BEILSTEIN JOURNAL OF NANOTECHNOLOGY

Atomic scale interface design and characterisation

Edited by Carla Bittencourt, Chris Ewels and Arkady K. Krasheninnikov

Generated on 28 February 2026, 14:19

Imprint

Beilstein Journal of Nanotechnology
www.bjnano.org
ISSN 2190-4286
Email: journals-support@beilstein-institut.de

The *Beilstein Journal of Nanotechnology* is published by the Beilstein-Institut zur Förderung der Chemischen Wissenschaften.

Beilstein-Institut zur Förderung der Chemischen Wissenschaften
Trakehner Straße 7–9
60487 Frankfurt am Main
Germany
www.beilstein-institut.de

The copyright to this document as a whole, which is published in the *Beilstein Journal of Nanotechnology*, is held by the Beilstein-Institut zur Förderung der Chemischen Wissenschaften. The copyright to the individual articles in this document is held by the respective authors, subject to a Creative Commons Attribution license.

BEILSTEIN JOURNAL OF NANOTECHNOLOGY

Atomic scale interface design and characterisation

Carla Bittencourt*[1], Chris Ewels*[2] and Arkady V. Krasheninnikov*[3,4]

Editorial

Open Access

Address:
[1]Chimie des Interactions Plasma-Surface (ChIPS), CIRMAP, Research Institute for Materials Science and Engineering, University of Mons, 7000 Mons, Belgium, [2]Institute des Matériaux Jean Rouxel, IMN, Université de Nantes, CNRS UMR6502 Nantes, France, [3]Department of Applied Physics, Aalto University, Finland and [4]Institute of Ion Beam Physics and Materials Research, Helmholtz Zentrum Dresden-Rossendorf, Germany

Email:
Carla Bittencourt* - carla.bittencourt@umons.ac.be; Chris Ewels* - chris.ewels@cnrs-imn.fr; Arkady V. Krasheninnikov* - arkady.krasheninnikov@aalto.fi

* Corresponding author

Keywords:
carbon; first-principles simulations; interface; nanomaterials; nanoscale; oxides; spectromicroscopy

Beilstein J. Nanotechnol. **2015,** *6,* 1708–1711.
doi:10.3762/bjnano.6.174

Received: 29 June 2015
Accepted: 28 July 2015
Published: 10 August 2015

This article is part of the Thematic Series "Atomic scale interface design and characterisation".

Editor-in-Chief: T. Schimmel

© 2015 Bittencourt et al; licensee Beilstein-Institut.
License and terms: see end of document.

While many major strides have been made in the last three decades concerning the synthesis, characterisation and properties of individual nanoobjects, their technological uptake necessarily requires integration into devices. To achieve this, detailed characterization, design and control of the interface between nanoobjects and their environment is essential. Nanomaterials differ significantly from their bulk counterparts and one important aspect of this is their high surface to volume ratios. For this reason interface properties typically dominate the behavior of nanomaterials. As a consequence, one immediately faces the problem of designing and controlling surfaces and, in case of embedded or layered systems, interfaces on atomic scales.

Engineering of electrical contacts is required for nanostructure integration. The performance of electronic devices based on nanostructures is affected by a potential barrier at the metal–nanostructure contact, thus investigation of the metal–nanostructure interaction aiming at understanding the physics and chemistry of this interface is critical for the design of optimal devices [1-3]. Potential applications of nanostructures such as spintronics, or light absorption and emission devices require doping [4,5]. In this context, conventional bulk doping techniques must be adapted, given the large surface to volume ratio of nanostructures, surface segregation of dopant atoms is a severe drawback. Therefore detailed knowledge and control of the physical and chemical properties and processes occurring at the surface on a nanoscale are of crucial concern.

Nanostructured materials show a great application potential in the areas of nanoelectronics, catalysis, and light harvesting/energy storage, an excellent example being the capability of titanate nanoribbons to simultaneously harvest and store energy in photobatteries [6]. In such systems, the exact nature of the interface between different nanostructures is the decisive factor determining the solar harvesting efficiency. The optimal inte-

gration of nanostructured materials into larger scale devices and their diverse applications, both are often hindered by technological constraints arising from the lack of precise knowledge and control of the interface formation at the nanoscale. To date, the main obstacle for the scientific community was posed by the limits of some conventional characterization tools when applied at the nanoscale: Tools such as vibrational and electronic spectroscopy were typically macroscopic probes sampling areas in the range of square millimeters or square micrometers, at best. Hence, these techniques are inadequate for the characterization of nanoscale interfaces. The development of new experimental tools and the detailed understanding of their impact on the sample structure will therefore provide a substantial contribution to the design and optimization of novel devices [7].

Addressing design, control and characterization of nanoscale interfaces and the development of new tools to facilitate this is a vast area of research, requiring multidisciplinary collaboration between chemists, physicists, biologists and engineers across a wide range of disciplines. It is clearly a very broad topic for a single Thematic Series, and for this reason the current volume has been jointly edited by Carla Bittencourt, Chris Ewels and Arkady Krasheninnikov, with the reviews covering key areas of advanced synthesis methods, controlled functionalization and post-processing routes, developments in nanoscale characterization tools as well as theoretical modeling of structure and dynamics, and electronic properties. Finally some reviews cover key examples of successful nanomaterial integration.

Recent drives to improve and refine nanomaterial synthesis routes have adopted different approaches. The increasingly important role played by organic chemists in the field of nanocarbon design has led to new families of atomically designed materials such as cycloparaphenylenes, the ultimate "short nanotubes" [8]. At slightly larger scales, atomic layer deposition allows the design of atomic-scale hybrid materials such as TiO_2 deposition on carbon nanotubes [9]. Post-growth engineering of nanomaterials is also considerably refined, for example new understandings of diffusion processes during growth and oxidation allow for the engineering of hollow nanostructures using the Kirkendall effect [10], the filling of carbon nanotubes and nanofibers to tune their properties [11], or the use of electron irradiation to produce carbon atom chains [12].

Graphene and related materials such as nanotubes, polycrystalline nanoparticles [13] and carbon onions [14] have seen significant progress in preparing samples of reasonable size and quality [15] and form a worldwide actively pursued field of research on understanding and modifying their properties [16,17]. Besides dealing with fundamental questions, contributions emphasize possible applications of the remarkable physical and chemical properties of this class of materials such as thermoelectrics [18], plasmonics [19] and gas sensing [20]. In the future, spatial control of doping may allow for surface modifications in a laterally controlled way. Controlled functionalization will allow for optimal integration of nanostructures in electronic devices but also for their use in biological applications. It is important to mention the use of carbon nanomaterials in neuroengineering, where these nanomaterials have been used as substrates for neural growth, as drug delivery systems and as electrodes for both extra cellular recordings and for in vivo recordings [21]. Finally, although carbon is often seen as the "poster child" of nanomaterials, it is important not to forget the expanding range of applications for related nanomaterials such as boron nitride nanotubes [22] and silicon and germanium nanocrystals [23].

Recent developments in X-rays collimation optics triggered the interest in synchrotron radiation-based techniques for the study of nanostructures. In this context, X-ray microscopy has shown to be a powerful tool for chemical analysis of radiation-sensitive nanomaterial [7]. Combining the chemical and magnetic information provided by XPEEM with the structural sensitivity of LEEM has created a complete characterization tool of material properties at the nanometer length scale. This can be complimentary with conventional XPS, whose peak assignments for identifying heteroatom doping behavior in nanocarbons are reviewed by Susi et al. [24].

Another important characterization tool for nanomaterials has emerged from the introduction of aberration correctors in transmission electron microscopes (TEM), which brings both increased spatial resolution and energy resolution allowing imaging at low voltage, crucial for nanomaterials which are sensitive to electron irradiation. Currently, the atomic structure of different nanomaterials can be revealed with a resolution of better than 0.1 nm, in addition to elemental analysis [25].

The analysis of experimental results can significantly profit from the comparison of the images to the results of first-principles calculations. Similarly, for the precise interpretation of experimental scanning tunneling microscopy (STM) and atomic force microscopy (AFM) images, the microscopy knowledge about the local electronic structure of the system is extremely important. Full understanding of the electronic structure and properties of a large number of solids can be credited to first principles simulations, and more specifically density-functional theory (DFT) approaches. In addition, using DFT-based molecular dynamics, the manipulation of nanostructures by SPM tools and the changes made to the system by the characterization tools, e.g., the production of defects under electron irradiation and their evolution over time, can be simulated.

An impressive example of how STM experiments and DFT calculations together can unravel the atomic structure of the material is given in the article by J. A. Lawlor and M. S. Ferreira [26] focused on the identification of dopant impurities in graphene. Synergy effects of TEM and DFT are illustrated in the article by M. Quintana et al. [15], by the examples of imaging molecules and clusters on graphene. Another example is the article by Barmparis et al. on Wulff construction [27], based on first-principle calculations. This method has become quite popular as a tool of choice for the simulation of nanoparticle shapes. In the past decade, many TEM and catalysis experiments were simulated using this multi-scale approach with remarkable success.

First-principle calculations have also provided insight into the electronic properties of low-dimensional materials, for example graphene doping by surface adsorbates [28], and nanosystems structured from misfit layer compounds [29]. Planar and bended misfit structures, such as tubes, scrolls or nanoparticles, with intriguing electronic and magnetic characteristics have been synthesized, while calculations explained their electronic structure and properties.

An important remark is related to the background of all contributions of the present volume. They represent a cross-section of research subjects from members of the European COST Action NMP 0901 "NanoTP", which ran from 2009 to 2014. The project brought together chemists, physicists, biologists and engineers across a wide range of disciplines, to share their common interest and pool their skills in the field of atomic-scale interface design. At its end the project had nearly 300 members drawn from 26 countries COST countries, along with members in Russia, Australia, Armenia, Belarus, Mexico and Canada. The network allowed researchers to mutually visit laboratories, organise training schools and workshops on diverse subjects including new spectroscopy and microscopy tools, latest developments in atomic scale simulations, and nanocarbon design and application. It helped to launch the ongoing "GraphITA" graphene conference series [30], and produced videos on YouTube explaining graphene and related science for the general public [31,32].

Within its broad scientific and technical objective, secondary objectives were identified including synthesis of novel nanostructures, engineering of metal-nanostructures contacts, development of new tools for characterization and manipulation nanostructures, atomic-scale quantum chemical modelling, and integration in potential devices. All of these are reflected in the 26 reviews presented here. They appropriately demonstrate the richness and diversity within the NanoTP Action, as well the active participation and enthusiasm of the project members which made the project such a success. This collection of articles is a fitting conclusion to the project, and we hope the collection will also serve to stimulate amongst its readers the most important motivation of all: scientific curiosity.

Last but not least, we would like to thank the Production Team of the Beilstein-Institut for their enthusiasm, encouragement, patience and engaged editorial support.

Carla Bittencourt, Chris Ewels and Arkady V. Krasheninnikov

Mons, Nantes and Helsinki, June 2015

References

1. Tersoff, J. *Nature* **2003,** *424,* 622–623. doi:10.1038/424622a
2. Liu, W.; Hierold, C.; Haluska, M. *Beilstein J. Nanotechnol.* **2014,** *5,* 2202–2215. doi:10.3762/bjnano.5.229
3. Gopal, V.; Radmilovic, V. R.; Daraio, C.; Jin, S.; Yang, P.; Stach, E. A. *Nano Lett.* **2004,** *4,* 2059–2063. doi:10.1021/nl0492133
4. Yu, J. H.; Liu, X.; Kweon, K. E.; Joo, J.; Park, J.; Ko, K.-T.; Lee, D. W.; Shen, S.; Tivakornsasithorn, K.; Son, J. S.; Park, J.-H.; Kim, Y.-W.; Hwang, G. S.; Dobrowolska, M.; Furdyna, J. K.; Hyeon, T. *Nat. Mater.* **2010,** *9,* 47–53. doi:10.1038/nmat2572
5. Djurišić, A. B.; Ng, A. M. C.; Chen, X. Y. *Prog. Quantum Electron.* **2010,** *34,* 191–259. doi:10.1016/j.pquantelec.2010.04.001
6. Rutar, M.; Rozman, N.; Pregelj, M.; Bittencourt, C.; Cerc Korošec, R.; Sever Škapin, A.; Mrzel, A.; Škapin, S. D.; Umek, P. *Beilstein J. Nanotechnol.* **2015,** *6,* 831–844. doi:10.3762/bjnano.6.86
7. Guttmann, P.; Bittencourt, C. *Beilstein J. Nanotechnol.* **2015,** *6,* 595–604. doi:10.3762/bjnano.6.61
8. Tran-Van, A.-F.; Wegner, H. A. *Beilstein J. Nanotechnol.* **2014,** *5,* 1320–1333. doi:10.3762/bjnano.5.145
9. Zhang, Y.; Utke, I.; Michler, J.; Ilari, G.; Rossell, M. D.; Erni, R. *Beilstein J. Nanotechnol.* **2014,** *5,* 946–955. doi:10.3762/bjnano.5.108
10. El Mel, A.-A.; Nakamura, R.; Bittencourt, C. *Beilstein J. Nanotechnol.* **2015,** *6,* 1348–1361. doi:10.3762/bjnano.6.139
11. Gately, R. D.; in het Panhuis, M. *Beilstein J. Nanotechnol.* **2015,** *6,* 508–516. doi:10.3762/bjnano.6.53
12. Banhart, F. *Beilstein J. Nanotechnol.* **2015,** *6,* 559–569. doi:10.3762/bjnano.6.58
13. Kempiński, W.; Łoś, S.; Kempiński, M.; Markowski, D. *Beilstein J. Nanotechnol.* **2014,** *5,* 1760–1766. doi:10.3762/bjnano.5.186
14. Bartelmess, J.; Giordani, S. *Beilstein J. Nanotechnol.* **2014,** *5,* 1980–1998. doi:10.3762/bjnano.5.207
15. Quintana, M.; Tapia, J. I.; Prato, M. *Beilstein J. Nanotechnol.* **2014,** *5,* 2328–2338. doi:10.3762/bjnano.5.242
16. Di Crescenzo, A.; Ettorre, V.; Fontana, A. *Beilstein J. Nanotechnol.* **2014,** *5,* 1675–1690. doi:10.3762/bjnano.5.178
17. Stergiou, A.; Pagona, G.; Tagmatarchis, N. *Beilstein J. Nanotechnol.* **2014,** *5,* 1580–1589. doi:10.3762/bjnano.5.170
18. Pennelli, G. *Beilstein J. Nanotechnol.* **2014,** *5,* 1268–1284. doi:10.3762/bjnano.5.141
19. Grochowska, K.; Siuzdak, K.; Atanasov, P. A.; Bittencourt, C.; Dikovska, A.; Nedyalkov, N. N.; Śliwiński, G. *Beilstein J. Nanotechnol.* **2014,** *5,* 2102–2112. doi:10.3762/bjnano.5.219

20. Chikkadi, K.; Muoth, M.; Roman, C.; Haluska, M.; Hierold, C. *Beilstein J. Nanotechnol.* **2014,** *5,* 2179–2191. doi:10.3762/bjnano.5.227
21. Monaco, A. M.; Giugliano, M. *Beilstein J. Nanotechnol.* **2014,** *5,* 1849–1863. doi:10.3762/bjnano.5.196
22. Kalay, S.; Yilmaz, Z.; Sen, O.; Emanet, M.; Kazanc, E.; Çulha, M. *Beilstein J. Nanotechnol.* **2015,** *6,* 84–102. doi:10.3762/bjnano.6.9
23. Capan, I.; Carvalho, A.; Coutinho, J. *Beilstein J. Nanotechnol.* **2014,** *5,* 1787–1794. doi:10.3762/bjnano.5.189
24. Susi, T.; Pichler, T.; Ayala, P. *Beilstein J. Nanotechnol.* **2015,** *6,* 177–192. doi:10.3762/bjnano.6.17
25. Ke, X.; Bittencourt, C.; van Tendeloo, G. *Beilstein J. Nanotechnol.* **2015,** *5,* 1541–1557. doi:10.3762/bjnano.6.158
26. Lawlor, J. A.; Ferreira, M. S. *Beilstein J. Nanotechnol.* **2014,** *5,* 1210–1217. doi:10.3762/bjnano.5.133
27. Barmparis, G. D.; Lodziana, Z.; Lopez, N.; Remediakis, I. N. *Beilstein J. Nanotechnol.* **2015,** *6,* 361–368. doi:10.3762/bjnano.6.35
28. Pinto, H.; Markevich, A. *Beilstein J. Nanotechnol.* **2014,** *5,* 1842–1848. doi:10.3762/bjnano.5.195
29. Lorenz, T.; Joswig, J.-O.; Seifert, G. *Beilstein J. Nanotechnol.* **2014,** *5,* 2171–2178. doi:10.3762/bjnano.5.226
30. GraphITA 2015 | NANOfutures. http://www.nanofutures.eu/event/graphita-2015 (accessed June 28, 2015).
31. What is Graphene? – YouTube. https://www.youtube.com/watch?v=EX8ClPVkD1g (accessed June 28, 2015).
32. The Future for Graphene? – YouTube. https://www.youtube.com/watch?v=-zpbIOpZ14Y (accessed June 28, 2015).

License and Terms

This is an Open Access article under the terms of the Creative Commons Attribution License (http://creativecommons.org/licenses/by/2.0), which permits unrestricted use, distribution, and reproduction in any medium, provided the original work is properly cited.

The license is subject to the *Beilstein Journal of Nanotechnology* terms and conditions: (http://www.beilstein-journals.org/bjnano)

The definitive version of this article is the electronic one which can be found at: doi:10.3762/bjnano.6.174

Beilstein Journal of Nanotechnology

Growth and characterization of CNT–TiO_2 heterostructures

Yucheng Zhang*[1], Ivo Utke[2], Johann Michler[2], Gabriele Ilari[1], Marta D. Rossell[1] and Rolf Erni[1]

Review

Open Access

Address:
[1]Electron Microscopy Center, EMPA, Swiss Federal Laboratories for Materials Science and Technology, Überlandstrasse 129, CH-8600 Dübendorf, Switzerland and [2]Laboratory of Mechanics of Materials and Nanostructure, EMPA, Swiss Federal Laboratories for Materials Science and Technology, Feuerwerkstrasse 39, CH-3602 Thun, Switzerland

Email:
Yucheng Zhang* - yucheng.zhang@empa.ch

* Corresponding author

Keywords:
atomic layer deposition (ALD); carbon nanotubes; electron energy loss spectroscopy (EELS); interface; titanium dioxide (TiO2); transmission electron microscopy (TEM)

Beilstein J. Nanotechnol. **2014,** *5,* 946–955.
doi:10.3762/bjnano.5.108

Received: 27 March 2014
Accepted: 12 June 2014
Published: 02 July 2014

This article is part of the Thematic Series "Atomic scale interface design and characterisation: Experimental aspects and methods".

Guest Editor: C. Bittencourt

© 2014 Zhang et al; licensee Beilstein-Institut.
License and terms: see end of document.

Abstract

A thriving field in nanotechnology is to develop synergetic functions of nanomaterials by taking full advantages of unique properties of each component. In this context, combining TiO_2 nanocrystals and carbon nanotubes (CNTs) offers enhanced photosensitivity and improved photocatalytic efficiency, which is key to achieving sustainable energy and preventing environmental pollution. Hence, it has aroused a tremendous research interest. This report surveys recent research on the topic of synthesis and characterization of the CNT–TiO_2 interface. In particular, atomic layer deposition (ALD) offers a good control of the size, crystallinity and morphology of TiO_2 on CNTs. Analytical transmission electron microscopy (TEM) techniques such as electron energy loss spectroscopy (EELS) in scanning transmission mode provides structural, chemical and electronic information with an unprecedented spatial resolution and increasingly superior energy resolution, and hence is a necessary tool to characterize the CNT–TiO_2 interface, as well as other technologically relevant CNT–metal/metal oxide material systems.

Introduction

Since the discovery by Iijima in 1991, carbon nanotubes (CNTs) have always been on the research frontier due to their extraordinary properties [1-5]. Applications based on CNTs including high sensitivity sensors, next generation transistors and high efficiency solar cells have been proposed, and tremendous progress has been achieved. A particularly interesting

research area is to combine CNTs with other inorganic nanomaterials, i.e., metal and metal oxide nanoparticles, and to exploit unique properties of each component to realize a synergetic effect of the ensemble. For example, while it has been long discovered that TiO_2, a semiconductor that can be obtained cost-effectively and environmentally friendly, is a good candidate for electrochemical photocatalysis [6], recent research shows that its limited absorption of only the UV part of the sunlight spectrum can be extended to visible light when forming a nanocomposite with CNTs [7-9]. This can significantly increase the efficiency of electrochemical photocatalysis, and benefits largely in areas such as acquiring sustainable energy and preventing environmental pollution.

In this context, this paper reviews growth of metal and/or metal oxide particles on CNTs and the characterisation by using analytical transmission electron microscopy (TEM) techniques with a focus on the TiO_2–CNT material system. The mechanisms of efficiency enhancement for photocatalysis by using the ensemble are reviewed. Methods to fabricate nanocomposites consisting of CNTs and metal/metal oxides are surveyed. In particular, an atomic layer deposition (ALD) has recently been used to deposit TiO_2 nanoparticles on CNTs in a controllable fashion. Characterization of the interface will help to understand the mechanisms, and requires techniques capable of revealing structural details on a nanometer and atomic scale, for which electron energy loss spectroscopy (EELS) is a good candidate. The physical principle of EELS is explained, and a survey of applying EELS to characterization of several technologically important nanomaterials including CNTs and metal/metal oxide nanoparticles is presented. The challenges of studying the TiO_2–CNT interface using EELS are also discussed.

Review

Photocatalysis using TiO_2–CNT

Among all the nanocomposites consisting of CNTs and metal/metal oxides, CNT–TiO_2 has attracted most research interest because of its unique properties and potential applications such as photocatalysis, especially since the recent discovery that with the addition of CNTs, the light absorption of TiO_2 can be extended to the visible-light region [8-14]. This can significantly increase the photocatalytic efficiency. In literature several photocatalysis enhancement mechanisms based on TiO_2–CNT have been proposed, as illustrated in Figure 1. Hoffmann et al. have proposed that electrons and holes are generated in TiO_2 after absorption of photons, and CNTs act as an electron scavenger due to their high electron storage capacity and conductivity, so that excessive holes are generated on the surface of TiO_2 for redox reactions [12]. Alternatively, Wang et al. propose that electrons and holes are generated in the semiconducting CNTs, which act as a sensitizer [9]. The electrons

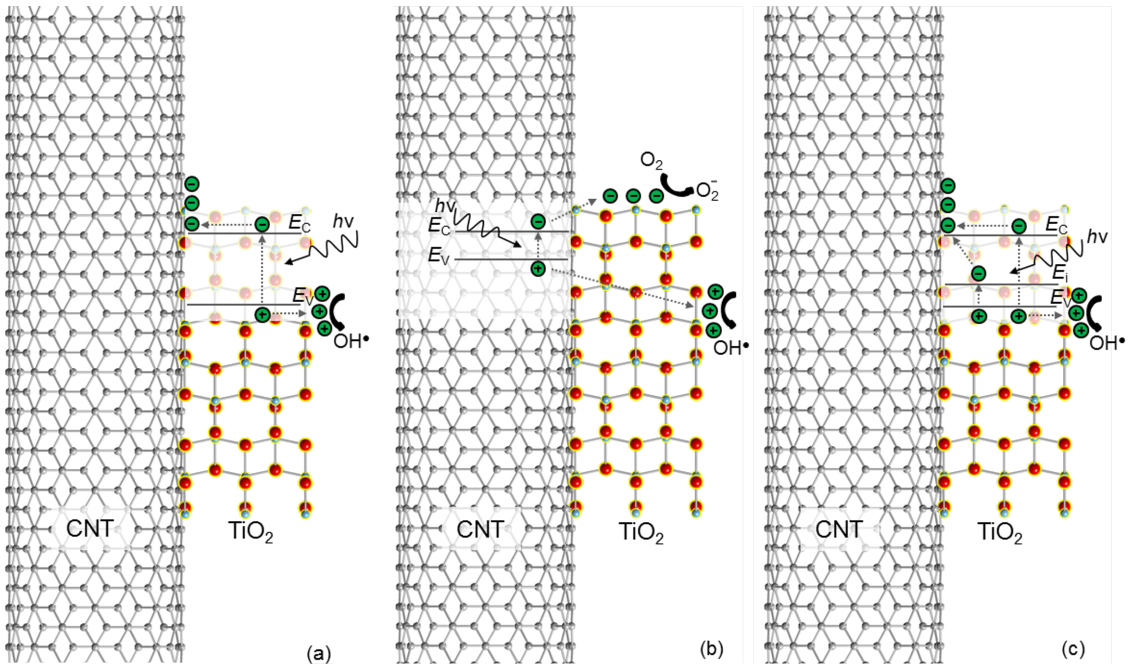

Figure 1: Efficiency enhancement mechanisms for photocatalysis using CNT–TiO_2 nanocomposites. (a) CNT scavenges electrons generated in TiO_2, resulting in excessive holes on the surface for redox actions. (b) CNT acts as a photosensitizer and injects electrons and holes into TiO_2 for redox actions. (c) CNT introduces energy states in the band gap of TiO_2 which can convert long wavelength photons to electrons and holes. Adapted from [18]. Copyright (2009) WILEY-VCH Verlag GmbH & Co. KGaA, Weinheim.

are injected into the conduction band of TiO_2 to form superoxide radicals and the holes into the valence band of TiO_2 to form hydroxyl radicals. The third mechanism was proposed by Pyrgiotakis [13], in which the C–O–Ti bond introduces energy states in the band gap of TiO_2, and is attributed to the extended absorption of longer wavelength light. In addition, they also found that the electronic structure of CNTs may have a bigger effect on the photocatalytic performance than the chemical bond between CNTs and TiO_2, since the arc-discharge-synthesized CNTs show a dramatically higher photocatalytic dye degradation rate than the CVD-synthesized CNTs, which is attributed to the smaller number of defects in the multi-wall (MW) tubes of the former. In reality, there are probably more than one mechanism acting in the photocatalysis. It is, however, crucial to investigate the interface so as to understand the dominant mechanism. A fundamental understanding of the mechanisms can also benefit other applications such as photoelectrochemical cells [15], sensors [16] and batteries [17] where the synergetic effect of the ensemble can be fully exploited.

It is therefore of paramount importance to achieve CNT–TiO_2 in a controllable way and further characterize the interface. Fundamental questions need to be answered, such as how TiO_2 nucleates and grows on CNTs, and what bonding is formed at the interface. Growth methods with a nanoscale precision are required to fabricate the ensemble. Characterization methods that can provide structural, chemical and electronic information on a nanometer or atomic scale are sought to investigate the interface. Some of the recent progress achieved in these areas is reviewed here.

ALD growth of CNT–TiO_2

Many methods have been developed to fabricate CNT–metal/metal oxide nanocomposites. For CNT–TiO_2, the methods that are mostly adopted are sol–gel and hydrothermal deposition. A good summary of the synthesis methods can be found in the review by Leary [19]. Recently, we have adopted the atomic layer deposition (ALD) technique to deposit TiO_2 on CVD-grown MW-CNTs. ALD relies on self-limiting surface reactions (dissociative chemisorption) of gases which are alternately introduced into and purged out of the reaction chamber. The surface reaction will establish a chemical bond of the precursor molecule with the substrate through the reaction of an organic ligand to a volatile compound. The remaining organic ligands still bound to the metal atom prevent further chemisorption. This self-limitation has two important consequences which make ALD very attractive: a) The thickness of deposited material will be limited to a monolayer at maximum, i.e., there is atomistic control of the thickness, and b) ultra-high aspect ratio structures can be deposited conformally as one can give enough time for the molecules to diffuse into the porous volume without clogging the surface. In order to continue the process the organometallic precursor gas needs to be purged and a second gas, the reactant will be introduced and reacting in a self-limiting manner with the remaining organic ligands. As a result of this full ALD cycle, the ligands react to volatile compounds and the reacted bonds constitute the reaction sites for the next ALD cycle starting again with the organometallic precursor. A schematic illustration of ALD is shown in Figure 2. For titanium isopropoxide $Ti(OCH(CH_3)_2)_4$ (TTIP) and H_2O the self-limiting surface reactions in Equation 1 and

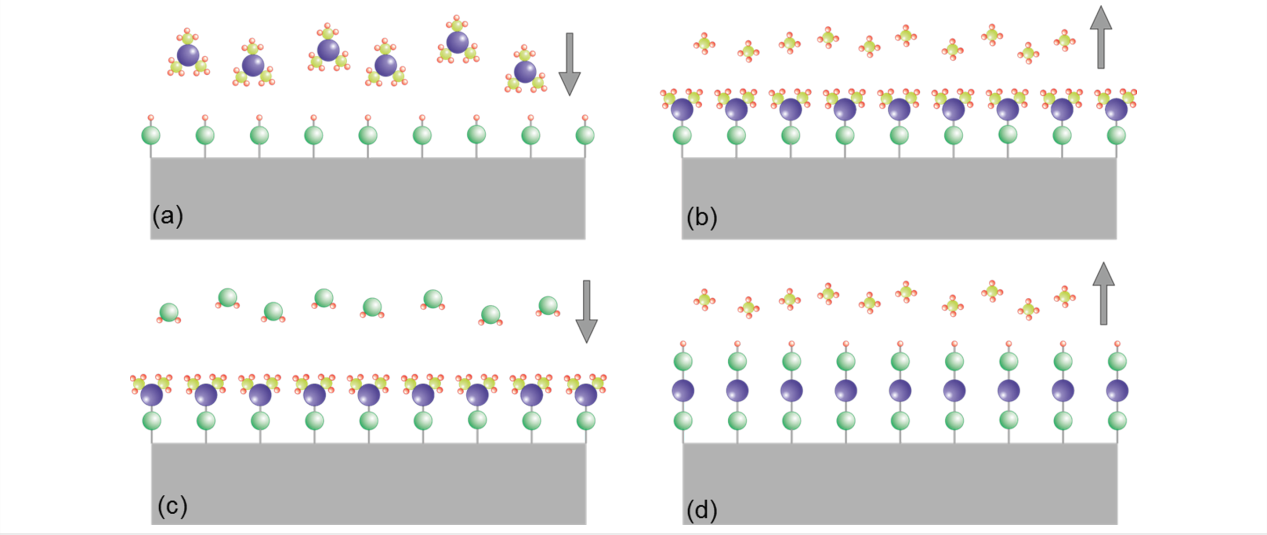

Figure 2: A schematic illustration of one cycle in ALD: (a) The first precursor flows into the chamber and reacts on the active sites of the substrate by partially losing ligands. (b) One mono-layer of reactant is formed and the chamber is purged to remove the remaining precursor and the intermediate product. (c) The second precursor is then introduced into the chamber to react with the remaining ligands and to form the desired compound molecule. (d) One cycle is complete when all of the ligands of the first precursor are consumed and one mono-layer of the compound is formed. The chamber is purged again for next cycle.

Equation 2 were proposed. TTIP/H_2O ALD results in amorphous TiO_2 for substrate temperatures between 100 and 150 °C while for substrate temperatures higher than 180 °C the crystalline anatase phase is obtained.

$$(-OH)_2 + Ti(OCH(CH_3)_2)_4 \rightarrow (-O)_2Ti(OCH(CH_3)_2)_2 + 2(CH_3)_2CHOH\uparrow \quad (1)$$

$$(-O)_2Ti(O(CH_3)_2)_2 + 2H_2O \rightarrow (-O)_2Ti(OH)_2 + 2(CH_3)_2CHOH\uparrow \quad (2)$$

Generally, the organo-metallic precursor molecules for metal oxide ALD, e.g., trimethylaluminium for Al_2O_3, titanium tetraisopropoxide for TiO_2, diethylzinc for ZnO, or tetrakis(ethylmethylamido)hafnium for HfO_2, need surfaces that are terminated with a functional group, which would allow for their dissociative chemisorption reaction. Hydroxy-(OH)-group terminated surfaces prevailing on many metaloxide surfaces are ideally suited [20,21]. However, single-wall (SW) carbon nanotubes, graphene, and a few noble metals do not possess naturally such a functional-group termination but rather inert surfaces and ALD nucleation is prohibited [22]. Hydrogen-terminated surfaces are also non-reactive and are used to render the ALD process selective in self-assembled monolayer molecules [23]. Only surface defects on CNTs and graphene allow for the chemisorption of metal-organic precursor molecules.

Basically, surface functional groups need to be generated on pristine single-wall CNTs or graphene by specific treatments which attack the surface and introduce defects [24]. The treatments can be divided into covalent and non-covalent functionalization. An ozone treatment, as an example for covalent functionalization, is simple to integrate into the ALD process and was shown to result in conformal Al_2O_3 coatings on graphene when using trimethylaluminium and ozone half-cycles, while the use of water resulted in inhomogeneous films [25]. This is due to the generation of oxygenated functional groups on the CNT surface. Also treatments of CNTs prior to ALD by using acids such as H_3PO_4 (together with a chromic acid) and HNO_3 triggered conformal growth of ruthenium [26] and SiO_2, TiO_2, and Al_2O_3 (after thermal annealing) [27]. Such surface defects seem to be naturally present on multi-wall CNTs with a given surface density. They are responsible for local metal oxide nucleation. The density of oxygenated defects can be increased by oxygen plasma treatment. A conformal film is obtained when the nanocrystals coalesce due to lateral growth after approximately 50–100 cycles (depending on the defect density) [28]. Similar results were obtained with Al_2O_3 coatings by using trimethylaluminium and water ALD half-cycles [29] and tetrakis(ethylmethylamido)hafnium with water [30]. In contrast, thin conformal metal oxide ALD films can be easily obtained on organic polymers like polystyrene. Conformal 20 nm thin ZnO coatings were deposited using diethylzinc half-cycles alternated with water on large area polystyrene bead arrays [31]. After removing the polystyrene, a transparent, electrically conductive, hollow sphere array was obtained on top of which an urchin-inspired nanobuilding block design of a solar cell with n-type ZnO nanowires could be realized by using electrochemical deposition [32].

Non-covalent surface functionalization leaves the pristine CNTs sp^2 structure and carbon atom conjugation intact. Examples include in-situ NO_2 physisorption which permitted the uniform growth of Al_2O_3 on SW-CNT [33], MW-CNT [34] and graphene [35], as well as the physisorption of ethanol and sodium dodecylsulfate on CNTs, which also permitted the ALD of Al_2O_3 [36]. So far only amorphous TiO_2 was deposited by ALD on graphene and CNTs by using an ALD interlayer of Al_2O_3 [37].

By using this method, TiO_2 of various crystallinity, size and morphology on MW-CNTs has been recently obtained in a controllable way. An example is shown in Figure 3, in which the deposition of TiO_2 for various numbers of cycles at 220 °C is presented. The morphology changes from small nuclei with diameters smaller than 2 nm after 20 cycles, to clustering of crystalline particles of about 5 nm after 200 cycles, until the formation of a coalesced and conformal layer of an anatase phase after 750 cycles. This provides an ideal scenario to study nucleation and growth of TiO_2 on CNTs, and especially assisted with the powerful TEM techniques, to investigate the interface that is crucial to applications based on the ensemble. In addition to the growth parameters in ALD, such as temperature and number of cycles, pre-treatment of the surface of the CNTs by using O_2 plasma is found to have an effect on the nucleation and morphology of TiO_2. The nuclei density is significantly increased after the surface treatment, probably due to the fact that the plasma introduces more defect sites on the tube-walls, which facilitate the nucleation. A similar effect has been previously reported when depositing various metals such as Ni, Cu, and Pt on MW-CNTs pre-treated with O_2 plasma [38,39].

Analytical-TEM characterization of functional nanomaterials

To fundamentally understand the interface between CNTs and metal/metal oxides on the nanometer or even on the atomic level, TEM plays an irreplaceable role due to its high spatial resolution. With the development of spherical aberration correctors, atomic-resolution imaging at a sub-0.5 Å level has already been demonstrated [40]. On the other hand, analytical TEM

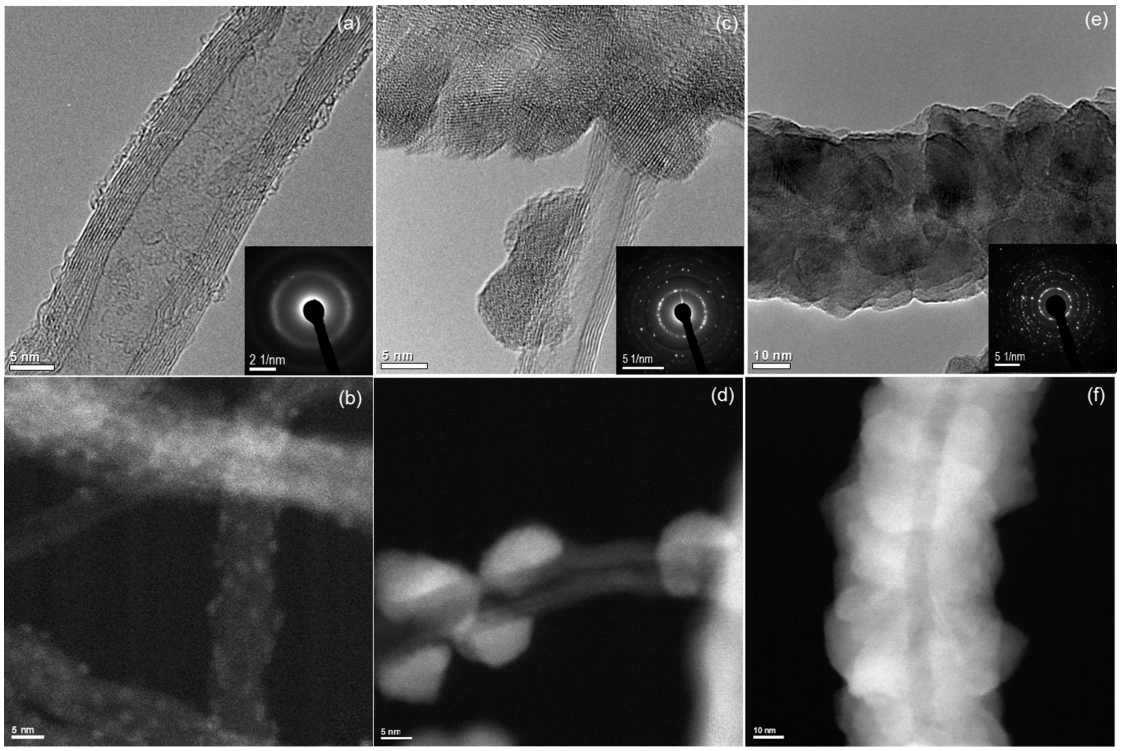

Figure 3: Micrographs of TiO_2 deposited on MW-CNT by using ALD with different number of cycles to control the particle size. (a), (c) and (e) are the high-resolution TEM images after 20, 200 and 750 cycles, respectively. The inset shows selected area diffraction pattern (SADP). (b), (d) and (f) are the respective STEM-HAADF images providing a higher contrast between the TiO_2 particles and the MW-CNTs.

provides chemical and electronic information about nanomaterials with an increasingly improved energy resolution. One powerful analytical TEM technique is electron energy loss spectroscopy (EELS). It detects electrons that lose a certain amount of energy due to inelastic scattering processes inside the specimen. Depending on the physical nature of the inelastic scattering processes, the EELS spectrum can be divided into two regions: the low-loss region, in which the energy loss, ΔE, is typically less than 50 eV, and the core-loss region, in which ΔE is above 50 eV. The physical principles of the inelastic scattering processes in EELS are schematically illustrated in Figure 4.

The low-loss region reflects a collective excitation of electrons in the conduction band, known as plasmons, as well as single electron excitations in the outer shells, i.e., excitations from the valence band to the conduction band. Hence, the low-loss signal contains information about the band structure of the specimen, and has been used to determine the band gaps of semiconductors [41]. Based on a dielectric model, the dielectric function can be extracted from the low-loss region by using a Kramers–Kronig analysis and its energy dependence can be measured at wavelengths beyond optical methods. However, the low-loss signals are complicated by other inelastic processes such as surface plasmons and retardation loss due to the Čerenkov emission, such that simulations based on a first-principle calculation is difficult [42]. Additionally, the spatial resolution of the low-loss is limited by the delocalization of the scattering processes, and it is yet to measure the low-loss signals on an atomic level.

The core-loss region contains the electrons that lose energy by exciting the core-shell electrons in the specimen. Because the energy levels in the core-shells are unique for every element, the core-loss signals can be used as a fingerprint of the elements present in the specimen, with a much higher energy resolution than energy dispersive X-ray (EDX) analysis. The core-shell excitation process is localized around the atoms, and hence atomic-resolution chemical mappings can be achieved by using EELS core-loss signals combined with a sub-nanometer sized electron probe [43-47]. For example, by using EELS at a low acceleration voltage of 60 kV to avoid beam damage, Suenaga et al. have been able to detect single calcium atoms inside the metallofullerence-doped single-wall nanotubes [46]. Nakagawa et al. have applied the atomic-scale EELS to the study of the (001) $LaAlO_3$ and $SrTiO_3$ interfaces, and observed an asymmetry between ionically and electronically compensated interfaces, which explains why some semiconductor interfaces

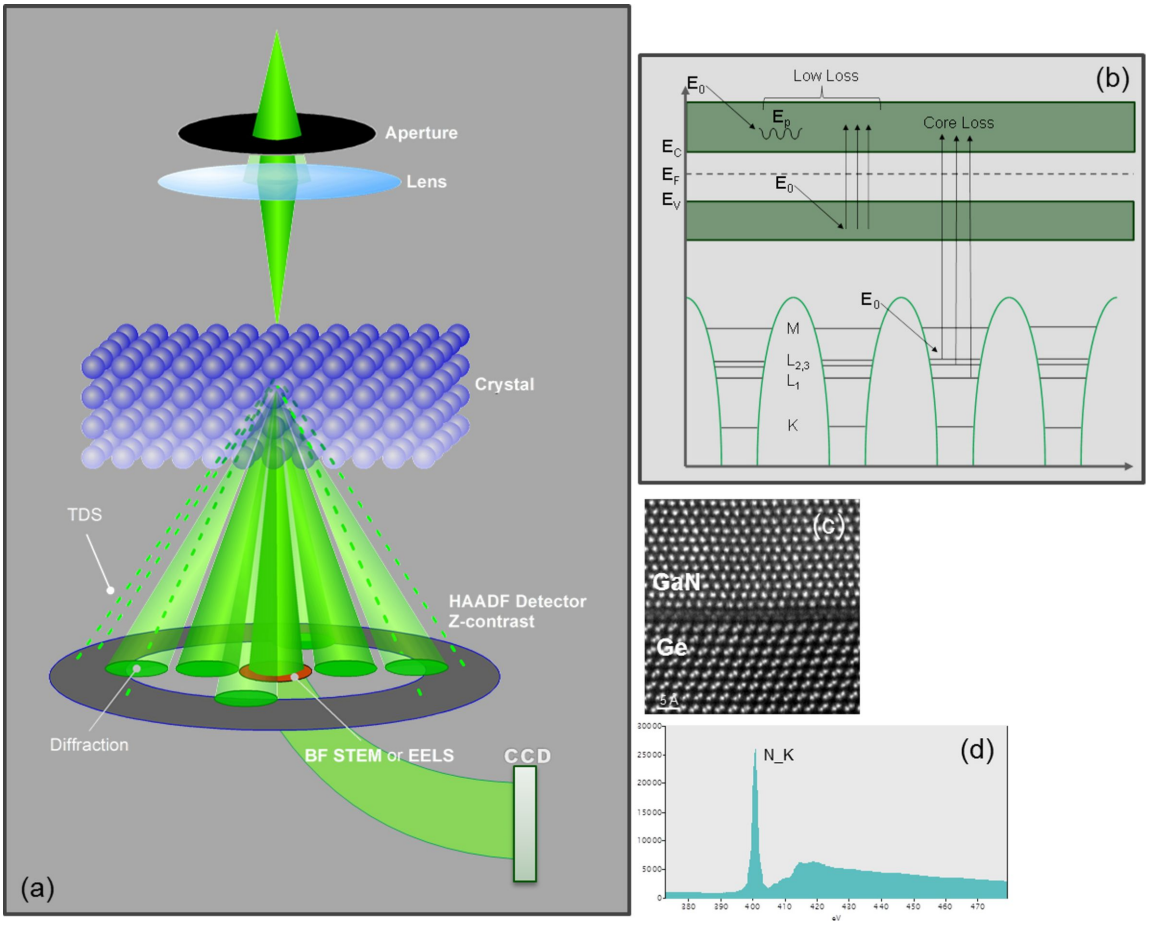

Figure 4: A schematic illustration of the principle in STEM-EELS: (a) the microscope configuration in the STEM mode; (b) the inelastic scattering processes in the TEM sample contributing to the low-loss and the core-loss EELS signals; (c) an atomic-resolution STEM-HAADF image of a GaN–Ge interface; (d) a EELS core-loss spectrum showing the N_K edge of gaseous N_2.

cannot be atomically sharp [48]. Recently, Rossell et al. [49] have adopted STEM-EELS combined with multivariate statistical analysis (MSA) to map the distribution of Ba dopant atoms in $SrTiO_3$ nanoparticles, as shown in Figure 5. The results provide direct evidence for clustering of the Ba atoms in the nanoparticles, which may explain the presence of the polar

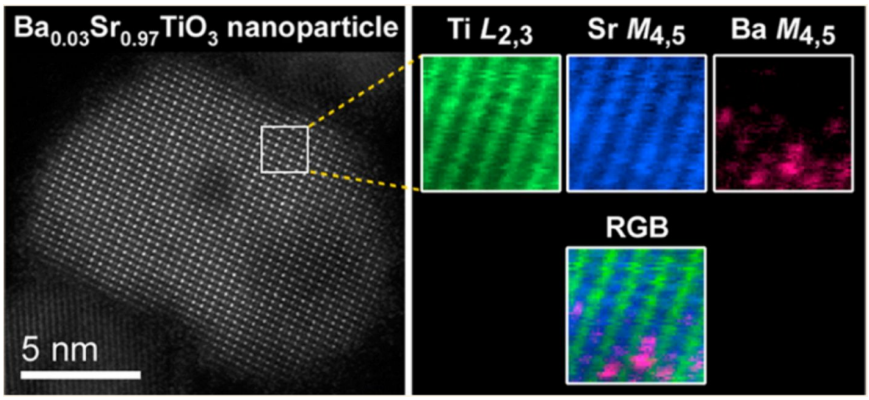

Figure 5: An atomic-resolution chemical mapping of Ba-doped $SrTiO_3$ nanoparticles: (a) the HAADF-STEM image of a Ba-doped STO nanoparticle along the [011] direction; (b) the simultaneous chemical mappings measuring the Ti_$L_{2,3}$, Sr_$M_{4,5}$, and Ba_$M_{4,5}$ edges, respectively, and the corresponding RGB map. Reprinted with permission from [49]. Copyright (2012) The American Chemical Society.

nanoregions in Ba:$SrTiO_3$. These results demonstrate the capability of EELS to characterize the interface of CNT–metal/metal oxides on the nanometer or the atomic level.

The electron loss near-edge fine structures (ELNES) in EELS provide additional information about the chemical and electronic environment of the ionized atoms. The spectrum region corresponds to the electrons with an energy loss within about 50 eV above the edge threshold. An example of ELNES at the N_K edge of N_2 is shown in Figure 4d. Within a certain approximation, the observed details represent a symmetry-projected density of unoccupied states above the Fermi level [50]. Hence, ELNES is very sensitive to the local atomic coordination and can be used to probe atomic bonding. The same element can have different ELNES signals if it is in different chemical states. Performed in the STEM mode, ELNES can provide the electronic information on a nanometer or atomic scale. It is an ideal technique to study CNTs and related nanomaterials. For example, by measuring the ratio of π* and σ* peaks at the C_K edge, the amount of sp^2 and sp^3 hybridizations can be quantified in amorphous carbon, which determines the physical properties [51,52]. Similarly, Muller et al. have used the ELNES signals to produce a map of sp^2 and sp^3 at the interface of diamond grown on Si/SiO_2 with a sub-nanometer spatial resolution, which helps to understand the nucleation of diamond [53]. Suenaga et al. have performed in-situ bending of SW-CNTs in TEM and observed a change in the C_K edge ELNES at kinks of the CNT bundles, indicating the change of the electronic structure with the deformation [54]. Theoretical calculations based on density functional theory (DFT) can be used to simulate the details in ELNES and to fundamentally predict the atomic and the electronic structure. Depending on the atomic potentials defined in the calculation, methods based on the band theory, the molecular orbitals or the multiple scattering are developed, either in the reciprocal space or in the real space, to simulate the ELNES of both crystalline and amorphous materials [50]. Titantah et al. performed DFT calculations of ELNES on CNTs, taking into consideration the effect of curvatures, the electron-beam orientation as well as the inclusion of the core hole [55]. Their calculation also predicted an energy shift of 5 eV in the σ* peak if the C–C bond length is increased to 1.7 Å, demonstrating the sensitivity of ELNES to the bond length [56]. Using EELS at a high energy resolution, Brydson et al. observed a difference in the ELNES of the $Ti_L_{2,3}$ and O_K edges between anatase and rutile TiO_2, which could be modelled using real-space multiple-scattering calculations [57].

With all the advancements in the analytical TEM techniques and their application to characterization of carbon-based nanomaterials and metal/metal oxides, it is now possible to study the interface of the nanocomposites formed of the two material systems on a nanometer or even atomic level, which is a determining factor for the nanodevices based on the ensemble. Recently, Ilari et al. have studied the interface between graphite and metals including Ni and Cu by using STEM-EELS, as well as between MW-CNTs and the metals, by using STEM-EELS with an electron probe down to sub-nanometer [58]. The interaction at the interface was found to be different for Ni and Cu, leading to different interfacial structures. The study helps to understand the behavior of metallic contacts on CNTs, a key step for electronic devices at a nanometer scale. Similarly, analytical TEM can also be used to study the interface between TiO_2 and CNTs. In particular, the $Ti_L_{2,3}$ and C_K edges in EELS contain important atomic and electronic information about the interface, which can shed light on the performance enhancement mechanisms in photocatalysis that is explained in the proceeding section. Particularly, with a high spatial resolution STEM-EELS can be used to probe the bonding at the interface between CNTs and the nanoparticle and, answer the question if any covalent bonds such as C–O or C–Ti are formed at the interface. Other analytical techniques such as X-ray photoelectron spectroscopy (XPS) [59] and Raman spectroscopy [60] can also provide information about the interfacial bonding, however on a much larger scale. The bonding information obtained using STEM-EELS on a nanometer or even on an atomic scale, when combined with first-principle calculation, can help to learn the atomic and electronic structure at the interface, which is crucial to understanding charge transfer and hence the working mechanisms of the applications including photocatalysis and photovoltaics based on the ensemble.

While analytical TEM, in particular EELS, is a powerful tool to study the interface between CNTs and metal/metal oxides, the task is quite challenging and several difficulties need to be overcome. The damage in the sample caused by the high energy electron can hinder acquisition of sufficient EELS signals. For example, as shown in Figure 6, it was found that the ALD-grown TiO_2 on MW-CNTs can be damaged only a few seconds after the beam is incident on the sample. The $Ti_L_{2,3}$ edge from the damaged TiO_2 shows a red-shift due to sputtering of oxygen atoms by the high energy electrons and the resulting change of the oxidation state [61]. The damage mechanism can however depend on the specific chemical environment in the sample. To avoid the damage, optimized experimental conditions are required, such as a lower acceleration voltage or a lower probe current density. This should be balanced with a reasonable acquisition time to minimize the carbon contamination that can also be an obstacle especially when studying carbon-based nanomaterials. In addition, it is more difficult to study interfaces consisting of CNTs than those in semiconductor thin films due to the curvature of the former. Especially for CNTs of small diameters, the signals at the interface may be embedded in those

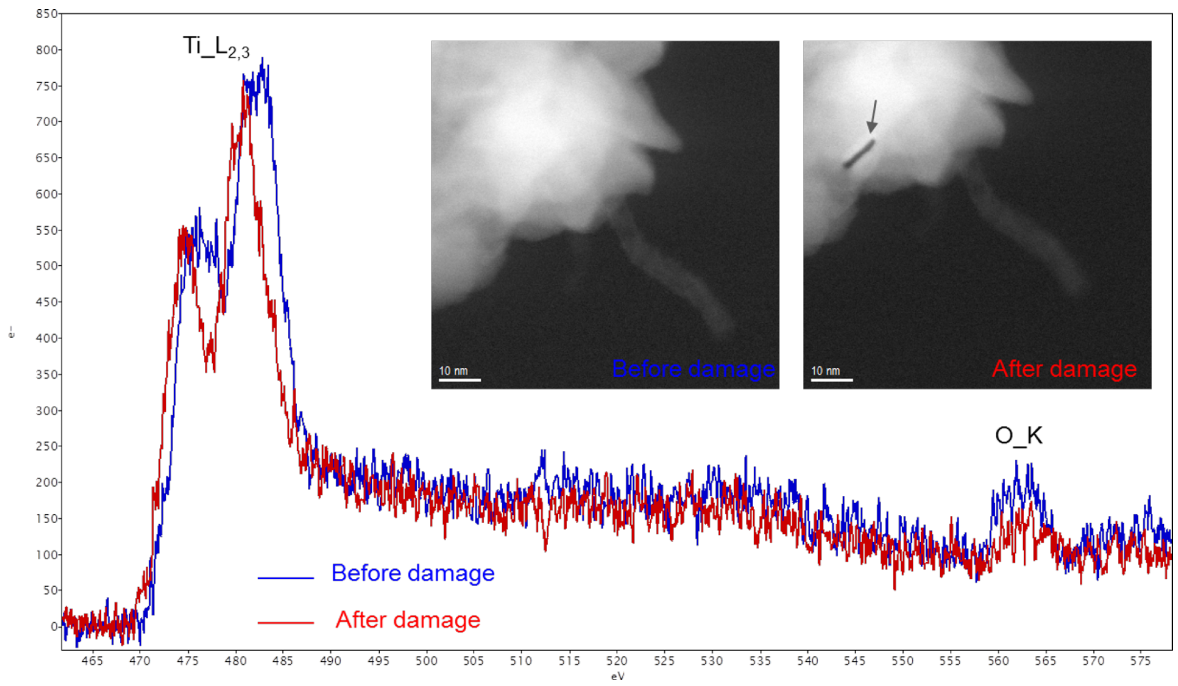

Figure 6: An example of electron beam damage during EELS acquisition. Note that there is a chemical shift in the Ti_$L_{2,3}$ edge after the damage. The damage is also visible in the STEM-HAADF image.

from the volume, due to 2D projection of TEM characterization While the length of CNTs does not affect the measurement, the radius can be an important factor, since the smaller the radius, the larger the curvature. The difficulty can be overcome as the spatial resolution and the chemical sensitivity of EELS is continuously increasing. Additionally, combined with electron tomography, it may be possible to use EELS to learn about the interfacial structure in 3D on a nanometer scale [62,63].

Conclusion

Nanocomposites combining CNTs and metal/metal oxides can achieve synergetic functions beyond the capability of each component. However, successful implementation relies on growing the ensemble with a good control and understanding the interface through advanced characterization. For the material system CNT–TiO_2, ALD offers the good control of growth conditions to obtain different morphology, size and crystallinity of TiO_2 on CNTs, which not only facilitates the study of nucleation mechanisms, but also is beneficial to various applications. As an important characterization tool for nanomaterials, EELS can be used to study the interface and gain fundamental knowledge of how CNTs interact with metal/metal oxides on a nanometer or atomic level. Difficulties exist when applying the growth and characterization methods, but can be overcome with the rapid advancement of both the techniques and the instrumentations.

Acknowledgements

The author Dr. Yucheng Zhang would like to acknowledge the Marie Curie Cofund scheme for the financial support.

References

1. Iijima, S. *Nature* **1991,** *354,* 56–58. doi:10.1038/354056a0
2. Collins, P. G.; Bradley, K.; Ishigami, M.; Zettl, A. *Science* **2000,** *287,* 1801–1804. doi:10.1126/science.287.5459.1801
3. Shulaker, M. M.; Hills, G.; Patil, N.; Wei, H.; Chen, H.-Y.; Wong, H.-S. P.; Mitra, S. *Nature* **2013,** *501,* 526–530. doi:10.1038/nature12502
4. Ajayan, P. M.; Lijima, S. *Nature* **1993,** *361,* 333–334. doi:10.1038/361333a0
5. De Volder, M. F. L.; Tawfick, S. H.; Baughman, R. H.; Hart, A. J. *Science* **2013,** *339,* 535–539. doi:10.1126/science.1222453
6. Fujishima, A.; Honda, K. *Nature* **1972,** *238,* 37–38. doi:10.1038/238037a0
7. Li, Q. Y.; Chen, L. A.; Lu, G. X. *J. Phys. Chem. C* **2007,** *111,* 11494–11499. doi:10.1021/jp072520n
8. Wang, Q.; Shang, J.; Song, H.; Zhu, T.; Ye, J. H.; Zhao, F. W.; Li, J.; He, S. J. *Mater. Sci. Semicond. Process.* **2013,** *16,* 480–484. doi:10.1016/j.mssp.2012.06.018
9. Wang, W. D.; Serp, P.; Kalck, P.; Faria, J. L. *J. Mol. Catal. A: Chem.* **2005,** *235,* 194–199. doi:10.1016/j.molcata.2005.02.027
10. Akhavan, O.; Abdolahad, M.; Abdi, Y.; Mohajerzadeh, S. *Carbon* **2009,** *47,* 3280–3287. doi:10.1016/j.carbon.2009.07.046
11. Guo, M. Y.; Liu, F. Z.; Leung, Y. H.; Ng, A. M. C.; Djurišić, A. B.; Chan, W. K. *Curr. Appl. Phys.* **2013,** *13,* 1280–1287. doi:10.1016/j.cap.2013.03.022

12. Hoffmann, M. R.; Martin, S. T.; Choi, W. Y.; Bahnemann, D. W. *Chem. Rev.* **1995,** *95,* 69–96. doi:10.1021/cr00033a004
13. Pyrgiotakis, G.; Lee, S.-H.; Sigmund, W. *MRS Online Proc. Libr.* **2005,** *876,* R5. doi:10.1557/PROC-876-R5.7
14. Ou, Y.; Lin, J. D.; Fang, S. M.; Liao, D. W. *Chem. Phys. Lett.* **2006,** *429,* 199–203. doi:10.1016/j.cplett.2006.08.024
15. Grätzel, M. *Nature* **2001,** *414,* 338–344. doi:10.1038/35104607
16. Santangelo, S.; Faggio, G.; Messina, G.; Fazio, E.; Neri, F.; Neri, G. *Sens. Actuators, B* **2013,** *178,* 473–484. doi:10.1016/j.snb.2013.01.005
17. Hyder, M. N.; Gallant, B. M.; Shah, N. J.; Shao-Horn, Y.; Hammond, P. T. *Nano Lett.* **2013,** *13,* 4610–4619. doi:10.1021/nl401387s
18. Woan, K.; Pyrgiotakis, G.; Sigmund, W. *Adv. Mater.* **2009,** *21,* 2233–2239. doi:10.1002/adma.200802738
19. Leary, R.; Westwood, A. *Carbon* **2011,** *49,* 741–772. doi:10.1016/j.carbon.2010.10.010
20. Puurunen, R. L. *J. Appl. Phys.* **2005,** *97,* 121301. doi:10.1063/1.1940727
21. George, S. M. *Chem. Rev.* **2010,** *110,* 111–131. doi:10.1021/cr900056b
22. Marichy, C.; Bechelany, M.; Pinna, N. *Adv. Mater.* **2012,** *24,* 1017–1032. doi:10.1002/adma.201104129
23. Lee, H.-B.-R.; Bent, S. F. Nanopatterning by Area-Selective Atomic Layer Deposition. In *Atomic Layer Deposition of Nanostructured Materials;* Pinna, N.; Knez, M., Eds.; Wiley-VCH Verlag GmbH & Co. KGaA: Weinheim, 2011; pp 193–225. doi:10.1002/9783527639915.ch9
24. Hirsch, A. *Angew. Chem., Int. Ed.* **2002,** *41,* 1853–1859. doi:10.1002/1521-3773(20020603)41:11<1853::AID-ANIE1853>3.0.CO;2-N
25. Speck, F.; Ostler, M.; Rohrl, J.; Emtsev, K. V.; Hundhausen, M.; Ley, L.; Seyller, T. *Phys. Status Solidi C* **2010,** *7,* 398–401. doi:10.1002/pssc.200982496
26. Min, Y. S.; Bae, E. J.; Jeong, K. S.; Cho, Y. J.; Lee, J. H.; Choi, W. B.; Park, G. S. *Adv. Mater.* **2003,** *15,* 1019–1022. doi:10.1002/adma.200304452
27. Gomathi, A.; Vivekchand, S. R. C.; Govindaraj, A.; Rao, C. N. R. *Adv. Mater.* **2005,** *17,* 2757–2761. doi:10.1002/adma.200500539
28. Yazdani, N.; Chawla, V.; Edwards, E.; Wood, V.; Park, H. G.; Utke, I. *Beilstein J. Nanotechnol.* **2014,** *5,* 234–244. doi:10.3762/bjnano.5.25
29. Herrmann, C. F.; Fabreguette, F. H.; Finch, D. S.; Geiss, R.; George, S. M. *Appl. Phys. Lett.* **2005,** *87,* 123110. doi:10.1063/1.2053358
30. Altun, A. O.; Youn, S. K.; Yazdani, N.; Bond, T.; Park, H. G. *Adv. Mater.* **2013,** *25,* 4431–4436. doi:10.1002/adma.201300571
31. Elias, J.; Utke, I.; Yoon, S.; Bechelany, M.; Weidenkaff, A.; Michler, J.; Philippe, L. *Electrochim. Acta* **2013,** *110,* 387–392. doi:10.1016/j.electacta.2013.04.168
32. Elias, J.; Bechelany, M.; Utke, I.; Erni, R.; Hosseini, D.; Michler, J.; Philippe, L. *Nano Energy* **2012,** *1,* 696–705. doi:10.1016/j.nanoen.2012.07.002
33. Farmer, D. B.; Gordon, R. G. *Nano Lett.* **2006,** *6,* 699–703. doi:10.1021/nl052453d
34. Cavanagh, A. S.; Wilson, C. A.; Weimer, A. W.; George, S. M. *Nanotechnology* **2009,** *20,* 255602. doi:10.1088/0957-4484/20/25/255602
35. Williams, J. R.; DiCarlo, L.; Marcus, C. M. *Science* **2007,** *317,* 638–641. doi:10.1126/science.1144657
36. Zhan, G. D.; Du, X. H.; King, D. M.; Hakim, L. F.; Liang, X. H.; McCormick, J. A.; Weimer, A. W. *J. Am. Ceram. Soc.* **2008,** *91,* 831–835. doi:10.1111/j.1551-2916.2007.02210.x
37. Sun, X.; Xie, M.; Travis, J. J.; Wang, G. K.; Sun, H. T.; Lian, J.; George, S. M. *J. Phys. Chem. C* **2013,** *117,* 22497–22508. doi:10.1021/jp4066955
38. Bittencourt, C.; Felten, A.; Douhard, B.; Colomer, J. F.; Van Tendeloo, G.; Drube, W.; Ghijsen, J.; Pireaux, J. J. *Surf. Sci.* **2007,** *601,* 2800–2804. doi:10.1016/j.susc.2006.12.045
39. Felten, A.; Bittencourt, C.; Colomer, J. F.; Van Tendeloo, G.; Pireaux, J. J. *Carbon* **2007,** *45,* 110–116. doi:10.1016/j.carbon.2006.07.023
40. Erni, R.; Rossell, M. D.; Kisielowski, C.; Dahmen, U. *Phys. Rev. Lett.* **2009,** *102,* 096101. doi:10.1103/PhysRevLett.102.096101
41. Erni, R.; Browning, N. D. *Ultramicroscopy* **2005,** *104,* 176–192. doi:10.1016/j.ultramic.2005.03.009
42. Erni, R.; Browning, N. D. *Ultramicroscopy* **2008,** *108,* 84–99. doi:10.1016/j.ultramic.2007.03.005
43. Bosman, M.; Keast, V. J.; García-Muñoz, J. L.; D'Alfonso, A. J.; Findlay, S. D.; Allen, L. J. *Phys. Rev. Lett.* **2007,** *99,* 086102. doi:10.1103/PhysRevLett.99.086102
44. Botton, G. A.; Lazar, S.; Dwyer, C. *Ultramicroscopy* **2010,** *110,* 926–934. doi:10.1016/j.ultramic.2010.03.008
45. Kimoto, K.; Asaka, T.; Nagai, T.; Saito, M.; Matsui, Y.; Ishizuka, K. *Nature* **2007,** *450,* 702–704. doi:10.1038/nature06352
46. Suenaga, K.; Sato, Y.; Liu, Z.; Kataura, H.; Okazaki, T.; Kimoto, K.; Sawada, H.; Sasaki, T.; Omoto, K.; Tomita, T.; Kaneyama, T.; Kondo, Y. *Nat. Chem.* **2009,** *1,* 415–418. doi:10.1038/nchem.282
47. Muller, D. A.; Kourkoutis, L. F.; Murfitt, M.; Song, J. H.; Hwang, H. Y.; Silcox, J.; Dellby, N.; Krivanek, O. L. *Science* **2008,** *319,* 1073–1076. doi:10.1126/science.1148820
48. Nakagawa, N.; Hwang, H. Y.; Muller, D. A. *Nat. Mater.* **2006,** *5,* 204–209. doi:10.1038/nmat1569
49. Rossell, M. D.; Ramasse, Q. M.; Findlay, S. D.; Rechberger, F.; Erni, R.; Niederberger, M. *ACS Nano* **2012,** *6,* 7077–7083. doi:10.1021/nn3021212
50. Egerton, F. R. *Electron Energy Loss Spectroscopy in the Electron Microscope,* 3rd ed.; Springer: New York Dordrecht Heidelberg London, 2000.
51. Yuan, J.; Brown, L. M. *Micron* **2000,** *31,* 515–525. doi:10.1016/S0968-4328(99)00132-8
52. Hamon, A. L.; Verbeeck, J.; Schryvers, D.; Benedikt, J.; Van der Sanden, R. M. C. M. *J. Mater. Chem.* **2004,** *14,* 2030–2035. doi:10.1039/b406468m
53. Muller, D. A.; Tzou, Y.; Raj, R.; Silcox, J. *Nature* **1993,** *366,* 725–727. doi:10.1038/366725a0
54. Suenaga, K.; Colliex, C.; Iijima, S. *Appl. Phys. Lett.* **2001,** *78,* 70–72. doi:10.1063/1.1335854
55. Titantah, J. T.; Jorissen, K.; Lamoen, D. *Phys. Rev. B* **2004,** *69,* 125406. doi:10.1103/PhysRevB.69.125406
56. Titantah, J. T.; Lamoen, D. *Phys. Rev. B* **2005,** *72,* 193104. doi:10.1103/PhysRevB.72.193104
57. Brydson, R.; Sauer, H.; Engel, W.; Thomas, J. M.; Zeitler, E.; Kosugi, N.; Kuroda, H. *J. Phys.: Condens. Matter* **1989,** *1,* 797–812. doi:10.1088/0953-8984/1/4/012
58. Ilari, G. M.; Kränzlin, N.; Longtin, R.; Sanchez-Valencia, J. R.; Schneider, S.; Rossell, M. D.; Niederberger, M.; Erni, R. *Carbon* **2014,** *73,* 146–154. doi:10.1016/j.carbon.2014.02.050
59. An, G. M.; Ma, W. H.; Sun, Z. Y.; Liu, Z. M.; Han, B. X.; Miao, S. D.; Miao, Z. J.; Ding, K. L. *Carbon* **2007,** *45,* 1795–1801. doi:10.1016/j.carbon.2007.04.034
60. Dai, K.; Zhang, X. H.; Fan, K.; Peng, T. Y.; Wei, B. Q. *Appl. Surf. Sci.* **2013,** *270,* 238–244. doi:10.1016/j.apsusc.2013.01.010

61. Tan, H.; Verbeeck, J.; Abakumov, A.; Van Tendeloo, G. *Ultramicroscopy* **2012,** *116,* 24–33. doi:10.1016/j.ultramic.2012.03.002
62. Gass, M. K.; Koziol, K. K. K.; Windle, A. H.; Midley, P. A. *Nano Lett.* **2006,** *6,* 376–379. doi:10.1021/nl052120g
63. Jin-Phillipp, N. Y.; Koch, C. T.; van Aken, P. A. *Ultramicroscopy* **2011,** *111,* 1255–1261. doi:10.1016/j.ultramic.2011.02.006

License and Terms

This is an Open Access article under the terms of the Creative Commons Attribution License (http://creativecommons.org/licenses/by/2.0), which permits unrestricted use, distribution, and reproduction in any medium, provided the original work is properly cited.

The license is subject to the *Beilstein Journal of Nanotechnology* terms and conditions: (http://www.beilstein-journals.org/bjnano)

The definitive version of this article is the electronic one which can be found at: doi:10.3762/bjnano.5.108

BEILSTEIN JOURNAL OF NANOTECHNOLOGY

Sublattice asymmetry of impurity doping in graphene: A review

James A. Lawlor*[1] and Mauro S. Ferreira[1,2]

Review

Open Access

Address:
[1]School of Physics, Trinity College Dublin, Dublin 2, Ireland and
[2]CRANN, Trinity College Dublin, Dublin 2, Ireland

Email:
James A. Lawlor* - jalawlor@tcd.ie

* Corresponding author

Keywords:
band gap; electronic transport; graphene; nitrogen doping; sublattice asymmetry

Beilstein J. Nanotechnol. **2014,** *5,* 1210–1217.
doi:10.3762/bjnano.5.133

Received: 29 April 2014
Accepted: 08 July 2014
Published: 05 August 2014

This article is part of the Thematic Series "Atomic scale interface design and characterisation: Theory – Electronic properties".

Guest Editor: A. Krasheninnikov

© 2014 Lawlor and Ferreira; licensee Beilstein-Institut.
License and terms: see end of document.

Abstract

In this review we highlight recent theoretical and experimental work on sublattice asymmetric doping of impurities in graphene, with a focus on substitutional nitrogen dopants. It is well known that one current limitation of graphene in regards to its use in electronics is that in its ordinary state it exhibits no band gap. By doping one of its two sublattices preferentially it is possible to not only open such a gap, which can furthermore be tuned through control of the dopant concentration, but in theory produce quasi-ballistic transport of electrons in the undoped sublattice, both important qualities for any graphene device to be used competetively in future technology. We outline current experimental techniques for synthesis of such graphene monolayers and detail theoretical efforts to explain the mechanisms responsible for the effect, before suggesting future research directions in this nascent field.

Review

Introduction

With its excellent transport properties and low dimensionality, graphene, an atomically thin layer of Carbon atoms bonded together in a hexagonal lattice, initially seems a strong candidate for use in many future commercial applications such as ultra high-speed transistors, integrated circuits and other novel devices [1-3]. One of the main problems with using regular graphene for such applications is the absence of a band gap in the electronic band structure [4], and as a result any field effect transistors (FETs) made using the material (so-called GFETs) would be unable to be switched off, rendering it useless as a logic device [5-7]. The most natural way to approach this issue is therefore to introduce a sizeable band gap and hence allowing more control over the current flow.

Although several methods exist to induce a band gap, for example 1D quantum confinement by construction of graphene

nanoribbons (GNRs) [8], stacking of monolayers with perpendicular electric fields [6,7], strain [9] and mounting on a substrate [10-12], these methods are not without problems. Alternatives are therefore sought after with the minimum standard to meet or exceed the limits of silicon semiconductor technology, which is characterised by a current on/off ratio of roughly 10^4–10^7 and a band gap of at least 340 meV whilst maintaining high carrier mobility [5,13,14].

Alteration of the crystal structure through the introduction of foreign dopants is one of the more realistic avenues of approach in realising this goal. Atomic dopants like boron (B) or nitrogen (N) are a similar size to carbon and can be introduced easily in a variety of graphene growth processes, typically replacing carbon sites and forming substitutional impurities in the lattice, positively (p-) and negatively (n-) doping the system for B and N dopants respectively [15]. Early theoretical attempts at investigating the electronic properties of such a material found that a periodic arrangement of B or N dopants, forming a dopant superlattice, would open a band gap [16], but that a random distribution of dopants among lattice sites yields no band gap [17]. Further investigations using vacancies, where carbon atoms are removed from the lattice, found that both superlattices [18] and random distributions restricted to one of the two graphene sublattices [19] both lead to a tunable band gap, and in the latter case an emergence of magnetic properties in the system [20,21].

Whilst these findings are certainly interesting, their scalability, and hence commercial application, is prohibited by the standard of precision that must be met in order to produce such materials. Circumventing these problems using nitrogen doped graphene has only come about relatively recently which we detail in the following section.

A brief history of nitrogen doped graphene

Exploiting the effects of nitrogen dopants on the transport properties of graphene has been an interesting experimental research topic for the last 5 years [22], whereby the methods and techniques to achieve this have been developed to include chemical vapour deposition (CVD), using NH_3 as a precursor, arc discharge [23], embedded nitrogen and carbon sources within a metal substrate [24], ion implantation [25,26], ammonia [27] or nitrogen plasma [28,29] treatments, and capable of achieving nitrogen dopant concentrations of up to around 10% [30] and with direct applicablity to GFET technology and bio-sensing [28]. Although CVD is one of the more challenging methods, it seems the most reliable option and yields the best quality nitrogen doped graphene sheets [31] and single continuous sheets can be synthesised on the centimeter scale [32]. Using nitrogen dopants alone through CVD can yield bandgaps up to 200 meV [33] and by inclusion of boron co-dopants, through a tailored growth process, this can be expanded to around 600 meV with 6% total dopant concentration [12]. Boron doping alone has shown to also open a band gap, tunable with dopant concentration [34,35]. This method results in small B–N domains embedded in the graphene sheet, so the precise mechanism behind the band gap opening may not be the same as that seen in a random B–N ensemble. Although these gaps are quite sizeable, the effect of scattering would lead to a detrimental impact on the transport characteristics. However, the recent theoretical prediction of sublattice asymmetry, a situation where dopants are distributed in one sublattice only, is expected to yield very low scattering transport properties. The electron wavefunctions in such a system are shown to mainly exist on the sublattice without dopants and can travel almost unhindered [36,37], which is very promising for overcoming the scattering problem.

It was not until 2011 that a viable experimental approach was found by Zhao et al. [38]. They discovered that graphene grown via chemical vapour deposition (CVD) in the presence of ammonia (NH_3) naturally incorporates nitrogen atoms as substitutional so-called 'graphitic' dopants (see Figure 1A) into the crystal, and with a distinct sublattice segregation of dopants. Indeed further research has uncovered a less pronounced asymmetry phenomenon using graphene implanted with nitrogen impurities followed by a high temperature annealing process [25], and it seems reasonable that there is a common mechanism with the CVD method. Due to the limited published work on this implantation and annealing method, our main focus will be on CVD and it is here that we begin our main discussions. We begin with a section covering in-depth the experimental work done to date, followed by a section on theoretical aspects and ending with a future outlook and conclusions.

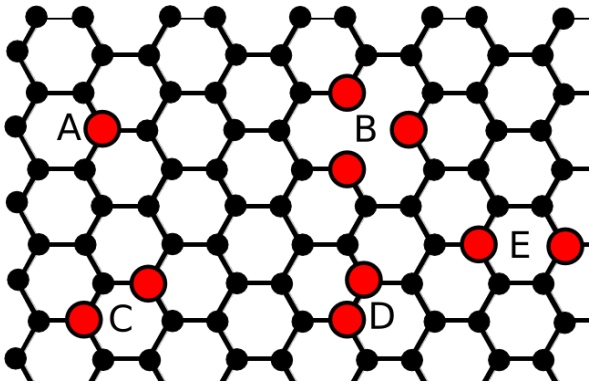

Figure 1: Schematic of a graphene lattice with the most common experimentally observed species of substitutional nitrogen dopants: (A) a single graphitic, (B) three pyridinics, (C) one N_2^{AA} pair, (D) one N_2^{AB} pair and (E) one $N_2^{AB'}$ pair.

Experimental observation of sublattice asymmetry of N-graphene

The main focus of the work by Zhao et al. was the observation and characterization of nitrogen dopants via scanning tunnel spectroscopy (STS), followed by a short investigation on the transport properties of the resulting graphene. Their experimental observation of same sublattice segregation, at least on local scales, was noted as a curiosity but was not discussed in depth. A key finding by the researchers was that by varying the ammonia precursor concentration they could adjust the resulting embedded dopant concentration. Further theoretical work confirmed that a tunable band gap would be obtainable using this method [36], and along with the findings of Zhao et al. this sparked further interest into this phenomenon. It should be noted that the experimental conditions were a high vacuum CVD process on a Cu(111) substrate with a temperature of 1000 °C, using CH_4 and NH_3 as graphene and nitrogen precursors respectively for 18 min reaction time achieving a dopant concentration of 0.3%.

Shortly after this work a more focussed investigation was undertaken by Lv et al. [39]. They were able to replicate the findings of the first group and synthesised large areas of N-doped monolayer graphene with the additional finding that by increasing the pressure in the growth phase from a high vacuum to atmospheric-pressure CVD would result in an abundance of so-called N_2^{AA} pairs [39] (see Figure 1C), which are thought to be a result of a higher number of intermolecule collisions during formation. Using the same substrate and precursors, they were also able to find that a minimum reaction time of 5 min and temperatures of 800 °C were optimum for the N-doped graphene synthesis and moreover it was found that singular nitrogen dopants are more frequently found for reaction times below 10 min with the ratio of N_2^{AA} to single N increasing with reaction time. The samples had a typical concentration of around 0.25% nitrogen dopants.

More recently the addition of boron dopants into the lattice and their effects have been studied [40] using high vacuum CVD growth and adding B_2H_6 diborane instead of ammonia as the dopant precursor, achieving concentrations on the order of 0.3%. The researchers compared B-doped and N-doped systems in detail and found no detectable sublattice asymmetry in the case of B-doped systems and thus the dopants were distributed evenly between sublattices. The reason for this is thought to be due to a strong interaction between the Cu(111) substrate and the boron impurity, in contrast to a very weak interaction with the substrate for nitrogen impurities [40].

The most recent and thorough study of asymmetric nitrogen dopants in graphene is by Zabet-Khosousi et al. [41] who again used the CVD growth process but with a pyridine (C_5H_5N) precursor for the nitrogen and graphene instead of the conventional ammonia/methane mix. Figure 2 shows a rather striking STM image of a large area of N-doped graphene grown using this method, showing two clearly defined domains of different sublattice preference where the sharp borders are thought to arise from terracing of the substrate disrupting the asymmetry effect. The method was tailored to use a very smooth Cu(111) substrate and so they were able to achieve domain sizes far larger than previous efforts. Typical concentrations found with this method were around 0.2%, very similar to the previous ammonia/methane method which points to an equivalent growth mechanism. By comparing N-doped graphene systems synthesised with this method to other systems made via nitrogen ion bombardement and ammonia post-treatment of a pristine graphene sheet, where no sublattice asymmetric configurations were found, it was suggested that the sublattice asymmetry must be occuring during formation of the graphene sheet. This is supported by the recent experiments using ion bombardement followed by high temperature annealing by Telychko et al. [25], where the impurities may be reconfiguring themselves locally during cooling. This phenomenon is not seen without the annealing process [26].

The common elements of all the aforementioned experimental reports are that they all use a Cu(111) substrate, all have reaction times exceeding 10 min in a temperature range of 800–900 °C, and all have used either ammonia or pyridine precursors to achieve concentrations of up to 0.3%. A review of other methods for N-doped graphene synthesis finds no mention of sublattice asymmetry [29,30], it is known that this effect is mainly detectable through careful scanning tunnel microscopy of large areas. The most natural explanation for this lack of observation is then either that it is not being observed due to simply not looking, or that sublattice asymmetry is not a very robust effect and therefore requires a careful choice of synthesis procedure. Research into the mechanisms behind the phenomenon is therefore paramount in answering this question and could shed light on whether other methods or even dopant species are at all possible and this leads us naturally to a review of the current theoretical models of the effect.

Theoretical models of the segregation effect

It is clear that any degree of asymmetry between the two equivalent sublattices is the result of a symmetry breaking operation. Current theoretical attempts to explain the sublattice asymmetry in the nitrogen doping seen in the experiments discussed in the previous section suggest that the effect comes from either the energetically preferable positioning of nitrogen on the graphene edge during the growth process [41,42], where the symmetry breaking effect is the edge structure, or from

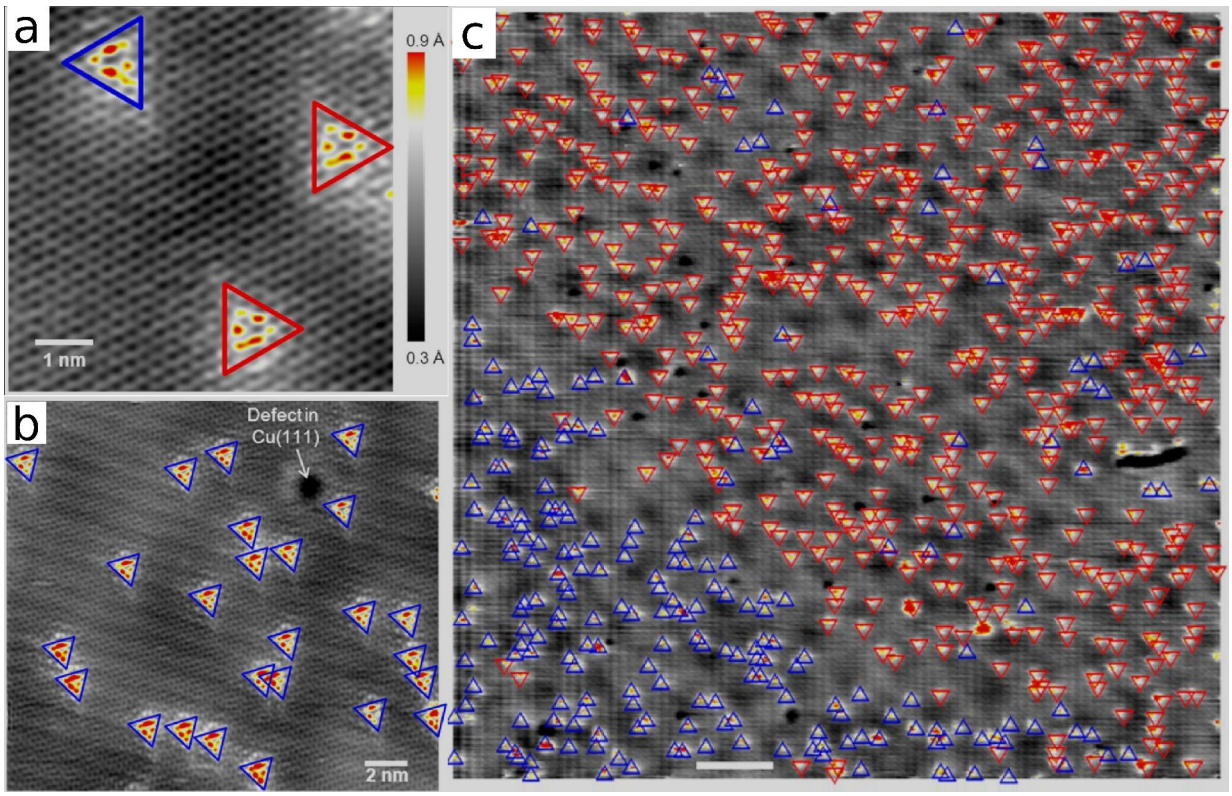

Figure 2: STM images of nitrogen doped graphene on (a) 7 nm^2, (b) 20 nm^2 and (c) 100 nm^2 scales, adapted with permission from Zabet-Khosousi et al. [41]. Copyright 2014 American Chemical Society. The dopants locations are identified by finding bright spots on the STM image, corresponding to slight perturbations in the positions of the neighbouring carbon atoms. The dopant sublattice can be found through the orientation of the bright triangle features, where opposite sublattices appear as mirror images of each other as demonstrated in (a). The red and blue triangles in each subfigure correspond to impurities on the different sublattices. Part (c) best demonstrates that although the distribution of dopants appears random, when their sublattice is identified we see two very large domains appear with opposite sublattice segregation. Shown at the bottom, off-center left of (c) is a white 10 nm scalebar.

inter-impurity interactions in the impurity ensemble [39,43] where the symmetry is broken by the impurities themselves. These models will hereafter be referred to as the edge growth and interaction models respectively.

The edge growth model suggests that during the growth phase the most energetically favourable position for a nitrogen dopant being incorporated into a graphene edge would be that which leads to a same sublattice configuration for all impurities in a domain. Through density functional theory (DFT) calculations involving a graphene nanoribbon on a Cu(111) substrate, aiming to reproduce experimental conditions, a thorough investigation into the energetic favourable position of single graphitic nitrogens in the GNR was undertaken and the energetic difference between placing the nitrogen at one edge site over another on the opposite sublattice was found to be a substantial 1.3 eV. One drawback of this method is that one would expect therefore that the clearly defined segregation domains seen experimentally (see Figure 2 and [41]) would naturally fall in with the graphene grain boundaries, but this has not been observed. The role of inter-impurity interactions has been considered as an alternative, through both tight binding [43] and DFT [39,44] formalisms, although with differing conclusions. The tight binding method by Lawlor et al. [43] was part of a more in-depth theoretical investigation, and suggests that a Friedel oscillation-like perturbation in the long-range inter-impurity interactions [45] arise from adding impurities to the system, leading to a shift in the system's Fermi energy. Such a mechanism would explain both the non-commensurability between crystal grain boundaries and segregation domains, and would suggest why the alternative synthesis method of nitrogen implantation followed by high temperature annealing also results in impurities preferring to occupy the same sublattice [25]. Furthermore, the authors predict that as a result of this interaction and the reduction in nearest neighbour distance with increasing concentration, there exists a critical dopant concentration beyond which no sublattice asymmetry would be observed, as the energetic minimum occurs when the impurities are distributed evenly between sublattices. Although the exact value of this critical concentration is dependant on

how the impurity is parameterised within the tight binding regime, the authors predict it to lie between 0.1% and 0.8%. Comparing to the highest experimentally reported doping concentrations for samples with sublattice asymmetry (0.3%), it is a hope that further experiments can clarify whether such a critical concentration exists. If the prediction of a critical concentration is accurate it would limit the band gap of a segregated device to around 100 meV [36]. This figure, however, comes from matching tight binding and DFT band structure results, a method which is known to systematically underestimate such band gaps. Nevertheless, the band gap obtained can be expected to be much below that required for a GFET device.

In-depth DFT calculations by Hou et al. [44] found that the interactions between nitrogen impurities are generally repulsive in nature. More specifically, when the two impurities are placed close together the system energy is minimised for opposite sublattice configurations, with the exception of N_2^{AB}. This contradicts the experimental reports of Lv et al. [39] who found an abundance of N_2^{AA} defects in their samples. A simplistic tight binding approach predicts that two identical impurities in close proximity to one another would indeed have an energetic minimum when both occupy the same sublattice [46], however this method ignores coulombic interaction which will be dominant at close separations. Interestingly, the DFT approach of Lv et al. of such nitrogen pairs finds that the lowest energy configuration would be $N_2^{AB'}$ (see Figure 1), approximately 0.3 eV lower than that of N_2^{AA}. This appears to be in disagreement with experiments where N_2^{AA} is more commonly found than $N_2^{AB'}$. As a final note their calculations have also shown that two N_2^{AA} pairs have a lower energy when they share the same sublattice, however further studies have shown that the overall energy change resulting from an N_2^{AA} pair in the sheet is very high [42]. It is possible that these impurities also come from edge growth, but the controllable presence of N_2^{AA} in nitrogen ion implanted graphene [25] indicates again that this may not be the full picture as in this case the complete graphene sheet is already fabricated.

Predicted electronic properties

The earliest attempts to study nitrogen dopants and their effect on the graphene electronic properties were purely theoretical. Beginning with impurity superlattices, this research preceded the experimental realistation of nitrogen doped graphene. By introducing a controlled periodic arrangement of boron and nitrogen impurities a band gap was seen to open [16], and although such superlattice structures were not feasible on large-scale it was further shown that a random distribution on one sublattice can also open a gap [37]. Further DFT studies showed that the band gap will increase with dopant concentration [36,47] and that a dopant level of over 8%, where impurities are all on the same sublattice, will produce a band gap of around 550 meV far surpassing the minimum required for a CMOS [14,36] and finding that the band gap scales with concentration to the power 3/4, as shown in Figure 3.

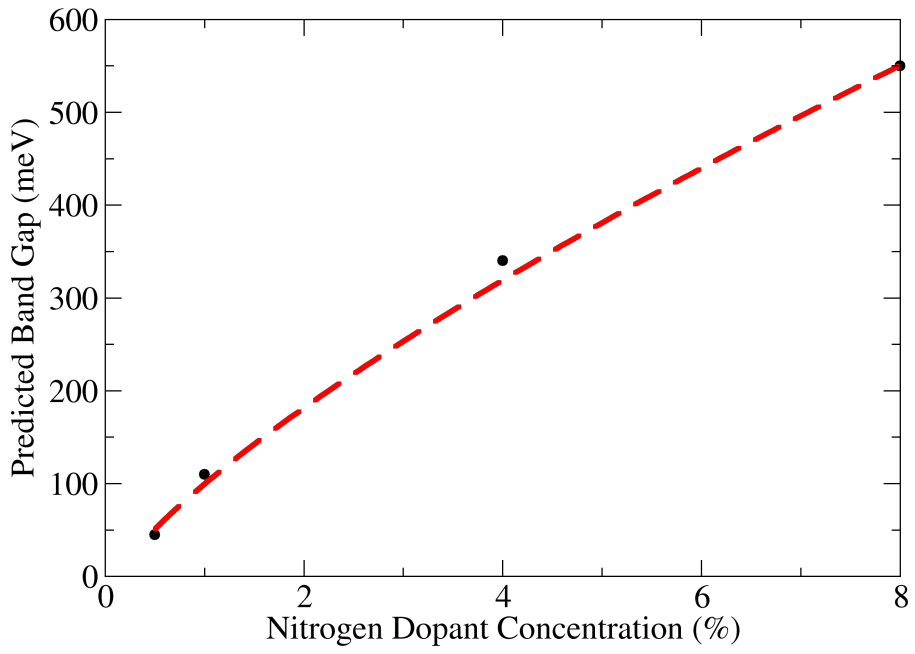

Figure 3: Predicted band gap against nitrogen dopant concentration. Black circles are calculated values from [36] and the red dashed line shows the expected band gap scaling with concentration, according to the power 3/4 as discussed in the text.

Even with a 4:1 doping ratio between sublattices, the band gap, although smaller, was shown to still exist. This is promising for scaleability where perfect asymmetric doping may not always be realizable. Beyond the realization of quasi-ballistic electron transport, sublattice segregated systems can also be used to induce magnetism [19,48-50] and produce spin-polarized current [51,52].

Much work has been done studying how the placement of dopants affects the properties of nanoribbons. DFT approaches, using a periodic system of dopants [53,54], and a more general Kubo–Greenwood approach [37] have shown that electron transport is enhanced when dopants are placed on one sublattice, compared to a random distribution, and that a band gap does indeed open. The difference in transport qualities between the asymmetrically doped versus completely randomly doped systems is illustrated by a conductance plot in Figure 4, where it is evident that the electrons in the former kind of device will be subjected to less scattering leading to an increase in the quantum conductance, closer to that of the pristine system when subjected to a positive bias.

It should also be noted that that symmetry breaking in nanoribbons occurs via edge effects and also results in a favourable sublattice [58], however the mechanism is distinctly different from that in graphene.

Outlook

At the time of writing, the synthesis of sublattice asymmetric graphene is only just now becoming practical. There are still many unanswered questions and the most important ones we outline in this section.

The natural question to ask is if this asymmetry is particular to nitrogen only, or if it can be found with other dopants. Theoretical findings in the past have shown that such an effect can be expected with a dilute concentration of certain adsorbates [59], and indeed more recent studies suggest that this could also be possible with other impurities [43]. Whilst it is known experimentally that molybdenum impurities exhibit same sublattice configurations in bilayer epitaxial graphene, the mechanism behind this is not currently understood [60]. Boron has been studied in a similar CVD growing regime to nitrogen where it has been proposed that the role of the substrate can play a critical role in the manifestation of segregation. In this case, it is thought that the strong interactions between the Cu(111) crystal and the boron dopants destroy any asymmetry effects [40]. It is then logical to ask whether suitable substrates can be identified to produce segregated boron doped graphene sheets, which would have the effect of p-doping the system, and then to ask whether this can be extended to other species of dopants. We note that it is known that there are weak interactions between graphene and Al, Ag, Au, Pt(111) substrates, all of which leave

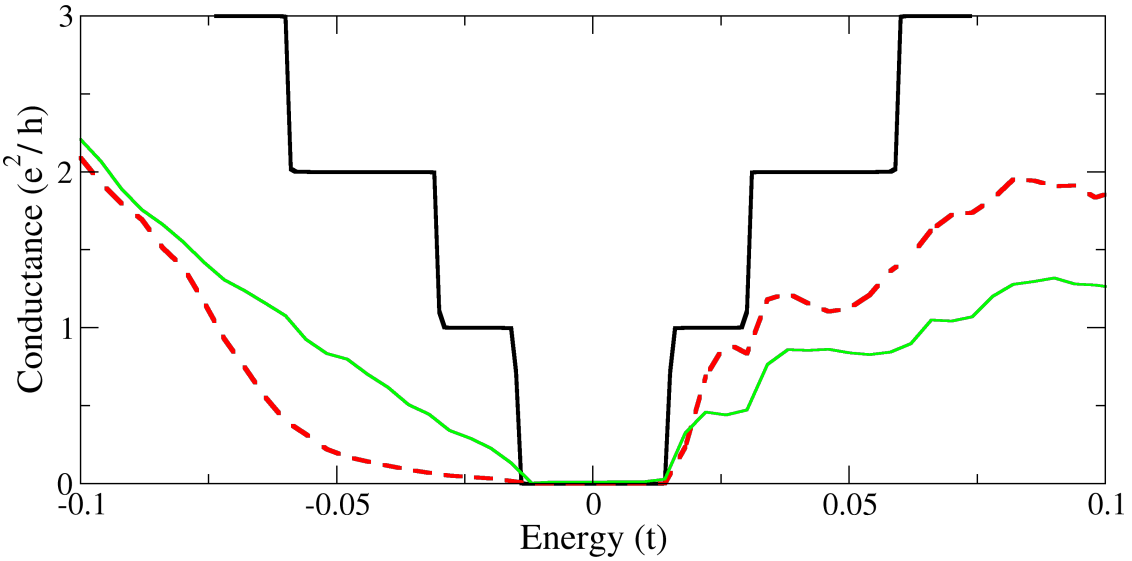

Figure 4: Quantum conductance through a 15 nm wide graphene nanoribbon with a 7.5 nm long scattering region containing a dispersion of substitutional nitrogen impurities, in a similar vein to the method of Botello-Mendez et al. [37], calculated using a recursive Green's Function method [55,56], the Kubo formula for conductance [57] and a configurational average of 50 systems. Energy is in units of the tight binding nearest neighbour hopping energy between carbon atoms, t = 2.7 eV. Shown is the predicted conductance for pristine (black), randomly doped (green solid) and single sublattice doped (red dashed) systems, where a dopant concentration of 1% nitrogen was used.

the electronic structure intact [61], whilst substrates such as Ni have considerably stronger interactions [62]. Another way to investigate the presence of sublattice asymmetry with dopants other than nitrogen is via ion bombardement [63], which could be combined with the high temperature annealing process discussed previously.

The experimental realisation of spin-polarized transport should also be pursued, and could spark additional interest in this research area beyond quasi-ballistic transport. Investigation of the effects of strain on such a system is difficult due to the technicalities of the CVD method, but could be explored using adsorbates instead of substitutions or by incorporation of the strain in to the nitrogen ion bombardement and annealing procedure discussed earlier. Another open question is if a critical concentration of dopants exists, as mentioned in the theory section, which would limit the available bandgap below the threshold needed for future use in GFET devices. Currently all experimental reports on sublattice asymmetry have very low concentrations of dopants around 0.3%, so it should be feasible to test the existence of a critical concentration of using available methods [30]. Consequentially this would shed more light on the mechanism responsible for the segregation, and whether in fact the inter-impurity interactions and edge growth effects are complementary effects.

Conclusion

This paper reviews the current state of experimental and theoretical research in sublattice asymmetric nitrogen doped graphene. Not only are such systems now able to be synthesised in the lab, we have seen that this area shows promise attaining graphene-based FET devices due to the opening of a bandgap whilst maintaining the excellent transport properties of graphene, something which is not realisable in graphene with no sublattice imbalance in dopant distribution. While there are still many open questions in the field these should be answerable within the scope of current techniques.

Acknowledgements

The authors acknowledge financial support from the Programme for Research in Third Level Institutions (PRTLI), Science Foundation Ireland (Grant No. SFI 11/ RFP.1/MTR/ 3083).

References

1. Geim, A. K.; Novoselov, K. S. *Nat. Mater.* **2007,** *6,* 183–191. doi:10.1038/nmat1849
2. Novoselov, K. S.; Fal'ko, V. I.; Colombo, L.; Gellert, P. R.; Schwab, M. G.; Kim, K. *Nature* **2012,** *490,* 192–200. doi:10.1038/nature11458
3. Chen, J.-H.; Jang, C.; Xiao, S.; Ishigami, M.; Fuhrer, M. S. *Nat. Nanotechnol.* **2008,** *3,* 206–209. doi:10.1038/nnano.2008.58
4. Allen, M. J.; Tung, V. C.; Kaner, R. B. *Chem. Rev.* **2010,** *110,* 132–145. doi:10.1021/cr900070d
5. Schwierz, F. *Nat. Nanotechnol.* **2010,** *5,* 487–496. doi:10.1038/nnano.2010.89
6. Lin, Y.-M.; Jenkins, K. A.; Valdes-Garcia, A.; Small, J. P.; Farmer, D. B.; Avouris, P. *Nano Lett.* **2009,** *9,* 422–426. doi:10.1021/nl803316h
7. Zhang, Y.; Tang, T.-T.; Girit, C.; Hao, Z.; Martin, M. C.; Zettl, A.; Crommie, M. F.; Shen, Y. R.; Wang, F. *Nature* **2009,** *459,* 820–823. doi:10.1038/nature08105
8. Li, X.; Wang, X.; Zhang, L.; Lee, S.; Dai, H. *Science* **2008,** *319,* 1229–1232. doi:10.1126/science.1150878
9. Naumov, I. I.; Bratkovsky, A. M. *Phys. Rev. B* **2011,** *84,* 245444. doi:10.1103/PhysRevB.84.245444
10. Novoselov, K. *Nat. Mater.* **2007,** *6,* 720–721. doi:10.1038/nmat2006
11. Zhou, S. Y.; Gweon, G.-H.; Fedorov, A. V.; First, P. N.; de Heer, W. A.; Lee, D.-H.; Guinea, F.; Castro Neto, A. H.; Lanzara, A. *Nat. Mater.* **2007,** *6,* 770–775. doi:10.1038/nmat2003
12. Chang, C.-K.; Kataria, S.; Kuo, C.-C.; Ganguly, A.; Wang, B.-Y.; Hwang, J.-Y.; Huang, K.-J.; Yang, W.-H.; Wang, S.-B.; Chuang, C.-H.; Chen, M.; Huang, C.-I.; Pong, W.-F.; Song, K.-J.; Chang, S.-J.; Guo, J.-H.; Tai, Y.; Tsujimoto, M.; Isoda, S.; Chen, C.-W.; Chen, L.-C.; Chen, K.-H. *ACS Nano* **2013,** *7,* 1333–1341. doi:10.1021/nn3049158
13. Avouris, P. *Nano Lett.* **2010,** *10,* 4285–4294. doi:10.1021/nl102824h
14. Kim, K.; Choi, J.-Y.; Kim, T.; Cho, S.-H.; Chung, H.-J. *Nature* **2011,** *479,* 338–344. doi:10.1038/nature10680
15. Islam, M. S.; Ushida, K.; Tanaka, S.; Makino, T.; Hashimoto, A. *Comput. Mater. Sci.* **2014,** in press. doi:10.1016/j.commatsci.2014.01.040
16. Casolo, S.; Martinazzo, R.; Tantardini, G. F. *J. Phys. Chem. C* **2011,** *115,* 3250–3256. doi:10.1021/jp109741s
17. Lherbier, A.; Blase, X.; Niquet, Y.-M.; Triozon, F.; Roche, S. *Phys. Rev. Lett.* **2008,** *101,* 036808. doi:10.1103/PhysRevLett.101.036808
18. Martinazzo, R.; Casolo, S.; Tantardini, G. F. *Phys. Rev. B* **2010,** *81,* 245420. doi:10.1103/PhysRevB.81.245420
19. Palacios, J. J.; Fernández-Rossier, J.; Brey, L. *Phys. Rev. B* **2008,** *77,* 195428. doi:10.1103/PhysRevB.77.195428
20. Cresti, A.; Ortmann, F.; Louvet, T.; Van Tuan, D.; Roche, S. *Phys. Rev. Lett.* **2013,** *110,* 196601. doi:10.1103/PhysRevLett.110.196601
21. Pereira, V. M.; Lopes dos Santos, J. M. B.; Castro Neto, A. H. *Phys. Rev. B* **2008,** *77,* 115109. doi:10.1103/PhysRevB.77.115109
22. Wei, D.; Liu, Y.; Wang, Y.; Zhang, H.; Huang, L.; Yu, G. *Nano Lett.* **2009,** *9,* 1752–1758. doi:10.1021/nl803279t
23. Guan, L.; Cui, L.; Lin, K.; Wang, Y. Y.; Wang, X. T.; Jin, F. M.; He, F.; Chen, X. P.; Cui, S. *Appl. Phys. A* **2011,** *102,* 289–294. doi:10.1007/s00339-010-6110-5
24. Zhang, C.; Fu, L.; Liu, N.; Liu, M.; Wang, Y.; Liu, Z. *Adv. Mater.* **2011,** *23,* 1020–1024. doi:10.1002/adma.201004110
25. Telychko, M.; Mutombo, P.; Ondráček, M.; Hapala, P.; Bocquet, F. C.; Kolorenč, J.; Vondráček, M.; Jelínek, P.; Švec, M. *ACS Nano* **2014,** *8,* 7318–7324. doi:10.1021/nn502438k
26. Bangert, U.; Pierce, W.; Kepaptsoglou, D. M.; Ramasse, Q.; Zan, R.; Gass, M. H.; Van den Berg, J. A.; Boothroyd, C. B.; Amani, J.; Hofsäss, H. *Nano Lett.* **2013,** *13,* 4902–4907. doi:10.1021/nl402812y
27. Lin, Y.-C.; Lin, C.-Y.; Chiu, P.-W. *Appl. Phys. Lett.* **2010,** *96,* 133110. doi:10.1063/1.3368697
28. Wang, Y.; Shao, Y.; Matson, D. W.; Li, J.; Lin, Y. *ACS Nano* **2010,** *4,* 1790–1798. doi:10.1021/nn100315s

29. Joucken, F.; Tison, Y.; Lagoute, J.; Dumont, J.; Cabosart, D.; Zheng, B.; Repain, V.; Chacon, C.; Girard, Y.; Botello-Mendez, A. R.; Rousset, S.; Sporken, R.; Charlier, J.-C.; Henrard, L. *Phys. Rev. B* **2012,** *85,* 161408. doi:10.1103/PhysRevB.85.161408
30. Wang, H.; Maiyalagan, T.; Wang, X. *ACS Catal.* **2012,** *2,* 781–794. doi:10.1021/cs200652y
31. Wang, H.; Xie, M.; Thia, L.; Fisher, A.; Wang, X. *J. Phys. Chem. Lett.* **2014,** *5,* 119–125. doi:10.1021/jz402416a
32. Gao, H.; Song, L.; Guo, W.; Huang, L.; Yang, D.; Wang, F.; Zuo, Y.; Fan, X.; Liu, Z.; Gao, W.; Vajtai, R.; Hackenberg, K.; Ajayan, P. M. *Carbon* **2012,** *50,* 4476–4482. doi:10.1016/j.carbon.2012.05.026
33. Usachov, D.; Vilkov, O.; Grüneis, A.; Haberer, D.; Fedorov, A.; Adamchuk, V. K.; Preobrajenski, A. B.; Dudin, P.; Barinov, A.; Oehzelt, M.; Laubschat, C.; Vyalikh, D. V. *Nano Lett.* **2011,** *11,* 5401–5407. doi:10.1021/nl2031037
34. Tang, Y.-B.; Yin, L.-C.; Yang, Y.; Bo, X.-H.; Cao, Y.-L.; Wang, H.-E.; Zhang, W.-J.; Bello, I.; Lee, S.-T.; Cheng, H.-M.; Lee, C.-S. *ACS Nano* **2012,** *6,* 1970–1978. doi:10.1021/nn3005262
35. Fan, X.; Shen, Z.; Liu, A.; Kuo, J.-L. *Nanoscale* **2012,** *4,* 2157–2165. doi:10.1039/c2nr11728b
36. Lherbier, A.; Botello-Méndez, A. R.; Charlier, J.-C. *Nano Lett.* **2013,** *13,* 1446–1450. doi:10.1021/nl304351z
37. Botello-Méndez, A. R.; Lherbier, A.; Charlier, J. C. *Solid State Commun.* **2013,** *175-176,* 90–100. doi:10.1016/j.ssc.2013.08.029
38. Zhao, L.; He, R.; Rim, K. T.; Schiros, T.; Kim, K. S.; Zhou, H.; Gutiérrez, C.; Chockalingam, S. P.; Arguello, C. J.; Pálová, L.; Nordlund, D.; Hybertsen, M. S.; Reichman, D. R.; Heinz, T. F.; Kim, P.; Pinczuk, A.; Flynn, G. W.; Pasupathy, A. N. *Science* **2011,** *333,* 999–1003. doi:10.1126/science.1208759
39. Lv, R.; Li, Q.; Botello-Méndez, A. R.; Hayashi, T.; Wang, B.; Berkdemir, A.; Hao, Q.; Elias, A. L.; Cruz-Silva, R.; Gutiérrez, H. R.; Kim, Y. A.; Muramatsu, H.; Zhu, J.; Endo, M.; Terrones, H.; Charlier, J.-C.; Pan, M.; Terrones, M. *Sci. Rep.* **2012,** *2,* 586. doi:10.1038/srep00586
40. Zhao, L.; Levendorf, M.; Goncher, S.; Schiros, T.; Pálová, L.; Zabet-Khosousi, A.; Rim, K. T.; Gutiérrez, C.; Nordlund, D.; Jaye, C.; Hybertsen, M.; Reichman, D.; Flynn, G. W.; Park, J.; Pasupathy, A. N. *Nano Lett.* **2013,** *13,* 4659–4665. doi:10.1021/nl401781d
41. Zabet-Khosousi, A.; Zhao, L.; Pálová, L.; Hybertsen, M. S.; Reichman, D. R.; Pasupathy, A. N.; Flynn, G. W. *J. Am. Chem. Soc.* **2014,** *136,* 1391–1397. doi:10.1021/ja408463g
42. Deretzis, I.; La Magna, A. *Phys. Rev. B* **2014,** *89,* 115408. doi:10.1103/PhysRevB.89.115408
43. Lawlor, J. A.; Gorman, P. D.; Power, S. R.; Bezerra, C. G.; Ferreira, M. S. *Carbon* **2014,** in press. doi:10.1016/j.carbon.2014.05.069
44. Hou, Z.; Wang, X.; Ikeda, T.; Terakura, K.; Oshima, M.; Kakimoto, M.-a.; Miyata, S. *Phys. Rev. B* **2012,** *85,* 165439. doi:10.1103/PhysRevB.85.165439
45. Lambin, P.; Amara, H.; Ducastelle, F.; Henrard, L. *Phys. Rev. B* **2012,** *86,* 045448. doi:10.1103/PhysRevB.86.045448
46. Lawlor, J. A.; Power, S. R.; Ferreira, M. S. *Phys. Rev. B* **2013,** *88,* 205416. doi:10.1103/PhysRevB.88.205416
47. Rani, P.; Jindal, V. K. *RSC Adv.* **2012,** *3,* 802–812. doi:10.1039/C2RA22664B
48. Nair, R. R.; Sepioni, M.; Tsai, I.-L.; Lehtinen, O.; Keinonen, J.; Krasheninnikov, A. V.; Thomson, T.; Geim, A. K.; Grigorieva, I. V. *Nat. Phys.* **2012,** *8,* 199–202. doi:10.1038/nphys2183
49. Singh, R.; Kroll, P. *J. Phys.: Condens. Matter* **2009,** *21,* 196002. doi:10.1088/0953-8984/21/19/196002
50. Santos, E. J.; Sánchez-Portal, D.; Ayuela, A. *Phys. Rev. B* **2010,** *81,* 125433. doi:10.1103/PhysRevB.81.125433
51. Park, H.; Wadehra, A.; Wilkins, J. W.; Castro Neto, A. H. *Phys. Rev. B* **2013,** *87,* 085441. doi:10.1103/PhysRevB.87.085441
52. Rakyta, P.; Kormányos, A.; Cserti, J. *Phys. Rev. B* **2011,** *83,* 155439. doi:10.1103/PhysRevB.83.155439
53. Owens, J. R.; Cruz-Silva, E.; Meunier, V. *Nanotechnology* **2013,** *24,* 235701. doi:10.1088/0957-4484/24/23/235701
54. Chen, T.; Li, X.-F.; Wang, L.-L.; Li, Q.; Luo, K.-W.; Zhang, X.-H.; Xu, L. *J. Appl. Phys.* **2014,** *115,* 053707. doi:10.1063/1.4863638
55. Economou, E. N. *Green's functions in quantum physics;* Springer, 1984; Vol. 3.
56. Lopez Sancho, M. P.; Lopez Sancho, J. M.; Rubio, J. *J. Phys. F: Met. Phys.* **1984,** *14,* 1205. doi:10.1088/0305-4608/14/5/016
57. Kubo, R. *Can. J. Phys.* **1956,** *34,* 1274–1277. doi:10.1139/p56-140
58. Power, S. R.; de Menezes, V. M.; Fagan, S. B.; Ferreira, M. S. *Phys. Rev. B* **2009,** *80,* 235424. doi:10.1103/PhysRevB.80.235424
59. Cheianov, V. V.; Syljuåsen, O.; Altshuler, B. L.; Fal'ko, V. I. *EPL* **2010,** *89,* 56003. doi:10.1209/0295-5075/89/56003
60. Wan, W.; Li, H.; Huang, H.; Wong, S. L.; Lv, L.; Gao, Y.; Wee, A. T. S. *ACS Nano* **2013,** *8,* 970–976. doi:10.1021/nn4057929
61. Khomyakov, P. A.; Giovannetti, G.; Rusu, P. C.; Brocks, G.; van den Brink, J.; Kelly, P. J. *Phys. Rev. B* **2009,** *79,* 195425. doi:10.1103/PhysRevB.79.195425
62. Xu, Z.; Buehler, M. J. *J. Phys.: Condens. Matter* **2010,** *22,* 485301. doi:10.1088/0953-8984/22/48/485301
63. Wang, H.; Wang, Q.; Cheng, Y.; Li, K.; Yao, Y.; Zhang, Q.; Dong, C.; Wang, P.; Schwingenschlögl, U.; Yang, W.; Zhang, X. X. *Nano Lett.* **2011,** *12,* 141–144. doi:10.1021/nl2031629

License and Terms

This is an Open Access article under the terms of the Creative Commons Attribution License (http://creativecommons.org/licenses/by/2.0), which permits unrestricted use, distribution, and reproduction in any medium, provided the original work is properly cited.

The license is subject to the *Beilstein Journal of Nanotechnology* terms and conditions: (http://www.beilstein-journals.org/bjnano)

The definitive version of this article is the electronic one which can be found at: doi:10.3762/bjnano.5.133

BEILSTEIN JOURNAL OF NANOTECHNOLOGY

Review of nanostructured devices for thermoelectric applications

Giovanni Pennelli

Review

Open Access

Address:
University of Pisa, Dipartimento di Ingegneria dell'Informazione, Via Caruso 16, I-56122 Pisa, Italy

Email:
Giovanni Pennelli - g.pennelli@iet.unipi.it

Keywords:
nanofabrication; nanostructures; silicon nanowires; thermoelectricity

Beilstein J. Nanotechnol. **2014,** *5,* 1268–1284.
doi:10.3762/bjnano.5.141

Received: 15 May 2014
Accepted: 22 July 2014
Published: 14 August 2014

This article is part of the Thematic Series "Atomic scale interface design and characterisation: Experimental aspects and methods".

Guest Editor: C. Bittencourt

© 2014 Pennelli; licensee Beilstein-Institut.
License and terms: see end of document.

Abstract

A big research effort is currently dedicated to the development of thermoelectric devices capable of a direct thermal-to-electrical energy conversion, aiming at efficiencies as high as possible. These devices are very attractive for many applications in the fields of energy recovery and green energy harvesting. In this paper, after a quick summary of the fundamental principles of thermoelectricity, the main characteristics of materials needed for high efficiency thermoelectric conversion will be discussed, and a quick review of the most promising materials currently under development will be given. This review paper will put a particular emphasis on nanostructured silicon, which represents a valid compromise between good thermoelectric properties on one side and material availability, sustainability, technological feasibility on the other side. The most important bottom-up and top-down nanofabrication techniques for large area silicon nanowire arrays, to be used for high efficiency thermoelectric devices, will be presented and discussed.

Introduction

The thermoelectric (TE) effect, known since the 19th century, offers an interesting perspective for the direct conversion of heat in electrical power, and vice versa. Given a thermal gradient, a thermoelectric generator (TEG) is capable of converting heat into electrical power even with small temperature differences. TEGs are simple, compact, robust and very reliable because they contain no moving mechanical parts. For all these reasons, TEGs are attractive for a large variety of applications, in particular in the fields of energy recovery and green energy harvesting. For example, they can be used as alternative to photovoltaic cells [1,2], or together with advanced photovoltaic cells [3,4], for the conversion of solar energy into electrical power.

Several industrial processes need a large amount of heat, which is wasted and dispersed in the environment at the end of the

productive cycle because it cannot be converted by conventional thermodynamic systems (as turbines or steam engines). All these industrial processes could conveniently exploit TEGs for recovering most of this otherwise wasted heat. Several studies are dedicated to the development of modules, based on TEGs, for exhaust heat recovery in cars [5,6]. Several car maker companies shows a growing interest in these modules, to be applied for the production of electrical power in hybrid cars and/or for the supply of the on-board car electronics and sensors. One more application field of TEGs is energy scavenging. For example, body heat can be used for powering wearable sensor systems or, eventually, for powering personal electronics as mobile phones. It must be mentioned that TEGs are also used as heat pumps and/or as generators in domestic plants for air conditioning or heating.

However, with the current state-of-the-art technology, the applications of TEGs are limited because their thermal to electrical conversion efficiency is still quite low. This is mainly due to the limitations of the materials currently available for the fabrication of thermoelectric generators. A great research effort is still needed for the development of materials with thermoelectric properties capable of conversion efficiencies greater than 10%. In particular, one of the most limiting factors that reduce the efficiency is the heat diffusion through the TEG for thermal conduction: Most of the heat passes through the generator and it is wasted on the cold side without being converted in useful electrical power. Thus, one of the main target of research efforts in thermoelectricity is to develop materials with a very low thermal conductivity, while still maintaining a high electrical conductivity. In this way, Joule heating, which is an irreversible process, is reduced and, furthermore, high electrical currents can be delivered to the external load.

In this review, first of all the general principles of thermoelectricity will be summarized (section I "Principles of thermoelectricity"). Section II, "Materials for thermoelectricity", will describe the principles for the optimization of TEG efficiency. Then, the most common thermoelectric materials currently available will be briefly illustrated. Section III will show the advantages of nanostructured materials, with respect to bulk ones, for the purposes of thermoelectric conversion. The development of materials for a large scale application of thermoelectric generation should consider a trade-off between optimal thermoelectric properties on the one hand and material availability, cost, sustainability and technological aspects [7] on the other hand. In this respect, silicon is the second most abundant element on the surface of Earth (after oxygen), it is a very sustainable and biocompatible material. Furthermore, due to its pervasiveness in the electronic market, silicon is one of the best known materials both from the physical and the technological point of views, and it is at the center of a worldwide manufacturing infrastructure. Thermoelectric applications of silicon are currently limited by its high thermal conductivity (148 W/mK). However, several studies have observed a strong reduction of thermal conductivity in rough silicon nanowires [8-10]. For this reason, section IV is dedicated to the review of the main techniques currently investigated for the fabrication of silicon nanostructures that can be integrated in devices for thermoelectric generation.

Review

Principles of thermoelectricity

A temperature gradient can be obtained placing a piece of conducting, or semiconducting, material between a hot (temperature T_H) and a cold (temperature T_C) heat source. As an effect of this temperature gradient, both heat and charge carriers (electrons or holes) tend to diffuse through the conductor, from the hot to the cold source. As a consequence of the charge carrier diffusion, a potential difference V is established between the hot and the cold extremity of the material (see Figure 1). This effect has been noted for the first time by Thomas Seebeck (1770–1831), who measured a current in a circuit made of different materials and subjected to a temperature gradient. The Seebeck coefficient S, also indicated as thermopower, can be written as:

$$S = \frac{V}{T_H - T_C} \tag{1}$$

A precise expression for S takes into account the temperature gradient $\partial T/\partial x$ and the generated electric field $\varepsilon = -\partial V/\partial x$ at the electrical equilibrium (current density $J = 0$):

$$S = \frac{\varepsilon}{\frac{\partial T}{\partial x}} \tag{2}$$

Following this definition, S is positive for p-doped semiconductors because if $\partial T/\partial x > 0$ (the temperature increases with x), holes tend to diffuse toward negative coordinates. Therefore, at the electrical equilibrium ($J = 0$) ε is positive (see Figure 1, in which a piece of p doped semiconductor is represented). In n-doped semiconductors, electrons diffuse from the hot part to the cold part, as do the holes, but their charge sign is opposite, so that S is negative.

Following Kirchhoff's law, at least two materials with different Seebeck coefficients must be used in order to obtain a potential drop in a circuit in which a temperature gradient is maintained. The basic cell of a thermoelectric generator is made of two semiconducting legs with opposite doping, placed thermally in

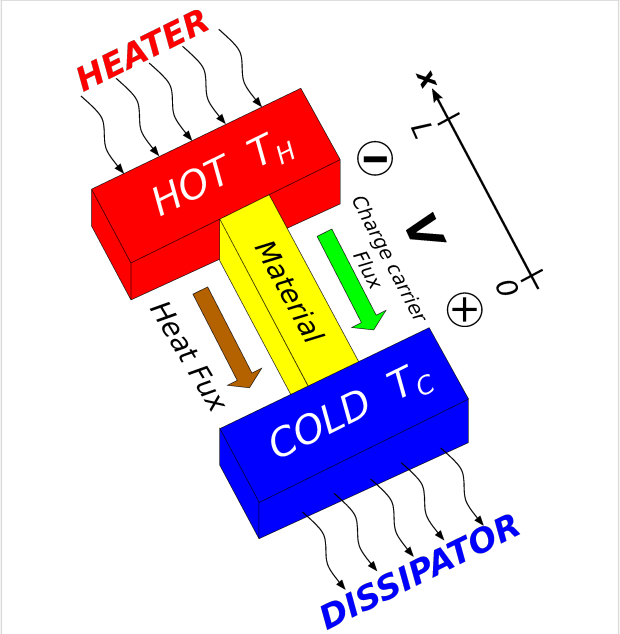

Figure 1: Sketch of a piece of semiconducting material, placed between a hot source (heater, temperature T_H) and a cold source (heat sink, temperature T_C). A potential difference V is established between the extremities, due to the charge carrier flux driven by the temperature gradient.

parallel and electrically in series as schematically shown in Figure 2. Both the heat flux and the charge carrier flux have the same direction, i.e., from T_H to T_C. The electrical series of the legs, that have opposite Seebeck coefficients ($S_p > 0$, $S_n < 0$), results in a potential drop proportional to the temperature difference:

$$V = \left(S_p - S_n\right)\left(T_H - T_C\right) = \left(S_p + \left|S_n\right|\right)\left(T_H - T_C\right) \quad (3)$$

An eventual load, applied to this generator (schematically represented by a resistor R_L in Figure 2a), can benefit of the carrier flux (electrical current) induced and sustained by the temperature gradient.

Conversely, if an electrical current is forced through the legs by means of an external generator (Figure 2b), heat is transferred from the cold side to the hot side by the charge carrier flux, and the system acts as a cooler. This effect has been investigated for the first time by Jean C. A. Peltier in 1834, who established a relationship between the heat flux Φ and the charge carrier flux (electrical current density J) imposed by the external generator:

$$\Phi = \Pi J \quad (4)$$

Where Π is the so-called Peltier coefficient. The Seebeck effect and Peltier effect have the same physical basis (the one is the reverse of the other), and an important relationship is established between S and Π: $\Pi = ST$. In principle, the same basic element made of two legs (electrically in series and thermally in parallel) can be used both to generate electrical power, if a temperature difference is maintained (by using for example a heater for T_H and a heat sink for T_C), and as a cooler, if electrical power is supplied by a battery. Even if in this review a particular emphasis on thermoelectric generation will be given, the same principles could be similarly applied to devices for thermoelectric cooling (Peltier cells). In practical applications, a

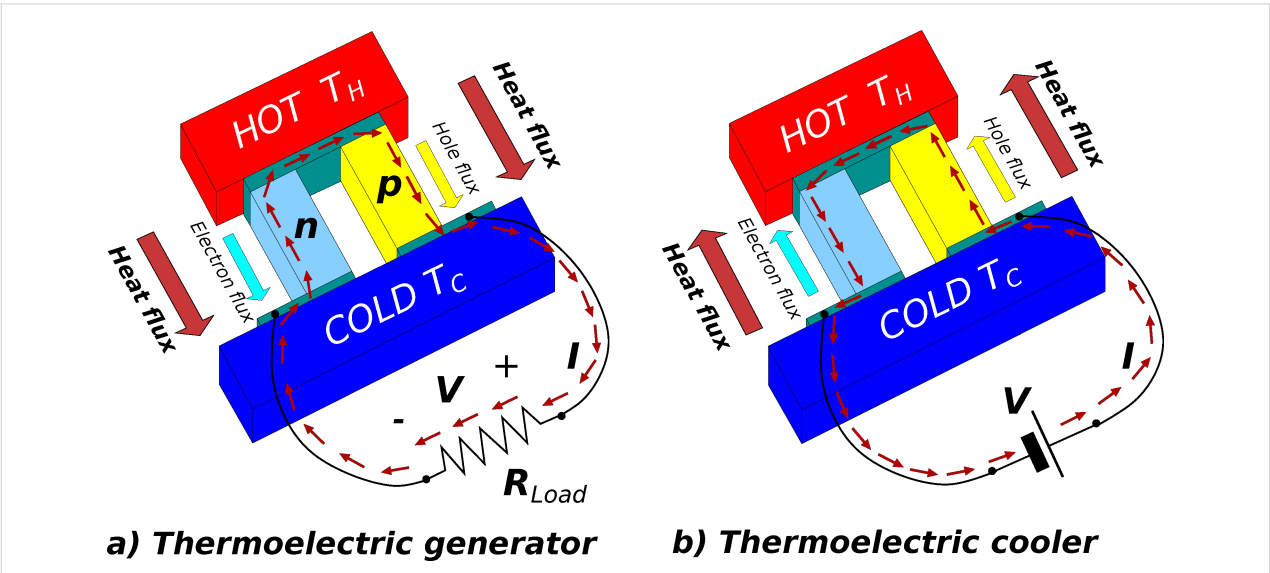

Figure 2: a) Sketch of a thermoelectric generator: two pieces of semiconducting materials with different (opposite) Seebeck coefficient can exploit a temperature gradient to deliver electrical power to an external load R_{Load}, indicated with R_L in the text. b) Sketch of a thermoelectric cooler: a battery imposes a current through the legs, so that the flux of the charge carriers brings heat from the cold extremity to the hot extremity of each leg.

TEG (or a Peltier cooler) is made of several basic elements placed in series (to increase the voltage) and/or in parallel (for high currents).

The properties of the electrical and thermal transports are resumed by two thermoelectric equations:

$$J = \sigma\varepsilon - S\sigma\frac{\partial T}{\partial x} \tag{5}$$

$$\Phi = STJ - k_t\frac{\partial T}{\partial x} \tag{6}$$

In these equations, the current density J is related to the electric field ε and to the field generated by the temperature gradient $S\partial T/\partial x$, because of the electrical conductivity of the material, σ. The heat flux Φ depends on the current density J, through the Peltier coefficient $\Pi = ST$, and on the temperature gradient $\partial T/\partial x$, because of the thermal conductivity of the material, k_t. A thermoelectric generator is characterized by its conversion efficiency η, defined as the electrical power delivered to the load R_L divided by the thermal power extracted from the hot source. In terms of heat flux, assuming that the legs are adiabatic on the lateral sides, the heat power exchanged with the hot source per surface unit is $\Phi_H = \Phi(x = 0)$. The heat drained by the cold source, and wasted, is $\Phi_C = \Phi(x = L)$. Therefore, the converted electrical power, delivered to the load, is $\Phi_H - \Phi_C$ multiplied by the total cross section surface of the legs, so that the efficiency is:

$$\eta = \frac{\Phi_H - \Phi_C}{\Phi_H} \tag{7}$$

without loss of generality, legs with constant cross section surface have been hypothesized for the sake of simplicity.

Given T_H and T_C, the total current I in the generator depends on the thermoelectric parameters (S, σ and k_t), on the geometrical parameters (length and cross section surface of the generator legs), and on the load resistance R_L. Combining the thermoelectricity Equation 5 and Equation 6 with the stationary heat equation $\partial\Phi/\partial x = \varepsilon J$, it is possible to determine $T(x)$ in the legs, and also Φ_H and Φ_C, so that an expression for the efficiency η can be obtained:

$$\eta = \frac{R_L I^2}{ST_H I - \frac{1}{2}R_g I^2 + K\left(T_H - T_C\right)} \tag{8}$$

where R_g and K are the total electrical resistance and the total thermal conductance of the generator, which can be evaluated respectively from the material electrical resistivity $\rho = 1/\sigma$ and from the material thermal conductivity k_t, to be combined with the geometrical parameters of the legs (length and cross-section surface). Given a temperature difference $T_H - T_C$, the generator acts as a voltage generator with an open circuit voltage $V_g = S_{total}(T_H - T_C)$, where $S_{total} = S_p + |S_n|$, and a series (parasitic) resistance R_G. The current I depends on the generator electrical resistance R_g and on the load resistance R_L. In the evaluation of these expressions, the variation with temperature of the thermoelectric parameters S, σ and k_t, has been neglected. These parameters need to be evaluated at the average temperature $\overline{T} = \left(T_H + T_C\right)/2$. In order to obtain the maximum conversion efficiency, the load resistance R_L, which appears both explicitly an through the current I in Equation 8, needs to be optimized. By simple mathematical passages, it is possible to show that the optimum load condition, for which η is maximum, is:

$$R_L = R_G\sqrt{Z\overline{T} + 1} \tag{9}$$

where the factor Z:

$$Z = S^2\frac{\sigma}{k_t} \tag{10}$$

is the parameter that qualifies the materials for thermoelectric conversion. If optimum load conditions are established, the maximum conversion efficiency is:

$$\eta_{max} = \frac{\Delta T}{T_H}\frac{\sqrt{Z\overline{T} + 1} - 1}{\sqrt{Z\overline{T} + 1} + \frac{T_C}{T_H}} \tag{11}$$

The first factor of this expression, $\Delta T/T_H$, is the Carnot efficiency, that is the maximum conversion efficiency fixed by the second principle of thermodynamics. The second factor depends on the parameter Z, or better on the dimensionless parameter $Z\overline{T}$, that must be as high as possible to have high efficiencies. If $Z\overline{T} \to \infty$, the efficiency η has the maximum value obtainable with the two heat sources T_H and T_C: $\eta = \Delta T/T_H$, i.e., the Carnot limit. The development of a good thermoelectric material should aim to obtain a factor $Z = S^2\sigma/k_t$ as high as possible: A good thermoelectric material should have high Seebeck coefficient S and electrical conductivity σ, and small thermal conductivity k_t.

Materials for thermoelectricity

Several experimental works on thermoelectric materials are devoted to maximize the power factor $S^2\sigma$, which is proportional to the power delivered to the load R_L. Given two heat sources (or better a heat source T_H and a heat sink T_C), the optimization of $S^2\sigma$ leads to the maximization of the power that a TEG can deliver to the load. In this respect, graphene [11] could offer interesting opportunities, in particular for its high electrical conductivity σ. The Seebeck coefficient of pristine graphene is of the order of 10–100 μV/K [12,13]. Several solutions for increasing this value up to several hundreds of μV/K, such as plasma etching treatments [11], have been carried out successfully. A great enhancement of S has been predicted in graphene nanoribbons [14,15], and the use of a suitable array of nanoelectrodes has been proposed for obtaining a giant thermoelectric power [16].

The maximization of the power factor $S^2\sigma$ is important in those applications that require a power as high as possible, and that have enough thermal energy available on the hot source. However, in many practical applications, one of the key points is to exploit as much as possible the thermal energy that is available on the heat source, so that energy conversion efficiency, more than maximum delivered power, is the main issue to be faced. In other words, for the majority of applications the main target is to optimize energy, instead of maximize power. As for example, the application of TEGs as alternative to photovoltaic cells must aim for the maximum exploitation of solar energy, hence to the maximum conversion efficiency. A strong increase of conversion efficiency would also allow for the minimization of the heat dissipated on the cold side, so that the exchanging surface of the dissipating system can be reduced.

Therefore, the development of a good thermoelectric material, useful for the majority of thermoelectric applications, should aim to maximize the efficiency η (see Equation 11). Hence, the figure of merit $Z\bar{T}$, and in particular the factor $Z = S^2\sigma/k_t$, must be as high as possible. This means that a good thermoelectric material, as previously stated, should have a high Seebeck coefficient S and a high electrical conductivity σ, but also a low thermal conductivity k_t. In this respect, graphene exhibits a very high thermal conductivity, higher than 3000 W/mK [17], so that the figure of merit of graphene-based thermoelectric generators would be very small.

In Figure 3 the efficiency of a thermoelectric generator is reported as a function of the hot source temperature T_H. The curves have been evaluated with Equation 11, assuming that the cold source is maintained at room temperature (T_C = 300 K). Curves for different values of the material-dependent parameter Z are shown. The maximum efficiency theoretically obtainable (Carnot efficiency $\Delta T/T_H$) is also reported as a function of T_H. In the figure, TEG efficiencies are also compared with a few conventional techniques for energy production (see the sketch on the right). It can be seen that if research can provide materials with sufficiently high values of the parameter Z, thermoelectric generation will become comparable with other techniques. It must be noted that the parameters S, σ and k_t, and thus the parameter Z, are strongly temperature dependent. Furthermore, these parameters depend on the temperature through nonlinear relationships, that in general can be determined only by experimental measurements. Therefore, a numerical solution of the thermoelectric equations (Equation 5 and Equation 6), which takes in account the dependence of the material parameters on the temperature, must be implemented for an exact calculation of the TEG efficiency [18]. The graphs reported in Figure 3 have been evaluated considering Z constant in the temperature range from T_H to T_C. Hence, these curves can be used only for a rough indication of the Z value that is required for a desired efficiency. The Z values suggested by the graph

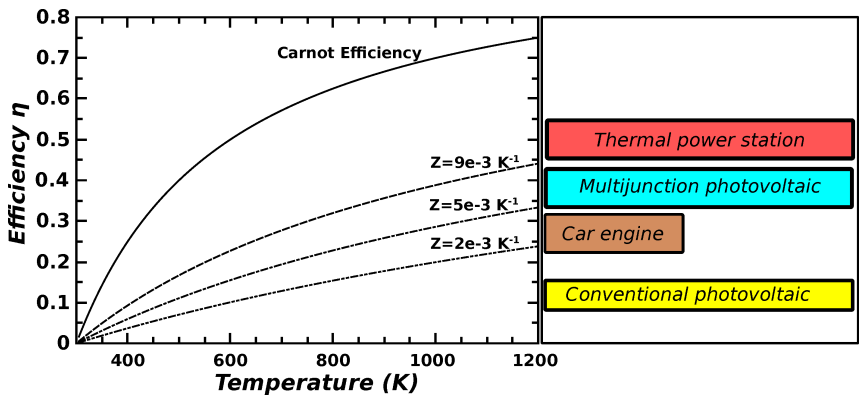

Figure 3: Efficiency of a thermoelectric generator for different values of the material-dependent parameter $Z = S^2\sigma/k_t$, as a function of the hot source temperature T_H. The cold source temperature is T_C = 300 K. The efficiency of conventional techniques for energy production is also reported for comparison.

can be interpreted as the optimum Z parameter that should be maintained in the temperature range between the selected T_H and 300 K.

In order to compare the thermoelectric performances, in previous works on thermoelectricity the so-called figure of merit $Z\overline{T}$ (in general ZT) has been introduced as a comparison parameter. ZT is a dimensionless parameter that appears explicitly in the efficiency expression (Equation 11), and a material with a ZT value greater than 1 is, in general, considered acceptable for thermoelectric applications. However, the use of the figure of merit ZT as performance parameter can be misleading, because it is not directly connected to the efficiency that strongly depends on the temperature difference. Furthermore, the temperature dependence of ZT is even stronger than that of the Z parameter. If for example a material shows $ZT = 2.0$ at an average temperature of 400 K, this means that Z must have an almost constant value of 5×10^{-3} K^{-1} in the temperature range between 300 and 500 K (assuming the room temperature of 300 K as cold source temperature T_C). For TEGs that must work with small temperature differences at about room temperature, as for example in cooling/generating systems for domestic plants, a material with $Z\overline{T} = 2.0$ can be thought to be a very good one because $Z = 7 \times 10^{-3}$. However, the temperature difference is very small, hence the the expected efficiency will be very low. For these reasons, in the following sections the Z parameter will be considered for comparing TE materials.

Many tellurium compounds showed interesting TE potentialities. The most widely used material for thermoelectricity, extensively studied since 1954 [19-21], is Bi_2Te_3. It is a narrow gap (about 160 mV at 300 K) semiconductor, whose electrical conductivity can be increased by doping, either n- or p-type. Its moderately high Seebeck coefficient (between 0.1 and 0.25 mV/K), and in particular its low thermal conductivity (between 2 and 3 W/mk at room temperature), gives a Z factor of about 2.5×10^{-3} K^{-1} at room temperature (ZT of the order of 0.7–0.8). However, the Z factor reaches its maximum value in a narrow temperature range (about 50 K wide) around 300 K. Hence, TEGs based on Bi_2Te_3 can be usefully employed only for small temperature differences at about room temperature. Higher Z factor values can be obtained by ternary alloys based on bismuth/tellurium and antimony (typically p-doped) or selenium (typically n-doped) [22-25]. Values of the Z factor in excess of 4.5×10^{-3} K^{-1} (ZT in excess of 1.4) at room temperature have been found. A further increase of the Z factor has been measured in nanostructured bismuth antimony telluride alloys, because phonon scattering at nanocrystal boundaries gives a reduced thermal conductivity [26]. Hovewer, TEGs based on bismuth telluride compounds have a small operating temperature range, because the Z factor rapidly decreases well below 2×10^{-3} K^{-1} for $T > 400$ K, as shown in Figure 4. Lead telluride (PbTe) compounds [27,28] exhibited a smaller Z value, of the order of 1.5×10^{-3} K^{-1}, but its value is almost stable on a large temperature range (from room temperature up to 800 K, see Figure 4). Therefore, PbTe-based TEGs can operate with large temperature differences, so that they can pursue higher efficiencies with respect to other tellurium based materials. Nanocrystalline PbTe compounds [29,30] showed an increment of the Z factor in excess of 2×10^{-3} K^{-1}, still maintaining a large temperature range. Even if all these TE characteristics (high Z factor and large temperature range) of tellurium compounds are very attractive for applications, it must be mentioned that tellurium is a very rare material on the surface of Earth. Moreover, tellurium is a toxic material, thus disposal of tellurium-based TEG devices would arise noticeable environmental problems. For these reasons, research on thermoelectricity is focussing on tellurium-free materials. Skutterudites ($CoSb_3$), filled with rare or alkaline earths or metals, show interesting perspectives because of their reduced thermal conductivity [31]. Slack suggested [32] that the random distribution of filling ions as well as their "rattling" effect increases the phonon scattering on a large spectrum, so that the thermal conductivity is strongly reduced and Z is quite high. Several filling elements, such as La [32], Co [33], Ta [34], and others, have been experimented. Recently, filled [35-37] skutterudites were found with Z factors of about 2×10^{-3} K^{-1}, for temperatures up to 800 K. Skutterudites are, in general, based on elements that are not very rare, however sustainability problems could arise from the presence of cobalt.

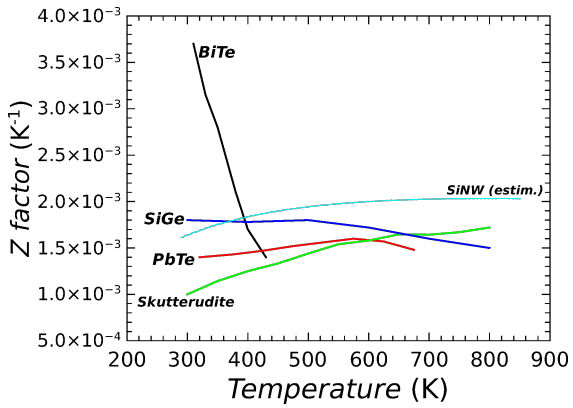

Figure 4: The Z parameter is reported as a function of temperature for few most common TE materials (n type). Experimental data from literature have been used, and in particular: curve BiTeSe from [23]; PbTe from [28]; skutterudites from [37]; and SiGe from [38]. Numerical estimation of the Z parameter for a silicon nanowire 50 nm wide and n-doped 5×10^{19} cm^{-3} is also reported.

A big research effort has been devoted to the enhancement of TE properties of compounds based on silicon. Silicon is one of

the most well known materials both from the physical and from the chemical point of view, it is abundant on the surface of Earth, and it is very sustainable. Furthermore, devices based on silicon could exploit a large operating temperature range, because silicon is a very stable material for temperatures in excess of 900 K. Silicon–germanium alloys, SiGe [38,39], and superlattices [40,41] showed a good Z factor value, of the order of 2×10^{-3} K^{-1} at 800 K. Furthermore, they can be used for power generation in devices exploiting temperature differences between 900 K and 300 K. Other silicon compounds are actually under development. Very promising results have been obtained with magnesium silicide (Mg_2Si) [42,43] compounds, which are low cost and non-toxic. Highly boron-doped nanocrystalline silicon [44] is another promising material for its increased electrical conductivity and Seebeck coefficient compared to bulk silicon.

Advantages of nanostructured materials for thermoelectricity

Thermoelectric parameters are enhanced in structures with reduced dimensionality. As pointed out by Dresselhaus and co-workers in pioneering theoretical works [45,46], and further investigated also by other authors [18,47,48], the Seebeck coefficient increases in bidimensional, or monodimensional (nanowires), structures. The Seebeck coefficient strongly depends on the distribution in energy of the charge carriers (electrons or holes), and in particular it increases when the average difference between the carrier energies and the Fermi energy increases. In low dimensional systems, the density of states is reshaped with respect to bulk systems, in such a way that charge carriers are spread to higher energies. This produces an increase not only of S but also, in principle, of the electrical conductivity σ, with a benefit for the $Z = S^2\sigma/k_t$ parameter. However, first of all structures with diameters of the order of a few nanometers are requested in order to obtain a noticeable increase of the Seebeck coefficient with respect to its bulk value. Moreover, the electrical conductivity of very small nanostructures is strongly reduced by the surface scattering of charge carriers. As an example, Figure 5 shows the Seebeck coefficient evaluated for silicon nanowires with triangular cross section [18], as a function of the nanowire width (triangular base) W: S increases only if the nanowire width is reduced below 5 nm. It is to be noted that S increases noticeably for low doping values, because the Fermi energy level decreases with respect to the bottom of the conduction band, and consequently the energy difference between charge carriers and Fermi level increases: Values of the order of 1 mV/K can be obtained in silicon for doping values smaller than 10^{16} cm^{-3}.

The main point in the use of nanostructured materials for thermoelectricity is the strong reduction of the thermal conductivity k_t compared to the bulk value. This strong reduction of k_t has been measured in experimental works on nanowires [8,49,50], and confirmed by several theoretical studies [51-54]. The thermal conductivity of the material k_t can be written as the sum of two main contributions, $k_t = k_e + k_{ph}$, hence the parameter Z can be written as $Z = S^2\sigma/(k_e + k_{ph})$. The first term k_e takes into account the heat brought by the charge carriers (electrons or holes) that diffuse from the hot part T_H to the cold part T_C. The second term k_{ph} takes into account the heat conduction through the material crystalline lattice, due to phonon propagation. k_e (e for electrons, the same for holes) depends on charge carrier concentration and mobility, and it is strictly connected with the electrical conductivity σ. The thermal conductivity of metals is principally due to k_e, which is related to the electrical conductivity σ through the well-known Wiedemann–Franz law:

$$\frac{k_e}{\sigma T} = \left(\frac{\pi}{3}\right)^2 \left(\frac{k}{q}\right)^2 = \left(156\,\mu V \cdot K^{-1}\right)^2 \qquad (12)$$

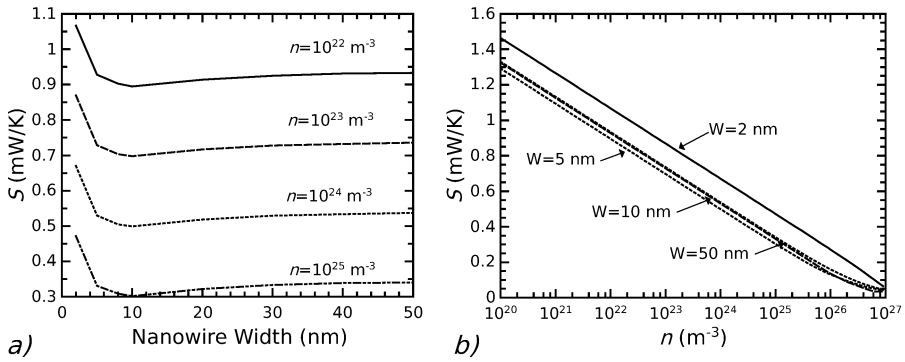

Figure 5: Panel (**a**): Seebeck coefficient in silicon nanowires with triangular cross section as a function of the nanowire width, for different values of n-doping. Panel (**b**): Seebeck coefficient in silicon nanowires as a function of the doping for different nanowire widths. Reproduced with permission from [18], Copyright (2013) AIP publishing LLC.

The phonon contribution to the thermal conductivity, k_{ph}, is instead predominant in semiconductors. For example, in bulk silicon k_t = 148 W/mK, meanwhile k_e, which depends on doping (i.e., on the electron or hole concentration), is always smaller than 1 W/mK for doping values up to 10^{19} cm^{-3}. When the dimensions of nanostructures (as for example the nanowire width/diameter) become comparable with the phonon mean free path, which is of the order of several tens of nanometers at room temperature, the phonon propagation is limited by the surface scattering. It has been observed that the effect of thermal conduction reduction by surface phonon scattering is enhanced in nanostructures with rough surfaces. Several experimental works have been dedicated to the measurement of the thermal conductivity in rough silicon nanowires [9,55-59], and it was found that k_t decreases down to few W/mK (bulk silicon thermal conductivity = 148 W/mK) in nanowires with diameters of several tens of nanometers (20–100 nm). This value is well below the so-called Casimir limit [60,61], which is the minimum thermal conductivity theoretically obtainable when a completely diffusive phonon scattering on the nanowire surface is assumed. On the basis of these intriguing experimental results, several works [62-67] developed theoretical models for phonon boundary scattering, taking into account coherent effects. For an appropriate scale of surface roughness, these coherent effects can be important for phonon reflection and suppression. Therefore, accordingly with the experimental results, these models confirm that a phonon thermal conductivity below the diffusive limit can be obtained in rough nanowires.

On the other hand, the electrical conductivity in rough nanowires is only slightly affected by the surface scattering of charge carriers. Figure 6 shows the electrical conductivity σ in n-doped silicon nanowires, normalized with respect to the value σ_{Bulk} obtained in bulk silicon with the same doping concentration. These curves have been numerically evaluated with a simple model that takes into account a completely diffusive scattering of electrons on the nanowire surfaces. Variations of the electrical conductivity, with respect to its bulk value, are significant only in nanowires narrower than 20 nm. This is especially true in particular for high doping values, for which electron mobility is limited by impurity scattering and the electron mean free path is very small with respect to the nanowire diameter. Thus, in nanowires wider than 20–40 nm, phonon thermal conduction k_{ph} can be strongly reduced by increasing the surface roughness, meanwhile the electrical conductivity remains comparable with that of bulk silicon. Therefore, a strong enhancement of the factor $Z = S^2\sigma/(k_e + k_{ph})$ can be obtained in rough nanowires wider than 20–40 nm. If k_{ph} is reduced to values smaller than k_e, doping can be optimized so that the Z factor can be further increased [18]. If $k_{ph} < k_e$, the Z factor becomes $Z = S^2\sigma/(k_e + k_{ph}) \approx S^2\sigma/k_e$ and, as mentioned above, the Wiedemann–Franz law states that the ratio σ/k_e is constant. Thus, a suitable decreasing of the doping leaves this value unchanged, while the Z factor improves because S, which appears squared in the Z expression, increases. In Figure 4 the estimated Z factor for a silicon nanowire 50 nm wide, n-doped 5 × 10^{19} cm^{-3}, is reported for a comparison with other TE materials. An optimistic value of k_{ph} = 0.8 W/mK (k_e given by the doping) has been assumed for the numerical estimation of Z.

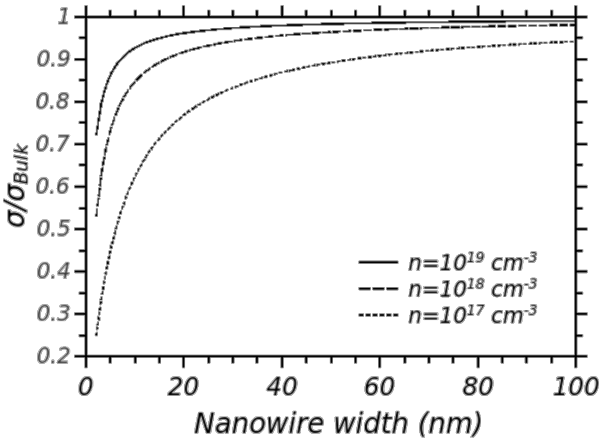

Figure 6: Electrical conductivity σ of a silicon nanowire as a function of the nanowire width (triangular cross section), normalized with respect to the bulk electrical conductivity σ_{Bulk}.

Nanostructured silicon for thermoelectricity

In the last years, nanowires have been extensively investigated for their potentialities as advanced electronic devices [68-70] and as sensing elements [71-73]. For these purposes, devices based on single, or very few, silicon nanowires have been fabricated exploiting both bottom-up and top-down approaches. However, devices for thermoelectric generation must be able to handle high powers, that means high currents and voltages. Thus, techniques for the massive and reliable production of a huge number of nanowires, well organized and electrically interconnected in a well determined way, need to be developed. Bottom-up approaches are based on the crystalline growth of nanowires by means of chemical vapour deposition (CVD) techniques. The most common CVD technique for the fabrication of silicon nanowires is the vapor–liquid–solid (VLS) growth [74,75], developed in particular by the group of Lieber at Harvard [76-80], and rapidly diffused and applied by several other groups [81-85]. The VLS growth is based on the catalytic effect of metal (gold or iron) nanoparticles, deposited on a silicon substrate. At high temperatures, an eutectic alloy is formed among metal and Si, supplied by a silane (SiH_4) flux (or

others silicon-based gases). A precise calibration of silane flux and reaction temperature gives a supersaturation of the melt and induces a transformation from the liquid alloy phase to solid Si that crystallizes under the metal nanoparticle. In this way, crystalline silicon nanowhiskers grow perpendicularly to the substrate.

Exploiting the VLS-CVD technique, silicon nanowires have been grown between small suspended silicon masses, fabricated by micromachining techniques applied to silicon-on-insulator (SOI) substrates [86,87]. The silicon masses are maintained at different temperatures, so that a thermoelectric microgeneration has been obtained.

The fabrication of silicon nanostructures [88,89] and nanowires [69,90-96] by means of top-down approaches starts from a macroscopic structure, such as a silicon wafer. Suitable patterns are defined on the wafer surface by advanced lithographic tools, such as electron beam lithography [90,91], atomic force lithography [94,95,97] and even optical lithography [69,93]. Etching, oxidation and other fabrication processes are then used to define structures with nanometric dimensions. Top-down fabrication is somewhat more complex compared to the bottom-up approach that allows for the massive, low-cost, production of nanostructures. However, the top-down fabrication allows for the simultaneous fabrication of nanostructures and nanowires together with contacts, connections and control gates, so that the fabrication process yields fully functional devices. Conversely, bottom-up approaches allow for an easier production of nanowires, but then the fabrication of devices requires the development of complex procedures for the positioning of nanowires with respect to contacts and connections.

A typical top-down process, based on electron beam lithography, anisotropic silicon etching and stress-limited oxidation, is shown in the sketches of Figure 7. This process [91-93] has been developed on a silicon-on-insulator (SOI) substrate, <100> oriented, which is becoming largely employed in the semiconductor industry for the production of integrated circuits. The same process can be used on substrates with different thicknesses of the silicon top layer, in the range between 100 and 300 nm, by adapting the mask dimensions and oxidation parameters. The doping of the silicon top layer can be tailored, both as a type (n or p) and as doping concentration, by exploiting standard silicon doping processes. A 50–80 nm thick silicon dioxide (SiO_2) top layer, to be used as a mask for the silicon etching, is grown by dry thermal oxidation. This top SiO_2 layer is patterned by means of electron beam lithography through standard poly(methyl methacrylate) (PMMA) resist. An etching with well calibrated buffered HF (BHF) allows for the transferring of the pattern from the PMMA to the SiO_2 layer (reactive ion etching can be used as alternative). Once the SiO_2 mask is defined, the top silicon layer is etched anisotropically. Plasma etching/ reactive ion etching (RIE), which is a standard process in integrated circuit fabrication, can be used. However, a simple and more convenient technique is the wet silicon anisotropic etching in alkaline solutions [98,99], typically based on potassium hydroxide (KOH) or tetramethylammonium hydroxide (TMAH). As for example, the silicon top layer can be etched in KOH 35% in volume at 43°C for 5–7 min: The etching time is not very critical, because the etching stops (it is very low) on the buried oxide layer, and on {111} silicon crystalline planes. At the end of the etching process, the nanowire has a very regular trapezoidal cross-section, the minor base of which at the top is a {100} plane with a width W_{top} determined by the lithog-

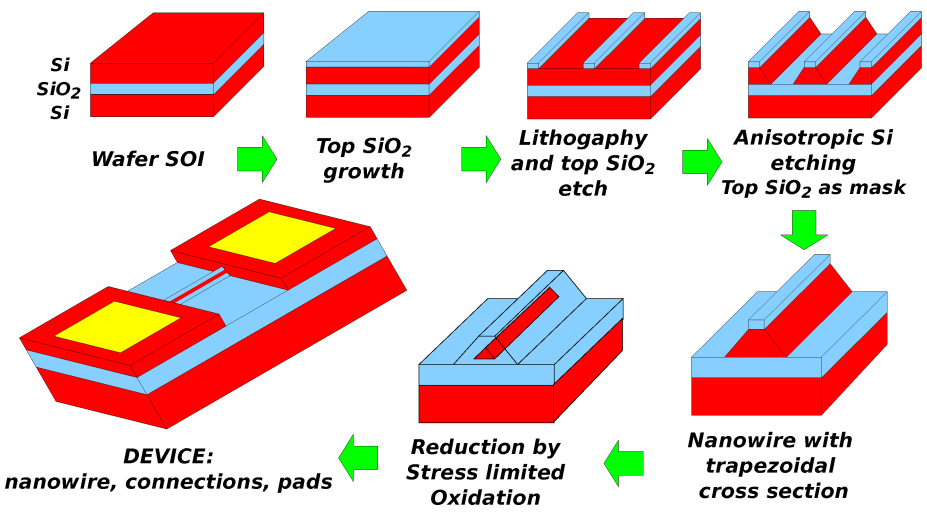

Figure 7: Sketch of a top-down fabrication process for a device based on a silicon nanowire.

raphy. The sloping walls are {111} crystalline planes, where the anisotropic etching stopped. The major base at the bottom has a width W that depends on W_{top} and on the thickness of the silicon top layer. A trapezoidal cross section allows for an easy and well controllable reduction of the nanowire width by stress-limited oxidation [91,92]. In particular, the silicon oxidation proceeds faster on the sloping sides (that are {111} planes) of the sections, because the oxide growth rate is faster in <111> directions.

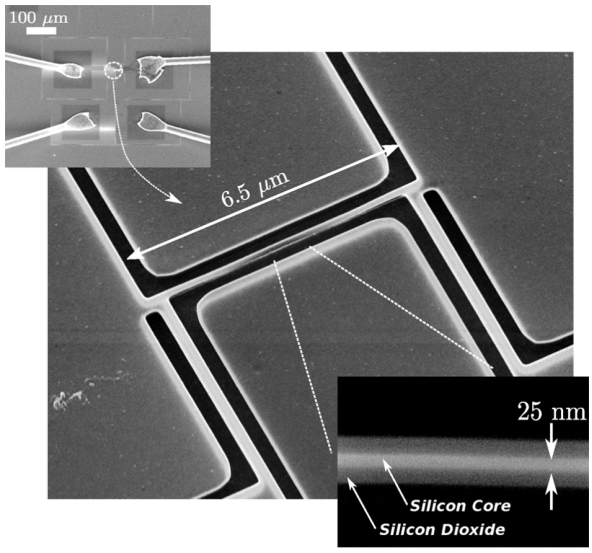

Figure 8: A composition of SEM images of a device, based on a single silicon nanowire positioned between four contacts to be used for electrical characterization. The top-down process allows the simultaneous fabrication of the nanowire and of the interconnections-contacts. Top left: overview of the device, middle: nanowire with two contacts at the extremities and two side contacts, bottom right: enlargement of the central region. For more details refer to the text.

A correct design of the top width W_{top}, defined by lithography, with respect to the top silicon layer thickness, allows for the formation of a triangular cross section during the oxidation process. Once a triangular cross section is obtained, the increasing of the oxide volume induces a mechanical stress that limits the oxidation rate. Therefore, a well controlled reduction of the nanowire width can be obtained simply by controlling the oxidation temperature and time. With this technique, a very narrow nanowire can be fabricated even if a relaxed lithography, as for example optical lithography, is used for the definition of the initial W_{top}. Figure 8 is a composition of SEM images of a typical device based on a top-down fabricated silicon nanowire. The top inset is a overview of the device, showing metal pads, bonded with microwires to external connections. The main image shows the nanowire, which is 6.5 μm long. It is fabricated together with two contacts at the extremities and two side contacts to be used for four point measurements. The bottom inset shows an enlargement of the central region: the silicon nanowire core, 25 nm wide, is embedded in silicon dioxide. A calibrated BHF etching, which can be performed at the end of the oxidation process, allows for the tailoring of the silicon dioxide thickness around the nanowire silicon core.

This top-down technique is very flexible and it can be used for the fabrication of well-organized networks made of a large amount (more than 10^5 nanowires/mm^2) of very small nanowires. Figure 9 shows sketches of networks, made of nanowires placed in multiple series and parallels between a top and a bottom contact. Figure 10 and Figure 11 are compositions of SEM images of typical silicon nanowire networks. The nanowires are 3 μm long in Figure 10 and 10 μm long in

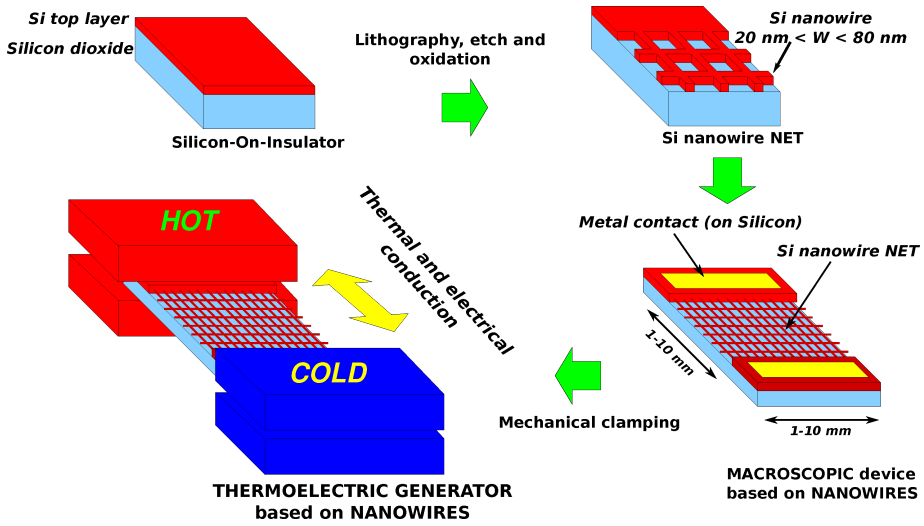

Figure 9: Sketches of the fabrication and mechanical clamping of a macroscopic thermoelectric generator based on nanowires.

Figure 11. It is easy to demonstrate [100,101] that these very large area arrays of very narrow, micrometers long, silicon nanowires are equivalent to the parallel arrangement of very narrow SiNWs with a total length of several millimeters (see the top right sketch of Figure 11). These networks can be used as devices for thermoelectric generation because their macroscopic dimensions make it possible to clamp them between a hot and a cold source, as shown in Figure 9. These macroscopic thermoelectric generators are able to exploit the properties shown by materials at the nanoscale, and in particular the reduced thermal conductivity of nanowires. Furthermore, nanowire networks are very reliable with respect to unavoidable failures (breakages) of nanowires, which can happen during the fabrication process or during the operation of the device. This high reliability is due to the high level of interconnections (vertical and horizontal branches) of the net. It has been demonstrated [100] that the total top to bottom electrical resistance of the net increases only negligibly for a nanowire failure percentage up to 40%, that means the failure (breaking) of almost half of the nanowires. The resistance of the net shows also a low sensitivity with respect to the non-uniformity (dispersion) of the nanowire width. The Seebeck coefficient of nanowire networks has been measured [101], and its value resulted in a good agreement with the doping, found by measuring the nanowire electrical conductivity. However, the measured doping concentration was slightly higher than the original doping concentration of the silicon top layer. A reduction of the thermal conductivity in devices based on top-down nanowires has been confirmed by means of a self-heating, self-measuring technique [102]. This technique is based on the principle of 3-ω thermal conductivity measurements [103], already applied to carbon nanotubes [104], and exploits the heat generated in the nanowire by the Joule effect when a current passes through it. The temperature is determined by means of an accurate *I*–*V* measurement, through a suitable model which uses the thermal conductivity as a parameter to be fitted with experimental data.

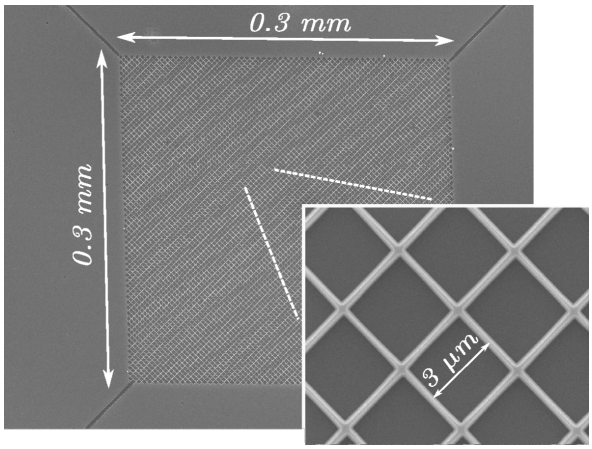

Figure 10: Composition of SEM images of a large area network, made of silicon nanowires 3 µm long.

The main disadvantage of top-down nanowire networks is that they are defined in a very thin layer which must be supported by a substrate. The silicon top layer can be easily detached from the silicon substrate, and positioned on another substrate that must be a good electrical and thermal insulator. Alternatively,

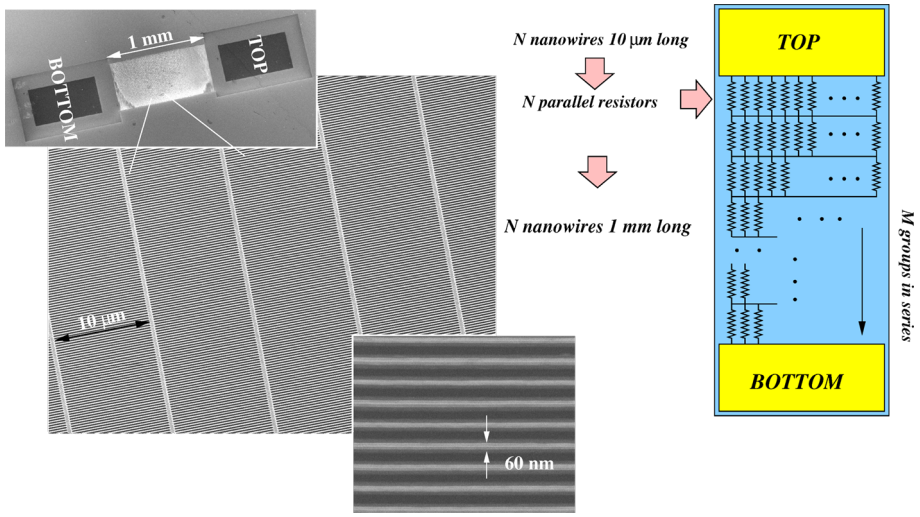

Figure 11: Composition of SEM images of a large area network with a different texture, with respect to Figure 10. An huge number of nanowires, 10 µm long and 60 nm wide, are placed in series and in parallel. The top right sketch shows a resistor network, that represents the silicon nanowire network both from the electrical and from the thermal point of view. Reproduced with permission from ref.[101], Copyright 2013 American Chemical Society.

with slight modifications to the process, a polysilicon layer deposited on a thermally insulating substrate can be used as starting material. Multiple parallel layers can be positioned and stacked on the same substrate, so that the total current (and electrical power) delivered by the device increases.

Another top-down technique for the fabrication of silicon nanowires is schematically represented in Figure 12. This technique exploits highly anisotropic silicon etching for the fabrication of dense arrays of nanowires perpendicular to the wafer surface. A suitable mask with nanometric features is patterned on the surface of a standard n- or p-doped crystalline silicon wafer, and then a vertical, highly anisotropic, etching allows for the definition of nanowires. The main advantage of this technique is that a huge number (more than 10^7 nanowires/mm^2) of parallel nanowires can be simultaneously fabricated on large surfaces. However, the nanowire length relies on the ability of performing high aspect ratio vertical etches, which is limited not only by the etching selectivity but also by the reduced mechanical stability of very long and narrow nanowires. Deep reactive ion etching (DRIE) is a plasma etching technique that alternates vertical etching steps (for example by SF_6) and polymerization steps (by CF_4) [105-108]. Each polymerization step provides a conformal polymer deposition, meanwhile each etching step that follows is anisotropic. Therefore, the etching step removes the polymer on the bottom of the feature while a passivating polymer layer is preserved (or only partially removed) on the sidewalls. In this way, the sidewalls of the features are protected, and the etching proceeds vertically during successive etching and passivation steps. Deep vertical etches can be obtained with a huge number of alternate etching/passivation steps. For its importance and utility also in other fields, such as integrated circuits and the fabrication of microelectromechanical systems (MEMS), this technique has been improved and developed in the course of the years, with respect to both etching/polimerizating chemical agents and process temperature and step time [106]. Silicon pillars smaller than 100 nm with aspect ratios greater than 50:1 [109] or even 100:1 [110,111] have been fabricated, and thermoelectric power generators based on vertical DRIE fabricated nanowires, few micrometers long, have been tested [112,113].

A very promising technique, which could allow for the fabrication of vertical nanowires with a length of several tens of micrometers, is the silicon metal assisted chemical etching (MaCE) [114-116]. The thermal conductivity of crystalline nanowires, obtained by MaCE, has been measured by Hochbaum and co-workers [9]. In the MaCE technique, a patterned film (or nanoparticles) of noble metals (most commonly gold or silver, but also platinum) on a silicon substrate is used to catalyze the chemical etching of silicon by an aqueous solution of HF and an oxidant as H_2O_2. Following the most accepted model, H_2O_2 is reduced at the metal through the reaction:

$$H_2O_2 + 2H^+ \rightarrow 2H_2O + 2h^+ \qquad (13)$$

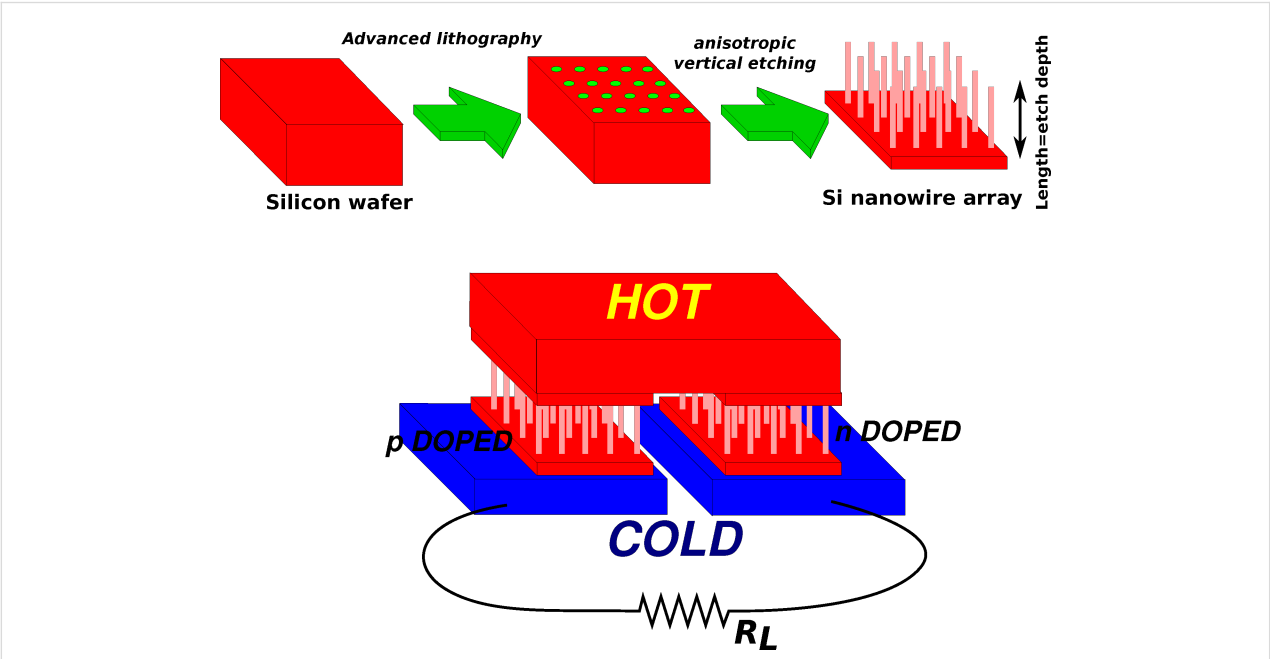

Figure 12: Sketch of the fabrication of vertical nanowire arrays. A sketch of a thermoelectric generator, based on vertical SiNWs, is also shown. Standard silicon doping processes can be used for the fabrication of both n- and p-doped nanowires.

Thus, the metal acts as a microscopic cathode injecting holes in the underlying silicon (i.e., withdrawing electrons from silicon) and the silicon undergoes oxidative dissolution in the presence of HF. Therefore, silicon in direct contact with the metal is dissolved so that the metal sinks into the substrate, and the metal–silicon (Schottky) junction is maintained. In this way, the etching front (metal–silicon interface) moves deeper and deeper into the silicon substrate. Conversely, the silicon etching is very slow in regions without metal coverage, because the electrochemical potential of H_2O_2 is much more positive than the silicon valence band energy, and direct injection of holes in silicon is very difficult. Therefore, vertical trenches with high aspect ratio [117-119] (Figure 13) and in particular silicon nanowires narrower than 100 nm and with a length of several micrometers [120-126] can be obtained by using metal masks with suitable patterning. However, if the generation of holes through the reducing reaction (Equation 13) is faster than the silicon oxidation/etching reaction, holes generated at the silicon–metal interface can diffuse toward confining, metal-free, regions [127]. Thus, silicon can become partially etched in neighbouring regions around the metal features [117,124,128] (Figure 14). This limits the minimum distances between metal patterns, as for example the nanowire pitch. Furthermore, hole diffusion in metal-free regions gives porous vertical structures. Porous nanowires must be avoided, because they have a reduced electrical conductivity with respect to bulk silicon, and their Z factor is not optimized. Conversely, if the hole generation rate at the metal interface is too low, the etching is not uniform and looses its verticality. In particular, very small metal features as nanoparticles [115,117,119,129] sink into the silicon following random paths, instead of proceeding vertically (perpendicular to the Si surface).

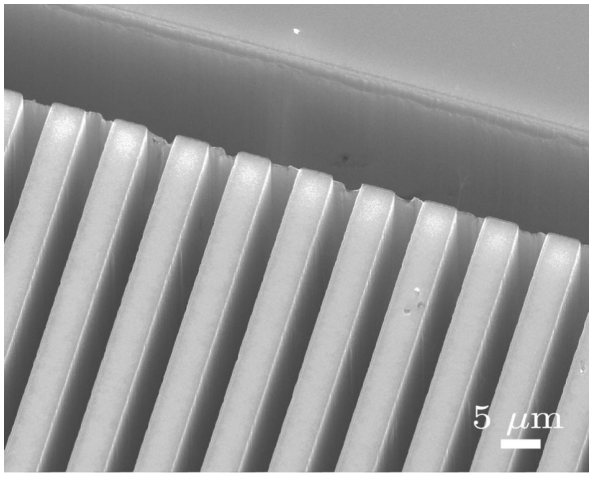

Figure 13: SEM image showing a top view of very deep trenches in silicon, obtained by MaCE. Patterned gold stripes have been used as catalyst.

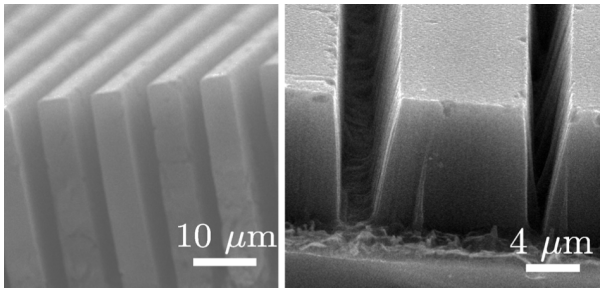

Figure 14: The SEM image on the left shows a cross section of vertical structures, obtained by MaCE etching: Patterned Au structures have been used as a catalyst. The etching solution was $HF:H_2O_2:H_2O$ 3:1:10 in volume. The cross section of the SEM image on the right shows trenches in a silicon substrate obtained by MaCE with an high concentration of hydrogen peroxide ($HF:H_2O_2:H_2O$ 3:3:10). The sidewalls are not vertical, and porous silicon is generated below the metal-free surfaces.

The critical parameter ε to be optimized for MaCE is the ratio between the concentrations of HF, which determines the silicon dissolution rate, and H_2O_2, which determines the hole generation rate: $\varepsilon = [HF]/[H_2O_2]$ [115] (sometimes the parameter $\rho = [HF]/([H_2O_2] + [HF])$ is used instead [119]). The ε parameter must be accurately calibrated in order to obtain vertical, and non-porous, structures. If ε is too low (high H_2O_2 concentration), the etching is more vertical but the silicon surrounding the etched regions becomes porous (porous nanowires). If ε is too high, the etching looses its verticality. The correct ε value depends on the crystalline orientation of the silicon wafer and, in particular, on the shape of the metal patterns [115,130]. Values of $\varepsilon > 3$ give random movements of the catalyst particles, while values of $\varepsilon < 1$ give porous structures [124].

Patterns of catalytic metals can be obtained by metal deposition (thermal or e-beam evaporation) and standard lithographic tools. Metal catalyst features for regular silicon nanowire arrays can also be produced by the simpler and cheaper innovative pattering technique nanosphere lithography [120,121]; The evaporation of Ag or Au through porous aluminum oxide membranes[122-124] gives a periodic and almost regular pattern for vertically etched nanowire arrays.

A thin evaporation of a uniform Au film on a silicon surface, with a successive rapid thermal annealing (RTA), can be used for the fabrication of Au nanoparticles on large surfaces. Even if the nanoparticles have a random position and diameter, the average diameter and diameter dispersion can be partially controlled by the initial film thickness and RTA time and temperature [131]. Metal nanoparticles on silicon, suitable for MaCE production of SiNWs, can be also obtained by sinking silicon in an aqueous solution of HF and metal salts, such as

$AgNO_3$ [132-135], for a very short time (galvanic displacement). Is is to be noted that $AgNO_3$ acts as oxidizing agent and it can be used as alternative to H_2O_2 for vertical etching. A long etching in a $HF/AgNO_3$ solution gives as a result vertical silicon nanowires with random diameter and position. This avoids the need of a preliminary metal pattern deposition and definition. See for example the SEM image of Figure 15, that shows a "forest" of nanowires longer than 20 μm, perpendicular to the Si surface, obtained with a $HF/AgNO_3$ based MaCE. The nanowire diameter is in the range of 100 nm. The drawback of this technique is that Ag is continuously deposited during the etching, so that nanoparticles grow and new nanoparticles are continuously deposited on the Si surface. Hence, non-uniform nanowires with a large dispersion in diameter distribution are obtained. However, some results in average nanowire diameter and diameter dispersion control have been obtained [134] by a suitable calibration of the $HF/AgNO_3$ concentration ratio and the reaction temperature.

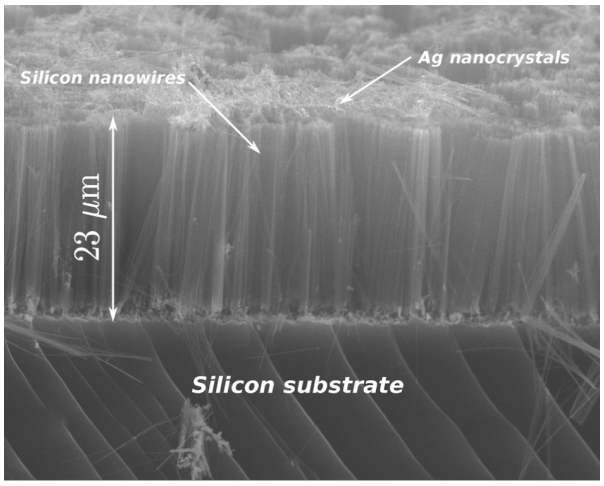

Figure 15: SEM image of a silicon nanowire "forest" (cross-section), fabricated by MaCE of silicon in an $HF/AgNO_3$ aqueous solution.

The fundamental point that still needs to be addressed in the development of TEGs based on vertical, large area nanowire arrays is the improvement of techniques for giving them mechanical stability and robustness, and for fabricating a metal structure on the top of the array, to be used as electrical and thermal contact. To these purposes, techniques for embedding vertical silicon nanowire arrays in polymers are under development [136,137]. However, the presence of the polymer limits the maximum working temperature of these TEGs. At the present state-of-the-art, only preliminary, very encouraging, characterizations of vertical silicon nanowire arrays have been performed [136,137] and the Seebeck coefficient has been measured [138].

Conclusion

In this review paper, after an introduction of the basic principles of thermoelectricity and of the basic parameters for a high TEG conversion efficiency, a quick summary of the most investigated TE materials is given. The aim of research on TE materials is to increase the parameter $Z = S^2\sigma/k_t$ (or equivalently the figure of merit ZT), hence to fabricate TEGs with a high conversion efficiency. In this respect, tellurium compounds seem to be very promising. However, tellurium is very rare on the surface of Earth: It has been estimated that its abundance is only slightly higher than that of platinum. Furthermore, tellurium is poisonous and polluting. Thus, in the case of a large-scale applications of tellurium-based devices their disposal would arise serious environmental problems.

The enhanced phonon surface scattering in rough silicon nanowires can reduce their thermal conductivity by two orders of magnitude (down to few W/mK), with respect to that of bulk silicon (that is 148 W/mK). Conversely, the electrical conductivity of silicon nanowires wider than 20 nm is almost unchanged with respect to bulk electrical conductivity, which is controllable by means of well-known silicon doping processes. Therefore, nanowires offer a very promising way to the use of silicon as TE material, with efficiencies comparable to, and even better than, those of other materials. Silicon is one of the most abundant elements on the surface of Earth, and it is a very sustainable and biocompatible material. Furthermore, silicon-based technologies are largely available and widespread, because their investigation and improvement are stimulated by the continuous growth of the electronic market. For example, the technology of metal contacts on silicon, which are essential for electrical interconnections between the elements of TEG devices, is very well known. Conversely, a full development of solutions and technologies for the fabrication of contacts is requested for many innovative TE materials.

The fabrication of TEGs based on SiNWs must face the challenging fabrication of large scale arrays of SiNW. In this paper, a considerable space has been given to the review of the most innovative technological solutions currently under development for this purpose. Several solutions are very interesting and promising. However, problems of reliability, repeatability on large areas and mechanical stability of very long, and very narrow, silicon nanowires still need to be addressed in future research works.

References

1. Kraemer, D.; Poudel, B.; Feng, H.-P.; Caylor, J. C.; Yu, B.; Yan, X.; Ma, Y.; Wang, X.; Wang, D.; Muto, A.; McEnaney, K.; Chiesa, M.; Ren, Z.; Chen, G. *Nat. Mater.* **2011,** *10,* 532–538. doi:10.1038/nmat3013

2. Baranowski, L. L.; Snyder, G. J.; Toberer, E. S. *Energy Environ. Sci.* **2012,** *5,* 9055–9067. doi:10.1039/C2EE22248E
3. Su, S.; Liu, T.; Wang, Y.; Chen, X.; Wang, J.; Chen, J. *Appl. Energy* **2014,** *120,* 16–22. doi:10.1016/j.apenergy.2014.01.048
4. Fisac, M.; Villasevil, F. X.; Lopez, A. M. *J. Power Sources* **2014,** *252,* 264–269. doi:10.1016/j.jpowsour.2013.11.121
5. Wang, Y.; Dai, C.; Wang, S. *Appl. Energy* **2013,** *112,* 1171–1180. doi:10.1016/j.apenergy.2013.01.018
6. Quan, R.; Tang, X.; Quan, S.; Huang, L. *J. Electron. Mater.* **2013,** *42,* 1469–1475. doi:10.1007/s11664-012-2291-3
7. Yadav, G. G.; Susoreny, J. A.; Zhang, G.; Yang, H.; Wu, Y. *Nanoscale* **2011,** *3,* 3555–3562. doi:10.1039/c1nr10555h
8. Li, D.; Wu, Y.; Kim, P.; Shi, L.; Yang, P.; Majumdar, A. *Appl. Phys. Lett.* **2003,** *83,* 2934–2936. doi:10.1063/1.1616981
9. Hochbaum, A. I.; Chen, R.; Delgrado, R. D.; Liang, W.; Garnett, C. E.; Najarian, M.; Majumdar, A.; Yang, P. *Nat. Lett.* **2008,** *451,* 163–167. doi:10.1038/nature06381
10. Shi, L. *Nanoscale Microscale Thermophys. Eng.* **2012,** *16,* 79–116. doi:10.1080/15567265.2012.667514
11. Xiao, N.; Dong, X.; Song, L.; Liu, D.; Tay, Y. Y.; Wu, S.; Li, L.; Zhao, Y.; Yu, T.; Zhang, H.; Huang, W.; Hng, H. H.; Ajayan, M.; Yan, Q. *ACS Nano* **2011,** *5,* 2749–2755. doi:10.1021/nn2001849
12. Zuev, Y. M.; Chang, W.; Kim, P. *Phys. Rev. Lett.* **2009,** *102,* 096807. doi:10.1103/PhysRevLett.102.096807
13. Babichev, A. V.; Gasumyants, V. E.; Butko, V. Y. *J. Appl. Phys.* **2013,** *113,* 076101. doi:10.1063/1.4792032
14. Ni, X.; Liang, G.; Wang, J.-S.; Li, B. *Appl. Phys. Lett.* **2009,** *95,* 192114. doi:10.1063/1.3264087
15. Sevinçli, H.; Cuniberti, G. *Phys. Rev. B* **2010,** *81,* 113401. doi:10.1103/PhysRevB.81.113401
16. Dragoman, D.; Dragoma, M. *Appl. Phys. Lett.* **2007,** *91,* 203116. doi:10.1063/1.2814080
17. Balandin, A. A.; Ghosh, S.; Bao, W.; Calizo, I.; Teweldebrhan, D.; Miao, F.; Lau, C. N. *Nano Lett.* **2008,** *8,* 902–907. doi:10.1021/nl0731872
18. Pennelli, G.; Macucci, M. *J. Appl. Phys.* **2013,** *114,* 214507. doi:10.1063/1.4842835
19. Goldsmid, H. J.; Douglass, R. W. *Br. J. Appl. Phys.* **1954,** *5,* 386. doi:10.1088/0508-3443/5/11/303
20. Goldsmid, H. J.; Sheard, A. R.; Wright, D. A. *Br. J. Appl. Phys.* **1958,** *9,* 365. doi:10.1088/0508-3443/9/9/306
21. Satterthwaite, C. B.; Ure, R. W., Jr. *Phys. Rev.* **1957,** *108,* 1164. doi:10.1103/PhysRev.108.1164
22. Hyun, D. B.; Hwang, J. S.; Oh, T. S.; Shim, J. D.; Kolomoets, N. V. *J. Phys. Chem. Solids* **1998,** *59,* 1039–1044. doi:10.1016/S0022-3697(97)00242-4
23. Yamashita, O.; Tomiyoshi, S.; Makita, K. *J. Appl. Phys.* **2003,** *93,* 368. doi:10.1063/1.1525400
24. Yamashita, O.; Tomiyoshi, S. *J. Appl. Phys.* **2004,** *95,* 6277. doi:10.1063/1.1712013
25. Yan, X.; Poudel, B.; Ma, Y.; Liu, W. S.; Joshi, G.; Wang, H.; Lan, Y.; Wang, D.; Chen, G.; Ren, Z. F. *Nano Lett.* **2010,** *10,* 3373–3378. doi:10.1021/nl101156v
26. Poudel, B.; Hao, Q.; Ma, Y.; Lan, Y.; Minnich, A.; Yu, B.; Yan, X.; Wang, D.; Muto, A.; Vashaee, D.; Chen, X.; Liu, J.; Dresselhaus, M. S.; Chen, G.; Ren, Z. *Science* **2008,** *320,* 634–638. doi:10.1126/science.1156446
27. Dughaish, Z. H. *Physica B* **2002,** *322,* 205–223. doi:10.1016/S0921-4526(02)01187-0
28. Gelbstein, Y.; Dashevsky, Z.; Dariel, M. P. *Physica B* **2005,** *363,* 196–205. doi:10.1016/j.physb.2005.03.022
29. Girard, S. N.; He, J.; Zhou, X.; Shoemaker, D.; Jaworski, C. M.; Uher, C.; Dravid, V. P.; Heremans, J. P.; Kanatzidis, M. G. *J. Am. Chem. Soc.* **2011,** *133,* 16588–16597. doi:10.1021/ja206380h
30. Biswas, K.; He, J.; Blum, I. D.; Wu, C.-I.; Hogan, T. P.; Seidman, D. N.; Dravid, V. P.; Kanatzidis, M. G. *Nature* **2012,** *489,* 414–418. doi:10.1038/nature11439
31. Sales, B. C.; Mandrus, D.; Williams, R. K. *Science* **1996,** *272,* 1325–1328. doi:10.1126/science.272.5266.1325
32. Nolas, G. S.; Cohn, J. L.; Slack, G. A. *Phys. Rev. B* **1998,** *58,* 164. doi:10.1103/PhysRevB.58.164
33. Puyet, M.; Lenoir, B.; Dauscher, A.; Weisbecker, P.; Clarke, S. J. *J. Solid State Chem.* **2004,** *177,* 2138–2143. doi:10.1016/j.jssc.2004.02.010
34. Sales, B. C.; Chakoumakos, B. C.; Mandrus, D. *Phys. Rev. B* **2000,** *61,* 2475. doi:10.1103/PhysRevB.61.2475
35. Shi, X.; Yang, J.; Salvador, J. R.; Chi, M.; Cho, J. Y.; Wang, H.; Bai, S.; Yang, J.; Zhang, W.; Chen, L. *J. Am. Chem. Soc.* **2011,** *133,* 7837–7846. doi:10.1021/ja111199y
36. Ballikaya, S.; Uzar, N.; Yildirim, S.; Salvador, J. R.; Uher, C. *J. Solid State Chem.* **2012,** *193,* 31–35. doi:10.1016/j.jssc.2012.03.029
37. Ballikaya, S.; Uher, C. *J. Alloys Compd.* **2014,** *585,* 168–176. doi:10.1016/j.jallcom.2013.09.124
38. Wang, X. W.; Lee, H.; Lan, Y. C.; Zhu, G. H.; Joshi, G.; Wang, D. Z.; Yang, J.; Muto, A. J.; Tang, M. Y.; Klatsky, J.; Song, S.; Dresselhaus, M. S.; Chen, G.; Ren, Z. F. *Appl. Phys. Lett.* **2008,** *93,* 193121. doi:10.1063/1.3027060
39. Slack, G. A.; Hussain, M. A. *J. Appl. Phys.* **1991,** *70,* 2694. doi:10.1063/1.349385
40. Yang, B.; Liu, W. L.; Liu, J. L.; Wang, K. L.; Chen, G. *Appl. Phys. Lett.* **2002,** *81,* 3588. doi:10.1063/1.1515876
41. Lee, S.-M.; Cahill, D. G.; Venkatasubramanian, R. *Appl. Phys. Lett.* **1997,** *70,* 2957. doi:10.1063/1.118755
42. Battiston, S.; Fiameni, S.; Saleemi, M.; Boldrini, S.; Famengo, A.; Agresti, F.; Stingaciu, M.; Toprak, M. S.; Fabrizio, M.; Barison, S. *J. Electron. Mater.* **2013,** *42,* 1956–1959. doi:10.1007/s11664-013-2482-6
43. Fiameni, S.; Battiston, S.; Boldrini, S.; Famengo, S.; Agresti, F.; Barison, S.; Fabrizio, M. *J. Solid State Chem.* **2012,** *193,* 142. doi:10.1016/j.jssc.2012.05.004
44. Neophytou, N.; Zianni, X.; Kosina, H.; Frabboni, S.; Lorenzi, B.; Narducci, D. *Nanotechnology* **2013,** *24,* 205402. doi:10.1088/0957-4484/24/20/205402
45. Hics, L. D.; Dresselhaus, M. S. *Phys. Rev. B* **1993,** *47,* 12727–12731. doi:10.1103/PhysRevB.47.12727
46. Hics, L. D.; Dresselhaus, M. S. *Phys. Rev. B* **1993,** *47,* 16631–16634. doi:10.1103/PhysRevB.47.16631
47. Heremans, J. P. *Acta Physica Polonica A* **2005,** *108,* 609–634.
48. Liang, G.; Huang, W.; Koong, S.; Wang, J.-S.; Lan, J. *J. Appl. Phys.* **2010,** *107,* 014317. doi:10.1063/1.3273485
49. Boukay, A. I.; Bunimovich, Y.; Tahir-Kheli, J.; Yu, J.-K.; Goddard, W. A., III; Heat, J. R. *Nat. Lett.* **2008,** *451,* 168–171. doi:10.1038/nature06458
50. Hippalgaonkar, K.; Huang, B.; Chen, R.; Sawyer, K.; Ercius, P.; Majumdar, A. *Nano Lett.* **2010,** *10,* 4341–4348. doi:10.1021/nl101671r
51. Mingo, N. *Phys. Rev. B* **2003,** *68,* 113308. doi:10.1103/PhysRevB.68.113308

52. Zou, J.; Balandin, A. *J. Appl. Phys.* **2001,** *89,* 2932–2938. doi:10.1063/1.1345515
53. Chantrenne, P.; Barrat, J. L.; Blase, X.; Gale, J. D. *J. Appl. Phys.* **2005,** *97,* 104318. doi:10.1063/1.1898437
54. Kazan, M.; Guisbiers, G.; Pereira, S.; Correia, M. R.; Masri, P.; Bruyant, A.; Volz, S.; Royer, P. *J. Appl. Phys.* **2010,** *107,* 083503. doi:10.1063/1.3340973
55. Lim, J.; Hippalgaonkar, K.; Andrews, C. S.; Majumdar, A.; Yang, P. *Nano Lett.* **2012,** *12,* 2475–2482. doi:10.1021/nl3005868
56. Park, Y.-H.; Kim, J.; Kim, H.; Kim, I.; Lee, K.-Y.; Seo, D.; Choi, H.-J.; Kim, W. *Appl. Phys. A* **2011,** *104,* 7–14. doi:10.1007/s00339-011-6474-1
57. Chen, R.; Hochbaum, A. I.; Murphy, P.; Moore, J.; Yang, P.; Majumdar, A. *Phys. Rev. Lett.* **2008,** *101,* 105501. doi:10.1103/PhysRevLett.101.105501
58. Kim, H.; Park, H.-Y.; Kim, I.; Kim, J.; Choi, J.-H.; Kim, W. *Appl. Phys. A* **2011,** *104,* 23–28. doi:10.1007/s00339-011-6475-0
59. Feser, J. P.; Sadhu, J. S.; Azeredo, B. P.; Hsu, H. K.; Ma, J.; Kim, J.; Seong, M.; Fang, N. X.; Li, X.; Ferreira, P. M.; Sinha, S.; Cahill, D. G. *J. Appl. Phys.* **2012,** *112,* 114306. doi:10.1063/1.4767456
60. Casimir, H. B. G. *Physica* **1938,** *5,* 495–500. doi:10.1016/S0031-8914(38)80162-2
61. Heron, J. S.; Fournier, T.; Mingo, N.; Bourgeois, O. *Nano Lett.* **2009,** *9,* 1861–1865. doi:10.1021/nl803844j
62. Moore, A. L.; Saha, S. K.; Prasher, R. S.; Li, S. *Appl. Phys. Lett.* **2008,** *93,* 083112. doi:10.1063/1.2970044
63. Martin, P.; Aksamija, Z.; Pop, E.; Ravaioli, U. *Phys. Rev. Lett.* **2009,** *102,* 125503. doi:10.1103/PhysRevLett.102.125503
64. Liu, L.; Chen, X. *J. Appl. Phys.* **2010,** *107,* 033501. doi:10.1063/1.3298457
65. Carrete, J.; Gallego, L. J.; Varela, L. M.; Mingo, N. *Phys. Rev. B* **2011,** *84,* 075403. doi:10.1103/PhysRevB.84.075403
66. Sadhu, J.; Sinha, S. *Phys. Rev. B* **2011,** *84,* 115450. doi:10.1103/PhysRevB.84.115450
67. Seong, M.; Sadhu, J. S.; Ma, J.; Ghossoub, M. G.; Sihna, S. *J. Appl. Phys.* **2012,** *111,* 124319. doi:10.1063/1.4728189
68. Wei, L.; Xie, P.; Lieber, C. M. *IEEE Trans. Electron Devices* **2008,** *55,* 2859–2876. doi:10.1109/TED.2008.2005158
69. Pott, V.; Moselund, E. K.; Bouvet, D.; DeMichielis, L.; Ionescu, A. M. *IEEE Trans. Nanotechnol.* **2008,** *7,* 733–744. doi:10.1109/TNANO.2008.2007215
70. Fu, J.; Sing, N.; Buddharaju, K. D.; Teo, S. H. G.; Shen, C.; Jiang, Y.; Zhu, C. X.; Yu, M. B.; Lo, G. Q.; Balasubramanian, N.; Kwong, D. L.; Gnani, E.; Baccarani, G. *IEEE Electron Device Lett.* **2008,** *29,* 518–521. doi:10.1109/LED.2008.920267
71. Cui, Y.; Wei, Q.; Park, H.; Lieber, C. M. *Science* **2001,** *293,* 1289–1292. doi:10.1126/science.1062711
72. Talin, A. A.; Hunter, L. L.; Léonard, F.; Rokad, B. *Appl. Phys. Lett.* **2006,** *89,* 153102. doi:10.1063/1.2358214
73. Stern, E.; Klemic, J. F.; Routenberg, D. A.; Wyrembak, P. N.; Turner-Evans, D. B.; Hamilton, A. D.; LaVan, D. A.; Fahmy, T. M.; Reed, M. A. *Nat. Lett.* **2007,** *445,* 519–522. doi:10.1038/nature05498
74. Wagner, R. S.; Ellis, W. C. *Appl. Phys. Lett.* **1964,** *4,* 89. doi:10.1063/1.1753975
75. Westwater, J.; Gosain, D. P.; Tomiya, S.; Usui, S.; Ruda, H. *J. Vac. Sci. Technol. B* **1997,** *15,* 554. doi:10.1116/1.589291
76. Morales, A. M.; Lieber, C. M. *Science* **1998,** *279,* 208–211. doi:10.1126/science.279.5348.208
77. Hu, J.; Ouyang, M.; Yang, P.; Lieber, C. M. *Nature* **1999,** *399,* 48–51. doi:10.1038/19941
78. Cui, Y.; Duan, X.; Hu, J.; Lieber, C. M. *J. Phys. Chem. B* **2000,** *104,* 5213–5216. doi:10.1021/jp0009305
79. Cui, Y.; Lauhon, L. J.; Gudiksen, M. S.; Wang, J.; Lieber, C. M. *Appl. Phys. Lett.* **2001,** *78,* 2214. doi:10.1063/1.1363692
80. Cui, Y.; Lieber, C. M. *Science* **2001,** *291,* 851–853. doi:10.1126/science.291.5505.851
81. Samuelson, L.; Björk, M. T.; Depperd, K.; Larsson, M.; Ohlsson, B. J.; Panev, N.; Persson, A. I.; Sköld, N.; Thelander, C.; Wallenberg, L. R. *Physica E* **2004,** *21,* 560–567. doi:10.1016/j.physe.2003.11.072
82. Hochbaum, A. I.; Fan, R.; He, R.; Yang, P. *Nano Lett.* **2005,** *5,* 457–460. doi:10.1021/nl047990x
83. Schmidt, V.; Senz, S.; Gösele, U. *Nano Lett.* **2005,** *5,* 931–935. doi:10.1021/nl050462g
84. Selzner, T.; Andrä, G.; Wendler, E.; Wesch, W.; Scholz, R.; Gösele, U.; Christiansen, S. *Nanotechnology* **2006,** *17,* 2895. doi:10.1088/0957-4484/17/12/012
85. Kayes, B. M.; Filler, M. A.; Putnam, M. C.; Kelzenberg, M. D.; Lewis, N. S.; Atwater, H. A. *Appl. Phys. Lett.* **2007,** *91,* 103110. doi:10.1063/1.2779236
86. Dávila, D.; Tarancón, A.; Fernández-Regúlez, M.; Calaza, C.; Salleras, M.; San Paulo, A.; Fonseca, L. *J. Micromech. Microeng.* **2011,** *21,* 104007. doi:10.1088/0960-1317/21/10/104007
87. Dávila, D.; Tarancón, A.; Calaza, C.; Salleras, M.; Fernández-Regúlez, M.; San Paulo, A.; Fonseca, L. *Nano Energy* **2012,** *1,* 812–819. doi:10.1016/j.nanoen.2012.06.006
88. Pennelli, G.; Piotto, M.; Barillaro, G. *Microelectron. Eng.* **2006,** *83,* 1710. doi:10.1016/j.mee.2006.01.144
89. Pennelli, G.; Piotto, M. *Microelectron. Eng.* **2006,** *83,* 1559. doi:10.1016/j.mee.2006.01.179
90. Ciucci, S.; D'Angelo, F.; Diligenti, A.; Pellegrini, B.; Pennelli, G.; Piotto, M. *Microelectron. Eng.* **2005,** *78–79,* 338. doi:10.1016/j.mee.2004.12.044
91. Pennelli, G.; Piotto, M. *J. Appl. Phys.* **2006,** *100,* 054507. doi:10.1063/1.2338599
92. Pennelli, G.; Pellegrini, B. *J. Appl. Phys.* **2007,** *101,* 104502. doi:10.1063/1.2722252
93. Pennelli, G. *Microelectron. Eng.* **2009,** *86,* 2139–2143. doi:10.1016/j.mee.2009.02.032
94. Chien, F. S.-S.; Hsieh, W.-F.; Gwo, S.; Vladar, A. E.; Dagata, J. A. *J. Appl. Phys.* **2002,** *91,* 10044. doi:10.1063/1.1476072
95. Legrand, B.; Dresmes, D.; Stiévenard, D. *J. Vac. Sci. Technol., B* **2002,** *20,* 862. doi:10.1116/1.1470519
96. Ferri, M.; Suriano, F.; Roncaglia, A.; Solmi, S.; Cerofolini, G. F.; Romano, E.; Narducci, D. *Microelectron. Eng.* **2011,** *88,* 877–881. doi:10.1016/j.mee.2010.11.034
97. Martinez, J.; Martinez, R. V.; Garcia, R. *Nano Lett.* **2008,** *8,* 3636. doi:10.1021/nl801599k
98. Seidel, H.; Csepregi, L.; Heuberger, A.; Baumgärtel, H. *J. Electrochem. Soc.* **1990,** *137,* 3612–3626. doi:10.1149/1.2086277
99. Madou, M. J. *Fundamentals of microfabrication;* CRC Press: London, U.K., 2002.
100. Totaro, M.; Bruschi, P.; Pennelli, G. *Microelectron. Eng.* **2012,** *97,* 157. doi:10.1016/j.mee.2012.04.007
101. Pennelli, G.; Totaro, M.; Piotto, M.; Bruschi, P. *Nano Lett.* **2013,** *13,* 2592. doi:10.1021/nl400705b
102. Pennelli, G.; Nannini, A.; Macucci, M. *J. Appl. Phys.* **2014,** *115,* 084507. doi:10.1063/1.4866994
103. Lu, L.; Yi, W.; Zhang, D. L. *Rev. Sci. Instrum.* **2001,** *72,* 2996. doi:10.1063/1.1378340

104. Choi, T.-Y.; Poulikakos, D.; Tharian, J.; Sennhauser, U. *Nano Lett.* **2006,** *6,* 1589. doi:10.1021/nl060331v
105. Laermer, F.; Schilp, A. Method of anisotropically etching silicon. U.S. Pat. 5501893A, March 26, 1996.
106. Wu, B.; Kumar, A.; Pamarthy, S. *J. Appl. Phys.* **2010,** *108,* 051101. doi:10.1063/1.3474652
107. Wang, X.; Zeng, W.; Lu, G.; Russo, O. L.; Eisenbraun, E. *J. Vac. Sci. Technol. B* **2007,** *25,* 1376. doi:10.1116/1.2756554
108. Ayón, A. A.; Braff, R.; Lin, C. C.; Sawin, H. H.; Schmidt, M. A. *J. Electrochem. Soc.* **1999,** *146,* 339–349. doi:10.1149/1.1391611
109. Morton, K. J.; Nieberg, G.; Bai, S.; Chou, S. Y. *Nanotechnology* **2008,** *19,* 345301. doi:10.1088/0957-4484/19/34/345301
110. Zeniou, A.; Ellinas, K.; Olziersky, A.; Gololides, E. *Nanotechnology* **2014,** *25,* 035302. doi:10.1088/0957-4484/25/3/035302
111. Parasuraman, J.; Summanwar, A.; Marty, F.; Basset, F.; Angelescu, D. E.; Bourouina, T. *Microelectron. Eng.* **2014,** *113,* 35–39. doi:10.1016/j.mee.2013.06.010
112. Stranz, A.; Kähler, J.; Merzsch, S.; Waag, A.; Peiner, E. *Microsyst. Technol.* **2012,** *18,* 857–862. doi:10.1007/s00542-011-1390-z
113. Stranz, A.; Waag, A.; Peiner, E. *J. Electron. Mater.* **2013,** *42,* 2233. doi:10.1007/s11664-013-2590-3
114. Huang, Z.; Geyer, N.; Werner, P.; de Boor, J.; Gösele, U. *Adv. Mater.* **2011,** *23,* 285. doi:10.1002/adma.201001784
115. Kim, J.; Han, H.; Kim, Y. H.; Choi, S.-H.; Kim, J.-C.; Lee, W. *ACS Nano* **2011,** *5,* 3222–3229. doi:10.1021/nn2003458
116. Li, X.; Bohn, P. W. *Appl. Phys. Lett.* **2000,** *77,* 2572. doi:10.1063/1.1319191
117. Tsujino, K.; Matsumura, M. *Electrochim. Acta* **2007,** *53,* 28. doi:10.1016/j.electacta.2007.01.035
118. Sharma, P.; Wang, Y.-L. *Appl. Phys. Express* **2011,** *4,* 025001. doi:10.1143/APEX.4.025001
119. Li, L.; Liu, Y.; Zhao, X.; Lin, Z.; Wong, C.-P. *ACS Appl. Mater. Interfaces* **2014,** *6,* 575–584. doi:10.1021/am4046519
120. Peng, K.; Zhang, M.; Lu, A.; Wong, N.-B.; Zhang, R.; Lee, S.-T. *Appl. Phys. Lett.* **2007,** *90,* 163123. doi:10.1063/1.2724897
121. Huang, Z.; Fang, H.; Zhu, J. *Adv. Mater.* **2007,** *19,* 744. doi:10.1002/adma.200600892
122. Huang, Z.; Zhang, X.; Reiche, M.; Liu, L.; Lee, T.; Shimizu, T.; Senz, S.; Gösele, U. *Nano Lett.* **2008,** *8,* 3046. doi:10.1021/nl802324y
123. Hong, J.; Kim, K.; Kwon, N.; Lee, J.; Whang, D.; Chung, Ilsub. *J. Vac. Sci. Technol. B* **2010,** *28,* 735. doi:10.1116/1.3336572
124. Liu, K.; Qu, S.; Tan, F.; Bi, Y.; Lu, S.; Wang, Z. *Mater. Lett.* **2013,** *101,* 96. doi:10.1016/j.matlet.2013.03.086
125. Ho, J.-W.; Wee, Q.; Dumond, J.; Tay, A.; Chua, S.-J. *Nanoscale Res. Lett.* **2013,** *8,* No. 506. doi:10.1186/1556-276X-8-506
126. Bollani, M.; Osmond, J.; Nicotra, G.; Spinella, C.; Narducci, D. *Nanotechnology* **2013,** *24,* 335302. doi:10.1088/0957-4484/24/33/335302
127. Huang, Z. P.; Geyer, N.; Liu, L. F.; Li, M. Y.; Zhong, P. *Nanotechnology* **2010,** *21,* 465301. doi:10.1088/0957-4484/21/46/465301
128. Chartier, C.; Bastide, S.; Lévy-Clément, C. *Electrochim. Acta* **2008,** *53,* 5509–5516. doi:10.1016/j.electacta.2008.03.009
129. Li, X.; Xiao, Y.; Yan, C.; Zhou, K.; Schweizer, S. L.; Sprafke, A.; Lee, J.-H.; Wehrspohn, R. B. *ECS Solid State Lett.* **2013,** *2,* P22–P24. doi:10.1149/2.010302ssl
130. Chern, W.; Hsu, K.; Chun, I. S.; de Azeredo, B. P.; Ahmed, N.; Kim, K.-H.; Zuo, J.-m.; Fang, N.; Ferreira, P.; li, X. *Nano Lett.* **2010,** *10,* 1582–1588. doi:10.1021/nl903841a
131. Pennelli, G.; Nannini, A. *e-J. Surf. Sci. Nanotechnol.* **2009,** *7,* 503. doi:10.1380/ejssnt.2009.503
132. Peng, K.; Yan, Y.; Gao, S.; Zhu, J. *Adv. Funct. Mater.* **2003,** *13,* 127. doi:10.1002/adfm.200390018
133. Peng, K.; Fang, H.; Hu, J.; Wu, Y.; Zhu, J.; Yan, Y.; Lee, S. *Chem.–Eur. J.* **2006,** *12,* 7942–7947. doi:10.1002/chem.200600032
134. Chen, C.-Y.; Wu, C.-S.; Chou, C.-J.; Yen, T.-J. *Adv. Mater.* **2008,** *20,* 3811. doi:10.1002/adma.200702788
135. Tsujino, K.; Matsumura, M. *Adv. Mater.* **2005,** *17,* 1045. doi:10.1002/adma.200401681
136. Zhang, T.; Wu, S.-l.; Zheng, R.-t.; Cheng, G.-a. *Nanotechnology* **2013,** *24,* 505718. doi:10.1088/0957-4484/24/50/505718
137. Weisse, J. M.; Marconnet, A. M.; Kim, D. R.; Rao, P. M.; Panzer, M. A.; Goodson, K. E.; Zheng, X. *Nanoscale Res. Lett.* **2012,** *7,* No. 554. doi:10.1186/1556-276X-7-554
138. Koukharenko, W.; Boden, S. A.; Platzek, D.; Bagnall, D. N.; White, N. M. *J. Electron. Mater.* **2013,** *42,* 2114. doi:10.1007/s11664-013-2539-6

License and Terms

This is an Open Access article under the terms of the Creative Commons Attribution License (http://creativecommons.org/licenses/by/2.0), which permits unrestricted use, distribution, and reproduction in any medium, provided the original work is properly cited.

The license is subject to the *Beilstein Journal of Nanotechnology* terms and conditions: (http://www.beilstein-journals.org/bjnano)

The definitive version of this article is the electronic one which can be found at: doi:10.3762/bjnano.5.141

BEILSTEIN JOURNAL OF NANOTECHNOLOGY

Nano-rings with a handle – Synthesis of substituted cycloparaphenylenes

Anne-Florence Tran-Van[1] and Hermann A. Wegner*[2]

Review

Open Access

Address:
[1]Department of Chemistry, Basel University, St Johanns-Ring 19, CH-4056 Basel, Switzerland and [2]Institut für Organische Chemie, Justus-Liebig-Universität, Heinrich-Buff-Ring 62, D-35392 Giessen, Deutschland

Email:
Hermann A. Wegner* - Hermann.A.Wegner@org.chemie.uni-giessen.de

* Corresponding author

Keywords:
aromatic compounds; carbon nanotubes; cycloparaphenylene; organic synthesis

Beilstein J. Nanotechnol. **2014,** *5,* 1320–1333.
doi:10.3762/bjnano.5.145

Received: 21 May 2014
Accepted: 25 July 2014
Published: 20 August 2014

This article is part of the Thematic Series "Atomic scale interface design and characterisation: Theory – Structure and dynamics" and is dedicated to Prof. Dr. Lawrence T. Scott, Boston College, on the occasion of his 70th birthday.

Guest Editor: C. Ewels

© 2014 Tran-Van and Wegner; licensee Beilstein-Institut.
License and terms: see end of document.

Abstract

The research of cycloparaphenylenes (CPPs), the smallest armchair carbon nanotube, has been a quest for the past decades which experienced a revival in 2008 when the first synthesis was achieved. Since then CPPs with various ring sizes have been realized. The incorporation of substituents and the synthesis of CPPs with building blocks different from phenyl rings bear challenges of their own. Such structures, however, are highly interesting, as they allow for an incorporation of CPPs as defined nano-objects for other applications. Therefore, this review provides a status report about the current efforts in synthesizing CPPs beyond the parent unsubstituted oligo-phenylene structure.

Introduction

Carbon is for organic chemists the essential building block. Besides graphite and diamond scientists have discovered new carbon allotropes such as fullerene [1], graphene [2] and carbon nanotubes (CNTs) [3]. Research on these materials has been originally conducted by physicists. Also, the preparation methods relied on physical processes [4,5]. In the past decade the field is also more and more a playground for organic chemists as these structures are great challenges for modern organic synthesis. In 2002 the first rational synthesis of C_{60} was presented showing the possibility to control each atom in the final target [6]. The choice of suitable synthetic methods is critical to cope with the strain as well as the lack of functional groups in the target molecule. For CNTs a selective synthesis, which controls all structural parameters, is of special interest as they determine the properties and, finally, the field of application [7-10]. For armchair carbon nanotubes, cycloparaphenylenes (CPPs) have been designed as potential template or building block for a bottom-up approach [11-13]. Since 2008 several groups have presented successful syntheses of CPPs with different diameters and their properties were studied [14-

24]. The main challenge of such a synthesis is, similar to C_{60}, to overcome the high strain energy. To circumvent this, different strategies have been developed. Bertozzi and Jasti used a bent cyclohexadiene that can be converted to a fully aromatic benzene unit [25-32]. Itami utilized a similar L-shaped building block based on cyclohexane [33-38]. Yamago [39-42] relied on a square-shaped tetranuclear platinum complex originally developed by Bäuerle [43] for the synthesis of macrocylic oligothiophenes. In all these methods a macrocyclic precursor is reaching full conjugation in the last step of the synthesis. The strain in a CPP is mainly due to the deviation of the phenyl rings from planarity. However, the phenyl units in all CPPs that were synthesized so far are not fully conjugated due to a torsion between the phenyl moieties to overcome the steric interactions of the protons in *ortho*-position. This effect has to be paid for through an increased energy to deviate the phenyl units from planarity. The incorporation of substituents into CPPs presents therefore a special synthetic challenge as it further increases the torsion angle and, hence, the strain energy. The installment of functionalities, however, is crucial for the application of CPPs. Therefore, this review gathers current endeavors in this direction and discusses the different strategies leading to these new classes of CPP molecules.

Review

Different types of substitutions have been incorporated in recent syntheses of CPPs. Classical CPP syntheses have opened the way to make phenyl-substituted CPPs, acene-containing CPPs, polycyclic CPPs as well as heteroatom-containing CPPs.

Phenyl- and alkyl-substituted cycloparaphenylenes

The synthesis of phenyl-substituted CPPs can be performed by using similar strategies as for the unsubstituted CPPs. For instance Jasti et al. applied their strategy to synthesize a tetraphenyl-substituted CPP as a model molecule for the synthesis of larger nanobelts via cyclodehydrogenation reaction (Scheme 1) [44]. The preparation of the modified building

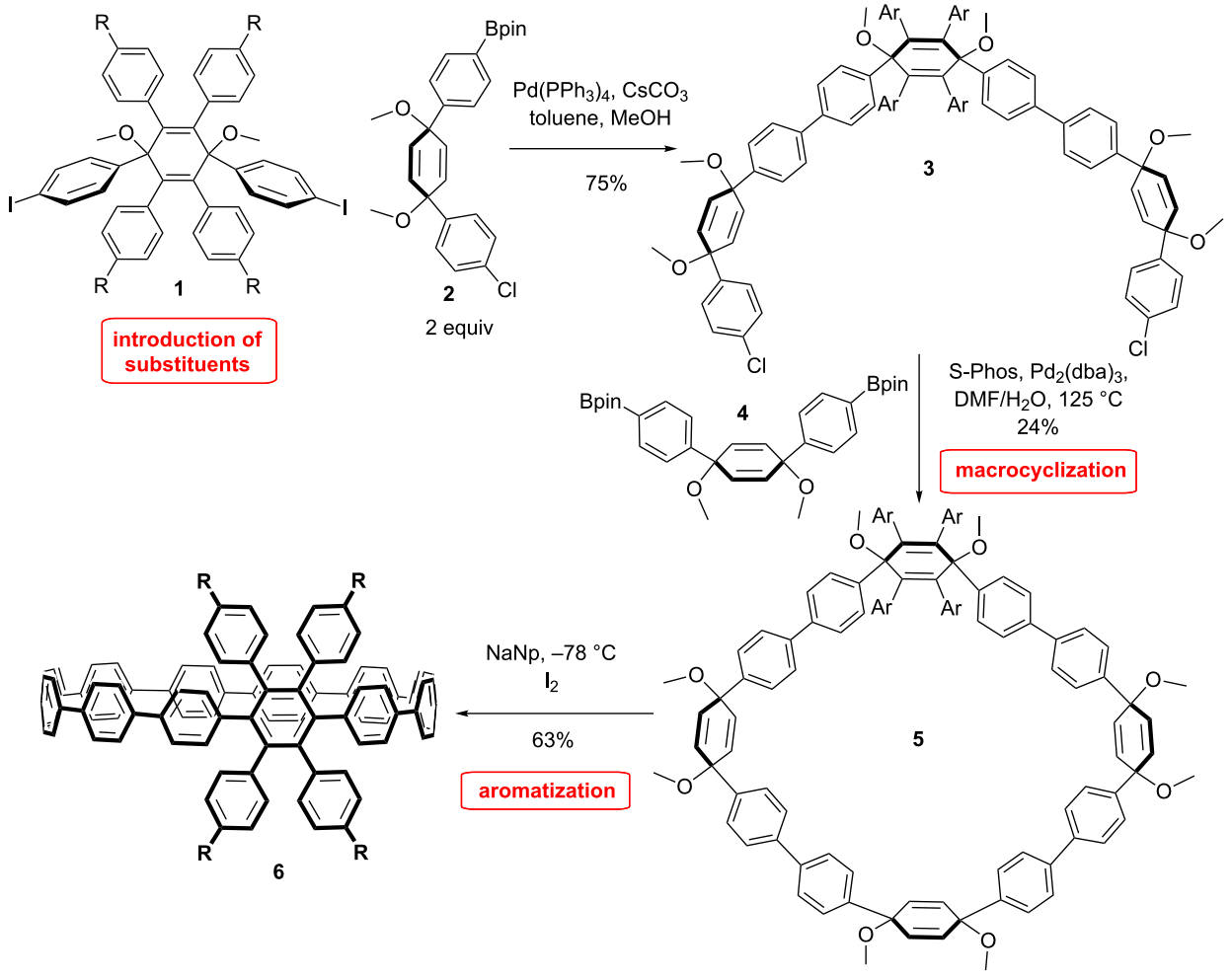

Scheme 1: Synthesis of a tetraphenyl-substituted CPP by Jasti et al.

block was performed with 1-bromo-4-*n*-butylphenyl that was transformed to the boronic acid. This compound was then coupled with tetrabromoquinone via Suzuki coupling and treated with DDQ to furnish the tetraphenylbenzoquinone. The addition of lithiated phenyl iodide gave the *syn*-diol after separation. The compound was subsequently methylated. They presented a multigram synthesis of this very useful building block **1**, which was coupled via Suzuki reaction with two equivalents of the boronic ester building block **2**. The macrocyclization was again achieved through Suzuki coupling with building block **4** in 24% yield. Finally, the aromatization reaction was conducted by using sodium naphthalenide affording the substituted [12]CPP **6** in 63% yield (Scheme 1).

With the same strategy dodecaphenyl-substituted [9]CPP **9** was prepared by Müllen et al. (Scheme 2) [45]. A tetraphenyl-substituted cyclohexadiene building block **7** was combined via nickel-mediated Yamamoto coupling reaction, and was consequently aromatized through reductive aromatization mediated by the use of low-valent titanium to produce the substituted [9]CPP in even better yields (73–81%) compared to Jasti. The aim of this synthesis was to achieve the synthesis of [3]cyclohexabenzocoronene ([3]CHBC) through cyclodehydrogenation reactions. Indeed, this would be the first three dimensional hexabenzocoronene (HBC) molecule. HBCs are interesting because of their supramolecular behavior and electronical properties [46-48]. However, the cyclodehydrogenation reaction on this molecule proved to be quite challenging due to ring strain and led to a complex mixture of partially dehydrogenated and chlorinated products. A clear evidence for the formation of [3]CHBC was not obtained.

DFT calculations showed that the molecule is C_3-symmetric with a twisted CPP core and a diameter of 12.2 Å in the gas phase. In the calculated structures the dihedral angle is 51.2° between substituted phenyls and unsubstituted phenyls and 78.7° between two unsubstituted phenyl rings. Therefore, π-conjugation is expected to be reduced, which corresponds to the observed shorter absorption and emission wavelengths compared to the unsubstituted [9]CPP. However, the X-ray structures differ from the computationally calculated structures with C_1-symmetry; the phenyl ring fills the cavity due to crystal packing forces, and the ring exhibits an ellipsoidal shape. The ring strain is calculated by using the homodesmotic reaction method to 93.9 kcal/mol. This is 28 kcal/mol more than for the corresponding unsubstituted [9]CPP, and closer to that of the [6]CPP. The NMR study showed that the rotational speed of each phenyl is fast, even at low temperatures, as broadening was only observed at −90 °C.

A different strategy was developed by Wegner et al. (Scheme 3) [49]. Initially, it was planned to utilize the [2 + 2 + 2] cycloaddition reaction to build the CPP scaffold by taking advantage of the aromaticity gained in the process to overcome the ring strain. However, studies on a model system revealed that under the conditions of the [2 + 2 + 2] cycloaddition reaction the reaction pathways deviate in strained systems to a formal [2 + 1 + 2 + 1] cycloaddition reaction [50]. Therefore, a building block was devised that combines a cyclohexane moiety, similar to that of Itami, and a diyne building block precursor for the cycloaddition reaction. With this strategy a modular access to substituted CPPs is provided, which differs from all other approaches in so far as the substituents are introduced after the macrocyclization and not before, which allows for a higher flexibility. The building block **12** was obtained by combining the L-shaped unit **10** with a protected diyne **11** via Sonogashira reaction and subsequent deprotection. Macrocyclization of **12** under Sonogashira reaction conditions provided the macrocyclic dimer **13**.

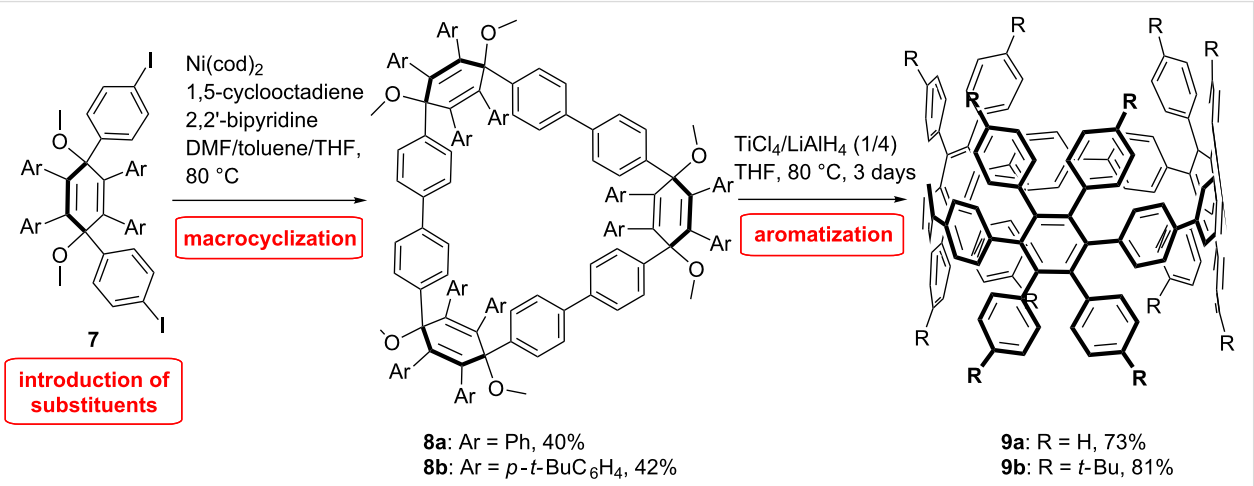

Scheme 2: Synthesis of tetraphenyl substituted CPP by Müllen et al.

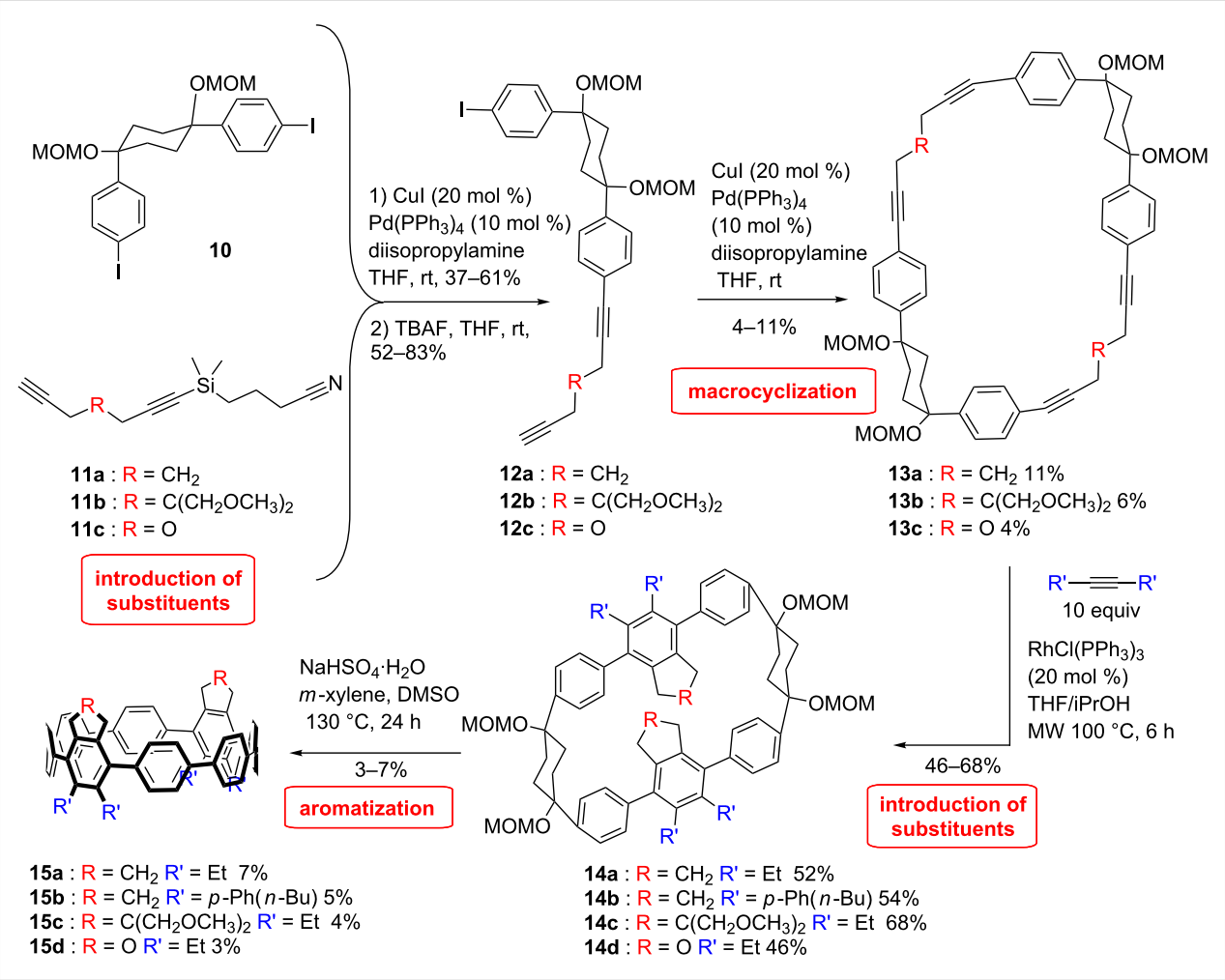

Scheme 3: Synthesis of substituted CPPs by Wegner et al.

The [2 + 2 + 2] cycloaddition was then performed on the macrocyclic precursor yielding variously substituted macrocycles in 46–52% yield. Finally, differently substituted [8]CPP were obtained through an aromatization reaction of the corresponding precursor **14** (Scheme 3). The low yield of the last step is attributed to the high strain energy to overcome.

Whereas the diameters of substituted rings are comparable to the diameters of unsubstituted [8]CPP, the dihedral angles between the substituted phenyl ring and the neighbouring rings are larger than for two unsubstituted rings, which exhibit a similar angle as in the unsubstituted CPP. Therefore, the conjugation in the substituted CPP is expected to be even less dominant than that in the unsubstituted CPP, which is again represented in the optical properties. The solid-state packing structure shows pairs of substituted CPP molecules arranged parallel to each other in a basket weave motif. Strain energies were calculated by using a different method than the homodesmotic reaction method described in previous publications. Indeed, in this case, the corresponding linear CPP fragments were placed in a repeating supercell. Strain energies between 51.1–73.6 kcal/mol were obtained. The ring strain can vary according to the substitution by around 11 kcal/mol from the strain energy of [8]CPP calculated with the same method (62 kcal/mol).

Nanorings with inserted acene units

One of the benefits of applying CPPs as templates for the preparation of CNTs is the possibility to control the chirality of the CNT by incorporating the desired chirality into the precursor. The Itami group applied their concept for the synthesis of the shortest chiral CNTs by inserting an acene unit in a CPP structure (Scheme 4) [51]. As a particular example they synthesized cyclo[13]*para*-phenylen-2,6-naphthylene ([13]CPPN). With this approach it is possible to synthesize all chiral nanohoops by including the appropriate acene. The synthesis follows the classical strategy developed by the group (Scheme 4). The required L-shaped building block **16** was synthesized according

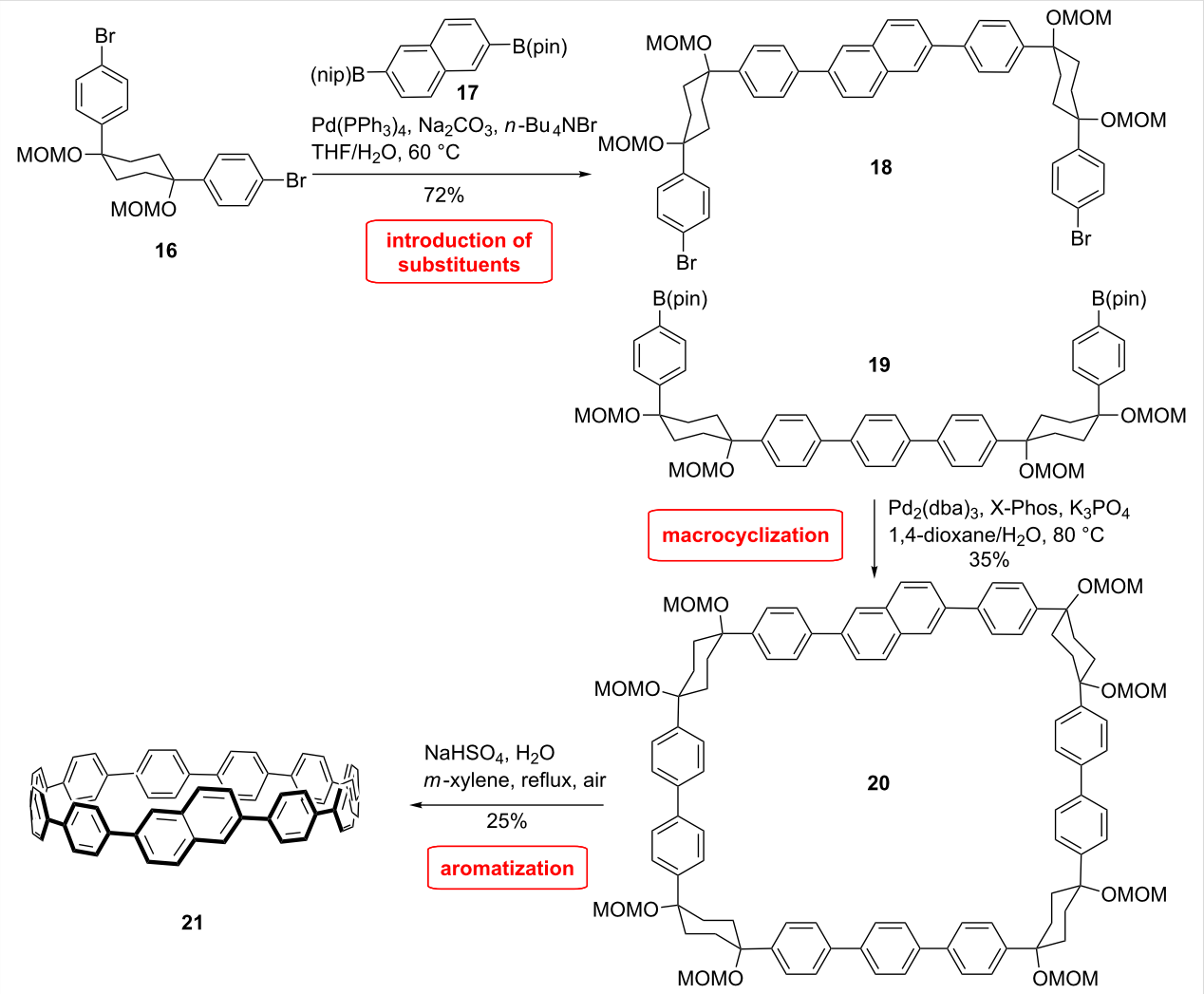

Scheme 4: Synthesis of acene inserted CPP by Itami et al.

to a previously developed methodology [37]. Two of these building blocks were coupled with 2,6-diborylated naphthalene **17** to give the first U-shaped building block **18**. The second U-shaped unit **19** was synthesized accordingly by Suzuki coupling of diborylated benzene with two equivalents of L-shaped building block **16**. The resulting compound was then borylated. The two units **18** and **19** were combined by Suzuki coupling to form the square-shaped macrocycle **20** in 35% yield. The CPP precursor was subsequently aromatized by a treatment with sodium bisulfate to furnish the desired [13]CPPN in 25% yield.

[13]CPPN **21** presents a helical chirality, although racemization occurs by rotation of the acene unit around the connecting bonds to the rest of the ring. Calculations showed that the molecule is racemizing rapidly at ambient temperature (8.4 kcal/mol). They also studied the racemization of other chiral nanorings to study the impact of the ring size. The racemization barrier increases as the ring diameter decreases and also as the acene unit becomes larger, which can be explained by the increase of ring strain.

Furthermore, a synthesis of a pyrene-inserted CPP was developed by the Itami group (Scheme 5) [52]. This molecule represents a CPP that was benzannulated and π-extended at the bay-region by converting two biphenyl units into a pyrene unit. Pyrene derivatives show interesting photophysical properties like long fluorescence life time and excimer emission. Therefore, it was of interest to see if these features appear in the CPPs containing pyrene units. The preparation of cycloparaphenylene-2,7-pyridylene (CPPyr) is described in Scheme 5. The synthesis relies on the same strategy as that for the corresponding non-annelated CPP. It uses the L-shaped building block **16** and the pyrene unit is incorporated via Suzuki coupling of the diborylated 2,7-pyrene **22** to access the U-shaped unit **23**. The two units were coupled using a nickel catalyst to give the macro-

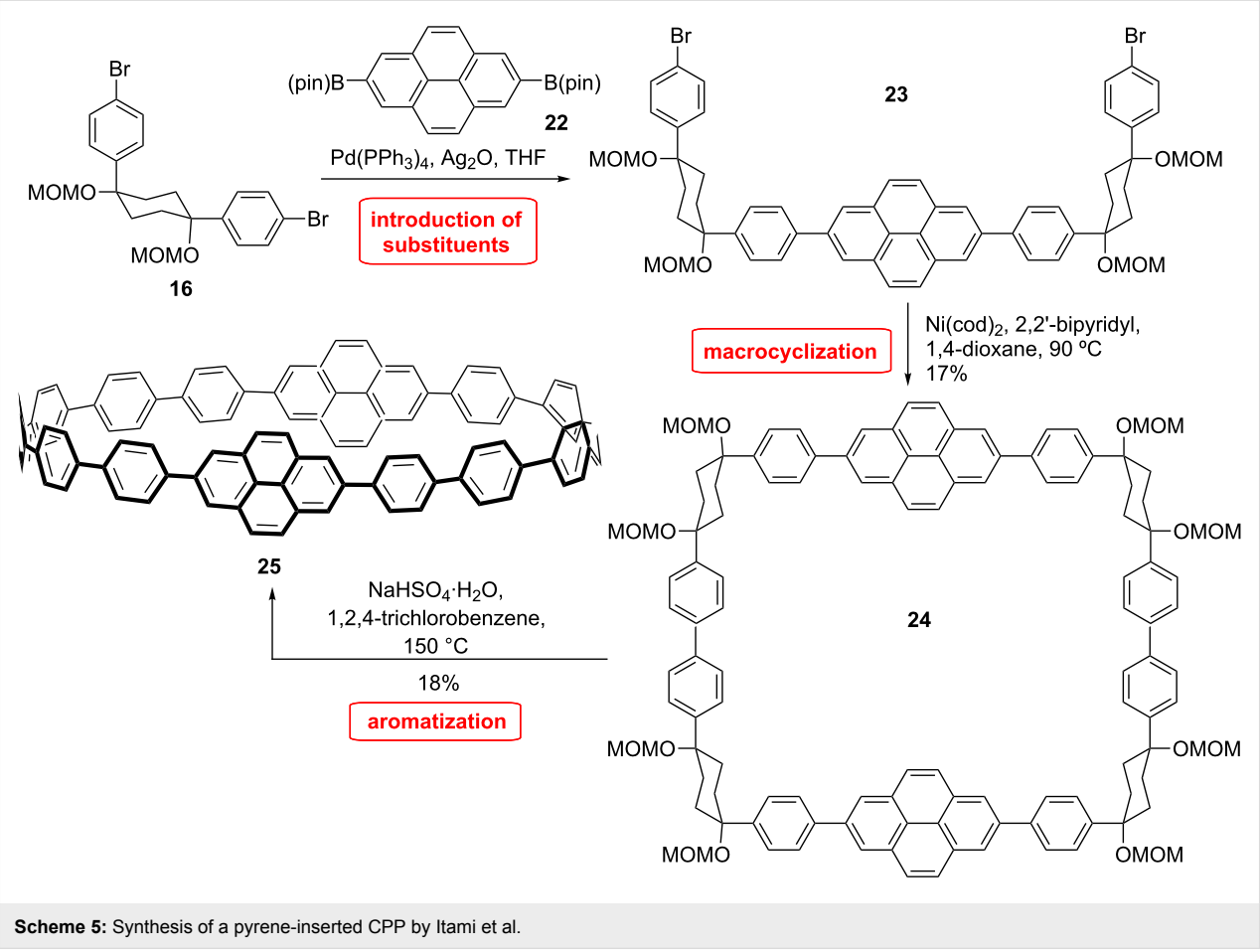

Scheme 5: Synthesis of a pyrene-inserted CPP by Itami et al.

cyclic dimer **24** in 17% yield. Aromatization of this CPP precursor was achieved by sodium bisulfate in 1,2,4-trichlorobenzene to give the desired [12,2]CPPyr **25**. Notably, the resulting pyrene product was soluble only in chlorinated solvents in contrast to the generally easily soluble CPPs.

The UV–vis absorption spectrum can be explained by a combination of the spectra of pyrene and [16]CPP, as a result of the poor conjugation between paraphenylene and 2,7-pyrenylene. The emission maximum appears at 430 nm similar to [12]–[18]CPPs. However, the quantum yield is found to be much smaller with 0.21 in comparison to [9]–[16]CPPs (0.73–0.90) [15]. The fluorescence life time is larger than that of other CPPs with 25.6 ns (10.6 ns for [12]CPP), which is in accordance with the long fluorescence life time of pyrenes. A computational study showed that HOMO−1 HOMO−2, LUMO+1 LUMO+2 are degenerated and localized on the two pyrene moieties and have a similar shape as the HOMO and LUMO of pyrene explaining the additivity of the UV spectra of [16]CPP and pyrene. The shape and energy of HOMO and LUMO are similar to those of [16]CPP. Therefore, the emission is mostly dependent on the CPP structure. Recently, Yamago and coworkers also reported the synthesis of a [4]cyclo-2,7-pyrenylene ([4]CPY) by using their method with a square-like tetra-Pt-complex [53]. DFT-calculations as well as electrochemical analysis revealed a strong resemblance with [8]CPP.

During the evolution of larger π-extended nanobelts, Itami applied the cyclohexadiene strategy that was initially presented by Jasti et al. with a modified naphthalene derivative to synthesize a cyclonaphthylene nanoring (CN) (Scheme 6) [54]. The building block was synthesized by addition of mono-lithiated 1,4-dibromonaphthalene (**26**) on 1,4-naphthoquinone (**27**), providing the desired *cis*-diol in 36% yield after separation. The diol was further methylated by using MeI and NaH as base. They combined the designed L-shaped naphthylene modified building block **28** in a nickel-mediated shotgun macrocyclization producing the trimer **29** in 2% yield. Final aromatization under reductive condition afforded desired π-extended [9]CN **30** in 59% yield [55].

The NMR spectrum of [9]CN is differentiated into numerous peaks that coalesce into three signals when heated to 150 °C.

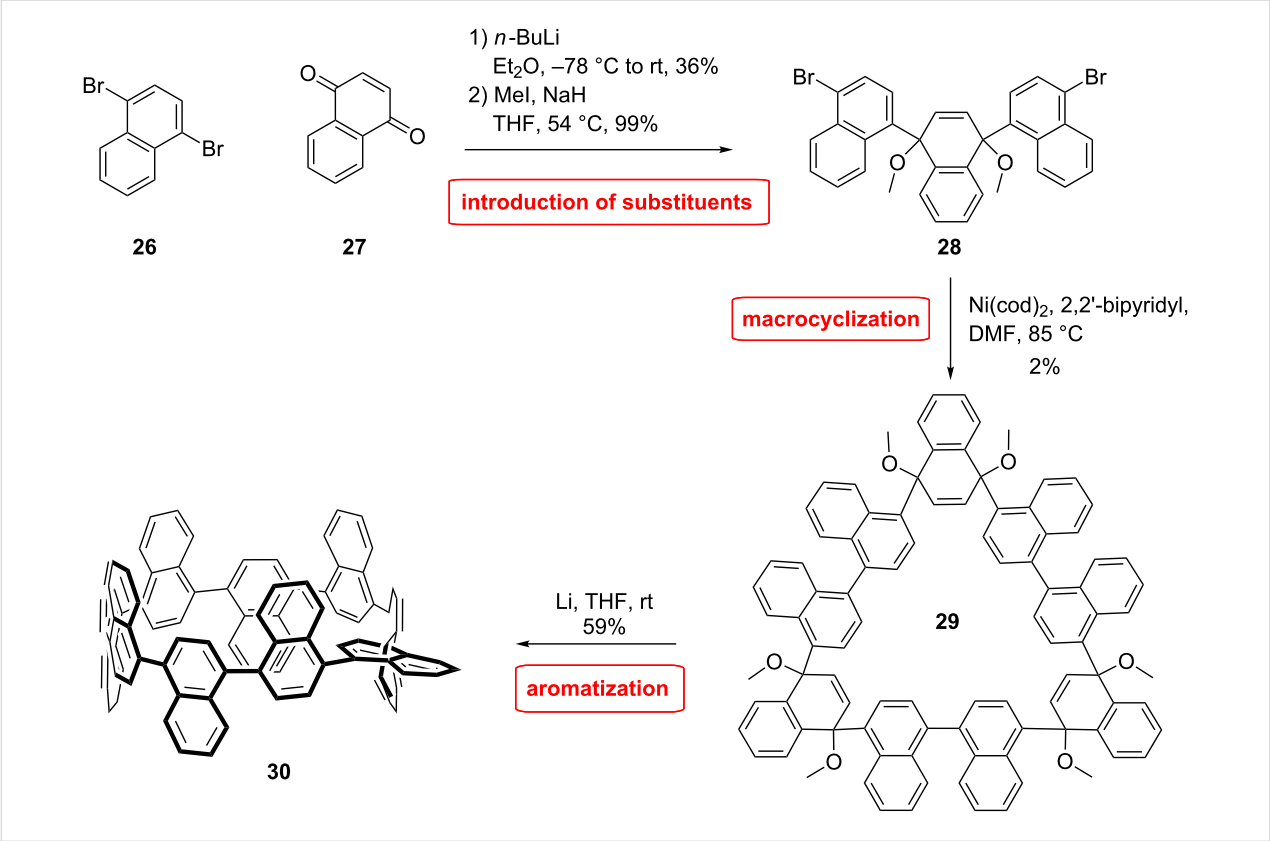

Scheme 6: Synthesis of a [9]cyclonaphthylene nanoring by Itami et al.

Therefore, the molecule has a low symmetry and dynamic conformational changes take place slowly on the NMR time scale at room temperature. Because of steric reasons, the dihedral angles between the naphthalene rings are around 60°, which is twice as much as in [9]CPP. [9]CPP as well as [9]CN are odd numbered which means it is not possible that the phenyl or naphthyl rings arrange in an alternated twisted structure. Therefore, a helical moiety has to be incorporated in the ring. In the case of [9]CN one of the naphthalene rings is parallel to the plane of the macrocyle. As a result, the molecule is chiral. The racemization was studied by computational models and compared with the rotation of 1,1'-binaphtyl moieties, observing an effect of the ring strain on the rotation mode. Compared to 1,1'-binaphthyl the interaction of the C8–H/C8'–H is less important due to the ring curvature. The maximum of absorption (378 nm) is shifted towards longer wavelengths than for the [9]CPP (340 nm) which can be attributed to the extension of the π-system. Fluorescence emission occurs at 491 nm which is similar to the corresponding CPP however with a quantum yield lowered by a factor of two [15].

Another naphthalene CPP has been synthesized by Batson and Swager [55], who used a similar strategy as the Itami group. They choose to use a benzene spacer to isolate 1,1'-binaphthyl units in order to facilitate the Scholl reaction to form perylene units (Scheme 7). Molecule **34** constitutes a good model for probing reaction conditions, which would be usable in the synthesis of larger nanobelts through cyclodehydrogenation.

The group of Wang [56] explored a different strategy to integrate a substituted naphthylene unit into CPP (Scheme 8). The square shaped subtituent was synthesized via Diels–Alder reaction of **35** and **31** selectively affording the *cis* product **36** after methylation. This building block was further submitted to macrocyclization using nickel-catalyzed homocoupling initially developed by Itami et al. The *syn* and *anti* trimers were isolated in 11% yield. Dimers were also isolated. The aromatization of **37** was performed by using DDQ yielding the corresponding [9]CPP with three 5,8-dimethoxynaphth-1,4-diyl units in 88% yield. However, the aromatization of the dimer precursor for the [6]CPP was not successful due to larger strain energy. The NMR study of **38** suggests that the phenyl units undergo fast rotation as only one set of signals was observed.

CPP dimers and other architectures

The structure of *para*-connected CPP resembles that of linear CNTs. The incorporation of other connectivities such as *meta* allows for the assembly of other complex geometries. The syn-

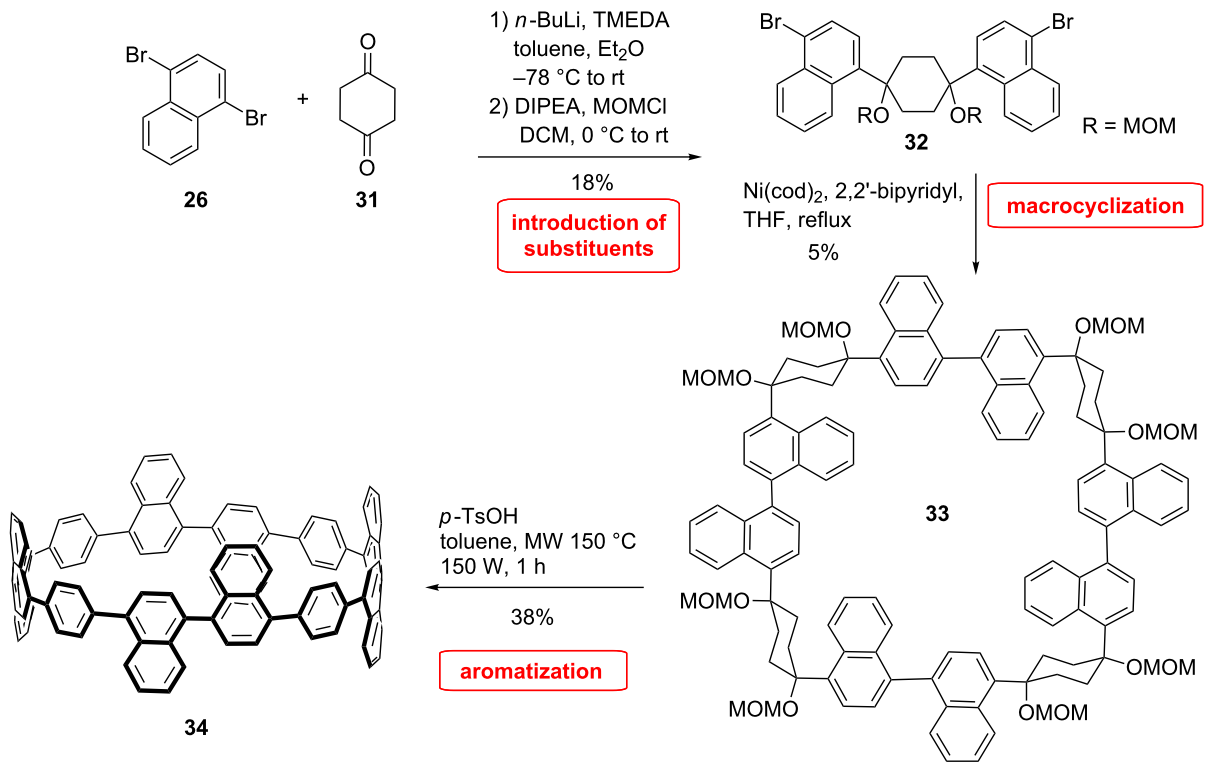

Scheme 7: Synthesis of a naphthylene-containing CPP by Swager and Batson.

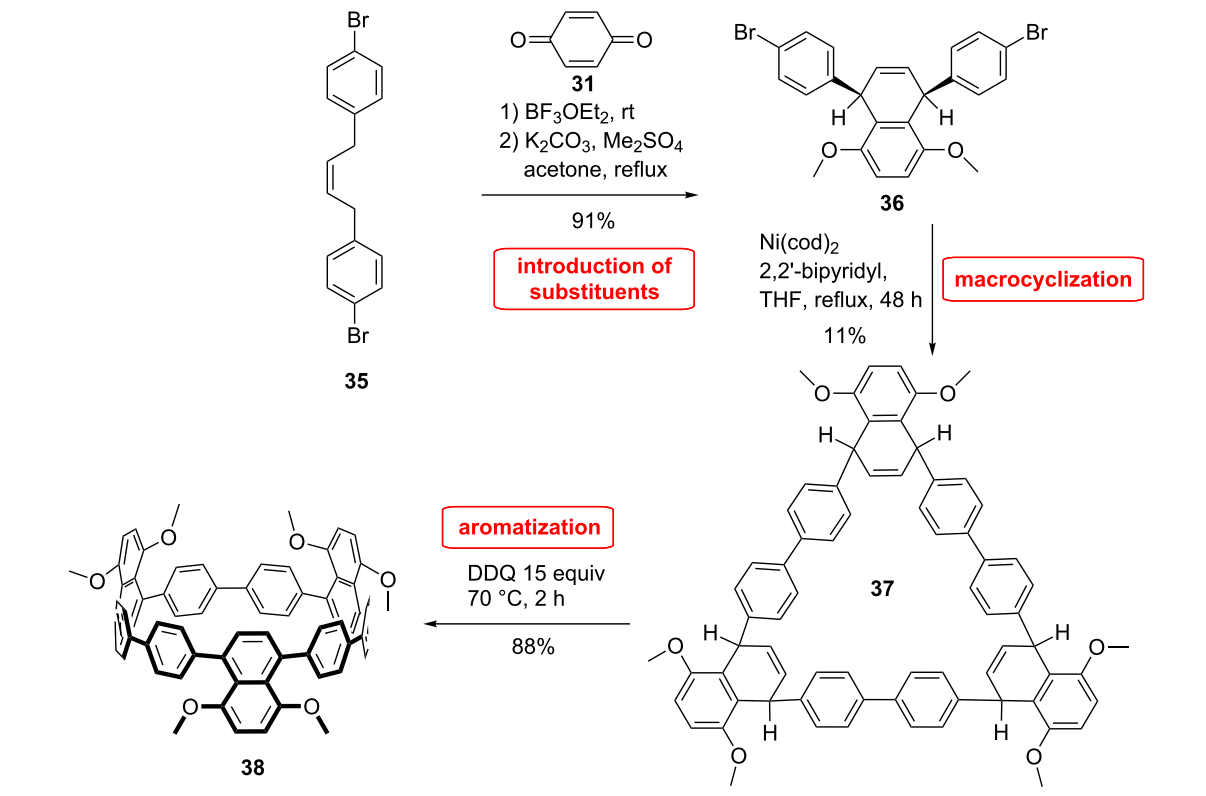

Scheme 8: Synthesis of functionalized cycloparaphenylenes by Wang et al.

thesis of a nanocage of interlinked CPP was performed by Itami et al. (Scheme 9) [57]. They used their L-shaped cyclohexane building block **16** coupled to a 1,3,5-triborylbenzene **39** as three-way unit. Suzuki coupling and macrocyclization afforded the precursor **41**. Aromatization of this cage precursor produced the beautiful conjugated nanocage molecule **42**, which could serve as template for a CNT junction.

Calculations show that the molecule has a D_3 symmetry, the trisubstituted benzene units are staggered by 12.5°, and the distance between these two connection units is 18.4 Å, which lies between the diameter of [13]CPP and [14]CPP. The strain energy was calculated through the homodesmotic reaction method to 67.2 kcal/mol.

Dimers of CPPs were prepared in the Jasti group by using a bromo-substituted CPP precursor (Scheme 10) [58]. The synthesis relied on a brominated cyclohexadiene building block **45**. This entity was then inserted in compound **46**, which was synthesized by a succession of Suzuki–Miyaura coupling reactions. With the bromo-functionalized macrocycle **47** in hand they performed the dimerization by coupling two macrocycles to an arene unit, either 1,4-benzene boronic ester (66%) or 1,5-naphtalene boronic ester (49%). The dimeric macrocycles were then aromatized under reductive conditions to obtain the corresponding CPP dimers **50** in 75% and 48% yield for the benzene and naphthalene junction, respectively. The molecules were rather insoluble, which is in sharp contrast to the monomeric CPP which is readily soluble in organic solvents.

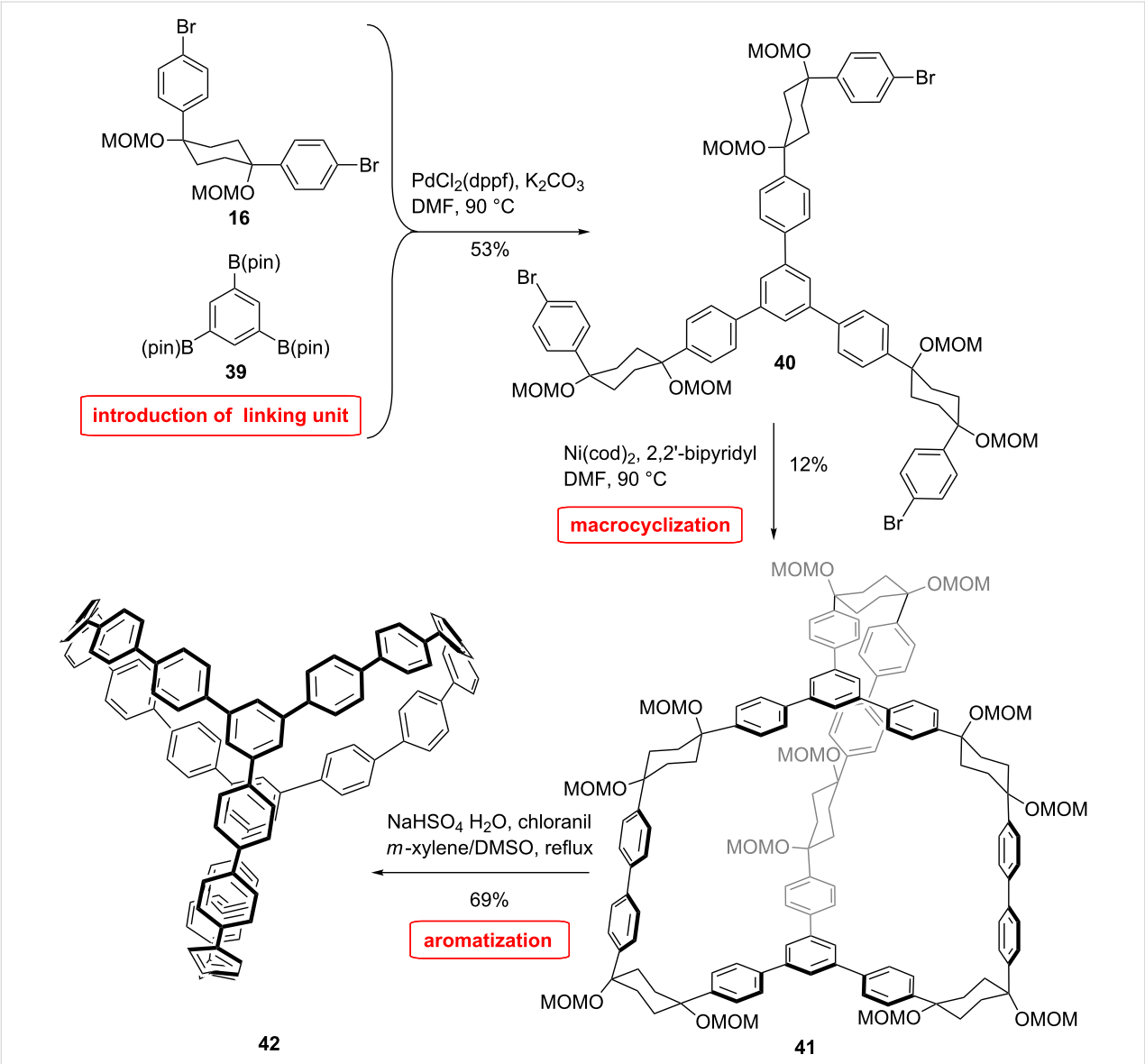

Scheme 9: Synthesis of a CNT junction by Itami et al.

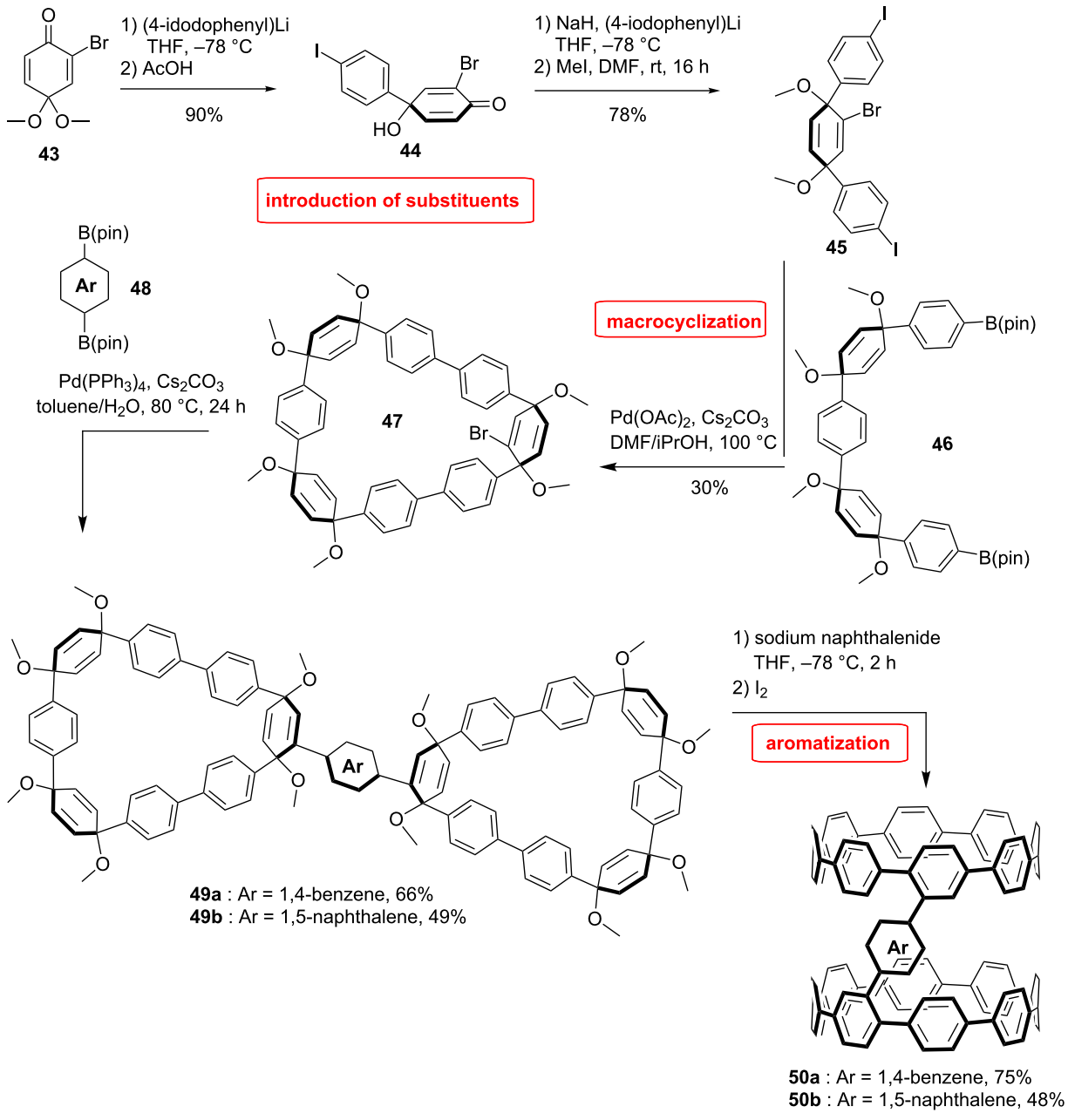

Scheme 10: Synthesis of CPP dimers by Jasti et al.

There are two conformers possible for the molecule: the *cis* conformer, in which the two rings are on top of each other like in a nanotube, and the *trans* conformer, in which the rings are far from each other. The *cis* conformer could serve as a starting point to construct a longer nanotube by closing more carbon–carbon bonds via Scholl reaction. Switching between the two configurations allows for interesting applications in host–guest chemistry. In the solid state, the *trans* structure was calculated to be lower in energy than the *cis* isomer. However, the dynamic change from *trans* to *cis* conformation was studied by DFT calculation and the energy barrier was found to be 13 kcal/mol and 20 kcal/mol for the reverse. The path with the lowest energy implies the flipping of one CPP ring over the other and not a simple rotation around the aryl linking unit. In this dynamic study the *cis* configuration was found to be the lowest in energy in the gas phase due to increased van der Waals interactions between the two CPP rings. Studies including solvent effects did not change the relative stability of the conformers compared to the gas phase calculations.

A directly linked CPP dimer has been synthesized by the group of Itami (Scheme 11) [59]. The synthesis relied again on the

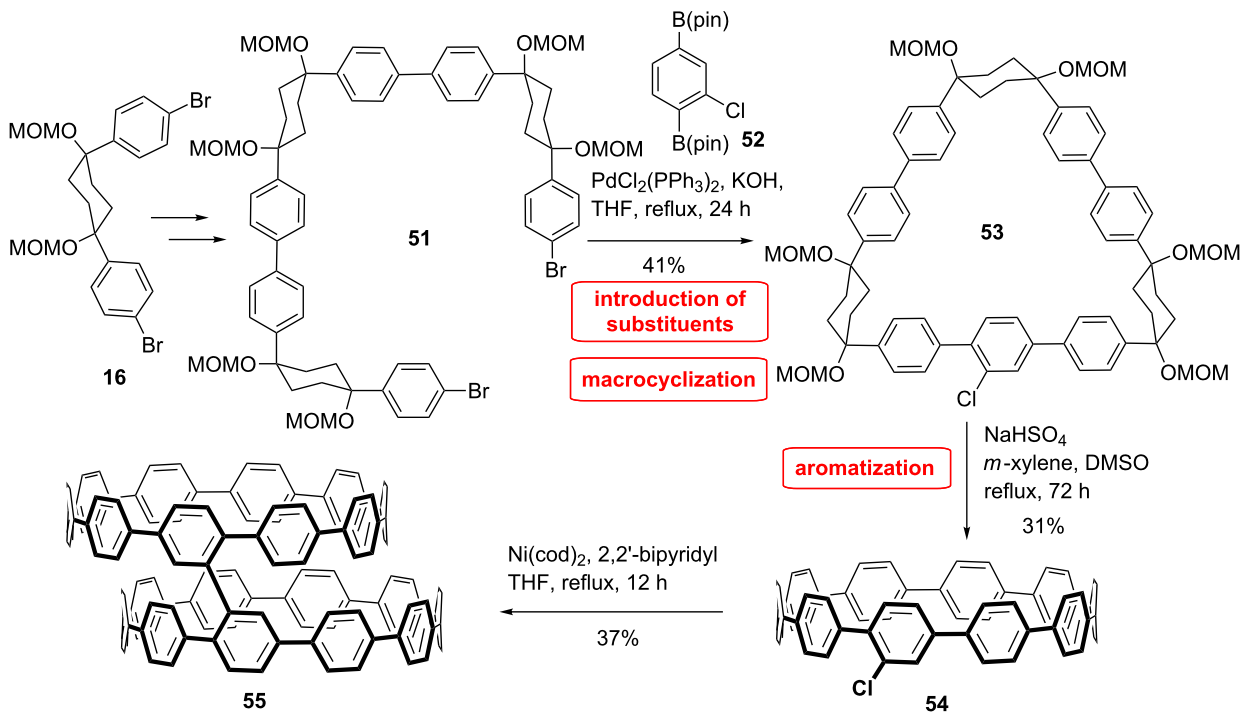

Scheme 11: Synthesis of a CPP dimer by Itami et al.

L-shaped building block **16** combined with a chlorobenzene unit **52**. This way, they accessed the first monohalogenated [10]CPP. This molecule offers various possibilities for further functionalization. They successfully managed the dimerization of the chloro[10]CPP **54** through Yamamoto coupling. The isomerization between the *cis* and *trans* configurations was studied by DFT calculations. Here again the most stable conformation is the *cis* form. The results show that the transition takes place through rotation of one of the CPP rings around the connected benzene ring with a barrier of 8.9 kcal/mol indicating a fast isomerisation process at room temperature.

Another synthesis of acene-based rings has being developed by the Isobe group (Scheme 12). Their work afforded different fragments of nanotubes [60,61], for instance, a fragment of a zig-zag CNT was targeted [60]. The shortest zig-zag nanotube is the cyclacene fragment. However, the synthesis of this molecule remains challenging, mainly because of the reactive edges. As an alternative, Isobe et al. prepared a fragment of zig-zag CNT by using chrysenylene building blocks coupled via platinum complexation and reductive elimination, featuring the strategy also applied by Yamago [60]. Surprisingly, only one diastereomer was obtained. Different atropisomers are possible depending on the orientation of the chrysene units. The two optically active enantiomers formed by this reaction could be separated.

The isolation of the enantiomers shows the strain induced atropisomerism. There is a strong rotational restriction at the single bond linkages maintaining the tube-like shape. Moreover, the

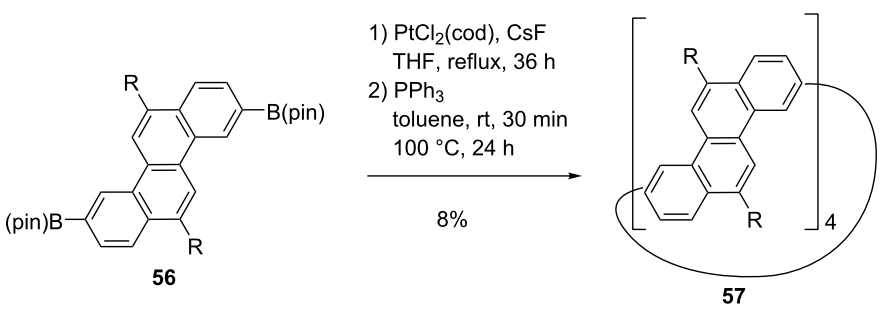

Scheme 12: Synthesis of a zig-zag CNT fragment by Isobe et al.

isomerization process could not be observed even at high temperatures showing a large rotation barrier and constriction at the single bond linkage. The solid state structure of the racemate presents a thread-in-bead columnar assembly with the hexyl chain of one enantiomer incorporated into the center of the other enantiomer forming pairs of enantiomers entangled together. Several pairs arrange in a tubular manner by incorporating hexyl chains of other pairs.

Heteroatomic cycloparaphenylenes

With all the strategies available, it is also possible to synthesize CPPs which contain heteroatoms, such as the nitrogen-containing CPP synthesized by Itami et al. by using bipyridine as a linear building block [62]. Such heteroatom-containing rings could pave the way to novel properties of CPPs through supramolecular assemblies, complex formation, or acid–base modifications and therefore offer access to new applications. The strategy for this synthesis relied on the same building block used by the Itami group for the synthesis of the parent CPP the only exception being the bipyridine building block which was inserted on two sides of compound **19** (Scheme 13). The bipyridine **58** was then again coupled with **19** in a Suzuki reaction to give the macrocyclic precursor **59** in 48% yield. Finally, the CPP **61** was obtained in 56% yield by an aromatiza-

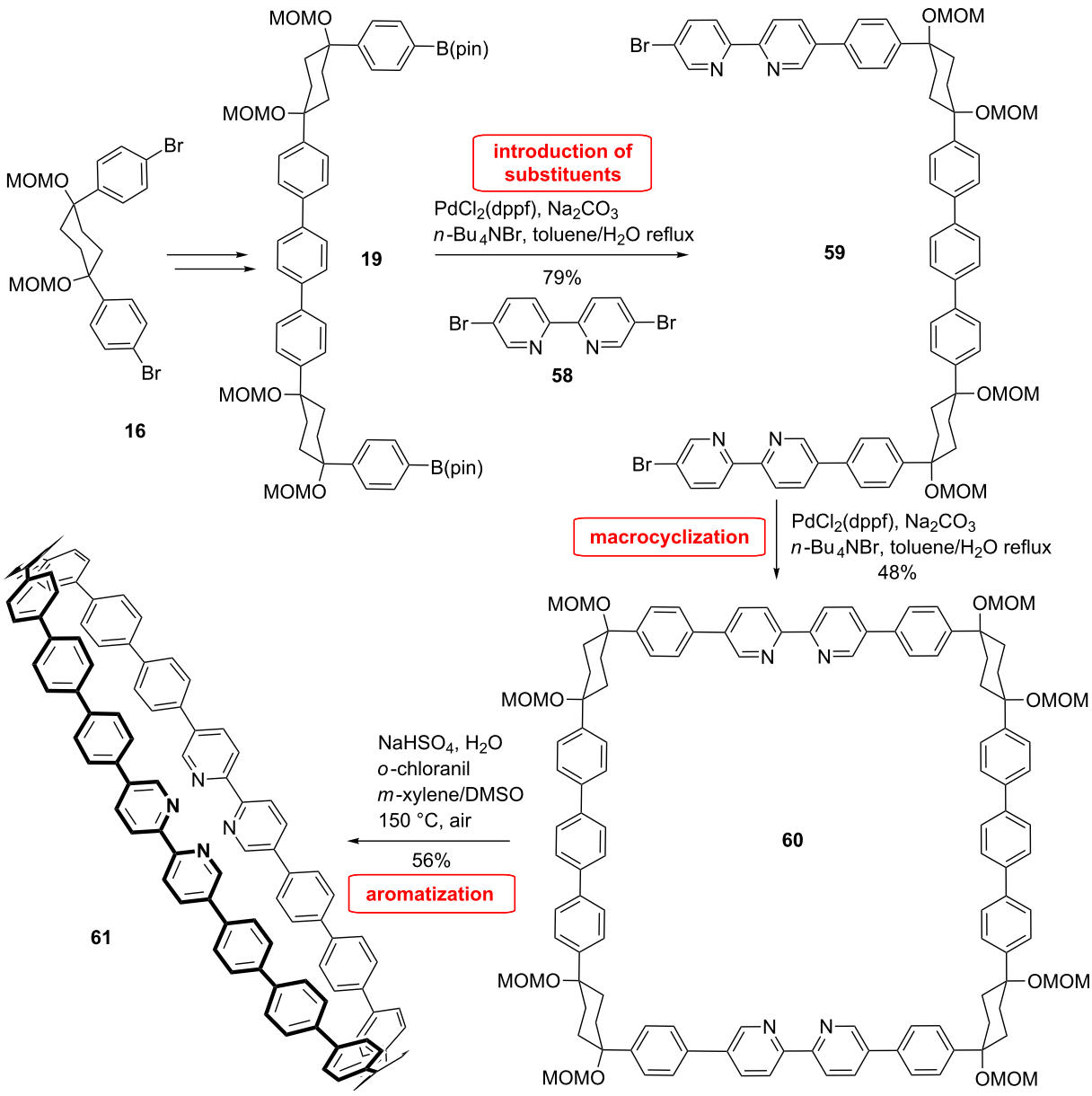

Scheme 13: Synthesis of a CPP with an inserted bipyridine by Itami et al.

tion reaction mediated by sodium bisulfate in the presence of chloranil.

Whereas the optical properties of **61** resemble those of large CPPs, a strong dependence on the pH value was observed. The absorption and emission spectra show broadening as well as red shift. This can be due a charge transfer excited state upon protonation of the bipyridine units. When the solution was neutralized, the previously observed absorption and fluorescence spectra were reproduced showing the reversibility of the process.

Conclusion

Different syntheses of CPPs of different diameters have been established. Based on these strategies a variety of substituted and non-phenyl containing CPPs have been prepared. All examples have the key steps of introducing the substituents, macrocyclization and finally aromatization. The possibility to add different substituents at a late stage in the synthesis is especially attractive. The incorporation of further functionalities into CPPs opens the way for the synthesis of larger nanobelts and other complex molecular architecture promising more and more creative new CPP-based structures in the near future.

Acknowledgements

The authors are thankful to the support by the COST action MP0901 NanoTP and Schweizer Staatssekretariat für Bildung und Forschung (SBF).

References

1. Kroto, H. W.; Heath, J. R.; O'Brien, S. C.; Curl, R. F.; Smalley, R. E. *Nature* **1985,** *318,* 162–163. doi:10.1038/318162a0
2. Novoselov, K. S.; Geim, A. K.; Morozov, S. V.; Jiang, D.; Zhang, Y.; Dubonos, S. V.; Grigorieva, I. V.; Firsov, A. A. *Science* **2004,** *306,* 666–669. doi:10.1126/science.1102896
3. Iijima, S. *Nature* **1991,** *354,* 56–58. doi:10.1038/354056a0
4. Huang, J.; Zhang, Q.; Zhao, M.; Wei, F. *Chin. Sci. Bull.* **2012,** *57,* 157–166. doi:10.1007/s11434-011-4879-z
5. Paradise, M.; Goswami, T. *Mater. Des.* **2007,** *28,* 1477–1489. doi:10.1016/j.matdes.2006.03.008
6. Scott, L. T.; Boorum, M. M.; McMahon, B. J.; Hagen, S.; Mack, J.; Blank, J.; Wegner, H.; de Meijere, A. *Science* **2002,** *295,* 1500–1503. doi:10.1126/science.1068427
7. Bianco, A.; Kostarelos, K.; Prato, M. *Curr. Opin. Chem. Biol.* **2005,** *9,* 674–679. doi:10.1016/j.cbpa.2005.10.005
8. Katz, E.; Willner, I. *ChemPhysChem* **2004,** *5,* 1084–1104. doi:10.1002/cphc.200400193
9. Baughman, R. H.; Zakhidov, A. A.; de Heer, W. A. *Science* **2002,** *297,* 787–792. doi:10.1126/science.1060928
10. Lieber, C. M. *Solid State Commun.* **1998,** *107,* 607–616. doi:10.1016/S0038-1098(98)00209-9
11. Omachi, H.; Nakayama, T.; Takahashi, E.; Segawa, Y.; Itami, K. *Nat. Chem.* **2013,** *5,* 572–576. doi:10.1038/nchem.1655
12. Omachi, H.; Segawa, Y.; Itami, K. *Acc. Chem. Res.* **2012,** *45,* 1378–1389. doi:10.1021/ar300055x
13. Li, H.-B.; Page, A. J.; Irle, S.; Morokuma, K. *ChemPhysChem* **2012,** *13,* 1479–1485. doi:10.1002/cphc.201200055
14. Camacho, C.; Niehaus, T. A.; Itami, K.; Irle, S. *Chem. Sci.* **2013,** *4,* 187–195. doi:10.1039/c2sc20878d
15. Segawa, Y.; Fukazawa, A.; Matsuura, S.; Omachi, H.; Yamaguchi, S.; Irle, S.; Itami, K. *Org. Biomol. Chem.* **2012,** *10,* 5979–5984. doi:10.1039/c2ob25199j
16. Nishihara, T.; Segawa, Y.; Itami, K.; Kanemitsu, Y. *J. Phys. Chem. Lett.* **2012,** *3,* 3125–3128. doi:10.1021/jz3014826
17. Fujitsuka, M.; Cho, D. W.; Iwamoto, T.; Yamago, S.; Majima, T. *Phys. Chem. Chem. Phys.* **2012,** *14,* 14585–14588. doi:10.1039/c2cp42712e
18. Fomine, S.; Zolotukhin, M. G.; Guadarrama, P. *J. Mol. Model.* **2012,** *18,* 4025–4032. doi:10.1007/s00894-012-1402-7
19. Iwamoto, T.; Watanabe, Y.; Sakamoto, Y.; Suzuki, T.; Yamago, S. *J. Am. Chem. Soc.* **2011,** *133,* 8354–8361. doi:10.1021/ja2020668
20. Iwamoto, T.; Watanabe, Y.; Sadahiro, T.; Haino, T.; Yamago, S. *Angew. Chem., Int. Ed.* **2011,** *50,* 8342–8344. doi:10.1002/anie.201102302
21. Sundholm, D.; Taubert, S.; Pichierri, F. *Phys. Chem. Chem. Phys.* **2010,** *12,* 2751–2757. doi:10.1039/b922175a
22. Segawa, Y.; Omachi, H.; Itami, K. *Org. Lett.* **2010,** *12,* 2262–2265. doi:10.1021/ol1006168
23. Bachrach, S. M.; Stück, D. *J. Org. Chem.* **2010,** *75,* 6595–6604. doi:10.1021/jo101371m
24. Wong, B. M. *J. Phys. Chem. C* **2009,** *113,* 21921–21927. doi:10.1021/jp9074674
25. Xia, J.; Jasti, R. *Angew. Chem., Int. Ed.* **2012,** *51,* 2474–2476. doi:10.1002/anie.201108167
26. Xia, J.; Bacon, J. W.; Jasti, R. *Chem. Sci.* **2012,** *3,* 3018–3021. doi:10.1039/c2sc20719b
27. Sisto, T. J.; Jasti, R. *Synlett* **2012,** *23,* 483–489. doi:10.1055/s-0031-1290360
28. Hirst, E. S.; Jasti, R. *J. Org. Chem.* **2012,** *77,* 10473–10478. doi:10.1021/jo302186h
29. Darzi, E. R.; Sisto, T. J.; Jasti, R. *J. Org. Chem.* **2012,** *77,* 6624–6628. doi:10.1021/jo3011667
30. Sisto, T. J.; Golder, M. R.; Hirst, E. S.; Jasti, R. *J. Am. Chem. Soc.* **2011,** *133,* 15800–15802. doi:10.1021/ja205606p
31. Jasti, R.; Bertozzi, C. R. *Chem. Phys. Lett.* **2010,** *494,* 1–7. doi:10.1016/j.cplett.2010.04.067
32. Jasti, R.; Bhattacharjee, J.; Neaton, J. B.; Bertozzi, C. R. *J. Am. Chem. Soc.* **2008,** *130,* 17646–17647. doi:10.1021/ja807126u
33. Sibbel, F.; Matsui, K.; Segawa, Y.; Studer, A.; Itami, K. *Chem. Commun.* **2014,** *50,* 954–956. doi:10.1039/c3cc48683d
34. Ishii, Y.; Nakanishi, Y.; Omachi, H.; Matsuura, S.; Matsui, K.; Shinohara, H.; Segawa, Y.; Itami, K. *Chem. Sci.* **2012,** *3,* 2340–2345. doi:10.1039/c2sc20343j
35. Segawa, Y.; Šenel, P.; Matsuura, S.; Omachi, H.; Itami, K. *Chem. Lett.* **2011,** *40,* 423–425. doi:10.1246/cl.2011.423
36. Segawa, Y.; Miyamoto, S.; Omachi, H.; Matsuura, S.; Šenel, P.; Sasamori, T.; Tokitoh, N.; Itami, K. *Angew. Chem., Int. Ed.* **2011,** *50,* 3244–3248. doi:10.1002/anie.201007232
37. Omachi, H.; Matsuura, S.; Segawa, Y.; Itami, K. *Angew. Chem., Int. Ed.* **2010,** *49,* 10202–10205. doi:10.1002/anie.201005734

38. Takaba, H.; Omachi, H.; Yamamoto, Y.; Bouffard, J.; Itami, K. *Angew. Chem., Int. Ed.* **2009,** *48,* 6112–6116. doi:10.1002/anie.200902617
39. Kayahara, E.; Patel, V. K.; Yamago, S. *J. Am. Chem. Soc.* **2014,** *136,* 2284–2287. doi:10.1021/ja413214q
40. Kayahara, E.; Iwamoto, T.; Suzuki, T.; Yamago, S. *Chem. Lett.* **2013,** *42,* 621–623. doi:10.1246/cl.130188
41. Kayahara, E.; Sakamoto, Y.; Suzuki, T.; Yamago, S. *Org. Lett.* **2012,** *14,* 3284–3287. doi:10.1021/ol301242t
42. Yamago, S.; Watanabe, Y.; Iwamoto, T. *Angew. Chem., Int. Ed.* **2010,** *49,* 757–759. doi:10.1002/anie.200905659
43. Fuhrmann, G.; Debaerdemaeker, T.; Bäuerle, P. *Chem. Commun.* **2003,** 948–949. doi:10.1039/b300542a
44. Sisto, T. J.; Tian, X.; Jasti, R. *J. Org. Chem.* **2012,** *77,* 5857–5860. doi:10.1021/jo301024g
45. Nishiuchi, T.; Feng, X.; Enkelmann, V.; Wagner, M.; Müllen, K. *Chem. – Eur. J.* **2012,** *18,* 16621–16625. doi:10.1002/chem.201203227
46. Tran-Van, A.-F.; Wegner, H. A. Strategies in Organic Synthesis for Condensed Arenes, Coronene, and Graphene. *Topics in Currrent Chemistry;* Springer: Berlin, Germany, 2013; pp 1–37. doi:10.1007/128_2013_465
47. Berresheim, A. J.; Müller, M.; Müllen, K. *Chem. Rev.* **1999,** *99,* 1747–1786. doi:10.1021/cr970073+
48. Müller, M.; Kübel, C.; Müllen, K. *Chem. – Eur. J.* **1998,** *4,* 2099–2109. doi:10.1002/(SICI)1521-3765(19981102)4:11<2099::AID-CHEM2099>3.0.CO;2-T
49. Tran-Van, A.-F.; Huxol, E.; Basler, J. M.; Neuburger, M.; Adjizian, J.-J.; Ewels, C. P.; Wegner, H. A. *Org. Lett.* **2014,** *16,* 1594–1597. doi:10.1021/ol500194s
50. Tran-Van, A.-F.; Götz, S.; Neuburger, M.; Wegner, H. A. *Org. Lett.* **2014,** *16,* 2410–2413. doi:10.1021/ol5007604
51. Omachi, H.; Segawa, Y.; Itami, K. *Org. Lett.* **2011,** *13,* 2480–2483. doi:10.1021/ol200730m
52. Yagi, A.; Venkataramana, G.; Segawa, Y.; Itami, K. *Chem. Commun.* **2014,** *50,* 957–959. doi:10.1039/c3cc48198k
53. Iwamoto, T.; Kayahara, E.; Yasuda, N.; Suzuki, T.; Yamago, S. *Angew. Chem., Int. Ed.* **2014,** *53,* 6430–6434. doi:10.1002/anie.201403624
54. Yagi, A.; Segawa, Y.; Itami, K. *J. Am. Chem. Soc.* **2012,** *134,* 2962–2965. doi:10.1021/ja300001g
55. Batson, J. M.; Swager, T. M. *Synlett* **2013,** *24,* 2545–2549. doi:10.1055/s-0033-1339882
56. Huang, C.; Huang, Y.; Akhmedov, N. G.; Popp, B. V.; Petersen, J. L.; Wang, K. K. *Org. Lett.* **2014,** *16,* 2672–2675. doi:10.1021/ol500904x
57. Matsui, K.; Segawa, Y.; Namikawa, T.; Kamada, K.; Itami, K. *Chem. Sci.* **2013,** *4,* 84–88. doi:10.1039/c2sc21322b
58. Xia, J.; Golder, M. R.; Foster, M. E.; Wong, B. M.; Jasti, R. *J. Am. Chem. Soc.* **2012,** *134,* 19709–19715. doi:10.1021/ja307373r
59. Ishii, Y.; Matsuura, S.; Segawa, Y.; Itami, K. *Org. Lett.* **2014,** *16,* 2174–2176. doi:10.1021/ol500643c
60. Hitosugi, S.; Yamasaki, T.; Isobe, H. *J. Am. Chem. Soc.* **2012,** *134,* 12442–12445. doi:10.1021/ja305723j
61. Hitosugi, S.; Nakanishi, W.; Isobe, H. *Chem. – Asian J.* **2012,** *7,* 1550–1552. doi:10.1002/asia.201200187
62. Matsui, K.; Segawa, Y.; Itami, K. *Org. Lett.* **2012,** *14,* 1888–1891. doi:10.1021/ol3005112

License and Terms

This is an Open Access article under the terms of the Creative Commons Attribution License (http://creativecommons.org/licenses/by/2.0), which permits unrestricted use, distribution, and reproduction in any medium, provided the original work is properly cited.

The license is subject to the *Beilstein Journal of Nanotechnology* terms and conditions: (http://www.beilstein-journals.org/bjnano)

The definitive version of this article is the electronic one which can be found at: doi:10.3762/bjnano.5.145

BEILSTEIN JOURNAL OF NANOTECHNOLOGY

Donor–acceptor graphene-based hybrid materials facilitating photo-induced electron-transfer reactions

Anastasios Stergiou, Georgia Pagona and Nikos Tagmatarchis*

Review

Open Access

Address:
Theoretical and Physical Chemistry Institute, National Hellenic Research Foundation, 48 Vassileos Constantinou Avenue, 11635 Athens, Greece

Email:
Nikos Tagmatarchis* - tagmatar@eie.gr

* Corresponding author

Keywords:
donor–acceptor; electron-transfer; functionalization; graphene; photophysical properties

Beilstein J. Nanotechnol. **2014,** *5,* 1580–1589.
doi:10.3762/bjnano.5.170

Received: 23 May 2014
Accepted: 22 August 2014
Published: 18 September 2014

This article is part of the Thematic Series "Atomic scale interface design and characterisation: Theory – Structure and dynamics".

Guest Editor: C. Ewels

© 2014 Stergiou et al; licensee Beilstein-Institut.
License and terms: see end of document.

Abstract

Graphene research and in particular the topic of chemical functionalization of graphene has exploded in the last decade. The main aim is to increase the solubility and thereby enhance the processability of the material, which is otherwise insoluble and inapplicable for technological applications when stacked in the form of graphite. To this end, initially, graphite was oxidized under harsh conditions to yield exfoliated graphene oxide sheets that are soluble in aqueous media and amenable to chemical modifications due to the presence of carboxylic acid groups at the edges of the lattice. However, it was obvious that the high-defect framework of graphene oxide cannot be readily utilized in applications that are governed by charge-transfer processes, for example, in solar cells. Alternatively, exfoliated graphene has been applied toward the realization of some donor–acceptor hybrid materials with photo- and/or electro-active components. The main body of research regarding obtaining donor–acceptor hybrid materials based on graphene to facilitate charge-transfer phenomena, which is reviewed here, concerns the incorporation of porphyrins and phthalocyanines onto graphene sheets. Through illustrative schemes, the preparation and most importantly the photophysical properties of such graphene-based ensembles will be described. Important parameters, such as the generation of the charge-separated state upon photoexcitation of the organic electron donor, the lifetimes of the charge-separation and charge-recombination as well as the incident-photon-to-current efficiency value for some donor–acceptor graphene-based hybrids, will be discussed.

Introduction

Among the outstanding forms of carbon nanostructures, graphene, a single layer of carbon, is a newly available material exhibiting unique mechanical [1] and electronic properties [2] and can be described as one of the most extensively examined materials of recent years [3,4]. Diverse approaches have been developed to obtain graphene sheets, including the mechanical cleavage of graphite [3], chemical vapor deposition on metal surfaces [5,6], liquid exfoliation via sonication [7,8], dissolu-

tion in superacids such as chlorosulfonic acid [9] and ball milling [10]. However, a major drawback of graphene, likewise of carbon nanotubes, stems from its insolubility in all solvents, which impedes the chemical manipulation toward applications. There are two main routes to overcome this hurdle. Namely, this can be accomplished by starting with water-soluble graphene oxide (GO), which can be reduced to the so-called reduced graphene oxide (rGO), followed by post-modification to acquire functionalized graphene [11]. However, the reduction of GO sometimes leads to amorphous carbon [12], and often the graphene sp^2-network is incompletely restored. Therefore the properties of the resulting rGO significantly deviate from those of pristine graphene. Hence, this particular approach in not suitable for applications in which the novel electronic properties of graphene are of primary importance. Alternatively, wet exfoliation of graphite followed by functionalization is a more efficient strategy. Although functionalization of exfoliated graphene can be achieved by either covalent anchoring of organic molecules onto the graphene lattice [13] or supramolecularly, by π–π stacking and/or van der Waals interactions [14], the latter methodology suffers from weak interactions between the two species (i.e., graphene and organic units), which often leads to a loss of the organic moiety. Apparently, covalent functionalization of exfoliated graphene, in which the organic unit is tightly attached on the graphene network, is the method of choice for preparing novel donor–acceptor hybrid materials that can potentially facilitate photo-induced electron-transfer phenomena.

Single-layer, bilayer and oligo-layer graphene sheets have been utilized to fabricate donor–acceptor ensembles potentially useful in energy conversion schemes. Actually, electrons can travel without scattering around the 2D crystal structure of graphene [15], thus guaranteeing a continuous lossless electron flow. In addition, considering that carbon nanotubes are generally produced as a mixture of metallic and semiconducting components, and also sometimes retain significant amounts of metal nanoparticles as impurities, the advantageous character of graphene in the construction of donor–acceptor systems is easily understood. Although the field is in its infancy, a few hybrid materials composed of graphene and photoactive components, such as porphyrins and phthalocyanines, have been prepared and evaluated regarding photo-induced charge transfer phenomena [16-18]. Moreover, semiconducting quantum dots such as CdS [19-22], CdSe [23-26], CdTe [27,28], ZnO [29,30] and composites thereof, for instance, Au nanoparticles [31,32] have been incorporated into graphene sheets (GO or rGO) to yield donor–acceptor systems. However, the aim of this mini-review is to highlight recent advances in the preparation of graphene-based hybrid materials with organic electron donors for energy conversion. Additonally, routes and strategies for the chemical functionalization of graphene with photoactive electron donors will be presented and common techniques for characterizing and evaluating the photophysical properties of the materials will be discussed.

Review

Chemical functionalization toward the formation of donor–acceptor hybrids

A plethora of soluble and easy-to-handle graphene-based materials have been prepared and methodologies for the functionalization of graphene have already been reviewed [12,33-37]. In Scheme 1, a collection of the major chemical reactions leading to the covalent modification of a graphene framework are displayed. Briefly, after the exfoliation of graphite, the following reactions can be performed to modify the graphene sheet (summarized in Scheme 1):

1. [3 + 2] 1,3-Dipolar cycloaddition of in situ generated azomethine ylides to introduce fused pyrrolidine rings into the skeleton of graphene [38]. Azomethine ylides are organic 1,3-dipoles possessing a carbanion next to an iminium ion and can be readily produced upon decarboxylation of the iminium salts derived from the condensation of α-amino acids with aldehydes or ketones. When azomethine ylides are added to graphene, a fused pyrrolidine ring is formed at the junction between two six-membered rings of the graphene lattice. Notably, functionalized aldehydes lead to the formation of 2-substituted pyrrolidines, whereas the reaction with N-substituted glycines leads to N-substituted pyrrolidines, thus allowing for the preparation of numerous custom-synthesized graphene-based materials;
2. [1 + 2] Cycloaddition of malonate derivatives, the so-called Bingel reaction, yielding cyclopropane rings on graphene [39]. This versatile modification involves the generation of carbon nucleophiles from α-halo esters and their subsequent regioselective addition to graphene. In general, the addition takes place on double bonds between two six-membered rings present on graphene, yielding methano-modified graphene-based materials. Moreover, modifications of the original Bingel reaction exist, utilizing (i) carbanionic precursors to methano-modified graphene other than malonates, and (ii) alternative pathways generating the reactive monohalomalonate intermediate in situ;
3. Addition of in situ generated aryl diazonium salts, proceeding via the release of dinitrogen [40]. The reaction mechanism involves an electron transfer from graphene to the diazonium salt, resulting in the formation of a radical aryl unit, which subsequently adds to the sp^2-carbon lattice of graphene;

4. Addition of azides forming aziridine adducts onto graphene [41-43]. The particular functionalization proceeds via nitrenes as generated upon the thermal (or photochemical) decomposition of azides and the liberation of dinitrogen.

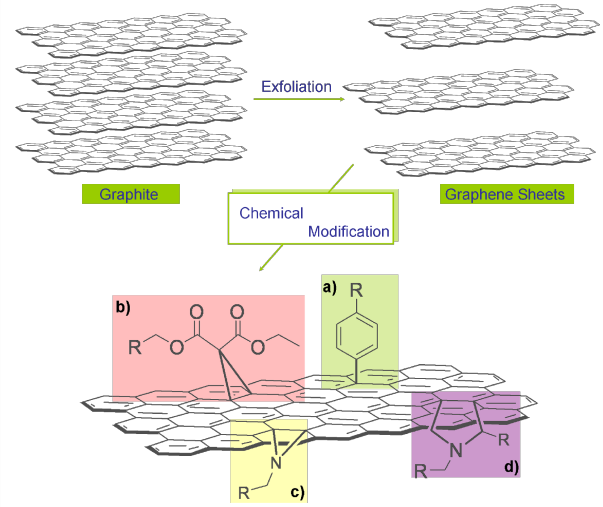

Scheme 1: General chemical modification routes for exfoliated graphene sheets. (a) [3 + 2] 1,3-dipolar cycloaddition of in situ generated azomethine ylides, (b) [1 + 2] Bingel cycloaddition, (c) aryl diazonium addition, and (d) azide addition.

Characterization, charge-separation and incident-photon-to-current efficiency

Raman spectroscopy is an extremely useful tool for characterizing graphene-based materials. Pristine graphite exhibits two characteristic Raman modes, namely the G-band, due to the presence of sp^2-hybridized carbon atoms at 1585 cm^{-1} and the 2D band at a higher frequency of around 2725 cm^{-1}. In addition, functionalized graphene sheets exhibit a new band, the so-called disorder D-band at around 1350 cm^{-1}, due to the presence of sp^3-hybridized carbon atoms, present at defects and/or anchor sites of functional groups. Furthermore, the 2D band in functionalized graphene shifts to lower frequencies and narrows compared to that of graphite. Thermal gravimetric analysis gives information about the degree of functionalization in modified graphene sheets because the covalent attachment of the organic moieties can be thermally eliminated, while intact graphite is thermally stable under inert atmosphere. Moreover, microscopy techniques such as TEM and AFM offer significant insight into the morphology of graphene and especially the number of layers in a particular sample. Overall, based on such complementary spectroscopic, microscopy and thermal techniques graphene-based hybrid materials can be qualitatively monitored, while at the same time information about the dimensions and purity is obtained.

With regard to energy conversion schemes, the challenge for constructing robust and functional architectures made of graphene and photo- and/or electro-active components is met by considering and applying to a large extent the aforementioned functionalization strategies. In this respect, a few covalently linked graphene sheets with organic electron-donor moieties to facilitate photo-induced electron-transfer processes have been synthesized. Briefly, photo-induced excitation of the organic electron donor in the graphene-based hybrid materials results on the formation of the singlet-excited state of the organic component. Then, charge-separation takes place and the efficiency of the whole process is governed by how fast or slow the recombination of charges occurs. A schematic description of such a process, which sometimes may be quite complex involving triplet states as derived upon intersystem crossing, is presented in Figure 1.

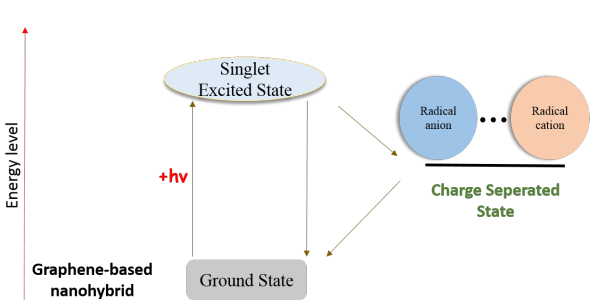

Figure 1: Illustrative energy diagram for the photo-induced formation of the charge-separated state of graphene-based hybrid materials.

Usually, the photoelectrochemical measurements of graphene-based hybrid materials with photoactive organic electron donors are carried out in a three-compartment cell using a potentiostat, employing a saturated calomel reference electrode, a working electrode and a Pt wire gauze counter electrode. This configuration allows for photocurrent measurements under electrochemical bias. Electrophoretic deposition is applied to fabricate films of the graphene-based hybrid material onto an optically transparent electrode (OTE) covered with nanostructured SnO_2. Typically, a suspension of the graphene-based hybrid material in THF is transferred to a cuvette, then, two OTEs cut from conducting glass are inserted, and a DC electric field is applied. Then, the graphene-based hybrid material from the suspension is driven to the surface of the positive electrode, and a robust thin-film (abbreviated as OTE/SnO_2/graphene-based hybrid material) is deposited within a short period of time. The photocurrent action spectrum of the OTE/SnO_2/graphene-based hybrid material electrode is evaluated by examining the wavelength dependence of the incident-photon-to-current conversion efficiency (IPCE). The IPCE values are calculated by normalizing the photocurrent densities by energy and intensity of the inci-

dent light according to the following equation:

$$\text{IPCE}\ (\%) = 100 \times 1240 \times i / \left(W_{\text{in}} \times \lambda\right),$$

where i is the photocurrent density ($A \cdot cm^{-2}$), W_{in} is the incident light intensity ($W \cdot cm^{-2}$), and λ is the excitation wavelength (nm).

Donor–acceptor hybrids based on graphene oxide or reduced graphene oxide

The unique and notable features of porphyrins and phthalocyanines as light-harvesting antennas with high extinction coefficients and remarkable redox properties make them promising electron donors to be associated with graphene. The very first approach of associating porphyrins with graphene was made by condensing an amino-modified tetraphenylporphyrin (TPP) to the carboxylic functionalities present in GO [44] providing the GO–TPP hybrid structure shown in Figure 2. The observed luminescence quenching of TPP in the GO–TPP hybrid material is indicative of a strong electronic interaction between TPP in the excited state and GO. Possible pathways for the fluorescence quenching of TPP are attributed either to an electron transfer or to an energy transfer to GO. Additionally, the formation of the charge-separated state $(GO)^{\bullet-}$–$(TPP)^{\bullet+}$ was shown to have an energy gap of 0.87 eV, while the IPCE was calculated to be 1.3% [45].

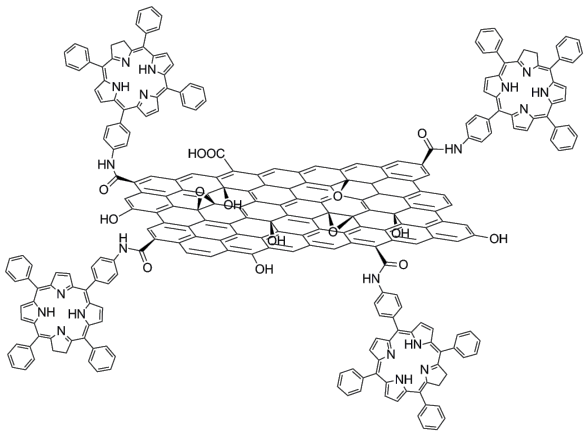

Figure 2: Tetraphenylporphyrin (TTP) condensed onto graphene oxide (GO) yielding GO–TPP hybrid material [44].

Along the same lines, when hydroxy-functionalized porphyrin (H_2P) was condensed onto GO sheets, the GO–H_2P hybrid material showed enhanced non-linear optical (NLO) properties, which were mainly ascribed to photo-induced electron-transfer from H_2P to GO [46]. Similarly, an amino-modified zinc phthalocyanine (ZnPc) was conjugated to GO furnishing the GO–ZnPc hybrid, which showed enhanced NLO properties due to strong electronic interactions between the donor and acceptor components within the nanohybrid material [47].

As a different route taken to associate porphyrin units with GO, an imidazolium ionic-liquid was conjugated to GO forming an amide bond. The presence of the positively charged imidazolium moiety allows the modulation of the dispersibility of the modified GO material in aqueous media and organic solvents by simply exchanging and altering the counter anion of the imidazolium unit. More importantly, when an anionic porphyrin was incorporated as counter anion to the GO–ionic-liquid hybrid material, electronic interactions between the porphyrin and the GO lattice were identified [48].

Zinc(II) phthalocyanine (ZnPc) as electron donor and C_{60} were added to GO through an esterification reaction between the carboxyl groups of GO and the hydroxy groups present on ZnPc as well as on the fullerene derivative. Photoexcitation of ZnPc–GO–C_{60} at 390 nm, the wavelength at which ZnPc was predominantly excited, resulted in the identification of the first singlet excited state of ZnPc. However, photoexcitation at 532 nm, at which mainly C_{60} was excited, revealed the formation of both a ZnPc radical cation and a C_{60} radical anion. The latter results, as obtained from nanosecond transient absorption spectroscopy measurements, ascertain the formation of a charge-separated state in the ZnPc–GO–C_{60} hybrid material [49].

Recently, the fabrication of a composite of GO and ferrocene moieties (GO–Fc, see Figure 3) was reported [50]. Although, the study refers to graphene oxide, it is the first report that describes the combination of graphene and ferrocene properties through chemical bonding. The photo-responsiveness of the developed composite was investigated by fabricating a Au/GO–Fc/Au device. Interestingly, a significant enhancement in current density under illumination with light was observed, which suggests charge-transfer processes within the GO–Fc hybrid material.

As described above, cations of transition metals are often present in chromophores (the central metal core of Pcs, porphyrins etc.) and take part in the electron/energy transfer processes. Very recently, a terpyridine (tpy) derivative, as a ligand for Fe(II) ions, was used to modify graphene oxide [51]. More precisely, Fe(II) coordinates tpy groups of the upper surface of one of the graphene sheets with the same groups of the lower surface of another graphene sheet, promoting the self-assembly of GO. The Fe–tpy–GO nanohybrid fully decomplexes when treated with EDTA and re-complexes after fresh addition of Fe(II) (Scheme 2). Furthermore, Fe–tpy–GO was tested as a catalyst for the oxygen reduction reaction (ORR) and

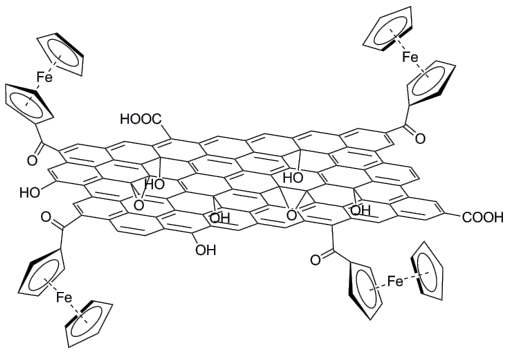

Figure 3: Ferrocene units anchored to graphene oxide (GO) forming a GO–Fc hybrid material [50].

found to be durable against carbon monoxide poisoning and to exhibit a higher fuel selectivity compared with commercially available Pt/C electro-catalysts. The ORR reactivity is tightly connected to electron transfer processes, thus indicating indirectly the occurrence of such phenomena. Ruthenium(II) was also employed as a coordinating cation and resulted in a Ru–tpy–GO hybrid material with an enhanced photocurrent response, higher than GO and Fe–tpy–GO, probably due to a more effective electron transfer from the Ru–tpy core to the graphene network. This class of self-assembled covalently functionalized GO-based nanohybrids is a promising new member in the family of graphene hybrid materials for potential applications in energy conversion and storage.

On similar grounds, rGO was initially modified by phenylacetylene units, which were used to mediate the grafting of zinc–porphyrin (ZnP) and ruthenium–phenanthroline (RuP) chromophores through a copper-catalyzed "click" chemistry reaction [52]. The preparation of the RuP–rGO hybrid material is illustrated in Scheme 3. The excellent dispersibility of the two novel types of graphene-based nanostructures in common organic solvents allowed for the easy characterization by various microscopy and spectroscopic techniques. Spectroscopic results of the ground and excited states gave important insights about the electronic communication between the chromophore moiety and rGO, which lead to the fabrication of photoelectrochemical cells. The photo-induced electron-transfer properties of ZnP–rGO and RuP–rGO were evaluated by examining the photocurrent responses in thin films on indium tin oxide (ITO).

In all the above studies, the hybrid materials were applied for energy conversion. However, the unique properties of graphene and in particular its ability to efficiently quench the photo-induced emission of electron donors have recently been used for other purposes. Thus, it is interesting to note that, although graphene-based biomaterials are out of the scope of this mini-review, GO has been covalently functionalized with peptides, antibodies and other biomolecules for applications in diagnostics, novel therapeutic approaches and near infrared (NIR) photo-thermal therapies [53]. A representative work demonstrates the usage of a GO–coumarin conjugate as an activated

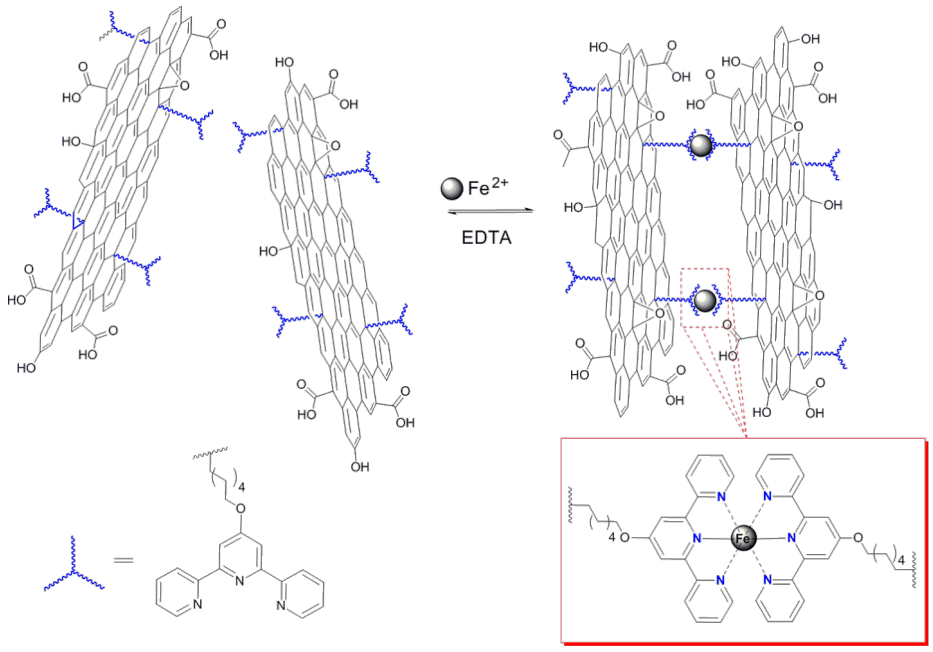

Scheme 2: Iron(II) coordinated on terpyridine (tpy) moieties covalently anchored to graphene oxide (GO) forming GO–tpy–Fe hybrids [51].

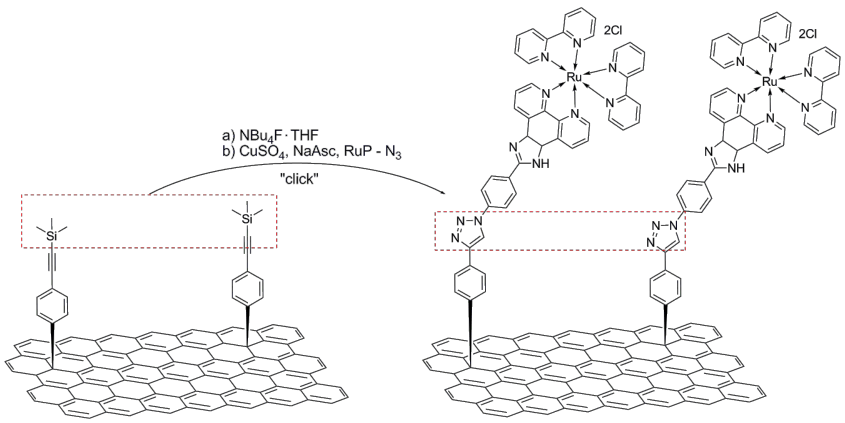

Scheme 3: "Click" reaction for the grafting of a porphyrin onto reduced graphene oxide sheets that was pre-modified by phenylacetylene units [52].

fluorescent imaging probe with high sensitivity in the visualization of cancer cells [54]. The fluorescence of the probe can be switched off or on during intracellular imaging. Normally, the probe shows no or weak fluorescence (off) due to the fluorescence quenching of the coumarin moiety. However, fluorescence is activated (on) and significantly enhanced inside the cells by glutathione-initiated dissociation.

Donor–acceptor hybrids based on exfoliated graphene

However, as mentioned earlier, the surface defects in the sp^2-network of GO influence the electronic and optical properties of the hybrid materials. Therefore, free TPP as well as Pd-metallated TPP were added to exfoliated graphene trough a 1,3-dipolar cycloaddition of azomethine ylides [55]. In this approach, graphite flakes were sonicated in *o*-DCB to induce exfoliation. In the following step, sarcosine and the corresponding aldehydes bearing the TPP and Pd–TPP moieties were added and the reaction mixture was stirred at 160 °C under N_2 for one week to yield the structures shown in Figure 4. The presence of TPP or Pd–TPP in the graphene-based hybrid materials was confirmed by standard spectroscopic methods, such as UV–vis, Raman, FTIR and XPS. Complementary electron microscopy studies showed that the functionalization processes did not affect the morphology of graphene in the hybrid materials. More importantly, fluorescence and phosphorescence quenching of either the free or the Pd-metallated porphyrin was observed, with a simultaneous decrease on the fluorescence emission lifetimes. These observations are indicative of intrahybrid interactions in the excited state through energy- and/or electron-transfer between graphene and the covalently bound porphyrin moieties. It is noteworthy, that the particular type of functionalization resulted in a relatively low loading of porphyrins on graphene, as calculated by thermogravimetry. Thus, the π-electronic network of graphene was preserved to large extent, which renders the hybrid materials suitable for applications in solar and/or photoelectrochemical cells.

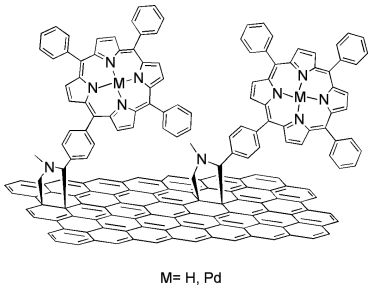

Figure 4: Free and Pd-metallated tetraphenylporphyrin moieties as substituents of pyrrolidine rings covalently anchored to exfoliated graphene [55].

Another graphene-based hybrid material was prepared in which a porphyrin was anchored to graphene through Suzuki coupling of iodophenyl-functionalized graphene and the corresponding porphyrin boronic ester [56]. The covalently linked graphene–porphyrin hybrid was especially designed to possess a short, yet rigid phenylene spacer between porphyrin and graphene. Photophysical measurements revealed the presence of a short-lived porphyrin singlet excited state (38 ps), however, without yielding the porphyrin radical cation, thus suggesting that energy transfer from the porphyrin excited state to the graphene sheets occurs. Moving a step forward, a prototype photoelectrochemical device, in which a SnO_2 electrode was coated with the aforementioned graphene–porphyrin hybrid material, was constructed. Photophysical and electrical measurements revealed the absence of any photocurrent response from the porphyrin absorption, leading to a maximum IPCE value of approximately 3%.

A further survey of the functionalization of graphene with organic electron donors revealed that phthalocyanines were introduced on exfoliated graphene in parallel and via two independent routes. In the first approach, the covalent grafting of (2-aminoethoxy)(tri-*tert*-butyl)phthalocyanine zinc (ZnPc) to exfoliated graphene sheets via direct nucleophilic addition of primary amines was accomplished (Figure 5) [57]. The ZnPc–graphene hybrid material was extensively characterized by complementary spectroscopic means as well as electron microscopy. Efficient fluorescence quenching of ZnPc in the ZnPc–graphene hybrid material was observed and the deactivation pathway was evaluated by using femtosecond transient absorption spectroscopy. The charge-separated state $ZnPc^{\bullet+}$–$graphene^{\bullet-}$ was identified. An electrode of the ZnPc–graphene hybrid material was prepared and its photoelectrochemical properties were examined. It was found to exhibit stable and reproducible photocurrent responses, and the incident-photon-to-current conversion efficiency was determined to be 2.2% at 420 nm. These results highlight the important role of the covalent grafting of ZnPc onto the graphene sheet for enhancing the photo-induced electron-transfer phenomena and achieving higher IPCE values as compared to non-covalently interacting ZnPc [58], or ZnPc-functionalized (phenylene vinylene) oligomers [59].

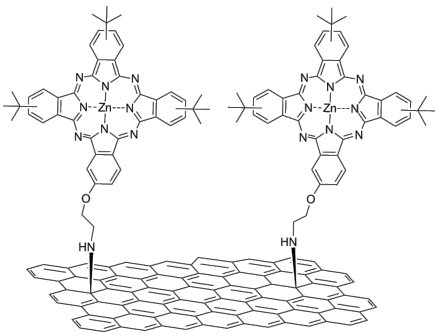

Figure 5: Covalent grafting of (2-aminoethoxy)(tri-*tert*-butyl)phthalocyanine zinc to exfoliated graphene sheets via direct nucleophilic addition of primary amines [57].

In the second strategy followed for the realization of a Pc–graphene hybrid, few-layered graphene, obtained by exfoliating graphite through sonication, was utilized. The exfoliated graphene sheets were then reacted with excess *N*-methylglycine and 4-formylbenzoic acid to yield functionalized graphene that carries pyrrolidine rings with pendant phenylcarboxylic acid units. In the next step, the condensation between the –COOH units of the pre-functionalized graphene and mono-OH-derivatized phthalocyanine, in the presence of EDC/HOBt as activators, resulted in the graphene–Pc hybrid material (Figure 6) [60]. Photoexcitation of Pc–graphene and evaluation of the species by pump-probe femtosecond transient absorption spectroscopy revealed the formation of the radical anion of graphene through a broad band in the NIR region. Based on multi-wavelength analysis, a short-lived and a long-lived component with lifetimes of 3.3 and 270 ps, respectively, in DMF were identified, suggesting that the ultra fast charge-separation in the Pc–graphene is followed by a slower charge-recombination.

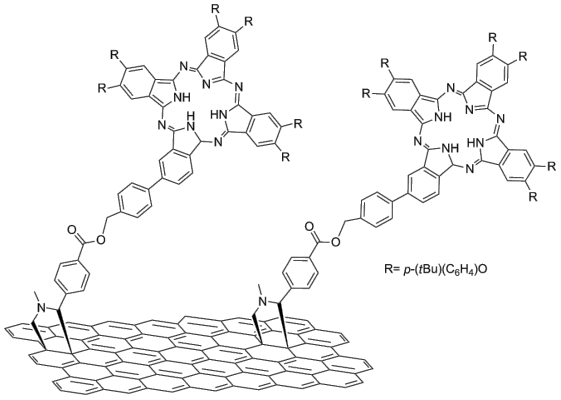

Figure 6: Phthalocyanine–graphene hybrid material, prepared upon condensation of mono-OH-derivatized phthalocyanine with pendant phenylcarboxylic acid units present as substituents of pyrrolidine rings on pre-modified graphene sheets [60].

Recently, a sulfonyl-substituted zinc phthalocyanine was synthesized and covalently bound to exfoliated graphene via "click" chemistry (Figure 7). Interestingly, due to the strong electron-withdrawing effect of the sulfonyl units, the particular phthalocyanine component acts as electron acceptor in the graphene–ZnPc hybrid material [61]. Complementary electrochemical measurements and photophysical assays, based on fluorescence emission and transient absorption spectroscopy, verified that electron transfer occurs from graphene to ZnPc.

Beyond the coupling of porphyrin and phthalocyanine dyes to graphene, other photo- and/or electro-active units have been also introduced. In this context, an extended tetrathiafulvalene (exTTF) was grafted to exfoliated graphene via a microwave-assisted Bingel reaction (Figure 8) [39]. The new exTTF-graphene material was fully characterized by spectroscopic, thermal, and microscopy means. Importantly, the electrochemical properties of exTTF-graphene were studied by cyclic voltammetry which allowed identification of the formation of a radical ion pair that includes one-electron oxidation of exTTF and one electron reduction of graphene.

Covalently functionalized few-layer graphene with the bipyridine ruthenium complex (2,2′-bipyridyl)-4-pyridyl-

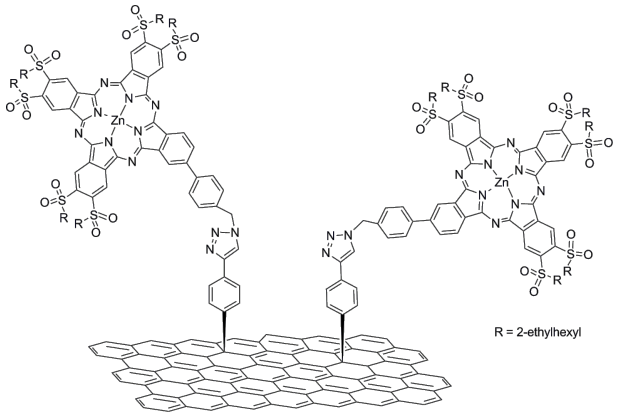

Figure 7: Sulfonyl-substituted zinc phthalocyanine covalently bound to pre-modified graphene via "click" chemistry [61].

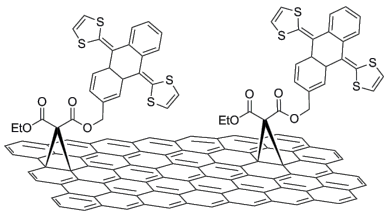

Figure 8: Extended tetrathiafulvalene units covalently attached to exfoliated graphene via Bingel cycloaddition reaction [39].

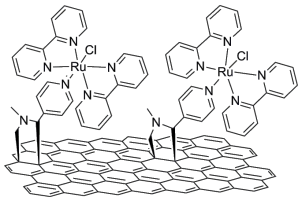

Figure 9: Graphene sheets covalently functionalized with a Ru-bipyridine complex [62].

ruthenium(II)chloride, $Ru(bpy)_2(py)Cl$, results in the formation of another novel nanohybrid material (Figure 9). A slow recombination of the photoexcited charges was identified and demonstrates the high potential of the hybrid material for immediate applications in photocatalysis as well as in solar energy conversion schemes [62]. The $Ru(bpy)_2(py)Cl$–graphene hybrid material highlights the importance of the covalent binding and the chemistry chosen for the particular functionalization methodology for the enhancement of photo-induced electron transfer. It is noteworthy that triazole rings constructed by "click" reaction of an alkyne-functionalized graphene sheet (or chromophore) and an azide-functionalized chromophore (or graphene sheet) were also shown to amplify the charge transfer [52].

An overview of common photophysical properties for some of the discussed graphene-based nanohybrids is given in Table 1.

Conclusion

To summarize, recent advances in the synthesis of graphene sheets that are covalently functionalized with photo- and/or electro-active moieties for the formation of novel hybrid materials were reviewed. Although in early stages oxidation was the method of choice for the functionalizing graphene, the introduction of numerous lattice defects that significantly alter the electronic properties of graphene, required the development of new routes for obtaining graphene sheets that preserve to a large extent the high conductivity of the material. Therefore, graphene-based hybrid materials are formed by exfoliating graphite and a subsequent chemical functionalization. Such graphene-based donor–acceptor hybrid materials were found to possess interesting optical and photophysical properties. Charge-transfer phenomena mainly from the photoexcited organic chromophore units to the graphene layers were observed. Although the potential of these materials to be applied in solar and photoelectrochemical cells is great, there is surely a need for the preparation and the evaluation of more graphene-based materials in order to fully understand and describe the electronic interaction processes of these systems.

Acknowledgements

Partial financial support from GSRT/NSRF 2007-2013 through action "ARISTEIA II" project FUNGRAPH (3150) "Functionalization of graphene with multichromophoric arrays of photoactive units for energy conversion" is acknowledged.

Table 1: Some photophysical properties for selected graphene-based hybrid materials.

hybrid material	references	IPCE[a]	τ_{CS} / ps[b]	k^{CS} / s^{-1} [c]	Φ^{CS} [d]	τ_{CR} / ns[e]	K^{CR} / s^{-1} [f]	ΔG_{CS} / eV[g]
GO–TPP	Figure 2 and [44]	1.3%	675	1.14×10^9	0.77	56	1.8×10^7	−1
exfoliated graphene–TPP	Figure 4 and [55]	—	<500	—	0.3	—	—	—
exfoliated graphene–Pd-TPP	Figure 4 and [55]	—	8,000	—	<0.01	—	—	—
exfoliated graphene–ZnPc	Figure 5 and [57]	2.2%	7.7	—	0.98	4.3	2.3×10^8	—
exfoliated graphene–Pc	Figure 6 and [60]	—	3.3	2.03×10^9	0.7	—	—	—
exfoliated graphene–ZnPc	Figure 7 and [61]	—	1	—	—	—	—	—
exfoliated graphene–exTTF	Figure 8 and [39]	—	—	—	—	—	—	0.69
exfoliated graphene–TPP	[31]	3%	30	—	—	—	—	—

[a]The incident-photon-to-current conversion efficiency of the fabricated devices. [b]Charge-separation lifetime of the photo-excited hybrids. [c]Charge-separation rate constant. [d]Quantum yield for charge-seperation. [e]Charge-recombination lifetime. [f]Charge-recombination rate constant. [g]Free energy of the charge-seperated state.

References

1. Lee, C.; Wei, X.; Kysar, J. W.; Hone, J. *Science* **2008,** *321,* 385–388. doi:10.1126/science.1157996
2. Du, X.; Skachko, I.; Barker, A.; Andrei, E. Y. *Nat. Nanotechnol.* **2008,** *3,* 491–495. doi:10.1038/nnano.2008.199
3. Novoselov, K. S.; Geim, A. K.; Morozov, S. V.; Jiang, D.; Zhang, Y.; Dubonos, S. V.; Grigorieva, I. V.; Firsov, A. A. *Science* **2004,** *306,* 666–669. doi:10.1126/science.1102896
4. Geim, A. K.; Novoselov, K. S. *Nat. Mater.* **2007,** *6,* 183–193. doi:10.1038/nmat1849
5. Li, X.; Cai, W.; An, J.; Kim, S.; Nah, J.; Yang, D.; Piner, R.; Velamakanni, A.; Jung, I.; Tutuc, E.; Banerjee, S. K.; Colombo, L.; Ruoff, R. S. *Science* **2009,** *324,* 1312–1314. doi:10.1126/science.1171245
6. Kim, K. S.; Zhao, Y.; Jang, H.; Lee, S. Y.; Kim, J. M.; Kim, K. S.; Ahn, J.-H.; Kim, P.; Choi, J.-Y.; Hong, B. H. *Nature* **2009,** *457,* 706–710. doi:10.1038/nature07719
7. Coleman, J. N. *Acc. Chem. Res.* **2013,** *46,* 14–22. doi:10.1021/ar300009f
8. Skaltsas, T.; Karousis, N.; Yan, H.-J.; Wang, C.-R.; Pispas, S.; Tagmatarchis, N. *J. Mater. Chem.* **2012,** *22,* 21507–21512. doi:10.1039/c2jm33245k
9. Behabtu, N.; Lomeda, J. R.; Green, M. J.; Higginbotham, A. L.; Sinitskii, A.; Kosynkin, D. V.; Tsentalovich, D.; Parra-Vasquez, A. N. G.; Schmidt, J.; Kesselman, E.; Cohen, Y.; Talmon, Y.; Tour, J. M.; Pasquali, M. *Nat. Nanotechnol.* **2010,** *5,* 406–411. doi:10.1038/nnano.2010.86
10. Jeon, I.-Y.; Shin, Y.-R.; Sohn, G.-J.; Choi, H.-J.; Bae, S.-Y.; Mahmood, J.; Jung, S.-M.; Seo, J.-M.; Kim, M.-J.; Chang, D. W.; Dai, L.; Baek, J.-B. *Proc. Natl. Acad. Sci. U. S. A.* **2012,** *109,* 5588–5593. doi:10.1073/pnas.1116897109
11. Dreyer, D. R.; Park, S.; Bielawski, C. W.; Ruoff, R. S. *Chem. Soc. Rev.* **2010,** *39,* 228–240. doi:10.1039/b917103g
12. Gao, W.; Alemany, L. B.; Ci, L.; Ajayan, P. M. *Nat. Chem.* **2009,** *1,* 403–409. doi:10.1038/nchem.281
13. Economopoulos, S. P.; Tagmatarchis, N. *Chem. – Eur. J.* **2013,** *19,* 12930–12936. doi:10.1002/chem.201302358
14. Georgakilas, V.; Otyepka, M.; Bourlinos, A. B.; Chandra, V.; Kim, N.; Kemp, K. C.; Hobza, P.; Zboril, R.; Kim, K. S. *Chem. Rev.* **2012,** *112,* 6156–6214. doi:10.1021/cr3000412
15. Geim, A. K.; Novoselov, K. S. *Nat. Mater.* **2007,** *6,* 183–191. doi:10.1038/nmat1849
16. Bottari, G.; Trukhina, O.; Ince, M.; Torres, T. *Coord. Chem. Rev.* **2012,** *256,* 2453–2477. doi:10.1016/j.ccr.2012.03.011
17. Chen, D.; Zhang, H.; Liu, Y.; Li, J. *Energy Environ. Sci.* **2013,** *6,* 1362–1387. doi:10.1039/c3ee23586f
18. Dirian, K.; Herranz, M.-A.; Katsukis, G.; Maliq, J.; Perez-Rodriquez, L.; Romero-Nieto, C.; Strauss, V.; Martin, N.; Guldi, D. M. *Chem. Sci.* **2013,** *4,* 4335–4353. doi:10.1039/c3sc51100f
19. Cao, A.; Liu, Z.; Chu, S.; Wu, M.; Ye, Z.; Cai, Z.; Chang, Y.; Wang, S.; Gong, Q.; Liu, Y. *Adv. Mater.* **2010,** *22,* 103–106. doi:10.1002/adma.200901920
20. Chang, H.; Lv, X.; Zhang, H.; Li, J. *Electrochem. Commun.* **2010,** *48,* 483–487. doi:10.1016/j.elecom.2010.01.025
21. Pham, T. A.; Choi, B. C.; Jeong, Y. T. *Nanotechnology* **2010,** *21,* 465603. doi:10.1088/0957-4484/21/46/465603
22. Feng, M.; Sun, R.; Zhan, H.; Chen, Y. *Nanotechnology* **2010,** *21,* 075601. doi:10.1088/0957-4484/21/7/075601
23. Lin, Y.; Zhang, K.; Chen, W.; Liu, Y.; Geng, Z.; Zeng, J.; Pan, N.; Yahn, L.; Wang, X.; Hou, J. G. *ACS Nano* **2010,** *4,* 3033–3038. doi:10.1021/nn100134j
24. Wang, T.; Zhang, S.; Mao, C.; Song, J.; Niu, H.; Jin, B.; Tian, Y. *Biosens. Bioelectron.* **2012,** *31,* 369–375. doi:10.1016/j.bios.2011.10.048
25. Lightgap, I. V.; Kamat, P. V. *J. Am. Chem. Soc.* **2012,** *134,* 7109–7116. doi:10.1021/ja3012929
26. Chen, J.; Xu, F.; Wu, J.; Quasim, K.; Zhou, Y.; Lei, W.; Sun, L.-T.; Zhang, Y. *Nanoscale* **2012,** *4,* 441–443. doi:10.1039/c2nr11656a
27. Wang, Y.; Lu, J.; Tang, L.; Chang, H.; Li, J. *J. Anal. Chem.* **2009,** *89,* 9710–9715. doi:10.1021/ac901935a

28. Lu, Z.; Guo, C. X.; Yang, H. B.; Qiao, Y.; Guo, J.; Li, C. M. *J. Colloid Interface Sci.* **2011,** *353,* 588–592. doi:10.1016/j.jcis.2010.10.007
29. Huang, Q.; Zeng, D.; Li, H.; Xie, C. *Nanoscale* **2012,** *4,* 5651–5658. doi:10.1039/c2nr31131c
30. Son, D. I.; Kwon, B. W.; Park, D. H.; Seo, W.-S.; Yi, Y.; Angadi, B.; Lee, C.-L.; Choi, W. K. *Nat. Nanotechnol.* **2012,** *7,* 465–471. doi:10.1038/NNANO.2012.71
31. Narayanan, R.; Deepa, M.; Srivastava, A. K. *Phys. Chem. Chem. Phys.* **2012,** *14,* 767–778. doi:10.1039/c1cp22548k
32. Zhiguo, G.; Shuping, Y.; Zaijun, L.; Xiulan, S.; Guangli, W.; Yinjun, F.; Junkang, L. *Electrochim. Acta* **2011,** *56,* 9162–9167. doi:10.1016/j.electacta.2011.07.117
33. Chua, C. K.; Pumera, M. *Chem. Soc. Rev.* **2013,** *42,* 3222–3233. doi:10.1039/c2cs35474h
34. Rodriguez-Perez, L.; Herranz, M. A.; Martin, N. *Chem. Commun.* **2013,** *49,* 3721–3735. doi:10.1039/c3cc38950b
35. Park, J.; Yan, M. *Acc. Chem. Res.* **2013,** *46,* 181–189. doi:10.1021/ar300172h
36. Karousis, N.; Economopoulos, S.; Tagmatarchis, N. *Functionalization of Graphene*. In *Handbook of Carbon Nano Materials;* D'Souza, F.; Kadish, K. M., Eds.; World Scientific: Singapore, 2012; Vol. 4, pp 1–54.
37. Hirsch, A.; Englert, J. M.; Hauke, F. *Acc. Chem. Res.* **2013,** *46,* 87–96. doi:10.1021/ar300116q
38. Quintana, M.; Spyrou, K.; Grzelczak, M.; Browne, W. R.; Rudolf, P.; Prato, M. *ACS Nano* **2010,** *4,* 3527–3533. doi:10.1021/nn100883p
39. Economopoulos, S. P.; Rotas, G.; Miyata, Y.; Shinohara, H.; Tagmatarchis, N. *ACS Nano* **2010,** *4,* 7499–7507. doi:10.1021/nn101735e
40. Bekyarova, E.; Itkis, M. E.; Ramesh, P.; Berger, C.; Sprinkle, M.; de Heer, W. A.; Haddon, R. C. *J. Am. Chem. Soc.* **2009,** *131,* 1336–1337. doi:10.1021/ja8057327
41. Liu, L.-H.; Yan, M. *J. Mater. Chem.* **2011,** *21,* 3273–3276. doi:10.1039/c0jm02765k
42. Castelain, M.; Martinez, G.; Merino, P.; Martin-Gago, J. A.; Segura, J. L.; Ellis, G.; Salavagione, H. J. *Chem. – Eur. J.* **2012,** *18,* 4965–4973. doi:10.1002/chem.201102008
43. Strom, T. A.; Dillon, E. P.; Hamilton, C. E.; Barron, A. R. *Chem. Commun.* **2010,** *46,* 4097–4099. doi:10.1039/c001488e
44. Xu, Y.; Liu, Z.; Zhang, X.; Wang, Y.; Tian, J.; Huang, Y.; Ma, Y.; Zhang, X.; Chen, Y. *Adv. Mater.* **2009,** *21,* 1275–1279. doi:10.1002/adma.200801617
45. Karousis, N.; Sandanayaka, A. S. D.; Hasobe, T.; Economopoulos, S. P.; Sarantopoulou, E.; Tagmatarchis, N. *J. Mater. Chem.* **2011,** *21,* 109–117. doi:10.1039/c0jm00991a
46. Liu, Z.-B.; Xu, Y.-F.; Zhang, X.-Y.; Zhang, X.-L.; Chen, Y.-S.; Tian, J.-G. *J. Phys. Chem. B* **2009,** *113,* 9681–9686. doi:10.1021/jp9004357
47. Zhao, X.; Yan, X.-Q.; Ma, Q.; Yao, Y.; Zhang, X.-L.; Liu, Z.-B.; Tian, J.-G. *Chem. Phys. Lett.* **2013,** *577,* 62–67. doi:10.1016/j.cplett.2013.04.023
48. Karousis, N.; Economopoulos, S. P.; Sarantopoulou, E.; Tagmatarchis, N. *Carbon* **2010,** *48,* 854–860. doi:10.1016/j.carbon.2009.10.039
49. Das, S. K.; KC, C. B.; Ohkubo, K.; Yamada, Y.; Fukuzumi, S.; D'Souza, F. *Chem. Commun.* **2013,** *49,* 2013–2015. doi:10.1039/c3cc38898k
50. Kalita, G.; Sharma, S.; Wakita, K.; Umeno, M.; Hayashi, Y.; Tanemura, M. *Phys. Chem. Chem. Phys.* **2013,** *15,* 1271–1274. doi:10.1039/c2cp43427j
51. Song, S.; Xue, Y.; Feng, L.; Elbatal, H.; Wang, P.; Moorefield, C. N.; Newkome, G. R.; Dai, L. *Angew. Chem., Int. Ed.* **2014,** *53,* 1415–1419. doi:10.1002/anie.201309641
52. Wang, H.-X.; Zhou, K.-G.; Xie, Y.-L.; Zeng, J.; Chai, N.-N.; Li, J.; Zhang, H.-L. *Chem. Commun.* **2011,** *47,* 5747–5749. doi:10.1039/c1cc11121c
53. Feng, L.; Wu, L.; Qu, X. *Adv. Mater.* **2013,** *25,* 168–186. doi:10.1002/adma.201203229
54. Zhang, H.; Huang, R.; Cang, H.; Cai, Z.; Sun, B. *J. Mater. Chem. B* **2014,** *2,* 1742–1750. doi:10.1039/c3tb21656j
55. Zhang, X.; Hou, L.; Cnossen, A.; Coleman, A. C.; Ivashenko, O.; Rudolf, P.; van Wees, B. J.; Browne, W. R.; Feringa, B. L. *Chem. – Eur. J.* **2011,** *17,* 8957–8964. doi:10.1002/chem.201100980
56. Umeyama, T.; Mihara, J.; Tezuka, N.; Matano, Y.; Stranius, K.; Chukharev, V.; Tkachenko, N. V.; Lemmetyinen, H.; Noda, K.; Matsushige, K.; Shishido, T.; Liu, Z.; Hirose-Takai, K.; Suenaga, K.; Imahori, H. *Chem. – Eur. J.* **2012,** *18,* 4250–4257. doi:10.1002/chem.201103843
57. Karousis, N.; Ortiz, J.; Ohkudo, K.; Hasobe, T.; Fukuzumi, S.; Sastre-Santos, A.; Tagmatarchis, N. *J. Phys. Chem. C* **2012,** *116,* 20564–20573. doi:10.1021/jp305783v
58. Malig, J.; Jux, N.; Kiessling, D.; Cid, J.-J.; Vazquez, P.; Torres, T.; Guldi, D. M. *Angew. Chem., Int. Ed.* **2011,** *50,* 3561–3565. doi:10.1002/anie.201003364
59. Brinkhaus, L.; Katsukis, G.; Malig, J.; Costa, R. D.; Garcia-Iglesias, M.; Vasquez, P.; Torres, T.; Guldi, D. M. *Small* **2013,** *9,* 2348–2357. doi:10.1002/smll.201202427
60. Ragoussi, M. E.; Malig, J.; Katsukis, G.; Butz, B.; Spiecker, E.; de la Torre, G.; Torres, T.; Guldi, D. M. *Angew. Chem., Int. Ed.* **2012,** *51,* 6421–6425. doi:10.1002/anie.201201452
61. Ragoussi, M.-E.; Katsukis, G.; Roth, A.; Malig, J.; de la Torre, G.; Guldi, D. M.; Torres, T. *J. Am. Chem. Soc.* **2014,** *136,* 4593–4598. doi:10.1021/ja411830x
62. Xiao, B.; Wang, X.; Huang, H.; Zhu, M.; Yang, P.; Wang, Y.; Du, Y. *J. Phys. Chem. C* **2013,** *117,* 21303–21311. doi:10.1021/jp405497j

License and Terms

This is an Open Access article under the terms of the Creative Commons Attribution License (http://creativecommons.org/licenses/by/2.0), which permits unrestricted use, distribution, and reproduction in any medium, provided the original work is properly cited.

The license is subject to the *Beilstein Journal of Nanotechnology* terms and conditions: (http://www.beilstein-journals.org/bjnano)

The definitive version of this article is the electronic one which can be found at: doi:10.3762/bjnano.5.170

BEILSTEIN JOURNAL OF NANOTECHNOLOGY

Non-covalent and reversible functionalization of carbon nanotubes

Antonello Di Crescenzo, Valeria Ettorre and Antonella Fontana*

Review

Open Access

Address:
Dipartimento di Farmacia, Università "G. d'Annunzio", Via dei Vestini, 66100 Chieti, Italy

Email:
Antonella Fontana* - fontana@unich.it

* Corresponding author

Keywords:
carbon nanotubes; non-covalent functionalization; π-stacking; reversible dispersion/precipitation

Beilstein J. Nanotechnol. **2014,** *5,* 1675–1690.
doi:10.3762/bjnano.5.178

Received: 03 May 2014
Accepted: 29 August 2014
Published: 30 September 2014

This article is part of the Thematic Series "Atomic scale interface design and characterisation: Theory – Electronic properties".

Guest Editor: A. Krasheninnikov

© 2014 Di Crescenzo et al; licensee Beilstein-Institut.
License and terms: see end of document.

Abstract

Carbon nanotubes (CNTs) have been proposed and actively explored as multipurpose innovative nanoscaffolds for applications in fields such as material science, drug delivery and diagnostic applications. Their versatile physicochemical features are nonetheless limited by their scarce solubilization in both aqueous and organic solvents. In order to overcome this drawback CNTs can be easily non-covalently functionalized with different dispersants. In the present review we focus on the peculiar hydrophobic character of pristine CNTs that prevent them to easily disperse in organic solvents. We report some interesting examples of CNTs dispersants with the aim to highlight the essential features a molecule should possess in order to act as a good carbon nanotube dispersant both in water and in organic solvents. The review pinpoints also a few examples of dispersant design. The last section is devoted to the exploitation of the major quality of non-covalent functionalization that is its reversibility and the possibility to obtain stimuli-responsive precipitation or dispersion of CNTs.

Introduction

Carbon nanotubes (CNTs) are hollow cylindrical tubes with nanometer scale diameters and lengths up to a few micrometers. They are ideally obtained by a rolled up graphene sheet and their diameter, curvature and electronic properties are uniquely defined by the combination of the rolling angle and radius, which is referred to as nanotube chirality (Figure 1) [1]. CNTs made up of a rolled up single graphene sheet and closed at their ends by hemispheric fullerene caps are referred to as single-walled nanotubes (SWCNTs) and their diameter ranges from 0.4 nm to 5 nm [2,3]. Multi-walled carbon nanotubes, made up of several concentric graphene cylinders, are much bigger with diameters from a few to tens of nanometers.

These one-dimensional nanostructures reveal exceptional thermal, electrical, mechanical and optical properties [4], which make them promising candidates for potential applications in various fields. CNTs have found applications in nanotechnology [5], electronics [6], sensors and biosensors [7-9], catal-

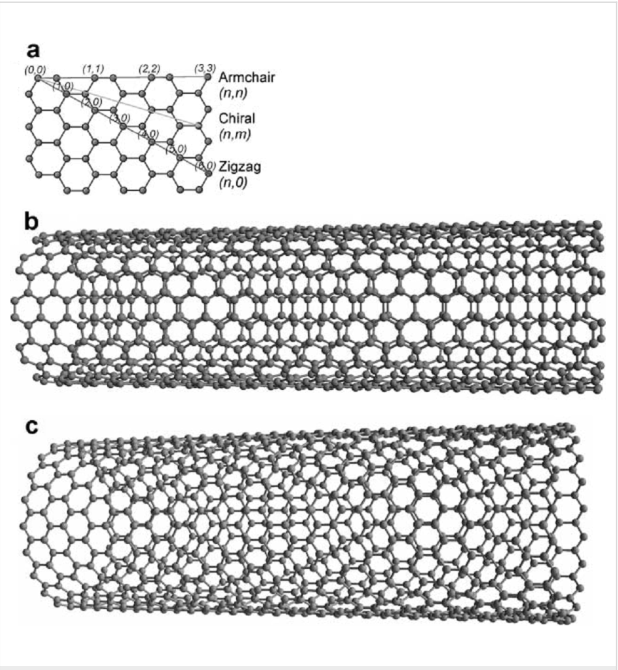

Figure 1: (a) The wrapping vector of a graphene sheet defines the structure (chirality) of a carbon nanotube. Examples of (b) ''armchair'' and (c)''zig-zag'' SWCNTs. [1]. – Reproduced by permission of The Royal Society of Chemistry.

ysis [10], energy conversion [11,12] storage devices [13], the delivery field [14,15], and in the polymer field [16] to name a few. However, CNTs applications have been hindered for a long time from their discovery [17] due to their limited solubility and processability. Individual CNTs tend to strongly interact with each other through van der Waals forces reaching ~500 eV per μm of CNT's length [18] and aggregate into bundles and ropes. In order to counteract these forces and favor CNTs manipulability and solubility mainly two strategies have been adopted: i) covalent functionalization through attachment of molecular pendants to the Csp^2 backbone [19,20] and ii) non-covalent functionalization by adsorption of molecules onto the nanotube surface [21]. Alternatively, in order to use CNTs for elected applications, encapsulation of molecules in the inner empty cavity of the nanotubes has been exploited [22-24]. To date, several successful strategies have been applied to covalently derivatize CNTs sidewalls. Typical approaches include acid oxidation [25], cycloadditions spanning from the widely known 1,3-dipolar cycloaddition, namely the Prato reaction [26-28] to the Bingel [2 + 1] cyclopropanation [29], radical additions via diazonium salts [30,31] grafting of polymers. Nevertheless the creation of novel covalent bonds disrupt the sp^2 network of non-derivatized CNTs and may thus alter their inherent properties [30,32]. The prospect of functionalizing CNTs outer surface via non-covalent ways through chemical adsorption of ordered architectures [33,34] and preserve the extended networks of the CNTs seems therefore very attractive.

In this review, starting from several examples of good dispersions and dispersants, we intend to systematically identify the features that allow a molecule to behave as a good CNTs dispersant both in organic and in aqueous solvents via non-covalent functionalization. Once the essential morphological characteristics of a dispersant have been outlined, it will be much easier to conceive novel molecules with additional properties but unchanged functionalities responsible for water or organic solvent solubility or nanotubes debundling. Several recent practical applications for CNTs involved in non-covalent interactions with elected molecules both in aqueous and organic environment are discussed. In particular, a light will be shed on the possibility of creating systems able to respond to elected external chemical or physical stimuli such as pH, temperature or light thanks to the major advantage of non-covalent functionalization, namely its reversibility.

Review

Morphological and electronic characteristics of CNTs

Despite we do not want to put forward an exhaustive CNTs description, we think that, in order to evaluate the features that a dispersant should possess to favor CNTs dispersion, it is important to briefly describe CNTs properties. Carbon nanotubes, as well as graphene, are built mainly of Csp^2 arranged in hexagons but, differently from benzene, carbon atoms in a nanotube are pyramidalized and π-orbitals are misaligned due to the curvature of the tube surface [1] .These conditions confer to nanotubes an intrinsic p-type semiconducting behavior and a reactivity much more pronounced than that of graphite. Accordingly, nanotubes with bigger diameter are less reactive than smaller nanotubes whereas the inner surface of carbon nanotubes appears to be much less reactive than the outer one. These differences manifest themselves as well when non-covalent interactions are concerned. In fact, Tournus et al. [35] showed that wider nanotubes tend to interact easier than narrow nanotubes with benzene due to the better geometric match between a planar molecule such as benzene and the not very pronounced π-orbital misalignment of bigger CNTs.

The chirality of CNTs, that depends on the way carbon hexagons are arranged in the nanotube (see Figure 1), and their diameter affects the conductance, density and honeycomb lattice structure of the tube and allow to divide them in two main types, semiconducting and metallic. The CNTs chirality appears to be severely involved in the dispersion of CNTs. As an example, the chirality of the tubes drives the interactions that nanotubes establish with the surrounding medium with semiconducting tubes favoring donor-acceptor interactions [36,37].

Non-covalent interactions and hydrophobicity of CNTs

Despite pristine carbon nanotubes possess a π-conjugative structure with a highly hydrophobic surface, they are scarcely soluble in most organic solvents due to the high molecular weight and their tendency to entangle and form 3D networks through persistent van der Waals interactions. Therefore, for CNTs applications, the prime aim is to promote CNTs entanglement by energetic agitation. Generally, agitation is provided by magnetic stirring, reflux, shear mixing, or, most commonly, ultrasonication either mild sonication in a bath or high-power sonication using a tip [16]. Once exfoliated, the simplest stable CNTs dispersions have been achieved by using solvent molecules able to efficiently interact with CNTs such as phenylethyl alcohol [38] or *N*-methylpyrrolidone (NMP) [39]. Indeed NMP has been demonstrated to enter the bundles during sonication and remain strongly bound to the nanotube surface. This leads to an enthalpy of mixing that is approximately zero conferring to the corresponding free energy of mixing a negative value. However, NMP molecules could be removed by heating to 340 °C, leaving perfectly intact nanotubes and demonstrating that NMP was physisorbed via van der Waals interactions onto the nanotube surface. Good and relatively stable dispersions have been obtained also by sonicating CNTs with *N*,*N*-dimethylformamide (DMF) [40], highlighting that a high value of β (the hydrogen bond acceptance basicity), a negligible value of R (the hydrogen bond donation parameter of Taft and Kamlet) and a high value for π* (solvochromic parameter) [41] are necessary, although not sufficient conditions, to ensure a good CNTs dispersion. Landi et al. [42] obtained a dispersion stable for days by sonicating CNTs with *N*,*N*-diethylacetamide (DEA) and imputed the stability of the dispersion to synergistic effective polar and π-stacking interactions. As a matter of fact solvents characterized by either dipole–dipole or π-orbital overlap interactions may not account for an equivalent dispersion performance, neither equally polar solvents such as acetonitrile (dielectric constant 36.00) and DMSO (dielectric constant 46.71) or 1,2-dichlorobenzene able to give higher π-orbital overlap interactions despite being less polar (dielectric constant 10.36) [43] than DEA.

An alternative strategy to favor CNTs dispersion in organic solvents is to coat CNTs with a dispersant phase, usually a molecule characterized by a high affinity towards nanotube sidewalls and at the same time particularly soluble in the elected solvent. In particular both small molecules and high weight polymers have been used as dispersants.

Aromatic molecules have a strong affinity for graphitic surfaces via π–stacking. The adsorption of different polycyclic aromatic hydrocarbons (PAH) such as pyrene, anthracene, tetracene and phenanthrene on SWCNTs has been extensively investigated. The strong interactions of different anthracene derivatives to shortened SWCNTs has been made clearly evident [44] by changes in both the UV–vis and FTIR spectra and shift in fluorescence spectra. The displacement of attached anthracene by an excess amount of pyrene in THF indicated that the adsorption process is reversible. Instead tetracene and pentacene were investigated by X-ray photoelectron spectroscopy [45]. The more than six times greater adsorption of tetracene with respect to that of phenanthrene was imputed to the nanoscale curvature of the tube surface, and the consequent difference in the contacts between the molecule and the tube surface. The observed shift of the radial breathing mode (RBM) of the Raman band towards high frequency confirmed the strong π–π interactions between PAH and the external SWCNT surface. Wang et al. demonstrated that sorption of phenanthrene and naphtalene to CNTs is correlated to the hydrophobicity of the corresponding PAH [46]. Stable dispersions of SWCNTs in THF have been easily achieved by sonicating CNTs with diazapentacene at room temperature [47] (see Table 1). The adsorption is solely imputable to π-stacking as no solvophobic forces can participate in the interactions with the SWCNT walls. This functionalization leaves virtually intact the inherent properties of SWCNTs, as observed by several photophysical measurements. Porphyrins (see Table 1) demonstrated [48] to physically adsorb onto the CNTs surface and dissolve both individual and bundled SWCNTs in organic solvents. The solid SWCNTs–Zn-protoporphyrin nanocomposite is readily separable from the solution and can be easily redissolved in DMF.

Typical dispersants are polymers formed by repetitive units of alkyl chains and aromatic moieties which exploit both π-stacking to the CNT surface and van der Waals interactions between the hydrophobic nanotube surface and alkyl tails. It has been demonstrated [49] that poly(*m*-phenylene vinylene-*co*-2,5-dioctyloxy-*p*-phenylene vinylene) (PmPV, see Table 1) effectively adsorbs onto the nanotube surface allowing to obtain a good dispersion of MWCNTs produced by arc discharge in toluene. Actually the method was used to purify the starting soot material from graphitic particles. Analogously, poly(*p*-phenylene vinylene), bearing cyano substituents, has been used to immobilize functional groups such as Zn-phthalocyanine onto the surface of SWCNT to generate active hybrid materials able to give, by photoexcitation, a metastable radical ion pair state, namely oxidized ZnPc and reduced SWCNT [50].

Vaisman et al. [51] have demonstrated that the dispersion of CNTs in water-insoluble polymers is favored by the presence of polymeric non-ionic surfactants containing a branched tail promoting a steric barrier that prevents aggregation and by unsaturated C–C bonds “securing” through π–π interactions the

Table 1: Some lipophilic molecules used for the dispersion of CNTs in organic solvents.

dispersant (structure or name)	acronym	organic solvent	ref.
anthracene and substituted-anthracene	–	THF	[44]
tetracene and pentacene	–	THF	[45]
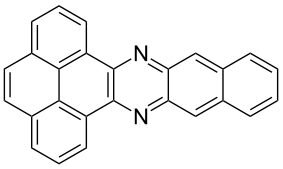	diazapentacene derivative	THF	[47]
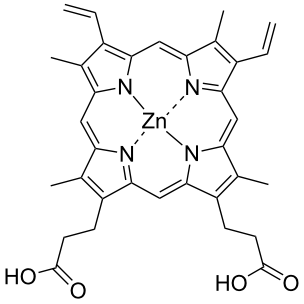	ZnPP	DMF	[48]
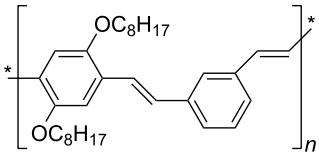	PmPV	toluene	[49]
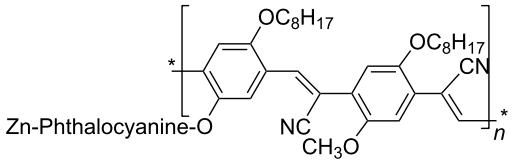	PPV	THF	[50]
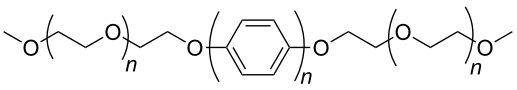	$(PEG)_8(Ph)_6(PEG)_8$	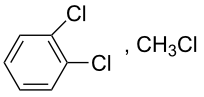	[52]
polystyrene-*b*-polyisoprene		DMF heptane	[53]
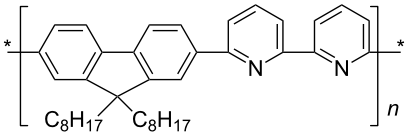	PFO-BPy	toluene, THF	[55]
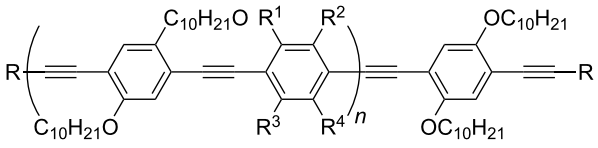	PPE 1	CH_3Cl	[56]
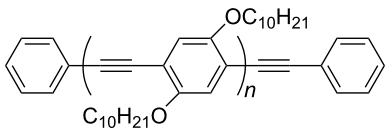	PPE 2	CH_3Cl	[56]

Table 1: Some lipophilic molecules used for the dispersion of CNTs in organic solvents. (continued)

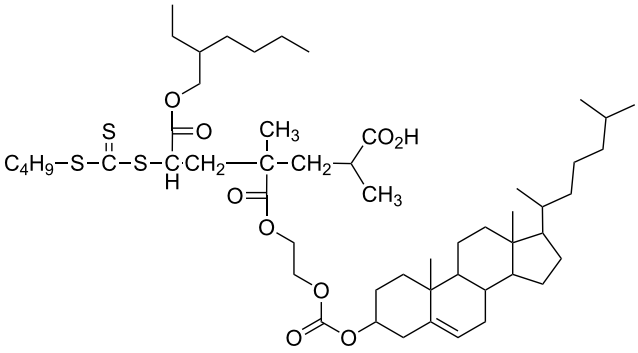	CEM-EHA	THF, toluene, isooctane	[57]
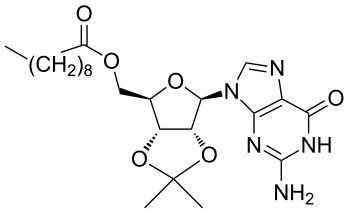	LipoG 1	$CHCl_3$	[58]
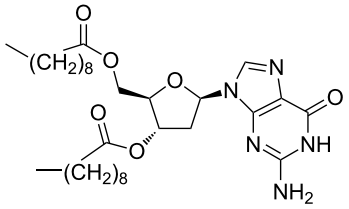	LipoG 2	$CHCl_3$	[58]

polymers to the Csp^2 backbone of the nanotubes. Diblock (A–B) and triblock (A–B–A) copolymers demonstrated to be very efficient dispersing agents for CNTs thanks to the adsorption of one of the blocks onto the nanotube surface and the formation, by the other blocks dangling into the solution, of a steric barrier that prevents the CNT–CNT approach. Nevertheless, the prevailing effect among the two is still under investigation. Polyethylene glycol (PEG) chains with PEG repeating units as long as 8, have been demonstrated [52] to favor both self-assembly and dispersion of SWCNTs in chloroform and 1,2-dichlorobenzene once chosen a hydrophobic domain B (i.e., hexa-*p*-phenylene) able to establish π–π interactions with the B block of another monomer or with the SWCNT surface, respectively. On the other hand, the capability of polystyrene-*b*-polyisoprene (PS-*b*-PI) diblock copolymers to disperse MWCNTs seems to be dominated by the solvent selectivity of the block copolymers, being the direct interaction between the nanotubes and the polymers of secondary importance [53]. Indeed PS-*b*-PI demonstrated to disperse MWCNTs both in dimethylformamide (DMF), a polar solvent selective for polystyrene, and heptane, a non-polar solvent that is selective for the polyisoprene block.

Conjugated polymers like polyfluorene derivatives have been recently used for dispersing SWCNTs into different organic solvents. Poly[(9,9-dioctylfluorenyl-2,7-diyl)-*alt*-*co*-(6,6'-{2,2'-bipyridine})] (PFO-BPy, see Table 1) has been demonstrated [54] to selectively wrap highly semiconducting SWCNT species with large diameters ranging from 1.3 to 1.7 nm and to disperse both arc discharge and HiPco SWCNT in toluene and THF. The obtained dispersions were used to align and deposit semiconducting SWCNTs (s-SWCNTs) with exceptional electronic-type purity and at high deposition velocity (i.e., 5 mm min^{-1}) with excellent control over the placement of stripes and quantity of deposited SWCNTs [55]. The rigid *non-wrapping* poly(arylenethynylene)s (PPEs) polymers (see Table 1), with backbone lengths less than 15 nm, have been demonstrated to make SWCNTs highly soluble in chloroform [56]. It is interesting to evidence that, depending of the bulkiness and/or the presence of ionic functional groups at the end of the side chains of PPE, it is possible to favor CNTs individualization or increase the adhesion between nanotubes via better π–π interactions eventually forming 2D "bucky papers", respectively [56].

Nguenda et al. demonstrated [57] for the cholesterol moiety of a multivalent cholesterol-containing polymer (CEM-EHA, see Table 1) an interaction very similar to that between pyrene and carbon nanotubes with cholesterol laying flat above the graphene surface. Supramolecular complexes of these copolymers with CNTs were soluble in THF, toluene and isooctane.

Supramolecular complexes can be formed between CNTs and a biopolymer such as DNA, in order to disperse CNTs in aqueous solutions (see next section). Recently two decanoyl-functionalized guanosines (LipoGs, see Table 1) have been used [58] for the disaggregation of SWCNTs in chloroform. Different spectroscopic and microscopic methods highlighted a well debundling of SWCNTs whereas fluorescence measurements showed the strong adsorption of LipoGs onto the CNT surface. The authors demonstrated that the ability of the investigated LipoGs to disperse SWCNTs depends on their tendency to self-assemble into ribbon-like supramolecular structures that wrap, although not specifically, around the nanotube. It is interesting to note that the self-aggregation properties of the dispersant are crucial as the tendency of super-aggregate into bigger fibers can favor their desorption from CNT surface and thus CNTs bundling.

Non-covalent interactions for solubilizing CNTs in water

In order to favor the dispersion of CNTs in water the widely and most used approach is the adsorption of surfactants onto the nanotube sidewalls. Their main advantages are their cheapness, their ready commercial disposability and simplicity of use. These small molecules have typically a hydrophobic tail and a hydrophilic head group, the former is intended to favor adsorption onto the hydrophobic nanotube walls and the latter to promote affinity with the aqueous bulk solvent. Indeed, surface active agents can modify the features of the interface between CNTs and the bulk medium providing additional repulsive forces, either electrostatic or steric, and decreasing the surface energy. In 1997 Bonard et al. [59] purified CNTs from graphitic nanoparticles by sonicating CNTs for a few minutes in a 1% aqueous solution of an ionic surfactant such as sodium dodecyl sulfate (SDS). The chemical adsorption of SDS molecules on the surface of the nanotube induces electrostatic repulsion between polar heads that expose in the aqueous solution thus preventing CNTs aggregation and inducing the formation of stable aqueous black suspensions.

During the years stable aqueous CNTs dispersions were obtained with differently charged and non-ionic commercial surfactants such as sodium dodecylbenzen sulfonate (SDBS), cetyltrimethylammonium *p*-toluenesulfonate (CTAT), cetyltrimethylammonium bromide (CTAB) and sodium cholate (SC) enhanced by sonication [60] (see Table 2). The most efficient dispersant, SDBS, was able to disperse as much as 0.06% w/w SWCNTs in water [60]. Very recently Oh et al. [61] determined that binding strengths of surfactants to SWCNTs follows the trend SDBS > SC ≈ Flavin mononucleotide (FMN, see Table 2) > SDS, irrespective of electronic types of SWCNTs. SC were demonstrated to be particularly efficient in dispersing CNTs also in the absence of any sonication. For this reason SC has been used in cases where integrity of carbon nanotubes has to be ensured, i.e., to sort water-filled and empty CNTs via ultracentrifugation to equilibrium by exploiting a density gradient (see Figure 2) [62].

Different papers have faced the possible organizations of surfactant molecules on the surface of CNTs and still several conflicting evidences are reported in the literature. Richard et al. were among the first authors envisaging the assembling of SDS on the nanotube surface [63]. They discovered, through TEM analysis, that surfactants characterized by long alkyl chains, either SDS, cationic octadecyltrimethylammonium bromide (OTABr) and nitrilotriacetic acid substituted with a single lipidic saturated chain of 10, 12, 14, or 18 carbon atoms (NTA) do arrange into half-cylinders oriented parallel to the tube axis (see Figure 3, arrangement A) highlighting the crucial role of supramolecular assembling for CNT-dispersant interactions.

The environment of nanotubes in SDS micelles was modeled also by O'Connell et al. [64] through molecular dynamics simulations run for 0.4 ns. The nanotube represented the core of a SDS cylindrical micelles were the hydrophobic tails of SDS molecules could adopt a wide range of orientations with respect to the tube (see Figure 3, arrangement B). As no water density was observed in the proximity of the tube, they speculated that the individual nanotubes were essentially in a pure hydrocarbon environment. On the other hand, SANS data, performed by Yurekli et al. [65] strongly suggested that the dispersion of SWCNTs by SDS is due to the formation of a structureless, adsorbed layer of surfactant on the individual SWCNTs (see Figure 3, arrangement C).

Analogously, we have evidenced [66,67] that gemini surfactants, characterized by two alkyl chains and two polar head groups separated by a spacer in a single molecule, are relatively effective dispersants also below their CMC or at very low surfactant concentrations confirming their compact alignment on the nanotube surface. Indeed, a gemini surfactant ensures (i) doubled hydrophobic interactions with the CNT sidewalls, due to the presence of twin chains rather than a single alkyl tail and (ii) favorable packing, thanks to the spacer that forces the twin ionic groups to reside in a space-filling geometry reduced with respect to that of two distinct single-chained surfactant mole-

Table 2: Some amphiphilic molecules used for the dispersion of CNTs in water.

dispersant (structure or name)	acronym	ref.
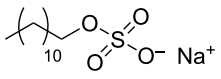	SDS	[59-61,63-65,68]
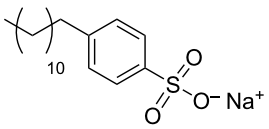	SDBS	[60,61,68]
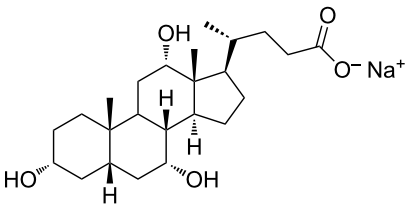	SC	[60-62]
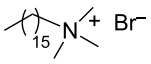	CTAB	[60]
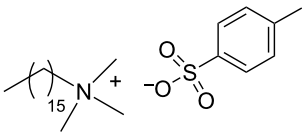	CTAT	[60]
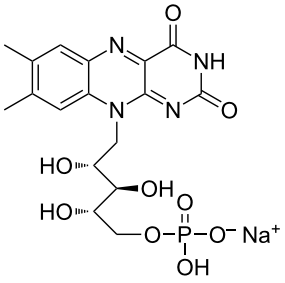	FMN	[61]
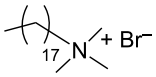	ODTABr	[63]
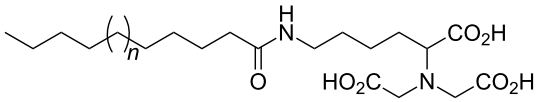	NTA	[63]
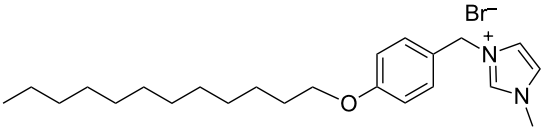	T3	[67]
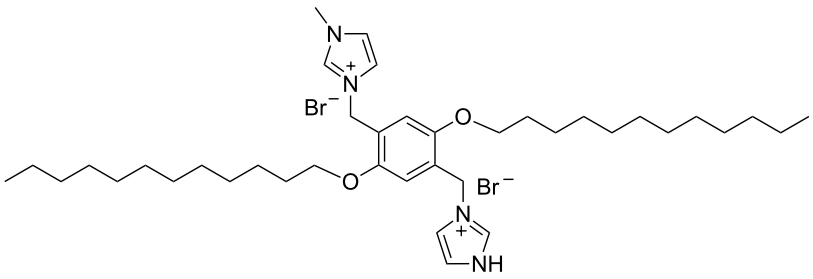	T1	[67]

Table 2: Some amphiphilic molecules used for the dispersion of CNTs in water. (continued)

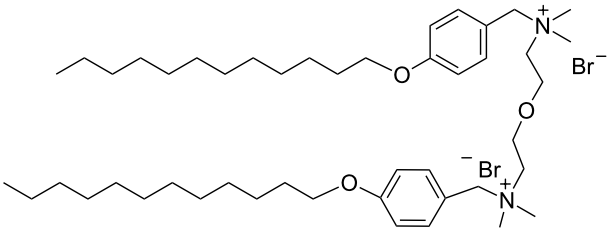	T4	[67]
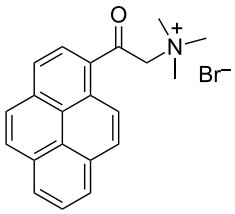	–	[72,76]
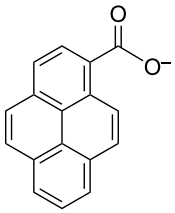	–	[73]
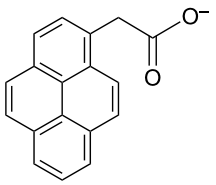	–	[73]
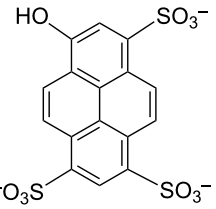	–	[73]
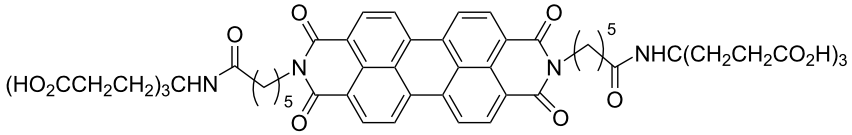	perylene dye	[74]

cules. Similarly, Zhong and Claverie demonstrated from adsorption isotherm measurements [68] that MWCNTs form stable aqueous dispersions when 90% of their surface is covered by the dispersant, while for SWCNTs, 45% of the surface has to be covered in order for the dispersion to be stable. Nevertheless, they also showed that a good dispersion is the result of a delicate compromise, i.e., at high surfactant concentrations a significant amount of the surfactant, at least more than 40%, is free in solution and can reduce the Debye length thus destabilizing the colloidal suspension. Analogously, Bonard et al. [59] evidenced that CNTs bundles form in the presence of a large excess of SDS surfactant (i.e., well above the CMC) due to the depletion interaction induced by the surfactant micelles on large colloidal particles.

Examples of polymers that favor CNTs dispersion in water are countless. This review is not intended to list all of the investigated polymers, nevertheless it is worth mentioning that the

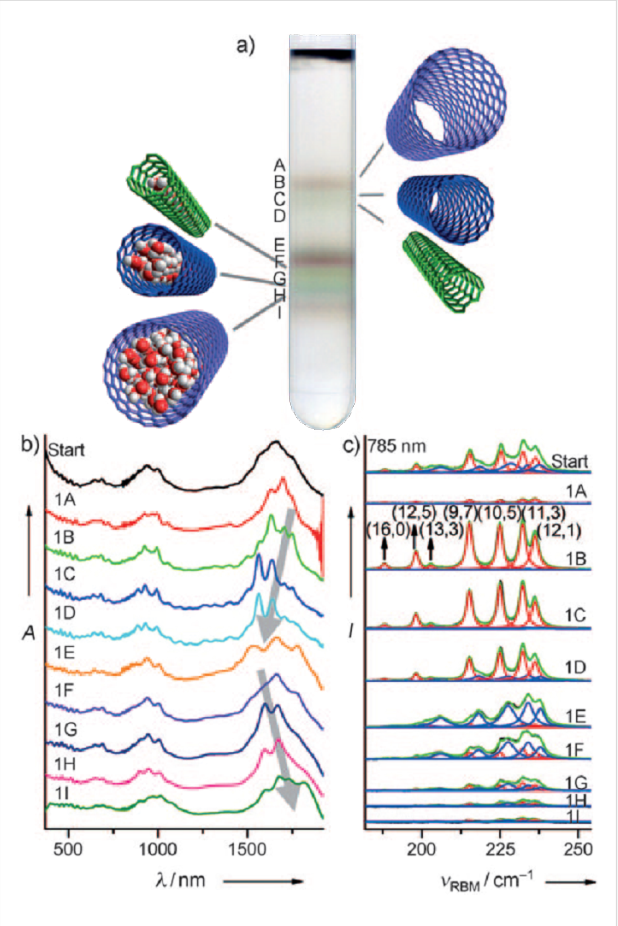

Figure 2: Sorting of empty and water-filled Arc SWCNTs (2% w/v SC). a) Centrifuge tube containing sorted Arc SWCNTs; b) Absorption spectra of the original solution and of the sorted fractions; c) Resonance Raman spectra of the different fractions excited at 785 nm. Reprinted with permission from [62]. Copyright 2011, Wiley VCH.

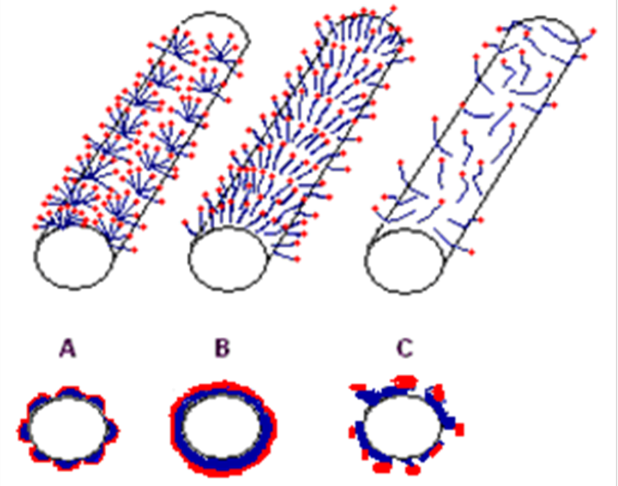

Figure 3: Schematic illustration of the different possible organizations of surfactant molecules on the surface of a CNT. Upper images refer to lateral projections; lower images refer to cross sections.

majority of polymers and block copolymers have been demonstrated [69] to wrap the nanotube exposing their polar domains towards the aqueous environments while favoring the contact of their hydrophobic domains with the nanotube surface. The wrapping of the SWCNTs by water-soluble polymers is a thermodynamically driven phenomenon because the free energy cost of forcing the polymer into a regular wrapping around the nanotube appears to be well counterbalanced by the reduction of the hydrophobic penalty consequent to the contact of CNT hydrophobic surface with the surrounding aqueous medium. Also in the case of polymers and similarly to what has already been underlined for classical surfactant molecules, we have demonstrated [70] that polymeric micelles concentration is not related to the formation of stable SWCNT dispersions, the outmost requirement in order to obtain a stable CNTs dispersion being the adsorption degree, up to an almost complete saturation, of the nanotube surface with proper dispersant molecules. Molecular dynamic simulations allowed us to highlight that the SWCNT surface coverage is systematically ensured by the hydrophobic domain of the amphiphilic dispersant. An increase of hydrophobicity therefore causes weaker inter-tube contacts, makes CNTs bundles precipitation more difficult, dehydrate the CNT interface and reduce water ordering around the CNTs [71] (see Figure 4). Unlikely, in none of our simulations we have observed hydrophilic chains extending and swelling in the aqueous environment. Nevertheless, our simulations considered always available SWCNT surfaces higher than the potential coverage area of the polymer [71].

Noteworthy are the numerous examples of PAH functionalized with hydrophilic domains used both to solubilize CNTs in water and to non-covalently functionalize CNTs with proper functionalities [72,73]. A perylene dye (see Table 2) has been used to exfoliate and suspend SWCNTs through strong π–π interactions in water. This hybrid system granted charge transfer chemistry of pristine SWCNTs used as an unusual electron donor towards the electron acceptor molecule perylene [74].

Regarding biocompatible polymers, the most representative one is DNA and different examples of non-covalently functionalized SWCNTs with DNA have been published. While double-stranded DNA (dsDNA), being more rigid, displayed a less efficient wrapping, single-stranded DNA (ssDNA) has been used to disperse CNTs or to separate and purify them. Indeed, by sonicating ssDNA with HiPco SWCNTs for ca. 1 h a solution as concentrated as 25 mg/L has been obtained [75]. These functionalized SWCNTs have proved to be able to internalize oligonucleotide chains into living cells whereas ssDNAs have been translocated into cell nucleus upon endosomal rupture triggered by NIR laser pulses. Continuous NIR radiation can cause cell death because of excessive in vitro local SWCNTs heating

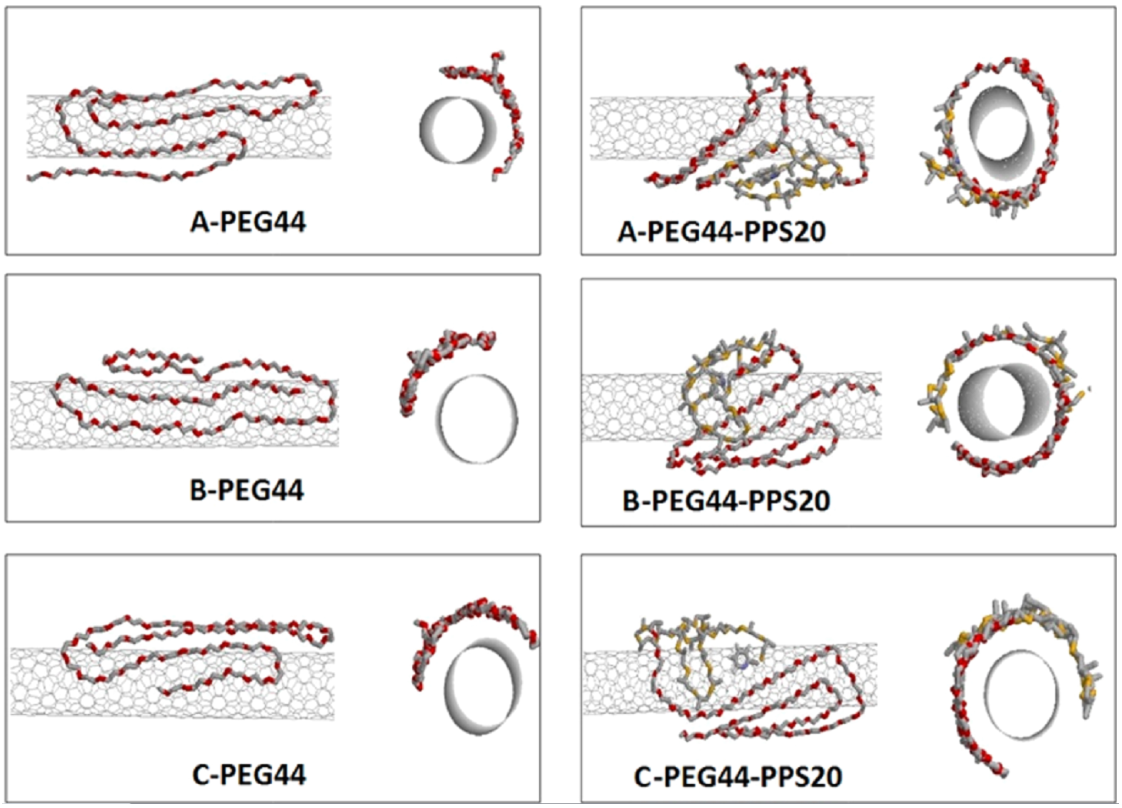

Figure 4: Representative structures of poly(ethylene glycol), PEG_{44}, and poly(ethylene glycol-*bl*-propylene sulfide), PEG_{44}−PPS_{20}, adsorbed on SWCNT as obtained by essential dynamics analysis. The presence of PPS (see structures on the right) enables the block copolymer chain to fully wrap the CNT thus minimizing nanotube−nanotube aggregating interactions. Reprinted with permission from [71]. Copyright 2012, American Chemical Society.

[75]. In these carbon scaffolds the nucleobases directly interact with SWCNT sidewalls, while the hydrophilic sugar-phosphate backbone is oriented towards the solvent [5].

Design of novel dispersant

At this point we have all the hints for properly designing an efficient dispersant for both aqueous and organic solvents. Different authors have already tried to improve the dispersing ability of commercial organic molecules in order to prepare stable CNTs dispersions. Tomonari et al. [76,77] described the design of ammonium-substituted polycyclic aromatic compounds (see Table 3) and showed the better performance of polycyclic aromatic moieties with respect to simple phenyl or naphthyl groups in favoring SWCNTs dispersions.

In the last five years we have synthesized different surfactants with the aim to increase the affinity of the dispersant for the nanotube surface or favor its hydrophilicity. Indeed, we have demonstrated that, in order to increase the efficiency of dispersants, is essential to reach an optimal hydrophobic/hydrophilic balance which favors adsorption onto the nanotube sidewalls over self-assembly. Exploiting the excellent capacity of imidazolium-based ionic liquids [78] to disperse CNTs, we conceived an ionic liquid-based surfactant, 1-hexadecyl-3-vinylimidazolium bromide (hvimBr, see Table 3) which demonstrated to be more effective than SDBS at high surfactant concentrations [79]. Despite the introduction in the polar head of the ionic liquid-derived surfactant of aromatic groups (i.e., benzene in hphimBr and pyrene in hpymimBr, see Table 3) enhances the affinity for SWCNTs, as confirmed by molecular dynamic simulations, it reduces the solubility of the surfactants in water and renders them more prone to self-assemble [80]. Starting from a good SWCNT dispersant such as *N*-[*p*-(*n*-dodecyloxybenzyl)]-*N*,*N*,*N*-trimethylammonium bromide (pDOTABr, see Table 3) we improved [66] its dispersing capability by preparing the corresponding gemini counterparts [66]. Indeed, the novel surfactants, namely 2,5-bis(*n*-dodecyloxy)-1,4-bis(*N*,*N*,*N*-trimethylammoniomethyl)phenyl bromide [pXDo$(TA)_2$Br] and 2,5-dimethoxy-1,4-bis[*N*-(*n*-dodecyl)-*N*,*N*-dimethylammoniomethyl]phenyl bromide [pXMo$(DDA)_2$Br] (see Table 3), demonstrated to disperse SWCNTs at much lower surfactant/

Table 3: Novel designed dispersants.

dispersant	acronym	ref.
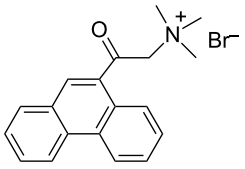	–	[76]
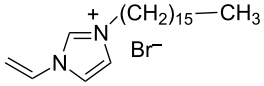	hvimBr	[79,80]
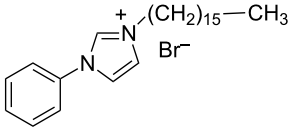	hphimBr	[80]
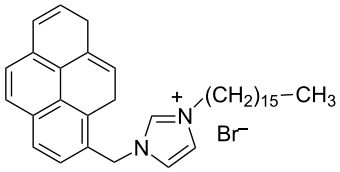	HpymimBr	[80]
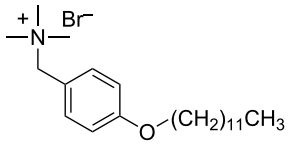	pDOTABr	[66]
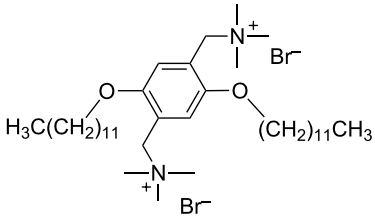	pXDo(TA)$_2$Br	[66]
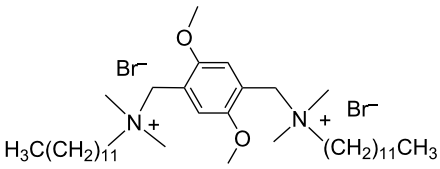	pXMo(DDA)$_2$Br	[66]

CNTs weight ratios with respect to conventional surfactants (i.e., 3 times lower than CTABr, 2 times lower than SDBS and 6 times lower than SDS). Besides their capacity to enrich the dispersed mixture in semiconducting tubes paves the way for applications in CNT fractionation. Analogously, the substitution of the ammonium groups with imidazolium moieties in pDOTABr ensured an increase of the water solubility of the corresponding surfactant and a consequent improvement of their CNTs dispersing ability [67].

Reversibility: the advantage of non-covalent functionalization

The non-covalent functionalization of carbon nanotubes, aside from preserving CNTs conjugated double bonds, has another feature that makes this approach even more interesting, which is the reversibility. Indeed, it is possible to regain the bare CNTs from the dispersant-coated counterparts both in aqueous or organic solvents. Among the numerous papers reporting on the subsequent functionalization and functionalization removal of

CNTs we review here the main examples in which such an approach is useful for purification, enrichment or separation of different types of nanotubes and extensive potential applications in different fields. An intelligent way to exploit at the same time the strong and selective interactions of many CNT dispersants and their ability to reversibly desorb from the CNT surface is the use of molecules capable of responding to different specific external stimuli [81] such as variation of the solvent, pH, temperature, light and redox conditions. Interestingly, many biomolecules have this capability, providing a viable alternative when reversibility of these processes is preferred.

Solvent variation. The first and easiest method to remove the non-covalent functionalization is to change the solvent system [82]. Anyway, due to the strong interactions with the nanotube sidewalls, the removal of the dispersant via solvent washing is often a difficult task as in the case of some polymers [83]. Lellouche et al. proposed to exploit the non-covalent interaction of neutral iron tricarbonyl complexes with MWCNTs to detect their sidewall oxygenated defects. A simple CH_3CN washing of the composite allows the complete desorption of the adsorbed complexes [84].

A similar result was obtained by adding CH_3CN to CNTs dispersed in chlorinated solvents by using foldamers (i.e., synthetic and designable oligomers) [85]. In this case, CH_3CN did not act as a simple "washing" solvent but rather induced a variation of the conformation of the foldamers due to the solvophobic effect associated to the increase of solvent polarity on passing from chlorinated solvents to CH_3CN.

A recent and interesting way to get a reversible functionalization of MWCNTs makes use of molecules that self-assemble around the nanotube forming supramolecular polymers. Llanes-Pallas et al. have shown that such a non-covalent solubilization can be realized by exploiting the formation of hydrogen bonds between the 2,6-di(acetylamino)pyridine and the imidic groups of uracil derivatives [86]. In apolar organic solvents such hydrogen bonding interactions are effective and keep the nanotube in solution, whereas the addition of polar solvents destroys the H-bonds causing the detachment of the polymer from CNT surface and the precipitation of the nanotubes.

pH responsive systems. It is possible to control the polymer-nanotube affinity, and consequently the CNTs aggregation/disaggregation state, by varying the proton concentration. An effective method of CNTs purification takes advantage of the use of 1-pyreneacetic acid (Py-COOH). This acid, with a high affinity to the nanotube surface thanks to the presence of pyrene, deprotonates under basic conditions and becomes able to solubilize and separate the nanotubes from carbonaceous impurities in water. The acidification of the solution to the original acid causes the precipitation of the nanotubes. Nevertheless, in order to recover the bare nanotubes they must be thoroughly washed with deionized water and ethyl acetate in repeated dispersion–centrifugation cycles, and eventually refluxed in ethyl acetate for 12 h [87].

Some polymers are able to undergo conformational changes in response to a pH change, basically due to a protonation or deprotonation step. Thus, Liang et al. [88,89] have recently studied a conjugated tetrathiafulvalene vinylogue-fluorene copolymer able to selectively disperse low-diameter semiconducting SWCNTs in organic solvents. Upon addition of trifluoroacetic acid to the dispersion a rapid precipitation of completely naked and extremely pure SWCNTs can be observed due to desorption of the polymer from the nanotube walls.

Single-stranded DNA is able to disperse SWCNTs in water at pH 7 and shows a selective affinity towards semiconducting CNTs. Arnold et al. demonstrated [90] an easily scalable and automatable method for the enrichment of SWCNTs by diameter size using density gradient ultracentrifugation. Isolated DNA-wrapped semiconducting SWCNTs are separated into colored bands according to the buoyant density. Besides, as the pH of the aqueous environment controls the secondary structure of DNA, a precipitation/redispersion sequence can be obtained upon simply lowering the pH below 4–5 and raising it to 7. The process is totally reversible, nondestructive and can be repeated several times [91].

Worth noting is also the pH response of poly-L-lysine (PLL)/SWCNTs complexes to pH variations. At pH values higher than 9 the aqueous dispersions of PLL/SWCNTs complexes lose their stability due to the different affinity of PLL towards the nanotubes in their neutral or charged state. Indeed, in aqueous solutions at pH < 9 PLL interacts with the nanotubes either via hydrophobic interactions between the PLL hydrocarbon linker moieties ($–C_4H_8–$) and the SWCNT surface and/or cation–π interaction between protonated amine groups and the nanotube π-electron system. Both interactions are affected by pH variation as PLL assumes an α-helix conformation at high pH but adopts an uncoiled conformation in acidic or neutral pH, whereas ammonium groups deprotonate at pH higher than 9 [92].

Another example is the polymer poly(acrylic acid) used as CNT dispersant. Upon changing the pH of the aqueous solution its charges, its ability to form hydrogen bonds and conformations may vary thus conferring to the polymer a different dispersing power [93].

Another example of reversible dispersion/precipitation of CNTs is the folic acid (FA)/SWCNT system. The insolubility of folic acid in acidic aqueous solutions prevents it acting as a CNT dispersant. Nevertheless, once CNTs have been FA-coated, the simple basification of the mixture results in a complete CNT redissolution without the need for sonication [94].

Guo et al. have shown that using CO_2-responsive polymers is possible to tune the dispersion and aggregation of SWCNT in organic and aqueous media [95]. The amidine groups of the adsorbed polymers in the presence of CO_2 do protonate thus leading to an increased polymer–polymer electrostatic repulsion and to the disassembly of the bundles. CNTs precipitation is induced by N_2 bubbling and CO_2 displacement.

Temperature responsive systems. The precipitation of a FA-coated SWCNT system can be controlled also through temperature variation. The simple heating of the dispersion at 80 °C for 20 minutes causes the peeling of the FA from the SWCNT surface and induces their precipitation. The drawback of this precipitation strategy is that, in order to regenerate the dispersion, it is mandatory to sonicate the sample [94].

Wang et al. showed that, upon increasing the temperature, poly(*N*-isopropylacrylamide) passes from the enthalpically favored to the entropically favored conformation leading to the precipitation of the initially dispersed SWCNTs [92]. The process is reversible and a 2 minutes sonication at 0 °C is enough to regenerate the dispersion. Etika et al. employed a thermo-responsive poly(*N*-cyclopropylacrylamide) copolymer with 5 mol % pyrene side groups to stabilize aqueous SWNT suspensions. At temperatures above the lower critical solution temperature of the copolymer, the conformation of the dispersant changes reducing the steric layer thickness on the CNT surface and inducing precipitation [96].

Light responsive systems. Another very interesting phenomenon is the light-controlled dispersion and reaggregation of SWCNTs in solution. This means realizing a change of the state of aggregation of nanotubes controlled by simple irradiating the sample under UV–visible light.

Chen et al. pointed out that the UV photoirradiation of well-dispersed SWCNTs coated with a poly(ethylene glycol)-terminated malachite green derivative is responsible for the CNTs reaggregation [97]. Indeed, UV light irradiation converts the dispersant into a cation with a superhydrophilic nature and thus more prone to interact with water than with the nanotube surface. The CNTs dispersing ability of azobenzene polymers is also tunable by the light-promoted *trans–cis* isomerization of azobenzene units that allow to switch the polymer conformation from a wrapping to an unwrapping state [98]. Shiraki et al. have shown that NIR laser irradiation coagulates a modified helical polysaccharide/SWCNT complex [99]. Recently, a UV-responsive supra-amphiphile based on the host–guest complexation of a water-soluble pillar[6]arene and a 2-nitrobenzyl ester derivative has been used to control the dispersion behavior of MWCNTs. After 30 minutes UV light irradiation CNT aggregate due to photocleavage of an hydrophilic segment from the hybrid [100].

Redox responsive systems. Oxidation or reduction of the dispersant can as well be favorably exploited for CNTs precipitation/dispersion cycles. Ortiz-Acevedo et al. obtained a diameter-selective solubilization of SWCNTs by using cyclic peptides containing thiol groups [101]. The oxidation induces polymerization of the peptides which wrap around the nanotube achieving a size-selective dispersion. The precipitation of SWCNTs is induced by reduction of newly formed disulfide bonds. Other experimental evidences have been reported on reversible nanotube dispersion via modulation of the oxidation state of a metal complex used as the dispersant. Nobusawa et al. demonstrated how the addition of ascorbic acid to a chloroform solution of SWCNT coated with a Cu(II) complex, in which the 2,2'-bipyridine derivative ligand bears two cholesteryl groups, induces the precipitation of the nanotubes due to the formation of the reduced Cu(I) complex [102]. The conformational change from the planar structure of the Cu(II) complex to the tetrahedral structure of the Cu(I) complex prevents π-stacking interactions between the complexes and the SWCNT surface. Moreover, the precipitate can be redissolved in solution by bubbling air into the mixture. Some foldamers, able to wrap and solubilize nanotubes, unfold and dissociate from the nanotube surface leading to CNTs precipitation upon oxidation [103].

Adsorption–desorption induction. Non-covalent functionalization of CNTs can be controlled by an adsorption–desorption equilibrium. As already highlighted above, when polymers are used as the dispersants some free polymer is always present in the solution. It has been demonstrated that too much free polymer in the bulk solution can lead to aggregation of the CNTs because of the depletion effect. As an example, Meuer et al. showed [104] that CNTs dispersed by pyrene-substituted poly(methyl methacrylate) do precipitate on addition of further polymer.

The adsorption–desorption equilibrium is a real critical point when dealing with dilution steps (i.e., administration of drug targeting SWCNTs in the blood stream) as it is important to ascertain that a proper amount of the dispersant keeps covering the nanotube surface even under very diluted states [105].

Non-covalent functionalization can be reversed also by means of thin-layer chromatography (TLC) experiments by exploiting the different affinity of the dispersant for the stationary or the mobile phase [106].

Conclusion

The reported findings highlight how it is possible to obtain stable and relatively concentrated dispersions of CNTs both in organic and in aqueous solvents. Once CNTs are properly disentangled by overcoming the strong van der Waals interactions among the tubes via sonication, it is essential to disfavor the approach of CNTs to each other. Thus, it is possible to simply obtain organic CNTs dispersions by exploiting synergistic effective polar and π-stacking interactions of CNTs with elected solvents such as NMP. A second and widely used approach involves the addition of proper molecules characterized by the capability to interact both with the nanotube surface (i.e., mainly through π-stacking and van der Waals interactions) and with the surrounding medium. Among the most used dispersants, we may recall PAH, porphyrines and lipophilic polymers for dispersion in organic solvents whereas surfactants, DNA and block copolymers are mainly used for dispersion in aqueous solutions. The possibility of processing CNTs with the use of proper dispersing agents and/or to control their bundling through external stimuli such as pH, temperature, redox reactions or light irradiation, thanks to the reversibility of non-covalent functionalization, represents nowadays one of the major challenges in overcoming their limited manipulability and therefore in developing applications for the future.

Acknowledgements

A. F. would like to acknowledge the COST Project MP0901 NanoTP for support and especially Carla Bittencourt and Chris Ewels for their commitment to the success of the project and the creation of an excellent scientific network. This work was supported by the University ‘G. d’Annunzio’ of Chieti-Pescara and MIUR (PRIN 2010-11, prot. 2010N3T9M4). A. D. C. thanks MIUR (PRIN 2010-11, prot. 2010N3T9M4) that funded his biennial postdoctoral fellowship.

References

1. Britz, D. A.; Khlobystov, A. N. *Chem. Soc. Rev.* **2006,** *35,* 637–659. doi:10.1039/b507451g
2. Qin, L.-C.; Zhao, X.; Hirahara, K.; Miyamoto, Y.; Ando, Y.; Iijima, S. *Nature* **2000,** *408,* 50. doi:10.1038/35040699
3. Yang, Q.-H.; Bai, S.; Sauvajol, J.-L.; Bai, J.-B. *Adv. Mater.* **2003,** *15,* 792–795. doi:10.1002/adma.200304567
4. De Volder, M. F. L.; Tawfick, S. H.; Baughman, R. H.; Hart, A. J. *Science* **2013,** *339,* 535–539. doi:10.1126/science.1222453
5. Battigelli, A.; Ménard-Moyon, C.; Da Ros, T.; Prato, M.; Bianco, A. *Adv. Drug Delivery Rev.* **2013,** *65,* 1899–1920. doi:10.1016/j.addr.2013.07.006
6. Avouris, P. *Acc. Chem. Res.* **2002,** *35,* 1026–1034. doi:10.1021/ar010152e
7. Yang, W.; Ratinac, K. R.; Ringer, S. P.; Thordarson, P.; Gooding, J. J.; Braet, F. *Angew. Chem., Int. Ed.* **2010,** *49,* 2114–2138. doi:10.1002/anie.200903463
8. Chen, Z.; Zhang, X.; Yang, R.; Zhu, Z.; Chen, Y.; Tan, W. *Nanoscale* **2011,** *3,* 1949–1956. doi:10.1039/c0nr01014f
9. Heller, D. A.; Jin, H.; Martinez, B. M.; Patel, D.; Miller, B. M.; Yeung, T.-K.; Jena, P. V.; Hobartner, C.; Ha, T.; Silverman, S. K.; Strano, M. S. *Nat. Nanotechnol.* **2009,** *4,* 114–120. doi:10.1038/nnano.2008.369
10. Cornelio, B.; Rance, G. A.; Laronze-Cochard, M.; Fontana, A.; Sapi, J.; Khlobystov, A. N. *J. Mater. Chem. A* **2013,** *1,* 8737–8744. doi:10.1039/c3ta11530e
11. Wei, J.; Jia, Y.; Shu, Q.; Gu, Z.; Wang, K.; Zhuang, D.; Zhang, G.; Wang, Z.; Luo, J.; Cao, A.; Wu, D. *Nano Lett.* **2007,** *7,* 2317–2321. doi:10.1021/nl070961c
12. Di Crescenzo, A.; Bardini, L.; Sinjari, B.; Traini, T.; Marinelli, L.; Carraro, M.; Germani, R.; Di Profio, P.; Caputi, S.; Di Stefano, A.; Bonchio, M.; Paolucci, F.; Fontana, A. *Chem. – Eur. J.* **2013,** *19,* 16415–16423. doi:10.1002/chem.201302704
13. Kim, J.-H.; Lee, K. H.; Overzet, L. J.; Lee, G. S. *Nano Lett.* **2011,** *11,* 2611–2617. doi:10.1021/nl200513a
14. Scheinberg, D. A.; McDevitt, M. R.; Dao, T.; Mulvey, J. J.; Feinberg, E.; Alidori, S. *Adv. Drug Delivery Rev.* **2013,** *65,* 2016–2022. doi:10.1016/j.addr.2013.07.013
15. Oberoi, H. S.; Nukolova, N. V.; Kabanov, A. V.; Bronich, T. K. *Adv. Drug Delivery Rev.* **2013,** *65,* 1667–1685. doi:10.1016/j.addr.2013.09.014
16. Coleman, J. N.; Khan, U.; Gun'ko, Y. K. *Adv. Mater.* **2006,** *18,* 689–706. doi:10.1002/adma.200501851
17. Iijima, S. *Nature* **1991,** *354,* 56–58. doi:10.1038/354056a0
18. Girifalco, L. A.; Hodak, M.; Lee, R. S. *Phys. Rev. B* **2000,** *62,* 13104–13110. doi:10.1103/PhysRevB.62.13104
19. Singh, P.; Campidelli, S.; Giordani, S.; Bonifazi, D.; Bianco, A.; Prato, M. *Chem. Soc. Rev.* **2009,** *38,* 2214–2230. doi:10.1039/b518111a
20. Peng, X.; Wong, S. S. *Adv. Mater.* **2009,** *21,* 625–642. doi:10.1002/adma.200801464
21. Lee, Y.; Geckeler, K. E. *Adv. Mater.* **2010,** *22,* 4076–4083. doi:10.1002/adma.201000746
22. Teizer, W.; Hallock, R. B.; Dujardin, E.; Ebbesen, T. W. *Phys. Rev. Lett.* **1999,** *82,* 5305–5308. doi:10.1103/PhysRevLett.82.5305
23. Suenaga, K.; Taniguchi, R.; Shimada, T.; Okazaki, T.; Shinohara, H.; Iijima, S. *Nano Lett.* **2003,** *3,* 1395–1398. doi:10.1021/nl034621c
24. Smith, B. W.; Monthioux, M.; Luzzi, D. E. *Nature* **1998,** *396,* 323–324. doi:10.1038/24521
25. Flavin, K.; Kopf, I.; Del Canto, E.; Navio, C.; Bittencourt, C.; Giordani, S. *J. Mater. Chem.* **2011,** *21,* 17881–17887. doi:10.1039/c1jm12217g
26. Guryanov, I.; Toma, F. M.; Montellano López, A.; Carraro, M.; Da Ros, T.; Angelini, G.; D'Aurizio, E.; Fontana, A.; Maggini, M.; Prato, M.; Bonchio, M. *Chem. – Eur. J.* **2009,** *15,* 12837–12845. doi:10.1002/chem.200901408
27. Tagmatarchis, N.; Prato, M. *J. Mater. Chem.* **2004,** *14,* 437–439. doi:10.1039/b314039c
28. Tasis, D.; Tagmatarchis, N.; Bianco, A.; Prato, M. *Chem. Rev.* **2006,** *106,* 1105–1136. doi:10.1021/cr050569o

29. Coleman, K. S.; Bailey, S. R.; Fogden, S.; Green, M. L. H. *J. Am. Chem. Soc.* **2003,** *125,* 8722–8723. doi:10.1021/ja0355675
30. Bahr, J. L.; Yang, J. P.; Kosynkin, D. V.; Bronikowski, M. J.; Smalley, R. E.; Tour, J. M. *J. Am. Chem. Soc.* **2001,** *123,* 6536–6542. doi:10.1021/ja010462s
31. Strano, M. S.; Dyke, C. A.; Usrey, M. L.; Barone, P. W.; Allen, M. J.; Shan, H.; Kittrell, C.; Hauge, R. H.; Tour, J. M.; Smalley, R. E. *Science* **2003,** *301,* 1519–1522. doi:10.1126/science.1087691
32. Chen, J.; Hamon, M. A.; Hu, H.; Chen, Y.; Rao, A. M.; Eklund, P. C.; Haddon, R. C. *Science* **1998,** *282,* 95–98. doi:10.1126/science.282.5386.95
33. Balavoine, F.; Schultz, P.; Richard, C.; Mallouh, V.; Ebbesen, T. W.; Mioskowski, C. *Angew. Chem., Int. Ed.* **1999,** *38,* 1912–1915. doi:10.1002/(SICI)1521-3773(19990712)38:13/14<1912::AID-ANIE1912>3.0.CO;2-2
34. Quintana, M.; Traboulsi, H.; Llanes-Pallas, A.; Marega, R.; Bonifazi, D.; Prato, M. *ACS Nano* **2012,** *6,* 23–31. doi:10.1021/nn203471t
35. Tournus, F.; Charlier, J.-C. *Phys. Rev. B: Condens. Matter Mater. Phys.* **2005,** *71,* 165421. doi:10.1103/PhysRevB.71.165421
36. Guldi, D. M.; Costa, R. D. *J. Phys. Chem. Lett.* **2013,** *4,* 1489–1501. doi:10.1021/jz4001714
37. Chen, Y.; Gunasinghe, R. N.; Wang, X.-Q.; Pang, Y. *RSC Adv.* **2013,** *3,* 25097–25102. doi:10.1039/c3ra43654c
38. Dumonteil, S.; Demortier, A.; Detriche, S.; Raes, C.; Fonseca, A.; Rühle, M.; Nagy, J. B. *J. Nanosci. Nanotechnol.* **2006,** *6,* 1315–1318. doi:10.1166/jnn.2006.316
39. Bergin, S. D.; Nicolosi, V.; Streich, P. V.; Giordani, S.; Sun, Z. Y.; Windle, A. H.; Ryan, P.; Niraj, N. P. P.; Wang, Z. T. T.; Carpenter, L.; Blau, W. J.; Boland, J. J.; Hamilton, J. P.; Coleman, J. N. *Adv. Mater.* **2008,** *20,* 1876–1881. doi:10.1002/adma.200702451
40. Ausman, K. D.; Piner, R.; Lourie, O.; Ruoff, R. S.; Korobov, M. *J. Phys. Chem. B* **2000,** *104,* 8911–8915. doi:10.1021/jp002555m
41. Marcus, Y. *J. Solution Chem.* **1991,** *20,* 929–944. doi:10.1007/BF01074953
42. Landi, B. J.; Ruf, H. J.; Worman, J. J.; Raffaelle, R. P. *J. Phys. Chem. B* **2004,** *108,* 17089–17095. doi:10.1021/jp047521j
43. Laurence, C.; Nicolet, P.; Dalati, M. T.; Abboud, J.-L. M.; Notario, R. *J. Phys. Chem.* **1994,** *98,* 5807–5816. doi:10.1021/j100074a003
44. Zhang, J.; Lee, J.-K.; Wu, Y.; Murray, R. W. *Nano Lett.* **2003,** *3,* 403–407. doi:10.1021/nl025952c
45. Gotovac, S.; Honda, H.; Hattori, Y.; Takahashi, K.; Kanoh, H.; Kaneko, K. *Nano Lett.* **2007,** *7,* 583–587. doi:10.1021/nl0622597
46. Wang, X.; Tao, S.; Xing, B. *Environ. Sci. Technol.* **2009,** *43,* 6214–6219. doi:10.1021/es901062t
47. Mateo-Alonso, A.; Ehli, C.; Chen, K. H.; Guldi, D. M.; Prato, M. *J. Phys. Chem. A* **2007,** *111,* 12669–12673. doi:10.1021/jp0765648
48. Murakami, H.; Nomura, T.; Nakashima, N. *Chem. Phys. Lett.* **2003,** *378,* 481–485. doi:10.1016/S0009-2614(03)01329-0
49. Murphy, R.; Coleman, J. N.; Cadek, M.; McCarthy, B.; Bent, M.; Drury, A.; Barklie, R. C.; Blau, W. J. *J. Phys. Chem. B* **2002,** *106,* 3087–3091. doi:10.1021/jp0132836
50. Bartelmess, J.; Ehli, C.; Cid, J.-J.; García-Iglesias, M.; Vázquez, P.; Torres, T.; Guldi, D. M. *Chem. Sci.* **2011,** *2,* 652–660. doi:10.1039/c0sc00364f
51. Vaisman, L.; Marom, G.; Wagner, H. D. *Adv. Funct. Mater.* **2006,** *16,* 357–363. doi:10.1002/adfm.200500142
52. Itzhak, R.; Raichman, D.; Shahar, Z.; Frey, G. L.; Frey, J.; Yerushalmi-Rozen, R. *J. Phys. Chem. C* **2010,** *114,* 3748–3753. doi:10.1021/jp908309f
53. Slusarenko, N. N.; Heurtefeu, B.; Maugey, M.; Zakri, C.; Poulin, P.; Lecommandoux, S. *Carbon* **2006,** *44,* 3207–3212. doi:10.1016/j.carbon.2006.06.034
54. Nish, A.; Hwang, J.-Y.; Doig, J.; Nicholas, R. J. *Nat. Nanotechnol.* **2007,** *2,* 640–646. doi:10.1038/nnano.2007.290
55. Joo, Y.; Brady, G. J.; Arnold, M. S.; Gopalan, P. *Langmuir* **2014,** *30,* 3460–3466. doi:10.1021/la500162x
56. Chen, J.; Liu, H. Y.; Weimer, W. A.; Halls, M. D.; Waldeck, D. H.; Walker, G. C. *J. Am. Chem. Soc.* **2002,** *124,* 9034–9035. doi:10.1021/ja026104m
57. Nguendia, J. Z.; Zhong, W.; Fleury, A.; De Grandpré, G.; Soldera, A.; Sabat, R. G.; Claverie, J. P. *Chem. – Asian J.* **2014,** *9,* 1356–1364. doi:10.1002/asia.201301687
58. Di Crescenzo, A.; Kopf, I.; Pieraccini, S.; Masiero, S.; Del Canto, E.; Spada, G. P.; Giordani, S.; Fontana, A. *Carbon* **2012,** *50,* 4663–4672. doi:10.1016/j.carbon.2012.05.056
59. Bonard, J.-M.; Stora, T.; Salvetat, J.-P.; Maier, F.; Stöckli, T.; Duschl, C.; Forró, L.; de Heer, W. A.; Châtelain, A. *Adv. Mater.* **1997,** *9,* 827–831. doi:10.1002/adma.19970091014
60. Attal, S.; Thiruvengadathan, R.; Regev, O. *Anal. Chem.* **2006,** *78,* 8098–8104. doi:10.1021/ac060990s
61. Oh, H.; Sim, J.; Ju, S.-Y. *Langmuir* **2013,** *29,* 11154–11162. doi:10.1021/la4022933
62. Cambré, S.; Wenseleers, W. *Angew. Chem., Int. Ed.* **2011,** *50,* 2764–2768. doi:10.1002/anie.201007324
63. Richard, C.; Balavoine, F.; Schultz, P.; Ebbesen, T. W.; Mioskowski, C. *Science* **2003,** *300,* 775–778. doi:10.1126/science.1080848
64. O'Connell, M. J.; Bachilo, S. M.; Huffman, C. B.; Moore, V. C.; Strano, M. S.; Haroz, E. H.; Rialon, K. L.; Boul, P. J.; Noon, W. H.; Kittrell, C.; Ma, J.; Hauge, R. H.; Weisman, R. B.; Smalley, R. E. *Science* **2002,** *297,* 593–596. doi:10.1126/science.1072631
65. Yurekli, K.; Mitchell, C. A.; Krishnamoorti, R. *J. Am. Chem. Soc.* **2004,** *126,* 9902–9903. doi:10.1021/ja047451u
66. Di Crescenzo, A.; Germani, R.; Del Canto, E.; Giordani, S.; Savelli, G.; Fontana, A. *Eur. J. Org. Chem.* **2011,** 5641–5648. doi:10.1002/ejoc.201100720
67. Di Crescenzo, A.; Cambré, S.; Germani, R.; Di Profio, P.; Fontana, A. *Langmuir* **2014,** *30,* 3979–3987. doi:10.1021/la500151j
68. Zhong, W. H.; Claverie, J. P. *Carbon* **2013,** *51,* 72–84. doi:10.1016/j.carbon.2012.08.014
69. Smalley, R. E.; Colbert, D.; O'Connell, M.; Smith, K. PCT Int. Appl. WO 2002012144 A2 20020214, 2002.
70. Di Meo, E. M.; Di Crescenzo, A.; Velluto, D.; O'Neil, C. P.; Demurtas, D.; Hubbell, J. A.; Fontana, A. *Macromolecules* **2010,** *43,* 3429–3437. doi:10.1021/ma902443j
71. Di Crescenzo, A.; Aschi, M.; Fontana, A. *Macromolecules* **2012,** *45,* 8043–8050. doi:10.1021/ma301534k
72. Toma, F. M.; Sartorel, A.; Iurlo, M.; Carraro, M.; Rapino, S.; Hoober-Burkhardt, L.; Da Ros, T.; Marcaccio, M.; Scorrano, G.; Paolucci, F.; Bonchio, M.; Prato, M. *ChemSusChem* **2011,** *4,* 1447–1451. doi:10.1002/cssc.201100089
73. Guldi, D. M.; Rahman, G. M. A.; Jux, N.; Balbinot, D.; Hartnagel, U.; Tagmatarchis, N.; Prato, M. *J. Am. Chem. Soc.* **2005,** *127,* 9830–9838. doi:10.1021/ja050930o

74. Ehli, C.; Oelsner, C.; Guldi, D. M.; Mateo-Alonso, A.; Prato, M.; Schmidt, C.; Backes, C.; Hauke, F.; Hirsch, A. *Nat. Chem.* **2009,** *1,* 243. doi:10.1038/nchem.214
75. Kam, N. W. S.; O'Connell, M.; Wisdom, J. A.; Dai, H. *Proc. Natl. Acad. Sci. U. S. A.* **2005,** *102,* 11600–11605. doi:10.1073/pnas.0502680102
76. Tomonari, Y.; Murakami, H.; Nakashima, N. *Chem. – Eur. J.* **2006,** *12,* 4027–4034. doi:10.1002/chem.200501176
77. Nakashima, N.; Tomonari, Y.; Murakami, H. *Chem. Lett.* **2002,** *31,* 638–639. doi:10.1246/cl.2002.638
78. Fukushima, T.; Kosaka, A.; Ishimura, Y.; Yamamoto, T.; Takigawa, T.; Ishii, N.; Aida, T. *Science* **2003,** *300,* 2072–2074. doi:10.1126/science.1082289
79. Di Crescenzo, A.; Demurtas, D.; Renzetti, A.; Siani, G.; De Maria, P.; Meneghetti, M.; Prato, M.; Fontana, A. *Soft Matter* **2009,** *5,* 62–66. doi:10.1039/b812022f
80. Di Crescenzo, A.; Aschi, M.; Del Canto, E.; Giordani, S.; Demurtas, D.; Fontana, A. *Phys. Chem. Chem. Phys.* **2011,** *13,* 11373–11383. doi:10.1039/c1cp20140a
81. Lemasson, F.; Tittmann, J.; Hennrich, F.; Stürzl, N.; Malik, S.; Kappes, M. M.; Mayor, M. *Chem. Commun.* **2011,** *47,* 7428–7430. doi:10.1039/c1cc11400j
82. O'Connell, M. J.; Boul, P.; Ericson, L. M.; Huffman, C.; Wang, Y.; Haroz, E.; Kuper, C.; Tour, J.; Ausman, K. D.; Smalley, R. E. *Chem. Phys. Lett.* **2001,** *342,* 265–271. doi:10.1016/S0009-2614(01)00490-0
83. Imin, P.; Imit, M.; Adronov, A. *Macromolecules* **2012,** *45,* 5045–5050. doi:10.1021/ma300403q
84. Lellouche, J.-P.; Piran, M.; Shahar, L.; Grinblat, J.; Pirlot, C. *J. Mater. Chem.* **2008,** *18,* 1093–1099. doi:10.1039/b715913g
85. Zhang, Z.; Che, Y.; Smaldone, R. A.; Xu, M.; Bunes, B. R.; Moore, J. S.; Zang, L. *J. Am. Chem. Soc.* **2010,** *132,* 14113–14117. doi:10.1021/ja104105n
86. Llanes-Pallas, A.; Yoosaf, K.; Traboulsi, H.; Mohanraj, J.; Seldrum, T.; Dumont, J.; Minoia, A.; Lazzaroni, R.; Armaroli, N.; Bonifazi, D. *J. Am. Chem. Soc.* **2011,** *133,* 15412–15424. doi:10.1021/ja2011516
87. Lu, F.; Wang, X.; Meziani, M. J.; Cao, L.; Tian, L.; Bloodgood, M. A.; Robinson, J.; Sun, Y.-P. *Langmuir* **2010,** *26,* 7561–7564. doi:10.1021/la904361e
88. Liang, S.; Chen, G.; Zhao, Y. *J. Mater. Chem. C* **2013,** *1,* 5477–5490. doi:10.1039/c3tc30317a
89. Liang, S.; Zhao, Y.; Adronov, A. *J. Am. Chem. Soc.* **2013,** *136,* 970–977. doi:10.1021/ja409918n
90. Arnold, M. S.; Stupp, S. I.; Hersam, M. C. *Nano Lett.* **2005,** *5,* 713–718. doi:10.1021/nl050133o
91. Maji, B.; Samanta, S. K.; Bhattacharya, S. *Nanoscale* **2014,** *6,* 3721–3730. doi:10.1039/c3nr05045a
92. Wang, D.; Chen, L. *Nano Lett.* **2007,** *7,* 1480. doi:10.1021/nl070172v
93. Grunlan, J. C.; Liu, L.; Kim, Y. S. *Nano Lett.* **2006,** *6,* 911–915. doi:10.1021/nl052486t
94. Ikeda, A.; Totsuka, Y.; Nobusawa, K.; Kikuchi, J.-i. *J. Mater. Chem.* **2009,** *19,* 5785–5789. doi:10.1039/b905387e
95. Guo, Z.; Feng, Y.; He, S.; Qu, M.; Chen, H.; Liu, H.; Wu, Y.; Wang, Y. *Adv. Mater.* **2013,** *25,* 584–590. doi:10.1002/adma.201202991
96. Etika, K. C.; Jochum, F. D.; Theato, P.; Grunlan, J. C. *J. Am. Chem. Soc.* **2009,** *131,* 13598–13599. doi:10.1021/ja905803f
97. Chen, S.; Jiang, Y.; Wang, Z.; Zhang, X.; Dai, L.; Smet, M. *Langmuir* **2008,** *24,* 9233–9236. doi:10.1021/la8020063
98. Umeyama, T.; Kawabata, K.; Tezuka, N.; Matano, Y.; Miyato, Y.; Matsushige, K.; Tsujimoto, M.; Isoda, S.; Takano, M.; Imahori, H. *Chem. Commun.* **2010,** *46,* 5969–5971. doi:10.1039/c0cc00709a
99. Shiraki, T.; Dawn, A.; Le, T. N. L.; Tsuchiya, Y.; Tamaru, S.-i.; Shinkai, S. *Chem. Commun.* **2011,** *47,* 7065–7067. doi:10.1039/c1cc11288k
100. Yang, J.; Yu, G.; Xia, D.; Huang, F. *Chem. Commun.* **2014,** *50,* 3993–3995. doi:10.1039/c4cc00590b
101. Ortiz-Acevedo, A.; Xie, H.; Zorbas, V.; Sampson, W. M.; Dalton, A. B.; Baughman, R. H.; Draper, R. K.; Musselman, I. H.; Dieckmann, G. R. *J. Am. Chem. Soc.* **2005,** *127,* 9512–9517. doi:10.1021/ja050507f
102. Nobusawa, K.; Ikeda, A.; Kikuchi, J.-i.; Kawano, S.-i.; Fujita, N.; Shinkai, S. *Angew. Chem., Int. Ed.* **2008,** *47,* 4577–4580. doi:10.1002/anie.200800095
103. Liang, S.; Chen, G.; Peddle, J.; Zhao, Y. *Chem. Commun.* **2012,** *48,* 3100–3102. doi:10.1039/c2cc17935k
104. Meuer, S.; Braun, L.; Schilling, T.; Zentel, R. *Polymer* **2009,** *50,* 154–160. doi:10.1016/j.polymer.2008.10.039
105. Di Crescenzo, A.; Velluto, D.; Hubbell, J. A.; Fontana, A. *Nanoscale* **2011,** *3,* 925–928. doi:10.1039/c0nr00444h
106. Zhang, W.; Silva, S. R. P. *Scr. Mater.* **2010,** *63,* 645–648. doi:10.1016/j.scriptamat.2010.05.037

License and Terms

This is an Open Access article under the terms of the Creative Commons Attribution License (http://creativecommons.org/licenses/by/2.0), which permits unrestricted use, distribution, and reproduction in any medium, provided the original work is properly cited.

The license is subject to the *Beilstein Journal of Nanotechnology* terms and conditions: (http://www.beilstein-journals.org/bjnano)

The definitive version of this article is the electronic one which can be found at: doi:10.3762/bjnano.5.178

BEILSTEIN JOURNAL OF NANOTECHNOLOGY

Experimental techniques for the characterization of carbon nanoparticles – a brief overview

Wojciech Kempiński*[1], Szymon Łoś[1], Mateusz Kempiński[2,3] and Damian Markowski[1]

Review

Open Access

Address:
[1]Institute of Molecular Physics, Polish Academy of Sciences, Mariana Smoluchowskiego 17, Poznań, 60-179, Poland, [2]Faculty of Physics, Adam Mickiewicz University, Umultowska 85, Poznań, 61-614, Poland and [3]NanoBioMedicalCentre, Adam Mickiewicz University, Umultowska 85, Poznań, 61-614, Poland

Email:
Wojciech Kempiński* - wojkem@ifmpan.poznan.pl;
Mateusz Kempiński - matt@amu.edu.pl

* Corresponding author

Keywords:
carbon nanoparticles; charge carrier transport; host–guest interactions; spin localization

Beilstein J. Nanotechnol. **2014,** *5,* 1760–1766.
doi:10.3762/bjnano.5.186

Received: 29 May 2014
Accepted: 23 September 2014
Published: 13 October 2014

This article is part of the Thematic Series "Atomic scale interface design and characterisation: Theory – Electronic properties".

Guest Editor: A. Krasheninnikov

© 2014 Kempiński et al; licensee Beilstein-Institut.
License and terms: see end of document.

Abstract

The review of four experimental methods: X-ray diffraction, Raman spectroscopy, electron paramagnetic resonance and four-point electrical conductivity measurements is presented to characterize carbon nanoparticles. Two types of carbon nanoparticle systems are discussed: one comprising the powder of individual carbon nanoparticles and the second as a structurally interconnected nanoparticle matrix in the form of a fiber. X-ray diffraction and Raman spectroscopy reveal the atomic structure of the carbon nanoparticles and allow for observation of the changes in the quasi-graphitic ordering induced by ultrasonic irradiation and with the so-called quasi-high pressure effect under adsorption conditions. Structural changes have strong influence on the electronic properties, especially the localization of charge carriers within the nanoparticles, which can be observed with the EPR technique. This in turn can be well-correlated with the four-point electrical conductivity measurements which directly show the character of the charge carrier transport within the examined structures.

Review

Introduction

Quasi-graphitic carbon nanoparticles (CNs) were found to show very interesting behavior with respect to the localization of charge carriers. Due to their large specific surface area, CNs are very sensitive to the adsorption of various molecules. Their electronic properties strongly depend on their structure and interactions between the molecules adsorbed in pores and the pore walls (host–guest interactions) and this behavior is the main interest of this work. It was shown that it is possible to control the charge carrier transport within the systems of CNs by varying the temperature, adsorbed molecules and external

electric field. Due to the significant changes in resistivity induced by the host–guest interactions, the systems of CNs might prove interesting in the fields of gas sensing, molecular electronics or spintronics. Localization of charge carriers (spins) within the CNs is the crucial phenomenon for such applications [1-3]. Dresselhaus' group described the process of charge carrier transport within the carbon nano-textures using two models – Coulomb gap variable range hopping (CGVRH) and charge energy limited tunneling conduction (CELTC) [4-6]. The latter model was also used by other researchers to describe disordered carbons [7]. Both models originate from the well-explored system of granular metals in which potential barriers are created with different dielectric separators [8]. The possibility to control the charge carrier transport ("tunable electrical conductivity") was shown in porous metal-organic frameworks (MOFs) with adsorbed guest molecules [9]. It was also shown that by appropriate choice of guest molecules, it is possible to control the charge (spin) transport in the nano-graphitic or graphene-like systems [10,11].

In this review we have collected results from four experimental methods: X-ray diffraction (XRD), Raman spectroscopy, electron paramagnetic resonance (EPR) and four-point electrical conductivity measurements, in order to characterize the two CN systems. These well-defined nanoparticle powders were comprised of separated CNs and a fiber formed by randomly connected CNs, referred to as the activated carbon fiber herein. With a comprehensive study of such systems, comprising the research of host–guest interactions of CNs with different molecules, the problem of controlled charge and spin localization within different systems based on nano-graphite or nano-graphene crystallites can be approached.

Individual carbon nanoparticles – the structure

Graphite crystals are layered materials with the strong carbon bonding within the atomic sheets and weak interaction between them [12]. It is relatively easily to pulverize this material to form CNs. XRD and Raman spectroscopy are suitable methods for crystal size approximation [13-15]. To obtain CNs similar to those forming activated carbon fibers described in the next paragraph, crystals of hexagonal graphite were treated with ultrasonic irradiation [16]. This procedure results in the development of an internal strain which generates the stacking fault by shifting the layers laterally as well as increasing the distance between them. The in-plane coherence length and the degree of three dimensional order of the crystallites can be calculated from the powder XRD data. The diffractograms presented in Figure 1 show a progressive decrease in the peak intensity as well as broadening of the linewidth. The most prominent peak of the hexagonal structure, (002), undergoes the strongest alteration. The intensity proportional to the number of atomic layers is gradually reduced with the irradiation time. Additionally, broadening of the peak width is observed due to the reduction of the coherence length. This effect is observed for all peaks present. This is a signature of the decay of the periodicity in the crystal, especially along the crystallographic *c* direction perpendicular to the graphene layers. Translation of these layers is the mechanical consequence of ultrasonic radiation. An accurate analysis reveals the presence of a set of extra peaks whose posi-

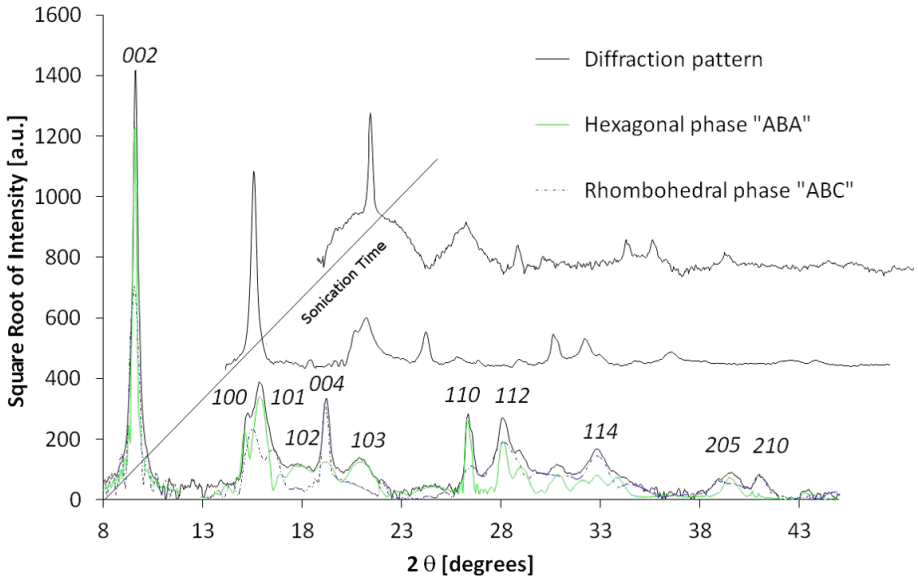

Figure 1: The experimental XRD diffraction pattern obtained for ultrasound-treated graphite. Both hexagonal and rhombohedral phase have been assumed to simulate the diffraction pattern. For clarity, the Miller indices have been assigned only to the hexagonal graphite phase.

tions suggest the occurrence of a rhombohedral phase [17]. It was shown that this phase can be generated locally by grinding the graphite [18-20] and constitutes up to 40% volume content of the sample. Figure 1 presents the diffractograms of pre-grinded graphite, irradiated with ultrasonic waves. The XRD pattern simulation (peak intensity and width) gives the average crystallite thickness calculated for the major reciprocal in-plane directions. The average domain dimension, L_a, can be calculated from the [100]* and [110]* directions, and coherent domain size, L_c along the c axis, from the [002]* direction. These values obtained from Fraunhofer analysis could also be calculated from the linewidth by Scherrer's equation [21]. Notwithstanding, in samples which contain the hexagonal and rhombohedral phases, the peaks which are characteristics of both phases overlap, resulting in a broadened linewidth, which may result in the over-estimation of the aforementioned values when compared to the samples comprising only one phase. The sonication procedure results in multiple mechanical effects such as: the disintegration of the three dimensional order, the separation of layers, the turbostratic structure formation, and the reduction of the layer size due to breaking of the C–C aromatic bonds. The presence of the two-dimensional graphene particles could not be observed with XRD.

First- and second-order Raman spectroscopy is a useful method which allows characterization of the powders from the point of view of CNs. This technique is based on the phonon scattering phenomena and much valuable information can be obtained from the relative intensities of the spectral components. It was shown by Tuinstra and Koenig in 1970 [22,23] and recently by Ferrari et al. [14,24] and Cançado et al. [25] that the D to G peak intensity ratio in the first order spectra can be correlated with the in-plane size of the crystallites. The D peak intensity depends on the defect concentration and indicates the presence of a crystalline border [26]. It is suppressed by the perfectly organized carbon layer since it is a hexagonal ring breathing mode [14]. Second order Raman spectra are presented in Figure 2. They are composed of the three different signals because the laser irradiates sample regions with different degrees of structural ordering. The first signal represents the well-organized graphite structure (3D structure) and is comprised of two peaks in the vicinity of 2697 cm^{-1} and 2728 cm^{-1}. This signal reconstruction was performed with the 1:2 amplitude ratio, respectively [27]. The second signal (marked with T) comes from the turbostratic fraction and is represented by the single Lorentzian line at 2710 cm^{-1} [28]. Each band from the above mentioned carbon types has a full width at half-maximum of approximately 30 cm^{-1}. For the sonicated sample, a third signal appears (marked with NG). Its position is shifted towards shorter wavenumbers. A similar peak was previously observed on graphene treated with an argon ion beam [29]. The width of the NG line is twice as broad as the width of the 3D and T signals. This can be due to the large number of defects. This result points at the creation of a large number of defects due to the ultrasonic treatment. The NG signal can also be interpreted as the line associated with few-layered graphene flakes since the signal of double-layered graphene flakes consists of four Lorentzian lines [30] and resembles a single broad line [31]. Furthermore, triple-layered graphene would result in six peaks, and so forth. Considering this, the broad peak at 2679 cm^{-1} might be inhomogeneously broadened and can be attributed to the strained nano-graphite appearing in the sample.

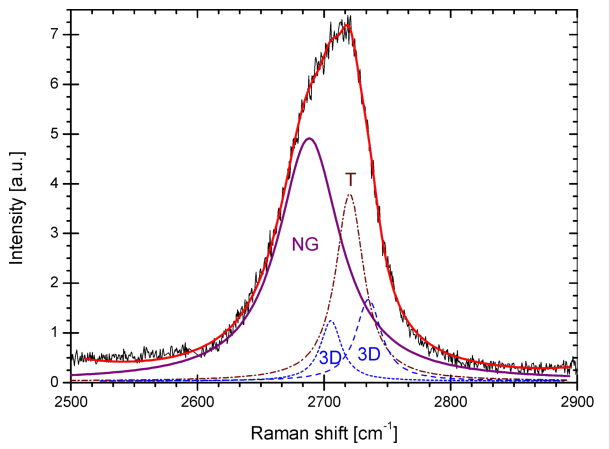

Figure 2: A typical second-order Raman spectra of an irradiated sample: the turbostratic (T) structure band (dotted line), the two peaks of the three dimensionally ordered graphite (3D) structure (dashed line), and the nano-graphite signal (solid line).

There are also other ways to determine the dimensions of the CNs. Among them are impedance measurements [32] and the EPR technique performed on the conducting electrons [33]. A more detailed analysis is provided in the next section.

Carbon nanoparticle matrix

The electric conductivity measurements were performed for activated carbon fibers (ACFs) formed from the quasi-graphitic CNs, which are mechanically connected by carbon chains or graphene fragments [36]. It was shown that the conductivity of such a system depends on the thermal energy allowing the hopping of charge carriers between the CNs [4,37]. Hopping charge carrier transport in the granular structures is described with the CGVRH model [4], from which the following equation has been derived:

$$\rho(T) = \rho_0 \exp(T_0/T)^{1/2}, \quad (1)$$

where ρ stands for the resistivity, ρ_0 is a temperature-independent constant, T is the temperature and T_0 is the energy needed for hopping of charge carriers.

In the low temperature regime (below 200 K) the amount of thermal excitations drastically decreases and charge carriers cannot overcome the potential barriers between the nano-crystallites and thus become localized within them [8]. The localization of charge carriers can be easily observed with the EPR technique [36]. This consists of the resonant absorption of microwave energy by unpaired spins (localized charge carriers) placed in the external magnetic field.

The EPR signal of ACFs can be observed only in the low temperature regime and its integral intensity significantly increases with the reduction of temperature [36], as represented in Figure 3.

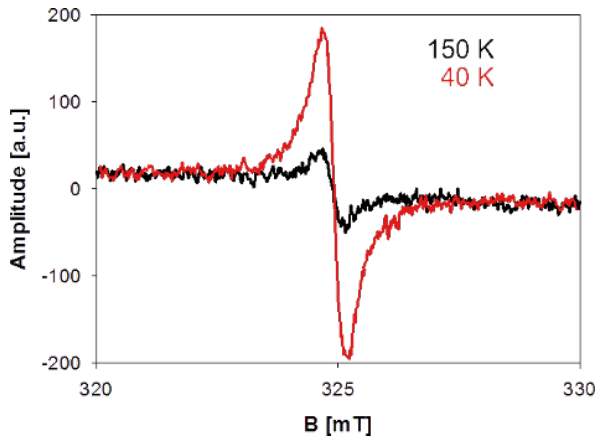

Figure 3: EPR signal of ACFs in different temperatures.

It was shown that this increase results from the Curie's law behavior, where integral intensity is inversely proportional to temperature, which is normally observed for paramagnetic systems with the fixed number of spins (Langevin paramagnetism) [36]. In the case of the ACFs, the number of spins observed in EPR changes according to Equation 1. This is related to the CGVRH model, where resistivity depends on the temperature. In the classical approach [37] the resistivity ρ (which is the reverse of conductivity σ) depends on the number of charge carriers N, their charge e, and mobility μ according to the equation:

$$\rho = \sigma^{-1} = (Ne\mu)^{-1}. \quad (2)$$

N decreases because charge carriers are localized within the system, thus the resistivity increases. The carriers localized within the individual CNs no longer take part in the charge transport and add to the EPR signal instead. Thus, Curie's law must be modified with the component resulting from the Equation 1 to take into account the changing number of localized spins. This result is presented in Figure 4 [36].

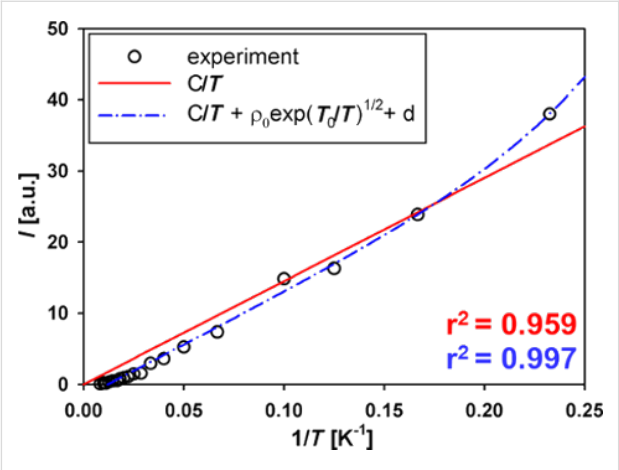

Figure 4: EPR signal intensity vs temperature fitted with the unmodified Curie's law (red) and Curie's law modified with Equation 1 (blue).

Another factor greatly influencing the EPR signal of ACFs is the adsorption of molecules at the surface of CNs which comprise the pore walls. The adsorption in ACF pores is of a physical nature (van der Waals forces), without any covalent bond formation. Fully reversible physisorption has been observed with EPR (see Figure 5).

The EPR spectrum of ACFs becomes strongly modified after the adsorption of guest molecules. Pure ACFs show a single narrow Lorentzian line, while the filled ones show the same narrow line plus two additional broad components in the EPR spectrum [35,38].

It was concluded that the three different lines originate from the different parts of the fibers, that is, areas not accessed by guest molecules, the pore walls and the fiber surface [35,38].

Figure 5 shows that the influence of various adsorbed molecules is varied. For example, water causes a more significant change of the EPR spectrum of the ACFs than CCl_4. This effect is particularly visible in the experiment where the number of spins localized due to the interaction of CNs with H_2O and CCl_4 molecules is estimated. In this case, water causes six-times stronger localization compared to CCl_4 [39].

The influence of H_2O and CCl_4 on the ACF properties is compared in several other experiments and theoretical approaches, as presented below [40-45].

XRD measurements show that guest molecules cause a strong change in the distance between graphene layers comprising the CNs in the ACF texture. Here, the lattice constant decreases from 3.78 Å (recorded for pure ACFs) to 3.33 Å and 3.30 Å for CCl_4- and water-filled fibers, respectively. Such significant changes appear due to the so-called quasi-high pressure effect, which appear in confined liquids (e.g., adsorbed inside small pores). This causes swelling of pores of a certain width due to the decrease of the CN size [40,41]. Water seems to cause a slightly larger shrinkage of the CNs than CCl_4, probably due to the large difference in wetting of graphitic pore walls by both liquids. The wetting in porous materials is commonly described with the microscopic wetting parameter α [42], which shows the interplay between the interactions within the liquid and of the liquid within the pore walls. The wetting parameter is given as:

$$\alpha = c(\varepsilon_{fw} / \varepsilon_{ff}), \quad (3)$$

where c is a constant that comprises the parameters related to the structure of the pore walls and ε is the energy parameter in the Lennard–Jones potential, where the index *fw* represents the fluid–wall, and *ff* the fluid–fluid interaction. For $\alpha \geq 1.15$, the system is considered wet, while for $\alpha \leq 1.15$ it is considered non-wet. The α value for CCl_4 in graphite is 1.9 while for water in graphite it is 0.48. A low α results in the strong hydrophobicity of the CN surface (ACF pore walls) [42].

Similar effects were observed in the spin susceptibility χ measurements, where adsorption of molecules containing the –OH groups (water amongst them) caused a larger increase in the χ-value than the adsorption of other molecules (such as CCl_4) [43].

A more significant difference between ACFs + H_2O and ACFs + CCl_4 was observed in the conductivity measurements, which clearly show that the dipolar molecules cause greater increase of the T_0 value than those without a dipole moment [44]. This concept is presented below.

It was proposed to consider the system of mechanically connected CNs as a quantum dots matrix [35,44]. In such a matrix, where CNs are structurally connected by some mechanical linkages (carbon chains or graphene fragments [34]), there exists a system of potential barriers, similar to the those formed by a dielectric separator in granular metals. The barriers depend on the dielectric constant of the separator [4,8] and in ACFs its value seems to be influenced by the existence of guest molecules inside the pores. It has been shown that the T_0 parameter increases with the value of the dipole moment of the guest molecules adsorbed within the ACF pores [44]. This behavior is consistent with the CELTC model. Recent measurements of ACFs + CCl_4 confirm this idea and Figure 6 shows that there is a clear difference between the influence of dipolar and non-dipolar guest molecules, represented by the value of the T_0 parameter.

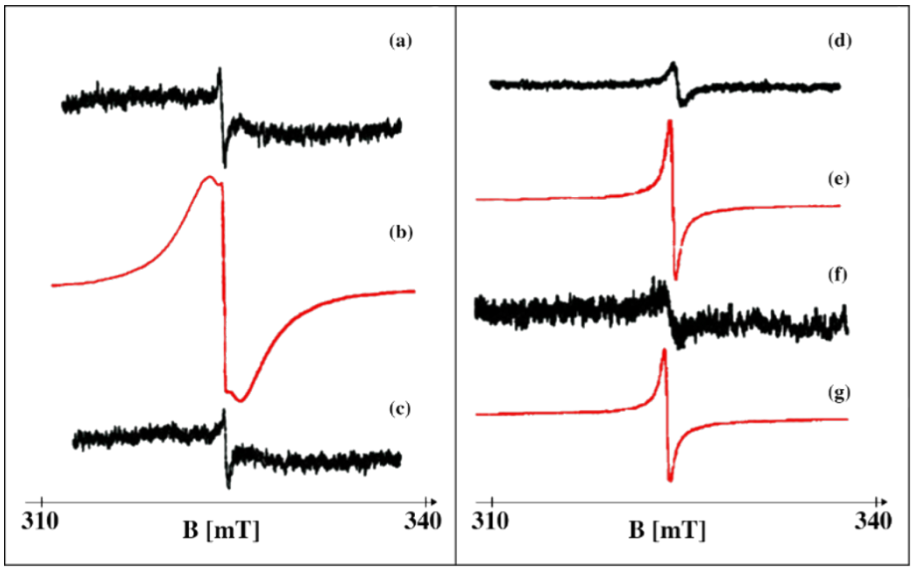

Figure 5: EPR signal of ACFs. Adsorption/desorption of H_2O: (a) initial signal of pure ACFs, signal gain $4 \cdot 10^4$; (b) ACFs + H_2O, s. g. $2 \cdot 10^3$; (c) ACFs after heating in vacuum (100 °C, 10^{-4}mbar), s. g. $4 \cdot 10^4$. Adsorption/desorption of CCl_4 (d) initial signal of pure ACFs, s. g. $2 \cdot 10^4$; (e) ACFs + CCl_4, s. g. $2.5 \cdot 10^3$; (f) ACFs after CCl_4 desorption, s. g. $1 \cdot 10^5$; (g) ACFs + CCl_4, s. g. $2 \cdot 10^3$.

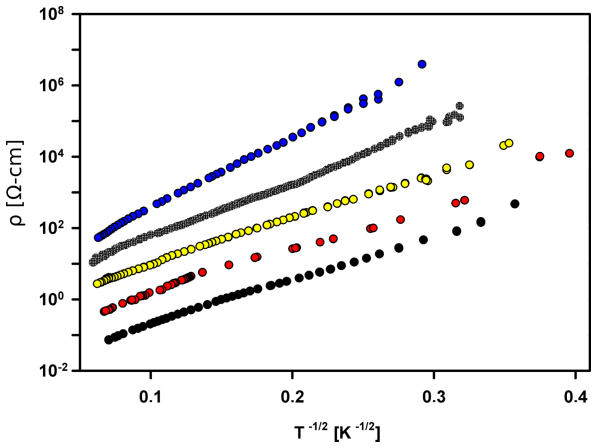

Figure 6: Resistivity vs the reciprocal square root of temperature for pure ACFs and ACFs filled with dipolar molecules (H_2O, D_2O and $C_6H_5NO_2$). This was adapted from a previous publication [38] with the addition of the result for ACFs + non-dipolar molecules (CCl_4). Black: pure ACF with T_0 = 809 K; red: ACF + CCl_4 with T_0 = 844 K; yellow: ACF + H_2O with T_0 = 876 K; green: ACF + D_2O with T_0 = 1282 K and blue: ACF + $C_6H_5NO_2$ with T_0 = 2162 K.

Another interesting feature is the "switching effect", which was reported for CN texture of ACFs [36,45]. An external electric field causes the sudden increase of the resistivity of ACFs filled with dipolar guest molecules. It confirms that the value of the T_0 parameter is influenced by the local electric fields created in the vicinity of individual CNs.

Conclusion

According to the above considerations it can be concluded that different systems of interconnected quasi-graphitic (or graphene-like) CNs may form a good basis for detectors of molecules and atoms of different types, as their electronic properties are very sensitive to adsorption. Another very interesting feature of the CN textures is the possibility to control certain physical properties of the carbon nanoparticle systems by choosing the specific molecules. The ability to control the structure and the charge or spin transport in nanostructured materials can be very useful from the point of view of many future applications.

Acknowledgements

Research was partially supported by the Polish grant MNiSW DPN/N174/COST/2010 and COST MP0901 "NanoTP".

References

1. Sato, H.; Kawatsu, N.; Enoki, T.; Endo, M.; Kobori, R.; Maruyama, S.; Kaneko, K. *Solid State Commun.* **2003,** *125,* 641–645. doi:10.1016/S0038-1098(02)00880-3
2. Nakayama, A.; Suzuki, K.; Enoki, T.; Ishii, C.; Kaneko, K.; Endo, M.; Shindo, N. *Solid State Commun.* **1995,** *93,* 323–326. doi:10.1016/0038-1098(94)00786-1
3. Kobayashi, N.; Enoki, T.; Ishii, C.; Kaneko, K.; Endo, M. *J. Chem. Phys.* **1998,** *109,* 1983. doi:10.1063/1.476774
4. Fung, A. W. P.; Wang, Z. H.; Dresselhaus, M. S.; Dresselhaus, G.; Pekala, R. W.; Endo, M. *Phys. Rev. B* **1994,** *49,* 17325–17335. doi:10.1103/PhysRevB.49.17325
5. Fung, A. W. P.; Rao, A. M.; Kuriyama, K.; Dresselhaus, M. S.; Dresselhaus, G.; Endo, M.; Shindo, N. *J. Mater. Res.* **1993,** *8,* 489–500. doi:10.1557/JMR.1993.0489
6. Rao, A. M.; Fung, A. W. P.; Dresselhaus, M. S.; Endo, M. *J. Mater. Res.* **1992,** *7,* 1788–1794. doi:10.1557/JMR.1992.1788
7. Deroide, B.; Zanchetta, J. V.; Diby, A. *Carbon* **1991,** *29,* 3–9. doi:10.1016/0008-6223(91)90088-Z
8. Abeles, B.; Sheng, P.; Coutts, M. D.; Arie, Y. *Adv. Phys.* **1975,** *24,* 407–461. doi:10.1080/00018737500101431
9. Talin, A. A.; Centrone, A.; Ford, A. C.; Foster, M. E.; Stavila, V.; Haney, P.; Kinney, R. A.; Szalai, V.; El Gabaly, F.; Yoon, H. P.; Léonard, F.; Allendorf, M. D. *Science* **2014,** *343,* 66–69. doi:10.1126/science.1246738
10. Schedin, F.; Geim, A. K.; Morozov, S. V.; Hill, E. W.; Blake, P.; Katsnelson, M. I.; Novoselov, K. S. *Nat. Mater.* **2007,** *6,* 652–655. doi:10.1038/nmat1967
11. Echtermeyer, T. J.; Lemme, M. C.; Baus, M.; Szafranek, B. N.; Geim, A. K.; Kurz, H. *IEEE Electron Device Lett.* **2008,** *29,* 952–954. doi:10.1109/LED.2008.2001179
12. Bonaccorso, F.; Lombardo, A.; Hasan, T.; Sun, Z.; Colombo, L.; Ferrari, A. C. *Mater. Today* **2012,** *15,* 564–589. doi:10.1016/S1369-7021(13)70014-2
13. Andersson, O. E.; Prasad, B. L. V.; Sato, H.; Enoki, T.; Hishiyama, Y.; Kaburagi, Y.; Yoskikawa, M.; Bandow, S. *Phys. Rev. B* **1998,** *58,* 16387–16395. doi:10.1103/PhysRevB.58.16387
14. Ferrari, A. C.; Robertson, J. *Phys. Rev. B* **2000,** *61,* 14095–14107. doi:10.1103/PhysRevB.61.14095
15. Chu, P. K.; Li, L. *Mater. Chem. Phys.* **2006,** *96,* 253–277. doi:10.1016/j.matchemphys.2005.07.048
16. Łoś, S.; Duclaux, L.; Alvarez, L.; Havełek, Ł.; Duber, S.; Kempiński, W. *Carbon* **2013,** *55,* 53–61. doi:10.1016/j.carbon.2012.12.005
17. McNaught, A. D.; Wilkinson, A. *The gold book IUPAC compendium of chemical terminology,* 2nd ed.; Blackwell Scientific Publications: Oxford, U.K., 1997.
18. Boehm, H.-P.; Hofmann, U. *Z. Anorg. Chem.* **1955,** *278,* 58–77. doi:10.1002/zaac.19552780109
19. Guerin, K.; Fevrier-Bouvier, A.; Flandrois, S.; Couzi, M.; Simon, B.; Biensan, P. *J. Electrochem. Soc.* **1999,** *146,* 3660–3665. doi:10.1149/1.1392530
20. Wilhelm, H. A.; Croset, B.; Medjahdi, G. *Carbon* **2007,** *45,* 2356–2364. doi:10.1016/j.carbon.2007.07.010
21. Hammond, C. *The basics of crystallography and diffraction,* 3rd ed.; Oxford University Press, 2009.
22. Tuinstra, F.; Koenig, J. L. *J. Chem. Phys.* **1970,** *53,* 1126–1130. doi:10.1063/1.1674108
23. Tuinstra, F.; Koenig, J. L. *J. Compos. Mater.* **1970,** *4,* 492–499.
24. Ferrari, A. C.; Robertson, J. *Phys. Rev. B* **2001,** *64,* 075414. doi:10.1103/PhysRevB.64.075414
25. Cançado, L. G.; Takai, K.; Enoki, T.; Endo, M.; Kim, Y. A.; Mizusaki, H.; Jorio, A.; Coelho, L. N.; Magalhães-Paniago, R.; Pimenta, M. A. *Appl. Phys. Lett.* **2006,** *88,* 163106. doi:10.1063/1.2196057

26. Cançado, L.; Pimenta, M. A.; Neves, B. R. A.; Dantas, M. S. S.; Jorio, A. *Phys. Rev. Lett.* **2004,** *93,* 247401. doi:10.1103/PhysRevLett.93.247401
27. Vidano, R. P.; Fischbach, D. B.; Willis, L. J.; Loehr, T. M. *Solid State Commun.* **1981,** *39,* 341–344. doi:10.1016/0038-1098(81)90686-4
28. Cançado, L. G.; Takai, K.; Enoki, T.; Endo, M.; Kim, Y. A.; Mizusaki, H.; Speziali, N. L.; Jorio, A.; Pimenta, M. A. *Carbon* **2008,** *46,* 272–275. doi:10.1016/j.carbon.2007.11.015
29. Ferreira, E. H. M.; Moutinho, M. V. O.; Stavale, F.; Lucchese, M. M.; Capaz, R. B.; Achete, C. A.; Jorio, A. *Phys. Rev. B* **2010,** *82,* 125429. doi:10.1103/PhysRevB.82.125429
30. Malard, M. L.; Pimenta, M. A.; Dresselhaus, G.; Dresselhaus, M. S. *Phys. Rep.* **2009,** *473,* 51–87. doi:10.1016/j.physrep.2009.02.003
31. Lee, D. S.; Riedl, C.; Krauss, B.; von Klitzing, K.; Starke, U.; Smet, J. H. *Nano Lett.* **2008,** *8,* 4320–4325. doi:10.1021/nl802156w
32. Łoś, S.; Duclaux, L.; Kempiński, W.; Połomska, M. *Microporous Mesoporous Mater.* **2010,** *130,* 21–25. doi:10.1016/j.micromeso.2009.10.007
33. Dyson, F. J. *Phys. Rev.* **1955,** *98,* 349–359. doi:10.1103/PhysRev.98.349
34. Pré, P.; Huchet, H.; Jeulin, D.; Rouzaud, J.-N.; Sennour, M.; Thorel, A. *Carbon* **2013,** *52,* 239–258. doi:10.1016/j.carbon.2012.09.026
35. Kempiński, M.; Kempiński, W.; Śliwińska-Bartkowiak, M. *Acta Phys. Pol., A* **2005,** *108,* 339–343.
36. Kempiński, M.; Kempiński, W.; Kaszyński, J.; Śliwińska-Bartkowiak, M. *Appl. Phys. Lett.* **2006,** *88,* 143103. doi:10.1063/1.2187416
37. Drude, P. *Ann. Phys. (Berlin, Ger.)* **1900,** *306,* 566–613. doi:10.1002/andp.19003060312
38. Kempiński, M.; Kempiński, W.; Śliwińska-Bartkowiak, M. *Rev. Adv. Mater. Sci.* **2006,** *12,* 72–77.
39. Kempiński, M.; Kempiński, W.; Śliwińska-Bartkowiak, M. *Rev. Adv. Mater. Sci.* **2007,** *14,* 163–166.
40. Śliwińska-Bartkowiak, M.; Drozdowski, H.; Kempiński, M.; Jażdżewska, M.; Long, Y.; Palmer, J. C.; Gubbins, K. E. *Phys. Chem. Chem. Phys.* **2012,** *14,* 7145–7153. doi:10.1039/c2cp22111j
41. Long, Y.; Śliwińska-Bartkowiak, M.; Drozdowski, H.; Kempiński, M.; Phillips, K. A.; Palmer, J. C.; Gubbins, K. E. *Colloids Surf., A* **2013,** *437,* 33–41. doi:10.1016/j.colsurfa.2012.11.024
42. Radhakrishnan, R.; Gubbins, K. E.; Śliwinska-Bartkowiak, M. *J. Chem. Phys.* **2002,** *116,* 1147–1155. doi:10.1063/1.1426412
43. Sato, H.; Kawatsu, N.; Enoki, T.; Endo, M.; Kobori, R.; Maruyama, S.; Kaneko, K. *Carbon* **2007,** *45,* 214–217. doi:10.1016/j.carbon.2006.09.017
44. Kempiński, W.; Markowski, D.; Kempiński, M.; Śliwińska-Bartkowiak, M. *Carbon* **2013,** *57,* 533–536. doi:10.1016/j.carbon.2013.01.087
45. Kempiński, W.; Markowski, D.; Kempiński, M. Porosity and Guest Molecules as a Potential Barrier Moderator in Activated Carbon Fibers. In *Conference materials of The Annual World Conference on Carbon,* Rio de Janeiro, Brazil, July 14–19, 2013; published on CD, ID 411.

License and Terms

This is an Open Access article under the terms of the Creative Commons Attribution License (http://creativecommons.org/licenses/by/2.0), which permits unrestricted use, distribution, and reproduction in any medium, provided the original work is properly cited.

The license is subject to the *Beilstein Journal of Nanotechnology* terms and conditions: (http://www.beilstein-journals.org/bjnano)

The definitive version of this article is the electronic one which can be found at:
doi:10.3762/bjnano.5.186

BEILSTEIN JOURNAL OF NANOTECHNOLOGY

Silicon and germanium nanocrystals: properties and characterization

Ivana Capan*[1], Alexandra Carvalho[2] and José Coutinho[3]

Review

Open Access

Address:
[1]Rudjer Boskovic Institute, P.O. Box 180, 10000 Zagreb, Croatia, [2]Graphene Research Centre and Department of Physics, National University of Singapore, 117542, Singapore and [3]Department of Physics and I3N, Campus Universitário de Santiago, 3810-193 Aveiro, Portugal

Email:
Ivana Capan* - Ivana.Capan@irb.hr

* Corresponding author

Keywords:
characterization; germanium; modelling; nanocrystals; silicon

Beilstein J. Nanotechnol. **2014,** *5,* 1787–1794.
doi:10.3762/bjnano.5.189

Received: 28 May 2014
Accepted: 24 September 2014
Published: 16 October 2014

This article is part of the Thematic Series "Atomic scale interface design and characterisation: Theory – Electronic properties".

Guest Editor: A. Krasheninnikov

© 2014 Capan et al; licensee Beilstein-Institut.
License and terms: see end of document.

Abstract

Group-IV nanocrystals have emerged as a promising group of materials that extends the realm of application of bulk diamond, silicon, germanium and related materials beyond their traditional boundaries. Over the last two decades of research, their potential for application in areas such as optoelectronic applications and memory devices has been progressively unraveled. Nevertheless, new challenges with no parallel in the respective bulk material counterparts have arisen. In this review, we consider what has been achieved and what are the current limitations with regard to growth, characterization and modeling of silicon and germanium nanocrystals and related materials.

Review

I Introduction

Nanocrystals (NCs) have emerged as one of the preferred ways to control quantum phenomena at the nanoscale. This control leads to spectacular properties and to a wide field of applications ranging from memory devices, solar cells and thermoelectrics to light emitters, spintronic devices and printable electronics.

The use of semiconductor NCs instead of two-dimensional floating gate devices such as metal oxide semiconductor (MOS) field effect transistors and memory devices makes memory less sensitive to common problems such as leakage current and dielectric breakdown and allows for an ultimate miniaturization without electrical instabilities [1]. Moreover, nanostructures offer significant breakthroughs in photovoltaics. It is believed that quantum dot (QD) solar cells have the potential to reach a maximum conversion efficiency of about 66% [2]. A colloidal nanocrystal solar cell, which combines all the advantages of organics (scalable and controllable synthesis) with transport properties comparable to traditional photovoltaic semiconductors, has been demonstrated [3]. Different approaches have been made to achieve light emission from group-IV semiconductor nanostructures despite the indirect nature of the energy gaps.

The quantum confinement of carriers has led to efficient luminescence and electroluminescence of semiconductor nanostructures, mostly Si and Ge NCs embedded in an oxide matrix [4].

Theoretical research on NCs was also triggered by the interest in their optical properties [5-7], namely following the work of Furukawa and Miyasato with Si NCs [8], which reported the opening of the optical gap of small Si QD by more than 100% with respect to bulk Si. Within a "particle-in-a-box" description, the effect was simply cast as a power law $E_{gap} = E_{bulk} + \alpha/R^n$ [9], where R is the particle size, α is a confinement factor and n is usually $1 < n < 2$, depending mostly on the surface termination and host material (for a review see [10]). Despite its popularity, such an empirical approach overlooks important physical aspects such as the chemical nature of the NCs or the dielectric mismatch across their boundaries [11].

One important issue that has led to considerable debate relates to the screening effects within the NCs [12-15]. An accurate theory for the dielectric screening is essential to understand the response of nanostructures to an external electro-magnetic field, or the localization of dopant states and excitations. There is consensus now that even for NCs with a diameter as small as 2 nm, the spatially averaged electronic screening within the core is virtually identical to that in bulk, decreasing to the vacuum value close to the polarized surface [16]. Confinement due to underscreening is essentially a surface/interface effect that manifests itself when the surface-to-volume ratio of the structures becomes large [14].

Many important questions related to impurities and surface chemistry have to be answered by using quantum-chemical models. With the development of efficient linear-scaling density functional methods along with the steady drop of CPU-time costs, we are now able to solve by first-principles the all-electron problem of systems with a few thousands of atoms [17]. This has led to the understanding of more complex problems such as doping [18-20], and electronic transport across NC solids [21,22]. These are among the advances that will be reviewed below.

II Growth and characterization

Much of current research on Si/Ge NCs is focused on the preparation and characterization of NCs embedded in a SiO_2 matrix. In this paper, we have restricted our analysis to growth techniques, such as magnetron co-sputtering and ion implantation. With these techniques, it is possible to produce and to control the space-/size-distribution and ordering of NCs. Both benefits and shortcomes of these techniques will be pointed out along the text. It should be noted that other important and widespread techniques are also used for the growth of Si and Ge NCs, namely PECVD (CVD) and MBE. From the experimental point of view, the synthesis of free-standing NCs will not be covered within this review. However, those issues are visited in Section III of this paper, which deals with the first principles modelling of the NCs.

II.1 Magnetron co-sputtering

This is basically a technique for thin film deposition. Together with thermal evaporation and pulsed laser deposition (PLD), they are all fabrication methods based on the production of substoichiometric oxides, with thermal evaporation being the simplest among them. The NCs size, distribution and shape can be controlled by varying sputtering time, composition of sputtered material, as well as the annealing temperature, time and atmosphere. Since NCs embedded in the oxide matrix have a large interface-area-to-volume ratio, they show a high density of interface defects [23]. In such cases, the role of the interface and interface-related traps cannot be neglected.

The interface traps are located at the substrate/oxide-matrix interface (most commonly Si–SiO_2) and at the NCs/oxide-matrix interface. Unlike the other traps located in the oxide matrix (fixed and mobile oxide charges), interface traps are in electrical communication with the underlying substrate, and therefore largely affect the electrical properties of such structures [24]. Passivation of deep levels caused by the interface is necessary before NC-based optoelectronic devices can become reality. Vacuum annealing, which is used for NC crystallization, is known to increase the density of the interface traps. However, most of the interface traps can be neutralized by low-temperature (about 450 °C) annealing with hydrogen or forming gas [24].

In general, the formation of Ge NC is much more complicated than that of Si NC because GeO_2 is thermodynamically less stable than SiO_2, which leads to a higher concentration of defect states [23]. Moreover, the high difference between the thermal expansion coefficients of Ge and SiO_2 and the large lattice constant of Ge results in mechanical stress in the system [25]. However, due to the lower binding energy of Ge atoms in comparison with Si atoms, Ge NCs can be formed in samples annealed at significantly lower temperatures (600–900 °C).

Martin-Sánchez et al. [26] have reported that a crystallization of as-deposited amorphous Ge NCs can be achieved by a short treatment at relatively low temperatures, which significantly decreases the thermal budget, when compared to other growth techniques. Moreover, it implies that PLD should be considered as an excellent alternative to the widely used magnetron co-sputtering technique for the deposition of complex oxide thin films and NCs.

II.2 Ion implantation

An ion beam stands as a highly versatile tool for a variety of purposes including synthesis, modification and characterization of materials. The synthesis of NCs made of silicon and germanium by means of ion beams has been extensively studied in the past years [23]. QDs size, shape and distribution can be controlled by varying the implantation conditions (implantation energy and dose) and subsequent annealing. It is a well-known fact that Si ion implantation of SiO_2 is characterized by the production of a large number of oxygen vacancies and other defects in the oxide matrix. These defects enhance the QD formation and the formation of the sub-oxide interface states [23].

As ion implantation is unavoidable for CMOS technology today, it is desirable to use it not only for the fabrication of NCs but for the doping of NCs as well. Over the past decade, phosphorus-and erbium-doped Si NCs have attracted a great deal of attention, due to the promising optoelectronic applications [27]. It has been shown that in order to study the donor doping and dependences of the PL intensity in such systems, it is crucial to understand and control the presence of defects. The effects of donors and defects to the PL of Si NCs are strongly overlapping [28]. Moreover, it was reported that the density of interface-related defects may be decreased by light phosphorus doping [29].

An alternative method to the doping of NCs by using ion implantation is by means of neutron transmutation doping (NTD). NTD is a technique commonly used to dope bulk semiconductors, but for NCs is not much explored. Recently, the promising application of NTD for arsenic-doping of Ge NCs has been reported [30].

II.3 Properties and characterization

To obtain all necessary information regarding the properties of NCs, it is desirable to perform a complete characterization that includes structural, optical and electrical specifications. Most characterization reports on semiconductor NCs start with transmission electron microscopy (TEM) data. This is a widespread and well-known technique, which gives extremely valuable structural information. TEM has been used to study Si NCs produced by reactive evaporation in one of the first approaches to produce embedded semiconductor NCs, the so-called superlattice approach [31]. This method enables an easy and well-defined control over the particle size, density and ordering.

Together with TEM, there are other useful techniques that can provide information regarding the structural properties of NCs. One of them is grazing incidence small X-ray scattering (GISAXS), which is a non-destructive technique for the structural characterization of NCs supported on a substrate [32] and NCs embedded in a matrix [33]. From the GISAXS analysis, it is possible to determine size, shape, inter-NC distance and size distribution of NCs.

Among all properties of semiconductor NCs, the optical properties have been the most extensively studied, usually by using photoluminescence (PL). Si NCs often show strong luminescence intensity in the visible and near-infrared region. A size-dependent blue shift of the luminescence comparable to porous Si is well documented. Figure 1 shows PL spectra of Si NCs produced by ion implantation and subsequent annealing [34]. The emission is tuned by varying the implantation and annealing conditions (yielding control over of the NC size).

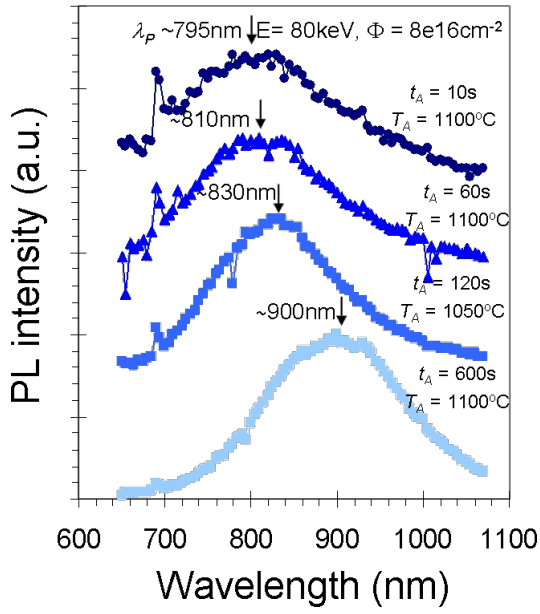

Figure 1: Evolution of the Si NC photoluminescence spectra (offseted for clarity) with high temperature annealing (t_A = time, T_A = temperature) for a thin (500 nm) oxide (on sapphire) implanted with Si^+ at E = 80 keV to a dose of 8 × 10^{16} cm^{-2}) [34].

Interaction of Si NCs with Er ions has attracted a special attention due to the possibility of producing optoelectronic devices operating in the telecommunications band around 1.5 μm. Recent studies have shown that doping with phosphorus can result in either a quenching or an enhancement of the Si NCs PL, depending on the dopant concentration and NC sizes [28,35]. Crowe et al. [35] have shown that as phosphorus accumulates at the nanocrystal oxide interface it leads to the passivation of the dangling bonds as observed by the luminescence enhancement. This is only valid for small NCs, while the enhancement diminishes as the density of larger NCs increases.

As already mentioned, one of the main applications of the embedded NCs is in memory devices. To check the charge trap-

ping properties of the embedded NCs, different electrical characterization techniques could be applied. The most common is the capacitance-voltage (C–V) technique that gives information about the memory window. Moreover, C–V gives valuable information as far as interface-defects and oxide defects are concerned. There are numerous studies on the charge-trapping properties of embedded NCs. However, it should be noted that in a significant number of those, the effects of defects (either interface-related or in the oxide) have been completely neglected, and the observed memory window (the flat band voltage shift ΔV_{FB}) has been unconditionally ascribed to the NCs trapping properties. As some studies indicate [1,26] these issues should be seriously considered.

To obtain even more information about defects in embedded NCs and at their interfaces, a capacitance transient measurement (through deep-level transient spectroscopy, DLTS) could be applied. DLTS has been mostly used for studying defects in semiconductors [36]. It has been successfully applied in studying the Si–SiO_2 interface related defects [37] and in studying NCs [25,38]. In the case of NCs, the DLTS can detect only charge carriers thermally emitted from the NCs. Figure 2 shows a typical DLTS spectrum of the simple MOS structure, with Ge NCs embedded in the SiO_2 film deposited on a Si substrate. In order to check for the existence of the deep level traps coming from the Si/SiO_2 interface, temperature dependent C–V measurements have been performed. The activation energy of the electron emission has been determined from the Arrhenius plot (given in the inset). The observed deep level trap at 0.22 eV resembles those already reported [25,38] and it has been already ascribed to charge trapping centers associated with Ge NCs.

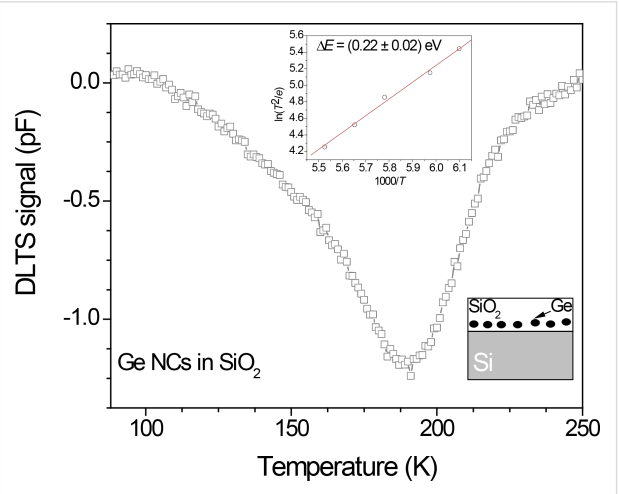

Figure 2: DLTS spectrum of a MOS structure with Ge NCs embedded in the oxide, with Arrhenius plot in the inset. By careful adjustments of the measurement settings, the thermal emission of electrons from the NCs is detected by DLTS (for more explanations on DLTS analysis see [24,36-38]).

Another open and still unresolved problem is the electrical transport across doped NC films. Here, significant progress has been made in free-standing Si NC films [22], but much more effort is needed, for instance by using different electrical characterization techniques, to understand the electrical properties of doped and embedded NCs.

III Electronic structure models

Effective mass models and the more elaborate k·p perturbation theory have been used to give insight into the quantum confinement [39], dispersion, as well as on the dependence of the electronic levels of nanocrystals and quantum dots on strain and electric fields [40]. Such results are general and have been helpful to understand the trends found by experimental and atomistic modeling studies. More recently, significant understanding of the relationships between structure, chemistry and electronic structure has been obtained from first-principles calculations based on density functional theory. From a theoretical perspective, group-IV nanocrystals are usually divided into free-standing and embedded. The first class of models mimics the NCs grown, for example, by using plasma methods; the second class comprises nanocrystals embedded in another material, as for example Si nanodots in SiO_2, or in a different phase of the same material, for example crystalline Si nanodots in amorphous Si.

Free-standing nanocrystals in vacuum can be modeled by using real-space boundary conditions, i.e., requiring the wavefunction to vanish far from the nanocrystal. An alternative approach is to impose periodic boundary conditions ("particle in a box"). This has the advantage of allowing for expansion of the charge density in plane-waves and the use of numerical approaches developed for crystalline solids. However, care has to be taken to ensure that there is little interaction between periodic images of the system. This is particularly relevant when treating systems with an electric charge or dipole [41]. Embedded nanocrystals are best modeled by using periodic boundary conditions. In that case, one of the main difficulties consists of reproducing the correct structure of the interface and the respective oxidation numbers [42]. The gap between such ideal models, which provide insight into quantum effects, and real scale systems is difficult to bridge, but there have been some attempts at building multi-scale modeling frameworks [43]. Still, there is ample room for development in the modeling of growth, interaction with solvents, and other multi-scale phenomena. In this review, however, we will concentrate on quantum-chemical modeling at the nanoscale.

III.1 The Hamiltonian and the many-body problem

The greatest challenge associated with modeling NCs is the huge number of atoms required for the model to meet the sizes

of even the smallest particles that were realized experimentally (about 1000 atoms for ca. 3 nm). Such sizes are close to the practical limits of present-day first-principles density functional theory implementations. Various full-DFT implementations by using localized basis sets such as Aimpro [17,44], Conquest [45], Onetep [46], OpenMX [47] and Siesta [48] exhibit order-N scaling [49] and are advertised as enabling calculations with up to $N \approx 10^4$ atoms. Larger systems have been treated by using tight binding or semi-empirical methods [50].

Further, localized basis sets, such as Gaussian-type orbitals, are convenient in the case of free-standing nanocrystals, both because they can be combined with real-space boundary conditions and because they result in sparse Hamiltonian and overlap matrices that can be efficiently diagonalized. Notwithstanding, many implementations of density functional theory traditionally used in solid state physics rely on the use of plane-wave basis sets for expansion of wavefunctions and charge density. A disadvantage of this approach is that to make the basis size finite it is then necessary to impose periodic boundary conditions, allowing for sufficiently large vacuum spaces in between a nanoparticle and its image. The large supercell size reflects then into a great number of plane waves, which is independent on the ratio between the volumes of matter and vacuum.

III.2 Theoretical prediction of observables

III.2.1 Optical response: The indirect band-gap nature of bulk Si has been one of the main drawbacks of this material. It has placed Si away from many optical applications such as lasers and LEDs, in favor of the more expensive and less environmental friendly III–V semiconductors. While radiative recombination on compound semiconductors is an efficient process, in Si such transitions are rather unlikely to take place as the large k-space mismatch between conduction band minimum and valence band maximum states implies the involvement of phonons. On the other hand, the dispersionless and tunable nature of the electronic structure of Si NCs holds many promises in all-Si optoelectronics. In this respect, theoretical modeling has provided many insights. Besides the size and shape effect to the energy and rate of optical transitions, the chemical nature of the surface, shell or host where the NC is embedded play a critical role [51]. For instance, Guerra and Ossicini [52] showed that while radiative recombination of H-saturated Si NC is strongly dependent on the size of the crystallites, in hydroxy-terminated or SiO_2-embedded NCs the optical yield is mostly determined by the fraction of oxygen termination.

First-principles modeling has also been insightful in the study of local polarizations that take place at Si NC/SiO_2 interfaces [53]. The abrupt change of chemical species (with different electronegativities) at the edge of the NCs induces charge displacements that can be accounted for by using pseudopotentials. It has been found that polarizations due to the oxide interface have two important effects, namely (i) to quench the low energy absorption region and (ii) a blue-shift of some particularly intense transitions.

Another important aspect is the role of defects. Si dangling bonds or radicals are strongly localized being effective traps for both electrons and holes [21]. They are therefore likely to degrade the optical yield. On the other hand, shallower states like those produced at the Si/SiO_2 core–shell interface of oxidized Si NCs are most likely to shift the absorption/emission spectra with respect to pristine NCs [54].

Inclusion of many-body effects is important especially for small nanoparticles in which the exciton binding energy can be large [55]. These can be calculated by using the Bethe–Salpeter equation [7]. However, for nanocrystals with a radius larger than 0.6 nm, the self-energy and the Coulomb corrections almost exactly cancel each other, and one-particle calculations actually give accurate values for the excitonic gap(s).

III.2.2 Doping of Si nanocrystals: The deliberate introduction of dopants into materials lies at the heart of microelectronics. A prototypical example is the replacement of a few lattice sites in a billion in crystalline Si, for instance by phosphorous or boron, to confer good electrical conductivity to an otherwise poor insulator. In the same way, doping NCs will play an analogous role in future artificial solids or meta-materials made of wave-function engineered particles.

Although many promising applications of Si NCs rely on the possibility to tune their electronic states by exploring surface effects, the fact is that this is only possible in ultra-small NCs in which effective electrical doping, which leads to a spontaneous ionization of dopants at room-temperature, is yet to be demonstrated. Notwithstanding, the introduction of dopants in Si NCs has been unequivocally demonstrated, for instance by monitoring the ^{31}P hyperfine splitting of the phosphorous donor state during electron paramagnetic resonance experiments [56], or from photoluminescent transitions of bound excitons to boron [57].

In small NCs, in which surface conditions affect the electronic states, theory predicts that phosphorous and boron levels are rather deep with carrier binding energies of the order of 1 eV, anticipating serious difficulties in finding suitable dopants to operate at room temperature [21,58-60].

In this respect other routes for doping have been under investigation. Namely, transfer doping by means of molecules with high electron affinity or low ionization potential stands as a rather promising alternative. For instance, Carvalho et al. [20] suggested that the F_4-TCNQ (7,7,8,8-tetracyano-2,3,5,6-tetrafluoroquinodimethane) molecule, which is commonly used as a p-dopant in organic electronics, could be a candidate to produce holes in the Si NCs, as shown in Figure 3. They also showed that about three to four molecules adsorbed to the NC surface are able to produce a positively charged NC, although the first excitation of the doped system was almost 1 eV, again indicating that free-holes are unlikely to be produced at room temperature. These results were confirmed recently by means of electrical measurements combined with first-principles calculations [22], demonstrating that F_4-TCNQ within a Si NC solid film is not a shallow acceptor, but rather a deep acceptor with levels that can edge the conduction band minimum of the Si NC film. In fact, this dopant was used to increase the conductivity of the films by more than two orders of magnitude, although the majority carriers were electrons.

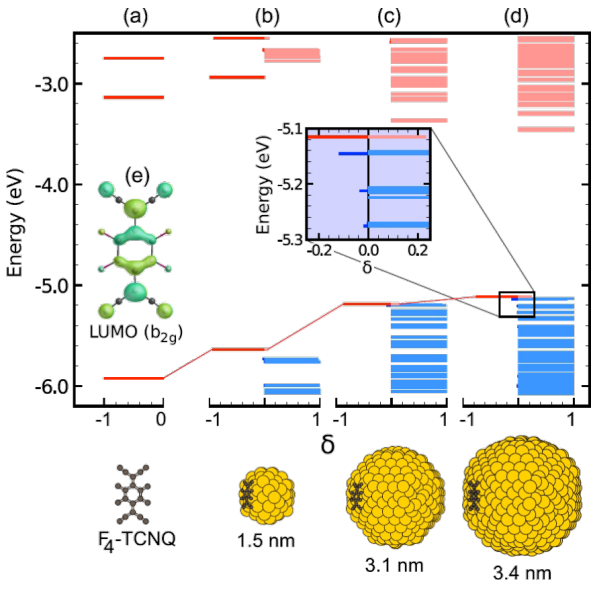

Figure 3: Hybridization between F_4-TCNQ and Si NC one-electron states. (a) Isosurface plot of the F_4-TCNQ lowest unoccupied state (b_{2g} symmetry), and (b–e) Kohn–Sham eigenvalue energy diagrams. The energy-level diagrams are for (a) isolated F_4-TCNQ and (b–e) for F_4-TCNQ adsorbed on Si NCs of increasing size. Each state is represented by a bar of unitary length, with the abscissa of the left- and right-hand ends of the bar indicating, respectively, the relative localization on the molecule (negative values) and on the NC (positive values). Reprinted with permission from [20]. Copyright 2011 The American Physical Society.

III.2.3 Surface properties: The NC surface is one of the most important variables in the engineering of its shape, intrinsic properties and stability in air and interaction with solvents and other substances. For nanoparticles with a clean surface or with a hydrogen-covered surface, the orientation dependence of the surface energy, as well as edge- and corner-energies (for less than 10^4 atoms) determine the shape of the NCs grown under near-equilibrium quasi-static conditions. It has been found that diamond NCs are most stable in a truncated octahedral structure, but Si and Ge NCs are stable in a nearly-spherical geometry [61]. In any case, free standing Si and Ge NCs are usually grown in conditions very far from equilibrium, justifying the use of spherical models [62]. Diamond nanocrystals, however, have been grown in different shapes and configurations, and their optical properties have been found to be in discrepancy with theoretical models, presumably due to the contribution of defects [63].

As nanocrystals have a very large surface-to-volume ratio, their electronic and optical properties are largely determined by the surface or interface morphology. Amongst group-IV NCs, Si NCs are especially reactive in air, immediately forming an oxide cap. Surface oxidation also decreases the gap energy of the NC, shifting its absorption and photoluminescence edges to the red [64,65]. Models of Si NCs embedded in SiO_2 also show an optical redshift following oxidation, and suggest that this effect is associated not only with the decreased quantum confinement, but also with the presence of silanone-like Si=O bonds [66]. As a consequence of the change in the electronic structure and dielectric screening, the ionization energy of dopants is also altered. The earliest oxidation stage corresponding to the formation of silanol surface groups was found to increase the electron binding energy of P, As and Sb, and to decrease the hole binding energy of B, Al, Ga and In [67].

Chlorine-covered Si NCs were found to have higher electron affinity, higher ionization energy and a lower optical absorption energy threshold than hydrogen-covered nanocrystals with the same size. Like the hydrogenated Si NCs, chlorinated Si NCs doped with phosphorus or boron require a high activation energy to transfer an electron or hole, respectively, to undoped Si NCs. The electronic levels of surface dangling bonds are similar for both types of surface passivation, although in the chlorinated Si NCs some fall off the narrower gap. Functionalisation with chlorine, nitrogen and fluorine was also found to be an effective way to control the bandgap of nanodiamonds [68].

Nanocrystals functionalized with organic groups have so far only been considered in a limited number of theoretical studies, for silicon [49,69-71] and diamond [72]. Functionalization with alkyl and aryl molecules is an important preparatory step for the conjugation of the surface to larger organic molecules. Regarding the direct influence on the physical properties, alkyl passivation was found to slightly change the optical gaps of

silicon QDs, but to substantially decrease their ionization potentials and electron affinities and to affect their excited state properties. Nevertheless, there is still ample space for the modeling of the interaction of functionalized nanocrystals with solvents, polymers and biological molecules. A tight-binding parameterization has been proposed for this family of systems, offering a cheaper approach that may become a basis for a function-oriented treatment of organic-inorganic interfaces [48].

Conclusion

Although group-IV NCs may emerge as a natural way to extend, enhance and control the properties of their respective bulk materials, the last two decades of research have shown that not only the device architecture, but also the growth, characterization and modeling techniques have to be redesigned to meet their very specific requirements.

Silicon and germanium NCs have revealed to be promising on the areas of optical luminescence, in which size-dependent luminescence and absorption of Si NCs is consistently reported. Memory devices are another promising area of application. So far, the greatest challenges continue to be the control of surface, interface and other deep levels, misfit strain, and doping efficiency.

From a theoretical point of view, even though one of the most important attributes of nanoparticles – their size-dependent optical gap – is a quantity hard to predict, modeling studies have been able to provide great insight into the fundamental optical and electronic properties of different types of NCs. An open issue still resides on the difficult task of bridging the length scales from the largest sizes achievable numerically to the smallest sizes produced experimentally.

Acknowledgements

The authors acknowledge financial support from the COST MP0901-NanoTP Action. JC thanks the FCT through Project No. PEst-C/CTM/LA0025/2013.

References

1. El Hdiy, A.; Gacem, K.; Troyon, M.; Ronda, A.; Bassani, F.; Berbezier, I. *J. Appl. Phys.* **2008,** *104,* 063716. doi:10.1063/1.2985909
2. Nozik, A. J. *Physica E* **2002,** *14,* 115–120. doi:10.1016/S1386-9477(02)00374-0
3. Gur, I.; Fromer, N. A.; Geier, M. L.; Alivisatos, A. P. *Science* **2005,** *310,* 462–465. doi:10.1126/science.1117908
4. Ray, S. K.; Maikap, S.; Banarjee, W.; Das, S. *J. Phys. D: Appl. Phys.* **2013,** *46,* 153001. doi:10.1088/0022-3727/46/15/153001
5. Wang, L.-W.; Zunger, A. *J. Phys. Chem.* **1994,** *98,* 2158–2165. doi:10.1021/j100059a032
6. Öğüt, S.; Chelikowsky, J. R.; Louie, S. G. *Phys. Rev. Lett.* **1997,** *79,* 1770–1773. doi:10.1103/PhysRevLett.79.1770
7. Delerue, C.; Lannoo, M.; Allan, G. *Phys. Rev. Lett.* **2000,** *84,* 2457. doi:10.1103/PhysRevLett.84.2457
8. Furukawa, S.; Miyasato, T. *Phys. Rev. B* **1988,** *38,* 5726–5729. doi:10.1103/PhysRevB.38.5726
9. Timmerman, D.; Gergorkiewicz, T. *Nanoscale Res. Lett.* **2012,** *7,* 389. doi:10.1186/1556-276X-7-389
10. Belyakov, V.; Burdov, V. A.; Lockwood, R.; Meldrum, A. *Adv. Opt. Technol.* **2008,** 279502.
11. Franceschetti, A.; Zunger, A. *Phys. Rev. B* **2000,** *62,* 2614–2623. doi:10.1103/PhysRevB.62.2614
12. Wang, L.-W.; Zunger, A. *Phys. Rev. Lett.* **1994,** *73,* 1039–1042. doi:10.1103/PhysRevLett.73.1039
13. Giustino, F.; Pasquarello, A. *Phys. Rev. B* **2005,** *71,* 144104. doi:10.1103/PhysRevB.71.144104
14. Delerue, C.; Lannoo, M.; Allan, G. *Phys. Rev. B* **2003,** *68,* 115411. doi:10.1103/PhysRevB.68.115411
15. Öğüt, S.; Burdick, R.; Saad, Y.; Chelikowsky, J. R. *Phys. Rev. Lett.* **2003,** *90,* 127401. doi:10.1103/PhysRevLett.90.127401
16. Trani, F.; Ninno, D.; Cantele, G.; Iadonisi, G.; Hameeuw, K.; Degoli, E.; Ossicini, S. *Phys. Rev. B* **2006,** *73,* 245430. doi:10.1103/PhysRevB.73.245430
17. Rayson, M. J.; Briddon, P. R. *Phys. Rev. B* **2009,** *80,* 205104. doi:10.1103/PhysRevB.80.205104
18. Ramos, L. E.; Degoli, E.; Cantele, G.; Ossicini, S.; Ninno, D.; Furthmüller, J.; Bechstedt, F. *Phys. Rev. B* **2008,** *78,* 235310. doi:10.1103/PhysRevB.78.235310
19. Chan, T.-L.; Tiago, M. L.; Kaxiras, E.; Chelikowsky, J. R. *Nano Lett.* **2008,** *8,* 596–600. doi:10.1021/nl072997a
20. Carvalho, A.; Coutinho, J.; Barroso, M.; Silva, E. L.; Öberg, S.; Rayson, M.; Briddon, P. R. *Phys. Rev. B* **2011,** *84,* 125437. doi:10.1103/PhysRevB.84.125437
21. Carvalho, A.; Öberg, S.; Rayson, M. J.; Briddon, P. R. *Phys. Rev. B* **2012,** *86,* 045308. doi:10.1103/PhysRevB.86.045308
22. Pereira, R. N.; Coutinho, J.; Niesar, S.; Oliveira, T. A.; Aigner, W.; Wiggers, H.; Rayson, M. J.; Briddon, P. R.; Brandt, M. S.; Stutzmann, M. *Nano Lett.* **2014,** *14,* 3817–3826. doi:10.1021/nl500932q
23. Barbagiovanni, E. G.; Lockwood, D. J.; Simpson, P. J.; Goncharova, V. *Appl. Phys. Rev.* **2014,** *1,* 011302. doi:10.1063/1.4835095
24. Schroder, D. K. *Semiconductor Material and Device Characterization;* Wiley: New Jersey, 2006.
25. Antonova, I. V.; Popov, V. I.; Smagulova, S. A.; Jedrzejewski, J.; Balberg, I. *J. Appl. Phys.* **2013,** *113,* 084308. doi:10.1063/1.4793586
26. Martin-Sánchez, J.; Capan, I.; Chahboun, A.; Pinto, S. R. C.; Vieira, E. M. F.; Rolo, A. G.; Gomes, M. J. M. *Appl. Surf. Sci.* **2013,** *280,* 632–640. doi:10.1016/j.apsusc.2013.04.170
27. Shah, M.; Wojdak, M.; Kenyon, A. J.; Halsall, M. P.; Li, H.; Crowe, I. F. *J. Lumin.* **2012,** *132,* 3103–3112. doi:10.1016/j.jlumin.2012.02.002
28. Murakami, K.; Shirakawa, R.; Tsujimura, M.; Uchida, N.; Fukata, N.; Hishita, S. *J. Appl. Phys.* **2009,** *105,* 054307. doi:10.1063/1.3088871
29. Mimura, A.; Fujii, M.; Hayashi, S.; Kovalev, D.; Koch, F. *Phys. Rev. B* **2000,** *62,* 12625. doi:10.1103/PhysRevB.62.12625
30. Chen, Q.; Lu, T.; Xu, M.; Meng, C.; Hu, Y.; Sun, K.; Shlimak, I. *Appl. Phys. Lett.* **2011,** *98,* 073103. doi:10.1063/1.3553770
31. Zacharias, M.; Heitmann, J.; Scholz, R.; Kahler, U.; Schmidt, M.; Bläsing, J. *Appl. Phys. Lett.* **2002,** *80,* 661–663. doi:10.1063/1.1433906
32. Kovačević, I.; Pivac, B.; Dubček, P.; Zorc, H.; Radić, N.; Bernstorff, S.; Campione, M.; Sassella, A. *Appl. Surf. Sci.* **2007,** *253,* 3034–3040. doi:10.1016/j.apsusc.2006.06.048

33. Bernstorff, S.; Dubček, P.; Kovačević, I.; Radić, N.; Pivac, B. *Thin Solid Films* **2007,** *515,* 5637–5640. doi:10.1016/j.tsf.2006.12.015
34. Iain Crowe (unpublished results).
35. Crowe, I. F.; Papachristodoulou, N.; Halsall, M. P.; Hylton, N. P.; Hulko, O.; Knights, A. P.; Yang, P.; Gwilliam, R. M.; Shah, M.; Kenyon, A. J. *J. Appl. Phys.* **2013,** *113,* 024304. doi:10.1063/1.4772947
36. Dobaczewski, L.; Peaker, A. R.; Bonde Nielsen, K. *J. Appl. Phys.* **2004,** *96,* 4689–4728. doi:10.1063/1.1794897
37. Capan, I.; Janicki, V.; Jacimovic, R.; Pivac, B. *Nucl. Instrum. Methods Phys. Res., Sect. B* **2012,** *282,* 59–62. doi:10.1016/j.nimb.2011.08.065
38. Buljan, M.; Grenzer, J.; Holý, V.; Radić, N.; Mišić-Radić, T.; Levichev, S.; Bernstorff, S.; Pivac, B.; Capan, I. *Appl. Phys. Lett.* **2010,** *97,* 163117. doi:10.1063/1.3504249
39. Bimberg, D.; Grundmann, M.; Ledentsov, N. N. *Quantum Dot Heterostructures;* John Willey and Sons: Chichester, 1999.
40. Chang, K.; Xia, J.-B. *J. Appl. Phys.* **1998,** *84,* 1454. doi:10.1063/1.368207
41. Makov, G.; Payne, M. C. *Phys. Rev. B* **1995,** *51,* 4014. doi:10.1103/PhysRevB.51.4014
42. Pasquarello, P.; Hybertsen, M. S.; Car, R. *Nature* **1998,** *396,* 58–60. doi:10.1038/23908
43. Zahi, I.; Mur, P.; Blaise, P.; Estève, A.; Djafari Rouhani, M.; Vergnes, H.; Caussat, B. *Thin Solid Films* **2011,** *519,* 7650–7658. doi:10.1016/j.tsf.2011.05.016
44. Rayson, M. J. *Comput. Phys. Commun.* **2010,** *181,* 1051–1056. doi:10.1016/j.cpc.2010.02.012
45. Bowler, D. R.; Miyazaki, T.; Gillan, M. J. *J. Phys.: Condens. Matter* **2002,** *14,* 2781. doi:10.1088/0953-8984/14/11/303
46. Skylaris, S.-K.; Haynes, P. D.; Mostofi, A.; Payne, M. C. *J. Chem. Phys.* **2005,** *122,* 084119. doi:10.1063/1.1839852
47. OpenMX code, available at: http://www.openmx-square.org
48. Soler, J. M.; Artacho, E.; Gale, J. D.; Garcia, A.; Junquera, J.; Ordejon, P.; Sánchez-Portal, D. *J. Phys.: Condens. Matter* **2002,** *14,* 2745–2779. doi:10.1088/0953-8984/14/11/302
49. Kohn, W. *Phys. Rev. Lett.* **1996,** *76,* 3168–3171. doi:10.1103/PhysRevLett.76.3168
50. Trani, F.; Baroni, V. *J. Chem. Theory Comput.* **2011,** *7,* 713–719. doi:10.1021/ct1006086
51. Puzder, A.; Williamson, A. J.; Grossman, J. C.; Galli, G. *J. Chem. Phys.* **2002,** *117,* 6721–6729. doi:10.1063/1.1504707
52. Guerra, R.; Ossicini, S. *Phys. Rev. B* **2010,** *81,* 245307. doi:10.1103/PhysRevB.81.245307
53. Guerra, R.; Marsili, M.; Pulci, O.; Ossicini, S. *Phys. Rev. B* **2011,** *84,* 075342. doi:10.1103/PhysRevB.84.075342
54. Koponen, L.; Tunturivuori, L. O.; Puska, M. J.; Nieminen, R. M. *Phys. Rev. B* **2009,** *79,* 235332. doi:10.1103/PhysRevB.79.235332
55. Rajadell, F.; Climente, J. I.; Planelles, J.; Bertoni, A. *J. Phys. Chem. C* **2009,** *113,* 11268–11272. doi:10.1021/jp902652z
56. Stegner, A. R.; Pereira, R. N.; Klein, K.; Lechner, R.; Dietmueller, R.; Brandt, M. S.; Stutzmann, M.; Wiggers, H. *Phys. Rev. Lett.* **2008,** *100,* 026803. doi:10.1103/PhysRevLett.100.026803
57. Fujii, M.; Hayashi, S.; Yamamoto, K. *J. Appl. Phys.* **1998,** *83,* 7953–7957. doi:10.1063/1.367976
58. Melnikov, D. V.; Chelikowsky, J. R. *Phys. Rev. Lett.* **2004,** *92,* 046802. doi:10.1103/PhysRevLett.92.046802
59. Cantele, G.; Degoli, E.; Luppi, E.; Magri, R.; Ninno, D.; Iadonisi, G.; Ossicini, S. *Phys. Rev. B* **2005,** *72,* 113303. doi:10.1103/PhysRevB.72.113303
60. Ni, Z.; Pi, X.; Yang, D. *Phys. Rev. B* **2014,** *89,* 035312. doi:10.1103/PhysRevB.89.035312
61. Barnard, A. S.; Zapol, P. *J. Chem. Phys.* **2004,** *121,* 4276. doi:10.1063/1.1775770
62. Mangolini, L.; Kortshagen, U. In *Silicon Nanocrystals; Fundamentals, Synthesis, and Applications;* Pavesi, L.; Turan, R., Eds.; Wiley-VCH: Weinheim, 2010.
63. Landt, L.; Klünder, K.; Dahl, J. E.; Carlson, R. M. K.; Möller, T.; Bostedt, C. *Phys. Rev. Lett.* **2009,** *103,* 047402. doi:10.1103/PhysRevLett.103.047402
64. Vasiliev, I.; Chelikowsky, J. R.; Martin, R. M. *Phys. Rev. B* **2002,** *65,* 121302. doi:10.1103/PhysRevB.65.121302
65. Zhou, Z.; Friesner, R. A.; Brus, L. *J. Am. Chem. Soc.* **2003,** *125,* 15599–15607. doi:10.1021/ja036443v
66. Luppi, M.; Ossicini, S. *Phys. Rev. B* **2005,** *71,* 035340. doi:10.1103/PhysRevB.71.035340
67. Carvalho, A.; Rayson, M. J.; Briddon, P. R. *J. Phys. Chem. C* **2012,** *116,* 8243–8250. doi:10.1021/jp300712v
68. Brown, N.; Hod, O. Controlling the Electronic Properties of Nanodiamonds Via Surface Chemical Functionalization: A DFT Study 2013, arXiv:1309.3906v1 [cond-mat.mtrl-sci].
69. Reboredo, F. A.; Schwegler, E.; Galli, G. *J. Am. Chem. Soc.* **2003,** *125,* 15243–15249. doi:10.1021/ja035254+
70. Reboredo, F. A.; Galli, G. *J. Phys. Chem. B* **2005,** *109,* 1072–1078. doi:10.1021/jp0462254
71. Zhou, Z.; Brus, L.; Friesner, R. *Nano Lett.* **2003,** *3,* 163–167. doi:10.1021/nl025890q
72. Zhong, Y. L.; Loh, K. P.; Midya, A.; Chen, Z.-K. *Chem. Mater.* **2008,** *20,* 3137–3144. doi:10.1021/cm703686w

License and Terms

This is an Open Access article under the terms of the Creative Commons Attribution License (http://creativecommons.org/licenses/by/2.0), which permits unrestricted use, distribution, and reproduction in any medium, provided the original work is properly cited.

The license is subject to the *Beilstein Journal of Nanotechnology* terms and conditions: (http://www.beilstein-journals.org/bjnano)

The definitive version of this article is the electronic one which can be found at: doi:10.3762/bjnano.5.189

BEILSTEIN JOURNAL OF NANOTECHNOLOGY

Electronic and electrochemical doping of graphene by surface adsorbates

Hugo Pinto*[1] and Alexander Markevich[2]

Review

Open Access

Address:
[1]COMP/Department of Applied Physics, Aalto University School of Sciences, FI-00076 Aalto, Finland and [2]School of Chemistry, University of Nottingham, NG7 2RD Nottingham, UK

Email:
Hugo Pinto* - hugo.pinto@aalto.fi

* Corresponding author

Keywords:
adsorbates; doping; electrochemical; electronic; graphene

Beilstein J. Nanotechnol. **2014,** *5,* 1842–1848.
doi:10.3762/bjnano.5.195

Received: 19 June 2014
Accepted: 26 September 2014
Published: 23 October 2014

This article is part of the Thematic Series "Atomic scale interface design and characterisation: Theory – Electronic properties".

Guest Editor: A. Krasheninnikov

© 2014 Pinto and Markevich; licensee Beilstein-Institut.
License and terms: see end of document.

Abstract

Many potential applications of graphene require its precise and controllable doping with charge carriers. Being a two-dimensional material graphene is extremely sensitive to surface adsorbates, so its electronic properties can be effectively modified by deposition of different atoms and molecules. In this paper, we review two mechanisms of graphene doping by surface adsorbates, namely electronic and electrochemical doping. Although, electronic doping has been extensively studied and discussed in the literature, much less attention has been paid to electrochemical doping. This mechanism can, however, explain the doping of graphene by adsorbates for which no charge transfer is expected within the electronic doping model. In addition, electrochemical doping is in the origin of the hysteresis effects often observed in graphene-based field effect transistors when operating in the atmospheric environment.

Introduction

Graphene is a monolayer of carbon atoms arranged in a honeycomb lattice [1]. With the discovery of graphene a new era of two-dimensional materials for science and technology has started. Due to its remarkable transport, optical and mechanical properties graphene has a great potential for being used in a wide range of applications [2,3]. For instance, high mobility of charge carriers [4] in graphene combined with its high optical transparency [5] and mechanical strength [6] makes graphene a promising material for ultrafast and flexible electronics [7-10]. Graphene is a zero gap semiconductor with its valence and conduction bands touching each other at the corners of the Brillouin zone in the so called Dirac points [11,12]. This implies that, neglecting the effect of thermal excitations, the intrinsic charge carrier concentration in graphene is, in principle, zero. However, for the development of graphene-based electronic devices the presence of charge carriers and the control of their type and concentration are required. Therefore, a lot of research has been devoted to find ways for controllable

doping of graphene with electrons and holes. It has been shown that the deposition of different adsorbates, either atoms or molecules, on the graphene surface can result in both n- and p-type doping.

In this paper, we present an overview of two mechanisms of graphene doping by surface adsorbates, namely, electronic and electrochemical doping and consider appropriate atomic and molecular dopants.

Review

Mechanisms of doping

Charge carriers, either electrons or holes, can be induced in graphene by the application of an electric field or by chemical doping. The electric field effect doping is usually performed in graphene-based field effect transistors (FET), in which charge carriers are induced by changing the electric potential between graphene and a gate, which can be, for example, a Si^+/SiO_2 substrate [1,13]. By varying the gate voltage, V_g, the type of carriers and their concentration in graphene can be tuned. The sign of the induced carriers is opposite to the sign of the applied gate voltage. A positive V_g induces electrons while a negative V_g induces holes. It was shown that for graphene on Si^+/SiO_2 the concentration of charge carriers induced by this method can be as high as 10^{13} cm^{-2} [1].

Chemical doping involves interactions of graphene with other chemical species [14]. There are two types of chemical doping, surface transfer and substitutional doping. In the latter case doping occurs when some of carbon atoms in the graphene lattice are substituted by other atoms with a different number of valence electrons. This type of doping has been observed for boron, B_s, and nitrogen, N_s, substitutional atoms and leads to p- and n-type conductivity, respectively [15,16]. However, the incorporation of foreign atoms into the graphene lattice can result in a significant modification of the electronic structure of graphene. For instance, N_s-doped graphene behaves like an n-type doped semiconductor but exhibits a low charge carrier mobility [16].

The surface transfer doping is non-destructive and occurs due to the charge transfer between graphene and surface adsorbates. Two mechanisms of charge transfer doping can be distinguished, electronic and electrochemical doping. The electronic doping is a consequence of the direct charge transfer between graphene and an adsorbate. This requires a difference in electronic chemical potentials at an interface, which is determined by the relative positions of the graphene Fermi level and the highest occupied (HOMO) and lowest unoccupied (LUMO) molecular orbitals of an adsorbate. If the LUMO of the adsorbate lies lower in energy than the Fermi level of graphene, Figure 1a, electrons will flow from graphene to the adsorbate making graphene p-type-doped. Adsorbates with the HOMO lying above the graphene Fermi level, Figure 1b, act as donors and dope graphene n-type. Although surface transfer doping is an effective method to control the concentration of charge carriers in graphene the ionized dopants can act as an additional source of scattering for charge carriers and reduce their mobility.

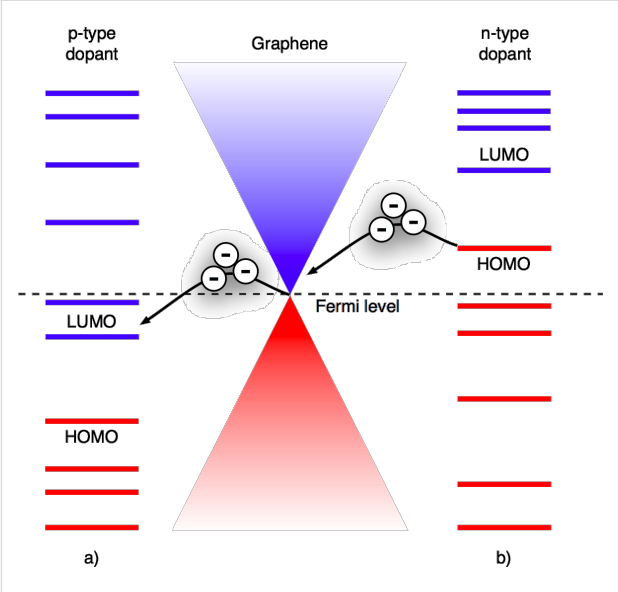

Figure 1: Scheme of the relative position of the highest occupied (HOMO) and lowest unoccupied (LUMO) molecular orbitals of an adsorbate to the Fermi level of graphene for a) p-type and b) n-type dopant.

The electrochemical doping of graphene occurs when certain surface adsorbates participate in electrochemical redox reactions in which graphene plays the role of an electrode. Such reactions occur spontaneously if the total Gibbs free energy is negative and the diffusion and reaction barriers are sufficiently low for the reaction proceed at room temperature. The total Gibbs free energy change is given by $\Delta G + W$ for p-doping and $\Delta G - W$ for n-doping, where ΔG is the free energy for the molecular reaction and W is the work function of graphene. The work function of graphene is expected to be similar to that of graphite, about 4.5 eV [17,18]. Although ΔG can be estimated from the Nernst equation the barrier heights are unknown and it must be assumed that they are sufficiently low for the reaction to occur [19].

Whether a reaction will result in p- or n-type doping of graphene depends on the relative position of the electrochemical redox potential E_{redox} to the graphene Fermi level. The E_{redox} is the equivalent of the Fermi level of an electrolyte solution. It measures the energy required to add or remove an elec-

tron in redox couples and is usually referenced to the standard hydrogen electrode (SHE) [20]. Thus, ΔG and E_{redox} measure the same property and are related by $\Delta G = -n \cdot F \cdot E_{redox}$, where n and F are the number of electrons and the Faraday constant, respectively. Furthermore, while the E_{redox} level lies higher (lower) than the Fermi level of graphene (E_F), electrons (holes) induced by a reaction will flow to graphene until equilibrium is reached, $E_{redox} = E_F$, making graphene n- (p-)type doped.

In contrast to electronic doping, which occurs instantaneously, electrochemical doping is a time-dependent process, which is affected by the rate of the reaction and diffusion rates of participating species. Therefore, in the case the reaction or diffusion rates are slower than the rate of change of gate voltage electrochemical doping can lead to hysteresis effects which are often observed in graphene-based FET devices [21-24].

Electronic dopants

The ability to dope graphene either n- or p-type has been demonstrated for various atomic and molecular adsorbates. Electropositive elements that easily donate their outer shell electrons are expected to be n-type dopants. Indeed, density functional theory (DFT) calculations predicted group I–III metals to be efficient electron donors for graphene [25-28]. Electron doping of graphene was observed experimentally for potassium (K) atoms (group I metal) deposited on graphene [29]. Figure 2 shows plots of the conductivity of graphene versus the gate voltage for different exposures to K. The shift of the neutrality point towards negative V_g with the increase of the potassium concentration is a clear indication of n-type doping.

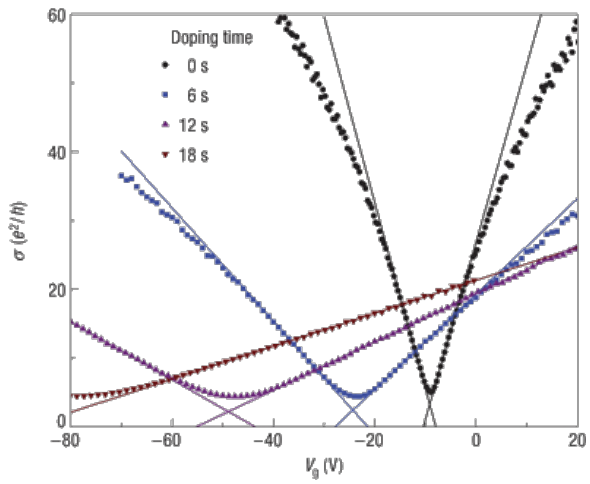

Figure 2: Conductivity as a function of the gate voltage ($\sigma(V_g)$) of graphene at different exposures to K. The shift of neutrality point to negative gate voltages indicates an increase of n-type doping with increasing exposure to K atoms. The change in the slope of the curves suggest a reduction of the mobility of the charge carriers. Reprinted with permission from [29]. Copyright 2008 Nature Publishing Group.

It was also observed that the mobility of the charge carriers decreases with the increase of the doping concentration. This is attributed to the additional scattering caused by the ionized potassium atoms. In agreement with the experimental results, DFT calculations have shown that K atoms act as electron donors [25-28]. Electronic band structure calculations show that adsorption of a K atom on graphene results in the shift of the Fermi level above the Dirac point, indicating the n-type doping of graphene, Figure 3a. Furthermore, it has been shown that the

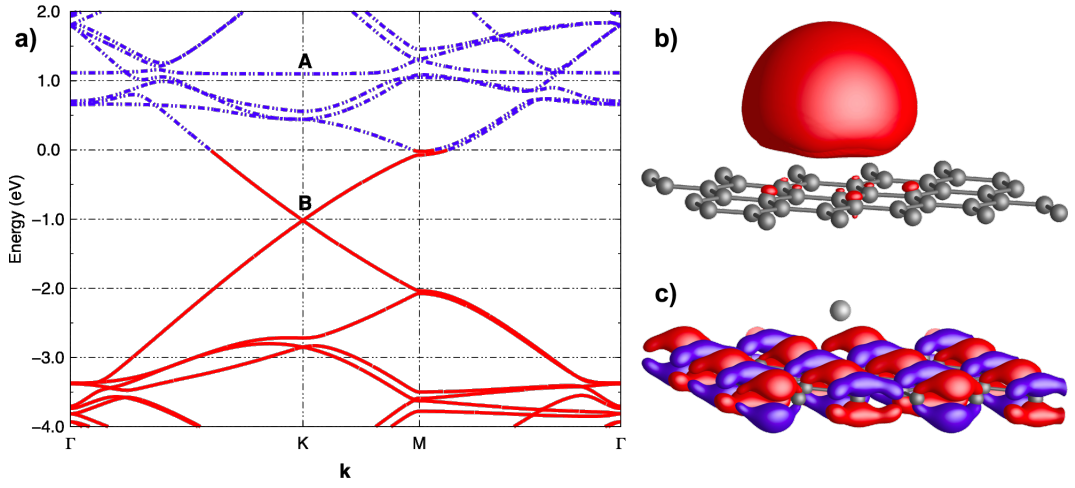

Figure 3: a) Electronic band structure (eV) of a K atom on top of a graphene layer in the vicinity of the Fermi energy. The Fermi level is set to zero. Full lines denote occupied states while dashed lines show empty levels. The bands around **B**, unoccupied for pristine graphene, are now occupied. b,c) Plots of the real part of the wavefunctions of electronic levels marked **A** and **B** in the electronic band structure of K on top of graphene. The wavefunction of the level marked **A** is localized on the K atom while the wavefunction of the highest occupied level, marked **B**, is delocalised over the graphene layer. These results confirm that charge transfer has occurred from the 4s occupied level of K to graphene. Reprinted with permission from [28]. Copyright 2010 American Physical Society.

$4s^1$ electronic level of potassium, Figure 3b, which is occupied for an isolated K atom, becomes empty when the K atom is adsorbed on graphene (level marked A in Figure 3a). On the other hand, the wavefunctions of the occupied levels above the graphene Dirac point (marked B in Figure 3a) are delocalized over the carbon atoms of graphene (Figure 3c) indicating the presence of free electrons. These results confirm that n-type doping of graphene occurs due to the transfer of electrons from K atoms to graphene. Integration of the graphene density of states between the Dirac point and the Fermi level shows that approximately one electron is transferred per adsorbed K atom.

The doping properties were also explored for different transition metal clusters (Ti, Fe and Pt) deposited on graphene by molecular beam epitaxy (MBE) [30]. The Ti and Fe metal clusters were found to be n-type dopants with Ti being the most effective donor. Interestingly, deposition of Pt may lead to either n- or p-type doping depending on the Pt coverage. The n-type doping observed at low Pt-coverages is attributed to the formation of a strong interfacial dipole, causing a potential step which in this case promotes the n-type doping [31].

Whereas one expects that electropositive adsorbates will dope graphene n-type, electronegative species should lead to p-type doping. By using angle-resolved photoemission spectroscopy Gierz et al. [32] demonstrated the doping of epitaxial graphene (EG) with holes by metal atoms with high electron affinity such as bismuth, antimony and gold. In the case of doping with bismuth and antimony the electron extraction from graphene only reduced the natural intrinsic n-type character of EG on SiC while gold actually shifted the Dirac point above the Fermi level, that is a clear evidence of induced p-type doping. Graphene layers with p-type conductivity can also be produced by deposition of some organic molecules. Tetrafluorotetracyanoquinodimethane (F_4-TCNQ), shown in Figure 4, is an organic molecule with a strong electron affinity, which was previously demonstrated to be an efficient acceptor for diamond [33] and carbon nanotubes [34].

As the workfunctions of diamond and graphene are similar, the F_4-TCNQ molecule was considered to be a good candidate for p-type doping of graphene. The effect of the F_4-TCNQ molecule on the electronic properties of epitaxial graphene was studied by synchrotron-based high resolution photoemission spectroscopy (PES) [35]. The increase of the graphene work function due to the deposition of F_4-TCNQ (Figure 5) suggests that there is an electron transfer from graphene to the molecule. In agreement with PES measurements DFT calculations have shown the electron transfer of 0.3 *e* per molecule from the highest occupied electronic state of graphene to the lowest unoccupied electronic state of the F_4-TCNQ molecule [36].

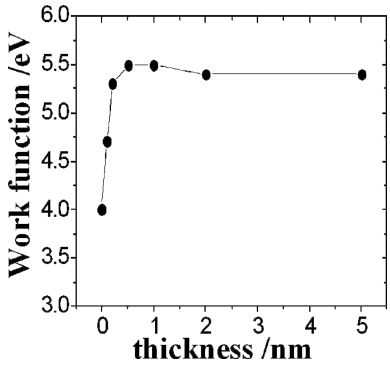

Figure 5: Plot of the workfunction of graphene (eV) as a function of the thickness (nm) of deposited F_4-TCNQ. The workfunction of graphene increases 1.3 eV after the deposition of 0.2 nm of F_4-TCNQ. For higher thicknesses the workfunction remains constant suggesting that the charge transfer occurs at the graphene/F_4-TCNQ interface. Reprinted with permission from [35]. Copyright 2007 American Chemical Socieity.

The p-type doping of graphene can also be achieved by depositing other organic molecules such as pyrenetetrasulfonic acid (TPA) or tetracyanoethylene (TCNE) [37,38], shown in Figure 6a and Figure 6b, respectively. After the deposition of TPA, Raman spectroscopic studies showed upshifts of both Raman G and 2D frequencies compared to single layer graphene indicating p-type doping [37]. Electronic structure calculations based on density functional theory demonstrated that a p-type graphene can be obtained through charge transfer between the TCNE molecule and graphene [38].

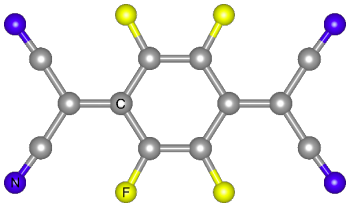

Figure 4: Molecular geometry of tetrafluorotetracyanoquinodimethane (F_4-TCNQ).

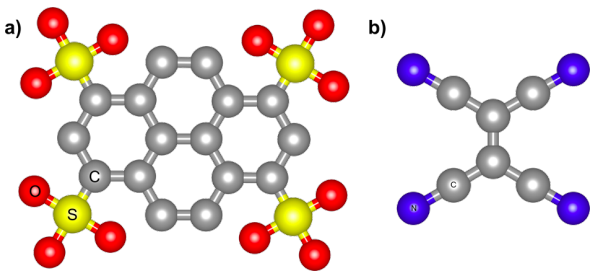

Figure 6: Molecular structure of a) pyrenetetrasulfonic acid (TPA) and b) tetracyanoethylene (TCNE).

Electrochemical dopants

It was observed that the exposure of graphene to a humid atmosphere causes p-type doping whereas exposure to toluene ($C_6H_5CH_3$), Figure 7, results in n-type doping [24,39,40]. However, doping of graphene in the presence of water and toluene cannot be understood within the electronic model. For instance, according to DFT calculations the Fermi level of graphene lies between the HOMO and LUMO levels of the adsorbed toluene molecules, which indicates the absence of electronic doping [41]. The doping effects in the above cases are instead attributed to electrochemical redox reactions occurring in aqueous layers at the graphene interface [41].

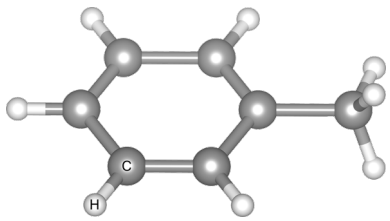

Figure 7: Molecular structure of toluene ($C_6H_5CH_3$).

The *p*-doping induced by humid atmosphere occurs via a redox reaction involving H_2O/O_2 and graphene as in

$$O_2 + 2H_2O + 4e^- = 4OH^- . \quad (1)$$

The value of ΔG of this reaction can be calculated from the tables of free energies to be −4.82 eV [19]. Under the assumption that electrons for the above reaction are taken from graphene the total Gibbs free energy change is $-4.82 + W$ or −0.3 eV. Thus, the reaction will occur spontaneously near the graphene surface, making graphene p-type doped. The rate of the reaction is, however, influenced by the molar concentration of O_2 and OH^-. According to the Nernst equation ΔG can range from −4.8 to −5.7 eV in basic (pH 14) and acidic (pH 1) conditions, respectively. Therefore, the reaction is inhibited in basic conditions and promoted in acidic conditions since the concentration of OH^- is low.

The electrochemical p-type doping of graphene on a SiO_2 substrate in the presence of O_2 and H_2O was confirmed experimentally by Raman spectroscopy measurements [39]. It was shown that the exposure of graphene to a mixture of O_2 and H_2O leads to a stronger doping than the exposure to O_2 or H_2O alone. The hysteresis effects commonly observed in graphene FETs doped under atmospheric conditions [21-24] were suppressed by treating the samples under vacuum for about 50 h or annealing at 473 K. The long evacuation time suggests that the doping species are strongly bound to graphene and difficult to be desorbed.

Similarly, the n-type doping of graphene caused by toluene can be explained by the electrochemical mechanism. In this case it is difficult to determine which particular reaction takes place. One possibility is the electrochemical oxidation of toluene to benzyl alcohol

$$\text{toluene} + 2OH^- = \text{benzyl alcohol} + H_2O + 2e^- . \quad (2)$$

This reaction is spontaneous as the change of the total Gibbs free energy is −0.5 eV. The released electron can be trapped by graphene and make it n-type doped.

Figure 8 shows the measured resistance of a typical graphene FET device as a function of the gate voltage V_g at different stages of the toluene-doping experiment. Firstly, the sample was annealed in vacuum and the resistance peak at positive V_g, Figure 8a, is an indication that the graphene is doped with holes. The exposure of graphene to toluene shifts the resistance peak to negative V_g showing that toluene acts as n-type dopant on graphene, Figure 8b. It is worth emphasizing that redox reactions are slow and thus graphene needs to be exposed to toluene for long periods of about 1 h for a doping effect to be seen. Furthermore, hysteresis is observed in the $R(V_g)$ measurement. The position of the resistance peak changes with the direction of the V_g sweep. The hysteresis vanished when the toluene is pumped out, but the doping effect remains, Figure 8c.

Hysteresis effects are often observed in graphene FETs based on Si^+/SiO_2 substrates [21-24]. Such effects are not expected in the case of electronic doping. However, they can be explained within the electrochemical doping model if a chemical reaction rate or diffusion rates of species involved in the reaction are slower than the rate of gate voltage change. The most obvious reaction in this case is the reaction in Equation 1. The water molecules required for the reaction are assumed to be located at the graphene/SiO_2 interface. Indeed, the presence of water layers on the surface of SiO_2 films grown on Si has been confirmed by Kelvin probe microscopy, X-ray spectroscopy and FTIR measurements [42,43]. Water molecules are also believed to be present in small voids in amorphous SiO_2. It has been found that for graphene FETs operating under ambient conditions the hysteresis is suppressed when Si^+/SiO_2 substrate was covered with a thin hydrophobic layer [23]. Another experiment showed that atmospheric doping does not occur in free standing graphene [39], supporting that the main source of water molecules is within the substrate or at the graphene/SiO_2 interface. The binding energy of OH^- to the SiO_2 network was estimated to be about 0.3 eV indicating that OH^- can easily

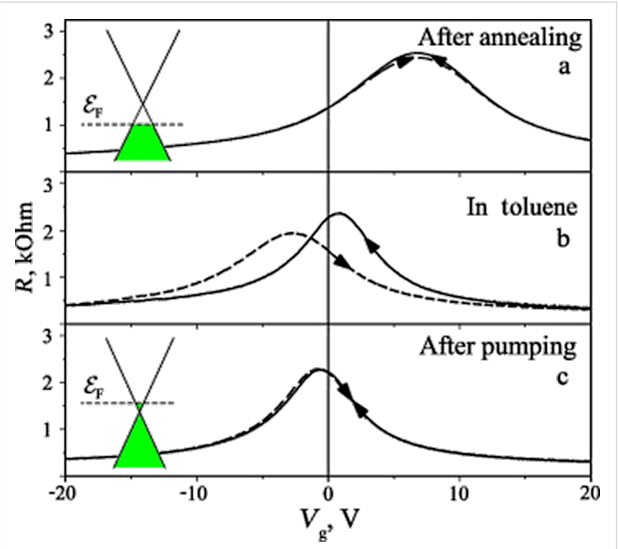

Figure 8: Resistance (kOhm) as a function of the gate voltage (V_g) a) for pristine graphene after annealing in vacuum, b) after exposure to toluene and c) and pumping out the toluene vapour. The shift of the resistance peak towards negative (V_g) after the exposure of toluene indicates that the molecule acts as a n-type dopant. Pumping out the toluene from the chamber removes the hysteresis but the doping effect remains. Reprinted with permission from [24]. Copyright 2011 Elsevier.

diffuse through SiO_2 at room temperature [44]. Therefore, the concentration of OH^- at the graphene/SiO_2 interface and thus the rate of the reaction is influenced by the gate voltage. A positive V_g results in the reduction of the OH^- concentration at the graphene interface promoting the further dissociation of H_2O molecules, which consequently increases the concentration of holes in graphene, as it was observed experimentally [21].

Some of these redox reactions were first discussed for diamond and carbon nanotubes [17,45] and were investigated for graphene because of the similarity in all their work functions. For instance, the exposure of hydrogenated diamond to a humid atmosphere results in p-type doping [46,47], which can be suppressed by NH_3 and enhanced by NO_2 [48]. Similar effects were reported for carbon nanotubes [49,50]. It would be interesting to see whether they could apply to graphite or indeed if some of the variant reactions tried on graphene could be applied to diamond, graphite and carbon nanotubes.

Conclusion

In this article we have revisited the surface dopants of graphene and the charge transfer mechanisms. The deposition of atoms or molecules is an effective method to control the type and concentration of charge carriers in graphene. Surface charge transfer can be mediated by two mechanisms, electronic and electrochemical doping. The electronic doping occurs by direct exchange of electrons between graphene and the adsorbates, either atoms or molecules. Electropositive elements that easily donate their outer shell electrons, such as potassium, are expected to be n-type dopants while adsorbates with a strong electron affinity, such as F_4-TCNQ, have been proved to be very efficient p-type dopants. This type of doping occurs instantaneously and should not cause hysteresis effects. However, the ionized dopants become additional charge scatterers leading to a reduction in the charge carrier mobility.

The electrochemical doping of graphene occurs as a result of redox reactions that can take place near the graphene surface. Unlike electronic doping it does not reduce the charge carriers mobility but it may require appreciable time to occur since the reaction and diffusion barriers have to be overcome. Moreover, the electrochemical doping model can explain the hysteresis effects usually observed in graphene based field effect transistors when operating in atmospheric environment.

Acknowledgements

The authors would like to thank R. Jones, J. P. Goss, D. W. Palmer and S. Öberg for helpful discussions and their important contribution into some of the theoretical work discussed in the present article. The financial support from the COST action MP0901 “NanoTP” is gratefully acknowledged.

References

1. Novoselov, K. S.; Geim, A. K.; Morozov, S. V.; Jiang, D.; Zhang, Y.; Dubonos, S. V.; Grigorieva, I. V.; Firsov, A. A. *Science* **2004,** *306,* 666–669. doi:10.1126/science.1102896
2. Novoselov, K. S.; Fal’ko, V. I.; Colombo, L.; Gellert, P. R.; Schwab, M. G.; Kim, K. *Nature* **2012,** *490,* 192–200. doi:10.1038/nature11458
3. Geim, A. K.; Novoselov, K. S. *Nat. Mater.* **2007,** *6,* 183–191. doi:10.1038/nmat1849
4. Novoselov, K. S.; Geim, A. K.; Morozov, S. V.; Jiang, D.; Katsnelson, M. I.; Grigorieva, I. V.; Dubonos, S. V.; Firsov, A. A. *Nature* **2005,** *438,* 197–200. doi:10.1038/nature04233
5. Nair, R. R.; Blake, P.; Grigorenko, A. N.; Novoselov, K. S.; Booth, T. J.; Stauber, T.; Peres, N. M. R.; Geim, A. K. *Science* **2008,** *320,* 1308. doi:10.1126/science.1156965
6. Lee, C.; Wei, X.; Kysar, J. W.; Hone, J. *Science* **2008,** *321,* 385–388. doi:10.1126/science.1157996
7. Bae, S.; Kim, H.; Lee, Y.; Xu, X.; Park, J.-S.; Zheng, Y; Balakrishnan, J.; Lei, T.; Kim, H. R.; Song, Y. I.; Kim, Y.-J.; Kim, K. S.; Özyilmaz, B.; Ahn, J.-H.; Hong, B. H.; Iijima, S. *Nat. Nanotechnol.* **2010,** *5,* 574–578. doi:10.1038/NNANO.2010.132
8. Li, X.; Zhu, Y.; Cai, W.; Borysiak, M.; Han, B.; Chen, D.; Piner, R. D.; Colombo, L.; Ruoff, R. S. *Nano Lett.* **2009,** *9,* 4359–4363. doi:10.1021/nl902623y
9. Xia, F.; Mueller, T.; Golizadeh-Mojarad, R.; Freitag, M.; Lin, Y.-m.; Tsang, J.; Perebeinos, V.; Avouris, P. *Nano Lett.* **2009,** *9,* 1039–1044. doi:10.1021/nl8033812
10. Lin, Y.-M.; Dimitrakopoulos, C.; Jenkins, K. A.; Farmer, D. B.; Chiu, H.-Y.; Grill, A.; Avouris, P. *Science* **2010,** *327,* 662. doi:10.1126/science.1184289

11. Wallace, P. R. *Phys. Rev.* **1947,** *71,* 622–634. doi:10.1103/PhysRev.71.622
12. Castro Neto, A. H.; Guinea, F.; Peres, N. M. R.; Novoselov, K. S.; Geim, A. K. *Rev. Mod. Phys.* **2009,** *81,* 109–162. doi:10.1103/RevModPhys.81.109
13. Reddy, D.; Register, L. F.; Carpenter, G. D.; Banerjee, S. K. *J. Phys. D: Appl. Phys.* **2011,** *44,* 313001. doi:10.1088/0022-3727/44/31/313001
14. Liu, H.; Liu, Y.; Zhu, D. *J. Mater. Chem.* **2011,** *21,* 3335–3345. doi:10.1039/c0jm02922j
15. Panchakarla, L. S.; Subrahmanyam, K. S.; Saha, S. K.; Govindaraj, A.; Krishnamurthy, H. R.; Waghmare, U. V.; Rao, C. N. R. *Adv. Mater.* **2009,** *21,* 4726–4730. doi:10.1002/adma.200901285
16. Wei, D.; Liu, Y.; Wang, Y.; Zhang, H.; Huang, L.; Yu, G. *Nano Lett.* **2009,** *9,* 1752–1758. doi:10.1021/nl803279t
17. Hansen, W. N.; Hansen, G. J. *Surf. Sci.* **2001,** *481,* 172–184. doi:10.1016/S0039-6028(01)01036-6
18. Sque, S. J.; Jones, R.; Briddon, P. R. *Phys. Status Solidi A* **2007,** *204,* 3078–3084. doi:10.1002/pssa.200776313
19. Lide, D. R., Ed. *CRC Handbook of Physics and Chemistry,* 76th ed.; CRC Press, 2005; pp 8–21.
20. Reiss, H. *J. Phys. Chem.* **1985,** *89,* 3783–3791. doi:10.1021/j100264a005
21. Lohmann, T.; von Klitzing, K.; Smet, J. H. *Nano Lett.* **2009,** *9,* 1973–1979. doi:10.1021/nl900203n
22. Xu, H.; Chen, Y.; Xu, W.; Zhang, H.; Kong, J.; Dresselhaus, M. S.; Zhang, J. *Small* **2011,** *7,* 2945–2952. doi:10.1002/smll.201100546
23. Lafkioti, M.; Krauss, B.; Lohmann, T.; Zschieschang, U.; Klauk, H.; von Klitzing, K.; Smet, J. H. *Nano Lett.* **2010,** *10,* 1149–1153. doi:10.1021/nl903162a
24. Kaverzin, A. A.; Strawbridge, S. M.; Price, A. S.; Withers, F.; Savchenko, A. K.; Horsell, D. W. *Carbon* **2011,** *49,* 3829–3834. doi:10.1016/j.carbon.2011.05.017
25. Chan, K. T.; Neaton, J. B.; Cohen, M. L. *Phys. Rev. B* **2008,** *77,* 235430. doi:10.1103/PhysRevB.77.235430
26. Liu, X.; Wang, C. Z.; Yao, Y. X.; Lu, W. C.; Hupalo, M.; Tringides, M. C.; Ho, K. M. *Phys. Rev. B* **2011,** *83,* 235411. doi:10.1103/PhysRevB.83.235411
27. Uchoa, B.; Lin, C.-Y.; Castro Neto, A. H. *Phys. Rev. B* **2008,** *77,* 035420. doi:10.1103/PhysRevB.77.035420
28. Pinto, H.; Jones, R.; Goss, J. P.; Briddon, P. R. *Phys. Rev. B* **2010,** *82,* 125407. doi:10.1103/PhysRevB.82.125407
29. Chen, J.-H.; Jang, C.; Adam, S.; Fuhrer, M. S.; Williams, E. D.; Ishigami, M. *Nat. Phys.* **2008,** *4,* 377–381. doi:10.1038/nphys935
30. Pi, K.; McCreary, K. M.; Bao, W.; Han, W.; Chiang, Y. F.; Li, Y.; Tsai, S.-W.; Lau, C. N.; Kawakami, R. K. *Phys. Rev. B* **2009,** *80,* 075406. doi:10.1103/PhysRevB.80.075406
31. Giovannetti, G.; Khomyakov, P. A.; Brocks, G.; Karpan, V. M.; van den Brink, J.; Kelly, P. J. *Phys. Rev. Lett.* **2008,** *101,* 026803. doi:10.1103/PhysRevLett.101.026803
32. Gierz, I.; Riedl, C.; Starke, U.; Ast, C. R.; Kern, K. *Nano Lett.* **2008,** *8,* 4603–4607. doi:10.1021/nl802996s
33. Qi, D.; Chen, W.; Gao, X.; Wang, L.; Chen, S.; Loh, K. P.; Wee, A. T. S. *J. Am. Chem. Soc.* **2007,** *129,* 8084–8085. doi:10.1021/ja072133r
34. Nosho, Y.; Ohno, Y.; Kishimoto, S.; Mizutani, T. *Nanotechnology* **2007,** *18,* 415202. doi:10.1088/0957-4484/18/41/415202
35. Chen, W.; Chen, S.; Qi, D. C.; Gao, X. Y.; Wee, A. T. S. *J. Am. Chem. Soc.* **2007,** *129,* 10418–10422. doi:10.1021/ja071658g
36. Pinto, H.; Jones, R.; Goss, J. P.; Briddon, P. R. *J. Phys.: Condens. Matter* **2009,** *21,* 402001. doi:10.1088/0953-8984/21/40/402001
37. Dong, X.; Fu, D.; Fang, W.; Shi, Y.; Chen, P.; Li, L.-J. *Small* **2009,** *5,* 1422–1426. doi:10.1002/smll.200801711
38. Lu, Y. H.; Chen, W.; Feng, Y. P.; He, P. M. *J. Phys. Chem. B* **2009,** *113,* 2–5. doi:10.1021/jp806905e
39. Xu, H.; Chen, Y.; Zhang, J.; Zhang, H. *Small* **2012,** *8,* 2833–2840. doi:10.1002/smll.201102468
40. Schedin, F.; Geim, A. K.; Morozov, S. V.; Hill, E. W.; Blake, P.; Katsnelson, M. I.; Novoselov, K. S. *Nat. Mater.* **2007,** *6,* 652–655. doi:10.1038/nmat1967
41. Pinto, H.; Jones, R.; Goss, J. P.; Briddon, P. R. *Phys. Status Solidi A* **2010,** *207,* 2131–2136. doi:10.1002/pssa.201000009
42. Verdaguer, A.; Weis, C.; Oncins, G.; Ketteler, G.; Bluhm, H.; Salmeron, M. *Langmuir* **2007,** *23,* 9699–9703. doi:10.1021/la700893w
43. Aarts, I. M. P.; Pipino, A. C. R.; Hoefnagels, J. P. M.; Kessels, W. M. M.; van de Sanden, M. C. M. *Phys. Rev. Lett.* **2005,** *95,* 166104. doi:10.1103/PhysRevLett.95.166104
44. Bakos, T.; Rashkeev, S. N.; Pantelides, S. T. *Phys. Rev. B* **2004,** *69,* 195206. doi:10.1103/PhysRevB.69.195206
45. Rezek, B.; Sauerer, C.; Nebel, C. E.; Stutzmann, M.; Ristein, J.; Ley, L.; Snidero, E.; Bergonzo, P. *Appl. Phys. Lett.* **2003,** *82,* 2266–2268. doi:10.1063/1.1564293
46. Maier, F.; Riedel, M.; Mantel, B.; Ristein, J.; Ley, L. *Phys. Rev. Lett.* **2000,** *85,* 3472–3475. doi:10.1103/PhysRevLett.85.3472
47. Chakrapani, V.; Angus, J. C.; Anderson, A. B.; Wolter, S. D.; Stoner, B. R.; Sumanasekera, G. U. *Science* **2007,** *318,* 1424–1430. doi:10.1126/science.1148841
48. Garrido, J. A.; Härtl, A.; Dankerl, M.; Reitinger, A.; Eickhoff, M.; Helwig, A.; Müller, G.; Stutzmann, M. *J. Am. Chem. Soc.* **2008,** *130,* 4177–4181. doi:10.1021/ja078207g
49. Kong, J.; Franklin, N. R.; Zhou, C.; Chapline, M. G.; Peng, S.; Cho, K.; Dai, H. *Science* **2000,** *287,* 622–625. doi:10.1126/science.287.5453.622
50. Bradley, K.; Gabriel, J.-C. P.; Briman, M.; Star, A.; Grüner, G. *Phys. Rev. Lett.* **2003,** *91,* 218301. doi:10.1103/PhysRevLett.91.218301

License and Terms

This is an Open Access article under the terms of the Creative Commons Attribution License (http://creativecommons.org/licenses/by/2.0), which permits unrestricted use, distribution, and reproduction in any medium, provided the original work is properly cited.

The license is subject to the *Beilstein Journal of Nanotechnology* terms and conditions: (http://www.beilstein-journals.org/bjnano)

The definitive version of this article is the electronic one which can be found at: doi:10.3762/bjnano.5.195

BEILSTEIN JOURNAL OF NANOTECHNOLOGY

Carbon-based smart nanomaterials in biomedicine and neuroengineering

Antonina M. Monaco[1] and Michele Giugliano*[1,2,3]

Review

Open Access

Address:
[1]Theoretical Neurobiology and Neuroengineering Lab, Department of Biomedical Sciences, University of Antwerp, Universiteitsplein 1, B-2610 Wilrijk, Belgium, [2]Brain Mind Institute, Swiss Federal Institute of Technology, Lausanne, CH-1015, Switzerland and [3]Department of Computer Science, University of Sheffield, S1 4DP Sheffield, UK

Email:
Michele Giugliano* - michele.giugliano@uantwerpen.be

* Corresponding author

Keywords:
carbon nanotubes; electrophysiology; graphene; microelectrodes; nanodiamonds; nanotechnology; neuroengineering; neuronal cultures; neuroscience

Beilstein J. Nanotechnol. **2014,** *5,* 1849–1863.
doi:10.3762/bjnano.5.196

Received: 25 June 2014
Accepted: 29 September 2014
Published: 23 October 2014

This article is part of the Thematic Series "Atomic scale interface design and characterisation: Theory – Structure and dynamics".

Guest Editor: C. Ewels

© 2014 Monaco and Giugliano; licensee Beilstein-Institut.
License and terms: see end of document.

Abstract

The search for advanced biomimetic materials that are capable of offering a scaffold for biological tissues during regeneration or of electrically connecting artificial devices with cellular structures to restore damaged brain functions is at the forefront of interdisciplinary research in materials science. Bioactive nanoparticles for drug delivery, substrates for nerve regeneration and active guidance, as well as supramolecular architectures mimicking the extracellular environment to reduce inflammatory responses in brain implants, are within reach thanks to the advancements in nanotechnology. In particular, carbon-based nanostructured materials, such as graphene, carbon nanotubes (CNTs) and nanodiamonds (NDs), have demonstrated to be highly promising materials for designing and fabricating nanoelectrodes and substrates for cell growth, by virtue of their peerless optical, electrical, thermal, and mechanical properties. In this review we discuss the state-of-the-art in the applications of nanomaterials in biological and biomedical fields, with a particular emphasis on neuroengineering.

Introduction

Over the past few years, the gap between materials sciences and biology has increasingly narrowed. This has enabled substantial progress within interdisciplinary approaches, particularly in those combining micro- and nanotechnologies in biological and biomedical applications. For example, the field of neuroengineering was established, as a recent new research discipline within the field of neuroscience. Neuroengineering focuses on the development of artificial devices and novel materials to be functionally and structurally interfaced with the central nervous system (CNS). Among its ultimate goals, repairing, replacing, and enhancing the function of damaged brain tissue is a priority, as witnessed by the recent progress in (pre)clinical neuroprosthetics and brain pacemakers. At the same time, neuroengineering also deals with serious clinical challenges, due to the

unique anatomy and physiology of the CNS, compared to other organs. Today, there is the expectation that materials science and nanotechnology will be able to address these challenges and lead to breakthroughs at the level of the interfaces between artificial transducers/actuators and living cells.

Nowadays, fundamental research in neuroengineering aims to open up new frontiers in tissue engineering through reconstructive/repairing strategies that will ultimately be able to provide a functional bridge to the damaged tissue and restore functions via implantable assisting devices. This calls for the use of new smart materials, whose interactions with living tissue can be controlled, engineered and modified. Nanomaterials are ideal candidates for such applications and by virtue of their nanoscale dimensions, share with biological (sub)cellular structures a similar level of organisation. This review presents some of the recent applications of nanomaterials that were reported in very recent years with an emphasis on carbon-based materials.

Review

Carbon and its nanoderivatives: chemical and physical properties

In nature, carbon is found in different forms or *allotropes*, depending on its chemical valence. The electron configuration of carbon in its fundamental state ($1s^2\ 2s^2\ 2p^2$) is such that it can form, at the most, two covalent bonds. However, in its chemical compounds, carbon is able to form up to four covalent bonds thanks to a rearrangement of its electron configuration: One of its 2s electrons "moves" into the empty 2p orbital, giving rise to four bonds due to four hybrid orbitals. The three possible hybridisations (sp, sp^2 and sp^3) differ according to the number of p orbitals mixed with the s orbital, and according to the angle between the orbitals themselves. This angle, in turn, defines the type of chemical bond carbon can establish; these consist of only simple bonds (σ type) in sp^3 hybridisation, double bonds (one σ and one π) in sp^2, and triple bonds (one σ and two π) in sp.

Among the existing allotropes, the most widely known are carbon nanotubes (CNTs) and fullerenes, graphite and graphene (sp^2), and diamond (sp^3). From these distinct hybridisations, different properties are inherent to these allotropes.

Carbon nanotubes (CNTs): CNTs, first reported by Iijima in 1991 [1], are hollow cylinders made of one (i.e., single-walled CNTs, SWCNTs) or several (i.e., multi-walled CNTs, MWCNTs) layers of graphene. They are obtained by a variety of methods, including chemical vapour deposition (CVD) and arc-discharge, and their electronic properties depend solely on geometric parameters, such as diameter and chiral angle. These parameters are in turn determined by the magnitude and the direction of the chiral vector [2], and their influence is clearly expressed in the electrical conductivity of the CNTs: SWCNTs can be either metallic or semiconducting [3], while MWCNTs show only metallic behaviour [4]. Moreover, the mechanical and electronic properties of SWCNTs can be altered by means of external electric fields [5,6].

The chemical bonds between carbon atoms in CNTs are among the strongest known and this, combined with their characteristic tubular structure, endows CNTs with an extremely high mechanical strength [7], while at the same time exhibiting a very low weight. Combined with a large surface area, these electronic and mechanical properties give CNTs a great potential for microelectronics and optics, and also for biomedical applications (e.g., as nanoelectrodes for neural stimulation and functional scaffolds for tissue engineering).

Nanodiamonds (NDs): As a result of the complete sp^3 hybridisation of its carbon atoms and its characteristic tetrahedral configuration, diamond shows interesting and peculiar properties such as an extreme hardness, low friction coefficient, high mobility of electrical charge carriers and high thermal conductivity [8,9]. Diamond exhibits these properties both in bulk as well as at the nanoscale and combines them with typical features of nanomaterials, such as a large surface area and small overall size.

NDs, mainly obtained by detonation of TNT-like explosives under oxygen-deprived conditions, are core–shell like particles with a diameter of 2–8 nm. Their structure consists of an sp^3-hybridised core surrounded by layers of amorphous and sp^2-hybridised carbon [10-12], and they show a strong tendency to agglomerate [13] in clusters with sizes ranging from 100–200 nm to 20–30 μm. This tendency is likely the consequence of several surface terminations, all containing oxygen functional groups such as carboxyl, hydroxyl, ketone and lactone. Ad hoc surface functionalisation of NDs is thus essential for improving the solubility of NDs and to make them suitable for biological applications [14].

The optical properties of NDs are remarkable: highly pure diamond is fully transparent and colourless, whereas the presence of lattice impurities and dopants render diamond coloured [15]. When NDs are excited by UV light [16], they display fluorescence over a broad emission band in the visible region [17] of the spectrum. One of the most common and studied defects in diamond lattice is the *nitrogen-vacancy* centre (NV centre) [18], formed by a lattice vacancy and an adjacent nitrogen atom in the NDs. The importance of these NV centres lies in their magnetic properties [19]: Given the coupling

between the spin state and luminescence, the luminescence of NDs can be modulated by local magnetic fields [20,21].

Graphene: Graphene is a mono-atomic, two-dimensional, sheet of sp^2-hybridised carbon atoms arranged as a honeycomb lattice. Since the first single-layer sample was isolated from graphite by Novoselov and colleagues [22] in 2004, graphene has attracted substantial interest and attention for its unique chemical and physical properties, because its existence had for a long time been considered to be impossible [23,24].

Its special electronic structure bestows graphene uncommon and astonishing electronic properties, such as the quantum Hall effect, which can be observed even at room temperature [25], a very high electron mobility [26], the ambipolar electric field effect, the ballistic conduction of electronic charge carriers [27], as well as the nature of the charge carriers themselves, which behave like massless relativistic particles and are thus better described by Dirac's rather than Schrödinger's equation [28]. These, and other remarkable properties, including its excellent mechanical strength [29], the high transparency of single-layer graphene [30], and its large surface area [31], make graphene and graphene oxide (GO) one of the most promising materials for technological and biomedical applications.

Carbon-based nanomaterials in biomedical applications

The peculiar ability of several nanomaterials to functionally integrate with biological systems is a consequence of their interactions with cells and membranes occurring at the subcellular level. However, due to their chemically inert surface and van der Waals forces occurring at the surface, carbon-based nanomaterials, particularly pristine CNTs, tend to agglomerate, which results in a limited dispersion in organic matrices. To overcome this problem and to improve the biocompatibility, or to specify the targeting of the particles, functionalisation methods have been developed and successfully used in the past decade. In the following paragraphs, we review some of the most important biological applications of these nanomaterials.

CNTs: The previously mentioned large surface area and their excellent chemical stability confers CNTs the ability to conjugate and absorb several therapeutic molecules, paving the way for using them as drug- and gene-delivery systems. Yang and colleagues [32], for example, exploited the ability of CNTs to cross the blood–brain barrier to deliver acetylcholine into the lysosomes of neurons in the experimental treatment of Alzheimer's disease in mice.

However, the biological applications of CNTs require their complete purification from both metal and carbonaceous particles [33]. In addition, their surface functionalisation must be designed to enhance their solubility in biological media [34]. In particular, two functionalisation procedures for CNTs are explored in the literature: (i) the non-covalent approach [35,36] that consists of coating CNTs with surfactants, peptides, polymers, or nucleic acids, which preserve their aromatic structure, and (ii) the covalent approach [37-39], by means of applying several protocols, such as oxidation in strong acids, fluorination [40], and Bingel [41] and Billups [42] reactions.

Given the nature of their applications, biocompatibility of CNTs is a crucial, yet still controversial point. How physicochemical characteristics (i.e., length, diameter, and surface functionalisation) affect the toxicity of CNTs [43], and by what mechanisms CNTs can enter the cellular cytoplasm, and where they are localised once internalised [44], remain open questions. In fact, both toxicity and biocompatibility have been reported and discussed extensively for CNTs in recent literature. Inhalation of pristine raw SWCNTs has been described to result in changes in pulmonary functions, inflammatory reactions, and the formation of granulomas [45]. Granulomas and inflammatory reactions have also been reported upon injection of CNTs in the peritoneal cavity, likely as a consequence of their asbestos-like structure [46]. The toxic effects of raw CNTs have also been reported in vitro [47-50], interpreted as a likely consequence of their hydrophobic surface and as a result, their tendency to aggregate. However, these adverse effects appear to be reduced for functionalised CNTs [49,50]. Therefore, the cyto- and genotoxicity of CNTs appear to be sample-specific, and require the evaluation of biocompatibility properties on a case-by-case basis.

Despite the debate on their biocompatibility when in solution, CNTs have been proposed as an ideal material over quite a wide range of biomedical applications; in addition to the discussed drug [51] and gene [52,53] delivery, CNTs have been used as biosensors [54], in hyperthermia therapy for tumours [55,56], in tissue engineering [57], for in vivo [58] and in vitro [59] imaging.

The electrical conductivity of CNTs lies at the foundation of the proposal for employing CNTs as smart-scaffolds for excitable cells such as neurons [60] and cardiac cells [61], within regenerative applications. Martinelli et al. [62,63] cultured neonatal rat ventricular myocytes on CNTs substrates and measured the active and passive membrane electrical properties of both single myocytes and multinucleated cells by patch-clamp cellular electrophysiology. In both cases, cells grown on CNTs substrates showed a more negative resting potential compared to the control condition, while no significant differences were found for input resistance and cell capacitance or for the occurrence

frequency and kinetics of action potentials (APs). However, this study further highlighted that interfacing cardiomyocytes with CNTs accelerates cells maturation, resulting in an increased expression of mature phenotype-related genes.

Lin and colleagues [64] studied in vitro how pristine SWCNTs dispersed in an extracellular medium can affect the viability of vascular adventitial fibroblasts and their transformation into myofibroblasts. Their results showed an up-regulated expression of a specific differentiation marker, accompanied, however, by an increased generation of the most biologically significant free radicals, the reactive oxygen species (ROS).

NDs: Among the applications of NDs, the most important include drug delivery [65,66], implants coating [67] and bioimaging [68]. Similarly to the use of CNTs, the first consideration in biological applications is the biocompatibility of NDs. Diamond, in its bulk form, is chemically inert. However, because surface chemistry is predominant at the nanoscale compared to that of the bulk scale, investigating ND biocompatibility has been a priority in recent years.

One of the first studies in this area was conducted by Yu and colleagues [69], who evaluated the cytotoxicity of fluorescent NDs by employing human embryonic kidney cells: they observed that NDs slightly affected cell viability, even for a concentration of about 400 μg/mL.

Schrand and co-workers [70-72] extensively studied this issue through standard in vitro cell viability assays (i.e., MTT) and also monitored adenosine triphosphate (ATP) production and ROS generation. They found that, compared to several carbon-based alternative nanomaterials (i.e., carbon black, SWCNTs and MWCNTs), NDs were the least toxic when exposed to neuroblastoma cells, as they did not induce significant ROS production and did not affect mitochondrial membrane integrity.

A different approach to biocompatibility of NDs has been proposed by several research groups, who monitored gene expression of cells. No significant change in the expression of Bcl-x and TNF-α genes [65] was found, while a decreased expression of genes responding to genotoxic compounds was described; in addition, no effects on the expression of genes responding to oxidative stress were observed [73]. However, Xing et al. [74] observed that embryonic stem cells responded to incubation with NDs with an increased expression of MOGG-1 and P53, which are proteins related to DNA repair processes. This genotoxicity was increased when cells were incubated with oxidised NDs, suggesting it was a specific consequence of the surface chemistry of NDs. Nonetheless, Xing and co-workers noted that NDs and oxidised NDs induce overall less DNA damage than that caused by MWCNTs.

The investigation of the cellular uptake mechanisms of NDs is also a key aspect for biological applications of NDs. Vaijayanthimala and colleagues [75] reported that cellular uptake was strictly related to the surface functionalisation of NDs and that it took place through clathrin-mediated, energy-dependent, endocytosis processes. Schrand et al. [76] also investigated the uptake of fluorophore-conjugated NDs by neuroblastoma cell line and observed that the fluorophore-conjugation was not affected by the different pH conditions encountered during the uptake process. In addition, NDs were described as localising mainly in endosomes, lysosome and in some cases, the cytoplasm.

Given the possibility for NDs in powder form to spread in the air during detonation synthesis, an in vivo evaluation of their toxicity also became relevant and timely; several studies have focused on this aspect and highlighted that NDs have no remarkable adverse effects in the lungs [77]. In addition, subcutaneous exposure to NDs does not trigger inflammatory responses and NDs do not affect the normal internal organs development or reproductive abilities [78]. In vivo system-level localisation of NDs, studied by labelling NDs with different radionuclides, revealed that NDs preferentially localise in the lungs, liver and spleen [79], and that the urinary system excrete them [80].

Hydrogels and thin-films based on NDs have also been used as drug delivery systems by virtue of their ease of surface functionalisation and small size. They have been reported for successfully delivering several anticancer drugs and preserving their activity under biological conditions [81-84].

The affinity of NDs for protein adsorption has been finally utilised to separate recombinant proteins from *Escherichia coli* [85], resulting not only in a radically faster process than the commonly used purification treatments, but also in a high degree of purity of the recovered proteins, which can be further analysed by mass spectrometry [86].

Graphene: Graphene, graphene oxide (GO) and reduced graphene oxide (r-GO) have been investigated as new biocompatible material by virtue of their unique properties, making them suitable for a broad variety of applications. The biocompatibility of graphene is, however, still disputed, given that very few studies are available and because several graphene forms can be employed (i.e., single or few layer, nanosheets, GO, r-GO) each with different chemical and physical properties.

These differences can induce distinct toxicological responses in biological systems and require a systematic investigation.

In vitro studies, carried out on human cell lines (i.e., HepG2, BEAS-2B, PC12, hMSCs), have demonstrated that the cyto- and genotoxicity of graphene depends on the dose, shape, and size of the nanomaterial itself [87-89], as well as on the presence of metal contaminants and the residues of the GO preparation method in graphene samples [90].

Biomedical applications of graphene and its derivatives range from photothermal tumour ablation therapy to biosensors, from gene therapy [91] and drug delivery to substrates for biomolecular imaging [92,93], and from tissue scaffolds [94] to electrodes for neural stimulation [95].

For instance, Yang and colleagues [96] investigated the possibility of using polyethylene glycol (PEG)-coated nanographene sheets showing absorption in the near-infrared region as a photothermal agent for in vivo cancer treatment, while scrutinising the effects originating from different graphene sizes and coatings [97].

Several research groups have focused on graphene as biosensors. Dey et al. [98] developed an amperometric cholesterol biosensor; Tang and co-workers [99] studied the electrochemical behaviour of reduced graphene sheet films as nicotinamide adenine dinucleotide (NADH) sensors, while Kim and colleagues [100] and Sun and colleagues [101] studied graphene/Pt-based sensors for the detection of dopamine, and uric and ascorbic acids.

The presence of reactive functional groups and of localised π-electrons, which promote the π–π bond with aromatic compounds, render graphene a suitable candidate as a drug delivery system. Several remarkable studies in this area have been performed, including those involving the functionalisation of GO by PEG and water-insoluble chemotherapeutic drugs [102], as well as research involving sulfonic acid groups bound with folic acid in order to target human breast cancer [103]. Furthermore, Weaver and co-workers [104], exploiting the conductive properties of GO sheets, developed an electrically-controlled system capable of a linear release profile of an anti-inflammatory drug.

Carbon-based nanomaterials in neuroscience

The (sub)cellular organisation of the CNS and carbon-based nanomaterials share some intriguing similarities. This has inspired several research groups to explore the use of these nanomaterials for developing nanosized sensing/actuating technologies, ultimately capable of functional interfacing with nerve cells and brain tissue, in order to repair the brain on the (sub)cellular scale.

CNTs: The first application of CNTs in neuroscience was the exploration of CNTs thin-films as ex vivo neuronal growth substrates [105]. Mattson and colleagues reported that MWCNTs favoured neuronal adhesion although neurite branching was reduced, with respect to control conditions. This pioneering work laid the foundations for subsequent studies aimed at establishing the ability of CNTs to support neural adhesion. Since then, several studies [106] have revealed that CNTs are able to guide neuronal adhesion and to impact neuronal networks.

Microelectrode arrays (MEAs – extracellular recording and stimulation of neuronal activity): MEAs are devices consisting of metallic microelectrodes (i.e., made of Au, Pt, or titanium nitrate) and embedded in a planar substrate, arranged in an array and connected to an external electrical circuitry. By using individual microelectrodes it is possible to stimulate or record neural electrical activity non-invasively, both in vivo and in vitro. For these applications, which represent the frontiers of neuroprosthetics and brain pacemakers, MEAs should exhibit excellent biocompatibility, large signal-to-noise ratio (S/N), large charge-injection limits, and high spatial resolution. While the latter aspect can be improved by microphotolitography and ultimately designing smaller microelectrodes, reducing the electrode surface exposed to the electrolyte or in close proximity to neuronal cell membranes, has been shown to lead to a significant electrochemical impedance of the interface, decreased injected charge limits and poor S/N properties.

CNTs, by their excellent electrical properties and large surface area, immediately presented themselves as top candidates for the fabrication of a new class of electrodes [107-110]. Gabay and colleagues [111] developed CNTs-MEAs with improved electrochemical properties by synthesizing “islands” of CNTs on silicon dioxide substrates, and confirmed the capability of the device for recording the spontaneous activity of cultured rat cortical neurons.

Gabriel and co-workers [112] deposited a solution of SWCNTs onto conventional platinum electrodes of a MEA, thus enhancing the electrical properties of the device and successfully tested it to record the extracellular activity of ganglion cells in rabbit retinas as a potentially important step for retinal prostheses.

Shein et al. [113] cultured neurons on specifically designed microelectrode arrays in which CNTs had been deposited by

CVD on TiN leads, and reported a direct electrical interfacing between neurons and microelectrodes made of CNTs.

Deposition of CNTs onto TiN microelectrode arrays was proposed by means of a micro-contact printing technique by Fuchsberger and colleagues [114], and showed superior recording properties compared to commercial TiN microelectrodes. The same microelectrodes were also employed to electrically stimulate and record neuronal activity, as well as to detect low concentrated amounts of dopamine.

To overcome the problems related to spatial resolution and S/N, more recently Gerwig et al. [115] developed a PEDOT–CNT composite that combined the ionic and electronic conductivity of poly(3,4-ethylenedioxythiophene) (PEDOT), a conductive polymer, with the high mechanical stability of CNTs. This combination, employed as a coating layer of conventional MEAs, resulted in reduced impedance, and thus in improved performances not only when compared with TiN or Au electrodes, but also compared to pure PEDOT electrodes. The interpretation of this phenomenon can most likely be found in the conductivity of the meshwork of CNTs, which enhances the electrical conductivity of the whole composite. Furthermore, PEDOT–CNTs-electrodes demonstrated excellent biocompatibility, allowing for the adhesion of primary chicken cardiomyocytes and the development of a two-dimensional syncytium, accompanied by good quality recording after six and ten days in vitro (DIV).

The MEAs thus far discussed are designed for in vitro electrophysiological stimulation and recording; however, they are not directly suitable for in vivo applications, in which flexible substrates must be employed. Lin and colleagues [116] were the first researchers to grow CNTs electrode arrays on a silicon substrate, transfer it onto a flexible and biocompatible polymeric film (Figure 1), and then successfully record the APs of crayfish nerve cords.

Another flexible MEA, completely made from CNTs that have been embedded in a polymeric support, has been presented by David-Pur et al. [117]. This device showed the same characteristics as planar CNTs-MEAs, combined with the advantages of being flexible and of consisting of a continuous rough surface, i.e., the CNTs film, which was demonstrated to improve cell adhesion.

Patch-clamp electrophysiology: One of the first studies reporting on the electrical activity of in vitro neuronal networks coupled to MWCNT-substrates was that of Lovat and co-workers [118]. They were the first researchers to intracellularly monitor the electrical activity of neurons developing ex vivo on CNT-substrates (Figure 2A–C). The researchers unexpectedly reported that CNTs had an effect on spontaneous synaptic activity (Figure 2D–F).

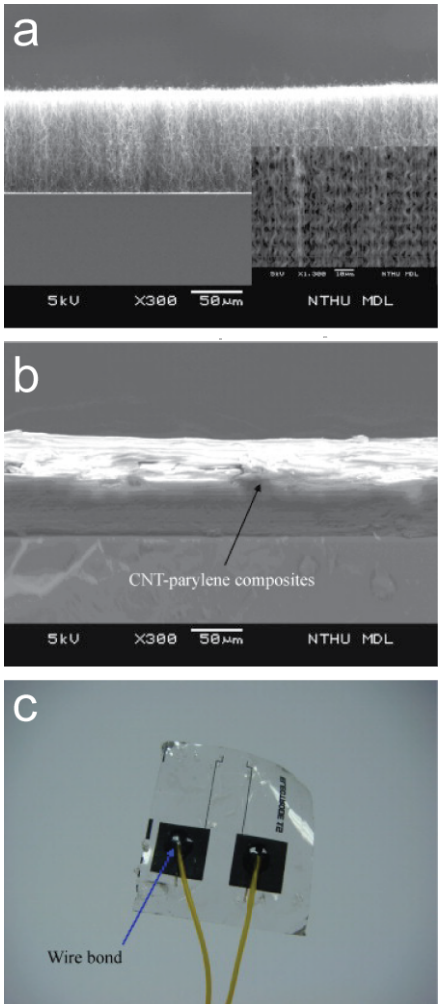

Figure 1: Flexible MEA developed by Lin and colleagues. SEM micrographs showing vertically aligned CNTs on Parylene-C (a,b) and a photo of the transparent flexible CNTs electrodes (c). Reproduced and modified from [116] with permission. Copyright 2009 Elsevier.

Mazzatenta and colleagues [119] further characterised and explored this phenomenon by culturing hippocampal neurons on pristine SWCNT-substrates. They also stimulated neurons electrically through the CNTs film and devised a mathematical model for the description of the electrical interface between neurons and CNTs. This work confirmed the improved synaptic activity observed by Lovat et al. [118], though no remarkable differences in cell morphology or neuronal density were found, suggesting that the reason for the enhanced network activity might have resulted from tighter connections between the neuronal membranes and the conductive CNT-substrates.

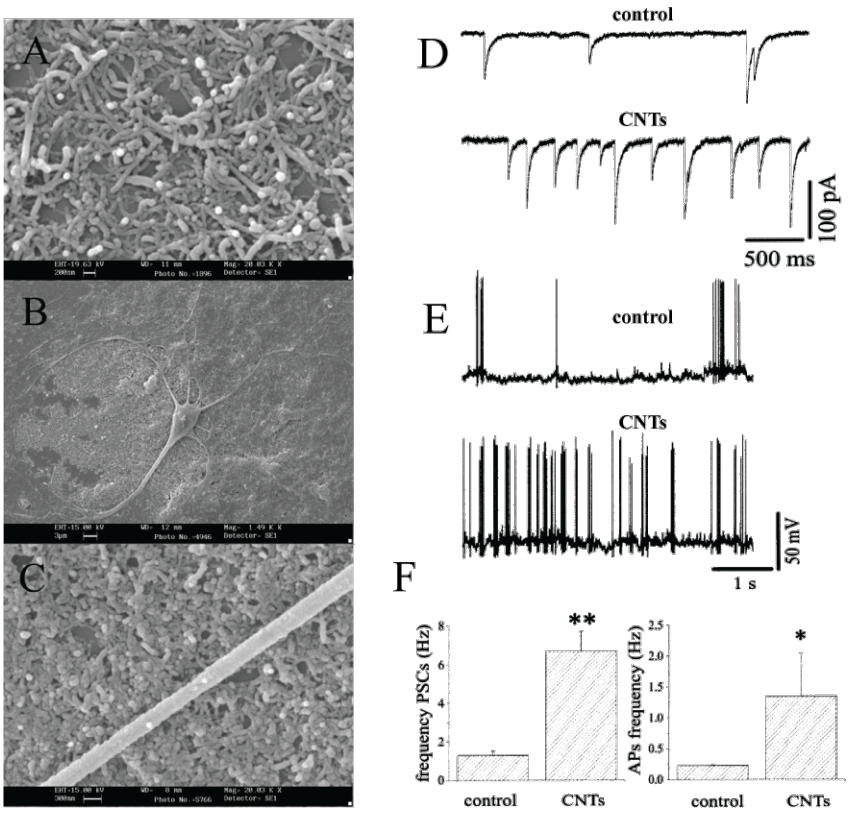

Figure 2: CNTs thin-films are optimal substrates for neuronal growth and development ex vivo (A–C) and improve spontaneous synaptic activity, as shown by the increased frequency of (D) post-synaptic currents and of (E) action potentials. Reproduced and modified from [118] with permission. Copyright 2005 American Chemical Society.

The presence of these intimate connections was then proved, by means of transmission electron microscopy (TEM), high resolution scanning electron microscopy (HRSEM) and immunofluorescence confocal laser scanning (CLS) microscopy, also conducted by Sorkin et al. [120], who suggested a correlation between mechanical forces and neuronal outgrowth, and by Cellot et al. [121], who reported a very tight yet discontinuous contact between CNTs substrates and neuronal membranes.

Another remarkable aspect is that the passive properties of the membrane (i.e., quantified in terms of electrical circuit equivalent, as the input resistance, the membrane capacitance and the resting membrane potential) were comparable to the control conditions [118,119,121,122] (Figure 3d). Ultimately, the increase in spontaneous activity, exhibited by neurons in the presence of CNTs, was not a result of an altered cell morphology.

Cellot and colleagues [121] also focused their efforts on the occurrence of an electrical coupling between CNTs and cell membranes. Using patch-clamp electrophysiology, they showed that CNTs strongly impacted the electrical regenerative properties of neuronal membranes upon inducing depolarising after-potentials, which might be related to Ca^{2+}-mediated electrogenesis and backpropagating APs (Figure 3a,b). It is worth noting that this behaviour was shown to be specifically attributable to CNTs, as it was not observed in neurons growing on other substrates exhibiting large electrical conductivity or nanoscale roughness (Figure 3c). Moreover, in the same work, mathematical modelling and electrophysiology were used to probe a contingent connection between the effects observed at single-neuron level and those detected at the level of neuronal networks, leading to the speculation that the tight discontinuous connections observed between cell bodies and CNTs might act as shortcuts and transfer electrical currents between different neuronal compartments. Cellot and co-workers [123] also investigated the effects of CNTs at the synaptic level and observed not only that growing neurons on CNT-substrates increased the possibility of finding synaptically-connected pairs of cells, but also that CNTs affected synaptic plasticity.

Another interesting feature of CNT-based substrates is that they are able to modulate the developmental onset of neuronal electrical activity in culture, as reported by Fabbro and colleagues

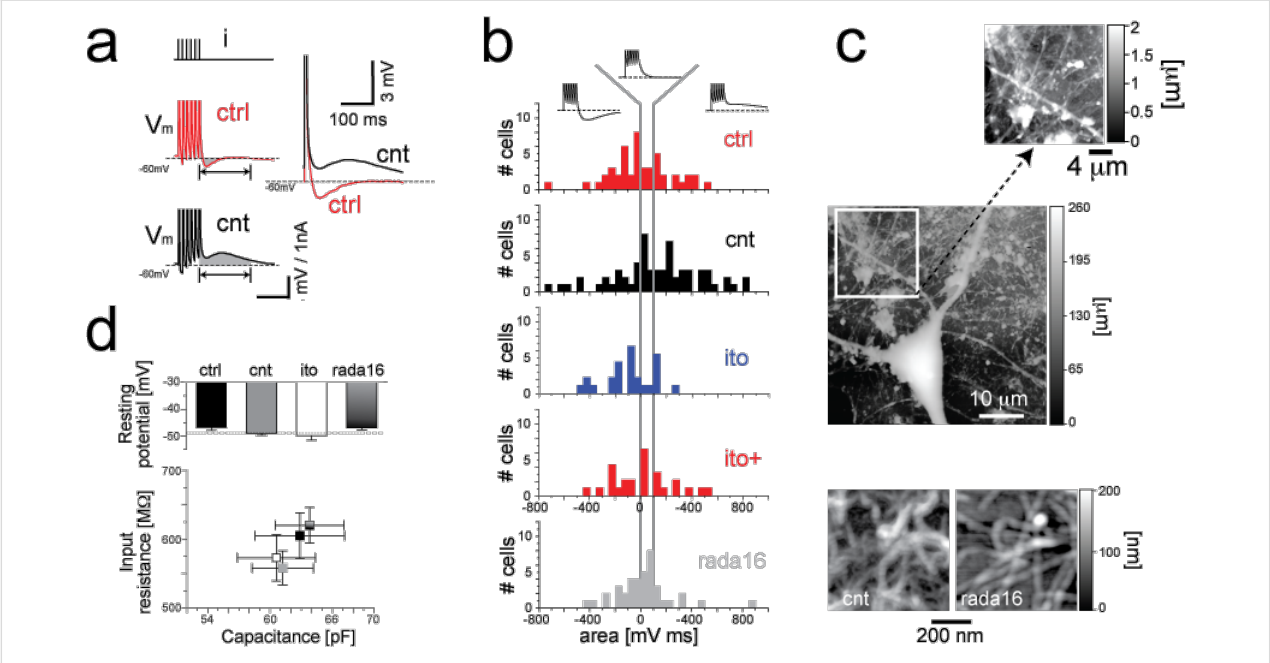

Figure 3: CNTs affect single-neuron excitability, inducing depolarising after-potentials (a). This behaviour is specifically attributable to CNTs, as it has been observed neither for cells grown on smooth and electrically conducting indium tin oxide substrates (ito) nor on electrically-insulating RADA16 peptide thin-films (b), characterised by a similar nanoscale roughness s CNTs (c). The culture substrates do not alter the electrical passive properties of neuronal membranes (d). Reproduced and modified from [121] with permission. Copyright 2009 Nature Publishing Group.

[122]. In their study, the researchers observed that spinal neurons grown on CNTs scaffolds displayed an early developmental onset for generating APs and voltage-gated currents, as well as changes in the expression of genes involved in cell communication, growth, differentiation and in neuronal maturation.

The chronic interface between CNTs and organotypic cultures of embryonic mouse spinal cord and dorsal root ganglia has also been investigated [124]. The researchers observed an improved outgrowth of cellular processes emerging from the dorsal root ganglia, despite having a slightly different morphology than in control conditions. Patch-clamp experiments finally revealed the effect of CNT on spontaneous electrical activity of spinal networks (i.e., an increased amplitude of spontaneous postsynaptic currents), as well as on neuronal signalling (i.e., increased efficacy of synaptic responses, even for neurons located several cell layers away).

NDs: ND particles and thin-films have found applications in neurosciences as substrates for neuronal growth [125-127] and as microelectrode material [128,129], by virtue of their peculiar electrical and chemical properties and stability. Specht et al. [125] were among the first to report on the suitability of ND as a substrate material. By micro-contact printing, they deposited laminin on NDs to form patterned microstructures, on which they then observed the ordered growth of primary cortical neurons.

Neuronal adhesion and cell excitability have been studied by Ariano and co-workers [126] and by Thalhammer and colleagues [130], who observed that oxygen functionalisation [126] and deposition of a layer of 5–10 nm sized ND particles (NDPs) [130] (Figure 4a) improved cell attachment and did not compromise neuronal electrical activity. This has been quantified by patch-clamp electrophysiology in terms of activation of voltage-gated Ca^{2+} channels [126] and of AP firing frequency [130] (Figure 4b). In the same researches, synaptic connectivity was also studied, by evoking inhibitory GABAergic responses [126] and by monitoring the spontaneous excitatory postsynaptic miniature currents (mEPSCs) [130]. The results showed that culturing neurons on ND did not affect synaptic activity.

The use of ND as a platform material for neural interfaces [131] has been studied both in vivo [132], ex vivo [133] and in vitro [128]. For these applications, boron doping of ND [134,135] has often been considered to bestow ND metallic properties, thus enabling superior S/N performances in the detection of neuronal activity and a wider electrochemical window for electrical stimulation.

Ariano et al. [128] developed a ND-based device in order to record the spontaneous extracellular electrical activity in a murine neuronal cell line, which yielded results in good agreement with recordings made by means of conventional MEAs (Figure 5).

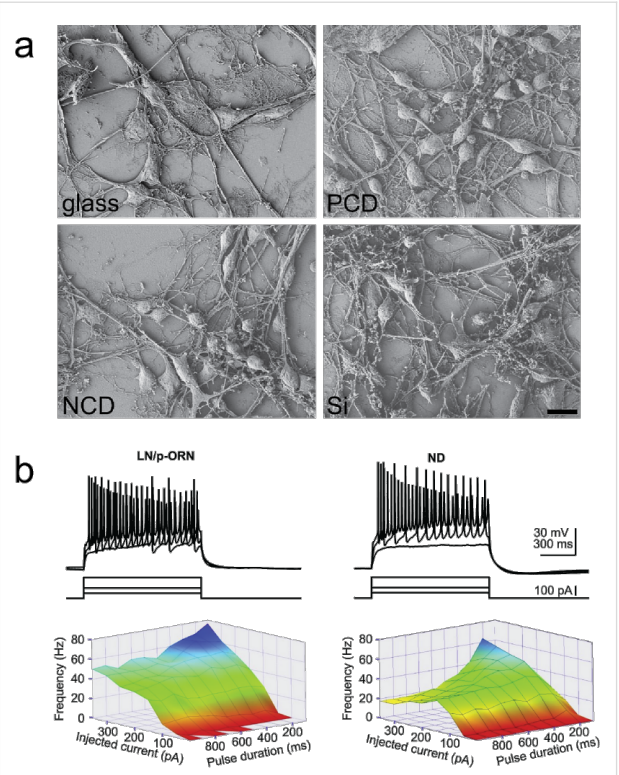

Figure 4: Scanning electron micrographs show that, when exposed to animal blood serum proteins, polycrystalline (PCD) and nanocrystalline diamond (NCD) substrates performed as good as glass or silicon substrates (a). NDs coating did not alter single-cell excitability (b). Reproduced and modified from [130] with permission. Copyright 2010 Elsevier.

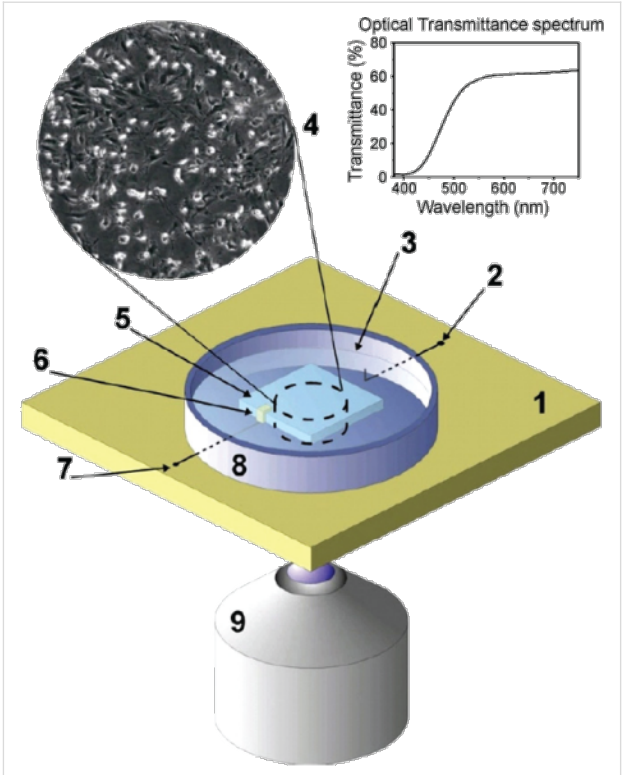

Figure 5: Sketch of the device for recording the extracellular electrical activity of cultured neuronal networks, developed by Ariano and co-workers. Cells (4) are plated in the recording chamber (8), directly onto hydrogen-terminated diamond (5). Reproduced from [128] with permission. Copyright 2009 Elsevier.

Single-spin NV-NDs embedded in an artificial lipid bilayer [136] and in a real cell membrane, in which there is a notable potential drop between the extra- and intracellular compartment, can be used as nanoscopic magnetic sensors of spin labels. Considering the typical values of membrane thickness and membrane potential, the order of magnitude for the expected electric fields is 10^7 V·m^{-1}, which can allow for the measurement of membrane potentials over a millisecond time-scale in real time.

Hall et al. [137] recently proposed the use of a single crystal ND substrate containing a layer of NV as a non-invasive model for a detection set-up based on Förster resonance energy transfer and optically detected magnetic resonance.

Graphene: Researchers have only recently begun to investigate graphene and its derivatives as potential scaffolds for neuronal growth, and as a conductive polymer for bio-interfacing. The interest that graphene has attracted was the result not only of its excellent conductive properties, but also because its nanostructure and its chemical stability render it a good candidate for favouring cell adhesion.

In one of the first studies, Li and co-workers [138] studied the biocompatibility of graphene and the contingent changes in the expression of the protein GAP43, which is associated with the growth of neurites. Their results showed high biocompatibility, and highlighted a longer average length of neurites, as well as better viability for cells grown on graphene, when compared to polystyrene control substrates. The authors also found an overexpression of the GAP43 protein, possibly the result of improved neurites outgrowth due to both the high electrical conductivity of graphene (as in CNTs) and by the wrinkled nanoscale morphology of graphene layer. These properties render graphene a good adhesion substrate to cells.

The use of graphene as an in vitro or an in vivo stimulator device was the primary focus of a study conducted by Heo and colleagues [95], who developed a graphene/PET film to test the effects of a non-contact field stimulation on cell-to-cell coupling. This film was found to be biocompatible and improved cell proliferation and viability compared to those observed in the control cultures; additionally, the electrical stimulation resulted in affecting the regulation of cytoskeleton protein related to cellular mobility, such as actin, resulting in morphological changes in cellular edges.

Sahni et al. [139] compared the neurite outgrowth of rat primary cortical neurons cultured on bare, graphene- and poly-D-lysine (PDL)-coated plastic polymer dishes, and found that neuronal viability showed remarkable differences between graphene and PDL substrates; the morphology of cells cultured on graphene displayed more linear dendritic structures compared to cells cultured on PDL and in control conditions. The improved neuronal adhesion on graphene, compared to the bare plastic polymeric dish, was ascribed by the authors to van der Waals forces between cell membranes and graphene.

Similarly to NDs [140], surface charges can influence adhesion and outgrowth of neuronal cells on graphene substrates. This aspect has been investigated by Tu and colleagues [141], who cultured primary rat hippocampal neurons on carboxylated GO (GO-COOH; negative surface charge; control condition), the surface of which had been chemically modified by functionalisation with three functional groups: methoxy (-OCH_3; almost neutral surface charge), amino (NH_2; positively charged surface) and poly-*m*-aminobenzene sulfonic acid (-NH_2/-SO_3H, PABS; zwitterionic). The viability of neurons after 7 DIV

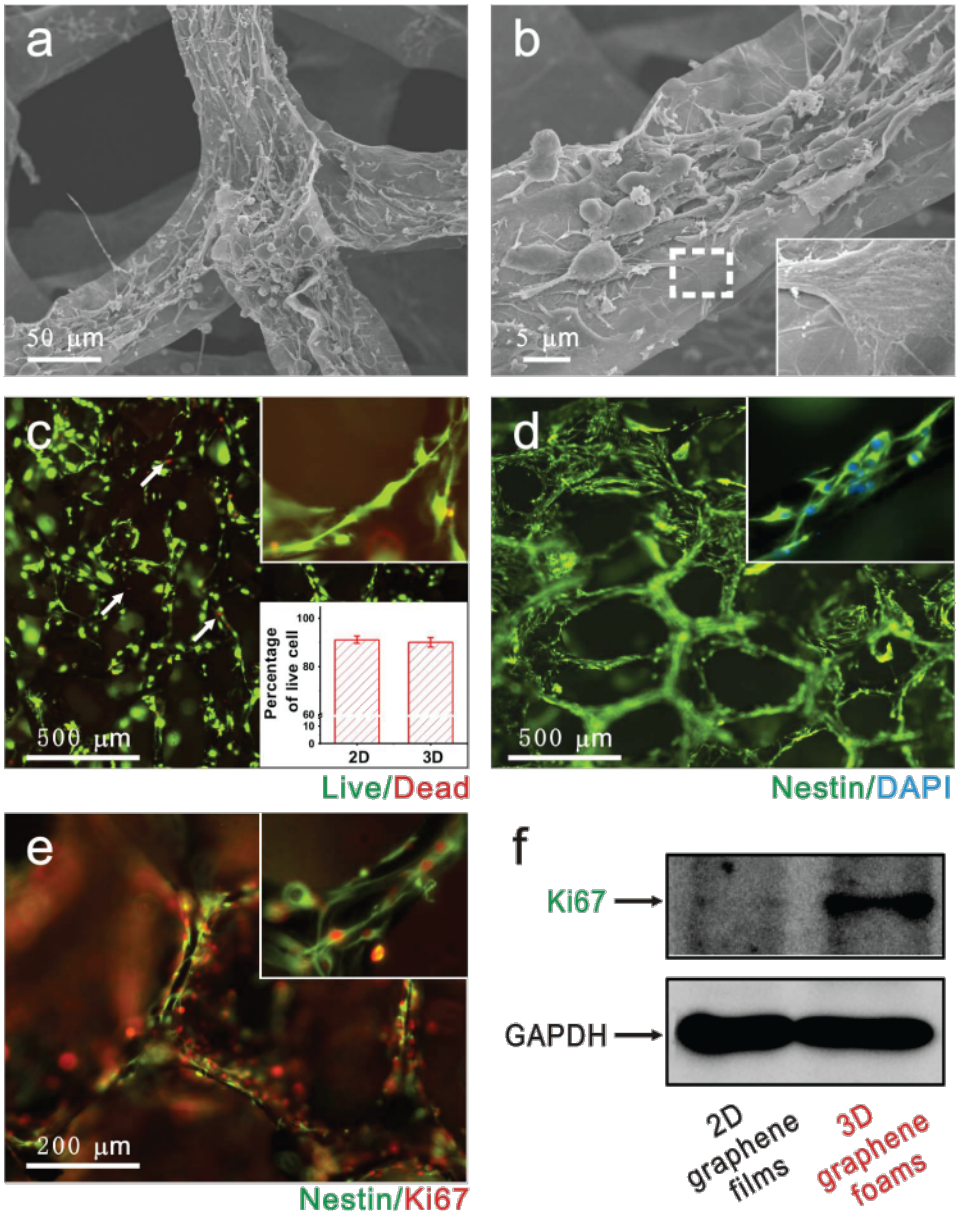

Figure 6: Three-dimensional graphene foam scaffolds allow neural stem cells to adhere and improve their proliferation by up-regulating Ki-67 protein expression. Reproduced from [146] with permission. Copyright 2013 Nature Publishing Group.

was estimated to be over 90% and, although no relevant differences in morphology were observed, neurons cultured on a positively charged surface showed a greater number of neurites per neuron, a longer length of neurites and a greater number of branches per neurite. However, the lack of a direct comparison with the conventional control conditions (i.e., glass or plastic, polymeric, culture substrates) makes it difficult to interpret these results in terms of a possible application for neural stimulation.

Graphene-based substrates have also been investigated as scaffolds for growth and for the differentiation of stem cells [142,143]. The differentiation into neurons of human neural stem cells (hNSCs), cultured on graphene has been studied by Park et al. [144]; the results showed not only an improved differentiation but also an enhanced cell adhesion and neurites formation compared to control conditions. Moreover, the expression of laminin-related receptors and of genes involved in the calcium signalling pathway was up-regulated for hNSCs grown on graphene.

Akhavan et al. [145] studied the differentiation of hNSCs on GO nanogrids deposited on a substrate made of TiO_2 nanoparticles over SiO_2, which made them photosensitive. The authors observed an increase in cell growth and alignment along the geometrical pattern of the nanogrids, further enhanced by means of a repeated photo stimulation.

Li and co-workers [146] designed a three-dimensional graphene foam scaffold for neural stem cells. This scaffold allowed the formation of a three-dimensional neural network, resulting in an excellent substrate for cell adhesion and proliferation by up-regulating Ki-67 protein expression (Figure 6). To test whether such a scaffold could be used as a neural stimulation electrode, its electrochemical properties were investigated by cyclic voltammetry, the results showing that electrical stimulation via a capacitive charge injection was enhanced compared to the use of conventional graphene film electrode; this was due to the larger specific surface area of the three-dimensional scaffold.

Conclusion

In this review, several reasons were established for why carbon-based nanomaterials have gained more importance over the past few years in the context of biomedical applications. We reviewed their most important applications, with an emphasis on the field of neuroscience and underlined their unique affinity for neuronal interfacing.

Ultimately, additional research is required before a complete understanding can be reached concerning how to best engineer these nanomaterials for their use in advanced applications in the fields of neuroscience and neuroprosthetics, as it relates to biocompatibility, biodegradability, biostability and the exact interaction mechanisms between these nanomaterials and neuronal networks. The most recent results in this field, however, are extremely promising and confirm the start of an important new discipline at the interface between nanotechnologies and neuroscience.

Acknowledgements

We are grateful to Drs. C. Bittencourt, M. Prato, L. Ballerini, and M. Nesládek for discussions. We are also grateful to Drs. Henry Markram, Sébastien Lasserre, and the Blue Brain Project team at the EPFL for contributing the graphical abstract. Financial support from the European Commission (FP7-PEOPLE-ITN "NAMASEN", contract n. 264872 and FP7-PEOPLE-IEF “INCA-NANEP”, contract n. 328214; FP7-NMP "MERIDIAN" project, contract n. 280778-02) and from the Belgian Science Policy Office (BELSPO) is kindly acknowledged.

References

1. Iijima, S. *Nature* **1991,** *354,* 56–58. doi:10.1038/354056a0
2. Dresselhaus, M. S.; Dresselhaus, G.; Avouris, P. *Carbon Nanotubes Synthesis, Structure, Properties, and Applications;* Springer: Berlin, Germany, 2001.
3. Wilder, J. W. G.; Venema, L. C.; Rinzler, A. G.; Smalley, R. E.; Dekker, C. *Nature* **1998,** *391,* 59–62. doi:10.1038/34139
4. Charlier, J.-C.; Blase, X.; Roche, S. *Rev. Mod. Phys.* **2007,** *79,* 677–732. doi:10.1103/RevModPhys.79.677
5. Shtogun, Y. V.; Woods, L. M. *J. Phys. Chem. C* **2009,** *113,* 4792–4796. doi:10.1021/jp807206m
6. Oliva-Avilés, A. I.; Avilés, F.; Sosa, V.; Oliva, A. I.; Gamboa, F. *Nanotechnology* **2012,** *23,* 465710. doi:10.1088/0957-4484/23/46/465710
7. Falvo, M. R.; Clary, G. J.; Taylor, R. M., II; Chi, V.; Brooks, F. P., Jr.; Washburn, S.; Superfine, R. *Nature* **1997,** *389,* 582–584. doi:10.1038/39282
8. Field, J. E. *The Properties of natural and synthetic diamond;* Academic Press, 1992.
9. Liu, H. D.; Dandy, D. S. *Diamond chemical vapor deposition: Nucleation and Early Growth Stages;* Noyes Publications: Park Ridge, NJ, United States, 1995.
10. Kulakova, I. I. *Phys. Solid State* **2004,** *46,* 636–643. doi:10.1134/1.1711440
11. Dement'ev, A. P.; Maslakov, K. I. *Phys. Solid State* **2004,** *46,* 678–680. doi:10.1134/1.1711450
12. Palosz, B.; Pantea, C.; Grzanka, E.; Stelmakh, S.; Proffen, Th.; Zerda, T. W.; Palosz, W. *Diamond Relat. Mater.* **2006,** *15,* 1813–1817. doi:10.1016/j.diamond.2006.09.001
13. Krüger, A.; Kataoka, F.; Ozawa, M.; Fujino, T.; Suzuki, Y.; Aleksenskii, A. E.; Vul', A. Ya.; Ōsawa, E. *Carbon* **2005,** *43,* 1722–1730. doi:10.1016/j.carbon.2005.02.020
14. Krüger, A.; Liang, Y.; Jarre, G.; Stegk, J. *J. Mater. Chem.* **2006,** *16,* 2322. doi:10.1039/b601325b

15. Aharonovich, I.; Castelletto, S.; Simpson, D. A.; Su, C.-H.; Greentree, A. D.; Prawer, S. *Rep. Prog. Phys.* **2011,** *74,* 076501. doi:10.1088/0034-4885/74/7/076501
16. Aleksenskii, A. E.; Osipov, V. Yu.; Vul', A. Ya.; Ber, B. Ya.; Smirnov, A. B.; Melekhin, V. G.; Adriaenssens, G. J.; Iakoubovskii, K. *Phys. Solid State* **2001,** *43,* 145–150. doi:10.1134/1.1340200
17. Kompan, M. E.; Terukov, E. I.; Gordeev, S. K.; Zhukov, S. G.; Nikolaev, Yu. A. *Phys. Solid State* **1997,** *39,* 1928–1929. doi:10.1134/1.1130202
18. Doherty, M. W.; Manson, N. B.; Delaney, P.; Jelezko, F.; Wrachtrup, J.; Hollenberg, L. C. L. *Phys. Rep.* **2013,** *528,* 1–45. doi:10.1016/j.physrep.2013.02.001
19. Lee, S.-Y.; Widmann, M.; Rendler, T.; Doherty, M. W.; Babinec, T. M.; Yang, S.; Eyer, M.; Siyushev, P.; Hausmann, B. J. M.; Loncar, M.; Bodrog, Z.; Gali, A.; Manson, N. B.; Fedder, H.; Wrachtrup, J. *Nat. Nanotechnol.* **2013,** *8,* 487–492. doi:10.1038/nnano.2013.104
20. Wrachtrup, J.; Jelezko, F. *J. Phys.: Condens. Matter* **2006,** *18,* S807–S824. doi:10.1088/0953-8984/18/21/S08
21. Tisler, J.; Balasubramanian, G.; Naydenov, B.; Kolesov, R.; Grotz, B.; Reuter, R.; Boudou, J.-P.; Curmi, P. A.; Sennour, M.; Thorel, A.; Börsch, M.; Aulenbacher, K.; Erdmann, R.; Hemmer, P. R.; Jelezko, F.; Wrachtrup, J. *ACS Nano* **2009,** *3,* 1959–1965. doi:10.1021/nn9003617
22. Novoselov, K. S.; Geim, A. K.; Morozov, S. V.; Jiang, D.; Zhang, Y.; Dubonos, S. V.; Grigorieva, I. V.; Firsov, A. A. *Science* **2004,** *306,* 666–669. doi:10.1126/science.1102896
23. Peierls, R. E. *Ann. Inst. Henri Poincare* **1935,** *5,* 177–222.
24. Mermin, N. D. *Phys. Rev.* **1968,** *176,* 250–254. doi:10.1103/PhysRev.176.250
25. Novoselov, K. S.; Jiang, Z.; Zhang, Y.; Morozov, S. V.; Stormer, H. L.; Zeitler, U.; Maan, J. C.; Boebinger, G. S.; Kim, P.; Geim, A. K. *Science* **2007,** *315,* 1379. doi:10.1126/science.1137201
26. Bolotin, K. I.; Sikes, K. J.; Jiang, Z.; Klima, M.; Fudenberg, G.; Hone, J.; Kim, P.; Stormer, H. L. *Solid State Commun.* **2008,** *146,* 351–355. doi:10.1016/j.ssc.2008.02.024
27. Novoselov, K. S.; Jiang, D.; Schedin, F.; Booth, T. J.; Khotkevich, V. V.; Morozov, S. V.; Geim, A. K. *Proc. Natl. Acad. Sci. U. S. A.* **2005,** *102,* 10451–10453. doi:10.1073/pnas.0502848102
28. Katsnelson, M. I.; Novoselov, K. S.; Geim, A. K. *Nat. Phys.* **2006,** *2,* 620–625. doi:10.1038/nphys384
29. Lee, C.; Wei, X.; Kysar, J. W.; Hone, J. *Science* **2008,** *321,* 385–388. doi:10.1126/science.1157996
30. Nair, R. R.; Blake, P.; Grigorenko, A. N.; Novoselov, K. S.; Booth, T. J.; Stauber, T.; Peres, N. M. R.; Geim, A. K. *Science* **2008,** *320,* 1308. doi:10.1126/science.1156965
31. Stoller, M. D.; Park, S.; Zhu, Y.; An, J.; Ruoff, R. S. *Nano Lett.* **2008,** *8,* 3498–3502. doi:10.1021/nl802558y
32. Yang, Z.; Zhang, Y.; Yang, Y.; Sun, L.; Han, D.; Li, H.; Wang, C. *Nanomedicine* **2010,** *6,* 427–441. doi:10.1016/j.nano.2009.11.007
33. Flavin, K.; Kopf, I.; Del Canto, E.; Navio, C.; Bittencourt, C.; Giordani, S. *J. Mater. Chem.* **2011,** *21,* 17881. doi:10.1039/c1jm12217g
34. Georgakilas, V.; Kordatos, K.; Prato, M.; Guldi, D. M.; Holzinger, M.; Hirsch, A. *J. Am. Chem. Soc.* **2002,** *124,* 760–761. doi:10.1021/ja016954m
35. Richard, C.; Balavoine, F.; Schultz, P.; Ebbesen, T. W.; Mioskowski, C. *Science* **2003,** *300,* 775–778. doi:10.1126/science.1080848
36. Zheng, M.; Jagota, A.; Semke, E. D.; Diner, B. A.; McLean, R. S.; Lustig, S. R.; Richardson, R. E.; Tassi, N. G. *Nat. Mater.* **2003,** *2,* 338–342. doi:10.1038/nmat877
37. Dyke, C. A.; Tour, J. M. *Chem. – Eur. J.* **2004,** *10,* 812–817. doi:10.1002/chem.200305534
38. Dyke, C. A.; Tour, J. M. *J. Phys. Chem. A* **2004,** *108,* 11151–11159. doi:10.1021/jp046274g
39. Tagmatarchis, N.; Prato, M. *J. Mater. Chem.* **2004,** *14,* 437. doi:10.1039/b314039c
40. Khabashesku, V. N. *Russ. Chem. Rev.* **2011,** *80,* 705–725. doi:10.1070/RC2011v080n08ABEH004232
41. Coleman, K. S.; Bailey, S. R.; Fogden, S.; Green, M. L. H. *J. Am. Chem. Soc.* **2003,** *125,* 8722–8723. doi:10.1021/ja0355675
42. Liang, F.; Sadana, A. K.; Peera, A.; Chattopadhyay, J.; Gu, Z.; Hauge, R. H.; Billups, W. E. *Nano Lett.* **2004,** *4,* 1257–1260. doi:10.1021/nl049428c
43. Yang, M.; Flavin, K.; Kopf, I.; Radics, G.; Hearnden, C. H.; McManus, G. J.; Moran, B.; Villalta-Cerdas, A.; Echegoyen, L. A.; Giordani, S.; Lavelle, E. C. *Small* **2013,** *9,* 4194–4206. doi:10.1002/smll.201300481
44. Porter, A. E.; Gass, M.; Muller, K.; Skepper, J. N.; Midgley, P. A.; Welland, M. *Nat. Nanotechnol.* **2007,** *2,* 713–717. doi:10.1038/nnano.2007.347
45. Shvedova, A. A.; Kisin, E. R.; Mercer, R.; Murray, A. R.; Johnson, V. J.; Potapovich, A. I.; Tyurina, Y. Y.; Gorelik, O.; Arepalli, S.; Schwegler-Berry, D.; Hubbs, A. F.; Antonini, J.; Evans, D. E.; Ku, B. K.; Ramsey, D.; Maynard, A.; Kagan, V. E.; Castanova, V.; Baron, P. *Am. J. Physiol.: Lung Cell. Mol. Physiol.* **2005,** *289,* L698–L708. doi:10.1152/ajplung.00084.2005
46. Poland, C. A.; Duffin, R.; Kinloch, I.; Maynard, A.; Wallace, W. A. H.; Seaton, A.; Stone, V.; Brown, S.; Macnee, W.; Donaldson, K. *Nat. Nanotechnol.* **2008,** *3,* 423–428. doi:10.1038/nnano.2008.111
47. Bottini, M.; Bruckner, S.; Nika, K.; Bottini, N.; Bellucci, S.; Magrini, A.; Bergamaschi, A.; Mustelin, T. *Toxicol. Lett.* **2006,** *160,* 121–126. doi:10.1016/j.toxlet.2005.06.020
48. Ding, L.; Stilwell, J.; Zhang, T.; Elboudwarej, O.; Jiang, H.; Selegue, J. P.; Cooke, P. A.; Gray, J. W.; Chen, F. F. *Nano Lett.* **2005,** *5,* 2448–2464. doi:10.1021/nl051748o
49. Dumortier, H.; Lacotte, S.; Pastorin, G.; Marega, R.; Wu, W.; Bonifazi, D.; Briand, J. P.; Prato, M.; Muller, S.; Bianco, A. *Nano Lett.* **2006,** *6,* 1522–1528. doi:10.1021/nl061160x
50. Yehia, H. N.; Draper, R. K.; Mikoryak, C.; Walker, E. K.; Bajaj, P.; Musselman, I. H.; Daigrepont, M. C.; Dieckmann, G. R.; Pantano, P. *J. Nanobiotechnol.* **2007,** *5,* No. 8. doi:10.1186/1477-3155-5-8
51. Wu, W.; Li, R.; Bian, X.; Zhu, Z.; Ding, D.; Li, X.; Jia, Z.; Jiang, X.; Hu, Y. *ACS Nano* **2009,** *3,* 2740–2750. doi:10.1021/nn9005686
52. Pantarotto, D.; Singh, R.; McCarthy, D.; Erhardt, M.; Briand, J.-P.; Prato, M.; Kostarelos, K.; Bianco, A. *Angew. Chem.* **2004,** *116,* 5354–5358. doi:10.1002/ange.200460437
53. Gao, L.; Nie, L.; Wang, T.; Qin, Y.; Guo, Z.; Yang, D.; Yan, X. *ChemBioChem* **2006,** *7,* 239–242. doi:10.1002/cbic.200500227
54. Cella, L. N.; Chen, W.; Myung, N. V.; Mulchandani, A. *J. Am. Chem. Soc.* **2010,** *132,* 5024–5026. doi:10.1021/ja100503b
55. Madani, S. Y.; Naderi, N.; Dissanayake, O.; Tan, A.; Seifalian, A. M. *Int. J. Nanomed.* **2011,** *6,* 2963–2979. doi:10.2147/IJN.S16923
56. Elhissi, A. M. A.; Ahmed, W.; Ul Hassan, I.; Dhanak, V. R.; D'Emanuele, A. *J. Drug Delivery* **2012,** 837327. doi:10.1155/2012/837327
57. Hirata, E.; Uo, M.; Takita, H.; Akasaka, T.; Watari, F.; Yokoyama, A. *Carbon* **2011,** *49,* 3284–3291. doi:10.1016/j.carbon.2011.04.002

58. Zavaleta, C.; de la Zerda, A.; Liu, Z.; Keren, S.; Cheng, Z.; Schipper, M.; Chen, X.; Dai, H.; Gambhir, S. S. *Nano Lett.* **2008,** *8,* 2800–2805. doi:10.1021/nl801362a
59. Jin, H.; Heller, D. A.; Strano, M. S. *Nano Lett.* **2008,** *8,* 1577–1585. doi:10.1021/nl072969s
60. Sucapane, A.; Cellot, G.; Prato, M.; Giugliano, M.; Parpura, V.; Ballerini, L. *J. Nanoneurosci.* **2009,** *1,* 10–16. doi:10.1166/jns.2009.002
61. Chan, V.; Raman, R.; Cvetkovic, C.; Bashir, R. *ACS Nano* **2013,** *7,* 1830–1837. doi:10.1021/nn401098c
62. Martinelli, V.; Cellot, G.; Toma, F. M.; Long, C. S.; Caldwell, J. H.; Zentilin, L.; Giacca, M.; Turco, A.; Prato, M.; Ballerini, L.; Mestroni, L. *Nano Lett.* **2012,** *12,* 1831–1838. doi:10.1021/nl204064s
63. Martinelli, V.; Cellot, G.; Toma, F. M.; Long, C. S.; Caldwell, J. H.; Zentilin, L.; Giacca, M.; Turco, A.; Prato, M.; Ballerini, L.; Mestroni, L. *ACS Nano* **2013,** *7,* 5746–5756. doi:10.1021/nn4002193
64. Lin, Z. Q.; Liu, L. H.; Xi, Z. G.; Huang, J. H.; Lin, B. C. *Int. J. Nanomed.* **2012,** *7,* 4199–4206. doi:10.2147/IJN.S34663
65. Huang, H.; Pierstorff, E.; Ōsawa, E.; Ho, D. *Nano Lett.* **2007,** *7,* 3305–3314. doi:10.1021/nl071521o
66. Li, J.; Zhu, Y.; Li, W.; Zhang, X.; Peng, Y.; Huang, Q. *Biomaterials* **2010,** *31,* 8410–8418. doi:10.1016/j.biomaterials.2010.07.058
67. Metzler, P.; von Wilmowsky, C.; Stadlinger, B.; Zemann, W.; Schlegel, K. A.; Rosiwal, S.; Rupprecht, S. *J. Cranio-Maxillofacial Surg.* **2013,** *41,* 532–538. doi:10.1016/j.jcms.2012.11.020
68. Chang, I. P.; Hwang, K. C.; Chiang, C.-S. *J. Am. Chem. Soc.* **2008,** *130,* 15476–15481. doi:10.1021/ja804253y
69. Yu, S.-J.; Kang, M.-W.; Chang, H.-C.; Chen, K.-M.; Yu, Y.-C. *J. Am. Chem. Soc.* **2005,** *127,* 17604–17605. doi:10.1021/ja0567081
70. Schrand, A. M.; Dai, L.; Schlager, J. J.; Hussain, S. M.; Ōsawa, E. *Diamond Relat. Mater.* **2007,** *16,* 2118–2123. doi:10.1016/j.diamond.2007.07.020
71. Schrand, A. M.; Huang, H.; Carlson, C.; Schlager, J. J.; Omacr Sawa, E.; Hussain, S. M.; Dai, L. *J. Phys. Chem. B* **2007,** *111,* 2–7. doi:10.1021/jp066387v
72. Schrand, A. M.; Lin, J. B. Characterization of Detonation Nanodiamonds. In *Ultrananocrystalline Diamond,* 2nd ed.; Shenderova, O. A.; Gruen, D. M., Eds.; Elsevier, 2012; pp 519–548. doi:10.1016/B978-1-4377-3465-2.00016-5
73. Bakowicz-Mitura, K.; Bartosz, G.; Mitura, S. *Surf. Coat. Technol.* **2007,** *201,* 6131–6135. doi:10.1016/j.surfcoat.2006.08.142
74. Xing, Y.; Xiong, W.; Zhu, L.; Ōsawa, E.; Hussin, S.; Dai, L. *ACS Nano* **2011,** *5,* 2376–2384. doi:10.1021/nn200279k
75. Vaijayanthimala, V.; Tzeng, Y.-K.; Chang, H.-C.; Li, C.-L. *Nanotechnology* **2009,** *20,* 425103. doi:10.1088/0957-4484/20/42/425103
76. Schrand, A. M.; Lin, J. B.; Hens, S. C.; Hussain, S. M. *Nanoscale* **2011,** *3,* 435–445. doi:10.1039/c0nr00408a
77. Yuan, Y.; Wang, X.; Jia, G.; Liu, J.-H.; Wang, T.; Gu, Y.; Yang, S.-T.; Zhen, S.; Wang, H.; Liu, Y. *Diamond Relat. Mater.* **2010,** *19,* 291–299. doi:10.1016/j.diamond.2009.11.022
78. Puzyr, A. P.; Baron, A. V.; Purtov, K. V.; Bortnikov, E. V.; Skobelev, N. N.; Mogilnaya, O. A.; Bondar, V. S. *Diamond Relat. Mater.* **2007,** *16,* 2124–2128. doi:10.1016/j.diamond.2007.07.025
79. Yuan, Y.; Chen, Y.; Liu, J.-H.; Wang, H.; Liu, Y. *Diamond Relat. Mater.* **2009,** *18,* 95–100. doi:10.1016/j.diamond.2008.10.031
80. Rojas, S.; Gispert, J. D.; Martín, R.; Abad, S.; Menchón, C.; Pareto, D.; Victor, V. M.; Álvaro, M.; García, H.; Herance, J. R. *ACS Nano* **2011,** *5,* 5552–5559. doi:10.1021/nn200986z
81. Lam, R.; Chen, M.; Pierstorff, E.; Huang, H.; Ōsawa, E.; Ho, D. *ACS Nano* **2008,** *2,* 2095–2102. doi:10.1021/nn800465x
82. Chen, M.; Pierstorff, E. D.; Lam, R.; Li, S. Y.; Huang, H.; Ōsawa, E.; Ho, D. *ACS Nano* **2009,** *3,* 2016–2022. doi:10.1021/nn900480m
83. Adnan, A.; Lam, R.; Chen, H.; Lee, J.; Schaffer, D. J.; Barnard, A. S.; Schatz, G. C.; Ho, D.; Liu, W. K. *Mol. Pharmaceutics* **2011,** *8,* 368–374. doi:10.1021/mp1002398
84. Li, Y.; Zhou, X.; Wang, D.; Yang, B.; Yang, P. *J. Mater. Chem.* **2011,** *21,* 16406. doi:10.1039/c1jm10926j
85. Bondar', V. S.; Pozdnyakova, I. O.; Puzyr', A. P. *Phys. Solid State* **2004,** *46,* 758–760. doi:10.1134/1.1711468
86. Kong, X. L.; Huang, L. C. L.; Hsu, C.-M.; Chen, W.-H.; Han, C.-C.; Chang, H.-C. *Anal. Chem.* **2005,** *77,* 259–265. doi:10.1021/ac048971a
87. Akhavan, O.; Ghaderi, E.; Akhavan, A. *Biomaterials* **2012,** *33,* 8017–8025. doi:10.1016/j.biomaterials.2012.07.040
88. Chang, Y.; Yang, S.-T.; Liu, J.-H.; Dong, E.; Wang, Y.; Cao, A.; Liu, Y.; Wang, H. *Toxicol. Lett.* **2011,** *200,* 201–210. doi:10.1016/j.toxlet.2010.11.016
89. Yuan, J.; Gao, H.; Sui, J.; Duan, H.; Chen, W. N.; Ching, C. B. *Toxicol. Sci.* **2012,** *126,* 149–161. doi:10.1093/toxsci/kfr332
90. Yue, H.; Wei, W.; Yue, Z.; Wang, B.; Luo, N.; Gao, Y.; Ma, D.; Ma, G.; Su, Z. *Biomaterials* **2012,** *33,* 4013–4021. doi:10.1016/j.biomaterials.2012.02.021
91. Feng, L.; Zhang, S.; Liu, Z. *Nanoscale* **2011,** *3,* 1252–1257. doi:10.1039/c0nr00680g
92. Sun, X.; Liu, Z.; Welsher, K.; Robinson, J. T.; Goodwin, A.; Zaric, S.; Dai, H. *Nano Res.* **2008,** *1,* 203–212. doi:10.1007/s12274-008-8021-8
93. Hong, H.; Yang, K.; Zhang, Y.; Engle, J. W.; Feng, L.; Yang, Y.; Nayak, T. R.; Goel, S.; Bean, J.; Theuer, C. P.; Barnhart, T. E.; Liu, Z.; Cai, W. *ACS Nano* **2012,** *6,* 2361–2370. doi:10.1021/nn204625e
94. Kalbacova, M.; Broz, A.; Kong, J.; Kalbac, M. *Carbon* **2010,** *48,* 4323–4329. doi:10.1016/j.carbon.2010.07.045
95. Heo, C.; Yoo, J.; Lee, S.; Jo, A.; Jung, S.; Yoo, H.; Lee, Y. H.; Suh, M. *Biomaterials* **2011,** *32,* 19–27. doi:10.1016/j.biomaterials.2010.08.095
96. Yang, K.; Zhang, S.; Zhang, G.; Sun, X.; Lee, S.-T.; Liu, Z. *Nano Lett.* **2010,** *10,* 3318–3323. doi:10.1021/nl100996u
97. Yang, K.; Wan, J.; Zhang, S.; Tian, B.; Zhang, Y.; Liu, Z. *Biomaterials* **2012,** *33,* 2206–2214. doi:10.1016/j.biomaterials.2011.11.064
98. Dey, R. S.; Raj, C. R. *J. Phys. Chem. C* **2010,** *114,* 21427–21433. doi:10.1021/jp105895a
99. Tang, L.; Wang, Y.; Li, Y.; Feng, H.; Lu, J.; Li, J. *Adv. Funct. Mater.* **2009,** *19,* 2782–2789. doi:10.1002/adfm.200900377
100. Kim, Y. R.; Bong, S.; Kang, Y. J.; Yang, Y.; Mahajan, R. K.; Kim, J. S.; Kim, H. *Biosens. Bioelectron.* **2010,** *25,* 2366–2369. doi:10.1016/j.bios.2010.02.031
101. Sun, C.-L.; Lee, H.-H.; Yang, J.-M.; Wu, C.-C. *Biosens. Bioelectron.* **2011,** *26,* 3450–3455. doi:10.1016/j.bios.2011.01.023
102. Yang, X.; Zhang, X.; Liu, Z.; Ma, Y.; Huang, Y.; Chen, Y. *J. Phys. Chem. C* **2008,** *112,* 17554–17558. doi:10.1021/jp806751k
103. Zhang, L.; Xia, J.; Zhao, Q.; Liu, L.; Zhang, Z. *Small* **2010,** *6,* 537–544. doi:10.1002/smll.200901680
104. Weaver, C. L.; Larosa, J. M.; Luo, X.; Cui, X. T. *ACS Nano* **2014,** *8,* 1834–1843. doi:10.1021/nn406223e
105. Mattson, M. P.; Haddon, R. C.; Rao, A. M. *J. Mol. Neurosci.* **2000,** *14,* 175–182. doi:10.1385/JMN:14:3:175

106. Voge, C. M.; Stegemann, J. P. *J. Neural Eng.* **2011,** *8,* 011001. doi:10.1088/1741-2560/8/1/011001
107. Malarkey, E. B.; Parpura, V. *Neurodegener. Dis.* **2007,** *4,* 292–299. doi:10.1159/000101885
108. Ben-Jacob, E.; Hanein, Y. *J. Mater. Chem.* **2008,** *18,* 5181. doi:10.1039/b805878b
109. Keefer, E. W.; Botterman, B. R.; Romero, M. I.; Rossi, A. F.; Gross, G. W. *Nat. Nanotechnol.* **2008,** *3,* 434–439. doi:10.1038/nnano.2008.174
110. Malarkey, E. B.; Fisher, K. A.; Bekyarova, E.; Liu, W.; Haddon, R. C.; Parpura, V. *Nano Lett.* **2009,** *9,* 264–268. doi:10.1021/nl802855c
111. Gabay, T.; Ben-David, M.; Kalifa, I.; Sorkin, R.; Abrams, Z. R.; Ben-Jacob, E.; Hanein, Y. *Nanotechnology* **2007,** *18,* 035201. doi:10.1088/0957-4484/18/3/035201
112. Gabriel, G.; Gómez, R.; Bongard, M.; Benito, N.; Fernández, E.; Villa, R. *Biosens. Bioelectron.* **2009,** *24,* 1942–1948. doi:10.1016/j.bios.2008.09.036
113. Shein, M.; Greenbaum, A.; Gabay, T.; Sorkin, R.; David-Pur, M.; Ben-Jacob, E.; Hanein, Y. *Biomed. Microdevices* **2009,** *11,* 495–501. doi:10.1007/s10544-008-9255-7
114. Fuchsberger, K.; Le Goff, A.; Gambazzi, L.; Toma, F. M.; Goldoni, A.; Giugliano, M.; Stelzle, M.; Prato, M. *Small* **2011,** *7,* 524–530. doi:10.1002/smll.201001640
115. Gerwig, R.; Fuchsberger, K.; Schroeppel, B.; Link, G. S.; Heusel, G.; Kraushaar, U.; Schuhmann, W.; Stett, A.; Stelzle, M. *Front. Neuroeng.* **2012,** *5,* No. 8. doi:10.3389/fneng.2012.00008
116. Lin, C.-M.; Lee, Y.-T.; Yeh, S.-R.; Fang, W. *Biosens. Bioelectron.* **2009,** *24,* 2791–2797. doi:10.1016/j.bios.2009.02.005
117. David-Pur, M.; Bareket-Keren, L.; Beit-Yaakov, G.; Raz-Prag, D.; Hanein, Y. *Biomed. Microdevices* **2014,** *16,* 43–53. doi:10.1007/s10544-013-9804-6
118. Lovat, V.; Pantarotto, D.; Lagostena, L.; Cacciari, B.; Grandolfo, M.; Righi, M.; Spalluto, G.; Prato, M.; Ballerini, L. *Nano Lett.* **2005,** *5,* 1107–1110. doi:10.1021/nl050637m
119. Mazzatenta, A.; Giugliano, M.; Campidelli, S.; Gambazzi, L.; Businaro, L.; Markram, H.; Prato, M.; Ballerini, L. *J. Neurosci.* **2007,** *27,* 6931–6936. doi:10.1523/JNEUROSCI.1051-07.2007
120. Sorkin, R.; Greenbaum, A.; David-Pur, M.; Anava, S.; Ayali, A.; Ben-Jacob, E.; Hanein, Y. *Nanotechnology* **2009,** *20,* 015101. doi:10.1088/0957-4484/20/1/015101
121. Cellot, G.; Cilia, E.; Cipollone, S.; Rancic, V.; Sucapane, A.; Giordani, S.; Gambazzi, L.; Markram, H.; Grandolfo, M.; Scaini, D.; Gelain, F.; Casalis, L.; Prato, M.; Giugliano, M.; Ballerini, L. *Nat. Nanotechnol.* **2009,** *4,* 126–133. doi:10.1038/nnano.2008.374
122. Fabbro, A.; Sucapane, A.; Toma, F. M.; Calura, E.; Rizzetto, L.; Carrieri, C.; Roncaglia, P.; Martinelli, V.; Scaini, D.; Masten, L.; Turco, A.; Gustincich, S.; Prato, M.; Ballerini, L. *PLoS One* **2013,** *8,* No. e73621. doi:10.1371/journal.pone.0073621
123. Cellot, G.; Toma, F. M.; Varley, Z. K.; Laishram, J.; Villari, A.; Quintana, M.; Cipollone, S.; Prato, M.; Ballerini, L. *J. Neurosci.* **2011,** *31,* 12945–12953. doi:10.1523/JNEUROSCI.1332-11.2011
124. Fabbro, A.; Villari, A.; Laishram, J.; Scaini, D.; Toma, F. M.; Turco, A.; Prato, M.; Ballerini, L. *ACS Nano* **2012,** *6,* 2041–2055. doi:10.1021/nn203519r
125. Specht, C. G.; Williams, O. A.; Jackman, R. B.; Schoepfer, R. *Biomaterials* **2004,** *25,* 4073–4078. doi:10.1016/j.biomaterials.2003.11.006
126. Ariano, P.; Baldelli, P.; Carbone, E.; Gilardino, A.; Lo Giudice, A.; Lovisolo, D.; Manfredotti, C.; Novara, M.; Sternschulte, H.; Vittone, E. *Diamond Relat. Mater.* **2005,** *14,* 669–674. doi:10.1016/j.diamond.2004.11.021
127. May, P. W.; Regan, E. M.; Taylor, A.; Uney, J.; Dick, A. D.; McGeehan, J. *Diamond Relat. Mater.* **2012,** *23,* 100–104. doi:10.1016/j.diamond.2012.01.023
128. Ariano, P.; Lo Giudice, A.; Marcantoni, A.; Vittone, E.; Carbone, E.; Lovisolo, D. *Biosens. Bioelectron.* **2009,** *24,* 2046–2050. doi:10.1016/j.bios.2008.10.017
129. Ho-Yin, C.; Aslam, D. M.; Wiler, J. A.; Casey, B. *J. Microelectromech. Syst.* **2009,** *18,* 511–521. doi:10.1109/JMEMS.2009.2015493
130. Thalhammer, A.; Edgington, R. J.; Cingolani, L. A.; Schoepfer, R.; Jackman, R. B. *Biomaterials* **2010,** *31,* 2097–2104. doi:10.1016/j.biomaterials.2009.11.109
131. Garrett, D. J.; Ganesan, K.; Stacey, A.; Fox, K.; Meffin, H.; Prawer, S. *J. Neural Eng.* **2012,** *9,* 016002. doi:10.1088/1741-2560/9/1/016002
132. Halpern, J. M.; Cullins, M. J.; Chiel, H. J.; Martin, H. B. *Diamond Relat. Mater.* **2010,** *19,* 178–181. doi:10.1016/j.diamond.2009.08.006
133. Bonnauron, M.; Saada, S.; Mer, C.; Gesset, C.; Williams, O. A.; Rousseau, L.; Scorsone, E.; Mailley, P.; Nesladek, M.; Arnault, J.-C.; Bergonzo, P. *Phys. Status Solidi A* **2008,** *205,* 2126–2129. doi:10.1002/pssa.200879733
134. Feoktistov, N. A.; Grudinkin, S. A.; Rybin, M. V.; Smirnov, A. N.; Aleksenskii, A. E.; Vul', A. Y.; Golubev, V. G. *Tech. Phys. Lett.* **2011,** *37,* 322–325. doi:10.1134/S1063785011040079
135. Bennet, K.; Lee, K.; Kruchowski, J.; Chang, S.-Y.; Marsh, M.; Van Orsow, A.; Paez, A.; Manciu, F. *Materials* **2013,** *6,* 5726–5741. doi:10.3390/ma6125726
136. Kaufmann, S.; Simpson, D. A.; Hall, L. T.; Perunicic, V.; Senn, P.; Steinert, S.; McGuinness, L. P.; Johnson, B. C.; Ohshima, T.; Caruso, F.; Wrachtrup, J.; Scholten, R. E.; Mulvaney, P.; Hollenberg, L. *Proc. Natl. Acad. Sci. U. S. A.* **2013,** *110,* 10894–10898. doi:10.1073/pnas.1300640110
137. Hall, L. T.; Beart, G. C. C.; Thomas, E. A.; Simpson, D. A.; McGuinness, L. P.; Cole, J. H.; Manton, J. H.; Scholten, R. E.; Jelezko, F.; Wrachtrup, J.; Petrou, S.; Hollenberg, L. C. L. *Sci. Rep.* **2012,** *2,* No. 401. doi:10.1038/srep00401
138. Li, N.; Zhang, X.; Song, Q.; Su, R.; Zhang, Q.; Kong, T.; Liu, L.; Jin, G.; Tang, M.; Cheng, G. *Biomaterials* **2011,** *32,* 9374–9382. doi:10.1016/j.biomaterials.2011.08.065
139. Sahni, D.; Jea, A.; Mata, J. A.; Marcano, D. C.; Sivaganesan, A.; Berlin, J. M.; Tatsui, C. E.; Sun, Z.; Luerssen, T. G.; Meng, S.; Kent, T. A.; Tour, J. M. *J. Neurosurg.: Pediatr.* **2013,** *11,* 575–583. doi:10.3171/2013.1.PEDS12374
140. Lechleitner, T.; Klauser, F.; Seppi, T.; Lechner, J.; Jennings, P.; Perco, P.; Mayer, B.; Steinmuller-Nethl, D.; Preiner, J.; Hinterdorfer, P.; Hermann, M.; Bertel, E.; Pfaller, K.; Pfaller, W. *Biomaterials* **2008,** *29,* 4275–4284. doi:10.1016/j.biomaterials.2008.07.023
141. Tu, Q.; Pang, L.; Chen, Y.; Zhang, Y.; Zhang, R.; Lu, B.; Wang, J. *Analyst* **2014,** *139,* 105–115. doi:10.1039/c3an01796f
142. Nayak, T. R.; Andersen, H.; Makam, V. S.; Khaw, C.; Bae, S.; Xu, X.; Ee, P.-L. R.; Ahn, J.-H.; Hong, B. H.; Pastorin, G.; Ozyilmaz, B. *ACS Nano* **2011,** *5,* 4670–4678. doi:10.1021/nn200500h
143. Lee, W. C.; Lim, C. H. Y. X.; Shi, H.; Tang, L. A. L.; Wang, Y.; Lim, C. T.; Loh, K. P. *ACS Nano* **2011,** *5,* 7334–7341. doi:10.1021/nn202190c

144. Park, S. Y.; Park, J.; Sim, S. H.; Sung, M. G.; Kim, K. S.; Hong, B. H.; Hong, S. *Adv. Mater.* **2011,** *23,* H263–H267. doi:10.1002/adma.201101503
145. Akhavan, O.; Ghaderi, E. *J. Mater. Chem. B* **2013,** *1,* 6291. doi:10.1039/c3tb21085e
146. Li, N.; Zhang, Q.; Gao, S.; Song, Q.; Huang, R.; Wang, L.; Liu, L.; Dai, J.; Tang, M.; Cheng, G. *Sci. Rep.* **2013,** *3,* No. 1604. doi:10.1038/srep01604

License and Terms

This is an Open Access article under the terms of the Creative Commons Attribution License (http://creativecommons.org/licenses/by/2.0), which permits unrestricted use, distribution, and reproduction in any medium, provided the original work is properly cited.

The license is subject to the *Beilstein Journal of Nanotechnology* terms and conditions: (http://www.beilstein-journals.org/bjnano)

The definitive version of this article is the electronic one which can be found at: doi:10.3762/bjnano.5.196

BEILSTEIN JOURNAL OF NANOTECHNOLOGY

Cathode lens spectromicroscopy: methodology and applications

T. O. Menteş*[1], G. Zamborlini[2,3], A. Sala[1] and A. Locatelli[1]

Review

Open Access

Address:
[1]Elettra - Sincrotrone Trieste S.C.p.A., Basovizza, Trieste 34149, Italy, [2]Department of Physics, University of Trieste, Via Valerio 2, Trieste 34137, Italy and [3]Peter Grünberg Institute (PGI-6) and JARA-FIT, Research Center Jülich, 52425 Jülich, Germany

Email:
T. O. Menteş* - tevfik.mentes@elettra.eu

* Corresponding author

Keywords:
gold (Au); graphene; intercalation; low-energy electron microscopy (LEEM); magnetism; nanostructures; X-ray magnetic circular dichroism (XMCD); X-ray photoemission electron microscopy (XPEEM)

Beilstein J. Nanotechnol. **2014,** *5,* 1873–1886.
doi:10.3762/bjnano.5.198

Received: 09 July 2014
Accepted: 25 September 2014
Published: 27 October 2014

This article is part of the Thematic Series "Atomic scale interface design and characterisation: Experimental aspects and methods".

Guest Editor: C. Bittencourt

© 2014 Menteş et al; licensee Beilstein-Institut.
License and terms: see end of document.

Abstract

The implementation of imaging techniques with low-energy electrons at synchrotron laboratories allowed for significant advancement in the field of spectromicroscopy. The spectroscopic photoemission and low energy electron microscope, SPELEEM, is a notable example. We summarize the multitechnique capabilities of the SPELEEM instrument, reporting on the instrumental aspects and the latest developments on the technical side. We briefly review applications, which are grouped into two main scientific fields. The first one covers different aspects of graphene physics. In particular, we highlight the recent work on graphene/Ir(100). Here, SPELEEM was employed to monitor the changes in the electronic structure that occur for different film morphologies and during the intercalation of Au. The Au monolayer, which creeps under graphene from the film edges, efficiently decouples the graphene from the substrate lowering the Dirac energy from 0.42 eV to 0.1 eV. The second field combines magnetism studies at the mesoscopic length scale with self-organized systems featuring ordered nanostructures. This example highlights the possibility to monitor growth processes in real time and combine chemical characterization with X-ray magnetic circular dichroism–photoemission electron microscopy (XMCD–PEEM) magnetic imaging by using the variable photon polarization and energy available at the synchrotron source.

Introduction

The cathode lens, or immersion objective lens, is used to image electrons emitted from surfaces [1]. In a microscope that uses this type of objective, the sample surface acts as the cathode held at a negative potential, whereas the anode (objective lens) has a central aperture to allow for the passage of the emitted electrons towards the imaging column. The imaged electrons

may originate from different processes such as thermionic emission, secondary emission, emission of photoelectrons from core levels and the valence band or elastic backscattering [2]. Methods based on the latter two, photoemission electron microscopy (PEEM) and low energy electron microscopy (LEEM), have found a special place in the field of surface science, and they will be the focus of our review.

During the evolution of PEEM [3], its first use as an X-ray microscope in a synchrotron environment in the late eighties stands out as one of the most significant developments [4]. Since then X-ray PEEM (XPEEM) has become a widespread analytical technique for surface investigation, which takes advantage of the high photon flux along with the tunable energy and polarization available at synchrotron sources [5]. In recent years, the natural combination of XPEEM with LEEM has created the powerful surface science facility, spectroscopic photoemission and low energy electron microscope (SPELEEM). In SPELEEM, the structural sensitivity of LEEM perfectly complements the chemical and magnetic information provided by XPEEM, thus creating a complete characterization tool of material properties at the nanometer length scale.

The following provides an overview on SPELEEM methods along with the recent examples predominantly considering the activity carried out at the Elettra Sincrotrone Trieste. The first part of the paper is organized as an extended introduction to LEEM and XPEEM methodology. Then, we give a detailed account of the instrumental aspects specific to the SPELEEM instrument at Elettra.

The bulk of this work is dedicated to applications of the SPELEEM technique. We put special emphasis on graphene, which has been extensively studied by using cathode lens microscopy, LEEM in particular, with numerous studies of epitaxial graphene grown on a variety of transition metal and silicon carbide supports. These microscopy experiments have been carried out by using well-established methodologies, which were formerly developed for the analysis of ultra-thin metal films on single crystal surfaces [6]. These methods were soon adapted to the needs of the rising research field of graphene, making LEEM one of the prominent methods to access the structural properties of graphene [7]. Since several review works have already addressed this subject [8-10], treating in depth also the experimental methods, the section on graphene is limited to an overview on the most recent research activity. The versatility of the LEEM and SPELEEM methodologies will be further illustrated by the effect of Au intercalation in graphene on Ir(100). The last part of the paper focuses on the studies of magnetism at the nanoscale using the SPELEEM.

Review

Low energy electron microscopy

Low energy electron microscopy (LEEM) is a surface-sensitive method based on the elastic backscattering of low energy electrons [6,11]. The concept was put forth by Ernst Bauer in the 1960s, and the first operating instrument was demonstrated by Telieps and Bauer [12]. “Low energy” stands for electron energies from a few to several hundred electronvolts. Importantly, due to the high elastic backscattering cross section in the very low energy range (2–20 eV), exposure times are short and data collection becomes possible at video frame rate in most cases. Figure 1a and Figure 1b provide a schematic diagram of typical LEEM and PEEM instrumentation. Backscattered electrons are collected by the objective lens (also known as cathode lens or immersion lens), of which the sample is part. The objective lens, which is the most important optical element of the microscope, accelerates the e-beam to an energy of several keV. The outgoing beam is manipulated by a dedicated set of electron optical elements in the imaging column, which produces a magnified image of the sample. In order to combine the low energy scattering and the high energy imaging stages, a high voltage bias between the sample and the objective lens acts as a decelerating/accelerating potential for the incident/scattered electrons. Besides the electron energy, the backscattering geom-

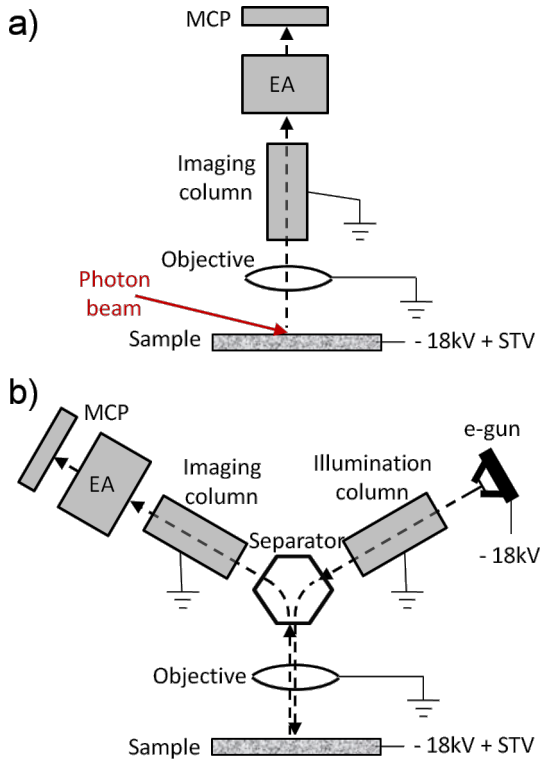

Figure 1: The simplified schematic description of a) XPEEM, b) LEEM. The energy analyzer (EA) is optional in both cases. Panel (b) with the energy analyzer represents also the SPELEEM setup.

etry at normal incidence distinguishes LEEM from other more conventional electron microscopies. This necessitates a beam separator, which is used to separate the incident and the scattered electron beams [6].

Contrast mechanism. Among all contrast mechanisms available in LEEM, "diffraction contrast" is the one that is most commonly used. This is derived from the strong energy dependence of electron diffraction intensities, making LEEM suitable for studying crystalline systems [13]. The backscattering intensity varies depending on the material, presence of adsorbates, formation of surface reconstructions and other ordered structures, giving the means to distinguish lateral variations in such properties. In the basic operation mode, only one of the low energy electron diffraction (LEED) beams is used to produce an image, in which the energy-dependent intensity provides information about the local morphology and crystal structure. This is done by filtering out undesired diffraction beams in the back-focal plane of the objective lens by using an aperture (usually called contrast aperture). The selection of the specular beam (zero-order diffraction) is commonly referred to as the bright field mode. An illustration of the intensity variations resulting from diffraction contrast is shown in Figure 2. The three curves belong to clean W(110), to W(110) covered with a pseudomorphic Fe monolayer, and to O(1 × 12)/W(110). As seen in the top panels, the first two surfaces give the same (1 × 1) LEED pattern, whereas the oxygen-covered surface features an additional superstructure. Nevertheless, all LEEM $I(V)$ curves show distinct differences. Similar differences are observed on surfaces with different structure and composition, which produces a contrast between regions of laterally-varying morphology by appropriate choice of the electron energy.

The sharp change in intensity at very low energy, seen in the inset of Figure 2, corresponds to the transition into the so-called mirror electron microscopy (MEM) regime. This MEM–LEEM transition marks the onset for the total reflection of incident electrons as the electron energy is lowered. The threshold energy predominantly depends on the surface work function and on the angle of incidence of the electrons. Therefore, imaging at or near the MEM transition allows to map the local work function as well as the variations in the surface topography. The effect of the work function is clear in the inset of Figure 2, in which the adsorption of oxygen on W(110) results in a work function more than 1.2 eV higher than that of the clean surface, with a corresponding shift in the MEM–LEEM transition. Fe adsorption, instead, induces a less pronounced shift towards a lower work function.

The diffraction contrast is also exploited in the dark field mode, obtained by imaging with higher order LEED beams. The diffraction order is selected by placing the contrast aperture on the desired beam. The resulting real space image gives a direct map of the corresponding structure. No intensity is seen elsewhere, except that originating from the diffuse background of the primary diffracted beam. The lateral resolution is comparable to that of the bright field mode, and the acquisition times, although slightly longer than the bright field operation, can be a few seconds to minutes depending on the intensity in the selected diffraction order.

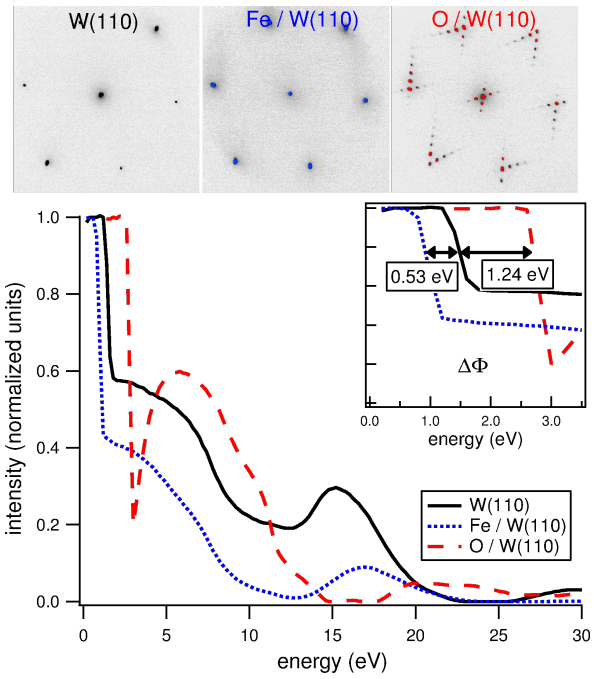

Figure 2: Energy dependence of the (00) beam intensity for clean, Fe-covered and O-covered W(110) surfaces. The top panels show the respective LEED patterns. The inset is a blowup of the MEM–LEEM transition at low energy. The increase (decrease) in the work function due to the presence of O or Fe is seen in the shift of the transition energy.

Due to the short inelastic mean free path (IMFP) at low electron energies below a few hundred electronvolts [14], LEEM is a surface sensitive technique, which probes only a few atomic layers near the surface. Nevertheless, below 10 eV the IMFP considerably increases (up to a few nanometers) giving depth information to LEEM. This is best reflected in the quantum size oscillations in electron reflectivity for thin films on crystalline surfaces [11,15]. As regularly observed in LEEM, the period of intensity oscillations as a function of the electron energy is highly dependent on the film thickness. Beyond their period, the amplitude of these quantum size oscillations depends on the film thickness and the IMFP, which was recently used to extract the IMFP in metal films at very low electron energies [16].

μ-LEED operation mode is a natural extension of LEEM. For crystalline surfaces, the backfocal plane of the objective lens contains the diffraction pattern from the probed area, which can be transferred to the detector with the proper lens excitation in the imaging column. By placing a small aperture in the illumination column or at the image plane of the objective lens, the probed area can be limited to a micrometer-sized region, thus giving rise to the micro-probe operation. When the length scale of the structural heterogeneity is below the size of the micro-probe, the contribution of different domains to the LEED pattern can still be sorted out by using LEED in combination with dark-field LEEM imaging. The micro-probe capability is especially useful in quantitative structure analyses of LEED $I(V)$ curves acquired from single domains on a heterogeneous surface. The first example of a full surface structural analysis at the micrometer scale by using LEED $I(V)$ in a LEEM instrument was given only recently for the case of the (4 × 4) reconstruction of oxygen on Ag(111) [17].

Beyond the laterally-resolved electron diffraction, LEED measurements in a LEEM instrument have practical advantages such as electron-energy independent spot positions and constant electron flux. The former is due to the acceleration stage at the objective lens, after which the electrons reach 18 keV regardless of the start energy (i.e., the energy of the elastically-scattered electrons at the sample surface). It should be underlined that this is particularly useful in the analysis of energy-dependent $I(V)$ data.

X-ray photoemission electron microscopy

PEEM uses UV or soft X-ray photons to stimulate the emission of photoelectrons to probe the state of the emitter. A simplified sketch of an XPEEM setup is given in Figure 1a. Similar to LEEM, it is based on the cathode lens, which accelerates the photoelectrons to an energy of several keV and directs them towards the imaging column of the instrument. The low photon energy of the conventional photon sources readily available in most laboratories presents a limitation, as the information on surface chemistry is available in core-level electronic transitions, which are only accessible by using higher photon energies from few tens of electronvolts to above 1 keV. By providing tunable high-brightness X-ray beams, synchrotron sources greatly extend the application field of XPEEM instruments, which can achieve chemical, magnetic and electronic structure contrast through the implementation of the most popular photoelectron spectroscopies such as X-ray absorption spectroscopy (XAS), photoelectron spectroscopy (XPS), and angle-resolved photoemission spectroscopy (ARPES) [5].

XAS based methods. XAS is the only method readily available when using the basic XPEEM instrument installed at a synchrotron beamline with a monochromator in place. Among the variety of detection methods to measure X-ray absorption [18], the secondary photoelectrons are collected in XPEEM as a close approximation to the total photoelectron yield measurement. The local XAS spectra are obtained by acquiring image sequences as a function of the photon energy, which can then be

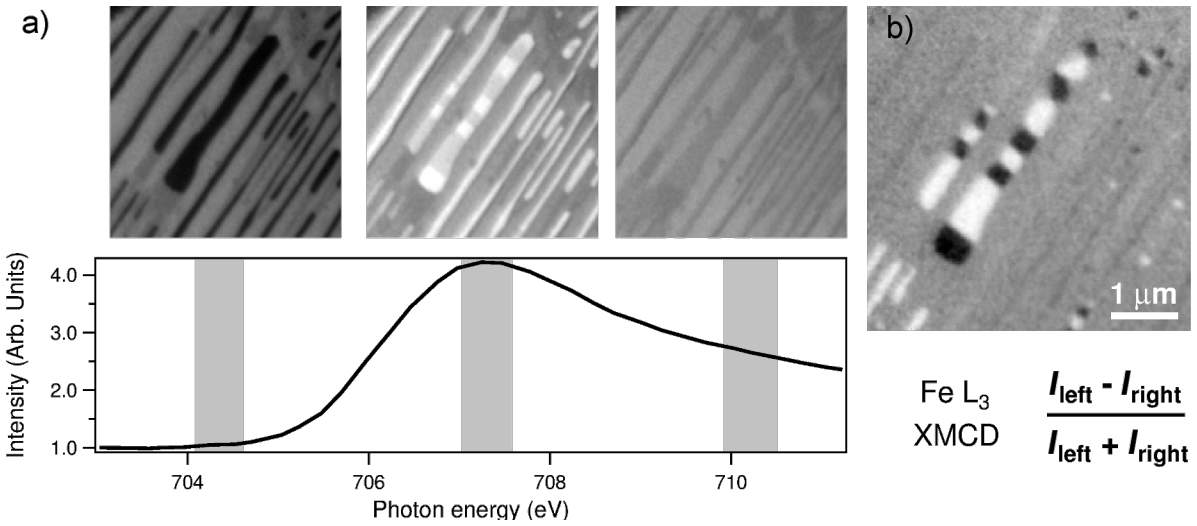

Figure 3: a) Illustration of imaging spectroscopy in XAS mode. Fe nanowires on W(110) appear dark on the left panel at a photon energy of 704.5 eV. At the Fe L_3 threshold, the wires become much brighter (middle panel). The XAS spectrum below is extracted from the largest nanowire in the center. b) Illustration of XMCD-PEEM imaging. The photon energy is tuned to the L_3 maximum. The field of view is 5 μm. The start voltage is 3 eV in order to collect secondary electrons. Within the image plane, the X-ray direction is perpendicular to the nanowire axis.

processed in order to extract the intensity variation within any region of interest in the image. Figure 3a illustrates XAS-PEEM imaging spectroscopy on a nanostructured Fe film on W(110). The off-resonant image contrast (leftmost panel) is due to the different secondary photoelectron yield from different surface structures, dominated by the variations in the work function. When the photon energy is tuned to the Fe absorption threshold (middle panel), the elongated Fe nanowires become much brighter, whereas the regions in between barely change intensity. The spectrum seen in the plot in Figure 3a is extracted from an individual nanowire.

Magnetic imaging. X-ray magnetic circular and linear dichroism techniques applied to magnetic surfaces constitute major branches of XPEEM research at synchrotrons. Aside from the photon energy, undulator sources provide also the possibility to manipulate the X-ray polarization. The scattering of circularly polarized X-rays is known to carry a contribution from magnetization, which is greatly enhanced at energies corresponding to certain absorption thresholds [19]. Therefore, XPEEM images can be used to obtain the magnetization distribution on a magnetic surface by a simple polarization analysis [20].

The XMCD-PEEM imaging is illustrated in Figure 3b, in which the magnetization distribution of Fe nanowires on W(110) is mapped along the beam direction corresponding to the $[1\bar{1}0]$ substrate axis. The photon energy is tuned to the Fe L_3 absorption threshold maximum at about 707.5 eV, and the XMCD image is obtained by taking the difference of the two images with opposing circular polarizations. The wires with magnetization along the perpendicular direction, [001] axis, appear gray as they do not produce an XMCD signal. The black and white regions evident in the central wires are the dipolar domains with magnetization parallel and antiparallel to the beam direction, respectively. Note that the strong magnetic contrast in the case of Fe nanowires is visible even in the single XAS image acquired with circular polarization as seen in Figure 3a (middle panel).

Core and valence band spectroscopy. Contrary to XAS-based PEEM, X-ray photoelectron spectroscopy requires a filtering of the kinetic energy of the photoemitted electrons [21]. Therefore, in order to implement XPS in an XPEEM, an energy analyzer has to be installed in the imaging column of the microscope. The most advanced PEEM experiments show a duality between imaging and diffraction operations. The real space image gives a map of the photoelectron intensity, whereas at the backfocal plane the angular distribution of the photoelectrons are imaged. The latter gives access to photoelectron diffraction or angle-resolved photoemission from a micrometer-sized region selected by a field-limiting aperture, which we will refer to as μ-ARPES.

Dark-field PEEM is the analogue of the dark-field method in LEEM, such that the same contrast aperture (i.e., diffraction-plane aperture) is used to filter out everything except the emission along a given angle. From a practical standpoint, the main difference of the dark-field XPEEM operation is the necessity to change the sample tilt angle in order to get the diffraction feature through the aperture [22,23]. The angular resolution in the dark-field XPEEM is determined by the size of the contrast aperture, which is typically a fraction of an inverse Å. The lateral resolution is comparable to that of the normal XPEEM operation, well below the micrometer scale. Therefore, dark-field XPEEM makes it possible to probe the electronic structure of small features, which cannot be distinguished in the μ-ARPES mode.

The SPELEEM at Elettra

Although LEEM and PEEM are widespread, only few instruments that combine both methods can be found in synchrotrons. Some prominent ones are situated at ALBA (Spain), BESSY (Germany), Diamond (UK), MAXLAB (Sweden), NSLS (USA), SOLEIL (France) and SPRING-8 (Japan). Among these, the end station of the Nanospectroscopy beamline at Elettra, the 3rd generation storage ring in Trieste, hosts a spectroscopic photoemission and low energy electron microscope (SPELEEM) [24]. This microscope is the commercial evolution (Elmitec GmbH, SPELEEM III) of the first prototype LEEM with a 120° separator and an energy analyzer, which has pioneered cathode lens spectromicroscopy measurements at synchrotrons during the mid-1990's [25]. The SPELEEM combines LEEM and XPEEM with energy filter in the same setup: LEEM operation uses an LaB_6 electron gun and dedicated illumination optics with three condenser lenses, which can deliver a well-collimated e-beam on the sample. In XPEEM operation, instead, the sample is illuminated by the monochromatized X-ray beam produced by the insertion device in the synchrotron ring.

A photograph of the experimental apparatus is shown in Figure 4. Traces indicating the optical path of the incident and scattered beams in LEEM and XPEEM modes are superimposed onto the photograph. Labels indicate the main electron-optical elements and other essential components. The X-ray beam, traced out as a (red) dashed line entering from the right hand side, is incident on the sample at a 16° grazing angle from the surface plane. The backscattered/emitted electrons are accelerated to 18 keV towards the electromagnetic objective lens. Next element along the optical path is the beam separator, which deflects the e-beam towards the imaging column in

which a magnified image of the sample is produced. Depending on the lens excitations, the diffraction pattern at the objective lens backfocal plane can be imaged. At the entrance of the energy analyzer, the electrons are decelerated from 18 keV to 908 eV, the pass energy of the filter. Upon exit from the analyzer, the e-beam is re-accelerated to 18 keV. The final image is projected onto the detector, a chevron multichannel plate followed by a phosphorous screen. The light produced in the phosphorous screen is collected by a CCD camera (PCO Sensicam QE) equipped with an external fan for vibrationless cooling. A more detailed explanation of the SPELEEM optics can be found in reference [25].

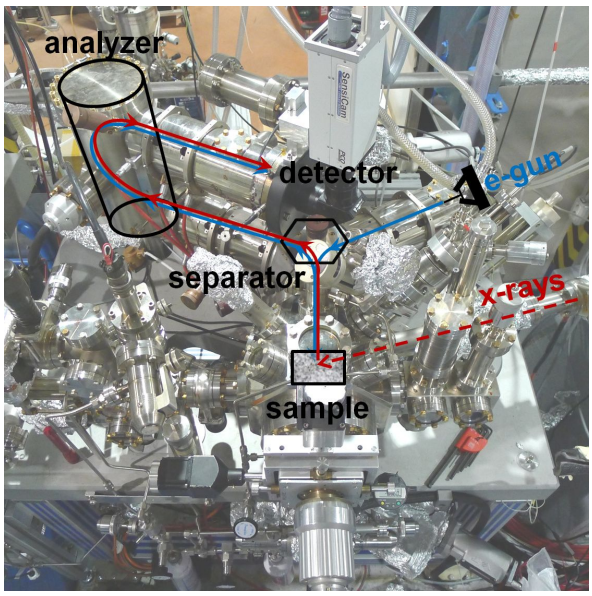

Figure 4: The SPELEEM instrument at the Nanospectroscopy beamline, Elettra Sincrotrone, Trieste. The sketch of the basic setup is superimposed onto the photograph. X-rays arrive from the right at 16° grazing angle to the sample surface.

Electron source. The SPELEEM is equipped with an LaB_6 thermionic emission cathode (Kimball Physics, model ES-423E, style 06-60). The emitter is a single crystal cut to a cone angle of 60° exposing a ⟨100⟩ microfacet of 6 µm diameter as tip, which offers high electron flux at a relatively low temperature of the emitter. In the SPELEEM instrument, the electron beam has a flux density of up to 1×10^{16} $e^-/cm^2 \cdot sec$ at the surface. The illumination optics focus the beam on the sample to a slightly elliptical shape with diameter of about 90 µm.

The energy spread of the LaB_6 source is set by its operation temperature, reaching 1900 K at a current of 2.12 A. Figure 5a shows the energy distribution of the electron source at the SPELEEM instrument for an operation current of 1.75 A. In order the determine the emitter characteristics, we fitted the experimental data modeling the energy dependence with a simple function taking into account instrumental and thermal broadening [26]. The long tail in the energy dependence of the intensity seen in Figure 5a reflects the LaB_6 temperature. By fitting the curve with a Fermi function, we determine a tip temperature of about 1750 K. The sharp rise on the left hand side represents the effect of the instrumental broadening. The broadening obtained from this leading edge is about 65 meV, providing a best estimate for the energy resolution of our electron energy analyzer in LEEM operation. Note that this figure is not limited by the size of the contrast aperture, as the angular spread in LEEM is smaller than the aperture size.

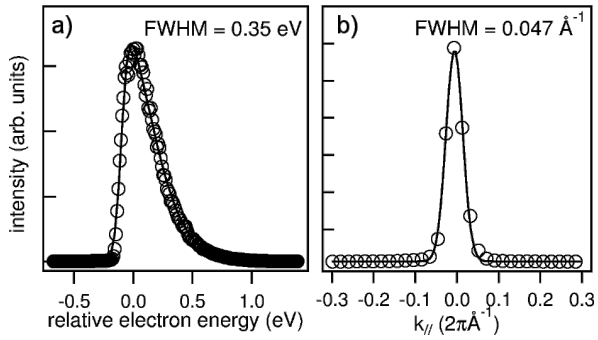

Figure 5: a) The energy distribution of the electron beam emitted from the LaB_6 source acquired by keeping the sample below the MEM transition using a negative start voltage bias. The intensity-vs-energy curve is obtained in dispersive plane operation, in which the exit plane of the energy analyzer is projected onto the detector. b) The (00) LEED spot profile from W(110).

The transfer width of the system was measured from the profile of the (00) specular diffraction spot originating from a virtually step-free region of a W(110) crystal, as shown in Figure 5b. Under normal operating conditions, when using a 2 µm illumination aperture and 0.05 µA total emission from the e-gun, the full width half maximum of the Gaussian spot profile was found to be 0.047 $Å^{-1}$. This corresponds to a transfer width of more than 130 Å in real space.

X-ray source. Two Apple-II type undulators provide an intense X-ray beam with linear horizontal, linear vertical, or circular polarization from below 10 eV up to 1000 eV [24,27,28]. The monochromator makes use of three gratings to cover the entire photon energy range. A spherical grating is used at the low energies below 50 eV, whereas two variable line spacing gratings of 200 lines/mm and 400 lines/mm cover the ranges of 50–250 eV and 250–1000 eV, respectively. The footprint of the X-ray beam is about 20×5 μm^2 ($H \times V$), horizontally elongated because of the grazing incidence. A larger area (up to 30 µm) can be illuminated by slightly defocusing the photon beam and by moving it along vertically during image acquisi-

tion, although this method usually causes striations in the illumination. The maximum flux is obtained at about 150 eV photon energy and is about 1.8×10^{13} photons/s with the exit slit of the monochromator set to 10 µm and with 200 mA synchrotron ring current [29].

Energy resolution in XPEEM. The photon source and the SPELEEM operation mode together determine the value of the energy resolution. The resolving power of the VLS400 grating of the beamline monochromator, $E/\Delta E$, is about 3000 for the photon energy range from 700 to 1000 eV. This figure nearly doubles at lower photon energies [30]. Therefore, in the majority of practical cases, the microscope energy analyzer is the limiting factor in terms of energy resolution.

In energy-filtered imaging and diffraction, where images are collected at a well-defined photoelectron kinetic energy, the energy resolution is mainly determined by the size of the analyzer exit slit. Two slits of different width can be used to set the bandpass of the energy filter, corresponding to energy windows of 0.33 eV and 0.79 eV, respectively. Note that the best energy resolution from the instrument can be obtained in the μ-spectroscopy operation, in which the dispersive plane of the analyzer is imaged onto the detector. In this way, the resolution is mainly determined by the radius of the analyzer hemisphere (r_0 = 10 cm), the pass energy (E = 908 eV), and the angular spread before the analyzer (α = 5 mrad full width) given by the size of the contrast aperture (d = 20 µm, smallest aperture), which also acts as the entrance slit. The energy spread ΔE (full width at half maximum) is parameterized as [31]:

$$\Delta E = E\left(0.43\frac{d}{r_0} + \alpha^2\right). \quad (1)$$

Inserting the values listed above, the best resolution is estimated to be 101 meV. The experimental energy resolution of the SPELEEM was measured from the W 4f core level of the clean W(110) surface. The dispersive plane spectrum and the corresponding Doniach–Šunjić fit are displayed in Figure 6 [32]. The resulting full-width half-maximum of the Gaussian broadening is found to be less than 110 meV for the optimal conditions (smallest contrast aperture, low photon flux, small field-limiting aperture), which is in excellent agreement with the above estimation. For the usual operating conditions with less stringent parameters, the energy resolution was found to be about 150 meV.

Lateral resolution. The SPELEEM spatial resolution is mainly determined by the spherical and chromatic aberrations of the objective lens. LEEM performs better compared to XPEEM.

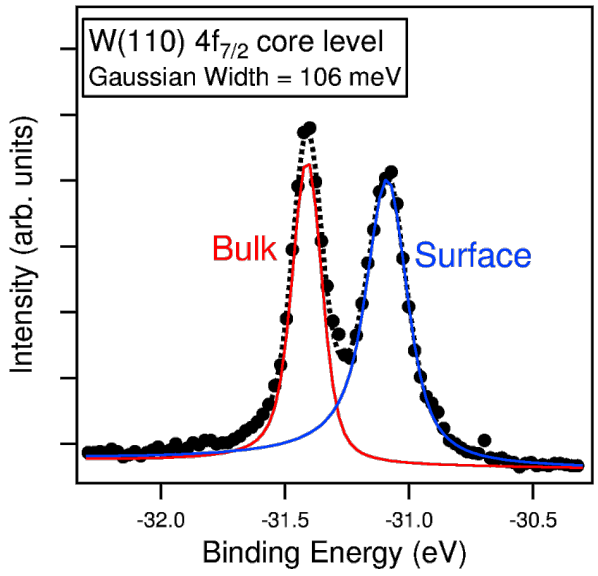

Figure 6: Tungsten $4f_{7/2}$ core level spectrum from a clean W(110) surface acquired in dispersive plane mode. The photon energy is 90 eV. The acquisition time is 80 s. The Lorentzian broadening for the bulk peak was fixed at 60 meV, with an asymmetry parameter of 0.035. The contrast aperture, which acts as the analyzer entrance slit, is 20 µm.

Low energy electron diffraction beams are generally much sharper than the broad photoelectron emission angles. As a result, the angular spread (thus spherical aberrations) in LEEM is considerably reduced compared to XPEEM. The same is true also for the energy spread and the chromatic aberrations, which are again reduced in the case of LEEM. The lateral resolution in LEEM mode for the SPELEEM at Nanospectroscopy is demonstrated in Figure 7. The plot shows the variation of the LEEM intensity across a profile through a ML thick Ni island on W(110), along with a sigmoid fit. The width of the sigmoid represents the instrumental broadening, corresponding to the distance identified by using the 16–84% intensity variation criterion often used to characterize the lateral resolution. By averaging over several profiles across the image, we obtained a value of about 9 nm. The same value is obtained when measuring the width of steps (providing phase instead of amplitude contrast) on clean W(110). Note that this value is better by more than 20% compared to the performance prior to the installation of the new electron source. This improvement is based on the smaller energy spread and the reduced transfer width, which are reported in Figure 5. The lateral resolution may possibly be further reduced by using a field-emission source with superior characteristics.

The spatial resolution in XPEEM is about 30 nm [24]. For comparison, consider that the wide angular spread observed when

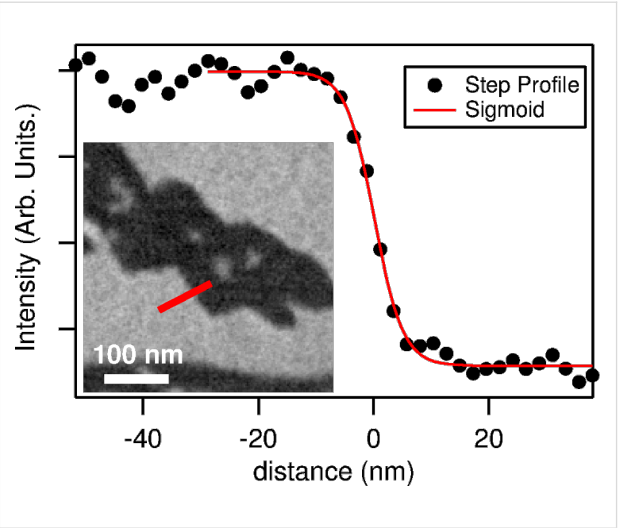

Figure 7: Lateral resolution in LEEM. The inset shows a Ni monolayer island (dark) on W(110). The profile in the plot is marked on the image. The full width of the sigmoid function is 8.2 nm. Averaging over several profiles, the value is found to be 8.6 ± 1.2 nm.

imaging the inelastically scattered energy-loss electrons in LEEM gives a spatial resolution of about 18 nm, similar to XPEEM [33]. It is important to note that the lateral resolution in XPEEM suffers from space-charge effects due to the highly brilliant synchrotron pulses [29]. The electron–electron interaction within the photoelectron pulse produced by the X-ray pulse (which has a low duty cycle of about 1/50) results in the degradation of the image quality as well as increasing the energy spread. As a result, even the aberration-corrected instruments are limited to a moderate lateral resolution in XPEEM [34]. Similar effects were not observed in LEEM with its monochromatic LaB_6 cathode providing a much lower current density than the peak photoelectron current in XPEEM.

SPELEEM studies of graphene epilayers

LEEM has found ample use in graphene research with its high structural sensitivity and video acquisition rate allowing for dynamic measurements of film growth. In such experiments, graphene is typically obtained by the chemical vapor deposition (CVD) technique. CVD utilizes transition metal catalysts as a means to promote the dissociative adsorption of gases such as ethylene or methane, which can readily deliver the carbon atoms required for island nucleation and growth. LEEM is widely employed to image the growth process; the accessible parameter space is explored by varying the gas pressure and/or sample temperature in a manner compatible with the operation limits of the instrument. In this regard, LEEM permits operation at elevated sample temperatures (approximately up to 1000°C) by using the experimental chamber as a gas flow reactor up to pressures approaching 1×10^{-5} mbar, still ensuring a lateral resolution nearing 10 nm. The growth of graphene on a variety of transition metal substrates provide catching examples of the potential of the LEEM method [35-37]. For instance, by measuring subtle variations in the low energy electron reflectivity of the substrate upon ethylene uptake, it has been shown that LEEM can quantitatively monitor the time evolution of the C adatom lattice gas that anticipates island nucleation. Tiny variations of the carbon coverage were detected in these experiments, achieving sensitivities below 0.1% of a ML. These experiments provided a formidable means to access to the thermodynamics governing carbon segregation, graphene nucleation and film growth [36-38]. In other cases, LEEM imaging was used to monitor the intercalation of adspecies below graphene [39-41]. As a further advantage, LEEM allows for thickness determination in multilayer systems, through the exploitation of quantum size contrast. Nevertheless, the understanding of the low energy electron reflectivity is not always straightforward, since it is extremely sensitive to the substrate–film interaction, as has been recently demonstrated by an ab initio study that clarified the interpretation of LEEM-$I(V)$ curves [42].

An important aspect is the integration of LEEM with low energy electron diffraction (LEED). Diffraction experiments permit a full characterization of the crystal structure and quality of graphene. For instance, μ-LEED methods have been devised to quantify the short-range roughness of multi-thickness SiO_2-supported and suspended exfoliated graphene films [43]. To date, the most frequent application of LEEM/LEED has been the study of rotational domains and complex moiré patterns in a wide variety of graphene epilayers. A notable example is that of graphene on Re(0001), in which a moiré cell made out of (10 × 10) graphene unit cells over (9 × 9) Re unit cells was determined in a μ-LEED experiment performed in a SPELEEM microscope; the atomic positions in the unit cell were subsequently obtained by means of ab initio calculations, which could prove the very large corrugation of graphene in this system and establish a correlation between C 1s binding energy and C–substrate separation [44]. On the same system, μ-probe diffraction analyses were carried out in combination with dark-field imaging, investigating the carburisation of the Re(0001) substrate as a function of temperature [45]. The literature shows a plethora of other experiments exploiting the LEED capabilities of LEEM with notable examples of graphene on single and polycrystalline copper [46-48], nickel [49] and on non-three-fold crystalline substrates such as Ir(100) [50,51] and Fe(110) [52].

There is also a growing literature on XPEEM applications in graphene research. In particular, μ-ARPES available in the SPELEEM has been successfully applied to exfoliated [53,54] as well as epitaxial graphene grown on metal [48,55,56] and

SiC substrates [57]. In many studies μ-ARPES was employed to access the π-band of graphene, to quantify the doping in graphene and to verify the strength of the film–substrate interaction. At length scales below the resolution of the μ-probe approach, the recently introduced dark-field XPEEM method is ideally suited to compare the density of states (DOS) of different, adjacent types of graphene exhibiting distinct electronic structure properties. Laterally resolved XAS was also utilized in an isolated study on exfoliated graphene, in which selected features in the K-edge spectrum of C were studied as a function of the thickness of graphene. A splitting of the π^* resonance was observed in multilayers and ascribed to specific interlayer states [58].

The intercalation of Au below graphene on Ir(100). Recently investigated by using a wide range of microscopy methods and theory, the graphene/Ir(100) system exhibits unique morphological and electronic properties, which originate from the different film and substrate symmetries [50]. At temperatures above 800 °C, micrometer-sized single layer graphene crystals can be obtained upon exposure to ethylene, oriented at 3° with respect to the main substrate direction. By cooling the sample from growth to room temperature, a phase transformation occurs in the graphene film, which develops neighboring phases characterized by flat and buckled morphology. Adjacent striped-shaped domains of different carbon surface density alternate on the film at microscopic length-scales, relieving the strain accumulated upon cooling to room temperature. Most interestingly, the buckled graphene phase is characterized by large and extremely regular one-dimensional ripples showing a periodicity of 2.1 nm. Dark-field PEEM experiments have demonstrated that the buckled graphene phase shows a negligible DOS at the *K* point of the π-band. These results point to the disruption of the Dirac cones and the formation of a metal-like DOS. Surprisingly, the hybridization of the π-band with Ir states is due to the chemisorption of just 11% of the C atoms in the unit cell of the buckled phase [50].

In order to modify the graphene–substrate interaction in this system, we have intercalated Au at elevated sample temperature, taking advantage of the fast diffusion of Au adatoms under such conditions. Au is expected to exert a weaker interaction than Ir, hindering the formation of the chemisorption bonds such as those observed in the buckled graphene phase on Ir(100). In our work, the related variations in C–substrate bonding and the electronic structure of graphene were quantified in μ-XPS and μ-ARPES experiments, taking the pristine graphene/Ir(100) system as reference. Experimentally, Au was deposited by using an e-beam evaporator (Elmitec GmbH) at a flux of 0.059 $eML_{Ir(100)}$ (equivalent monolayer of Ir(100)) per minute at a sample temperature of about 600 °C.

The evolution of the interface upon increasing Au dose was monitored in situ employing LEEM. Figure 8a illustrates the initial state of the surface, with a graphene island (bright) located in the lower half of the image. The same image (upper half) shows the bare Ir surface, rendered in medium gray; a few thin curved lines can be spotted here, which identify morphological features of the surface such as steps and step bunches. The first stages of the Au growth are shown in Figure 8b, the Au-covered areas appearing darker than the Ir substrate at the chosen electron energy (12 eV). As can be seen, Au has already decorated the steps and has formed a step-flow growth front, its local thickness being just one layer. Note that Au is not found on or below graphene, but adsorbs exclusively on the iridium substrate. Only when the bare Ir surface has been fully covered, the intercalation process starts. At this stage, the Au growth front propagates quickly under the film, as shown in Figure 8c and Figure 8d, until a full Au monolayer is formed below graphene.

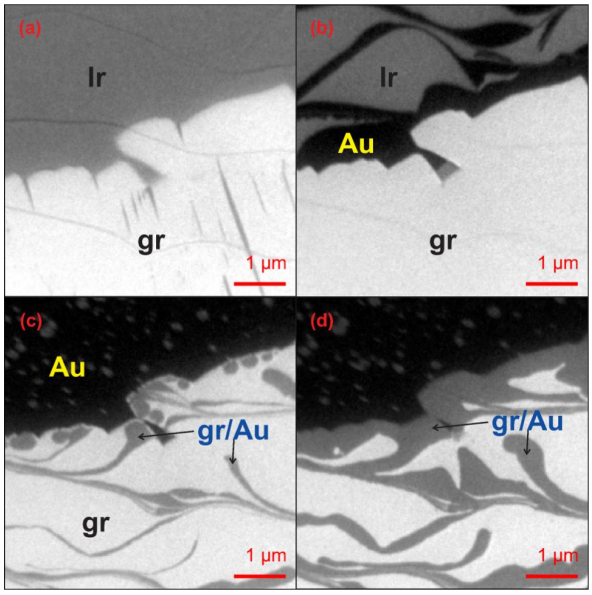

Figure 8: LEEM images at a start voltage of 12 eV illustrating the evolution of the graphene/Ir(100) interface upon deposition of Au. A large graphene crystal (gr) is visible in all images (lower half), brighter than the Ir surrounding it (upper half). (a) Initial configuration of the sample at T = 520 °C. (b) The same area after a dose of 0.25 ML Au at sample temperature of 600 °C. Au (dark areas) has decorated steps and step bunches. (c) The same area after a dose of 0.85 ML of Au. At this stage, Au has entirely covered the initially bare Ir surface and the intercalation under graphene has just started (darker areas). Note also that small graphene islands have nucleated on the Au/Ir surface. (d) The same area after a dose of 0.9 ML of Au.

There are two interesting findings that need to be highlighted. First, it appears that Au can intercalate below graphene only after accumulation of a full Au ML at the island edges, and before the nucleation of second or multilayer Au islands.

Second, small graphene islands nucleate at the Au-covered surface far from the large graphene crystal, as was verified by μ-LEED analysis. The former observation gives the order of energetics for Au adsorption on Ir versus its intercalation under graphene. The intercalation is facilitated by the lifting of the chemisorbed graphene edges upon Au adsorption at the edges. To explain the appearance of small graphene islands on Au, we must consider that 0.1 ML carbon is chemisorbed to the Ir surface, forming a carbidic c(2 × 2) structure [51]. In such a structure, C is strongly bound to the substrate, with a binding energy of almost 8 eV at a coverage of 0.5 $eML_{Ir(100)}$ [59]. We note, however, that Au binds strongly to other noble metal substrates. For instance, on Rh(110) the binding energy of Au is 3.5 eV at ML-coverage [60]. Due to the strong interaction with Ir, the adsorption of Au weakens the C–Ir bonds, and the high density of C adatom gas on the Au layer readily condense to form graphene islands.

Upon subsequent cooling to room temperature, the morphology and structure of graphene remain unchanged. In fact, we could not detect any evidence of phase transformation or formation of stripe-shaped domains resembling those of observed on Ir(100). Instead, LEEM imaging at high lateral resolution evidenced the formation of wrinkles in the graphene film, a process which helps relieving the thermal strain, because of the different thermal contraction of film and substrate. Similar features have been previously observed for graphene on Pt(111) and Ir(111) surfaces [61,62]. Importantly, no coincidence structures are observed in the LEED pattern, which exhibits only the first order graphene spots plus an extremely week moiré structure, identical to that observed on the flat phase of graphene on Ir(100). This finding further confirms that, after Au intercalation, graphene is entirely physisorbed and no chemisorption bonds are established between C and the substrate.

The C 1s μ-XPS spectrum of the graphene/Ir(100) system exhibits two components. The dominant one, at about 283.95 eV binding energy, has been previously ascribed to physisorbed C [50], consistent with the binding energy values observed for weakly-interacting graphene on a variety of fcc(111) and hcp(0001) substrates [44,63]; the second peak appears at higher binding energy (about 284.9 eV) and is due to the small fraction of chemisorbed carbon atoms in the buckled phase. Conversely, the C 1s spectrum measured on the graphene/Au system shows only the physisorbed component, proving that no chemisorption to the substrate has been established upon cooling to room temperature.

Clearly, the Au layer induces important variations in the graphene–substrate interaction, which in turn affect the charge transfer processes occurring between substrate and film and, consequently, the doping. Figure 9 shows μ-ARPES patterns (a, top) and momentum distribution curves (b, bottom) along the high symmetry directions for the graphene/Au system (on the left-hand side of the Figure) and pristine graphene on Ir(100) (on the right-hand side), respectively. Visual inspection of the full μ-ARPES pattern at E_F shown in (a) instantly reveals that Au intercalation is manifested by a change in the doping: The circular features identifying the Dirac cones for the graphene/Au system appear narrower than those recorded on pristine graphene, suggesting that the Dirac energy is now closer to the Fermi level. By accurately fitting of momentum distribution curves we could determine a positive doping of just 0.09 ± 0.06 eV for graphene/Au/Ir(100), which has to be compared with the value of 0.42 ± 0.03 eV obtained on graphene/Ir(100) [50]. Our results are in fair agreement with μ-ARPES data for the graphene/Au/Ni(111) system [64]. On the Ni substrate, the Au intercalation leads to a non-rigid shift of the bands of graphene towards lower binding energies, the π-band moving by approximately 2 eV; the Dirac energy E_D is found at just 25 meV above the Fermi level, so that quasi free-standing conditions for the film are claimed. Referring to an analytical model [65,66], the Fermi level shift in graphene translates to the graphene–Au distance beng in the range of 3.4–3.6 Å, slightly larger than the calculated graphene–Ir distance [50].

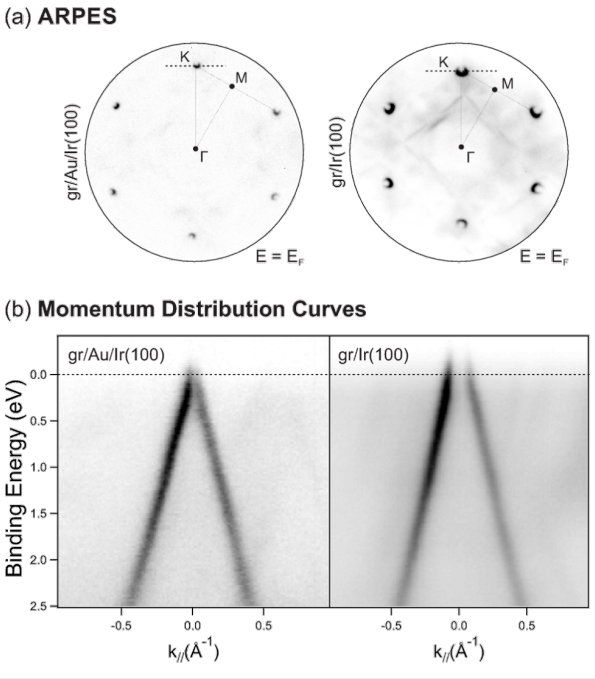

Figure 9: Graphene on Au/Ir(100) (left column) and Ir(100) (right column). (a) μ-ARPES near E_F; the high symmetry points in the first Brillouin zone (FBZ) are indicated. Photon energy is 40 eV. The probed area has a diameter of 2 μm. (b) Momentum distribution curves along the normal to the Γ–K direction, as indicated by the dashed line in (a).

Self-organized nanomagnets

*S*elf-organization may be ascribed the general meaning "spontaneous appearance of a particular form". Even though the definition may be stretched about to describe nearly all observed shapes in nature, static and dynamic, we assign the term to the formation of regular structures. SPELEEM methods perfectly lend themselves to studies of self-organization phenomena, particularly in the field of nanomagnetism. In a nutshell, LEEM is used to monitor the growth process in real time at high temperatures; spectromicroscopy with XPEEM provides the chemical map of the resulting heterogeneous surface; and finally XMCD-PEEM reveals the magnetization distribution of this nanostructured surface.

Stress-induced adsorbate stripes have been recently observed on crystalline surfaces at high temperatures. The mechanism is based on the competition between the cost of a boundary and the gain due to long range elastic interactions between boundaries [67]. The temperature determines the relative strength of the long- and short-ranged energy terms [68].

In the case of monolayer Pd stripes on W(110) forming at about 1100 K [68], it was recently shown that the addition of oxygen modifies the pattern anisotropy while preserving the periodic structure [69]. Moreover, the Pd–O bispecies layer is stable upon lowering the temperature from above 1000 K down to room temperature. The different adlayer patterns that can be obtained by varying the amount of oxygen on the surface are depicted in Figure 10a. The changes in the pattern anisotropy are driven by the magnitude and sign of stress variations on the surface, which are both dependent on the presence and amount of oxygen [69].

The stability of the Pd–O stripes on W(110) at lower temperatures allows for a further growth of magnetic wires following the self-organized template. Fe/Pd–O stripes on W(110) have been demonstrated very recently [70]. XPEEM imaging at the Fe L_3 absorption threshold has confirmed the expected Fe distribution as seen in Figure 10b (left panel). In the resulting picture, Fe preferentially wets the Pd-covered parts of the striped template. Furthermore, at about 200 °C Fe and Pd rearrange to make a surface alloy with a Pd-rich surface layer. The magnetization of the FePd stripes was found to be along the $[1\,\bar{1}0]$ direction perpendicular to the stripe axis, as shown in the XMCD map in Figure 10b (right panel). This is a surprising confirmation of the magnetocrystalline anisotropy strength dominating the shape anisotropy.

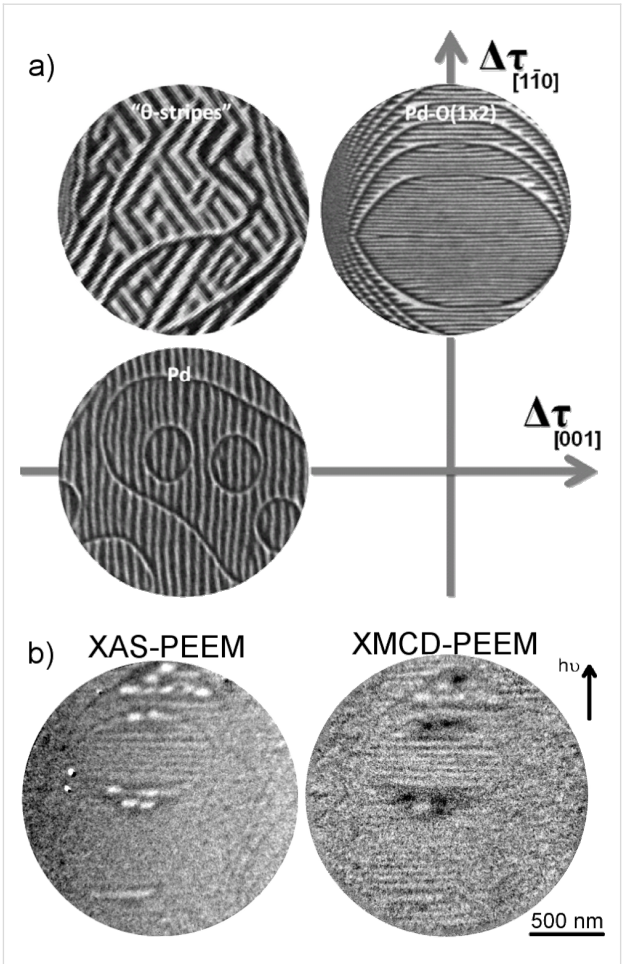

Figure 10: a) LEEM images (2 µm diameter) of monolayer Pd stripes on W(110). The lower left panel shows Pd on a clean substrate, whereas the other two panels display the progressive change in pattern anisotropy upon addition of 0.1 ML and 0.33 ML oxygen. (Reprinted from [69]. Copyright 2011 IOP Publishing.) b) Fe grown on Pd–O stripes at 225 °C. Left panel is the XAS-PEEM image at the Fe L_3 edge showing the Fe distribution. On the right, the Fe XMCD image indicates that the wires are uniformly magnetized perpendicular to the long axis. (Reprinted from [70]. Copyright 2013 Elsevier.)

Iron oxides find wide application in several fields of research, among others magnetism and heterogeneous catalysis. In both cases, the heteroepitaxial growth of nanostructured FeO_x offers a versatile means to tune the material properties. Recently, SPELEEM techniques were applied to characterize the reactive growth of FeO_x on Ru(0001) [71]. Fe growth in an oxygen ambient (5×10^{-7} mbar) at 900 K resulted in the formation of perfectly triangular micrometer-sized Fe_3O_4 islands on a FeO wetting layer. The combination of spatially-resolved XPS and XAS spectra, along with µ-LEED patterns, allowed the unequivocal identification of the specific iron-oxide phases.

From the screening of substrate core-level photoelectrons, the thickness of the micrometer-sized magnetite islands was found to be about 1 nm, which corresponds to two unit cells [72]. XMCD-PEEM measurements on these ultrathin islands (seen in Figure 11a) show that magnetite preserves its ferrimagnetic properties at 1 nm thickness up to 520 K (above which the

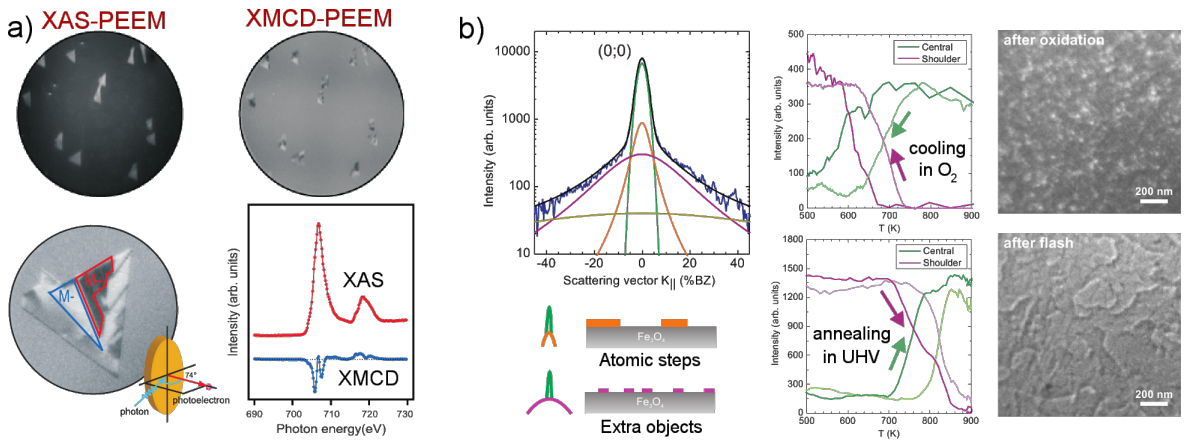

Figure 11: a) Magnetite islands and the FeO wetting layer on Ru(0001). Top panels show the island and magnetization distribution within a region of 30 µm diameter, illuminated homogeneously by vertically scanning the photon beam during acquisition. Bottom panels show the details of the magnetic domains (left, field of view 4 µm) and the Fe L_3 XMCD spectrum extracted from a single domain (right). (Reprinted with permission from [72]. Copyright 2012 American Physical Society.) b) Morphology of Fe_3O_4/Pt(111) from LEEM and µ-LEED spot profile analysis. The large tail in the (00) spot profile (seen on the left) is identified with the formation of oxygen-related agglomorates as sketched below. Middle panels show the effect of cooling/annealing on the spot profile. LEEM images on the right (at an energy of 24 eV) present the surface before and after the annealing cycle. (Reprinted with permission from [73]. Copyright 2012 American Physical Society.)

morphology changes irreversibly). This observation corresponds to the thinnest magnetite crystal that shows magnetism.

Beyond the self-organized crystal shapes at the micrometer scale, epitaxial iron-oxide films provide a variety of complex surface reconstructions at the atomic scale as usual for oxide surfaces [74]. Fe_3O_4 films on Pt(111) are known to give a (2 × 2) reconstruction with an additional moiré superstructure. Nevertheless, the details of the Fe_3O_4 surface structure is still under study. The recent work by using an aberration-corrected XPEEM-LEEM setup, SMART (BESSY II, Helmholtz Zentrum, Berlin), showed distinct differences between LEED $I(V)$ curves obtained from surfaces with differing preparation pathways [73]. The role of surface preparation was revealed in the LEED spot-profile analysis of the Fe_3O_4(111) surface as summarized in Figure 11b, which showed the formation of oxygen-related defects. In particular, the different contributions to the LEED spot-profile were observed in real-time as a function of temperature, which resulted in a model of oxygen-induced extended surface defects [73].

Aside structure and magnetism, transformations between different iron-oxide phases were studied by using the SPELEEM methods. In the above example of FeO_x growth on Ru(0001), further oxidation by using NO_2 as atomic oxygen source resulted in the transformation of the FeO wetting layer to hematite (α-Fe_2O_3) and the triangular Fe_3O_4 islands to maghemite (γ-Fe_2O_3) [71]. In an independent study, the real-time observation of thermal reduction with LEEM and LEED was crucial in understanding the reversible changes in thin magnetite and hematite films grown on several substrates [75]. In particular, annealing in UHV led to substrate-dependent transformations of the iron oxide thin film: from hematite to magnetite on a Pt(111) substrate and vice-versa on Ag(111). The conversion has been explained as a competition between the dilution of Fe cations in the substrate, predominant only in the former case, and the desorption of oxygen.

Summary

We have given a review of SPELEEM methods along with recent applications in the fields of graphene and nanomagnetism. The extensive introduction to LEEM and XPEEM techniques illustrates the basic operation principles, with the intention to serve as a guideline for those unfamiliar with the field. A working example of a SPELEEM instrument is the one available at the Nanospectroscopy beamline at Elettra. Details on the instrumental aspects of the Nanospectroscopy microscope have been given both as an update on the performance of this particular setup, and also as a reference for the typical SPELEEM properties regarding parameters such as energy resolution, lateral resolution, electron beam characteristics and the transfer function of the instrument. After the instrumental part, recent scientific activity in graphene research by using LEEM-PEEM methods have been reviewed. Then, the original example of Au intercalation at the graphene–Ir(100) interface has been presented, showing the effective role of Au in breaking the C–Ir chemisorption bonds and in restoring the neutral Dirac point nearly at the Fermi level. The review has been concluded with examples on self-organized nanomagnetism studies taking advantage of the possibility to perform magnetic imaging with

an XPEEM, based on the X-ray magnetic circular dichroism contrast.

References

1. Septier, A. Geometrical Electron Optics. In *Electron Microscopy in Material Science;* Valdrè, U., Ed.; Academic Press, 1971; pp 15–73.
2. Bauer, E. *J. Phys.: Condens. Matter* **2009,** *21,* 314001. doi:10.1088/0953-8984/21/31/314001
3. Bauer, E. *J. Electron Spectrosc. Relat. Phenom.* **2012,** *185,* 314–322. doi:10.1016/j.elspec.2012.08.001
4. Tonner, B. P.; Harp, G. R. *Rev. Sci. Instrum.* **1988,** *59,* 853. doi:10.1063/1.1139792
5. Locatelli, A.; Bauer, E. *J. Phys.: Condens. Matter* **2008,** *20,* 093002. doi:10.1088/0953-8984/20/9/093002
6. Bauer, E. *Rep. Prog. Phys.* **1994,** *57,* 895. doi:10.1088/0034-4885/57/9/002
7. Man, K. L.; Altman, M. S. *J. Phys.: Condens. Matter* **2012,** *24,* 314209. doi:10.1088/0953-8984/24/31/314209
8. Wintterlin, J.; Bocquet, M.-L. *Surf. Sci.* **2009,** *603,* 1841–1852. doi:10.1016/j.susc.2008.08.037
9. Batzill, M. *Surf. Sci. Rep.* **2012,** *67,* 83–115. doi:10.1016/j.surfrep.2011.12.001
10. Tetlow, H.; Posthuma de Boer, J.; Ford, I. J.; Vvedensky, D. D.; Coraux, J.; Kantorovich, L. *Phys. Rep.* **2014,** *542,* 195–295. doi:10.1016/j.physrep.2014.03.003
11. Altman, M. S. *J. Phys.: Condens. Matter* **2010,** *22,* 084017. doi:10.1088/0953-8984/22/8/084017
12. Telieps, W.; Bauer, E. *Ultramicroscopy* **1985,** *17,* 57–65. doi:10.1016/0304-3991(85)90177-9
13. Bauer, E. *Surf. Rev. Lett.* **1998,** *5,* 1275. doi:10.1142/S0218625X98001614
14. Tanuma, S.; Powell, C. J.; Penn, D. R. *Surf. Interface Anal.* **2011,** *43,* 689–713. doi:10.1002/sia.3522
15. Altman, M. S.; Chung, W. F.; He, Z. Q.; Poon, H. C.; Tong, S. Y. *Appl. Surf. Sci.* **2001,** *169-170,* 82–87. doi:10.1016/S0169-4332(00)00644-9
16. Zdyb, R.; Menteş, T. O.; Locatelli, A.; Niño, M. A.; Bauer, E. *Phys. Rev. B* **2013,** *87,* 075436. doi:10.1103/PhysRevB.87.075436
17. Reichelt, R.; Günther, S.; Wintterlin, J.; Moritz, W.; Aballe, L.; Menteş, T. O. *J. Chem. Phys.* **2007,** *127,* 134706. doi:10.1063/1.2779028
18. de Groot, F. M. F. *J. Electron Spectrosc. Relat. Phenom.* **1994,** *67,* 529–622. doi:10.1016/0368-2048(93)02041-J
19. Hannon, J. P.; Trammell, G. T.; Blume, M.; Gibbs, D. *Phys. Rev. Lett.* **1988,** *61,* 1245. doi:10.1103/PhysRevLett.61.1245
20. Schneider, C. M.; Schönhense, G. *Rep. Prog. Phys.* **2002,** *65,* 1785. doi:10.1088/0034-4885/65/12/202
21. Hüfner, S. *Photoelectron Spectroscopy;* Springer-Verlag: Berlin Heidelberg New York, 2003.
22. Menteş, T. O.; Locatelli, A. *J. Electron Spectrosc. Relat. Phenom.* **2012,** *185,* 323–329. doi:10.1016/j.elspec.2012.07.007
23. Barrett, N.; Conrad, E.; Winkler, K.; Krömker, B. *Rev. Sci. Instrum.* **2012,** *83,* 083706. doi:10.1063/1.4746279
24. Locatelli, A.; Aballe, L.; Menteş, T. O.; Kiskinova, M.; Bauer, E. *Surf. Interface Anal.* **2006,** *38,* 1554–1557. doi:10.1002/sia.2424
25. Schmidt, T.; Heun, S.; Slezak, J.; Diaz, J.; Prince, K. C.; Lilienkamp, G.; Bauer, E. *Surf. Rev. Lett.* **1998,** *5,* 1287. doi:10.1142/S0218625X98001626
26. Gadzuk, W.; Plummer, E. W. *Rev. Mod. Phys.* **1973,** *45,* 487. doi:10.1103/RevModPhys.45.487
27. Tosi, L.; Diviacco, B.; Iazzourene, F.; Roux, R.; Walker, R. P.; Zangrando, D. Commissioning of elliptical undulators in Elettra. In *Proceedings of EPAC 2000,* 2000; pp 2349 ff.
28. Locatelli, A.; Bianco, A.; Cocco, D.; Cherifi, S.; Heun, S.; Marsi, M.; Pasqualetto, M.; Bauer, E. *J. Phys. IV* **2003,** *104,* 99–102. doi:10.1051/jp4:200300038
29. Locatelli, A.; Menteş, T. O.; Niño, M. A.; Bauer, E. *Ultramicroscopy* **2011,** *111,* 1447–1454. doi:10.1016/j.ultramic.2010.12.020
30. Cocco, D.; Marsi, M.; Kiskinova, M.; Prince, K. C.; Schmidt, T.; Heun, S.; Bauer, E. *Proc. SPIE* **1999,** *3767,* 271. doi:10.1117/12.371126
31. Imhof, R. E.; Adams, A.; King, G. C. *J. Phys. E: Sci. Instrum.* **1976,** *9,* 138. doi:10.1088/0022-3735/9/2/024
32. The Doniach–Šunjić lineshape for the bulk/surface components were fitted with 60/129 meV Lorentzian broadening and 0.035/0.063 asymmetry, respectively. The surface component was found to be at 320 meV lower binding energy.
33. Menteş, T. O.; Niño, M. A.; Locatelli, A. *e-J. Surf. Sci. Nanotechnol.* **2011,** *9,* 72–79. doi:10.1380/ejssnt.2011.72
34. Schmidt, T.; Sala, A.; Marchetto, H.; Umbach, E.; Freund, H.-J. *Ultramicroscopy* **2013,** *126,* 23–32. doi:10.1016/j.ultramic.2012.11.004
35. Sutter, P. W.; Flege, J.-I.; Sutter, E. A. *Nat. Mater.* **2008,** *7,* 406–411. doi:10.1038/nmat2166
36. Loginova, E.; Bartelt, N. C.; Feibelman, P. J.; McCarty, K. F. *New J. Phys.* **2008,** *10,* 093026. doi:10.1088/1367-2630/10/9/093026
37. Loginova, E.; Bartelt, N. C.; Feibelman, P. J.; McCarty, K. F. *New J. Phys.* **2009,** *11,* 063046. doi:10.1088/1367-2630/11/6/063046
38. McCarty, K. F.; Feibelman, P. J.; Loginova, E.; Bartelt, N. C. *Carbon* **2009,** *47,* 1806–1813. doi:10.1016/j.carbon.2009.03.004
39. Sutter, P.; Sadowski, J. T.; Sutter, E. A. *J. Am. Chem. Soc.* **2010,** *132,* 8175–8179. doi:10.1021/ja102398n
40. Sutter, P.; Albrecht, P.; Tong, X.; Sutter, E. *J. Phys. Chem. C* **2013,** *117,* 6320–6324. doi:10.1021/jp400838j
41. Alfé, D.; Pozzo, M.; Miniussi, E.; Günther, S.; Lacovig, P.; Lizzit, S.; Larciprete, R.; Burgos, B. S.; Menteş, T. O.; Locatelli, A.; Baraldi, A. *Sci. Rep.* **2013,** *3,* No. 2430. doi:10.1038/srep02430
42. Feenstra, R. M.; Srivastava, N.; Gao, Q.; Widom, M.; Diaconescu, B.; Ohta, T.; Kellogg, G. L.; Robinson, J. T.; Vlassiouk, I. V. *Phys. Rev. B* **2013,** *87,* 041406. doi:10.1103/PhysRevB.87.041406
43. Locatelli, A.; Knox, K. R.; Cvetko, D.; Menteş, T. O.; Niño, M. Á.; Wang, S.; Yilmaz, M. B.; Kim, P.; Osgood, R. M., Jr.; Morgante, A. *ACS Nano* **2010,** *4,* 4879–4889. doi:10.1021/nn101116n
44. Miniussi, E.; Pozzo, M.; Baraldi, A.; Vesselli, E.; Zhan, R. R.; Comelli, G.; Menteş, T. O.; Niño, M. A.; Locatelli, A.; Lizzit, S.; Alfé, D. *Phys. Rev. Lett.* **2011,** *106,* 216101. doi:10.1103/PhysRevLett.106.216101
45. Miniussi, E.; Pozzo, M.; Menteş, T. O.; Niño, M. A.; Locatelli, A.; Vesselli, E.; Comelli, G.; Lizzit, S.; Alfè, D.; Baraldi, A. *Carbon* **2014,** *73,* 389–402. doi:10.1016/j.carbon.2014.02.081
46. Kraus, J.; Böcklein, S.; Reichelt, R.; Günther, S.; Santos, B.; Menteş, T. O.; Locatelli, A. *Carbon* **2013,** *64,* 377–390. doi:10.1016/j.carbon.2013.07.090
47. Wofford, J. M.; Nie, S.; McCarty, K. F.; Bartelt, N. C.; Dubon, O. D. *Nano Lett.* **2010,** *10,* 4890–4896. doi:10.1021/nl102788f
48. Walter, A. L.; Nie, S.; Bostwick, A.; Kim, K. S.; Moreschini, L.; Chang, Y. J.; Innocenti, D.; Horn, K.; McCarty, K. F.; Rotenberg, E. *Phys. Rev. B* **2011,** *84,* 195443. doi:10.1103/PhysRevB.84.195443

49. Sun, J.; Hannon, J. B.; Tromp, R. M.; Johari, P.; Bol, A. A.; Shenoy, V. B.; Pohl, K. *ACS Nano* **2010,** *4,* 7073–7077. doi:10.1021/nn102167f
50. Locatelli, A.; Wang, C.; Africh, C.; Stojić, N.; Menteş, T. O.; Comelli, G.; Binggeli, N. *ACS Nano* **2013,** *7,* 6955–6963. doi:10.1021/nn402178u
51. Locatelli, A.; Zamborlini, G.; Menteş, T. O. *Carbon* **2014,** *74,* 237–248. doi:10.1016/j.carbon.2014.03.028
52. Vinogradov, N. A.; Zakharov, A. A.; Kocevski, V.; Rusz, J.; Simonov, K. A.; Eriksson, O.; Mikkelsen, A.; Lundgren, E.; Vinogradov, A. S.; Mårtensson, N.; Preobrajenski, A. B. *Phys. Rev. Lett.* **2012,** *109,* 026101. doi:10.1103/PhysRevLett.109.026101
53. Knox, K. R.; Wang, S.; Morgante, A.; Cvetko, D.; Locatelli, A.; Menteş, T. O.; Niño, M. Á.; Kim, P.; Osgood, R. M., Jr. *Phys. Rev. B* **2008,** *78,* 201408. doi:10.1103/PhysRevB.78.201408
54. Knox, K. R.; Locatelli, A.; Yilmaz, M. B.; Cvetko, D.; Menteş, T. O.; Niño, M. Á.; Kim, P.; Morgante, A.; Osgood, R. M., Jr. *Phys. Rev. B* **2011,** *84,* 115401. doi:10.1103/PhysRevB.84.115401
55. Sutter, P.; Hybertsen, M. S.; Sadowski, J. T.; Sutter, E. *Nano Lett.* **2009,** *9,* 2654–2660. doi:10.1021/nl901040v
56. Sutter, P.; Sadowski, J. T.; Sutter, E. *Phys. Rev. B* **2009,** *80,* 245411. doi:10.1103/PhysRevB.80.245411
57. Zakharov, A. A.; Mikkelsen, A.; Andersen, J. N. *J. Electron Spectrosc. Relat. Phenom.* **2012,** *185,* 417–428. doi:10.1016/j.elspec.2012.03.002
58. Pacilé, D.; Papagno, M.; Rodríguez, A. F.; Grioni, M.; Papagno, L.; Girit, Ç. Ö.; Meyer, J. C.; Begtrup, G. E.; Zettl, A. *Phys. Rev. Lett.* **2008,** *101,* 066806. doi:10.1103/PhysRevLett.101.066806
59. Johnson, K.; Ge, Q.; Sauerhammer, B.; Titmuss, S.; King, D. *Surf. Sci.* **2001,** *478,* 49–56. doi:10.1016/S0039-6028(00)01092-X
60. Locatelli, A.; Sbraccia, C.; Heun, S.; Baroni, S.; Kiskinova, M. *J. Am. Chem. Soc.* **2005,** *127,* 2351–2357. doi:10.1021/ja045285k
61. N'Diaye, A. T.; van Gastel, R.; Martínez-Galera, A. J.; Coraux, J.; Hattab, H.; Wall, D.; Meyer zu Heringdorf, F.-J.; Horn-von Hoegen, M.; Gómez-Rodríguez, J. M.; Poelsema, B.; Busse, C.; Michely, T. *New J. Phys.* **2009,** *11,* 113056. doi:10.1088/1367-2630/11/11/113056
62. Hattab, H.; N'Diaye, A. T.; Wall, D.; Klein, C.; Jnawali, G.; Coraux, J.; Busse, C.; van Gastel, R.; Poelsema, B.; Michely, T.; Meyer zu Heringdorf, F.-J.; Horn-von Hoegen, M. *Nano Lett.* **2012,** *12,* 678–682. doi:10.1021/nl203530t
63. Preobrajenski, A. B.; Ng, M. L.; Vinogradov, A. S.; Mårtensson, N. *Phys. Rev. B* **2008,** *78,* 073401. doi:10.1103/PhysRevB.78.073401
64. Varykhalov, A.; Sánchez-Barriga, J.; Shikin, A. M.; Biswas, C.; Vescovo, E.; Rybkin, A.; Marchenko, D.; Rader, O. *Phys. Rev. Lett.* **2008,** *101,* 157601. doi:10.1103/PhysRevLett.101.157601
65. Khomyakov, P. A.; Giovannetti, G.; Rusu, P. C.; Brocks, G.; van den Brink, J.; Kelly, P. J. *Phys. Rev. B* **2009,** *79,* 195425. doi:10.1103/PhysRevB.79.195425
66. Giovannetti, G.; Khomyakov, P. A.; Brocks, G.; Karpan, V. M.; van den Brink, J.; Kelly, P. J. *Phys. Rev. Lett.* **2008,** *101,* 026803. doi:10.1103/PhysRevLett.101.026803
67. Alerhand, O. L.; Vanderbilt, D.; Meade, R. D.; Joannopoulos, J. D. *Phys. Rev. Lett.* **1988,** *61,* 1973. doi:10.1103/PhysRevLett.61.1973
68. Menteş, T. O.; Locatelli, A.; Aballe, L.; Bauer, E. *Phys. Rev. Lett.* **2008,** *101,* 085701. doi:10.1103/PhysRevLett.101.085701
69. Menteş, T. O.; Stojić, N.; Locatelli, A.; Aballe, L.; Binggeli, N.; Niño, M. A.; Kiskinova, M.; Bauer, E. *EPL* **2011,** *94,* 38003. doi:10.1209/0295-5075/94/38003
70. Menteş, T. O.; Locatelli, A.; Aballe, L.; Niño, M. A.; Bauer, E. *Ultramicroscopy* **2013,** *130,* 82–86. doi:10.1016/j.ultramic.2013.03.012
71. Monti, M.; Santos, B.; Mascaraque, A.; Rodríguez de la Fuente, O.; Niño, M. A.; Menteş, T. O.; Locatelli, A.; McCarty, K. F.; Marco, J. F.; de la Figuera, J. *J. Phys. Chem. C* **2012,** *116,* 11539–11547. doi:10.1021/jp300702d
72. Monti, M.; Santos, B.; Mascaraque, A.; Rodríguez de la Fuente, O.; Niño, M. A.; Menteş, T. O.; Locatelli, A.; McCarty, K. F.; Marco, J. F.; de la Figuera, J. *Phys. Rev. B* **2012,** *85,* 020404(R). doi:10.1103/PhysRevB.85.020404
73. Sala, A.; Marchetto, H.; Qin, Z.-H.; Shaikhutdinov, S.; Schmidt, T.; Freund, H.-J. *Phys. Rev. B* **2012,** *86,* 155430. doi:10.1103/PhysRevB.86.155430
74. Noguera, C. *J. Phys.: Condens. Matter* **2010,** *12,* R367. doi:10.1088/0953-8984/12/31/201
75. Genuzio, F.; Sala, A.; Schmidt, T.; Menzel, D.; Freund, H.-J. *J. Phys. Chem. C*, in press. doi:10.1021/jp504020a

License and Terms

This is an Open Access article under the terms of the Creative Commons Attribution License (http://creativecommons.org/licenses/by/2.0), which permits unrestricted use, distribution, and reproduction in any medium, provided the original work is properly cited.

The license is subject to the *Beilstein Journal of Nanotechnology* terms and conditions: (http://www.beilstein-journals.org/bjnano)

The definitive version of this article is the electronic one which can be found at: doi:10.3762/bjnano.5.198

BEILSTEIN JOURNAL OF NANOTECHNOLOGY

Carbon nano-onions (multi-layer fullerenes): chemistry and applications

Juergen Bartelmess and Silvia Giordani*

Review

Open Access

Address:
Istituto Italiano di Tecnologia, Nano Carbon Materials, Via Morego 30, 16163 Genova, Italy

Email:
Silvia Giordani* - silvia.giordani@iit.it

* Corresponding author

Keywords:
carbon nanomaterials; carbon nano-onions; fullerenes; functionalization

Beilstein J. Nanotechnol. **2014,** *5,* 1980–1998.
doi:10.3762/bjnano.5.207

Received: 13 May 2014
Accepted: 10 October 2014
Published: 04 November 2014

This article is part of the Thematic Series "Atomic scale interface design and characterisation: Theory – Structure and dynamics".

Guest Editor: C. Ewels

© 2014 Bartelmess and Giordani; licensee Beilstein-Institut.
License and terms: see end of document.

Abstract

This review focuses on the development of multi-layer fullerenes, known as carbon nano-onions (CNOs). First, it briefly summarizes the most important synthetic pathways for their preparation and their properties and it gives the reader an update over new developments in the recent years. This is followed by a discussion of the published synthetic procedures for CNO functionalization, which are of major importance when elucidating future applications and addressing drawbacks for possible applications, such as poor solubility in common solvents. Finally, it gives an overview over the fields of application, in which CNO materials were successfully implemented.

Review

Introduction

Since the discovery of the fullerene C_{60} in 1985 by Curl, Kroto and Smalley [1], carbon nanomaterials have been the focus of interdisciplinary chemical research. In the following years, several other carbon based nanomaterials were discovered, namely carbon nanotubes (CNTs) [2-4], carbon nanohorns [5], nanodiamonds [6] and graphene [7]. Multi-shell fullerenes, known as carbon nano-onions (CNOs) and discovered by Ugarte in 1992 [8], are structured by concentric shells of carbon atoms. Over the last years, different methods for their synthesis have been developed and their properties have been widely studied. In addition, the chemical functionalization of CNOs has been investigated and several synthetic pathways were found to be applicable for the introduction of a variety of functional groups. Chemically modified CNOs were probed in different fields of application and have revealed to be a promising nanomaterial that attracts a growing interest among researchers and opens new avenues for investigation.

Preparation and structural properties of carbon nano-onions

Carbon nano-onions were first discovered by Ugarte in 1992, who obtained them by intense electron irradiation of carbon soot [8]. CNOs were later found to be part of detonation soot [9], and a variety of different methods for their synthesis were reported. For a detailed review of the different methods and related mechanisms of CNO formation, we refer to the book chapter of Luis Echegoyen and co-workers [10]. A common method, for the preparation of small CNOs consisting of approx. 5–8 carbon shells, uses nanodiamonds as starting material. Nanodiamonds can be converted to graphitic CNOs by heat treatment (Figure 1) [11,12] or by electron radiation [13]. Another method is the formation of CNOs by arc discharge of graphite in liquids such as liquid nitrogen or water [14,15]. A recent novel method for the preparation of large CNOs (30 nm diameter) includes the use of inorganic starting material, such as $CuCl_2{\cdot}2H_2O$ and CaC [16]. Large CNOs with distinct fluorescence emission were produced from wood wool, a natural resource, which was pyrolized and then subsequently treated with concentrated nitric acid [17]. Nowadays, CNOs can be produced in gram-scale quantities by treatment of commercially available nanodiamonds, or by the combustion of naphthalene [18]. This good availability of different CNO materials, grants the future investigation of the applications of CNOs in a variety of fields.

The characteristic properties of CNOs render them of great interest for a large number of applications, as we will elucidate in the corresponding section of this review article. The diameter of the CNO nanomaterial depends on the synthetic protocol, but nevertheless, CNOs exhibit in general a high surface area to volume ratio. In his initial studies, Ugarte reported distances between the carbon layers of 0.34 nm, which is in good accordance to the distance of the layers in bulk graphite [8]. In a report from 1995, Daniel Ugarte refers to CNOs as onion-like graphitic particles, which display a wide range of structures, explicitly including polyhedral to nearly spherical morphologies in his definition of CNOs [19]. It is worth to mention, that in some reports the authors utilize the term onion-like carbons (OLCs), when referring to CNOs. In this review article, we have usually included the diameter of the utilized CNO nanomaterial, together with their fabrication method. If there are any divergent structural properties from the common definition of CNOs observed, we have included this information as well.

High-resolution transmission electron microscopy (HRTEM) has been widely employed to visualize CNOs and to study the mechanisms of CNO formation and their structural properties. Raman spectroscopy is another useful technique for the structural characterization of CNOs and corroborates the basic graphitic structure of carbon nano-onions [10,12,20,21]. Typically, two broad Raman bands can be readily observed in the area between 1300 and 1600 cm^{-1} (Figure 2). The D-band at around 1350 cm^{-1} resembles structural disorder due to the presence of sp^3 carbons, while the G-band at around 1580 cm^{-1} corresponds to the E_{2g} mode of sp^2-hybridized carbon frameworks. Covalent CNO functionalization usually leads to an increase of the D-band intensity, due to the increase of sp^3-hybridized carbon atoms.

Functionalization of carbon nano-onions

The access to soluble CNOs is important for different applications. Analogous to carbon nanotubes, CNOs display poor solubility in both aqueous and organic solvents. This is due to aggregation, promoted by strong intermolecular interactions such as van-der-Waals forces. To overcome this tendency to

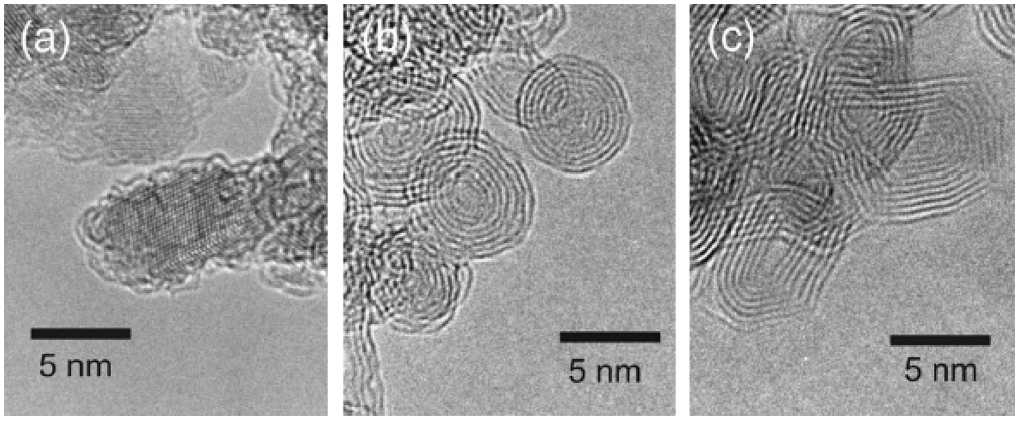

Figure 1: HRTEM images of (a) diamond nanoparticles, (b) spherical carbon onions, and (c) polyhedral carbon onions. Diamond nanoparticles are transformed into spherical onions at about 1700 °C. Polyhedral onions are dominant in the sample annealed above 1900 °C. Reprinted with permission from [12]. Copyright 2001 AIP Publishing LLC.

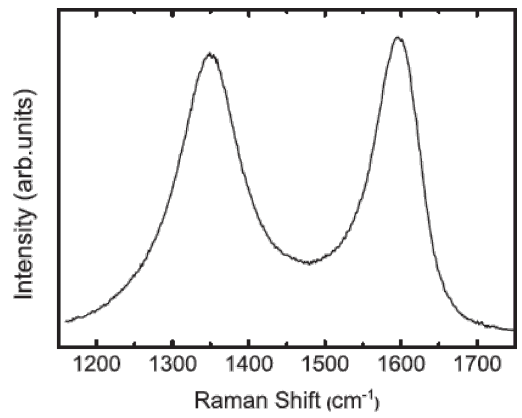

Figure 2: Typical Raman spectra of pristine CNOs. Reprinted with permission from [21]. Copyright 2013 Elsevier.

aggregate, functionalization of the surface of the carbon materials is the method of choice. The covalent as well as the non-covalent functionalization of CNTs [22-24] have been widely studied in the past decades and can serve as inspiration for possible synthetic strategies to decorate CNOs with a variety of functional groups and also to increase the solubility of CNO materials.

The following chapter summarizes the published literature regarding the reported methods for the covalent functionalization of CNOs (Scheme 1 and Table 1). In addition, we will give an overview over some CNO-containing composite materials. Except for some of these composites, the non-covalent functionalization of CNOs, especially with small molecules or surfactants, which is widely described for CNTs [23], has not been reported so far.

Covalent functionalization

Synthetic procedures for the covalent functionalization of CNOs are largely based on previously described strategies for the functionalization of CNTs [22,24]. The first study reporting covalently functionalized CNOs was published in 2003, in which Prato et al. described an azomethine ylide addition reaction on CNOs [25] (Scheme 2). The CNO material was part of raw arc-discharge soot, which was processed as produced. The crude material was heated with an amino acid and paraformaldehyde. Following filtration and washing with toluene, the solid was suspended in chloroform. After one week, the formed precipitate was removed and the functionalized CNO material was obtained by evaporation of the chloroform. The authors reported that the final product was well soluble in

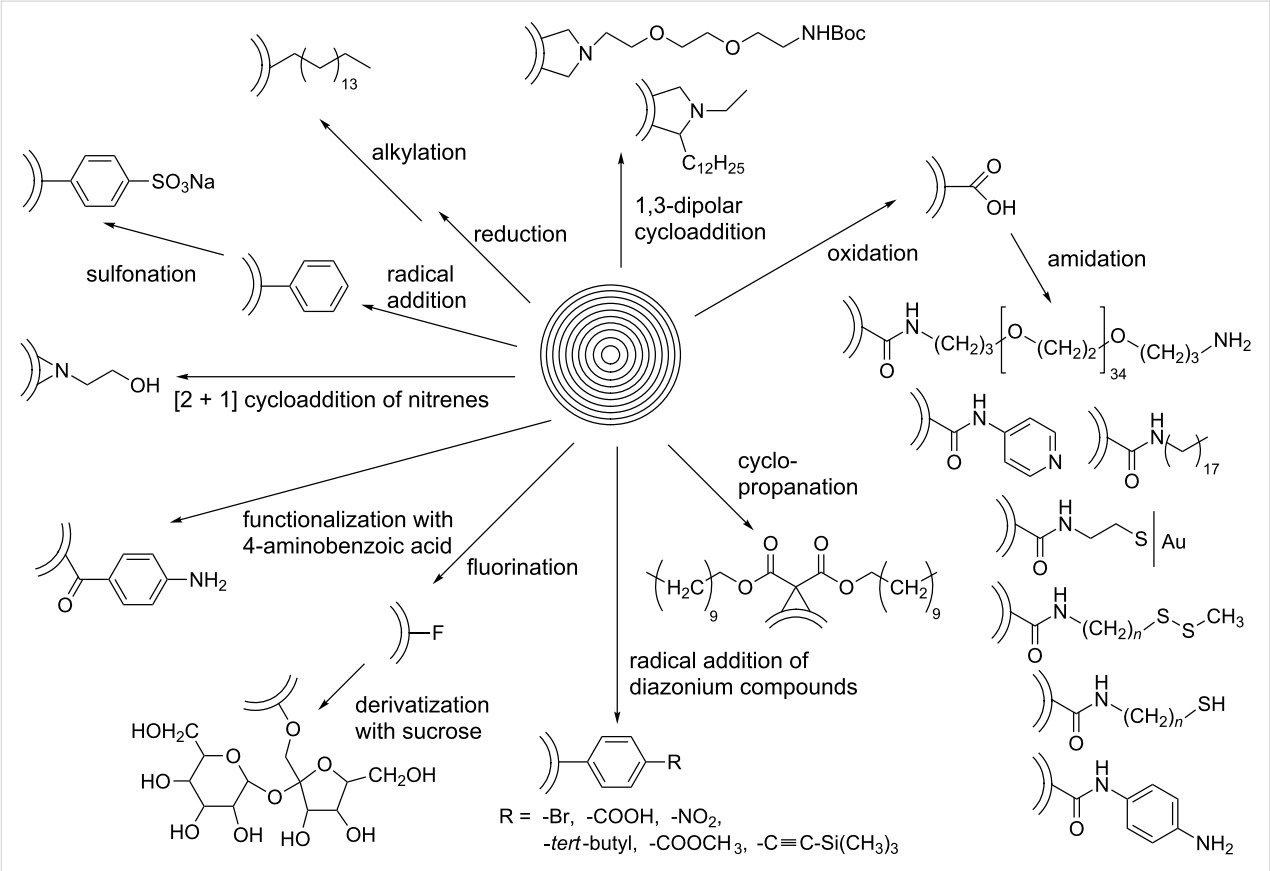

Scheme 1: Covalent functionalization pathways for CNOs.

Table 1: Overview of covalent functionalization of CNOs.

reaction	description and added functional groups	reference
1,3-dipolar cycloaddition	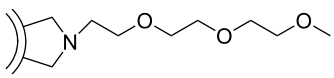	[25]
	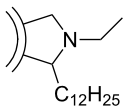	[26]
	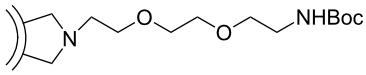	[34]
	and subsequent amidation with ferrocene	
oxidation	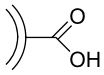	[26,27,36,59]
amidation of oxidized CNOs	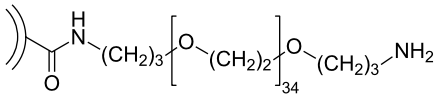	[26]
	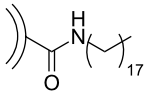	[26]
	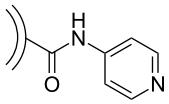	[32]
	and subsequently Zn-tetraphenylporphyrin (ZnTPP)	
	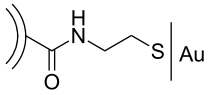	[36]
	further CNO functionalization with biotinamidohexanoic acid and subsequently avidin	
	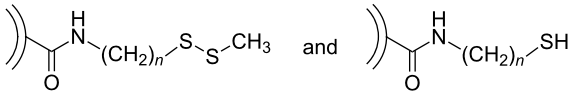	[83]
	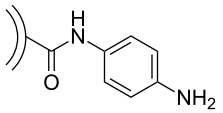	[45]
	and subsequent polymerization with *p*-phenylenediamine	
cyclopropanation	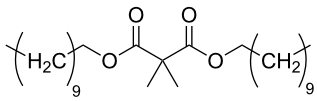	[27]
radical addition and subsequent sulfonation	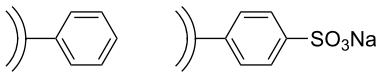	[27]
fluorination and subsequent derivatization with sucrose		[28]
	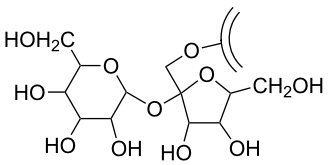	[29]

Table 1: Overview of covalent functionalization of CNOs. (continued)

radical addition	bis-*o*-diynyl arene (BODA) co-polymers (Figure 2)	[30]
[2 + 1] cycloaddition of nitrenes	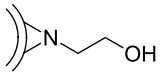 and subsequent polymerizations (Scheme 6)	[33]
radical addition of diazonium compounds	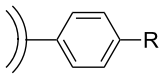 R = -Br, -COOH, -NO_2, -*tert*-butyl, -$COOCH_2C{\equiv}C\text{-}Si(CH_3)_3$ and subsequent Huisgen click-addition of Zn-porphyrin	[37]
reduction and alkylation	reduction with Na-K alloy followed by alkylation 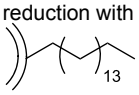	[42]
functionalization with 4-aminobenzoic acid	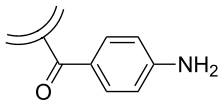 and subsequent polymerization with *p*-phenylenediamine	[45,46]

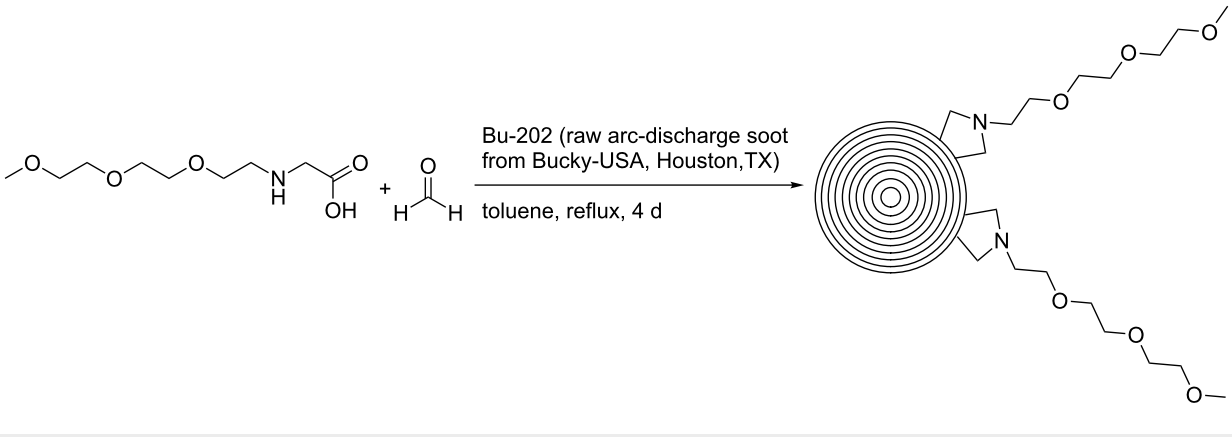

Scheme 2: Covalent functionalization of CNOs by an azomethine ylide addition [25].

common organic solvents such as ethanol, chloroform and dichloromethane. Evidence for a successful CNO functionalization was derived from ^{1}H NMR spectroscopy, MALDI mass spectrometry and elemental analysis. TEM suggested that the individual CNOs had diameters between 60 and 300 nm. In addition, steady-state absorption and fluorescence spectroscopy was performed. It was found that the functionalized CNOs exhibit a distinct CNO-centered, excitation-wavelength-dependent fluorescence with a fluorescence quantum yield of 0.08. The fluorescence lifetimes depended on the emission wavelength and were determined to be 3.13 ns (at 550 nm) and 1.85 ns (at 400 nm) for the major component of a multiexponential fit. Transient absorption measurements indicated a strong difference of the absorption coefficients in the ground and excited state. However, some concerns were risen later, whether the investigated carbon nanomaterial in the present study was comparable to the CNOs described by Ugarte [26]. Especially since the authors report the distance between the internal shells of the CNOs to be ca. 4 nm, while Ugarte reported much smaller values of 0.34 nm.

Further functionalization strategies for CNOs were reported three years later by Echegoyen et al. [26], who described two novel methods for the functionalization of CNOs and, in addition, a variation of the mentioned 1,3-dipolar cycloaddition of an azomethine ylide (Scheme 3). The CNOs were prepared by arc discharge of graphite in water and had diameters of about 20 nm. For the 1,3-dipolar cycloaddition, the CNOs were purified by thermal annealing followed by heating under reflux in 3 N HNO_3 and subsequent thermal annealing to remove potential organic functionalities. The reaction mixture, containing the purified CNOs, *N*-ethylglycine and dodecanal (or in another approach tridecanal) was refluxed, yielding the covalently functionalized CNO materials (Scheme 3A). The other two reac-

tions presented in this study were carried out with purified carboxylated CNOs, which were fabricated from raw CNO material through thermal annealing and subsequent oxidation by reflux heating in 3 N HNO_3. The first reaction utilizing oxidized CNOs was the functionalization with a diamine-terminated poly(ethylene glycol) (PEG_{1500N}), realized by heating the CNOs in the PEG for 19 days (Scheme 3B). The second reaction was the functionalization of carboxylated CNOs with octadecylamine. In order to obtain this, the authors followed two different approaches. One was a solid state synthetic procedure, in which the CNOs were heated with 1-octadecylamine in an evacuated, sealed glass ampoule. The second approach was a microwave-assisted synthesis, in which CNOs and 1-octadecylamine were heated in DMF in a microwave reactor. Both approaches were successful and led to the desired octadecylated CNOs (Scheme 3C). To summarize, the synthetic pathways described in this study yielded functionalized CNO materials that were soluble in various organic solvents. One derivative, (CNO-PEG_{1500N}), was also soluble in water.

In a comparative research work, Echegoyen et al. studied the reactivity of CNO materials of different sizes, which were prepared by different synthetic methods [27] (Scheme 4). A comparison was presented between larger and smaller CNOs. The former were produced by arc discharge of graphite under water (A-CNO), with a diameter of 15–20 nm and approx. 20–30 carbon shells while the latter were obtained by annealing nanodiamonds (N-CNO) and presented an average diameter of about 5 nm, having 6–8 carbon shells. The difference in diameter was found to be of great importance for the reactivity of the CNOs. The first reaction studied was a [2 + 1] Bingel–Hirsch cyclopropanation, which was successful only for the N-CNOs. The CNOs were reacted with a mixture of dodecyl malonate ester, carbon tetrabromide, and 1,8-diazabicyclo[5.4.0]undec-7-ene (DBU) in *o*-dichlorobenzene (Scheme 4A). The second reaction studied was a free-radical addition, in which the CNOs were heated under reflux with benzoyl peroxide as radical source in toluene. Also this reaction could be accomplished only with N-CNOs, while the A-CNOs did not react. The obtained phenylated CNOs were not soluble in organic solvents, but sulfonation with oleum, followed by treatment with aqueous NaOH lead to a highly soluble product, which formed stable dispersions in water as well as in ethanol (Scheme 4B). The last reaction investigated was based on an earlier reported oxidation of the N-CNOs by heating under reflux in 3 N HNO_3 [26]. This treatment led to the introduction of carboxylic acid functionalities and caused, as verified by Raman spectroscopy, an increase of the number of defect sites on the CNO surface (Scheme 4C). In a similar procedure, A-CNOs were not oxidized. However, oxidation of A-CNOs was accomplished under much harsher conditions (conc. HNO_3/H_2SO_4, 1:1 v/v, reflux) and led to comparable observations made for the oxidized N-CNO ma-

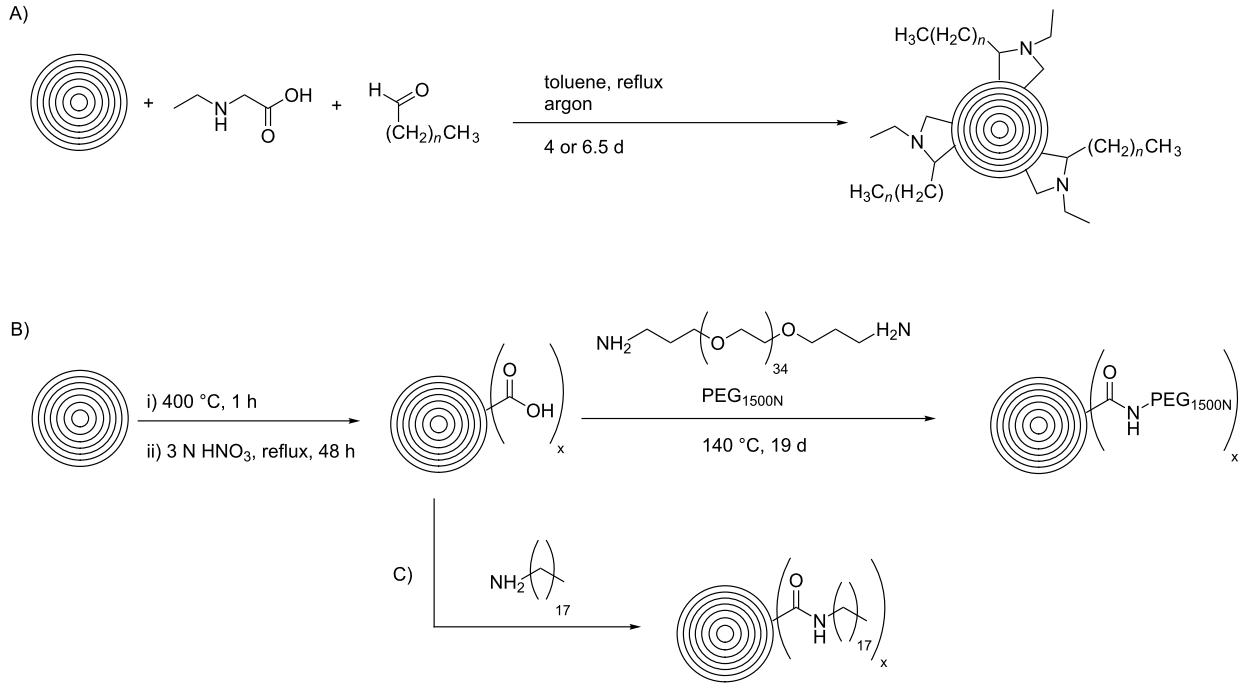

Scheme 3: Methods for the covalent functionalization of CNOs by azomethine ylide addition on CNOs and amidation reactions of carboxylated CNOs [26].

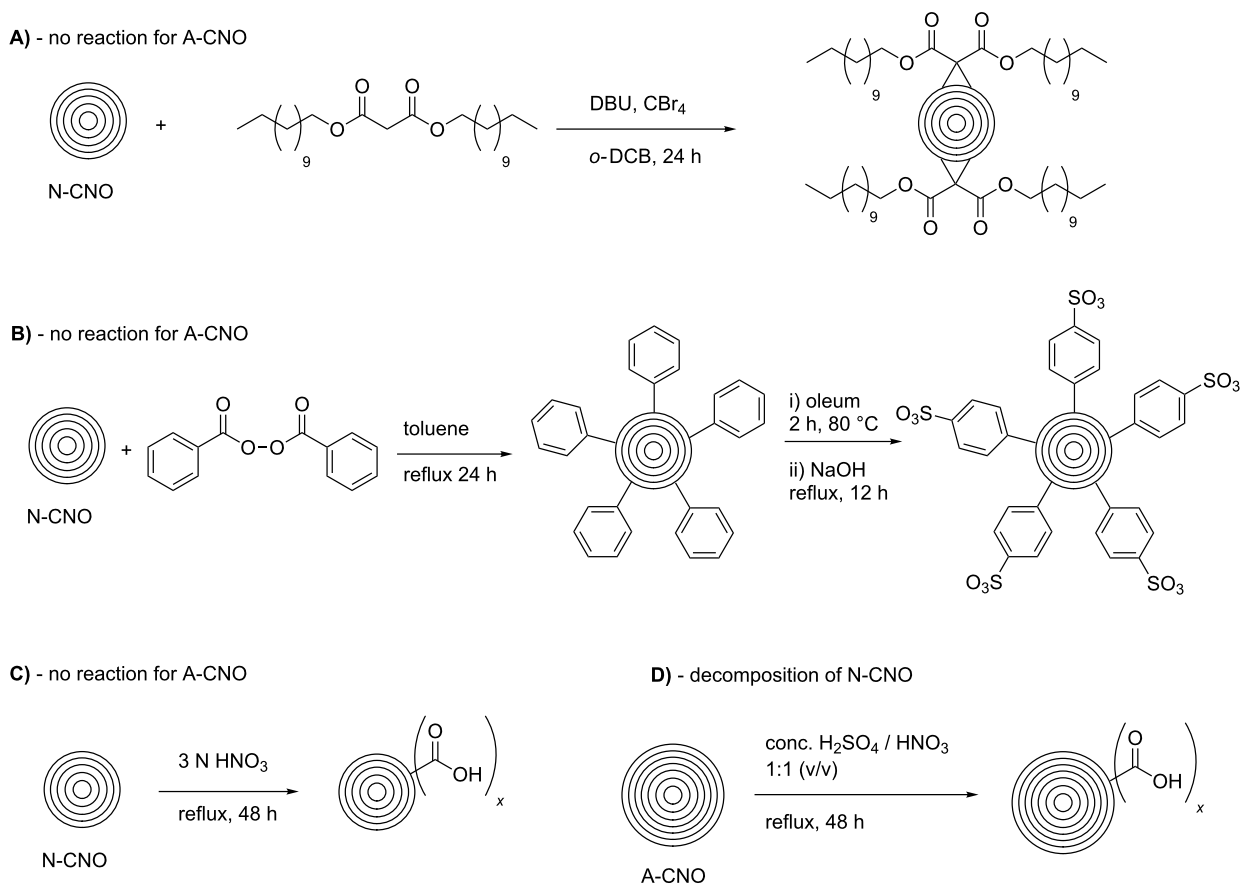

Scheme 4: Comparison of the reactivity of small N-CNOs and larger A-CNOs, prepared by different methods [27].

terial. It is important to note that N-CNOs were completely destroyed under the harsh reaction conditions mentioned above (Scheme 4D). In conclusion, the authors found that the smaller N-CNO are much more accessible for covalent functionalization, while the functionalization of A-CNO requires an aggressive treatment. This observation is led back to a higher surface-to-volume ratio in the N-CNOs, compared to A-CNOs, as well as to a larger curvature increasing the degree of surface strain.

Another example for the functionalization of CNOs in a highly reactive environment was published by Khabashesku et al., who directly fluorinated CNOs under a stream of F_2 and H_2 [28]. CNO fluorination was carried out in a custom-built reactor with different fluorination temperatures. The CNOs used in this study were prepared from carbon black by heating and the formed individual CNOs had diameters between 50 and 100 nm. HF was generated in situ under the given reaction conditions in a continuous flow of a F_2 gas mixture (10% F_2/90% He) and H_2. The successful fluorination led to an increase of the mass of the CNO material and the fluorinated CNOs (F-CNO) were well soluble in ethanol and other alcohols as well as in DMF. Characterization of the F-CNOs was carried out by a multitude of techniques such as FTIR, Raman and UV–vis spectroscopy, SEM/EDX, XRD, XPS, TGA and TEM. In addition, the authors reported that the fluorination of the F-CNOs was reversible upon treatment with hydrazine, which interestingly led also to a regeneration of the "broken" graphene layers of the CNO.

Some years later, based on the F-CNO material, the same group reported the preparation of water-soluble sucrose-functionalized CNOs [29]. In this case, F-CNOs were reacted with a lithium monosucrate derivative, which was previously synthesized from sucrose and lithium hydroxide. The sucrose-decorated CNOs showed an improved solubility of up to 200 $mg \cdot L^{-1}$ in water and 400 $mg \cdot L^{-1}$ in DMF.

Smith et al. reported the first radical addition of a polymer to CNOs in 2007 [30]. The CNO starting material was prepared and purified following an earlier reported procedure [26], and then further functionalized with bis-*o*-diynyl arene (BODA), which is known to thermally form reactive bis-radicals [31]. After ultrasonication and heating of the CNOs and BODA in *N*-methyl-2-pyrrolidone (NMP) in a pressure vessel, a

CNO–BODA copolymer was obtained. NMP suspensions of the CNO–BODA copolymer were found to be very stable, even at high concentrations of up to 0.67 mg·mL^{-1} (Figure 3). Characterization was carried out by a multitude of different techniques, such as GPC, TEM, TGA, XPS and Raman spectroscopy.

In 2008, Echegoyen et al. reported a first supramolecular CNO/Zn-porphyrin complex [32] (Scheme 5). In this set up, acid-treated CNOs bearing carboxylic acid functionalities, which were prepared by the oxidation of CNOs (diameter approx. 6 nm) with conc. HNO_3/H_2SO_4 (3:1, v/v), were reacted with 4-aminopyridine in an amidation reaction. The synthesized water-soluble CNO material was characterized by using TEM, NMR, UV–vis and Raman spectroscopy. Based on TGA studies, the authors estimated that approximately one pyridine functionality per 120 CNO surface carbon atoms was present. The pyridine groups were then decorated with Zn-tetraphenylporphyrin (ZnTPP) what was confirmed by NMR spectroscopy and electrochemistry. No further spectroscopic studies were carried out with the presented CNO–ZnTPP supramolecular complex.

A further example of a [2 + 1] cycloaddition on CNOs was reported by Kong et al., who used different nitrene derivatives to covalently functionalize pristine CNOs [33] (Scheme 6). The

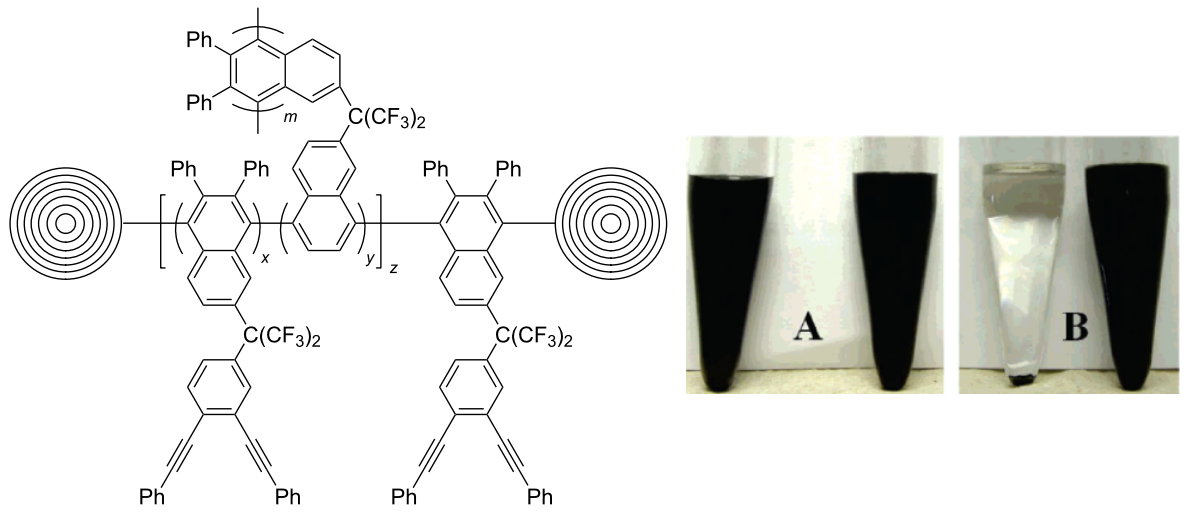

Figure 3: Structure of a CNO–BODA copolymer. (A) CNO starting material (left) and BODA-functionalized CNOs (right) suspended in NMP (0.67 mg·mL^{-1}) immediately after sonication. (B) CNO starting material (left) and BODA-functionalized CNOs (right) suspended in NMP (0.67 mg·mL^{-1}) after 2 h and 48 h of centrifugation. Reprinted with permission from [30]. Copyright 2007 American Chemical Society.

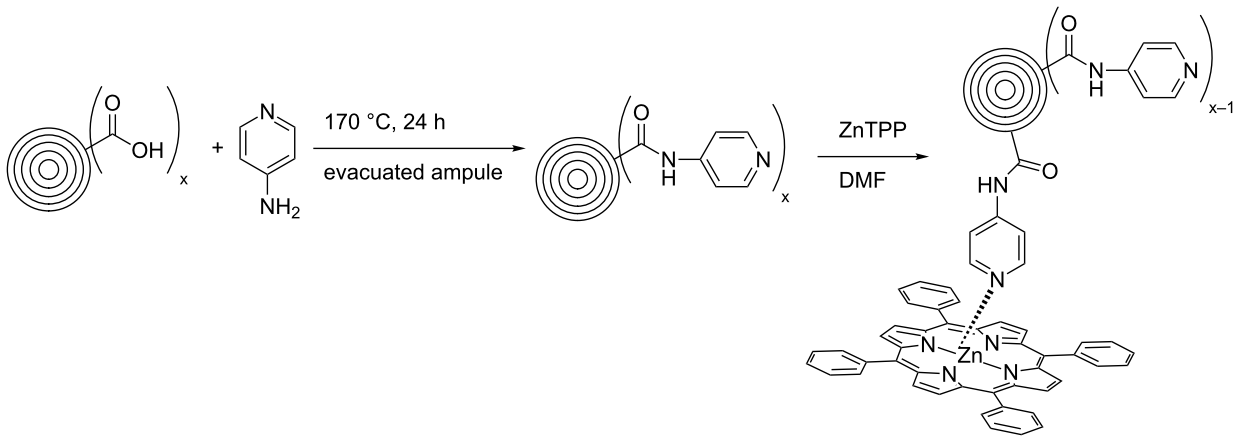

Scheme 5: Preparation of pyridyl-CNOs and an illustration of their supramolecular interaction with Zn-tetraphenylporphyrin (ZnTPP) [32].

CNO starting material was reacted with either 2-azidoethanol, leading to OH-functionalized CNOs (CNO-OH) or azidoethyl 2-bromo-2-methylpropanoate, yielding Br-functionalized CNOs (CNO-Br). The functionalized CNOs showed an increased solubility in organic solvents and water and were characterized by various techniques, such as TGA, XPS, TEM and Raman spectroscopy. Interestingly, the CNO-OH showed distinct fluorescence emission with an emission maximum at 453 nm in aqueous solution, while CNO-Br did not fluoresce. Based on these two CNO derivatives, the authors reported different polymerization reactions, where the CNOs served as macroinitiators. Firstly, CNO-OHs were used for a ring opening polymerization with ε-caprolactone in the presence of stannous octoate. In a second approach, CNO-Brs were decorated with polystyrene in an atom transfer radical polymerization reaction. Both polymer-functionalized CNO materials showed a good solubility in common organic solvents and give rise to potential future applications in various fields of technology.

The synthesis of ferrocene (Fc)-decorated CNOs was reported by Prato et al. [34]. CNOs were functionalized in a 1,3-dipolar cycloaddition reaction with a BOC-protected amin/amino acid [35] and paraformaldehyde. Subsequent deprotection of the amino functionality and reaction with Fc-carboxylic acid chloride lead to Fc-functionalized CNOs. By utilizing a TGA-based method for estimating the number of functionalizations per surface carbon atom of a CNO, the authors reported that the CNOs presented in this study contained one functional group per 36 surface carbon atoms. The properties of the Fc-CNO conjugates and the electronic interactions between the Fc and the CNO were investigated by electrochemical and spectroscopic methods, and supported by quantum chemical calculations.

A covalent functionalization of CNOs with biomolecules was reported by the groups of Plonska-Brzezinska, Simionescu and Echegoyen in 2010 [36]. In the first step, small CNOs (6–8 shells) were oxidized by using conc. H_2SO_4/HNO_3 and subsequently functionalized with PEG to study their cytotoxicity on rat dermal fibroblasts. The result was that no significant cytotoxicity was observable, which renders this CNO material ideal for future biological applications. Toward the fabrication of CNO-biosensors, gold electrodes were initially decorated with a self-assembled monolayer of cysteamine on which the oxidized CNOs were deposited by an amidation reaction. In another amidation step, some of the unreacted carboxylic acid groups on the CNO surface were functionalized with biotin, which allows the attachment of biomolecules such as avidin. This first covalent functionalization of CNOs with biomolecules, promoted by biotin–avidin interactions, gives rise to future biological applications such as bio-sensors, especially since the authors of this study reported that the attached protein retains its biological activity.

A novel strategy for the surface functionalization of CNOs was published by our group in 2010 [37] (Scheme 7).

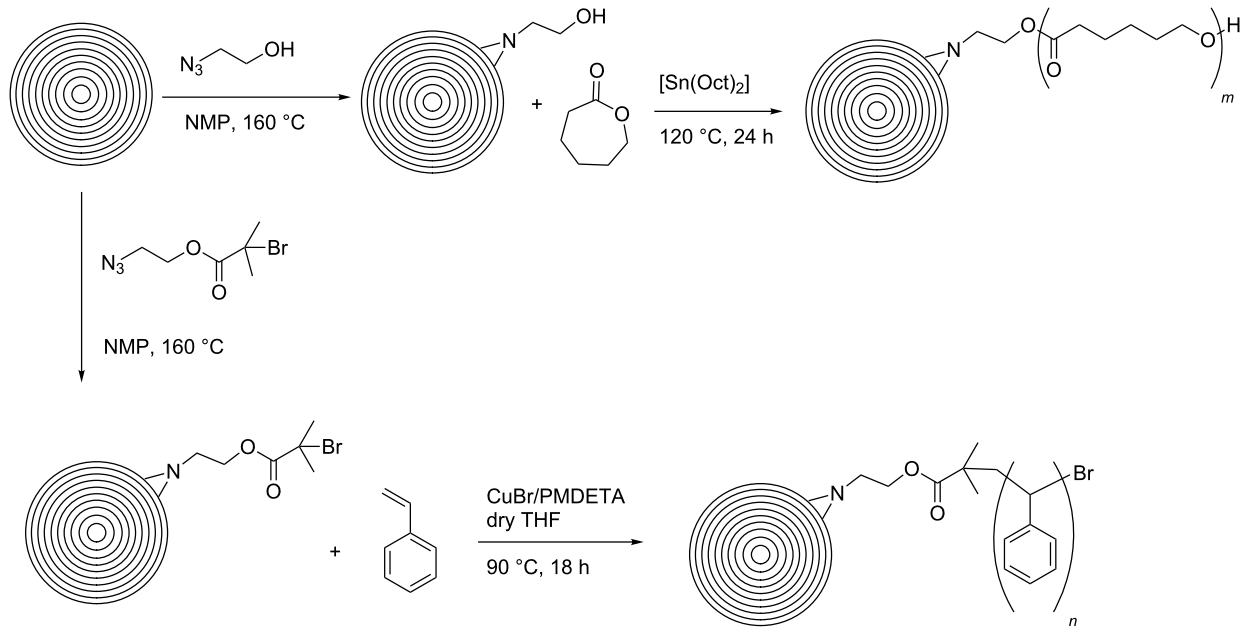

Scheme 6: Illustration of polymerization reactions on CNOs following initial [2 + 1] cycloaddition reaction of nitrenes [33].

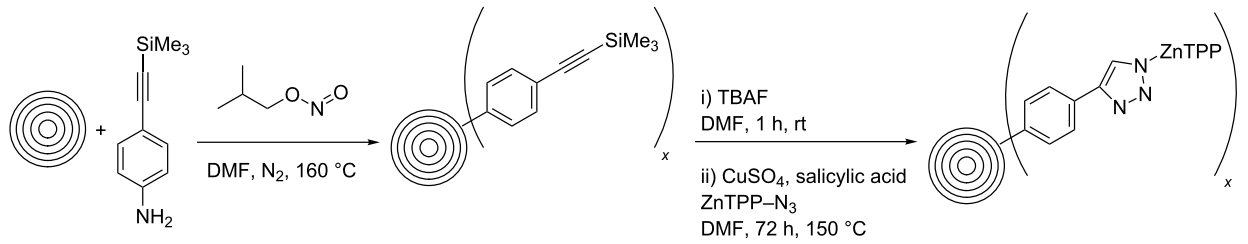

Scheme 7: "Tour" functionalization of CNOs and subsequent "click"-addition of a ZnTPP-derivative [37].

The so-called Tour reaction is well studied for the covalent functionalization of carbon nanotubes by reacting them with in situ generated diazonium compounds [38]. This versatile reaction was used in the present study to attach different aniline derivatives to the surface of CNOs and thus introducing a variety of functional groups, such as bromides, benzoic acids, *tert*-butyl groups, nitro groups, methyl esters, and trimethylsilyl (TMS) acetylenes. For all reactions, the CNO starting material was suspended in DMF by ultrasonication and then the aniline derivative and isoamyl nitrite were subsequently added. After stirring, the different functionalized CNOs were obtained and characterized by Raman and TGA analysis. The Raman spectroscopy showed an increase of the D-band at 1354 cm^{-1}, a clear confirmation of a successful covalent functionalization. In addition, TGA showed a significant weight loss at temperatures below 450 °C upon functionalization. Based on the method of Prato et al. [34], the number of surface carbon atoms per functionality was calculated to be between 22 and 60, depending on the different aniline derivatives used for functionalization. Multiple repetitions of the reaction lead to a further increase of the degree of functionalization (Figure 4). All kinds of functionalization led to an increased dispersibility of the CNOs. In a next step, the CNO–TMS acetylide material was first deprotected and then the free acetylene group was coupled with zinc triphenyl azidophenyl porphyrin in a copper-mediated "click" reaction. The successful functionalization was verified by TGA analysis as well as by Raman, absorption and fluorescence spectroscopy.

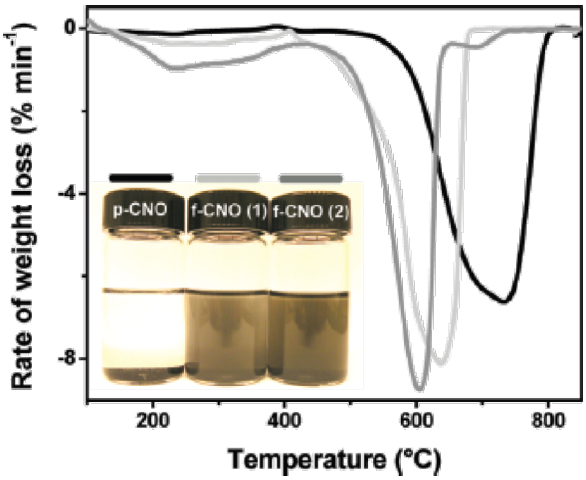

Figure 4: First derivative TGA weight-loss curves of pristine CNO (black), treated once (light gray) and treated three times with 4-bromoaniline (dark gray). Inset shows the enhanced CNO dispersibility in THF upon functionalization. Reprinted with permission from [37]. Copyright 2010 American Chemical Society.

Following the aforementioned functionalization of CNOs with benzoic acid [37], fluoresceinamine-based fluorophores [39] as well as NIR-emitting aza-borondipyrromethenes (azaBODIPYs) were attached to the CNOs through an amidation reaction [40]. In another very recent study, we attached a *meso*-phenol-substituted borondipyrromethene (BODIPY) fluorophore on the same benzoic acid functionalized CNO nanomaterial through an esterification reaction [41]. These fluorescent-tagged CNOs (Scheme 8) were then used for in vitro fluorescence imaging, which will be discussed in the corresponding section of this review article.

Recently, Echegoyen et al. reported for the first time the alkylation of CNOs [42], which was achieved by a reductive process utilizing a Na–K alloy. CNOs were added to a previously prepared, deep-blue solution of the Na–K alloy in 1,2-dimethoxyethane under inert atmosphere affording a brownish dispersion. Then an excess of 1-bromohexadecane was added as electrophile and the alkylated CNO material (CNO-C_{16}) could be recovered. TGA analysis and IR as well as Raman spectroscopy were used to verify the successful alkylation of the CNOs. It was reported that the CNO-C_{16} exhibits an outstanding solubility in a multitude of organic solvents, even in high concentrations of up to 0.1 $mg \cdot mL^{-1}$. This high solubility enabled the use of ^1H NMR spectroscopy, which corroborated the presence of alkyl groups on the CNO surface. Additional HRTEM and SEM experiments were carried out to further support the successful functionalization and excellent solubility of CNO-C_{16}. The authors also studied the reversibility of this alkylation reaction, which could be accomplished by annealing the CNO-C_{16} material at 415 °C, which was supported by Raman spectroscopy.

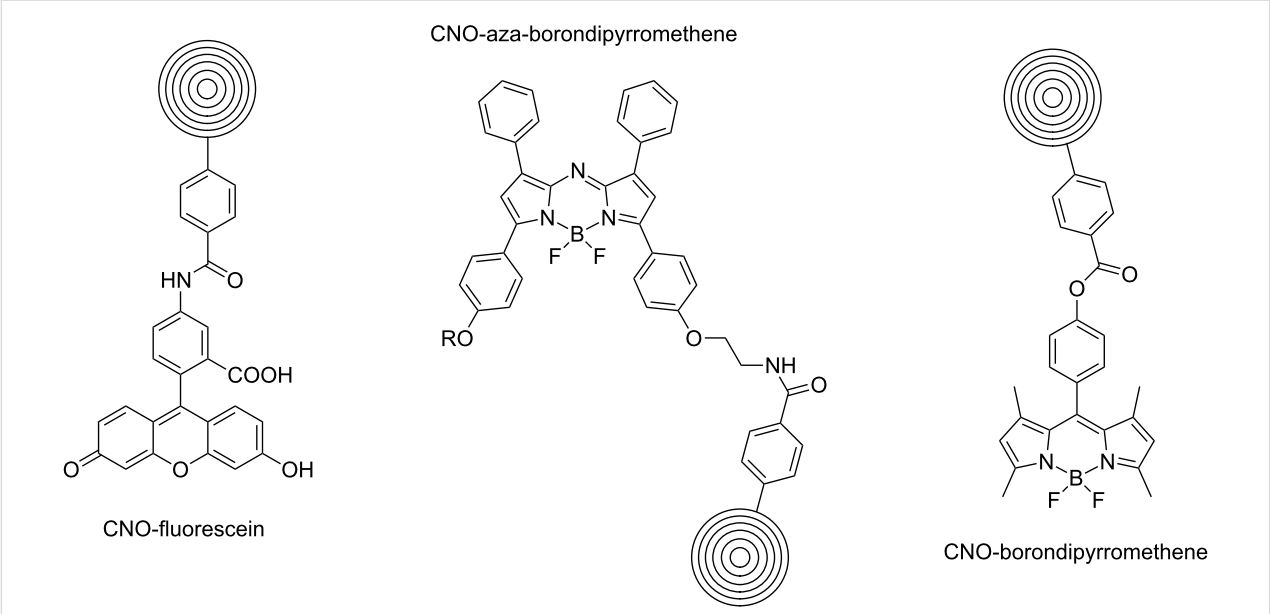

Scheme 8: Fluorophore–CNO conjugates derived from benzoic acid-functionalized CNOs [39-41].

CNO composites

In addition to the previously mentioned BODA-based CNO nanocomposites [30] and polymer-functionalized CNOs prepared by a [2 + 1] cycloaddition of nitrenes [33], several other CNO-containing composites have been reported (Scheme 9). In one study, composites consisting of CNOs and poly(diallyldimethylammonium chloride) (PDDA) or chitosan (Chit) were prepared and their electrochemical properties were studied [43]. In another study, CNO–PDDA composite films were used for the detection of dopamine in the presence of ascorbic acid and uric acid in solution [44]. The concentration of dopamine could be determined in a range between 5×10^{-5} and 4×10^{-3} mol·L^{-1}. They also reported the in situ polymerization of aniline on phenylene amine-terminated CNO derivatives [45]. This polyaniline (PANI)-functionalized CNOs were characterized by a multitude of techniques and showed an excellent solubility in protic solvents, which gives rise to several future applications of this material. In a follow-up study, the properties of CNO–PANI composites were compared to other PANI-decorated carbon nanostructures [46]. In general, PANI films containing carbon nanostructures showed improved properties like a lower resistance and higher mechanical stability than pure PANI films. Another CNO-containing composite material was prepared from unmodified or oxidized CNOs and poly(3,4-ethylenedioxythiophene):poly(styrenesulfonate) (PEDOT:PSS) [47]. In a very recent study, they reported the non-covalent functionalization of CNOs with poly(4-vinylpyridine-*co*-styrene) (PVPS) and poly(ethylene glycol)/Polysorbate 20 (PEG/P20) [48]. The PVPS polymers were then further functionalized with thiols. Both CNO-containing polymers, could be modified with flavonoid compounds, for the example quercitin, a compound known for its anti-inflammatory potential [49], giving rise to future applications in nanomedicine.

Some additional metal oxide-containing composite materials were studied for applications as electrode materials in capacitors and lithium-ion batteries and will be discussed in the corresponding part of this review article.

Toxicological aspects

In the context of applications in biology and medicine, newly employed nanomaterials should be carefully evaluated with regard to biocompatibility, environmental health and safety, secure processing and sustainable engineering.

In the case of CNOs, limited data regarding their biocompatibility has been published. An initial report, investigating the toxicity of large CNOs with a diameter of about 30 nm was published in 2005 by Chen et al. [50]. They probed the effects of large CNOs produced by an underwater carbon-arc discharge, as well as of multi-wall carbon nanotubes (MWCTNs) on human skin fibroblasts and found more adverse effects upon exposure to MWCNTs as compared to CNOs. However, CNOs were also found to cause negative effects on the studied cell cultures. The first report investigating the toxicity of small CNOs dates back to 2010, when Echegoyen et al. investigated the biocompatibility of PEGylated CNOs by exposing rat dermal fibroblasts to different CNO concentrations [37]. The authors could show almost 100% viability of

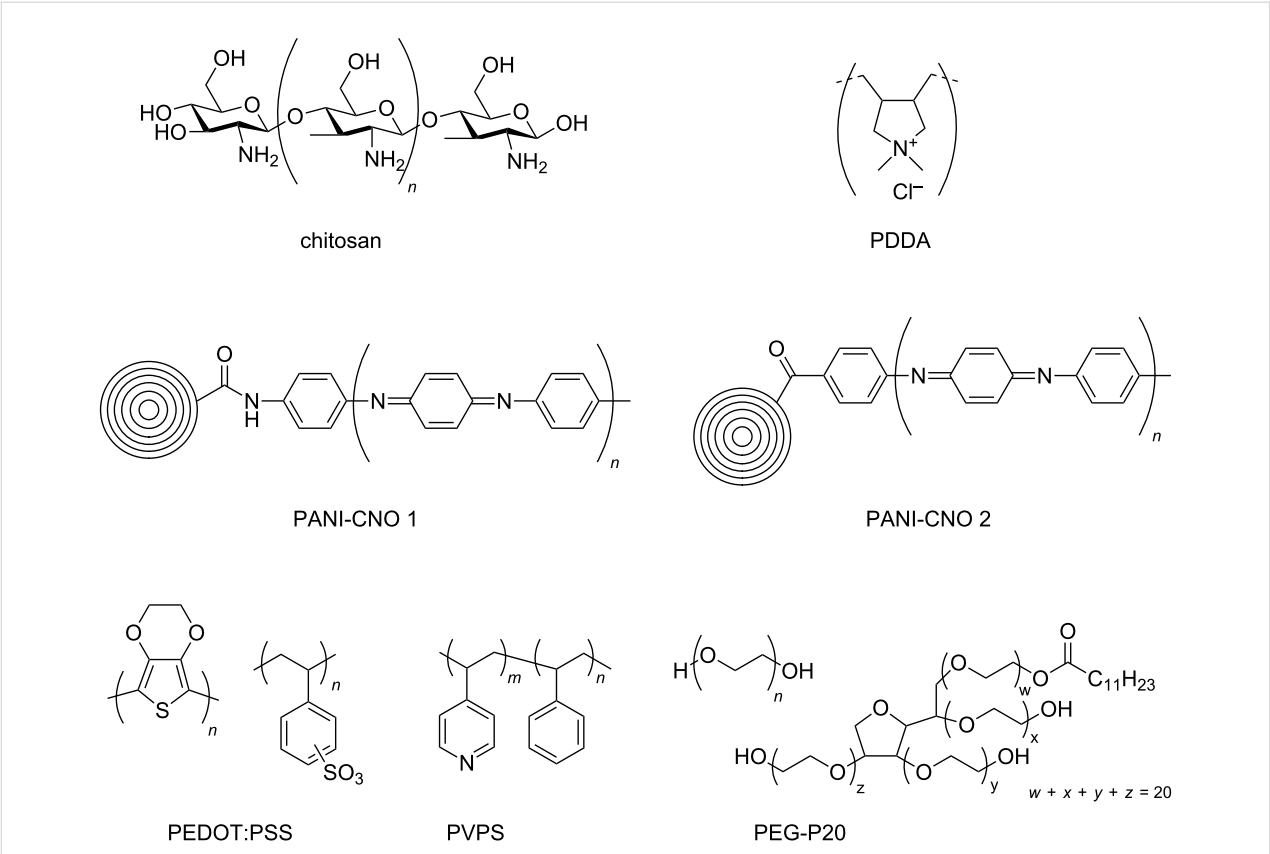

Scheme 9: Schematic overview over the different polymeric structures utilized to functionalize CNOs [43-48].

cells for concentrations of 30 and 300 μg·mL^{-1}, and a minor reduction of approx. 15% for 3,000 μg·mL^{-1}. Thus, it follows that small CNOs are not cytotoxic and can be used safely for biological studies. In two other reports, highly oxidized CNOs, derived from pyrolized wood wool, were used for in vivo imaging of *Drosophila melanogaster*, *Escherichia coli* and *Caenorhabditis elegans* [17,51]. In both studies, no toxic effects of the water-soluble CNOs on the investigated organisms were observed.

We recently reported the weak inflammatory potential and low cytotoxicity in vitro and in vivo of CNOs and their ability to be up-taken by antigen-displaying cells. In our work, small benzoic acid functionalized CNOs were compared with similar functionalized single wall carbon nanotubes [39]. CNOs showed a lower inflammatory potential than CNTs and we demonstrated that chemical functionalization attenuates their inflammatory properties. This was evidenced by a reduced secretion of the inflammatory cytokine IL-1β, and a pronounced decrease in the recruitment of neutrophils and monocytes following injection into mice. Subsequently, in two recent studies, we investigated the effects of two different, fluorophore functionalized CNOs on HeLa Kyoto [40] and MCF-7 cells [41] and did not observe any significant cytotoxicity. Our results let us believe that CNOs are promising materials for biological and medicinal applications.

Applications

In the following chapter we give an overview over the different applications of CNOs. We have selected representative studies from all areas of materials science, nano- and biotechnology and chemistry where CNOs have been successfully applied. The presented functionalization pathways usually led to a largely improved solubility of the CNO materials and thus to an enhanced processability and applicability. In addition, the introduction of functional groups and functionalities for specific applications further improved the usability of CNO materials. However, while other carbon nanostructures have drawn large attention in a variety of fields of applications, CNOs can still be considered as being a niche of the research on carbon nanostructures.

Biological and environmental applications

Biological imaging: In contrast to other carbon nanomaterials such as CNTs [52] or carbon quantum dots [53], CNOs have not been widely employed in biological marking, yet. A first report

was published in 2011 by Sarkar et al. by using large, defect rich CNOs, synthesized from wood waste, for imaging the life cycle of *D. melanogaster* (Figure 5) [17]. The authors claim that solubility in water was achieved by the presence of a large number of carboxylate groups on the CNO surface that originate from the production process. These carboxylate functional groups, together with the defective nature of the CNOs, also led to the observed fluorescence emission in the visible and NIR, which was imposed by spontaneous surface passivation and quantum confinement and allowed for multicolor biological imaging. The specimens were fed with fluorescent CNO nanomaterial that accumulated in the organisms and could be observed by fluorescence microscopy. Control experiments with non-CNO fed specimens were performed, excluding autofluorescence as reason for the observed luminescence of the organisms. Following their initial work describing in vivo biological marking of *D. melanogaster*, they used fluorescent CNOs also as imaging agents to study *E. coli* and *C. elegans* in vivo [51].

In a recent report from our group [40], we used fluorescein-functionalized CNOs in a comparative toxicological study in vitro and in vivo, including biological marking (Figure 6). The cytotoxicity and immunomodulatory properties of the synthesized fluorescein-CNO derivative were elucidated and compared with similarly functionalized CNTs. We could show that CNOs exhibit efficient cellular uptake, weak inflammatory potential, and low cytotoxicity and are therefore promising material for biomedical applications.

Recently we demonstrated the cellular imaging of HeLa Kyoto [40] and MCF-7 cells [41] after incubating them with azaBODIPY- or BODIPY-functionalized CNOs (Scheme 8 and Figure 7). In both cases the CNO conjugates were readily inter-

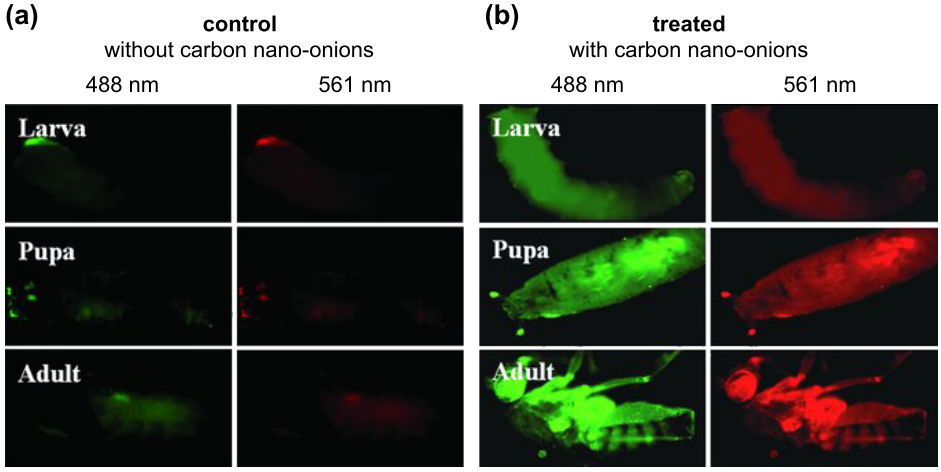

Figure 5: a) Autofluorescence images of different developmental stages of *Drosophila melanogaster* from larva to adult. b) *D. melanogaster* fed with water-soluble CNO, under 488 and 561 nm filters. Reprinted with permission from [17]. Copyright 2011 John Wiley and Sons.

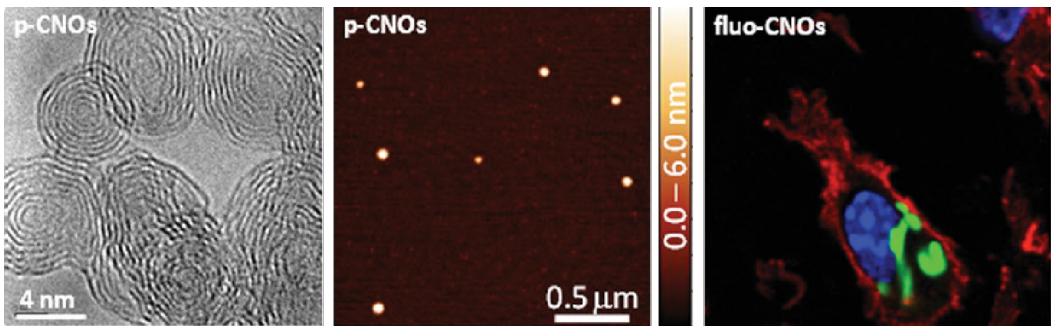

Figure 6: High-resolution TEM images of pristine CNOs (left). AFM topographs of pristine CNOs deposited on mica (center). Confocal microscopy of C57BL/6 BMDCs incubated in the presence of fluorescein-labelled-CNOs and stained with wheat germ agglutinin-Alexa Fluor594 (red), fluorescein (green) and nuclei stain Hoechst (blue) (right). Reprinted with permission from [39]. Copyright 2013 John Wiley and Sons.

nalized by the cells. In the earlier study, one of the azaBODIPY-CNO derivatives showed a pH-dependent switching (on–off) of the fluorescence, a feature that could also be observed inside the cells. The latter CNO nanomaterial was subject to co-localization experiments with Lysotracker Red dye and it was confirmed by high-resolution imaging that the CNOs were deposited in the lysosomes of the cells.

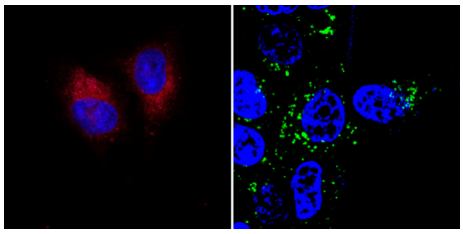

Figure 7: Confocal images of azaBODIPY-CNOs in HeLa Kyoto cells (left) and BODIPY-CNOs in MCF-7 cells (right). The blue luminescence is due to Hoechst 33342 nuclear stain. Reproduced with permission from [40] and [41]. Copyright 2014 The Royal Society of Chemistry.

Biological sensing: In the aforementioned study of Luszczyn et al. [36], CNOs were covalently functionalized with biomolecules and studied for the first time as biosensors by using avitin–biotin interactions. The CNO served as linking layers between the biomolecules and the gold surface of the sensor and led to an amplified signal of the biosensor, as determined by surface plasmon resonance spectroscopy. In addition, the biocompatibility of CNOs was investigated and found to be excellent.

Environmental remediation: An application of CNO in environmental remediation was studied by Li group [54], who revealed that surface-oxidized CNO in aqueous suspensions have a high sorption capacity for heavy metal ions such as Pb^{2+}, Cu^{2+}, Cd^{2+}, Ni^{2+} and Zn^{2+}. The sorption capacity of oxidized CNOs was found to be up to ten times higher than the one of fullerene C_{60}. These encouraging results could be a first step toward in situ remediation of heavy metal contaminants.

Electronic applications

Capacitors: Carbon materials are commonly used as electrode materials in capacitors, but the first study probing CNOs as electrode materials in electrical double layer capacitors (EDLC) with an organic electrolyte was published only in 2007. The electrochemical performance of CNO electrodes was compared with electrodes made with nanodiamonds, multi-wall carbon nanotubes and carbon black [55]. Following this initial work, several groups studied CNO materials in supercapacitor electrodes. Bushueva et al. for example, found capacitance values of the investigated CNO material of 20–40 $F{\cdot}g^{-1}$ and 70–100 $F{\cdot}g^{-1}$ with acidic or basic electrolyte solutions, respectively [56]. In 2010, Pech et al. published the preparation and characterization of ultrahigh-power micrometer-sized supercapacitors based on CNOs [57]. In an extensive electrochemical study in different aqueous and organic electrolytes, McDonough et al. investigated the influence of the CNO structure on their electrochemical performance in supercapacitor electrodes [58]. The increase of the capacitance of CNO materials was the subject of two further studies. Borgohain et al. firstly oxidized the CNOs and subsequently functionalized the surface with polar carboxylic acid groups, which enabled them to precipitate RuO_2 [59]. This functionalization led to an increase of the capacitance from 45 $F{\cdot}g^{-1}$ (for the pure CNO material) to 334 $F{\cdot}g^{-1}$ (for the $RuO_2{\cdot}H_2O$–CNO composite material). Another strategy to increase the CNO capacitance is the activation of the CNO surface by treatment with 6 M KOH, creating porosity in the outer shells of the CNOs (Figure 8) [60]. The activated CNOs show largely improved properties compared to pristine CNOs with a maximum specific capacitance of 122 $F{\cdot}g^{-1}$ (vs 25.8 $F{\cdot}g^{-1}$), a power density of 153 $kW{\cdot}kg^{-1}$ (vs 123 $kW{\cdot}kg^{-1}$) and an energy density of 8.5 $Wh{\cdot}kg^{-1}$ (vs 1.5 $Wh{\cdot}kg^{-1}$).

Composite materials were studied for application in capacitors as well. The group of Echegoyen found that incorporation of CNOs in a Chit- or PDDA-polymer matrix leads to a large increase of the capacitance of the composite films (from 4–10 $F{\cdot}g^{-1}$ for the pure Chit or PDDA films to 20–30 $F{\cdot}g^{-1}$ for the corresponding CNO composite material) [43]. Also the specific electrochemical capacitance of a CNO–PANI composite (206.64 $F{\cdot}g^{-1}$) was much larger than for pure oxidized CNOs (12.15 $F{\cdot}g^{-1}$) [45]. After optimization in a follow-up study, the highest specific capacitance for a CNO–PANI composite was measured to be 525 $F{\cdot}g^{-1}$, which renders this composite material interesting for applications in supercapacitor electrodes [46]. Also the CNO/PEDOT:PSS composites, which were previously discussed, showed promising properties for the application as electrode material in supercapacitors, such as a specific capacity of 96 $F{\cdot}g^{-1}$, good cation-exchange properties and a simple synthesis [47]. In a recent study, the same group decorated the surface of CNO with $Ni(OH)_2$ or NiO as pseudocapacitive redox material and showed that these composites can be promising materials for the development of supercapacitors [61]. In order to achieve this, the CNO surface was modified with nickel particles, which were synthesized in situ from nickel nitrate hexahydrate and ammoniumhydroxide in ethanol in the presence of (4-dimethylamino)pyridine (4-DMAP) as modifier in a one-pot multi-step reaction. Calcination of the CNO/4-DMAP/$Ni(OH)_2$ composite led to the CNO/4-DMAP/NiO composite material. The electrochemical properties were promising, especially the specific

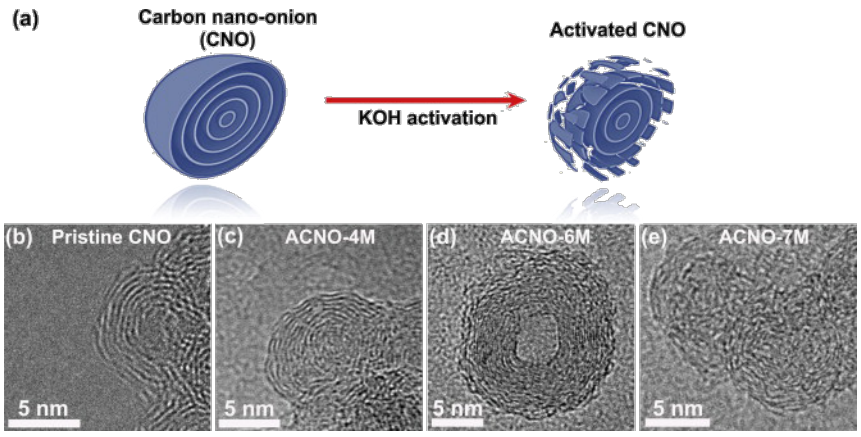

Figure 8: (a) A schematic showing the chemical activation of CNOs in KOH. TEM images of pristine CNO (b), ACNO-4M (c), ACNO-6M (d), and ACNO-7M (e). "ACNO-nM" denotes the activated CNO prepared using *n* mol·L^{-1} KOH solution. Reprinted with permission from [60]. Copyright 2013 Elsevier.

electrochemical capacitance could be increased largely to 290.6 F·g^{-1} for the CNO/4-DMAP/NiO and 1225.2 F·g^{-1} for the CNO/4-DMAP/$Ni(OH)_2$ composite, compared to pristine CNOs with 30.6 F·g^{-1}.

Another example for CNO composite-based capacitors was reported by the group of H. Y. Yang [62]. The composite was prepared from $KMnO_4$ and CNOs in different weight ratios in deionized water by heating in an autoclave. The formed CNO–MnO_2 composite was then implemented in an asymmetric pseudocapacitor with the CNO–MnO_2 composite as working electrode and nickel foam as counter electrode. The capacitance of pure MnO_2 (40 F·g^{-1}) could be increased by the incorporation of CNO up to 177.5 F·g^{-1}. In addition, the authors report an excellent cycling stability with 99–101% retention of the specific capacitance after 1000 cycles.

Lithium-Ion batteries: Carbon nanotubes are widely studied for a use in lithium ion batteries [63]. However, also CNOs were studied for a potential application as anode materials. Han et al., for example, reported the large scale synthesis of CNOs starting from $CuCl_2$·2 H_2O and CaC_2 and found that they exhibit a high capacity in combination with a promising cycling performance, which renders these as-prepared CNOs as potential anode materials for lithium-ion batteries [16]. However, no prototype batteries were prepared by the authors of this report. In two recent studies, H. Y. Yang and co-workers reported lithium-ion batteries incorporating CNOs in combination with Co_3O_4 [64] and MnO_2 [65] as electrode material. In the earlier study, the CNO-containing anode material was prepared by a solvo-thermal method from cobalt acetate and CNOs and the authors found that the novel composite material showed improved electrochemical properties, compared to pristine Co_3O_4 electrodes. They observed, for example, an increase of the specific capacity from 190 mA·h·g^{-1} to 632 mA·h·g^{-1} at a current density of 200 mA·g^{-1} and also an increased rate capability [64]. In the latter report, the CNO hybrid material was prepared from $KMnO_4$ and CNOs by a hydrothermal method (Figure 9) similar to the one the group reported earlier for the preparation of electrode materials for pseudocapacitors [62]. This material was then probed as anode material in lithium-ion batteries. It was found that the performance of pure MnO_2 anodes could be significantly enhanced by the incorporation of CNOs. The specific capacity increased from 260 mA·h·g^{-1} to 630 mA·h·g^{-1}, at a current density of 50 mA·g^{-1}. In addition, the authors report an increased rate capability, stable cycling performance, and coulomb efficiency of nearly 100% [65].

Fuel cells: CNOs were also investigated as catalyst support for application in direct methanol fuel cells. For this, Xu et al. prepared CNOs decorated with Pt nanoparticles (Pt-CNO) and compared the performance of this novel catalyst material with common Pt/Vulcan XC-72 with encouraging results [66]. The novel Pt-CNO catalyst showed a higher surface area and smaller Pt particle size (3.05 nm vs 4.10 nm) than the reference system and the catalytic activity for the electro oxidation of methanol was increased by about 20%, rendering CNOs as a promising catalyst support for fuel cells.

Terahertz-shielding: In recent years, terahertz devices, circuits and terahertz-based communication systems have become important in many fields. This makes the development of materials for terahertz shielding essential, to limit electromagnetic interferences and thus reduce for example noise in cables and communication systems and signal coupling. Carbon materials

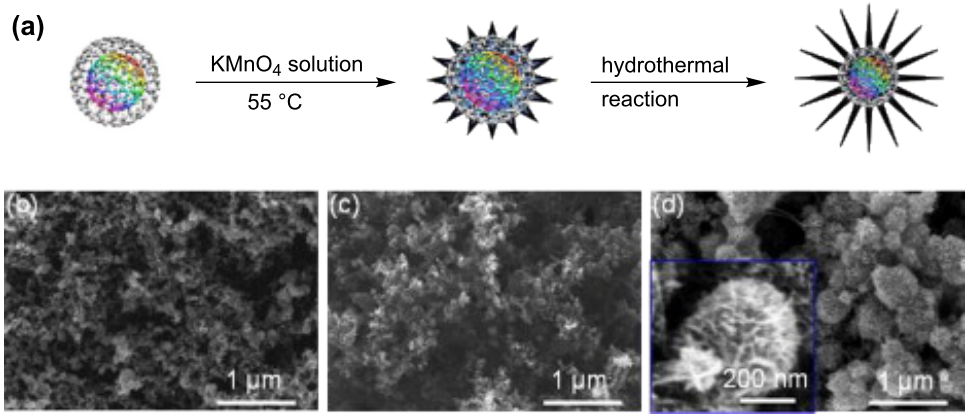

Figure 9: Note: The authors of the original report refer to CNOs as onion-like carbon (OLC) (a) Schematic diagram of the synthesis procedure of the core–leaf OLC–MnO_2 hybrid nano-urchins. Scanning electron micrographs of (b) pure OLC, (c) intermediate product, and (d) final hybrid nano-urchins. Inset in (d) is the magnified image of a single urchin-like nano-architecture. Reprinted with permission from [65]. Copyright 2013 Elsevier.

have been widely studies for this application [67], including CNOs. The main research investigating the usability for CNOs for terahertz shielding was carried out by an international group of scientists and published in four papers in 2007 and 2008 [68-71]. After studying the terahertz absorption properties of CNO and CNO composites in a wide range of frequencies [68-70], the authors prepared CNO–poly(methyl methacrylate) (PMMA) composite films and studied the terahertz shielding properties in a frequency range of 0.1–3 THz and found a shielding of up to 14 dB [67,71].

Catalysis

One of the most important catalytical reactions in industry is the oxidative dehydrogenation (ODH) of ethylbenzene to styrene. In 2002, Keller et al. published a study showing the potential of CNOs as catalyst for this reaction with conversion levels of up to 92% after an activation period of 2 h and stable styrene yields of 62%, outperforming industrial K–Fe catalysts and other carbon materials [72]. In a later study, the groups of Su and Keller compared the catalytic behavior of nanodiamonds and CNOs for ODH catalysis [73]. Special attention was dedicated to the reactional behavior of sp^3 and sp^2 carbons of the catalyst surface as a function of time during catalysis. The authors conclude that the activity of the nanocarbon catalyst is largely influenced by the presence of oxygenated carbon species on the catalyst surface, which may eventually be formed during an initial period.

Tribology

In tribology, CNOs are widely studied and have shown promising results as lubricants. In 2002, Cabioc'h et al. reported that CNOs incorporated in silver layers significantly reduced wear, while the friction coefficient is largely unaffected by their presence [74]. Further studies investigated the use of CNOs as a solid state lubricant [75] and as an additive to the oil Krytox 143AB, where the aim was to improve the lubricating lifetime for space applications [76]. In the following years, several reports were published on the characterization of the tribological properties of CNO materials, produced through different methods [77-80]. Mechanisms by which CNOs can reduce friction and wear were investigated in greater detail in 2009 by Martin and collaborators in a combined experimental and computational study [81]. Computer simulations suggest that the lubrication of CNOs between two surfaces is caused by rolling–sliding of the CNO nanoparticles. These findings were corroborated by TEM observations of the wear particles and AFM imaging of the wear tracks.

Optical limiting

CNOs were also studied in optics and found to exhibit very efficient optical limiting [82]. Furthermore, the authors of this study compared the nonlinear optical response (upon pulsed laser excitation with 10 ns pulses, at 532 nm wavelength) of CNOs with nanodiamonds and concluded, that the optical response of CNOs is stronger than the one of nanodiamonds. In addition, the nonlinear optical refraction of the CNOs was found to be negligible. Finally, transient absorption studies of covalently functionalized CNOs yielded evidence for a strong difference of the absorption coefficients in the ground and excited state, which gives further rise to a possible application of this CNO material in optical limiting [25].

Molecular junctions in STM

In another recent report, the groups of Plonska-Brzezinska and Echegoyen prepared sulfide-terminated CNO derivatives, which can be used as molecular junctions in scanning tunneling

microscopy (STM) [83]. This enabled the authors to study the conductivity of CNOs and compare their properties with comparable fullerene-C_{60} derivatives. The measured data suggests that the intrinsic conductivity of CNOs and C_{60} is within the same order of magnitude.

Conclusion

Multi-shell fullerenes, known as carbon nano-onions (CNOs), were discovered in 1992 and are structured by concentric shells of carbon atoms in a graphitic interlayer distance. Analogous to carbon nanotubes, CNOs display poor solubility in both aqueous and organic solvents as well as a high surface area, compared to their volume. In order for their full potential to be realized, the solubility of the CNO nanomaterial has to be increased. To achieve this, a multitude of different synthetic pathways for the covalent surface functionalization has been reported. An alternative to the covalent functionalization is the surface decoration of CNOs with polymers or their incorporation into composites. CNOs have been implemented in different electronic applications, as electrode materials in capacitors, as anode materials in lithium-ion batteries, as catalyst support in fuel cells. They have even attracted the interest of NASA researchers for their tribological properties as additives for aerospace applications. Despite much interest in different carbon-based nano-materials, CNOs as functional constructs for intracellular transport have not been widely explored. However, given their size, homogeneity and purity (compared with carbon nanotubes) they could in principle add an important new avenue for the transport of imaging and therapeutic agents. These carbon particles have demonstrated high cellular uptake, low cytotoxicity and lower inflammatory potential than CNTs and a very promising future for biomedical applications.

Acknowledgements

Financial support from the Istituto Italiano di Tecnologia (IIT) is greatly appreciated. We also thank the Cost Action MP0901: “Designing novel materials for nanodevices: From Theory to Practice”.

References

1. Kroto, H. W.; Heath, J. R.; O’Brien, S. C.; Curl, R. F.; Smalley, R. E. *Nature* **1985,** *318,* 162–163. doi:10.1038/318162a0
2. Bollmann, W.; Spreadborough, J. *Nature* **1960,** *186,* 29–30. doi:10.1038/186029a0
3. Iijima, S. *Nature* **1991,** *354,* 56–58. doi:10.1038/354056a0
4. Iijima, S.; Ichihashi, T. *Nature* **1993,** *363,* 603–605. doi:10.1038/363603a0
5. Iijima, S.; Yudasaka, M.; Yamada, R.; Bandow, S.; Suenaga, K.; Kokai, F.; Takahashi, K. *Chem. Phys. Lett.* **1999,** *309,* 165–170. doi:10.1016/S0009-2614(99)00642-9
6. Danilenko, V. V. *Phys. Solid State* **2004,** *46,* 595–599. doi:10.1134/1.1711431
7. Novoselov, K. S.; Geim, A. K.; Morozov, S. V.; Jiang, D.; Zhang, Y.; Grigorieva, I. V.; Firsov, A. A. *Science* **2004,** *306,* 666–669. doi:10.1126/science.1102896
8. Ugarte, D. *Nature* **1992,** *359,* 707–709. doi:10.1038/359707a0
9. Kuznetsov, V. L.; Chuvilin, A. L.; Moroz, E. M.; Kolomiichuk, V. N.; Shaikhudtdinov, S. K.; Butenko, Y. V.; Mal’kov, I. Y. *Carbon* **1994,** *32,* 873–882. doi:10.1016/0008-6223(94)90044-2
10. Echegoyen, L.; Ortiz, A.; Chaur, M. N.; Palkar, A. J. Carbon Nano Onions. In *Chemistry of Nanocarbons;* Akasaka, T.; Wudl, F.; Nagase, S., Eds.; John Wiley & Sons: Chichester, UK, 2010; pp 463–483. doi:10.1002/9780470660188.ch19
11. Kuznetsov, V. L.; Chuvilin, A. L.; Butenko, Y. V.; Mal’kov, I. Y.; Titov, V. M. *Chem. Phys. Lett.* **1994,** *222,* 343–348. doi:10.1016/0009-2614(94)87072-1
12. Tomita, S.; Sakurai, T.; Ohta, H.; Fujii, M.; Hayashi, S. *J. Chem. Phys.* **2001,** *114,* 7477–7482. doi:10.1063/1.1360197
13. Qin, L.-C.; Iijima, S. *Chem. Phys. Lett.* **1996,** *262,* 252–258. doi:10.1016/0009-2614(96)01037-8
14. Sano, N.; Wang, H.; Chhowalla, M.; Alexandrou, I.; Amaratunga, G. A. J. *Nature* **2001,** *414,* 506. doi:10.1038/35107141
15. Alexandrou, I.; Wang, H.; Sano, N.; Amaratunga, G. A. J. *J. Chem. Phys.* **2004,** *120,* 1055–1058. doi:10.1063/1.1629274
16. Han, F.-D.; Yao, B.; Bai, Y.-J. *J. Phys. Chem. C* **2011,** *115,* 8923–8927. doi:10.1021/jp2007599
17. Ghosh, M.; Sonkar, S. K.; Saxena, M.; Sarkar, S. *Small* **2011,** *7,* 3170–3177. doi:10.1002/smll.201101158
18. Choucair, M.; Stride, J. A. *Carbon* **2012,** *50,* 1109–1115. doi:10.1016/j.carbon.2011.10.023
19. Ugarte, D. *Carbon* **1995,** *33,* 989–993. doi:10.1016/0008-6223(95)00027-B
20. Roy, D.; Chhowalla, M.; Wang, H.; Sano, N.; Alexandrou, I.; Clyne, T. W.; Amaratunga, G. A. J. *Chem. Phys. Lett.* **2003,** *373,* 52–56. doi:10.1016/S0009-2614(03)00523-2
21. Krishnamurthy, S.; Butenko, Y. V.; Dhanak, V. R.; Hunt, M. R. C.; Šiller, L. *Carbon* **2013,** *52,* 145–149. doi:10.1016/j.carbon.2012.09.015
22. Singh, P.; Campidelli, S.; Giordani, S.; Bonifazi, D.; Bianco, A.; Prato, M. *Chem. Soc. Rev.* **2009,** *38,* 2214–2230. doi:10.1039/b518111a
23. Herranz, M. A.; Martin, N. Noncovalent Functionalization of Carbon Nanotubes. In *Carbon Nanotubes and Related Structures: Synthesis, Characterization, Functionalization, and Applications;* Guldi, D. M.; Martin, N., Eds.; Wiley-VCH Verlag GmbH & Co. KGaA: Weinheim, Germany, 2010; pp 103–134. doi:10.1002/9783527629930.ch5
24. Hauke, F.; Hirsch, A. Covalent Functionalization of Carbon Nanotubes. In *Carbon Nanotubes and Related Structures: Synthesis, Characterization, Functionalization, and Applications;* Guldi, D. M.; Martin, N., Eds.; Wiley-VCH Verlag GmbH & Co. KGaA: Weinheim, Germany, 2010; pp 135–198. doi:10.1002/9783527629930.ch6
25. Georgakilas, N.; Guldi, D. M.; Signorini, R.; Bozio, R.; Prato, M. *J. Am. Chem. Soc.* **2003,** *125,* 14268–14269. doi:10.1021/ja0342805
26. Rettenbacher, A. S.; Elliott, B.; Hudson, J. S.; Amirkhanian, A.; Echegoyen, L. *Chem. – Eur. J.* **2006,** *12,* 376–387. doi:10.1002/chem.200500517
27. Palkar, A.; Melin, F.; Cardona, C. M.; Elliott, B.; Naskar, A. K.; Edie, D. D.; Kumbhar, A.; Echegoyen, L. *Chem. – Asian J.* **2007,** *2,* 625–633. doi:10.1002/asia.200600426
28. Liu, Y.; Vander Wal, R. L.; Khabashesku, V. N. *Chem. Mater.* **2007,** *19,* 778–786. doi:10.1021/cm062177j

29. Kuznetsov, O. V.; Pulikkathara, M. X.; Lobo, R. F. M.; Khabashesku, V. N. *Russ. Chem. Bull.* **2010,** *59,* 1495–1505. doi:10.1007/s11172-010-0269-y
30. Rettenbacher, A. S.; Perpall, M. W.; Echegoyen, L.; Hudson, J.; Smith, D. W., Jr. *Chem. Mater.* **2007,** *19,* 1411–1417. doi:10.1021/cm0626132
31. Bergman, R. G. *Acc. Chem. Res.* **1973,** *6,* 25–31. doi:10.1021/ar50061a004
32. Palkar, A.; Kumbhar, A.; Athans, A. J.; Echegoyen, L. *Chem. Mater.* **2008,** *20,* 1685–1687. doi:10.1021/cm7035508
33. Zhou, L.; Gao, C.; Zhu, D.; Xu, W.; Chen, F. F.; Palkar, A.; Echegoyen, L.; Kong, E. S.-W. *Chem. – Eur. J.* **2009,** *15,* 1389–1396. doi:10.1002/chem.200801642
34. Cioffi, C. T.; Palkar, A.; Melin, F.; Kumbhar, A.; Echegoyen, L.; Melle-Franco, M.; Zerbetto, F.; Rahman, G. M. A.; Ehli, C.; Sgobba, V.; Guldi, D. M.; Prato, M. *Chem. – Eur. J.* **2009,** *15,* 4419–4427. doi:10.1002/chem.200801818
35. Kordatos, K.; Da Ros, T.; Bosi, S.; Vázquez, E.; Bergamin, M.; Cusan, C.; Pellarini, F.; Tomberli, V.; Baiti, B.; Pantarotte, D.; Georgakilas, V.; Spalluto, G.; Prato, M. *J. Org. Chem.* **2001,** *66,* 4915–4920. doi:10.1021/jo015608k
36. Luszczyn, J.; Plonska-Brzezinska, M. E.; Palkar, A.; Dubis, A. T.; Simionescu, A.; Simionescu, D. T.; Kalska-Szostko, B.; Winkler, K.; Echegoyen, L. *Chem. – Eur. J.* **2010,** *16,* 4870–4880. doi:10.1002/chem.200903277
37. Flavin, K.; Chaur, M. N.; Echegoyen, L.; Giordani, S. *Org. Lett.* **2010,** *12,* 840–843. doi:10.1021/ol902939f
38. Bahr, J. L.; Yang, J.; Kosynkin, D. V.; Bronikowski, M. J.; Smalley, R. E.; Tour, J. M. *J. Am. Chem. Soc.* **2001,** *123,* 6536–6542. doi:10.1021/ja010462s
39. Yang, M.; Flavin, K.; Kopf, I.; Radics, G.; Hearnden, C. H. A.; McManus, G. J.; Moran, B.; Villalta-Cerdas, A.; Echegoyen, L. A.; Giordani, S.; Lavelle, E. C. *Small* **2013,** *9,* 4194–4206. doi:10.1002/smll.201300481
40. Giordani, S.; Bartelmess, J.; Frasconi, M.; Biondi, I.; Cheung, S.; Grossi, M.; Wu, D.; Echegoyen, L.; O'Shea, D. F. *J. Mater. Chem. B* **2014,** *2,* 7459–7463. doi:10.1039/C4TB01087F
41. Bartelmess, J.; De Luca, E.; Signorelli, A.; Baldrighi, M.; Becce, M.; Brescia, R.; Nardone, V.; Parisini, E.; Echegoyen, L.; Pompa, P. P.; Giordani, S. *Nanoscale* **2014,** *6,* 13761–13769. doi:10.1039/C4NR04533E
42. Molina-Ontaria, A.; Chaur, M. N.; Plonska-Brzezinska, M. E.; Echegoyen, L. *Chem. Commun.* **2013,** *49,* 2406–2408. doi:10.1039/c3cc39077b
43. Breczko, J.; Winkler, K.; Plonska-Brzezinska, M. E.; Villalta-Cerdas, A.; Echegoyen, L. *J. Mater. Chem.* **2010,** *20,* 7761–7768. doi:10.1039/c0jm01213k
44. Breczko, J.; Plonska-Brzezinska, M. E.; Echegoyen, L. *Electrochim. Acta* **2012,** *72,* 61–67. doi:10.1016/j.electacta.2012.03.177
45. Plonska-Brzezinska, M. E.; Mazurczyk, J.; Palys, B.; Breczko, J.; Lapinski, A.; Dubis, A. T.; Echegoyen, L. *Chem. – Eur. J.* **2012,** *18,* 2600–2608. doi:10.1002/chem.201102175
46. Plonska-Brzezinska, M. E.; Breczko, J.; Palys, B.; Echegoyen, L. *ChemPhysChem* **2013,** *14,* 116–124. doi:10.1002/cphc.201200759
47. Plonska-Brzezinska, M. E.; Lewandowski, M.; Blaszyk, M.; Molina-Ontario, A.; Luciński, T.; Echegoyen, L. *ChemPhysChem* **2012,** *13,* 4134–4141. doi:10.1002/cphc.201200789
48. Plonska-Brzezinska, M. E.; Brus, D. M.; Breczko, J.; Echegoyen, L. *Chem. – Eur. J.* **2013,** *19,* 5019–5024. doi:10.1002/chem.201300009
49. Lei, H.; Luo, J.; Tong, L.; Peng, L.-q.; Qi, Y.; Jia, Z.-g.; Wei, Q. *Food Chem.* **2011,** *127,* 1169–1174. doi:10.1016/j.foodchem.2011.01.119
50. Ding, L.; Stilwell, J.; Zhang, T.; Elboudwarej, O.; Jiang, H.; Selegue, J. P.; Cooke, P. A.; Gray, J. W.; Chen, F. F. *Nano Lett.* **2005,** *5,* 2448–2464. doi:10.1021/nl051748o
51. Sonkar, S. K.; Ghosh, M.; Roy, M.; Begum, A.; Sarkar, S. *Mater. Express* **2012,** *2,* 105–114. doi:10.1166/mex.2012.1064
52. Gong, H.; Peng, R.; Liu, Z. *Adv. Drug Delivery Rev.* **2013,** *65,* 1951–1963. doi:10.1016/j.addr.2013.10.002
53. Shen, J.; Zhu, Y.; Yang, X.; Li, C. *Chem. Commun.* **2012,** *48,* 3686–3699. doi:10.1039/c2cc00110a
54. Seymour, M. B.; Su, C.; Gao, Y.; Lu, Y.; Li, Y. *J. Nanopart. Res.* **2012,** *14,* 1087. doi:10.1007/s11051-012-1087-y
55. Portet, C.; Yushin, G.; Gogotsi, Y. *Carbon* **2007,** *45,* 2511–2518. doi:10.1016/j.carbon.2007.08.024
56. Bushueva, E. G.; Galkin, P. S.; Okotrub, A. V.; Bulusheva, L. G.; Gavrilov, N. N.; Kuznetsov, V. L.; Moiseekov, S. I. *Phys. Status Solidi B* **2008,** *245,* 2296–2299. doi:10.1002/pssb.200879608
57. Pech, D.; Brunet, M.; Durou, H.; Huang, P.; Mochalin, V.; Gogotsi, Y.; Taberna, T.-L.; Simon, P. *Nat. Nanotechnol.* **2010,** *5,* 651–654. doi:10.1038/nnano.2010.162
58. McDonough, J. K.; Frolov, A. I.; Presser, V.; Niu, J.; Miller, C. H.; Ubieto, T.; Fedorov, M. V.; Gogotsi, Y. *Carbon* **2012,** *50,* 3298–3309. doi:10.1016/j.carbon.2011.12.022
59. Borgohain, R.; Li, J.; Selegue, J. P.; Cheng, Y.-T. *J. Phys. Chem. C* **2012,** *116,* 15068–15075. doi:10.1021/jp301642s
60. Gao, Y.; Zhou, Y. S.; Qian, M.; He, X. N.; Redepenning, J.; Goodman, P.; Li, H. M.; Jiang, L.; Lu, Y. F. *Carbon* **2013,** *51,* 52–58. doi:10.1016/j.carbon.2012.08.009
61. Plonska-Brzezinska, M. E.; Brus, D. M.; Molina-Ontaria, A.; Echegoyen, L. *RSC Adv.* **2013,** *3,* 25891–25901. doi:10.1039/c3ra44249g
62. Wang, Y.; Yu, S. F.; Sun, C. Y.; Zhu, T. J.; Yang, H. Y. *J. Mater. Chem.* **2012,** *22,* 17584–17588. doi:10.1039/c2jm33558a
63. Landi, B. J.; Ganter, M. J.; Cress, C. D.; DiLeo, R. A.; Raffaelle, R. P. *Energy Environ. Sci.* **2009,** *2,* 638–654. doi:10.1039/b904116h
64. Wang, Y.; Yan, F.; Liu, S. W.; Tan, A. Y. S.; Song, H.; Sun, X. W.; Yang, H. Y. *J. Mater. Chem. A* **2013,** *1,* 5212–5216. doi:10.1039/c3ta10559h
65. Wang, Y.; Han, Z. J.; Yu, S. F.; Song, R. R.; Song, H. H.; Ostrikov, K.; Yang, H. Y. *Carbon* **2013,** *64,* 230–236. doi:10.1016/j.carbon.2013.07.057
66. Xu, B.; Yang, X.; Wang, X.; Guo, J.; Liu, X. *J. Power Sources* **2006,** *162,* 160–164. doi:10.1016/j.jpowsour.2006.06.063
67. Liu, L.; Das, A.; Megaridis, C. M. *Carbon* **2014,** *69,* 1–16. doi:10.1016/j.carbon.2013.12.021
68. Shenderova, O.; Tyler, T.; Cunningham, G.; Ray, M.; Walsh, J.; Casulli, M.; Hens, S.; McGuire, G.; Kuznetsov, V.; Lipa, S. *Diamond Relat. Mater.* **2007,** *16,* 1213–1217. doi:10.1016/j.diamond.2006.11.086
69. Maksimenko, S. A.; Rodionova, V. N.; Slepyan, G. Y.; Karpovich, V. A.; Shenderova, O.; Walsh, J.; Kuznetsov, V. L.; Mazov, I. N.; Moseenkov, S. I.; Okotrub, A. V.; Lambin, P. *Diamond Relat. Mater.* **2007,** *16,* 1231–1235. doi:10.1016/j.diamond.2006.11.025
70. Shenderova, O.; Grishko, V.; Cunningham, G.; Moseekov, S.; McGuire, G.; Kuznetsov, V. *Diamond Relat. Mater.* **2008,** *17,* 462–466. doi:10.1016/j.diamond.2007.08.023

71. Macutkevic, J.; Adomavicius, R.; Krotkus, A.; Seliuta, D.; Valusis, G.; Maksimenko, S.; Kuzhir, P.; Batrakov, K.; Kuznetsov, V.; Moseenkov, S.; Shenderova, O.; Okotrub, A. V.; Langlet, R.; Lambin, P. *Diamond Relat. Mater.* **2008,** *17,* 1608–1612. doi:10.1016/j.diamond.2007.11.018
72. Keller, N.; Maksimova, N. I.; Roddatis, V. V.; Schur, M.; Mestl, G.; Butenko, Y. V.; Kuznetsov, V. L.; Schlögl, R. *Angew. Chem., Int. Ed.* **2002,** *41,* 1885–1888. doi:10.1002/1521-3773(20020603)41:11<1885::AID-ANIE1885>3.0.CO;2-5
73. Su, D.; Maksimova, N. I.; Mestl, G.; Kuznetsov, V. L.; Keller, V.; Schlögl, R.; Keller, N. *Carbon* **2007,** *45,* 2145–2151. doi:10.1016/j.carbon.2007.07.005
74. Cabioc'h, T.; Thune, E.; Rivière, J. P.; Camelio, S.; Girard, J. C.; Guérin, P.; Jaouen, M.; Henrard, L.; Lambin, P. *J. Appl. Phys.* **2002,** *91,* 1560–1567. doi:10.1063/1.1421222
75. Hirata, A.; Igarashi, M.; Kaito, T. *Tribol. Int.* **2004,** *31,* 899–905. doi:10.1016/j.triboint.2004.07.006
76. Street, K. W.; Marchetti, M.; Vander Wal, R. L.; Tomasek, A. J. *Tribol. Lett.* **2004,** *16,* 143–149. doi:10.1023/B:TRIL.0000009724.01711.f4
77. Matsumoto, N.; Joly-Pottuz, L.; Kinoshita, H.; Ohmae, N. *Diamond Relat. Mater.* **2007,** *16,* 1227–1230. doi:10.1016/j.diamond.2007.01.031
78. Joly-Pottuz, L.; Vacher, B.; Ohmae, N.; Martin, J. M.; Epicier, T. *Tribol. Lett.* **2008,** *30,* 69–80. doi:10.1007/s11249-008-9316-3
79. Yao, Y.; Wang, X.; Guo, J.; Yang, X.; Xu, B. *Mater. Lett.* **2008,** *62,* 2524–2527. doi:10.1016/j.matlet.2007.12.056
80. Joly-Pottuz, L.; Matsumoto, N.; Kinoshita, H.; Vacher, B.; Belin, M.; Montagnac, G.; Martin, J. M.; Ohmae, N. *Tribol. Int.* **2008,** *41,* 69–78. doi:10.1016/j.triboint.2007.05.001
81. Joly-Pottuz, L.; Bucholz, E. W.; Matsumoto, N.; Phillpot, S. R.; Sinnott, S. B.; Ohmae, N.; Martin, J. M. *Tribol. Lett.* **2010,** *37,* 75–81. doi:10.1007/s11249-009-9492-9
82. Koudoumas, E.; Kokkinaki, O.; Konstantaki, M.; Couris, S.; Korovin, S.; Detkov, P.; Kuznetsov, V.; Pimenov, S.; Pustovoi, V. *Chem. Phys. Lett.* **2002,** *357,* 336–340. doi:10.1016/S0009-2614(02)00557-2
83. Sek, S.; Breczko, J.; Plonska-Brzezinska, M. E.; Wilczewska, A. Z.; Echegoyen, L. *ChemPhysChem* **2013,** *14,* 96–100. doi:10.1002/cphc.201200624

License and Terms

This is an Open Access article under the terms of the Creative Commons Attribution License (http://creativecommons.org/licenses/by/2.0), which permits unrestricted use, distribution, and reproduction in any medium, provided the original work is properly cited.

The license is subject to the *Beilstein Journal of Nanotechnology* terms and conditions: (http://www.beilstein-journals.org/bjnano)

The definitive version of this article is the electronic one which can be found at: doi:10.3762/bjnano.5.207

BEILSTEIN JOURNAL OF NANOTECHNOLOGY

Properties of plasmonic arrays produced by pulsed-laser nanostructuring of thin Au films

Katarzyna Grochowska*[1], Katarzyna Siuzdak[1], Peter A. Atanasov[2], Carla Bittencourt[3], Anna Dikovska[2], Nikolay N. Nedyalkov[2] and Gerard Śliwiński[1]

Review

Open Access

Address:
[1]Centre for Plasma and Laser Engineering, The Szewalski Institute, Polish Academy of Sciences, 14 Fiszera St., 80-231 Gdańsk, Poland, [2]Institute of Electronics, Bulgarian Academy of Sciences, 72 Tzarigradsko Shousse, 1784 Sofia, Bulgaria and [3]Chemistry of Interaction Plasma Surface (ChiPS), University of Mons, Rue du Parc 20, B-7000 Mons, Belgium

Email:
Katarzyna Grochowska* - kgrochowska@imp.gda.pl

* Corresponding author

Keywords:
Au nanostructures; laser dewetting; laser nanostructuring; plasmonic enhancement; self-organization

Beilstein J. Nanotechnol. **2014,** *5,* 2102–2112.
doi:10.3762/bjnano.5.219

Received: 01 July 2014
Accepted: 10 October 2014
Published: 13 November 2014

This article is part of the Thematic Series "Atomic scale interface design and characterisation: Theory – Structure and dynamics".

Guest Editor: C. Ewels

© 2014 Grochowska et al; licensee Beilstein-Institut.
License and terms: see end of document.

Abstract

A brief description of research advances in the area of short-pulse-laser nanostructuring of thin Au films is followed by examples of experimental data and a discussion of our results on the characterization of structural and optical properties of gold nanostructures. These consist of partially spherical or spheroidal nanoparticles (NPs) which have a size distribution (80 ± 42 nm) and self-organization characterized by a short-distance order (length scale ≈140 nm). For the NP shapes produced, an observably broader tuning range (of about 150 nm) of the surface plasmon resonance (SPR) band is obtained by renewal thin film deposition and laser annealing of the NP array. Despite the broadened SPR bands, which indicate damping confirmed by short dephasing times not exceeding 4 fs, the self-organized Au NP structures reveal quite a strong enhancement of the optical signal. This was consistent with the near-field modeling and micro-Raman measurements as well as a test of the electrochemical sensing capability.

Introduction

The capability of pulsed-laser beams to deliver energy to a precise space at a precise time stimulated developments of laser technology and a variety of applications in scientific research and in the fields of medicine, metrology and optoelectronic devices. Among studies on short-pulse laser interactions with materials, the topic of nanostructuring by photothermally induced instabilities at the liquid–solid interface due to fast heating and solidifying of thin metal films evoked noticeable interest in the last two decades [1-7]. The formation of particulates observed in the case of a Au film irradiated with

nanosecond laser pulses has been ascribed by Bischof et al. to the substrate dewetting and two mechanisms were postulated: the nucleation and spinodal (instability driven) separation [1]. They are both dependent on the laser irradiation conditions. From time-resolved studies of the transport phenomena, droplet formation and dynamics of the thermocapillary effect in Al, Au and Co films, thermal gradients of about 10^9 K/m were concluded [2-4]. This was confirmed by investigation of the surface tension-driven flow leading to the Rayleigh–Taylor (R–T) instability. The R–T process has been concluded from coincidence between the droplet dimension (0.5 μm) obtained from the experiment and the model simulations, and with values of the Weber number as reported by Willis and Xu [5]. Using the R–T instability criterion, the dimensions of nanoislands formed by laser-irradiated metal films on Si-supported SiO_2 substrate were analyzed by Henley et al. [6,7]. More recently, Kalyanaraman and coworkers discussed the dewetting mechanism basing on hydrodynamic theory with the temperature gradients both lateral and normal to the film surface taken into account [8-10].

The gold nanoparticles produced from thin Au films on Si and indium tin oxide (ITO) substrates using a 532 nm laser operated in a single-pulse regime were studied in detail by Ruffino et al. [11] and Kuznetsov et al. [12]. It was found that the NP morphology changes markedly depending on the deposited pulse energy. For characterization of the particle size and shape distributions, the authors proposed that both the average values and also the "most probable" ones are required to describe the particle shape variations which range from partially spherical to cup-like to partial spheroids. Nanostructuring via the photothermal effect associated with strong plasmonic absorption (i.e., collective oscillation of the free electrons between the metal and dielectric when excited around the resonant frequency) was reported by Hubenthal and coworkers who obtained controlled rearrangement of the NP population and morphology using laser pulses of energy tunable in the range of 0.7–4 eV (1771–310 nm) [13]. For thin, granular Au films, the photothermal effect at a wavelength corresponding to the surface plasmon resonance (SPR) peak around 520 nm resulted in the observable decrease of the film roughness and resistivity [14]. In case of nanostructuring of a thin Au film by a pulsed-laser beam passing through a pinhole (60 μm), the forced arrangement of nanospheres into micro-circular patterns due to diffraction was observed [15].

Properties of the Au, Ag, and Cu nanostructures and also bi-metal nanosystems (known for broader tunability) such as Au/Ag and Au/Ni were reported in a number of papers where the keyword "laser nanostructuring" (or annealing) is used rather than "laser dewetting" [16-18]. It should be understood that laser dewetting refers to a physical phenomenon resulting from rapid heating and cooling while nanostructuring is a technological process characterized by nanoscale morphology. Therefore, the equivalent use of both terms is justified by the same underlying basic mechanisms and final effect. Mechanisms relevant to the laser nanostructuring (LNS) of thin metal films are often discussed in the broader context of the non-equilibrium processes due to pulsed-laser interaction at time scales from micro- to femto-seconds and with nanofabrication by material ablation and pulsed laser deposition (PLD) and also with the effect of environment (gaseous, liquid) taken into account [19-21]. Numerous experimental data confirm that the electrostatic, thermal and non-thermal regimes of the laser–surface interaction depend critically on the laser fluence and pulse length. For laser pulses of duration longer than 50 ps, the interaction effect is photothermal in nature, while for shorter pulses, the ballistic energy transfer dominates [22,23]. In a recent paper on the nanosecond laser effect, Kneier et al. reported time-resolved data from interferometric measurements and obtained the different velocities of the metallic (Au and Ta) film surfaces of 0.6 m/s and 1.9 m/s below and above the melting threshold, respectively [24]. Interestingly, the velocity values in the range of 20–70 m/s characteristic of the instability driven processes (i.e., film detachment from Si substrate, followed by dewetting and droplet formation) are in reasonable agreement with those observed in femtosecond experiments [25].

Similar to other laser-based methods, LNS results in a variety of unique properties not reproducible by other production routes. This contributes to new research on nanomaterials exhibiting properties markedly different from their bulk counterparts and shows application possibilities in surface enhanced Raman spectroscopy, plasmonic optical circuits, light harvesting and solid state lighting. Results published so far validate the conclusion that the controlled laser nanostructuring by nanosecond laser irradiation of thin metal films is a simple and cost-effective approach, providing a reasonable alternative to the relatively expensive and time-consuming fabrication of NP arrays of regular geometries with the use of ion beam and plasma techniques [26,27].

In this paper, the properties of the plasmonic arrays produced from thin Au films by short-pulse-laser nanostructuring are reported and illustrated with experimental data obtained for samples of Au nanostructures produced and analyzed in collaboration with the laboratories of The Institute of Electronics BAS (Sofia, BG), The Szewalski Institute PASci (Gdańsk, PL) and The Cirmap at University of Mons (BE). In the discussion, particular attention is paid to the main process observables characteristic of the self-organized plasmonic nanostructures, that is, their morphology and optical properties attainable from results

of the microscope and inspection spectroscopic measurements. The effect of the nanostructure morphology on plasmonic properties (such as resonance position and damping), the near- and mid-field enhancement of the optical signal, and evidence of sensing capability are discussed. Moreover, the possibility of tuning the plasmon resonance peak resulting from repeated film deposition and laser annealing observed for the first time is reported.

Results and Discussion

Nanoparticle structures

The photothermally stimulated patterning path from a thin metal film to a nanostructured array of particles is initiated by nanosecond laser pulses of energy absorbed at the film surface, transferred and converted into heat. This results in fast material melting, dewetting of the substrate and fast cooling after termination of each pulse. The process of dewetting is typical for most liquid metals on SiO_2 and is characterized by contact angle values around 90º and higher (e.g., 105º, 120º, 131º for Ni, Au and Cu, respectively) [28]. Recently, increasing interest in dewetting of thin metal films has occurred due to the fabrication potential for self-organized nanostructures [1-9], which can be applied for light harvesting, spintronics and catalysis. The reproducibly functionalized nanostructures are documented by numerous experimental data and the scaling-up potential of this technique is an additional advantage from the perspective of possible applications [6-8].

The self-organization of structures represents an important characteristic resulting from the LNS process and is observed in numerous works [29,30]. The degree of order is described by the distribution of the particle size, shape and inter-particle distance, which can be controlled by the process conditions discussed in our previous works [16,31]. In short, LNS was performed on thin Au films of thickness in the range of 5–60 nm produced from bulk Au (99.99% purity) by means of discharge sputtering (K550X, Emitech) or by PLD. The films were nanostructured in vacuum at a pressure of $(1–3) \times 10^{-4}$ Pa using a pulsed laser (Quantel Bw, 6 ns full pulsewidth) operated at 266 nm and at a laser fluence not exceeding 412 mJ/cm^2.

The properties of the NP arrays produced by the nanosecond laser pulses from the Au thin films on SiO_2 and ITO substrates can be inferred from SEM images (EVO-40 microscope, Zeiss) shown in Figure 1.

In the process of nanostructuring, the grainy, thin metal film sputtered onto the substrate (e.g., glass, ITO, or Si) is melted and fragmented by irradiation with laser pulses under defined conditions. The film fragmentation starts at the grain boundaries. The poor wetting of the substrate by the liquid metal, in this case Au, and coalescence both result in the formation of the NP structure. The final geometry and NP distribution depends on the surface tension forces at equilibrium characterized by a minimal ratio of the NP surface-area-to-volume [31]. The short-range order observed for structures in Figure 1a–c confirms the NP self-organization, which is characteristic for the instability-driven dewetting [8,32]. This order is evidenced by data (extracted from SEM images using the ImageJ package [33]) such as average size distributions between 63 nm and 80 nm and periodic intensity fluctuations (bright rings) in the FFT spectra of the SEM images (see insets of Figure 1). The distance-related peak positions of the integrated radial intensity distribution (shown for example in the FFT inset of Figure 1c) allow for the length scale estimation of the structure, which was found to be about 135 ± 40 nm. Interestingly, the NP structures produced with ≈0.6 J/cm^2 of total irradiation fluence reveal a mono-modal size distribution (see Figure 1c), while the distribution of structures produced with ≈1 J/cm^2 resulted in observ-

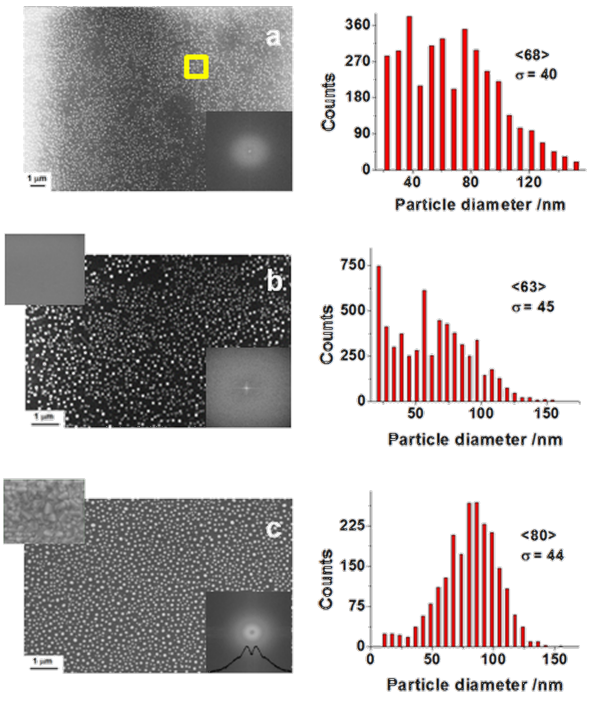

Figure 1: SEM images and size distributions (with the mean diameter value in brackets and standard deviation, σ, given) of Au nanoparticle arrays obtained from films of a thickness of d = 10 nm deposited on SiO_2 glass (a,b) and ITO/BK-7 glass (c) substrates by irradiation with 15 (a), 10 (b), and 4 (c) laser pulses at 266 nm and fixed fluences of 60 (a), 100 (b), and 160 (c) mJ/cm^2. The top-left insets in b) and c) show the substrate structures where the scale is the same as for the NPs. The bottom-right insets show power distributions of the FFT-processed SEM images. The yellow-selected area in a) was used as the model system for FDTD calculations.

able amounts of small particles (Figure 1a,b). This may be an indication of the size redistribution due to prolonged irradiation.

As viewed from above, circularly symmetric particles might be inferred. However, SEM investigations performed at 45° incidence show that, in reality, the particles are partially spherical and/or spheroidal [18]. This observation agrees with results obtained by Gupta et al. who analyzed and postulated how the NP shapes depend on the equilibrium of the surface tension forces [34]. The partially spherical/spheroidal shapes correspond to the case of partial wetting of the substrate by the molten metal and are characterized by a contact angle value of less than 90°. This angle approaches 180° in the case of weak wetting, that is, with a decrease in the metal–substrate interface. While a variety of NP shapes can be easily considered by means of numerical methods (see, e.g., the results discussed in [35,36]), analytical approaches based on Mie theory with a Drude model of the metallic sphere (i.e., a single metallic spherical particle) can be quite useful in view of approximate solutions. This can even be the case for self-organized NP arrays as is demonstrated below.

Observation of plasmon resonances

The data extracted from absorbance spectra contain the key information on the optical response of the nanostructured Au films. Shown in Figure 2 are the spectra acquired with a spectrophotometer (UV–vis, Perkin Elmer) for the NP structures of Figure 1. Here, the red shift and also the broadening of the resonance band from 110 nm to about 170 nm with an increase of the particle radius are clearly visible.

The position and shape of the absorbance band can be derived from the Mie solution of Maxwell equations describing interaction of a metallic, spherical particle embedded in medium of a fixed refractive index in an external electromagnetic field. With the particle material (Au) treated as a Drude metal, the absorption cross section of spherical nanoparticles is given by [37]:

$$\alpha(\omega) = 9\varepsilon_m^{3/2} V \frac{\omega}{c}\left(\frac{\varepsilon_2(\omega)}{[\varepsilon_1(\omega)+2\varepsilon_m]^2+\varepsilon_2^2(\omega)}\right), \qquad (1)$$

where ω is the irradiation frequency, c is the speed of light, V is the particle volume and ε_m, ε_1, ε_2 are the dielectric constants of the medium, and the real and imaginary parts of the metal dielectric function, respectively. If ε_2 is small and weakly dependent on ω, the resonance condition is fulfilled when $\varepsilon_1(\omega) = -2\cdot\varepsilon_2$. Validity of this approach is limited to isolated particles, but the mean inter-particle distance ranges from about 95 to 175 nm which indicates that this condition is fulfilled. At

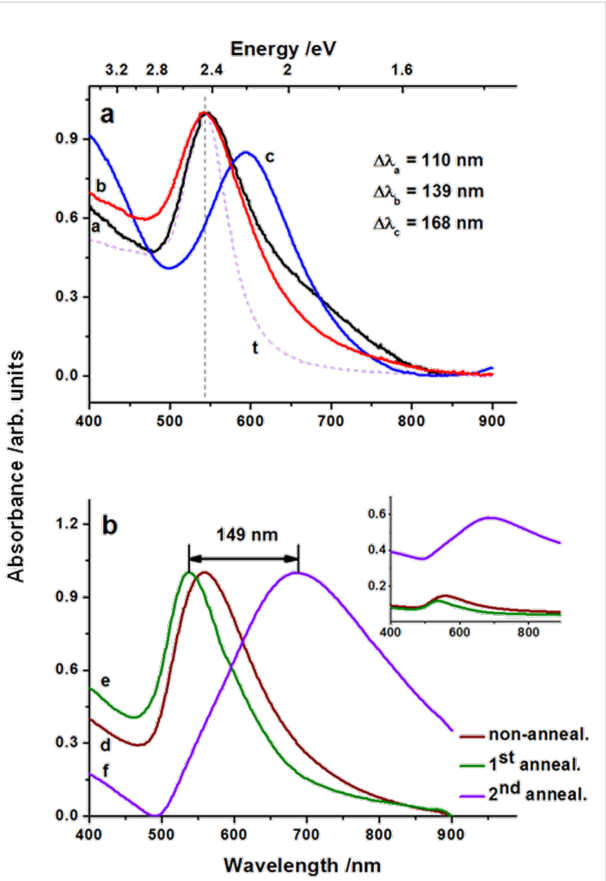

Figure 2: Absorbance spectra (normalized): a) profiles a, b, and c of nanostructures shown in Figure 1a, b, and c, respectively; spectrum t is calculated for the structure in Figure 1b. b) Absorbance spectra recorded for structures in a two-stage process: non-irradiated 5 nm thick film - spectrum d, the same film irradiated with 5 pulses at fluence of 60 mJ/cm^2 - spectrum e, and after renewal sputtering of 5 nm Au film and successive irradiation under the same conditions - spectrum f; the inset shows intensity relations between lines d, e, and f.

these distances the NPs are either not interacting with each other or the interactions are rather insignificant in terms of single particle scattering. In case of spectrum t of Figure 2a, R = 31.5 nm and a refractive index value of n_m = 1.33 have been employed for the calculation. This is the intermediate value between n_m = 1.5 (glass) and n_m = 1 (air) ensuring the best fit of the peak position while taking into account that NPs are deposited on the glass substrate rather than embedded in the matrix. Nevertheless, the experimental profile is broader than calculated. This can be caused by the presence of large particles in the arrays and also by the NP size distribution, neither of which are taken into account in the calculations conducted for the average size NPs. The structureless peaks in Figure 2a indicate a relatively strong dipolar response to irradiation, even in the case of this self-organized nanostructure. However, excitation of high-order multipoles can occur too, especially when the symmetry is broken by differences in the particle shape and size

or by the presence of the substrate [38]. This leads to the appearance of additional red-shifted maxima and results in structured absorbance spectra. On the other hand, such effects can be used for tuning of the SPR. Comparison of the absorbance spectra of the non-processed Au film, the NP structures obtained from its processing, and also of the structure produced by renewal film deposition (5 nm) and re-processing are presented in Figure 2b. The gold layer of thickness of 5 nm (spectrum d) shows plasmonic behavior due to film discontinuity. The irradiation results in a smoother film surface observed in SEM images and the spectrum shows a blue shift and narrowing (see spectrum e). After coverage of the structure with an additional 5 nm thick Au film and its subsequent annealing by the laser, the broadening and a red shift of ≈149 nm follow from peak positions of spectra e as compared to c. This indicates an effective tuning possibility which, to our knowledge, has not been previously reported.

Values of the resonance energy and linewidths (FWHM, full-width-at-half-maximum) as a function of the particle radius obtained for self-organized Au NP arrays are presented in Figure 3. The experimental peak positions and FWHMs are shown as full circles and squares, respectively.

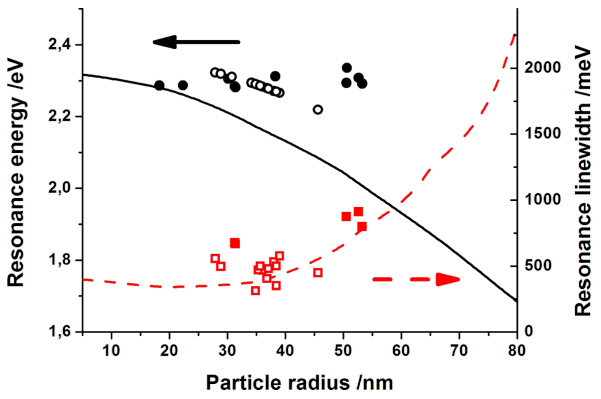

Figure 3: The particle size influence on the resonance peak position (circles) and linewidth (squares) of the absorbance spectra of Au NPs; empty and filled symbols correspond to particle sizes estimated from Equation 2 and obtained from analysis of SEM images, respectively; the lines represent the resonance position (solid line) and linewidth (dashed line) calculated from Mie theory with an assumed value of the refractive index of n_m = 1.5.

The experimental data points corresponding to the resonance positions which lie above the solid line which represents values calculated for the model, single and non-interacting Au NPs embedded in a medium of n_m = 1.5. The experimental data fulfill the assumption that the n_m value (in the case of supported NPs) is smaller than that of the embedded ones. Using the semi-empirical relation given by Haiss et al. [39]:

$$d[\mathrm{nm}] = \frac{\ln\left(\frac{\lambda_{SPR} - \lambda_0}{L_1}\right)}{L_2}, \quad (2)$$

where λ_{SPR} (in nm) is the experimental peak position, λ_0 = 512 nm, L_1 = 6.53, L_2 = 0.0216, and assuming the value of n_m = 1.33, the particle size was estimated and the dependences of the resonance position and linewidth on NPs dimension are presented as empty circles and squares, respectively. The good agreement of the calculated and experimental data validates usage of Equation 2 in the case of semi-regular NP arrays supported on glass substrates.

The linewidth of the plasmonic absorption band observed experimentally describes an important property of the plasmon resonance, namely its dephasing. As stated by Link and El-Sayed [40] there are two main decay mechanisms of the coherent electron motion postulated and discussed in the literature. The first one assumes that plasmons can decay by "pure" dephasing, which means a decay of the fixed-phase correlation between the individual electronic excitations of the whole oscillator ensemble (elastic process). The second explains the decay in terms of the energy transfer into quasi-particles (electron–hole pairs; inelastic processes). The dephasing results in the loss of coherence of the collective electron motion and is characterized by the time constant T_2, which is size-dependent and is given by the expression [31]:

$$\frac{1}{T_2} = \frac{1}{T_r} + A\frac{v_F}{R}, \quad (3)$$

where T_r is the bulk-specific, purely free-electron relaxation time, v_F is the Fermi velocity and A is a constant. The reported value of T_r for Au is 18 fs and can be used as a reference for estimations of the quantum efficiency of the resonant scattering [38,40]. From Equation 3 it follows that T_2 decreases with increasing particle size. Moreover, the constant A ($1 < A < 2$) represents a dependence of the dephasing time on the particle shape as discussed in [41,42]. This makes evident that the dephasing mechanisms can seriously limit the resonant scattering of the NP structure, which in turn determines the plasmonic enhancement of the electromagnetic field in the vicinity of the particles, and finally determines the application capability (e.g., for SERS (surface enhanced Raman spectroscopy)). In the estimation of the plasmon damping effect, the relation between the observable Γ and dephasing time $T_2 = 2\hbar/\Gamma$ can be applied, where Γ is the FWHM of the plasmon resonance. For simplified analysis, it is assumed that the line broadening effects are independent and additive. Thus, the linewidth consists of the sum of the contributions from the homogeneous

and radiative widths and those originating from bulk, surface and interface effects [41]:

$$\Gamma = \Gamma_t + \gamma_{rad} + \gamma_{bulk} + \gamma_{surface} + \gamma_{interface}. \quad (4)$$

In this sum the three latter terms can be neglected, being much smaller than the prominent radiative and homogeneous contributions [43,44]. The above assumptions make possible the analysis based on experimental data. Sample values of T_2 extracted from absorbance spectra of nanostructures fabricated from Au films of a thickness of 10–30 nm at various pulse fluencies from the range of 60–420 mJ/cm^2 together with literature data taken from [45] are shown as a function of the particle size in Figure 4.

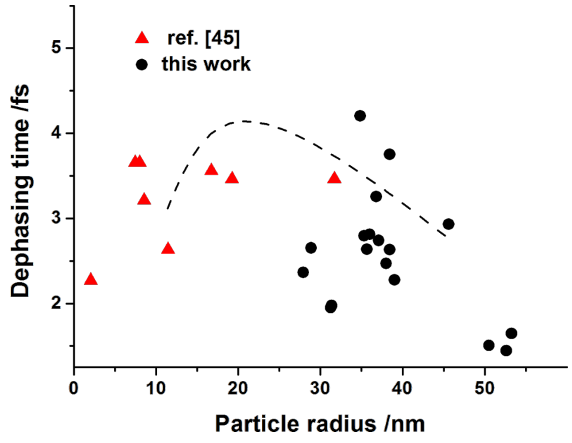

Figure 4: Influence of the gold NP size on the dephasing time of the plasmonic resonance; data from this work were obtained from absorbance spectra of Au NP arrays produced from 10–30 nm thick films (circles) and data from [45] are given for comparison (triangles); the dashed line is a guide for the eye.

It can be concluded from both sets of data obtained for the NP structures that in the range of particle size increase from 40 to about 100 nm the maximal values of T_2 do not exceed ≈4 fs and decrease observably. This indicates a strong plasmon damping when compared with the longest coherence time reported (T_2 = 18 fs, i.e., no damping) [41]. This observation agrees with other literature results that reveal an even more drastic reduction of T_2 for larger particles (size > 100 nm) [42]. In the following it is shown that despite the strong damping of the plasmon resonance, the self-organized Au nanostructures reveal sufficient enhancement of the optical signal from the application point of view.

Evidence of plasmonic enhancement

Near-field effect

In the analysis of the electromagnetic field in the vicinity of the particle-surrounding interface the finite-difference time-domain (FDTD) method represents a widely used tool. It allows for flexible modeling and effective problem solutions for isolated and simple particle systems, as well as for large particle populations and with interactions with the environment taken into account [35,38]. An example of FDTD results for a model system having a geometry corresponding to that of the semi-regular structure of the fragment marked by a square in Figure 1a and consisting of 14 spherical particles of averaged size 2·R = 73 nm is shown in Figure 5 [31].

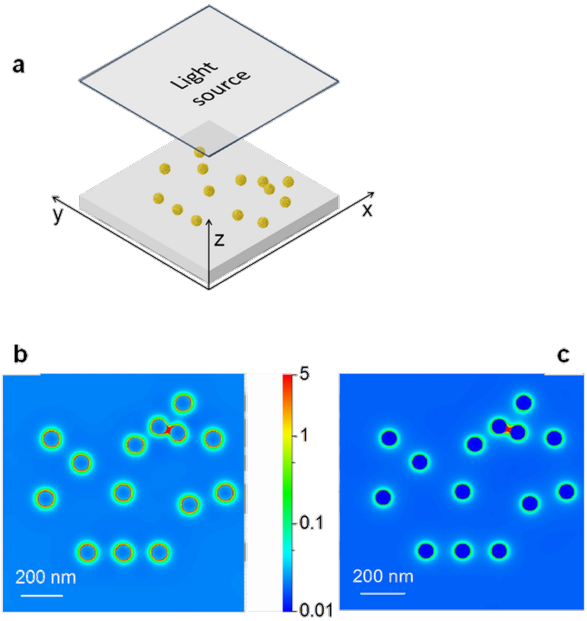

Figure 5: Near-field intensity distributions in the vicinity of Au nanoarrays on SiO_2 glass: a) scheme of the structure geometry adopted from the SEM image in Figure 1a inset, assumed particle size 68 nm, and distributions calculated for excitation at 785 nm - b) and 514 nm - c); intensities (logarithmic scale) are related to a constant illumination of 1 (V/cm)^2 - adapted from [31].

The calculated data of the near-field intensities $|E|^2$ refer to the plane parallel to substrate surface and distanced by R from it. Magnitude of the electromagnetic field enhancement is related to the electric field strength of the incident light (E = 1 V/m) which is illuminating the surface orthogonally. Distributions obtained under illumination at wavelengths used typically in Raman spectrometers of 514 nm (Figure 5a) and 785 nm (Figure 5b), are dominated by the dipolar effect localized on individual particles. The coupling between the local dipole fields decreases rapidly with the distance from the particle surface (≈1/r^6) and does not build up because of the large inter-particle separations. The enhancement due to field intensities in the inter-particle areas is practically negligible with the exception of two closely spaced particles in the upper right corner of the structure. Similar intensity “hot spots” are most often observed for more closely-packed NP structures which in the

case of partial structural order also reveal partially symmetrical spot patterns of the EM-field distributions reported in a number of works [18]. The corresponding broad and structured absorbance profiles result in different resonant responses depending on the excitation energy where the distribution in particle size, shape and also inter-particle distance are the main contributions to the observed effect. Values of the field enhancement due to SPR lie within one order of magnitude for the sparsely-packed Au nanostructures in Figure 1a and increase by a factor of about 10 with increasing NP packing density when the Au nanoarrays are produced using the method of [18,31]. The distributions indicate that in the case of the low density structures, the resonant response due to light scattering is similar to that of a single particle, in agreement with theory [37]. Accordingly, similar peak positions of the absorbance spectra are observed for such structures (see Figure 2a) and for particles of the same size, while differences in the spectral bandwidth and shape result from differences in inter-particle distances. In fact, the 514 nm excitation is more efficient than at 785 nm, which follows from a comparison of the field distributions. This is in general agreement with results obtained by means of simplified models and reported for the resonant response of regular NP structures [46]. This is also confirmed for self-organized NPs, including those produced by other techniques such as ion beam lithography and colloidal synthesis [47].

Mid-field enhancement

Measurements of the micro-Raman spectra and quantitative data on the SERS effect provide a reliable check of the sensing capability from the point of view of the ultrasensitive detection based on the refractive index variations [18]. In the particular case of the self-organized NP arrays, such data are crucial for understanding the relation between the structure morphology, the near-field distribution of the optical signal due to the plasmonic resonance effect, the SERS signal enhancement in the mid-field, and the far-field resonant response observed via the SPR spectrum. The enhancement factor (EF) can be estimated from relation [48]:

$$\mathrm{EF} = \frac{I_{\mathrm{SERS}}/N_{\mathrm{SERS}}}{I_{\mathrm{R}}/N_{\mathrm{R}}}, \qquad (5)$$

where I_{SERS} and I_{R} are intensities of SERS and Raman signals, and N_{R} and N_{SERS} are the number of molecules contributing to Raman and SERS intensities, respectively. If the values of N_{R} and N_{SERS} are unknown or there is no Raman signal recorded for bulk samples, another EF estimation method described thoroughly by Gupta and Weimer [49] can be used, which is shown further in this work.

An example of Raman spectra obtained for the laser-nanostructured, thin Au films and of reference samples (SiO_2 glass and continuous Au film) covered with a dried solution of ≈10^{-5} M R6G in ethanol are shown in Figure 6. The spectra were recorded with a micro-Raman spectrometer (InVia, Renishaw) with excitation wavelengths of 514 and 785 nm and a microscope magnification of 50×.

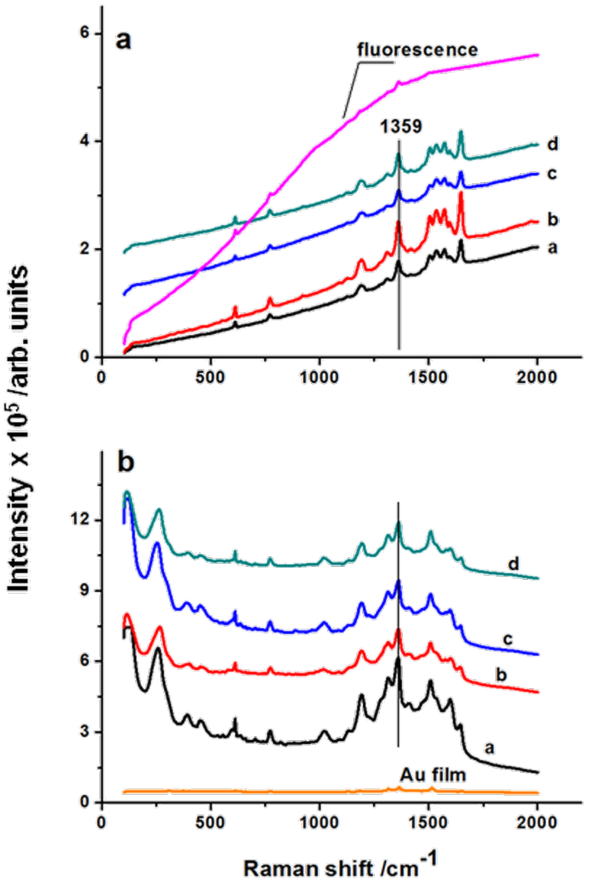

Figure 6: Raman spectra of a 10^{-5} M dried solution of rhodamine R6G deposited on laser-nanostructured thin Au films, excited at λ = 514 nm (a) and 785 nm (b) together with reference spectra of R6G on SiO_2 glass (fluorescence) and on the gold film prior to processing (Au film).

It can be observed that for samples prepared under the same conditions, the recorded spectra show a lower Raman signal when excited at 514 nm than at 785 nm, while the FDTD model calculation reveal a stronger field enhancement in case of the 514 nm excitation compared to that at 785 nm (see distributions in Figure 5) [31]. The effect originates in the difference of surface coverage by the R6G dried film and by the Au nanoparticles. The latter is low and does not exceed 30%, while the dye film covers the entire nanoarray surface together with the inter-particle areas. In consequence, a large part of the illuminating radiation is absorbed by the dye molecules and does not contribute to the scattering signal. Moreover, the strong absorp-

tion band of R6G at 530 nm matches nearly perfectly with the broad plasmon band at around 546 nm (FWHM ≈110 nm). This leads to a decrease of the AuNPs illumination with an instantaneously lower contribution of the resonant scattering and finally results in lower values of the optical field enhancement. For excitation at 785 nm, the plasmon absorption is higher compared to the weak R6G absorption at this wavelength and this results in higher Raman enhancement.

By comparison of spectra recorded for NP arrays and the reference in Figure 6b, the distinctly higher Raman peak intensities can be observed for the NP structures, while the spectrum of the metal film shows only weak signals of the characteristic peaks due to the structure of the DC-sputtered film (grain size ≤0.5 nm) as revealed by SEM inspection. The quantitative estimation of the Raman enhancement can be performed according to the abovementioned method [49]. The evaluation of the EF is based on the comparison of the Raman and fluorescence intensities for R6G with an assumed sample illumination well below the saturation level and a constant ratio of the illuminated Au and R6G molecules of about 10^3. For excitation at 514 nm, the intensity of the fluorescence signal in Figure 6a is 5.1×10^5 at 1359 cm^{-1} while intensities of the corresponding Raman peaks in spectra a–d are in the range of $(1.6–3.7) \times 10^5$ indicating that the latter are slightly lower. Given the fluorescence cross section σ_F of R6G equal to 10^{-16} cm^2 at 514 nm, and that of Raman scattering $\sigma_{SC} \approx 10^{-30}$ cm^2 and taking into account that Raman scattering of R6G is enhanced by about 10^4 due to resonance at 514 nm, the factor of about 10^7 of the Raman signal enhancement due to surface effect can be estimated. For the spectra excited at 785 nm (used to ensure non-resonant Raman excitation) the maximum Raman peak heights in Figure 6b are $\approx 12 \times 10^5$ at 1359 cm^{-1}, which is close to the intensities of the fluorescence signal at 514 nm (Figure 6a). Thus, the cross section for non-resonant SERS signal is on the order of $\approx 10^{-19}$–10^{-20} cm^2 which corresponds to the enhancement factor of about 10^{10}.

For the semi-regular (random) structures, the reported average values of the EF lie in the range of 10^1–10^3 for non-optimized conditions (that is in the absence of "hot spots") and 10^3–10^6 for very good SERS substrates, while those of template-based structures vary between 10^4 and 10^7 [50-52] and are an order of magnitude larger than for randomly ordered structures [50]. Despite the fact that for the individual "hot spots" a huge enhancement up to 10^{14} can be observed [18,49,53], the EF of NP assemblies is usually 10^7–10^8 times smaller. This is due to statistical averaging as particles are contributing equally to the recorded mid-field signal and only small amounts of them are "optically hot" showing an exceptionally high enhancement [54]. Therefore, the EF values of 10^7–10^{10} reported in this work for semi-regular structures are considered comparable to values reported for template-based ones.

Sensing capability attributable to laser nanostructuring

Short-pulse laser processing represents an advantageous solution to the synthesis problem of sensor materials based on the SPR effect. This has been confirmed by using the patterning effect induced by a single laser pulse at 532 nm and intensities up to 1000 mJ/cm^2 in a thin Au film deposited onto an ITO substrate [12]. The Au nanoclusters (20–40 nm) produced in this way have a surface density in the range $(0.2–2) \times 10^{10}$ cm^{-2}, which is sufficient for enhancement of the optical signal. Similarly, improved sensor performance is observed for electrodes modified by deposition of catalytic metals by means of a direct laser transfer of material [15]. Among metallic structures showing the SPR effect, Au NPs play important role in the construction of electrochemical sensors [55]. This is confirmed by numerous results obtained with the use of Au-modified, conducting oxide materials, such as indium tin oxide, fluorine tin oxide and others. In particular, the ITO substrate is widely used and investigated because of its stable physical and electrochemical properties and finds application in optoelectronic and photovoltaic devices, as well as in the sensitive detection of species such as glucose, hydrogen peroxide and DNA fragments [56,57].

Samples of the Au–ITO interface discussed here were formed in a controlled process using multiple UV laser pulses applied to the thin Au films [58]. The resulting structures shown in Figure 1c were obtained from 5–30 nm thick Au films, produced by discharge sputtering on substrates of ITO at BK7 glass. The laser processing resulted in nano-arrays of Au particles characterized by self-organization despite the granular structure revealed by the continuous ITO layer (see Figure 1c, inset on the left). As concluded from the previous section, these NP arrays revealed the SPR-related enhancement of the optical signal. Testing of their sensing capacity was performed by means of the voltammetric measurements described in detail elsewhere [58]. In brief, the CV curves were recorded using a potentiostat–galvanostat (PGStat 302N, Metrohm) in a standard three-electrode assembly, operated at 295 K. Measurements were performed in solutions of 10 mM $K_3[Fe(CN)_6]$ + 1 M KCl and 0.1 M NaOH without and with 2 mM of glucose added. The electrolytes were purged with argon for about 1 h prior the measurements, and during the electrochemical tests the Ar-cushion above the electrolyte has been applied. For the samples on ITO substrates, the Au films and NP arrays stayed as a working electrode, and the Pt mesh and Ag/AgCl/0.1 M KCl served as the counter and reference electrodes, respectively.

Figure 7 shows data collected for the reference ITO electrodes covered by continuous gold films of a thickness of 10 and 20 nm and also for ITO modified by Au NP arrays obtained by laser processing of such films. The reversibility of the electrochemical reactions can be concluded from the CV data obtained for ferricyanide as a model substance according to method described in [59]. Curves acquired for electrodes modified by Au nanoarrays and immersed in the $K_3[Fe(CN)_6]$ solution show pronounced oxidation and reduction peaks of the Fe^{2+}/Fe^{3+} redox couple (see Figure 7a). For the ITO reference sample, a weak reversibility with peak separation of ΔE = 0.166 V is observed. In the case of the modified electrodes, the higher current values are recorded and the separation of the oxidation and reduction peaks are lower, which indicates an enhanced redox reversibility [60].

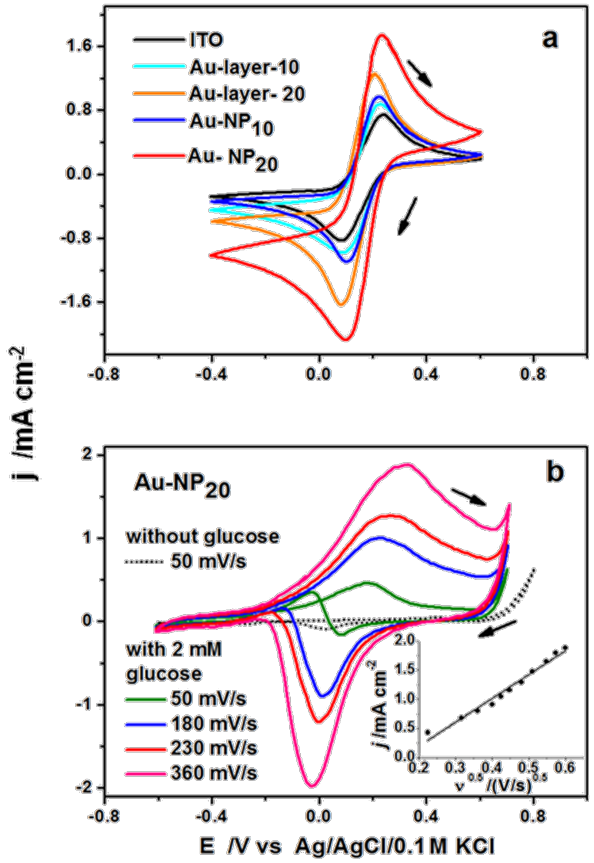

Figure 7: a) Voltammetric curves of the reference electrodes of uncovered ITO and covered by non-processed 10 and 20 nm thick Au film, and modified by Au NPs produced by laser nanostructuring of these films, for electrodes immersed in 10 mM $K_3[Fe(CN)_6]$ + 1 M KCl and recorded at a scan rate of 50 mV/s; b) CV curves of the ITO electrode modified by Au NPs produced from 20 nm thick films, in 0.1 M NaOH without and with 2 mM of glucose, recorded at scan rates of 50, 180, 230, and 360 mV/s; the inset shows a linear dependence of the peak current on square root of the scan rate - adapted from [58].

A minimal peak separation of 0.127 V and a high peak current (exceeding that of the Au-NP10 sample by factor of two) are obtained for the Au-NP20 electrodes, thus they are preferred from the point of view of electrochemical properties. The preference is closely related to the presence of Au NPs having a larger size and lower inter-particle distances thus effectively covering the ITO surface as compared to Au-NP10, which is also revealed by the SEM inspection. For the selected electrode (Au-NP20) the sensing capability was observed via electrochemical response towards glucose oxidation and the CV curves were recorded for electrodes immersed in 0.1 M NaOH with and without 2 mM of glucose as shown in Figure 7b. In the range from −0.6 V to +0.7 V the signals corresponding to the gold oxidation and reduction are observed at −0.11 V and +0.51 V, respectively. The addition of glucose to the solution leads to the increase of current and clearly resolved peaks in the CV curves are observed. The wide shoulder (−0.1 V) in the anodic component of the potential sweep can be ascribed to glucose electrosorption and formation of gluconolactone [61]. In the cathodic potential scan another oxidation peak is visible around −0.11 V due to release of the Au sites by reduction of gold oxide [61]. This is due to the re-oxidation of glucose instantaneously with the reduction of gold oxide and both the oxidation and reduction peaks overlap. The linear dependence of the current density vs square root of the scan rate in the inset in Figure 7b confirms the diffusion-controlled glucose electro-oxidation in agreement with literature [62]. This and the values of the peak current density registered in the presence of $K_3[Fe(CN)_6]$ and glucose both confirm the improved electrode performance. This indicates that the laser processing of the ITO–Au interface makes possible a cost-effective, non-enzymatic detection of glucose, distinct from the production and use of enzyme-based sensors [63]. The result obtained for samples Au-NP20 indicates that modification of ITO electrodes by NP arrays produced from thin Au films by short laser pulses represents a new production path of hybrid sensor materials for medicine, the food industry and environmental protection.

Conclusion

For gold nanoarrays characterized by low and moderate packing densities that are produced by sequences of short laser pulses under mild irradiation conditions, the morphology, optical properties and in particular the enhancement of the optical signal were investigated. It was shown that the nanostructures reveal self-organization characterized by a short-range order and by distributions of the particle and inter-particle size and also particle shape. The partially spherical/spheroidal shape of the particles contributes to the broadening of the absorbance band and provides observable effects in the optical response of the nanoarrays. The resonance peak position can be selected by the array preparation conditions. Moreover, for nanostructures

obtained by repeated film deposition and nanostructuring, a new possibility for a relatively broad-range tuning of the plasmon peak position is observed. Despite the fact that the resonance lifetime was reduced to below ≈4 fs, the data for the optical field enhancement obtained from SERS and electrochemical measurements of the self-organized Au nanoarrays indicate an application capability in areas of light harvesting [34], ultra-sensitive detection (SERS), spintronics [64] and optical switching [65]. Results of this work confirm that semi-regular Au NP arrays produced by short-pulse laser irradiation of thin metal films represent cost-effective and relatively unexplored fabrication route for nanomaterials of the required structural and chemical stability, which is of crucial importance for industrial-scale plasmonic technologies.

Acknowledgements

The authors appreciate the support from the Cost Action 0901 and fruitful discussions with the NanoTP Community as well as the inspiration towards biomedical sensing from Cost Action 1202. KG and KS acknowledge the National Science Centre – NCN for funding under contracts 2012/07/N/ST5/02139 and 2012/07/D/ST5/02269, respectively. Additionally, the support of colleagues A. Belfiore and L. Dangreau from Univ. of Mons and of M. Sawczak and A. Sobczyk of the Szewalski Institute PASci Gdańsk is gratefully acknowledged.

References

1. Bischof, J.; Scherer, D.; Herminghaus, S.; Leiderer, P. *Phys. Rev. Lett.* **1996,** *77,* 1536–1539. doi:10.1103/PhysRevLett.77.1536
2. Seifert, N.; Betz, G.; Husinsky, W. *Appl. Surf. Sci.* **1996,** *103,* 63–70. doi:10.1016/0169-4332(96)00469-2
3. Bostanjoglo, O.; Nink, T. *Appl. Surf. Sci.* **1997,** *109–110,* 101–105. doi:10.1016/S0169-4332(96)00912-9
4. Simon, P.; Ihleman, J. *Appl. Surf. Sci.* **1997,** *109–110,* 25–29. doi:10.1016/S0169-4332(96)00615-0
5. Willis, D. A.; Xu, X. *J. Heat Transfer* **2000,** *122,* 763–770. doi:10.1115/1.1288931
6. Henley, S. H.; Carey, J. D.; Silva, S. R. P. *Phys. Rev. B* **2005,** *72,* 195408. doi:10.1103/PhysRevB.72.195408
7. Henley, S. J.; Poa, C. H. P.; Adikaari, A. A. D. T.; Giusca, C. E.; Carey, J. D.; Silva, S. R. P. *Appl. Phys. Lett.* **2004,** *84,* 4035–4038. doi:10.1063/1.1751226
8. Krishna, H.; Sachan, R.; Strader, J.; Favazza, C.; Khenner, M.; Kalyanaraman, R. *Nanotechnology* **2010,** *21,* 155601. doi:10.1088/0957-4484/21/15/155601
9. Krishna, H.; Favazza, C.; Gangopadhyay, A. K.; Kalyanaraman, R. *JOM* **2008,** *60,* 37–42. doi:10.1007/s11837-008-0115-y
10. Sachan, R.; Ramos, V.; Malasi, A.; Yadavali, S.; Bartley, B.; Garcia, H.; Duscher, G.; Kalyanaraman, R. *Adv. Mater.* **2013,** *25,* 2045–2050. doi:10.1002/adma.201204920
11. Ruffino, F.; Pugliara, A.; Carria, E.; Romano, L.; Bongiorno, C.; Fisicaro, G.; La Magna, A.; Spinella, C.; Grimaldi, M. G. *Appl. Surf. Sci.* **2012,** *258,* 9128–9137. doi:10.1016/j.apsusc.2011.12.087
12. Kuznetsov, A. I.; Unger, C.; Koch, J.; Chichov, B. N. *Appl. Phys. A* **2012,** *106,* 479–487. doi:10.1007/s00339-011-6747-8
13. Hubenthal, F. *Eur. J. Phys.* **2009,** *30,* S49–S61. doi:10.1088/0143-0807/30/4/S05
14. Cheng, Y.-T.; Uang, R.-H.; Wanga, Y.-M.; Chiou, K.-C.; Lee, T.-M. *Microelectron. Eng.* **2009,** *86,* 865–867. doi:10.1016/j.mee.2008.12.058
15. Haro-Poniatowski, E.; Alonso-Huitrón, J. C.; Acosta-Zepeda, A.; Acosta-García, M. C.; Batina, N. *Nanotechnology* **2009,** *2,* 355304. doi:10.1088/0957-4484/20/35/355304
16. Nedyalkov, N. N.; Nikov, R.; Dikovska, A. O.; Atanasov, P. A.; Obara, G.; Obara, M. *Appl. Surf. Sci.* **2012,** *258,* 9162–9166. doi:10.1016/j.apsusc.2011.12.023
17. Nikov, R. G.; Nedyalkov, N. N.; Atanasov, P. A.; Grochowska, K.; Iwulska, A.; Śliwiński, G. In *Proc. SPIE 8770,* 17th International School on Quantum Electronics: Laser Physics and Applications, Nessebar, Bulagia, Nov 24, 2012; Dreischuh, T. N.; Daskalova, A. T., Eds.; 2013; pp 1–7. doi:10.1117/12.2014758
18. Imamova, S. E.; Dikovska, A.; Nedyalkov, N. N.; Atanasov, P. A.; Sawczak, M.; Jendrzejewski, R.; Śliwiński, G.; Obara, M. *J. Optoelectron. Adv. Mater.* **2010,** *12,* 500–504.
19. Verma, S.; Rao, B. T.; Rai, S.; Ganesan, V.; Kukreja, L. M. *Appl. Surf. Sci.* **2012,** *258,* 4898–4905. doi:10.1016/j.apsusc.2012.01.111
20. Zavestovskaya, I. N. *Quantum Electron.* **2010,** *40,* 942–954. doi:10.1070/QE2010v040n11ABEH014447
21. Kabashin, A. V.; Delaporte, P.; Pereira, A.; Grojo, D.; Torres, R.; Sarnet, T.; Sentis, M. *Nanoscale Res. Lett.* **2010,** *5,* 454–463. doi:10.1007/s11671-010-9543-z
22. Gamaly, E.; Rode, A.; Luther-Davies, B.; Tikhonchuk, V. *Phys. Plasmas* **2002,** *9,* 949–957. doi:10.1063/1.1447555
23. Stuart, B. C.; Feit, M. D.; Herman, S.; Rubenchik, A. M.; Shore, B. W.; Perry, M. D. *J. Opt. Soc. Am. B* **1996,** *13,* 459–468. doi:10.1364/JOSAB.13.000459
24. Kneier, F.; Geldhauser, T.; Scheer, E.; Leiderer, P.; Boneberg, J. *Appl. Phys. A* **2013,** *110,* 321–327. doi:10.1007/s00339-012-7235-5
25. Kuznetsov, A. I.; Koch, J.; Chichkov, B. N. *Appl. Phys. A* **2009,** *94,* 221–230. doi:10.1007/s00339-008-4859-6
26. Di Fonzo, F.; Casari, C. S.; Russo, V.; Brunella, M. F.; Li Bassi, A.; Bottani, C. E. *Nanotechnology* **2009,** *20,* 1–7. doi:10.1088/0957-4484/20/1/015604
27. Kawashima, N.; Zhu, Q. Y.; Gerson, A. R. *Thin Solid Films* **2012,** *520,* 3884–3891. doi:10.1016/j.tsf.2012.01.021
28. De Jonghe, V.; Chatain, D. Wettability of Real Surfaces in Liquid Metal/Monocrystalline Alumina and Contact Angle Hysteresis. In *Interfaces in New Materials;* Grange, P., Ed.; Elsevier: Cambridge/MA, USA, 1991; pp 219–228. doi:10.1007/978-94-011-3680-8_22
29. Brissonneau, V.; Escoubas, L.; Flory, F.; Berginc, G.; Maire, G.; Giovannini, H. *Appl. Surf. Sci.* **2012,** *258,* 9171–9174. doi:10.1016/j.apsusc.2011.10.137
30. Nakata, Y.; Momoo, K.; Miyanaga, N.; Hiromoto, T.; Tsuchida, K. *Appl. Phys. A* **2013,** *112,* 173–177. doi:10.1007/s00339-012-7236-4
31. Grochowska, K.; Śliwiński, G.; Iwulska, A.; Sawczak, M.; Nedyalkov, N.; Atanasov, P.; Obara, G.; Obara, M. *Plasmonics* **2013,** *8,* 105–113. doi:10.1007/s11468-012-9428-3
32. Krishna, H.; Shirato, N.; Yadavali, S.; Sachan, R.; Strader, J.; Kalyanaraman, R. *ACS Nano* **2011,** *5,* 470–476. doi:10.1021/nn1022632
33. http://imagej.nih.gov/ij/ (accessed Sept 8, 2014).
34. Gupta, G.; Tanaka, D.; Ito, Y.; Shibata, D.; Shimojo, M.; Furuya, K.; Mitsui, K.; Kajikawa, K. *Nanotechnology* **2009,** *20,* 025703. doi:10.1088/0957-4484/20/2/025703

35. Papoff, F.; Hourahine, B. *Opt. Express* **2011,** *19,* 21432–21444. doi:10.1364/OE.19.021432
36. Kolwas, K.; Derkachova, A. *Opto-Electron. Rev.* **2010,** *18,* 429–437. doi:10.2478/s11772-010-0043-6
37. Kreibig, U.; Vollmer, M. *Optical Properties of Metal Clusters;* Springer-Verlag: Berlin, Germany, 1995. doi:10.1007/978-3-662-09109-8
38. Moroz, A. *Opt. Commun.* **2010,** *283,* 2277–2287. doi:10.1016/j.optcom.2010.01.061
39. Haiss, W.; Thanh, N. T. K.; Aveyard, J.; Fernig, D. G. *Anal. Chem.* **2007,** *79,* 4215–4221. doi:10.1021/ac0702084
40. Link, S.; El-Sayed, M. A. *Annu. Rev. Phys. Chem.* **2003,** *54,* 331–366. doi:10.1146/annurev.physchem.54.011002.103759
41. Sönnichsen, C.; Franzl, C. T.; Wilk, T.; von Plessen, G.; Feldmann, J.; Wilson, O.; Mulvaney, P. *Phys. Rev. Lett.* **2002,** *88,* 077402. doi:10.1103/PhysRevLett.88.077402
42. Dahmen, C.; Schmidt, B.; von Plessen, G. *Nano Lett.* **2007,** *7,* 318–322. doi:10.1021/nl062377u
43. Kolwas, K.; Derkachova, A. *J. Quant. Spectrosc. Radiat. Transfer* **2013,** *114,* 45–55. doi:10.1016/j.jqsrt.2012.08.007
44. Heilweil, E. J.; Hochstrasser, R. M. *J. Chem. Phys.* **1985,** *82,* 4762–4770. doi:10.1063/1.448693
45. Austin, J.; Anthony, J.; Rigo, M. V.; Seo, J.; Tabiti, B.; Jung, S.; Kim, W.-J. *World J. Eng.* **2010,** *7,* 141.
46. Auguié, B.; Barnes, W. L. *Phys. Rev. Lett.* **2008,** *101,* 143902. doi:10.1103/PhysRevLett.101.143902
47. Nishijima, Y.; Rosa, L.; Juodkazis, S. *Opt. Express* **2012,** *20,* 11466–11477. doi:10.1364/OE.20.011466
48. Fazio, E.; Neri, F.; D'Andrea, C.; Ossi, P. M.; Santo, N.; Trusso, S. *J. Raman Spectrosc.* **2011,** *42,* 1298–1304. doi:10.1002/jrs.2861
49. Gupta, R.; Weimer, W. A. *Chem. Phys. Lett.* **2003,** *374,* 302–306. doi:10.1016/S0009-2614(03)00737-1
50. Tessier, P. M.; Velev, O. D.; Kalambur, A. T.; Rabolt, J. F.; Lenhoff, A. M.; Kaler, E. W. *J. Am. Chem. Soc.* **2000,** *122,* 9554–9555. doi:10.1021/ja0022831
51. Mahajan, S.; Hutter, T.; Steiner, U.; Goldberg Oppenheimer, P. *J. Phys. Chem. Lett.* **2013,** *4,* 4153–4159. doi:10.1021/jz4018688
52. Banaee, M. G.; Crozier, K. B. *Opt. Lett.* **2010,** *35,* 760–762. doi:10.1364/OL.35.000760
53. Du, Y.; Shi, L.; He, T.; Sun, X.; Mo, Y. *Appl. Surf. Sci.* **2008,** *255,* 1901–1905. doi:10.1016/j.apsusc.2008.06.140
54. Nie, S.; Emory, S. R. *Science* **1997,** *275,* 1102–1106. doi:10.1126/science.275.5303.1102
55. Katz, E.; Willner, I.; Wang, J. *Electroanalysis* **2004,** *16,* 19–44. doi:10.1002/elan.200302930
56. Siuzdak, K.; Abbas, M.; Vignau, L.; Devynck, M.; Dubacheva, G.; Lisowska-Oleksiak, A. *J. Appl. Phys.* **2012,** *112,* 123110. doi:10.1063/1.4770490
57. Wu, M.-S.; Yuan, D.-J.; Yu, J.-J.; Chen, H.-Y. *Anal. Chem.* **2013,** *85,* 11960–11965. doi:10.1021/ac402889z
58. Grochowska, K.; Siuzdak, K.; Śliwiński, G. *Eur. J. Inorg. Chem.* **2014**. doi:10.1002/ejic.201402485
59. Ahammad, A. J. S.; Choi, Y.-H.; Koh, K.; Kim, J.-H.; Lee, J.-J.; Lee, M. *Int. J. Electrochem. Sci.* **2011,** *6,* 1906–1916.
60. Zhang, J.; Oyama, M. *Anal. Chim. Acta* **2005,** *540,* 299–306. doi:10.1016/j.aca.2005.03.054
61. Ben Aoun, S.; Dursun, Z.; Koga, T.; Bang, G. S.; Sotomura, T.; Taniguchi, I. *J. Electroanal. Chem.* **2004,** *567,* 175–183. doi:10.1016/j.jelechem.2003.12.022
62. Silva, A. T. B.; Coelho, A. G.; da S. Lopes, L. C.; Martins, M. V. A.; Crepilho, F. N.; Merkoçi, A.; da Silva, W. C. *J. Braz. Chem. Soc.* **2013,** *24,* 1237–1245. doi:10.5935/0103-5053.20130157
63. Xu, F.; Cui, K.; Sun, Y.; Guo, C.; Liu, Z.; Zhang, Y.; Shi, Y.; Li, Z. *Talanta* **2010,** *82,* 1845–1852. doi:10.1016/j.talanta.2010.07.087
64. Karmakar, S.; Kumar, S.; Rinaldi, R.; Maruccio, G. *J. Phys.: Conf. Ser.* **2011,** *292,* 012002. doi:10.1088/1742-6596/292/1/012002
65. Maier, S. A.; Brongersma, M. L.; Kik, P. G.; Meltzer, S.; Requicha, A. A. G.; Atwater, H. A. *Adv. Mater.* **2001,** *13,* 1501–1505. doi:10.1002/1521-4095(200110)13:19<1501::AID-ADMA1501>3.0.CO;2-Z

License and Terms

This is an Open Access article under the terms of the Creative Commons Attribution License (http://creativecommons.org/licenses/by/2.0), which permits unrestricted use, distribution, and reproduction in any medium, provided the original work is properly cited.

The license is subject to the *Beilstein Journal of Nanotechnology* terms and conditions: (http://www.beilstein-journals.org/bjnano)

The definitive version of this article is the electronic one which can be found at: doi:10.3762/bjnano.5.219

BEILSTEIN JOURNAL OF NANOTECHNOLOGY

Two-dimensional and tubular structures of misfit compounds: Structural and electronic properties

Tommy Lorenz*[1,2], Jan-Ole Joswig[1] and Gotthard Seifert[1]

Review

Open Access

Address:
[1]Theoretische Chemie, Technische Universität Dresden, 01069 Dresden, Germany and [2]Helmholtz-Zentrum Dresden-Rossendorf e.V., Institute of Ion Beam Physics and Materials Research, P.O. Box 51 01 19, 01314 Dresden, Germany

Email:
Tommy Lorenz* - tommy.lorenz@chemie.tu-dresden.de

* Corresponding author

Keywords:
2D layered materials; misfit layer compounds

Beilstein J. Nanotechnol. **2014,** *5,* 2171–2178.
doi:10.3762/bjnano.5.226

Received: 28 July 2014
Accepted: 30 October 2014
Published: 19 November 2014

This article is part of the Thematic Series "Atomic scale interface design and characterisation: Theory – Electronic properties".

Guest Editor: A. Krasheninnikov

© 2014 Lorenz et al; licensee Beilstein-Institut.
License and terms: see end of document.

Abstract

Misfit layer compounds are structures that consist of two sublattices differing in at least one of their lattice constants. The two different layers are stacked either an alternating or in a more complex series resulting in mono- or multi-layer misfit compounds. To date, planar and bent misfit structures, such as tubes, scrolls or nanoparticles, have been synthesized and interesting magnetic and physical properties have been observed as a result of their special structures. Based on these observations, we present an overview of such misfit systems and summarize and discuss their electronic structure as well as the interlayer bonding behaviour, which is not completely understood yet. Furthermore, a more detailed insight into the SnS–SnS_2 system is given, which was the first tubular misfit compound that has been synthesized and extensively investigated.

Review

Introduction

Sheets of different two-dimensional, layered materials can assemble to form composite materials. As the compounds usually exhibit their own symmetry and space groups, their unit cells differ in most cases in either one, two, or all three directions. The combination of any two or more layers of these sheets results in a so-called misfit layer compound (MLC) [1,2], in which the difference in the compound layers leads to different effects. Figure 1a demonstrates the misfit-compound concept schematically: two different layered, 2D materials are stacked alternately in different sequences. These materials exhibit the stoichiometries MX and TMX_2, and their total chemical formula is $(MX)_{1+x}(TMX_2)_m$ (with M = Sn, Pb, Bi, Sb, rare earths; TM = Ti, V, Cr, Nb, Ta; X = S, Se, $0.08 < x < 0.28$, m = 1–3) [3]. The unit cell parameters are dissimilar at least in one direction (crystallographic direction a in Figure 1). The review by Meerschaut [4] considered misfit compounds with

different unit cell lengths in one direction (a) only. Additionally, compounds that are different in both in-plane directions (a and b) are also known. For example, $(SnS)_{1.32}SnS_2$, $(PbSe)_{0.99}WSe_2$, $(PbSe)_{1.00}MoSe_2$, and $(SnSe)_{1.03}MoSe_2$ [5-8], and misfit layer compounds consisting of other elements such as tellurium [9] or lanthanides [10] have been synthesized. Although some misfit compounds occur naturally [1,11], the recent developments in the synthesis, exfoliation, and handling of layered, two-dimensional (2D) materials gave access to the preparation of numerous misfit compounds.

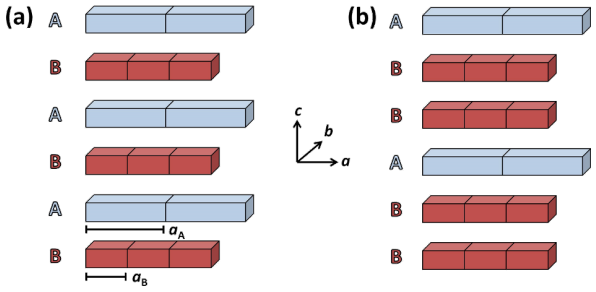

Figure 1: Schematic representation of two stacks of misfit compounds: (a) a misfit compound of type AB and (b) a misfit compound of type ABB.

To date, three comprehensive reviews have dealt with planar [3,4] and tubular [6] misfit compounds, which were as well the foundation for the present overview. In the following, planar and tubular misfit structures are discerned and their individual structural and electronic properties are discussed. Note that the following sections are sorted with respect to the reviewed properties. A section containing special examples will be followed by a summary.

Structures

Layered chalcogenides most commonly form misfit compounds [3] with stoichiometries MX/TMX_2 (chemical formula $(MX)_{1+y}(TMX_2)_m$ with M = Sn, Pb, Bi, Sb, rare earths; TM = Ti, V, Cr, Nb, Ta; X = S, Se , $0.08 < y < 0.28$, m = 1–3). The lengths of the lattice vectors $\vec{a}_1$ and $\vec{a}_2$ (the indices label the two components of the misfit compound) in the mismatched direction determine the ratio of MX to $(TMX_2)_m$. This is expressed in the sum formula by the variable y and can be derived as $y = (4/2)\cdot(a_2/a_1) - 1$. The individual layer types, that is, MX and TMX_2, have different stoichiometries, and thus, differing structures. Whereas MX layers show a distorted rock salt structure (Figure 2a), the TMX_2 layers have a sandwich structure, where a sheet of (transition) metal atoms is sandwiched by two layers of chalcogenide atoms (Figure 2b,c). The transition metal atoms can assemble in a trigonal prismatic or octahedral coordination in the TMX_2 layer (Figure 2d,e). The TMX_2 labeling is according to the polytypes of their lamellar compounds, that is, their stacking order (number of layers in the unit cell) and symmetry (T, H, R for trigonal, hexagonal, rhombohedral symmetry, respectively) generate the labels.

As can be seen in Figure 1, different sequences of stacking are possible: Either an alternating A–B–A–B–… stacking (Figure 1a) or bi- (m = 2) and trilayer (m = 3) systems are known. Here, the parameter m indicates the number of successive layers of the same type. In the latter two cases, two or three TMX_2 layers follow directly and are embedded into two MX layers as shown in Figure 1b. In these cases, the TMX_2 layers are held together by van der Waals forces, whereas the interaction between MX and TMX_2 layers is based on van der Waals interaction and a charge transfer (CT) from MX to TMX_2 [12].

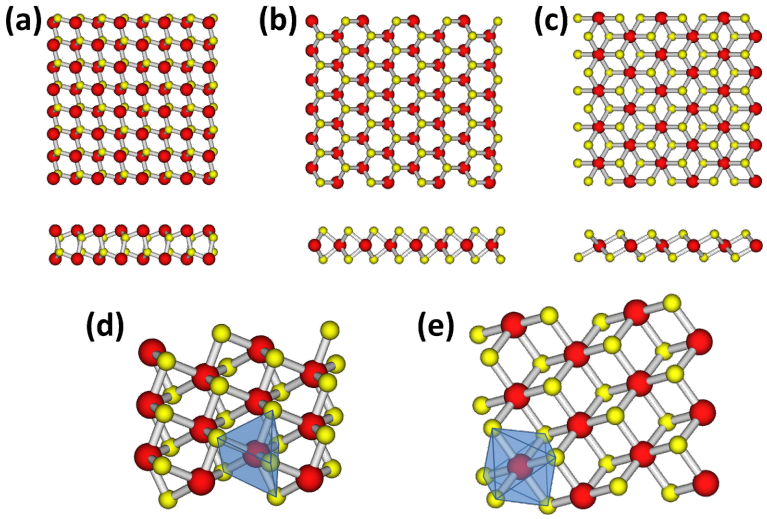

Figure 2: Structures of a monolayer of (a) MX and (b–e) TMX_2. The TMX_2 layer occurs in two configurations with the metal atoms coordinated either (b)/(d), trigonal prismatically, or (c)/(e), octahedrally. The metal and chalcogenide atoms are shown as red and yellow spheres, respectively.

Thus, misfit compounds do not only differ by stoichiometry, difference in structure, and individual coordination in the TMX_2 layer, but also by the ratio between the two subsystems, MX and TMX_2.

Planar structures

We will now focus on a discussion of crystallographic data obtained from different planar misfit compounds. In most cases, the angle between the in-plane lattice vectors $\vec{a}$ and $\vec{b}$ (as defined in Figure 1) is 90°, so that the $\vec{a}$ and $\vec{b}$ vectors in both interacting compounds are parallel. If the $\vec{b}$ vectors have the same length, $\vec{b}_1 = \vec{b}_2$ results. An exception is reported by Ren et al. [13] for $(SbS)_{1.15}TiS_2$ with angles of γ_1 = 84.06° and γ_2 = 90.01°. Generally, the differences occur regularly in both directions as a result of right-angled in-plane lattice vectors.

Most of the systems with NbX_2 or TaX_2 sublayers in a trigonal prismatic coordination have α angles of nearly 90°. There are, however, misfit compounds with different $\vec{c}$ vectors and α or β angles deviating from 90°, for example, $(YS)_{1.23}NbS_2$ [14] and $(HoS)_{1.23}NbS_2$ [15] with trigonal prismatic TMX_2 layers, monoclinic $(PbS)_{1.18}TiS_2$ [16] and $(PbS)_{1.12}VS_2$ [17], or triclinic $(LaS)_{1.20}CrS_2$ [18] and $(SnS)_{1.20}TiS_2$ [19], all four with octahedral coordination in the TMX_2 layer. The unit cell parameters of some misfit compounds are given in Table 1.

As mentioned above, different types of stacking are possible for these composite structures. They may differ, for example, in the number of sub-layers, their symmetry and orientation. The most common structures are 2*H* and 3*R*. Due to the weak interlayer forces, layer exfoliation is easily possible [24].

As a consequence of their structure, interaction between the M atoms of the MX layer and the X atoms of the TMX_2 layer exists in all misfit compounds. In each unit cell this interaction occurs twice: at the top and the bottom sides of the layers. This can be seen in Figure 3. Additionally, this figure shows that the symmetry of the misfit compound's unit cell is determined by the sublayers and their symmetries. The metal atoms of the TMX_2 sublayer can be coordinated trigonal prismatically by the chalcogenide atoms (Figure 3a), so that the symmetry of the whole cell is orthorhombic as, for example, in $(SnS)_{1.17}NbS_2$. On the other hand, for a monoclinic misfit compound such as $(PbS)_{1.18}TiS_2$, the TMX_2 sublayers have a (distorted) octahedral symmetry (Figure 3b).

In cases where the misfit occurs in only one direction, for example, in *b*, the number of stacking possibilities grows, since the individual layers may be centered differently with respect to the *b* direction (see Figure 4). Each subsystem has either a so-called C-centered or an F-centered lattice. In both cases, the *c* axes match. In the F-centered structure, the length of the *c* axis in the unit cell is doubled due to an additional shift of 1/2*c*. Accordingly, four different possibilities of stacking are possible: CC, CF, FC, and FF (see Figure 4). In the CC system, the two *c* axes of the subsystems completely match (in direc-

Table 1: Cell parameters of different misfit layer compounds. This table has been taken from Rouxel et al. [3].

Compound	a_1 [Å]	a_2 [Å]	$y = 2\cdot(a_2/a_1) - 1$	$b_1 = b_2$ [Å]	$c_1 = c_2$ [Å]	α [deg.]	Ref.
$(SnS)_{1.17}NbS_2$	5.673	3.321	0.1708	5.751	11.761	90	[20,21]
$(LaS)_{1.14}NbS_2$	5.828	3.310	0.1359	5.797	c_1 = 11.52[a] c_2 = 23.94	90	[22,23]
$(PbS)_{1.18}TiS_2$	5.800	3.409	0.1755	5.881	11.76	95.28	[16]

[a]$c_2 = 2c_1$.

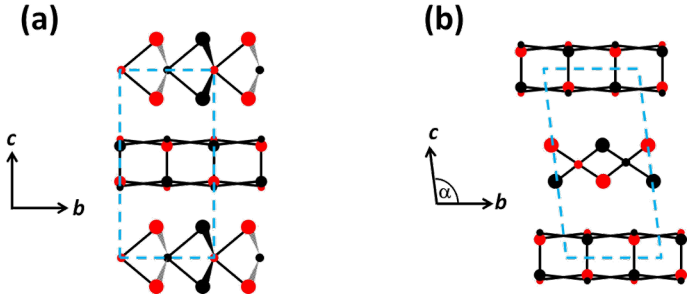

Figure 3: Side view of two unit cells of misfit layer compounds with the TMX_2 component either in trigonal prismatic (a) or octahedral coordination (b). The unit cells are denoted by the blue boxes. Adapted with permission from [3]. Copyright 1995 Elsevier.

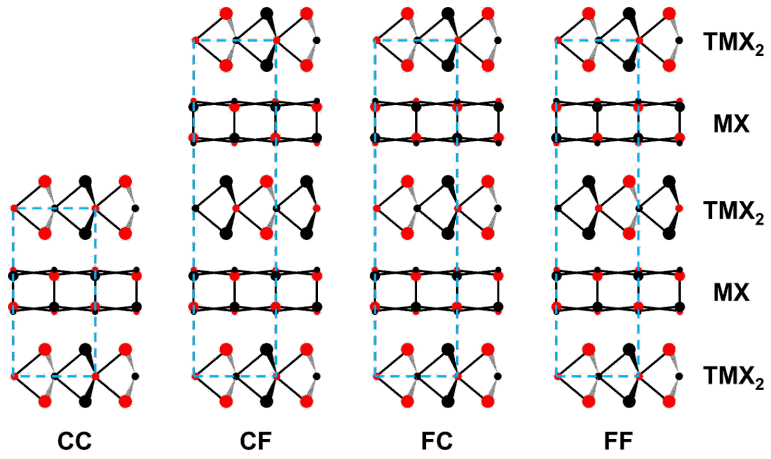

Figure 4: Different possible stacking types of misfit compounds projected along the [100] direction. The blue boxes denote the unit cell and the colored circles represent the metal (small circles) and chalcogenide atoms (large circles), where the different colors represent the different positions in space: black atoms above the paper-plane and red ones beneath it. Adapted with permission from [3]. Copyright 1995 Elsevier.

tion and length) which is the case, for example, in the compound $(SnS)_{1.17}NbS_2$. In the FC system, $c_1 = 2{\cdot}c_2$ as it occurs in, for example, $(YS)_{1.23}NbS_2$, whereas $c_2 = 2{\cdot}c_1$ is seen in CF systems such as $(LaS)_{1.14}NbS_2$. In misfit compounds of the FF type, both $\vec{c}$ vectors have the same direction and norm, but twice the length as the CC type. The structure of $(PbS)_{1.13}TaS_2$ is an example of the latter type.

Non-planar structures

In addition to the previously discussed planar misfit structures, bent systems are common as well [5,6,25-29]. Such tubular or cylindrical misfit layer compounds have been mentioned for the first time in relation to the mineral cylindrite [1,30]. Generally, it is assumed that a misfit in *a* and *b* directions leads to the formation of tubular structures by reason of energy minimizing [6]. The advantage of these structures is the absence of any dangling bonds, which leads to more energetically stable systems compared to the finite planar ones (stripes, flakes, platelets) [31,32]. Hence, the act of bending or rolling can be seen as a relaxation process, although the relative thickness of the tube walls and the rigidity of the interatomic bonds were seen as a steric hindrance. The rolling process has been discussed in relation to the misfit compounds $(PbS)_{1.14}(NbS_2)_2$ [29], $(BiS)_{1.17}(NbS_2)_n$ [33] with n = 1–4 or $(SnS)_{1.32}SnS_2$ [25]. Just as for planar misfit compounds, different stacking types are possible in the bent misfit systems as well regarding the number of sublayers, or rather, the stacking order (as shown in Figure 1), and also regarding the possibility of different structures and orientations of the sublayers, as shown in Figure 3 and Figure 4. For example, several different stacking configurations have been observed for $(SnS)_{1.32}(SnS_2)_n$, such as ABAB, ABBABB, ABABBABABB [6,26]. As in planar misfit systems, the composite has a global super-symmetry that may differ from that of the two subsystems. Due to two different lattice vectors ($\vec{a}$ and $\vec{b}$), multiple in-plane orientations of the sublayers are possible, which leads to different rolling vectors and therefore, to a manifold of chiral nanotubes. However, aside from tubular misfit layer compounds, nanoscrolls and nanoparticles containing sublayers with different lattices were produced [5,6,25,26], which can have the same structural parameters (stacking order, number and orientation of sublayers, etc.) as tubes and planar misfit compounds.

Electronic structure and interlayer bonding

Meerschaut [4] suggests that the properties of misfit layer compounds might be attributed to the properties of the individual compounds or subsystems. For example, the van der Waals gap in TMX_2 systems can be chemically intercalated [34]. A misfit compound can, thus, be viewed as a TMX_2 system intercalated by another layered MX system. As a consequence, the electronic properties of some misfit compounds have been successfully described by a rigid-band formalism. In this description, the electronic bands are taken as immutable characteristics and only the filling is changed depending on the intercalated species.

In addition to theoretical considerations, the electronic structure is discernible by spectroscopy as Ohno [12,35] presented in 1991. By performing X-ray photoelectron and absorption spectroscopy (XPS, XAS) and reflection electron energy loss spectroscopy (REELS), it was revealed that the electronic structure indeed can be well-described by a superposition of bands of individual single layers. From these results it was concluded that a charge transfer from MX to TMX_2 takes place, which is independent from the nature of the metal M (either M^{2+}: Sn, Pb, or M^{3+}: La, Ce, Sm). In that case, MX can be viewed as a donor

and TMX_2 as an acceptor of the transferred electron density. This claim was based on studies of valence band XPS and XAS spectra of the misfit compounds, compared to those of the individual layers, and a spectrum of iron intercalated titanium disulfide ($Fe_{1/3}TiS_2$), which can be interpreted as a true intercalated system. Figure 5 in [35] shows this XAS spectra of the *K* absorption edge of sulfur for the systems TiS_2, PbS, $PbTiS_3$ (=MLC $(PbS)_{1.18}TiS_2$), and $Fe_{1/3}TiS_2$. The shapes of the $PbTiS_3$ and $Fe_{1/3}TiS_2$ spectra are quite similar. From this, charge transfer was concluded, which should result from the filling of the t_{2g} energy levels coming from the titanium d states.

Further studies used a comparable argument for the claim of charge transfer in other misfit layer compounds. One example is the electron transfer from PbSe to $NbSe_2$ in $[(PbSe)_{1.14}]_m(NbS_2)_1$ with m = 1–6 [36]. The electronic structure has been predicted by density functional theory calculations using the generalized gradient approximation. From the overlap of the empty bands in NbS_2 with the filled valence band of PbSe, the authors concluded that "only a small fraction of an electron's charge is transferred per atom" [36]. In Figure 5 the density of states of the electronic bands of PbSe and $NbSe_2$ near the Fermi level are displayed schematically. The overlap of the Se(PbSe) 4p states with the Nb d_{z^2} states can be seen clearly, which is used as an argument for potential charge transfer. Additionally, the dependence on the number of PbSe sublayers in one unit cell of the misfit compound has been investigated (varying m in the sum formula) with the result that the interlayer charge transfer increases with increasing m.

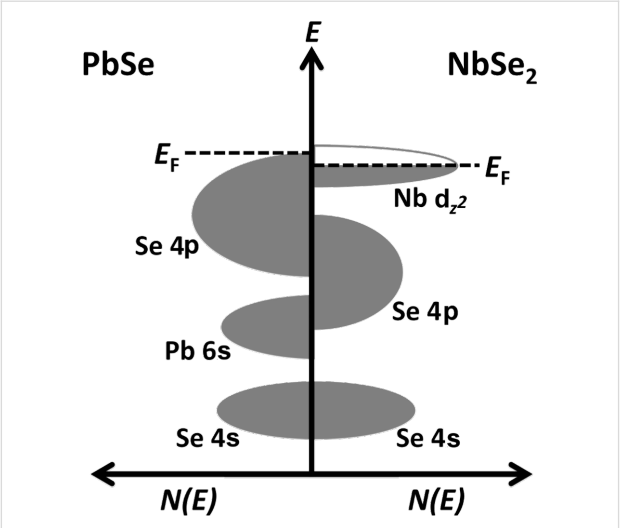

Figure 5: Schematic representation of the density of states of a PbSe layer (left) and a $NbSe_2$ layer (right). The electron transfer takes place from the PbSe valance band to the conduction band of the $NbSe_2$ layer. Adapted with permission from [36]. Copyright 2014 American Chemical Society.

Another theoretical work [37] analysed the band structure of $(SnS)_{1.17}NbS_2$ by using a ratio of $\vec{a}$ vectors of 5:3 resulting in a $(SnS)_{1.20}NbS_2$ stoichiometry. The authors concluded a charge transfer of 0.4 electrons per niobium atom from their calculations. Furthermore, they showed that the Sn 5s orbitals mix strongly with the S 3p orbitals from NbS_2.

Moreover, vibrational spectroscopy has been used to investigate a possible interlayer charge transfer. The Raman spectra of $(SnS)_{1.17}NbS_2$ and $(PbS)_{1.18}TiS_2$ (powdered samples and single crystals) as well as single crystals of $(PbS)_{1.14}NbS_2$ were compared to those of the pure substances and showed a superposition of the interlayer vibrations of the individual layers. Shifts in the NbS_2 modes relative to those in 2H-NbS_2 were interpreted to be a result of charge transfer. These spectra are published in [38,39].

In contrast to the previously shown examples, Ettema and Haas [40] performed XPS measurements for the core states of misfit layer compounds. This work can be seen as an extension of Ohno's work [12,35], which was limited to the valence bands and has been discussed above. They showed that tin and lead are divalent in compounds of the structure $(MX)_{1+y}TMX_2$ due to the fact that the core-level binding energies of these elements do not differ in either the misfit compounds or the isolates systems (SnS, PbS). If a (small) charge transfer took place, the core-level energies of the TM atoms in the TMS_2 sublayer would have stayed nearly constant. Experimentally, this shift in binding energy was not observed for the 2s, 2p, 3s, 3p levels of Ti, the 3s, 3p, 3d, 4s, 4p levels of Nb and the 4p, 4d, 5p, and 4f levels of Ta. From this fact, the authors concluded that there is no significant interlayer charge transfer and the stability of the misfit layer compounds results from covalent bonds between the several sublayers.

Moëlo et al. [41] investigated different misfit systems consisting of Sn and Pb (single-, double- and triple-layer, i.e., m = 1–3) using electron microprobe analysis. Since the M and TM atoms are in oxidation states +2 and +4, respectively, each sublayer should be uncharged and electronically balanced. Hall and Seebeck measurements performed by Auriel et al. [42] showed a highly anisotropic metallic behaviour of misfit layer compounds; some of them even showed a transition to superconductivity at temperatures less than 6 K. A small intrinsic charge transfer could explain such physical properties. However, it is quite improbable that (especially) lead has oxidation states higher than +2 in a Pb–S system. Thus, a charge transfer from Pb (MX) to TMX_2 is unlikely. The concept of cationic coupling assumes an M (e.g., Pb or Sn) deficiency in the MX layer and therefore a TM (e.g., Nb) excess. In fact, some of the M^{2+} cations in the MX sublayer are substituted by

TM^{3+} ions. The excess of positive charge must then be adjusted by reduction of the same amount of TM^{4+} ions in the TMX_2 layer. Thus, the MX sublayer is positively charged and, as a consequence, the TMX_2 layer becomes negative, so that a charge transfer is introduced. The resulting strong, attractive, electrostatic interaction between the two sublayers is the origin of the stability of the misfit compounds within the concept of cationic coupling.

To conclude this section, we will briefly mention the so-called graphite intercalation compounds (GICs) [43] that consist of several graphene layers, which are intercalated by different atoms or fragments, for example, alkali and alkaline earth derivatives or metal halide derivatives. Those components are held together by charge transfer and not every van der Waals gap is intercalated by guest atoms. The systems are called "stage 1 compounds" in the case of an alternating arrangement, and "stage 2 compounds", if every second graphene layer is intercalated, and so on. In contrast to misfit structures, which were the focus of this review, the host molecules and atoms in GICs are intercalated and do not have the same or comparable lattice structure as they have in their bulk phases. For this reason we will not go beyond mentioning GICs here and refer the interested reader to the respective literature.

Examples

SnS–SnS_2 layers and nanotubes

In 2003, inorganic fullerene-like nanoparticles and small nanotubes were synthesized [5]. These structures have spherical or polyhedral shapes and consist of orthorhombic SnS and hexagonal SnS_2 lattices. The two sublattices have the same structure and orientation as the "classical" layered misfit compounds discussed above. Meanwhile, SnS–SnS_2 nanostructures have been further produced, such as nanotubes and nanoscrolls (see Figure 6). These structures have been extensively experimentally and theoretically investigated to date [6,25,26,44]. Selected area electron diffraction (SAED) measurements showed that the interlayer distance between the SnS and SnS_2 substructures is nearly unchanged relative to the bulk structures (error 3%) [26]. For this reason, it is estimated that the sublattice structures in the SnS–SnS_2 system are almost the same as in the pristine bulk material. As a consequence, both in-plane directions are different from one another. The resulting SnS–SnS_2 nanotubes result in the stoichiometries $(SnS)_{1.32}SnS_2$, $(SnS)_{1.32}(SnS_2)_2$ and $[(SnS)_{1.32}]_2(SnS_2)_3$. SAED patterns further show that the SnS_2 subsystems in these misfit tubes have two different rolling directions. This is equivalent to two different SnS_2 chiralities (zig-zag, armchair tubes) in the misfit tube.

A recent theoretical study performed with density functional-based tight-binding calculations investigated a possible charge transfer between the SnS and SnS_2 layers. By comparing the density of states (DOS) for a hypothetical SnS–SnS_2 misfit system with the sum of the DOSs of the two isolated monolayers, the authors showed that additional states arise in the gap region hinting at an electronic interaction between the layers. Furthermore, the atomic charges in the combined system obtained by Mulliken population analysis surprisingly showed that the SnS_2 layer was slightly positively charged, whereas the SnS layer was negatively charged. Although the received charge transfer is quite small (approx. 0.1 electrons per SnS_2 unit) the direction of the electron transfer was perplexing, especially because this direction is unexpected because the Sn^{4+} system transfers electron density to the Sn^{2+} system. The explanation might be that the charge transfer does not take place from metal to metal ($Sn^{2+} \rightarrow Sn^{4+}$), because Sn is not a transition metal, in contrast to the TMX_2 systems discussed above. Thus, the sulfur atoms of the SnS_2 layer could act as donors and Sn^{2+} atoms in the SnS layer as acceptors. Generally, Sn^{2+} can act as an acceptor if a stronger reducer is present. By comparing the standard potentials of the S^{2-}/S and Sn/Sn^{2+} systems, it appears that this explanation is possible and is supported by the fact that in the SnS_2–SnS bilayer, only the SnS_2-sulfur atoms facing the SnS layer become slightly positive (see Figure 5 in [44]).

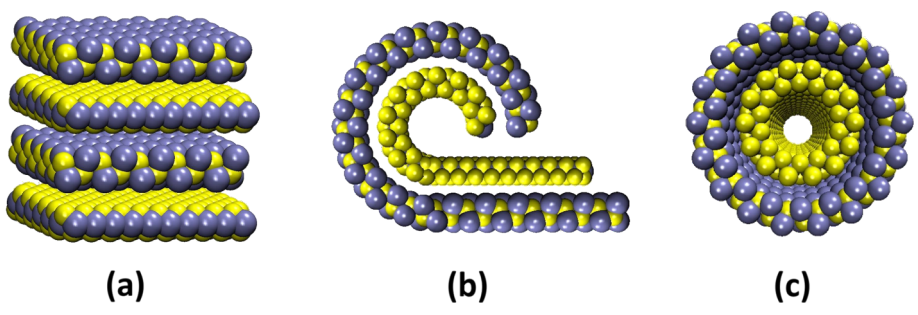

Figure 6: SnS–SnS_2 misfit compounds forming nanoscrolls and nanotubes. Yellow spheres represent sulfur atoms and blue spheres tin atoms.

SiO_x-coated carbon nanotubes

In 2002, carbon–SiO_x-based nanocomposites were synthesized [27,28]. Although these structures differ significantly from the discussed misfit compounds, the two host lattices adjust and the mechanical strain is reduced by a spontaneous bending. Figure 7a shows the two planar sublattices in which the hexagonal carbon structure (graphene) and the six-membered SiO_4 rings align their lattice constants. To minimize the energy, the C–Si-bonded system bends spontaneously (Figure 7b). This relaxation process leads to the formation of tubular structures and Si–O–Si bond angles of 140°. In this system, a real covalent bond between the two subsystems can be observed, which partly changes the hybridization of the carbon atoms from sp^2 to sp^3.

Conclusion

In this review, the structures of misfit layer compounds were discussed. As was illustrated, MLCs consist of two different sublattices with at least one lattice vector of different length in the subsystems. By aligning their lattices, the layers with stoichiometries MX and TMX_2 can be stacked alternating or in more complex sequences connecting to a misfit compound. They can adopt planar or bent structures, and the resulting super-symmetry usually differs from the symmetry of the pristine systems. To date, layers, tubes, nanoparticles, and nanoscrolls formed by misfit layer compounds are known and have been synthesized. In the non-alternating A–B–B–… stacking, the successive layers of the same type are bonded only by van der Waals interaction. This is one reason why it is possible to intercalate metal atoms within this van der Waals gap. Due to the fact that layered materials show exceptional lubricating properties originating in strong intra-layer, but weak inter-layer interactions, lubricating properties can be expected for misfit layer compounds as well.

For the purpose of structure determination, many measurements and experiments have been performed for misfit layer compounds. Furthermore, the determination of their electronic structure has been implemented considerably. From this data, estimations of the bonding behaviour between the sublayers were made. On the one hand, a charge transfer from the MX to the TMX_2 layer is mentioned, on the other hand the concept of cation coupling is discussed, which assumes the substitution of M^{2+} by TM^{3+} cations in the MX layer. This might introduce a charge transfer through the necessity of electroneutrality for the whole system. The presented concepts may explain the stability of the misfit layer compounds and their properties, but further studies are necessary for a comprehensive description of these interesting systems.

Acknowledgements

The authors acknowledge financial support by the European Union via ERC grant INTIF 226639 and Dr. Igor Baburin for fruitful discussions.

References

1. Makovicky, E.; Hyde, B. G. Non-commensurate (misfit) layer structures. In *Inorganic Chemistry;* Mingos, D. M. P., Ed.; Structure and Bonding, Vol. 46; Springer: Berlin, Heidelberg, 1981; pp 101–170.
2. Meerschaut, A., Ed. *Incommensurate Sandwiched Layered Compounds;* Trans Tech: Zürich, 1992.
3. Rouxel, J.; Meerschaut, A.; Wiegers, G. A. *J. Alloys Compd.* **1995,** *229,* 144–157. doi:10.1016/0925-8388(95)01680-5
4. Meerschaut, A. *Curr. Opin. Solid State Mater. Sci.* **1996,** *1,* 250–259. doi:10.1016/S1359-0286(96)80092-1
5. Hong, S. Y.; Popovitz-Biro, R.; Prior, Y.; Tenne, R. *J. Am. Chem. Soc.* **2003,** *125,* 10470–10474. doi:10.1021/ja036057d
6. Radovsky, G.; Popovitz-Biro, R.; Stroppa, D. G.; Houben, L.; Tenne, R. *Acc. Chem. Res.* **2014,** *47,* 406–416. doi:10.1021/ar400138h
7. Smeller, M. M.; Heideman, C. L.; Lin, Q.; Beekman, M.; Anderson, M. D.; Zschack, P.; Anderson, I. M.; Johnson, D. C. *Z. Anorg. Allg. Chem.* **2012,** *638,* 2632–2639. doi:10.1002/zaac.201200408
8. Lin, Q.; Smeller, M.; Heideman, C. L.; Zschack, P.; Koyano, M.; Anderson, M. D.; Kykyneshi, R.; Keszler, D. A.; Anderson, I. M.; Johnson, D. C. *Chem. Mater.* **2010,** *22,* 1002–1009. doi:10.1021/cm901952v

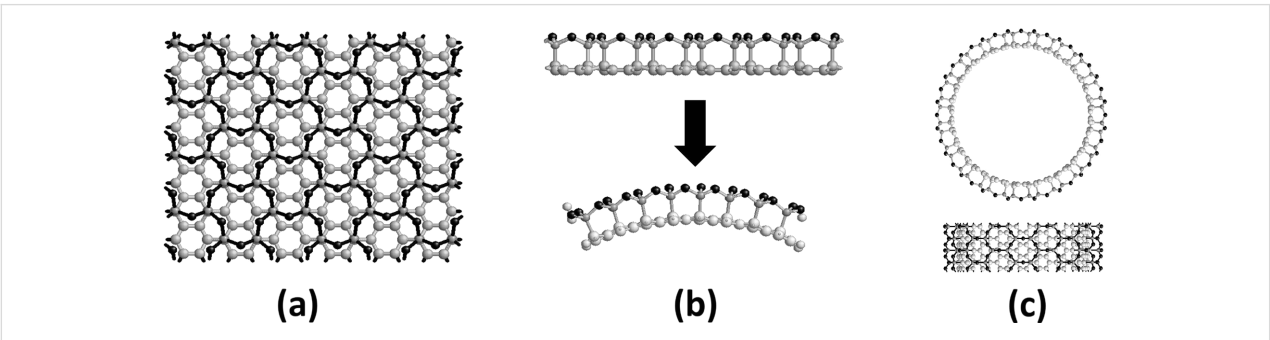

Figure 7: Superposition of the hexagonal carbon lattice and the six-membered SiO_4 rings. (a) Top view, (b) side view with the depiction of the spontaneous bending of the layers and the C–Si bonds and (c) a carbon nanotube is surrounded by a cylindrical SiO_x (x = 5/2) layer. Carbon, oxygen, and silicon atoms are colored in light gray, dark gray, and black, respectively.

9. Moore, D. B.; Beekman, M.; Disch, S.; Johnson, D. C. *Angew. Chem., Int. Ed.* **2014,** *53,* 5672–5675. doi:10.1002/anie.201401022
10. Panchakarla, L. S.; Popovitz-Biro, R.; Houben, L.; Dunin-Borkowski, R. E.; Tenne, R. *Angew. Chem., Int. Ed.* **2014,** *53,* 6920–6924. doi:10.1002/anie.201404189
11. Makovicky, E.; Hyde, B. G. *Mater. Sci. Forum* **1992,** *100–101,* 1–100. doi:10.4028/www.scientific.net/MSF.100-101.1
12. Ohno, Y. *Solid State Commun.* **1991,** *79,* 1081–1084. doi:10.1016/0038-1098(91)90015-N
13. Ren, Y.; Meetsma, A.; Petricek, V.; van Smaalen, S.; Wiegers, G. *Acta Crystallogr., Sect. B: Struct. Sci.* **1995,** *51,* 275–287. doi:10.1107/S0108768194014035
14. Rabu, P.; Meerschaut, A.; Rouxel, J.; Wiegers, G. A. *J. Solid State Chem.* **1990,** *88,* 451–458. doi:10.1016/0022-4596(90)90241-O
15. Wiegers, G. A.; Meetsma, A.; Haange, R. J.; de Boer, J. L. *J. Alloys Compd.* **1992,** *178,* 369–378. doi:10.1016/0925-8388(92)90277-G
16. Van Smaalen, S.; Meetsma, A.; Wiegers, G. A.; de Boer, J. L. *Acta Crystallogr., Sect. B: Struct. Sci.* **1991,** *47,* 314–325. doi:10.1107/S0108768190013477
17. Onoda, M.; Kato, K.; Gotoh, Y.; Oosawa, Y. *Acta Crystallogr., Sect. B: Struct. Sci.* **1990,** *46,* 487–492. doi:10.1107/S0108768190003950
18. Kato, K.; Kawada, I.; Takahashi, T. *Acta Crystallogr., Sect. B: Struct. Crystallogr. Cryst. Chem.* **1977,** *33,* 3437–3443. doi:10.1107/S0567740877011157
19. Wiegers, G. A.; Meetsma, A.; de Boer, J. L.; van Smaalen, S.; Haange, R. J. *J. Phys.: Condens. Matter* **1991,** *3,* 2603–2612. doi:10.1088/0953-8984/3/16/001
20. Wiegers, G. A.; Meetsma, A.; Haange, R. J.; de Boer, J. L. *Mater. Res. Bull.* **1988,** *23,* 1551–1559. doi:10.1016/0025-5408(88)90243-7
21. van Smaalen, S. *J. Phys.: Condens. Matter* **1989,** *1,* 2791–2800. doi:10.1088/0953-8984/1/17/002
22. Meerschaut, A.; Rabu, P.; Rouxel, J.; Monceau, P.; Smontara, A. *Mater. Res. Bull.* **1990,** *25,* 855–861. doi:10.1016/0025-5408(90)90062-7
23. Wiegers, G. A.; Meetsma, A.; Haange, R. J.; van Smaalen, S.; de Boer, J. L.; Meerschaut, A.; Rabu, P.; Rouxel, J. *Acta Crystallogr., Sect. B: Struct. Sci.* **1990,** *46,* 324–332. doi:10.1107/S0108768190001252
24. Bonneau, P.; Mansot, J. L.; Rouxel, J. *Mater. Res. Bull.* **1993,** *28,* 757–766. doi:10.1016/0025-5408(93)90016-7
25. Radovsky, G.; Popovitz-Biro, R.; Staiger, M.; Gartsman, K.; Thomsen, C.; Lorenz, T.; Seifert, G.; Tenne, R. *Angew. Chem., Int. Ed.* **2011,** *50,* 12316–12320. doi:10.1002/anie.201104520
26. Radovsky, G.; Popovitz-Biro, R.; Tenne, R. *Chem. Mater.* **2012,** *24,* 3004–3015. doi:10.1021/cm301491v
27. Grobert, N.; Seeger, T.; Seifert, G.; Rühle, M. *J. Ceram. Process. Res.* **2003,** *4,* 1–5.
28. Seeger, T.; Cöhler, T.; Frauenheim, T.; Grobert, N.; Terrones, M.; Seifert, G.; Rühle, M. *Z. Metallkd.* **2002,** *93,* 455–458. doi:10.3139/146.020455
29. Bernaerts, D.; Amelinckx, S.; Van Tendeloo, G.; Van Landuyt, J. *J. Cryst. Growth* **1997,** *172,* 433–439. doi:10.1016/S0022-0248(96)00747-6
30. Williams, T. B.; Hyde, B. G. *Phys. Chem. Miner.* **1988,** *15,* 521–544. doi:10.1007/BF00311023
31. Seifert, G.; Köhler, T.; Tenne, R. *J. Phys. Chem. B* **2002,** *106,* 2497–2501. doi:10.1021/jp0131323
32. Brüser, V.; Popovitz-Biro, R.; Albu-Yaron, A.; Lorenz, T.; Seifert, G.; Tenne, R.; Zak, A. *Inorganics* **2014,** *2,* 177–190. doi:10.3390/inorganics2020177
33. Gómez-Herrero, A.; Landa-Cánovas, A. R.; Hansen, S.; Otero-Díaz, L. C. *Micron* **2000,** *31,* 587–595. doi:10.1016/S0968-4328(99)00141-9
34. Hernán, L.; Morales, J.; Pattanayak, J.; Tirado, J. L. *J. Solid State Chem.* **1992,** *100,* 262–271. doi:10.1016/0022-4596(92)90100-A
35. Ohno, Y. *Phys. Rev. B* **1991,** *44,* 1281–1291. doi:10.1103/PhysRevB.44.1281
36. Alemayehu, M. B.; Mitchson, G.; Ditto, J.; Hanken, B. E.; Asta, M.; Johnson, D. C. *Chem. Mater.* **2014,** *26,* 1859–1866. doi:10.1021/cm404018a
37. Fang, C. M.; Ettema, A. R. H. F.; Haas, C.; Wiegers, G. A.; van Leuken, H.; de Groot, R. A. *Phys. Rev. B* **1995,** *52,* 2336–2347. doi:10.1103/PhysRevB.52.2336
38. Sourisseau, C.; Cavagnat, R.; Tirado, J. L. *J. Raman Spectrosc.* **1992,** *23,* 647–651. doi:10.1002/jrs.1250231114
39. Hangyo, M.; Nakashima, S.; Hamada, Y.; Nishio, T.; Ohno, Y. *Phys. Rev. B* **1993,** *48,* 11291–11297. doi:10.1103/PhysRevB.48.11291
40. Ettema, A. R. H. F.; Haas, C. *J. Phys.: Condens. Matter* **1993,** *5,* 3817–3826. doi:10.1088/0953-8984/5/23/008
41. Moëlo, Y.; Meerschaut, A.; Rouxel, J.; Auriel, C. *Chem. Mater.* **1995,** *7,* 1759–1771. doi:10.1021/cm00058a003
42. Auriel, C.; Meerschaut, A.; Deudon, C.; Wiegers, G. A.; Baas, J.; Chen, J.; Monceau, P. *Eur. J. Solid State Inorg. Chem.* **1995,** *32,* 947–962.
43. Rüdorff, W. *Adv. Inorg. Chem. Radiochem.* **1959,** *1,* 223–266.
44. Lorenz, T.; Joswig, J.-O.; Seifert, G. *Semicond. Sci. Technol.* **2014,** *29,* 064006. doi:10.1088/0268-1242/29/6/064006

License and Terms

This is an Open Access article under the terms of the Creative Commons Attribution License (http://creativecommons.org/licenses/by/2.0), which permits unrestricted use, distribution, and reproduction in any medium, provided the original work is properly cited.

The license is subject to the *Beilstein Journal of Nanotechnology* terms and conditions: (http://www.beilstein-journals.org/bjnano)

The definitive version of this article is the electronic one which can be found at: doi:10.3762/bjnano.5.226

BEILSTEIN JOURNAL OF NANOTECHNOLOGY

Advances in NO_2 sensing with individual single-walled carbon nanotube transistors

Kiran Chikkadi*, Matthias Muoth, Cosmin Roman, Miroslav Haluska and Christofer Hierold

Review

Open Access

Address:
Micro and Nanosystems, Department of Mechanical and Process Engineering, ETH Zurich, Switzerland

Email:
Kiran Chikkadi* - kiranc@ethz.ch

* Corresponding author

Keywords:
carbon nanotube field-effect transistors (CNFETs); cross-sensitivity; functionalization; gas sensors; hysteresis; low power; selectivity; self-heating; single walled carbon nanotubes

Beilstein J. Nanotechnol. **2014,** *5,* 2179–2191.
doi:10.3762/bjnano.5.227

Received: 08 July 2014
Accepted: 29 October 2014
Published: 20 November 2014

This article is part of the Thematic Series "Atomic scale interface design and characterisation: Theory – Structure and dynamics".

Guest Editor: C. Ewels

© 2014 Chikkadi et al; licensee Beilstein-Institut.
License and terms: see end of document.

Abstract

The charge carrier transport in carbon nanotubes is highly sensitive to certain molecules attached to their surface. This property has generated interest for their application in sensing gases, chemicals and biomolecules. With over a decade of research, a clearer picture of the interactions between the carbon nanotube and its surroundings has been achieved. In this review, we intend to summarize the current knowledge on this topic, focusing not only on the effect of adsorbates but also the effect of dielectric charge traps on the electrical transport in single-walled carbon nanotube transistors that are to be used in sensing applications. Recently, contact-passivated, open-channel individual single-walled carbon nanotube field-effect transistors have been shown to be operational at room temperature with ultra-low power consumption. Sensor recovery within minutes through UV illumination or self-heating has been shown. Improvements in fabrication processes aimed at reducing the impact of charge traps have reduced the hysteresis, drift and low-frequency noise in carbon nanotube transistors. While open challenges such as large-scale fabrication, selectivity tuning and noise reduction still remain, these results demonstrate considerable progress in transforming the promise of carbon nanotube properties into functional ultra-low power, highly sensitive gas sensors.

Introduction

New materials often generate entirely new possibilities, pushing the limits of the accepted boundaries of material properties within which engineers operate. The identification of carbon nanotubes (CNTs) [1-4] and later, single-walled nanotubes (SWNTs) [5,6] is one example of this phenomenon. One such exciting prospect for carbon nanotubes is in the field of chemical sensing. First reports of the sensitivity of the electrical characteristics of carbon nanotubes to adsorbed gases were reported by Kong et al. [7] and Collins et al. [8] in 2000. Kong et al. showed that gases such as NO_2 and NH_3 caused a large shift of

the threshold voltage in carbon nanotube field-effect transistors (CNFETs). SWNTs possess several properties that make them attractive candidates for gas sensors. They have all their atoms on the surface, endowing them with the highest specific surface area possible together with graphene. Therefore, all the carbon atoms in the nanotube can, in principle, interact with the analyte gas, while simultaneously supporting charge transport in the device. Thus, adsorbates and electrostatic charges and dipoles close to the nanotube can greatly impact charge transport. At the same time, the carbon nanotube lattice is held together by strong sp^2 C–C bonds, which provide the necessary chemical stability to the carbon nanotube.

The sensitivity of SWNTs towards NO_2 at ambient temperatures, as reported by Kong et al. [7] is particularly interesting. NO_2 is a well-known toxic gas and air pollutant and monitoring its concentration is crucial for applications such as air quality monitoring. Leveraging the NO_2 sensitivity of carbon nanotubes to build highly sensitive, low-power gas sensors is therefore not only of academic, but also of great commercial interest. As such, we will focus on the NO_2-SWNT system, as it is one of the most extensively discussed in literature.

Several device architectures have been used for fabricating NO_2 sensors by using carbon nanotubes – as individual elements in the transistor channel [7,9-11], as low density networks [12-15] or as forests [16]. SWNT networks and forests have been shown to be effective for gas sensing, and can be fabricated efficiently on a large scale at low cost. However, the sensing behavior of nanotube networks is very complex due to the large variety of available adsorption sites, the presence of grooves and junctions between nanotubes, photoresist and other processing residues, interfaces with the substrate and tube-metal junctions. Their role in carrier transport and their response to analyte exposure can be diverse and difficult to reproduce. To circumvent this difficulty, empirical or phenomenological models are typically employed to evaluate the gas sensor response in SWNT network sensors. Furthermore, there is recent evidence that the electronic nature of the nanotubes (semiconducting or metallic) and the fabrication processes typically used to fabricate these devices play a substantial role in device performance [17] and the ensuing sensor response [18]. Thus, the behavior of a random ensemble of unsorted nanotubes cannot be used to elucidate the interactions between the analyte molecules and the surface of the nanotube without the interference of the aforementioned effects. Individual SWNT sensors, on the other hand, have a much simpler structure which eases understanding and reproducibility.

One concern for NO_2 sensing with carbon nanotubes is the selectivity of nanotubes to NO_2, i.e., their ability to distinguish NO_2 in the presence of other interfering analytes. For individual, pristine single-walled carbon nanotubes, calculations and experiments have shown that the interactions with other gases present in the atmosphere, such as N_2, H_2, CO, H_2O and CO_2 are negligible [19]. However, nanotubes are sensitive to other interfering pollutants, such as SO_2 [20], NH_3 [12] and O_3 [21]. Therefore, the task of enhancing the selectivity of SWNT sensors to NO_2 must also be considered. Employing arrays of such individual SWNT sensors may be a viable option for enhancing the selectivity, sensitivity and robustness of SWNT gas sensor products.

In this review, we will focus on individual nanotube gas sensors and collate the theoretical and experimental achievements of the past few years in understanding the interaction of individual, single-walled carbon nanotubes with their environment. First, a summary of the effects of adsorbate molecules on electronic transport is presented, after which the effect of nearby charges and dipoles on the nanotube carrier transport, which constitutes the major challenge for the stability, resolution and drift of these sensors, is discussed. The list of cited works is by no means exhaustive, but we attempt to highlight the pioneering reports showing relevant information to individual single-walled carbon nanotubes for NO_2 sensing.

Review

Individual-nanotube transistors for gas sensing

The typical individual-SWNT gas sensor is a 3-terminal device, in which the nanotube is contacted by a source and a drain electrode and a current flowing through it is measured. Depending on the work function difference between the metal and the nanotube, a Schottky barrier is commonly formed at both contacts. The channel conductivity is controlled by a gate electrode that is separated from the nanotube channel by a gate dielectric. In Schottky barrier field-effect transistors, the effect of the gate voltage is to change the width of the Schottky barrier, which controls the current through the device. Carbon nanotube transistors often operate as Schottky-barrier field-effect transistors because the back-gated architecture that is typically employed for CNFET gas sensors covers the entire channel and overlaps the source and drain contacts. Top-gate architectures, which have a closer resemblance to CMOS architectures, are less common for gas sensors due to the need for an exposed channel. Side-gate configurations are not typically used due to their poor gate coupling. Variants of this basic architecture, with suspended or on-substrate tubes, and passivated or unpassivated contacts have been reported (Figure 1).

The conductivity of a CNFET can be influenced by surface adsorbates. In particular, the adsorption of electron-with-

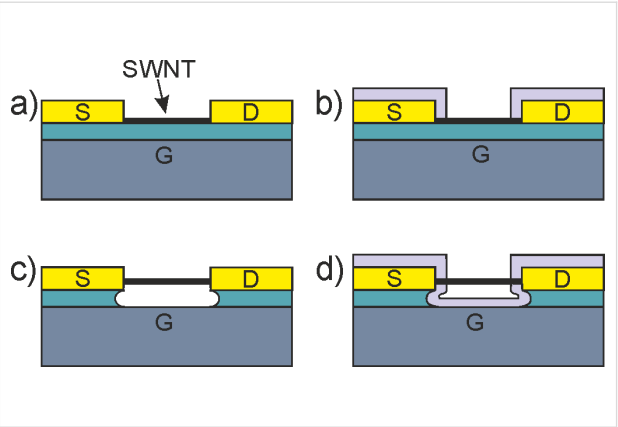

Figure 1: Examples of different back-gated device architectures employed for carbon nanotube field-effect transistor gas sensors. a) On-substrate, unpassivated devices, where the entire device is exposed to the analyte. The substrate acts as the back gate, and the nanotube lies on a dielectric which is deposited on top of this electrode [7,14]. b) Contact-passivated CNFETs. In these devices, only the carbon nanotube is exposed to the gas, while the contacts are passivated against a gas exposure. Passivation layers may include polymers [22] or oxides [9,10]. c) Suspended, unpassivated devices. In this case, the SWNT can be released after fabrication [23,24] the SWNT is either placed [25] or grown [26-28] onto prefabricated electrodes. d) Contact-passivated, suspended-SWNT transistors that are fabricated either through post-fabrication release [29] or using selective film nucleation [30].

drawing gases, such as NO_2, or electron-donating gases such as NH_3 can influence the electron transport in the devices by changing the transfer characteristics. However, the devices also react strongly to charges in their vicinity, which leads to problems such as hysteresis and noise. We will examine these effects in detail in the next sections.

Effect of adsorbate gases

The sensitivity of carbon nanotube devices to adsorbate gases was reported in 2000 by two groups. Collins et al. [8] showed that carbon nanotube mats contacted by metal showed oxygen sensitivity, while Kong et al. [7] showed the sensitivity of individual CNFETs to NO_2 and NH_3, and discussed the possible mechanisms behind the device response. They reported that the CNFET responded to gas exposure by showing a large shift of the transfer (I_d–V_g) characteristics, with the direction of the shift dependent on the gas type.

The remarkable feature of the observations by Kong et al. [7] is that the nanotubes were sensitive to gases at ambient temperature. Most solid-state semiconducting gas sensors that operate as chem-FETs require elevated temperatures for operation. Heating is an energy-expensive operation, due to which their application in large numbers or in sensor network nodes is challenging. Carbon nanotubes also appeared to be highly sensitive even without optimization, hinting at their promise for NO_2 detection.

Several studies, both experimental and theoretical, have been conducted to understand the effect of gas molecules on carbon nanotube devices. Understanding the effect of gases on the CNFET electrical transport is crucial to sensor design and architecture. For a CNFET to be sensitive to a certain gas, the gas molecules must be able to interact and bind to the device surface and produce a change in the electrical transport of the device. A lively debate is prevalent in literature about the sensing mechanisms involved, and both contact-related and channel-related mechanisms have been suggested. For the sake of discussion it is convenient to distinguish the effect of gas adsorption on the two different regions: the contact metal surface and the nanotube surface. In the next few paragraphs, the different sensing mechanisms which may be present in a CNFET sensor are discussed in detail.

Adsorption on the metal

The work function of a metal is known to be sensitive to the adsorption of gaseous surface species. Methods such as Kelvin probe [31], scanning tunneling spectroscopy, X-ray and ultraviolet photoelectron spectroscopy [32] (XPS and UPS) have been used to understand the mechanism of this work function change. For polar molecules such as NO_2, a dipole layer is expected to be formed at the surface of the metal, thereby modifying the metal work function [33,34]. In Schottky barrier CNFETs, a change of metal work function means a net change in the metal–nanotube work function difference, which in turn determines the height of the Schottky barrier. For carbon nanotube gas sensors, any sensor response associated with on-metal adsorption is therefore related to a change in the height of the carrier injection barrier at the contacts. As an example, consider the case of a device that has dominant n-type conductivity, i.e., the electron Schottky barrier is smaller than the hole Schottky barrier. The adsorption of NO_2 can lead to an increase of the metal work function (and thereby an increase in the Schottky barrier height for electrons), leading to a lower current in the n-branch and an increase in the p-branch [35].

On the other hand, a work function change for devices with ohmic contacts will depend on magnitude and direction of the change. For example, if the work function change induces a Schottky barrier in the device (i.e., the device becomes non-ohmic), it could lead to a visible change in the transfer characteristics, resulting in a sensor response. However, if the result of work function change is to turn the Schottky barrier more negative within the same n-type device thought experiment, then no sensor response is expected.

Sensor response of devices with unpassivated contacts tend to be a tilt of the transfer characteristics (visible in the linear part of the curve) as well as a shift of the threshold voltage; this is

often attributed to the effect of adsorption on both the metal (leading to a Schottky barrier change) as well as the nanotube channel (leading to doping) [35], as shown in Figure 2. This is because the devices are unpassivated, and gas adsorption could occur on both the nanotube and the metal surfaces. So far, there have been no successful attempts at measuring the effect of on-metal adsorption separately, due to the fabrication challenges involved in completely passivating the nanotube alone, while leaving the metal unpassivated.

Adsorption on the nanotube

The nature of interaction between NO_2 and the nanotube is heavily debated, and the current understanding of the NO_2–nanotube interaction is far from complete. A brief review of the reports so far will be made before further discussing their effects on the electrical characteristics of the CNFET.

Several experimental reports have shown that the undisturbed recovery time of a nanotube sensor after exposure to NO_2 is in the range of several hours [12,30,37,38]. This alone suggests that the desorption barrier for NO_2 on the nanotube is relatively high – of the order of −1 eV. However, many theoretical calculations (see Figure 3) contend that pure NO_2 adsorption is physisorption [19,39-43]. Although the first calculations [39,40] suggested a charge transfer upon physisorption, Santucci et al. [43] showed that this charge transfer disappeared when spin-polarized treatment was used in the calculations. Yim et al. [44] have suggested that a pairwise chemisorption of NO_2 molecules is more favorable than the chemisorption of individual molecules, but the energy of interaction they report is far lower than the observed experimental results as well as theoretical calculations in other reports [41,45].

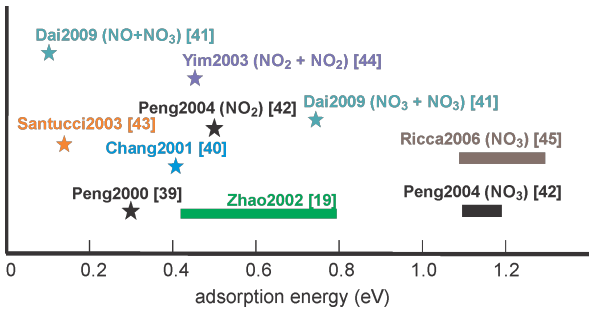

Figure 3: Theoretically calculated adsorption energies for various NO_x–CNT systems. The calculations show widely varying interactions for the systems, which may be partly explained due to the different simulation methods used as well as the different chiralities for the SWNTs.

Another possibility is dissociative adsorption of NO_2. Goldoni et al. [46-48] performed photoemission spectroscopy measurements of NO_2 adsorption on purified SWNTs. Their data showed indications suggestive of the formation of NO_3 and NO on the surface of the nanotube. This is in agreement with the calculations of Peng et al. [42] who reported a strong binding energy for NO_3 on the nanotube. However, it has since been pointed out that the methods used in this paper tend to overestimate the binding energy [41,45] and charge transfer. Dai et al. [41] found that chemisorption of two NO_3 molecules, on the other hand, is found to be favorable, with an adsorption energy (for two molecules) between −1.4 and 1.9 eV. On the other hand, the results from Ellison et al. [49] by using temperature-programmed desorption (TPD) and Fourier-transform infrared (FTIR) spectroscopy disagree with this suggestion, as they found no evidence for chemisorption. In addition, these studies

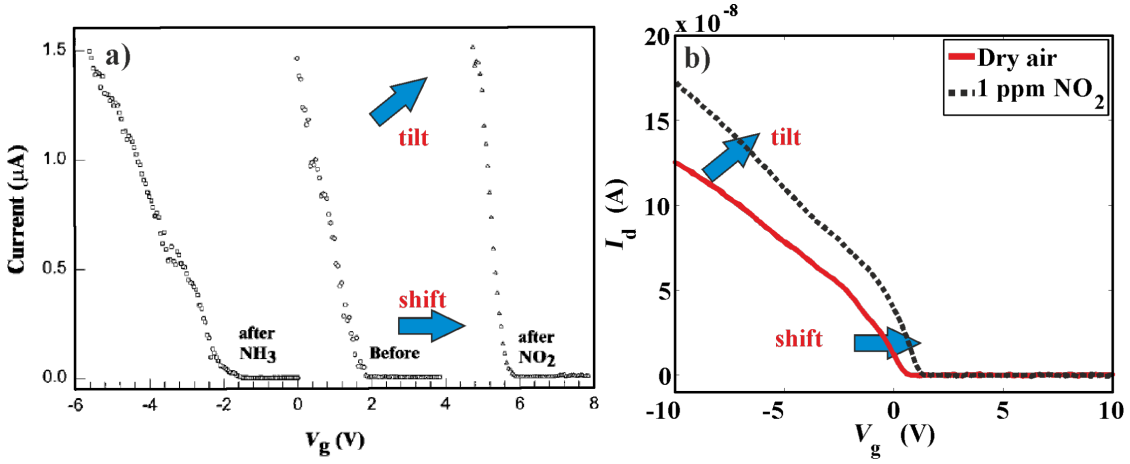

Figure 2: Effects of NO_2 adsorption on unpassivated nanotube transistors. a) Measurements from Kong et al. [7] show a shift and a tilt of the characteristics, as shown above. In their case, the Ni–Au contacts are likely to have Schottky barriers, due to which the effects may be due to both on-tube and on-metal adsorption. Adapted with permission from [7]. Copyright 2000 American Academy for the Advancement of Sciences. b) The authors have also observed similar effects in [36] for Pd-contacted nanotubes. Adapted with permission from [36]. Copyright 2014 Elsevier.

also suggest a strong dependence of binding energy on the nanotube curvature, but a systematic experimental investigation of this dependence has not yet been performed.

There are also suggestions that the presence of an electric field or charges on the nanotube may have a strong influence on the binding energy and charge transfer of NO_2 [50]. Although there have not been any direct studies with NO_2, Chen et al. [51] calculated the binding energy of water molecules on an SWNT surface and found that it increased from 0.03 eV at zero electric field to 0.6 eV at an electric field of 0.33 V/Å. For comparison, the electric field from the gate in the vicinity of the nanotube in typical CNFET gas sensors can be around 0.1 V/Å [7,52]. As such, the effect of an electric field on the binding energy of NO_2 on a SWNT remains poorly understood.

A further possibility is that interfaces between the nanotube and the substrate provide more favorable sites for adsorption, where the NO_2 molecules may have a higher binding energy. However, suspended nanotubes have also been shown to be sensitive to NO_2 [30,53], and the recovery time even in the absence of a substrate appears to be comparable. This suggests that the nanotube is capable of responding to NO_2 without the assistance of a substrate.

More recently, evidence has emerged on the possible role of the electronic nature of the nanotube (metallic or semiconducting) in the response of carbon nanotube gas sensors. Ruiz-Soria et al. [18] investigated the NO_2–SWNT system by utilizing metallicity-sorted, ultrapure carbon nanotubes. They used X-ray photoelectron spectroscopy (XPS) and X-ray absorption spectroscopy (XAS) to investigate the nature of bonding and chemical interaction. Their conclusions, supported by theoretical calculations, are that the process is a charge transfer mediated physisorption. In their studies, both semiconducting and metallic nanotubes showed evidence of NO_2 physisorption, but the interaction energy was twice as high (as indicated by the C–N peak intensity ratios in their spectroscopic measurements) for metallic nanotubes compared to semiconducting nanotubes. They also found very little NO_3 and NO formation in their measurements, suggesting that these mechanisms may not be dominant. However, their experiments were based on spectroscopic measurements at low temperature, and they performed no direct electrical measurements, due to which the implications of their conclusions to FET-type devices is not yet completely clear.

In recent studies, we have shown that a single, suspended nanotube with passivated contacts is sensitive to NO_2 [30], as shown in Figure 4. On the other hand, a fully-passivated device does not respond to gas exposure. This excludes other possibilities such as substrate-assisted adsorption and response from the contacts suggesting that the nanotube itself is indeed sensitive even in the absence of other contributing mechanisms. Furthermore, the long recovery time is observed here as well, suggesting a high desorption barrier for the tube–NO_2 interaction.

The effect of adsorption on the nanotube on the transistor characteristics can also depend on the device architecture and contact type. Bradley et al. [10] discuss a similar response in contact-passivated CNFETs for NH_3 sensors, but indicate that this may be related to the screening length in their short-channel FETs. Similar observations are made by Mattmann et al. [9]. On the other hand, Zhang et al. [22] discuss the response of polymer-passivated long-channel FETs which also show an

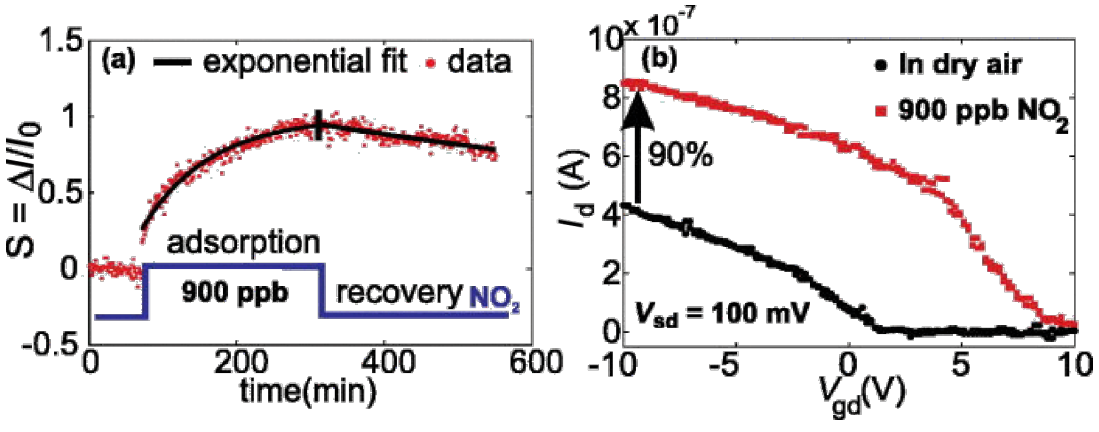

Figure 4: Response of contact-passivated, pristine suspended carbon nanotube gas sensors. a) Transient response of the sensor to an NO_2 step. The exponential fits to the data are shown. The recovery time is in excess of 12 h, which corresponds to an equivalent desorption barrier of −1.01 eV. b) Transfer characteristics recorded for the same experiment as (a). The black circles were recorded just before the NO_2 entered the chamber, while the red circles were recorded just before the NO_2 step ended. Reproduced with permission from [30]. Copyright 2013 AIP Publishing LLC.

apparent shift of the characteristics. They suggest that the response of the CNFETs to gas can be attributed not to channel doping, but to a change in the Schottky barrier. They further account for the gas diffusion through the polymer membranes and argue that the long response times in their contact-passivated devices are related to the time constants associated with this diffusion, while the unpassivated devices exhibit a faster response. These arguments further suggest that adsorption on the nanotube could indeed generate different responses depending on the contact type. In a Schottky barrier CNFET, if the adsorption on the nanotube close to the barrier changes the screening length, the result on the transfer characteristics could be similar to that produced by a change in the metal work function (the Schottky barrier width changes instead of the height). Adsorption in the bulk of the nanotube causing a doping effect could produce no measurable response in Schottky barrier FETs, as the device conductance is not limited by the channel. On the other hand, in ohmic or near-ohmic contact nanotubes with extremely thin Schottky barriers (e.g., Pd-contacted nanotubes), the modulation of the conductance of the bulk channel could have a more profound effect. This is consistent with the observations made by the authors on Pd-contacted, contact-passivated carbon nanotube transistors [30]. Nevertheless, more detailed experiments on long-channel, ohmic transistors would be necessary to further clarify this question.

Thus, the apparent contradictions and the multitude of sensing mechanisms proposed in literature is a strong indication that the actual sensing mechanism predominant in a device depends not only on the number, quality (i.e., defects [54-56]) and the dimensions of the nanotubes used but also on the device architecture, contact type (Schottky or ohmic), the fabrication process and contact materials. In general, the desorption energies for NO_2 adsorbed on the metal contacts, defect sites and other interfaces are higher than the interaction between NO_2 and the nanotube. For low recovery times, therefore, exploiting the NO_2–SWNT interaction alone, while suppressing other interactions, may be beneficial. In this respect, suspended, contact-passivated devices show great potential.

Effect of surface functionalization

So far, there have been very few investigations on individual, functionalized SWNTs for NO_2 sensing. Covalent functionalization on individual SWNTs, in particular, is very challenging because any covalent bonding tends to drastically reduce the conductivity of the SWNT channel by disrupting the sp^2-C network. Consequently, the conductivity of a single nanotube decreases substantially upon covalent functionalization, making it very challenging to measure its sensor response. Furthermore, fabricating single-tube devices is far more challenging as the yields are lower compared to devices with mats or networks of tubes. As a result, most investigations on functionalized nanotubes involve networks [14,15,37] or forests of nanotubes [16,57].

Non-covalent functionalization, such as metal or polymer functionalization, has been extensively studied. For example, Penza et al. [16] have shown that the sensitivity of multiwalled nanotubes to NO_2 is enhanced by the use of Pt nanoparticles. However, a comparable study on individual SWNT FETs, for which the mechanisms may be different, is not available. On the other hand, polyethyleneimine (PEI) functionalization for NO_2 sensing has been shown to dramatically enhance the response of SWNT sensors [14]. There, the authors argue that the main mechanism of sensitivity enhancement is the increased sticking coefficient (by two orders of magnitude) compared to pristine nanotube devices that were also reported by the same group elsewhere [42]. This has the effect of increasing the sensitivity of the nanotube–PEI composite which makes it sensitive to NO_2 concentrations as low as 100 parts per trillion (ppt). As a comparison, the lowest measured detection limit for unfunctionalized individual SWNTs for NO_2 is about 5 ppb [13]. Therefore, it may be of further interest to investigate functional groups to enhance the sensitivity of individual carbon nanotube devices to NO_2.

Gate hysteresis

Carbon nanotube transistors are well-known for their sensitivity to the charges in their environment. Several detailed investigations have shown that gate hysteresis is an important problem for the stability of the readout in carbon nanotube transistors and gas sensors based on them. When a bi-directional gate sweep is performed, it is often observed that the forward and reverse sweeps are not concurrent, and the measured effect can often be over 50% of the gate sweep range. For gas sensors, this effect can be problematic due to the instability of the device current that arises from the drift and fluctuations associated with this hysteresis. For instance, a device biased at a constant gate voltage often drifts in time, thereby interfering with the gas sensitivity of the sensor.

The source of the hysteresis is attributed to several mechanisms, depending on the device architecture. Kim et al. [58] discuss the effect of water adsorption on substrate-bound carbon nanotube devices, lying on SiO_2 substrates (Figure 5a and Figure 5b). Due to the hydrophilic surface chemistry of SiO_2, a thin water layer is present close to the nanotube. These water molecules then act as charge traps that screen the gate voltage and create a field-dependent hysteresis in the transfer characteristics. They further show that annealing in vacuum followed by passivation can drastically reduce the amount of hysteresis, due to the removal of the water species. Franklin et al. [59] have recently

shown that passivating the substrate with HMDS is highly effective in reducing hysteresis. In their work, the hysteresis decreases gradually with passivation duration, achieving complete passivation after 24 h and reducing the hysteresis by 83% (Figure 5c and Figure 5d). From these studies, the contribution of water to hysteresis appears to be substantial when present in combination with a hydrophilic substrate.

Other investigations [9,60] showed that even with vacuum annealing and passivation with Al_2O_3, although the hysteresis decreases, it does not completely disappear. This suggests other mechanisms at play, such as charge trapping in the oxide and the dielectrics surrounding the nanotube. Robert-Peillard et al. [61] developed a model to qualitatively describe this phenomenon by using Fowler–Nordheim-type behavior for charge trapping by tunneling through the oxide layer. Although this model qualitatively describes the behavior of such devices, it is currently unclear if it reflects the underlying physics of gate hysteresis. More recent investigations have discussed gate hysteresis by using the Schottky–Reed–Hall framework [62].

Several methods to minimize hysteresis have been proposed. For unpassivated devices, methods suggested previously, such as exposure to HMDS or other hydrophobic coatings, as well as vacuum annealing are known to reduce hysteresis. Alternatively, Lin et al. [63] showed that by performing gate sweeps in the form of short pulses instead of quasi-static sweeps, hysteresis could be reduced. By pulsing the gate voltage, the duration in which trapping can occur is reduced, and the charges have time to de-trap in the time between gate pulses, thereby reducing the induced screening. Building on this idea, Mattmann et al. [64,65] showed that by applying alternating gate pulses, i.e, every positive gate pulse is followed by a negative gate pulse, hysteresis could be completely suppressed, as

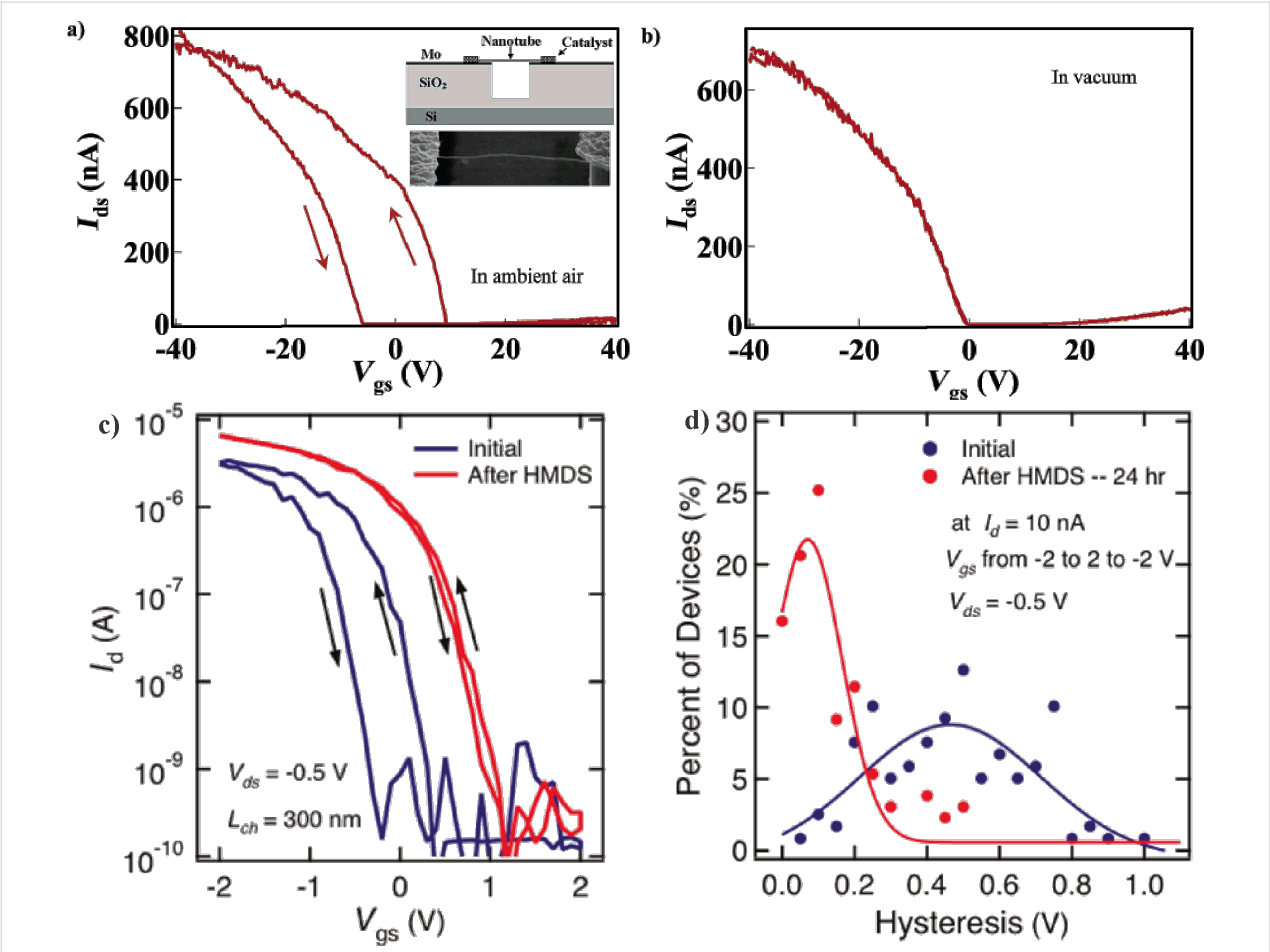

Figure 5: Hysteretic effects in carbon nanotubes lying on a substrate, as shown by Kim et al. [58] (a, b): a) A CNFET partially suspended on SiO_2, showing hysteresis in ambient air. b) The same device after annealing in vacuum, thereby eliminating the water molecules on the substrate. Reproduced with permission from [58]. Copyright 2013 American Chemical Society. Suppression of hysteresis by surface treatment with an HMDS layer, as shown by Franklin et al. [59] (c, d): c) Transfer characteristics of devices on a substrate, before and after HMDS treatment. d) After 24 h treatment with HMDS, the hysteresis nearly vanishes, as visible from the histograms of the hysteresis width. Reproduced with permission from [59]. Copyright 2012 American Chemical Society.

the charges trapped in the positive pulse were immediately de-trapped in the subsequent negative gate pulse (see Figure 6). Nonetheless, pulsed measurement schemes are complex and challenging to implement in sensor readout electronics.

If charge trapping in the nanotube surroundings is the primary cause of hysteresis, eliminating these sources, for example by using a protective layer to avoid resist contamination on the SWNT, could be effective in reducing hysteresis [17,66]. By using a protective layer that can later be removed selectively, it is possible to improve the contact resistance as well as reduce the hysteresis simultaneously, as shown by Khamis et al. [66] with organic layers, and Liu et al. [17] with an aluminium oxide layer.

Another possibility is to eliminate dielectrics altogether, for example by suspending the nanotube, while simultaneously keeping the SWNT surface contamination-free [28]. Initial reports on suspended nanotube devices which were fabricated through top-down lithography followed by release failed to show this behavior, as substantial hysteresis was still present in such devices. However, further work showed that preventing resist residues and wet chemical processing was just as important, as common fabrication process steps created undesirable surface modifications on the SWNT. Reports [26,67] have shown that suspending the nanotube often results in a reduction of hysteresis. Furthermore, Muoth et al. [25,28,68] have shown that in the absence of wet chemical processing, dielectrics or resist residues on the nanotube, hysteresis completely disappears even in ambient air (see Figure 7), further suggesting that the water-related hysteresis mechanisms observed in previous studies are present only when the nanotube is in contact with a substrate such as SiO_2.

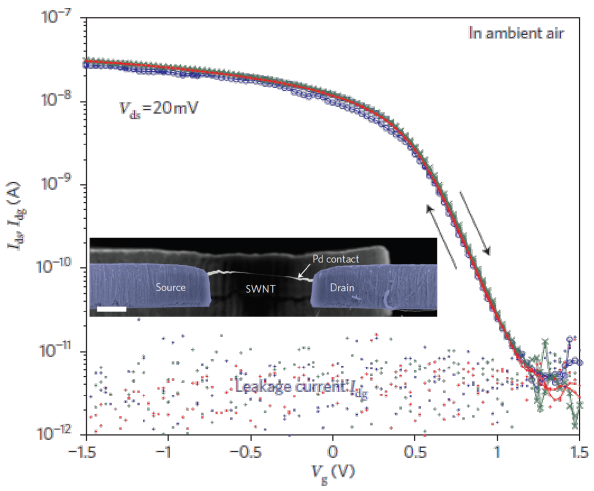

Figure 7: Hysteresis-free transistors using ultraclean, suspended carbon nanotubes. Gate sweeps for a suspended transistor fabricated using on-chip shadow-masking and ultraclean nanotubes shows no measurable hysteresis even in humid air. Reproduced with permission from [28]. Copyright 2010 Macmillan Publishers Ltd.

Drift and low-frequency noise

Drift of a sensor may have several origins, related to the ageing of the device, changes in materials properties over time, or ultra-low frequency noise. For example, if a substrate-bound CNFET sensor is measured under constant bias, the signal tends to drift monotonically over several hours due to the continuous accumulation of charges in the vicinity of the nanotube. In this respect, this source of drift is closely related to the hysteresis in the device, since they have common origins in charge trapping in the vicinity of the nanotube. This effect could be minimized by using suspended device architectures, as the authors have

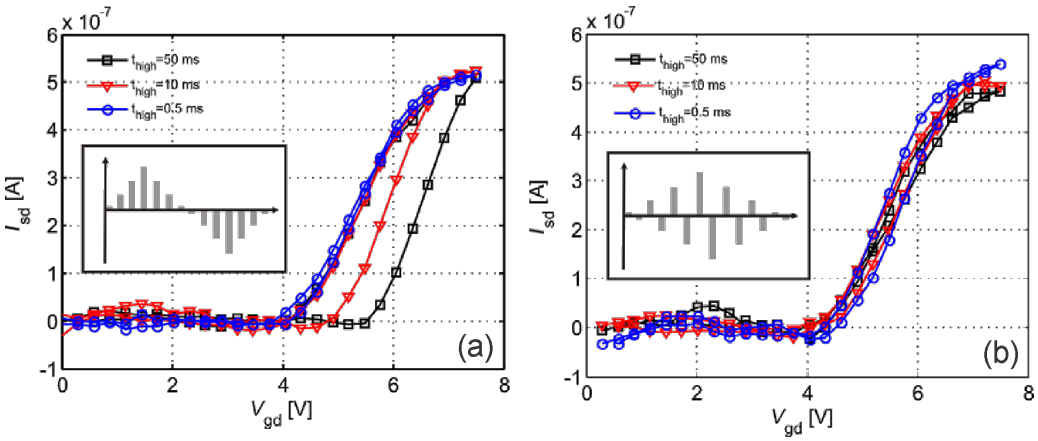

Figure 6: Pulsed gate sweep strategies to eliminate hysteresis in CNFETs [64]. a) Pulsed (p++) gate sweeps show a gradual decrease in the hysteresis width depending on the pulse duration. b) Pulsed (p+-) sweeps with alternating positive and negative pulses show an effective suppression of hysteresis even at high pulse widths. Reproduced with permission from [64]. Copyright 2010 AIP Publishing LLC.

shown in [36]. Comparing a suspended, ultra-clean carbon nanotube transistor and a substrate-bound sensor (Figure 8), we see that the drift is strongly suppressed in the suspended transistor, due to the absence of charge traps in the vicinity.

Another closely-related aspect is the current fluctuation that is observed over very long periods of time, which can also contribute towards sensor drift. This ultra-low frequency noise in CNFETs has a 1/*f* power spectral density. In the range of a few Hz to a few μHz, where sensor readout is commonly performed, this noise can be a significant roadblock to sensor performance. Collins et al. [69] first reported the presence of significant 1/*f* noise in carbon nanotube nanodevices. In 2006, Lin et al. [70] studied the gate–voltage dependence of this noise, which was later explained by Tersoff [71] by introducing the so-called charge-noise model. According to this model, the injection of charges into traps near the Schottky barrier can lead to changes in the width of the barrier, which is then manifested as a change in the current through the transistor that is determined by the local gate potential. As an extension, the model contains another term to model 1/*f*-fluctuations that do not depend on the gate voltage. The noise amplitude A is then modeled dependent on gate voltage V_g and drain current I_d as:

$$A = \left(\gamma_g S_g\right)^2 \left(\frac{d \ln I_d}{dV_g}^2 \right) + \alpha_c I_d^2 \,. \qquad (1)$$

Here γ_g is related to the oxide quality and is influenced by the charge traps available around the nanotube, S_g is proportional to the subthreshold slope and α_c is the noise parameter independent of the gate voltage. This model was developed for ballistic carbon nanotube transistors, but has found validity in long-channel Schottky-barrier CNFETs as well. For example, Männik et al. [72] and Helbling et al. [73] showed that these low-frequency fluctuations in carbon nanotube sensors on a substrate could also be explained by the extended charge-noise model, and studied the gate-voltage dependence to identify the ideal quiescent point for operating these sensors.

Lin et al. [23] also showed by comparing suspended and on-substrate devices on the same carbon nanotube, that the 1/*f*-noise in the suspended sections decreased by an order of magnitude due to the elimination of the oxide layer (Figure 9a). Building on this concept, the authors have recently shown in [36] that combined with the use of ultraclean fabrication processes for gas sensors, suspended gas sensors showed a 9-fold

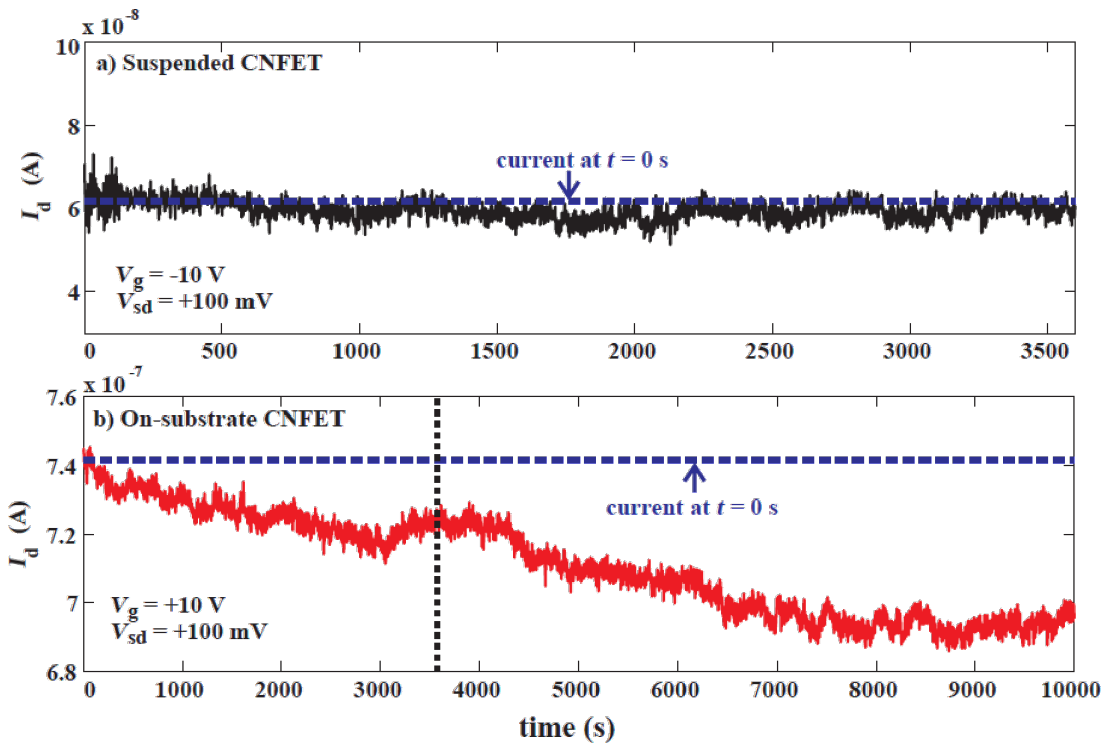

Figure 8: Drift suppression in suspended carbon nanotubes a) suspended carbon nanotube transistor and b) substrate-bound carbon nanotube transistor under constant bias. Over the same time span (marked by the vertical dotted line), the on-substrate transistor shows a 4% drop in current compared to the suspended transistor. The on-substrate transistor continues to decay beyond this point, decaying by about 10% over 10000 s of measurement. Reproduced with permission from [36]. Copyright 2014 Elsevier.

improvement in the signal-to-noise ratio compared to on-substrate sensors as well as improved stability of the threshold voltage (Figure 9b). This increase in signal-to-noise ratio directly implies improved sensor resolution.

Recovery

For a sensor to be functional, it must be fully recoverable after each cycle of exposure to gas. For NO_2 sensing using carbon nanotubes, this is a unique challenge. As discussed earlier, the undisturbed recovery time of nanotubes from NO_2 exposure is of the order of several hours. This is impractical for sensor applications.

In order to accelerate the recovery of the sensor, energy is supplied to the device in the form of heat or UV radiation. UV light has been used for carbon nanotube networks to recover the sensor [12,13]. However, Chen et al. [13] suggest that their individual-tube devices were not exposed to UV, citing the vulnerability of the single-tube device. Indeed, they also showed a drastic reduction in the conductivity of their SWNT-mat upon exposure to UV radiation. A single nanotube would likely be damaged over repeated UV-cycling for recovery, and therefore this may not be a viable long-term recovery solution.

Kong et al. [7] on the other hand showed that the sensor could be recovered by heating in vacuum for 1 h at 200 °C. Other papers [9] have subsequently shown that heating between 100 °C and 200 °C for between 10 min and 1 h recovers the sensor. Therefore, this approach appears to be a promising method, but it requires the integration of heaters into the device architecture. Heaters generally consume substantial power (around 10–100 mW for microheaters [74,75]), which nullifies the substantial power advantage that is achieved through the room-temperature operation of carbon nanotube gas sensors.

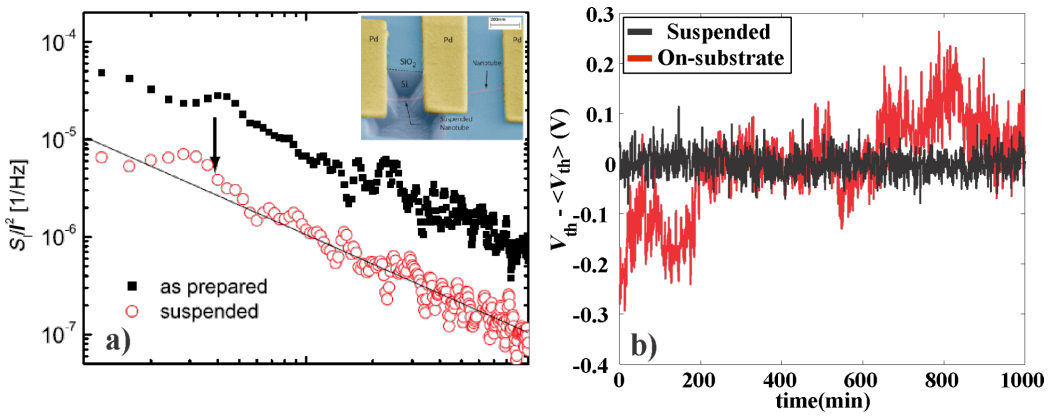

Figure 9: Reduction of 1/*f* noise in suspended CNFETs. a) The results from Lin et al. [23] show a 10-fold decrease in noise amplitude for a suspended transistor compared to a on-substrate transistor on the same nanotube. Reproduced with permission from [23]. Copyright 2007 IOP publishing. b) We have shown ultraclean, suspended transistors that exhibit remarkably low threshold-voltage fluctuations compared to on-substrate transistors [36]. Reproduced with permission from [36]. Copyright 2014 Elsevier.

Table 1: Performance summary of individual or few-tube SWNT-based NO_2 sensors. Sensors incorporating mats or forests of nanotubes are not considered. PEI: polyethyleneimine. It must be noted that the electrically refreshed gas sensors reported by Chang et al. [76] has been disputed by a subsequent article from Ervin et al. [77] who suggest that hysteretic contributions may be responsible for this effect.

authors	functional material	lowest conc.	response time (min)	recovery time (min)	recovery method
Kong et al. [7]	none	2 ppm	5 at 2 ppm	60	heating to 200 °C
Qi et al. [14]	PEI	0.1 ppb	1–2 at ppb	1–2	UV light (254 nm)
Zhang et al. [22]	none	n.a.	41 at 200 ppm	10	heating at 100 °C
Suehiro et al. [78]	none	0.5 ppm	1[a]	n.a.	UV light
Chang et al. [76]	none	300 ppm	n.a.	few seconds	voltage pulses
Mattmann et al. [65]	none	50 ppb	30	60	heating at 110 °C
Chen et al. [13]	none	5 ppb	30 at 5 ppb	n.a.	n.a.
Chikkadi et al. [11]	none	200 ppb	90 at 900 ppb	10	self-heating

[a]estimated value

Instead of an external heater, the authors have recently reported on a self-heated, suspended carbon nanotube gas sensor, that can recover from NO_2 exposure at a power below 3 μW within 10 min. The suspended architecture of the device plays a significant role in minimizing the power consumed by the device, since the isolated nanotube does not have any heat loss paths to the substrate. This ultra-low power consumption for the sensor provides a promising approach to sensor recovery while maintaining the power advantage of the sensors.

Performance Summary

Table 1 provides a summary of the performance of individual carbon nanotube gas sensors reported so far. In some cases, the numbers are extrapolated from the results reported in the papers, and are appropriately indicated.

Conclusion

Individual, single-walled CNFETs have long been used as model systems to study interactions between specific analytes and the nanotube, but several advances in fabrication processes as well as understanding of their behavior has enabled the prospect of using individual-tube devices directly in applications. Substantial progress has been made in understanding the source of noise, drift and hysteresis, and techniques have been introduced to counteract them, such as pulsed measurements and suspended device architectures. Furthermore, elimination of process residues and dielectrics leads to a complete suppression of hysteresis and an approximate 9-fold improvement in the noise performance [36]. Suspended devices are also attractive for self-heated, low-power architectures [30].

There are still several challenges to be addressed, particularly in the large-scale fabrication of these devices. Although integration of individual-nanotube devices on a wafer-scale has been achieved with moderate yield, the placement, length and chirality control remain challenging. Additional challenges remain in characterizing these devices in humid environments. Humid environments may be challenging for on-substrate devices owing to the induced hysteresis and noise, but suspended, ultraclean devices are expected to cope better with this problem due to the absence of hysteresis. Furthermore, the effect of functionalization must be studied in more detail on individual, suspended SWNTs in order to gain a better understanding of the mechanisms involved, and reliable techniques must be developed to extend these functionalization techniques on a large scale.

Although the debate on the precise nature of the NO_2-nanotube binding is not fully settled, experiments have made progress on understanding the nature of this interaction. From a theoretical perspective, the effect of NO_2 on the electron transport in the SWNT must be explored in more detail, and a hypothesis that consistently explains the observations from several papers must be developed. As it has increasingly grown clear, the cleanliness and type of the nanotube may play a significant role in the sensor response, and a clear link between the theoretical understanding and the experimental result will contribute significantly towards a better design for all gas sensors employing carbon nanotubes as their functional material.

The utility of individual-tube devices, furthermore, is not limited to addressing academic questions regarding sensing mechanisms and probing the limits of the technology. With improving control over fabrication processes and employing arrays of such individually-contacted SWNT devices, either for enhanced selectivity or noise performance, gas sensor products operating at extremely low powers can be envisioned. Compared to nanotube networks employing the same number of nanotubes, a better signal-to-noise ratio, lower power and smaller sizes could then be achieved. In this direction, suspended gas sensors appear to be the preferred architecture due to the low-power recovery and low noise performance.

Acknowledgements

We thank Roland Pohle, Max Fleischer, Wanda Andreoni and Wei Liu for useful discussions. The authors also acknowledge financial support from the EU FP7 program Technotubes, KTI discovery project 8885.2, ETH Zürich and EU COST action MP0901 and TD1105 for enabling networking possibilities.

References

1. Iijima, S. *Nature* **1991,** *354,* 56–58. doi:10.1038/354056a0
2. Radushkevich, L. V.; Lukyanovich, V. M. *Zh. Fiz. Khim.* **1952,** *26,* 88–95.
3. Oberlin, A.; Endo, M.; Koyama, T. *J. Cryst. Growth* **1976,** *32,* 335–349. doi:10.1016/0022-0248(76)90115-9
4. Tennent, H. G. Carbon fibrils, method for producing same and compositions containing same. U.S. Patent US4663230 A, May 5, 1987.
5. Iijima, S.; Ichihashi, T. *Nature* **1993,** *363,* 603–605. doi:10.1038/363603a0
6. Bethune, D. S.; Klang, C. H.; de Vries, M. S.; Gorman, G.; Savoy, R.; Vazquez, J.; Beyers, R. *Nature* **1993,** *363,* 605–607. doi:10.1038/363605a0
7. Kong, J.; Franklin, N. R.; Zhou, C.; Chapline, M. G.; Peng, S.; Cho, K.; Dai, H. *Science* **2000,** *287,* 622–625. doi:10.1126/science.287.5453.622
8. Collins, P. G.; Bradley, K.; Ishigami, M.; Zettl, A. *Science* **2000,** *287,* 1801–1804. doi:10.1126/science.287.5459.1801
9. Mattmann, M.; Helbling, T.; Durrer, L.; Roman, C.; Hierold, C.; Pohle, R.; Fleischer, M. *Appl. Phys. Lett.* **2009,** *94,* 183502–183502-3. doi:10.1063/1.3125259
10. Bradley, K.; Gabriel, J.-C. P.; Star, A.; Grüner, G. *Appl. Phys. Lett.* **2003,** *83,* 3821–3823. doi:10.1063/1.1619222

11. Chikkadi, K.; Muoth, M.; Hierold, C. Hysteresis-free, suspended pristine carbon nanotube gas sensors. 17th International Conference on Solid-State Sensors, Actuators and Microsystems (TRANSDUCERS EUROSENSORS XXVII); 2013; pp 1637–1640.
12. Li, J.; Lu, Y.; Ye, Q.; Cinke, M.; Han, J.; Meyyappan, M. *Nano Lett.* **2003,** *3,* 929–933. doi:10.1021/nl034220x
13. Chen, G.; Paronyan, T. M.; Pigos, E. M.; Harutyunyan, A. R. *Sci. Rep.* **2012,** *2,* No. 343. doi:10.1038/srep00343
14. Qi, P.; Vermesh, O.; Grecu, M.; Javey, A.; Wang, Q.; Dai, H.; Peng, S.; Cho, K. J. *Nano Lett.* **2003,** *3,* 347–351. doi:10.1021/nl034010k
15. Star, A.; Joshi, V.; Skarupo, S.; Thomas, D.; Gabriel, J.-C. P. *J. Phys. Chem. B* **2006,** *110,* 21014–21020. doi:10.1021/jp064371z
16. Penza, M.; Cassano, G.; Rossi, R.; Alvisi, M.; Rizzo, A.; Signore, M. A.; Dikonimos, Th.; Serra, E.; Giorgi, R. *Appl. Phys. Lett.* **2007,** *90,* 173123. doi:10.1063/1.2722207
17. Liu, W.; Chikkadi, K.; Lee, S.-W.; Hierold, C.; Haluska, M. *Sens. Actuators, B* **2014,** *198,* 479–486. doi:10.1016/j.snb.2014.03.039
18. Ruiz-Soria, G.; Pérez Paz, A.; Sauer, M.; Mowbray, D. J.; Lacovig, P.; Dalmiglio, M.; Lizzit, S.; Yanagi, K.; Rubio, A.; Goldoni, A.; Ayala, P.; Pichler, T. *ACS Nano* **2014,** *8,* 1375–1383. doi:10.1021/nn405114z
19. Zhao, J.; Buldum, A.; Han, J.; Lu, J. P. *Nanotechnology* **2002,** *13,* 195–200. doi:10.1088/0957-4484/13/2/312
20. Yu, S.; Yi, W. *IEEE Trans. Nanotechnol.* **2007,** *6,* 545–548. doi:10.1109/TNANO.2007.903800
21. Wongwiriyapan, W.; Honda, S.-i.; Konishi, H.; Mizuta, T.; Ikuno, T.; Ohmori, T.; Ito, T.; Shimazaki, R.; Maekawa, T.; Suzuki, K.; Ishikawa, H.; Oura, K.; Katayama, M. *Jpn. J. Appl. Phys., Part 1* **2006,** *45,* 3669–3671. doi:10.1143/JJAP.45.3669
22. Zhang, J.; Boyd, A.; Tselev, A.; Paranjape, M.; Barbara, P. *Appl. Phys. Lett.* **2006,** *88,* 123112. doi:10.1063/1.2187510
23. Lin, Y.-M.; Tsang, J. C.; Freitag, M.; Avouris, P. *Nanotechnology* **2007,** *18,* 295202. doi:10.1088/0957-4484/18/29/295202
24. Helbling, T.; Pohle, R.; Durrer, L.; Stampfer, C.; Roman, C.; Jungen, A.; Fleischer, A.; Hierold, C. *Sens. Actuators, B* **2008,** *132,* 491–497. doi:10.1016/j.snb.2007.11.036
25. Muoth, M.; Hierold, C. Transfer of carbon nanotubes onto microactuators for hysteresis-free transistors at low thermal budget. IEEE 25th International Conference on Micro Electro Mechanical Systems (MEMS); 2012; pp 1352–1355.
26. Cao, H.; Wang, Q.; Wang, D.; Dai, H. *Small* **2005,** *1,* 138–141. doi:10.1002/smll.200400015
27. Tseng, Y.-C.; Xuan, P.; Javey, A.; Malloy, R.; Wang, Q.; Bokor, J.; Dai, H. *Nano Lett.* **2004,** *4,* 123–127. doi:10.1021/nl0349707
28. Muoth, M.; Helbling, T.; Durrer, L.; Lee, S.-W.; Roman, C.; Hierold, C. *Nat. Nanotechnol.* **2010,** *5,* 589–592. doi:10.1038/nnano.2010.129
29. Chaste, J.; Eichler, A.; Moser, J.; Ceballos, G.; Rurali, R.; Bachtold, A. *Nat. Nanotechnol.* **2012,** *7,* 301–304. doi:10.1038/nnano.2012.42
30. Chikkadi, K.; Muoth, M.; Maiwald, V.; Roman, C.; Hierold, C. *Appl. Phys. Lett.* **2013,** *103,* 223109. doi:10.1063/1.4836415
31. Hückstädt, C.; Schmidt, S.; Hüfner, S.; Forster, F.; Reinert, F.; Springborg, M. *Phys. Rev. B* **2006,** *73,* 075409. doi:10.1103/PhysRevB.73.075409
32. De Renzi, V.; Rousseau, R.; Marchetto, D.; Biagi, R.; Scandolo, S.; del Pennino, U. *Phys. Rev. Lett.* **2005,** *95,* 046804. doi:10.1103/PhysRevLett.95.046804
33. Qazi, M.; Koley, G.; Park, S.; Vogt, T. *Appl. Phys. Lett.* **2007,** *91,* 043113. doi:10.1063/1.2760168
34. Oprea, A.; Bârsan, N.; Weimar, U. *Sens. Actuators, B* **2009,** *142,* 470–493. doi:10.1016/j.snb.2009.06.043
35. Heller, I.; Janssens, A. M.; Männik, J.; Minot, E. D.; Lemay, S. G.; Dekker, C. *Nano Lett.* **2008,** *8,* 591–595. doi:10.1021/nl072996i
36. Chikkadi, K.; Muoth, M.; Liu, W.; Maiwald, V.; Hierold, C. *Sens. Actuators, B* **2014,** *196,* 682–690. doi:10.1016/j.snb.2014.02.058
37. Kong, J.; Chapline, M. G.; Dai, H. *Adv. Mater.* **2001,** *13,* 1384–1386. doi:10.1002/1521-4095(200109)13:18<1384::AID-ADMA1384>3.0.CO;2-8
38. Randeniya, L. K.; Martin, P. J. *Carbon* **2013,** *60,* 498–505. doi:10.1016/j.carbon.2013.04.071
39. Peng, S.; Cho, K. *Nanotechnology* **2000,** *11,* 57–60. doi:10.1088/0957-4484/11/2/303
40. Chang, H.; Lee, J. D.; Lee, S. M.; Lee, Y. H. *Appl. Phys. Lett.* **2001,** *79,* 3863–3865. doi:10.1063/1.1424069
41. Dai, J.; Giannozzi, P.; Yuan, J. *Surf. Sci.* **2009,** *603,* 3234–3238. doi:10.1016/j.susc.2009.09.010
42. Peng, S.; Cho, K.; Qi, P.; Dai, H. *Chem. Phys. Lett.* **2004,** *387,* 271–276. doi:10.1016/j.cplett.2004.02.026
43. Santucci, S.; Picozzi, S.; Di Gregorio, F.; Lozzi, L.; Cantalini, C.; Valentini, L.; Kenny, J. M.; Delley, B. *J. Chem. Phys.* **2003,** *119,* 10904–10910. doi:10.1063/1.1619948
44. Yim, W.-L.; Gong, X. G.; Liu, Z.-F. *J. Phys. Chem. B* **2003,** *107,* 9363–9369. doi:10.1021/jp027647l
45. Ricca, A.; Bauschlicher, C. W., Jr. *Chem. Phys.* **2006,** *323,* 511–518. doi:10.1016/j.chemphys.2005.10.019
46. Goldoni, A.; Larciprete, R.; Petaccia, L.; Lizzit, S. *J. Am. Chem. Soc.* **2003,** *125,* 11329–11333. doi:10.1021/ja034898e
47. Goldoni, A.; Petaccia, L.; Gregoratti, L.; Kaulich, B.; Barinov, A.; Lizzit, S.; Laurita, A.; Sangaletti, L.; Larciprete, R. *Carbon* **2004,** *42,* 2099–2112. doi:10.1016/j.carbon.2004.04.011
48. Goldoni, A.; Petaccia, L.; Lizzit, S.; Larciprete, R. *J. Phys.: Condens. Matter* **2010,** *22,* 013001. doi:10.1088/0953-8984/22/1/013001
49. Ellison, M. D.; Crotty, M. J.; Koh, D.; Spray, R. L.; Tate, K. E. *J. Phys. Chem. B* **2004,** *108,* 7938–7943. doi:10.1021/jp049356d
50. Yao, F.; Duong, D. L.; Lim, S. C.; Yang, S. B.; Hwang, H. R.; Yu, W. J.; Lee, I. H.; Güneş, F.; Lee, Y. H. *J. Mater. Chem.* **2011,** *21,* 4502–4508. doi:10.1039/c0jm03227a
51. Chen, C.-W.; Lee, M.-H.; Clark, S. J. *Diamond Relat. Mater.* **2004,** *13,* 1306–1313. doi:10.1016/j.diamond.2003.11.081
52. Chikkadi, K.; Roman, C.; Durrer, L.; Süss, T.; Pohle, R.; Hierold, C. *Procedia Eng.* **2012,** *47,* 1374–1377. doi:10.1016/j.proeng.2012.09.412
53. Helbling, T.; Hierold, C.; Durrer, L.; Roman, C.; Pohle, R.; Fleischer, M. *Phys. Status Solidi B* **2008,** *245,* 2326–2330. doi:10.1002/pssb.200879599
54. Valentini, L.; Cantalini, C.; Armentano, I.; Kenny, J. M.; Lozzi, L.; Santucci, S. *Diamond Relat. Mater.* **2004,** *13,* 1301–1305. doi:10.1016/j.diamond.2003.11.011
55. Robinson, J. A.; Snow, E. S.; Bădescu, Ş. C.; Reinecke, T. L.; Perkins, F. K. *Nano Lett.* **2006,** *6,* 1747–1751. doi:10.1021/nl0612289
56. Salehi-Khojin, A.; Khalili-Araghi, F.; Kuroda, M. A.; Lin, K. Y.; Leburton, J.-P.; Masel, R. I. *ACS Nano* **2011,** *5,* 153–158. doi:10.1021/nn101995f
57. Llobet, E. *Sens. Actuators, B* **2013,** *179,* 32–45. doi:10.1016/j.snb.2012.11.014
58. Kim, W.; Javey, A.; Vermesh, O.; Wang, O.; Li, Y.; Dai, H. *Nano Lett.* **2003,** *3,* 193–198. doi:10.1021/nl0259232
59. Franklin, A. D.; Tulevski, G. S.; Han, S.-J.; Shahrjerdi, D.; Cao, Q.; Chen, H.-Y.; Wong, H.-S. P.; Haensch, W. *ACS Nano* **2012,** *6,* 1109–1115. doi:10.1021/nn203516z

60. Helbling, T.; Hierold, C.; Roman, C.; Durrer, L.; Mattmann, M.; Bright, V. M. *Nanotechnology* **2009,** *20,* 434010. doi:10.1088/0957-4484/20/43/434010
61. Robert-Peillard, A.; Rotkin, S. V. *IEEE Trans. Nanotechnol.* **2005,** *4,* 284–288. doi:10.1109/TNANO.2004.842053
62. Islam, A. E. *Electronics (Basel, Switz.)* **2013,** *2,* 332–367. doi:10.3390/electronics2040332
63. Lin, H.; Tiwari, S. *Appl. Phys. Lett.* **2006,** *89,* 073507. doi:10.1063/1.2337104
64. Mattmann, M.; Bechstein, D.; Roman, C.; Chikkadi, K.; Hierold, C. *Appl. Phys. Lett.* **2010,** *97,* 153103. doi:10.1063/1.3499363
65. Mattmann, M.; Roman, C.; Helbling, T.; Bechstein, D.; Durrer, L.; Pohle, R.; Fleischer, M.; Hierold, C. *Nanotechnology* **2010,** *21,* 185501. doi:10.1088/0957-4484/21/18/185501
66. Khamis, S. M.; Jones, R. A.; Johnson, A. T. C. *AIP Adv.* **2011,** *1,* 022106. doi:10.1063/1.3582820
67. Sangwan, V. K.; Ballarotto, V. W.; Fuhrer, M. S.; Williams, E. D. *Appl. Phys. Lett.* **2008,** *93,* 113112. doi:10.1063/1.2987457
68. Muoth, M.; Lee, S. W.; Hierold, C. In *2011 IEEE 24th International Conference on Micro Electro Mechanical Systems (Mems),* 2011; pp 83–86.
69. Collins, P. G.; Fuhrer, M. S.; Zettl, A. *Appl. Phys. Lett.* **2000,** *76,* 894–896. doi:10.1063/1.125621
70. Lin, Y.-M.; Appenzeller, J.; Knoch, J.; Chen, Z.; Avouris, P. *Nano Lett.* **2006,** *6,* 930–936. doi:10.1021/nl052528d
71. Tersoff, J. *Nano Lett.* **2007,** *7,* 194–198. doi:10.1021/nl062141q
72. Männik, J.; Heller, I.; Janssens, A. M.; Lemay, S. G.; Dekker, C. *Nano Lett.* **2008,** *8,* 685–688. doi:10.1021/nl073271h
73. Helbling, T.; Roman, C.; Hierold, C. *Nano Lett.* **2010,** *10,* 3350–3354. doi:10.1021/nl101031e
74. Ali, S. Z.; Udrea, F.; Milne, W. I.; Gardner, J. W. *J. Microelectromech. Syst.* **2008,** *17,* 1408–1417. doi:10.1109/JMEMS.2008.2007228
75. Courbat, J.; Canonica, M.; Teyssieux, D.; Briand, D.; de Rooij, N. F. *J. Micromech. Microeng.* **2011,** *21,* 015014. doi:10.1088/0960-1317/21/1/015014
76. Chang, Y. W.; Oh, J. S.; Yoo, S. H.; Choi, H. H.; Yoo, K.-H. *Nanotechnology* **2007,** *18,* 435504. doi:10.1088/0957-4484/18/43/435504
77. Ervin, M. H.; Dorsey, A. M.; Salaets, N. M. *Nanotechnology* **2009,** *20,* 345503. doi:10.1088/0957-4484/20/34/345503
78. Suehiro, J.; Imakiire, H.; Hidaka, S.-i.; Ding, W.; Zhou, G.; Imasaka, K.; Hara, M. *Sens. Actuators, B* **2006,** *114,* 943–949. doi:10.1016/j.snb.2005.08.043

License and Terms

This is an Open Access article under the terms of the Creative Commons Attribution License (http://creativecommons.org/licenses/by/2.0), which permits unrestricted use, distribution, and reproduction in any medium, provided the original work is properly cited.

The license is subject to the *Beilstein Journal of Nanotechnology* terms and conditions: (http://www.beilstein-journals.org/bjnano)

The definitive version of this article is the electronic one which can be found at: doi:10.3762/bjnano.5.227

BEILSTEIN JOURNAL OF NANOTECHNOLOGY

Electrical contacts to individual SWCNTs: A review

Wei Liu*, Christofer Hierold and Miroslav Haluska

Review

Open Access

Address:
Micro and Nanosystems, Department of Mechanical and Process Engineering, ETH Zurich, CH-8092 Zurich, Switzerland

Email:
Wei Liu* - wei.liu@micro.mavt.ethz.ch

* Corresponding author

Keywords:
charge carrier transport; CNFET; electrical contact; metal–SWCNT interface; SWCNT

Beilstein J. Nanotechnol. **2014,** *5,* 2202–2215.
doi:10.3762/bjnano.5.229

Received: 05 July 2014
Accepted: 30 October 2014
Published: 21 November 2014

This article is part of the Thematic Series "Atomic scale interface design and characterisation: Theory – Structure and dynamics".

Guest Editor: C. Ewels

© 2014 Liu et al; licensee Beilstein-Institut.
License and terms: see end of document.

Abstract

Owing to their superior electrical characteristics, nanometer dimensions and definable lengths, single-walled carbon nanotubes (SWCNTs) are considered as one of the most promising materials for various types of nanodevices. Additionally, they can be used as either passive or active elements. To be integrated into circuitry or devices, they are typically connected with metal leads to provide electrical contacts. The properties and quality of these electrical contacts are important for the function and performance of SWCNT-based devices. Since carbon nanotubes are quasi-one-dimensional structures, contacts to them are different from those for bulk semiconductors. Additionally, some techniques used in Si-based technology are not compatible with SWCNT-based device fabrication, such as the contact area cleaning technique. In this review, an overview of the investigations of metal–SWCNT contacts is presented, including the principle of charge carrier injection through the metal–SWCNT contacts and experimental achievements. The methods for characterizing the electrical contacts are discussed as well. The parameters which influence the contact properties are summarized, mainly focusing on the contact geometry, metal type and the cleanliness of the SWCNT surface affected by the fabrication processes. Moreover, the challenges for widespread application of CNFETs are additionally discussed.

Review

Introduction

The unique crystalline and electronic structure of single-walled carbon nanotubes (SWCNTs) afford extraordinary mechanical properties [1-3] as well as thermal and electrical conductivity [4,5], enabling ballistic charge carrier transport up to the microscale at room temperature [6,7]. The emergence of carbon nanotube field-effect transistors (CNFETs) using SWCNTs as the device channel provides a possible solution to the problem of undesirable, short-channel effects occurring in metal oxide semiconductor field-effect transistors (MOSFETs) on the order of tens of nanometers [8]. Furthermore, the diameter-normalized charge carrier density in sub-10 nm CNFETs is four times higher than for silicon-based devices [9]. Recently, the concept of a CNFET-based single processor was successfully implemented by Shulaker et al. [10]. These achievements reflect the great progress in fabrication technology that is advancing carbon nanotube technology closer to reality.

For SWCNT-based devices, the nanotubes must be connected to electrical circuitry, which is typically achieved by contacting the SWCNTs with metal. Due to possible low channel resistance (or even ballistic conduction), the metal–nanotube contact resistance can dominate the performance of these transistors. Devices with a low Schottky barrier height (SBH) or even with Ohmic contacts are often required. The principles of charge carrier transport developed for Si-based devices must be reconsidered for SWCNT-based devices due to the reduced dimensionality of the metal–SWCNT interface. In this review, the technological progress in the improvement of the electrical performance of metal–SWCNT contacts in CNFETs is reviewed. The approaches used to characterize the contact performance using two-, four- and multi-terminal measurements are described. The role of the contact geometry, metal type, cleanliness of the SWCNT surface, and post-metallization annealing process and their effect on the device with respect to resistance are summarized. Finally, the challenges in obtaining high-performance CNFETs are discussed, covering the reproducibility, long term stability of electrical contact properties, and large-scale fabrication options.

Carrier transport mechanism at metal–SWCNT interface

When a metal and a semiconductor are brought into intimate contact, the electric charges are redistributed to reach equilibrium at the metal–semiconductor interface due to the difference in their material work functions. Because of the charge redistribution, a Schottky barrier is formed at the metal–semiconductor contact if the position of the Fermi level of the metal lies between the edges of the semiconductor conduction and valence bands. This barrier impacts charge carrier transport through the electrical contact. Ideally, for a preselected semiconductor, the height of the Schottky barrier should depend on the work function of the chosen metals. In fact this rule is commonly violated for bulk semiconductors due to the existence of metal induced gap states (MIGS) at the metal–semiconductor interface [11,12]. For bulk semiconductors, MIGS cause a dipole sheet at the metal–semiconductor interface and lead to the so-called Fermi level pinning effect, that is, when the Fermi level tends to be fixed at a constant position in the band gap of the semiconductor [13]. The net result is that the Schottky barrier height is less sensitive to the work function difference between the metal and the semiconductor than theoretically expected.

However, the situation is different for the 1D, nanoscale, metal–semiconductor interfaces. The band bending structures for two types of contact geometries have been studied. For a SWCNT with an end-bonded contact (see the configuration shown in Figure 1b), MIGS cause a dipole ring instead of a dipole sheet at the metal–SWCNT interface, which only locally influences the band structures of SWCNTs within a few nanometers (Figure 2a) [14]. In contrast, for the planar contact, the dipole sheet affects the semiconductor band structure over a relatively longer distance (shown in the inset of Figure 2a).

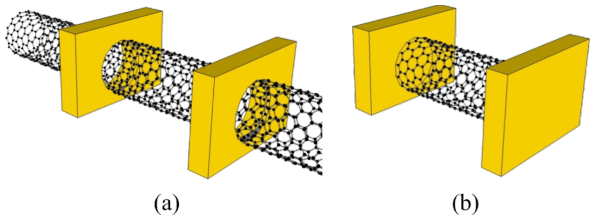

Figure 1: Contact geometries: (a) side-bonded and (b) end-bonded contact configurations.

For SWCNT with a side-bonded contact (configuration shown in Figure 1b), it was predicted as well that Fermi level pinning plays a minor role in the charge carrier injection effect at the electrical contact [16]. The experimental results [17] are consistent with this theoretical prediction [16]. Chen et al. [15] also reported that the Schottky barrier height decreased with increasing SWCNT diameter for the metals tested (Figure 2b). Meanwhile, for SWCNTs of the same diameter, a clear difference in electrical current (and Schottky barrier height) was observed for the contacts fabricated with Pd, Ti or Al [15] (Figure 2b).

As a result, for a given SWCNT, the height of the Schottky barrier can be adjusted by choosing the proper type of metal for the electrical contact. The work function of SWCNTs has been determined by the thermionic emission method to be 4.7–4.9 eV [18]. By choosing a metal with a high or low work function, it is possible to prepare the Schottky barrier favoring hole or electron conduction, respectively. Therefore, the types of transistors can be obtained by choosing the appropriate metal, ranging from fully p-type to ambipolar and to fully n-type.

Assuming the intrinsic Fermi level of SWCNTs is in the middle of the band gap (i.e., the intrinsic work function of the SWCNTs is approximated as the electron affinity plus half of the bandgap: $\varnothing_{\mathrm{CNT}} \approx x + E_{\mathrm{g}}/2$), the corresponding Schottky barrier height for a metal with a low work function can be estimated as

$$\begin{cases} \varnothing_{\mathrm{e}} \approx E_{\mathrm{g}}/2 - (\varnothing_{\mathrm{CNT}} - \varnothing_{\mathrm{m}}) & \text{for electrons} \\ \varnothing_{\mathrm{h}} \approx E_{\mathrm{g}}/2 + (\varnothing_{\mathrm{CNT}} - \varnothing_{\mathrm{m}}) & \text{for holes} \end{cases} \quad (1)$$

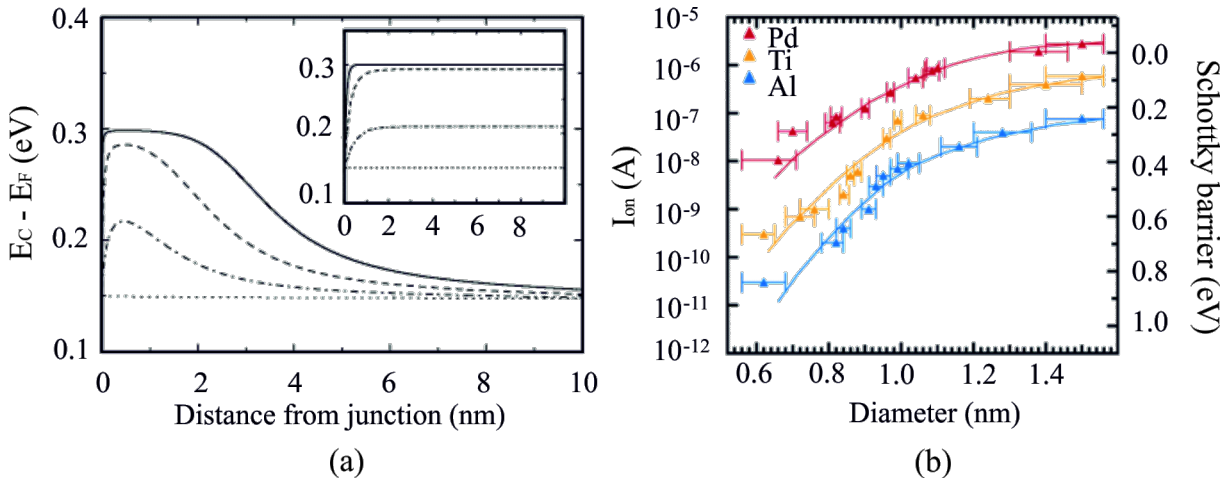

Figure 2: The role of the Fermi level pinning effect at the metal–semiconductor interface. a) Simulation of band bending at the metal–SWCNT (semiconducting SWCNT, diameter: 1.4 nm) interface for a low work function metal. The dotted, dash-dotted, dashed, and solid lines correspond to the different pinning strength 0, 0.01, 0.1, and 1 state/(atom eV), respectively. The pinning effect for the planar junction is shown in the inset for comparison using the same simulation parameters. b) The experimental results of the on current as a function of CNT diameter with different metals. The clear dependence of the Schottky barrier height on the type of metal and the SWCNT diameter is observed. This indicates that no Fermi level pinning effect exists at the metal–SWCNT interface. Figure reprinted with permission from (a) [14] copyright 2000 American Physical Society, (b) [15] copyright 2005 American Chemical Society.

where $\varnothing_m$ and $\varnothing_{CNT}$ represent the work function of metal and SWCNT, respectively, and E_g is the band gap of the SWCNT, which is inversely proportional to its diameter (approximated as $0.71 \approx 1.1/d$ [19-21]).

For a CNFET with a Schottky barrier (SB) at the contacts, the electrical current through the barrier contains the contributions from two components: the thermionic emission current (over the Schottky barrier) and the tunneling current (through the depletion region) [22]. The band bending diagram at the metal–SWCNT interface is illustrated in Figure 3a, assuming the drain–source electrode is biased with a positive voltage and the gate electrode is set to zero voltage potential. The electrical modulation of the CNFET conductance is the consequence of the Schottky barrier width (W) modulation [23]. The shape of Schottky barrier can be modulated by the gate and drain–source voltages, therefore, the transmission probability, $T(E)$, of carriers across the SB is determined by the electric field induced by both the gate and drain–source bias. This effect is illustrated in the inset of Figure 3b, showing typical transfer characteristics of an n-type CNFET. Under a low gate bias (less than the threshold voltage), the Schottky barrier is too high and wide to allow the charge carrier flow over or to tunnel through the barrier. When the gate voltage is positively increased (greater than the threshold voltage), the bands bend downward and narrow the Schottky barrier width, enabling more electrons to tunnel through (the n-branch shown in the inset of Figure 3b). In this regime, the current grows exponentially with an increase in the gate bias. As the gate voltage increases further, the gate-field-induced band bending effect slows down causing the source–drain current to become "saturated" beyond a certain gate voltage. The bands bend upward when a negative voltage is applied to the gate electrode and the Schottky barrier for holes is reduced. Under this condition, the activated hole carriers tunnel through the Schottky barrier (the p-branch shown in the inset of Figure 3b). Due to this, a current (for holes) is observed under a negatively biased gate voltage.

Characterization methods

The overall resistance (R_{tot}) of a CNFET includes the contact resistances ($2R_c$) and the device channel resistance ($r_{ch}L_{ch}$) given as [24]:

$$R_{tot} = 2R_c + r_{ch}L_{ch} = \left(R_q + \frac{2\rho_c}{L_c d}\right) + R_q \frac{L_{ch}}{L_e}, \qquad (2)$$

where the quantum resistance for a SWCNT is defined as $R_q = h/4e^2$, r_{ch} is the channel resistance per unit length, R_c is the single contact resistance, ρ_c is the specific contact resistivity, L_c and L_{ch} represent the contact width and the channel length, respectively, d is the diameter of the SWCNT, and L_e is the mean free path for carrier scattering (which varies with the temperature [25]). L_e is in the range of few hundreds nanometers [24,26] to a few micrometers [27], which reflects the quality of

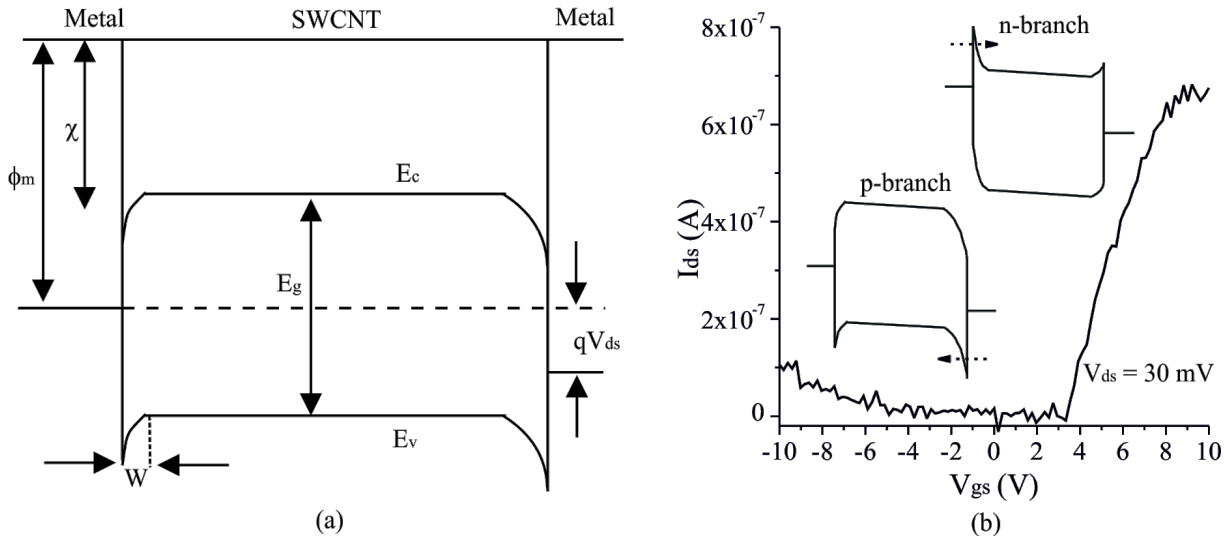

Figure 3: The energy band diagram of a CNFET. a) The band bending effect at the metal–SWCNT interface for a metal with a low work function. A positive voltage bias is applied between drain–source electrodes and the gate bias is set to zero. b) The transfer characteristics of an n-type CNFET. Inset sketches show the Schottky barrier width modulation with respect to the different bias conditions from the gate electrodes.

the SWCNTs (defects or imperfections) influenced by the SWCNT synthesis and the device fabrication processes.

The overall resistance for the on-state of CNFETs obtained from the experiments are typically much higher than the theoretically calculated value for CNFETs with a 1D channel ($h/4e^2$ = 6.5 kΩ) for SWCNTs [28]. Thus, it is necessary to determine the resistance contributions from the electrical contacts and the device channels. The common experimental techniques used to determine the contribution of the individual resistance components are: 1) extraction of the Schottky barrier height from the CNFET transfer characteristics measured at different temperatures, 2) estimation of the channel resistance through a four-terminal measurement, and 3) evaluation of the contact and channel resistances by a multi-terminal experiment using the transmission line model.

Determination of the Schottky barrier height

As mentioned previously, CNFETs (using SWCNTs as the active channel) are SB-modulated devices (SB-CNFETs). The width of the Schottky barrier can be determined by locally excited photo-voltage experiments [29] or by checking the bright segment in the SEM image [30]. The width of the Schottky barrier is modulated by the applied electric field from the gate and source–drain electrodes [23], but the height of Schottky barrier is mainly determined by the work function difference between metal and carbon nanotube. To some extent, the height of the Schottky barrier reflects the intrinsic property of electrical contact. The approaches used to evaluate the height of the Schottky barrier are detailed in this section.

Although a capacitance–voltage (C–V) measurement was developed to extract the Schottky barrier height for silicon planar devices [31], it requires a more sophisticated setup for CNFETs due to the small capacitance in the metal–SWCNT contact area [32]. Current–voltage (I–V) measurements performed at different temperatures (also called the thermal activation energy method) are more suitable for extracting the Schottky barrier height at the metal–SWCNT contacts in CNFETs [33,34]. According to the thermionic emission theory, the thermionic current through the metal–semiconductor contact is proportional to the measurement temperature [35]. The SB height can be determined from the following equation [36]:

$$\mathrm{Log}\left(\frac{I_{\mathrm{ds}}}{T}\right) = \mathrm{Log}\left(AA^{*}\right) - \frac{q\varphi_{\mathrm{b}}}{k_{\mathrm{b}}T}, \qquad (3)$$

where A is the contact area, A^* is the effective Richardson constant, q and k_b represent the elementary charge and Boltzmann constant, respectively, $q\varphi_b$ is the activation energy, and T is the temperature.

Figure 4a shows the transfer characteristics of the same CNFET obtained at different temperatures. The off-state current reveals a stronger temperature dependence because it mainly represents the thermally activated carrier transport (where charge flow over the Schottky barrier dominates). The trend is more obvious in the Arrhenius plot (Figure 4b). The maximum slope is obtained at a certain gate bias where the minimum current is

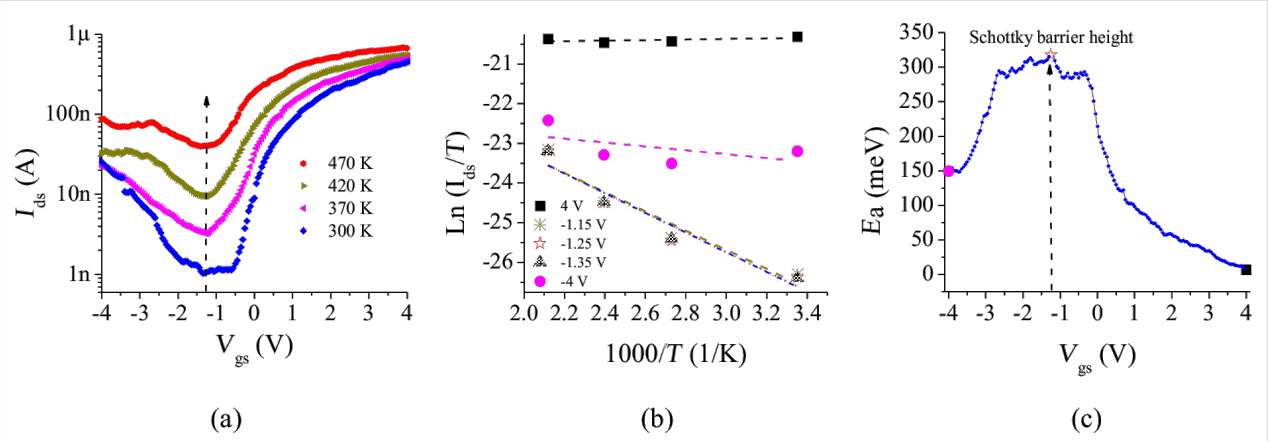

Figure 4: The procedures for determining the Schottky barrier height. (a) CNFET transfer characteristics measured at different temperatures. (b) Arrhenius plot with linear fits for different gate biases, V_{gs}. For the better visualization, only the data points obtained for five different gate voltages: 4 V, −1.15 V, −1.25 V, −1.35 V, −4 V are shown. (c) Activation energy (E_a) as a function of gate bias (V_{gs}) estimated from (a). The highlighted data points represent the activation energies derived from the corresponding slopes of linear fits in (b).

obtained. This corresponds to the flat band condition, that is, no band bending occurs at the metal–SWCNT interface at the source electrode for this condition [36]. On the other hand, the currents measured at the more positive and negative biases reveal only a weak temperature dependence due to carrier transport dominated by tunneling. Utilizing this characteristic, the activation energy ($q\varphi_b$, Figure 4c) is extracted according to Equation 3. Its maximum value corresponds to the Schottky barrier height. The activation energy becomes smaller when the energy bands are no longer in the flat band condition because of the added contribution of the tunneling current through the thinner part of the Schottky barrier.

It is worth noting that the Schottky barrier height could be influenced by the surrounding atmosphere. As reported in [37,38], the oxygen molecules at the metal–CNT contact had an effect on the Schottky barrier height. Therefore, the measurement conditions (in vacuum or in air) should be considered during the electrical characterization.

Determination of the contact and channel resistances

Four-terminal measurement: The four-terminal measurement is often used to determine the sheet resistance of thin films. The contact resistance can be extracted indirectly by subtracting the thin film resistance from the overall resistance. Two pairs of terminals are contacted to the target material and a constant current (I_{con}) is forced from two outside terminals and the voltage drop (V_{sen}) along the object is measured between the two inner "sensing" terminals. This method has been adapted to determine the resistance in CNFETs [39-42]. The channel resistance between the two inner terminals is determined by $R_{ch} = V_{sen}/I_{con}$. The contact resistance can be obtained by subtracting the channel resistance from the overall resistance measured from the inner electrode pair. However, those electrodes can cause deformation of the SWCNT structure and/or induce additional current scattering under the contacts [43,44], which can perturb the carrier transport along the SWCNT. For the bottom contact configuration, the nanotube deformation was also detected near the edges of the electrodes where the SWCNTs passed from the top electrodes to the substrate [45]. Therefore, it is necessary to set up a suitable measurement platform to eliminate the negative influence of the contacts on the nanotubes. Gao et al. [26] presented an approach to solve this problem by using noninvasive electrodes. As shown in Figure 5a, two MWCNTs acting as the sensing electrodes were placed on a SWCNT by an AFM manipulator. As a result, the additional barriers caused by the deformation of the SWCNT were avoided [26].

Transmission line model: CNFETs with longer channel lengths exhibit a higher on-resistance due to the electron scattering effect along the channels [46]. This could be caused by intrinsic structural defects or by the mechanical bending of CNTs lying on the substrate as well as by the chemical inhomogeneity induced during the fabrication process. The transmission line model (TLM) developed for planar devices [47] provides an approach to determine both the contact resistance and the channel resistance. The applicability of this approach was extended to nanoscale devices, such as CNFETs [24,48]. As shown in Figure 5b, multi-electrodes are defined on the same SWCNT. The overall resistance is measured for CNFETs with different channel lengths. For the CNFET with a short channel length made from a high quality SWCNT and measured at a low source–drain bias, the resistance contributed from the device channel plays a minor role in the total resistance when

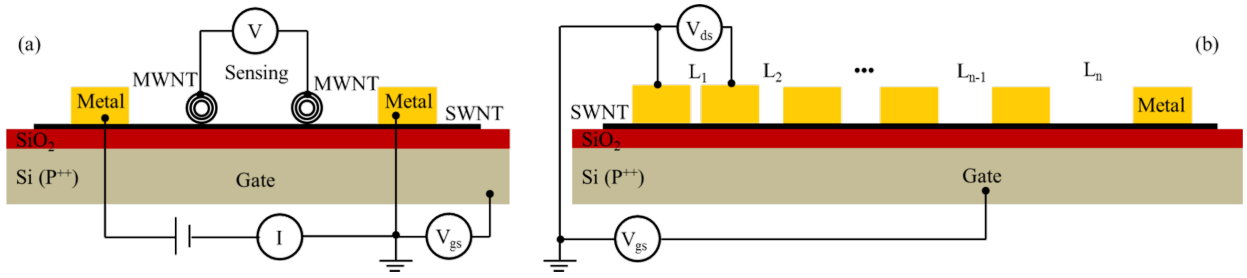

Figure 5: Schematics of different approaches for characterizing the electrical contacts of CNFETs. a) An optimized configuration for the four-terminal measurement by using MWCNTs as the voltage sensing electrode according to the reference [26]. b) Multiple contacts are defined on the same individual SWCNT with different channel lengths. Potential drops can be measured between any two electrodes.

approaching ballistic transport. The total resistance (R_{tot}) is determined as shown in Equation 2. Based on the assumption that each contact is of equal quality and the nanotube is consistent along the entire length, the contact resistance and the channel resistance can be determined by plotting the overall resistance versus the channel length. The corresponding resistances can be determined from the intercept ($2R_c$) and the slope (r_{ch}) of the curve.

Factors influencing the contact properties

The device architecture and characterization conditions often vary from device to device, as prepared by different research groups. For this reason, we will discuss the results obtained by different groups separately to better understand the effect of contact geometry, metal type, and the nanotube cleanliness, as well as the post-metallization annealing treatment.

Contact geometry

The contact geometries of CNFETs can be classified into two types: end-bonded and side-bonded contacts (as shown in Figure 1a,b). For end-bonded contacts, metal leads are directly touching the open ends of nanotube. In this case, the defect sites (dangling bonds) on the ends of the CNTs are intended to provide additional reaction sites to greatly increase the interaction energy between the metal and the CNT [49]. As an example, nanotube/carbide heterojunctions (such as TiC) can be formed at an optimized temperature [50]. This has been shown to be a great advantage for MWCNT interconnects. As demonstrated in [51], the caps of vertically (with respect to the horizontal substrate) aligned MWCNTs were removed by chemical mechanical polishing (CMP) followed by metal deposition to form the top electrodes. By this approach, the inner shells of MWCNTs are also contacted by metal, thereby enhancing the carrier transport capability. However, this fabrication process cannot be easily applied to horizontally aligned SWCNTs. Instead, side-bonded contacts are implemented and widely used in SWCNT-based device fabrication. SWCNTs can be deposited on the predefined metal electrodes, or the other way around. The effective contact area between the metal and SWCNT allows for the charge carrier transport capability. As a result, a term called the transfer length, L_T, is introduced to quantify the carrier transfer distance under the electrical contact. Nosho et al. [48] experimentally determined the transfer length to be a few tens of nanometers. Investigations by another group [24] showed that the contact resistance increased exponentially when the contact length decreased from 200 to 20 nm. This inconsistency could be caused by the different process conditions, such as the contact materials (Au vs Pd), annealing treatment, and the different properties of the individual SWCNTs used. The results imply that the carrier transport mainly occurs at or close to the edge of the metal–SWCNT contact.

Another crucial factor which could influence the charge carrier transport at the metal contact is the shape of the electrode. It was shown [52] that a needle-like contact is preferred to improve the gate-field efficiency and thus enhance the charge carrier transport at the metal–SWCNT interface. This approach has been experimentally implemented by Muoth and coworkers [53]. As shown in Figure 6, the thickness of the metal coating on the SWCNT gradually decreases from tens of nanometers to a few nanometers. Owing to the nano-tapered contacts, a remarkable subthreshold swing (230 mV dec^{-1} using air as the gate dielectric) was obtained for a device fabricated on a suspended SWCNT using a 3 μm air gap as the dielectric material between the gate electrode and the transistor channel.

Contact metal

Work function and wettability: The presence of a Schottky barrier at the metal–SWCNT contact largely impacts the CNFET performance. Since the pinning effect at the metal–CNT interface is nearly negligible [14,16], the height of the Schottky barrier could be minimized by choosing an appropriate metal with a relatively high (low) work function for high performance p-type (n-type) CNFETs. The Schottky barrier height is also inversely proportional to the diameter of the SWCNT. The discussion in this section will be focused on how

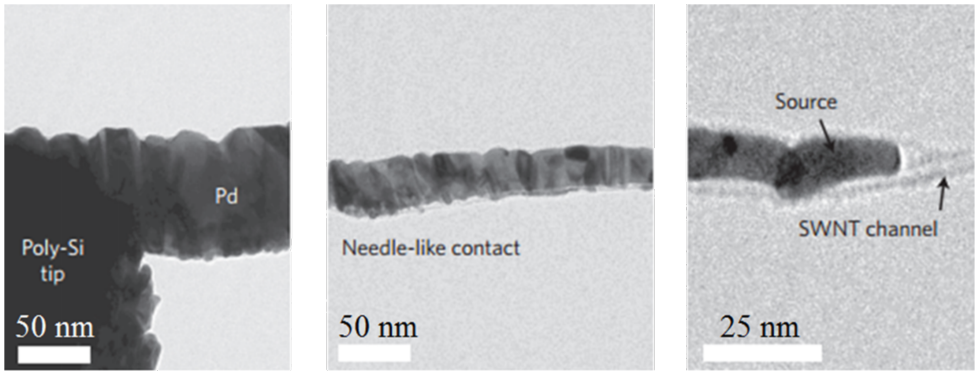

Figure 6: Needle-like side-bonded contact. Reprinted with permission from [53]. Copyright 2010 Macmillan Publisher.

the device performance is affected by the metal properties, for a given SWCNT.

High-performance n-type CNFETs were achieved by using Sc contacts [54], where the device conductance reached $0.5 \cdot G_0$ ($1/R_q = G_0 = 154$ μS) measured at room temperature. However, the strong propensity of oxidation for low work function metals cause low yield and degradation in the reproducibility of device performance. Recently, Shahrjerdi et al. [55] reported a remarkable improvement in n-type transistors by using erbium (Er) as the contact metal. A high device yield was obtained through controlling the metal deposition conditions, such as the base pressure and deposition rate. For p-type CNFETs, Pd has proven to be the most appropriate metal, forming nearly Ohmic contacts with superb device yield [56].

Other than the work function differences between the metals and the SWCNTs, the wettability of metals to SWCNTs is another critical factor affecting the contact properties. Although Au and Pd have comparable work functions (shown in Table 1), Au–CNT contacts possess a higher on-resistance in most cases. This can be explained by the relatively poor wettability of gold to SWCNTs. As shown in Figure 7a, discrete Au nanoparticles are formed on suspended SWCNTs [57]. In contrast, Pd forms a nearly continuous coating on the SWCNT [57], which indicates a good adhesion to the sidewall of carbon nanotube. Another promising metal with a high work function is Pt. Although it possesses a work function higher than Pd, non-Ohmic contacts were observed from the CNFETs with Pt–SWCNT contacts [27]. The effective contact area of Pt on SWCNT is limited by the poor wettability of Pt [58]. All these experimental observations point to the importance of metal wettability to SWCNTs [56,58,59]. A metal with better wettability provides a greater contact interface area per unit length of the nanotube, which enhances the current injection capability. On the other hand, metals with poor wettability cause a discontinuous coating resulting in the presence of vacuum voids at the metal–CNT interface. Therefore, it is not surprising that Pd exhibits the best quality of electrical contacts owing to both properties, that is, a high work function as well as good wettability to the SWCNT [60]. As reported by Franklin et al. [24], the total resistance (including the channel and contact resistances) reached 6.6 kΩ for metallic SWCNT contacted by Pd. Ti also shows excellent wettability to SWCNTs (Figure 7a). Using Ti as a contact material may result in Ohmic contact [7] as well as Schottky contact [61]. The variation in results is probably caused by the easy oxidation of Ti [62]. As was presented in [27], a maximum of a 20% success rate for the formation of Ohmic contacts was obtained for Ti–SWCNT contacts. Obviously, the chemical inertness of the contact metal in air is another important requirement for forming reliable electrical contacts.

Carbon interfacial layer: The imperfect wettability of the metal to the nanotube leads to the occurrence of atomic-level physical gaps between the metal and the nanotube, thus causing

Table 1: Work function of various metals [63] (units: eV).

Metal	Work function	Metal	Work function	Metal	Work function	Metal	Work function
Er	3.0	Al	4.28	W	4.55	Au	5.1
Sc	3.5	Ti	4.33	Mo	4.6	Pd	5.12
Mn	4.1	Cr	4.5	Cu	4.65	Ni	5.15
Ag	4.26	Fe	4.5	Rh	4.98	Pt	5.65

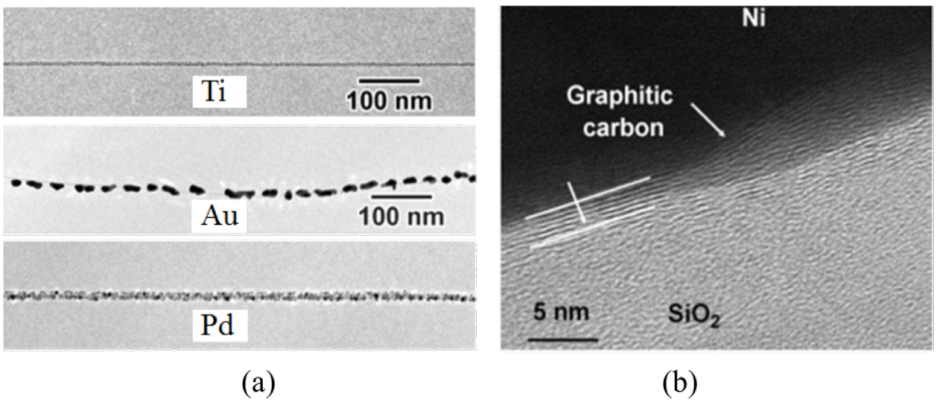

Figure 7: TEM images for (a) metal deposition on suspended, as-grown SWCNTs. Ti displays the best wettability to the SWCNT. Compared to Au, Pd showed better wettability to the SWCNT. (b) The graphitic carbon interfacial layer formed under a Ni layer through annealing treatment. Figure reprinted with permission from (a) [57] copyright 2000 American Institute of Physics and (b) [64] copyright IEEE Electron Devices Society.

the presence of an additional barrier which hinders charge carrier injection at the contacts. Although Pt provides poor coverage of the nanotubes [59], the electrical contact could be improved by introducing a graphitic interfacial layer between the SWCNT and the Pt electrode. As pointed out in [65], Pt acts as a catalyst for hydrocarbon residues (inevitably present in the vacuum chamber) which can be graphitized by an annealing treatment above 607 °C. However, the uncertainty of hydrocarbon residue concentration in the process chamber constrains the reproducibility of fabrication of low-resistance contacts. Chai et al. [64] developed another approach to obtain a graphitic interfacial layer in a more controllable manner. Amorphous carbon was deposited between Ni (as catalysts for graphitization) and semiconducting SWCNTs. The amorphous carbon transforms to graphitic carbon by annealing at 850 °C (as shown in Figure 7b). By this approach, the effective contact area between the metal and the SWCNTs is increased, thus improving the charge carrier transport. In this way, the on-current was improved by one order of magnitude [64].

Cleanliness of SWCNT surface

It is challenging to avoid resist residue from resist-based lithographic fabrication processes on SWCNTs. Although oxygen plasma etching is an efficient approach to remove the resist residue in silicon-based device fabrication processes [66], this harsh treatment destroys the CNT structure [67]. Several different approaches have been explored to preserve the clean surface of SWCNTs. Optimizing the resist wet-stripping procedure only partly helped to improve removability of the resist residue from the contact area [68]. To better clean SWCNTs, a dry-cleaning technique was developed. As presented in [69], the resist residue on SWCNTs can be removed by annealing (350 °C) the sample in forming gas (95% N_2, 5% H_2). However, neither wet-cleaning nor dry-cleaning techniques are applicable to remove the resist residue from the contact area, as they would destroy the preferably undercut profile of the resists required for the subsequent metal lift-off process. Khamis et al. [70] introduced a buffer layer between SWCNTs and a novolac-based photoresist to prevent SWCNTs from directly contacting the photoresist. However, the relatively high on-resistance (250 ± 100 kΩ) indicates the necessity for further optimization. Recently, the authors [71] have investigated an approach by using a thin layer of alumina to protect the SWCNTs during the device fabrication. The results presented in Figure 8a,b show that the resist residue is dramatically reduced at the contact area by using an alumina protective layer. Owing to the improvement in cleanliness of the SWCNT surface, the median value of the on-resistance was reduced from 247 kΩ for unprotected SWCNTs (381 n-type CNFETs) to 134 kΩ for protected SWCNTs (110 n-type CNFETs) (Figure 8d) [71]. The median value of the hysteresis width also narrowed from 2.2 V to 0.5 V (Figure 8e) [71]. In addition, the widths (see the insets in Figure 8d,e) of the dispersions of on-resistance and the hysteresis width were reduced to 152 kΩ and 0.6 V, respectively. Another option to avoid the impact of contamination induced by the photo/e-beam resists is stencil lithography. As reported by Muoth et al. [53], hysteresis-free devices were achieved by using a shadow mask to define the electrical contacts (resist-free). In this process, SWCNTs were grown between two suspended poly-Si tips. Then an on-chip shadow mask covered the SWCNT to protect the device channel. With the assist of a shadow mask, the electrical contacts were formed by directly depositing metals onto the poly-Si tips, which were bridged by a nanotube (as shown in Figure 8c). This approach eliminates contamination from the photo/e-beam resists completely.

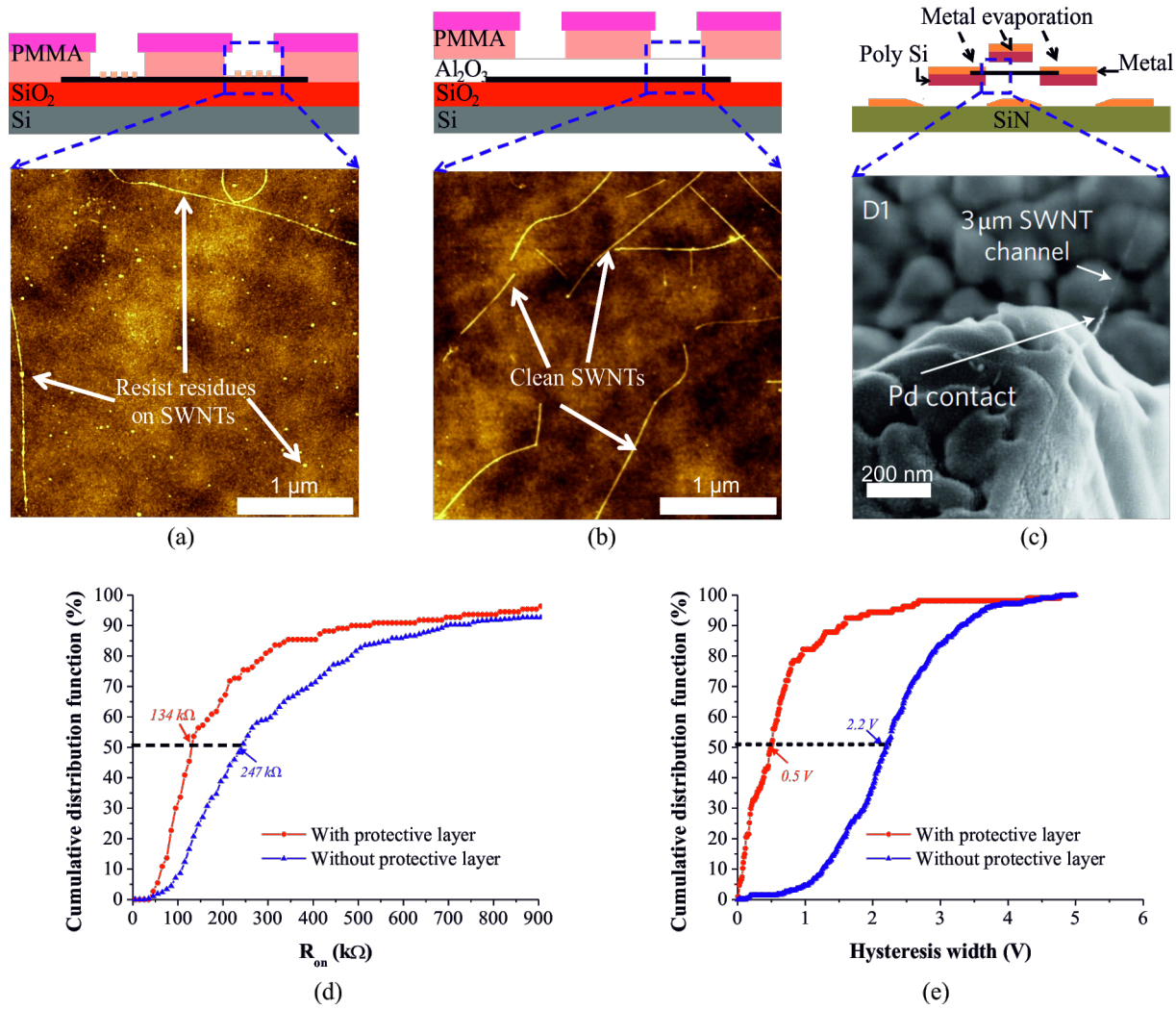

Figure 8: Inspection of the cleanliness of SWCNTs. a) AFM image obtained after developing a PMMA resist from the SiO_2-supported SWCNTs. b) AFM image obtained after PMMA and following alumina removal from the contact area. c) SEM image of a Pd contact on a suspended SWCNT using a shadow mask process. d) The cumulative distribution function of on-resistance for n-type CNFETs. Red circles and blue triangles represent the experimental results with and without using the protective layer, respectively. e) The distribution of the hysteresis width for n-type CNFETs. Figure reprinted with permission from (c) [53] copyright 2010 Macmillan Publisher and (d,e) [71] copyright 2014 Elsevier.

However, the large-scale applicability is constrained by the complexity of the fabrication process. Nevertheless, other groups have developed wafer-scale stencil lithography processes which could be used as a scale-up process for patterning metal–nanotube contacts. For instance, Vazquez-Mena et al. [72] developed a stencil lithography process to fabricate metallic nanowires at the wafer level. Nanoslits with a width down to 70 nm were defined on a wafer level membrane made of low-stress silicon nitride. Nanowires were thus formed by depositing metal through the nanoslits without using any photo/e-beam resist.

Post-metallization annealing

The metal–SWCNT contact performance can be further improved by post-metallization annealing. With this approach, the following benefits can be attained: 1) the removal of possible organic contaminations from the metal–SWCNT contact area in the case of a bottom contact configuration, 2) the change in metal morphology at the contact area, and 3) the formation of covalent bonds between the nanotube and the metal, leading to the formation of metal carbides. Several combinations of metals and annealing conditions (temperatures, duration) have been investigated, as summarized in Table 2.

Table 2: Different annealing conditions for commonly used contact metals in CNFETs.

Contact metals (thickness in nm)	Types of nanotubes[a,b]	Contact geometry	Annealing conditions	Reduction of resistance
Cr/Au [70]	s-SWCNTs	top contact	300 °C in air for 1 h	≈2–3 orders of magnitude
Cr/Au = 5/50 [73]	s-SWCNTs	top contact	600 °C in Ar atmosphere for 10 min	reduced the SB height
Ti/Pd = 0.8/50 [74]	m-SWCNTs	top contact	≈177 °C in vacuum	≈1 order of magnitude
Ti = 50 [74]	m-SWCNTs	top contact	327 to 627 °C in vacuum	≈1–2 orders of magnitude
Ti probe [75]	CNT fiber	bottom contact	400 to 700 °C in vacuum	≈4 orders of magnitude
Ti = 50 [76]	s-SWCNTs	top contact	700 to 800 °C in Ar atmosphere for 30 s	≈2–3 orders of magnitude
Ti [50]	SWCNT matrix	bottom contact	≈970 °C in vacuum for 20 min	SB-contacts turned to Ohmic contacts
Ti/Pt = 0.8/30 [65]	m-SWCNTs	top contact	627 °C in vacuum	14 times (average)

[a]s-SWCNTs: semiconducting SWCNTs, [b]m-SWCNTs: metallic SWCNTs.

Khamis et al. [70] pointed out that the device properties (for Au/Cr–SWCNT top contact) were improved at 300 °C, which helped to remove contamination attached to the channels of devices (Figure 9a). Another group [73] also highlighted the importance of the annealing treatment for Au/Cr–SWCNT contacts (top contact). The on-conductance was increased by 2–3 orders of magnitude through annealing at 600 °C in Ar atmosphere [73]. It was intended that the Au should penetrate the Cr layer and create a direct contact with SWCNTs after the annealing treatment [73]. Actually, evidence can be found in [77] which illustrates the inter-diffusion between the Cr (6 nm) layer and the Au (200 nm) as observed through the scanning Auger depth profile after 8 hours of annealing at 400 °C.

For Pd top contacts deposited on SWCNT, annealing at a relatively low temperature is preferred. As it was reported in [74], the overall resistance was reduced by three orders of magnitude after annealing at ≈177 °C. A further annealing step at 325 °C degraded the contact performance. This can be explained by the change of the Pd morphology, specifically by an increasing grain size of Pd at increased temperatures [78].

The performance of Ti–CNT top contacts [74] was investigated by annealing in vacuum in the range of 350–700 °C. The overall resistance was dramatically reduced by 1–2 orders of magnitude, owing to the chemical change at the metal–SWCNT–silicon oxide interface as well as the structure change of the Ti metal. Further annealing at a higher temperature has also been explored to form TiC by quenching the Ti contacts at 800–850 °C [76]. Thus, the conductance of ambipolar CNFET was improved by more than two orders of magnitude [76]. Zhang et al. [50] reported that the resistance of Ti-SWCNT bottom contacts was reduced by annealing the devices at temperatures greater than 800 °C due to the formation of nanorod-like TiC (Figure 9b). On the contrary, Tomimoto et al. [75] observed the gradually decreased conductance for Ti–SWCNT bottom contacts annealed at a temperature

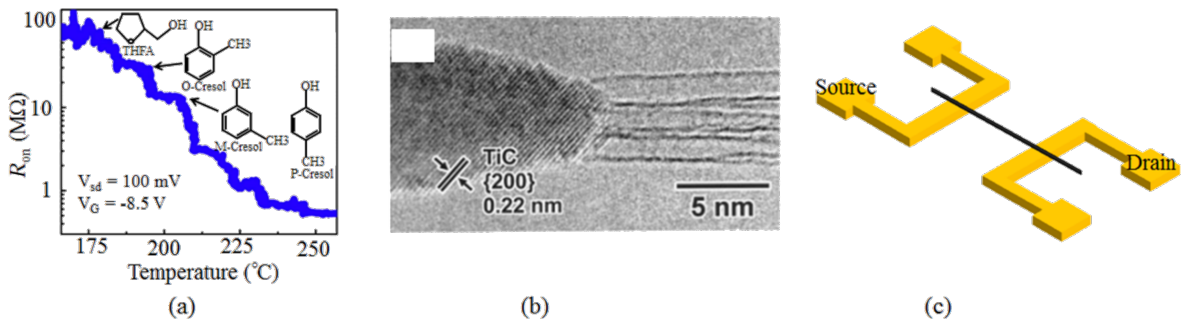

Figure 9: Improving the contact performance by post-metallization annealing. a) The process of removing contamination from the sidewalls of SWCNTs by annealing at modest temperatures. b) The TEM image shows the TiC formation through annealing Ti–SWCNT contacts above 800 °C. c) The schematic of contact design using the Joule heating method for local annealing of the metal–SWCNT contact (using Pd as the contact metal) by pulsed current. Figure reprinted with permission from (a) [70] copyright 2011 Author(s) and (b) [50] copyright 1999 The American Association for the Advancement of Science.

greater than 700 °C, which was explained as the reduction of the effective contact area between the conductor (Ti and TiC) and nanotube. The effective contact area could be the cross section or the partially carbidized side wall of SWCNT. However, it is difficult to experimentally inspect the effective contact area. Further investigation must be carried out.

The concept of electrically heating the contacts has also been explored. Figure 9c shows the schematic of using Joule heating to improve the contact properties. A constant or pulsed current [37,79-81] was applied through the electrodes. An instant heating locally in the contact area could remove the adsorbates remaining on the SWCNTs after wet deposition, thus reducing the tunneling barrier for carrier injection at the metal–SWCNT interface.

Challenges

Several milestones have been achieved regarding the improvement of electrical transport at the metal–CNT interface over the past decades. Nevertheless, there are still some challenges to be resolved before CNFET-based devices can be extensively used in a variety of applications. The most important challenges are reproducibility, predictability and long-term stability of device performance, as well as the feasibility of large-scale fabrication.

Comparing the performance of CNFETs obtained from the same fabrication batch, a large variation in the on-resistance was observed among thousands of devices [70]. The poor reproducibility of CNFET characteristics could be partially (but not entirely) explained by the variation in the CNT properties. Indeed, the current measured under the same conditions varies by nearly an order of magnitude for CNFETs fabricated using the same SWCNTs [82]. This suggests that the specific process steps during device fabrication, such as photo/e-beam resist contamination and the unclear effect caused by wet chemicals (developers, resist removers and etchants), affect the properties of SWCNTs. Therefore, the impact of the individual fabrication steps on SWCNT properties or the metal–SWCNT interface must be further investigated.

The long-term stability of CNFET transfer characteristics is another major concern for their applicability, which has been studied by several authors [83-85]. For devices with the Cr/Au (3 nm/20 nm) contacts, the electrical contacts were reported to be stable for 5 months without a passivation layer [83]. However, a contradictory observation was presented in [84], where severe degradation of electrical contact (Cr/Au: 2 nm/40 nm) was observed within a few days. The short lifetime of devices using Cr/Au (20 nm/75 nm) electrodes were reported in [85], where 92% of the devices did not function after 8 days. Even for the contact-passivated (by 1 μm PMMA) devices, 69% of them were not functional after a few days [85]. Without the passivation layer, the lifetime of devices using the same contact metals varies from a few months [41,83] to a few days [41,84]. Even for the passivated devices, the instability of CNFET performance was observed in [85,86]. The root cause of these seemingly contradictory results is unclear. It may be related to the different processes used for sample preparation or the inhomogeneity of SWCNT quality. This further highlights the necessity to clarify the factors influencing the stability of electrical contacts.

So far, the results presented in literature were mainly obtained from devices fabricated on the chip-scale. Results on wafer-scale fabrication are still lacking. Han et al. [87] have developed a process flow for wafer-scale CNFET fabrication, which is compatible with the current CMOS fabrication processes, but the SWCNTs require transfer to a target wafer. The physically and chemically induced impacts on the SWCNT properties which occur during the SWCNT transfer process must be further investigated. In particular, the organic contamination and gold etching issues must be examined. Park et al. [88] presented another wafer-level scalable process to disperse SWCNTs onto the pre-patterned substrate. A high density of SWCNTs were selectively deposited onto an array of HfO_2 trenches by using an ion exchange surface chemistry approach. Tens of thousands of CNFETs were fabricated on the chip level with 78% yield. Chikkadi et al. [89] introduced a photolithography-based scalable fabrication process which provides a good platform for investigating the uniformity of CNFET performance on a large scale. To further optimize the capability of the fabrication process, more statistical analysis on wafer-level fabrication is needed.

Conclusion

Both a theoretical understanding of the electrical transport in CNFETs and experimental techniques required for fabrication of high quality CNFETS with targeted characteristics have grown rapidly in recent years. Unlike for the case of planar contacts in Si-based devices, the Fermi level pinning effect at the metal–SWCNT interface is negligible. The Schottky barrier height at the metal–SWCNT contact can therefore be determined by selecting a metal with a suitable work function. So far, Pd is considered as the best metal for p-type CNFETs, owing to its high work function, good wettability to SWCNTs, as well as its stability in ambient conditions. Low work function metals were found to be extremely sensitive to oxidation, which leads to a low device yield. High-performance n-type CNFETs can be obtained by using Er as the contact material. The device yield can be largely improved by controlling the metal deposition conditions.

In addition to the choice of metal type, the CNFET performance can be further improved by annealing at modest temperatures, which may result in an improvement of the metal morphology or the formation of metal carbides at the contact interface. In the case of a solution-based SWCNT deposition onto metal electrodes, the annealing of the sample can reduce the amount of liquid residuals at the metal–SWCNT interface.

Another factor determining the metal–nanotube contact performance is the cleanliness of the metal–SWCNT interface. Using a protective layer to protect SWCNTs during the device fabrication helps to improve the contact performance.

The fabrication processes must be further optimized to improve the reproducibility and predictability of CNFETs to further their applicability. The critical factors which impact the long term stability of device performance must be clarified more precisely. The wafer-level fabrication processes require further development to promote CNFET-based applications, such as gas sensors and superior transistors with ultralow power consumption.

Acknowledgements

The financial support from Swiss COST-NanoTP (Project No.: C09.0156) is gratefully acknowledged. The authors highly appreciate the help from Prof. Vojislav Krstic (Trinity College Dublin) for his valuable suggestions about the Schottky barrier height measurement. Discussions with Kiran Chikkadi and Tobias Süss are also cordially acknowledged.

References

1. Yu, M.-F.; Files, B. S.; Arepalli, S.; Ruoff, R. S. *Phys. Rev. Lett.* **2000,** *84,* 5552–5555. doi:10.1103/PhysRevLett.84.5552
2. Krishnan, A.; Dujardin, E.; Ebbesen, T. W.; Yianilos, P. N.; Treacy, M. M. J. *Phys. Rev. B* **1998,** *58,* 14013–14019. doi:10.1103/PhysRevB.58.14013
3. Wang, M.-S.; Golberg, D.; Bando, Y. *Adv. Mater.* **2010,** *22,* 4071–4075. doi:10.1002/adma.201001463
4. Hone, J.; Whitney, M.; Piskoti, C.; Zettl, A. *Phys. Rev. B* **1999,** *59,* R2514–R2516. doi:10.1103/PhysRevB.59.R2514
5. Yao, Z.; Kane, C. L.; Dekker, C. *Phys. Rev. Lett.* **2000,** *84,* 2941–2944. doi:10.1103/PhysRevLett.84.2941
6. White, C. T.; Todorov, T. N. *Nature* **1998,** *393,* 240–242. doi:10.1038/30420
7. Kong, J.; Yenilmez, E.; Tombler, T. W.; Kim, W.; Dai, H. J.; Laughlin, R. B.; Liu, L.; Jayanthi, C. S.; Wu, S. Y. *Phys. Rev. Lett.* **2001,** *87,* 106801. doi:10.1103/PhysRevLett.87.106801
8. Appenzeller, J. *Proc. IEEE* **2008,** *96,* 201–211. doi:10.1109/Jproc.2007.911051
9. Franklin, A. D.; Luisier, M.; Han, S.-J.; Tulevski, G.; Breslin, C. M.; Gignac, L.; Lundstrom, M. S.; Haensch, W. *Nano Lett.* **2012,** *12,* 758–762. doi:10.1021/Nl203701g
10. Shulaker, M. M.; Hills, G.; Patil, N.; Wei, H.; Chen, H.-Y.; Philip Wong, H.-S.; Mitra, S. *Nature* **2013,** *501,* 526–530. doi:10.1038/Nature12502
11. Louie, S. G.; Cohen, M. L. *Phys. Rev. B* **1976,** *13,* 2461–2469. doi:10.1103/PhysRevB.13.2461
12. Heine, V. *Phys. Rev.* **1965,** *138,* 1689–1696. doi:10.1103/PhysRev.138.A1689
13. Cowley, A. M.; Sze, S. M. *J. Appl. Phys.* **1965,** *36,* 3212–3220. doi:10.1063/1.1702952
14. Léonard, F.; Tersoff, J. *Phys. Rev. Lett.* **2000,** *84,* 4693–4696. doi:10.1103/PhysRevLett.84.4693
15. Chen, Z.; Appenzeller, J.; Knoch, J.; Lin, Y.-m.; Avouris, P. *Nano Lett.* **2005,** *5,* 1497–1502. doi:10.1021/Nl0508624
16. Léonard, F.; Talin, A. A. *Phys. Rev. Lett.* **2006,** *97,* 026804. doi:10.1103/Physrevlett.97.026804
17. Nosho, Y.; Ohno, Y.; Kishimoto, S.; Mizutani, T. *Nanotechnology* **2006,** *17,* 3412–3415. doi:10.1088/0957-4484/17/14/011
18. Liu, P.; Sun, Q.; Zhu, F.; Liu, K.; Jiang, K.; Liu, L.; Li, Q.; Fan, S. *Nano Lett.* **2008,** *8,* 647–651. doi:10.1021/Nl0730817
19. Wildoer, J. W. G.; Venema, L. C.; Rinzler, A. G.; Smalley, R. E.; Dekker, C. *Nature* **1998,** *391,* 59–62. doi:10.1038/34139
20. Weisman, R. B.; Bachilo, S. M. *Nano Lett.* **2003,** *3,* 1235–1238. doi:10.1021/Nl034428i
21. Odom, T. W.; Huang, J.-L.; Kim, P.; Lieber, C. M. *J. Phys. Chem. B* **2000,** *104,* 2794–2809. doi:10.1021/Jp993592k
22. Appenzeller, J.; Radosavljević, M.; Knoch, J.; Avouris, P. *Phys. Rev. Lett.* **2004,** *92,* 048301. doi:10.1103/Physrevlett.92.048301
23. Appenzeller, J.; Knoch, J.; Derycke, V.; Martel, R.; Wind, S.; Avouris, P. *Phys. Rev. Lett.* **2002,** *89,* 126801. doi:10.1103/Physrevlett.89.126801
24. Franklin, A. D.; Chen, Z. *Nat. Nanotechnol.* **2010,** *5,* 858–862. doi:10.1038/Nnano.2010.220
25. Purewal, M. S.; Hong, B. H.; Ravi, A.; Chandra, B.; Hone, J.; Kim, P. *Phys. Rev. Lett.* **2007,** *98,* 186808. doi:10.1103/Physrevlett.98.186808
26. Gao, B.; Chen, Y. F.; Fuhrer, M. S.; Glattli, D. C.; Bachtold, A. *Phys. Rev. Lett.* **2005,** *95,* 196802. doi:10.1103/Physrevlett.95.196802
27. Mann, D.; Javey, A.; Kong, J.; Wang, Q.; Dai, H. J. *Nano Lett.* **2003,** *3,* 1541–1544. doi:10.1021/Nl034700o
28. Datta, S. *Quantum Transport: Atom to Transistor;* Cambridge University Press: Cambridge, U.K., 2005.
29. Freitag, M.; Tsang, J. C.; Bol, A.; Yuan, D.; Liu, J.; Avouris, P. *Nano Lett.* **2007,** *7,* 2037–2042. doi:10.1021/Nl070900e
30. He, Y.; Zhang, J.; Li, D.; Wang, J.; Wu, Q.; Wei, Y.; Zhang, L.; Wang, J.; Liu, P.; Li, Q.; Fan, S.; Jiang, K. *Nano Lett.* **2013,** *13,* 5556–5562. doi:10.1021/Nl403158x
31. Sze, S. M.; Kwok, K. N. *Physics of Semiconductor Devices;* John Willy & Sons: Hoboken, 2006.
32. Tseng, Y. C.; Bokor, J. *Appl. Phys. Lett.* **2010,** *96,* 013103.
33. Skákalová, V.; Kaiser, A. B.; Woo, Y.-S.; Roth, S. *Phys. Rev. B* **2006,** *74,* 085403. doi:10.1103/Physrevb.74.085403
34. Svensson, J.; Sourab, A. A.; Tarakanov, Y.; Lee, D. S.; Park, S. J.; Baek, S. J.; Park, Y. W.; Campbell, E. E. B. *Nanotechnology* **2009,** *20,* 175204. doi:10.1088/0957-4484/20/17/175204
35. Rhoderick, E. H. *IEE Proc., Part I: Solid-State Electron Devices* **1982,** *129,* 1–14. doi:10.1049/ip-i-1.1982.0001
36. Svensson, J.; Campbell, E. E. B. *J. Appl. Phys.* **2011,** *110,* 111101. doi:10.1063/1.3664139
37. Derycke, V.; Martel, R.; Appenzeller, J.; Avouris, P. *Appl. Phys. Lett.* **2002,** *80,* 2773–2775. doi:10.1063/1.1467702

38. Yamada, T. *Phys. Rev. B* **2004,** *69,* 125408. doi:10.1103/Physrevb.69.125408
39. Dockendorf, C. P. R.; Steinlin, M.; Poulikakos, D.; Choi, T.-Y. *Appl. Phys. Lett.* **2007,** *90,* 193116. doi:10.1063/1.2737821
40. Kanbara, T.; Takenobu, T.; Takahashi, T.; Iwasa, Y.; Tsukagoshi, K.; Aoyagi, Y.; Kataura, H. *Appl. Phys. Lett.* **2006,** *88,* 053118. doi:10.1063/1.2171481
41. Lee, J.-O.; Park, C.; Kim, J.-J.; Kim, J.; Park, J. W.; Yoo, K.-H. *J. Phys. D: Appl. Phys.* **2000,** *33,* 1953–1956. doi:10.1088/0022-3727/33/16/303
42. Ebbesen, T. W.; Lezec, H. J.; Hiura, H.; Bennett, J. W.; Ghaemi, H. F.; Thio, T. *Nature* **1996,** *382,* 54–56. doi:10.1038/382054a0
43. Cha, J. J.; Weyland, M.; Briere, J.-F.; Daykov, I. P.; Arias, T. A.; Muller, D. A. *Nano Lett.* **2007,** *7,* 3770–3773. doi:10.1021/Nl072251c
44. Bockrath, M.; Cobden, D. H.; Lu, J.; Rinzler, A. G.; Smalley, R. E.; Balents, L.; McEuen, P. L. *Nature* **1999,** *397,* 598–601. doi:10.1038/17569
45. Bezryadin, A.; Verschueren, A. R. M.; Tans, S. J.; Dekker, C. *Phys. Rev. Lett.* **1998,** *80,* 4036–4039. doi:10.1103/PhysRevLett.80.4036
46. Dai, H.; Wong, E. W.; Lieber, C. M. *Science* **1996,** *272,* 523–526. doi:10.1126/science.272.5261.523
47. Berger, H. H. *Solid-State Electron.* **1972,** *15,* 145–158. doi:10.1016/0038-1101(72)90048-2
48. Nosho, Y.; Ohno, Y.; Kishimoto, S.; Mizutani, T. *Jpn. J. Appl. Phys.* **2007,** *46,* L474–L476. doi:10.1143/Jjap.46.L474
49. Matsuda, Y.; Deng, W.-Q.; Goddard, W. A. *J. Phys. Chem. C* **2010,** *114,* 17845–17850. doi:10.1021/Jp806437y
50. Zhang, Y.; Ichihashi, T.; Landree, E.; Nihey, F.; Iijima, S. *Science* **1999,** *285,* 1719–1722. doi:10.1126/science.285.5434.1719
51. Yokoyama, D.; Iwasaki, T.; Yoshida, T.; Kawarada, H.; Sato, S.; Hyakushima, T.; Nihei, M.; Awano, Y. *Appl. Phys. Lett.* **2007,** *91,* 263101. doi:10.1063/1.2824390
52. Heinze, S.; Tersoff, J.; Martel, R.; Derycke, V.; Appenzeller, J.; Avouris, P. *Phys. Rev. Lett.* **2002,** *89,* 106801. doi:10.1103/Physrevlett.89.106801
53. Muoth, M.; Helbling, T.; Durrer, L.; Lee, S.-W.; Roman, C.; Hierold, C. *Nat. Nanotechnol.* **2010,** *5,* 589–592. doi:10.1038/Nnano.2010.129
54. Zhang, Z.; Liang, X.; Wang, S.; Yao, K.; Hu, Y.; Zhu, Y.; Chen, Q.; Zhou, W.; Li, Y.; Yao, Y.; Zhang, J.; Peng, L.-M. *Nano Lett.* **2007,** *7,* 3603–3607. doi:10.1021/Nl0717107
55. Shahrjerdi, D.; Franklin, A. D.; Oida, S.; Ott, J. A.; Tulevski, G. S.; Haensch, W. *ACS Nano* **2013,** *7,* 8303–8308. doi:10.1021/Nn403935v
56. Javey, A.; Guo, J.; Wang, Q.; Lundstrom, M.; Dai, H. *Nature* **2003,** *424,* 654–657. doi:10.1038/nature01797
57. Zhang, Y.; Dai, H. *Appl. Phys. Lett.* **2000,** *77,* 3015–3017. doi:10.1063/1.1324731
58. Lim, S. C.; Jang, J. H.; Bae, D. J.; Han, G. H.; Lee, S.; Yeo, I.-S.; Lee, Y. H. *Appl. Phys. Lett.* **2009,** *95,* 264103. doi:10.1063/1.3255016
59. Maiti, A.; Ricca, A. *Chem. Phys. Lett.* **2004,** *395,* 7–11. doi:10.1016/j.cplett.2004.07.024
60. Lee, S.; Kahng, S.-J.; Kuk, Y. *Chem. Phys. Lett.* **2010,** *500,* 82–85. doi:10.1016/j.cplett.2010.09.082
61. Manohara, H. M.; Wong, E. W.; Schlecht, E.; Hunt, B. D.; Siegel, P. H. *Nano Lett.* **2005,** *5,* 1469–1474. doi:10.1021/Nl050829h
62. Felten, A.; Suarez-Martinez, I.; Ke, X.; Van Tendeloo, G.; Ghijsen, J.; Pireaux, J.-J.; Drube, W.; Bittencourt, C.; Ewels, C. P. *ChemPhysChem* **2009,** *10,* 1799–1804. doi:10.1002/cphc.200900193
63. Michaelson, H. B. *J. Appl. Phys.* **1977,** *48,* 4729–4733. doi:10.1063/1.323539
64. Chai, Y.; Hazeghi, A.; Takei, K.; Chen, H.-Y.; Chan, P. C. H.; Javey, A.; Wong, H.-S. P. *IEEE Trans. Electron Devices* **2012,** *59,* 12–19. doi:10.1109/Ted.2011.2170216
65. Kane, A. A.; Sheps, T.; Branigan, E. T.; Apkarian, V. A.; Cheng, M. H.; Hemminger, J. C.; Hunt, S. R.; Collins, P. G. *Nano Lett.* **2009,** *9,* 3586–3591. doi:10.1021/Nl9017995
66. Macintyre, D. S.; Ignatova, O.; Thoms, S.; Thayne, I. G. *J. Vac. Sci. Technol., B* **2009,** *27,* 2597–2601. doi:10.1116/1.3243176
67. Felten, A.; Bittencourt, C.; Pireaux, J. J.; Van Lier, G.; Charlier, J. C. *J. Appl. Phys.* **2005,** *98,* 074308. doi:10.1063/1.2071455
68. Kim, Y. L.; Jung, H. Y.; Kar, S.; Jung, Y. J. *Carbon* **2011,** *49,* 2450–2458. doi:10.1016/j.carbon.2011.02.013
69. Döring, V.; Süss, T.; Hierold, C. *Sens. Actuators, A* **2014,** *208,* 152–158. doi:10.1016/j.sna.2013.12.034
70. Khamis, S. M.; Jones, R. A.; Johnson, A. T. C. *AIP Adv.* **2011,** *1,* 022106. doi:10.1063/1.3582820
71. Liu, W.; Chikkadi, K.; Lee, S.-W.; Hierold, C.; Haluska, M. *Sens. Actuators, B* **2014,** *198,* 479–486. doi:10.1016/j.snb.2014.03.039
72. Vazquez-Mena, O.; Villanueva, G.; Savu, V.; Sidler, K.; van den Boogaart, M. A. F.; Brugger, J. *Nano Lett.* **2008,** *8,* 3675–3682. doi:10.1021/Nl801778t
73. Yaish, Y.; Park, J.-Y.; Rosenblatt, S.; Sazonova, V.; Brink, M.; McEuen, P. L. *Phys. Rev. Lett.* **2004,** *92,* 046401. doi:10.1103/Physrevlett.92.046401
74. Kane, A. A.; Loutherback, K.; Goldsmith, B. R.; Collins, P. G. *Appl. Phys. Lett.* **2008,** *92,* 083506. doi:10.1063/1.2885092
75. Tomimoto, H.; Nakayama, T. *Jpn. J. Appl. Phys.* **2010,** *49,* 035002. doi:10.1143/Jjap.49.035002
76. Martel, R.; Derycke, V.; Lavoie, C.; Appenzeller, J.; Chan, K. K.; Tersoff, J.; Avouris, P. *Phys. Rev. Lett.* **2001,** *87,* 256805. doi:10.1103/Physrevlett.87.256805
77. Moody, N. R.; Adams, D. P.; Medlin, D.; Headley, T.; Yang, N.; Volinsky, A. *Int. J. Fract.* **2003,** *119,* 407–419. doi:10.1023/A:1024979829573
78. Samavat, F.; Ahmad, P. T.; Mahmoodi, F.; Samavat, M. F.; Tavakoli, M. H. *Am. J. Condens. Matter Phys.* **2012,** *2,* 73–76. doi:10.5923/j.ajcmp.20120203.04
79. Maki, H.; Suzuki, M.; Ishibashi, K. *Jpn. J. Appl. Phys.* **2004,** *43,* 2027–2030. doi:10.1143/Jjap.43.2027
80. Dong, L.; Youkey, S.; Bush, J.; Jiao, J.; Dubin, V. M.; Chebiam, R. V. *J. Appl. Phys.* **2007,** *101,* 024320. doi:10.1063/1.2430769
81. Woo, Y.; Duesberg, G. S.; Roth, S. *Nanotechnology* **2007,** *18,* 095203. doi:10.1088/0957-4484/18/9/095203
82. Zhang, X.; Chenet, D.; Kim, B.; Yu, J.; Tang, J. Z.; Nuckolls, C.; Hone, J. *J. Vac. Sci. Technol., B* **2013,** *31,* 06FI01. doi:10.1116/1.4820903
83. Pisana, S.; Zhang, C.; Ducati, C.; Hofmann, S.; Robertson, J. *IEEE Trans. Nanotechnol.* **2008,** *7,* 458–462. doi:10.1109/Tnano.2008.917849
84. Helbling, T.; Hierold, C.; Roman, C.; Durrer, L.; Mattmann, M.; Bright, V. M. *Nanotechnology* **2009,** *20,* 434010. doi:10.1088/0957-4484/20/43/434010
85. Crockett, L. Carbon Nanotube Transistor Fabrication and Reliability Characterization. *National Nanotechnology Infrastructure Network Research Experience for Undergraduates Program;* University of California: Santa Barbara, 2007; pp 46–47.
86. Rispal, L.; Tschischke, T.; Yang, H.; Schwalke, U. *Jpn. J. Appl. Phys.* **2008,** *47,* 3287–3291. doi:10.1143/Jjap.47.3287

87. Han, S.-J.; Chang, J.; Franklin, A. D.; Bol, A. A.; Loesing, R.; Guo, D.; Tulevski, G. S.; Haensch, W.; Chen, Z. Wafer scale fabrication of carbon nanotube FETs with embedded poly-gates. IEEE nternational Electron Devices Meeting, San Francisco, CA, Dec 6–8, 2010; 9.1.1–9.1.4. doi:10.1109/IEDM.2010.5703326
88. Park, H.; Afzali, A.; Han, S.-J.; Tulevski, G. S.; Franklin, A. D.; Tersoff, J.; Hannon, J. B.; Haensch, W. *Nat. Nanotechnol.* **2012,** *7,* 787–791. doi:10.1038/Nnano.2012.189
89. Chikkadi, K.; Roman, C.; Durrer, L.; Süss, T.; Pohle, R.; Hierold, C. *Procedia Eng.* **2012,** *47,* 1374–1377. doi:10.1016/j.proeng.2012.09.412

License and Terms

This is an Open Access article under the terms of the Creative Commons Attribution License (http://creativecommons.org/licenses/by/2.0), which permits unrestricted use, distribution, and reproduction in any medium, provided the original work is properly cited.

The license is subject to the *Beilstein Journal of Nanotechnology* terms and conditions: (http://www.beilstein-journals.org/bjnano)

The definitive version of this article is the electronic one which can be found at: doi:10.3762/bjnano.5.229

BEILSTEIN JOURNAL OF NANOTECHNOLOGY

Localized surface plasmon resonances in nanostructures to enhance nonlinear vibrational spectroscopies: towards an astonishing molecular sensitivity

Dan Lis* and Francesca Cecchet*

Review

Open Access

Address:
Research Centre in Physics of Matter and Radiation (PMR), University of Namur (UNamur), 61 rue de Bruxelles, B-5000 Namur, Belgium

Email:
Dan Lis* - dan.lis@unamur.be; Francesca Cecchet* - francesca.cecchet@unamur.be

* Corresponding author

Keywords:
coherent anti-Stokes Raman scattering (CARS); nonlinear optical spectroscopies; sum-frequency generation (SFG); surfaces plasmon resonance; vibrational spectroscopies

Beilstein J. Nanotechnol. **2014,** *5,* 2275–2292.
doi:10.3762/bjnano.5.237

Received: 02 June 2014
Accepted: 04 November 2014
Published: 28 November 2014

This article is part of the Thematic Series "Atomic scale interface design and characterisation: Experimental aspects and methods".

Guest Editor: C. Bittencourt

© 2014 Lis and Cecchet; licensee Beilstein-Institut.
License and terms: see end of document.

Abstract

Vibrational transitions contain some of the richest fingerprints of molecules and materials, providing considerable physicochemical information. Vibrational transitions can be characterized by different spectroscopies, and alternatively by several imaging techniques enabling to reach sub-microscopic spatial resolution. In a quest to always push forward the detection limit and to lower the number of needed vibrational oscillators to get a reliable signal or imaging contrast, surface plasmon resonances (SPR) are extensively used to increase the local field close to the oscillators. Another approach is based on maximizing the collective response of the excited vibrational oscillators through molecular coherence. Both features are often naturally combined in vibrational nonlinear optical techniques. In this frame, this paper reviews the main achievements of the two most common vibrational nonlinear optical spectroscopies, namely surface-enhanced sum-frequency generation (SE-SFG) and surface-enhanced coherent anti-Stokes Raman scattering (SE-CARS). They can be considered as the nonlinear counterpart and/or combination of the linear surface-enhanced infrared absorption (SEIRA) and surface-enhanced Raman scattering (SERS) techniques, respectively, which are themselves a branching of the conventional IR and spontaneous Raman spectroscopies. Compared to their linear equivalent, those nonlinear vibrational spectroscopies have proved to reach higher sensitivity down to the single molecule level, opening the way to astonishing perspectives for molecular analysis.

Review

1. Introduction – linear vibrational spectroscopies

A widespread approach in molecular analysis relies on the vibrational fingerprint of matter to obtain an intrinsic chemical selectivity, and to identify specific molecules with no added labels. The two major techniques that have dominated for a long time in this field are infrared (IR) spectroscopy and spontaneous (incoherent) Raman scattering. In IR spectroscopy, IR radiation is absorbed by matter at specific frequencies matching the energy gap between vibrational states (Figure 1). Physically, it corresponds to oscillators presenting a variation of the dipole moment. In fine, the transmitted or reflected beam intensity is reduced because of the light absorption. In spontaneous Raman spectroscopy, a monochromatic visible (vis) radiation interacts with the investigated medium. Most of the illuminating light is scattered, reflected, and transmitted at the same frequency as the illumination. However, a small portion of light undergoes a change in energy during the scattering process. The energy difference between the illumination and the scattered frequencies matches a transition between vibrational states and is associated to oscillators owing a variation of polarisability: $\omega_{Raman} = \omega_{vis} \pm \Delta\omega$. The shift in frequency towards the lower energy is defined as the Stokes Raman line, while the shift toward higher energy is the anti-Stokes Raman line (Figure 1).

In the frame of molecular detection at surfaces (i.e., molecular films on solid substrates), IR and Raman spectroscopies have often suffered from a lack of sensitivity due to the reduced number of oscillators in thin films on surfaces compared to bulk materials. Therefore, to make vibrational techniques more efficient for surface science purposes, many efforts have been made to increase the surface sensitivity of IR and Raman spectroscopies. For instance, from IR spectroscopy is born polarization-modulation IR reflection–absorption spectroscopy (PM-IRRAS) [1], and surface-enhanced infrared absorption (SEIRA), the latter relying on the use of surface plasmon resonances in the near-mid IR range [2]. Similarly, plasmon resonances have been used in the visible range to boost the sensitivity of Raman spectroscopy as well, in the so-called surface-enhanced Raman scattering (SERS). Indeed, spontaneous Raman scattering possesses an intrinsically weak cross section, typically lower than one Raman photon over 10^{18} [3]. However, the paths of development of SEIRA and SERS have been rather different. The success of SEIRA remains uncertain because of the limited bandwidth of plasmon resonances that makes the amplification irregular over a broad frequency window, and because of the restricted choice of efficient plasmonic materials over the extended IR range [2,4-6]. More successfully, the coupling with plasmon resonances has enhanced the Raman signal by a factor of up to 10^{12} [7]. This is possible thanks to the strong electromagnetic (EM) field amplification achieved with surface plasmon resonances, especially when the field is confined in nanometric metallic structures under the form of a localized surface plasmon resonance (LSPR) [8-16].

Up to now, a very high molecular surface sensitivity has been reached with SERS (and to a lesser extent with SEIRA),

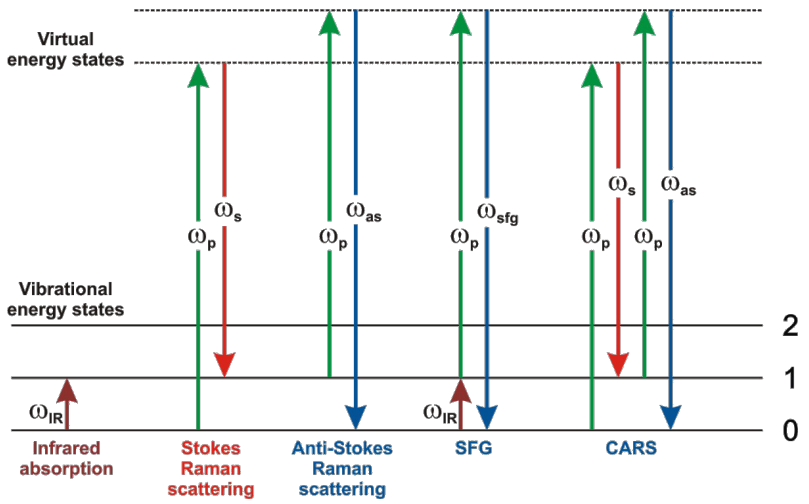

Figure 1: Photon diagrams for different linear and nonlinear optical processes. Solid horizontal lines are real vibrational energy states of matter, while dashed lines are virtual states. Upward pointing arrows correspond to incoming photons that lead to an excitation of matter, while downward pointing arrows correspond to emitted photons that relax the energy excitation of matter. The optical processes depicted here are linear infrared, spontaneous Stokes and anti-Stokes Raman, nonlinear sum-frequency generation, and coherent anti-Stokes Raman transitions, from left to right.

offering incredible perspectives in various fields, especially in nano-biosciences [2] in which probing tissues at the molecular level has allowed for a deeper understanding of biological properties and behaviours, and has opened the way to fascinating biomedical and biotechnological applications of single molecules and nanomaterials [7,17-20]. This success is mostly due to the electromagnetic near-field enhancement achieved thanks to more and more sophisticated nanostructures and laser sources, coupled with efficient acquisition methods.

A step forward has been achieved with nonlinear optics. Indeed, while SERS and SEIRA intrinsically possess a linear dependence on the incident laser power, nonlinear optical phenomena, instead, may benefit from a power-law relationship. Moreover, besides strict EM field intensity concerns, additional features can offer incontestable advantages, such as exploiting the molecular coherence that improves the spectroscopic yield. Many nonlinear optical processes intrinsically exhibit such coherence and are good candidates to push forward the sensitivity of vibrational spectroscopies. Within the limited number of nonlinear vibrational spectroscopies, this review will specifically focus on surface-enhanced sum-frequency generation (SE-SFG) and surface-enhanced coherent anti-Stokes Raman scattering (SE-CARS) to highlight the advantageous combination of their coherent nature with their surface-enhanced potentialities.

2. Nonlinear vibrational spectroscopies – SFG and CARS principles and properties

Sum-frequency generation (SFG) is a second-order nonlinear optical process in which an IR absorption is coupled to an anti-Stokes Raman process within a coherent three-wave mixing mechanism (Figure 1) [21-23]. Commonly, it is performed by focussing simultaneously one visible beam ω_{vis} and one infrared beam ω_{IR} on the interface to be probed (Figure 2a and Figure 2b). When the infrared frequency ω_{IR} matches an IR active vibrational transition, it drives all resonant oscillators in the probed volume to vibrate at that frequency. If the molecular vibration is Raman active as well, the infrared transition further interacts coherently with the visible field to drive the resonant oscillators at the sum-frequency $\omega_{SFG} = \omega_{vis} + \omega_{IR}$. Thanks to the very high electric field achieved with pulsed laser sources, the illuminated medium is thus polarized in a nonlinear regime and able to reemit electromagnetic waves at the SFG frequency. Being a hybrid mechanism that shares infrared and Raman activities, SFG adds up both selection rules, making it selective to a reduced number of vibrational transitions which however contain much physicochemical information about the molecular interfaces. Indeed, the analysis of the SFG signatures can provide quantitative information about the molecular orientation, and very sensitive information about the environment close to the interface from which many local properties can be deduced. Distinctly, coherent anti-Stokes Raman scattering (CARS) is a third-order optical process coupling both Stokes Raman and anti-Stokes Raman processes within a coherent four-wave mixing mechanism (Figure 1) [24,25]. It is performed by simultaneously mixing three distinct photons at two different frequencies ω_p and ω_s in the medium (see Figure 2c and Figure 2d). The pump beam ω_p and the Stokes beam ω_s interact with matter and lead to a coherent excitation of all resonant oscillators in the probed volume at the beat frequency $\omega_p - \omega_s$ (Figure 2e). If this frequency matches a Raman active molecular vibration, the Stokes emission interacts coherently with the pump beam to drive the resonant oscillators at the anti-Stokes frequency $\omega_{as} = 2\omega_p - \omega_s$. This leads to the emission of a CARS photon at the anti-Stokes frequency. Because CARS is based on Stokes and anti-Stokes processes, it inherits the Raman selection rules [3,4]. It is noteworthy that when using the same laser source for the visible beam in SFG and for the pump beam in CARS, a given vibrational mode at $\omega_{IR} = \omega_p - \omega_s$ will lead to the emission of identical photons for both SFG and CARS, at a frequency $\omega_{vis/p} + \omega_{IR}$ (see Figure 1).

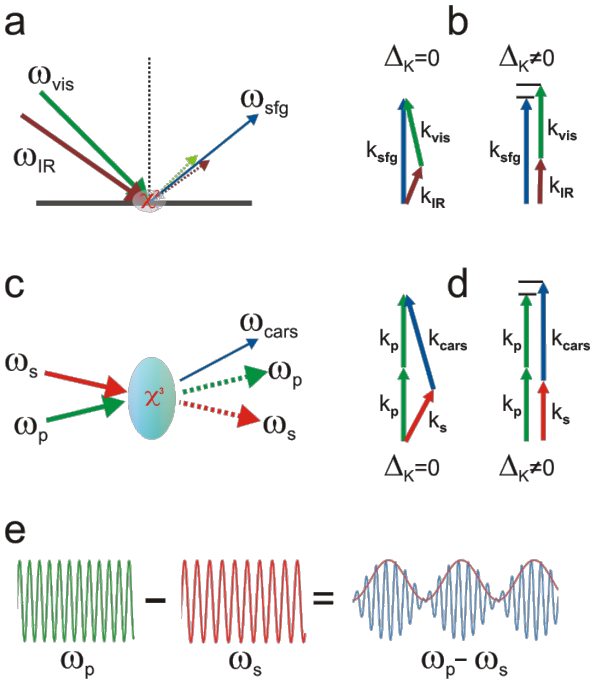

Figure 2: (a) Schematic representation of SFG spectroscopy in a reflection configuration on a surface. (b) The momentum conservation promotes the collinear geometry to fulfil the phase-matching condition (this condition is however relaxed for interfacial SFG). (c) Schematic representation of CARS spectroscopy performed in the bulk phase. (d) The momentum conservation requires the non-collinear geometry to be adopted to fulfil the phase-matching condition. (e) Generation of a beat frequency between the pump and the Stokes waves.

The macroscopic polarization of the matter at the SFG and CARS frequencies results from the nonlinear interaction of the visible (ω_{vis}) with the infrared (ω_{IR}) fields, and the pump (ω_p) with the Stokes (ω_s) fields, respectively:

$$P_i^{(2)}\left(\omega_{SFG}\right) \propto \chi_{ijk}^{(2)} E_j\left(\omega_{\text{vis}}\right) E_k\left(\omega_{\text{IR}}\right),$$

$$P_i^{(3)}\left(\omega_{\text{as}}\right) \propto \chi_{ijkl}^{(3)} E_j\left(\omega_{\text{p}}\right) E_k\left(\omega_{\text{p}}\right) E_l\left(\omega_{\text{s}}\right),$$

where $\chi_{ijk}^{(2)}$ and $\chi_{ijkl}^{(3)}$ are the tensors of the second-order and third-order electrical susceptibility of the probed matter, respectively.

Two terms contribute to the measured SFG or CARS signal. The first one is referred to as the resonant term, and occurs whenever the infrared frequency ω_{IR} matches an active vibrational transition in a SFG experiment, or when the beat frequency $\omega_p - \omega_s$ matches a Raman active vibration in a CARS experiment. This term gives rise to a signal corresponding to the amplitude of the vibrational mode. However, even far from any vibrational transition, a residual SFG or CARS intensity can be measured as well. This non-resonant term, which may be significant, is considered as a background signal, and origins from electronic contributions either from the substrate and/or from the molecular adsorbate [3,24-28]. Thus, the electrical susceptibility tensors are described as:

$$\begin{aligned}\chi_{ijk}^{(2)} &= \chi_{ijk\ (\text{NR})}^{(2)} + \chi_{ijk\ (\text{R})}^{(2)} \\ &= \left|A_{ijk\ (\text{NR})}\right| e^{i\phi} + \sum_q \frac{\left|A_{ijk\ (q)}\right|}{\omega_q - \omega_{\text{IR}} - i\Gamma_q},\end{aligned}$$

$$\begin{aligned}\chi_{ijkl}^{(3)} &= \chi_{ijkl\ (\text{NR})}^{(3)} + \chi_{ijkl\ (\text{R})}^{(3)} \\ &= \left|A_{ijkl\ (NR)}\right| e^{i\phi} + \sum_q \frac{\left|A_{ijkl\ (q)}\right|}{\omega_q - \left(\omega_{\text{p}} - \omega_{\text{S}}\right) - i\Gamma_q},\end{aligned}$$

where $A_{ijk(l)\ (\text{NR})}$ and ϕ are the non-resonant amplitudes and phase; $A_{ijk(l)\ (q)}$, Γ_q and ω_q are the oscillator strength, the damping factor and the vibrational frequency of the q-th vibrational mode; ω_{IR}, ω_p and ω_S are the infrared, the pump and the Stokes beam frequencies. The oscillator strengths in SFG and CARS are defined as follows:

$$\left|A_{ijk\ (q)}\right| \propto N \sum_{lmn} \left\langle T_{lmn}^{ijk} \right\rangle \beta_{lmn}^{(2)},$$

$$\left|A_{ijkl\ (q)}\right| \propto N \sum_{mnop} \left\langle T_{mnop}^{ijkl} \right\rangle \beta_{mnop}^{(3)},$$

where N is the density number of involved individual oscillators, the brackets indicate the average over the molecular orientation distribution, T links the microscopic coordinates to the macroscopic ones through the Euler transformation, and $\beta^{(2)}$ and $\beta^{(3)}$ are the second and third order hyperpolarizability tensors, respectively. More details can be found in the literature [21,26,29-32].

The intensities of the SFG and CARS signals are given by:

$$I_{\text{SFG}} \propto \left|\chi^{(2)}\right|^2 I_{\text{vis}}\, I_{\text{IR}}\, L^2\ \sin c^2\left(\frac{\Delta kL}{2}\right),$$

$$I_{\text{CARS}} \propto \left|\chi^{(3)}\right|^2 I_{\text{p}}^2\, I_{\text{S}}\, L^2\ \sin c^2\left(\frac{\Delta kL}{2}\right),$$

where L is the length over which the beams are mixed through the sample, $\sin c(x) = \sin(x)/x$, and Δk is the momentum mismatch. For SFG, $\Delta k_{SFG} = k_{SFG} - k_{vis} - k_{IR}$, while for CARS $\Delta k_{CARS} = k_{AS} - (2k_p - k_S)$. Since $|k| = n\omega/c$, and because the energy conservation imposes that $\omega_{AS} - (2\omega_p - \omega_S) = 0$ and $\omega_{SFG} - \omega_{vis} - \omega_{IR} = 0$, the distinct refractive indexes n resulting from the medium dispersion over the distinct propagating wave frequencies, promote to fulfil the phase matching condition $\Delta k = 0$ in a collinear geometry (see Figure 2b and Figure 2d). Therefore, specific beam propagation angles have to be set to achieve the phase matching and ensure an optimal energy transfer from the incident beams to the nonlinear radiation over L [3,24]. However, for both SFG and CARS spectroscopies, this phase matching condition is relaxed under specific conditions.

Indeed, the $\chi^{(2)}$ tensor equals to zero in any centro-symmetric medium within the frame of the dipolar approximation, making the SFG photons to be generated only where the centro-symmetry is broken. Therefore, aside birefringent bulk materials, the SFG signal is commonly emitted from interfaces, such as thin films on surfaces (Figure 2a). The thickness of the emission region is thus much smaller than the coherence length ($l_c = 1/\Delta k$) which is usually larger than one micron. Basically, the SFG output intensity increases nearly quadratic with the probed film thickness irrespective of the propagative angles of the laser [21]. The conservation of momentum is however applicable and determines the emission direction of the SFG in the form of a collimated beam.

Likewise, although CARS is sensitive to the bulk, it has been shown that with tightly focused laser beams, the interaction volume is rather limited and can reach dimensions smaller than

the coherence length ($l_c = 1/\Delta k$). The medium dispersion is thus unable to lead to a significant phase mismatch whatever the configuration [3,26,33]. This allows one to adopt either the backward- or forward-generated CARS geometry with collinear pump and Stokes beams, as largely exploited for CARS imaging with the use of commercial confocal scanning microscopes [34].

In terms of intensity, SFG scales linearly with the intensities of the infrared and of the visible beam, respectively, while CARS is proportional to the intensity of the Stokes beam and to the square of the pump beam intensities. Both of them scale with the square of the density number of oscillators, N^2, in the probed volume. Interestingly, with N being a density number (oscillators per volume), and L defining the probed volume length, both SFG and CARS actually scale with the square of the oscillator surface density.

Overall, the intrinsic properties and the selection rules of SFG and CARS spectroscopies make them highly competitive with their linear counterparts regarding the sensitivity and the ability to deduce fine physicochemical information. Overall, the relative superiority of SFG and CARS derives from several factors: i) the molecular coherence that ensures a much higher conversion efficiency; ii) the emission directionality; iii) the power-law dependence of the intensities of SFG and CARS on the total incident power; iv) the square dependence of the SFG and CARS intensities on the resonant oscillators density N^2; v) the blue-shifted conversion processes, which avoid any interference with fluorescence, and vi) the overall higher spatial resolution from up-frequency conversion, both lateral and for 3D layering.

Based on those arguments, on the one hand SFG, being a spectroscopy method specific to interfaces, it possesses a very high surface sensitivity and has proved to be able to provide the vibrational signature of sub-monolayer coverages [35] as well as unique orientational information about molecules at interfaces [36-47]. On the other hand, CARS has enabled rapid tissue imaging in biomedical applications. Proper image contrast can be obtained with CARS microscopy within one second and with a concentration contrast weaker than 10^6 CH_2 oscillators in the probed volume, corresponding to several 10^4 lipid molecules, which are easily achieved in lipid-rich structures [3,48,49]. Nowadays, SFG and CARS techniques are established vibrational spectroscopies, overall more sensitive than conventional linear IR or spontaneous Raman spectroscopies.

To push forward the performance of both techniques, the coupling of the molecular coherence and power-law intensity dependence with the near-field enhancement from surface plasmon resonance has been initiated, and some demonstrations of an extreme sensitivity for the study and detection of surface molecules have already been given. Since both SFG and CARS mechanisms deal with visible photons, they represent ideal candidates to obtain large intensity gains from surface-enhanced (SE) mechanisms in metallic nanostructures, alike to SERS. Basically, the surface-enhanced SE-SFG and SE-CARS signals become stronger if any of the photons involved in the wave mixing process is in resonance with a SPR. Ideally, to reach the highest enhancements, all involved photons should be in resonance with the nanostructure plasmon resonances simultaneously. Similarly to SERS, this is partially achievable for low frequency vibrational bands that keep the visible and SFG radiation, or the Stokes, the pump and the CARS radiation, close to each other in frequency. However, high frequency vibrational bands spread away the different involved visible frequencies. Since it is difficult to tailor metallic nanostructures that can support very broad or multi-frequency resonances, only partial and limited plasmonic oscillations are usually obtained. Therefore, though very high theoretical enhancements have been predicted (up to 10^{12} for SE-CARS [50]), this is barely reproduced in experiments. As we will show in detail in this review, up to now, the best enhancement reported equals 10^5 for SE-SFG, and reaches 10^7 with SE-CARS, by comparison with the conventional SFG and CARS, respectively.

3 Localized surface plasmon resonance in nanostructures

As mentioned earlier, the intensity of the nonlinear conversion process can be amplified if the electric field is enhanced at least at one wave-mixing frequency, and more successfully if all fields are simultaneously enhanced. Therefore, the coupling of SFG and CARS spectroscopies with surface-enhanced fields has begun to be investigated, in particular by using propagating surface plasmon polaritons (SPP) in thin metal sheets and localized surface plasmon resonances in metal nanostructures.

SPP refers to the possibility of propagating an electromagnetic wave within a very thin metallic interface [51-53]. The propagating plasmon wave possesses a momentum $k_{sp(x)}$ which is purely directed along the interface. Its excitation requires using light that has a momentum component k_x equal to $k_{sp(x)}$. Because in air k_x is smaller than $k_{sp(x)}$, a dispersive material with a higher refractive index is commonly used as coupling medium to increase the incident light wave vector and fulfil $k_x = k_{sp(x)}$. In practical devices, a prism-metal interface is employed (Figure 3a). The incident angle of the excitation light can be precisely adjusted to phase-match both wave vectors along the interface and propagate the EM field through the SPP.

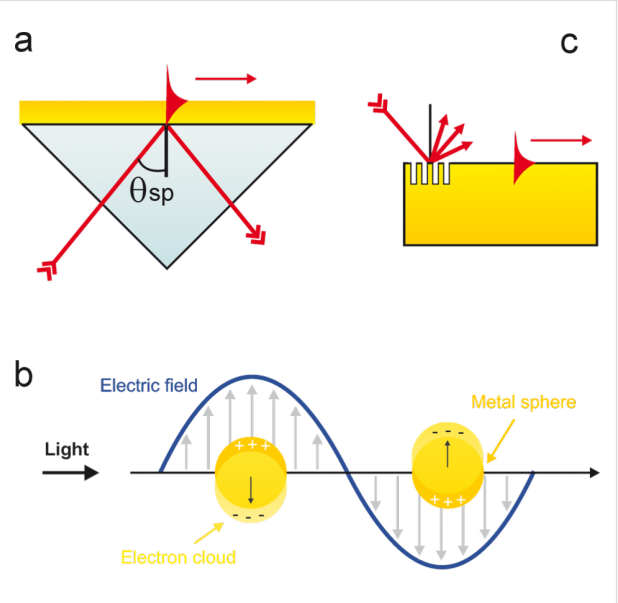

Figure 3: (a) Schematic representation of a SPP excitation (Kretschmann configuration) in which the plasmon mode propagates into a metal film adjacent to a prism. The incident angle should be accurately chosen so as to phase-match the momentums of the illuminated light and the SPP. (b) The excitation of a LSPR in nanoparticles confines the light energy into sub-wavelength volume, leading to strongly enhanced local electromagnetic field. (c) The excitation of a SPP can be coupled with the light diffraction on a grating.

While the local field amplification (denoted as g) can reach up to 100 times with SPP, it may goes up to 1000 times when condensing the metal sheet into nanostructures, e.g., virtually rolling it up into wires, or folding it into spheres [6]. Such strong local field amplification arises from the tridimensional shrinkage of the material into nanometric dimensions, which confines the EM field into sub-wavelength volumes (Figure 3b). Since the field is not propagating anymore but is well localized, the momentum matching condition is not required any longer. The LSPR can thus be excited by a simple reflection without considering dispersion issues. The only excitation condition is now the rigorous matching of the LSPR frequency, and eventually the use of adequate light polarization. Note that such external excitation of a LSPR can be used to funnel the SPR into a propagative mode in a metal sheet, thanks to diffraction, without considering the dispersion issue. This is currently achieved by using a metallic grating in external reflection geometry (Figure 3c).

The strong EM field enhancements g achieved with noble metal nanostructures have been extensively exploited in SERS. While the SERS intensity is proportional to $|g|^2 \cdot |E_0|^2 = |g|^2 \cdot I_0$, the specific case in which both the incident and scattered fields are in resonance with a (broad) plasmon mode makes the SERS intensity to scale up with $|g|^4 \cdot I_0$, leading to an enhancement factor of 10^{12}. Accordingly, LSPR represents the most commonly used technique for state of the art surface-enhanced spectroscopies.

The frequency of the LSPR spectral peak is very sensitive to the nanostructure environment through the local refractive index. Thereby, shifts of the LSPR frequency are widely used as a method for detecting molecular interaction close to the surface of the nanoparticle [54-58]. Besides, the near-field enhancement has led to a very large variety of advances in many fundamental and applied areas of science. Large boosts in the sensitivity and intensity have been reported for a very wide variety of nanoparticle shapes, dimensions and compositions, which altogether define the light absorbance, and so the LSPR spectral peak. As shown in Figure 4, depending on those parameters, the resonance frequency can be tuned over all the visible and near-infrared ranges [9-12,15]. For example, gold nanorods (Figure 4a) present two plasmon resonances, a transverse one around 515 nm which weakly depends on the aspect ratio of the rod, and a longitudinal mode which is strongly red-shifted with increasing aspect ratio (Figure 4b). Similarly, gold octahedra (Figure 4c) display a plasmon mode highly red-shifted for increasing dimensions (Figure 4d).

Figure 5 shows the nonlinear emission of a rectangular gold nanowire illuminated simultaneously with two laser pulses at ω_1 = 817 nm and ω_2 = 1064 nm [32,59]. The blue spectrum plots the collected light intensity with an incident light polarization perpendicular to the wire axis, matching therefore the transverse LSPR mode of the wire. The red curve is for a light polarization parallel to the wire. The collected nonlinear response is purely non-resonant (electronic) and appears as a broad emission from the plasmon-enhanced two-photon absorption (TPA) by gold, over which three sharp peaks are observed and correspond to the nonlinear wave mixing: SFG, SHG (second harmonic generation) and CARS signals.

Interestingly, coupling nano-objects, i.e., tuning the distance between gold nanoparticles until they get in contact [60], shifts the frequency of the LSPR. For an optimal distance, i.e., when LSPR matches one of the involved laser frequencies, the nonlinear optical generation has been reported to be enhanced by four orders of magnitude because of the EM field enhancement [61].

It is important to emphasize that although using LSPR phenomena can bring a huge benefit in term of field enhancement, those effects are definitively associated with metallic surfaces, and accordingly, enhancement occurs only in the proximity of the metal surface. Because the field intensity decays

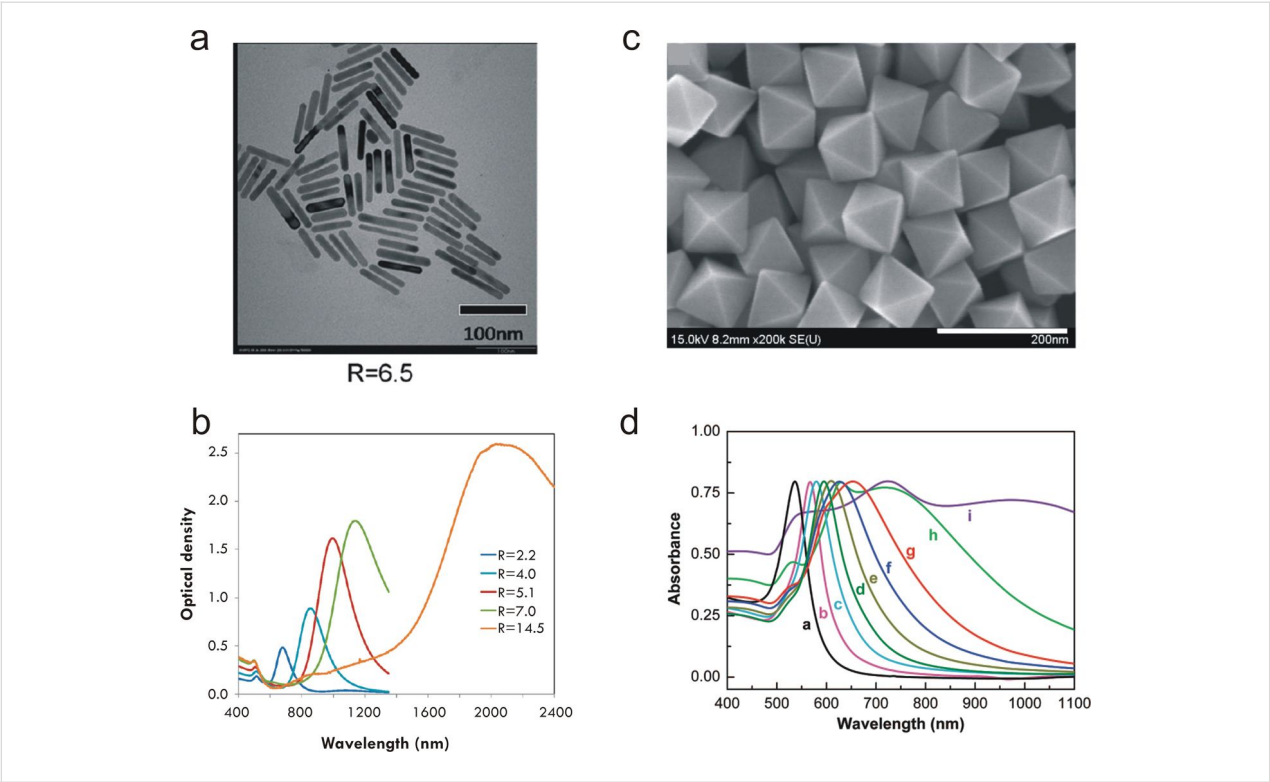

Figure 4: (a) TEM image of gold nanorods (AuNRs) with an aspect ratio *R* equal to 6.5. (b) UV–vis measurements showing the experimental spectra of longitudinal and transverse LSPRs for AuNRs with various aspect ratios (c) TEM image of gold octahedra with an edge length of 95 nm. (d) UV–vis absorption spectra for Au octahedra with different edge lengths (20, 50, 63, 80, 95, 110, 125, 160, and 230 nm, from curve a to curve i, respectively) dispersed in water. Figures adapted with permission from [9], Copyright 2008 American Chemical Society, and from [12], Copyright 2009 American Chemical Society.

exponentially, the amplification typically occurs only a few tens of nanometres away from the surface. To some extent, exploiting surface-enhanced (SE) fields limits the possibility to probe bulk materials. An alternative approach, which overcomes this limitation, consists in dispersing the nanostructures in the bulk of the medium to be probed, and use them as a contrast agent to enhance the optical signal in their surroundings, as we will discuss later.

4 SE-SFG spectroscopy

Sum-frequency generation emission can be increased if the electric field of the visible and/or the infrared radiation is enhanced. In principle, both SERS and SEIRA effects can contribute to the observed increase of SFG intensity, since the SFG amplification depends on the enhancement of the Raman activity, in the visible range (SERS), and/or on that of the IR activity (SEIRA) [5,62-65]. In practice, up to now, plasmon-assisted SFG enhancement has been demonstrated only with visible LSPR, due to the easier availability and development of nanostructures resonating in that range, and also due to the better amplifications obtained with plasmon-assisted SERS compared to those obtained with SEIRA [2]. It is interesting to note that such enhancement due to the LSPR excitation in the visible range indirectly enables the amplification of the signature of the infrared absorption thanks to the nonlinear wave mixing.

4.1 Surface enhancement from SPP

The first age of surface-enhanced SFG spectroscopy through plasmon waves dates back to 1991 when Chen and Zhang demonstrated theoretically end experimentally the excitation of surface plasmon wave (SPW) in a silver film adsorbed on a prism and covered with a Langmuir–Blodgett (LB) film of arachidic acid [66]. The authors measured the transmitted SFG signal as a function of the Vis angle in the counter-propagating geometry, and observed the excitation of the SPW through the amplification of the non-resonant SFG signal of both the silver film and the LB monolayer. In particular, they highlighted that the SFG signal from the LB film was increased by about 25% and was angularly shifted by comparison with the pure silver film. Combining their experimental results with theoretical calculations modelling the SFG emission from the interface, the authors obtained a nonlinear polarizability coefficient of the arachidic acid molecule. These results made the authors optimistic on the future possibility to use SPWs to identify molecular adsorbates.

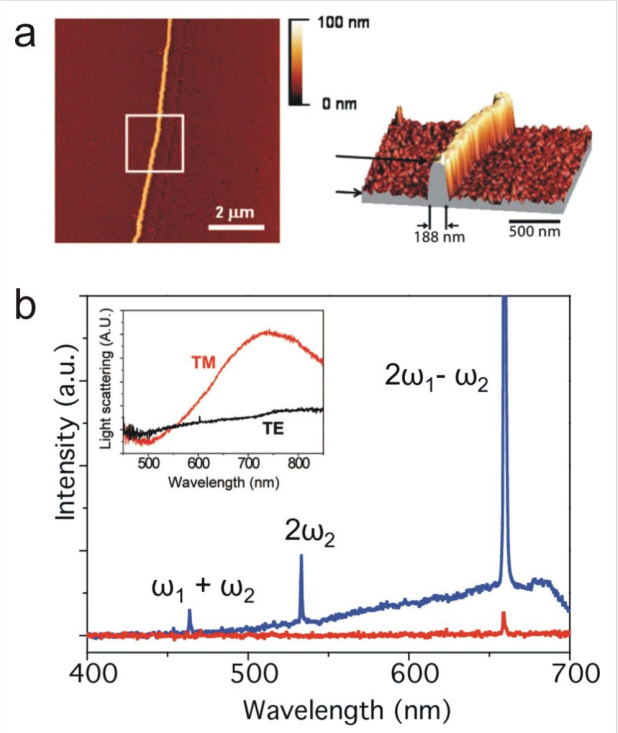

Figure 5: (a) AFM image of a single rectangular gold nanowire with an aspect ratio of ca. 7. (b) CARS, SFG and SHG emission from the rectangular gold nanowire. The red and blue curves correspond to a light polarization parallel and normal to the wire, respectively. The inset shows the white light scattering spectra of the wire with TM and TE polarized light. Figures adapted with permission from [32], Copyright 2010 Optical Society of America, and from [59], Copyright 2008 American Chemical Society.

In 1997, Alieva et al. used a grating coated with silver (200 nm thick) to couple the excitation of a surface plasmon polariton within the metal sheet and, thus, enhance the SFG signal (as shown in Figure 3c) [67]. The grating was illuminated in external reflection and counter-propagating geometry. Although no molecular signature was recorded, the enhancement of the non-resonant SFG intensity from the metallic surface itself was mentioned to be greater than 10^4. Later in 1999, the authors demonstrated the feasibility to use a similar plasmonic substrate to amplify the resonant SFG signals of copper phthalocyanine and fullerene films adsorbed onto the silver grating [68].

4.2 Surface enhancement from porosity

In 2005, Mattei et al. observed a SFG enhancement by tuning the optical properties of silicon layers through porosity [69]. While this work does not strictly rely on plasmon excitation, tuning the electronic and optical properties of matter through morphology is an interesting alternative that, under some conditions, can lead to enhancement of the electromagnetic field at the interface. Indeed, the authors successfully amplified the SFG signal of the H-terminated porous silicon surfaces (with increasing porosity). Although they did not provide any explanation about the amplification mechanism, they were able to ascribe the result to both optical and structural effects. More interestingly, the authors studied the possibility to increase the SFG signal of H-terminated surfaces in a photonic crystal structure, namely a Fabry–Perot microcavity, made of alternating silicon layers of low and high porosity. From calculations and experiments, they predicted and verified the possibility to enhance the SFG signal up to one order of magnitude for adequate incident and SFG propagation directions. Lastly, the authors also predicted that an even better amplification could be obtained if conceiving a porous silicon photonic structure with two levels of defects, so that it could be in resonance with the visible and the SFG beams simultaneously.

4.3 Surface enhancement from LSPR

Besides few examples of surface-enhanced SFG from SPP waves coupled with a prism or a grating, and from photonic structures, the most successful and promising results were certainly obtained from localized surface plasmon resonances in nanostructures.

4.3.1 Spherical nanoparticles: In 2009, Pluchery et al. and Humbert et al. demonstrated that the vibrational SFG signature of thiophenol-functionalized gold nanoparticles (17 nm of diameter) grafted on flat silicon could be detected at a surface coverage as low as about 1% [70,71]. The SFG spectra displayed a single mode corresponding to the CH groups of the aromatic core of thiophenol at 3055 cm^{-1} (Figure 6).

The Au NPs surface coverage on a prefunctionalized aminopropyl-triethoxysilane (APTES) silicon substrate could be varied from 1.5% (5 min) to 15% (24 h) depending on the dipping time in the colloidal solution (Figure 6). When comparing the SFG signal of the thiophenol molecules chemisorbed on the NPs substrate (15% of surface coverage) with the same thiophenol SAM (self-assembled monolayer) chemisorbed on a Au(111) monocrystal, the normalized intensity enhancement was estimated to be 21. Actually, a 1.5% NPs surface coverage already led to a significant SFG vibrational signature, which underlines the remarkable sensitivity of SFG given that the intensity scale with N^2. Also, thanks to this signal amplification, Humbert et al. succeeded to obtain the SFG signature of thiophenol in the fingerprint spectral range (ring deformation vibrations), where nonlinear activities are intrinsically rather weak. This was achieved by scanning the infrared between 980 and 1100 cm^{-1} with a free electron laser (CLIO) [72].

Significant amplifications of the SFG intensity from LSPR excitation were reported by other groups. In 2009, Li et al. demon-

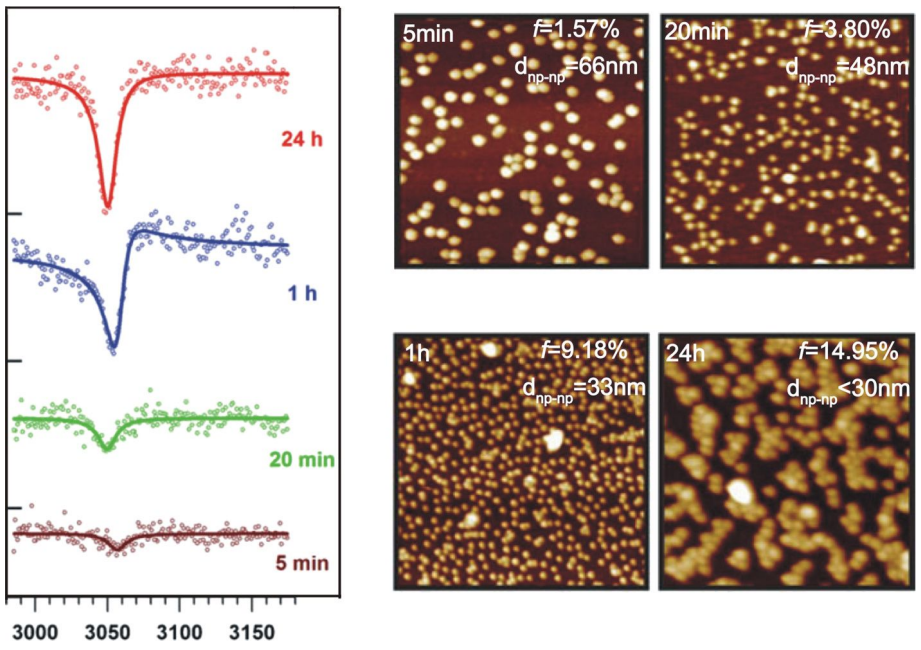

Figure 6: (Left) SFG spectra of silicon substrate immersed in a colloidal solution of gold NPs (17 nm diameters) for increasing times and subsequently functionalized with thiophenol. Depending on the immersion time, the NPs surface coverage ranged from 1.5 to 15%. (Right) Corresponding SEM images showing the progressive surface coverage with immersion time. Figure adapted with permission from [71], Copyright 2013 Springer, and from [72], Copyright 2012 Royal Society of Chemistry.

strated that a noble metal surface with a controlled roughness could lead to an important SFG enhancement [73]. To do that, a 200 nm thick silver or gold film was evaporated over polystyrene beads with various diameters (from 300 to 620 nm). The visible laser source being fixed at 532 nm, the best excitation of the LSPR mode was obtained with the 360 nm beads, no matter whether silver or gold was used as coating material. This latter fact was rather surprising since the SPR frequencies are well distinct between the two metals. However, the authors explained that, irrespective of the metal, the strong SFG enhancement was mainly due to the electromagnetic field increase at the junction between the nanospheres, with a strong dipolar contribution parallel to the substrate. This explains the necessity to use *ssp* polarization (in the order of SFG, vis, IR) to obtain a strong amplification for such dense nanoparticle layer. As a result, an octadecanethiol SAM chemisorbed on silver coated beads gave an SFG signal enhancement of 730 when considering the asymmetric stretching mode, which possesses a dipole moment mainly parallel to the surface. The enhancement of the methyl symmetric stretching was one order of magnitude weaker, according to the fact that its dipole moment change was perpendicular to the substrate, and thus penalized with regard to the directional SPR resonance lying at the nanosphere junction.

Although the amplification factor appeared much larger in this work by comparison with the result of Humbert et al., one should take into account that different normalizations were used to estimate the amplification. Indeed, in an attempt of comparison, a naive extrapolation of the surface coverage from 15% to 100% (from Humbert et al.) would increase the amplification factor from 21 to 933. This last value is much closer to the factor of 730 set by Li, although the nanoparticle size was 20 times smaller (17 nm vs 360 nm). Also, when considering the gold-coated 360 nm spheres of Li instead of the silver coated ones, the best amplification was weaker, with a factor of 190. Finally, the authors underlined that the SFG emission was strongly scattered by the surface, and that only a limited fraction of the chemisorbed molecules was precisely located at the nanosphere junctions, thereby estimating the local enhancement factor to range from 10^4 to 10^6. It is interesting to notice that for both gold and silver coating, the SFG vibrational modes appeared as clear peaks when amplified, while they were dip-shaped on a flat sample.

Whereas the amplification factor reflects the efficiency of the local field enhancement, spectroscopy applications are more concerned by the absolute SFG intensity that can be collected. For this sake, a common reference signal in SFG experiment is the non-resonant gold contribution in *ppp* polarization that gives an intense SFG emission. For instance, in the two above works, the intensity contrast for the strongest vibrational mode (either under the shape of a peak or a dip) never exceeded a fair 10% of that gold reference.

A hybrid configuration was studied by Tourillon et al. [74], for which the SFG spectroscopy was performed on a dense gold nanoparticles monolayer (11 nm) on a quartz prism surface. The interface was probed in the total internal reflection (TIR) configuration, in *ppp* polarization, with the visible frequency matching the LSPR of the Au NPs. According to the authors, the overall SFG signal from a dodecanethiol SAM was increased by one order of magnitude. If considering an ideal 100% surface coverage in Au NPs (which was not the case), the minimum amplification factor that can be deduced is 100. Also an important improvement of the signal-to-noise and signal-to-background ratios was obtained by comparing the TIR to the external reflection geometry. However, according to the authors, it was unclear if this enhancement resulted only from the TIR geometry, which maximized the surface EM field, or also from the excitation of a LSPR in the Au NPs. Since Tourillon et al. obtained a rather low SFG intensity when working with the same Au NPs layer functionalized with DDT, but probed in the external reflection geometry, one could believe that the contribution of the LSPR excitation was rather limited in the reported enhancement.

Nonetheless, these results underlined that the TIR configuration offers undisputable advantages for surface-enhanced SFG spectroscopy. To go further, Tourillon et al. applied this hybrid configuration to demonstrate the label-free recognition of biomolecules, namely in the case of the avidin–biocytin interaction [75]. Because SFG is sensitive to molecular order and conformation through centro-symmetry, it can address detailed molecular properties of the adlayer, which otherwise are inaccessible for most of the more conventional techniques. This enabled the authors to guarantee the specific detection of the bio-recognition and of a subsequent molecular re-ordering.

4.3.2 Nano-antennas: Up to now, SE-SFG has been demonstrated in only a few studies with a limited variety of nanostructures. Asides from spherical nanoparticles, the other reported nanostructure was nano-antennas. Supporting two distinct plasmon resonances, a transverse and a longitudinal mode, nano-antennas have been shown to allow large amplification of molecular signals.

In 2000, Baldelli et al. demonstrated that strong enhancements of the SFG signal could be obtained through exciting the plasmon mode in a nanopillar array [76]. They reported a significant amplification of the CO signature on an array of platinum nanopillars, prepared by electron beam lithography, and possessing uniform spacing and size (Figure 7a).

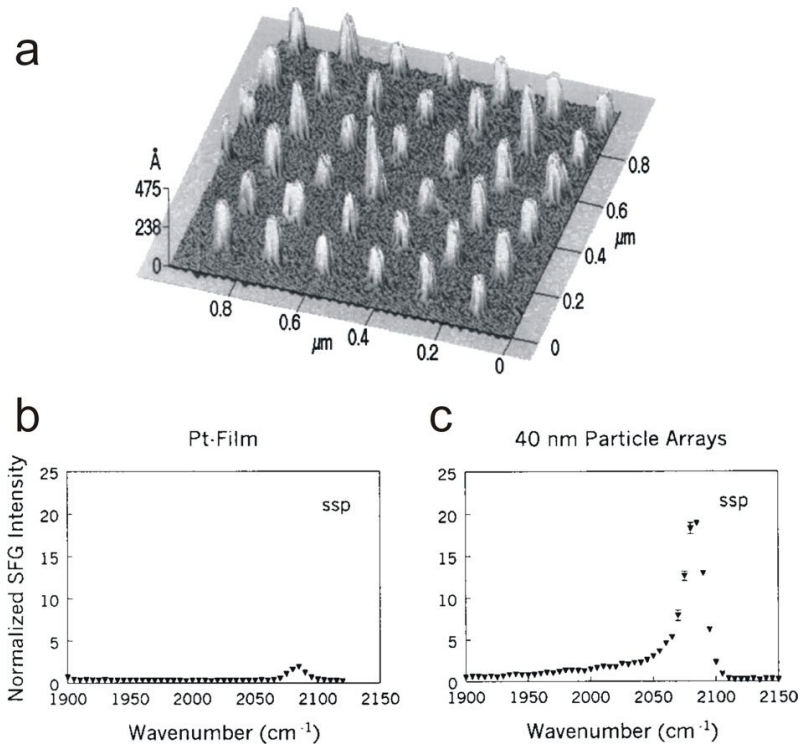

Figure 7: (a) AFM image of the platinum nano-antenna array, the antennas sizing 40 nm in diameter and being spaced by 150 nm. SFG spectra in *ssp* polarization of CO adsorbed on (b) a smooth Pt film and on (c) 40 nm Pt nano-antenna arrays. Figure adapted with permission from [76], Copyright 2000 AIP Publishing LLC.

As demonstrated by the authors, the amplification was maximal in the *ssp* polarization. The calculated SFG amplification was greater than 10^4 for a 45 nm pillar diameter and an inter-pillar distance of 150 nm (NPs surface coverage of about 5%) by comparison to the signal of CO on smooth Pt films. Note however that given the low molecular coverage, the collected SFG signal enhancement was only of a factor ca. 10 (Figure 7b,c).

In 2011, Lis et al. reported the enhancement of an alkanethiol SAM on randomly distributed gold nanopillars vertically-aligned on either a flat platinum or gold surface (Figure 8a) [77].

The authors achieved a selective excitation of the nanopillar LSPR modes by tuning the visible frequency over the visible range. They showed that both the transverse (TM) and the longitudinal (LM) excitation modes of the pillars could be selectively used to enhance the SFG vibrational intensity of bounded molecules. Further, because of the different EM field enhancement around the pillars when exciting either the TM or the LM mode, the authors estimated that the TM excitation could preferentially enhance the EM field at the pillar side-wall (Figure 8b), while the LM mode excitation preferentially enhanced the EM field at the pillar top (Figure 8c), leading to different areas of the nanostructured substrate to be probed. Besides, far from the LSPR excitation,

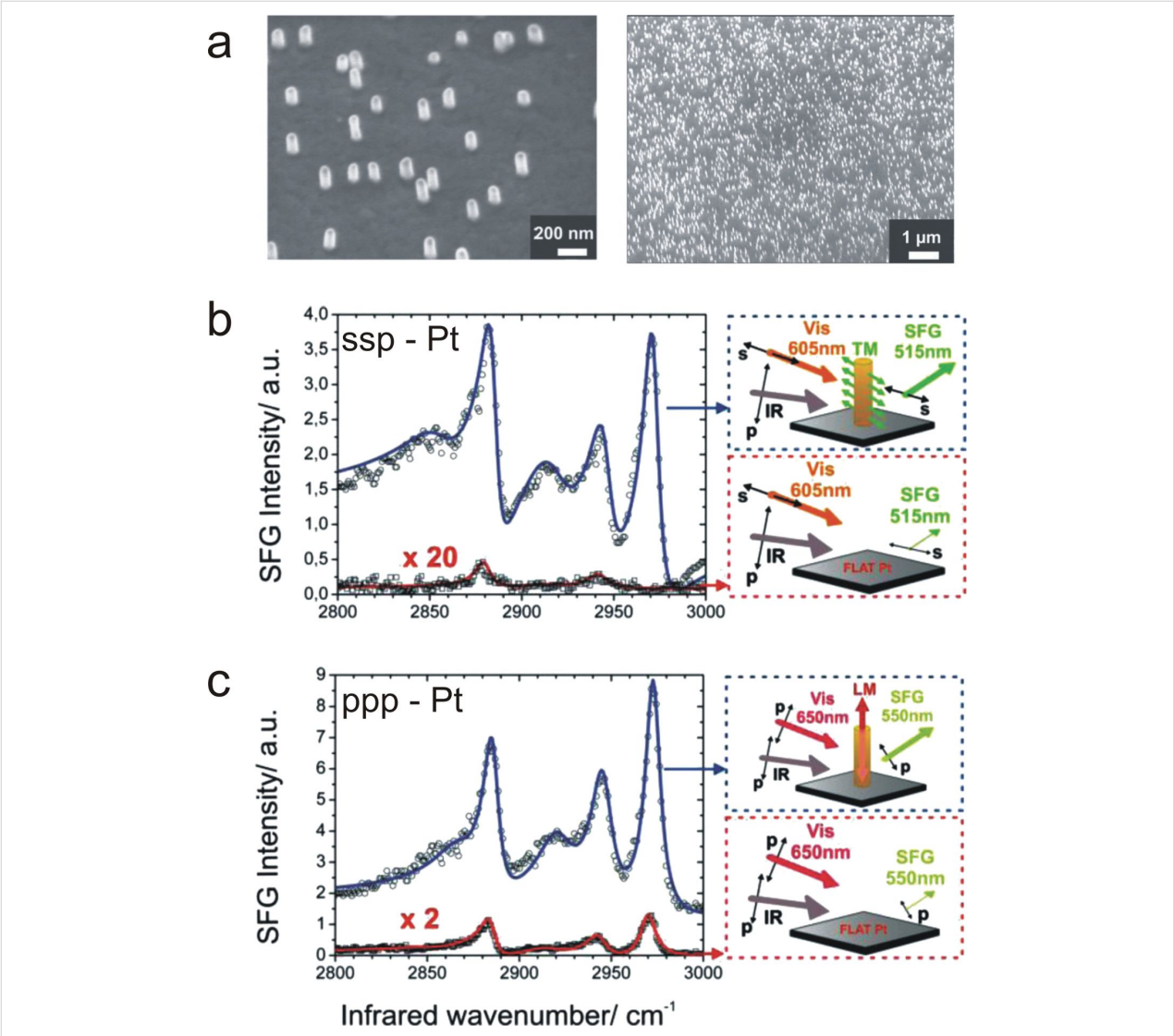

Figure 8: (a) Scanning electron microscopy (SEM) images of gold nano-antennas possessing an average height of 140 nm and diameter of 70 nm. SFG spectra of a dodecanethiol SAM (b) in *ssp* polarization with a selective excitation of the transverse plasmon mode and (c) in *ppp* polarization with a selective excitation of the longitudinal plasmon mode. The red curves stand for a DDT SAM chemisorbed on a flat platinum substrate, whereas the blue curves correspond to a DDT SAM over gold nano-antennas standing on flat platinum. Pictures on the right illustrate the experimental conditions in which the spectra have been recorded. Figure adapted from [77], Copyright 2013 Wiley-VCH Verlag GmbH & Co. KGaA, Weinheim.

the SFG signature was dominated from molecules bonded in-between the pillars on the flat substrate, which accounted for most of the sample surface. The raw SFG intensity enhancement was spectacular, and reached up to a factor of 200. By comparison to the previously used reference, that is the non-resonant gold contribution in *ppp* polarization, the resonant amplitude could reach a value of 150%. The local amplification reported by the author was several 10^3 (10^5 if adopting the same calculation method as used in [76]).

As mentioned earlier, optimizing the enhancement factor would require both the visible and SFG fields to match the plasmon resonance, simultaneously. In a SFG experiment, this is difficult since the commonly used nanostructures possess rather narrow LSPR modes, which indeed promotes multi-frequency resonances. However, the use of nanostructures that support multi-LSPR modes could potentially be a solution, as it is the case with nano-antennas, which present two modes at distinct frequencies. However the directionality of the required electric field imposes specific beam polarizations. For example, Lis et al. showed that the high frequency TM mode had to be excited with *s*-polarized SFG at 515 nm, while the low frequency LM mode had to be excited with *p*-polarized visible at 605 nm. Exciting simultaneously both modes with the visible and SFG photons would therefore impose to adopt the *sps* or polarization set which is unfavorable for the SFG signal on metals [77].

Finally, it is important to point out that in the majority of those reported SE-SFG studies, the strong amplification of the resonant features occurred with a comparable amplification of the non-resonant background. This might be explained through the surface selectivity of the SFG that makes the nanoparticle bulk contribution to be zero in the dipolar approximation. Therefore, the electronic SFG signal is limited to the surface contribution and is evenly amplified with the molecule adjacent to the nanostructure. However, care should be taken since it is known that a strong quadrupolar (and magnetic dipolar) contribution can be collected from metallic nanoparticles and could somehow lead to a SE-SFG signal as well.

5 SE-CARS spectroscopy

Surface-enhanced CARS performed on metallic nanostructures can be considered as the third-order nonlinear counterpart of SERS. In fact, they both rely on the Raman selection rules and benefit from the confined electromagnetic field produced by surface plasmon modes. However, as mentioned earlier, SE-CARS signal scales with the cube of the total incident intensity, and could gain an important benefit if the plasmon resonance is adequately chosen. Moreover, contrary to SERS, SE-CARS emission is coherent leading to large conversion yields over the coherence length, and ensuring a directional emission.

5.1 Surface enhancement from SPP

The first experimental evidence of SE-CARS dates back to 1979 and was given by Shen et al. They performed a nonlinear mixing of four surface plasmon polariton waves that were propagated in a smooth silver film coated over a prism [78]. The surface-enhanced CARS signal was obtained from benzene molecules close to the metal interface. This work demonstrated the possibility for sub-monolayer detection at surfaces with SE-CARS.

5.2 Surface enhancement from LSPR

While the possibility to obtain a higher electric field in nanostructures through LSPR drove researchers towards using nanoparticles, the first investigations dealt with bulk solutions.

5.2.1 Bulk solutions: In 1984, Chew et al. analytically calculated that CARS amplification of benzene molecules close to silver particles, averaged over all scattering angles, could be as large as 10^{21} [50]. Then, in 1994, Liang et al. experimentally demonstrated an enhancement of the CARS signature of benzene in the bulk phase, by adding colloidal silver nanoparticles directly into the liquid [79]. Although the phase matching condition was not fulfilled, the average particle spacing had been adjusted such as to be smaller than the coherence length, while the pump wavelength was matching the localized surface plasmon resonance of the silver NPs. In this first experimental proof, the CARS signal enhancement was limited to two orders of magnitude.

Opposite to SFG, a major drawback of CARS is the uneven amplification of the electronic contribution from the nanostructure body that can be orders of magnitude stronger than the molecular signal from the adsorbate [21,80]. To circumvent that, various experimental means have been envisioned. In 2005, Koo et al. used a polarization-sensitive CARS setup to preferentially enhance the signal coming from the analytes with respect to the background. This procedure enabled them to achieve an extremely high signal to noise ratio and single molecule sensitivity [81]. The authors used a colloidal silver mixture in which the molecular concentration was chosen so that only a single molecule was found within the probed volume, in average. They reported the SE-CARS detection of single DNA nucleotide (dAMP and dGMP, 90 pM concentration), with much stronger intensity than what could be obtained with SERS (higher by a factor of 10^3–10^{10}). Because the signal originated from single molecules, which were diffusing in and out the illuminated volume, the SE-CARS intensity was fluctuating between quantized states, proving the single molecule detection.

Furthermore, this weak molecular contribution was still higher than the non-resonant contributions of water and silver particles. The authors confirmed the high sensitivity of the system with the peptide angiotensin I, as testified by the 40 times higher signal than that of SERS, while working with a molecular concentration 10^4 times lower. This ultra-sensitive detection of non-labelled peptides achieved with SE-CARS is a brilliant example of single molecular detection and offers great perspectives for biomedical detection with very low molecular concentration threshold.

Schlücker et al. showed in 2011 that SE-CARS could be used to obtain large scale images of tissues, for diagnostic purposes [82]. The authors demonstrated that, similarly to immunohistochemistry (IHC) that labels antibodies with dyes or enzymes to image the tissue with conventional light microscope, antibody-labeled metallic nanoshells could be used as well for accurate imaging with SE-CARS (Figure 9).

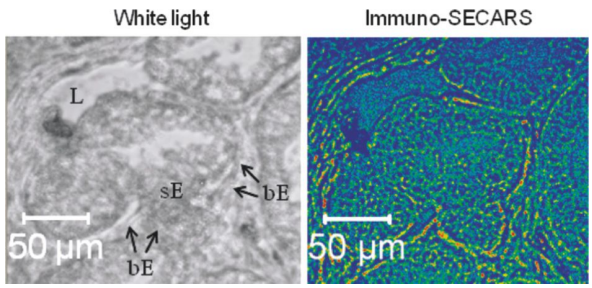

Figure 9: White light (left) and SECARS (right) images of prostate biopsies incubated with SERS-labeled p63-antibodies. p63 is only abundant in the p63-(+) basal epithelium (bE, arrows) but not in the p63-(−) secretory epithelium (sE) and lumen (L). Figure adapted with permission from [82], Copyright 2011 American Chemical Society.

They showed the high sensitivity of the method to selectively image basal cell proteins p63 in normal prostate tissues. The authors also underlined the key advantages of immuno-SE-CARS microscopy: it enables to get very high resolution and potentially to detect different targets in the same SE-CARS experiment, by playing with the wavelength activities of different SERS labels; moreover, SE-CARS is promising for gaining time analysis, and also enables one to avoid fluorescence processes typical of biological matter, which often reduces image contrast in common immunofluorescence images. These properties promoted SE-CARS and CARS microscopy as a new tool for biomedical analysis.

Still in 2011, Namboodiri et al. investigated the SERS and SE-CARS contribution from a mixture of pyridine molecules and silver colloids [83]. They reported a SERS enhancement of pyridine up to 10^4, while the SE-CARS signal increased barely by a factor of 10. This fact is rather surprising given that the authors took care to fulfil the phase matching condition by adopting a three-dimensional forward geometry with specific incident angles for the pump, Stokes, and probe beams, while they further delayed the pump and the probe by 1ps to reduce the non-resonant contribution, and therefore enhance the signal-to-noise ratio. The authors attributed this poor enhancement factor to the increased scattering of light due to the NPs, to the limited amount of silver clusters possessing the right shape and size to fulfil the requirements of the nonlinear coherent Raman scattering, and also to the possible destruction of those silver clusters by the high energy femtosecond-pulsed laser.

In 2014, Yamplosky et al. showed a new proof of single molecule detection threshold, as they succeeded in detecting the motion of a single bipyridylethylene (BPE) molecule in a time-resolved SE-CARS experiment [84].

5.2.2 Surfaces: With the perspective of a better reproducibility of the signal enhancement, different researches have been carried on solid sample devices built up with controlled parameters. Such SE-CARS spectroscopy on solid surfaces led to promising results. In 2004, Ichimura et al. succeeded to measure the SE-CARS signal from a 20 nm thick layer of adenine molecules adsorbed on isolated gold nanoparticles (60 nm) supported on a substrate [85]. The SE-CARS spectrum collected over a region of ca. 1000 µm^2, including several tens of NPs, showed a dominant vibrational mode at 1329.5 cm^{-1}, attributed to the ring breathing mode of the diazole. Further, they recorded the CARS spectrum emitted from a single nanoparticle. The local intensity was estimated to be multiplied by 2000 by comparison to the same adenine layer without nanoparticle.

Very interestingly, by using the adenine vibrational mode at 1330 cm^{-1}, Hayazawa et al. succeeded to obtain a CARS vibrational mapping of a nanometric DNA network structure [86]. To do that, they used an alternative technique, namely the tip-enhanced CARS microscopy, which exploits the confined excitation of a LSPR in the extremity of a metallic tip apex to map the surface, as it is done in near-field scanning optical microscopy. This enabled to move the source of the surface-enhanced field at any place of the studied surface and achieved enhanced optical imaging at high resolution. This method also provided an enhanced CARS imaging of carbon nanotubes [86].

In 2011, Liu et al. demonstrated an advantageous configuration that coupled the use of SPP waves to generate a four-wave mixing SE-CARS signal from individual Si nanoparticles [87]. The nanoparticle was positioned over a thin gold metal film in which two distinct SSP waves counter-propagated. Although the two SPP waves were excited far from the NP itself, the

propagating nature of the waves enabled the NP to generate a SE-CARS signal, free of any surface background. Also, the authors succeeded to obtain an interference pattern from the CARS generation of two adjacent NPs, proving the coherent nature of the emission. In a similar work, Wang et al. employed the Kretschmann geometry through a prism coated with a thin gold film [88]. Again, the authors used a SPP wave to locally generate a SE-CARS emission from NPs adsorbed on the gold surface. By comparison to the non-propagative wave configuration relying solely on an evanescent field, an amplification of two orders of magnitude was obtained. Finally, the authors collected the nonlinear generation on the air side of the Au film by using a lens with high numerical aperture. This enabled obtaining a SE-CARS imaging in the far-field with an emission originating exclusively from the nanostructure. Indeed, the radiation from the Au surface was prohibited in this configuration and only the dipole-like nature of the NPs radiation could lead to a light emission. In such way, the authors successfully imaged carbon nanotubes and neocyanine nanosized clusters by using a wide-field surface-sensitive SE-CARS microscope.

As mentioned earlier, the optimum and most promising enhancement should take benefit of multi-frequency resonant devices. Those nanostructured platforms are supposed to support multiple or broad resonances, ideally matching the pump, the Stokes, and the anti-Stokes frequencies, so that CARS enhancement could be maximized. In 2011, Steuwe et al. achieved an astonishing result by using spherical gold nanovoids with intermediate depths (see Figure 10a) [89].

Figure 10b presents a mapping of the UV–vis absorption spectrum of the void structure as a function of the thickness (for a diameter of 800 nm). An evolution of the plasmonic resonance was observed with the degree of completeness of the void sphere. When the void was approximately grown up to 60% in height, the absorption was substantial for both the pump and the anti-Stokes frequencies, which led to a CARS enhancement factor of 10^5. Besides, the authors also demonstrated that such a large enhancement factor was achievable with commercial SERS substrates (Figure 10c). They used a Klarite sample functionalized with various molecules (ferrocyanide, nitrobenzenthiol, benzenthiol). Given the broad resonances that those substrates offer, LSPR were simultaneously excited at multiple frequencies, which allowed for the very fast recording of CARS images with an estimated reproducibility over 10^4 measurements. It is worth to mention that the authors compared the SE-CARS intensity with the conventional SERS signal (which is already 10^7 times higher than Raman). The enhancement was 10^3 times more intense, making SE-CARS 10^{10} times higher than conventional Raman spectroscopy on plasmonic substrates. This study demonstrated the possibility of using reproducible

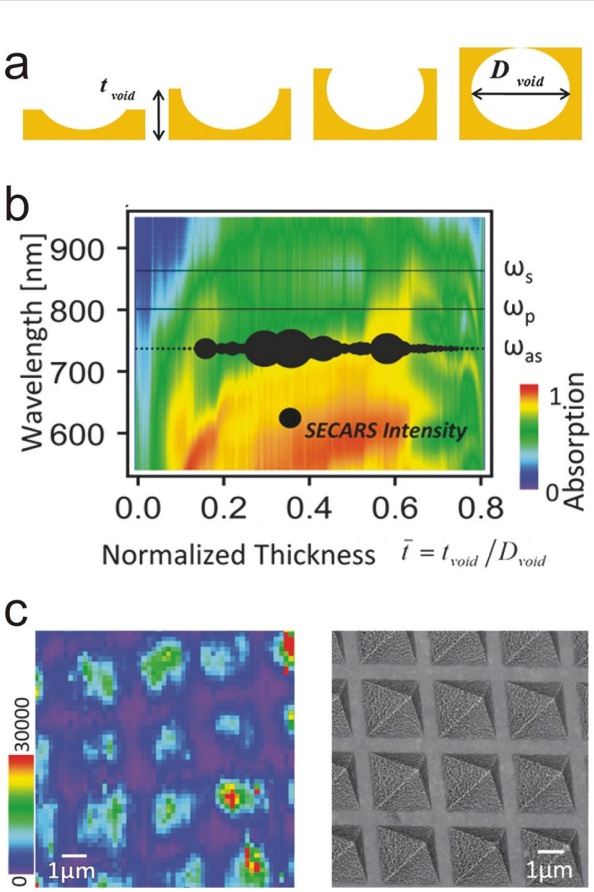

Figure 10: (a) Schematic representation of the gold nanovoids. Depending on the gold film thickness, the voids present various completeness levels. (b) UV–vis absorption mapping of 800 nm nanovoids as a function of their degree of completeness. For a specific thickness, the CARS and the pump frequencies can be both in resonance leading to large CARS intensities (black spot). (c) SE-CARS image of benzenethiol monolayer on the commercially available plasmonic surface Klarite (left) and corresponding SEM image showing the pyramidal pits of Klarite (right). Figure adapted with permission from [89], Copyright 2011 American Chemical Society.

plasmonic surfaces able to support strong and repeatable SE-CARS intensity enhancements, and in consequence, fast vibrational imaging.

Aside from those important achievements, investigations demonstrated that the electronic background that derives from the water and the metal could also be reduced on such kind of solid substrates. Voronine et al. used time-resolved surface-enhanced CARS, which combines delayed laser pulses of different widths, to obtain a high spectral resolution with the suppression of the non-resonant background [90]. To provide quantitative signal intensity comparisons, the SE-CARS spectroscopy was applied to a 12 µm thick pyridine–Au NPs layer (red trace in Figure 11a), while conventional CARS was done on a 2 mm thick pyridine film (blue trace in Figure 11a).

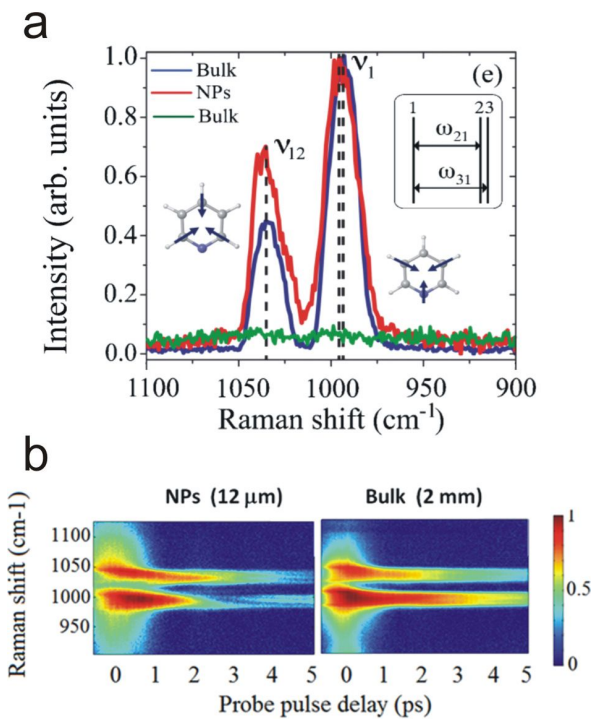

Figure 11: (a) SE-CARS spectrum obtained from a 12 µm thick layer of pyridine on the surface of NPs (red spectrum). The bulk CARS signal (without NPs) showed no detectable spectral features for a 12 µm thick sample (green), whereas a 2 mm thick layer gave the blue spectrum. Three vibrational modes were resolved: at 990 cm^{-1} and 997 cm^{-1} due to the ring breathing mode of free pyridine and hydrogen-bonded pyridine-water complexes, respectively; and at 1030 cm^{-1} due to the triangle mode of a mixture of both species. (b) 2D (SE)-CARS spectrograms obtained by scanning the probe pulse delay. A delay of 1 ps led to a sharp improvement of the signal-to-background ratio, while narrow band probe pulse and adequate slit in the detection set-up led to a high spectral resolution. Figure adapted with permission from [90], Copyright 2012 Nature Publishing Group.

Note that a 12 µm pyridine sample did not provide any measurable CARS signal (green trace in Figure 11a). The spectra showed three vibrational modes of the free and H-bonded pyridine–water complexes. Basically, the authors used femtosecond pump and Stokes laser pulses with frequencies matching the large plasmon resonance of the aggregated gold NPs. The broadband pulses enabled to efficiently excite the vibrational coherence of the pyridine–water complex molecules in contact with gold nanoparticles. Then, they used a picosecond narrow-band probe pulse to generate the coherent anti-Stokes signal, with a very good spectral resolution. Because this probe pulse was delayed in time with the pump (1 ps), it enabled to suppress the non-resonant contribution, which possesses a shorter lifetime (Figure 11b). Finally, by comparing the peak ratio between the CARS intensity collected from the bulk pyridine (estimated coherence length of 300 µm) with the SE-CARS intensity from the 12 µm film, an enhancement factor of 10^7 was estimated. This was 10^6 times higher than that previously reported by Namboodiri et al. in 2011 with a similar system. This value is closer to the theoretical estimate of 10^{10} for isolated NPs [27].

Very recently, a new record for SE-CARS enhancement has been set by Zhang et al. [91], who obtained an amplification of 11 orders of magnitude compared to spontaneous Raman, by exploiting the Fano resonance generated from a nanostructure made of four discs of gold arranged in a diamond-shaped structure. This is an ultimate exciting proof of the potentialities of those coherent and nonlinear spectroscopies coupled to sophisticate and controlled plasmonic nanostructures.

Conclusion

We have reviewed the main achievements in vibrational nonlinear optical spectroscopies enhanced through their coupling with surface plasmon waves, in particular localized surface plasmon resonances in nanostructures. It emerges that the overall development of those uncommon surface-enhanced spectroscopies is still at an early stage, as demonstrated by the small number of works in the field, and that their potential application remains very specialized. In the meantime, it is unquestionable that these works have set the basis to make SE-SFG and SE-CARS powerful and unique tools to address fundamental questions in cutting edge researches carried out in laboratories. Moreover, the constant progress in the development of stable, miniaturized, easy-to-use and cheaper laser sources, together with an optimized control and design of nanomaterials and nanostructures for plasmonics, are driving SE-SFG and SE-CARS to concrete applications, for instance in the field of bioanalytical or biomedical applications.

The advantages and limitations of SE-SFG and SE-CARS are closely related to their non-enhanced counterparts, SFG and CARS. SE-SFG, like SFG, takes advantage of the centrosymmetry selectivity which makes them specific techniques to probe the vibrational response of interfacial systems, with a high sensibility to molecular conformation and order. SFG selection rules combining both IR and Raman features, it may be advantageous to study specific vibrational modes with no interference from neighbouring modes. However, because of the reduced complexity of the fingerprint, SFG offers restricted possibilities of chemical identification. Moreover, the requirement for a vibrational mode to be strongly IR and Raman active, generally entails a large loss of intensity for most of the detected modes. Hopefully, this lack of intensity may be overcome with SE-SFG, which has demonstrated to lead to very significant amplifications. Besides, an advantageous strength of SE-SFG stands in its ability to not favour the non-resonant contribution of the substrate over the resonant vibrational

contribution, and, under specific conditions, this may even improve the signal-to-noise/background ratio, thus making its surface sensitivity always better. Therefore, although SE-SFG is not yet used in practical applications or as routine techniques, it appears very promising thanks to its interfacial sensitivity and represents an extreme tool for interface investigations in fundamental science.

On the other side, SE-CARS being a third-order nonlinear process, it does not possess a specific surface sensitivity. However, this insensitivity to symmetry and the sole necessity of Raman activity usually lead to a larger SE-CARS signal over SE-SFG. This makes SE-CARS more appropriate for practical applications, such as real-time in situ label-free molecular imaging (in biomedicine for example). Also, it is overall easier to implement SE-CARS because of the requirement of laser sources exclusively tuneable in the visible range. Meanwhile, SE-CARS allows for measuring the vibrational transitions from 4000 cm^{-1} up to few 100 cm^{-1}, which is extremely useful. Regarding the SE ability, scaling with the third power of the total incident intensity gives a supplementary advantage for spectroscopy performed with short laser pulses (fs) at high repetition rate (MHz), which are now widely available on the market.

Overall, while each of those spectroscopies appears to be suitable for distinct aims, there is no doubt that both SFG and CARS take large advantage in plasmon-assisted configurations. This enables to combine the high sensitivity of nonlinear processes to the physicochemical properties of matter with a unique detection threshold. Those features promote both spectroscopies as must tools to investigate fundamental properties and processes, and set the basis for further technical and analytical developments, with the purpose of practical applications, such as (bio)-molecular detection devices, or (bio)-imaging tools with improved single-molecule sensitivity.

Acknowledgements

D. L. and F. C. are postdoctoral researcher and research associate of the Belgian National Fund for the Scientific Research F.R.S.-FNRS, respectively. The authors acknowledge the Cost Actions MP0901 “Designing novel materials for nanodevices: From Theory to Practice”. This work was performed in the context of the European COST Action MP1302 "Nanospectroscopy".

References

1. Frey, B. L.; Corn, R. M.; Weibel, S. C. Polarization-Modulation Approaches to Reflection-Absorption pectroscopy. In *Handbook of Vibrational Spectroscopy;* Chalmers, J. M.; Griffith, P. R., Eds.; John Wiley and Sons, Ltd.: Chichester, UK, 2001; Vol. 2, pp 1042–1056.
2. Aroca, R. *Surface-Enhanced Vibrational Spectroscopy;* John Wiley and Sons, Ltd.: Chichester, UK, 2006. doi:10.1002/9780470035641
3. Evans, C. L.; Xie, X. S. *Annu. Rev. Anal. Chem.* **2008,** *1,* 883–909. doi:10.1146/annurev.anchem.1.031207.112754
4. Aroca, R.; Ross, D. J.; Domingo, C. *Appl. Spectrosc.* **2004,** *58,* 324A–338A. doi:10.1366/0003702042475420
5. Hartstein, A.; Kirtley, J. R.; Tsang, J. C. *Phys. Rev. Lett.* **1980,** *45,* 201. doi:10.1103/PhysRevLett.45.201
6. Lamy de la Chapelle, M.; Pucci, A., Eds. *Nanoantenna - Plasmon Enhanced Spectroscopies for Biotechnological Applications;* Pan Stanford Publishing: Singapore, 2013. doi:10.1201/b14594
7. Kneipp, K.; Wang, Y.; Kneipp, H.; Perelman, L. T.; Itzkan, I.; Dasari, R. R.; Feld, M. S. *Phys. Rev. Lett.* **1997,** *78,* 1667–1670. doi:10.1103/PhysRevLett.78.1667
8. Haes, A. J.; Zou, S.; Schatz, G. C.; Van Duyne, R. P. *J. Phys. Chem. B* **2004,** *108,* 109–116. doi:10.1021/jp0361327
9. Li, C.; Shuford, K. L.; Chen, M.; Lee, E. J.; Cho, S. O. *ACS Nano* **2008,** *2,* 1760–1769. doi:10.1021/nn800264q
10. Willets, K. A.; Van Duyne, R. P. *Annu. Rev. Phys. Chem.* **2007,** *58,* 267–297. doi:10.1146/annurev.physchem.58.032806.104607
11. Schwartzberg, A. M.; Zhang, J. Z. *J. Phys. Chem. C* **2008,** *112,* 10323–10337. doi:10.1021/jp801770w
12. Duan, J.; Park, K.; MacCuspie, R. I.; Vaia, R. A.; Pachter, R. *J. Phys. Chem. C* **2009,** *113,* 15524–15532. doi:10.1021/jp902448f
13. Mayer, K. M.; Hafner, J. H. *Chem. Rev.* **2011,** *111,* 3828–3857. doi:10.1021/cr100313v
14. Kottmann, J. P.; Martin, O. J. F. *Opt. Express* **2001,** *8,* 655–663. doi:10.1364/OE.8.000655
15. Sajanlal, P. R.; Sreeprasad, T. S.; Samal, A. K.; Pradeep, T. *Nano Rev.* **2011,** *2,* 5883–5975. doi:10.3402/nano.v2i0.5883
16. Coello, V.; Bozhevolnyi, S. I. *Opt. Commun.* **2009,** *282,* 3032–3036. doi:10.1016/j.optcom.2009.04.012
17. Kneipp, K.; Kneipp, H.; Bohr, H. Single-molecule SERS spectroscopy. In *Surface-enhanced Raman Scattering: Physics and Applications;* Kneipp, K.; Moskovits, M.; Kneipp, H., Eds.; Springer-Verlag: Berlin, Germany, 2006; pp 261–277. doi:10.1007/3-540-33567-6_13
18. Kneipp, J.; Kneipp, H.; Kneipp, K. *Chem. Soc. Rev.* **2008,** *37,* 1052–1060. doi:10.1039/b708459p
19. Stiles, P. L.; Dieringer, J. A.; Shah, N. C.; Van Duyne, R. P. *Annu. Rev. Anal. Chem.* **2008,** *1,* 601–626. doi:10.1146/annurev.anchem.1.031207.112814
20. Sharma, B.; Frontiera, R. R.; Henry, A.-I.; Ringe, E.; Van Duyne, R. P. *Mater. Today* **2012,** *15,* 16–25. doi:10.1016/S1369-7021(12)70017-2
21. Shen, Y. R. *Principles of Nonlinear Optics;* Wiley: New York, 1984.
22. Shen, Y. R. *Nature* **1989,** *337,* 519–525. doi:10.1038/337519a0
23. Shen, Y. R. *Pure Appl. Chem.* **2001,** *73,* 1589–1598. doi:10.1351/pac200173101589
24. Tolles, W. M.; Nibler, J. W.; McDonald, J. R.; Harvey, A. B. *Appl. Spectrosc.* **1977,** *31,* 253–271. doi:10.1366/000370277774463625
25. Begley, R. F.; Harvey, A. B.; Byer, R. L. *Appl. Phys. Lett.* **1974,** *25,* 387–390. doi:10.1063/1.1655519
26. Cheng, J.; Xie, S. X. *Coherent Raman Scattering Microscopy;* CRC Press: Boca Raton, FL, 2013.
27. Chung, C.-Y.; Boik, J.; Potma, E. O. *Annu. Rev. Phys. Chem.* **2013,** *64,* 77–99. doi:10.1146/annurev-physchem-040412-110103
28. Day, J. P. R.; Domke, K. F.; Rago, G.; Kano, H.; Hamaguchi, H.-o.; Vartiainen, E. M.; Bonn, M. *J. Phys. Chem. B* **2011,** *115,* 7713–7725. doi:10.1021/jp200606e

29. Dick, B. *Chem. Phys.* **1987,** *113,* 131–147. doi:10.1016/0301-0104(87)80226-4
30. Boyd, R. W. *Nonlinear Optics,* 2nd ed.; Academic Press: UK, 2003.
31. Lin, S. H.; Hayashi, M.; Islampour, R.; Yu, J.; Yang, D. Y.; Wu, G. Y. C. *Physica B* **1996,** *222,* 191–208. doi:10.1016/0921-4526(96)00008-7
32. Wang, Y.; Lin, C.-Y.; Nikolaenko, A.; Raghunathan, V.; Potma, E. O. *Adv. Opt. Photonics* **2011,** *3,* 1–52. doi:10.1364/AOP.3.000001
33. Zumbusch, A.; Holtom, G. R.; Xie, X. S. *Phys. Rev. Lett.* **1999,** *82,* 4142–4145. doi:10.1103/PhysRevLett.82.4142
34. Cheng, J.-X.; Jia, Y. K.; Zheng, G.; Xie, X. S. *Biophys. J.* **2002,** *83,* 502–509. doi:10.1016/S0006-3495(02)75186-2
35. Geiger, F. M. *Annu. Rev. Phys. Chem.* **2009,** *60,* 61–83. doi:10.1146/annurev.physchem.59.032607.093651
36. Guyot-Sionnest, P.; Hunt, J. H.; She, Y. R. *Phys. Rev. Lett.* **1987,** *59,* 1597–1600. doi:10.1103/PhysRevLett.59.1597
37. Epple, M.; Bittner, A. M.; Kuhnke, K.; Kern, K.; Zheng, W.-Q.; Tadjedinne, A. *Langmuir* **2002,** *18,* 773–784. doi:10.1021/la0109819
38. Roke, S. *ChemPhysChem* **2009,** *10,* 1380–1388. doi:10.1002/cphc.200900138
39. Noguchi, H.; Ito, M.; Uosaki, K. *Chem. Lett.* **2005,** *34,* 950–951. doi:10.1246/cl.2005.950
40. Bordenyuk, A. N.; Weeraman, C.; Yatawara, A. K.; Jayathilake, H. D.; Stiopkin, I. V.; Liu, Y.; Benderskii, A. V. *J. Phys. Chem. C* **2007,** *111,* 8925–8933. doi:10.1021/jp069062n
41. Wang, H.-F.; Gan, W.; Lu, R.; Rao, Y.; Wu, B.-H. *Int. Rev. Phys. Chem.* **2005,** *24,* 191–256. doi:10.1080/01442350500225894
42. Rao, Y.; Comstock, M.; Eisenthal, K. B. *J. Phys. Chem. B* **2006,** *110,* 1727–1732. doi:10.1021/jp055340r
43. Gan, W.; Wu, B.; Zhang, Z.; Guo, Y.; Wang, H.-f. *J. Phys. Chem. C* **2007,** *111,* 8716–8725. doi:10.1021/jp067062h
44. Bourguignon, B.; Zheng, W.; Carrez, S.; Ouvrard, A.; Fournier, F.; Dubost, H. *Phys. Rev. B* **2009,** *79,* 125433. doi:10.1103/PhysRevB.79.125433
45. Lis, D.; Peremans, A.; Sartenaer, Y.; Caudano, Y.; Mani, A. A.; Dreesen, L.; Thiry, P. A.; Guthmuller, J.; Champagne, B.; Cecchet, F. *J. Phys. Chem. C* **2009,** *113,* 9857–9864. doi:10.1021/jp900217d
46. Cecchet, F.; Lis, D.; Guthmuller, J.; Champagne, B.; Fonder, G.; Mekhalif, Z.; Caudano, Y.; Mani, A. A.; Thiry, P. A.; Peremans, A. *J. Phys. Chem. C* **2010,** *114,* 4106–4113. doi:10.1021/jp911836k
47. Cecchet, F.; Lis, D.; Guthmuller, J.; Champagne, B.; Caudano, Y.; Silien, C.; Mani, A. A.; Thiry, P. A.; Peremans, A. *ChemPhysChem* **2010,** *11,* 607–615. doi:10.1002/cphc.200900733
48. Huff, T. B.; Shi, Y.; Fu, Y.; Wang, H.; Cheng, J.-X. *IEEE J. Sel. Top. Quantum Electron.* **2008,** *14,* 4–9. doi:10.1109/JSTQE.2007.913419
49. Henry, F. P.; Côté, D.; Randolph, M. A.; Rust, E. A.; Redmond, R. W.; Kochevar, I. E.; Lin, C. P.; Winograd, J. M. *Plast. Reconstr. Surg.* **2009,** *123,* 123S–130S. doi:10.1097/PRS.0b013e318191c5b8
50. Chew, H.; Wang, D.-S.; Kerker, M. *J. Opt. Soc. Am. B* **1984,** *1,* 56–66. doi:10.1364/JOSAB.1.000056
51. Pelton, M.; Bryant, G. *Introduction to Metal-Nanoparticle Plasmonics;* John Wiley & Sons and Science Wise Publishing: Hoboken, NJ, 2013.
52. Sarid, D.; Challener, W. *Modern Introduction to Surface Plasmons -Theory, Mathematica Modeling, and Applications;* Cambridge University Press : Cambridge, UK, 2010. doi:10.1017/CBO9781139194846
53. Pitarke, J. M.; Silkin, V. M.; Chulkov, E. V.; Echenique, P. M. *Rep. Prog. Phys.* **2007,** *70,* 1–87. doi:10.1088/0034-4885/70/1/R01
54. Zijlstra, P.; Paulo, P. M. R.; Orrit, M. *Nat. Nanotechnol.* **2012,** *7,* 379–382. doi:10.1038/nnano.2012.51
55. Shopova, S. I.; Rajmangal, R.; Holler, S.; Arnold, S. *Appl. Phys. Lett.* **2011,** *98,* 243104. doi:10.1063/1.3599584
56. Sönnichsen, C.; Reinhard, B. M.; Liphardt, J.; Alivisatos, A. P. *Nat. Biotechnol.* **2005,** *23,* 741–745. doi:10.1038/nbt1100
57. Sannomiya, T.; Hafner, C.; Voros, J. *Nano Lett.* **2008,** *8,* 3450–3455. doi:10.1021/nl802317d
58. Chen, S.; Svedendahl, M.; Van Duyne, R. P.; Käll, M. *Nano Lett.* **2011,** *11,* 1826–1830. doi:10.1021/nl2006092
59. Kim, H.; Xiang, C.; Güell, A. G.; Penner, R. M.; Potma, E. O. *J. Phys. Chem. C* **2008,** *112,* 12721–12727. doi:10.1021/jp8032758
60. Danckwerts, M.; Novotny, L. *Phys. Rev. Lett.* **2007,** *98,* 026104. doi:10.1103/PhysRevLett.98.026104
61. Simkhovich, B.; Bartal, G. *Phys. Rev. Lett.* **2014,** *112,* 056802. doi:10.1103/PhysRevLett.112.056802
62. Hatta, A.; Suzuki, Y.; Suëtaka, W. *Appl. Phys. A* **1984,** *35,* 135–140. doi:10.1007/BF00616965
63. Nakao, Y.; Yamada, H. *Surf. Sci.* **1986,** *176,* 578–592. doi:10.1016/0039-6028(86)90056-7
64. Kamata, T.; Kato, A.; Umemura, J.; Takenaka, T. *Langmuir* **1987,** *3,* 1150–1154. doi:10.1021/la00078a049
65. Badilescu, S.; Ashrit, P. V.; Truong, V.-V. *Appl. Phys. Lett.* **1988,** *52,* 1551–1553. doi:10.1063/1.99078
66. Chen, Z.; Zhang, Z. *J. Appl. Phys.* **1991,** *69,* 7406–7410. doi:10.1063/1.348928
67. Alieva, E. V.; Petrov, Y. E.; Yakovlev, V. A.; Eliel, E. R.; van der Ham, E. W. M.; Vrehen, Q. H. F.; van der Meer, A. F. G.; Sychugov, V. A. *JETP Lett.* **1997,** *66,* 609–613. doi:10.1134/1.567569
68. Alieva, E. V.; Knippels, G. M. H.; Kuzik, L. A.; Mattei, G.; van der Meer, A. F. G.; Yakovlev, V. A. *Phys. Status Solidi A* **1999,** *175,* 109–114. doi:10.1002/(SICI)1521-396X(199909)175:1<109::AID-PSSA109>3.0.CO;2-Q
69. Mattei, G.; Valentini, V.; Yakovlev, V. A.; Mani, A. A.; Sartenaer, Y.; Thiry, P. A.; Peremans, A.; Caudano, Y.; Dreesen, L.; Humbert, C.; Busson, B.; Vidal, F.; Tadjeddine, A. *Phys. Status Solidi A* **2005,** *202,* 1487–1491. doi:10.1002/pssa.200461155
70. Pluchery, O.; Humbert, C.; Valamanesh, M.; Lacaze, E.; Busson, B. *Phys. Chem. Chem. Phys.* **2009,** *11,* 7729–7737. doi:10.1039/b902142f
71. Humbert, C.; Pluchery, O.; Lacaze, E.; Tadjeddine, A.; Busson, B. *Gold Bull.* **2013,** *46,* 299–309. doi:10.1007/s13404-013-0126-5
72. Humbert, C.; Pluchery, O.; Lacaze, E.; Tadjeddine, A.; Busson, B. *Phys. Chem. Chem. Phys.* **2012,** *14,* 280–289. doi:10.1039/c1cp21091b
73. Li, Q.; Kuo, C. W.; Zheng, Y.; Chen, P.; Chou, K. C. *Phys. Chem. Chem. Phys.* **2009,** *11,* 3436–3442. doi:10.1039/b821045d
74. Tourillon, G.; Dreesen, L.; Volcke, C.; Sartenaer, Y.; Thiry, P. A.; Peremans, A. *Nanotechnology* **2007,** *18,* 415301. doi:10.1088/0957-4484/18/41/415301
75. Tourillon, G.; Dreesen, L.; Volcke, C.; Sartenaer, Y.; Thiry, P. A.; Peremans, A. *J. Mater. Sci.* **2009,** *44,* 6805–6810. doi:10.1007/s10853-009-3572-y
76. Baldelli, S.; Eppler, A. S.; Anderson, E.; Shen, Y.-R.; Somorjai, G. A. *J. Chem. Phys.* **2000,** *113,* 5432–5438. doi:10.1063/1.1290024
77. Lis, D.; Caudano, Y.; Henry, M.; Demoustier-Champagne, S.; Ferain, E.; Cecchet, F. *Adv. Opt. Mater.* **2013,** *1,* 244–255. doi:10.1002/adom.201200034
78. Chen, C. K.; de Castro, A. R. B.; Shen, Y. R.; DeMartini, F. *Phys. Rev. Lett.* **1979,** *43,* 946–949. doi:10.1103/PhysRevLett.43.946

79. Liang, E. J.; Weippert, A.; Funk, J.-M.; Materny, A.; Kiefer, W. *Chem. Phys. Lett.* **1994,** *227,* 115–120. doi:10.1016/0009-2614(94)00779-9
80. Cheng, J.-X.; Book, L. D.; Xie, X. S. *Opt. Lett.* **2001,** *26,* 1341–1343. doi:10.1364/OL.26.001341
81. Koo, T.-W.; Chan, S.; Berlin, A. A. *Opt. Lett.* **2005,** *30,* 1024–1026. doi:10.1364/OL.30.001024
82. Schlücker, S.; Salehi, M.; Bergner, G.; Schütz, M.; Ströbel, P.; Marx, M.; Petersen, I.; Dietzek, B.; Popp, J. *Anal. Chem.* **2011,** *83,* 7081–7085. doi:10.1021/ac201284d
83. Namboodiri, V.; Namboodiri, M.; Cava Diaz, G. I.; Oppermann, M.; Flachenecker, G.; Materny, A. *Vib. Spectrosc.* **2011,** *56,* 9–12. doi:10.1016/j.vibspec.2010.08.005
84. Yampolsky, S.; Fishman, D. A.; Dey, S.; Hulkko, E.; Banik, M.; Potma, E. P.; Apkarian, V. A. *Nat. Photonics* **2014,** *8,* 650–656. doi:10.1038/nphoton.2014.143
85. Ichimura, T.; Hayazawa, N.; Hashimoto, M.; Inouye, Y.; Kawata, S. *J. Raman Spectrosc.* **2003,** *34,* 651–654. doi:10.1002/jrs.1047
86. Hayazawa, N.; Ichimura, T.; Hashimoto, M.; Inouye, Y.; Kawata, S. *J. Appl. Phys.* **2004,** *95,* 2676–2681. doi:10.1063/1.1642735
87. Liu, X.; Wang, Y.; Potma, E. O. *Opt. Lett.* **2011,** *36,* 2348–2350. doi:10.1364/OL.36.002348
88. Wang, Y.; Liu, X.; Halpern, A. R.; Cho, K.; Corn, R. M.; Potma, E. O. *Appl. Opt.* **2012,** *51,* 3305–3312. doi:10.1364/AO.51.003305
89. Steuwe, C.; Kaminski, C. F.; Baumberg, J. J.; Mahajan, S. *Nano Lett.* **2011,** *11,* 5339–5343. doi:10.1021/nl202875w
90. Voronine, D. V.; Sinyukov, A. M.; Hua, X.; Wang, K.; Jha, P. K.; Munusamy, E.; Wheeler, S. E.; Welch, G.; Sokolov, A. V.; Scully, M. O. *Sci. Rep.* **2012,** *2,* 891. doi:10.1038/srep00891
91. Zhang, Y.; Zhen, Y.-R.; Neumann, O.; Day, J. K.; Nordlander, P.; Halas, N. J. *Nat. Commun.* **2014,** *5,* 4424. doi:10.1038/ncomms5424

License and Terms

This is an Open Access article under the terms of the Creative Commons Attribution License (http://creativecommons.org/licenses/by/2.0), which permits unrestricted use, distribution, and reproduction in any medium, provided the original work is properly cited.

The license is subject to the *Beilstein Journal of Nanotechnology* terms and conditions: (http://www.beilstein-journals.org/bjnano)

The definitive version of this article is the electronic one which can be found at: doi:10.3762/bjnano.5.237

BEILSTEIN JOURNAL OF NANOTECHNOLOGY

Liquid-phase exfoliated graphene: functionalization, characterization, and applications

Mildred Quintana*[1], Jesús Iván Tapia[1] and Maurizio Prato*[2]

Review

Open Access

Address:
[1]Instituto de Física, Universidad Autónoma de San Luis Potosí, Manuel Nava 6, Zona Universitaria 78290, San Luis Potosí, SLP, Mexico and [2]Center of Excellence for Nanostructured Materials (CENMAT), INSTM UdR di Trieste, Dipartimento di Scienze Chimiche e Farmaceutiche, University of Trieste, Piazzale Europa 1, 34127 Trieste, Italy

Email:
Mildred Quintana* - mildred@ifisica.uaslp.mx; Maurizio Prato* - prato@units.it

* Corresponding author

Keywords:
applications; dispersions; graphene; organic functionalization; ultrasonication

Beilstein J. Nanotechnol. **2014,** *5,* 2328–2338.
doi:10.3762/bjnano.5.242

Received: 15 July 2014
Accepted: 14 November 2014
Published: 04 December 2014

This article is part of the Thematic Series "Atomic scale interface design and characterisation: Theory – Electronic properties".

Guest Editor: A. Krasheninnikov

© 2014 Quintana et al; licensee Beilstein-Institut.
License and terms: see end of document.

Abstract

The development of chemical strategies to render graphene viable for incorporation into devices is a great challenge. A promising approach is the production of stable graphene dispersions from the exfoliation of graphite in water and organic solvents. The challenges involve the production of a large quantity of graphene sheets with tailored distribution in thickness, size, and shape. In this review, we present some of the recent efforts towards the controlled production of graphene in dispersions. We also describe some of the chemical protocols that have provided insight into the vast organic chemistry of the single atomic plane of graphite. Controlled chemical reactions applied to graphene are expected to significantly improve the design of hierarchical, functional platforms, driving the inclusion of graphene into advanced functional materials forward.

Review

Introduction

Various methodologies for the production of graphene and chemically modified graphene have been described during the last years [1]. Among them, micromechanical exfoliation [2] and metal supported growth [3] produced the best layers in terms of electrical and structural quality. Unfortunately, these strategies are time consuming, expensive or produce low material yield. It is crucial to push these methodologies forward towards the large-scale and low-cost production of graphene for the development of applications. Recently, using chemical vapour deposition (CVD) techniques (as reported in [4]), it was possible to produce transferable, large graphene sheets that were included in transparent conductive films for mobile phones [5]. However, for the development of composite materials in large quantities, good quality graphene dispersions

must be produced. In this direction, wet chemistry methodologies are proficient for the mass fabrication of graphene, since the starting material is usually graphite, an inexpensive substance [6].

To exfoliate graphite by wet chemistry techniques, it is necessary to decrease the π–π staking interactions between the graphene layers. In achieving this, the sp^2 lattice is partially disrupted into layers containing sp^2–sp^3 carbon atoms. The most drastic example is probably graphene oxide (GO), where the extreme oxidation of the carbon lattice causes a detriment in the electrical and mechanical properties of the sheets [7]. As consequence, even today, chemically-produced graphene is suitable for the development of low performance applications. In order to produce graphene dispersions within satisfactory optical and electrical property specifications, experimental techniques must be improved. More research must be performed to better understand and manipulate: the mechanochemical forces required for weakening the van der Waals cohesive forces in graphite, the organic chemistry of the two-dimensional graphene layers and the colloidal mechanisms that guide stabilization of graphene sheets possessing diverse physical and chemical features such as charge, size and shape.

To date, the exfoliation of graphite in dispersions has been obtained by a number of mechanochemical methods. Each one of these strategies presents advantages and disadvantages depending on the type of application. In this contribution, we summarize some of the chemical procedures used to obtain graphene dispersions for various applications. Special emphasis is placed on the liquid-phase exfoliation of graphite by ultrasonic techniques, since this is a straightforward process for the production of clean graphene layers ready for organic functionalization. Importantly, the exfoliation of graphite by ultrasonication is a very versatile technique that has already demonstrated its effectiveness in dispersing graphene in solvents with different physical and chemical properties. This flexibility allows the incorporation of additives such as surfactants [8], antioxidants [9], and polymers [10] during the ultrasonication process, while increasing the affinity for the solvent, the quality of the resulting graphene layers, or their functionality. Finally, we describe recent efforts in the chemical design of tailored graphene nanohybrids using graphene dispersions as the starting material.

Discussion

Graphene in dispersions

As previously mentioned, a number of chemical strategies can be followed for the production of graphene in dispersions. Until now, the most widely used methodology has involved the production of GO [11]. In this approach, strong oxidizing agents cause exfoliation of graphite by altering the chemical structure of the 2D graphene layer, introducing oxygen moieties that constrain π–π stabilization. Oxidation of the carbon lattice creates organic functional groups such as epoxides, alcohols, ketones, carbonyls, and carboxylic groups [12]. As result, GO presents completely different physical and chemical properties from that of graphene. The presence of oxidized carbon species modifies the conductive properties of GO from that of a semimetal to an insulating material, while its chemical stability is considerably reduced.

As an alternative, charged species can be used to induce the exfoliation of graphite. For example, the addition of electrons from alkali metal intercalation compounds resulted in the spontaneous exfoliation of graphite in water or polar solvents. This procedure yields stable solutions of negatively charged graphene sheets [13].

As charged, intercalating species, ionic liquids are considered a green alternative. The negligible vapour pressure, thermal stability, wide electrochemical potential window, good conductivity, recyclability, and the high dielectric constant of ionic liquids induce the exfoliation of graphite by weakening the π–π stacking interactions. Indeed, the use of ionic liquids is considered a highly versatile and industrially scalable method for the preparation of graphene nanomaterials [14].

Some neutral molecules are also able to exfoliate graphite by producing polarized π-systems [15]. For example, we recently reported the production of graphene layers by the mechanochemical activation of graphite with melanine (2,4,6-triamine-1,3,5-triazine) under solid conditions through a ball milling process [16]. The melamine-coated graphene layers are easily dispersed in polar solvents. Later, following a similar methodology, the stabilization of a high concentration of graphene sheets in different solvents was achieved by using diverse aminotriazine molecules [17].

The methodologies used for the exfoliation of graphite described thus far might pose a challenge to the further modification of graphene layers by covalent organic reactions. The presence of additional chemical species could yield unexpected products. Thus, different approaches are followed for the production of clean graphene sheets. For example, graphene can be produced by supercritical solvent exfoliation of graphite. In this procedure, solvents reach or exceed their critical point, presenting outstanding wetting properties, low interfacial tension, low viscosity, and high diffusion coefficients. Under these conditions, graphite is exfoliated as high-quality graphene [18].

Ultrasonic techniques

A versatile and simple strategy to exfoliate graphite in liquid phase is based on the use of ultrasonic wave treatment. Ultrasound techniques have important applications in a wide range of materials synthesis strategies [19]. The physical and chemical phenomena associated with ultrasonic waves are cavitation and nebulization. Cavitation induces extreme conditions by collapsing air bubbles which initiates chemical reactions, while nebulization furthers the reaction within the heated droplets. These processes induce the production of highly reactive chemical species including peroxides and radicals formed from the sonochemical reaction of the solvent in air [20]. The combined mechanochemical effects of ultrasonication prompt the exfoliation of graphite in organic solvents, surfactant solutions, or mixed organic solvents. After the ultrasonication process, graphene dispersions are typically centrifuged in order to eliminate graphite microcrystals. From the obtained, stable dispersions, it is possible to calculate the concentration of the graphene layers by UV–vis absorption, as shown in Figure 1 [21]. This protocol allows the quantification of the graphene sheets in the dispersion, enabling further organic functionalization by stoichiometric reactions. This approach is suitable for the tailored design of materials with applications in many different research fields [22].

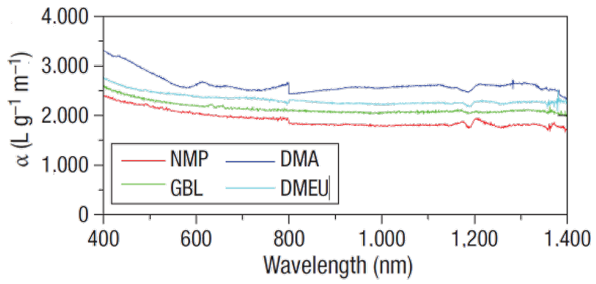

Figure 1: Absorption spectra of graphene layers dispersed in *N*-methylpyrrolidone (NMP), γ-butyrolactone (GBL), *N*,*N*-dimethylacetamide (DMA) and 1,3-dimethyl-2-imidazolidinone (DMEU) at concentrations from 2 to 8 μg·mL^{-1}. Reprinted with permission from [21], copyright 2008 Nature Publishing Group.

Ultrasonic processes are successful at exfoliating graphite only if the net energetic cost of the process is very small. The enthalpy of mixing depends on the affinity between graphene layers and solvent molecules. Then, in order to obtain high yields of exfoliated graphite, the surface energy of the solvent must compete with the surface energy of graphite (≈70–80 mJ·m^{-2}). This relatively high surface energy results in solvents with high boiling points and high surface tensions, for example, *N*,*N*-dimethylformamide (DMF) and *N*-methyl-1,2-pyrrolidone (NMP), which are well-known as good dispersing solvents for carbon nanostructures such as fullerenes and carbon nanotubes (CNTs) [23-25]. Using these solvents, it is possible to exfoliate graphite, resulting in defect-free graphene layers of high concentration. One limitation of this methodology is its inability to completely eliminate the absorbed solvent from the graphene surface. The strong molecular interactions between graphene layers and DMF or NMP molecules, in addition to the fact that both solvents have a high boiling point and high surface tension, make their complete evaporation or removal very difficult. The presence of these residual molecules modifies the physical properties of graphene, which is detrimental to their electrical performance.

As an alternative, it is possible to prepare graphene dispersions in chloroform, acetone, or isopropanol. These are all volatile solvents that have generally lower surface tensions, and are therefore more easily evaporated. Unfortunately, in order to achieve graphene layers of reasonable concentrations in volatile solvents, it is necessary to increase the ultrasonication time, which increases the oxidative processes that cut the graphene sheets into smaller layers, resulting in a higher content of oxidized carbon atoms [26].

The exfoliation of graphite in water is also possible by adding surfactants as stabilizing agents. For example, graphite and sodium cholate were ultrasonicated in water for long periods up to 400 h [27]. This process easily produces stable dispersions of high-quality, free-standing graphene films. In order to obtain more information related to the interaction between graphene sheets and surfactants, graphene was stabilized in water dispersions using twelve different surfactants [28]. The authors found that ionic surfactants stabilize graphene sheets with a concentration that increases with the square of the zeta potential of the surfactant-coated sheets. This means that the concentration is proportional to the magnitude of the electrostatic potential barrier, which prevents graphene π–π stabilization. In contrast, for non-ionic surfactants, the dispersed graphene concentration increased linearly with the magnitude of the steric potential barrier.

Production of larger graphene sheets

As previously mentioned, ultrasonication is a highly energetic process that produces strongly oxidizing chemical species, such as radicals and peroxides. These radicals typically oxidize carbon atoms in graphene close to the defects and at the edges. Under prolonged periods of ultrasonication, the oxidation can cut graphene sheets into small pieces. A well-known strategy to mitigate the damage induced by radicals in different biological processes is through the addition of antioxidant. Following this approach, the ultrasonication of graphite upon addition of *N*-(2-

mercaptopropionyl)glycine (tiopronin) was reported [9]. Tiopronin is an antioxidant molecule that traps electrons, radicals and peroxides. The ultrasonication of graphite in the presence of tiopronin produced larger graphene layers as compared to pure DMF. In this process, carbon nanofibers (CNFs) are formed revealing the occurrence of chemical reactions. During the ultrasonication process, graphene sheets were cut close to the edges, producing small fragments which later aggregate into CNFs. To verify the mechanism of CNF formation, gold nanoparticles (Au NPs) were introduced as contrast markers. Tiopronin and its fragments are well-known stabilizers for Au NPs. The analysis by transmission electron microscopy (TEM) showed Au NPs mostly resided on the nanofibers, thus supporting the proposed mechanism as shown in Figure 2. This methodology produces dispersions of larger graphene sheets of higher concentration than common ultrasonication in DMF. With this, it was demonstrated that the use of antioxidant molecules during ultrasonication treatments reduces the damage caused by radicals and other oxidizing chemical species, attacking mainly the edge carbon atoms.

Rolling and sealing graphene

An important potential application of exfoliated graphene is the tailored production of other carbon nanostructures such as fullerenes [29] and CNTs. To this effect, we have demonstrated the longstanding visualised strategy of rolling and sealing a graphene sheet [30]. This process is possible due to the ultrasonication of graphene upon addition of ferrocenecarboxaldehyde (Fc–CHO) in DMF, Figure 3. Fc–CHO is a reducing agent that prevents oxidation and radical reactions. Additionally, ferrocene derivatives are used in the synthesis of CNTs as carbon source and catalyst.

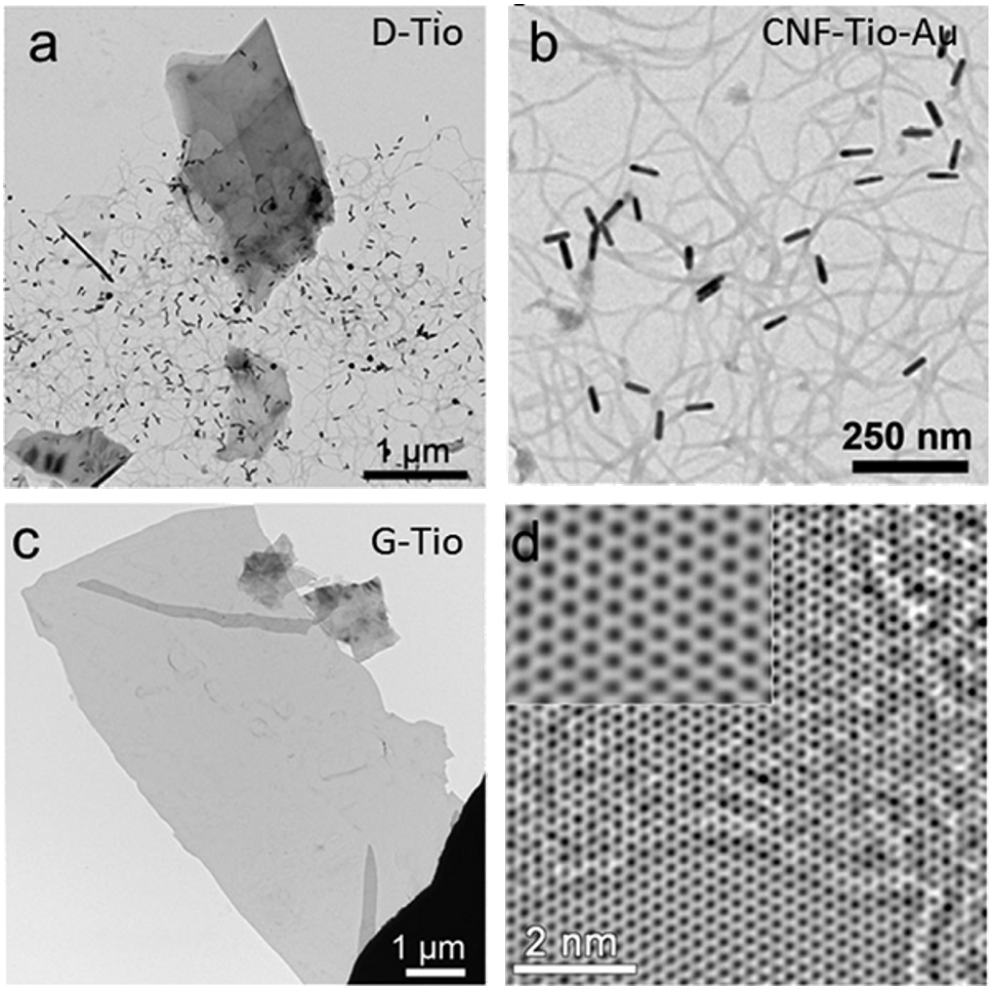

Figure 2: Carbon nanostructures produced with the addition of tiopronin. (a) TEM micrograph of a solution cast including graphene layers and carbon nanofibers. (b) Carbon nanofibers marked with Au Nanorods. (c) Representative TEM micrograph of a graphene sheet. (d) HR-TEM image of graphene. Reprinted with permission from [9], copyright 2012 The Royal Society of Chemistry.

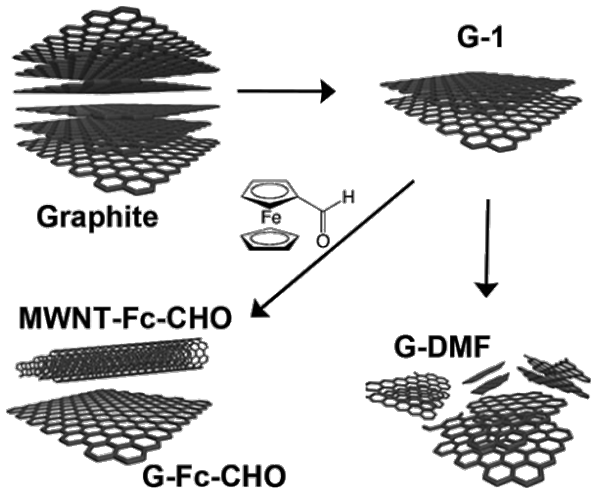

Figure 3: Ultrasound-assisted synthesis of MWNTs from graphite upon the addition of ferrocene aldehyde. Reprinted with permission from [30], copyright 2012 American Chemical Society.

The proposed mechanism for the formation of the MWNTs from graphene is as follows [31]: (1) the production of graphene layers by ultrasonication of graphite in DMF, (2) the antioxidant effect of Fc–CHO which reduces the concentration of radical reactive species, reducing the cutting and damage of graphene layers, (3) the Fc–CHO adsorption at the edges of graphene layers inducing the rolling up of a sheet to form a nanoscroll (schematically indicated in Figure 4), (4) the trapping of Fc–CHO into the scroll, and (5) finally, Fc–CHO accepts and donates unpaired electrons to the graphene edges and converts the less stable scroll into a MWNT. This is an important step towards the controlled synthesis of carbon nanostructures. The interaction between graphene sheets and template molecules is expected to produce carbon nanostructures with well-defined properties such as diameter, chirality, shape and size.

Organic chemistry of graphene

From an organic chemistry perspective, graphene is a very exciting material as it can be functionalized on the two faces, at the edges and at the defects. Initially, graphene was expected to behave as a chemically inert surface, similar to graphite. However, it was experimentally and theoretically shown [32] that functional moieties attack graphene at both faces. This provides the changed energetics allowing the formation of chemical bonds that would be unstable if only one surface was exposed. This mechanism explains the exceptional reactivity of the graphene layer [33,34]. Unpaired electrons created at sites adjacent to the point of covalent bonding lead to a chain reaction from the initial point of attack [35]. For example, cycloaddition reactions onto graphene by means of first-principle calculations show a cooperative behaviour. The cycloaddition of benzynes were found to be energetically as strong as the attachment of hydrogen atoms, while for the 1,3-dipolar cycloaddition, the free energy of the reaction is slightly smaller [36]. Additionally, carbon atoms which localize at graphene edges are considered to be more reactive than carbon atoms at the bulk surface faces.

There are two types or graphene edges: zigzag and armchair. Zigzag edges are considered more reactive as compared to the armchair ones (Figure 5). Defects are considered to be reactive sites as well. The chemical methods reported to date yield graphene with different types and amounts of defects, including damage in the carbon lattice, structural imperfections, adatoms, and solvent molecules randomly adsorbed.

Thus, reactions occur at both faces of the graphene layer and different types of edges show different chemical reactivity. Additionally, defects such as vacancies, adatoms or substitutional atoms might act as active chemical sites on the graphene layer [37]. These features make the organic chemistry of graphene very accessible, but only partially understood.

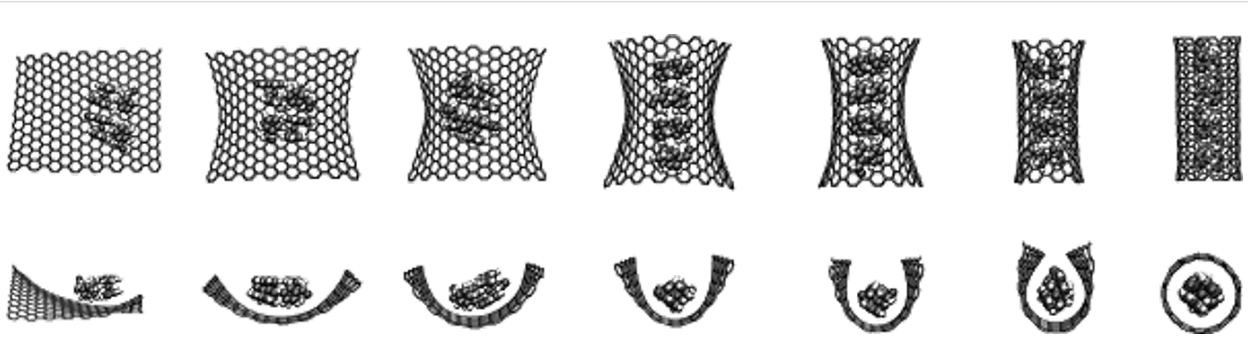

Figure 4: Slow-motion roll up of a graphene layer. Fc–CHO molecules template the rolling of the graphene sheet. Reprinted with permission from [31], copyright 2013 Wiley-VCH.

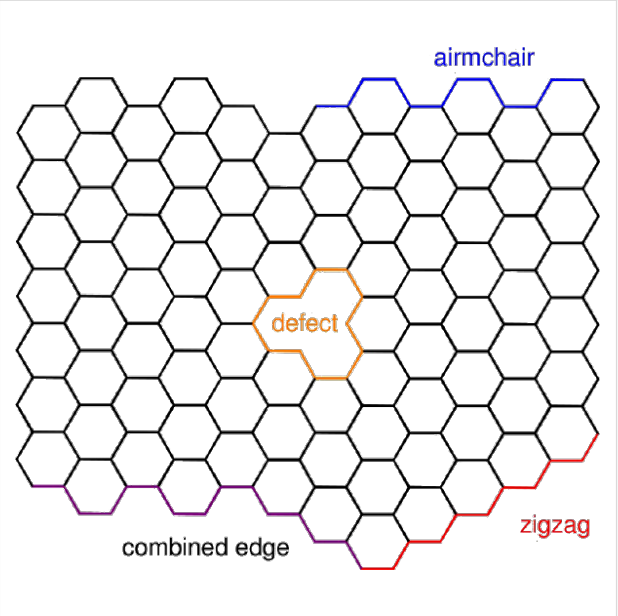

Figure 5: Schematic representation of reactive sites in graphene: surface faces, edges, and defects. Reprinted with permission from [22], copyright 2013 American Chemical Society.

Improvement in the chemical knowledge of the two dimensional material is expected to increase the tailored design of advanced materials.

The covalent organic functionalization of graphene is necessary for several purposes. For example: (1) to increase the dispersibility in common organic solvents and water and (2) to combine the properties of graphene with the properties of other functional materials such as nanoparticles, polymers or chromophores [38,39]. The appropriate design and construction of the graphene chemical surface are essential to reach the best material performance in the composite.

Visualizing graphene reactivity

Organic reactions might present different reactivity on the graphene surface when compared with other carbon nanostructures. The characterization of functionalized graphene layers typically requires the use of advanced analytic techniques. Graphene layers in dispersions are normally present at low concentrations and functional groups appear only sporadically. Thus, high-resolution techniques such as X-ray photoelectron spectroscopy (HR-XPS) and HR-TEM are very useful for the identification of functional groups.

A common organic reaction used for the functionalization of carbon nanostructures such as fullerenes, nanotubes, nano onions, nano horns and currently graphene, is the use of dienophiles as reactive species. One of the most successfully applied dienophiles to form covalent bonds with the hexagonal sp^2 lattice of carbon nanostructures is the azomethine ylide [40]. This intermediate reacts through a 1,3-dipolar cycloaddition mechanism.

The 1,3-dipolar cycloaddition, performed on graphene by employing an aldehyde and an α-amino acid as precursors, attacks both graphene faces and edges. This reactivity was observed by introducing protonated terminal amino groups that selectively bind gold nanorods allowing the recognition of the reactive sites by low resolution TEM (Figure 6). The HR-XPS analysis allowed for the determination of the concentration of functional groups [41].

In order to acquire more knowledge related to the organic chemistry of exfoliated graphene by ultrasonication, carboxylic groups where introduced on the graphene sheets by applying the 1,3-dipolar cycloaddition. This product was compared with

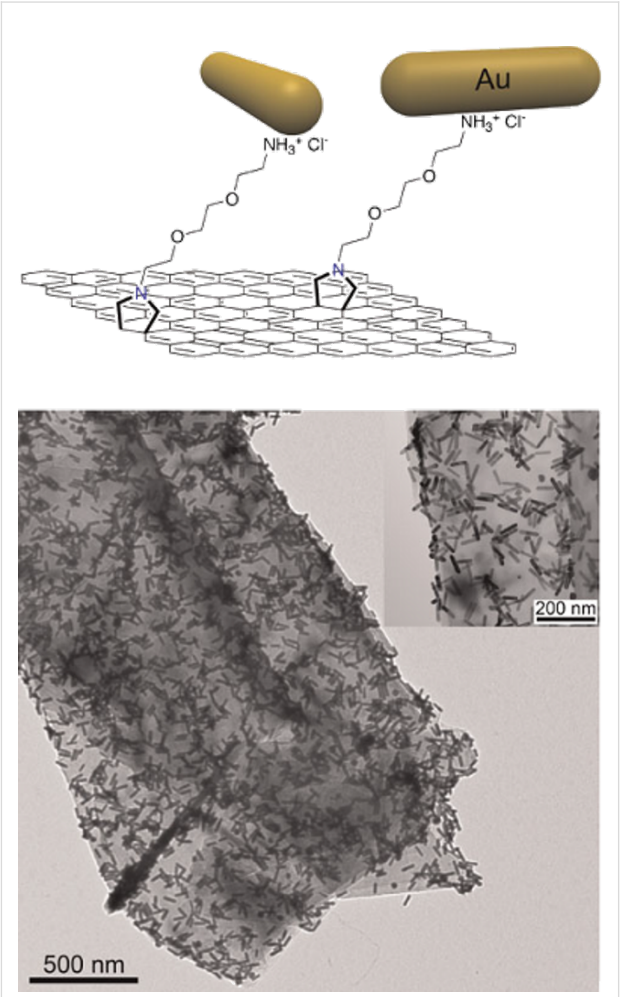

Figure 6: Graphene functionalization on the faces and edges by the 1,3-dipolar cycloaddition in DMF dispersions. Reproduced with permission from [41], copyright 2010 Wiley-VCH.

fresh exfoliated graphene by the derivatization of both products with PAMAN dendrons using an amide-bond condensation reaction [42]. Using Au NPs as markers, it was possible to visualize the reactive sites against each reaction.

As expected, for the 1,3-dipolar cycloaddition reaction, the TEM micrographs showed Au NPs completely dispersed on graphene faces and edges. In contrast, for the amide-bond condensation reaction, Au NPs were mainly found on the graphene edges. These results were corroborated by HR-XPS analysis of the products. A higher concentration of functional groups was found in graphene functionalized by using the 1,3-dipolar cycloaddition. With this, we demonstrated that graphene sheets could be selectively functionalized on the borders or in the entire lattice (Figure 7).

These results corroborate the success of the production of graphene layers by ultrasonication techniques. Oxidized carbon atoms on graphene sheets are introduced mainly on the edges of the layers when compared with GO. Additionally, the presence of the adatoms is not revealed by HR-XPS or HR-TEM.

Graphene nanohybrids

As described above, organic chemical reactions can be chosen to attack the complete graphene sheets or mostly the edges. Strategies such as this enable the integration of the outstanding properties of graphene in different applications. For example, graphene–polyoxometalate hybrids are considered important materials for the development of artificial photosynthesis. The properties of graphene enhance the electrocatalytic performance of the catalytic polyoxometalate and minimize the applied overpotential, increasing the long-term robustness of the device [43]. Recently, we demonstrated the feasibility of mimicking the oxygen-evolving centre of natural PSII by using functionalized graphene by the 1,3-dipolar cycloaddition with positively charged dendrons. The charged moieties recognize the inorganic tetraruthenate (Ru_4POM) anionic catalyst by electrostatic interactions, as illustrated in Figure 8. The device produced by deposition of the nanohybrid showed better performance when compared with similar substrates produced with functionalized CNTs. Our results support the importance of the rational chemical design of the carbon platform for the preservation of electron transport and accumulation processes associated with pristine graphene.

In order to introduce higher loadings of functional materials, stronger chemical reactions for graphene functionalization can be achieved by the attack of radical species. As reactive radical species, aryl diazonium salts are attractive and popular sources. These radicals covalently graft to carbon sp^2 surfaces [44]. Using this radical reaction, graphene was covalently functionalized using a positively charged *N*,*N*,*N*-trimethylbenzenammonium, as illustrated in Figure 9 [45]. This strategy produces

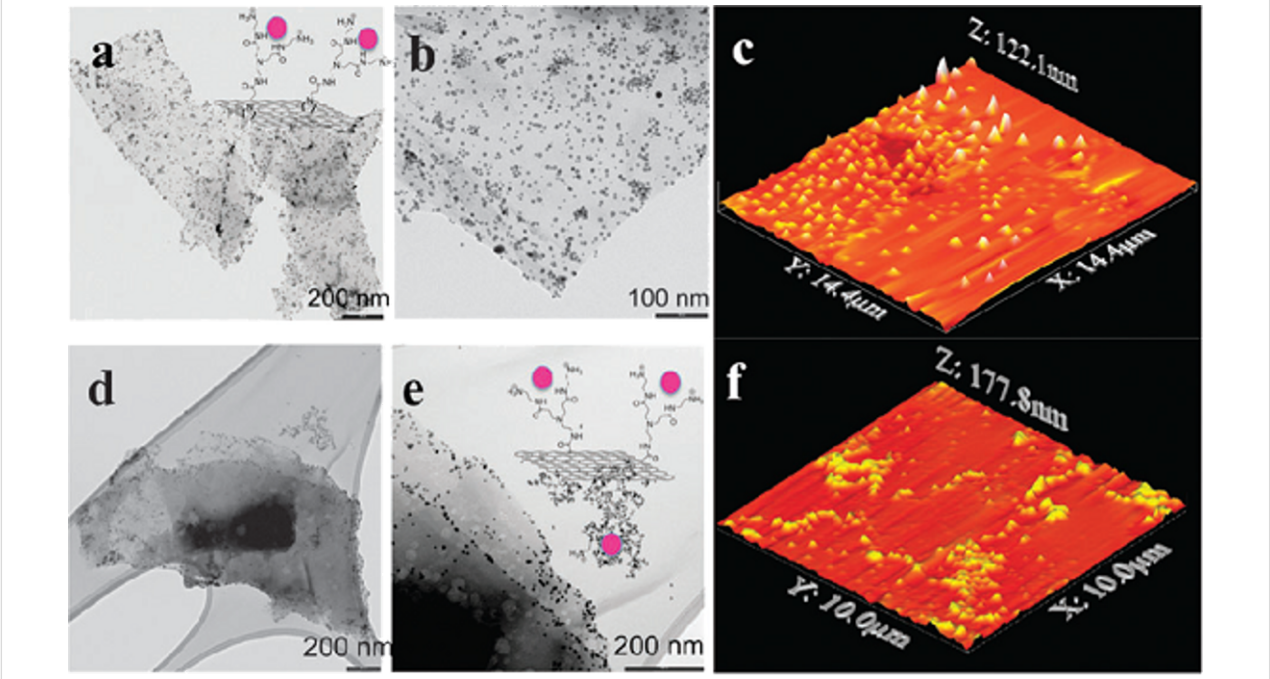

Figure 7: TEM and AFM micrographs after the addition of Au NPs for the identification of reactive sites against 1,3-dipolar cycloaddition (a–c) and amidation reaction on carboxylic groups created during the sonication process (d–f). Reproduced with permission from [42], copyright 2011 The Royal Society of Chemistry.

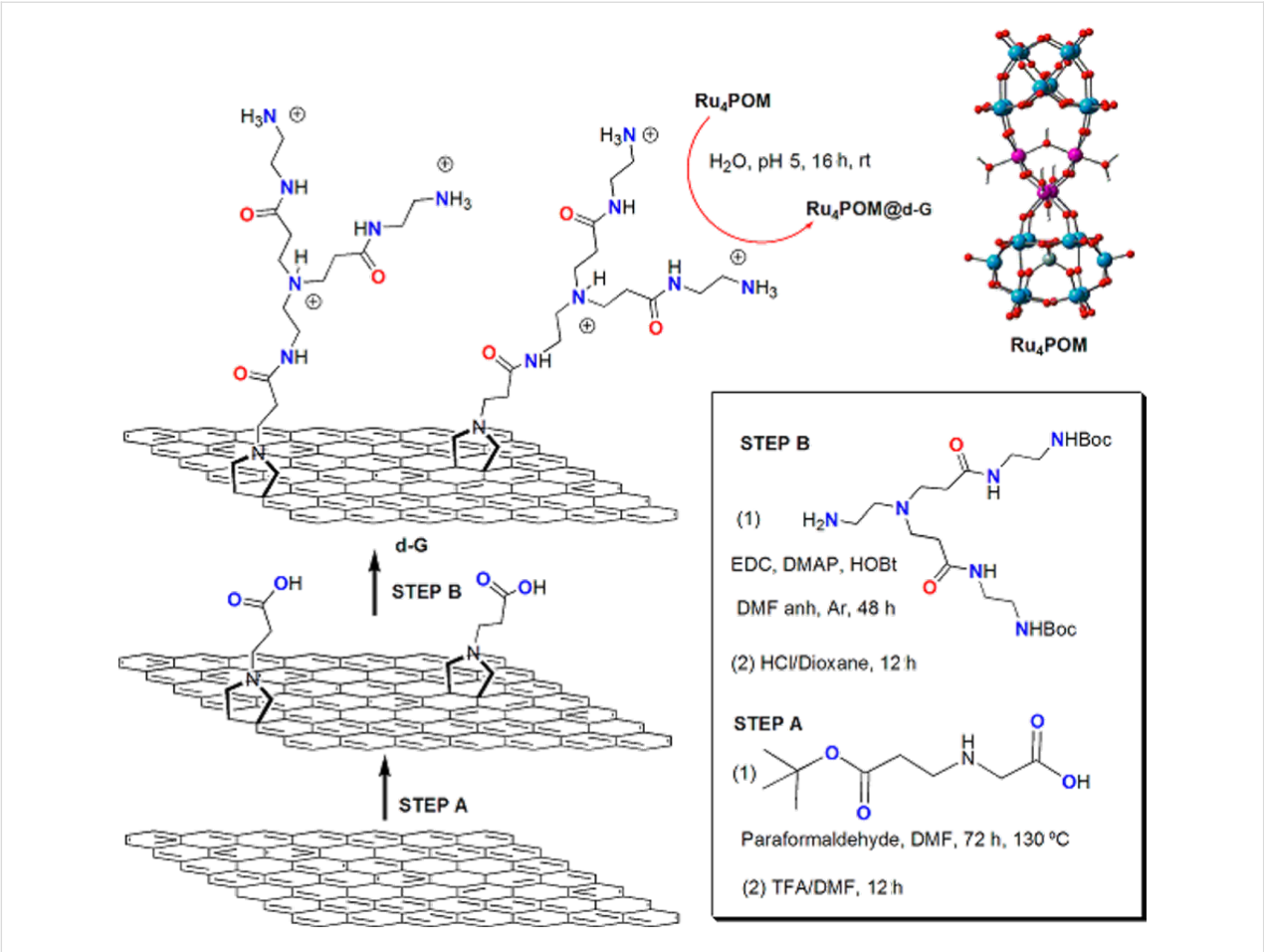

Figure 8: Synthesis of a graphene nano-platform supporting Ru_4POM. Reproduced with permission from [43], copyright 2013 American Chemical Society.

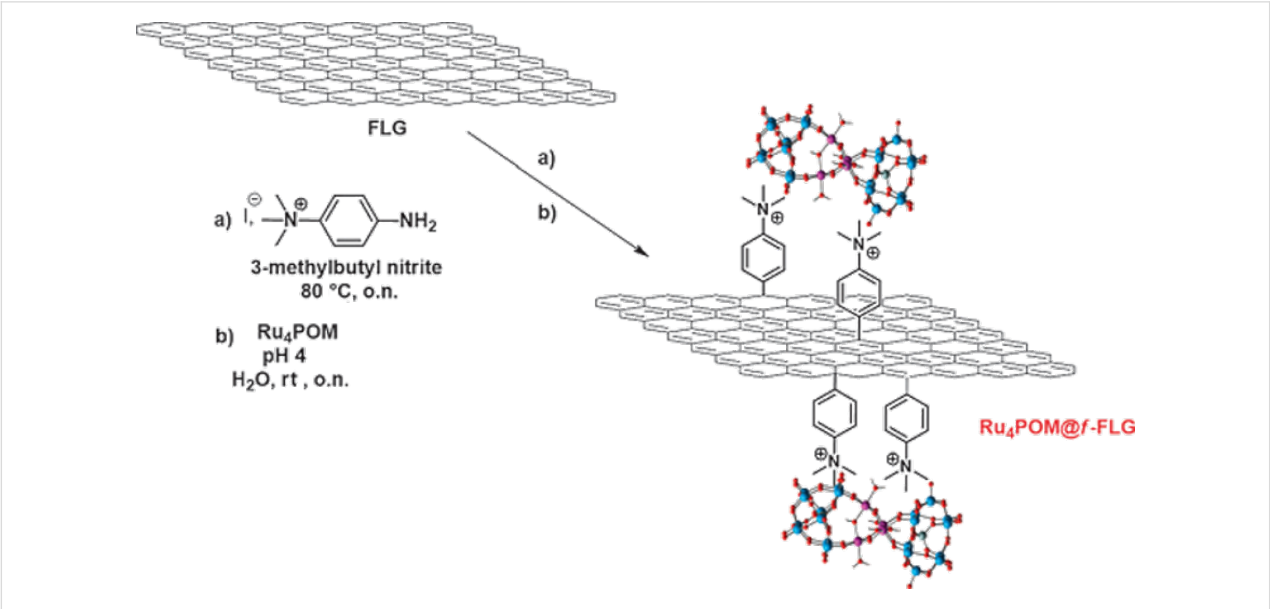

Figure 9: Synthesis of a polyoxometalate–graphene nanohybrid by using the diazonium-based reaction. Reproduced with permission from [45], copyright 2014 The Royal Society of Chemistry.

graphene layers with a substantial coverage of positive charges. Later, functional anions of Ru_4POM in the charged functional moieties by complementary electrostatic interactions were introduced. Comparing the insertion of a shorter moiety by the diazonium arylation reaction with the positively charged dendrons attached by the 1,3-dipolar cycloaddition described before, we confirmed the interplay of electrostatic forces and π-electron clouds on graphene. The proximity of the Ru_4POM to the graphene surface in the arylation reaction leads to a tight immobilization.

Imaging on graphene

Finally, the optical properties of graphene for the high contrast imaging of the two previously described graphene–polyoxometalate nanohybrids can be exploited. For this, Ru_4POM molecules were identified on functionalized graphene surfaces by low voltage aberration-corrected TEM (AC-TEM) [46]. Following this, a time sequence analysis of the dynamical rotation of individual Ru_4POM anions on functionalized graphene was performed. When comparing the Ru_4POM anions accompanying short carbon moieties with those attached to dendrons with longer carbon chains, a higher degree of motion and frequency were observed for the latter, as shown in Figure 10. For both samples, the presence of the functional moiety constrains the lateral motion of the anion catalyst with no preference with respect to the graphene surface. Our results are exciting because this implies that the graphene morphology might influence the performance of functional materials. Thus,

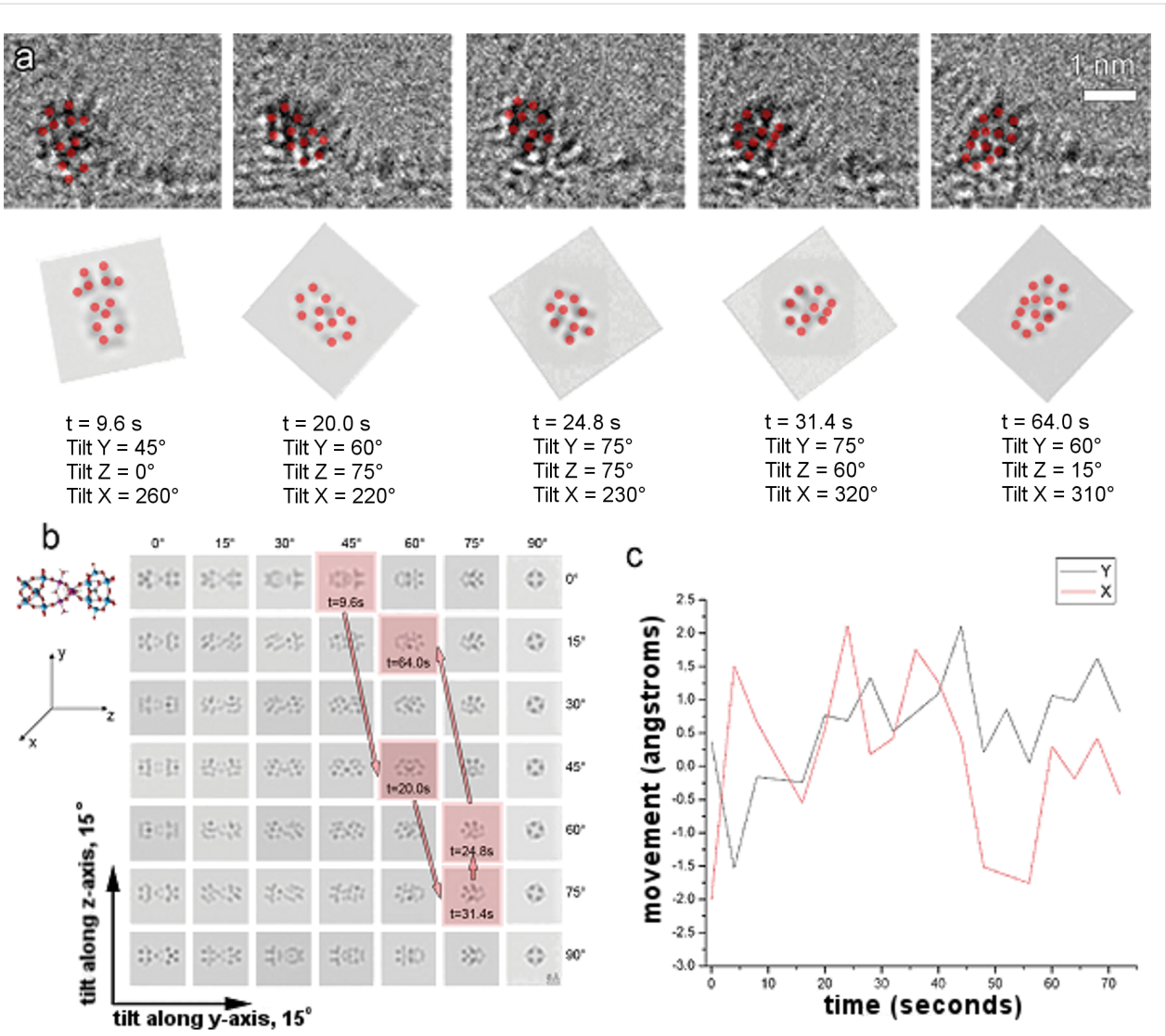

Figure 10: (a) Projections from a time sequence of dendron-functionalized Ru_4POM together with their corresponding orientations. (b) A plot showing the orientation changes as highlighted by the red squares. The movement path is indicated by arrows. (c) A diagram showing 2D translation of Ru_4POM with time. Reproduced with permission from [46], copyright 2013 Wiley-VCH.

it is essential to carefully design the functional moieties to covalently attach to the graphene surface as well as the functionalization strategy.

Conclusion

Substantial efforts have been performed for the mass scale-up and low-cost production of graphene. Thus far, wet chemical strategies have been demonstrated as the most efficient for the inclusion of graphene in low performance applications. To improve the physical properties of chemically produced graphene, it is necessary to gain better control of the experimental techniques by increasing the knowledge of the physical and chemical properties of both graphite and graphene. Likewise, it is critical to acquire detailed comprehension of the organic chemistry of the two dimensional material. The tailored chemical design of graphene platforms is essential for the development of new exciting functional materials.

Acknowledgements

Thanks are given to CONACYT through the project CB-166014. JIT thanks CONACYT for the scholarship 237551. We acknowledge the participation in the COST Action NanoTP.

References

1. Soldano, C.; Mahmood, A.; Dujardin, E. *Carbon* **2010,** *48,* 2127–2150. doi:10.1016/j.carbon.2010.01.058
2. Novoselov, K. S.; Geim, A. K.; Morozov, S. V.; Jiang, D.; Katsnelson, M. I.; Grigorieva, V.; Dubonos, S. V.; Firsov, A. A. *Nature* **2005,** *408,* 197–200. doi:10.1038/nature04233
3. Reina, A.; Jia, X.; Ho, J.; Nezich, D.; Son, H.; Bulovic, V.; Dresselhaus, M. S.; Kong, J. *Nano Lett.* **2009,** *9,* 30–35. doi:10.1021/nl801827v
4. Lee, J.-H.; Lee, E. K.; Joo, W.-J.; Jang, Y.; Kim, B. S.; Lim, J. Y.; Choi, S.-H.; Ahn, S. J.; Ahn, J. R.; Park, M.-H.; Yang, C.-W.; Choi, B. L.; Hwang, S.-W.; Whang, D. *Science* **2014,** *344,* 286–289. doi:10.1126/science.1252268
5. Ryu, J.; Kim, Y.; Won, D.; Kim, N.; Park, J. S.; Lee, E.-K.; Cho, D.; Cho, S.-P.; Kim, S. J.; Ryu, G. H.; Shin, H.-A.-S.; Lee, Z.; Hong, B. H.; Cho, S. *ACS Nano* **2014,** *8,* 950–956. doi:10.1021/nn405754d
6. Park, S.; Ruoff, R. S. *Nat. Nanotechnol.* **2009,** *4,* 217–224. doi:10.1038/nnano.2009.58
7. Dreyer, D. R.; Park, S.; Bielawski, C. W.; Ruoff, R. S. *Chem. Soc. Rev.* **2010,** *39,* 228–240. doi:10.1039/b917103g
8. Coleman, J. N. *Acc. Chem. Res.* **2012,** *46,* 14–33. doi:10.1021/ar300009f
9. Quintana, M.; Grzelczak, M.; Spyrou, K.; Kooi, B.; Bals, S.; Van Tendeloo, G.; Rudolf, P.; Prato, M. *Chem. Commun.* **2012,** *48,* 12159–12161. doi:10.1039/c2cc35298b
10. Xu, H.; Suslick, K. S. *J. Am. Chem. Soc.* **2011,** *133,* 9148–9151. doi:10.1021/ja200883z
11. Vélez, G. Y.; Encinas, A.; Quintana, M. Immobilization of Metal and Metal Oxide Nanoparticles on Graphene. In *Functionalization of Graphene;* Georgakilas, V., Ed.; Wiley-VCH: Weinheim, Germany, 2014; pp 219–254. doi:10.1002/9783527672790.ch8
12. Stankovich, S.; Dikin, D. A.; Piner, R. D.; Kohlhaas, K. A.; Kleinhammes, A.; Jia, Y.; Wu, Y.; Nguyen, S. T.; Ruoff, R. S. *Carbon* **2007,** *45,* 1558–1565. doi:10.1016/j.carbon.2007.02.034
13. Vallés, C.; Drummond, C.; Saadaoui, H.; Furtado, C. A.; He, M.; Roubeau, O.; Ortolani, L.; Monthioux, M.; Pénicaud, A. *J. Am. Chem. Soc.* **2008,** *130,* 15802–15804. doi:10.1021/ja808001a
14. Hardacre, C.; Holbrey, J. D.; Nieuwenhuyzen, M.; Youngs, T. G. A. *Acc. Chem. Res.* **2007,** *40,* 1146–1155. doi:10.1021/ar700068x
15. Martínez, R. C.; Iverson, B. L. *Chem. Sci.* **2012,** *3,* 2191–2201. doi:10.1039/c2sc20045g
16. León, V.; Quintana, M.; Herrero, M. A.; Fierro, J. L. G.; de la Hoz, A.; Prato, M.; Vázquez, E. *Chem. Commun.* **2011,** *47,* 10936–10938. doi:10.1039/c1cc14595a
17. León, V.; Rodríguez, A. M.; Prieto, P.; Prato, M.; Vázquez, E. *ACS Nano* **2014,** *8,* 563–571. doi:10.1021/nn405148t
18. Liu, C.; Hu, G.; Gao, H. *J. Supercrit. Fluids* **2012,** *63,* 99–104. doi:10.1016/j.supflu.2012.01.002
19. Suslick, K. S.; Hyeon, T.; Fang, M. *Chem. Mater.* **1996,** *8,* 2172–2179. doi:10.1021/cm960056l
20. Tapia, J. I.; Quintana, M. Chemical Manipulation of Graphene in Dispersions. In *Handbook of Carbon Nano Materials;* D'Souza, F.; Kadish, K. M., Eds.; *World Scientific Series on Carbon Nanoscience:*, Vol. 5,6; World Scientific, 2014; pp 185–217. doi:10.1142/9789814566704_0003
21. Hernandez, Y.; Nicolsi, V.; Loyta, M.; Blighe, F. M.; Sun, Z.; De, S.; McGovern, I. T.; Holland, B.; Byrne, M.; Gun'Ko, Y. K.; Boland, J. J.; Niraj, P.; Duesberg, G.; Krishnamurty, S.; Goodhue, R.; Hutchinson, J.; Scardaci, V.; Ferrari, A. C.; Coleman, J. N. *Nat. Nanotechnol.* **2008,** *3,* 563–568. doi:10.1038/nnano.2008.215
22. Quintana, M.; Vazquez, E.; Prato, M. *Acc. Chem. Res.* **2013,** *46,* 138–148. doi:10.1021/ar300138e
23. Giordani, S.; Bergin, S. D.; Nicolosi, V.; Lebedkin, S.; Kappes, M. M.; Blau, W. J.; Coleman, J. N. *J. Phys. Chem. B* **2006,** *110,* 15708–15718. doi:10.1021/jp0626216
24. Furtado, C. A.; Kim, U. J.; Gutierrez, H. R.; Pan, L.; Dickey, E. C.; Eklud, P. C. *J. Am. Chem. Soc.* **2004,** *126,* 6095–6105. doi:10.1021/ja039588a
25. Landi, B. J.; Ruf, H. J.; Worman, J. J.; Raffaelle, R. P. *J. Phys. Chem. B* **2004,** *108,* 17089–17095. doi:10.1021/jp047521j
26. ONeil, A.; Khan, U.; Nirmalraj, P. N.; Boland, J.; Coleman, J. N. *J. Phys. Chem. C* **2011,** *115,* 5422–5428.
27. Lotya, M.; King, P. J.; Khan, U.; De, S.; Coleman, J. N. *ACS Nano* **2010,** *4,* 3155–3162. doi:10.1021/nn1005304
28. Smith, R. J.; Loyta, M.; Coleman, J. N. *New J. Phys.* **2010,** *12,* 125008. doi:10.1088/1367-2630/12/12/125008
29. Chuvilin, A.; Kaiser, U.; Bichoutskaia, E.; Besley, N. A.; Khlobystov, A. N. *Nat. Chem.* **2010,** *2,* 450–453. doi:10.1038/nchem.644
30. Quintana, M.; Grzelczak, M.; Spyrou, K.; Calvaresi, M.; Bals, S.; Kooi, B.; VanTendeloo, G.; Rudolf, P.; Zerbeto, F.; Prato, M. *J. Am. Chem. Soc.* **2012,** *134,* 13310–13315. doi:10.1021/ja303131j
31. Calvaresi, M.; Quintana, M.; Rudolf, P.; Zerbetto, F.; Prato, M. *ChemPhysChem* **2013,** *14,* 3447–3453. doi:10.1002/cphc.201300337
32. Sofo, J. O.; Chaudhari, A. S.; Barber, G. D. *Phys. Rev. B* **2007,** *75,* 153401. doi:10.1103/PhysRevB.75.153401
33. Sharma, R.; Baik, J. H.; Perera, J. C.; Strano, M. S. *Nano Lett.* **2010,** *10,* 398–405. doi:10.1021/nl902741x
34. Quintana, M.; Spyrou, K.; Grzelczak, M.; Browne, W. R.; Rudolf, P.; Prato, M. *ACS Nano* **2010,** *4,* 3527–3533. doi:10.1021/nn100883p

35. Loh, K. P.; Bao, Q.; Ang, P. K.; Yang, J. *J. Mater. Chem.* **2010,** *2,* 2277–2289. doi:10.1039/b920539j
36. Denis, P. A.; Iribarne, F. *Chem. Phys. Lett.* **2012,** *550,* 111–117. doi:10.1016/j.cplett.2012.08.062
37. Banhart, F.; Kotakoski, J.; Krasheninnikov, A. V. *ACS Nano* **2011,** *5,* 26–41. doi:10.1021/nn102598m
38. Rodríguez-Pérez, L.; Herranz, M. A.; Martín, N. *Chem. Commun.* **2013,** *49,* 3721–3735. doi:10.1039/c3cc38950b
39. Georgakilas, V.; Otyepka, M.; Bourlinos, A. B.; Chandra, V.; Kemp, C.; Hobza, P.; Pavel, H.; Zboril, R.; Kim, K. S. *Chem. Rev.* **2012,** *112,* 6156–6214. doi:10.1021/cr3000412
40. Georgakilas, V.; Bourlinos, A. B.; Gournis, D.; Tsoufis, T.; Trapalis, C.; Alonso, A. M.; Prato, M. *J. Am. Chem. Soc.* **2008,** *130,* 8733. doi:10.1021/ja8002952
41. Quintana, M.; Grzelczak, M.; Prato, M. *Phys. Status Solidi B* **2010,** *247,* 2645–2648. doi:10.1002/pssb.201000310
42. Quintana, M.; Montellano, A.; del Rio-Castillo, A. E.; Van Tendeloo, G.; Bittencourt, C.; Prato, M. *Chem. Commun.* **2011,** *47,* 9330–9332. doi:10.1039/c1cc13254g
43. Quintana, M.; Montellano López, A.; Rapino, S.; Toma, F. M.; Iurlo, M.; Carraro, M.; Sartorel, A.; Maccato, C.; Ke, X.; Bittencourt, C.; Da Ros, T.; Van Tendeloo, G.; Marcaccio, M.; Paolucci, F.; Prato, M.; Bonchio, M. *ACS Nano* **2013,** *7,* 811–817. doi:10.1021/nn305313q
44. Chua, C. K.; Pumera, M. *Chem. Soc. Rev.* **2013,** *42,* 3222–3233. doi:10.1039/c2cs35474h
45. Hadad, C.; Ke, X.; Carraro, M.; Sartorel, A.; Bittencourt, C.; Van Tendeloo, G.; Bonchio, M.; Quintana, M.; Prato, M. *Chem. Commun.* **2014,** *50,* 885–887. doi:10.1039/c3cc47056c
46. Ke, X.; Turner, S.; Quintana, M.; Hadad, C.; Montellano-López, A.; Carraro, M.; Sartorel, A.; Bonchio, M.; Prato, M.; Bittencourt, C.; Van Tendeloo, G. *Small* **2013,** *9,* 3922–3927. doi:10.1002/smll.201300378

License and Terms

This is an Open Access article under the terms of the Creative Commons Attribution License (http://creativecommons.org/licenses/by/2.0), which permits unrestricted use, distribution, and reproduction in any medium, provided the original work is properly cited.

The license is subject to the *Beilstein Journal of Nanotechnology* terms and conditions: (http://www.beilstein-journals.org/bjnano)

The definitive version of this article is the electronic one which can be found at: doi:10.3762/bjnano.5.242

BEILSTEIN JOURNAL OF NANOTECHNOLOGY

Synthesis of boron nitride nanotubes and their applications

Saban Kalay, Zehra Yilmaz, Ozlem Sen, Melis Emanet, Emine Kazanc and Mustafa Çulha*

Review

Open Access

Address:
Department of Genetics and Bioengineering, Yeditepe University, Atasehir, 34755 Istanbul, Turkey

Email:
Mustafa Çulha* - mculha@yeditepe.edu.tr

* Corresponding author

Keywords:
boron nitride nanotubes; chemical modifications; medical applications; synthesis methods; toxicity

Beilstein J. Nanotechnol. **2015,** *6,* 84–102.
doi:10.3762/bjnano.6.9

Received: 13 May 2014
Accepted: 04 December 2014
Published: 08 January 2015

This article is part of the Thematic Series "Atomic scale interface design and characterisation: Experimental aspects and methods".

Guest Editor: C. Bittencourt

© 2015 Kalay et al; licensee Beilstein-Institut.
License and terms: see end of document.

Abstract

Boron nitride nanotubes (BNNTs) have been increasingly investigated for use in a wide range of applications due to their unique physicochemical properties including high hydrophobicity, heat and electrical insulation, resistance to oxidation, and hydrogen storage capacity. They are also valued for their possible medical and biomedical applications including drug delivery, use in biomaterials, and neutron capture therapy. In this review, BNNT synthesis methods and the surface modification strategies are first discussed, and then their toxicity and application studies are summarized. Finally, a perspective for the future use of these novel materials is discussed.

Review

Introduction

Boron nitride nanotubes (BNNTs) are known as structural analogs of carbon nanotubes (CNTs) but with superior properties [1-3]. Although they have structural similarities, they significantly differ in their chemical and physical properties. In contrast to CNTs, their electrical properties are not dependent on their chirality and diameter since they have a large band gap of about 5.5 eV. BNNTs also have excellent radiation shielding properties when compared to CNTs [4]. Since the BNNTs are composed of B and N atoms, their electronic structures are expected to be rather different from that of CNTs. The charge distribution is asymmetric in B–N bonds in BNNTs as compared to the C–C bonds in CNTs [5]. The electron density of B is attracted to the N atoms due to its higher electronegativity. Thus, the B–N bonds have a partially ionic character, which causes a gap between the valence and conduction bands. Therefore, the B–N bonds behave as a wide band gap semiconductor. Some relevant properties of BNNTs are as follows: high hydrophobicity, resistance to oxidation and heat, high hydrogen storage capacity and radiation absorption. Their electrical insulation is indeed very high, despite a high thermal conductivity [6]. Due to these properties, they can be used in a wide range of applications. BNNTs can resist oxidation in air up to 1000 °C while CNTs are resistant only up to 500 °C under the same conditions [7]. This makes BNNTs useful additives to increase

stability against the oxidation of surfaces [4]. Due to their highly hydrophobic character, BNNTs were also used to prepare super hydrophobic surfaces [8,9]. A hydrophobic surface was prepared by the synthesis of BNNTs on the surface of a stainless steel substrate where the contact angle was found to be more than 170° [8]. The origin of this super hydrophobicity was attributed to the surface morphology and adsorption capacity of BNNTs for airborne molecules [9].

BNNTs were also used to prepare composite materials to enhance their physical properties. Bansal et al. fabricated a glass composite by adding 4 wt % BNNTs and measured the strength and fracture toughness as 90% and 35%, respectively, which were greater than that of the constituents [10]. BNNTs also have significant hydrogen storage capacity, which was measured as 0.85 wt % – two times larger than that of the commercial CNTs [11].

The use of BNNTs in medical and biomedical applications has also been increasingly investigated [12-14]. Their hydrophobicity and toxicity concerns are the two factors that may limit their use in such applications. Due to their high hydrophobicity, BNNTs can only be used in biological applications after noncovalent [7] or covalent [15,16] modifications to increase their water dispersibility. Thus, they have been modified with several surface modifiers such as PEGylated phospholipids [17], and molecules of biological origin including DNA [18], proteins [13], and flavin mononucleotides (FMN) [19].

The synthesis of BNNTs was first reported in 1995 [20] by Chopra, based on an arc discharge method. Following the first report, several methods including arc discharge [20-22], chemical vapor deposition (CVD) [23-26], substitution reactions [27-29], ball milling [30-35], laser ablation [36-38], and low temperature methods [39-41] were reported. The CVD and ball milling methods are currently the two most widely used methods for the synthesis of BNNTs.

In this review, the most important BNNT synthesis methods are summarized first, then in vitro and in vivo studies of their toxicity are addressed. Finally, the investigations utilizing BNNTs in applications such as drug delivery, biomaterials preparation, biosensors, hydrogen storage, and neutron capture therapy are summarized by giving examples from the literature.

BNNT synthesis methods

There are several reports on the synthesis of BNNTs. The type of boron precursor, catalyst, temperature, mode of heat and duration are the key parameters in the synthesis procedure. Depending on these conditions, the length and size of the BNNTs will vary. In this section, a summary of the synthesis methods and the nature of the generated BNNTs are discussed. The precursors used in the synthesis of the BNNTs, formation mechanisms; application areas and physical properties (such as diameters and length) are summarized in Table 1.

Arc discharge

BNNTs were first synthesized by an arc discharge method resulting in a 1–3 nm inner diameter and a length of 200 nm [20]. An arc discharge was generated between a hexagonal BN (h-BN)-filled tungsten rod as an anode and a cooled copper electrode as cathode. The dark gray BNNTs were collected from the surface of the copper cathode. Later, hafnium diboride (HfB_2) electrodes [21], and conductive boron substances such as YB_6 [22] were used to obtain BNNTs using this arc discharge method.

Substitution reaction

Due to the structural similarity between CNTs and BNNTs, BNNTs can be obtained from CNTs via substitution reactions. BNNTs have been synthesized in high yields from CNTs and B_2O_3 under a $N_{2(g)}$ atmosphere at 1773 K [27]. A representative substitution reaction is given below.

$$B_2O_3+3C(CNTs)+N_2 \rightarrow 2BN(BNNTs)+3CO$$

Another substitution reaction was performed by interacting aligned carbon–nitrogen nanotubes (CNxNTs) or CNTs and B_2O_3 under NH_3 atmosphere at 1260 °C for 30 min to synthesize $B_xC_yN_z$/NTs [28]. The $B_xC_yN_z$/NTs were obtained from CNxNTs with a higher yield than that of the $B_xC_yN_z$/NTs obtained from CNTs. Finally, single-walled carbon nanotubes (SWCNTs) were used to obtain multi-walled boron nitride nanotubes (MWBNNTs) by mixing with B_2O_3 (as the B precursor) and MoO_3 (as the catalyst) under $N_{2(g)}$ atmosphere at 1500 °C for 30 min [29]. Although this method can be used to produce BNNTs, the outcome is not always pure BNNTs but rather some B- and N-doped CNTs result in addition [48].

Chemical vapor deposition

Chemical vapor deposition (CVD) is a well-known, economical method that is widely used for CNT and BNNT synthesis since it generates high yield products and requires simple experimental procedures. Lourie et al. performed the synthesis of BNNTs from borazine ($B_3N_3H_6$) based on the reaction provided below [49].

$$3(NH_4)_2SO_4+6NaBH_4 \rightarrow 2B_3N_3H_6+3Na_2SO_4+18H_2$$

Although Co, Ni, NiB and Ni_2B were found to be successful catalysts for the synthesis, NiB and Ni_2B were the most efficient precursors to obtain the highest BNNT yield. Later,

Table 1: Reaction conditions, growth mechanisms and applications of BNNTs reported in literature.[a]

Precursor	*T* [°C]; *t* [h]	Substrate	Method	Growth mechanism	Physical properties	Modification	Application	Ref.
B, h-BN, NH_3	<1100; 2 1200; 2	iron deposits alumina	ball milling (20 h), CVD	base-growth	40–100 nm diam., bamboo-like 40–100 nm diam., cylindrical shape	–	–	[42]
B:FeO:MgO (2:1:1), NH_3	1200; 0.5	Si/SiO_2	mechanic. mixed CVD	base-growth	30 nm diam., random direction, closed tip ends	–	–	[43]
	1300; 0.5			tip-growth	60 nm diam., random direction, closed tip ends			
	1400; 0.5			mixed-growth	10 nm diam., flower-like, closed tip ends			
B:FeO:MgO (1:1:1), NH_3	1300; 0.5			tip-/base-growth	100–500 nm diam., closed tip ends			
B:FeO:MgO (4:1:1), NH_3	1300; 0.5			tip-/base-growth	50–150 nm diam., closed tip ends			
B_2O_3, CaB_6, Mg, NH_3	1150; 6	–	CVD	base-growth	150 nm diam., >10 μm length	–	–	[23]
h-BN, N_2	1250–1300; 10	–	ball milling (100 h), CVD	–	30–60 nm diam., cylindirical shape, 500 nm length	covalent with NH_4HCO_3	reinforced material for Al-matrix composite	[44]
B, FeO, MgO	1100–1700; 1	–	ball milling, CVD	metal catalytic growth	50–80 nm diam., up to 10 μm length, straight nanowires	noncoval. polyaniline/ Pt/GO_X	amper. glucose biosensor	[45]
B, iron particle, N_2	1100; 15	Si/SiO_2	ball milling (50 h), CVD	metal catalytic growth	50–200 nm diam., up to 1 mm length, bamboo-like	–	insulators for electromechanical systems	[30]
MWCNT, H_3BO_3, NH_3	1300; 3	–	substitution	–	40–50 nm diam.	noncoval. trioctylam., tributylam., triphenyphos.	gel nanocomposite	[46]
B, $Co(NO_3)_2$, N_2, H_2	1100; 0.5–3	stainless steel	ball milling, CVD	–	bamboo-like	–	superhydrophobic surface	[8]
B, N_2	1200; 16	–	ball milling (150 h), CVD	–	20–50 nm diam. cylindrical, cylindrical capped by iron, bamboo-like	–	–	[32]

Table 1: Reaction conditions, growth mechanisms and applications of BNNTs reported in literature.[a] (continued)

KBH_4, NH_4Cl, N_2	1200–1300; 5–10	–	CVD	–	10–30 nm diam., up to 5 μm length, bamboo-like	–	–	[24]
B, Fe_2O_3, NH_3	1200–1300; 2.25	–	CVD	–	64–136 nm diam., bamboo-like	–	–	[25]
MWCNT, H_3BO_3, NH_3	1080; 6	–	substitution	–	10–100 nm diam., 10 μm length	coval. PVA and HP-MEC	imp. mechanical performance of polymer	[47]
ammon. borane, ferrocn., N_2	1450; 1	graphite crucible (graphite paper inner line)	CVD	(large diam. catalyst) vapor–liquid–solid (small diam. catalyst)	300 nm diam., 10 μm length, bamboo-like 15–200 nm diam., 100 μm length, cylindrical shape	–	–	[26]
B, Fe_2O_3, NH_3 B, Fe^{3+}-MCM-41, NH_3	600; 1	–	CVD	–	20–60 nm diam. 2.5–4 nm diam.	–	hydrogen storage	[11]
YB_6, N_2/Ar	–	–	arc discharge	mixed-growth	4–10 nm diam., 4–6 μm length, closed or open tip	–	–	[22]

[a]PVA: polyvinyl alcohol, HP-MEC: hydroxypropyl methylcellulose.

Ma et al. demonstrated that BNNTs could be synthesized without any metal catalyst using melamine diborate ($C_3N_6H_6{\cdot}2H_3BO_3$) [50]. A comprehensive study also showed that $B_3N_3H_6$ and decaborane could be used as precursors [51].

In a recent study, a large scale, high-yield BNNT synthesis method was demonstrated based on CVD using boron and metal oxides to produce so-called BOCVD methods [43,52-55]. The chemical mechanism of BOCVD [43] is shown below.

$$2MgO_{(s)}+2B_{(s)} \rightarrow B_2O_{2(g)}+2Mg_{(g)}$$
$$2FeO_{(s)}+2B_{(s)} \rightarrow B_2O_{2(g)}+2Fe_{(g)}$$
$$B_2O_{2(g)}+2NH_{3(g)} \rightarrow 2BN_{(s)}+2H_2O_{(g)}+H_{2(g)}$$

This mechanism is called vapor–liquid–solid (VLS). The high yield of BNNTs was observed as a white powder in the inner wall of the aluminum boat and on the substrate. Note that for the BOCVD mechanism to occur, variation in the types of catalysts, boron compounds and nitrogen-containing gases should be used.

The first successful synthesis of patterned BNNTs was performed by catalytic CVD [56]. To produce pure and vertically aligned BNNTs, a Si substrate was coated with Al_2O_3 of 30 nm thickness, then MgO, Ni, or Fe catalysts was deposited on the surface of the Al_2O_3 by pulsed laser deposition. This substrate was placed into a quartz tube with one end closed. The quartz tube was placed in a tube furnace for the growth of high yield BNNTs at 1100–1200 °C based on the growth vapor trapping (GVT) mechanism as seen in the SEM image in Figure 1.

The latest BOCVD method was studied by Nithya et al. [57]. They claim that large-scale production of BNNTs can be obtained using a mixture of $B/V_2O_5/Fe_2O_3$ and $B/V_2O_5/Ni_2O_3$ as precursors. In this experiment, the diameter and length of BNNTs was controlled and various BN nanostructures were obtained [57].

Recently, our group synthesized BNNTs from a boron ore, colemanite ($Ca_6B_6O_{11}{\cdot}5H_2O$), for the first time by means of CVD [58]. The reaction parameters such as type of catalyst, colemanite/catalyst ratio, reaction temperature and duration were

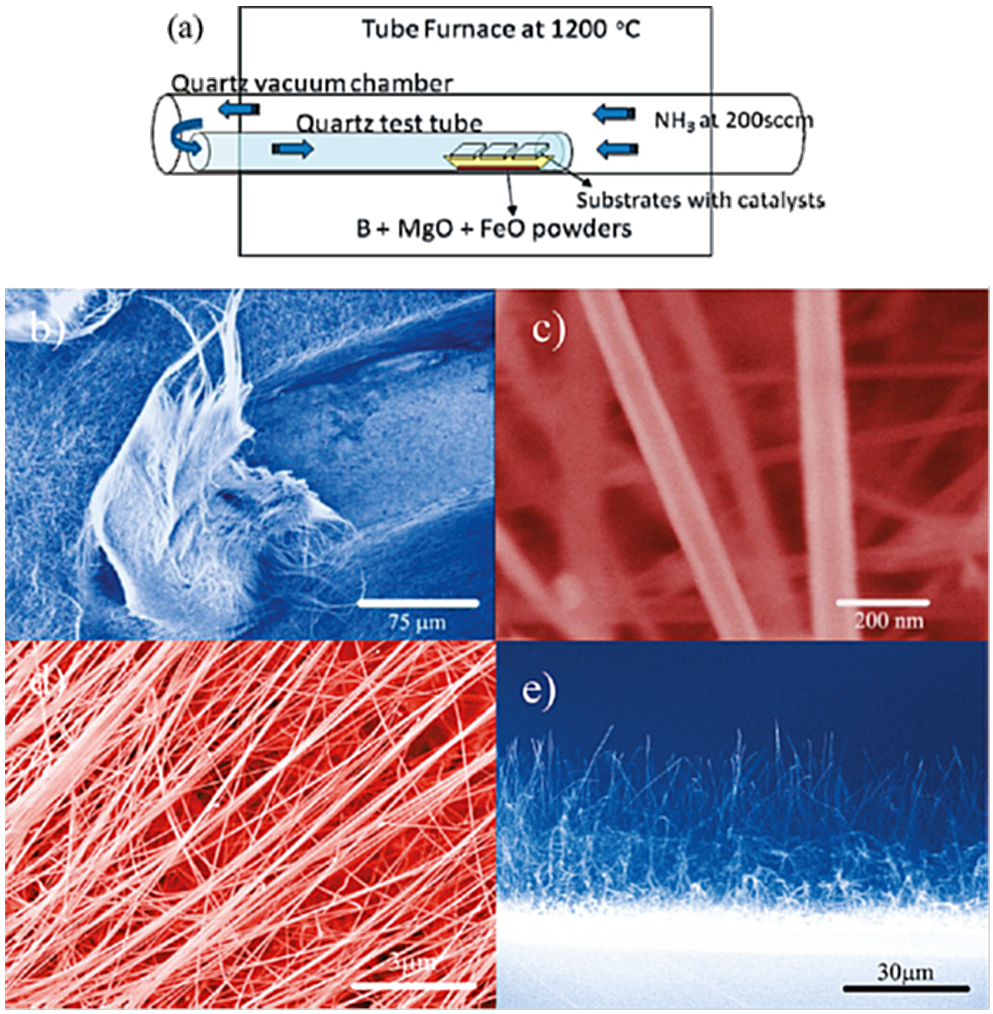

Figure 1: SEM images of BNNTs grown based on a CVD method. (a) Experimental setup, (b) stretching of dense BNNTs from the sample surface, (c) high magnification SEM image of BNNTs, (d) SEM images of slightly compressed BNNTs on a Si substrate, and (e) cross-sectional view of vertically aligned BNNTs. Figure adapted with permission from [56], copyright 2010 American Chemical Society.

optimized. ZnO, Al_2O_3, Fe_3O_4 and Fe_2O_3 catalysts were investigated with respect to their differences in performance. It was found that only Fe_2O_3 was effective as a catalyst. Figure 2 shows the SEM images of the results of the BNNT synthesis under several experimental conditions. The synthesized MWBNNTs were in the range of 10–30 nm in diameter, with a 5 nm wall thicknesses and 0.34 nm between walls. This simple method can be used to synthesize pure MWBNNTs on a large scale. The mechanism of BNNT formation was from base-growth, which included the conversion of Fe_2O_3 into metallic iron, the formation of an initial complex between metallic iron and BN, and the growth of a BN core into BNNTs on the surface of the metallic iron when the surface was supersaturated with B and N atoms.

In addition to the base-growth mechanism, BNNTs were also formed using the tip-growth, mixed-growth, and metal-catalytic-growth mechanisms (Table 1). During the annealing step in the metal-catalytic-growth mechanism (same as for base-growth), B atoms diffuse into the catalyst particle while the N_2 is decomposed to N atoms on the surface of the catalyst. The precursors precipitate layer-by-layer to form the BNNTs [30]. In the tip-growth mechanism, the catalyst is located on the tip of growing BNNTs [59]. Thus, the BNNTs are generally formed as bamboo-like structures.

The base- and tip-growth mechanisms of the BNNTs were revealed by TEM showing that the tube diameter and catalysts ratio were the important factors for the selection of growth mechanisms [43]. A ratio of 8:1 colemanite:catalyst caused the formation of BNNTs with a large diameter, thickness and a zigzag structure (Figure 2e) [59]. Under the similar experimental conditions with high catalyst content, the formation of thick BNNTs was reported [43].

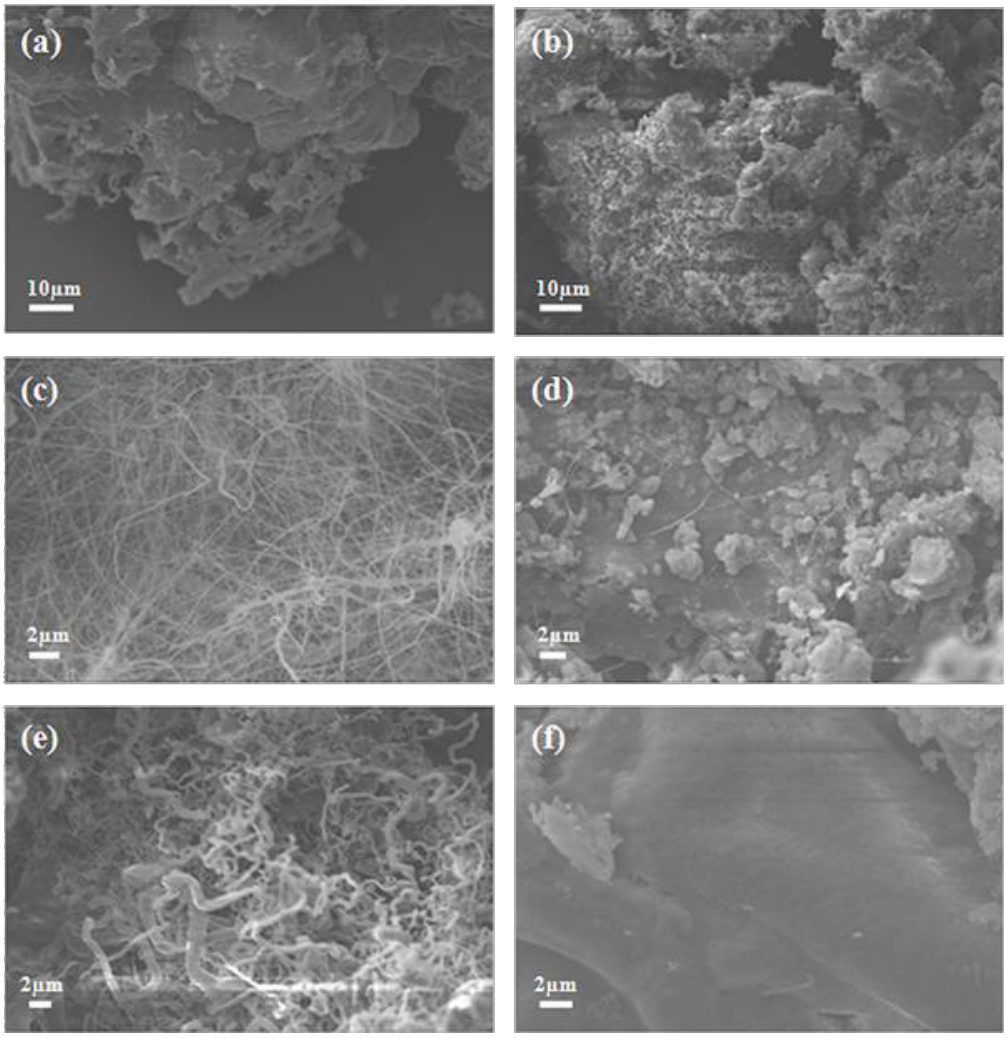

Figure 2: SEM images of the BNNTs products at the different reaction time and colemanite/catalyst ratios (w/w) after CVD application. The respective reaction time and colemanite/catalyst ratio (w/w) were (a) 30 min and 12:1, (b) 60 min and 12:1, (c) 120 min and 12:1, (d) 120 min and 32:1, and (e) 120 min and 8:1. (f) Boat surface after removal of the BNNTs, at 120 min and with a ratio of 12:1.

Ball milling method

Ball milling is commonly used in many studies to obtain a high yield of BNNTs [30]. The main objective of the ball milling method is to increase the surface area to bring the catalyst, boron and nitrogen precursors into contact as much as possible [32]. Although the impurities originating from the steel surface may interfere with the reaction, the synthesis of high-yield BNNTs was claimed [31]. The ball milling method allows transfers a high amount of mechanical energy to the boron powder, which results in an increased surface area and increased number of contact points among the catalyst, boron and nitrogen precursors, resulting in improved yield and product quality [31]. The structural changes in the boron compounds in the reaction mixture during ball milling were observed using X-ray diffraction [33]. It was also reported that there was no chemical reaction between NH_3 and boron powder during the ball milling process [33]. In the process, the boron precursor is ground either with or without catalyst. However, there is no report comparing both approaches. Li et al. reported that only amorphous boron was ball milled under a NH_3 atmosphere (300 kPa) for 150 h, at 155 rpm [60]. The milled boron and $Fe(NO_3)_3$ were sonicated in ethanol for 30 min followed by an annealing step under an 85% N_2 and 15% H_2 gas mixture. Bamboo-like, 40–80 nm diameter BNNTs were synthesized. Lim et al. reported that amorphous boron powder and NiB_x were ball milled in the presence of NH_3 atmosphere for 48 h at 180 rpm and annealed in the presence of N_2 and H_2 gases [34]. Bamboo-like BNNTs of 20–40 nm diameter and >250 nm length were obtained. Recently, Li et al. reported that the ball milling of amorphous boron powder and $Fe(NO_3)_3{\cdot}9H_2O$ is a more effective precursor for a high-yield BNNT synthesis [35]. It was possible to obtain relatively long BNNTs, up to 1 mm in

length, using ball milling annealing technique [30]. These long BNNTs were produced over the duration of a 50 h annealing step in the presence of N_2 gas at 1100 °C.

Laser ablation method

The synthesis of single- or double-walled BNNTs can generally be achieved using laser ablation [36-38]. It was reported that the only way to synthesize single-walled BNNTs (SWBNNTs) was by the laser vaporization method [37]. Golberg et al. synthesized pure BNNTs with 3–8 walls from BN under high N_2 pressure [36]. A single crystalline, 1–20 μm thick BN substrate and a CO_2 laser with a spot size of 80 μm diameter and 240 W power were used to synthesize pure BNNTs at temperatures higher than 5000 K. Naumov et al. synthesized MWBNNTs using a continuous wave CO_2 laser at 500 W power based on a BN substrate [61] and Lee et al. obtained gram quantities of SWBNNTs using continuous wave CO_2 laser [62].

BNNT synthesis methods at low temperatures

BNNT synthesis at low temperature is of great interest since it reduces the synthesis cost. However, the temperature has an important effect on the formation mechanism of the BNNTs [42,43]. It has been reported that the BNNT formation mechanism and tube diameter can be varied depending on the temperature or substrate/catalyst ratio [42,43]. Bae et al. obtained exclusively bamboo-liked BNNTs when processed at temperatures below 1100 °C and cylindrical-shaped BNNTs at 1200 °C from the ball-milled boron and $FeCI_2{\cdot}4H_2O$ precursors [42].

At low temperature, Xu et al. produced 60–350 nm diameter MWBNNTs at 450–600 °C with 50% yield [39]. Wang et al. synthesized BNNTs by means of microwave plasma at a temperature lower than 520 °C [40]. In this technique, a 6–100 nm pore size, aluminum oxide template was used along with microwave plasma. The BNNTs were grown on the surface of this template in the presence of B_2H_6/Ar and NH_3/N_2 at 10^{-4} Pa pressure at 520 °C. The diameter of the synthesized BNNTs was the same as the pore size diameter of the aluminum oxide template. The BNNTs were synthesized in a stainless steel autoclave at 380 °C from amorphous boron, NaN_3, and CH_3CN for 14 h. The obtained product was washed with ethanol, dried and a 5% BNNTs yield was calculated [41].

Modifications

Although the BNNTs have several unique properties, they are highly hydrophobic and difficult to use when an aqueous media is involved. Significant effort has been dedicated to increase the dispersibility of the BNNTs in aqueous media to extend their applicability to a variety of fields including medicine and biomedical applications. Two approaches to alter the surface properties of BNNTs are commonly employed: one is through covalent attachment of a molecule or molecular structure, and the other involves the physical adsorption of a molecular structure or a polymer onto BNNT surfaces. The chemical modification can be achieved through the –OH groups on the B atom and the $–NH_2$ groups at the edges or defects of the BNNTs. There are several polymeric structures that can be physical adsorbed onto the BNNTs to generate coated nanotubes or composites. In this section, examples of these two routes are addressed.

Chemical modifications

Due to their high resistance to harsh chemical conditions, BNNTs are consequently difficult materials for covalent functionalization (similar to CNTs). However, recent studies demonstrate that covalent modification is possible. The most commonly preferred chemical functionalization is through the –OH on B atoms and $–NH_2$ groups at the edges and defects, as shown in Figure 3 [15,44,63-65].

In one study, BNNTs were functionalized with amine groups by ammonia plasma irradiation [63]. It was predicted that $NH_2{\cdot}$ radicals produced by NH_3 plasma attached to B atom at the defects and edges whereas H· radicals attached to the N atoms of BNNTs. It was shown the amine-functionalized BNNTs (AF-BNNTs) were dispersible in chloroform. To investigate further chemical functionalization, the AF-BNNTs were coated with 3-bromopropanoyl chloride (BPC) via amide groups of acid chloride of BPC molecules and the amine groups of BNNTs. The study concluded that formation of amine groups on BNNT surfaces was helpful to increase the stability of molecules and polymers on the BNNTs surfaces [63].

3-aminopropyltriethoxysilane (APTES) is a widely-employed, aminosilane used in many applications. Ciofani et al. used APTES as an agent for silica coating to functionalize BNNTs [15]. For cellular uptake studies, a fluorescent dye, Oregon Green 488 carboxylic acid, succinimidyl ester was covalently bound to the functionalized BNNTs. The NIH/3T3 fibroblast cells were treated with this fluorescent dye labeled with the functionalized BNNTs. The study found that the labeled BNNTs were localized in the cytosol (Figure 4) [15].

A method to functionalize N–H at the defects on BNNTs with the –COCl groups of stearoyl chloride was successfully implemented [66]. This functionalization increased the dispersibility of the BNNTs in many organic solvents including chloroform, ethanol, acetone, toluene, *N*,*N*-dimethylacetamide, *N*,*N*-dimethylformamide, and tetrahydrofuran. BNNTs functionalized with proteins may increase their potential applications in the field of nanomedicine. The covalent grafting of BNNTs

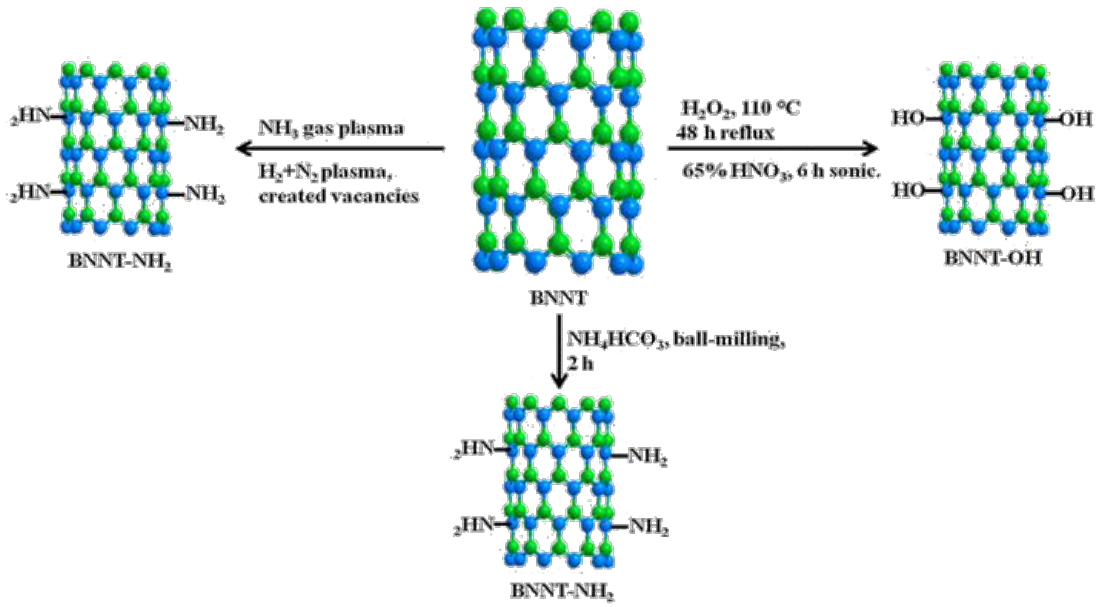

Figure 3: Summary of chemical modification routes of BNNTs.

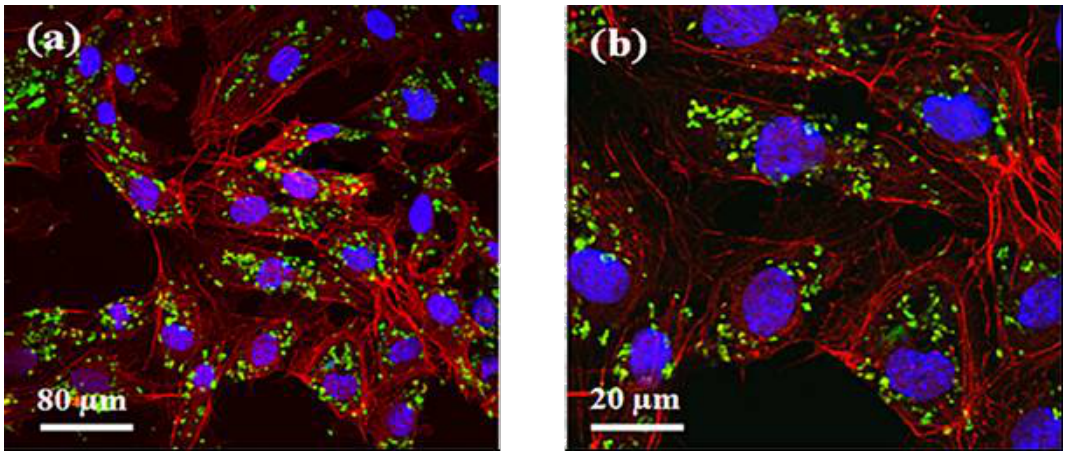

Figure 4: Low (a) and high (b) magnification confocal images of fluorescently labeled, functionalized BNNTs, where red, green, and blue are the cytoskeletal actin, functionalized BNNT, and nuclei, respectively. Figure adapted with permission from [15], copyright 2012 Elsevier.

with human transferrin, linked through a carbamide bond, was reported [67]. The transferrin–BNNTs were tested on primary human umbilical vein endothelial cells (HUVECs) to investigate their cellular uptake. It was concluded that the functionalization of the BNNTs via a targeting protein could generate smart and selective nanocarriers to be used in nanomedicine [67].

Physical modifications

For these types of modifications, weak interactions such as π–π, hydrophobic, and van der Waals forces are utilized to coat the BNNTs with mostly a polymeric material. Poly[*m*-phenylene-vinylene-co-(2,5-dioctoxy-*p*-phenylenevinylene)] (PmPV) was used to cover BNNTs via π–π interactions [7]. The prepared structure was more soluble in chloroform and ethanol than water. It was claimed that this composition had potential use in optical devices because of its luminescence properties and good dispersibility in organic solvents [7].

The BNNTs were also coated with PEGylated phospholipid 1,2-distearoyl-*sn*-glycero-3-phosphoethanolamine-*N*-[methoxy(poly(ethylene glycol))] conjugates (mPEG–DSPE)]

[17]. This polymer was selected due to its water solubility and biocompatibility. The mPEG–DSPE/BNNTs suspension was expected to be stable in water because fatty acids from DSPE should noncovalently interact with BNNTs and the hydrophilic mPEG could aid in the dispersion of the BNNTs in water. Indeed, the mPEG–DSPE/BNNTs were highly dispersed in water and slightly so in ethanol, acetone, methanol and chloroform. Furthermore, it was noted that sonication for long time periods (hours) could help to better disperse the BNNTs [17].

FMN is derived from vitamin B_2 and is a well-known phosphorylated biomolecule. The interaction of vitamin B_2 with BNNTs resulted in a highly fluorescent FMN–BNNT complex under daylight and UV light irridation [19]. Furthermore, the fluorescence from this complex was thermally stable and pH-dependent. It was suggested that FMN–BNNT nanohybrids could be used for biomedical imaging.

The adsorption of ferritin onto BNNTs was also reported. It was found that there was a natural affinity of this protein to the BNNT surfaces [13]. Figure 5 shows TEM images of ferritin immobilized onto the BNNTs. As seen, the ferritin not only can be adsorbed onto the BNNT surface but can also penetrate into the BNNTs. In addition, 1-pyrenebutyric acid *N*-hydroxysuccinimide ester (PAHE) was used to obtain more efficient immobilization. Because the PAHE has aromatic pyrenyl groups in its structure, a strong π–π interaction between the BNNT surface and PAHE is expected. When PAHE was used, a denser ferritin immobilization was observed [13].

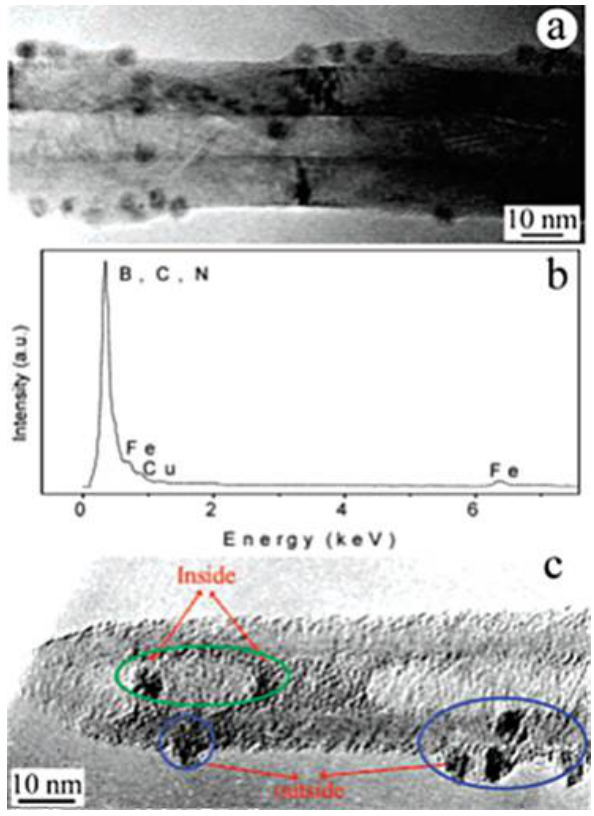

Figure 5: TEM images of ferritin molecules immobilized onto BNNT surfaces (a), EDS spectrum of BNNTs with immobilized ferritin molecules (b), ferritin molecules on the surface and inside of a BNNT (c). Figure adapted with permission from [13], copyright 2005 American Chemical Society.

A computational investigation concerning the interactions of BNNTs with tryptophan (Trp), aspartic acid (Asp), and arginine (Arg) was also carried out [68]. It was found that the polar Asp and Arg interacted with the BNNT surface through the charge transfer and electrostatic interactions while Trp, a neutral amino acid, had no interaction with the surface of the BNNTs. This study provides a deeper understanding into the nature of the interactions of amino acids (and perhaps similar molecules) with surface of the BNNTs [68].

The interaction of a peptide, HWSAWWIRSNQS, with BNNTs was studied using AFM [69]. It was found that the peptide–BNNT structure had an excellent dispersibility in water since the BNNTs were covered by this peptide. The study revealed that the presence of Trp (W), which has a benzene ring in the peptide sequence, exhibited a strong π–π interaction with the BNNT surfaces [69].

Dendrimers prepared from synthetic carbohydrate ligands were used to coat the BNNTs to mimic the cell surface receptors. The [G-2] dendrimers possessing R-mannose moieties ([G-2] Man) [70] were used to coat the BNNTs. Although uncoated BNNTs were precipitated very quickly, the [G-2] Man-coated BNNTs formed a stable suspension in water for weeks. The carbohydrates provide specific molecular recognition sites on cell membranes. The [G-2] Man-coated BNNTs were incubated with the R-mannose-specific receptor *Canavalia ensiformis* agglutinin (Con A). To observe the fluorescence of this complex, they were conjugated with fluorescein isothiocyanate (FITC). Chinese hamster ovary (CHO) cells were treated with this complex. It was found that the coated BNNTs had specific molecular recognition capability [70].

Glycol chitosan (GC) is widely used due to its biocompatibility and good solubility over a broad pH range [71]. The BNNTs were coated with GC during a 12 h sonication process. The TEM results indicated that the GC–BNNTs had two different configurations: bamboo-like shaped and noncontinuous walled. HUVECs were treated with the GC–BNNTs and the cellular uptake of the GC–BNNTs was observed. However, the uptake mechanism remains unclear and it might be worthwhile to further investigate it [71].

BNNT-grafted, poly(glycidyl methacrylate) and polystyrene brushes were prepared via atom transfer radical polymerization [72]. The resulting nanocomposite material was characterized using FTIR, TGA, SEM and TEM. The TEM images clearly show the formation of polymer grafts on the BNNT surface.

Toxicity of BNNTs

The potential adverse effect of nanomaterials on living systems is a growing concern. Although many engineered nanomaterials (ENMs) are already in use in several applications, there is no clear consensus regarding their possible impacts on living systems and the environment. The main reason behind this uncertainty is the lack of significant data on the subject. In addition, the diversity of nanomaterials and parameters further adds to the uncertainty for the proper assessment of the safety of these novel materials. Similar to many other ENMs, there are several issues with the assessment of the possible toxic effects of BNNTs. In early studies, there was no clear consensus regarding their cytotoxicity. In some reports it was found that BNNTs were toxic [73], and in others, not [74]. Naturally, first, in vitro studies were undertaken to assess the toxicity of the BNNTs. Similar to CNTs, one of the major problems in toxicity assessment of BNNTs is their low dispersibility in aqueous media, due to their high hydrophobicity. In order to increase the dispersion, either a surfactant or hydrophilic polymer is used to alter the surface properties. However, this process adds further uncertainties to the assessment since another material is introduced into the system. For example, polyethylenimine (PEI) is a cytocompatible polymer and principally used for DNA transfection and cell permeabilization. The BNNTs were coated with PEI for dispersion in aqueous media for biological applications [12]. The effect of the PEI-coated BNNTs with respect to viability, metabolism and cell proliferation of human neuroblastoma cell line (SH-SY5Y) was investigated. The PEI-coated BNNTs exposed cells analyzed at different time intervals. The viability, metabolic activity and proliferation of the cells were analyzed with MTT and trypan blue assays. The results showed that the PEI-coated BNNTs did not affect the viability of neuroblastoma cells up to 5 μg/mL [12].

Lahiri et al. studied the behavior of osteoblast cells in a scaffold constructed from the BNNT-embedded polylactide-polycaprolactone (PLC–BNNT) in orthopedic implants [75]. Using real-time PCR methods, they studied the *RunX2* gene expression profile, which is a transcription factor responsible for enhancing the cell proliferation. The results of the experiments showed that the PLC–BNNTs increased the *RunX2* gene expression of the osteoblast cells up to sevenfold. It was concluded that the positive effect of the BNNTs embedded into the scaffold on the cell proliferation was due to the natural affinity of proteins to the hydrophobic BNNTs [75].

Ciofani et al. investigated the cytotoxicity of GC–BNNTs [74]. The production of reactive oxygen species (ROS), DNA content in cell lysates, and apoptosis of cells were assessed using SH-SY5Y cells. The cells were exposed to GC–BNNTs up to 100 μg/mL. They found that the GC–BNNT-dependent toxic concentration was lower than the 50 μg/mL. On the other hand, 100 μg/mL of GC–BNNTs significantly decreased the cell viability. It was also found that the ROS production was not significant [74].

The hemolytic and cytotoxic effects of pure BNNTs on the malignant U87 (wild type p53), T98 (mutant p53) glioblastoma, MCF-7 adenocarcinoma mammary gland cells and normal MRC-5 fibroblast lung cells were investigated [76]. The hemolytic activity of the pure BNNTs was investigated by UV–vis spectroscopy and the results showed no significant hemolysis of cells that were exposed to the BNNTs. The metabolic activity of the BNNT-exposed cells using an MTT assay was studied and found that the BNNTs were significantly toxic at 200 μg/mL. The biocompatibility tests indicated that the pure BNNTs were good candidates at nontoxic concentrations for pharmacological applications [76].

The cell lines A549, RAW264.7, 3T3-L1 and HEK293 were exposed to BNNTs. The authors studied the cells with MTT and fluorometric microculture cytotoxicity assay (FMCA). As an indirect cytotoxicity measurement technique, FMCA assesses the esterase activity of cells. In general, the results indicated that the BNNTs were cytotoxic for the studied cell types even at low concentrations. In addition, the authors evaluated the toxicity of BNNTs according to the cell type and endocytosis ability of the cells. In particular, RAW 264.7 had high endocytosis capability as compared to A549 and 3T3-L1 cell types, and HEK293 showed low endocytosis capability. The results showed that the BNNTs slightly affected the growth and metabolic activity of HEK293 cells [77]. On the other hand, the effect of the BNNTs on A549 and 3T3-L1 cell types was worse than that of the HEK293 cells. The BNNTs were highly toxic for the RAW 264.7 cell type. From this study, one can be conclude that the toxicity of BNNTs is related to the cell type and the ability to perform endocytosis [77].

The morphology and viability of the GC–BNNTs-exposed HUVECs cells were also investigated [71]. The cells were incubated at increasing concentrations of GC–BNNTs for 48 and 72 h. The cell morphology and cell viability by amido black assay and trypan blue were studied. The total protein content and E1/1 protein expression profile were determined. It was found that a 50 μg/mL concentration of GC–BNNTs added to the cell medium caused a decreased proliferation. On the other hand, a 100 μg/mL concentration of GC–BNNTs showed a

modestly reduced proliferation at hours 48 and 72. Similar to the results reported by Ciofani et al., the GC–BNNTs were nontoxic at low concentrations [71].

The toxicity of glucosamine (GA)-, poly(ethylene glycol)$_{1000}$ (PEG_{1000})- and chitosan (CH)-coated BNNTs using MRC-5 cells was studied [78]. The study found that the BNNT–CH and BNNT–PEG were nontoxic in the range from 0.1 to 50.0 μg/mL but they were significantly toxic at 100 μg/mL. It was concluded that the GA–BNNT, PEG–BNNT and CH–BNNT were nontoxic at low concentrations but further evaluation on more cell types was suggested for their reliable use in biomedical applications [78]. The GA–BNNTs were found to be nontoxic to MRC-5 cells, but the previous studies claimed that glucosamine prevented the cellular uptake of glucose by pancreatic beta cells and caused cell death [73].

Poly-L-lysine (PLL) is known for its cytocompatibility due to the presence of amino groups and its use as a good dispersion agent [79]. The BNNTs were first coated with PLL and then with quantum dots (QDs) to observe the cellular uptake of PLL–BNNTs in C2C12 mouse myoblast cells. To observe the energy dependence of the uptake mechanism of the PLL–BNNTs, sodium azide was used to block ATP. They concluded that the PLL–BNNTs accumulation occurred in the cell membrane with energy dependent pathways. At a concentration of up to 10 μg/mL, the PLL–BNNTs exhibited no evidence of apoptosis, necrosis and membrane permeabilization [79].

Danti et al. investigated the cellular uptake of the BNNTs in the primary human osteoblasts (hOBs) under the exposure of low frequency ultrasound (US) [80]. The BNNTs were wrapped with PLL for stabilization in water. Furthermore, they found that the PLL–BNNTs were localized in the cytoplasm in the vesicles. Although the experimental system was complex, and further studies were necessary to understand the molecular mechanism, an obvious result was the increasing osteoblastic maturation. The findings of this study indicated that the BNNTs had potential use as nanotransducers for cellular therapies [80].

Ciofani et al. first reported a pilot investigation on the in vivo toxicity of BNNTs and they applied a single intravenous dose of BNNTs at 1 mg/mL. The changes in blood, kidneys and liver parameters were observed [81]. In the following study, 5 and 10 mg/kg of the BNNTs were intravenously injected into rabbits [82]. After the injection, the white blood cells, red blood cells and hematocrit levels were analyzed to investigate the possible adverse effects of the BNNTs. The authors did not see any adverse toxicological effect of BNNTs in blood [82].

Some of the important studies from the literature are summarized above and some of the toxicity assessment attempts are provided in Table 2. As seen, a number of reports claim that the BNNTs are nontoxic. Since the BNNTs are highly hydrophobic, it is difficult to perform toxicity assays for these materials. Therefore, a surface modification approach is generally performed to increase their dispersibility in aqueous media (Table 2). However, this may mask the real toxicity of the BNNTs since mostly the surface coating comes in contact with the cells. Based on the reports to date, their toxicity depends on the concentration, cell type and surface modifications, as is the case for all nanomaterials. A possible reason for the disagreement among the reports could arise from the synthesis procedure of the BNNTs, since the chemicals for the synthesis vary from synthesis to synthesis. Therefore, a careful purification step is vital for the further use of the BNNTs after the synthesis. Finally, although all in vitro studies provide very valuable data for the toxicity assessment, evaluation of this novel material

Table 2: Toxicity behavior of the BNNTs on cultured cells and animals.

Physical coating	In vitro / In vivo	Type of assay	Result	Ref.
PEI	SH-SY5Y	Trypan Blue, MTT	Nontoxic at 5 μg/mL	[12]
glycol chitosan	SH-SY5Y	MTT, WST-1, Apo. kit, Image-IT Green ROS kit	Low toxicity <100 μg/mL	[74]
PLC	Osteoblast cells (*RunX2*)	Real-time PCR	Increased cell growth	[75]
nonfunctionalized	U87, T98, MCF-7, MRC-5	MTT	Low toxicity <200 μg/mL	[76]
nonfunctionalized	A549, RAW264.7, 3T3-L1, HEK293	MTT, FMCA	Related to cell type	[77]
glycol chitosan	HUVECs	Amido Black assay, Trypan Blue	Nontoxic <50 μg/mL	[71]
glucosamine, PEG, chitosan	MRC-5	MTT	Nontoxic <50 μg/mL	[78]
PLL	C2C12	Trypan Blue, MTT, LIVE/DEAD, annexin V-FITC	Low toxicity <10 μg/mL	[79]
PLL	hOB	MTT	Low toxicity <10 μg/mL	[80]
glycol chitosan	Rabbit	Blood tests	Nontoxic	[81,82]

under in vivo conditions is critically important. At the moment, a lack of in vivo data is one reason a solid conclusion about the toxicity of the BNNTs cannot be drawn.

Drug delivery

The use of nanomaterials in drug delivery has also been investigated in recent years. Although the BNNTs can potentially be used for drug delivery, their behavior in biological environment is not very well understood at the moment. However, there are a few early reports and a review is included here.

A multifunctional, BNNT-based nanocarrier was synthesized using an Fe catalyst to render them magnetic and coated with PEI whereby QDs were attached to the PEI-coated BNNTs [83]. The cellular uptake of the BNNTs was tracked by QDs which revealed that the cellular uptake of the BNNTs depends upon the distance from the external magnetic field. A superconducting quantum interference device (SQUID) magnetometer analysis was carried out and revealed that the magnetic properties of the BNNTs were related to the Fe catalysts. Considering the magnetic properties and the ability to bind molecules on a large surface area of the BNNTs, it was concluded that the constructed structure was ideal for drug delivery purposes [83].

The core–shell structures of BNNTs with europium-doped, sodium gadolinium fluoride ($NaGdF_4$:Eu) were fabricated by using urea to demonstrate the chemotherapy efficiency of the BNNT–$NaGdF_4$:Eu composites in the presence and absence of a magnetic field [84]. The BNNT–$NaGdF_4$:Eu composites simultaneously show fluorescent and magnetic properties. Thus, imaging and targeting of the composites can be more easily achieved. Human LNCaP prostate cancer cells were treated with the BNNT–$NaGdF_4$:Eu composites in the presence and absence of a magnetic field and higher cell-associated uptake was found in the presence of a magnetic field. Then, the composites were loaded with doxorubicin (dox) to investigate the viability of LNCaP prostate cancer cells in the magnetic field. It was found that dox-loaded BNNT–$NaGdF_4$:Eu composites had higher toxicity in the presence of a magnetic field due to increased cellular uptake of the composites and thus increased doxorubicin delivery. It can be said that the BNNT–$NaGdF_4$:Eu composites increase the chemotherapy efficiency by the use of an external magnetic field [84].

The BNNT–mesoporous silica (BNNT–MS) hybrids were reported for their use in drug delivery [85]. In this study, a negatively and positively charged BNNT–mesoporous silica, BNNT–MS and BNNT–MS–NH_2, respectively, were produced. These structures were loaded with dox. The loading efficiency was found to be pH dependent and both negatively and positively charged structures had the same dox loading capacity. The BNNT–MS–NH_2 had higher uptake potential in LNCaP prostate cancer cells due to its charge. Thus, it had a higher toxicity towards LNCaP prostate cancer cells. It was concluded that the prepared structures have potential in cancer therapy [85].

To investigate in vivo biodistribution of the BNNTs, they were functionalized with GC then radiolabeled with ^{99m}Tc [86]. After 30 min of injection into mice, the BNNTs were in the systemic circulation and accumulated in the liver, spleen and intestinal tissues. After 4 h, radiolabeled BNNTs were found in the bladder. They were eliminated from body by renal excretion and the BNNTs conjugated with chitosan were degraded through enzymatic degradation. After 24 h, there was a reduction of radiation in the related organs (Figure 6). These promising results showed that the BNNTs have potential to carry new drugs or radioisotopes [86].

Electroporation is used for increasing the cell permeability for introduction of molecules into cells. However, it requires a high voltage, which is one of the problems for drug delivery. The applicability of BNNTs in an electroporation process was investigated [87]. The BNNTs were stabilized in phosphate buffered solution (PBS) with the help of PLL. Before applying electroporation to human neuroblastoma SH-SY5Y cells, the cells were incubated in the BNNT suspension, and then the electroporation was performed. The results demonstrated that a low electric field was adequate for electroporation. The BNNTs acted as mediators for electroporation as they interacted with the cell membrane. These experimental findings indicated that the BNNTs are promising tools for drug and gene delivery using electroporation [87].

A theoretical study revealed that platinum-based anticancer drugs preferentially interacted with Al-doped BNNTs as compared to pristine, zigzag and armchair BNNTs [88]. Cisplatin (cis-Pt) and nedaplatin (neda-Pt) molecules were used as platinum-based anticancer drugs. An aluminum (Al) atom is substituted for a boron atom. The Al atom induced a protrusion out of the plane of the BNNT and a distortion occurred at the doping site to relieve the stress. Density functional theory was performed to observe the absorption of cis-Pt and neda-Pt on pristine and Al-doped BNNTs. The results indicated that the chlorine atom of cis-Pt and the oxygen atom of the carbonyl group of neda-Pt interacted with the Al-doped BNNTs [88].

Biomaterial applications

The addition of BNNTs into a polymeric matrix could increase the physical strength, degradation rate and durability of the final product. Therefore, their use in polymeric biomaterials was investigated.

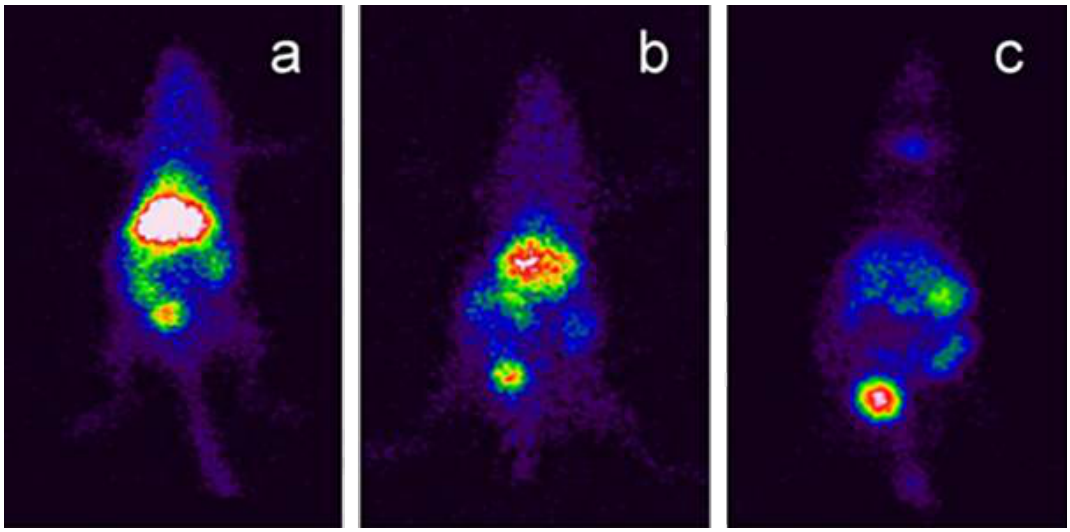

Figure 6: Scintigraphic image of radiolabeled, glycol chitosan BNNTs after (a) 30 min, (b) 1 h, and (c) 4 h after injection. Figure adapted with permission from [86], copyright 2012 Elsevier.

In one study, the BNNTs were used in polylactide-polycaprolactone (PLC) copolymer as additives to improve the properties of the polymer as an orthopedic implant [75]. With the addition of BNNTs, a 1370% increase in the mechanical strength of the polymer was observed. The reason for such an improvement was attributed to the formation of BNNT bridges among the polymeric structures. Figure 7 shows such structures as marked in red. When the osteoblast cell viability was evaluated with respect to the BNNT–PLC composite, and compared only to PLC, an increased cell viability was observed. In addition, it was found that the *RunX2* gene, which is the major regulator for the differentiation of the osteoblasts cells, increased the expression level with the addition of the BNNTs into the polymer. These results indicated that BNNTs plays an important role to improve mechanical properties of a scaffold and up regulated the gene expression for increased cell viability for orthopedic applications [75].

Hydroxypatite (HA) is an important material used in orthopedic implant applications [89]. 4 wt % of BNNTs were added into HA to improve its mechanical properties. It was found that compared to HA alone, an increase in elasticity of up to 120%, a 129% increase in hardness, and an 86% increase in fracture toughness were possible. The BNNT–HA composite also showed a 75% increase in the wear resistance. It was noted that the addition of BNNTs to HA did not have any adverse effect on osteoblasts cell proliferation and viability [89].

Sensing applications

One interesting application area of BNNTs is the field of sensors. Although there are not many reports regarding their use in sensors, a few available reports are included here as examples. The unique properties of the BNNTs can be combined with the properties of other nanomaterials to construct novel sensor devices for humidity, carbon dioxide detection, and clinical diagnostics.

A highly sensitive humidity sensor using BNNTs and silver nanoparticles (AgNPs) for the rapid detection of humidity was fabricated [90]. Figure 8 shows the humidity sensor system. The adsorption–desorption tests showed that the AgNP–BNNT material had a potentially fast response/recovery time of 100/15 s for the detection of relative humidity at room temperature [90].

The use of Ni-encapsulated BNNTs in optomagnetic-based sensors with respect to their magnetic and optical band gap properties was evaluated [91]. Two intense blue emission peaks at ~480 nm and ~365 nm were observed upon encapsulation of BNNTs with Ni. The time-resolved photoluminescence spectroscopy (TRPL) provided a photoluminescence spectrum with a bi-exponential decay of 280 ps. It was suggested that the Ni-encapsulated BNNTs could be used in clinical diagnostics and bioimaging applications due to their TRPL properties [91].

Hydrogen storage in BNNTs

Hydrogen is considered to be an exceptional energy source material since it produces clean energy in high yield. Although there are several techniques that can generate an abundant amount of hydrogen, its storage and transportation is an obstacle for its widespread use. In this respect, BNNTs were also investigated for their hydrogen adsorption capacity. Molecular dynamics simulations indicated that the collision and

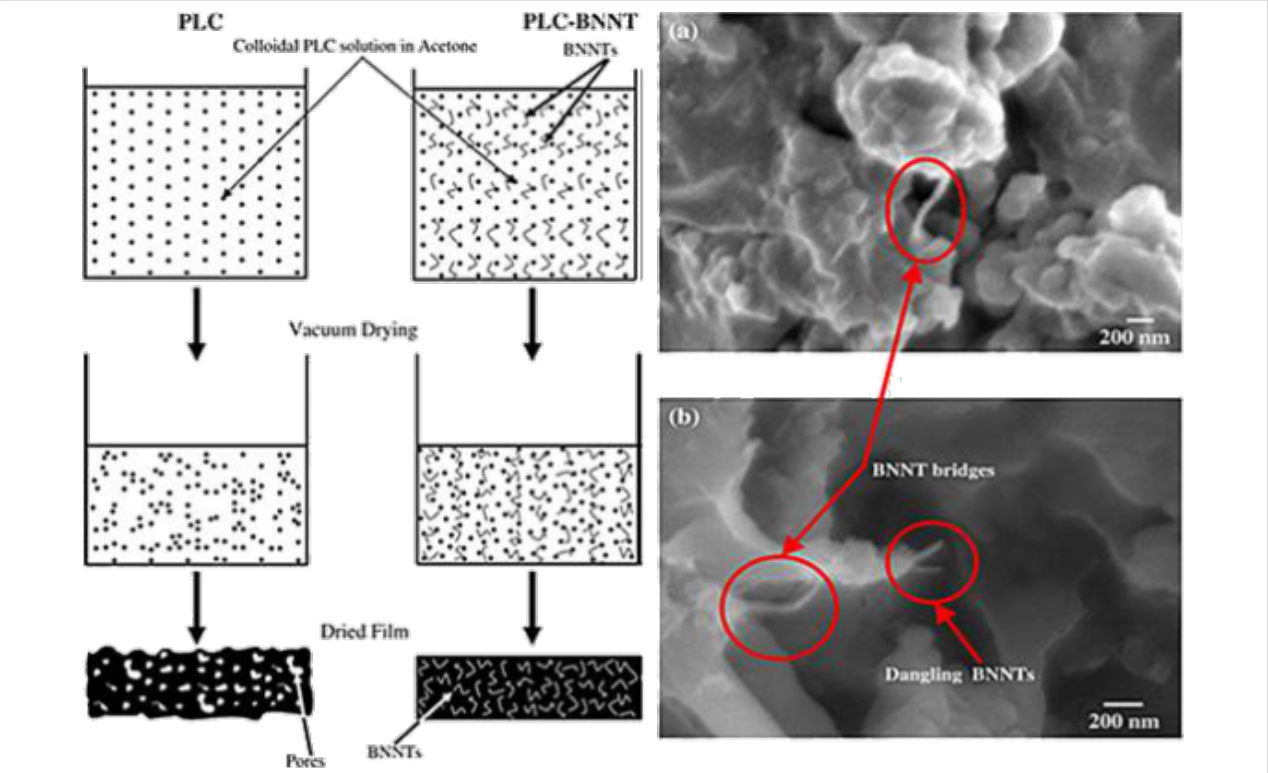

Figure 7: Preparation process of PLC (left) and PLC–BNNTs (right) and (a,b) SEM images of a PLC–BNNT composite exhibiting improved mechanical properties due to BNNTs bridges (red). Figure adapted with permission from [75], copyright 2010 Acta Biomaterialia.

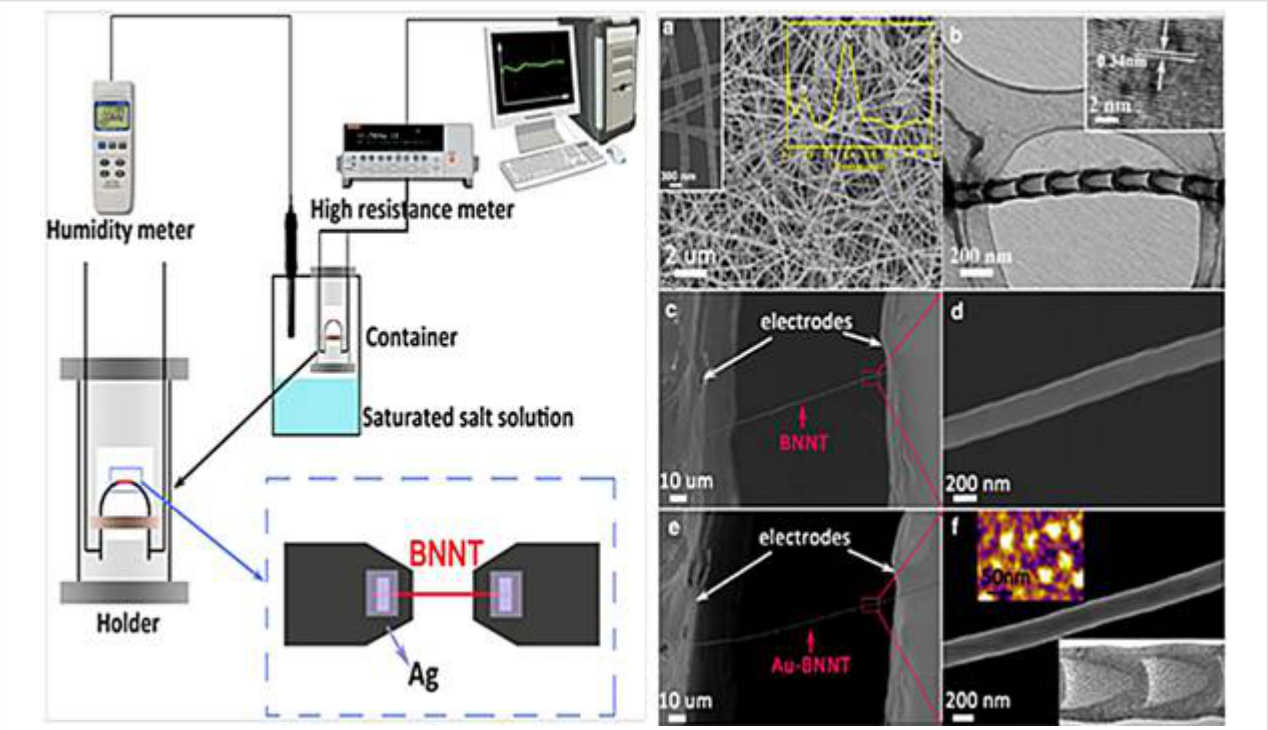

Figure 8: Schematic representation of a humidity sensor test system with a single BNNT and a single BNNT–AgNPs. (a) SEM image (left) and EDS spectrum (right) and (b) TEM and HRTEM image of the BNNTs, (c) and (e) the SEM images with a single BNNT and single AgNP–BNNT, (d) and (f) the higher magnification SEM images in (c) and (e) marked with red square (f) AFM (upper) and TEM (lower) images. Figure adapted with permission from [90], copyright 2013 Elsevier.

adsorption behavior of hydrogen molecules in single-walled BNNTs varies according to hydrogen incident energy. Additionally, the theoretical investigations showed that the B–N bond length (1.46 Å) of the BNNTs was larger than the C–C bond length of CNTs (1.42 Å). Therefore, the penetration of hydrogen molecules through the BNNT walls is faster than that through the CNT walls [92]. On the other hand, the B–N heteropolar bonding structure of the BNNTs induced an extra dipole moment on the hydrogen molecules contrary to the CNTs [34]. In addition, there are experimental reports supporting the simulation studies [11]. For the BNNTs, which were synthesized with Fe^{3+}/MCM-41 (mobile composition of matter) complex catalysts, the percentage of the adsorbed hydrogen molecules was two times larger than for the commercial CNTs. The adsorption capacity of hydrogen molecules by BNNTs was measured as 0.85 wt % by the Intelligent Gravimetric Analyser at room temperature [11].

Margulis at al. theoretically investigated the preferable adsorption sites on the BNNT surface by using the semi-empirical AM1 method [93]. The computational models showed that the hydrogen atoms favorably bonded to the nitrogen atoms as compared to boron atoms due to the higher electronegativity of the nitrogen atoms. Because of the high electronegativity of the nitrogen atoms, the hydrogen atoms can come into closer contact than the boron atoms can, but with the same energy. The simulations indicated that the diameter was an important property of the BNNTs to increase the amount of stored hydrogen molecules [93].

The binding positions of the hydrogen molecules on the surface of the SWBNNTs were also investigated [94]. It was claimed that the hydrogen molecules had a capacity to bind to the SWBNNTs as perpendicular, longitudinal and transversal positions in an ab initio theoretical study. The hydrogen molecules approached the SWBNNTs in perpendicular position to the surface, which slightly polarized and raised the binding energy of the molecules. On the other hand, the hydrogen atoms interacted with the nitrogen atoms more than the boron atoms [94].

The number of walls and the diameter of each wall affect the hydrogen molecule storing capacity of the BNNT. The hydrogen physisorption capacity of the SWBNNTs and MWBNNTs was theoretically investigated by grand canonical Monte Carlo theoretical studies [95]. The simulations showed that the triple-walled (TW) BNNTs provided the necessary limited spaces for hydrogen atoms between the tube walls. The double-walled (DW) BNNTs were predicted to store more hydrogen atoms due to the large space within the nanotubes as compared to the TWBNNTs with the condition that the inner tube diameter was sufficiently large in the DWBNNTs. As a conclusion, the number of BNNT walls was found to be very important as well as the wall diameter, which could be chosen to inhibit the hydrogen–hydrogen repulsion in the inner space of the BNNTs for improved hydrogen atom storage capability [95].

The hydrogen molecule storage capacity for BNNTs of several morphologies were also investigated experimentally [96]. The studies showed that the number of absorbed hydrogen molecules increased with the hydrogen pressure. The flower-type, straight-walled and bamboo-type BNNTs were evaluated for their hydrogen adsorption capacity. It was found that the adsorption of the flower-type was 2.5 wt % at about 100 bar hydrogen pressure. The straight-walled BNNTs exhibited an increased hydrogen storage capacity up to 2.7 wt % and the bamboo-type BNNTs had the highest hydrogen uptake capacity of 3.0 wt % [96].

The BNNTs were synthesized using annealing and ball milling methods and the hydrogen storage on the BNNTs was investigated experimentally by pressure–composition isotherms (PCI) and temperature-programmed desorption (TPD) methods [34]. The results showed that the hydrogen uptake capacity of purified BNNTs was 2.2 wt %. The temperature effect on the hydrogen storage capacity of the BNNTs was also investigated in the study. The BNNTs were exposed to the hydrogen atoms at 180 and 250 °C and with resulting hydrogen absorption in the range of 1.6–1.2 wt % [34].

The theoretical investigation of the hydrogen storage capacity of BNNTs showed that the nature of the electronic structure of boron and nitrogen atoms, as well as the diameter and dimensions of the BNNT walls have an impact on their hydrogen adsorption capacity. Although there are limited numbers of reports, the studies show that BNNTs are possibly valuable materials for hydrogen storage. It is important to note that further experimental investigations addressing the parameters such as temperature, gas pressure, and purity of the BNNTs should be conducted.

BNNTs for neutron capture therapy

The neutron absorption capacity of BNNTs was also reported [97]. Ciofani at al. investigated the use of BNNTs as contrast agents for neutron capture therapy, which could be an innovative approach for treatment of several aggressive cancers such as cerebral glioblastoma multiform. The main purpose of the therapy was to target the tumor cells by ^{10}B atoms. Accordingly, BNNTs were used as carriers of boron atoms. Figure 9 shows how the BNNTs were functionalized with PLL, a fluorescent probe (quantum dots) and folic acids. PLLs were wrapped around the BNNTs to induce a hydrophilic property. In

addition, the BNNTs were coated with folic acids for selective interaction with the tumor cells. The malignant glioblastoma cells were exposed to functionalized BNNTs under in vitro conditions. It was observed that the PLL–F–BNNTs were effectively taken up by the malignant glioblastoma cells. This study suggests that the use of BNNTs should be further investigated for neutron capture therapy [97].

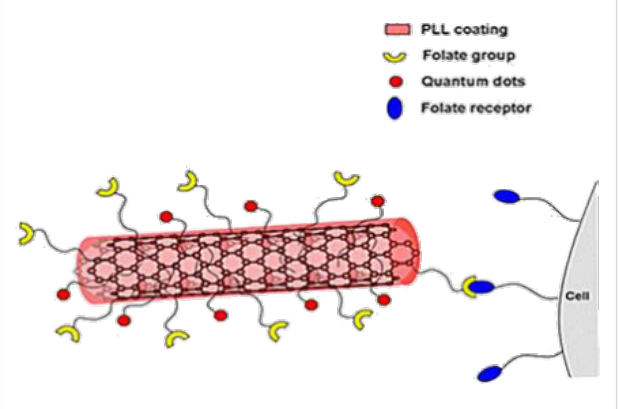

Figure 9: Schematic representation of a poly-L-lysine-, fluorescent probe- and folate-modified BNNT. Figure adapted with permission from the authors [97].

Gadolinium-doped BNNTs were fabricated as an effective contrast agent in clinical applications of BNNTs [98]. Due to the high magnetic moment property of gadolinium, Gd-doped BNNTs can be applied as an MRI contrast agent. The high in vitro biocompatibility property of the Gd-doped BNNTs and the labeling of cell populations due to the Gd and B content, make these structures a novel negative contrast agent [98].

Conclusion

It is clear that there is an increasing trend for the application of BNNTs in several fields from medicine to sensors. Although their synthesis is rather straightforward, it is still not possible to produce large quantities with high purity and uniformity. Since their physicochemical properties are independent of chirality, a simple synthesis method can be suitable, in contrast to CNTs. However, the choice of boron and nitrogen precursor catalysts can be important factors for their possible medical and biomedical applications. The other important point is the cost of the preparation of BNNTs. In this sense, there is an effort to reduce the synthesis temperature. However, to date, it seems that a reasonably high temperature of around 1000 °C is currently required for synthesis. The mechanism of BNNT formation is mostly defined by the synthesis conditions, which should be better understood for the control of the experimental parameters. Another problem limiting their applicability is their low dispersibility in aqueous media due to their high hydrophobicity. In order to increase their hydrophilicity, either covalent modifications or physical adsorption of a molecule or polymer is typically performed. Covalent modification can be achieved through –OH groups on B atoms and $–NH_2$ groups converted from N atoms at the edges and at defects.

The toxicity issues appear partially resolved in recent reports after conflicting early reports. However, there is a lack of in vivo data for the complete understanding of their toxicity. Most of the toxicity studies reported to date involve a polymer or a molecule attached to the BNNT surfaces to increase the dispersion in aqueous media, which might give misleading results since toxicity is mostly defined by the coating material. In addition, there is not much information about the fate of these materials in biological systems and the environment, such as their degradation after their release.

Acknowledgements

We acknowledge the support from the Scientific and Technological Research Council of Turkey (TUBITAK) (Project No.: 112M480) and Yeditepe University. We also acknowledge support of the COST action MP0901 NanoTP (Designing novel materials for nanodevices: From Theory to Practice).

References

1. Golberg, D.; Bando, Y.; Huang, Y.; Terao, T.; Miyome, M.; Tang, C.; Zhi, C. *ACS Nano* **2010,** *4,* 2979–2993. doi:10.1021/nn1006495
2. Wang, J.; Lee, C. H.; Yap, Y. K. *Nanoscale* **2010,** *2,* 2028–2034. doi:10.1039/c0nr00335b
3. Golberg, D.; Bando, Y.; Tang, C. C.; Zhi, C. Y. *Adv. Mater.* **2007,** *19,* 2413–2432. doi:10.1002/adma.200700179
4. Sauti, G.; Park, C.; Kang, J. H.; Kim, J.-W.; Harrison, J. S.; Smith, M. W.; Jordon, K.; Lowther, S. E.; Lillehei, P. T.; Thibeault, S. A. U.S. Pat. Appl. 2013/0119316 A1, May 16, 2013.
5. Cohen, M. L.; Zettl, A. *Phys. Today* **2010,** *63,* 34–38. doi:10.1063/1.3518210
6. Terao, T.; Zhi, C.; Bando, Y.; Mitome, M.; Tang, C.; Golberg, D. *J. Phys. Chem. C* **2010,** *114,* 4340–4344. doi:10.1021/jp911431f
7. Zhi, C.; Bando, Y.; Tang, C.; Xie, R.; Sekiguchi, T.; Golberg, D. *J. Am. Chem. Soc.* **2005,** *127,* 15996–15997. doi:10.1021/ja053917c
8. Li, H. L.; Chen, Y. *Langmuir* **2010,** *26,* 5135–5140. doi:10.1021/la903604w
9. Boinovich, L. B.; Emelyanenko, A. M.; Pashini, A. S.; Lee, C. H.; Drelich, J.; Yap, Y. K. *Langmuir* **2012,** *28,* 1206–1216. doi:10.1021/la204429z
10. Bansal, N. P.; Hurst, J. B.; Choi, S. R. *J. Am. Ceram. Soc.* **2006,** *89,* 388–390. doi:10.1111/j.1551-2916.2005.00701.x
11. Okan, B. S.; Kocabaş, Z. O.; Ergün, A. N.; Baysal, M.; Letofsky-Papst, I. L.; Yürüm, Y. *Ind. Eng. Chem. Res.* **2012,** *51,* 11341–11347. doi:10.1021/ie301605z
12. Ciofani, G.; Raffa, V.; Menciassi, A.; Cuschieri, A. *Biotechnol. Bioeng.* **2008,** *101,* 850–858. doi:10.1002/bit.21952
13. Zhi, C.; Bando, Y.; Tang, C.; Goldberg, D. *J. Am. Chem. Soc.* **2005,** *127,* 17144–17145. doi:10.1021/ja055989

14. Ricotti, L.; Fujie, T.; Vazão, H.; Ciofani, G.; Marotta, R.; Brescia, R.; Filippeschi, C.; Corradini, I.; Matteoli, M.; Mattoli, V.; Ferreira, L.; Menciassi, A. *PLoS One* **2013,** *8,* e71707. doi:10.1371/journal.pone.0071707
15. Ciofani, G.; Genchi, G. G.; Liakos, I.; Athanassiou, A.; Dinucci, D.; Chiellini, F.; Mattoli, V. *J. Colloid Interface Sci.* **2012,** *374,* 308–314. doi:10.1016/j.jcis.2012.01.049
16. Sainsbury, T.; Ikuno, T.; Okawa, D.; Pacilé, D.; Fréchet, J. M. J.; Zettl, A. *J. Phys. Chem. C* **2007,** *111,* 12992–12999. doi:10.1021/jp072958n
17. Lee, C. H.; Zhang, D.; Yap, Y. K. *J. Phys. Chem. C* **2012,** *116,* 1798–1804. doi:10.1021/jp2112999
18. Zhi, C.; Bando, Y.; Wang, W.; Tang, C.; Kuwahara, H.; Golberg, D. *Chem. – Asian J.* **2007,** *2,* 1581–1585. doi:10.1002/asia.200700246
19. Gao, Z.; Zhi, C.; Bando, Y.; Golberg, D.; Serizawa, T. *ACS Appl. Mater. Interfaces* **2011,** *3,* 627–632. doi:10.1021/am1010699
20. Chopra, N. G.; Luyken, R. J.; Cherrey, K.; Crepsi, V. H.; Cohen, M. L.; Louie, S. G.; Zettl, A. *Science* **1995,** *269,* 966–967. doi:10.1126/science.269.5226.966
21. Loiseau, A.; Willaime, F.; Demoncy, N.; Hug, G.; Pascard, H. *Phys. Rev. Lett.* **1996,** *76,* 4737–4740. doi:10.1103/PhysRevLett.76.4737
22. Narita, I.; Oku, T. *Solid State Commun.* **2002,** *122,* 465–468. doi:10.1016/S0038-1098(02)00188-6
23. Wang, J.; Gu, Y.; Zhang, L.; Zhao, G.; Zhang, Z. *J. Nanomater.* **2010,** *80,* No. 540456. doi:10.1155/2010/540456
24. Singhal, S. K.; Srivastava, A. K.; Singh, B. P.; Gupta, A. K. *Indian J. Eng. Mater. Sci.* **2008,** *15,* 419–424.
25. Özmen, D.; Sezgi, N. A.; Balcı, S. *Chem. Eng. J.* **2013,** *219,* 28–36. doi:10.1016/j.cej.2012.12.057
26. Zhong, B.; Huang, X.; Wen, G.; Yu, H.; Zhang, X.; Zhang, T.; Bai, H. *Nanoscale Res. Lett.* **2011,** *6,* No. 36. doi:10.1007/s11671-010-9794-8
27. Golberg, D.; Han, W.; Bando, Y.; Bourgeois, L.; Kurashima, K.; Sato, T. *J. Appl. Phys.* **1999,** *86,* 2364–2366. doi:10.1063/1.371058
28. Han, W.-Q.; Cumings, J.; Huang, X.; Bradley, K.; Zettl, A. *Chem. Phys. Lett.* **2001,** *346,* 368–372. doi:10.1016/S0009-2614(01)00993-9
29. Borowiak-Palen, E.; Pichler, T.; Fuentes, G.-G.; Bendjemil, B.; Liu, X.; Graff, A.; Behr, G.; Kalenczuk, R.-J.; Knupfer, M.; Fink, J. *Chem. Commun.* **2003,** 82–83. doi:10.1039/b208214d
30. Chen, H.; Chen, Y.; Liu, Y.; Fu, L.; Huang, C.; Llewellyn, D. *Chem. Phys. Lett.* **2008,** *463,* 130–133. doi:10.1016/j.cplett.2008.08.007
31. Wang, J.; Lee, C. H.; Bando, Y.; Golberg, D.; Yap, Y. K. Multiwalled Boron Nitride Nanotubes: Growth, Properties and Applications. In *B-C-N Nanotubes and Related Nanostructures;* Yap, Y. K., Ed.; Lecture Notes in Nanoscale Science and Technology, Vol. 6; Springer-Verlag: Berlin, Germany, 2009; pp 23–44. doi:10.1007/978-1-4419-0086-9_2
32. Chen, Y.; Conway, M.; Williams, J. S.; Zou, J. *J. Mater. Res.* **2002,** *17,* 1896–1899. doi:10.1557/JMR.2002.0281
33. Kim, J.; Lee, S.; Uhm, Y. R.; Jun, J.; Rhee, C. K.; Kim, G. M. *Acta Mater.* **2011,** *59,* 2807–2813. doi:10.1016/j.actamat.2011.01.019
34. Lim, S. H.; Luo, J.; Ji, W.; Lin, J. *Catal. Today* **2007,** *120,* 346–350. doi:10.1016/j.cattod.2006.09.016
35. Li, L.; Li, L. H.; Chen, Y.; Dai, X. J.; Xing, T.; Petravic, M.; Liu, X. *Nanoscale Res. Lett.* **2012,** *7,* 417–425. doi:10.1186/1556-276X-7-417
36. Golberg, D.; Bando, Y.; Eremets, M.; Takemura, K.; Kurashima, K.; Yusa, H. *Appl. Phys. Lett.* **1996,** *69,* 2045–2047. doi:10.1063/1.116874
37. Arenal, R.; Stephan, O.; Cochon, J.-L.; Loiseau, A. *J. Am. Chem. Soc.* **2007,** *129,* 16183–16189. doi:10.1021/ja076135n
38. Smith, M. W.; Jordan, K. C.; Park, C.; Kim, J.-W.; Lillehei, P. T.; Crooks, R.; Harrison, J. S. *Nanotechnology* **2009,** *20,* 505604. doi:10.1088/0957-4484/20/50/505604
39. Xu, L.; Peng, Y.; Meng, Z.; Yu, W.; Zhang, S.; Liu, X.; Qian, Y. *Chem. Mater.* **2003,** *15,* 2675–2680. doi:10.1021/cm0208531
40. Wang, X. Z.; Wu, Q.; Hu, Z.; Chen, Y. *Electrochim. Acta* **2007,** *52,* 2841–2844. doi:10.1016/j.electacta.2006.08.047
41. Hou, L.; Gao, F.; Sun, G.; Gou, H.; Tian, M. *Cryst. Growth Des.* **2007,** *7,* 535–540. doi:10.1021/cg060747m
42. Bae, S. Y.; Seo, H. W.; Park, J.; Choi, Y. S.; Park, J. C.; Lee, S. Y. *Chem. Phys. Lett.* **2003,** *374,* 534–541. doi:10.1016/S0009-2614(03)00745-0
43. Pakdel, A.; Zhi, C.; Bando, Y.; Nakayama, N.; Golberg, D. *Nanotechnology* **2012,** *23,* 215601. doi:10.1088/0957-4484/23/21/215601
44. Singhal, S. K.; Srivastava, A. K.; Pasricha, R.; Mathur, R. B. *J. Nanosci. Nanotechnol.* **2011,** *11,* 5179–5186. doi:10.1166/jnn.2011.4182
45. Wu, J.; Yin, L. *ACS Appl. Mater. Interfaces* **2011,** *3,* 4354–4362. doi:10.1021/am201008n
46. Samanta, S. K.; Gomathi, A.; Bhattacharya, S.; Rao, C. N. R. *Langmuir* **2010,** *26,* 12230–12236. doi:10.1021/la101150p
47. Zhou, S.-J.; Ma, C.-Y.; Meng, Y.-Y.; Su, H.-F.; Zhu, Z.; Deng, S.-L.; Xie, S.-Y. *Nanotechnology* **2012,** *23,* 055708. doi:10.1088/0957-4484/23/5/055708
48. Golberg, D.; Bando, Y.; Han, W.; Kurashima, K.; Sato, T. *Chem. Phys. Lett.* **1999,** *308,* 337–342. doi:10.1016/S0009-2614(99)00591-6
49. Lourie, O. R.; Jones, C. R.; Bartlett, M. B.; Gibbons, P. C.; Ruoff, R. S.; Buhro, W. E. *Chem. Mater.* **2000,** *12,* 1808–1810. doi:10.1021/cm000157q
50. Ma, R.; Bando, Y.; Sato, T. *Chem. Phys. Lett.* **2001,** *337,* 61–64. doi:10.1016/S0009-2614(01)00194-4
51. Chatterjee, S.; Kim, M. J.; Zakharov, D. N.; Kim, S. M.; Stach, E. A.; Maruyama, B.; Sneddon, L. G. *Chem. Mater.* **2012,** *24,* 2872–2879. doi:10.1021/cm3006088
52. Tang, C.; Bando, Y.; Sato, T.; Kurashima, K. *Chem. Commun.* **2002,** 1290–1291. doi:10.1039/b202177c
53. Lee, C. H.; Wang, J.; Kayatsha, V. K.; Huang, J. Y.; Yap, Y. K. *Nanotechnology* **2008,** *19,* 455605. doi:10.1088/0957-4484/19/45/455605
54. Zhi, C.; Bando, Y.; Tang, C.; Golberg, D.; Xie, R.; Sekigushi, T. *Appl. Phys. Lett.* **2005,** *86,* 213110. doi:10.1063/1.1938002
55. Li, J.; Li, J.; Yin, Y.; Chen, Y.; Bi, X. *Nanotechnology* **2013,** *24,* 365605. doi:10.1088/0957-4484/24/36/365605
56. Lee, C. H.; Xie, M.; Kayastha, V.; Wang, J.; Yap, Y. K. *Chem. Mater.* **2010,** *22,* 1782–1787. doi:10.1021/cm903287u
57. Nithya, J. S. M.; Pandurangan, A. *RSC Adv.* **2014,** *4,* 26697–26705. doi:10.1039/C4RA01204F
58. Kalay, S.; Yilmaz, Z.; Çulha, M. *Beilstein J. Nanotechnol.* **2013,** *4,* 843–851. doi:10.3762/bjnano.4.95
59. Chadderton, L. T.; Chen, Y. *J. Cryst. Growth* **2002,** *240,* 164–169. doi:10.1016/S0022-0248(02)00855-2
60. Li, L.; Chen, Y.; Stachurski, Z. H. *Prog. Nat. Sci.: Mater. Int.* **2013,** *23,* 170–173. doi:10.1016/j.pnsc.2013.03.004
61. Naumov, V. G.; Kosyrev, F. K.; Vostrikov, V. G.; Arutyunyan, N. R.; Obraztsova, E. D.; Konov, V. I.; Jiang, H.; Nasibulin, A.; Kauppinen, E. *Laser Phys.* **2009,** *19,* 1198–1200.

62. Lee, R. S.; Gavillet, J.; de la Chapelle, M. L.; Loiseau, A.; Cochon, J.-L.; Pigache, D.; Thibault, J.; Willaime, F. *Phys. Rev. B* **2001,** *64,* 121405. doi:10.1103/PhysRevB.64.121405
63. Ikuno, T.; Sainsbury, T.; Okawa, D.; Fréchet, J. M. J.; Zettl, A. *Solid State Commun.* **2007,** *142,* 643–646. doi:10.1016/j.ssc.2007.04.010
64. Dai, X.; Chen, Y.; Chen, Z.; Lamb, P. R.; Li, L. H.; du Plessis, J.; McCulloch, D. G.; Wang, X. *Nanotechnology* **2011,** *22,* 245301. doi:10.1088/0957-4484/22/24/245301
65. Huang, X.; Zhi, C.; Jiang, P.; Golberg, D.; Bando, Y.; Tanaka, T. *Adv. Funct. Mater.* **2013,** *23,* 1824–1831. doi:10.1002/adfm.201201824
66. Zhi, C.; Bando, Y.; Tang, C.; Honda, S.; Sato, K.; Kuwahara, H.; Golberg, D. *Angew. Chem., Int. Ed.* **2005,** *44,* 7932–7935. doi:10.1002/anie.200502846
67. Ciofani, G.; Del Turco, S.; Genchi, G. G.; D'Alessandro, D.; Basta, G.; Mattoli, V. *Int. J. Pharm.* **2012,** *436,* 444–453. doi:10.1016/j.ijpharm.2012.06.037
68. Mukhopadhyay, S.; Scheicher, R. H.; Pandey, R.; Karna, P. *J. Phys. Chem. Lett.* **2011,** *2,* 2442–2447. doi:10.1021/jz2010557
69. Gao, Z.; Zhi, C.; Bando, Y.; Godlberg, D.; Serizawa, T. *J. Am. Chem. Soc.* **2010,** *132,* 4976–4977. doi:10.1021/ja910244b
70. Chen, X.; Wu, P.; Rousseas, M.; Okawa, D.; Gartner, Z.; Zettl, A.; Bertozzi, C. R. *J. Am. Chem. Soc.* **2009,** *131,* 890–891. doi:10.1021/ja807334b
71. Del Turco, S.; Ciofani, G.; Cappello, V.; Gemmi, M.; Cervelli, T.; Saponaro, C.; Nitti, S.; Mazzolai, B.; Basta, G.; Mattoli, V. *Colloids Surf., B* **2013,** *111,* 142–149. doi:10.1016/j.colsurfb.2013.05.031
72. Ejaz, M.; Rai, S. C.; Wang, K.; Zhang, K.; Zhou, W.; Grayson, S. M. *J. Mater. Chem. C* **2014,** *2,* 4073–4079. doi:10.1039/c3tc32511c
73. Kim, Y.-K.; Park, J.-H.; Park, S.-H.; Lim, B.; Baek, W.-K.; Suh, S.-I.; Lim, J.-G.; Ryu, G. R.; Song, D.-K. *Cell. Physiol. Biochem.* **2010,** *25,* 211–220. doi:10.1159/000276555
74. Ciofani, G.; Danti, S.; D'Alessandro, D.; Moscato, S.; Menciassi, A. *Biochem. Biophys. Res. Commun.* **2010,** *394,* 405–411. doi:10.1016/j.bbrc.2010.03.035
75. Lahiri, D.; Rouzaud, F.; Richard, T.; Keshri, A. K.; Bakshi, S. R.; Kos, L.; Agarwal, A. *Acta Biomater.* **2010,** *6,* 3524–3533. doi:10.1016/j.actbio.2010.02.044
76. Ferreira, T.; Silva, P. R. O.; Santos, R. G.; Sousa, E. M. B. *J. Biomater. Nanobiotechnol.* **2011,** *2,* 426–434.
77. Horváth, L.; Magrez, A.; Golberg, D.; Zhi, C.; Bando, Y.; Smajda, R.; Horváth, E.; Forró, L.; Schwaller, B. *ACS Nano* **2011,** *5,* 3800–3810. doi:10.1021/nn200139h
78. Ferreira, T. H.; Soares, D. C. F.; Moreira, L. M. C.; Ornelas da Silva, P. R.; Gouvêa dos Santos, R.; Barros de Sousa, E. M. *Mater. Sci. Eng., C* **2013,** *33,* 4616–4623. doi:10.1016/j.msec.2013.07.024
79. Ciofani, G.; Ricotti, L.; Danti, S.; Moscato, S.; Nesti, C.; D'Alessandro, D.; Dinucci, D.; Chiellini, F.; Pietrabissa, A.; Petrini, M.; Menciassi, A. *Int. J. Nanomed.* **2010,** *5,* 285–298. doi:10.2147/IJN.S9879
80. Danti, S.; Ciofani, G.; Moscato, S.; D'Alessandro, D.; Ciabatti, E.; Nesti, C.; Brescia, R.; Bertoni, G.; Pietrabissa, A.; Lisanti, M.; Petrini, M.; Mattoli, V.; Berrettini, S. *Nanotechnology* **2013,** *24,* 465102. doi:10.1088/0957-4484/24/46/465102
81. Ciofani, G.; Danti, S.; Genchi, G. G.; D'Alessandro, D.; Pellequer, J.-L.; Odorico, M.; Mattoli, V.; Giorgi, M. *Int. J. Nanomed.* **2012,** *7,* 19–24. doi:10.2147/IJN.S28144
82. Ciofani, G.; Danti, S.; Nitti, S.; Mazzolai, B.; Mattoli, V.; Giorgi, M. *Int. J. Pharm.* **2013,** *444,* 85–88. doi:10.1016/j.ijpharm.2013.01.037
83. Ciofani, G.; Raffa, V.; Yu, J.; Chen, Y.; Obata, Y.; Takeoka, S.; Menciassi, A.; Cuschieri, A. *Curr. Nanosci.* **2009,** *5,* 33–38. doi:10.2174/157341309787314557
84. Li, X.; Hanagata, N.; Wang, X.; Yamaguchi, M.; Yi, W.; Bando, Y.; Golberg, D. *Chem. Commun.* **2014,** *50,* 4371–4374. doi:10.1039/c4cc00990h
85. Li, X.; Zhi, C.; Hanagata, N.; Yamaguchi, M.; Bandoa, Y.; Golberg, D. *Chem. Commun.* **2013,** *49,* 7337–7339. doi:10.1039/c3cc42743a
86. Soares, D. C. F.; Ferreira, T. H.; de Aguiar Ferreira, C.; Cardoso, V. N.; Barros de Sousa, E. M. *Int. J. Pharm.* **2012,** *423,* 489–495. doi:10.1016/j.ijpharm.2011.12.002
87. Raffa, V.; Ciofani, G.; Cuschieri, A. *Nanotechnology* **2009,** *20,* 075104. doi:10.1088/0957-4484/20/7/075104
88. Shakerzadeh, E.; Noorizadeh, S. *Physica E* **2014,** *57,* 47–55. doi:10.1016/j.physe.2013.09.019
89. Lahiri, D.; Singh, V.; Benaduce, A. P.; Seal, S.; Kos, L.; Agarwal, A. *J. Mech. Behav. Biomed. Mater.* **2011,** *4,* 44–56. doi:10.1016/j.jmbbm.2010.09.005
90. Yu, Y.; Chen, H.; Liu, Y.; Li, L. H.; Chen, Y. *Electrochem. Commun.* **2013,** *30,* 29–33. doi:10.1016/j.elecom.2013.01.026
91. Reddy, A. L. M.; Gupta, B. K.; Narayanan, T. N.; Marti, A. A.; Ajayan, P. M.; Walker, G. C. *J. Phys. Chem. C* **2012,** *116,* 12803–12809. doi:10.1021/jp210597m
92. Han, S. S.; Kang, J. K.; Lee, H. M.; van Duin, A. C. T.; Goddard, A. *J. Chem. Phys.* **2005,** *123,* 114704. doi:10.1063/1.1999629
93. Veziroglu, T. N.; Zaginaichenko, S. Yu.; Schur, D. V.; Baranowski, B.; Shpak, A. P.; Skorokhod, V. V.; Kale, A. Atomic hydrogen adsorption on boron nitride nanotube surfaces. In *Hydrogen Materials Science and Chemistry of Carbon Nanomaterials;* Margulis, V. A.; Muryumin, E. E.; Tomilin, O. B., Eds.; NATO Security through Science Series A: Chemistry and Biology; Springer-Verlag: Amsterdam, Netherlands, 2007; pp 275–278. doi:10.1007/978-1-4020-5514-0_36
94. Mpourmpakis, G.; Froudakis, G. E. *Catal. Today* **2007,** *120,* 341–345. doi:10.1016/j.cattod.2006.09.023
95. Ahadi, Z.; Shadman, M.; Yeganegi, S.; Asgari, F. *J. Mol. Model.* **2012,** *18,* 2981–2991. doi:10.1007/s00894-011-1316-9
96. Reddy, A. L. M.; Tanur, A. E.; Walker, G. C. *Int. J. Hydrogen Energy* **2010,** *35,* 4138–4143. doi:10.1016/j.ijhydene.2010.01.072
97. Ciofani, G.; Raffa, V.; Menciassi, A.; Cuschieri, A. *Nanoscale Res. Lett.* **2008,** *4,* 113–121. doi:10.1007/s11671-008-9210-9
98. Ciofani, G.; Boni, A.; Calucci, L.; Forte, C.; Gozzi, A.; Mazzolai, B.; Mattoli, V. *Nanotechnology* **2013,** *24,* 315101. doi:10.1088/0957-4484/24/31/315101

License and Terms

This is an Open Access article under the terms of the Creative Commons Attribution License (http://creativecommons.org/licenses/by/2.0), which permits unrestricted use, distribution, and reproduction in any medium, provided the original work is properly cited.

The license is subject to the *Beilstein Journal of Nanotechnology* terms and conditions: (http://www.beilstein-journals.org/bjnano)

The definitive version of this article is the electronic one which can be found at: doi:10.3762/bjnano.6.9

BEILSTEIN JOURNAL OF NANOTECHNOLOGY

X-ray photoelectron spectroscopy of graphitic carbon nanomaterials doped with heteroatoms

Toma Susi*, Thomas Pichler and Paola Ayala

Review

Open Access

Address:
University of Vienna, Faculty of Physics, Boltzmanngasse 5, A-1090 Vienna, Austria

Email:
Toma Susi* - toma.susi@iki.fi

* Corresponding author

Keywords:
carbon nanotubes; core level photoemission; graphene; substitutional doping; X-ray photoelectron spectroscopy (XPS)

Beilstein J. Nanotechnol. **2015,** *6,* 177–192.
doi:10.3762/bjnano.6.17

Received: 29 July 2014
Accepted: 08 December 2014
Published: 15 January 2015

This article is part of the Thematic Series "Atomic scale interface design and characterisation: Experimental aspects and methods".

Guest Editor: C. Bittencourt

© 2015 Susi et al; licensee Beilstein-Institut.
License and terms: see end of document.

Abstract

X-ray photoelectron spectroscopy (XPS) is one of the best tools for studying the chemical modification of surfaces, and in particular the distribution and bonding of heteroatom dopants in carbon nanomaterials such as graphene and carbon nanotubes. Although these materials have superb intrinsic properties, these often need to be modified in a controlled way for specific applications. Towards this aim, the most studied dopants are neighbors to carbon in the periodic table, nitrogen and boron, with phosphorus starting to emerge as an interesting new alternative. Hundreds of studies have used XPS for analyzing the concentration and bonding of dopants in various materials. Although the majority of works has concentrated on nitrogen, important work is still ongoing to identify its precise atomic bonding configurations. In general, care should be taken in the preparation of a suitable sample, consideration of the intrinsic photoemission response of the material in question, and the appropriate spectral analysis. If this is not the case, incorrect conclusions can easily be drawn, especially in the assignment of measured binding energies into specific atomic configurations. Starting from the characteristics of pristine materials, this review provides a practical guide for interpreting X-ray photoelectron spectra of doped graphitic carbon nanomaterials, and a reference for their binding energies that are vital for compositional analysis via XPS.

Introduction

Graphitic carbon nanomaterials consist of carbon bonded via sp^2-hybridized covalent bonds into structures with dimensionalities in the nanometer scale. Although two naturally occurring forms of carbon, graphite and diamond, have been known for millennia, several new carbon nanomaterials have been created and identified in the last decades. Three recent stages have received major attention, starting with the discovery of fullerenes in the late 1980s [1,2], followed by the proliferation of

carbon nanotube research from the early 1990s [3-5], and coming finally to the latest stage when graphene rose into prominence in the mid-2000s [6-8].

Due to the unique nature of sp^2 hybridization [9], strong σ bonds are formed between carbon atoms in fullerenes, nanotubes and graphene (Figure 1), along with delocalized π orbitals [10]. These materials each have superb intrinsic properties. Fullerenes are very stable nanocontainers [11], exhibiting interesting selective surface reactivity [12]. Carbon nanotubes have the highest length-to-diameter ratio of any material, with an extremely high specific strength [13]. Moreover, the single-walled types are either semiconducting or metallic ballistic conductors even at room temperature [14,15], and capable of sustaining current densities 1000 times higher than copper [16,17]. Finally, atomically thin single-layer graphene is extremely elastic yet impermeable [18], and the stiffest and strongest material ever measured [19]. Furthermore, the charge carriers in graphene behave as massless Dirac fermions [7], leading to unparalleled mobility and a number of exotic quantum phenomena [7,20,21].

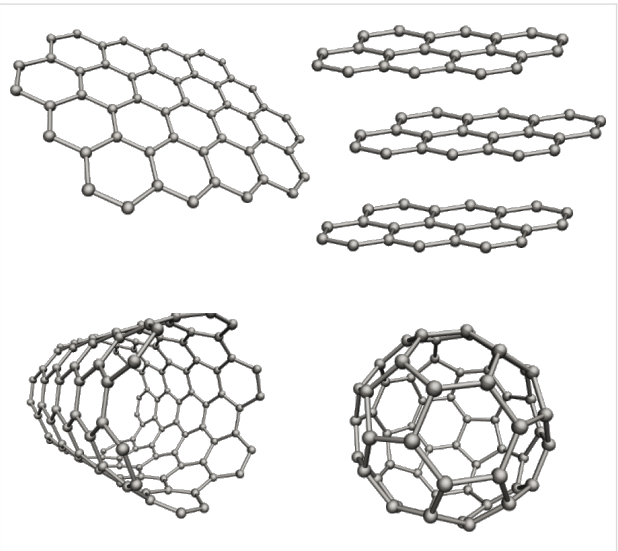

Figure 1: Structural models of graphitic carbon nanomaterials. Clockwise from top left: graphene, graphite, C_{60} fullerene, and a single-walled carbon nanotube.

However, for many real applications, additional control over the intrinsic properties of a material is needed. Heteroatom doping, the intentional replacement of some carbon atoms of the lattice with other elements, has been long studied for this and other purposes [22,23]. One of the key issues for controlled heteroatom doping is the detection and identification of the dopant atoms, and the further analysis of their concentration and atomic bonding environment in the studied materials. Compared to bulk solids, individual nano-objects are composed of far fewer atoms, and thus usual dopant concentrations correspond to a rather limited number of heteroatoms in the lattice. A typical sample must therefore be composed of innumerable such nanostructures in order to reach a measurable quantity, and thus any variability in their properties or in the distribution of dopants poses additional challenges for characterization.

Furthermore, although local methods such as scanning tunneling microscopy (STM) [24,25] and transmission electron microscopy based electron energy loss spectroscopy (TEM/EELS) [23,26] can these days be used to directly visualize and study individual atoms (e.g., [27-32]), it is vital to obtain information about the distribution of the dopants in an entire sample. For this purpose, X-ray photoelectron spectroscopy (XPS) is one of the most attractive techniques, and as such has been widely used to characterize doped materials [33,34]. However, XPS is commonly applied as a laboratory analytical tool, without taking into account important physical factors relevant for carbon nanostructured materials that might affect the resulting analyses. These include, for example, the significant influence of the substrate for measurements of graphene [35,36], and the disentanglement of the intrinsic photoemission responses of semiconducting and metallic single-walled carbon nanotubes (SWCNTs) [37]. Furthermore, as we shall see, identifying the binding energies associated with specific atomic structures is rarely straightforward.

The purpose of this review is to provide a practical guide for interpreting the X-ray photoelectron spectra of doped graphitic carbon nanomaterials, and act as a useful reference for the binding energies that are vital for their compositional analysis via XPS. Angle-resolved photoemission spectroscopy (ARPES), also based on the photoelectric effect [38,39], will only be mentioned briefly in our discussion related to graphene. Graphite has an important role in the context of the carbon 1s line, but our focus will be on graphene and carbon nanotubes, especially single-walled. We will likewise only briefly describe measurement-specific issues and extrinsic effects.

Most importantly, we will only consider heteroatom doping in the lattice itself. This explicitly leaves outside our scope the many forms of functionalization and surface chemistry that have been widely studied [2,12,40-45]. Since the binding energies of even the simplest dopant structures are still being debated, discussion of complicated hybrid structures or doping with more than one element at the same time will be omitted. However, we will endeavor to comprehensively survey the range of binding energy values reported for various configurations to help ensure that the reader has at hand the most complete available evidence for their assignment to specific atomic structures.

Review

X-ray photoemission

Physical background

We shall divide the X-ray photoemission process conceptually into three stages in a simplified single-particle picture. First, an X-ray photon is absorbed and transfers its energy to a core electron. Then, the target atom responds to this excitation by emitting a photoelectron, creating a core hole, i.e., an empty core state. Finally, the photoelectron transports to the surface of the material and escapes into the vacuum, where its energy is measured by an electron analyzer.

The first step defines to a large degree the binding energy of the core electron (this is called the initial state energy, including any chemical shift characteristic of the material). However, this energy gets modified by the interaction between the photoelectron and the resulting core hole (the so-called final state effects, including many-body interactions and core hole relaxation). Finally, inelastic scattering processes cause some of the photoelectrons to lose kinetic energy on the way to the surface, contributing to a continuous photoemission intensity background (extrinsic effects).

Following the above division of the photoemission process, two types of methodologies can be applied for calculating the core level binding energies: the so-called initial and final state methods [46-52]. In the initial state methods, only the energy level of the core electron before ionization is considered, and shifts in this value between different atoms in the system are calculated. In the final state methods, a core hole is explicitly included in the calculation, and the electronic structure of the system is relaxed in its presence. The core level binding energy is then computed from the total energy difference between a calculation with the core hole and a ground state calculation. More advanced methods aimed at directly simulating the dynamical screening of the core hole and thus the lifetimes and resulting line shapes have also been developed [53-55]. However, since the topic of calculating the core level binding energies in doped carbon nanomaterials is an active area of our research, we will for brevity leave a more detailed discussion of the topic for a later time.

Experimentally speaking, since the carbon core electrons are localized and do not participate in chemical bonding, core level signals could be expected to exhibit very narrow linewidths. However, several factors do cause broadening of the signal and can also influence its shape. Each XPS measurement setup has an intrinsic energy spread of the X-ray source and a finite energy resolution of the analyzer, resulting in so-called instrumental broadening that can be well described by a Gaussian line shape. It is therefore extremely difficult to establish good references when non-monochromatic X-ray sources are used, as is often the case. In addition, a finite sample temperature causes thermal broadening due to phonon vibrations, but this is usually negligible compared to the other factors (since the thermal energy is only approx. 25 meV at 300 K). Finally, each peak has a natural linewidth that is related to the excited state lifetime, usually well described by a Lorentzian profile. Thus, a convolution of Gaussian (G) and Lorentzian (L) profiles, also called the Voigtian (V), is the most adequate way to describe the line shapes $I_V(E)$ of the photoemission responses:

$$I_{\mathrm{V}}\left(E\right)=\left(\mathrm{G}\times\mathrm{L}\right)\left(E\right)\propto\int_{-\infty}^{\infty}\mathrm{G}\left(E'\right)\mathrm{L}\left(E-E'\right)dE' \quad (1)$$

$$\mathrm{G}\left(E\right)=\frac{e^{-E^2/(2\sigma^2)}}{\sigma\sqrt{2\pi}} \quad (2)$$

$$\mathrm{L}\left(E\right)=\frac{\gamma}{\pi\left(E^2+\gamma^2\right)}, \quad (3)$$

where G(E) and L(E) are the Gaussian and Lorentzian contributions, σ is the instrumental broadening, and γ the intrinsic lifetime broadening.

However, for a metallic system such as graphite, graphene or metallic carbon nanotubes, in addition to the Gaussian instrumental broadening, the carbon 1s line will exhibit significant asymmetry towards higher binding energies. This is due to excitation of many low-energy electron–hole pairs, which screen the core hole and manifest as higher binding energy events. This asymmetric line shape $I_{DS}(E)$ can be described in the Doniach–Šunjić (DS) [56] form:

$$I_{\mathrm{DS}}\left(E\right)=\frac{\Gamma\left(1-\alpha\right)}{\left(E^2+\gamma^2\right)^{(1-\alpha)/2}}\cos\left(\frac{\pi\alpha}{2}+\left(1-\alpha\right)\arctan\left(E/\gamma\right)\right), \quad (4)$$

where Γ is the Gamma function

$$\left(\Gamma\left(z\right)=\int_0^{\infty}t^{z-1}e^{-t}dt\right)$$

and α is the so-called asymmetry parameter. The asymmetry is zero for semiconductors and insulators, recovering the symmetric Lorentzian form.

Measurement

A typical XPS spectrum consists of a so-called primary spectrum, which is a convolution of the final state binding energies of each excited core state, broadened by lifetime and instru-

mental effects as described above. Superimposed over this is a stepped secondary spectrum, resulting from the inelastically scattered photoelectrons contributing to the higher binding energy sides of each peak. Photoelectrons have a material- and energy-dependent inelastic mean free path λ, which describes their scattering probability before reaching the surface. The sampling depth of XPS is usually taken to be 3λ (i.e., the depth from which 95% of photoelectrons with a normal take-off angle originate; note that 63.3% come from within 1λ), which is between 3 and 10 nm for commonly used Al Kα radiation. While this is well understood for uniform thin films, the sampling depth for nanostructured materials will depend on the sample. For instance, for graphite it is 8.7 nm [57], corresponding to about 26 graphene layers. Thus, for graphitic carbon nanomaterials (apart from thick multiwalled carbon nanotubes) XPS is in effect a bulk-probing technique.

A careful subtraction of the secondary background is vital for a correct analysis of the primary spectrum. Although a number of different background models are in widespread use, a linear background subtraction and the formulations by Shirley [58] and Tougaard [59] are often used.

For evaluating the concentration and the bonding of the dopants, the first sensible step is to focus on the carbon 1s response to evaluate contributions to the spectrum from synthesis byproducts or carbonaceous contaminants. This serves as a prerequisite to further analyze the dopant core states, namely 1s for nitrogen and boron and 2p for phosphorus. Finally, when the background-subtracted areas a_X of the responses of the sought elements X are multiplied by the corresponding energy-dependent sub-shell photoionisation cross sections σ_x [60], their ratios to the area of the carbon response gives the dopant concentration in atomic percent (atom %). As an example, the atomic concentration of nitrogen c_N would be evaluated as

$$c_N = \frac{a_N \sigma_{N1s}}{a_C \sigma_{C1s}}. \quad (5)$$

For phosphorus it should be noted that for the commonly considered photoemission from the 2p level, each core state is expected to split into two components due to spin–orbit coupling, corresponding to orbital angular momentum quantum numbers of j = 1/2 and 3/2. The magnitude of the spin–orbit splitting is thought to be rather insensitive to the chemical environment and predicted by theory to have a value of 0.87 eV for the P 2p level, with the lower binding energy j = 3/2 component having an area twice as large as the j = 1/2 component [61]. However, in the studies reported so far, it has not been established whether these predictions directly apply to molecular carbon nanostructures.

A further measurement-related issue is the practice of using the carbon 1s line for calibrating the energy scale, since adventitious carbon often provides a convenient common reference. However, when measuring carbon nanomaterials, the position of the C 1s line should obviously be carefully determined for each sample, and not assumed as a common reference by which the energy scale is calibrated. The absolute position of the C 1s line as well as those signals corresponding to the measured heteroatoms must be calibrated by using a reference. In most cases, a clean metallic sample with a well-understood XPS response is used for this purpose.

Carbon nanomaterials

In this section, we will briefly introduce the main classes of graphitic carbon nanomaterials, but will refer the reader elsewhere for further information on their properties. Instead, we will concentrate on describing the current state of the art on X-ray photoelectron spectroscopy of each pristine material, including the measured C 1s binding energies and line shapes. In the case of graphite, a consensus has been established in the literature (apart from the existence of a surface state, as discussed below), while for single-walled carbon nanotubes, we have focused on the few measurements made on metallicity-sorted samples, and two representative studies for double-walled and multiwalled nanotubes. For graphene, we have selected studies representing the full range of values measured on various substrates. Table 1 contains an overview.

Graphite is a semimetallic solid composed entirely of sp^2-bonded planar hexagonal carbon layers loosely stacked together by van der Waals interactions. Due to its close kinship to the nanoscale forms, especially graphene, the C 1s line of graphite is the logical starting point for understanding the photoemission response of all carbon nanomaterials. A further advantage specific to highly oriented pyrolytic graphite (HOPG) is that it is relatively straightforward to prepare large but extremely pure and uniform samples.

As mentioned above, in a metallic system such as graphite, the line shape of the C 1s line has the asymmetric Doniach–Šunjić form. The position of the maximum of the peak has been measured at 284.42 eV [62-64,66,84,85], with a lifetime broadening between 160–180 meV and an asymmetry parameter of 0.05–0.065 [62,85]. Some authors have identified another component in the spectra at certain excitation energies or emission angles shifted to higher binding energies by 120–194 meV, and assigned it to the surface layer [65,66]. However, this view has been disputed by others [78,85].

Graphene, a single layer of graphite, is a truly 2-dimensional solid that was originally thought to be fundamentally unstable.

Table 1: Photoemission measurements of the carbon 1s line for various graphitic carbon nanomaterials reported in the literature. The columns show the material, position of the maximum of the carbon 1s response, the energy width of the Lorentzian/Gaussian component, or, the full width at half maximum if these contributions have not been separated, the asymmetry index α, and the literature citation for each measurement.

material	C 1s max. (eV)	L/G width (eV)	FWHM (eV)	asymm. α	references
graphite (G)	284.42	0.16–0.18/0.08–0.1	—	0.05–0.065	[62-64]
G(0001) bulk	284.4[a]	0.095/0.294	—	0.10	[65]
G(0001) surface	284.6[b]	0.231/0.294	—	0.05	[65]
G(0001) bulk	284.4[c]	0.16/0.06	—	0.048	[66]
G(0001) surface	284.52[d]	0.16/0.06	—	0.048	[66]
FLG[e]	284.47	—	0.7	0.1	[67]
SLG/Ni(111)	284.7	0.216	—	0.1	[68]
SLG/Au/Ni(111)	284.2	—	—	—	[69,70]
SLG/Au/Ni(111)	284.42	0.155/0.258	—	0.061	[71]
SLG/Cu	284.5	0.170	—	0.068	[72]
SLG/SiC	284.83	0.12–0.2/0.4–0.7	—	—/0[f]	[64,73,74]
SLG/H/SiC	284.6	—	—	—	[75]
SLG/Pt(111)	283.97	0.13/0.34	—	0.13	[76,77]
4LG/Pt(111)	284.0	—	—	—	[77]
SLG/Ir(111)	284.15	0.130/0.165	—	0.093	[78]
m-SWCNT[g]	284.48	—	0.26	0.11	[37]
s-SWCNT[g]	284.43	—	0.30	0	[37]
(6,5) s-SWCNT	284.52	—	0.41	0	[79]
(6,4) s-SWCNT	284.42	—	0.41	0	[79]
DWCNT	284.6	—	0.64–0.8	0	[80,81]
MWCNT	284.42	—	>0.63	—[h]	[82]
C_{60}	285.2	0.11/0.60	—	0	[83]

[a]Value not explicitly reported, estimated from graph. [b]Bulk value not explicitly reported, 195 meV split between the lines attributed to bulk and surface components. [c]Value not explicitly reported, estimated from graph. [d]Bulk value not explicitly reported, 120 meV split between the lines attributed to bulk and surface components. [e]Synchrotron-based scanning X-ray photoelectron microscopy measurements on suspended few-layer graphene. [f]Either not reported or symmetric line shapes used in the fitting. [g]Metallicity separated sample with narrow diameter distributions centered at 1.4 nm. [h]Value not explicitly reported, but remarked to be similar to graphite.

When it was experimentally isolated by Geim and Novoselov in 2004 [6], an unprecedented amount of ongoing research activity was launched [8]. The interest was largely due to the unique electronic structure of graphene, whereby the charge carriers behave as massless Dirac fermions [7,86].

The exact position of the intrinsic graphene C 1s line would logically be the one corresponding exclusively to free-standing single-layer graphene. However, this is challenging to measure due to sample-related issues. It is still necessary to understand how the absence of other layers could affect the screening of the core hole and thus cause possible shifts compared to the graphite value. If the assignment of the higher binding energy component discussed above is correct and could be expected to better describe freestanding graphene, this would give it a C 1s value of around 284.6 eV. However, even if this were the case, the influence of the second layer might still have an effect. As we discuss below, in the available measurements on monolayer graphene, it is clear that the role of the surface cannot be discounted.

A recent measurement of graphene on Pt(111) by Rajasekaran et al. [77] found no difference between single- and few-layer graphene (both measured at 284.0 eV). On the other hand, Emtsev et al. [64] and Hibino et al. [73] measured the C 1s energy of mono- to few-layer graphene epitaxial on silicon carbide as a function of the number of layers, and found that the monolayer value is about 0.4 eV higher than the bulk graphite value at 284.8 eV [64,73] (more precisely, 284.83 eV with a lifetime broadening of 0.12–0.2 eV [74]). However, the shift has been attributed to charge transfer from the substrate, similar in magnitude to what has been observed in the Fermi level shift via ARPES [87]. After intercalating hydrogen between the SiC substrate and monolayer graphene, a value of 284.6 eV has been reported [75].

As graphene is commonly grown by chemical vapor deposition on catalytic metals, several XPS measurements on metal surfaces are available. Values of 284.15 [76,78] and 284.2 eV [69,70] have been measured on Ir(111) and Au-intercalated Ni(111) surfaces, respectively. C 1s values for graphene on

other metal surfaces range from as low as 283.97 eV on Pt(111) [76,77], to 284.5 eV on Cu(111) [72], and 284.7 eV on Ni(111) [68]. The range of values should make it clear that charge transfer or screening by any particular substrate greatly affects the measured value.

Carbon nanotubes [88] can be conceptually understood as sheets of graphene rolled into seamless cylinders along a certain lattice vector direction, denoted by the so-called chiral indices (n,m). In single-walled carbon nanotubes, quantum confinement of the electronic wave function around the circumference of the tube results in one third of the tubes being metallic (when $n - m = 3 \times$ integer), while the remaining two thirds are semiconducting with band gaps proportional to their diameter [14,89]. It is also possible that there are several concentric walls approximately separated by the graphite interlayer distance; such tubes are called multiwalled (MWCNTs), with the double-walled (DWCNT) being a somewhat special case [90].

Carbon nanotube samples have two crucial differences compared to graphene in terms of their X-ray photoelectron spectroscopy response. The first difference is an advantage, in that films consisting entirely of self-supported nanotubes (so-called buckypapers) can be made without any substrate. However, it should be noted that depending on the sample preparation, the nanotubes can have a wide range of disorder, diameters, lengths, and degrees of bundling, factors which may all affect the measurement. The second difference, on the other hand, is the complication that samples of SWCNTs typically contain a mixture of semiconducting and metallic tubes, and thus their photoemission response is a convolution of these two different signals. In the past few years, this challenge has been overcome by the development of methods for separating nanotube samples according to their metallicity or even chirality [91-93].

Photoemission measurements from both all-metallic and all-semiconducting SWCNT buckypapers were reported in 2009 [37] (see Figure 2). A further advantage of this study was that both samples had narrow diameter distributions with the same mean, minimizing the variability of properties related to diameter. It was found that the C 1s line of metallic nanotubes exhibits an asymmetric DS shape, with a peak maximum at 284.48 eV and an asymmetry index slightly higher than for graphite at 0.11, and a full width at half maximum (FWHM) of 0.26 eV (narrower than the 0.32 eV found for graphite). On the other hand, the semiconducting sample exhibited a symmetric Voigtian line shape centered at 284.43 eV (FWHM: 0.30 eV). The 0.05 eV difference in the peak position was attributed to differing chemical potentials.

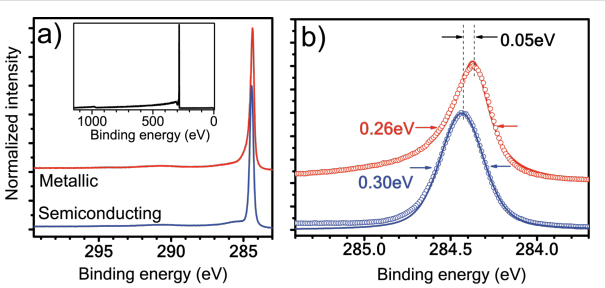

Figure 2: The photoemission response of metallicity-separated and purified single-walled carbon nanotube buckypapers. (a) C 1s photoemission of metallic (red upper curve) and semiconducting (blue lower curve) SWCNTs measured with a 400 eV photon excitation. The inset shows a survey scan, demonstrating the purity of the samples. (b) An expanded view of the C 1s line. The response of the metallic sample has been fitted with a Doniach–Šunjić and the semiconducting with a Voigtian lineshape. Reproduced with permission from [37], copyright 2009 The American Physical Society.

For double-walled carbon nanotubes, a value of 284.6 eV (FWHM: 0.64–0.8 eV) has been reported [80,81]. There is a plethora of measurements on multiwalled nanotubes as surveyed by Schiessling et al., who reported the same position of the C 1s line as for graphite but a larger FWHM at 0.63 eV [82]. However, they attributed this at least partly to remaining disorder or impurities even in the best samples, and cited a number of other measurements on MWCNTs with greater widths even when measured with the same energy resolution.

Although many different fullerene structures are known, the term fullerene (or "buckyball") often simply refers to the spherical C_{60} molecule resembling a soccer ball, which was the first of their kind to be discovered in 1985 by Kroto et al. [1]. The core level photoemission response of C_{60} is well described by a Voigtian centered at 285.2 eV, with a FWHM of the Lorentzian component measured at 0.11 eV [83].

Heteroatom doping

After these important considerations of the pristine structures, we turn to our main topic of heteroatom doping. By this we mean the intentional replacement of carbon atoms in the lattice of graphene or the walls of carbon nanotubes by atoms of other elements. Boron (B) and nitrogen (N) are the neighbors of carbon in the periodic table, meaning they have a similar atomic size but one valence electron less (B) or more (N). This makes them the most suitable candidates for heteroatom doping. Individual studies are too numerous to cite here, but a number of reviews are available for general information [33,34,94,95]. Here we will instead only consider the photoemission response of doped carbon nanomaterials.

Although phosphorus (P) was theoretically proposed a long time ago as a possible alternative n-type dopant [96], the first

experimental reports on phosphorus doping of CNTs and graphene have only been published recently [97-100]. Like nitrogen, phosphorus has five valence electrons, but since they are on the third electron shell, P has a significantly larger covalent atomic radius (106 pm, compared to 82 pm for B, 77 pm for C, and 75 pm for N), which is expected to cause it to protrude from the graphitic lattice [97,101].

Other heteroatoms such as S, Si, Al and Ni have also been proposed. However, since work in those directions is still rather limited and no XPS data available yet, we will omit them from this review. However, the interested reader can find more information elsewhere [28,102-107].

Nitrogen

Nitrogen is undoubtedly the most extensively studied heteroatom dopant for carbon nanomaterials. Stephan et al. pioneered the use of the arc-discharge technique for doping [23], followed by reports on the synthesis of nitrogen-doped multiwalled carbon nanotubes (N-MWCNTs) from several groups [108-110]. Successful nitrogen-doped SWCNT (N-SWCNT) synthesis was reported by Glerup et al. in 2004 by using arc discharge [111], later followed by laser ablation [112] and many different variations of chemical vapor deposition methods [113-125] (see also [33,34]). Nitrogen-doped graphene (N-graphene) has since been synthesized by using numerous methods, amongst them chemical vapor deposition [126,127], post-synthesis treatments [128,129], and ion implantation [30] (see also [107,130]).

Accordingly, there are hundreds of studies that use XPS to study nitrogen doping. However, it does not make sense to try to establish patterns for multiwalled tubes whose photoemission response is in general less well defined [82], and where the internal compartments of N-MWCNTs complicate matters further [131]. Instead, we concentrate on the subset of the literature related to single- and double-walled carbon nanotubes, and for N-MWCNTs and N-graphene restrict ourselves to summarize studies in which synchrotron radiation or an additional complementary technique (such as STM, EELS or X-ray absorption spectroscopy) was used for probing the doping. Table 2 contains our survey, with both the C 1s and N 1s values listed.

In most studies, the C 1s core level of only the doped material is reported, making it difficult to conclude if doping has caused any shift in the binding energy of the bulk system. However, a number of studies have explicitly compared a doped material to a corresponding pristine material [120,128,147-150]. In cases in which comparative data is available, it has been found that the position of the C 1s line is shifted to higher binding energies upon nitrogen doping, with the magnitude of the shift varying from 0.1 up to 0.4 eV depending on the study. Two additional components, most commonly found around 285.8 ± 0.1 and 287.1 ± 0.1 eV, have been tentatively identified and assigned to carbon in sp^2 C=N and sp^3 C–N bonds, respectively. However, since higher binding energy contributions could also arise from, e.g., carbon–oxygen bonds, very pure samples would be needed to draw confident conclusions about the identity of such components. Occasionally, values as high as 288.2 ± 0.1 eV have been similarly assigned [121,151], but these seem to be outliers in the literature and perhaps rather attributable to bonds with other elements.

An important and often overlooked starting point for interpreting the N 1s core level are fullerenes containing a single nitrogen substitution, which are called azafullerenes ($C_{59}N$). These are one of the only systems where there is no ambiguity about the underlying atomic structure. Thus even though curvature, the influence of the bonding of azafullerene dimers, or differences in the core hole screening compared to other nitrogen-doped systems may affect the measured value by at most a few hundred meV, the N 1s core level of $C_{59}N$ measured at 400.7 eV [132,152] should provide the first estimate for the energy of the N substitution (i.e., graphitic N).

In general, the N 1s response in XPS has been used for identifying many distinct components in different systems (see Figure 3d for a schematic illustration of many of the different atomic configurations that have been considered). Binding energy values for a N substitution have been variously assigned from around 400.2 eV up to 401.8 eV (e.g., [116,119,121,126,127,132,135,140,149-159]). Even within nominally the same systems (“N-SWCNTs” or “N-graphene”), the spread of the N 1s values is well over 1 eV. There are at least three clear explanations for such a large range of values: inaccuracies in either the measurement or the spectral deconvolution; the assignment of correctly measured binding energies to incorrect atomic configurations; or the effect of differences in core hole screening.

A level of variability could be expected for different systems, and values reported for graphene often tend to be in the higher end of the range. This may be due to the influence of hybridization between the valence orbitals of N with the underlying substrate [32], which reduces core hole screening and thus raises the binding energy, or to an effect of curvature (as proposed for the C 1s line [160]). Figure 3 shows a measurement of N-graphene where a binding energy of 401.3 eV was assigned to the substitutional configuration, and the influence of the substrate clearly elucidated by an intercalation procedure. Perhaps eliminating some of these factors, a very recent measurement

Table 2: XPS measurements of the carbon 1s and nitrogen 1s lines for various nitrogen-doped graphitic carbon nanomaterials reported in the literature. The columns show the material, diameter of the nanostructure, the carbon 1s energy assigned to C–C bonds, and to C–N bonds, the nitrogen 1s energies assigned to pyridinic (pnic), pyrrolic (plic) and substitutional (subs) nitrogen, the concentration of nitrogen in atomic percent, and the citation for each measurement.

		C 1s (eV)		N 1s (eV)				
material	*d* (nm)	C–C	C–N[a]	pnic	plic	subs	N atomic %	references
$(C_{59}N)_2$	0.71	285.2	—	—	—	400.72	1.6	[132]
SW	1–1.6	284.5	—	398.5	—	400.6	0.3	[119]
SW	<2	284.8	286.3, 288.3	399.8	—	401.8	3	[121]
SW	1–1.8	284.7[b]	287	397.9	—	401.1	2	[120]
SW	1.1–1.2	—	—	398.6	—	400.5	1.1	[133]
SW	0.9–1.8	—	—	397.6	—	400.5	1	[124]
SW	0.8–1.0	284.5	285.8, 287	398.4	400.9	—	3.2	[134]
S/DW	0.8–2	284.5	—	398.6	—	400.6	0.2	[117]
DW	—	284.5	285.5	398.3	—	400.2	3	[135]
DW	1.6–3.2	284.3	—	398.0	—	401.3	1	[136]
FW	1–5	284.5	287	398.6	—	400.88	6	[116]
MW	15–80	284.5	285.5	398.4	—	400.2	8	[137]
MW	10–40	284.7	285.7 ± 0.1	398.5	—	400.8	4	[138]
MW	30–80	284.5	—	398.6	—	400.5	5	[139]
MW	30–60	284.5	—	398.2	—	400.5	25.7	[140]
MW	20–60	284.1	285.9	398.2	400.2	401.1	5.2	[141]
SLG/Cu	∞	284.8	285.8, 287.5	398.2	400.1	401.7	8.9	[126] [c]
SLG/Au/Ni(111)[d]	∞	284.4	—	398.4	400.3	401.3	0.48	[127]
SLG/Cu	∞	284.6	285.8	398.6	—	400.6	0.25	[142]
SLG/SiO_2	∞	284.5	—	398.0	398.9	400	0.4	[143] [e]
FLG	∞	284.6[f]	—	398.45	399.45	400.92	12.8	[67]
graphite	∞	—	—	398.5	399.9	401.1	2.7	[144]

[a]When two values are listed, the lower binding energy component has been assigned to sp^2 C–N and the higher to sp^3 C–N bonds. [b]Shifted from 284.5 eV upon doping. [c]Predominant presence of graphitic nitrogen subsequently verified by transmission electron microscopy [145,146]. [d]Quasi-freestanding graphene via Au intercalation as in [69,70]. [e]Most values not explicitly reported, estimated from spectrum graph. A slight C 1s downshift and broadening is observed in the doped sample. [f]Synchrotron-based scanning X-ray photoelectron microscopy measurements on ion-implanted few-layer graphene samples. The pristine sample was measured at 284.47 eV.

using synchrotron-based scanning X-ray photoelectron microscopy assigned a value of 400.92 eV to substitutional N in suspended ion-irradiated few-layer graphene [67]. In any case, the range of values cited for the substitution seems so large that experimental inaccuracies or misassignments likely need to be invoked to explain the variability.

Less controversially, a peak around 398.3 ± 0.3 eV is commonly attributed to pyridinic nitrogen, that is, to nitrogen with a lone electron pair, located either at the edge of the graphitic network or next to a vacancy, and bonded to two carbon atoms [161] (structures 2 and 3, respectively, in Figure 3d). However, occasionally values as low as 397.9 eV [120] and as high as 399.8 eV [121] have been thus assigned. Although this is rarely mentioned, "pyridinic" can implicitly refer to three N atoms surrounding a vacancy (3NV, structure 4 in Figure 3d), or possibly even four N around a divacancy [162]. This is because the formation energy of a single pyridinic vacancy (1NV, structure 3 in Figure 3d) is very high, especially in graphene [163]. While many studies do not find any corresponding local structures in samples where "pyridinic" binding energies are present [164], the 1NV was recently directly observed by STM in ion-implanted graphite [144]; see also [129] for a tentative identification of the 3NV in plasma-treated graphene. Thus it seems the exact atomic configuration of the sites responsible for these peaks still remains somewhat unresolved.

Between these two, binding energies around 400.1 ± 0.3 eV are commonly attributed to "pyrrolic" nitrogen (N in a five-membered ring), which is thought to be responsible for the inner compartments typical for N-MWCNTs [131]. Recently, some authors have suggested that an N substitution in a Stone–Wales defect [165,166] (or otherwise asymmetric local bonding [167]) could also be the origin of this signal. However, it should be noted that amine, pyridone, nitroso and cyano groups could all fall close to this energy [161,168], and thus it is not possible to conclusively determine the exact atomic structure merely based on XPS. Furthermore, considering the N 1s

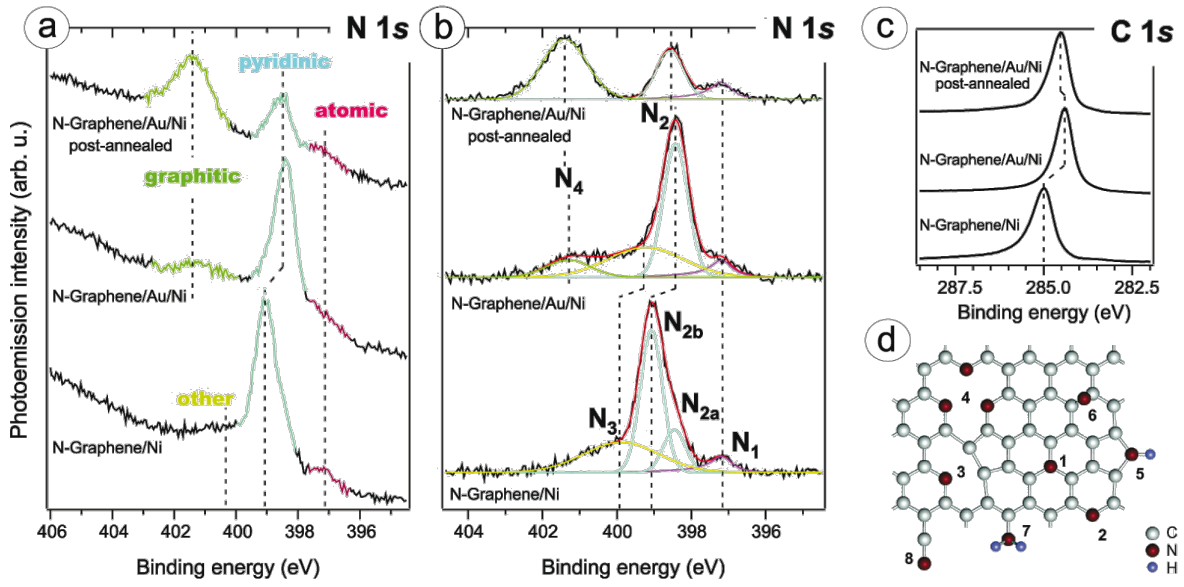

Figure 3: An XPS measurement and peak assignment of nitrogen-doped graphene prepared by chemical vapor deposition. (a–c) N 1s and C 1s spectra of N-graphene freshly prepared on nickel, intercalated by gold, and treated by post-annealing. Note the large shifts caused by interaction with the substrate in the non-intercalated spectrum. The N 1s spectra shown in (b) have been background-subtracted. In the post-annealed sample, a peak at 401.3 eV was assigned to graphitic nitrogen, and another at 398.4 eV to pyridinic N. (d) Some proposed possible configurations of graphene nitrogen impurities: (1) graphitic (substitutional) N; three varieties of pyridinic bonding: (2) edge pyridinic N, (3) single N pyridinic vacancy (1NV), and (4) triple N pyridinic vacancy (3NV); (5) pyrrole-like N, (6) interstitial N or adatom, and (7) amine or (8) nitrile groups. Adapted with permission from [127], copyright 2011 The American Chemical Society.

binding energy of $C_{59}N$, it is possible that binding energies at the higher end of this range are incorrectly assigned to pyrrolic N, and are actually graphitic N. If this were the case, however, the atomic origin of the next higher binding energy component around 401.5 eV would have to be rethought (notably, some have attributed this to absorbed N–O instead [143]).

Although not included in our survey in Table 2, components with even higher binding energies between 402 and 405 eV are occasionally also detected. Energies of about 402–403.5 eV have been typically assigned to various oxidized nitrogen configurations ([116,138,141,144,168-170]), pyridine-*N*-oxide being the most widely suggested one [168]). However, binding energies in the same range have also been suggested for clustered N substitutions [67,164,168,171]. Furthermore, hydrogenation of the nitrogen dopants (perhaps of substitutional N, but maybe more plausibly of edge pyridinic N atoms [172,173]) would also be expected to raise the measured binding energies, possibly contributing to the observed overlaps. More studies are needed to elucidate which, if any, of these suggestions play an important role, and in which materials. Finally, values between 404–405 eV (possibly shifted due to physisorption) have been typically assigned to N_2 molecules trapped inside carbon nanotubes or between graphene layers (e.g., [120,137,140,174,175]).

Boron

In boron-doped systems, the identification of the B 1s response is somewhat easier than in the case of nitrogen since a simple substitution is the sole favorable bonding configuration for boron in the lattice [34,176-178]. Very recently, direct local observations of this configuration in graphene were reported by STM [32] and TEM/EELS [30].

The synthesis of boron-doped SWCNTs has mainly been successful through the use of high-temperature techniques, i.e., arc-discharge [23,179] and laser ablation [180]. Identification of dopants was initially mainly via TEM/EELS measurements made directly on the bundles, and as such the presence of elemental boron in the targets or rods was not resolved until a recent XPS study of such a material, in which those bonding environments were clearly discerned [181]. The first successful synthesis of B-doped SWCNTs was carried out by using chemical vapor deposition in a high-vacuum system and a triisopropyl borate precursor [182], and the important role of B adhesion to Fe catalyst particles was also highlighted. For boron-doped graphene, successful synthesis recipes range from the mechanical exfoliation of boron-doped graphite [183] to thermochemical annealing of graphite oxide [184], microwave plasma decomposition of trimethylboron on SiO_2 [185], and CVD of phenylboronic acid on a copper substrate [186].

It has been consistently reported that the incorporation of B in a nanotube structure is responsible for the formation of an additional lower binding energy peak in the C 1s region [34], which can, depending on the concentration, either appear as broadening of the main peak [181] or as a separate feature [182]. A B 1s response at 187 eV has been assigned to elemental boron, a peak at 189 eV to BC_3, a peak at 190 eV to B in disordered carbon, and signals between 191.5 and 192.1 eV to substitutional B in the SWCNT wall [181,182]. Higher binding energy components corresponding to boric acid and various boron oxides can sometimes also be found [182], but boron has few gaseous compounds that could attach to the inner walls of nanotubes or adsorb onto the surface of either graphene or nanotubes.

In boron-doped graphene (B-graphene), significantly lower binding energy values from 187 to 189 eV have been assigned to the substitutional B configuration [183-185,187]. At the lower end of the range, Kim et al. [183] assigned a B 1s response of boron-doped graphite at 187.0 eV to substitutional boron. They also saw a downshift of about 0.2 eV of the C 1s line in their doped sample, along with a new peak at 282.2 eV. Sheng et al. [184] similarly measured a downshift of about 0.3 eV of the C 1s line of B-graphene, and assigned B 1s responses at 187.7 and 189.0 eV to B_4C and B_3C, respectively; and those at 190.4 and 191.9 eV to BC_2O and BCO_2. On the other hand, Tang et al. [185] found a single B 1s response at 189.7 eV, which upshifted to about 190.1 eV with increasing B content. Correlating the XPS measurements by EELS, they assigned this to substitutional boron. Yet higher in energy, Wang et al. [186] measured a single B 1s response at 190.9 eV, again assigning it to substitutional B.

As even the C 1*s* is very sensitive to the substrate on which the measurements are made, determining a fixed value for the binding energy for substitutional boron is not as straightforward in the case of graphene. The effect of the substrate may also be stronger for boron than for nitrogen, since there is evidence that B interacts more strongly with metallic substrates [32].

Phosphorus

The production of phosphorus-doped SWCNTs has been reported in a small number of works. Triphenylphosphine [98,188,189], and very recently also trimethylphosphine [190], have been used as P precursors to synthesize P-SWCNTs by using CVD, while Krstič et al. used arc discharge with red phosphorus mixed into the anode rod [99]. The synthesis of P-doped graphene has also been successful to a certain extent, by using ionic liquid 1-butyl-3-methylimidazolium hexafluorophosphate [191]. In addition, the synthesis of P/N-heterodoped graphene has been reported using triphenylphosphine and triphenylamine [100] and by chemical treatment of N-graphene using phosphoric acid [192].

However, unambiguous direct evidence for the bonding of phosphorus in graphitic carbon nanomaterials has been lacking. Based on DFT simulations, it is expected that P will predominantly bond to three C neighbors, but buckle significantly out of the surface due its larger atomic radius [97,101,104]. The curvature in small diameter SWCNTs might make the incorporation of P more favorable by a release of strain [98]. Krstič et al. have further suggested that P substitutions are readily oxidized in ambient, with the P-O bond formation predicted to be exothermic by as much as 3.3 eV [99].

Very limited XPS data is currently available on phosphorus dopants, and the samples used typically contain large amounts of impurities. A P 2p signature around 130.5 eV has been attributed to substitutional phosphorus in P-doped and P/N-co-doped MWCNTs [193,194] and graphene [100]. An additional peak around 132 eV has commonly been attributed to P–O bonds [195,196] (although some authors have instead assigned this peak to the P substitution in purely P-doped graphene [191]). Larrude et al. measured XPS on P-MWCNTs synthesized by spray pyrolysis [197], and assigned two lower binding energy components separated by the expected spin–orbit splitting to substitutional P, with P $2p_{3/2}$ at 129.3 eV and P $2p_{1/2}$ at 130.0 eV, with corresponding higher BE components at 133.1 and 133.9 eV assigned to P–O bonds. However, these measurements were performed on an unpurified multiwalled material of relatively poor crystallinity. For P-SWCNTs, the first available measurement found a lower binding energy component at 129.3 eV after annealing purified samples in vacuum, with two higher contributions at 133.3 and 134.2 eV [190].

Remarks

Considering the literature summarized above, it is clear that large and often overlapping ranges of binding energies has been assigned to allegedly the same atomic configurations. Thus we need to stress that the material in question (e.g., SWCNTs, MWCNTs, graphene on different substrates) must taken into account [37,198], and great care taken when assigning measured binding energies. Careful experiments done under ontrolled conditions using ultrapure materials are still needed to firmly establish reliable signatures for XPS in doped carbon nanomaterials [37]. Furthermore, new theoretical calculations to elucidate the binding energies of various configurations would prove useful, and XPS should be directly correlated with atomically resolved techniques.

With the data at hand, it is interesting to note that in the XPS spectra of nitrogen-doped carbon nanotubes, regardless of the synthesis method there always seems to be at best an approximately equal ratio of binding energy components attributed to pyridinic and graphitic nitrogen, especially in single-walled tubes [115,117,120,124,133]. On the contrary, when graphene crystallinity is high, several studies have reported a clear predominance of the higher binding energy component (e.g., [126,127,142]), often found around 401.5 eV. Although this energy seems rather high to be attributable to (at least single) graphitic nitrogen atoms, local measurements of such samples have seen a clear preference for the simple substitution [27,30,127,142,143,145,146]. It is currently not known whether this difference is due to differences in the formation energies for the various configurations (highly curved structures could favor the formation of pyridinic configurations to release strain energy [162]), or to differences in the morphologies of the respective catalysts, i.e., flat surfaces versus nanosized particles. Further work on elucidating the origin of the differences in the attributed binding energies and their relative abundances in different systems remains greatly needed.

Conclusion

Significant progress has been made in recent years in synthesizing graphitic carbon nanomaterials doped with various heteroatoms. However, even – or rather, especially – for the most studied dopant, nitrogen, a clear consensus on the core level binding energies and their atomic origin in various systems is still lacking. Furthermore, most of the commonly used binding energy references are still based on measurements made on molecules or by using limited or outdated computational methods, making new theoretical work on the subject desirable in the future. Although studies combining multiple complementary techniques, which thus have the best chances of conclusively identifying the atomic structures, are starting to emerge, much remains to be done to firmly establish the metrology of dopants in carbon nanomaterials.

Acknowledgements

We thank Danny Haberer-Gehrmann, Chris Ewels, Duncan Mowbray and Mathias Ljungberg for several useful discussions.

References

1. Kroto, H. W.; Heath, J. R.; O'Brien, S. C.; Curl, R. F.; Smalley, R. E. *Nature* **1985,** *318,* 162–163. doi:10.1038/318162a0
2. Hirsch, A., Ed. *Fullerenes and Related Structures;* Topics in Current Chemistry, Vol. 199; Springer: Berlin, Germany, 1999. doi:10.1007/3-540-68117-5
3. Iijima, S. *Nature* **1991,** *354,* 56–58. doi:10.1038/354056a0
4. Iijima, S.; Ichihashi, T. *Nature* **1993,** *363,* 603–605. doi:10.1038/363603a0
5. Bethune, D. S.; Klang, C. H.; de Vries, M. S.; Gorman, G.; Savoy, R.; Vazquez, J.; Beyers, R. *Nature* **1993,** *363,* 605–607. doi:10.1038/363605a0
6. Novoselov, K. S.; Geim, A. K.; Morozov, S. V.; Jiang, D.; Zhang, Y.; Dubonos, S. V.; Grigorieva, I. V.; Firsov, A. A. *Science* **2004,** *306,* 666–669. doi:10.1126/science.1102896
7. Novoselov, K. S.; Geim, A. K.; Morozov, S. V.; Jiang, D.; Katsnelson, M. I.; Grigorieva, I. V.; Dubonos, S. V.; Firsov, A. A. *Nature* **2005,** *438,* 197–200. doi:10.1038/nature04233
8. Geim, A. K.; Novoselov, K. S. *Nat. Mater.* **2007,** *6,* 183–191. doi:10.1038/nmat1849
9. Pauling, L. *J. Am. Chem. Soc.* **1931,** *53,* 1367–1400. doi:10.1021/ja01355a027
10. Kekulé, A. *Justus Liebigs Ann. Chem.* **1866,** *137,* 129–196. doi:10.1002/jlac.18661370202
11. Kroto, H. W. *Nature* **1987,** *329,* 529–531. doi:10.1038/329529a0
12. Prato, M. *J. Mater. Chem.* **1997,** *7,* 1097–1109. doi:10.1039/A700080D
13. Peng, B.; Locascio, M.; Zapol, P.; Li, S.; Mielke, S. L.; Schatz, G. C.; Espinosa, H. D. *Nat. Nanotechnol.* **2008,** *3,* 626–631. doi:10.1038/nnano.2008.211
14. Saito, R.; Fujita, M.; Dresselhaus, G.; Dresselhaus, M. S. *Appl. Phys. Lett.* **1992,** *60,* 2204–2206. doi:10.1063/1.107080
15. Charlier, J.-C.; Blase, X.; Roche, S. *Rev. Mod. Phys.* **2007,** *79,* 677. doi:10.1103/RevModPhys.79.677
16. Frank, S.; Poncharal, P.; Wang, Z. L.; de Heer, W. A. *Science* **1998,** *280,* 1744–1746. doi:10.1126/science.280.5370.1744
17. Hong, S.; Myung, S. *Nat. Nanotechnol.* **2007,** *2,* 207–208. doi:10.1038/nnano.2007.89
18. Bunch, J. S.; Verbridge, S. S.; Alden, J. S.; van der Zande, A. M.; Parpia, J. M.; Craighead, H. G.; McEuen, P. L. *Nano Lett.* **2008,** *8,* 2458–2462. doi:10.1021/nl801457b
19. Lee, C.; Wei, X.; Kysar, J. W.; Hone, J. *Science* **2008,** *321,* 385–388. doi:10.1126/science.1157996
20. Zhang, Y.; Tan, Y.-W.; Stormer, H. L.; Kim, P. *Nature* **2005,** *438,* 201–204. doi:10.1038/nature04235
21. Gusynin, V. P.; Sharapov, S. G. *Phys. Rev. Lett.* **2005,** *95,* 146801. doi:10.1103/PhysRevLett.95.146801
22. Yi, J.-Y.; Bernholc, J. *Phys. Rev. B* **1993,** *47,* 1708–1711. doi:10.1103/PhysRevB.47.1708
23. Stephan, O.; Ajayan, P. M.; Colliex, C.; Redlich, P.; Lambert, J. M.; Bernier, P.; Lefin, P. *Science* **1994,** *266,* 1683–1685. doi:10.1126/science.266.5191.1683
24. Ge, M.; Sattler, K. *Appl. Phys. Lett.* **1994,** *65,* 2284–2286. doi:10.1063/1.112719
25. Odom, T. W.; Huang, J.-L.; Kim, P.; Lieber, C. M. *Nature* **1998,** *391,* 62–64. doi:10.1038/34145
26. Colliex, C. *J. Electron Microsc.* **1996,** *45,* 44–50.
27. Zhao, L.; He, R.; Rim, K. T.; Schiros, T.; Kim, K. S.; Zhou, H.; Gutiérrez, C.; Chockalingam, S. P.; Arguello, C. J.; Pálová, L.; Nordlund, D.; Hybertsen, M. S.; Reichman, D. R.; Heinz, T. F.; Kim, P.; Pinczuk, A.; Flynn, G. W.; Pasupathy, A. N. *Science* **2011,** *333,* 999–1003. doi:10.1126/science.1208759
28. Zhou, W.; Kapetanakis, M.; Prange, M.; Pantelides, S.; Pennycook, S.; Idrobo, J.-C. *Phys. Rev. Lett.* **2012,** *109,* 206803. doi:10.1103/PhysRevLett.109.206803
29. Ramasse, Q. M.; Seabourne, C. R.; Kepaptsoglou, D.-M.; Zan, R.; Bangert, U.; Scott, A. J. *Nano Lett.* **2013,** *13,* 4989–4995. doi:10.1021/nl304187e

30. Bangert, U.; Pierce, W.; Kepaptsoglou, D. M.; Ramasse, Q.; Zan, R.; Gass, M. H.; Van den Berg, J. A.; Boothroyd, C. B.; Amani, J.; Hofsäss, H. *Nano Lett.* **2013,** *13,* 4902–4907. doi:10.1021/nl402812y
31. Nicholls, R. J.; Murdock, A. T.; Tsang, J.; Britton, J.; Pennycook, T. J.; Koós, A.; Nellist, P. D.; Grobert, N.; Yates, J. R. *ACS Nano* **2013,** *7,* 7145–7150. doi:10.1021/nn402489v
32. Zhao, L.; Levendorf, M. P.; Goncher, S. J.; Schiros, T.; Palova, L.; Zabet-Khosousi, A.; Rim, K. T.; Gutierrez, C.; Nordlund, D.; Jaye, C.; Hybertsen, M. S.; Reichman, D. R.; Flynn, G. W.; Park, J.; Pasupathy, A. N. *Nano Lett.* **2013,** *13,* 4659–4665. doi:10.1021/nl401781d
33. Ayala, P.; Arenal, R.; Rümmeli, M. H.; Rubio, A.; Pichler, T. *Carbon* **2010,** *48,* 575–586. doi:10.1016/j.carbon.2009.10.009
34. Ayala, P.; Arenal, R.; Loiseau, A.; Rubio, A.; Pichler, T. *Rev. Mod. Phys.* **2010,** *82,* 1843. doi:10.1103/RevModPhys.82.1843
35. Enderlein, C. Graphene and its Interaction with Different Substrates Studied by Angular-Resolved Photoemission Spectroscopy. Ph.D. Thesis, Freie Universität Berlin, Berlin, Germany, 2010.
36. Lim, H.; Song, H. J.; Son, M.; Baik, J. Y.; Shin, H.-J.; Choi, H. C. *Chem. Commun.* **2011,** *47,* 8608–8610. doi:10.1039/C1CC12953H
37. Ayala, P.; Miyata, Y.; De Blauwe, K.; Shiozawa, H.; Feng, Y.; Yanagi, K.; Kramberger, C.; Silva, S.; Follath, R.; Kataura, H. *Phys. Rev. B* **2009,** *80,* 205427. doi:10.1103/PhysRevB.80.205427
38. Smith, N. V.; Traum, M. M.; Di Salvo, F. J. *Solid State Commun.* **1974,** *15,* 211–214. doi:10.1016/0038-1098(74)90743-1
39. Himpsel, F. *Adv. Phys.* **1983,** *32,* 1–51. doi:10.1080/00018738300101521
40. Georgakilas, V.; Kordatos, K.; Prato, M.; Guldi, D. M.; Holzinger, M.; Hirsch, A. *J. Am. Chem. Soc.* **2002,** *124,* 760–761. doi:10.1021/ja016954m
41. Sinnott, S. B. *J. Nanosci. Nanotechnol.* **2002,** *2,* 113–123. doi:10.1166/jnn.2002.107
42. Sun, Y.-P.; Fu, K.; Lin, Y.; Huang, W. *Acc. Chem. Res.* **2002,** *35,* 1096–1104. doi:10.1021/ar010160v
43. Balasubramanian, K.; Burghard, M. *Small* **2005,** *1,* 180–192. doi:10.1002/smll.200400118
44. Georgakilas, V.; Otyepka, M.; Bourlinos, A. B.; Chandra, V.; Kim, N.; Kemp, K. C.; Hobza, P.; Zboril, R.; Kim, K. S. *Chem. Rev.* **2012,** *112,* 6156–6214. doi:10.1021/cr3000412
45. Kuila, T.; Bose, S.; Mishra, A. K.; Khanra, P.; Kim, N. H.; Lee, J. H. *Prog. Mater. Sci.* **2012,** *57,* 1061–1105. doi:10.1016/j.pmatsci.2012.03.002
46. Casanovas, J.; Ricart, J. M.; Rubio, J.; Illas, F.; Jiménez-Mateos, J. M. *J. Am. Chem. Soc.* **1996,** *118,* 8071–8076. doi:10.1021/ja960338m
47. Cole, R. J.; Macdonald, B. F.; Weightman, P. *J. Electron Spectrosc. Relat. Phenom.* **2002,** *125,* 147–152. doi:10.1016/S0368-2048(02)00084-1
48. Kudashov, A. G.; Okotrub, A. V.; Bulusheva, L. G.; Asanov, L. P.; Shubin, Yu. V.; Yudanov, N. F.; Yudanova, L. I.; Danilovich, V. S.; Abrosimov, O. G. *J. Phys. Chem. B* **2004,** *108,* 9048–9053. doi:10.1021/jp048736w
49. Hellgren, N.; Guo, J.; Luo, Y.; Såthe, C.; Agui, A.; Kashtanov, S.; Nordgren, J.; Ågren, H.; Sundgren, J.-E. *Thin Solid Films* **2005,** *471,* 19–34. doi:10.1016/j.tsf.2004.03.027
50. Cabellos, J. L.; Mowbray, D. J.; Goiri, E.; El-Sayed, A.; Floreano, L.; de Oteyza, D. G.; Rogero, C.; Ortega, J. E.; Rubio, A. *J. Phys. Chem. C* **2012,** *116,* 17991–18001. doi:10.1021/jp3004213
51. Susi, T.; Kaukonen, M.; Havu, P.; Ljungberg, M. P.; Ayala, P.; Kauppinen, E. I. *Beilstein J. Nanotechnol.* **2014,** *5,* 121–132. doi:10.3762/bjnano.5.12
52. Ruiz-Soria, G.; Pérez Paz, A.; Sauer, M.; Mowbray, D. J.; Lacovig, P.; Dalmiglio, M.; Lizzit, S.; Yanagi, K.; Rubio, A.; Goldoni, A.; Ayala, P.; Pichler, T. *ACS Nano* **2014,** *8,* 1375–1383. doi:10.1021/nn405114z
53. Shirley, E. L. *Phys. Rev. Lett.* **1998,** *80,* 794–797. doi:10.1103/PhysRevLett.80.794
54. Despoja, V.; Mowbray, D. J.; Vlahović, D.; Marušić, L. *Phys. Rev. B* **2012,** *86,* 195429. doi:10.1103/PhysRevB.86.195429
55. Despoja, V.; Šunjić, M. *Phys. Rev. B* **2013,** *88,* 245416. doi:10.1103/PhysRevB.88.245416
56. Doniach, S.; Šunjić, M. *J. Phys. C* **1970,** *3,* 285–291. doi:10.1088/0022-3719/3/2/010
57. Tanuma, S.; Shiratori, T.; Kimura, T.; Goto, K.; Ichimura, S.; Powell, C. J. *Surf. Interface Anal.* **2005,** *37,* 833–845. doi:10.1002/sia.2102
58. Shirley, D. A. *Phys. Rev. B* **1972,** *5,* 4709–4714. doi:10.1103/PhysRevB.5.4709
59. Tougaard, S. *J. Vac. Sci. Technol., A* **1990,** *8,* 2197–2203. doi:10.1116/1.577037
60. Scofield, J. *Theoretical photoionization cross sections from 1 to 1500 keV;* Lawrence Livermore National Laboratory, 1973.
61. Moulder, J. F.; Stickle, W. F.; Sobol, P. E.; Bomben, K. D. *Handbook of X-ray photoelectron spectroscopy;* Perkin Elmer: Eden Prairie, MN, USA, 1992; Vol. 40.
62. Prince, K. C.; Ulrych, I.; Peloi, M.; Ressel, B.; Cháb, V.; Crotti, C.; Comicioli, C. *Phys. Rev. B* **2000,** *62,* 6866–6868. doi:10.1103/PhysRevB.62.6866
63. Speranza, G.; Minati, L.; Anderle, M. *J. Appl. Phys.* **2007,** *102,* 043504. doi:10.1063/1.2769332
64. Emtsev, K. V.; Speck, F.; Seyller, T.; Ley, L.; Riley, J. D. *Phys. Rev. B* **2008,** *77,* 155303. doi:10.1103/PhysRevB.77.155303
65. Hunt, M. R. C. *Phys. Rev. B* **2008,** *78,* 153408. doi:10.1103/PhysRevB.78.153408
66. Balasubramanian, T.; Andersen, J. N.; Walldén, L. *Phys. Rev. B* **2001,** *64,* 205420. doi:10.1103/PhysRevB.64.205420
67. Scardamaglia, M.; Aleman, B.; Amati, M.; Ewels, C.; Pochet, P.; Reckinger, N.; Colomer, J.-F.; Skaltsas, T.; Tagmatarchis, N.; Snyders, R.; Gregoratti, L.; Bittencourt, C. *Carbon* **2014,** *73,* 371–381. doi:10.1016/j.carbon.2014.02.078
68. Grüneis, A.; Kummer, K.; Vyalikh, D. V. *New J. Phys.* **2009,** *11,* 073050. doi:10.1088/1367-2630/11/7/073050
69. Haberer, D.; Vyalikh, D. V.; Taioli, S.; Dora, B.; Farjam, M.; Fink, J.; Marchenko, D.; Pichler, T.; Ziegler, K.; Simonucci, S.; Dresselhaus, M. S.; Knupfer, M.; Büchner, B.; Grüneis, A. *Nano Lett.* **2010,** *10,* 3360–3366. doi:10.1021/nl101066m
70. Haberer, D.; Giusca, C. E.; Wang, Y.; Sachdev, H.; Fedorov, A. V.; Farjam, M.; Jafari, S. A.; Vyalikh, D. V.; Usachov, D.; Liu, X.; Treske, U.; Grobosch, M.; Vilkov, O.; Adamchuk, V. K.; Irle, S.; Silva, S. R. P.; Knupfer, M.; Büchner, B.; Grüneis, A. *Adv. Mater.* **2011,** *23,* 4497–4503. doi:10.1002/adma.201102019
71. Haberer, D. Electronic Properties of Functionalized Graphene Studied With Photoemission Spectroscopy. Ph.D. Thesis, TU Dresden / IWF Dresden, Dresden, Germany, 2012.
72. Avila, J.; Razado, I.; Lorcy, S.; Fleurier, R.; Pichonat, E.; Vignaud, D.; Wallart, X.; Asensio, M. C. *Sci. Rep.* **2013,** *3,* No. 2439. doi:10.1038/srep02439
73. Hibino, H.; Kageshima, H.; Kotsugi, M.; Maeda, F.; Guo, F.-Z.; Watanabe, Y. *Phys. Rev. B* **2009,** *79,* 125437. doi:10.1103/PhysRevB.79.125437

74. Merino, P.; Švec, M.; Martinez, J. I.; Jelinek, P.; Lacovig, P.; Dalmiglio, M.; Lizzit, S.; Soukiassian, P.; Cernicharo, J.; Martin-Gago, J. A. *Nat. Commun.* **2014,** *5,* No. 3054. doi:10.1038/ncomms4054
75. Riedl, C.; Coletti, C.; Iwasaki, T.; Zakharov, A. A.; Starke, U. *Phys. Rev. Lett.* **2009,** *103,* 246804. doi:10.1103/PhysRevLett.103.246804
76. Preobrajenski, A. B.; Ng, M. L.; Vinogradov, A. S.; Mårtensson, N. *Phys. Rev. B* **2008,** *78,* 073401. doi:10.1103/PhysRevB.78.073401
77. Rajasekaran, S.; Abild-Pedersen, F.; Ogasawara, H.; Nilsson, A.; Kaya, S. *Phys. Rev. Lett.* **2013,** *111,* 085503. doi:10.1103/PhysRevLett.111.085503
78. Lizzit, S.; Zampieri, G.; Petaccia, L.; Larciprete, R.; Lacovig, P.; Rienks, E. D. L.; Bihlmayer, G.; Baraldi, A.; Hofmann, P. *Nat. Phys.* **2010,** *6,* 345–349. doi:10.1038/nphys1615
79. De Blauwe, K.; Mowbray, D. J.; Miyata, Y.; Ayala, P.; Shiozawa, H.; Rubio, A.; Hoffmann, P.; Kataura, H.; Pichler, T. *Phys. Rev. B* **2010,** *82,* 125444. doi:10.1103/PhysRevB.82.125444
80. Choi, H. C.; Kim, S. Y.; Jang, W. S.; Bae, S. Y.; Park, J.; Kim, K. L.; Kim, K. *Chem. Phys. Lett.* **2004,** *399,* 255–259. doi:10.1016/j.cplett.2004.10.042
81. Kim, S. Y.; Lee, J. Y.; Park, J.; Park, C. J.; Lee, C. J.; Shin, H.-J. *Chem. Phys. Lett.* **2006,** *420,* 271–276. doi:10.1016/j.cplett.2005.12.084
82. Schiessling, J.; Kjeldgaard, L.; Rohmund, F.; Falk, L. K. L.; Campbell, E. E. B.; Nordgren, J.; Brühwiler, P. A. *J. Phys.: Condens. Matter* **2003,** *15,* 6563. doi:10.1088/0953-8984/15/38/022
83. Leiro, J.; Heinonen, M.; Laiho, T.; Batirev, I. *J. Electron Spectrosc. Relat. Phenom.* **2003,** *128,* 205–213. doi:10.1016/S0368-2048(02)00284-0
84. van Attekum, P. M. T. M.; Wertheim, G. K. *Phys. Rev. Lett.* **1979,** *43,* 1896–1898. doi:10.1103/PhysRevLett.43.1896
85. Lizzit, S.; Petaccia, L.; Goldoni, A.; Larciprete, R.; Hofmann, P.; Zampieri, G. *Phys. Rev. B* **2007,** *76,* 153408. doi:10.1103/PhysRevB.76.153408
86. Castro Neto, A. H.; Guinea, F.; Peres, N. M. R.; Novoselov, K. S.; Geim, A. K. *Rev. Mod. Phys.* **2009,** *81,* 109–162. doi:10.1103/RevModPhys.81.109
87. Zhou, S. Y.; Gweon, G. H.; Fedorov, A. V.; First, P. N.; de Heer, W. A.; Lee, D.-H.; Guinea, F.; Castro Neto, A. H.; Lanzara, A. *Nat. Mater.* **2007,** *6,* 770–775. doi:10.1038/nmat2003
88. Dresselhaus, M. S.; Dresselhaus, G.; Avouris, P., Eds. *Carbon Nanotubes: Synthesis, Structure, Properties, and Applications;* Topics in Applied Physics, Vol. 80; Springer: Berlin, Germany, 2001. doi:10.1007/3-540-39947-X
89. Saito, R.; Dresselhaus, G.; Dresselhaus, M. S. *Phys. Rev. B* **2000,** *61,* 2981. doi:10.1103/PhysRevB.61.2981
90. Shen, C.; Brozena, A. H.; Wang, Y. *Nanoscale* **2011,** *3,* 503–518. doi:10.1039/C0NR00620C
91. Krupke, R.; Hennrich, F.; Löhneysen, H.; Kappes, M. *Science* **2003,** *301,* 344. doi:10.1126/science.1086534
92. Arnold, M.; Green, A.; Hulvat, J.; Stupp, S.; Hersam, M. *Nat. Nanotechnol.* **2006,** *1,* 60. doi:10.1038/nnano.2006.52
93. Yanagi, K.; Iitsuka, T.; Fujii, S.; Kataura, H. *J. Phys. Chem. C* **2008,** *112,* 18889–18894. doi:10.1021/jp806822x
94. Ewels, C.; Glerup, M. *J. Nanosci. Nanotechnol.* **2005,** *5,* 1345–1363. doi:10.1166/jnn.2005.304
95. Terrones, M.; Souza Filho, A. G.; Rao, A. M. Doped Carbon Nanotubes: Synthesis, Characterization and Applications. In *Carbon Nanotubes;* Jorio, A.; Dresselhaus, G.; Dresselhaus, M. S., Eds.; Topics in Applied Physics, Vol. 111; Springer: Berlin, Germany, 2008; pp 531–566. doi:10.1007/978-3-540-72865-8_17
96. Strelko, V. V.; Kuts, V. S.; Thrower, P. A. *Carbon* **2000,** *38,* 1499–1503. doi:10.1016/S0008-6223(00)00121-4
97. Cruz-Silva, E.; Cullen, D. A.; Gu, L.; Romo-Herrera, J. M.; Muñoz-Sandoval, E.; López-Urías, F.; Sumpter, B. G.; Meunier, V.; Charlier, J.-C.; Smith, D. J.; Terrones, H.; Terrones, M. *ACS Nano* **2008,** *2,* 441–448. doi:10.1021/nn700330w
98. Cruz-Silva, E.; López-Urías, F.; Muñoz-Sandoval, E.; Sumpter, B. G.; Terrones, H.; Charlier, J.-C.; Meunier, V.; Terrones, M. *ACS Nano* **2009,** *3,* 1913–1921. doi:10.1021/nn900286h
99. Krstić, V.; Ewels, C. P.; Wågberg, T.; Ferreira, M. S.; Janssens, A. M.; Stéphan, O.; Glerup, M. *ACS Nano* **2010,** *4,* 5081–5086. doi:10.1021/nn1009038
100. Some, S.; Kim, J.; Lee, K.; Kulkarni, A.; Yoon, Y.; Lee, S.; Kim, T.; Lee, H. *Adv. Mater.* **2012,** *24,* 5481–5486. doi:10.1002/adma.201202255
101. Garcia, A. G.; Baltazar, S. E.; Castro, A. H. R.; Robles, J. F. P.; Rubio, A. *J. Comput. Theor. Nanosci.* **2008,** *5,* 2221–2229. doi:10.1166/jctn.2008.1123
102. Sumpter, B. G.; Huang, J.; Meunier, V.; Romo-Herrera, J. M.; Cruz-Silva, E.; Terrones, H.; Terrones, M. *Int. J. Quantum Chem.* **2009,** *109,* 97–118. doi:10.1002/qua.21893
103. Jiang, H.; Zhang, D.; Wang, R. *Nanotechnology* **2009,** *20,* 145501. doi:10.1088/0957-4484/20/14/145501
104. Denis, P. A. *Chem. Phys. Lett.* **2010,** *492,* 251–257. doi:10.1016/j.cplett.2010.04.038
105. Yang, S.; Zhi, L.; Tang, K.; Feng, X.; Maier, J.; Müllen, K. *Adv. Funct. Mater.* **2012,** *22,* 3634–3640. doi:10.1002/adfm.201200186
106. Audiffred, M.; Elías, A. L.; Gutiérrez, H. R.; López-Urías, F.; Terrones, H.; Merino, G.; Terrones, M. *J. Phys. Chem. C* **2013,** *117,* 8481–8490. doi:10.1021/jp312427z
107. Terrones, H.; Lv, R.; Terrones, M.; Dresselhaus, M. S. *Rep. Prog. Phys.* **2012,** *75,* 062501. doi:10.1088/0034-4885/75/6/062501
108. Yudasaka, M.; Kikuchi, R.; Ohki, Y.; Yoshimura, S. *Carbon* **1997,** *35,* 195–201. doi:10.1016/S0008-6223(96)00142-X
109. Sen, R.; Satishkumar, B. C.; Govindaraj, A.; Harikumar, K. R.; Renganathan, M. K.; Rao, C. N. R. *J. Mater. Chem.* **1997,** *7,* 2335–2337. doi:10.1039/A705891H
110. Terrones, M.; Terrones, H.; Grobert, N.; Hsu, W. K.; Zhu, Y. Q.; Hare, J. P.; Kroto, H. W.; Walton, D. R. M.; Kohler-Redlich, P.; Rühle, M.; Zhang, J. P.; Cheetham, A. K. *Appl. Phys. Lett.* **1999,** *75,* 3932–3934. doi:10.1063/1.125498
111. Glerup, M.; Steinmetz, J.; Samaille, D.; Stéphan, O.; Enouz, S.; Loiseau, A.; Roth, S.; Bernier, P. *Chem. Phys. Lett.* **2004,** *387,* 193–197. doi:10.1016/j.cplett.2004.02.005
112. Lin, H.; Lagoute, J.; Chacon, C.; Arenal, R.; Stéphan, O.; Repain, V.; Girard, Y.; Enouz, S.; Bresson, L.; Rousset, S.; Loiseau, A. *Phys. Status Solidi B* **2008,** *245,* 1986–1989. doi:10.1002/pssb.200879634
113. Keskar, G.; Rao, R.; Luo, J.; Hudson, J.; Chen, J.; Rao, A. M. *Chem. Phys. Lett.* **2005,** *412,* 269. doi:10.1016/j.cplett.2005.07.007
114. Min, Y.-S.; Bae, E. J.; Asanov, I. P.; Kim, U. J.; Park, W. *Nanotechnology* **2007,** *18,* 285601. doi:10.1088/0957-4484/18/28/285601

115. Villalpando-Paez, F.; Zamudio, A.; Elias, A. L.; Son, H.; Barros, E. B.; Chou, S. G.; Kim, Y. A.; Muramatsu, H.; Hayashi, T.; Kong, J.; Terrones, H.; Dresselhaus, G.; Endo, M.; Terrones, M.; Dresselhaus, M. S. *Chem. Phys. Lett.* **2006,** *424,* 345–352. doi:10.1016/j.cplett.2006.04.074
116. Ayala, P.; Grüneis, A.; Gemming, T.; Büchner, B.; Rümmeli, M. H.; Grimm, D.; Schumann, J.; Kaltofen, R.; Freire, F., Jr.; Fonseca Filho, H. D.; Pichler, T. *Chem. Mater.* **2007,** *19,* 6131–6137. doi:10.1021/cm0715592
117. Ayala, P.; Grüneis, A.; Gemming, T.; Grimm, D.; Kramberger, C.; Rümmeli, M. H.; Freire, F. L., Jr.; Kuzmany, H.; Pfeiffer, R.; Barreiro, A.; Büchner, B.; Pichler, T. *J. Phys. Chem. C* **2007,** *111,* 2879. doi:10.1021/jp0658288
118. Ayala, P.; Freire, F. L., Jr.; Rümmeli, M. H.; Grüneis, A.; Pichler, T. *Phys. Status Solidi B* **2007,** *244,* 4051–4055. doi:10.1002/pssb.200776180
119. Elías, A. L.; Ayala, P.; Zamudio, A.; Grobosch, M.; Cruz-Silva, E.; Romo-Herrera, J. M.; Campos-Delgado, J.; Terrones, H.; Pichler, T.; Terrones, M. *J. Nanosci. Nanotechnol.* **2010,** *10,* 3959–3964. doi:10.1166/jnn.2010.2009
120. Ibrahim, E. M. M.; Khavrus, V. O.; Leonhardt, A.; Hampel, S.; Oswald, S.; Rümmeli, M. H.; Büchner, B. *Diamond Relat. Mater.* **2010,** *19,* 1199–1206. doi:10.1016/j.diamond.2010.05.008
121. Liu, Y.; Jin, Z.; Wang, J.; Cui, R.; Sun, H.; Peng, F.; Wei, L.; Wang, Z.; Liang, X.; Peng, L. *Adv. Funct. Mater.* **2011,** *21,* 986–992. doi:10.1002/adfm.201002086
122. Susi, T.; Nasibulin, A. G.; Ayala, P.; Tian, Y.; Zhu, Z.; Jiang, H.; Roquelet, C.; Garrot, D.; Lauret, J.-S.; Kauppinen, E. I. *Phys. Status Solidi B* **2009,** *246,* 2507–2510. doi:10.1002/pssb.200982338
123. Pint, C. L.; Sun, Z.; Moghazy, S.; Xu, Y.-Q.; Tour, J. M.; Hauge, R. H. *ACS Nano* **2011,** *5,* 6925–6934. doi:10.1021/nn201252z
124. Koós, A. A.; Dillon, F.; Nicholls, R. J.; Bulusheva, L.; Grobert, N. *Chem. Phys. Lett.* **2012,** *538,* 108–111. doi:10.1016/j.cplett.2012.04.047
125. Thurakitseree, T.; Kramberger, C.; Zhao, P.; Aikawa, S.; Harish, S.; Chiashi, S.; Einarsson, E.; Maruyama, S. *Carbon* **2012,** *50,* 2635–2640. doi:10.1016/j.carbon.2012.02.023
126. Wei, D.; Liu, Y.; Wang, Y.; Zhang, H.; Huang, L.; Yu, G. *Nano Lett.* **2009,** *9,* 1752–1758. doi:10.1021/nl803279t
127. Usachov, D.; Vilkov, O.; Grüneis, A.; Haberer, D.; Fedorov, A.; Adamchuk, V. K.; Preobrajenski, A. B.; Dudin, P.; Barinov, A.; Oehzelt, M.; Laubschat, C.; Vyalikh, D. V. *Nano Lett.* **2011,** *11,* 5401–5407. doi:10.1021/nl2031037
128. Lin, Y.-C.; Lin, C.-Y.; Chiu, P.-W. *Appl. Phys. Lett.* **2010,** *96,* 133110. doi:10.1063/1.3368697
129. Joucken, F.; Tison, Y.; Lagoute, J.; Dumont, J.; Cabosart, D.; Zheng, B.; Repain, V.; Chacon, C.; Girard, Y.; Botello-Méndez, A. R.; Rousset, S.; Sporken, R.; Charlier, J.-C.; Henrard, L. *Phys. Rev. B* **2012,** *85,* 161408. doi:10.1103/PhysRevB.85.161408
130. Wang, H.; Maiyalagan, T.; Wang, X. *ACS Catal.* **2012,** *2,* 781–794. doi:10.1021/cs200652y
131. Trasobares, S.; Stephan, O.; Colliex, C.; Hsu, W. K.; Kroto, H. W.; Walton, D. R. M. *J. Chem. Phys.* **2002,** *116,* 8966–8972. doi:10.1063/1.1473195
132. Schulte, K.; Wang, L.; Moriarty, P. J.; Prassides, K.; Tagmatarchis, N. *J. Chem. Phys.* **2007,** *126,* 184707. doi:10.1063/1.2730787
133. Susi, T.; Kaskela, A.; Zhu, Z.; Ayala, P.; Arenal, R.; Tian, Y.; Laiho, P.; Mali, J.; Nasibulin, A. G.; Jiang, H.; Lanzani, G.; Stephan, O.; Laasonen, K.; Pichler, T.; Loiseau, A.; Kauppinen, E. I. *Chem. Mater.* **2011,** *23,* 2201–2208. doi:10.1021/cm200111b
134. Barzegar, H. R.; Gracia-Espino, E.; Sharifi, T.; Nitze, F.; Wågberg, T. *J. Phys. Chem. C* **2013,** *117,* 25805–25816. doi:10.1021/jp409518m
135. Kim, S. Y.; Lee, J.; Na, C. W.; Park, J.; Seo, K.; Kim, B. *Chem. Phys. Lett.* **2005,** *413,* 300–305. doi:10.1016/j.cplett.2005.07.093
136. Panchakarla, L. S.; Govindaraj, A.; Rao, C. N. R. *ACS Nano* **2007,** *1,* 494–500. doi:10.1021/nn700230n
137. Choi, H. C.; Park, J.; Kim, B. *J. Phys. Chem. B* **2005,** *109,* 4333–4340. doi:10.1021/jp0453109
138. Point, S.; Minea, T.; Bouchet-Fabre, B.; Granier, A.; Turban, G. *Diamond Relat. Mater.* **2005,** *14,* 891–895. doi:10.1016/j.diamond.2004.10.011
139. Droppa, R., Jr.; Ribeiro, C. T. M.; Zanatta, A. R.; dos Santos, M. C.; Alvarez, F. *Phys. Rev. B* **2004,** *69,* 045405. doi:10.1103/PhysRevB.69.045405
140. Ghosh, K.; Kumar, M.; Maruyama, T.; Ando, Y. *J. Mater. Chem.* **2010,** *20,* 4128–4134. doi:10.1039/B923139K
141. Ghosh, K.; Kumar, M.; Maruyama, T.; Ando, Y. *Carbon* **2010,** *48,* 191–200. doi:10.1016/j.carbon.2009.09.003
142. Lv, R.; Li, Q.; Botello-Méndez, A. R.; Hayashi, T.; Wang, B.; Berkdemir, A.; Hao, Q.; Elías, A. L.; Cruz-Silva, R.; Gutiérrez, H. R.; Kim, Y. A.; Muramatsu, H.; Zhu, J.; Endo, M.; Terrones, H.; Charlier, J.-C.; Pan, M.; Terrones, M. *Sci. Rep.* **2012,** *2,* No. 586. doi:10.1038/srep00586
143. Schiros, T.; Nordlund, D.; Pálová, L.; Prezzi, D.; Zhao, L.; Kim, K. S.; Wurstbauer, U.; Gutiérrez, C.; Delongchamp, D.; Jaye, C.; Fischer, D.; Ogasawara, H.; Pettersson, L. G. M.; Reichman, D. R.; Kim, P.; Hybertsen, M. S.; Pasupathy, A. N. *Nano Lett.* **2012,** *12,* 4025–4031. doi:10.1021/nl301409h
144. Kondo, T.; Casolo, S.; Suzuki, T.; Shikano, T.; Sakurai, M.; Harada, Y.; Saito, M.; Oshima, M.; Trioni, M. I.; Tantardini, G. F.; Nakamura, J. *Phys. Rev. B* **2012,** *86,* 035436. doi:10.1103/PhysRevB.86.035436
145. Meyer, J. C.; Kurasch, S.; Park, H. J.; Skakalova, V.; Künzel, D.; Groü, A.; Chuvilin, A.; Algara-Siller, G.; Roth, S.; Iwasaki, T.; Starke, U.; Smet, J. H.; Kaiser, U. *Nat. Mater.* **2011,** *10,* 209–215. doi:10.1038/nmat2941
146. Susi, T.; Kotakoski, J.; Arenal, R.; Kurasch, S.; Jiang, H.; Skakalova, V.; Stephan, O.; Krasheninnikov, A. V.; Kauppinen, E. I.; Kaiser, U.; Meyer, J. C. *ACS Nano* **2012,** *6,* 8837–8846. doi:10.1021/nn303944f
147. Liu, H.; Zhang, Y.; Li, R.; Sun, X.; Désilets, S.; Abou-Rachid, H.; Jaidann, M.; Lussier, L.-S. *Carbon* **2010,** *48,* 1498–1507. doi:10.1016/j.carbon.2009.12.045
148. Maldonado, S.; Morin, S.; Stevenson, K. J. *Carbon* **2006,** *44,* 1429–1437. doi:10.1016/j.carbon.2005.11.027
149. Podila, R.; Chacón-Torres, J.; Spear, J. T.; Pichler, T.; Ayala, P.; Rao, A. M. *Appl. Phys. Lett.* **2012,** *101,* 123108. doi:10.1063/1.4752736
150. Sheng, Z.-H.; Shao, L.; Chen, J.-J.; Bao, W.-J.; Wang, F.-B.; Xia, X.-H. *ACS Nano* **2011,** *5,* 4350–4358. doi:10.1021/nn103584t
151. Lu, Y.-F.; Lo, S.-T.; Lin, J.-C.; Zhang, W.; Lu, J.-Y.; Liu, F.-H.; Tseng, C.-M.; Lee, Y.-H.; Liang, C.-T.; Li, L.-J. *ACS Nano* **2013,** *7,* 6522–6532. doi:10.1021/nn402102y

152. Pichler, T.; Knupfer, M.; Golden, M. S.; Haffner, S.; Friedlein, R.; Fink, J.; Andreoni, W.; Curioni, A.; Keshavarz-K, M.; Bellavia-Lund, C.; Sastre, A.; Hummelen, J.-C.; Wudl, F. *Phys. Rev. Lett.* **1997,** *78,* 4249–4252. doi:10.1103/PhysRevLett.78.4249
153. Panchakarla, L. S.; Subrahmanyam, K. S.; Saha, S. K.; Govindaraj, A.; Krishnamurthy, H. R.; Waghmare, U. V.; Rao, C. N. R. *Adv. Mater.* **2009,** *21,* 4726–4730. doi:10.1002/adma.200901285
154. Li, X.; Wang, H.; Robinson, J. T.; Sanchez, H.; Diankov, G.; Dai, H. *J. Am. Chem. Soc.* **2009,** *131,* 15939–15944. doi:10.1021/ja907098f
155. Long, D.; Li, W.; Ling, L.; Miyawaki, J.; Mochida, I.; Yoon, S.-H. *Langmuir* **2010,** *26,* 16096–16102. doi:10.1021/la102425a
156. Qu, L.; Liu, Y.; Baek, J.-B.; Dai, L. *ACS Nano* **2010,** *4,* 1321–1326. doi:10.1021/nn901850u
157. Wang, Y.; Shao, Y.; Matson, D. W.; Li, J.; Lin, Y. *ACS Nano* **2010,** *4,* 1790–1798. doi:10.1021/nn100315s
158. Zhang, C.; Fu, L.; Liu, N.; Liu, M.; Wang, Y.; Liu, Z. *Adv. Mater.* **2011,** *23,* 1020–1024. doi:10.1002/adma.201004110
159. Deng, D.; Pan, X.; Yu, L.; Cui, Y.; Jiang, Y.; Qi, J.; Li, W.-X.; Fu, Q.; Ma, X.; Xue, Q.; Sun, G.; Bao, X. *Chem. Mater.* **2011,** *23,* 1188–1193. doi:10.1021/cm102666r
160. Sun, C. Q.; Sun, Y.; Nie, Y. G.; Wang, Y.; Pan, J. S.; Ouyang, G.; Pan, L. K.; Sun, Z. *J. Phys. Chem. C* **2009,** *113,* 16464–16467. doi:10.1021/jp905336j
161. Gammon, W. J.; Kraft, O.; Reilly, A. C.; Holloway, B. C. *Carbon* **2003,** *41,* 1917. doi:10.1016/S0008-6223(03)00170-2
162. Rocha, A. R.; Rossi, M.; da Silva, A. J. R.; Fazzio, A. *J. Phys. D: Appl. Phys.* **2010,** *43,* 374002. doi:10.1088/0022-3727/43/37/374002
163. Fujimoto, Y.; Saito, S. *Phys. Rev. B* **2011,** *84,* 245446. doi:10.1103/PhysRevB.84.245446
164. Telychko, M.; Mutombo, P.; Ondráček, M.; Hapala, P.; Bocquet, F. C.; Kolorenč, J.; Vondráček, M.; Jelínek, P.; Švec, M. *ACS Nano* **2014,** *8,* 7318–7324. doi:10.1021/nn502438k
165. Gong, K.; Du, F.; Xia, Z.; Durstock, M.; Dai, L. *Science* **2009,** *323,* 760–764. doi:10.1126/science.1168049
166. Shan, B.; Cho, K. *Chem. Phys. Lett.* **2010,** *492,* 131–136. doi:10.1016/j.cplett.2010.04.050
167. Arenal, R.; March, K.; Ewels, C. P.; Rocquefelte, X.; Kociak, M.; Loiseau, A.; Stéphan, O. *Nano Lett.* **2014,** *14,* 5509–5516. doi:10.1021/nl501645g
168. Pels, J. R.; Kapteijn, F.; Moulijn, J. A.; Zhu, Q.; Thomas, K. M. *Carbon* **1995,** *33,* 1641–1653. doi:10.1016/0008-6223(95)00154-6
169. Lee, D. H.; Lee, W. J.; Kim, S. O. *Nano Lett.* **2009,** *9,* 1427–1432. doi:10.1021/nl803262s
170. Kundu, S.; Nagaiah, T. C.; Xia, W.; Wang, Y.; Dommele, S. V.; Bitter, J. H.; Santa, M.; Grundmeier, G.; Bron, M.; Schuhmann, W.; Muhler, M. *J. Phys. Chem. C* **2009,** *113,* 14302–14310. doi:10.1021/jp811320d
171. Sharifi, T.; Hu, G.; Jia, X.; Wågberg, T. *ACS Nano* **2012,** *6,* 8904–8912. doi:10.1021/nn302906r
172. Kroke, E.; Schwarz, M. *Coord. Chem. Rev.* **2004,** *248,* 493–532. doi:10.1016/j.ccr.2004.02.001
173. Ewels, C. P.; Erbahar, D.; Wagner, P.; Rocquefelte, X.; Arenal, R.; Pochet, P.; Rayson, M.; Scardamaglia, M.; Bittencourt, C.; Briddon, P. *Faraday Discuss.* **2014,** *173,* 215–232. doi:10.1039/C4FD00111G
174. Wiggins-Camacho, J. D.; Stevenson, K. J. *J. Phys. Chem. C* **2009,** *113,* 19082–19090. doi:10.1021/jp907160v
175. Kramberger, C.; Thurakitseree, T.; Koh, H.; Izumi, Y.; Kinoshita, T.; Muro, T.; Einarsson, E.; Maruyama, S. *Carbon* **2013,** *55,* 196–201. doi:10.1016/j.carbon.2012.12.026
176. Kweon, K. E.; Hwang, G. S. *Phys. Rev. B* **2010,** *82,* 195439. doi:10.1103/PhysRevB.82.195439
177. Hanafusa, A.; Muramatsu, Y.; Kaburagi, Y.; Yoshida, A.; Hishiyama, Y.; Yang, W.; Denlinger, J. D.; Gullikson, E. M. *J. Appl. Phys.* **2011,** *110,* 053504. doi:10.1063/1.3631108
178. Faccio, R.; Fernández-Werner, L.; Pardo, H.; Goyenola, C.; Ventura, O. N.; Mombrú, A. W. *J. Phys. Chem. C* **2010,** *114,* 18961–18971. doi:10.1021/jp106764h
179. Czerw, R.; Terrones, M.; Charlier, J.-C.; Blase, X.; Foley, B.; Kamalakaran, R.; Grobert, N.; Terrones, H.; Tekleab, D.; Ajayan, P. M.; Blau, W.; Rühle, M.; Carroll, D. L. *Nano Lett.* **2001,** *1,* 457–460. doi:10.1021/nl015549q
180. Gai, P.; Stephan, O.; McGuire, K.; Rao, A.; Dresselhaus, M.; Dresselhaus, G.; Colliex, C. *J. Mater. Chem.* **2004,** *14,* 669–675. doi:10.1039/b311696d
181. Ayala, P.; Reppert, J.; Grobosch, M.; Knupfer, M.; Pichler, T.; Rao, A. M. *Appl. Phys. Lett.* **2010,** *96,* 183110. doi:10.1063/1.3427432
182. Ayala, P.; Plank, W.; Grüneis, A.; Kauppinen, E.; Rümmeli, M.; Kuzmany, H.; Pichler, T. *J. Mater. Chem.* **2008,** *18,* 5676. doi:10.1039/b809050e
183. Kim, Y. A.; Fujisawa, K.; Muramatsu, H.; Hayashi, T.; Endo, M.; Fujimori, T.; Kaneko, K.; Terrones, M.; Behrends, J.; Eckmann, A.; Casiraghi, C.; Novoselov, K. S.; Saito, R.; Dresselhaus, M. S. *ACS Nano* **2012,** *6,* 6293–6300. doi:10.1021/nn301728j
184. Sheng, Z.-H.; Gao, H.-L.; Bao, W.-J.; Wang, F.-B.; Xia, X.-H. *J. Mater. Chem.* **2012,** *22,* 390. doi:10.1039/c1jm14694g
185. Tang, Y.-B.; Yin, L.-C.; Yang, Y.; Bo, X.-H.; Cao, Y.-L.; Wang, H.-E.; Zhang, W.-J.; Bello, I.; Lee, S.-T.; Cheng, H.-M.; Lee, C.-S. *ACS Nano* **2012,** *6,* 1970–1978. doi:10.1021/nn3005262
186. Wang, H.; Zhou, Y.; Wu, D.; Liao, L.; Zhao, S.; Peng, H.; Liu, Z. *Small* **2013,** *9,* 1316–1320. doi:10.1002/smll.201203021
187. Jung, S.-M.; Choi, I. T.; Lim, K.; Ko, J.; Kim, J. C.; Lee, J.-J.; Ju, M. J.; Kim, H. K.; Baek, J.-B. *Chem. Mater.* **2014,** *26,* 3586–3591. doi:10.1021/cm5013119
188. Maciel, I. O.; Campos-Delgado, J.; Cruz-Silva, E.; Pimenta, M. A.; Sumpter, B. G.; Meunier, V.; López-Urías, F.; Muñoz-Sandoval, E.; Terrones, H.; Terrones, M.; Jorio, A. *Nano Lett.* **2009,** *9,* 2267–2272. doi:10.1021/nl9004207
189. Campos-Delgado, J.; Maciel, I. O.; Cullen, D. A.; Smith, D. J.; Jorio, A.; Pimenta, M. A.; Terrones, H.; Terrones, M. *ACS Nano* **2010,** *4,* 1696–1702. doi:10.1021/nn901599g
190. Ruiz-Soria, G.; Susi, T.; Sauer, M.; Yanagi, K.; Pichler, T.; Ayala, P. *Carbon* **2015,** *81,* 91–95. doi:10.1016/j.carbon.2014.09.028
191. Li, R.; Wei, Z.; Gou, X.; Xu, W. *RSC Adv.* **2013,** *3,* 9978–9984. doi:10.1039/C3RA41079J
192. Choi, C. H.; Chung, M. W.; Kwon, H. C.; Park, S. H.; Woo, S. I. *J. Mater. Chem. A* **2013,** *1,* 3694–3699. doi:10.1039/C3TA01648J
193. Yu, D.; Xue, Y.; Dai, L. *J. Phys. Chem. Lett.* **2012,** *3,* 2863–2870. doi:10.1021/jz3011833
194. Liu, J.; Liu, H.; Zhang, Y.; Li, R.; Liang, G.; Gauthier, M.; Sun, X. *Carbon* **2011,** *49,* 5014–5021. doi:10.1016/j.carbon.2011.07.018
195. Gorham, J.; Torres, J.; Wolfe, G.; d'Agostino, A.; Fairbrother, D. H. *J. Phys. Chem. B* **2005,** *109,* 20379–20386. doi:10.1021/jp0521196
196. Puziy, A. M.; Poddubnaya, O. I.; Socha, R. P.; Gurgul, J.; Wisniewski, M. *Carbon* **2008,** *46,* 2113–2123. doi:10.1016/j.carbon.2008.09.010

197. Larrude, D. G.; Maia da Costa, M. E. H.; Monteiro, F. H.; Pinto, A. L.; Freire, F. L., Jr. *J. Appl. Phys.* **2012,** *111,* 064315. doi:10.1063/1.3695452
198. Mowbray, D. J.; Ayala, P.; Pichler, T.; Rubio, A. *Mater. Express* **2011,** *1,* 225–230. doi:10.1166/mex.2011.1027

License and Terms

This is an Open Access article under the terms of the Creative Commons Attribution License (http://creativecommons.org/licenses/by/2.0), which permits unrestricted use, distribution, and reproduction in any medium, provided the original work is properly cited.

The license is subject to the *Beilstein Journal of Nanotechnology* terms and conditions: (http://www.beilstein-journals.org/bjnano)

The definitive version of this article is the electronic one which can be found at: doi:10.3762/bjnano.6.17

BEILSTEIN JOURNAL OF NANOTECHNOLOGY

Nanoparticle shapes by using Wulff constructions and first-principles calculations

Georgios D. Barmparis[1,2], Zbigniew Lodziana[3], Nuria Lopez[4] and Ioannis N. Remediakis[*1]

Review

Open Access

Address:
[1]Department of Materials Science and Technology, University of Crete, Heraklion, 71003, Greece, [2]Department of Physics and Astronomy, Vanderbilt University, Nashville, TN, 37235, USA, [3]INP, Polish Acad Sci, ul. Radzikowskiego 152, PL-31342 Krakow, Poland and [4]Institute of Chemical Research of Catalonia, ICIQ, Av. Paisos Catalans 16, Tarragona 43007, Spain

Email:
Ioannis N. Remediakis[*] - remed@materials.uoc.gr

* Corresponding author

Keywords:
density functional theory (DFT); hydrogen storage; multi-scale simulations; nanoparticles; surface energies; surfactants; Wulff construction

Beilstein J. Nanotechnol. **2015,** *6,* 361–368.
doi:10.3762/bjnano.6.35

Received: 28 June 2014
Accepted: 15 December 2014
Published: 03 February 2015

This article is part of the Thematic Series "Atomic scale interface design and characterisation: Theory – Electronic properties".

Guest Editor: A. Krasheninnikov

© 2015 Barmparis et al; licensee Beilstein-Institut.
License and terms: see end of document.

Abstract

Background: The majority of complex and advanced materials contain nanoparticles. The properties of these materials depend crucially on the size and shape of these nanoparticles. Wulff construction offers a simple method of predicting the equilibrium shape of nanoparticles given the surface energies of the material.

Results: We review the mathematical formulation and the main applications of Wulff construction during the last two decades. We then focus to three recent extensions: active sites of metal nanoparticles for heterogeneous catalysis, ligand-protected nanoparticles generated as colloidal suspensions and nanoparticles of complex metal hydrides for hydrogen storage.

Conclusion: Wulff construction, in particular when linked to first-principles calculations, is a powerful tool for the analysis and prediction of the shapes of nanoparticles and tailor the properties of shape-inducing species.

Introduction

The functionality of nanoparticles in modern materials is intimately linked to their structure in terms of size and shape [1]. Structures at the nanoscale have found myriads of applications out of the traditional field of heterogeneous catalysis and more are discovered almost on a daily basis. Nowadays, nanoparticles can be found in sensors, especially with biomedical interest, as agents to induce the death of cancer cells, as drug delivery vehicles, in emerging energy technologies, either in harvesting or for storage, as additives for fuels, in optics, and as part of smart fluids, just to name a few applications. The "plenty of room at the bottom" described by Feynman, is thus being filled with technological uses [2]. Indeed, several road-

maps have been established to improve our knowledge and control for such powerful technologies. It is well-known that, for nanotechnology to be successful, a higher degree of control over the synthesis at the nanoscale, better characterization techniques and simulation methods are required. The main aim of simulations is to provide guiding tools for the tailored synthesis of desired architectures. Concerning nanoparticles, a high degree in nanoparticle size control was achieved very early. This is demonstrated by the famous Lycurgus cup, that changes color due to directional light scattering combined with adsorption by the nanoparticle plasmon resonances, or the colorful windows in the facades of medieval cathedrals. Therefore, the real challenge we are facing today is to be able to control the shapes of nanoparticles [3]. The shape of nanoparticles can have a big impact on their properties, not only in catalysis in which the number of active sites is clearly shape-dependent [4], but also in other applications such as optics [5,6].

Theoretical simulations based on the Wulff construction hold the key to understand the shapes of nanoparticles. The Wulff construction revolutionized geology and crystallography especially at the beginning of the twentieth century, as it provided a systematic way to classify characteristic shapes and habits found in mineral crystals. Near the end of the twentieth century, Wulff construction was re-discovered in materials science and was used to characterize shapes of nanoparticles. Today, multiscale simulations that use Wulff constructions based on first-principles quantum-mechanical calculations of surface energies are routinely employed to explain experimental findings and lead to the design of better materials with tailored properties.

In the following, we review the concept of Wulff construction, present its mathematical formulation and limitations, and review modern uses in the analysis and the prediction of findings in microscopy experiments. We then present three recent extensions to this methodology: (a) the atomistic Wulff construction that allows for the detailed analysis of nanoparticles at the atomic level; (b) the inclusion of surfactants that gives rise to nanoparticles with shapes that have a lower symmetry than the bulk form of the same material and (c) Wulff constructions for complex materials with many metastable crystal structures.

Review

Wulff construction: definition and basic properties

In his famous paper of 1874 ”On the Equilibrium of Heterogeneous Substances”, J. Willard Gibbs concluded that a given quantity of matter will attain a shape such that the total surface energy is minimal [7]. For perfect crystalline solids, atomic planes are members of a countable set characterized by integer Miller indexes (*hkl*). The shape of a crystalline solid will therefore be a polyhedron for which only faces parallel to (*hkl*) planes are allowed. It is only reasonable to assume that faces with a relatively low surface energy will dominate the equilibrium shape.

Several decades later, mineralogist Georg Wulff suggested [8] that the polyhedron that corresponds to the lowest surface energy of a crystalline substance can be constructed in the following way (the so-called Wulff construction): One chooses a constant c, and a Cartesian set of axes. Starting from the origin, O, one draws a plane that is normal to the [*hkl*] vector and has a distance $d_{hkl} = c\cdot\gamma_{hkl}$ from O. The quantity γ_{hkl} is the energy required to create a surface of unit area normal to the [*hkl*] vector, and is the analogous of the surface tension for liquids. This process is repeated for all sets of Miller indexes, (*hkl*). The space that lies inside all these planes defines the equilibrium shape for this material. The first proof of the Wulff theorem came in 1943 by von Laue [9]; for more details, see [10,11]. More general proofs of Wulff's theorem have appeared in the recent years [12], and it is still a subject of on-going research in applied mathematics [13]. For instance, the Wulff–Kaishew theorem is a generalization that considers lateral strain [14].

When the material under study is at equilibrium with another gas- or liquid-phase material, the interface tension, $\gamma^{\text{int}}_{hkl}$, is used in the Wulff construction instead of the surface tension, γ_{hkl}. The two are connected by a simple formula that involves the surface coverage, θ, the adsorption energy, E_{ads}, and the area per surface atom, A_{at} [15]:

$$\gamma^{\text{int}}_{hkl} = \gamma_{hkl} + \theta\frac{E_{\text{ads}}}{A_{\text{at}}}. \qquad (1)$$

Interactions between adsorbates are implicitly taken into account in Equation 1, as these interactions will affect the values of both E_{ads} and θ.

An example of Wulff construction is shown in Figure 1 for a hypothetical orthorhombic material with $\gamma_{100} = \gamma_{110} = 1/2\,\gamma_{010}$. All other (*hkl*) planes have much higher surface energies. The resulting equilibrium shape is a rod-like prism. Interestingly, the cross-section of the crystal is an (almost regular) hexagon, although the material does not posses hexagonal symmetry. Similar pseudo-hexagonal shapes are often found in minerals of orthorhombic crystals, such as aragonite $CaCO_3$ [16].

The Wulff construction results in a polyhedron that:

1. depends only on ratios between surface tensions and not on their absolute values;

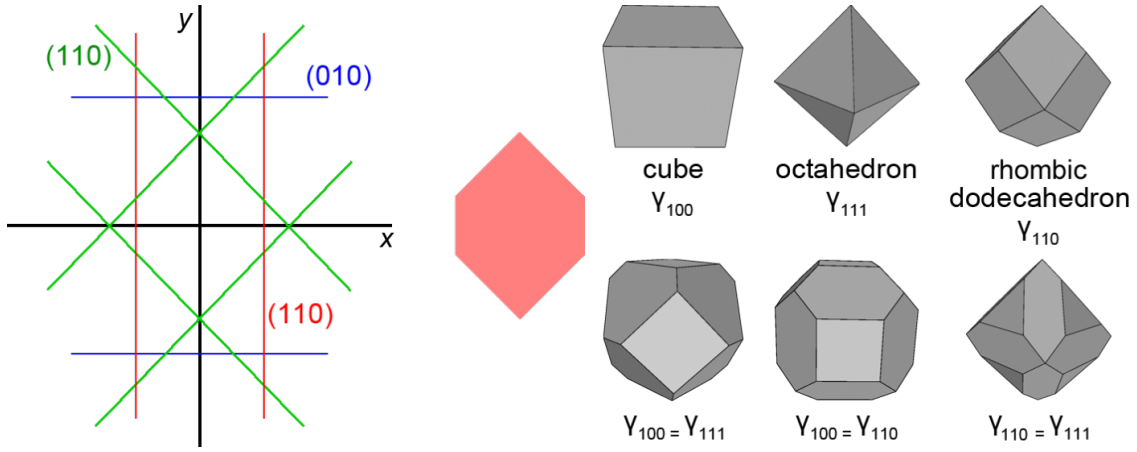

Figure 1: Left: Example of Wulff construction for orthorhombic material. *xy* plane is parallel to the (001) plane of the material. Center: The cross-section of the resulting equilibrium shape. Right: Some common Wulff constructions for materials with full cubic symmetry (O_h or $m\bar{3}m$), such as fcc metals. The surface energies that have been used in the Wulff construction are shown below each shape.

2. contains few faces with high Miller indexes as in most cases, they have a much higher surface tension than low-index faces; (if a high-index surface and a low-index surface have equal surface tensions, the low-index will have a greater area as the high-index face will be steeper and will be hidden in the Wulff construction);
3. does not take into account edge- and vertex-energies; and
4. bears the same symmetry (belonging to the same point group) as the bulk material.

Point 2 of the aforementioned list allows for a truncation of the set of (*hkl*) planes for small values of *h*, *k* and *l*. In most cases, the essential features of the shape can be found by considering only planes with indexes of zeros and ones. An exception might be nanoparticles with strong interactions with their environment. In that case, high-index surfaces that contain steps and kinks offer better binding of adsorbates which will lower their surface energy (see Equation 1). However, due to the fact given in brackets in point 2, the equilibrium shape rarely contains faces with indexes higher than three [17].

Point 4 is correct at the thermodynamic limit for very large nanoparticles. Smaller nanoparticles that have Wulff shapes could in principle belong to a subgroup of the original point group, as the center of the nanoparticle might not coincide with the symmetry center of the crystal structure. For Au nanoparticles, for example, two different classes of nanoparticles can be found depending on whether the center of the nanoparticle is at an fcc lattice point or at the octahedral site of the structure. However, these two types become indistinguishable for nanoparticles larger than a few angstroms [15]. Some characteristic equilibrium shapes that are often found in materials with cubic symmetry are shown in the right panel of Figure 1.

Symmetry, through point 4, can be used to rule out shapes of larger nanoparticles that are clearly out of equilibrium. However, it was recently found that when complex ligands are attached to their surfaces, nanoparticles may have equilibrium shapes that do not belong in the same point group as the material (see section about ligands below).

Wulff construction in the modern era: shapes of nanoparticles

In the past, equilibrium shapes were only associated with minerals and gemstones. Superb chemical stability and equilibration over millions of years under extreme pressure and temperature seemed to be the necessary (but often not sufficient) conditions for a piece of matter to be in its equilibrium shape. In the last two decades, however, it has been realized that due to their small sizes, nanoparticles can reach equilibrium within seconds or less. Moreover, the equilibrium shapes of nanoparticles are the same as those of gemstones with the same chemical composition. For example, the octahedral shape characteristic of natural diamonds is also observed for nanoparticles that consist entirely of C atoms in the diamond crystal structure [18].

The Wulff construction offers a simple and rigorous way to describe nanoparticle shapes without the need to use complex mathematical language. The shapes can be described by two or three parameters (the surface energies of some (*hkl*) faces and the point group of the material). These parameters can be plugged in to a Wulff construction code to reproduce the shape of the nanoparticle. Popular examples of free Wulff construction implementations are Wulffman [19] and VESTA [20].

Among the first uses of the Wulff construction for the characterization of nanoparticles are experiments by H. Topsøe and

co-workers for Cu-based catalysts [21,22], and the theory of Müller and Kern for epitaxially strained semiconductor quantum dots [23]. Since then, Wulff shapes have been observed in a variety of microscopy experiments with nanoparticles. Some characteristic examples include Ru [24], Pt [25], Au [26-30], Ni [31] and Si [32] nanoparticles.

The increase of computational power and the emergence of smart codes for the electronic structure of materials allowed for calculations of interface tensions from first principles. These data were often used in Wulff constructions for the prediction of the shape of nanoparticles in a variety of environments. Some characteristic examples include supported Au [33,34], diamond [35], TiO_2 [36], Si in amorphous SiO_2 [37], diamond in amorphous C [38], Rh and Pd under oxidizing conditions [39], Cu in N gas [40], Au under oxidizing conditions [41], noble metals with an environment [42], complex metal hydrides [43], iron carbides [44] and dawsonites [45,46], just to name a few.

Atomistic Wulff construction

The atomistic Wulff construction emerged through the field of heterogeneous catalysis, in which the shape of transition metal nanoparticles is a key factor of their functionality. Atomistic models for an equilibrium-shaped Ru nanoparticle were part of a long-term project to model an industrial ammonia-synthesis catalyst from first principles [47-49]. Density functional calculations were used to obtain accurate surface energies for several faces of hcp Ru. These values were used in a standard Wulff-construction software to create the polyhedron that corresponded to the equilibrium shape. In the last step, this polyhedron was filled with atoms in order to create a model of a cluster at thermodynamic equilibrium. This model was then used to calculate various atomistic properties of Ru nanoparticles that were measured experimentally, such as the number of moles of B-type step atoms per gram of catalyst.

Nanoparticles that are relevant to catalysis have diameters of the order of 5 nm and contain of the order of 5000 transition metal atoms. Direct simulation of such systems by using quantum-mechanical techniques is difficult at present. Modern DFT codes that can tackle several thousands of atoms are presently limited to atoms with few valence electrons, such as simple metals or semiconductors [50-52]. Late transition metals are typically simulated by using advanced force-fields or other approaches [53-55]. The advantage of the atomistic Wulff construction is that one avoids being trapped at one of the metastable structures of the nanoparticle as they do not need to span the full configurational space of the problem.

The turnover frequency (TOF) of a catalyst is proportional to the density of active sites (usually expressed as μmol of active sites per gram of catalyst). Microscopy and/or first-principles simulations are typically used to identify what the active sites for each catalytic reaction are. For example, B-type step atoms are the only active sites for ammonia synthesis on Ru-based catalysts [56]. Atomistic Wulff constructions can be then used to calculate the number of such atoms in a nanoparticle of a given diameter [47-49]. This procedure was recently used to account for the nanoparticle size-dependent TOF of a Ag catalyst in the selective semi-hydrogenation of alkyne–alkene mixtures [57].

Another advantage of the atomistic Wulff construction is that it enables the study of the equilibrium shape of the nanoparticle as a function of its size. The Wulff polyhedron is the equilibrium shape of the nanoparticle at the thermodynamic limit of large particles. At the nanoscale, some faces of the Wulff polyhedron might be so small that they cannot accommodate a single atom, let alone a unit cell of the (*hkl*) plane they represent. This leads to shapes for small nanoparticles that are significantly simpler than the Wulff polyhedron. For example, Au nanoparticles with diameter less than 16 nm contain only (111) and (100) surfaces, although the Wulff shape contains (111), (332), (100), (211), and (322) [15].

An example of atomistic Wulff construction for relatively large Au nanoparticles is shown in Figure 2. Upon exposure to CO or CH_3S radical gas, the nanoparticle changes towards more spherical shapes, in accordance with experiments [58].

Nanoparticles with surfactants

Metal-only nanoparticles or metal-adsorbate interactions have been the leading force that has helped the evolution of the presented methodology for the shape of nanocrystals. However, recent developments to design colloidal suspensions of nanoparticles with interesting physical and chemical properties have pushed forward the simulation frontier. Indeed, the synthesis of nanoparticles through wet chemistry methods is usually quite complex. When nanoparticles are to be employed in optics or as sensors, many formulations employ the seed-growth methodologies. First a nucleus (1–2 Å diameter) is formed by the fast reduction of a metal salt and in a subsequent step these nanoparticles are placed in a second solution in which they are allowed to grow. The second solution contains an important amount of surfactants, in some cases secondary metals and other shape inducing agents, typically halides. Depending on the mixture of surfactants, secondary ions and anions nanoparticles with different shapes can be observed [3]. From the point of view of modeling, the growth of these nanoparticles is difficult, but relevant information can still be extracted. For instance, the preferential adsorption of halides to particular facets reduces the surface energy of those facets and

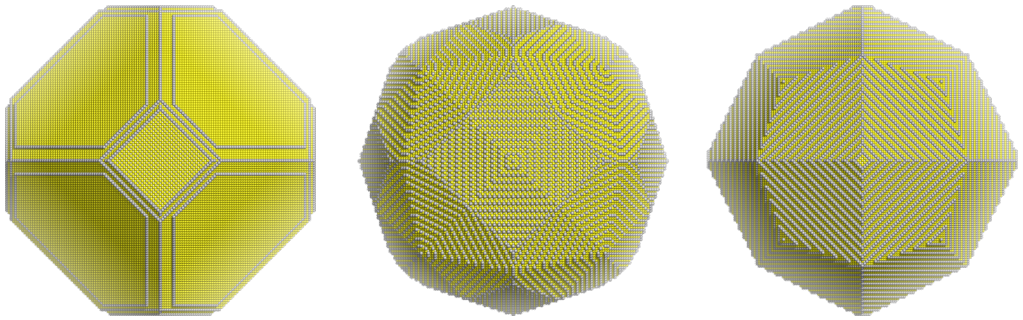

Figure 2: Atomistic Wulff constructions for Au nanoparticles using surface energies published in Refs. [15] and [17]. Atoms that have coordination numbers less than nine are colored in gray. Left: in vacuum or inert environment (28 nm in diameter, 539500 atoms, 2980 of which are step-edge atoms; (111) faces occupy 62% of the total area). Center: In low-pressure CO gas (27 nm in diameter, 533600 atoms, 7610 of which are step-edge atoms; (321) faces occupy 61% of the total area). Right: With adsorbed SCH_3 radicals (29 nm in diameter, 502900 atoms, 10600 of which are step-edge atoms; (211) faces occupy almost 100% of the total area).

typically they are represented more in the equilibrium state of the particle. This has been observed for the appearance of nanocubes of Ag grown on Au seeds in the presence of chlorine [59].

In some cases a symmetry breakdown (i.e., that the nanoparticle does not belong strictly to the same point group as the bulk) of the metal particle is desired, as nanoparticles with spikes have enhanced spectroscopic features. According to the Wulff rules this is not possible (see above the constraint in point 4). However, experimentally it has been found that objects such as nanorods can be systematically produced with an adequate selection of the solution growth. In that case the symmetry breaking appears very early in the formation of the seed as then some of the facets (but not all those equivalent by symmetry) can be blocked and in this way anisotropy can be easily induced [60]. A typical model for a metal surface in equilibrium with surfactants is shown in Figure 3.

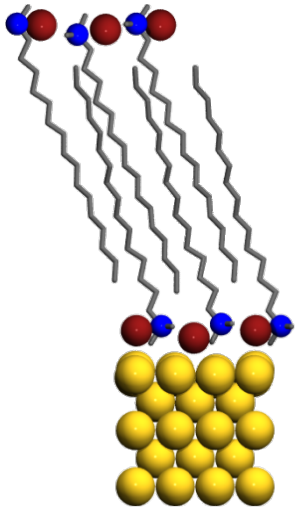

Figure 3: Schematic representation of the adsorption of a surfactant on a gold surface. Spheres represent gold (yellow), silver (grey) and bromine (red) and the tails of the surfactant are represented by sticks.

Complex materials

Complex materials such as those proposed in hydrogen storage also benefit from nanoparticle properties that are linked to improved atomic transport crucial for reversibility and fast kinetics of hydrogen cycling. For instance, lithium borohydride ($LiBH_4$) has a high gravimetric and volumetric hydrogen density, and it was considered recently as a promising hydrogen storage material or as new superionic conductor [61,62]. The lack of the long range order in $LiBH_4$ confined in 2–4 nm pores in nanoporous carbon is connected to the reduction of the barriers for the rotational motion of BH_4^- anions and the high- temperature behavior even at temperatures well below the bulk T_c [63]. The experimental insight to the properties of nano-confined $LiBH_4$ encounters severe difficulties: Techniques such as X-ray diffraction (XRD) or neutron scattering are not always applicable to systems with reduced length-scales and those consisting of the light elements. Only the local methods, such as solid state NMR, quasielastic neutron scattering (QENS), provide indirect information about structural properties.

Theoretical understanding of the nanocrystalline $LiBH_4$ can provide an insight into structural and dynamical properties of crystallites confined in the smallest pores with dimension below 3 nm. The Wulff construction is the starting point for these studies. The surface energy of the low-index facets of $LiBH_4$ was reported and the most consistent data point out that for (100), (010), (101), (011) facets the surface energy is below 0.115 J/m^2 [64]. The shape of the nanocrystallite is presented in Figure 4.

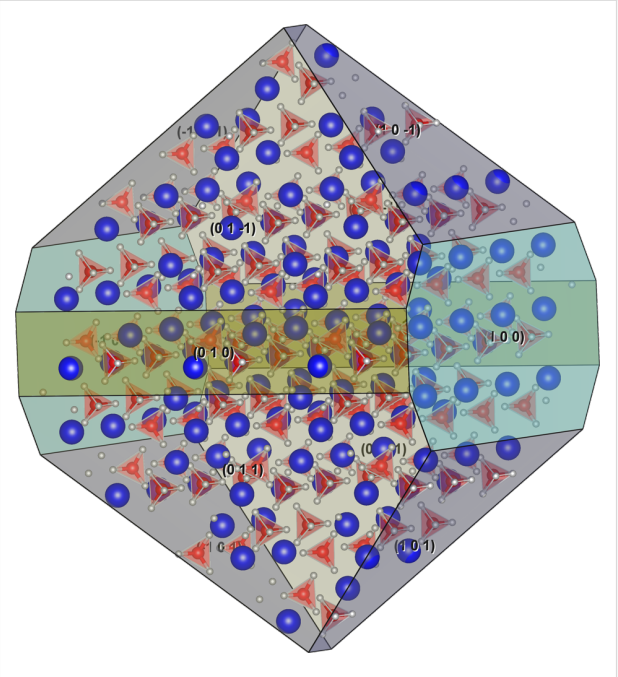

Figure 4: Wulff construction for the nanoparticles of $LiBH_4$. The blue spheres are for lithium, red for boron and white are hydrogen atoms.

Contrary to the pure elements or metal oxides, for lithium borohydride the Wulff construction of the nanocrystal does not provide features that can confirm or match experimental evidence. The reason is the low surface energy of compound, fast rotational motion of anions, and large enthalpy of formation of small clusters. Due to the weak interaction with the host matrix the shape of $LiBH_4$ cluster is not perturbed by the interfacial interaction. However, NMR experiments indicate a larger shielding of the boron nucleus (^{11}B) in nanoconfined state, this can be explained only if the coordination of BH_4^- anions is lower than three (the coordination number is four in the bulk) [65]. Such low coordination is possible only for two dimensional structures; the surface anions in the Wulff shape crystal have coordination three. However, the intensity of NMR lines suggest that the number of low coordinated atoms is larger than the number found in the Wulff construction.

Conclusion

The Wulff construction offers a simple way to characterize nanoparticles, based on symmetry and a few parameters (ratios of surface tensions and symmetry type). Coupled to first-principles calculations for surface- and interface tensions of crystals, it proves a powerful tool that can successfully account for the nanoparticle shapes observed in experiments, including nanoparticles that interact strongly with their environment. Being a multi-scale, first-principles thermodynamics technique, it offers a parameter-free model for the key components of modern functional materials. Recent additions to the method can account for detailed atomistic structure of the nanoparticles, including coordination numbers of their atoms and density of active sites, while it can even take into account complex crystal structures and attached ligands. As such, it is expected to play a key role within theoretical materials science in the years to come.

Acknowledgements

INR acknowledges valuable discussions on Wulff construction with Prof. Phoebus Rosakis. ZL acknowledges CPU allocation at the PL-Grid Infrastructure. The work of GDB and INR was partly supported by the Research Committee, University of Crete (grants 03131 and 03627) and by COST action MP0901 (nanoTP). We thank the nanoTP organizers, Carla Bittencourt and Chris Ewels, for creating and maintaining a great network for the exchange of scientific ideas.

References

1. Sun, Y.; Xia, Y. *Science* **2002,** *298,* 2176–2179. doi:10.1126/science.1077229
2. Feynman, R. P. *J. Microelectromech. Syst.* **1992,** *1,* 60–66. doi:10.1109/84.128057
3. Grzelczak, M.; Pérez-Juste, J.; Mulvaney, P.; Liz-Marzán, L. M. *Chem. Soc. Rev.* **2008,** *37,* 1783–1791. doi:10.1039/b711490g
4. Mostafa, S.; Behafarid, F.; Croy, J. R.; Ono, L. K.; Li, L.; Yang, J. C.; Frenkel, A. I.; Cuenya, B. R. *J. Am. Chem. Soc.* **2010,** *132,* 15714–15719. doi:10.1021/ja106679z
5. Hourahine, B.; Papoff, F. *Meas. Sci. Technol.* **2012,** *23,* 084002. doi:10.1088/0957-0233/23/8/084002
6. Hourahine, B.; Papoff, F. *Opt. Express* **2013,** *21,* 20322–20333. doi:10.1364/OE.21.020322
7. Gibbs, J. W. On the Equilibrium of Heterogeneous Substances. In *Transactions of the Connecticut Academy of Arts and Sciences*, 1876, III, pp. 108-248, Oct. 1875-May 1876, and pp. 343-524, May 1877-July 1878.
8. Wulff, G. *Z. Kristallogr.* **1901,** *34,* 449. doi:10.1524/zkri.1901.34.1.449
9. von Laue, M. *Z. Kristallogr.* **1943,** *105,* 124–133. doi:10.1524/zkri.1943.105.1.124
10. Herring, C. *Phys. Rev.* **1951,** *82,* 87. doi:10.1103/PhysRev.82.87
11. Cerf, R. *The Wulff Crystal in Ising and Percolation Models;* Springer: Berlin, Germany, 2006.
12. Fonseca, I. *Proc. R. Soc. London, Ser. A* **1991,** *432,* 125–145. doi:10.1098/rspa.1991.0009
13. Rosakis, P. *Networks Heterogeneous Media* **2014,** *9,* 453–476. doi:10.3934/nhm.2014.9.453
14. Winterbottom, W. L. *Acta Metall.* **1967,** *15,* 303–310. doi:10.1016/0001-6160(67)90206-4
15. Barmparis, G. D.; Remediakis, I. N. *Phys. Rev. B* **2012,** *86,* 085457. doi:10.1103/PhysRevB.86.085457
16. Jones, B.; Renaut, R. W. *Sedimentology* **1996,** *43,* 323–340. doi:10.1046/j.1365-3091.1996.d01-7.x
17. Barmparis, G. D.; Honkala, K.; Remediakis, I. N. *J. Chem. Phys.* **2013,** *138,* 064702. doi:10.1063/1.4790368
18. Turner, S.; Lebedev, O. I.; Shenderova, O.; Vlasov, I. I.; Verbeeck, J.; Van Tendeloo, G. *Adv. Funct. Mater.* **2009,** *19,* 2116–2124. doi:10.1002/adfm.200801872

19. Roosen, A. R.; McCormack, R. P.; Carter, W. C. *Comput. Mater. Sci.* **1998,** *11,* 16. doi:10.1016/S0927-0256(97)00167-5
20. Momma, K.; Izumi, F. *J. Appl. Crystallogr.* **2011,** *44,* 1272–1276. doi:10.1107/S0021889811038970
21. Clausen, B. S.; Schiøtz, J.; Gråbæk, L.; Ovesen, C. V.; Jacobsen, K. W.; Nørskov, J. K.; Topsøe, H. *Top. Catal.* **1994,** *1,* 367. doi:10.1007/BF01492289
22. Hansen, P. L.; Wagner, J. B.; Helveg, S.; Rostrup-Nielsen, J. R.; Clausen, B. S.; Topsøe, H. *Science* **2002,** *295,* 2053. doi:10.1126/science.1069325
23. Müller, P.; Kern, R. *Surf. Sci.* **2000,** *457,* 229. doi:10.1016/S0039-6028(00)00371-X
24. Nielsen, R. M.; Murphy, S.; Strebel, C.; Johansson, M.; Chorkendorff, I.; Nielsen, J. H. *J. Nanopart. Res.* **2010,** *12,* 1249–1262. doi:10.1007/s11051-009-9830-8
25. Barnard, A. S.; Chang, L. Y. *ACS Catal.* **2011,** *1,* 76–81. doi:10.1021/cs100025y
26. Bittencourt, C.; Felten, A.; Douhard, B.; Colomer, J.-F.; Van Tendeloo, G.; Drube, W.; Ghijsen, J.; Pireaux, J.-J. *Surf. Sci.* **2007,** *601,* 2800. doi:10.1016/j.susc.2006.12.045
27. Espinosa, E.; Ionescu, R.; Bittencourt, C.; Felten, A.; Erni, R.; Van Tendeloo, G.; Pireaux, J.-J.; Llobet, E. *Thin Solid Films* **2007,** *515,* 8322. doi:10.1016/j.tsf.2007.03.017
28. Quintana, M.; Ke, X.; Van Tendeloo, G.; Meneghetti, M.; Bittencourt, C.; Prato, M. *ACS Nano* **2010,** *4,* 6105. doi:10.1021/nn101183y
29. Behafarid, F.; Roldan Cuenya, B. *Nano Lett.* **2011,** *11,* 5290–5296. doi:10.1021/nl2027525
30. Rawalekar, S.; Mokari, T. *Adv. Energy Mater.* **2013,** *3,* 12–27. doi:10.1002/aenm.201200511
31. Aguilhon, J.; Thomazeau, C.; Boissière, C.; Durupthy, O.; Sanchez, C. *Part. Part. Syst. Charact.* **2013,** *30,* 532–541. doi:10.1002/ppsc.201300023
32. Yang, X.; Fujiwara, K.; Maeda, K.; Nozawa, J.; Koizumi, H.; Uda, S. *Prog. Photovoltaics* **2014,** *22,* 574–580. doi:10.1002/pip.2290
33. Molina, L. M.; Hammer, B. *Phys. Rev. Lett.* **2003,** *90,* 206102. doi:10.1103/PhysRevLett.90.206102
34. Lopez, N.; Nørskov, J. K.; Janssens, T. V. W.; Carlsson, A.; Puig-Molina, A.; Clausen, B. S.; Grunwaldt, J.-D. *J. Catal.* **2004,** *225,* 86–94. doi:10.1016/j.jcat.2004.03.036
35. Barnard, A. S.; Zapol, P. *J. Chem. Phys.* **2004,** *121,* 4276–4283. doi:10.1063/1.1775770
36. Barnard, A. S.; Curtiss, L. A. *Nano Lett.* **2005,** *5,* 1261–1266. doi:10.1021/nl050355m
37. Hadjisavvas, G.; Remediakis, I. N.; Kelires, P. C. *Phys. Rev. B* **2006,** *74,* 165419. doi:10.1103/PhysRevB.74.165419
38. Kopidakis, G.; Remediakis, I. N.; Fyta, M. G.; Kelires, P. C. *Diamond Relat. Mater.* **2007,** *16,* 1875. doi:10.1016/j.diamond.2007.07.013
39. Mittendorfer, F.; Seriani, N.; Dubay, O.; Kresse, G. *Phys. Rev. B* **2007,** *76,* 233413. doi:10.1103/PhysRevB.76.233413
40. Soon, A.; Wong, L.; Delley, B.; Stampfl, C. *Phys. Rev. B* **2008,** *77,* 125423. doi:10.1103/PhysRevB.77.125423
41. Shi, H.; Stampfl, C. *Phys. Rev. B* **2008,** *77,* 094127. doi:10.1103/PhysRevB.77.094127
42. Cortes-Huerto, R.; Goniakowski, J.; Noguera, C. *J. Chem. Phys.* **2013,** *138,* 244706. doi:10.1063/1.4811670
43. Kim, K. C.; Dai, B.; Johnson, J. K.; Sholl, D. S. *Nanotechnology* **2009,** *20,* 204001. doi:10.1088/0957-4484/20/20/204001
44. Pham, T. H.; Duan, X.; Qian, G.; Zhou, X.; Chen, D. *J. Phys. Chem. C* **2014,** *118,* 10170–10176. doi:10.1021/jp502225r
45. Łodziana, Z.; Stoica, G.; Pérez-Ramírez, J. *Inorg. Chem.* **2011,** *50,* 2590–2598. doi:10.1021/ic102443h
46. Honkala, K.; Łodziana, Z.; Remediakis, I. N.; Lopez, N. *Top. Catal.* **2014,** *57,* 14–24. doi:10.1007/s11244-013-0158-3
47. Honkala, K.; Hellman, A.; Remediakis, I. N.; Logadottir, A.; Carlsson, A.; Dahl, S.; Christensen, C. H.; Nørskov, J. K. *Science* **2005,** *307,* 555. doi:10.1126/science.1106435
48. Hellman, A.; Honkala, K.; Remediakis, I. N.; Logadóttir, Á.; Carlsson, A.; Dahl, S.; Christensen, C. H.; Nørskov, J. K. *Surf. Sci.* **2006,** *600,* 4264–4268. doi:10.1016/j.susc.2005.11.070
49. Hellman, A.; Honkala, K.; Remediakis, I. N.; Logadóttir, Á.; Carlsson, A.; Dahl, S.; Christensen, C. H.; Nørskov, J. K. *Surf. Sci.* **2009,** *603,* 1731–1739. doi:10.1016/j.susc.2008.10.059
50. Rayson, M. J.; Briddon, P. R. *Phys. Rev. B* **2009,** *80,* 205104. doi:10.1103/PhysRevB.80.205104
51. Carvalho, A.; Öberg, S.; Barroso, M.; Rayson, M. J.; Briddon, P. *Phys. Status Solidi A* **2012,** *209,* 1847–1850. doi:10.1002/pssa.201200149
52. Carvalho, A.; Öberg, S.; Barroso, M.; Rayson, M. J.; Briddon, P. *Phys. Status Solidi B* **2013,** *250,* 1799–1803. doi:10.1002/pssb.201349104
53. McKenna, K. P.; Shluger, A. L. *J. Phys. Chem. C* **2007,** *111,* 18848–18852. doi:10.1021/jp710043s
54. Gavnholt, J.; Schiøtz, J. *Phys. Rev. B* **2008,** *77,* 035404. doi:10.1103/PhysRevB.77.035404
55. McKenna, K. P. *Phys. Chem. Chem. Phys.* **2009,** *11,* 4145–4151. doi:10.1039/b821408p
56. Dahl, S.; Logadottir, A.; Jacobsen, C. J. H.; Nørskov, J. K. *Appl. Catal., A* **2001,** *222,* 19–29. doi:10.1016/S0926-860X(01)00826-2
57. Vilé, G.; Baudouin, D.; Remediakis, I. N.; Copéret, C.; López, N.; Pérez-Ramírez, J. *ChemCatChem* **2013,** *5,* 3750–3759. doi:10.1002/cctc.201300569
58. Ueda, K.; Kawasaki, T.; Hasegawa, H.; Tanji, T.; Ichihashi, M. *Surf. Interface Anal.* **2008,** *40,* 1725. doi:10.1002/sia.2947
59. Gómez-Graña, S.; Goris, B.; Altantzis, T.; Fernández-López, C.; Carbó-Argibay, E.; Guerrero-Martínez, A.; Almora-Barrios, N.; López, N.; Pastoriza-Santos, I.; Pérez-Juste, J.; Bals, S.; Van Tendeloo, G.; Liz-Marzán, L. M. *J. Phys. Chem. Lett.* **2013,** *4,* 2209–2216. doi:10.1021/jz401269w
60. Almora-Barrios, N.; Novell-Leruth, G.; Whiting, P.; Liz-Marzán, L. M.; López, N. *Nano Lett.* **2014,** *14,* 871–875. doi:10.1021/nl404661u
61. Saldan, I. *Cent. Eur. J. Chem.* **2011,** *9,* 761. doi:10.2478/s11532-011-0068-9
62. Züttel, A.; Borgschulte, A.; Orimo, S.-I. *Scr. Mater.* **2007,** *56,* 823–828. doi:10.1016/j.scriptamat.2007.01.010
63. Remhof, A.; Mauron, P.; Züttel, A.; Embs, J. P.; Łodziana, Z.; Ramirez-Cuesta, A. J.; Ngene, P.; de Jongh, P. *J. Phys. Chem. C* **2013,** *117,* 3789. doi:10.1021/jp311064d
64. Hazrati, E.; Brocks, G.; de Wijs, G. A. *J. Phys. Chem. C* **2012,** *116,* 18038. doi:10.1021/jp303720v
65. Łodziana, Z.; Błoński, P. *Int. J. Hydrogen Energy* **2014,** *39,* 9842. doi:10.1016/j.ijhydene.2014.02.150

License and Terms

This is an Open Access article under the terms of the Creative Commons Attribution License (http://creativecommons.org/licenses/by/2.0), which permits unrestricted use, distribution, and reproduction in any medium, provided the original work is properly cited.

The license is subject to the *Beilstein Journal of Nanotechnology* terms and conditions: (http://www.beilstein-journals.org/bjnano)

The definitive version of this article is the electronic one which can be found at: doi:10.3762/bjnano.6.35

BEILSTEIN JOURNAL OF NANOTECHNOLOGY

Filling of carbon nanotubes and nanofibres

Reece D. Gately[1] and Marc in het Panhuis[*1,2]

Review

Open Access

Address:
[1]Soft Materials Group, School of Chemistry, University of Wollongong, Wollongong, NSW 2522, Australia and [2]Intelligent Polymer Research Institute, ARC Centre of Excellence for Electromaterials Science, AIIM Facility, University of Wollongong, Wollongong, NSW 2522, Australia

Email:
Marc in het Panhuis[*] - panhuis@uow.edu.au

* Corresponding author

Keywords:
applications; carbon nanostructures; filling; nanofibers; nanotubes

Beilstein J. Nanotechnol. **2015,** *6,* 508–516.
doi:10.3762/bjnano.6.53

Received: 28 June 2014
Accepted: 29 January 2015
Published: 19 February 2015

This article is part of the Thematic Series "Atomic scale interface design and characterisation: Theory – Structure and dynamics".

Guest Editor: C. Ewels

© 2015 Gately and in het Panhuis; licensee Beilstein-Institut.
License and terms: see end of document.

Abstract

The reliable production of carbon nanotubes and nanofibres is a relatively new development, and due to their unique structure, there has been much interest in filling their hollow interiors. In this review, we provide an overview of the most common approaches for filling these carbon nanostructures. We highlight that filled carbon nanostructures are an emerging material for biomedical applications.

Introduction

Carbon nanotubes are well-known, 1D nanostructures, which are comprised of single, double or multiple coaxial layers of graphene [1]. The synthesis method and conditions greatly affect their structural characteristics such as number of layers, length and diameter distribution [2]. For example, the arc discharge synthesis method can be used to produce multiwalled carbon nanotubes (MWCNTs) with an inside diameter as small as 0.4 nm [3] and an outside diameter of up to 200 nm [4]. It has been shown that the inside diameter of MWCNTs produced using chemical vapour deposition is proportional to the size of the metal catalyst used during production [5]. Their high specific surface area (SSA, 1315 m^2/g) [6] makes MWCNTs an ideal material for application in hydrogen storage [7], capacitors [8] and sensing [9].

Single-walled carbon nanotubes (SWCNTs) were discovered during investigations into the filling of MWCNTs with iron and cobalt [10,11]. Rather than producing a filled MWCNT, the metals acted as a catalyst to create a nanotube with a single wall. Similar to MWCNTs, the physical properties (inside diameter, length, degree of graphitization) of SWCNTs vary with the production method [12]. For example, during the synthesis of SWCNTs using pulsed laser vaporization (PLV), the temperature of the deposition chamber was used to influence the average inside diameter range. It was demonstrated that at 780 °C the average diameter was 1.0 nm, whereas at 1000 °C the average diameter increased to 1.2 nm [13]. PLV has also been used to produce large quantities of pure SWCNTs and MWCNTs [14]. Other research showed that applying a

magnetic field had a large effect on the size of the SWCNTs [15-18]. The SSA of the SWCNTs can be between 124 and 1024 m^2/g depending on the production method used by the various manufacturers [19]. Arc discharge has also been used to produce bundles of SWCNTs with a yield of up to 90% [20]. This technique is now one of the more common production techniques, in addition to catalytic carbon vapour deposition (CCVD).

Carbon nanofibres (CNFs) are larger (≈100 nm outer diameter), cylindrical, carbon structures that have multiple possible structures. In order to ease the complexity that surrounds all of these possible structures, the nomenclature proposed by Suares-Martinez et al. shall be used for the most part [21]. The structures that have been observed include: hollow- and filled-core, stacked nanocones; partitioned, stacked nanocones; and partitioned nanotubes. The filled-core, stacked nanocone structure consists of bowed sheets of graphene, which are stacked to produce a cylindrical, solid structure [22,23]. As this produces solid structures (and thus not applicable as a material to be filled), this review will focus on those produced by catalytic thermal chemical vapour deposition using a floating catalyst, henceforth referred to as vapour-grown CNFs (VGCNFs) [24]. This technique can be used to produce partitioned, stacked nanocones or partitioned nanotubes. VGCNFs are produced (depending on the structure of the catalyst) with a hollow interior cavity [25] and have been shown to consist of two primary structures, single layer and double layer. The internal arrangement is the same for both structures, that is, a series of parallel graphitic layers at an angle of 4–36° relative to the hollow core. The double layer CNFs have an additional second layer (outside the angled layer) consisting of multiple sheets of graphene, which are aligned parallel with the core [12,26]. Since it has been shown that thermal treatment between 1300 °C and 1700 °C leads to improved electrical and mechanical properties, VGCNFs are typically heat treated [27]. Typical dimensions of CNFs are: outside diameters of up to 200 nm, inside diameters of 12.5 nm (single layer) or 22 nm (double layer), and lengths of up to 20 µm [24,26]. The SSA depends on the degree of heat treatment. For example, a SSA of 37 m^2/g results from heat treatment at 1200 °C and is reduced to 15 m^2/g after heat treatment at 2800 °C. Pyrolitic stripping can also be performed on as-grown nanofibres to remove unreacted polyaromatic hydrocarbons that may have fused onto the surface of the VGCNFs. This has been shown to increase the SSA from 20 m^2/g to 62 m^2/g [28]. Even higher values (348 m^2/g) have been reported when using a metal catalyst and C_3H_8 decomposition [29]. Due to their unique internal structure, there has been significant interest in the filling of CNFs for the alignment of atoms [30,31].

Figure 1 shows the morphological differences between a typical MWCNT and a typical VGCNF. Due to their large (average) inside radius, VGCNFs have a larger inside area as compared to SWCNTs and MWCNTs of the same length. The main interest in the filling of VGCNFs comes from their unique angled structure: the slight angle produces internal "shelves". This unique structure is clearly visible in the microscopy image (Figure 1b,d) and the schematic representation (Figure 1c).

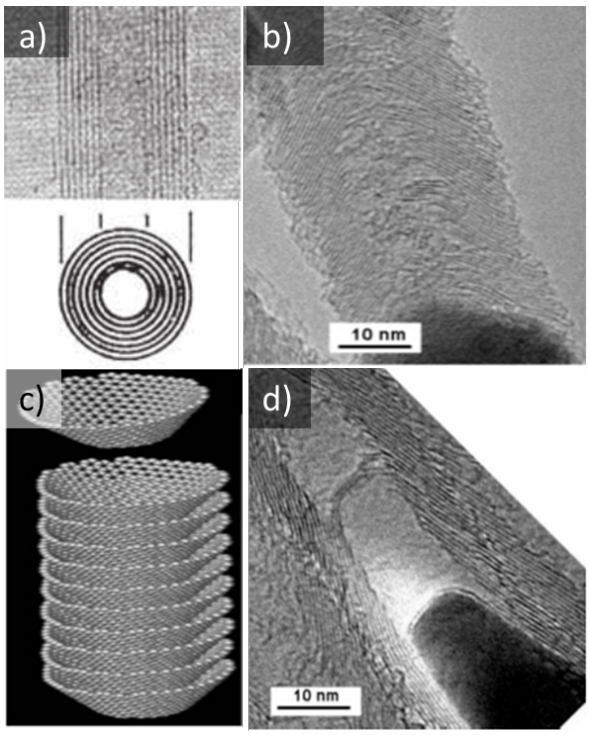

Figure 1: Images of (a) a typical MWCNT and (b,d) typical VGCNFs. A schematic representation is given in (c) of the "cup-stacked" VGCNFs, resulting in a hollow core. (a) Adapted with permission from [3], copyright 2006 the Royal Society of Chemistry and (b,c,d) with permission from [23], copyright 2007 the Royal Society of Chemistry.

The filling of these specific tubular carbon nanostructures (TCNSs) has attracted much interest due to their applications in gas storage (in particular H_2) [32,33], electrochemical energy storage [34,35], battery electrodes [24,36], catalysis [37,38] and nanowelding [39]. Shortly after their discovery in 1991, MWCNTs were filled with metals in order to create metal nanowires encapsulated within the CNT [10]. While this was the original inspiration behind the filling of TCNSs, it is still very much prevalent today. The main advantages of using CNTs to produce metallic nanowires is that the CNTs act as a template for self-assembly of the nanowires [40,41] and the CNT structure can act as a protective sheath to protect the nanowire from being damaged by chemicals in harsh conditions/environments [42]. CNTs have also been used as sacrificial templates. The

CNTs can be removed by heat treating (generally requiring temperatures greater than 600 °C), thereby leaving the metal structures unaltered and exposed [43,44]. It has also been shown that the irradiation of a filled MWCNT with a focused, high energy (200 keV) electron beam results in MWCNT–Co–MWCNT junction sites [45,46].

There has been considerable interest in the filling of SWCNTs and MWCNTs for drug delivery applications, for example, tip functionalization of the filled CNT for selective drug release [47,48]. A recent review focussed on the use of CNTs filled with antitumour medication for use in chemotherapy and immunotherapy [49]. In particular, they noted that the high level of selectivity (when functionalized) gave the CNTs the ability to "seek out" and selectively deliver the contained drugs to the tumours. The same article also discussed the potential use of SWCNTs for the treatment of central nervous system disorders due to their ability to pass through blood–brain barriers [50].

In this article, selected avenues for the filling of carbon nanotubes and nanofibres as well as applications of the filled TCNSs (including biomedical and catalytic applications) are discussed. We will present the progression of selected TCNS filling techniques beginning from the earliest papers that can be found as well as how the techniques have adapted to modern methods and applications, and finally reviewing some of the most recent papers that have been released. The most common ex situ techniques for opening (decapping the TCNSs) and filling are also described in detail, as this is one of the main problems to overcome when filling TCNSs. The unique advantages with regards to the filling of these two TCNSs are also discussed in this review, as it is important to emphasize that both serve their own purposes.

Review

Approaches for filling carbon nanostructures

Opening the capped ends

It is well known that the as-produced TCNSs have one end capped [51], thus in order to achieve filling, the TCNSs must be opened. The initial work focussed on the opening of MWCNTs using bismuth in the presence of oxygen at 850 °C [52]. This was then further expanded by suspending the MWCNTs in 68% nitric acid and refluxing at 140 °C for 4.5 h [53]. This wet chemistry method of opening MWCNTs was also attempted on SWCNTs using a heated hydrochloric acid solution, as nitric acid was found to be too harsh for SWCNTs. Similar to the MWCNTs, the SWCNTs were then easily filled directly after opening [54]. This was followed by more sophisticated methods such as oxygen plasma treatment [55], electrochemical treatment (which was able to remove the caps for both SWCNTs and MWCNTs) [56], heat treatment in carbon dioxide/air [57], sonication-induced shearing [58,59], partial opening due to purification [60], precision cutting [61] and water-assisted etching [62].

The main issue with these methods is that etching the CNTs in this way damages their surface or alters their morphology in undesired ways (e.g., reduction in length). Due to this challenge, much research has been focussed on producing CNTs that are open at both ends. This has been achieved by using an anodic aluminium oxide (AAO) film as a template for the thermal decomposition of hydrocarbon gases, followed by removal of the template by etching in 46% HF solution [63,64]. This technique has since been refined to produce tailored CNTs of desired length and diameter [65] and to allow the template to be dissolved in NaOH (rather than concentrated HF) [66]. This method has also been employed to produce SWCNTs [67] and VGCNFs [68], as well as long (10 μm) MWCNTs that can be nested or joined to create long MWCNTs [69].

The three primary methods for opening TCNSs are: electrochemical filling, functionalization of the TCNSs, and a method that takes advantage of the capillary forces within the TCNSs. Although it is also possible to combine more than one technique (e.g., chemical and capillary [70]), here we describe the general principle of each method individually.

Electrochemical filling

Electrochemical deposition on both the interior and exterior surfaces of TCNSs has been achieved [71]. MWCNT samples decorated with gold nanoparticles on the interior and exterior surfaces were produced by first functionalizing the CNTs with carboxylic acid groups [65]. This was followed by sonication of the functionalized MWCNTs in water and application of a large (225 V) potential across two gold electrodes [72]. This was shown to not only decorate the external surface, but also to fill some MWCNTs with a gold nanowire. Ordered, open MWCNTs produced from the AAO template method have also undergone an electrochemical filling process with nickel–iron alloys [73]. It was shown that this technique could be used to control the nickel/iron ratio and the amount of filling. Electrochemical methods have also been used to fill TCNSs with water [74] and can take advantage of the presence of oxygen within TCNSs applied as an electrode for Li–O_2 rechargeable batteries [75].

Filling through functionalization

The functionalization of TCNSs is a proven, effective method to coat the exterior [8,76,77] or interior [78] surface with metal particles. This method produces TCNSs with a single-atom-thick layer (plus the functional group, typically a carboxylate

group) of metal particles. It has been utilised to create nanoscale capacitors with high energy storage rates, high specific capacitance (329 F/g) [8,79] in addition to high surface area electrodes [76,77,80]. TCNSs have also been used as a membrane for water and gas filtration [81]. It has been proposed that by chemically functionalizing the TCNSs, the selectivity of the membrane can be adapted to remove specific contaminants [82,83]. Tip functionalization has also been used as a method to selectively separate various analytes [84,85] and can be performed at room temperature using ozone and small amounts of water vapour [86].

Capillary filling

It is well known that a tubular structure with a high aspect ratio will have strong capillary forces, and this is especially true for TCNSs [87,88]. These forces can be exploited to achieve the filling of TCNSs. Capillary filling was achieved by depositing drops of metallic lead onto the external surface of MWCNTs, followed by heat treating the sample to 400 °C [89]. This heat treatment removed the capped ends and the resulting capillary action led to the filling of the MWCNT through the absorbance of the liquid lead. This process has been modelled to determine the extent of the capillary action [90]. In addition, the effect of the molecular weight of a polymer on the capillary action has also been investigated [91]. Microscopy has been used to visualize the filling of a MWCNT with gold via Joule heating and capillary action [92]. A mathematical model has been developed to evaluate the relationship between the TCNS radius, the radius of the nanoscale drop of material used to fill the TCNS, and the contact angle between the filler and the TCNS. This model successfully predicted the capillary absorption of non-wettable nanoparticles [93] and has been employed to achieve filling [94] as well as removal of the encapsulated nanoparticles [95]. Sonication has also been employed to fill MWCNTs in solution. Sonication acted to shear the MWCNT, resulting in the filling of the MWCNT with the surrounding metal solution [96].

Other methods have employed focused electron irradiation to produce SWCNTs within the core of a filled MWCNT. This was achieved by first filling a MWCNT with iron, cobalt, nickel, or an iron–cobalt alloy using capillary action. Following this step, the sample was placed inside a transmission electron microscope (with the sample stage temperature set at 600 °C) and subjected to electron irradiation [97]. This resulted in the growth of a SWCNT within the inner core of the MWCNT.

Vapour-phase filling

Filled SWCNTs and MWCNTs have been achieved by exposure to a metallic vapour. This resulted in metal nanowires within the core of the CNT [98-101]. A general summary of this method is as follows: the as-produced SW/MWCNTs were processed in a furnace under vacuum at a temperature that vaporizes the compound/element to be filled into the CNT. Next, a stream of the metallic vapour was sent into the furnace. In one such study, purified double-walled CNTs (DWCNTs) were added to an evacuated furnace at 400 °C and 10^{-3} Pa containing VCl_3 vapour [101]. The resulting material was then cooled to 100 °C for 48 h and cleaned with a HF solution. This filling method not only fills the interior cavity, but also coats the exterior of the CNTs with the vapour. Therefore, an additional cleaning step is required to remove these species.

It is important to note that this filling method (along with many others mentioned in this article) is not restricted to metallic filling, although it is one of the more prevalent topics. Botka et al. have performed multiple studies on methods to efficiently fill SWCNTs with coronene [102,103]. In both cases, the filling was performed by first opening the SWCNTs, then placing them in a furnace with coronene at temperatures of up to 450 °C and at a pressure of 10^{-4} mbar – the ideal conditions for the sublimation of coronene. After processing it was found that the coronene had both coated the SWCNT, as well as filled it. In some instances, this annealing and vapour filling caused a structural change in the coronene (which formed dicoronylene, the dimer of coronene) or in the SWCNT itself (which produced a DWCNT at high temperatures). This effect along with the unique structure of CNTs was exploited to produce linear diamondoid assemblies of adamantine within the core of the DWCNTs using a method based on that proposed by Zhang et al. [104].

In situ filling

Although a significant amount of effort has gone into developing approaches for opening the end caps of TCNSs, some research has focussed on methods that either fill in situ (during growth) or that simultaneously open and fill. These methods make use of the strong capillary action that exists within the nanoscale cavities. Filled SWCNTs and MWCNTs have been produced using layered sheets of graphene, decorated with palladium particles via arc discharge in solution [105,106] (see Figure 2). This approach was able to produce filled SWCNTs or MWCNTs, depending on the number of layers of graphene used. In addition, it has been proposed that other metallic particles can be used. This has been demonstrated with Pd–Ag nanoparticles on graphene sheets, however, they were not "rolled" into CNTs [107].

Both vapour phase filling and in situ filling techniques have been combined to produce MWCNTs that are doped with various other elements, such as phosphorous and nitrogen, which can then later be released under high temperature condi-

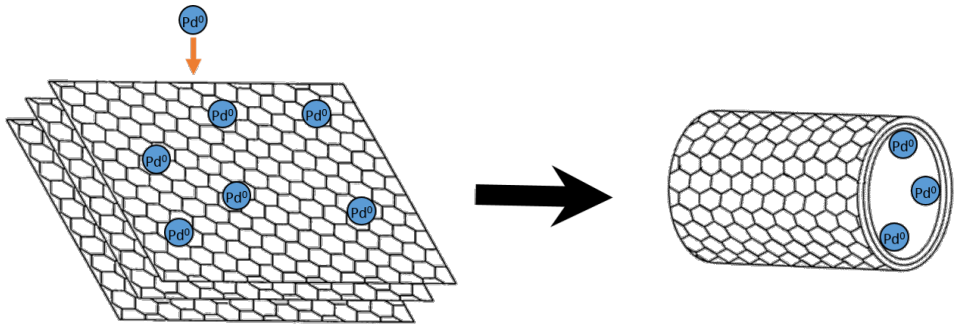

Figure 2: Schematic of a method for producing filled SWCNTs and MWCNTs via arc discharge in solution. Metallic palladium particles decorated the exterior surface of graphene sheets, which were then processed as filled CNTs. This schematic was inspired by a figure appearing in reference [106].

tions [108,109]. One method to produce nitrogen-doped MWCNTs is a modified, floating catalyst, CVD technique, which is most commonly used to produce VGCNFs. The catalyst (ferrocene) was placed into the CVD chamber under an argon/ethylene flow, and melamine was used as an efficient source for N-doping [110]. The chamber was then heated to 950 °C, with an effective heating of the ferrocene and melamine to 350 °C. At this temperature both compounds undergo sublimation. After the purification steps, it was found that the resulting MWCNTs were highly doped with nitrogen, demonstrating yet another method to produce MWCNTs to be used as a source of nitrogen storage. The nitrogen could be removed by heating to 700 °C. A very detailed review on one-dimensional nitrogen-containing carbon nanostructures by Ćirić-Marjanović et al. contains a very detailed list of other structures and methods used to achieve nitrogen storage [111].

The arc discharge method was also modified to produce filled SWCNTs and MWCNTs [112,113]. This was achieved by first producing a powdered mixture of graphite and the various metals performed in the study (YB_2, YNi_2, and NiB). Next, standard arc discharge methods were utilised (25–35 V, 100 A). This method produced filled MWCNTs, as well as filled, graphitic nanoparticles. This method has been employed in conjunction with an AAO template lined with the filler material [114] or completely filled with the metal [115]. Moreover, a variety of bismuth–tin nanostructures covered by CNTs have been produced via in situ filling. It was demonstrated that the $MSnO_2/MBi_2O_3$ ratio was instrumental in the formation of the encased nanostructures (nanoparticles, nanorods, and nanowires) [116].

Recent developments

Although several drug delivery and medical imaging applications of SWCNT and MWCNTs have been identified, this line of research has only very recently emerged [117-119]. Further investigations into the selective binding of functional groups and various viruses or tumours could provide for an effective drug delivery system for treating various difficult-to-treat ailments. However, effective CNT filling methods that do not negatively impact the drug require further investigation. To date, only SWCNTs and MWCNTs have been evaluated for their use in drug delivery. Although potentially promising for affordable, targeted, drug release, VGCNFs have not yet been evaluated. Whilst they have not demonstrated the same nanoscale interactions as CNTs (such as crossing the blood–brain barrier, which is still under investigation), they may have other applications on the larger scale and allow for higher drug storage capacity.

The use of focused electron beam irradiation for the removal of the outside layers of SW/MWCNTs has promise as an effective method to produce pure or alloyed nanowires for conductive applications [120]. This, however, is also a relatively new research field where very little investigation into developing a scalable method for producing larger quantities of nanowires has been undertaken. As TCNSs have shown promise in the field of tissue engineering, with further development, this method may be used to produce channels for cell growth. Filled with appropriate drugs and medium, TCNSs may provide a platform for the growth of various cells.

Although significant research has gone into the filling of TCNSs, possibility for further exploration still remains. For example, most of the current methods are harsh (i.e., employing concentrated acids, high temperature/pressure conditions) and damage either the filler material or the TCNS itself. In addition, the filling process can be complex and can require multiple steps using custom-built equipment. These methods could be improved to provide a simple method to completely fill the TCNSs with the desired material, without damage to the TCNS, and in a timely manner. Simplicity is key for scale-up to large quantities of filled TCNSs, which is a requirement for any commercially viable application.

TCNSs provide a unique structure with a high aspect ratio, large filling volume, and good stability, which can be useful for many applications. For example, it is well known that they can improve the mechanical and electrical properties of various dispersants [121-124]. However, the properties of the resulting materials prepared from dispersions of TCNSs filled with various materials have not been fully investigated. One interesting application area is in the field of repair (healing) of polymer materials [106]. Traditionally crack healing, which can repair the detrimental effects of mechanical degradation and fatigue in polymer adhesives, was primarily investigated this field. One application of this concept could be in the area of polymer materials (such as hydrogels) for cartilage replacement.

Most interest in the filling of VGCNFs is due to their unique internal structure, which allows for the alignment of atoms along the ridges of the graphene sheets [38], as shown in Figure 3. The internal structure has been demonstrated to be a good site for the catalytic growth of nanoparticles of desired dimensions (Figure 3a,d). When the nanoparticles grow too large, they simply flow through and out of the VGCNF, as indicated in Figure 3d [125,126]. The structure of VGCNFs in the context of filling has not been extensively studied [127], leaving much to be discovered as to how this unique internal "layering" can assist with self-assembly and size-controlled particle growth.

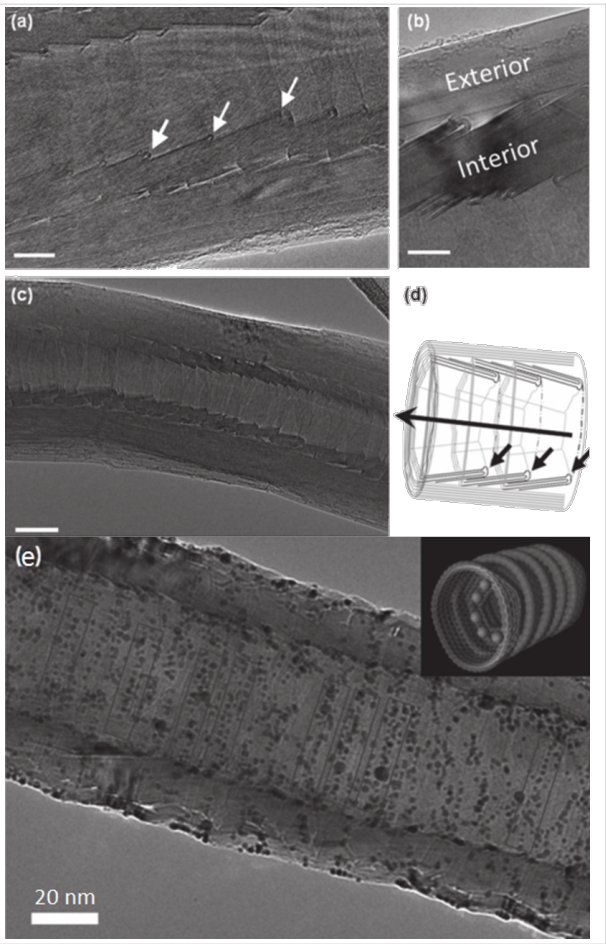

Figure 3: (a,b,c) Transmission electron micrographs of a hollow CVD-grown CNF with the graphene caps indicated by the white arrows. (d) Schematic of the structure of the CNFs with the caps as well as nucleation sites indicated by the black arrows. (e) Transmission electron micrograph of the filled CNFs with gold nanoparticles. Inset: a computer generated model. Reprinted with permission from [30], copyright 2012 Wiley-VCH.

Conclusion

The filling of TCNSs has shown much promise regarding the synthesis of nanowires, hydrogen storage, and drug delivery. Although most of the research has focussed on the development of the actual methods for filling, there are a number of biomedical applications of these fascinating materials that remain to be explored and developed. In this review, we aimed to provide an overview of the most common methods for filling of SWCNTs, MWCNTs and VGCNFs. Most of the reviewed literature relates to MWCNTs, as this material has been extensively studied. VGCNFs are an emerging material for filling applications, but not all VGCNFs are suitable. For example, the VGCNFs with a "deck of cards" morphology (i.e., a series of parallel graphene sheets stacked on top of each other [128]) cannot be filled due to the lack of a hollow core [22]. SWCNTs have significant promise, however, their high production cost has limited research in the past. As research into the efficient production of pristine SWCNTs has progressed, their cost has correspondingly rapidly decreased, which should lead to future SWCNT filling applications.

This article highlighted TCNSs as a suitable material for applications requiring filled nanostructures, as well as the unique strengths of both CNTs and CNFs. The remaining challenge is to prepare filled TCNS materials that achieve one or both of the following properties: (1) selective drug delivery using nanostructures, which is important for the development of nano-sized needles or patches for the localised treatment of diseases; (2) autonomic healing of polymeric materials, such as tough hydrogels, which is important for load-bearing biomedical materials such as cartilage replacement. While there is much research into the filling of SWCNTs and MWCNTs, there is very limited research regarding the filling of VGCNFs, which have been demonstrated to be as efficient (if not more) for certain filling applications such as storage and self-assembly. However, a more reliable and thorough method to completely fill VGCNFs must be established, as current methods either result in partial filling, or can only fill with certain types of materials. In conclusion, it is clear that filled TCNSs offer great opportunities for a broad variety of applications, yet a number of challenges remain to be addressed.

References

1. Dresselhaus, M. S.; Jorio, A.; Saito, R. *Annu. Rev. Condens. Matter Phys.* **2010,** *1,* 89–108. doi:10.1146/annurev-conmatphys-070909-103919
2. Cadek, M.; Murphy, R.; McCarthy, B.; Drury, A.; Lahr, B.; Barklie, R. C.; in het Panhuis, M.; Coleman, J. N.; Blau, W. J. *Carbon* **2002,** *40,* 923–928. doi:10.1016/S0008-6223(01)00221-4
3. Ando, Y.; Zhao, X. *New Diamond Front. Carbon Technol.* **2006,** *16,* 123–137.
4. Wang, X. K.; Lin, X. W.; Dravid, V. P.; Ketterson, J. B.; Chang, R. P. H. *Appl. Phys. Lett.* **1995,** *66,* 2430–2432. doi:10.1063/1.113963
5. Andrews, R.; Jacques, D.; Qian, D.; Rantell, T. *Acc. Chem. Res.* **2002,** *35,* 1008–1017. doi:10.1021/ar010151m
6. Peigney, A.; Laurent, C.; Flahaut, E.; Bacsa, R. R.; Rousset, A. *Carbon* **2001,** *39,* 507–514. doi:10.1016/S0008-6223(00)00155-X
7. Ritschel, M.; Uhlemann, M.; Gutfleisch, O.; Leonhardt, A.; Graff, A.; Täschner, C.; Fink, J. *Appl. Phys. Lett.* **2002,** *80,* 2985. doi:10.1063/1.1469680
8. Sankapal, B. R.; Gajare, H. B.; Dubal, D. P.; Gore, R. B.; Salunkhe, R. R.; Ahn, H. *Chem. Eng. J.* **2014,** *247,* 103–110. doi:10.1016/j.cej.2014.02.092
9. Verma, A. L.; Saxena, S.; Saini, G. S. S.; Gaur, V.; Jain, V. K. *Thin Solid Films* **2011,** *519,* 8144–8148. doi:10.1016/j.tsf.2011.06.034
10. Iljima, S.; Ichihashi, T. *Nature* **1993,** *363,* 603–605. doi:10.1038/363603a0
11. Bethune, D. S.; Klang, C. H.; de Vries, M. S.; Gorman, G.; Savoy, R.; Vazquez, J.; Beyers, R. *Nature* **1993,** *363,* 605–607. doi:10.1038/363605a0
12. Endo, M.; Kim, Y. A.; Hayashi, T.; Fukai, Y.; Oshida, K.; Terrones, M.; Yanagisawa, T.; Higaki, S.; Dresselhaus, M. S. *Appl. Phys. Lett.* **2002,** *80,* 1267–1269. doi:10.1063/1.1450264
13. Bandow, S.; Asaka, S.; Saito, Y.; Rao, A. M.; Grigorian, L.; Richter, E.; Eklund, P. C. *Phys. Rev. Lett.* **1998,** *80,* 3779–3782. doi:10.1103/PhysRevLett.80.3779
14. Maser, W. K.; Benito, A. M.; Martınez, M. T. *Carbon* **2002,** *40,* 1685–1695. doi:10.1016/S0008-6223(02)00009-X
15. Keidar, M.; Shashurin, A.; Li, J.; Volotskova, O.; Kundrapu, M.; Zhuang, T. S. *J. Phys. D: Appl. Phys.* **2011,** *44,* 174006. doi:10.1088/0022-3727/44/17/174006
16. Keidar, M.; Levchenko, I.; Arbel, T.; Alexander, M.; Waas, A. M.; Ostrikov, K. *Appl. Phys. Lett.* **2008,** *92,* 043129. doi:10.1063/1.2839609
17. Volotskova, O.; Fagan, J. A.; Huh, J. Y.; Phelan, F. R., Jr.; Shashurin, A.; Keidar, M. *ACS Nano* **2010,** *4,* 5187–5192. doi:10.1021/nn101279r
18. Waldorff, E. I.; Waas, A. M.; Friedmann, P. P.; Keidar, M. *J. Appl. Phys.* **2004,** *95,* 2749–2754. doi:10.1063/1.1642737
19. Panella, B.; Hirscher, M.; Roth, S. *Carbon* **2005,** *43,* 2209–2214. doi:10.1016/j.carbon.2005.03.037
20. Journet, C.; Mased, W. K.; Bernier, P.; Loiseau, A.; Lamy de la Chapelle, M.; Lefrant, S.; Deniard, P.; Lee, R.; Fischer, J. E. *Nature* **1997,** *388,* 756–758.
21. Suarez-Martinez, I.; Grobert, N.; Ewels, C. P. *Carbon* **2012,** *50,* 741–747. doi:10.1016/j.carbon.2011.11.002
22. Yoon, S.-H.; Lim, S.; Hong, S.-h.; Mochida, I.; An, B.; Yokogawa, K. *Carbon* **2004,** *42,* 3087–3095. doi:10.1016/j.carbon.2004.07.022
23. Monthioux, M.; Noé, L.; Dussault, L.; Dupin, J.-C.; Latorre, N.; Ubieto, T.; Romeo, E.; Royo, C.; Monzón, A.; Guimon, C. *J. Mater. Chem.* **2007,** *17,* 4611–4618. doi:10.1039/b707742d
24. Endo, M.; Kim, Y. A.; Hayashi, T.; Nishimura, K.; Matusita, T.; Miyashita, K.; Dresselhaus, M. S. *Carbon* **2001,** *39,* 1287–1297. doi:10.1016/S0008-6223(00)00295-5
25. Rodriguez, N. M.; Chambers, A.; Baker, R. T. K. *Langmuir* **1995,** *11,* 3862–3866. doi:10.1021/la00010a042
26. Uchida, T.; Anderson, D. P.; Minus, M. L.; Kumar, S. *J. Mater. Sci.* **2006,** *41,* 5851–5856. doi:10.1007/s10853-006-0324-0
27. Howe, J. Y.; Tibbetts, G. G.; Kwag, C.; Lake, M. L. *J. Mater. Res.* **2006,** *21,* 2646–2652. doi:10.1557/JMR.2006.0325
28. Elias, K. L.; Price, R. L.; Webster, T. J. *Biomaterials* **2002,** *23,* 3279–3287. doi:10.1016/S0142-9612(02)00087-X
29. Lee, B. O.; Woo, W. J.; Kim, M.-S. *Macromol. Mater. Eng.* **2001,** *286,* 114–118. doi:10.1002/1439-2054(20010201)286:2<114::AID-MAME114>3.0.CO;2-8
30. La Torre, A.; Fay, M. W.; Rance, G. A.; del Carmen Gimenez-Lopez, M.; Solomonsz, W. A.; Brown, P. D.; Khlobystov, A. N. *Small* **2012,** *8,* 1222–1228. doi:10.1002/smll.201102007
31. Solomonsz, W. A.; Rance, G. A.; Suyetin, M.; La Torre, A.; Bichoutskaia, E.; Khlobystov, A. N. *Chem. – Eur. J.* **2012,** *18,* 13180–13187. doi:10.1002/chem.201201542
32. Liu, C.; Chen, Y.; Wu, C.-Z.; Xu, S.-T.; Cheng, H.-M. *Carbon* **2010,** *48,* 452–455. doi:10.1016/j.carbon.2009.09.060
33. Rashidi, A. M.; Nouralishahi, A.; Khodadadi, A. A.; Mortazavi, Y.; Karimi, A.; Kashefi, K. *Int. J. Hydrogen Energy* **2010,** *35,* 9489–9495. doi:10.1016/j.ijhydene.2010.03.038
34. Che, G.; Lakshmi, B. B.; Martin, C. R.; Fisher, E. R. *Langmuir* **1999,** *15,* 750–758. doi:10.1021/la980663i
35. Candelaria, S. L.; Shao, Y.; Zhou, W.; Li, X.; Xiao, J.; Zhang, J.-G.; Wang, Y.; Liu, J.; Li, J.; Cao, G. *Nano Energy* **2012,** *1,* 195–220. doi:10.1016/j.nanoen.2011.11.006
36. Kumar, T. P.; Ramesh, R.; Lin, Y. Y.; Fey, G. T.-K. *Electrochem. Commun.* **2004,** *6,* 520–525. doi:10.1016/j.elecom.2004.03.009
37. Pan, X.; Bao, X. *Chem. Commun.* **2008,** 6271–6281. doi:10.1039/b810994j
38. La Torre, A.; del Carmen Giménez-López, M.; Fay, M. W.; Rance, G. A.; Solomonsz, W. A.; Chamberlain, T. W.; Brown, P. D.; Khlobystov, A. N. *ACS Nano* **2012,** *6,* 2000–2007. doi:10.1021/nn300400z
39. Dong, L.; Tao, X.; Zhang, L.; Zhang, X.; Nelson, B. J. *Nano Lett.* **2007,** *7,* 58–63. doi:10.1021/nl061980+
40. Ye, X.-R.; Lin, Y.; Wang, C.; Wai, C. M. *Adv. Mater.* **2003,** *15,* 316–319. doi:10.1002/adma.200390077
41. Elías, A. L.; Rodríguez-Manzo, J. A.; McCartney, M. R.; Golberg, D.; Zamudio, A.; Baltazar, S. E.; López-Urías, F.; Muñoz-Sandoval, E.; Gu, L.; Tang, C. C.; Smith, D. J.; Bando, Y.; Terrones, H.; Terrones, M. *Nano Lett.* **2005,** *5,* 467–472. doi:10.1021/nl0479583
42. Gao, X. P.; Zhang, Y.; Chen, X.; Pan, G. L.; Yan, J.; Wu, F.; Yuan, H. T.; Song, D. Y. *Carbon* **2004,** *42,* 47–52. doi:10.1016/j.carbon.2003.09.015
43. Grandhe, B. K.; Bandi, V. R.; Jang, K.; Kim, S. S.; Shin, D.-S.; Lee, Y.; Lim, J.-M.; Song, T. *Met. Mater. Int.* **2013,** *19,* 507–511. doi:10.1007/s12540-013-3019-5
44. Ajayan, P. M.; Stephan, O.; Redlich, P.; Colliex, C. *Nature* **1995,** *375,* 564–567. doi:10.1038/375564a0

45. Rodríguez-Manzo, J. A.; Banhart, F.; Terrones, M.; Terrones, H.; Grobert, N.; Ajayan, P. M.; Sumpter, B. G.; Meunier, V.; Wang, M.; Bando, Y.; Golberg, D. *Proc. Natl. Acad. Sci. U. S. A.* **2009,** *106,* 4591–4595. doi:10.1073/pnas.0900960106
46. Tang, D.-M.; Yin, L.-C.; Li, F.; Liu, C.; Yu, W.-J.; Hou, P.-X.; Wu, B.; Lee, Y.-H.; Ma, X.-L.; Cheng, H.-M. *Proc. Natl. Acad. Sci. U. S. A.* **2010,** *107,* 9055–9059. doi:10.1073/pnas.0914970107
47. Zhang, W.; Zhang, Z.; Zhang, Y. *Nanoscale Res. Lett.* **2011,** *6,* 555. doi:10.1186/1556-276X-6-555
48. Chen, M.-L.; He, Y.-J.; Chen, X.-W.; Wang, J.-H. *Langmuir* **2012,** *28,* 16469–16476. doi:10.1021/la303957y
49. Zhang, Y.; Bai, Y.; Yan, B. *Drug Discovery Today* **2010,** *15,* 428–435. doi:10.1016/j.drudis.2010.04.005
50. Ménard-Moyon, C.; Venturelli, E.; Fabbro, C.; Samorì, C.; Da Ros, T.; Kostarelos, K.; Prato, M.; Bianco, A. *Expert Opin. Drug Discovery* **2010,** *5,* 691–707. doi:10.1517/17460441.2010.490552
51. Reich, S.; Li, L.; Robertson, J. *Phys. Rev. B* **2005,** *72,* 165423. doi:10.1103/PhysRevB.72.165423
52. Ajayan, P. M.; Ebbesen, T. W.; Ichihashi, T.; Iljima, S.; Tanigaki, K.; Hiura, H. *Nature* **1993,** *362,* 522–525. doi:10.1038/362522a0
53. Tsang, S. C.; Chen, Y. K.; Harris, P. J. F.; Green, M. L. H. *Nature* **1994,** *372,* 159–162. doi:10.1038/372159a0
54. Sloan, J.; Hammer, J.; Zwiefka-Sibley, M.; Green, M. L. H. *Chem. Commun.* **1998,** 347–348. doi:10.1039/a707632k
55. Mathur, A.; Roy, S. S.; Hazra, K. S.; Wadhwa, S.; Ray, S. C.; Mitra, S. K.; Misra, D. S.; McLaughlin, J. A. *Mater. Chem. Phys.* **2012,** *134,* 425–429. doi:10.1016/j.matchemphys.2012.03.012
56. Holloway, A. F.; Toghill, K.; Wildgoose, G. G.; Compton, R. G.; Ward, M. A. H.; Tobias, G.; Llewellyn, S. A.; Ballesteros, B.; Green, M. L. H.; Crossley, A. *J. Phys. Chem. C* **2008,** *112,* 10389–10397. doi:10.1021/jp802127p
57. Yamada, Y.; Kimizuka, O.; Machida, K.; Suematsu, S.; Tamamitsu, K.; Saeki, S.; Yamada, Y.; Yoshizawa, N.; Tanaike, O.; Yamashita, J.; Don, F.; Hata, K.; Hatori, H. *Energy Fuels* **2010,** *24,* 3373–3377. doi:10.1021/ef9015203
58. Liu, J.; Rinzler, A. G.; Dai, H.; Hafner, J. H.; Bradley, R. K.; Boul, P. J.; Lu, A.; Iverson, T.; Shelimov, K.; Huffman, C. B.; Rodriguez-Macias, F.; Shon, Y.-S.; Lee, T. R.; Colbert, D. T.; Smalley, R. E. *Science* **1998,** *280,* 1253–1256. doi:10.1126/science.280.5367.1253
59. Hennrich, F.; Krupke, R.; Arnold, K.; Rojas Stütz, J. A.; Lebedkin, S.; Koch, T.; Schimmel, T.; Kappes, M. M. *J. Phys. Chem. B* **2007,** *111,* 1932–1937. doi:10.1021/jp065262n
60. Cambré, S.; Schoeters, B.; Luyckx, S.; Goovaerts, E.; Wenseleers, W. *Phys. Rev. Lett.* **2010,** *104,* 207401. doi:10.1103/PhysRevLett.104.207401
61. Wang, S.; Liang, Z.; Wang, B.; Zhang, C.; Rahman, Z. *Nanotechnology* **2007,** *18,* 055301. doi:10.1088/0957-4484/18/5/055301
62. Zhu, L.; Xiu, Y.; Hess, D. W.; Wong, C.-P. *Nano Lett.* **2005,** *5,* 2641–2645. doi:10.1021/nl051906b
63. Kyotani, T.; Tsai, L.-f.; Tomita, A. *Chem. Mater.* **1996,** *8,* 2109–2113. doi:10.1021/cm960063+
64. Kyotani, T.; Tsai, L.-f.; Tomita, A. *Chem. Mater.* **1995,** *7,* 1427–1428. doi:10.1021/cm00056a001
65. Hou, P.; Liu, C.; Shi, C.; Cheng, H. *Chin. Sci. Bull.* **2012,** *57,* 187–204. doi:10.1007/s11434-011-4892-2
66. Hou, P.-X.; Yu, W.-J.; Shi, C.; Zhang, L.-L.; Liu, C.; Tian, X.-J.; Dong, Z.-L.; Cheng, H.-M. *J. Mater. Chem.* **2012,** *22,* 15221–15226. doi:10.1039/c2jm31680c
67. Maschmann, M. R.; Franklin, A. D.; Amama, P. B.; Zakharov, D. N.; Stach, E. A.; Sands, T. D.; Fisher, T. S. *Nanotechnology* **2006,** *17,* 3925–3929. doi:10.1088/0957-4484/17/15/052
68. Kasi, J. K.; Kasi, A. K.; Wongwiriyapan, W.; Afzulpurkar, N.; Dulyaseree, P.; Hasan, M.; Tuantranont, A. *Adv. Mater. Res.* **2012,** *557–559,* 544–549. doi:10.4028/www.scientific.net/AMR.557-559.544
69. Lee, J. S.; Gu, G. H.; Kim, H.; Jeong, K. S.; Bae, J.; Suh, J. S. *Chem. Mater.* **2001,** *13,* 2387–2391. doi:10.1021/cm0014076
70. Capobianchi, A.; Foglia, S.; Imperatori, P.; Notargiacomo, A.; Giammatteo, M.; Del Buono, T.; Palange, E. *Carbon* **2007,** *45,* 2205–2208. doi:10.1016/j.carbon.2007.06.050
71. Du, D.; Wang, M.; Qin, Y.; Lin, Y. *J. Mater. Chem.* **2010,** *20,* 1532–1537. doi:10.1039/b919500a
72. Samant, K. M.; Chaudhari, V. R.; Kapoor, S.; Haram, S. K. *Carbon* **2007,** *45,* 2126–2129. doi:10.1016/j.carbon.2007.06.020
73. Wang, X.-H.; Orikasa, H.; Inokuma, N.; Yang, Q.-H.; Hou, P.-X.; Oshima, H.; Itoh, K.; Kyotani, T. *J. Mater. Chem.* **2007,** *17,* 986–991. doi:10.1039/b614300h
74. Babu, S.; Ndungu, P.; Bradley, J.-C.; Rossi, M. P.; Gogotsi, Y. *Microfluid. Nanofluid.* **2005,** *1,* 284–288. doi:10.1007/s10404-005-0037-8
75. Mitchell, R. R.; Gallant, B. M.; Thompson, C. V.; Shao-Horn, Y. *Energy Environ. Sci.* **2011,** *4,* 2952–2958. doi:10.1039/c1ee01496j
76. Guo, D. J.; Li, H. L. *Carbon* **2005,** *43,* 1259–1264. doi:10.1016/j.carbon.2004.12.021
77. Metz, K. M.; Colavita, P. E.; Tse, K.-Y.; Hamers, R. J. *J. Power Sources* **2012,** *198,* 393–401. doi:10.1016/j.jpowsour.2011.09.098
78. Balan, B. K.; Unni, S. M.; Kurungot, S. *J. Phys. Chem. C* **2009,** *113,* 17572–17578. doi:10.1021/jp9042655
79. Wang, J.-G.; Yang, Y.; Huang, Z.-H.; Kang, F. *Electrochim. Acta* **2011,** *56,* 9240–9247. doi:10.1016/j.electacta.2011.07.140
80. Nitze, F.; Mazurkiewicz, M.; Malolepszy, A.; Mikolajczuk, A.; Kędzierzawski, P.; Tai, C.-W.; Hu, G.; Kurzydłowski, K. J.; Stobinski, L.; Borodzinski, A.; Wågberg, T. *Electrochim. Acta* **2012,** *63,* 323–328. doi:10.1016/j.electacta.2011.12.104
81. Sears, K.; Dumée, L.; Schütz, J.; She, M.; Huynh, C.; Hawkins, S.; Duke, M.; Gray, S. *Materials* **2010,** *3,* 127–149. doi:10.3390/ma3010127
82. Srivastava, A.; Srivastava, O. N.; Talapatra, S.; Vajtai, R.; Ajayan, P. M. *Nat. Mater.* **2004,** *3,* 610–614. doi:10.1038/nmat1192
83. Liang, H.-W.; Wang, L.; Chen, P.-Y.; Lin, H.-T.; Chen, L.-F.; He, D.; Yu, S.-H. *Adv. Mater.* **2010,** *22,* 4691–4695. doi:10.1002/adma.201001863
84. Majumder, M.; Chopra, N.; Hinds, B. J. *J. Am. Chem. Soc.* **2005,** *127,* 9062–9070. doi:10.1021/ja043013b
85. Corry, B. *Energy Environ. Sci.* **2011,** *4,* 751–759. doi:10.1039/c0ee00481b
86. Peng, K.; Liu, L.-Q.; Li, H.; Meyer, H.; Zhang, Z. *Carbon* **2011,** *49,* 70–76. doi:10.1016/j.carbon.2010.08.043
87. Whitby, M.; Quirke, N. *Nat. Nanotechnol.* **2007,** *2,* 87–94. doi:10.1038/nnano.2006.175
88. Mezgebe, M.; Jiang, L.-H.; Shen, Q.; Du, C.; Yu, H.-R. *Colloids Surf., A* **2012,** *415,* 86–90. doi:10.1016/j.colsurfa.2012.09.046
89. Ajayan, P. M.; Lijima, S. *Nature* **1993,** *361,* 333–334. doi:10.1038/361333a0
90. Hilder, T. A.; Hill, J. M. *Small* **2009,** *5,* 300–308. doi:10.1002/smll.200800321
91. Dhondi, S.; Pereira, G. G.; Hendy, S. C. *Langmuir* **2012,** *28,* 10256–10265. doi:10.1021/la300903w

92. Zou, R.; Zhang, Z.; Liu, Q.; Xu, K.; Lu, A.; Hu, J.; Li, Q.; Bando, Y.; Golberg, D. *Adv. Mater.* **2013,** *25,* 2693–2699. doi:10.1002/adma.201300257
93. Schebarchov, D.; Hendy, S. C. *Nano Lett.* **2008,** *8,* 2253–2257. doi:10.1021/nl080875s
94. Schebarchov, D.; Lefèvre, B.; Somerville, W. R. C.; Hendy, S. C. *Nanoscale* **2013,** *5,* 1949–1954. doi:10.1039/c3nr32649g
95. Edgar, K.; Hendy, S. C.; Schebarchov, D.; Tilley, R. D. *Small* **2011,** *7,* 737–740. doi:10.1002/smll.201001857
96. Nguyen, T. T.; Serp, P. *ChemCatChem* **2013,** *5,* 3595–3603. doi:10.1002/cctc.201300527
97. Rodríguez-Manzo, J. A.; Terrones, M.; Terrones, H.; Kroto, H. W.; Sun, L.; Banhart, F. *Nat. Nanotechnol.* **2007,** *2,* 307–311. doi:10.1038/nnano.2007.107
98. Sauer, M.; Shiozawa, H.; Ayala, P.; Ruiz-Soria, G.; Kataura, H.; Yanagi, K.; Krause, S.; Pichler, T. *Phys. Status Solidi B* **2012,** *249,* 2408–2411. doi:10.1002/pssb.201200127
99. Du, G.; Li, W.; Liu, Y. *J. Phys. Chem. C* **2008,** *112,* 1890–1895. doi:10.1021/jp710543u
100. Kiang, C.-H.; Choi, J.-S.; Tran, T. T.; Bacher, A. D. *J. Phys. Chem. B* **1999,** *103,* 7449–7451. doi:10.1021/jp991424m
101. Zhang, H.; Pan, X.; Bao, X. *J. Energy Chem.* **2013,** *22,* 251–256. doi:10.1016/S2095-4956(13)60031-5
102. Botka, B.; Füstös, M. E.; Tóháti, H. M.; Németh, K.; Klupp, G.; Szekrényes, Z.; Kocsis, D.; Utczás, M.; Székely, E.; Váczi, T.; Tarczay, G.; Hackl, R.; Chamberlain, T. W.; Khlobystov, A. N.; Kamarás, K. *Small* **2014,** *10,* 1369–1378. doi:10.1002/smll.201302613
103. Botka, B.; Füstös, M. E.; Klupp, G.; Kocsis, D.; Székely, E.; Utczás, M.; Simándi, B.; Botos, Á.; Hackl, R.; Kamarás, K. *Phys. Status Solidi B* **2012,** *249,* 2432–2435. doi:10.1002/pssb.201200349
104. Zhang, J.; Feng, Y.; Ishiwata, H.; Miyata, Y.; Kitaura, R.; Dahl, J. E. P.; Carlson, R. M. K.; Shinohara, H.; Tománek, D. *ACS Nano* **2012,** *6,* 8674–8683. doi:10.1021/nn303461q
105. Bera, D.; Kuiry, S. C.; McCutchen, M.; Seal, S.; Heinrich, H.; Slane, G. C. *J. Appl. Phys.* **2004,** *96,* 5152. doi:10.1063/1.1786347
106. Seal, S.; Bera, D.; Kuiry, S. C.; Meyyappan, M.; McCutchen, M. L. In-situ synthesis of carbon nanotubes filled with metallic nanoparticles using arc discharge in solution. U.S. Pat. Appl. 7,968,072, June 28, 2011.
107. Li, L.; Chen, M.; Huang, G.; Yang, N.; Zhang, L.; Wang, H.; Liu, Y.; Wang, W.; Gao, J. *J. Power Sources* **2014,** *263,* 13–21. doi:10.1016/j.jpowsour.2014.04.021
108. Tsierkezos, N. G.; Szroeder, P.; Fuge, R.; Ritter, U. *Ionics* **2014**. doi:10.1007/s11581-014-1277-y
109. Liu, H.; Zhang, Y.; Li, R.; Sun, X.; Abou-Rachid, H. *J. Nanopart. Res.* **2012,** *14,* 1016. doi:10.1007/s11051-012-1016-0
110. Liu, H.; Zhang, Y.; Li, R.; Sun, X.; Désilets, S.; Abou-Rachid, H.; Jaidann, M.; Lussier, L.-S. *Carbon* **2010,** *48,* 1498–1507. doi:10.1016/j.carbon.2009.12.045
111. Ćirić-Marjanović, G.; Pašti, I.; Mentus, S. *Prog. Mater. Sci.* **2015,** *69,* 61–182. doi:10.1016/j.pmatsci.2014.08.002
112. Maser, W. K.; Lambert, J. M.; Ajayan, P. M.; Stephan, O.; Bernier, P. *Synth. Met.* **1996,** *77,* 243–247. doi:10.1016/0379-6779(96)80096-8
113. Demoncy, N.; Stéphan, O.; Brun, N.; Colliex, C.; Loiseau, A.; Pascard, H. *Eur. Phys. J. B* **1998,** *4,* 147–157. doi:10.1007/s100510050363
114. Zheng, G.; Yang, Y.; Cha, J. J.; Hong, S. S.; Cui, Y. *Nano Lett.* **2011,** *11,* 4462–4467. doi:10.1021/nl2027684
115. Bao, J.; Tie, C.; Xu, Z.; Suo, Z.; Zhou, Q.; Hong, J. *Adv. Mater.* **2002,** *14,* 1483–1486. doi:10.1002/1521-4095(20021016)14:20<1483::AID-ADMA1483>3.0.CO;2-6
116. Jeong, N.; Hwang, K. S.; Yang, S.; Lee, S.-p. *Mater. Charact.* **2014,** *89,* 69–80. doi:10.1016/j.matchar.2013.12.016
117. Smith, B. R.; Ghosn, E. E. B.; Rallapalli, H.; Prescher, J.; Larson, T.; Herzenberg, L.; Gambhir, S. S. *Nat. Nanotechnol.* **2014,** *9,* 481–487. doi:10.1038/nnano.2014.62
118. Singh, R. K.; Patel, K. D.; Kim, J.-J.; Kim, T.-H.; Kim, J.-H.; Shin, U. S.; Lee, E.-J.; Knowles, J. C.; Kim, H.-W. *ACS Appl. Mater. Interfaces* **2014,** *6,* 2201–2208. doi:10.1021/am4056936
119. Goenka, S.; Sant, V.; Sant, S. *J. Controlled Release* **2014,** *173,* 75–88. doi:10.1016/j.jconrel.2013.10.017
120. Xu, T.; Xie, X.; Yin, K.; Sun, J.; He, L.; Sun, L. *Small* **2014,** *10,* 1724–1728. doi:10.1002/smll.201303377
121. Deshpande, H. D.; Dean, D. R.; Thomas, V.; Clem, W. C.; Jose, M. V.; Nyairo, E.; Mishra, M. *Curr. Nanosci.* **2012,** *8,* 753–761. doi:10.2174/157341312802884409
122. Sanoj, P.; Kandasubramanian, B. *J. Compos.* **2014,** *2014,* 1–15. doi:10.1155/2014/825607
123. Thomassin, J.-M.; Jérôme, C.; Pardoen, T.; Bailly, C.; Huynen, I.; Detrembleur, C. *Mater. Sci. Eng., R* **2013,** *74,* 211–232. doi:10.1016/j.mser.2013.06.001
124. Aldalbahi, A.; in het Panhuis, M. *Carbon* **2012,** *50,* 1197–1208. doi:10.1016/j.carbon.2011.10.034
125. Balan, B. K.; Kale, V. S.; Aher, P. P.; Shelke, M. V.; Pillai, V. K.; Kurungot, S. *Chem. Commun.* **2010,** *46,* 5590–5592. doi:10.1039/c0cc00571a
126. Baaziz, W.; Begin-Colin, S.; Pichon, B. P.; Florea, I.; Ersen, O.; Zafeiratos, S.; Barbosa, R.; Begin, D.; Pham-Huu, C. *Chem. Mater.* **2012,** *24,* 1549–1551. doi:10.1021/cm300293b
127. Zhang, G.; Lou, X. W. *Sci. Rep.* **2013,** *3,* No. 1470. doi:10.1038/srep01470
128. De Jong, K. P.; Geus, J. W. *Catal. Rev.: Sci. Eng.* **2000,** *42,* 481–510. doi:10.1081/CR-100101954

License and Terms

This is an Open Access article under the terms of the Creative Commons Attribution License (http://creativecommons.org/licenses/by/2.0), which permits unrestricted use, distribution, and reproduction in any medium, provided the original work is properly cited.

The license is subject to the *Beilstein Journal of Nanotechnology* terms and conditions: (http://www.beilstein-journals.org/bjnano)

The definitive version of this article is the electronic one which can be found at: doi:10.3762/bjnano.6.53

BEILSTEIN JOURNAL OF NANOTECHNOLOGY

Chains of carbon atoms: A vision or a new nanomaterial?

Florian Banhart

Review

Open Access

Address:
Institut de Physique et Chimie des Matériaux de Strasbourg, UMR 7504 CNRS, University of Strasbourg, 23 rue du Loess, 67034 Strasbourg, France

Email:
Florian Banhart - Florian.Banhart@ipcms.unistra.fr

Keywords:
atom chains; carbon; carbyne; one-dimensional solids; sp^1 hybridization

Beilstein J. Nanotechnol. **2015,** *6,* 559–569.
doi:10.3762/bjnano.6.58

Received: 26 June 2014
Accepted: 02 February 2015
Published: 25 February 2015

This article is part of the Thematic Series "Atomic scale interface design and characterisation: Theory – Structure and dynamics".

Guest Editor: C. Ewels

© 2015 Banhart; licensee Beilstein-Institut.
License and terms: see end of document.

Abstract

Linear strings of sp^1-hybridized carbon atoms are considered as a possible phase of carbon since decades. Whereas the debate about the stability of the corresponding bulk phase carbyne continues until today, the existence of isolated chains of carbon atoms has meanwhile been corroborated experimentally. Since graphene, as the two-dimensional sp^2-bonded allotrope of carbon, has become a vast field, the question about the importance of one-dimensional carbon became of renewed interest. The present article gives an overview of the work that has been carried out on chains of carbon atoms in the past one or two decades. The review concentrates on isolated chains of carbon atoms and summarizes the experimental observations to date. While the experimental information is still very limited, many calculations of the physical and chemical properties have been published in the past years. Some of the most important theoretical studies and their importance in the present experimental situation are reviewed.

Introduction

Carbon is a unique element due to its ability to form bonds in three different hybridizations. The hybridizations, sp^1, sp^2, and sp^3, correspond to bonding geometries in one-, two-, and three-dimensional space. Accordingly, the modifications of carbon have completely different appearance. The sp^2- and sp^3-bonded modifications, graphite and diamond, are known since ancient times, however it took until the beginning of the 21st century until the synthesis and investigation of graphene, as the two-dimensional modification of carbon, became possible. Graphene has meanwhile evolved into a field of unprecedented activity in physics, chemistry, and materials research. Many of the unique and most interesting properties of graphene were found to originate from its two-dimensional nature. While extensive knowledge exists about the two- and three-dimensional allotropes of carbon, the sp^1-hybridized one-dimensional modification [1] remains elusive. Although carbon chains have already been proposed by Tammann in 1921 [2], it is still not clear if sp^1-hybridized carbon in a pure bulk form is chemically stable [3-5]. It is certain, however, that it is very reactive and it is possible that it is even explosive [6]. Some effort has been

devoted to the synthesis and investigation of this phase, called carbyne or linear acetylenic carbon [7,8]. Attempts have been undertaken to synthesize this modification by using chemical techniques that stabilize the ends of the chains with nonreactive groups [9-11]. The synthesis of carbyne in its pure form, i.e., without end groups, turned out to be much more challenging and has been carried out, e.g., by cluster beam deposition [12,13].

It has even been proposed that carbyne could be the stable phase of carbon in a certain temperature-pressure regime, leading to its appearance in the phase diagram of carbon at very high temperatures [3]. Indications for natural carbynes have been reported in shock-compressed graphite in an impact crater [14], in meteorites [15], and by spectroscopic information from interstellar molecules [16,17]. However, the debate about the existence of carbyne at ambient conditions continues until today [6]. Nevertheless, it is undisputed that carbyne represents an exceptional state among the other modifications of carbon and will, most likely, never become available as a standard bulk material like graphite or diamond.

In the same way as graphite is composed of stacked sheets of graphene, carbyne is considered as an arrangement of linear chains of carbon atoms. The chains are therefore the elementary building blocks of sp^1-hybridized carbon and the only real one-dimensional carbon phase (carbon nanotubes have often been denoted as one-dimensional carbon, however, they are cylinders and their properties depend strongly on the atomic arrangement in the two other dimensions). Like graphene sheets that can be rolled up in cylinders to form nanotubes, chains might also close their ends by forming atomic rings [18]. It has been recognized that chains of carbon atoms are not only remarkable (macro-)molecules; they may also have most interesting properties [19]. Two isomeric bonding types, involving either alternating single-triple bonds or only double bonds, lead to a variety of electrical properties, ranging from semiconducting to metallic. Furthermore, the strong covalent σ-bonds raise expectations of exceptional mechanical strength.

Producing isolated chains of carbon atoms has remained a challenge for a long time, due to the difficulties in their synthesis and characterization. It is clear that only techniques allowing imaging with atomic resolution would give reliable information about the existence of carbon chains. A few years ago, the first electron microscopy images of carbon chains appeared [20-22]. This gave the field a new impetus; in particular since a new generation of transmission electron microscopes (TEM) with improved spatial resolution became available. Most recently, the integration of scanning tunneling microscopy tips into the specimen stages of TEMs allowed the first electrical characterization [23] and therefore a more detailed investigation of carbon chains. The study of the electrical conductivity has been motivated by measurements on chains of metal atoms that showed quantized conductance [24].

Carbon chains have been subject of numerous theoretical studies since more than a decade. Calculations are facilitated by the fact that chains consist of typically 10 atoms only and constitute very small systems as compared to two- or three-dimensional nanomaterials. Of high importance, however, is the nature of the contacts at the ends of the chains. The mechanical and electrical properties of carbon chains have been calculated long before they became accessible to experimental observation (quantitative experimental information about the mechanical properties is still lacking). However, several difficulties in the modeling of chains appeared that made their simulation quite laborious.

Bulk carbyne with its unclear stability and chemistry will not be discussed in detail in this review. Instead, we will focus on isolated chains of carbon atoms as the elementary building blocks of sp^1-hybridized carbon. We will not address the interaction between different chains (although this interaction is important in a bulk solid) and, hence, study the interesting properties of linear arrangements of carbon atoms.

Review

The model of linear sp^1-hybridized carbon

Linear sp^1-hybridized carbon already results from the logical reduction of dimensions in carbon materials. Due to the similarity with the bonding characteristics in alkynes, in particular acetylene, the structure of sp^1-hybridized carbon is addressed in many textbooks of chemistry although carbyne is not a standard phase of carbon like graphite or diamond. Two extreme cases for the electronic structure can be imagined, namely cumulene with double bonds throughout the chain (=C=C=C=C=) and polyyne with alternating single and triple bonds (-C≡C-C≡C-). Cumulene has a uniform distribution of the π-electrons along the chain, leading to metallic conductivity. In polyyne, however, the π-electrons are localized at the shorter bonds so that the continuous distribution is interrupted at each single bond (Figure 1).

Carbon chains are, as a one-dimensional system, susceptible to Peierls distortion [25]. According to Peierls' theorem, the electron system of a perfectly one-dimensional crystal is unstable. The atomic periodicity is broken in such a way that the elementary period of the undistorted chain a is doubled to $2a$. The calculated length of the double bond in cumulene is 1.282 Å; the single and triple bond lengths in polyyne are 1.265 Å and 1.301 Å, respectively [26]. The alternating shorter and longer

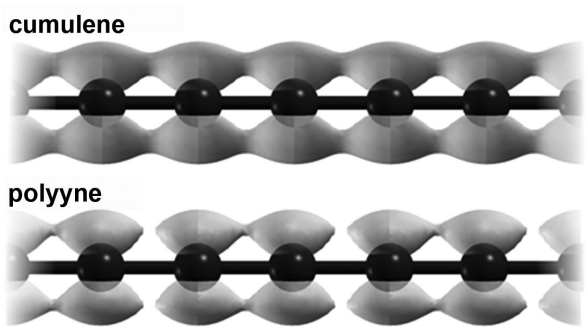

Figure 1: π-Electron distribution in cumulene (top) and polyyne (bottom). Calculation by A. Botello-Mendez and J.-C. Charlier. Reprinted with permission from [23]. Copyright 2013 American Chemical Society.

bonds in polyyne result in an electronic bandgap. The gain in electronic energy due to the formation of a bandgap outweighs the increase in strain energy [27]. However, the gain in energy of the (unstrained) polyyne structure is only 70 meV/atom [28]. This is a small difference in comparison to the total cohesive energy of the order of 7.0 eV/atom in a chain.

Long-range interactions in the electron system of carbon chains determine their properties [26]. The π-electrons of carbon chains can be considered as a one-dimensional system of free electrons. If one atom in the chain experiences a small displacement, the local perturbation of charge leads to oscillations of charge density and interatomic forces, extending over longer distances along the chain. Such Friedel oscillations in one-dimensional systems decay as $1/r$.

Experimental observations of carbon chains

The first experimental indication for the existence of carbon chains has been deduced from a study of field emission from carbon nanotubes [29,30]. The emission characteristics of open tube ends were not in accordance with the expected emission from a perfect tube. It was suspected that an unraveling of the tubes had taken place so that the electrons were emitted from dangling chains of carbon atoms. Unexplained features in the electrical characteristics of graphene [31] or in the conductivity of breaking nanotubes [32] as well as in the Raman spectra from heat-treated carbon nanotubes [33] have been attributed to the formation of carbon chains. However, no independent proof for the presence of atomic chains has been obtained.

Early indications for the existence of chains have also been obtained from electron microscopy images of carbon nanotubes. Sometimes an unexplained fringe in the interior of a tube has been taken as an indication for the presence of an atomic wire located on the axis of a tube [34]. Much clearer indications, however, came from the observation of double-wall carbon nanotubes where the disintegration of the inner shell led to very short chains in the axial direction between the vanishing peapod-like residues [35]. Quite convincing pictures from carbon chains were also obtained when single-wall carbon nanotubes shrank under electron irradiation [20,36]. Just before the hourglass-shaped tube broke, a linear fringe, bridging the conical tube ends, appeared in the images. The studies have been extended recently and give some indications for the interaction between neighbouring chains [37]. Indications for the appearance of short segments of chains migrating on graphene layers have also been found [38].

The first direct observations of the transformation from graphene to linear chains of carbon atoms have been reported in 2009 by Jin et al. [21] and Chuvilin et al. [22]. Both groups studied graphene monolayers by aberration-corrected high-resolution electron microscopy (Figure 2). The procedure has been quite simple: graphene membranes were irradiated with the electron beam that is used for imaging in the microscope. Sputtering of carbon atoms from the layers led to growing vacancies and holes. The phenomenon has been confirmed later [39,40]; in some experiments even two parallel chains were observed once a graphene ribbon has been thinned laterally to a certain minimum width. The narrowing graphene ribbons between two holes ended in atomic chains as the smallest

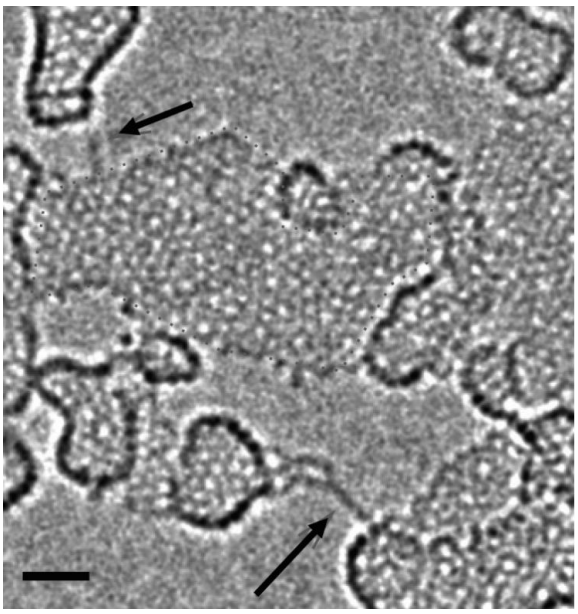

Figure 2: Electron microscopy image of carbon chains (arrowed). The carbon chains span between aggregates on top of a graphene layer (the contrast from the graphene lattice has been removed from the image by Fourier filtering). The scale bar is 1 nm. Courtesy of U. Kaiser, reprinted with permission from [22]. Copyright 2009 IOP publishing & Deutsche Physikalische Gesellschaft.

possible bridges between neighbouring graphene areas. The chains had lifetimes of a few seconds under the electron beam until they ruptured. This was an unexpected observation, given the high stability of graphene. Why should not graphene ribbons just disintegrate or fold back to the neighboring graphene layers? This was the first indication that atomic chains are more stable than narrow graphene ribbons, at least under an electron beam.

Phase contrast images taken by TEM are often difficult to interpret; it is easy to mix up chains with graphene ribbons in side view. In this context, not all published images from carbon chains might be unambiguous. Despite some efforts, the atoms in chains have not been clearly resolved by TEM although aberration-corrected microscopes should have the necessary resolution power. Besides the contrast problem (single carbon atoms are rather weak electron scatterers), the vibration of the chain under the electron beam makes atomic resolution difficult. Therefore, the atoms in a chain could not be counted reliably until now; the measurement of the bond length and the question whether cumulene or polyyne has been observed is still unanswered although some indications have been given [37]. Since TEM only gives projections of the chains onto a screen and the chains may be curved or aligned randomly, not even the length of the chains could be measured with high accuracy.

Another electron microscopy experiment allowed not only the generation of carbon chains but also their electrical characterization [23]. By contacting a graphitic aggregate with a transition metal tip and passing an electrical current through the junction, carbon chains could be unraveled from the graphitic materials when the tip was retracted (Figure 3). The experiment was carried out under the electron beam in the microscope; therefore electron irradiation might have played a certain role during the formation of chains. Once the chains were created, current-voltage characteristics were taken. The conductivity of the chains was much lower than predicted from theoretical work. By applying a voltage of 1 V, currents of typically less than 10 nA were measured.

As mentioned above, Peierls distortion is an important effect that favours the electronic structure of polyyne. If tensile strain is induced by an external force, it is clear that the weaker single bonds will stretch by a larger amount than the stronger triple bonds. Therefore, strain has a considerable influence on the conductivity of chains [23,26,28,41]. Increasing strain leads to a decreasing π-electron density over the longer single bonds. This, in turn, hinders the electron transfer over the single bonds and opens the bandgap. Simulations show that a strain of 10% leads to a bandgap of 1.5–3.0 eV, depending on the approximation (DFT, GW) [19,23].

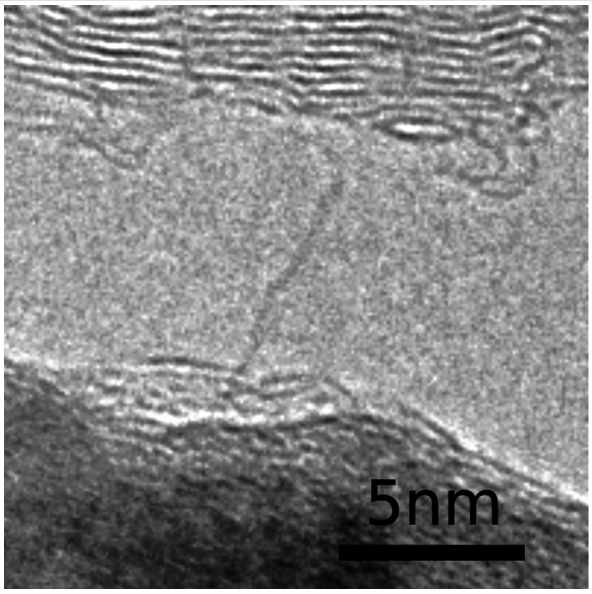

Figure 3: A carbon chain spanning between an iron crystal (bottom) and a graphitic aggregate (top). Both act as electrodes so that the electrical properties of the chain can be measured. Reprinted with permission from [23]. Copyright 2013 American Chemical Society.

The electrical properties of chains can only be measured by contacts through single atoms. The bonding characteristics at this particular point are of paramount importance. One single bond will have a decisive influence on the transport. At the contact between a chain and a metal, the delocalization of the conduction electrons and their overlap with the π-electrons of the chain could lead to an ohmic contact with low resistivity. Contacts with graphene or other sp^2 carbon structures, on the other hand, can be quite different, depending on a local sp^2 or sp^3 character at the junction. In the case of local sp^3 bonding, the π-electron density would be low at the contact and make the electron transfer difficult.

The measured current–voltage characteristics show, for most chains, an S-type behaviour (Figure 4). This is characteristic of the existence of a bandgap. In view of the preferred configuration of polyyne and possible strain, the current–voltage curves are qualitatively understandable.

A conductance measurement on a related system has been carried out by STM [42]. Oligoynes functionalized with anchor groups have been contacted by an STM tip, in part in solution. However, it is unclear whether individual monoatomic chains without side-links to other molecules have been present between the anchors and served as conductivity-limiting molecular junctions.

The predicted outstanding mechanical properties of carbon chains still have to be confirmed experimentally. Preliminary

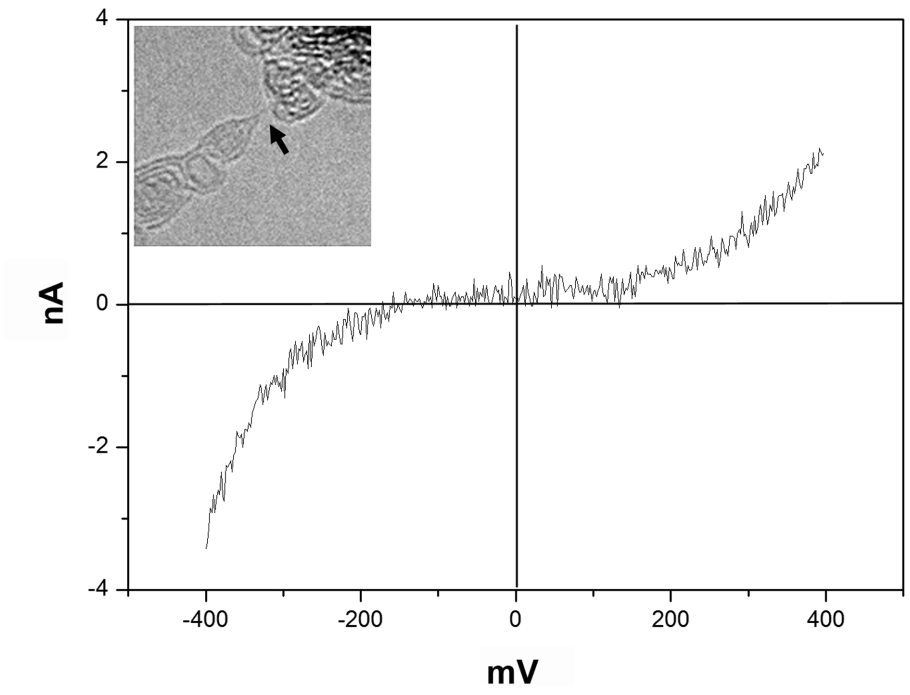

Figure 4: Measured current–voltage characteristic of a carbon chain (measurements by A. La Torre). A TEM image of the chain is shown in the inset.

results show qualitatively that chains have a high tensile stability against rupture. After the formation of chains between two contacts in the above-described procedure [23], the rupture of the chains after a few seconds of observation is often accompanied by a visible rebounding of the contacts. Since the system is under stress while one contact is retracted, the jumping of the contacts upon rupture of the chain is a convincing proof for a certain strength of the chains. If the elastic properties of the contacts were known or the forces could be measured, the ultimate strength of carbon chains could be determined quantitatively.

Theoretical work on carbon chains

Due to the difficulties in the synthesis of these elusive atomic-scale objects, the last decade has only seen few experimental reports about carbon chains. On the other hand, there is no lack of theoretical work. Since carbon chains are typically just ten-atom systems, the computational effort seemed in the first instance to be moderate. However, several unexpected difficulties in conventional computation schemes such as density functional theory (DFT) occurred, leading to the application of more sophisticated and, accordingly, more computationally intensive techniques of simulation. While DFT gave correct calculations of lattice constants and energies, the bandgaps have been considerably underestimated. Many-body perturbation theory (MBPT) in the GW approximation including electron–electron interactions resulted in more accurate calculations. Without discussing the applicability and reliability of different computational techniques, a short overview of some predicted properties of carbon chains will be given in this chapter.

Electrical properties

Due to the continuous overlap of the π-electrons along the chain, cumulene is metallic. Two degenerate half-filled p_x and p_y bands cross the Fermi level of cumulene that shows a quantum ballistic conductance of $4e^2/h$. In polyyne, however, the unit cell is doubled by the difference in length of the alternating bonds. This leads to a bandgap of 0.32 eV at the edge of the Brillouin zone, lowering the total energy per atom by 2 meV. The electrical current flowing through a chain is expected to be axially symmetric with vanishing current on the axis where the non-conducting σ-electrons are localized. The conducting π-electrons carry the current with a maximum in a bulge at about 1 Å from the axis [19].

Although the chains should theoretically have a high conductivity, experiments showed much lower values than predicted. Yuzvinsky et al. reported conductivities one order of magnitude lower than expected [32], but in this preliminary study the occurrence of the chains was just assumed. Later experiments, where the chains were clearly visible [23,43], showed still lower conductivities. Current–voltage curves are rather simple two-terminal measurements that give access to the electrical characteristics of carbon chains. Different behaviours have been

predicted, depending on the nature of the contacts and the number of atoms in the chain. Low-bias I–V curves should be linear whereas a negative differential resistance could occur at higher bias due to a shift of the conduction channels relative to the electronic states of the contact electrodes by the external bias [44,45]. The negative differential resistance has been proposed in order to explain an experimentally observed feature in the electrical characterization of breaking nanotubes [32].

Several computational studies predict that the electrical properties of chains with an even number of atoms are different from those with an odd number [46-49]. Generally, even-number chains should have a higher conductivity. In short chains, however, ballistic transport has only been predicted for chains with odd numbers of carbon atoms [49]. By considering cumulene chains between two metal electrodes, Lang and Avouris [46] have found that even-number chains have a lower density of states (DOS) at the Fermi level than odd-number chains. In free chains (no contacts), the highest occupied molecular orbital (HOMO) is half occupied if the chain has an even number and full occupied for an odd number of atoms. When the chains have metal contacts at their ends, however, the HOMO level of even chains is essentially full, leading to a low DOS at the Fermi energy whereas odd chains have a partially filled HOMO level. A high DOS at the Fermi level leads to a high conductance. Song et al. [48] have calculated the influence of even/odd number of atoms on the I–V characteristics of chains. Plateaus are found where the current becomes independent of bias for even chains whereas in odd chains the current increases monotonically with bias. Even chains should have a better conductivity at low bias whereas odd chains conduct more at high bias. The dimerization resulting from the Peierls distortion is assumed to be responsible for this behavior.

It is obvious that the nature of the contacts has a high influence on the electrical behavior of the system. The conductivity of a one-dimensional π-electron system with ideal contacts (transmission $T = 1$) would be $4e^2/h$. However, when the contacts are made of graphene, the characteristics are different from metal-chain systems. The transport at the contacts occurs through narrow resonant states in the chain, due to reflections at the interface to the contacts [50]. Close to the Fermi energy of perfect graphene, the transmission T decreases linearly with electron energy. The low transmission results from the vanishing of the DOS in undoped graphene. The reflection is high if the density of states in the contacting material at low energy is small. Another aspect is the local hybridization of the carbon atoms at the contact. A sp^3-hybridized carbon atom (e.g., when the chain is connected to the middle of a graphenic sheet or the wall of a carbon nanotube as shown in Figure 5) leads to a missing π-electron and, accordingly, to a reduced charge transfer. On the other hand, when the chain is attached to a graphene edge, the contact atom is sp^2-hybridized, allowing a continuous π-electron system over the contact and better conductivity. Therefore, the choice of sp^3 or sp^2 termination would allow switching the chain on and off [51].

The contact can also be considered in the context of doping since electrons can be transferred from the electrodes to the chain (charge transfer doping) [47], thus increasing the carrier density. The Fermi level of metallic contacts would be aligned to the LUMO of the carbon chain. Localized charge at the metal-chain contacts would also generate Schottky barriers. In contrast to conventional semiconductors, doping by introducing foreign atoms (donors or acceptors) into the chain would not be appropriate since these important perturbations would lead to electron localization.

It is well known that the electrical properties of graphene depend strongly on adsorbed species that might even act as dopants. A similar influence of attached atoms or molecules might occur in carbon chains since their conductivity is also

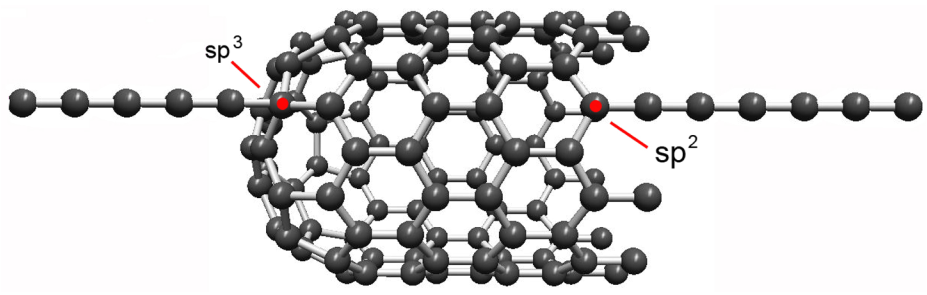

Figure 5: Different hybridization states of the end atoms of carbon chains when they are connected to a graphitic contact. The contact atoms are marked in red. As an example, chains are attached to the closed end of a carbon nanotube (left), leading to local sp^3-hybridization, and to an open end where the contact atom is sp^2-hybridized (right).

carried by the π-electron system. The influence of imperfections such as adsorbed impurities on the electrical properties of chains has been studied by Shen et al. [49]. If ballistic conductance occurs, adsorbed species such as hydrogen should have no influence. Oxygen impurities, on the other hand, are predicted to lower the conductivity of chains. Of particular experimental importance but not studied in detail yet would be the conductivity of a chain that is lying on a substrate.

For possible applications in devices, a rectifying behavior of the contact would be of interest. It has been suggested that changing the number of atoms by one (switching between odd and even number of atoms) can change the direction of rectification [52]. On the other hand, asymmetric contacts, e.g., different metals or a metal and a carbon contact at the two ends of the chain, should lead to rectification. It has also been proposed that switching might be possible when chains are terminated by five-membered carbon rings and exposed to strain [40].

Of further interest is spin transport that has been predicted by Zanolli et al. for carbon chains with covalent bonds to graphene ribbons [53]. Chains with odd number of atoms should carry such a spin polarization whether they are metallic or semiconducting (depending on the edge of the graphene ribbon at the contact). Hence, carbon chains connected to graphene ribbons could be used as spin polarized semiconductors. While Zanolli et al. did not obtain a magnetic moment on even-number chains, a triplet state appeared in even-number chains upon twisting by 90 degrees [28]. It has already been predicted in 1972 that twisted odd- or even-number chains have a triplet ground state [54].

Mechanical properties

Motivated by the outstanding mechanical properties of graphene, the response of carbon chains to stress, bending, or torsion has been addressed in several theoretical studies. Quantitative experimental information, however, is still lacking. The ultimate tensile strength (fracture) of a chain has been predicted to be of the order 10^{-8} N [19,55] whereas it is approximately 40 N/m in graphene [56]. Liu et al. [19] have related the fracture strength to a specific strength of carbon chains of 6.0–7.5 × 10^7 Nm/kg which would be the highest of all known materials.

A Young's modulus of 3.3 × 10^{13} Pa has been calculated [19] which is much higher than for graphene (approx. 10^{12} Pa). In sp^2 networks like graphene or carbon nanotubes, the hexagons are able to elongate in the direction of strain and contract in the normal direction. In that case, the bond angles change but not the bond lengths. In carbon chains, however, the bonds are loaded along their alignment and strained which needs a much higher force. Carbon chains could thus be considered as the stiffest known material. This is supported by the specific stiffness, which for carbyne is predicted to be 10^9 Nm/kg [19], clearly larger than for graphene (4.5 × 10^8 Nm/kg [56]) or diamond (3.5 × 10^8 Nm/kg [57]). The ultimate tensile strength corresponds to an ultimate strain of the order of 15% (graphene can be strained up to 20%). Liu et al. have also calculated a bending stiffness K= 3.56 eV·Å. This can be related to a persistence length $l_p = K/k_BT$ = 14 nm (corresponding to a chain of 110 atoms) at T = 300 K which is comparable to many polymers. Taking into account that different values for the thickness of carbon chains have been assumed, quite similar values have been found by other authors [58,59].

The high ultimate strength of carbon chains is reflected in the simulation of fracture of graphene-like networks under mechanical stress. Before a graphene ribbon breaks, carbon chains appear at the breaking edge as the ultimate junctions before rupture [60]. Even the behavior under twist has been calculated [19,51]. However, this is only applicable when rotationally non-symmetric groups are added to the ends of the chain (a chain is perfectly symmetric under rotation so that a twist is not defined). The chains can, for example, be stabilized by sp^3 or sp^2 end groups; the latter are sensitive to torsional strain [51].

Chains should also disintegrate in electric fields exceeding 4 × 10^{10} V/m [30]. This has already been discussed in the 1990s in the context of field emission from carbon nanotubes and the possible unraveling of carbon chains from their ends [29].

Chemical stability

The first question concerning the stability of chains is their energy in comparison to other carbon allotropes. It has been shown by calculations that carbon chains are energetically lower (more favourable) than extremely thin single-wall carbon nanotubes [5,61]. Indeed, no nanotubes with diameters below 4 Å have ever been observed. It has been shown by DFT calculations that an infinite chain is more favourable than an armchair (3,0) or zigzag (2,2) single-wall carbon nanotube [61]. The smallest experimentally identified carbon nanotube is the (3,3) nanotube with a diameter of 4 Å. The instability of extremely thin nanotubes is due to the increasing pyramidalization angle in small sp^2 structures, leading to an increasing sp^3 character of the bonds. The stability in comparison with narrow graphene ribbons will be discussed below in the context of defects and irradiation.

One of the most discussed properties of sp^1-hybridized carbon is its chemical stability. Two parallel chains develop cross-links; this is an exothermic reaction with an activation barrier of

0.6 eV. In the lowest energy configuration the chains would have cross-links every 2.2 nm (17 atoms) [19]. The formation of such cross-links, where local sp^2 hybridization occurs, is considered as the mechanism of degradation of carbyne [62].

An important question is whether isolated chains have a maximum length above which they become unstable. By electron microscopy observation, lengths up to 15–20 atoms have been found [21,23]. In other experiments, the synthesis of chains with lengths up to 44 atoms has been claimed [8]. It has become clear that the end termination has an important influence on the length of the chains. Linear chains of up to 28 atoms have been stabilized by nonreactive groups at the ends [10]. Hydrogen-terminated polyyne chains with lengths up to 20 atoms have already been synthesized [11,63]. The synthesis of the less stable cumulene appeared to be more difficult. Only short chains with two H atoms at each end have been found [64,65]. In a most recent study, carbon chains terminated with Pt atoms at their ends have been observed [66]. Chains might close their ends by forming rings. These have been proposed in several studies [67-69] but never seen. Carbon rings might be the ground state for carbon clusters with less than 20 atoms or precursors for the formation of more complex structures such as carbon nanotubes or fullerenes [18]. The rings might also consist of equal aromatic or alternated antiaromatic bonds.

Of current interest are also chemically related linear modifications, e.g., chains of B and N atoms that might have an even higher cohesive energy per unit cell than carbon chains [70]. A recent electron microscopy study shows the first observation of BN chains that formed under electron irradiation of BN layers [71]. These chains are predicted to be insulating with a bandgap comparable to two-dimensional BN. The Peierls theorem is therefore not applicable and no bond alternation is expected.

Formation and behaviour under electron irradiation

Carbon chains appear in the disintegration of both carbon nanotubes and graphene under electron irradiation. Apparently, the sputtering of carbon atoms from sp^2 materials favours the transformation to the sp^1 phase under certain conditions. Carbon atoms are displaced when the electron energy exceeds a certain threshold [72-74]. For perfect (infinite) graphene, the threshold energy of the electrons is around 80 keV [75]. Undercoordinated edge atoms can be sputtered off at lower energies although the edges tend to reconstruct [76]. The same holds for atoms next to unreconstructed vacancies. As for graphene, the displacement threshold for carbon chains should be highly asymmetric, being much higher on the axis than normal to it. Accordingly, atoms should be displaced normal to the chain. For carbon chains, the values have not been determined yet, neither experimentally nor theoretically. First experimental indications are the lifetimes of chains under the electron beam. Under typical conditions for electron microscopy observations (electron energy 200 keV, beam current density 10 A/cm^2), a displacement rate of 0.1/s is obtained under the assumption that the lifetime of the chains is limited by irradiation [23]. The ends of the chains are contacted by graphene or metals in this case.

The formation of chains under irradiation of graphene indicates that either the chains are energetically more stable than narrow graphene ribbons (resp. extremely thin tubes) [61] or that the atom displacement rate is smaller in chains. Jin et al. considered a ribbon that is thinned by the electron beam down to a line of hexagons that can be considered as two interlinked chains [21]. The calculated formation energy of a zigzag-terminated single-hexagon ribbon is 1.22 eV/Å which is higher than that of a carbon chain (0.76 eV/Å). The splitting of such a narrow graphene ribbon into two isolated chains would therefore be energetically favorable. The simulation of the breaking of graphene ribbons under irradiation shows the appearance of chains, bridging the gap between the separating ribbons for a short time (Figure 6) [76]. This occurs although the separation of a narrow graphene ribbon into two chains requires a high energy (18 eV/atom). A similar picture has been obtained in calculations of the fracture of strained graphene ribbons at grain boundaries [77]. Chains often appear as the last link between two separating grains. The kinetics of disintegration is also of importance as shown by Kotakoski et al. [76]. Carbon atoms from zigzag edges at a graphene ribbon are sputtered much

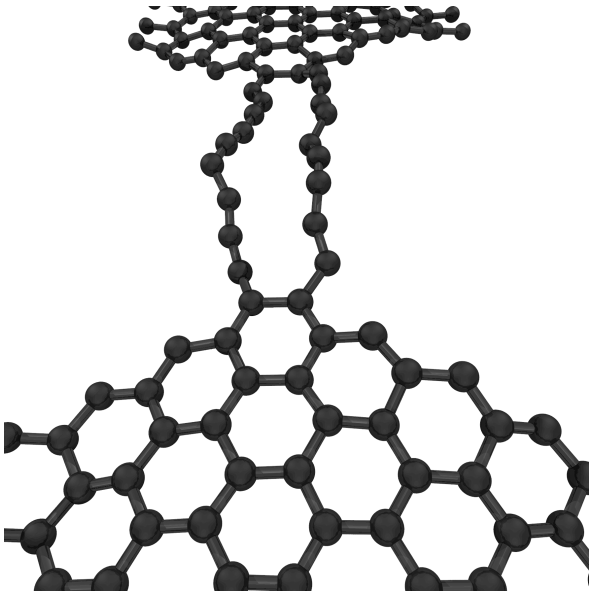

Figure 6: Formation of a pair of carbon chains during the breakage of a graphene ribbon under electron irradiation. The calculation shows the effect of continuous atom removal from a graphene sheet. Courtesy of J. Kotakoski.

faster than from armchair edges; the latter having almost the same stability under irradiation as bulk graphene. Exposing a square sheet of graphene to irradiation would lead to shrinkage from the zigzag edges until a chain of atoms is left.

Conclusion

The existence of sp^1-hybridized carbon has been secured experimentally and is undisputed. The high instability of bulk carbyne, however, due to cross-linking between chains of carbon atoms, made the availability of this material in bulk quantities and under ambient conditions very unlikely. The research concentrates therefore on isolated chains. Their outstanding mechanical and electronic properties, as theoretical work predicts, are still waiting for experimental confirmation. Preliminary experiments [23] do not confirm the predicted electrical conductivity. No experimental determination of the mechanical properties has been undertaken yet. The difficulty in all experiments is the production and handling of these atomic-size objects that appear to be highly reactive. Therefore, many questions remain open and need to be answered. It is not even clear if isolated chains are inherently unstable, e.g., above a certain length. It is clear, however, that the termination of the chains is crucial. End contacts transfer charge to the chains and determine the ultimate mechanical strength. Open chains react immediately with their environment or close by forming rings. Experimental efforts to synthesize longer chains have to be undertaken. The influence of end contacts as well as the stability of chains with a side contact, e.g., attached on a substrate, needs to be clarified.

In view of the predicted properties of carbon chains, the question arises if we can ever make use of their outstanding specifications. In many applications, bulk materials containing a large quantity of long chains would be needed. However, in nanoelectronic devices, working with single molecules or few-atom clusters, isolated chains of carbon atoms could find their applications in the future. In some respect, they might be superior to graphene ribbons whose properties depend strongly on the saturation of the edges. As we have seen from different electron microscopy studies, carbon chains are more stable than extremely narrow graphene ribbons. It could therefore be speculated that, once graphene comes to its limits, chains of carbon atoms become the building blocks in the ultimate miniaturization of carbon electronics. But even if this will never come, carbon chains will remain of interest as the textbook case of an extreme hybridization of the carbon atom.

Acknowledgements

The author is indebted to O. Cretu, A. La Torre, C. Pham-Huu, A. Botello-Mendez, and J.-C. Charlier for fruitful collaboration in the field of carbon chains. Financial support from the Agence Nationale de Recherche (grants NANOCONTACTS NT09 507527 and NANOCELLS ANR12 BS1000401) is gratefully acknowledged.

References

1. Heimann, R. B.; Evsyukov, S. E.; Kavan, L., Eds. *Carbyne and Carbynoid Structures;* Kluwer Acad. Publ.: Dordrecht, The Netherlands, 1999. doi:10.1007/978-94-011-4742-2
2. Tammann, G. *Z. Anorg. Allg. Chem.* **1921,** *115,* 145–158. doi:10.1002/zaac.19211150110
3. Greenville Whittaker, A. *Science* **1978,** *200,* 763–764. doi:10.1126/science.200.4343.763
4. Smith, P. P. K.; Buseck, P. R. *Science* **1982,** *216,* 984–986. doi:10.1126/science.216.4549.984
5. Kim, S. *Angew. Chem., Int. Ed.* **2009,** *48,* 7740–7743. doi:10.1002/anie.200904145
6. Baughman, R. H. *Science* **2006,** *312,* 1009–1010. doi:10.1126/science.1125999
7. Cataldo, F., Ed. *Polyynes: Synthesis, Properties, and Applications;* CRC Press: London, UK, 2005. doi:10.1201/9781420027587
8. Chalifoux, W. A.; Tykwinski, R. R. *Nat. Chem.* **2010,** *2,* 967–971. doi:10.1038/nchem.828
9. Kavan, L.; Kastner, J. *Carbon* **1994,** *32,* 1533–1536. doi:10.1016/0008-6223(94)90149-X
10. Lagow, R. J.; Kampa, J. J.; Wei, H.-C.; Battle, S. L.; Genge, J. W.; Laude, D. A.; Harper, C. J.; Bau, R.; Stevens, R. C.; Haw, J. F.; Munson, E. *Science* **1995,** *267,* 362–367. doi:10.1126/science.267.5196.362
11. Eisler, S.; Slepkov, A. D.; Elliott, E.; Luu, T.; McDonald, R.; Hegmann, F. A.; Tykwinski, R. R. *J. Am. Chem. Soc.* **2005,** *127,* 2666–2676. doi:10.1021/ja044526l
12. Ravagnan, L.; Siviero, F.; Lenardi, C.; Piseri, P.; Barborini, E.; Milani, P.; Casari, C. S.; Li Bassi, A.; Bottani, C. E. *Phys. Rev. Lett.* **2002,** *89,* 285506. doi:10.1103/PhysRevLett.89.285506
13. Ravagnan, L.; Piseri, P.; Bruzzi, M.; Miglio, S.; Bongiorno, G.; Baserga, A.; Casari, C. S.; Li Bassi, A.; Lenardi, C.; Yamaguchi, Y.; Wakabayashi, T.; Bottani, C. E.; Milani, P. *Phys. Rev. Lett.* **2007,** *98,* 216103. doi:10.1103/PhysRevLett.98.216103
14. Goresy, A. E.; Donnay, G. *Science* **1968,** *161,* 363–364. doi:10.1126/science.161.3839.363
15. Hayatsu, R.; Scott, R. G.; Studier, M. H.; Lewis, R. S.; Anders, E. *Science* **1980,** *209,* 1515–1518. doi:10.1126/science.209.4464.1515
16. Van Orden, A.; Saykally, R. J. *Chem. Rev.* **1998,** *98,* 2313–2358. doi:10.1021/cr970086n
17. Webster, A. *Mon. Not. R. Astron. Soc.* **1980,** *192,* 7–9. doi:10.1093/mnras/192.1.7P
18. Jones, R. O.; Seifert, G. *Phys. Rev. Lett.* **1997,** *79,* 443–446. doi:10.1103/PhysRevLett.79.443
19. Liu, M.; Artyukhov, V. I.; Lee, H.; Xu, F.; Yakobson, B. I. *ACS Nano* **2013,** *7,* 10075–10082. doi:10.1021/nn404177r
20. Troiani, H. E.; Miki-Yoshida, M.; Camacho-Bragado, G. A.; Marques, M. A. L.; Rubio, A.; Ascencio, J. A.; Jose-Yacaman, M. *Nano Lett.* **2003,** *3,* 751–755. doi:10.1021/nl0341640
21. Jin, C.; Lan, H.; Peng, L.; Suenaga, K.; Iijima, I. *Phys. Rev. Lett.* **2009,** *102,* 205501. doi:10.1103/PhysRevLett.102.205501
22. Chuvilin, A.; Meyer, J. C.; Algara-Siller, G.; Kaiser, U. *New J. Phys.* **2009,** *11,* 083019. doi:10.1088/1367-2630/11/8/083019

23. Cretu, O.; Botello-Mendez, A. R.; Janowska, I.; Pham-Huu, C.; Charlier, J.-C.; Banhart, F. *Nano Lett.* **2013,** *13,* 3487–3493. doi:10.1021/nl4018918
24. Ohnishi, H.; Kondo, Y.; Takayanagi, K. *Nature* **1998,** *395,* 780–783. doi:10.1038/27399
25. Peierls, R. E. *Quantum Theory of Solids;* Clarendon: Oxford, UK, 1964.
26. Cahangirov, S.; Topsakal, M.; Ciraci, S. *Phys. Rev. B: Condens. Matter Mater. Phys.* **2010,** *82,* 195444. doi:10.1103/PhysRevB.82.195444
27. Kertesz, M.; Koller, J.; Azman, A. *J. Chem. Phys.* **1978,** *68,* 2779–2782. doi:10.1063/1.436070
28. Artyukhov, V. I.; Liu, M.; Yakobson, B. I. *Nano Lett.* **2014,** *14,* 4224–4229. doi:10.1021/nl5017317
29. Rinzler, A. G.; Hafner, J. H.; Nikolaev, P.; Nordlander, P.; Colbert, D. T.; Smalley, R. E.; Lou, L.; Kim, S. G.; Tománek, D. *Science* **1995,** *269,* 1550–1553. doi:10.1126/science.269.5230.1550
30. Kim, S. G.; Lee, Y. H.; Nordlander, P.; Tománek, D. *Chem. Phys. Lett.* **1997,** *264,* 345–350. doi:10.1016/S0009-2614(96)01328-0
31. Standley, B.; Bao, W.; Zhang, H.; Bruck, J.; Lau, C. N.; Bockrath, M. *Nano Lett.* **2008,** *8,* 3345–3349. doi:10.1021/nl801774a
32. Yuzvinsky, T. D.; Mickelson, W.; Aloni, S.; Begtrup, G. E.; Kis, A.; Zettl, A. *Nano Lett.* **2006,** *6,* 2718–2722. doi:10.1021/nl061671j
33. Fantini, C.; Cruz, E.; Jorio, A.; Terrones, M.; Terrones, H.; Van Lier, G.; Charlier, J.-C.; Dresselhaus, M. S.; Saito, R.; Kim, Y. A.; Hayashi, T.; Muramatsu, H.; Endo, M.; Pimenta, M. A. *Phys. Rev. B: Condens. Matter Mater. Phys.* **2006,** *73,* 193408. doi:10.1103/PhysRevB.73.193408
34. Zhao, X.; Ando, Y.; Liu, Y.; Jinno, M.; Suzuki, T. *Phys. Rev. Lett.* **2003,** *90,* 187401. doi:10.1103/PhysRevLett.90.187401
35. Börrnert, F.; Börrnert, C.; Gorantla, S.; Liu, X.; Bachmatiuk, A.; Joswig, J.-O.; Wagner, F. R.; Schäffel, F.; Warner, J. H.; Schönfelder, R.; Rellinghaus, B.; Gemming, T.; Thomas, J.; Knupfer, M.; Büchner, B.; Rümmeli, M. H. *Phys. Rev. B* **2010,** *81,* 085439. doi:10.1103/PhysRevB.81.085439
36. Marques, M. A. L.; Troiani, H. E.; Miki-Yoshida, M.; Jose-Yacaman, M.; Rubio, A. *Nano Lett.* **2004,** *4,* 811–815. doi:10.1021/nl049839t
37. Casillas, G.; Mayoral, A.; Liu, M.; Ponce, A.; Artyukhov, V. I.; Yakobson, B. I.; Jose-Yacaman, M. *Carbon* **2014,** *66,* 436–441. doi:10.1016/j.carbon.2013.09.019
38. Meyer, J. C.; Girit, C. O.; Crommie, M. F.; Zettl, A. *Nature* **2008,** *454,* 319–322. doi:10.1038/nature07094
39. Song, B.; Schneider, G. F.; Xu, Q.; Pandraud, G.; Dekker, C.; Zandbergen, H. *Nano Lett.* **2011,** *11,* 2247–2250. doi:10.1021/nl200369r
40. Robertson, A. W.; Warner, J. H. *Nanoscale* **2013,** *5,* 4079–4093. doi:10.1039/c3nr00934c
41. Akdim, B.; Pachter, R. *ACS Nano* **2011,** *5,* 1769–1774. doi:10.1021/nn102403j
42. Moreno-García, P.; Gulcur, M.; Manrique, D. Z.; Pope, T.; Hong, W.; Kaliginedi, V.; Huang, C.; Batsanov, A. S.; Bryce, M. R.; Lambert, C.; Wandlowski, T. *J. Am. Chem. Soc.* **2013,** *135,* 12228–12240. doi:10.1021/ja4015293
43. La Torre, A.; Ben Romdhane, F.; Baaziz, W.; Janowska, I.; Pham-Huu, C.; Begin-Colin, S.; Pourroy, G.; Banhart, F. *Carbon* **2014,** *77,* 906–911. doi:10.1016/j.carbon.2014.06.004
44. Larade, B.; Taylor, J.; Mehrez, H.; Guo, H. *Phys. Rev. B* **2001,** *64,* 075420. doi:10.1103/PhysRevB.64.075420
45. Khoo, K. H.; Neaton, J. B.; Son, Y. W.; Cohen, M. L.; Louie, S. G. *Nano Lett.* **2008,** *8,* 2900–2905. doi:10.1021/nl8017143
46. Lang, N. D.; Avouris, P. *Phys. Rev. Lett.* **1998,** *81,* 3515–3518. doi:10.1103/PhysRevLett.81.3515
47. Lang, N. D.; Avouris, P. *Phys. Rev. Lett.* **2000,** *84,* 358–361. doi:10.1103/PhysRevLett.84.358
48. Song, B.; Sanvito, S.; Fang, H. *New J. Phys.* **2010,** *12,* 103017. doi:10.1088/1367-2630/12/10/103017
49. Shen, L.; Zeng, M.; Yang, S.-W.; Zhang, C.; Wang, X.; Feng, Y. *J. Am. Chem. Soc.* **2010,** *132,* 11481–11486. doi:10.1021/ja909531c
50. Chen, W.; Andreev, A. V.; Bertsch, G. F. *Phys. Rev. B* **2009,** *80,* 085410. doi:10.1103/PhysRevB.80.085410
51. Ravagnan, L.; Manini, N.; Cinquanta, E.; Onida, G.; Sangalli, D.; Motta, C.; Devetta, M.; Bordoni, A.; Piseri, P.; Milani, P. *Phys. Rev. Lett.* **2009,** *102,* 245502. doi:10.1103/PhysRevLett.102.245502
52. Zhang, Z.; Zhang, J.; Kwong, G.; Li, J.; Fan, Z.; Deng, X.; Tang, G. *Sci. Rep.* **2013,** *3,* No. 2575. doi:10.1038/srep02575
53. Zanolli, Z.; Onida, G.; Charlier, J.-C. *ACS Nano* **2010,** *4,* 5174–5180. doi:10.1021/nn100712q
54. Ukrainsky, I. I. *Int. J. Quantum Chem.* **1972,** *6,* 473–489. doi:10.1002/qua.560060309
55. Castelli, I. E.; Salvestrini, P.; Manini, N. *Phys. Rev. B* **2012,** *85,* 214110. doi:10.1103/PhysRevB.85.214110
56. Lee, C.; Wei, X.; Kysar, J. W.; Hone, J. *Science* **2008,** *321,* 385–388. doi:10.1126/science.1157996
57. Spear, K. E.; Dismukes, J. P. *Synthetic Diamond: Emerging CVD Science and Technology;* Wiley: New York, 1994.
58. Nair, A. K.; Cranford, S. W.; Buehler, M. J. *EPL* **2011,** *95,* 16002. doi:10.1209/0295-5075/95/16002
59. Itzhaki, L.; Altus, E.; Basch, H.; Hoz, S. *Angew. Chem.* **2005,** *117,* 7598–7601. doi:10.1002/ange.200502448
60. Erdogan, E.; Popov, I.; Rocha, C. G.; Cuniberti, G.; Roche, S.; Seifert, G. *Phys. Rev. B* **2011,** *83,* 041401. doi:10.1103/PhysRevB.83.041401
61. Hu, Y. H. *Phys. Lett. A* **2009,** *373,* 3554–3557. doi:10.1016/j.physleta.2009.07.067
62. Kavan, L.; Hlavatý, J.; Kastner, J.; Kuzmany, H. *Carbon* **1995,** *33,* 1321–1329. doi:10.1016/0008-6223(95)00081-N
63. Pino, T.; Ding, H.; Güthe, F.; Maier, J. P. *J. Chem. Phys.* **2001,** *114,* 2208–2212. doi:10.1063/1.1338530
64. Hino, S.; Okada, Y.; Iwasaki, K.; Kijima, M.; Shirakawa, H. *Chem. Phys. Lett.* **2003,** *372,* 59–65. doi:10.1016/S0009-2614(03)00360-9
65. Gu, X.; Kaiser, R. I.; Mebel, A. M. *ChemPhysChem* **2008,** *9,* 350–369. doi:10.1002/cphc.200700609
66. Kano, E.; Takeguchi, M.; Fujita, J.-i.; Hashimoto, A. *Carbon* **2014,** *80,* 382–386. doi:10.1016/j.carbon.2014.08.077
67. Hunter, J.; Fye, J.; Jarrold, M. F. *Science* **1993,** *260,* 784–786. doi:10.1126/science.260.5109.784
68. von Helden, G.; Gotts, N. G.; Bowers, M. T. *J. Am. Chem. Soc.* **1993,** *115,* 4363–4364. doi:10.1021/ja00063a065
69. Kiang, C.-H.; Goddard, W. A., III. *Phys. Rev. Lett.* **1996,** *76,* 2515–2518. doi:10.1103/PhysRevLett.76.2515
70. Abdurahman, A.; Shukla, A.; Dolg, M. *Phys. Rev. B* **2002,** *65,* 115106. doi:10.1103/PhysRevB.65.115106
71. Cretu, O.; Komsa, H.-P.; Lehtinen, O.; Algara-Siller, G.; Kaiser, U.; Suenaga, K.; Krasheninnikov, A. V. *ACS Nano* **2014,** *8,* 11950–11957. doi:10.1021/nn5046147
72. Banhart, F. *Rep. Prog. Phys.* **1999,** *62,* 1181–1221. doi:10.1088/0034-4885/62/8/201

73. Krasheninnikov, A. V.; Banhart, F. *Nat. Mater.* **2007,** *6,* 723–733. doi:10.1038/nmat1996
74. Banhart, F.; Kotakoski, J.; Krasheninnikov, A. V. *ACS Nano* **2011,** *5,* 26–41. doi:10.1021/nn102598m
75. Meyer, J. C.; Eder, F.; Kurasch, S.; Skakalova, V.; Kotakoski, J.; Park, H. J.; Roth, S.; Chuvilin, A.; Eyhusen, S.; Benner, G.; Krasheninnikov, A. V.; Kaiser, U. *Phys. Rev. Lett.* **2012,** *108,* 196102. doi:10.1103/PhysRevLett.108.196102
76. Kotakoski, J.; Santos-Cottin, D.; Krasheninnikov, A. V. *ACS Nano* **2012,** *6,* 671–676. doi:10.1021/nn204148h
77. Jhon, Y. I.; Zhu, S.-E.; Ahn, J.-H.; Jhon, M. S. *Carbon* **2012,** *50,* 3708–3716. doi:10.1016/j.carbon.2012.03.044

License and Terms

This is an Open Access article under the terms of the Creative Commons Attribution License (http://creativecommons.org/licenses/by/2.0), which permits unrestricted use, distribution, and reproduction in any medium, provided the original work is properly cited.

The license is subject to the *Beilstein Journal of Nanotechnology* terms and conditions: (http://www.beilstein-journals.org/bjnano)

The definitive version of this article is the electronic one which can be found at: doi:10.3762/bjnano.6.58

BEILSTEIN JOURNAL OF NANOTECHNOLOGY

Overview of nanoscale NEXAFS performed with soft X-ray microscopes

Peter Guttmann*[1] and Carla Bittencourt[2]

Review

Open Access

Address:
[1]Institute for Soft Matter and Functional Materials, Helmholtz-Zentrum Berlin für Materialien und Energie GmbH, Albert-Einstein-Str. 15, 12489 Berlin, Germany and [2]ChIPS, University of Mons, B-7000, Mons, Belgium

Email:
Peter Guttmann* - peter.guttmann@helmholtz-berlin.de

* Corresponding author

Keywords:
NEXAFS; STXM; TXM; X-ray microscopy

Beilstein J. Nanotechnol. **2015,** *6,* 595–604.
doi:10.3762/bjnano.6.61

Received: 09 December 2014
Accepted: 05 February 2015
Published: 27 February 2015

This article is part of the Thematic Series "Atomic scale interface design and characterisation: Experimental aspects and methods".

Guest Editor: C. Ewels

© 2015 Guttmann and Bittencourt; licensee Beilstein-Institut.
License and terms: see end of document.

Abstract

Today, in material science nanoscale structures are becoming more and more important. Not only for the further miniaturization of semiconductor devices like carbon nanotube based transistors, but also for newly developed efficient energy storage devices, gas sensors or catalytic systems nanoscale and functionalized materials have to be analysed. Therefore, analytical tools like near-edge X-ray absorption fine structure (NEXAFS) spectroscopy has to be applied on single nanostructures. Scanning transmission X-ray microscopes (STXM) as well as full-field transmission X-ray microscopes (TXM) allow the required spatial resolution to study individual nanostructures. In the soft X-ray energy range only STXM was used so far for NEXAFS studies. Due to its unique setup, the TXM operated by the Helmholtz-Zentrum Berlin (HZB) at the electron storage ring BESSY II is the first one in the soft X-ray range which can be used for NEXAFS spectroscopy studies which will be shown in this review. Here we will give an overview of the different microscopes used for NEXAFS studies and describe their advantages and disadvantages for different samples.

Review

Introduction

Several analysis tools and techniques have been developed over the last century to explore electronic and structural properties of materials. Laboratory-source based techniques have compared to methods performed at synchrotron radiation sources the disadvantage of less brilliant X-ray beams and are not tunable over a wide photon energy range. Therefore, with the availability of synchrotron radiation sources several techniques could be developed having smaller spot sizes which allows studies of the properties of small samples or details of larger materials. Protein crystallography is one of the widely used techniques becoming high productive at synchrotron sources. Macromolecular crystals of proteins, viruses or nuclic acids are studied at the atomic structural level [1]. The development of drugs by understanding the interaction is greatly influenced by this tech-

nique. X-ray microscopy techniques enable the study of thick (i.e., up to 10 μm) specimens in materials and biological sciences using photon energies that covers the K- and L-X-ray absorption edges of elements of major interest [2-5]. High-photon energy X-ray diffraction used in operando studies can correlate changes in size of the unit cell of catalysts with their deactivation [6]. Studies of the pore structure of rocks can be performed by using X-ray micro tomography. This allows visualizing and investigating changes of the 3D pore structure by injecting CO_2 saturated brine [7,8]. The storage of CO_2 in underground reservoir rocks is a promising approach to reduce the greenhouse gas emissions.

Parallel to the development of novel synchrotron sources, the nanoscale of the current technologies triggered the revision of X-ray absorption spectroscopy [9,10] or photoelectron spectroscopy [11,12] techniques. These techniques can be used to study the electronic structure of materials; however they probe typically areas of larger than 50 × 50 μm^2. By applying them for nanostructures or nanoparticles the electronic structure information will be averaged over different individual nanostructures. To investigate the electronic structure of isolated nanostructures needs spatial resolution in the nanoscale range together with X-ray spectroscopy methods. X-ray microscopy reaches a higher Rayleigh resolution than optical microscopy as the resolution is decreasing linear with the wavelength. Additionally, the larger penetration depth and smaller radiation damage compared to electron microscopy has to be noted. Atmospheric pressure operation using a helium atmosphere is possible [13]. Electronic properties of samples can be studied due to the interaction of X-ray with matter. Therefore, the combination of X-ray microscopy and spectroscopy denominated X-ray spectromicroscopy having the capability of offering both spatial and chemical/physical information opens avenues for detailed characterization of nanostructures. Other spatially resolved techniques or spectromicroscopy as, e.g., electron energy loss spectroscopy (EELS) [14] have been chosen to study individual nanostructures/nanoparticles. By using monochromatic, aberration-corrected transmission electron microscopes (TEM) operating at low voltages spectromicroscopy of isolated nanostructures can be performed. Here, energy resolutions comparable to classical synchrotron based spectroscopy techniques can be achieved. A drawback of this technique is that it cannot handle samples which are thicker than a few atomic diameters [15-17]. By using linear polarized X-rays available at synchrotron radiation sources effects by dichroism in materials can be studied. Thus, in this case, the degree of alignment, molecular orientation as well as spectral assignments can be determined [9,18-20]. Such measurements of the polarization dependence (linear dichroism) relative to a characteristic direction of isotropic samples using the momentum transfer directional dependence in an electron microscope is possible, but highly affordable [21].

In the past, spectroscopic methods with high spatial resolution in the nanometer range were restricted to EELS microscopy [22,23] or scanning transmissions X-ray microscopes (STXM) [3,24]. These methods are well adapted to study the electronic structure of isolated nanostructures as their typical image fields contain only one or few nanostructures. Though STXMs operating at an undulator beamline allow polarization dependent studies it is time consuming to gather statistical information because of the sequential image formation process in the STXM: The focal spot of the objective is raster-scanned over the sample to form the image by detecting the transmitted X-ray photons. Additionally, only a small fraction of the spatially coherent undulator flux can be used whereas the recently reported HZB TXM operates with partial coherent X-rays from an undulator source and therefore, using a higher amount of the available flux [25].

Soft X-ray microscopes

In general three modes of soft X-ray microscopes can be distinguished [26] and are schematically illustrated in Figure 1:

Mode 1 – scanning mode: Producing an image by raster scanning the sample through a small focal spot generated by a focusing lens which is in most cases a zone plate (ZP). In a scanning transmission X-ray microscopy (STXM) the transmitted X-rays are detected. Scanning photoelectron microscopy (SPEM) is a method where the emitted photoelectrons are kinetic-energy-resolved detected. Additionally, fluorescence photons emitted from the sample can be detected.

Mode 2 – full field mode: Direct imaging of the sample using a zone plate objective is provided by transmission X-ray microscopy (TXM). In the past a condenser ZP has been used to illuminate the sample and an objective ZP projects a magnified image of the sample to an appropriate area detector. A similar direct imaging is available in X-ray photo-electron emission microscopy (X-PEEM) where monochromatic X-rays illuminate the sample. Here, electron optics, which can be electrostatic or magnetic lenses, are used producing a magnified image of the distribution of the ejected electrons on an electron sensitive camera.

Mode 3 – diffraction mode: Coherent diffraction imaging (CDI) methods use coherent monochromatic X-rays normally without any optical element to illuminate the sample. A suitable X-ray detector records the far-field coherent scattering signal. With the help of computer algorithms this pattern is inverted into a real space image. So far, samples with weak

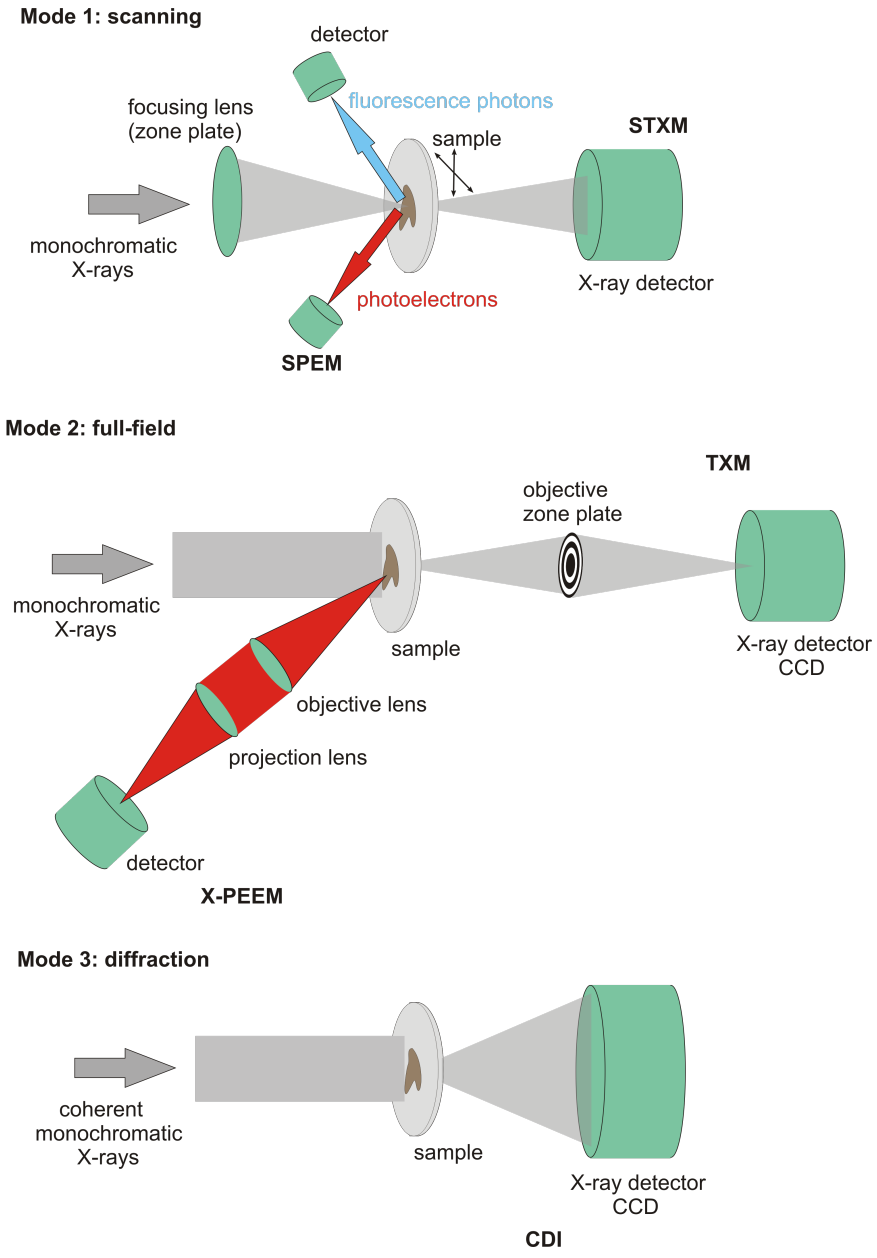

Figure 1: Schematic layout of general modes of soft X-ray microscopy. STXM and SPEM are focused probe methods, whereas TXM and X-PEEM are direct imaging methods. CDI needs computer algorithms to reconstruct an image from the recorded diffraction pattern.

contrast are not easily reconstructed. NEXAFS possibilities are missing.

Nowadays, the spatial resolution for zone plate based X-ray microscopes reaches 10 nm for real, even having weak contrast, samples [27-29].

The information depth by using soft X-ray microscopes depends strongly on the applied method. For SPEM and X-PEEM electrons emitted from the sample surface are detected. These electrons are generated in the surface layer not deeper than 10 nm. STXM and TXM are bulk sensitive methods as they normally detect the photons which are transmitted through the sample. The penetration depth of X-rays and therefore the usable sample thickness correlates with the X-ray photon energy used for the analysis and is much larger than for electrons (Figure 2) [30]. In the soft X-ray regime penetration depths in the order of several microns are accessible. This allows probing buried nanostructures within a bulk sample. Note, that the interaction of electrons with matter is mainly determined through Coulomb

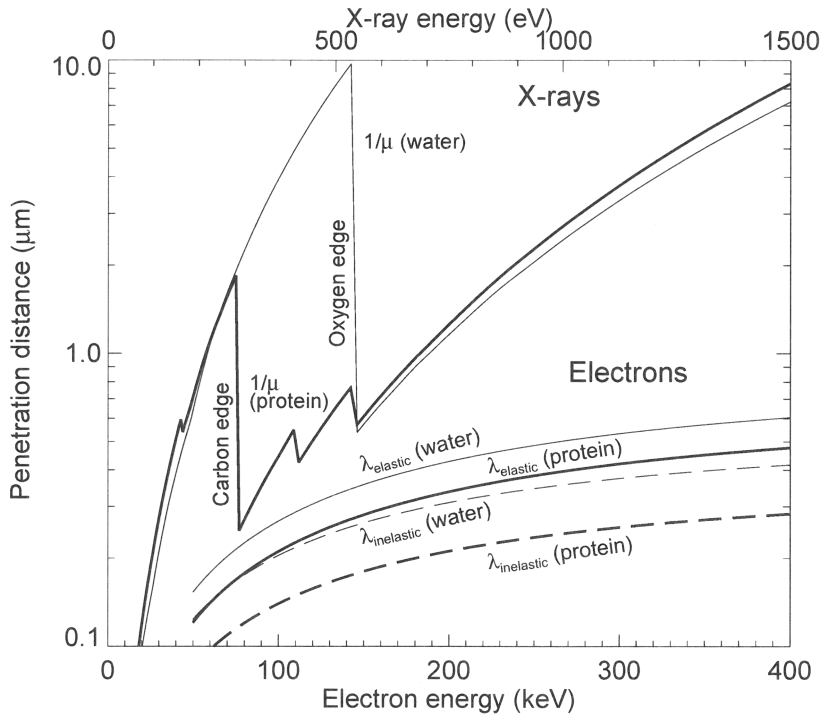

Figure 2: Calculated penetration depths of X-rays and electrons in dependence of their energy. The penetration depth of X-rays is larger than for electrons. In the so called “water window”, i.e., between the carbon and oxygen absorption edges at 284 and 543 eV protein and water have quite different absorption values which leads to a natural absorption contrast. Reprinted with permission from [30]. Copyright 1995 Cambridge University Press.

forces, whereas the interaction of X-rays with matter is caused by the valence electron cloud which will give different information.

In this review only methods for bulk sensitive NEXAFS spectroscopy using STXM and TXM in the soft X-ray range will be further discussed.

The Stony Brook group at the National Synchrotron Light Source (NSLS) at Brookhaven National Laboratory built the first STXM having a zone plate lens to produce the scanning spot [31,32]. In order to get the diffraction limited resolution a STXM needs spatially coherent light. The schematic setup of most STXMs is shown in Figure 3: The coherent part of the X-ray beam passing through a monochromator is collected by a zone plate. The zone plate produces a diffraction limited spot in the sample plane. An order sorting aperture (OSA) filters the unwanted diffraction orders of the ZP. The sample is mounted on a stage having stepping or piezoelectric driven motors to perform the raster scan. The X-ray sensitive detector collects the transmitted X-ray photons. No low efficiency optic is upstream of the sample. Therefore, the radiation load to the

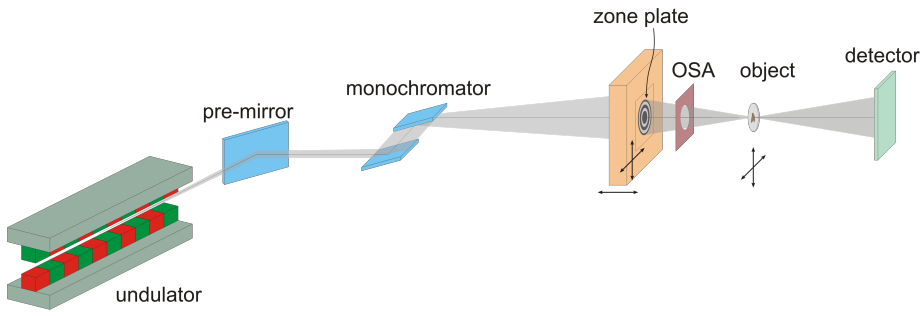

Figure 3: Schematic setup of a scanning transmission X-ray microscope (STXM).

sample is minimized. The pixel by pixel data format can be easily used for spectromicroscopy applications. In the STXM, the contrast transfer function (CTF) follows that one of an incoherent microscope due to the image formation process (pixel by pixel) and due to the fact that normally the detector aperture is equal or larger than that of the zone plate [33].

The first TXM having a higher resolution than light microscopes was constructed by the group of Günter Schmahl, University of Göttingen at the electron storage ring ACO in Orsay, France [34,35]. Figure 4 shows the set-up of a typical TXM at a bending magnet source. In similarity to a conventional light microscope the electron storage ring is used as the light source. The condenser zone plate collects the incoming X-rays and is used for the illumination of the sample. A high resolution zone plate objective generates a magnified image of the illuminated sample area on the X-ray sensitive CCD camera. A pinhole is required between the condenser and the sample which acts together with the condenser zone plate as monochromator. Additionally, a central stop near the condenser zone plate is used to block direct light and to produce a hollow cone illumination.

Depending on the available photon flux from the source, the efficiency of the zone plate objective and the sensitivity of the CCD detector exposure times in the range of a few seconds for acquiring a full-field image are state of the art. TXMs are not requiring precise scanning stages as STXMs and do not need spatially coherent illumination. So far, large diameter zone plates [36] or multilayer mirrors [37,38] were used as condenser. The drawback of these condenser types is their limited monochromaticity ($E/\Delta E$) in the range of a few hundred hindering spectroscopic applications. The full field TXM at the undulator beamline U41-FSGM at the electron storage ring BESSY II operated by the Helmholtz-Zentrum Berlin (HZB) uses a different optical concept [25]: The spectral resolution needed for NEXAFS studies is provided by the monochromator in front of the condenser. Therefore, a spectral resolution $E/\Delta E$ in the range of 5000 which is comparable to STXM setups can be reached. The achromatic condenser is a novel ellipsoidal shaped capillary which has an efficiency one order of magnitude higher than ZPs [39]. Due to the setup at an undulator beamline and the smaller size of the condenser compared to a ZP condenser partial coherent X-rays illuminates the condenser. The maximum possible resolution in this partial coherent case is lower compared to the incoherent case, but the contrast transfer function (CTF) shows higher contrast values at medium to higher spatial frequencies [25,29]. Combining partial coherence with a high-resolution objective, the capillary optic of the HZB TXM leads to high contrast C_{object} for nanoscale features which reduces artefacts of the measured absorption values. The radiation dose for detecting small object features is proportional to $(C_{object} \cdot CTF)^{-2}$ [29,40]. As a consequence of this favourable shape of the contrast transfer function exposure time and sample damage are minimized.

Results and Discussion

Today, several STXMs in the soft X-ray region are in operation at many synchrotron light sources worldwide [41]. Here, we restrict ourselves to a short overview of the most used instruments by the scientific community: At the Advanced Light Source (ALS) in Berkeley, California, USA, two STXMs [42-44] are operated for polymer sciences [45] and for the investigation of magnetic nanostructures [46,47]. In the latter case the magnetic properties as a function of an applied magnetic field as well as time resolved measurements [48] are performed to study the electronic functionalities for example in magnetic random access memories (MRAMS) or hard discs. The Hitchcock team of the McMaster University operates a STXM at an undulator beamline at the Canadian Light Source (CLS), Saskatoon, Canada, for many applications as, e.g., polymer sciences at the carbon K-edge [49], studies on graphene [50] and investigations of biological materials [51]. The STXM "Pollux" [52,53] installed at the Swiss Light Source operated by the Paul Scherrer Institute, Villingen, Switzerland, is a versatile instrument also covering polymer and magnetic investigations [54,55]. "Maxymus" (Magnetic X-ray Micro- and UHV Spectroscope) at the BESSY II electron storage ring, Helmholtz-

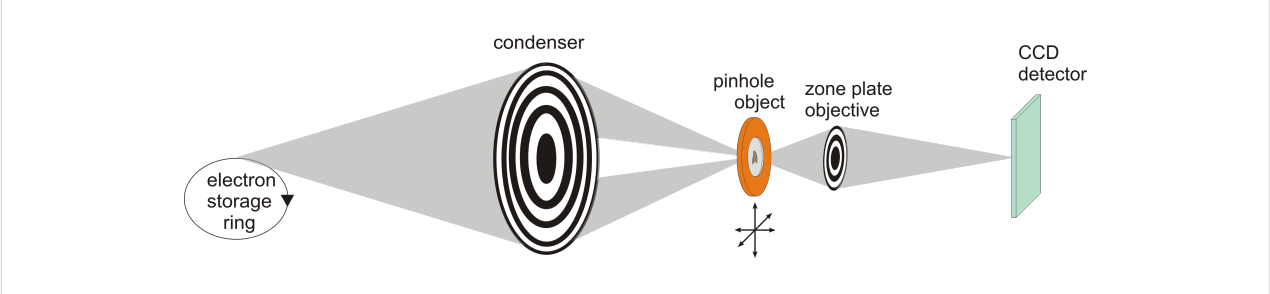

Figure 4: A full field transmission X-ray microscope (TXM) for a bending magnet source uses two zone plate lenses, condenser and objective, to form a 2D image on the detector. Additionally, a pinhole close to the sample is necessary which acts together with the condenser as a monochromator.

Zentrum Berlin, Germany, is operated by the Max-Planck-Institut for Intelligent Systems, Stuttgart, Germany and allows – compared to other STXMs – investigations under ultrahigh vacuum conditions [56]. This instrument is dedicated for studies of the magnetic behaviour of solids in the nanoscale range and allows time resolved measurements [57].

With the new optical concept of the HZB-TXM it was demonstrated for the first time that NEXAFS by studying sodium titanate nanostructures at the Ti-L-absorption edge in the soft X-ray region can be performed with a full field microscope (Figure 5) [58]. It should be noted that the collection rate for similar field of views is about two orders of magnitude faster than is possible with STXMs. By combining multichannel multiple-scattering calculations with the NEXAFS-TXM data specific spectral features at the Ti-L-edge could be associated to titanium atoms in distinct atomic sites within the lattice [58,59].

After these first encouraging investigations further spectroscopic studies on nanostructures containing metal atoms like copper were performed. It was shown that chemical analysis of nanowires for solar cells can be performed by NEXAFS-TXM. As a result of this investigation it was found that neither Cd nor S diffuse into the CuO phase after the deposition of CdS on the CuO nanowires [60,61]. The possibility to study the oxidation state of Mn dopants in titanate nanostructures was reported in [62].

Additionally, using the capability to investigate cryogenic samples in the HZB-TXM, the electronic structure of individual hybrid colloid particles in their hydrated environment were analysed [63]. Here, the structural homogeneity of nanoparticles in the hybrid particle was examined. Nanoscale valence changes in resistive switching thin film devices ($SrTiO_3$) could be demonstrated [64]. The change of resistance in a RRAM device could be assigned to a redox-process. The switching filament could be allocated to extended growth defects which are already present in the virgin films. Synthesis of anisotropic core-shell Fe_3O_4@Au magnetic nanoparticles which will have future applications in photo thermal therapy or drug delivery can be optimized by different analysis methods including NEXAFS spectroscopy with the HZB-TXM [65]. In the latter case as well as in the case of hybrid colloid particles the nanoparticles have sizes below the spatial resolution of the TXM, but still provide signals which can be used for NEXAFS spectroscopy.

Spectroscopic studies at the carbon K-edge are very challenging because nearly in all beamlines the photon flux is sharply reduced within the carbon K-edge photon energy range (280 up to 320 eV) due to the absorption of the X-ray beam by a thin carbon film contamination deposited on the optical elements (grating, mirrors, objectives). This contamination is caused by the interaction of the X-ray beam with residual hydrocarbon molecules in the vacuum of the beamline. The integrated photon flux at the sample position in the U41-FSGM beamline at the electron storage ring BESSY II (Figure 6) is reduced by one order of magnitude and, in addition, a peak related to second harmonic radiation (double photon energy) exists in the carbon K-edge energy region. Suppression of these higher energies can be accomplished by the use of appropriate filters. In the case of the carbon K-edge normally Ti-filters are in use. The sharp decrease in the photon flux at the photon energy range of the carbon K-edge add difficulties in the analysis of the carbon nanostructure due to the low contrast images recorded in this region. It is important to mention that the study of the carbon K-edge is also a challenge in non-microscopic NEXAFS set-ups due to uncertainties in the normalization by the photon flux. Nevertheless, carbon nanostructures, like suspended carbon nanohorns (CNH) [66], or thin graphite sheets [2] could be studied with the HZB-TXM. The electronic states of freestanding CNH aggregate in a dahlia-like shape

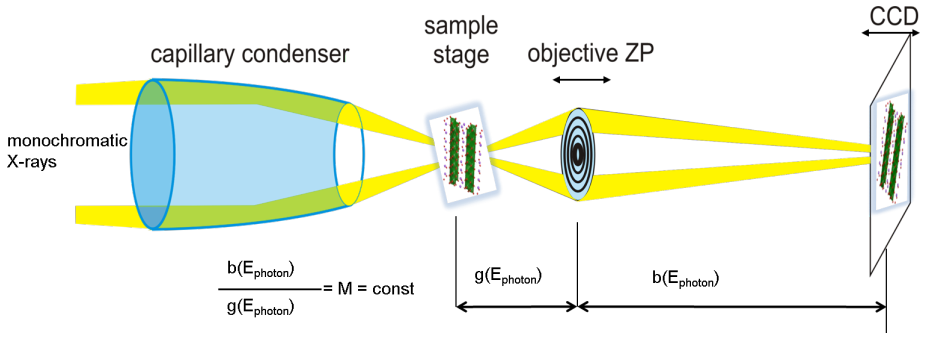

Figure 5: Schematic setup of the HZB-TXM for NEXAFS studies: Monochromatic X-rays are collected with an achromatic capillary condenser to illuminate the sample. At each photon energy a highly magnified 2D image of the sample is taken whereupon the magnification (M) is kept constant [58].

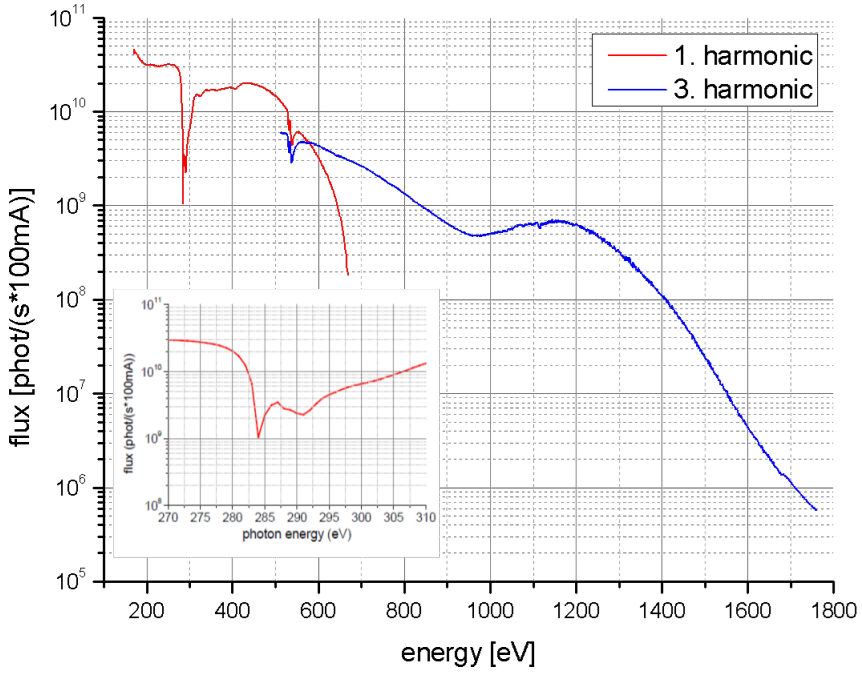

Figure 6: Measured integrated photon flux at the sample position of the HZB-TXM using a 10 µm exit slit of the monochromator for the 1. and 3. harmonic of the undulator. The inset shows the situation at the carbon-K-edge: A decrease of the flux due to the carbon contamination of the optical elements and the effect of the second order radiation (double photon energy, without using any filter).

were investigated and could be related to the presence of pentagonal rings and folding of the graphene sheet in the CNH [66]. Metal impurities due to the exfoliation process of graphite give rise to a pre-edge signal at 284.2 eV. Topological defects added additional spectral features in the π and σ region of the absorption edge [2].

STXMs have no optical element between the sample and the detector. Therefore, the radiation dose applied to the sample during the investigation might be lower. This is helpful in the case of very radiation sensitive materials like some polymers [45] which cannot be analysed in the TXM. Cryo preservation can be used for the structural integrity of the sample [67] but even at these low temperatures atomic bindings of sensible materials are damaged, i.e., the electronic structure is changed. The resulting STXM spectra of those sensitive materials have to be checked very carefully to avoid misinterpretations due to possible radiation induced changes.

Some interesting nanostructure materials like boron nitride could not be investigated so far at the boron-K-edge with the HZB-TXM, as no adapted objective with a longer focal length is available. However, such NEXAFS studies were performed with the STXM at the Canadian Light Source (CLS, Saskatoon, SK, Canada) [68].

Experimental

For NEXAFS spectroscopy, it is necessary to measure one data set for all photon energies E of the transmitted intensity $I(E)$ through the sample and another data set $I_0(E)$ without sample. The absorption spectrum normally will be displayed as an optical density $\mathrm{OD}(E) = -\log[I(E)/I_0(E)]$ [69]. So far, nearly all absorption spectroscopy techniques cannot measure $I(E)$ and $I_0(E)$ at the same time which can lead to errors in the normalization due to instabilities of the photon beam. For nanostructures the photon flux ($I_0(E)$) and the signal ($I(E)$) can be recorded in the full field HZB TXM simultaneously at near the same position reducing the uncertainties in the normalization of the NEXAFS signal. For this, near the nanostructure we should have a bare region (or a hole) where the $I_0(E)$ can be extracted (Figure 7). The analysis software package aXis2000 [66] which was originally written for STXM data analysis can now also handle the HZB TXM data sets.

Conclusion

Bulk sensitive nanoscale NEXAFS spectroscopy was restricted in the past to STXMs as TXMs did not allow the necessary spectral resolution. With the recently developed setup of the HZB-TXM at the BESSY electron storage ring this restriction could be overcome. As shown in this review, several published NEXAFS-TXM studies of low dimensional nanostructures pave

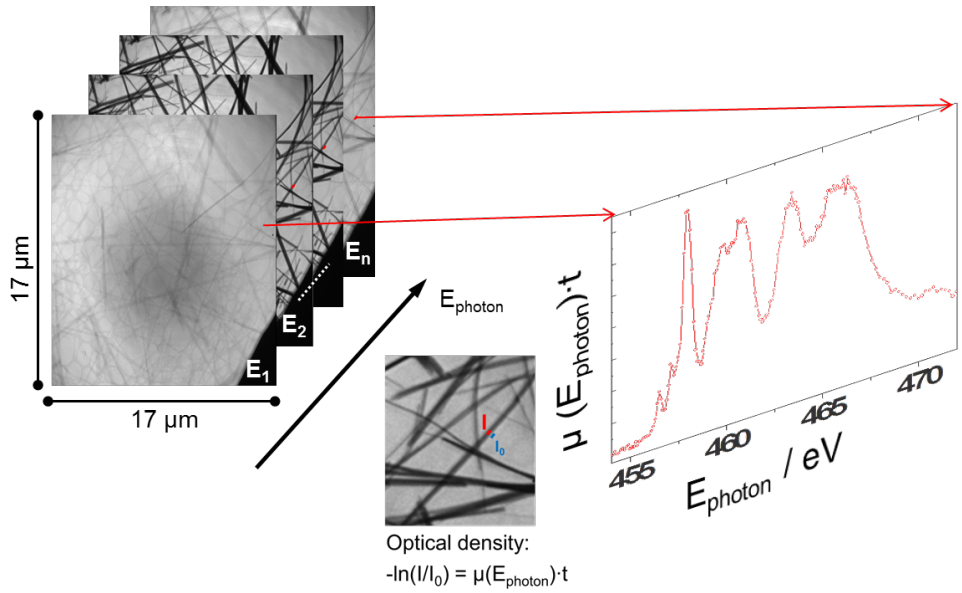

Figure 7: Workflow for NEXAFS-TXM: A data set of images at different photon energies is taken with the HZB-TXM. A NEXAFS spectrum can be generated out of this data set by using defined areas of the sample to measure $I(E)$ and neighbouring blank areas for $I_0(E)$ [58].

the way for understanding the electronic structure towards the atomic scale and will help in the design of tailored functional systems. The investigated carbon nanotubes, nanowires as well as nanoscale oxides have due to their high surface to volume ratio an enormous potential in nanoelectronics, catalysis, light harvesting and energy storage applications. The newly developed NEXAFS-TXM together with further complementary physicochemical methods and spectroscopic techniques will allow a more complete understanding of the function of low dimensional nanostructures.

Acknowledgements

This work was funded in part by the German Federal Ministry of Education and research under contract number 05KS4BY1/7, the Human Frontier Science Program Research Grant Ref. RGP0053/2005-C, the 7th framework program under grant agreement 226716 (WP23 NANOFOX), the Helmholtz-Zentrum Berlin für Materialien und Energie GmbH and the COST Action MP0901. We thank HZB for the allocation of synchrotron radiation beamtime. The research leading to these results has received funding from the European Community's Seventh Framework Programme (FP7/2007-2013) under grant agreement no. 226716 (ELISA) and no. 312284 (CALIPSO). This work was partially funded by the Belgian Fund for Scientific Research (FRS-FNRS) under FRFC contract “Chemographene” (convention no. 2.4577.11). C. Bittencourt is a research associate at the National Funds for Scientific Research (FRS-FNRS, Belgium).

References

1. Rowland, P.; Blaney, F. E.; Smyth, M. G.; Jones, J. J.; Leydon, V. R.; Oxbrow, A. K.; Lewis, C. J.; Tennant, M. G.; Modi, S.; Eggleston, D. S.; Chenery, R. J.; Bridges, A. M. *J. Biol. Chem.* **2006,** *281,* 7614–7622. doi:10.1074/jbc.M511232200
2. Bittencourt, C.; Hitchock, A. P.; Ke, X.; Van Tendeloo, G.; Ewels, C. P.; Guttmann, P. *Beilstein J. Nanotechnol.* **2012,** *3,* 345–350. doi:10.3762/bjnano.3.39
3. Felten, A.; Bittencourt, C.; Pireaux, J.-J.; Reichelt, M.; Mayer, J.; Hernandez-Cruz, D.; Hitchcock, A. P. *Nano Lett.* **2007,** *7,* 2435–2440. doi:10.1021/nl071134e
4. Weiner, A.; Kapishnikov, S.; Shimoni, E.; Cordes, S.; Guttmann, P.; Schneider, G.; Elbaum, M. *J. Struct. Biol.* **2013,** *181,* 77–81. doi:10.1016/j.jsb.2012.10.005
5. Schneider, G.; Guttmann, P.; Rehbein, S.; Werner, S.; Follath, R. *J. Struct. Biol.* **2012,** *177,* 212–223. doi:10.1016/j.jsb.2011.12.023
6. Wragg, D. S.; Brien, M. G. O.; Bleken, F. L.; Di Michiel, M.; Olsbye, U.; Fjellvåg, H. *Angew. Chem., Int. Ed.* **2012,** *51,* 7956–7959. doi:10.1002/anie.201203462
7. Gouze, P.; Luquot, L. *J. Contam. Hydrol.* **2011,** *120–121,* 45–55. doi:10.1016/j.jconhyd.2010.07.004
8. Noiriel, C.; Luquot, L.; Madé, B.; Raimbault, L.; Gouze, P.; van der Lee, J. *Chem. Geol.* **2009,** *265,* 160–170. doi:10.1016/j.chemgeo.2009.01.032
9. Stöhr, J. *NEXAFS Spectroscopy;* Springer Series in Surface Sciences, Vol. 25; Springer: Berlin, Germany, 1992. doi:10.1007/978-3-662-02853-7
10. Fadley, C. S. *J. Electron Spectrosc. Relat. Phenom.* **2010,** *178,* 2–32. doi:10.1016/j.elspec.2010.01.006
11. Hüfner, S. *Photoelectron Spectroscopy: Principles and Applications;* Springer: Berlin, Germany, 2003. doi:10.1007/978-3-662-09280-4

12. Wende, H. *Rep. Prog. Phys.* **2004,** *67,* 2105–2181. doi:10.1088/0034-4885/67/12/R01
13. Attwood, D. *Soft X-Rays and Extreme Ultraviolet Radiation: Principles and Applications;* Cambridge University Press: Cambridge, United Kingdom, 2007.
14. Egerton, R. F. *Rep. Prog. Phys.* **2009,** *72,* 016502. doi:10.1088/0034-4885/72/1/016502
15. Sasaki, T.; Sawada, H.; Hosokawa, F.; Kohno, Y.; Tomita, T.; Kaneyama, T.; Kondo, Y.; Kimoto, K.; Sato, Y.; Suenaga, K. *J. Electron Microsc.* **2010,** *59* (Suppl. 1), S7–S13. doi:10.1093/jmicro/dfq027
16. Suenaga, K.; Koshino, M. *Nature* **2010,** *468,* 1088–1090. doi:10.1038/nature09664
17. Krivanek, O. L.; Ursin, J. P.; Bacon, N. J.; Corbin, G. J.; Dellby, N.; Hrncirik, P.; Murfitt, M. F.; Own, C. S.; Szilagyi, Z. S. *Philos. Trans. R. Soc. London, A* **2009,** *367,* 3683–3697. doi:10.1098/rsta.2009.0087
18. Ade, H.; Hsiao, B. *Science* **1993,** *262,* 1427–1429. doi:10.1126/science.262.5138.1427
19. Stöhr, J.; Padmore, H. A.; Anders, S.; Stammler, T.; Scheinfein, M. R. *Surf. Rev. Lett.* **1998,** *5,* 1297–1308. doi:10.1142/S0218625X98001638
20. Smith, A. P.; Ade, H. *Appl. Phys. Lett.* **1996,** *69,* 3833–3835. doi:10.1063/1.117120
21. Hitchcock, A. P.; Dynes, J. J.; Johansson, G.; Wang, J.; Botton, G. *Micron* **2008,** *39,* 741–748. doi:10.1016/j.micron.2007.09.010
22. Krivanek, O. L.; Dellby, N.; Murfitt, M. F.; Chisholm, M. F.; Pennycook, T. J.; Suenaga, K.; Nicolosi, V. *Ultramicroscopy* **2010,** *110,* 935–945. doi:10.1016/j.ultramic.2010.02.007
23. Suenaga, K.; Sato, Y.; Liu, Z.; Kataura, H.; Okazaki, T.; Kimoto, K.; Sawada, H.; Sasaki, T.; Omoto, K.; Tomita, T.; Kaneyama, T.; Kondo, Y. *Nat. Chem.* **2009,** *1,* 415–418. doi:10.1038/nchem.282
24. Felten, A.; Hody, H.; Bittencourt, C.; Pireaux, J. J.; Hernández Cruz, D.; Hitchcock, A. P. *Appl. Phys. Lett.* **2006,** *89,* 093123. doi:10.1063/1.2345258
25. Schneider, G.; Guttmann, P.; Heim, S.; Rehbein, S.; Mueller, F.; Nagashima, K.; Heymann, J. B.; Müller, W. G.; McNally, J. G. *Nat. Methods* **2010,** *7,* 985–987. doi:10.1038/nmeth.1533
26. Hitchcock, A. P. Soft X-Ray Imaging and Spectromicroscopy. *Handbook of Nanoscopy;* Wiley-VCH Verlag GmbH & Co. KGaA: Weinheim, Germany, 2012; pp 745–791.
27. Chao, W.; Kim, J.; Rekawa, S.; Fischer, P.; Anderson, E. H. *Opt. Express* **2009,** *17,* 17669–17677. doi:10.1364/OE.17.017669
28. Keskinbora, K.; Grévent, C.; Bechtel, M.; Weigand, M.; Goering, E.; Nadzeyka, A.; Peto, L.; Rehbein, S.; Schneider, G.; Follath, R.; Vila-Comamala, J.; Yan, H. F.; Schütz, G. *Opt. Express* **2013,** *21,* 11747–11756. doi:10.1364/OE.21.011747
29. Rehbein, S.; Guttmann, P.; Werner, S.; Schneider, G. *Opt. Express* **2012,** *20,* 5830–5839. doi:10.1364/OE.20.005830
30. Kirz, J.; Jacobsen, C.; Howells, M. *Q. Rev. Biophys.* **1995,** *28,* 33–130. doi:10.1017/S0033583500003139
31. Kirz, J.; Rarback, H. *Rev. Sci. Instrum.* **1985,** *56,* 1–13. doi:10.1063/1.1138464
32. Rarback, H.; Shu, D.; Feng, S. C.; Ade, H.; Kirz, J.; McNulty, I.; Kern, D. P.; Chang, T. H. P.; Vladimirsky, Y.; Iskander, N.; Attwood, D.; McQuaid, K.; Rothman, S. *Rev. Sci. Instrum.* **1988,** *59,* 52–59. doi:10.1063/1.1139965
33. Misell, D. L.; Stroke, G. W.; Halioua, M. *J. Phys. D: Appl. Phys.* **1974,** *7,* L113. doi:10.1088/0022-3727/7/10/103
34. Schmahl, G.; Rudolph, D.; Niemann, B.; Christ, O. *Q. Rev. Biophys.* **1980,** *13,* 297–315. doi:10.1017/S0033583500001700
35. Niemann, B.; Rudolph, D.; Schmahl, G. *Nucl. Instrum. Methods Phys. Res.* **1983,** *208,* 367–371. doi:10.1016/0167-5087(83)91152-3
36. Schmahl, G.; Rudolph, D.; Niemann, B.; Guttmann, P.; Thieme, J.; Schneider, G.; David, C.; Diehl, M.; Wilhein, T. *Optik (Munich, Ger.)* **1993,** *93,* 95–102.
37. Stollberg, H.; Yulin, S.; Takman, P. A. C.; Hertz, H. M. *Rev. Sci. Instrum.* **2006,** *77,* 123101. doi:10.1063/1.2400665
38. Takman, P. A. C.; Stollberg, H.; Johansson, G. A.; Holmberg, A.; Lindblom, M.; Hertz, H. M. *J. Microsc. (Oxford, U. K.)* **2007,** *226,* 175–181. doi:10.1111/j.1365-2818.2007.01765.x
39. Guttmann, P.; Zeng, X.; Feser, M.; Heim, S.; Yun, W.; Schneider, G. *J. Phys.: Conf. Ser.* **2009,** *186,* 012064. doi:10.1088/1742-6596/186/1/012064
40. Schneider, G. *Ultramicroscopy* **1998,** *75,* 85–104. doi:10.1016/S0304-3991(98)00054-0
41. Obst, M.; Schmidt, G. 3D Chemical Mapping: Application of Scanning Transmission (Soft) X-ray Microscopy (STXM) in Combination with Angle-Scan Tomography in Bio-, Geo-, and Environmental Sciences. In *Electron Microscopy;* Kuo, J., Ed.; Humana Press: New York, NY, U.S.A., 2014; Vol. 1117, pp 757–781.
42. Warwick, T.; Ade, H.; Hitchcock, A. P.; Padmore, H.; Rightor, E. G.; Tonner, B. P. *J. Electron Spectrosc. Relat. Phenom.* **1997,** *84,* 85–98. doi:10.1016/S0368-2048(97)00026-1
43. Warwick, T.; Franck, K.; Kortright, J. B.; Meigs, G.; Moronne, M.; Myneni, S.; Rotenberg, E.; Seal, S.; Steele, W. F.; Ade, H.; Garcia, A.; Cerasari, S.; Delinger, J.; Hayakawa, S.; Hitchcock, A. P.; Tyliszczak, T.; Kikuma, J.; Rightor, E. G.; Shin, H.-J.; Tonner, B. P. *Rev. Sci. Instrum.* **1998,** *69,* 2964–2973. doi:10.1063/1.1149041
44. Warwick, T.; Ade, H.; Kilcoyne, D.; Kritscher, M.; Tyliszczak, T.; Fakra, S.; Hitchcock, A.; Hitchcock, P.; Padmore, H. *J. Synchrotron Radiat.* **2002,** *9,* 254–257. doi:10.1107/S0909049502005502
45. Ade, H.; Smith, A. P.; Zhang, H.; Zhuang, G. R.; Kirz, J.; Rightor, E.; Hitchcock, A. *J. Electron Spectrosc. Relat. Phenom.* **1997,** *84,* 53–72. doi:10.1016/S0368-2048(97)00013-3
46. Amaladass, E.; Ludescher, B.; Schütz, G.; Tyliszczak, T.; Eimüller, T. *Appl. Phys. Lett.* **2007,** *91,* 172514. doi:10.1063/1.2802075
47. Eimueller, T.; Ulbrich, T. C.; Amaladass, E.; Guhr, I. L.; Tyliszczak, T.; Albrecht, M. *Phys. Rev. B* **2008,** *77,* 134415. doi:10.1103/PhysRevB.77.134415
48. Höllinger, R.; Killinger, A.; Krey, U. *J. Magn. Magn. Mater.* **2003,** *261,* 178–189. doi:10.1016/S0304-8853(02)01471-3
49. Hitchcock, A. P.; Tyliszczak, T.; Koprinarov, I.; Stover, H.; Li, W. H.; Heng, Y. M.; Murti, K.; Gerroir, P.; Dutcher, J. R.; Dalnoki-Veress, K.; Ade, H. W. X-ray spectromicroscopy studies of polymer microstructure. In *X-Ray Microscopy, Proceedings;* Meyer-Ilse, W.; Warwick, T.; Attwood, D., Eds.; 2000; Vol. 507, pp 231–234.
50. Schultz, B. J.; Patridge, C. J.; Lee, V.; Jaye, C.; Lysaght, P. S.; Smith, C.; Barnett, J.; Fischer, D. A.; Prendergast, D.; Banerjee, S. *Nat. Commun.* **2011,** *2,* No. 372. doi:10.1038/ncomms1376
51. Yangquanwei, Z.; Neethirajan, S.; Karunakaran, C. *Nanoscale Res. Lett.* **2013,** *8,* 463. doi:10.1186/1556-276X-8-463
52. Flechsig, U.; Quitmann, C.; Raabe, J.; Böge, M.; Fink, R.; Ade, H. *AIP Conf. Proc.* **2007,** *879,* 505–508. doi:10.1063/1.2436109
53. Raabe, J.; Tzvetkov, G.; Flechsig, U.; Böge, M.; Jaggi, A.; Sarafimov, B.; Vernooij, M. G. C.; Huthwelker, T.; Ade, H.; Kilcoyne, D.; Tyliszczak, T.; Fink, R. H.; Quitmann, C. *Rev. Sci. Instrum.* **2008,** *79,* 113704. doi:10.1063/1.3021472

54. Watts, B.; McNeill, C. R. *Macromol. Rapid Commun.* **2010,** *31,* 1706–1712. doi:10.1002/marc.201000269
55. Wintz, S.; Strache, T.; Körner, M.; Fritzsche, M.; Markó, D.; Mönch, I.; Mattheis, R.; Raabe, J.; Quitmann, C.; McCord, J.; Erbe, A.; Fassbender, J. *Appl. Phys. Lett.* **2011,** *99,* 149901. doi:10.1063/1.3646545
56. Follath, R.; Schmidt, J. S.; Weigand, M.; Fauth, K. In *The X-ray microscopy beamline UE46-PGM2 at BESSY,* 10th International Conference on Synchrotron Radiation Instrumentation (SRI 2009), Melbourne, Australia; Garrett, R.; Gentle, I.; Nugent, K.; Wilkins, S., Eds.; American Institute of Physics: College Park, MD, USA, 2010; pp 323–326.
57. https://www.is.mpg.de/de/schuetz/roentgenmikroskopie (accessed Feb 4, 2015).
58. Guttmann, P.; Bittencourt, C.; Rehbein, S.; Umek, P.; Ke, X.; Van Tendeloo, G.; Ewels, C. P.; Schneider, G. *Nat. Photonics* **2012,** *6,* 25–29. doi:10.1038/nphoton.2011.268
59. Bittencourt, C.; Krüger, P.; Lagos, M. J.; Ke, X.; Van Tendeloo, G.; Ewels, C.; Umek, P.; Guttmann, P. *Beilstein J. Nanotechnol.* **2012,** *3,* 789–797. doi:10.3762/bjnano.3.88
60. El Mel, A. A.; Buffiére, M.; Bouts, N.; Gautron, E.; Tessier, P. Y.; Henzler, K.; Guttmann, P.; Konstantinidis, S.; Bittencourt, C.; Snyders, R. *Nanotechnology* **2013,** *24,* 265603. doi:10.1088/0957-4484/24/26/265603
61. Mel, A. A. E.; Buffiere, M.; Bouts, N.; Gautron, E.; Bittencourt, C.; Guttmann, P.; Tessier, P. Y.; Konstantinidis, S.; Snyders, R. Growth control of CuO nanowires on copper thin films: Toward the development of pn nanojunction arrays. 2013 IEEE 5th International Nanoelectronics Conference (INEC), Singapore, Jan 2–4, 2013; 2011; pp 201–202. doi:10.1109/INEC.2013.6465997
62. Umek, P.; Bittencourt, C.; Guttmann, P.; Gloter, A.; Škapin, S. D.; Arčon, D. *J. Phys. Chem. C* **2014,** *118,* 21250–21257. doi:10.1021/jp5063989
63. Henzler, K.; Guttmann, P.; Lu, Y.; Polzer, F.; Schneider, G.; Ballauff, M. *Nano Lett.* **2013,** *13,* 824–828. doi:10.1021/nl3046798
64. Koehl, A.; Wasmund, H.; Herpers, A.; Guttmann, P.; Werner, S.; Henzler, K.; Du, H.; Mayer, J.; Waser, R.; Dittmann, R. *APL Mater.* **2013,** *1,* 042102. doi:10.1063/1.4822438
65. Zengin, A.; Bozkurt, A.; Boyaci, I. H.; Özcan, S.; Daniel, P.; Lagarde, F.; Gibaud, A.; Cetin, D.; Suludere, Z.; Guttmann, P.; Tamer, U. *Pure Appl. Chem.* **2014,** *86,* 967–978. doi:10.1515/pac-2013-0915
66. Bittencourt, C.; Ke, X.; Van Tendeloo, G.; Tagmatarchis, N.; Guttmann, P. *Chem. Phys. Lett.* **2013,** *587,* 85–87. doi:10.1016/j.cplett.2013.09.034
67. Schneider, G.; Niemann, B.; Guttmann, P.; Schmahl, G. A. Low-temperature X-ray microscopy of biological samples in amplitude and phase contrast. In *X-Ray Microfocusing: Applications and Techniques,* San Diego, CA, USA, July 19, 1998; McNulty, I., Ed.; SPIE: Bellingham, WA, USA, 1998; pp 2–11. doi:10.1117/12.330331
68. Kaznatcheev, K. V.; Karunakaran, Ch.; Lanke, U. D.; Urquhart, S. G.; Obst, M.; Hitchcock, A. P. *Nucl. Instrum. Methods Phys. Res., Sect. A* **2007,** *582,* 96–99. doi:10.1016/j.nima.2007.08.083
69. Jacobsen, C.; Wirick, S.; Flynn, G.; Zimba, C. *J. Microsc. (Oxford, U. K.)* **2000,** *197,* 173–184. doi:10.1046/j.1365-2818.2000.00640.x

License and Terms

This is an Open Access article under the terms of the Creative Commons Attribution License (http://creativecommons.org/licenses/by/2.0), which permits unrestricted use, distribution, and reproduction in any medium, provided the original work is properly cited.

The license is subject to the *Beilstein Journal of Nanotechnology* terms and conditions: (http://www.beilstein-journals.org/bjnano)

The definitive version of this article is the electronic one which can be found at:
doi:10.3762/bjnano.6.61

BEILSTEIN JOURNAL OF NANOTECHNOLOGY

The Kirkendall effect and nanoscience: hollow nanospheres and nanotubes

Abdel-Aziz El Mel[*1,§], Ryusuke Nakamura[2] and Carla Bittencourt[3]

Review

Open Access

Address:
[1]Institut des Matériaux Jean Rouxel, IMN, Université de Nantes, CNRS, 2 rue de la Houssinière, BP 32229, 44322 Nantes cedex 3, France, [2]Department of Materials Science, Graduate School of Engineering, Osaka Prefecture University, Gakuen-cho 1-1, Naka-ku, Sakai 599-8531, Japan and [3]Chimie des Interactions Plasma-Surface (ChIPS), CIRMAP, Research Institute for Materials Science and Engineering, University of Mons, 23 Place du Parc, B-7000 Mons, Belgium

Email:
Abdel-Aziz El Mel[*] - Abdelaziz.elmel@cnrs-imn.fr

* Corresponding author
§ Telephone: +33(0)240 376325, Fax: +33(0)240 373 959

Keywords:
hollow nanospheres; Kirkendall effect; metals; nanotubes; oxides

Beilstein J. Nanotechnol. **2015,** *6,* 1348–1361.
doi:10.3762/bjnano.6.139

Received: 09 March 2015
Accepted: 27 May 2015
Published: 18 June 2015

This article is part of the Thematic Series "Atomic scale interface design and characterisation: Theory – Structure and dynamics".

Guest Editor: C. Ewels

© 2015 El Mel et al; licensee Beilstein-Institut.
License and terms: see end of document.

Abstract

Hollow nanostructures are ranked among the top materials for applications in various modern technological areas including energy storage devices, catalyst, optics and sensors. The last years have witnessed increasing interest in the Kirkendall effect as a versatile route to fabricate hollow nanostructures with different shapes, compositions and functionalities. Although the conversion chemistry of nanostructures from solid to hollow has reached a very advanced maturity, there is still much to be discovered and learned on this effect. Here, the recent progress on the use of the Kirkendall effect to synthesize hollow nanospheres and nanotubes is reviewed with a special emphasis on the fundamental mechanisms occurring during such a conversion process. The discussion includes the oxidation of metal nanostructures (i.e., nanospheres and nanowires), which is an important process involving the Kirkendall effect. For nanospheres, the symmetrical and the asymmetrical mechanisms are both reviewed and compared on the basis of recent reports in the literature. For nanotubes, in addition to a summary of the conversion processes, the unusual effects observed in some particular cases (e.g., formation of segmented or bamboo-like nanotubes) are summarized and discussed. Finally, we conclude with a summary, where the prospective future direction of this research field is discussed.

Review

Introduction

In the years following the discovery of the diffusion of gold in solid lead by Roberts-Austen in 1896 [1,2], it was believed that atomic diffusion in metals could occur by a direct exchange of atomic position (Figure 1a) or by a ring mechanism in which the atoms exchange their positions by following a ring path (Figure 1b) [3]. However, in 1942, Kirkendall reported on a

new diffusion phenomenon, known today as the Kirkendall effect, explaining the interdiffusion between copper and zinc in a copper/brass system [3,4]. The experimental data reported by Kirkendall supported the theory that atomic interdiffusion at the interface of two metals occurs through a vacancy exchange mechanism (Figure 1c). Despite the high importance of this discovery, at that time, it did not receive much attention [3]. In April 1946, together with his student Smigelskas, Kirkendall submitted a manuscript to the editorial office of Transactions of the AIME describing new results supporting the theory he had proposed four years before [3]. Unfortunately, this manuscript was rejected by the referee (R. F. Mehl from the Carnegie Institute of Technology) who was convinced that the new diffusion mechanism proposed by Kirkendall was wrong. In 1947, Smigelskas and Kirkendall succeeded in publishing their article [5] after including the criticisms and comments of Mehl in the comments and discussion section [3]. In 1950, Mehl acknowledged the validity of the Kirkendall effect [3] and one year later he and his student DaSilva published new data validating the reproducibility of the Kirkendall effect for different metal alloys [6].

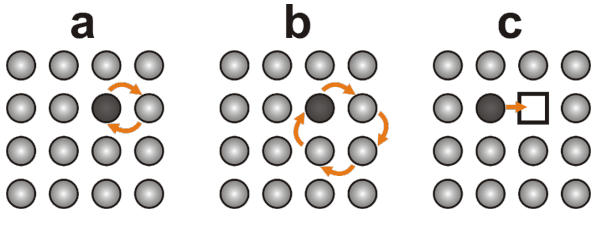

Figure 1: Atomic diffusion based on (a) the direct exchange mechanism, (b) the ring mechanism and (c) the vacancy mechanism. Figure adapted with permission from [3], copyright 1997 Springer Science and Business Media.

The Kirkendall effect describes the motion of the boundary between two metals due to a thermally activated, unbalanced diffusion. Upon annealing of two stacked metals, A and B, at a temperature high enough to thermally activate the diffusion of atoms, atomic migration can occur at the interface where atoms diffuse from metal A to metal B and vice versa (Figure 2a). Such an annealing process results in the formation of an A/B alloy layer located between the two sides of the interface where the final thickness is dependent on both the annealing temperature and time. According to the Kirkendall effect, the position of the initial interface changes during the annealing process since the atomic diffusion coefficients of atom A in metal B and of atom B in metal A are different. As a consequence of the unbalanced diffusion rates between the two stacked metals, vacancies will be injected at the interface region within the faster diffusing metal. For example, if we consider that atom A diffuses in metal B much faster than atom B in metal A, the flux of atoms migrating from metal A to metal B ($J_{A/B}$) will be much higher than atoms of B diffusing in the opposite direction ($J_{B/A}$). In such case, the A/B alloy region will be more extended within metal B and vacancies will be injected at the interface region within metal A (Figure 2b). The coalescence of excess of vacancies leads to the formation of small voids distributed all along the interface. As the annealing process progresses in time, vacancies will be generated leading to the enlargement of the formed voids (Figure 2c) that will coalesce and form pores within the material.

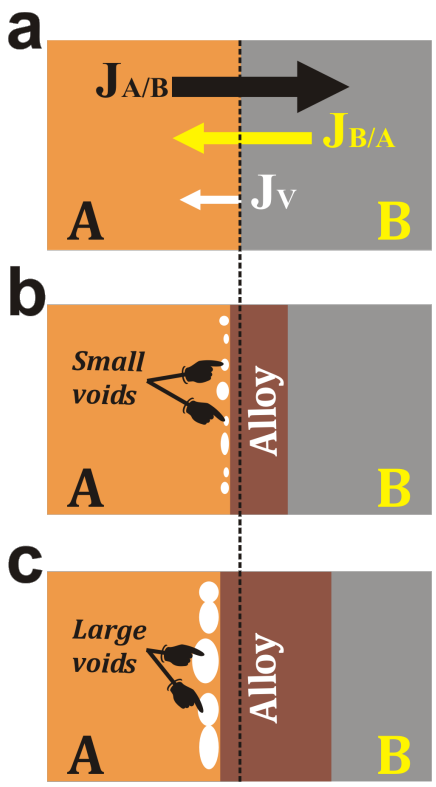

Figure 2: Schematic illustration describing the different stages occurring during the formation of voids at the interface of two different metals, A and B, as a consequence of the Kirkendall effect induced by thermal annealing. (a) Two stacked metals A and B before annealing; the arrows describe the flux of the different species diffusing from metal A to B and vice versa. Formation of small (b) and large (c) voids within metal A, as a consequence of the unbalanced diffusion rate.

Until recently, the formation of pores in metal alloys as a consequence of the Kirkendall effect was considered as a serious problem in metallurgy. For example, porosity at the interface of two soldered metals deteriorates the mechanical properties of the interface, resulting in a reduced mutual adhesion between them. For this reason, the main purpose of the research carried out in the past on the Kirkendall effect was to develop technological solutions to avoid the mentioned drawbacks, which lead to the failure of interfaces between soldered metals. However, in 2004, Yin et al. brought the Kirkendall effect to light when

they demonstrated for the first time that at the nanoscale, this effect becomes an extremely useful "tool" for the engineering and design of hollow nanomaterials [7]. Since this discovery, the Kirkendall effect applied to nano-objects has been considered as a very powerful synthesis strategy for hollow nanomaterials. The importance here rises from the fact that hollow nanostructures find applications in various technological applications including biotechnology [8], batteries [9-13], sensors [14-16], catalysis [17-19], photodetectors [20], electrochromic devices [21] and supercapacitors [22]. Three years after the pioneering work of Yin et al. [7], the progress in the synthesis of nanotubes and hollow nanoparticles using the Kirkendall effect was reviewed by Fan et al. [23]. In this first review, they summarized and discussed the achievements from both the experimental and theoretical point of view. In 2012, a review focusing mainly on the synthesis of hollow nanospheres using the Kirkendall effect was reported by Wang et al. [24]. While this present review was in preparation, Anderson and Tracy published a review on the progress of different synthesis approaches of hollow nanoparticles, including the anion and galvanic exchange reaction and the Kirkendall effect [25].

This review has two main goals: (i) expanding the knowledge on hollow nanospheres by addressing some issues which were not taken into account in the previous reviews (e.g., dynamic transformation of nanospheres from solid to hollow) and (ii) providing an updated account on the recent progress in the synthesis of nanotubes using the Kirkendall effect. We begin by summarizing the state of the art on the synthesis of Kirkendall hollow nanospheres with a special emphasis on the conversion mechanisms (i.e., symmetric and asymmetric) which require, in some cases, in situ dynamic analysis to be understood. We follow with a brief summary on the growth strategies developed so far to synthesize nanotubes using the Kirkendall effect. After, we mainly focus on the Kirkendall oxidation process of metal nanowires with special attention to some unusual effects observed for Kirkendall nanotubes which, until today, remain unclear.

Hollow nanospheres

First observation: symmetrical conversion mechanism

The formation of hollow Kirkendall nanospheres was first reported by Yin et al. in 2004 [7]. They observed the formation of hollow nanospheres while exploring the sulfidation of cobalt nanoparticles by injecting a solution of sulfur in 1,2-dichlorobenzene into hot Co nanocrystals. They demonstrated that both the annealing temperature and the annealing time have a direct impact on the transformation kinetics of the nanoparticles from solid Co into hollow CoS. In this same study, the authors show that a similar effect occurs during oxidation or selenization of Co nanocrystals. Since this first report, the nanoscale Kirkendall effect has become very popular and been adopted by many research groups for the synthesis of hollow nanoparticles covering a wide range of materials including sulfides [8,26-30], oxides [9-11,30-52], selenides [30,42,53], telurides [14,30], fluorides [53,54], phosphides [17,55] and metals [56-59]. Through these studies, two conversion mechanisms were identified: symmetrical and asymmetrical. In this subsection, we focus on the symmetrical mechanism and the following we discuss the asymmetrical mechanism. The terms "symmetrical" and "asymmetrical" are in general employed to indicate whether the shell of the hollow nanosphere is isotropic or nonuniform, respectively.

An early example of the symmetrical conversion mechanism is the pioneering work of Yin et al. on the selenization of cobalt nanoparticles [7]. They have shown that the conversion reaction starts by the formation of a very thin cobalt selenide shell on the outer skin of the Co nanoparticle (Figure 3). As the reaction proceeds in time, the Co atoms tend to diffuse outward through the cobalt selenide shell until reaching the outer surface of the nanoparticle. Simultaneously, the Se atoms were reported to diffuse inward through the shell until reaching the Co core. Due to the high outward diffusion flux of Co compared to the slower inward flux of Se, vacancies are created and injected at the Co(core)/CoSe(shell) interface. The migration and agglomeration of vacancies result in the formation and merging of the initial voids located at the interface and extended along the Co core (Figure 4a). The increase in size of these voids was found to lead to the formation of Co bridges, linking the Co core and the CoSe shell (Figure 4b). The authors found that these bridges persist until the Co core is completely consumed during the reaction and the particle becomes fully hollow. Such bridges were also reported for other materials; it is believed that at this stage the metal atoms leaving the core are transported by

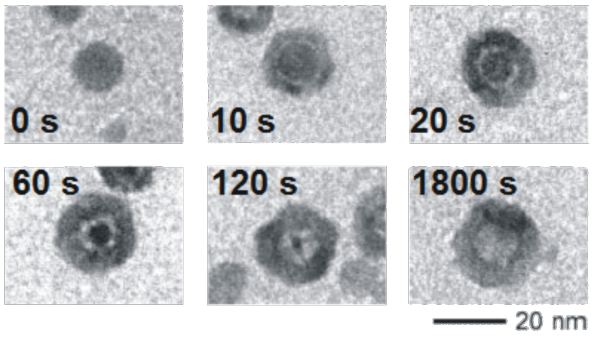

Figure 3: Morphological evolution of CoSe hollow nanocrystals as a function of the selenization time. Figure adapted with permission from [7], copyright 2004 American Association for the Advancement of Science.

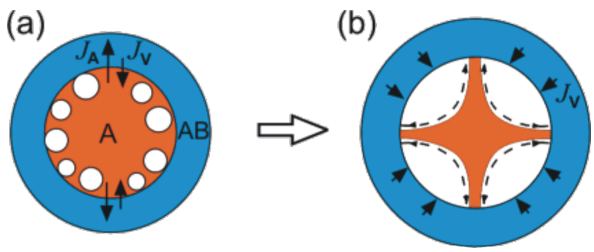

Figure 4: A scheme describing the Kirkendall-induced hollowing process of nanospheres consisting of a core/shell structure. (a) Generation of small Kirkendall voids along the core/shell interface and (b) surface migration of atoms along the bridges linking the core A to the shell AB. Figure adapted with permission from [61], copyright 2007 American Chemical Society.

diffusing mainly on the surface of the voids along the bridges until reaching the inner surface of the shell where they spread before diffusing outward across it [7,23,29,60,61]. Since the surface diffusion coefficients are several orders of magnitude higher than the bulk diffusion coefficients, at this stage, the growth kinetics of voids was reported to be faster than in the early stage of the growth were the formation of voids is mainly governed by a bulk diffusion mechanism [23,61].

Asymmetrical conversion mechanism

The stages of the hollowing process previously described were found to vary according to the selected metal and the reactive atmosphere [25,27,28,43]. For example, when oxidizing nickel nanospheres under ambient atmosphere, Nakamura et al. found that the shape of the resulting nickel oxide hollow nanoparticles was asymmetric with a nonuniform shell thickness [32]. This effect was also observed recently by other groups [25,43,48]. On the basis of these studies, one can briefly summarize the stages of the asymmetric conversion mechanism. In the early stage of conversion, it is believed that the vacancies migrate and then agglomerate into a single void at the Ni/NiO interface on one side of the nanoparticle (Figure 5a–d) instead of being distributed along the metal/metal oxide interface as observed in the case of the symmetrical conversion mechanism during the oxidation of Cu nanospheres (Figure 5e). As the oxidation process proceeds in time, the growth of NiO was reported to occur preferentially at the adjacent side of the void (Figure 5b–d). In general, most authors report that the shell is thinner on the side where a large void is present during oxidation and thicker on the opposite side (Figure 5d). The formation of a single large void during the conversion process was assumed to be more favorable as compared to the formation of multiple smaller voids and filaments observed in the symmetrical mechanism, illustrated in Figure 4 and Figure 5e. Indeed, since the sum of surface energies of multiple small voids is higher than the surface energy of a single large void, during the conversion process, multiple small voids tend to agglomerate and form a single large void to minimize the surface energy [32].

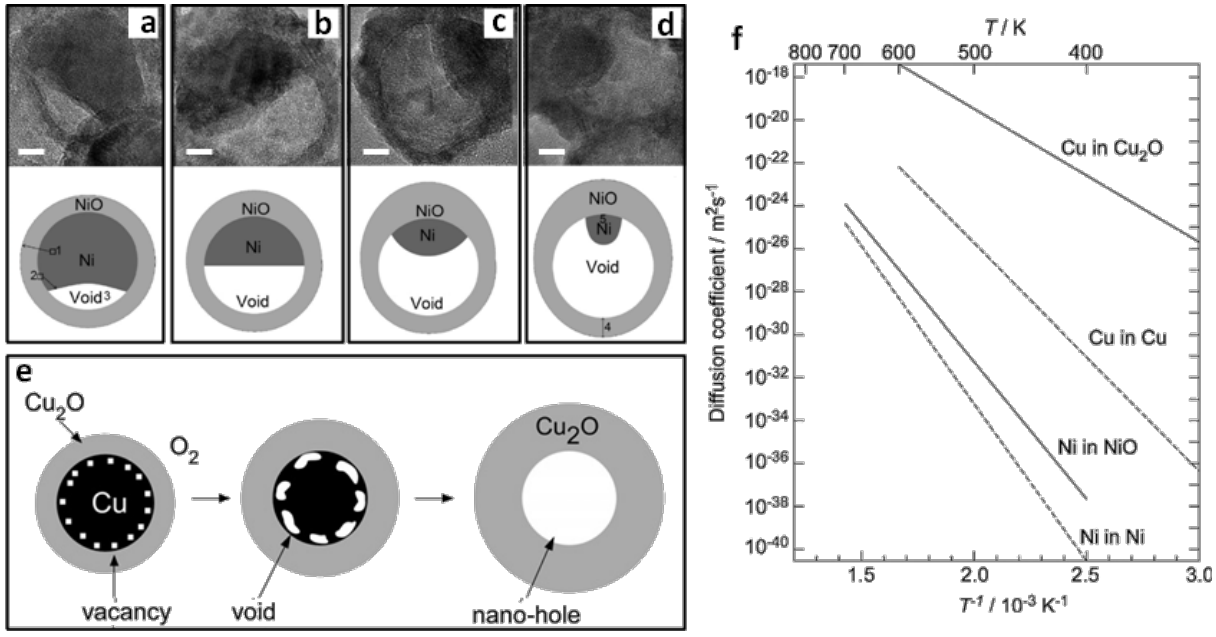

Figure 5: TEM micrographs and corresponding schemes of 26 nm nickel nanospheres oxidized in air at 300 °C for (a) 120, (b) 150, (c) 180, and (d) 210 min. Scale bar: 5 nm. Figure adapted with permission from [43], copyright 2010 American Chemical Society. (e) Scheme of the oxidation process of a Cu nanoparticle. (f) Self-diffusion coefficients of Ni and Cu and diffusion coefficients of Ni and Cu ions in NiO and Cu_2O, respectively. Figure adapted with permission from [32], copyright 2008 Taylor & Francis.

Until today, the explanation of such asymmetrical conversion mechanism is still under discussion. In their early report, Nakamura et al. concluded that the formation of an off-centered, single void during oxidation of nickel is related to the intrinsic properties of nickel itself [32]. They came to such a conclusion by comparing the ratio between the diffusion coefficient of Ni in NiO and the self-diffusion coefficient of Ni (i.e., diffusion of Ni ions in Ni) (Figure 5f). Since this ratio is quite low compared to other metals, they concluded that the generation/migration rate of vacancies is well-balanced [32]. This led to the conclusion that when the generation and the migration rate of vacancies injected at the Ni/NiO interface as a consequence of the outward diffusion of Ni are comparable, the vacancies have the ability to migrate toward a position over a long-range distance where they aggregate and form a large single void instead of forming small voids distributed along the Ni/NiO interface. This effect was not observed with Cu because the generation rate of vacancies in Cu during oxidation was found to be much faster than the migration rate since the diffusion coefficient of Cu in Cu_2O is much higher (up to nine times at 100 °C) than the self-diffusion coefficient of Cu. Thus, in the case of Cu, the generated vacancies do not have sufficient mobility to migrate over a long-range distance before they aggregate into one single large void. Rather, they form multiple small voids distributed along the Cu/Cu_2O interface (as illustrated in Figure 5e), which leads to an additional step in the formation of a hollow Cu_2O nanoparticle with a uniform shell thickness. The asymmetrical conversion mechanism identified when oxidizing spherical nickel nanoparticles was recently encountered by Railsback et al. who have shown that such an effect becomes more or less pronounced according to the size of the nanoparticles [25,43].

The formation of an off-centered, single void during the conversion process may also not be the only mechanism leading to the asymmetric shape of the hollow nanospheres. An example is the case of sulfidation of Cd nanospheres reported in the study by Cabot et al. who shown that, although an off-centered single void forms during the conversion process (Figure 6) [27], the spherical CdS shell grows isotropically resulting in the formation of hollow CdS nanospheres with a uniform shell thickness [27]. This puts in doubt the conclusions making a direct link between the formation of nonuniform shell thickness and the formation of a single void during the conversion of the particles. One obstacle preventing this phenomenon from being fully understood is related to the fact that the TEM observations are in general carried out ex situ. This means that the TEM micrographs collected during the different stages of the conversion process are not recorded on the same nanosphere. To provide a clearer interpretation of this phenomenon, direct monitoring of the conversion process using dynamic in situ TEM is mandatory.

Dynamic formation of hollow nanospheres

Very recently, Niu et al. reported on the dynamic formation of bismuth oxide hollow nanospheres using a TEM liquid cell, allowing the in situ oxidization of bismuth nanoparticles to be observed [48]. Figure 7a presents a sequence of TEM micrographs recorded by the authors on a bismuth nanoparticle during oxidation. At the early stage, the oxidation process started with the formation of a thin layer of bismuth oxide on the outer skin of the bismuth nanoparticle (Figure 7a). An off-centered, single void was then formed at the bismuth/bismuth oxide core/shell interface. As the oxidation process proceeds in

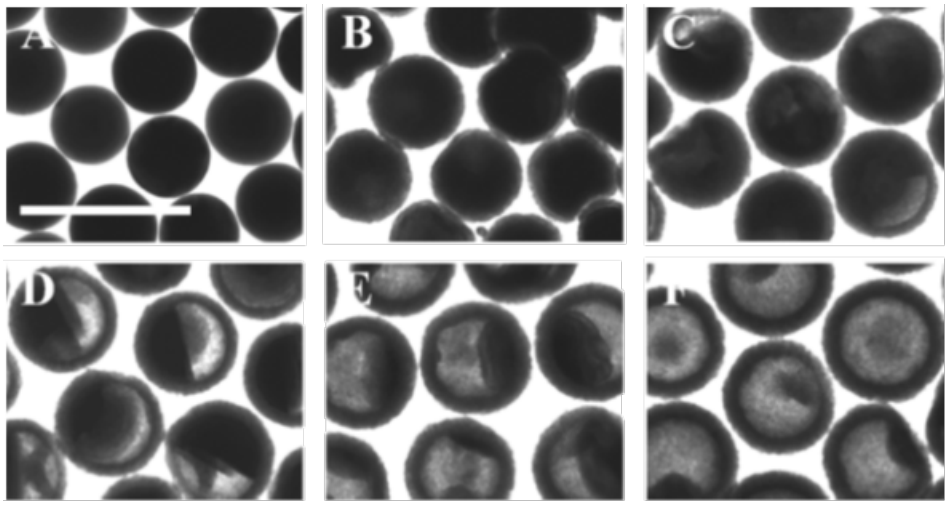

Figure 6: TEM micrographs showing the conversion stages of the CdS shell during the sulfidation of Cd nanospheres. The conversion process is monitored from the as-synthesized Cd nanospheres (A) until the fully hollow CdS nanospheres were obtained (B–F). Scale bar: 500 nm. Figure adapted with permission from [27], copyright 2008 American Chemical Society.

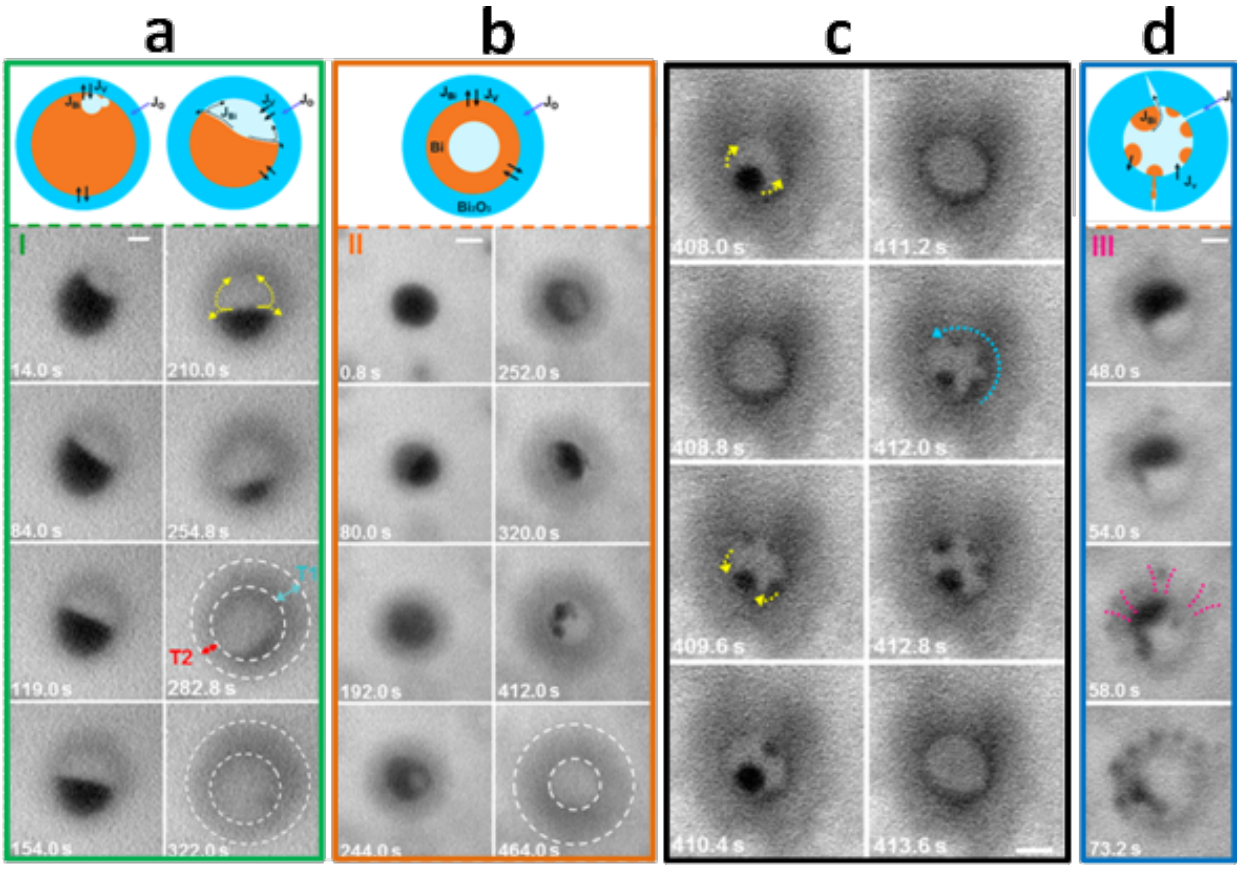

Figure 7: Sequential TEM micrographs recorded in situ to monitor the dynamic transformation of bismuth nanospheres during oxidation. The final product of the reaction was reported to be dependent on the considered nanosphere, which may transform by the end of the process into an: (a) asymmetric shell, (b, c) isotropic shell or (d) oxide shell decorated with bismuth nanoclusters. The data show that bismuth behaves like a liquid with frequent changes in the morphology of the nanodroplets inside the oxide shell. Scale bar: 50 nm. Figure adapted with permission from [48], copyright 2013 American Chemical Society.

time, the void was found to become bigger while the bismuth core disappeared in a layer-by-layer fashion. By the end of the conversion process, a nonuniform oxide shell was formed. The authors demonstrated that this effect is related to the fact that bismuth diffuses out of the oxide shell nonuniformly with a faster diffusion rate through the shell adjacent to the void. In the same study, Niu et al. demonstrated that other particles oxidized under the same conditions do not show the same behavior (Figure 7b). Indeed, after the formation of an off-centered, single void, in the case of the second particle, they observed that the small amount of bismuth residue forming the core became unstable during the conversion process and behaves like a liquid rather than a solid. The bismuth core was found to suddenly split into several small nanodroplets (Figure 7b, 412 s) which then quickly vanish (Figure 7b, 464 s). The authors attributed the observed frequent changes of the bismuth configuration during oxidation to the local temperature which exceeds the melting point of the residual bismuth core evaluated in the same study of about 180 °C [48]. It is important to mention that this particle results in a uniform shell thickness at the end of the conversion process (Figure 7b, 464 s).

The liquid behavior of bismuth was also identified by the authors while imaging another particle (Figure 7c). They found that before achieving fully-hollow nanospheres, several unexpected events take place. Their data, presented in Figure 7c, show that after 408 s of oxidation, the bismuth nanoparticle becomes hollow with a bismuth nanodroplet on the curved inner surface of the shell. For an additional 0.8 s of oxidation, the formed bismuth nanodroplet wet the inner surface of the oxide shell. Then, when reaching 409.6 s, the authors observed that the nanodroplet tends to split into multiple tiny dewetting metal bismuth nanodroplets. The droplets then migrate and aggregate on the curved inner surface of the oxide shell before the bismuth wets the surface again (between 410.4 and 413.6 s). They attributed this reversible wetting transition to the interplay between the surface tension of the metal bismuth present in a liquid phase and the curved inner surface of the oxide shell. It

is also believed that the wetting behavior of bismuth on the inner surface of the oxide shell can be influenced by other parameters such as the vapor pressure inside the oxide shell and the annealing temperature.

Niu et al. [48] have also remarked that in addition to the conversion mechanisms previously described, for some nanoparticles, bismuth nanoclusters can be formed on the outer surface of the particle (Figure 7d). They assumed that the defects present within the formed bismuth oxide shell (such as grain boundaries) serve as diffusion channels which enhance the outward diffusion of bismuth. They have further demonstrated that before being oxidized, bismuth tends to condense into several nanodroplets on the outer layer of the nanoparticle (Figure 7d, 73.2 s). In such a case, the growth rate of the oxide shell was found to be enhanced compared to the cases previously described.

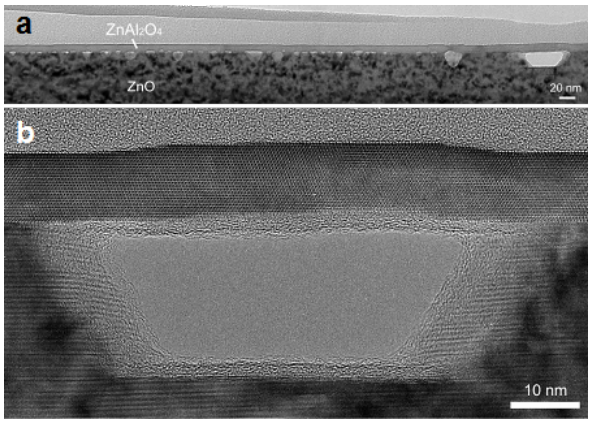

Figure 8: TEM (a) and high-resolution TEM (b) micrographs showing the Kirkendall voids formed at a ZnO–Al_2O_3 planar interface after annealing. Figure adapted with permission from [61], copyright 2007 American Chemical Society.

Nanotubes

Growth strategies

Following the report on hollow nanoparticles by Yin et al. in 2004 [7], Li and Penner [20] demonstrated in 2005 that the Kirkendall effect can be extended to the fabrication of nanotubes. CdS nanotubes were synthesized by high temperature sulfidation of Cd nanowires prepared by electrochemical step-edge decoration on graphite electrode surfaces. Since the as-grown nanowires were in contact with the surface of the graphite substrate, the diffusion of S was partially hindered, resulting in the formation of hemicylindrical CdS nanotubes instead of cylindrical ones. In 2006, Fan et al. [62] also showed that the Kirkendall effect can be used to synthesize monocrystalline spinel $ZnAl_2O_4$ nanotubes. In this case, the conversion method was based on a solid state reaction, occurring upon thermal annealing of core–shell ZnO/Al_2O_3 nanowires [23,62]. In such a process, the material forming the nanotube is defined by the two initial compounds constituting the core and the shell. As it can be seen in Figure 8, the formation of voids occurs at the interface within the ZnO which, in this case, plays the role of the fast diffusing material.

The strategy demonstrated by Li and Penner in 2005 was adopted by many groups for the synthesis of nanotubes by thermal annealing of metal nanowires under a controlled atmosphere such as sulfur, selenium or oxygen [15,63]. Among these materials, a preference was shown for metal oxide nanotubes due to the simplicity of oxidation of metals at ambient air conditions, as compared to sulfidation and selenization, where the use of toxic gases such as H_2S and H_2Se is required. On the basis of the large number of reports on this topic, similar to the case of the spherical nanoparticles presented in the previous section, the hollowing process of nanowires can now be easily described (Figure 9) [12,15,23,33,63-71]. Briefly, the conversion process starts with the adsorption of oxygen on the outer skin of the metal nanowire resulting in the formation of a thin layer of metal oxide (Figure 9a). After the formation of a metal/metal oxide core/shell nanowire, the metal ions diffuse outward through the oxide layer until reaching the outer surface. Simultaneously, the oxygen adsorbed on the outside of the wire diffuses through the oxide layer and penetrates toward the metal core. For some metals, such as Co, Cu, Fe, and Ni, the diffusion coefficients of metal ions through their own oxides are much higher than those of oxygen ions [34]. This fact results in the formation of multiple supersaturated vacancy clouds all over the metal/metal oxide interface along the wire axis which, in a further stage, condense and form multiple separated small voids within the metal core (Figure 9b,c) [63]. The coalescence of voids is the final mechanism occurring during the synthesis, which finally leads to the formation of hollow oxide nanostructures (Figure 9d and Figure 10).

Unusual effect in Kirkendall nanotubes

Several reports have shown that the injection and the diffusion rates of vacancies play a key role in the Kirkendall-induced hollowing process of nanostructures [65-67]. In the case of oxidation of metal nanowires, the injection rate of vacancies can be defined as the difference between the outward and inward diffusion flux of the metal and oxygen ions through the oxide shell, respectively. The diffusion rate of vacancies within the metal is dependent on the self-diffusion rate of the metal ions. To create metal oxide nanotubes, two different annealing approaches can be used: (i) rapid thermal annealing [65] and (ii) gradient thermal annealing [66]. In general, the first approach is preferred over the second since the annealing time for a fixed temperature can be precisely controlled. For NiO nanotubes

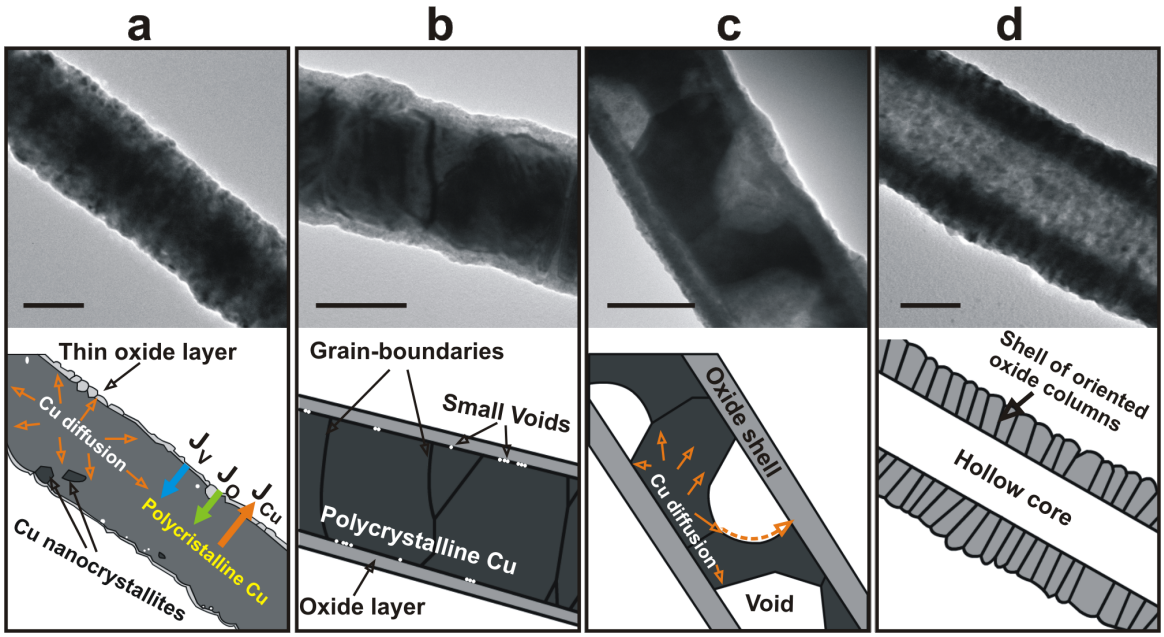

Figure 9: TEM micrographs and corresponding illustrations showing the chronological evolution of a Cu nanowire during thermal oxidation in air at 300 °C. The oxidation time was varied: (a) 1 min, (b) 2 min, (c) 3 min, and (d) 4 min. Scale bar: 100 nm. Figure adapted with permission from [63], copyright 2013 Wiley-VCH.

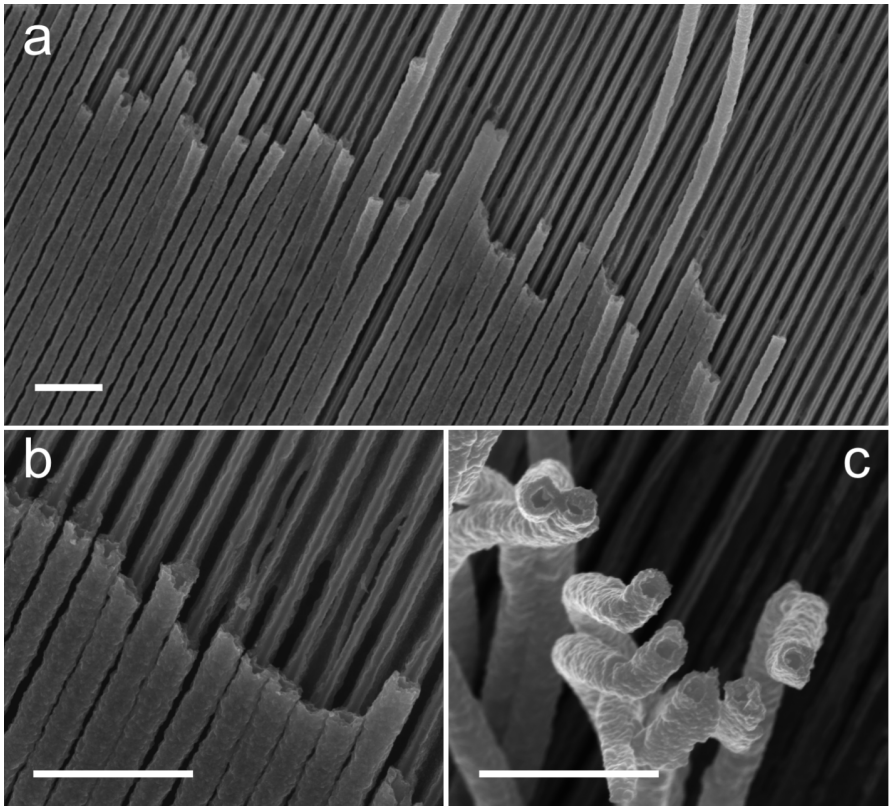

Figure 10: (a,b) SEM micrographs showing the high fidelity of copper oxide nanotubes prepared on nanograted silicon substrate by thermal oxidation of copper nanowires for 1 h at 300 °C. (c) SEM micrograph of copper oxide nanotubes disengaged from the nanograted substrate due to the cutting procedure applied to the specimen before observation with SEM. Scale bar: 1 μm. Figure adapted with permission from [63], copyright 2013 Wiley-VCH.

created by thermal oxidation of nickel nanowires, a systematic study was reported where both approaches were investigated (Figure 11) [66]. Through these studies, it was made clear that to obtain nanotubes with a uniform wall thickness, the diffusion rate of vacancies must be much lower than their injection rate [65-67]. When these conditions are not maintained, bamboo-like nanotubes may be formed [65-67]. This was first reported by Nakamura et al. while investigating the oxidation of nickel nanowires [65]. So far, this irregularity was only observed when oxidizing nickel nanowires. Although ramping (Figure 11a) and rapid (Figure 11b) thermal annealing approaches were investigated, the nanotubes were found to show the same bamboo-like structure at the final stage of the conversion process [66]. The formation of bamboo-like structures was attributed to the fact that nickel vacancies exhibit a very high diffusion length compared to other metals such as copper [65]. In a recent study, Ren et al. demonstrated that such irregularity originates from the fact that the diameter of the nickel nanowires used to create oxide nanotubes by means of the Kirkendall effect is in general much smaller than the diffusion length of nickel vacancies [67]. In their study, Ren et al. investigated the oxidation of nickel nanowires with two different diameters: ≈250 nm (Figure 12a,b) and ≈140 nm (Figure 12c,d) [67]. When the diameter of the nanowires is comparable to the vacancy diffusion length, the authors found that the vacancies were able to diffuse and agglomerate along the Ni/NiO interface (Figure 12a,b). As a consequence, multiple voids form along the Ni/NiO interface, which results in a further stage in the formation of nanotubes with uniform wall thickness. When the diameter of the nanowires becomes smaller or comparable to the diffusion length of vacancies in nickel, Ren et al. showed that a wall-to-wall diffusion can occur (Figure 12c,d) [67]. In other words, during oxidation, a vacancy generated at the interface on one side of the wire can travel across the wire and reach the opposite side before agglomerating with another vacancy (Figure 12d). This results in the formation of segmented-like nanotubes with a NiO shell and periodic nickel nanoparticles. As the oxidation process progress in time, the nickel atoms forming the nanoparticles undergo two diffusion mechanisms: lateral (perpendicular to the axis of the tube) and longitudinal (along the tube axis). Since no metal bridges are formed between the segmented metal particles, the diffusion along the tube axis was reported to be reduced and the lateral mechanism dominates. In the regions where the nanoparticles are formed, the Ni ions will diffuse laterally toward the outside of the nanotube. As this event occurs during oxidation, the segmented-like nanostructure transforms into a bamboo-like one.

The presence of very high strain generated during oxidation due to the lattice mismatch between the metal core and the metal oxide shell is another factor that can amplify the formation of a bamboo-like structure. Güder et al. reported on a new approach based on stress engineering to control the spatial positioning and distribution of Kirkendall voids in ZnO/Al_2O_3 core–shell nanowires [72]. In this study, they applied their novel approach to synthesize $ZnAl_2O_4$ nanotubes containing ZnO nanocrystals. First, rippled ZnO nanowires coated with a 12 nm thick Al_2O_3 layer were synthesized (Figure 13a) and then annealed at 700 °C for 5 h (Figure 13b). The annealing process results in the transformation of the ZnO/Al_2O_3 nanowires into a peapod structure, where large nanocavities were formed in the thin areas (i.e., narrower section) of the wires, while the thick regions (i.e., wider sections) remained filled with ZnO (Figure 13b). The authors further demonstrate that such transformation is a consequence of the presence of an oscillating

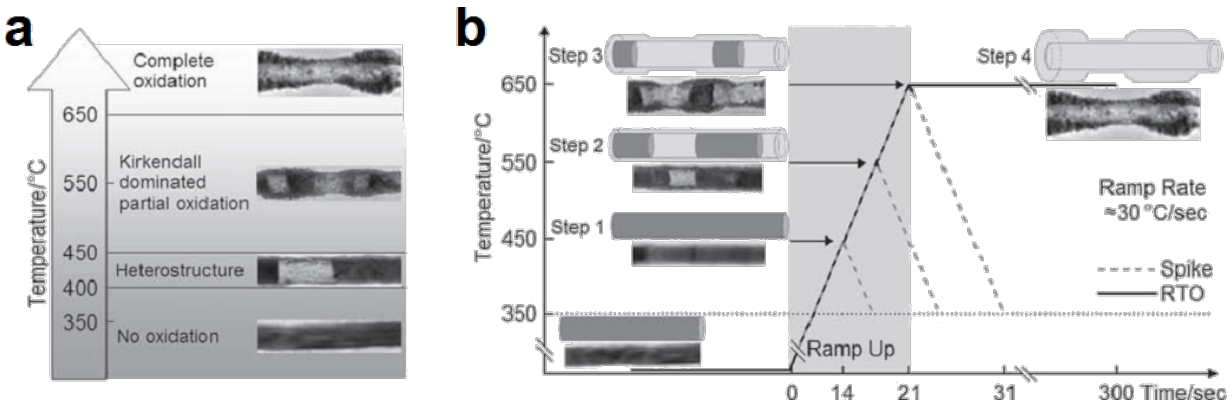

Figure 11: Representations of the different morphologies that can be obtained by thermal oxidation of nickel nanowires at different annealing temperatures and times. Two regimes are considered: (a) rapid thermal annealing and (b) ramp annealing. In the case of ramp annealing, the nanostructures in steps 1 to 3 are formed during the ramp up stage. The dashed lines in (b) represent the spike annealing temperature profiles. Figure adapted with permission from [66], copyright 2010 Wiley-VCH.

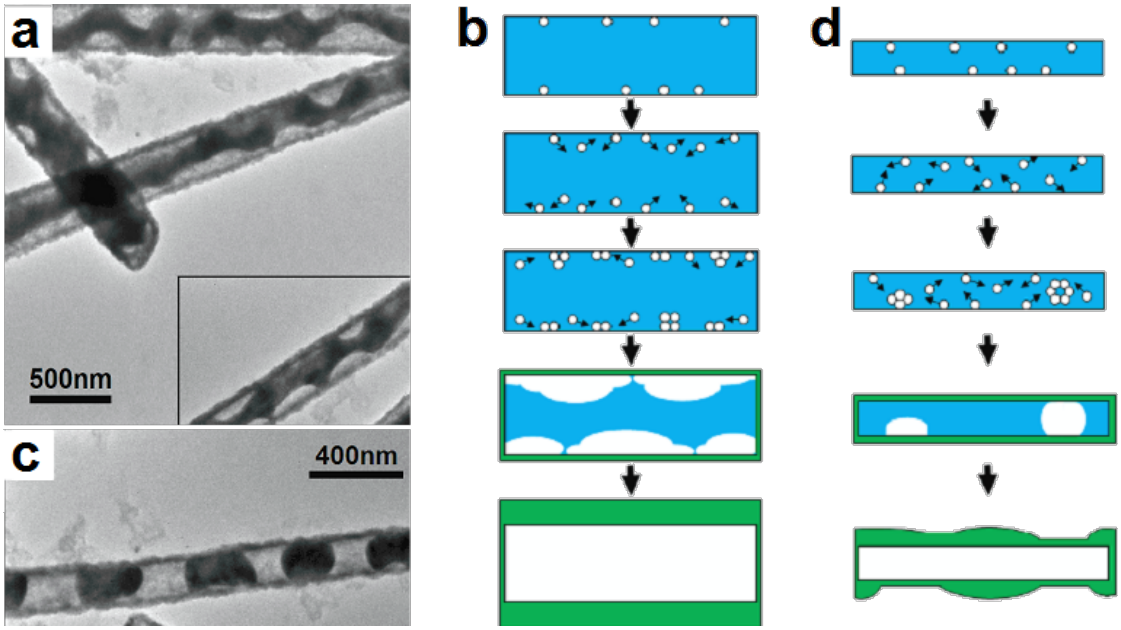

Figure 12: TEM micrograph of (a) thick (≈250 nm in diameter) and (c) thin (≈140 nm) nickel nanowires after thermal oxidation for 5 min at 500 °C in ambient air. Schematic showing the type of voids formed during oxidation of a nickel nanowire with a thick (b) and a thin (d) diameter. Figure adapted with permission from [67], copyright 2011 IOP Publishing.

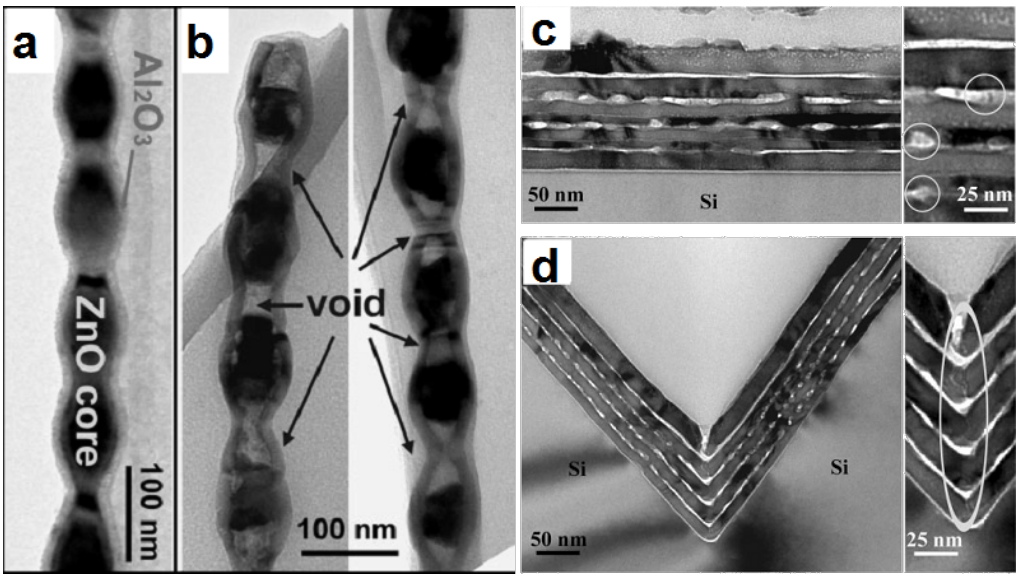

Figure 13: TEM micrographs of ZnO/Al_2O_3 core/shell oscillatory nanowires before (a) and after (b) annealing at 700 °C for 5 h. Cross-sectional TEM micrographs of $ZnAl_2O_4$ multilayers formed by a solid state reaction between ZnO and Al_2O_3 layers at 700 °C for 3 h in two different configurations: (c) planar (i.e., thin films) and (d) 3D (i.e., silicon V-trench). Figure adapted with permission from [72], copyright 2010 Wiley-VCH.

stress field with a periodic fluctuation along the wire's axis due to the initial rippled structure of the core/shell nanowire [72]. Indeed, the fact that the stress gradient is higher in the thin areas of the wire compared to the thick ones, the void nucleation becomes more favorable in the narrower section of the wire compared to the rest of the regions. The theory proposed for core/shell ZnO/Al_2O_3 nanowires was further confirmed by the authors by annealing ZnO (24 nm)/Al_2O_3 (12 nm) periodic

stacked layers. Two configurations were investigated: planar (Figure 13c) and 3D (V-trench substrate) (Figure 13d). In the planar configuration, disconnected Kirkendall channels/voids distributed without an ordered pattern were formed between the resulting $ZnAl_2O_4$ layers after annealing at 700 °C for 3 h (Figure 13c). On the other hand, the V-trench configuration shows a significant difference after annealing, where disordered smaller voids are distributed along the planar interface and large voids are pinned at the bottom of the V-trench (Figure 13d) [72]. From these results, the authors concluded that the formation of large voids at the bottom of the V-groove area is a consequence of the periodic stress pattern formed along the symmetry axis of the V-groove area of the deposited nanolayers, which results in the preferential nucleation and growth of voids.

Conclusion

Recently, the Kirkendall effect has been considerably developed and used as a powerful process to synthesize hollow nanostructures of different shapes. We summarized the recent progress on the Kirkendall effect and discussed why it is considered as a versatile route to hollow nanostructures such as nanospheres and nanotubes. For nanospheres, we focused mainly on the comparison between the symmetrical and the asymmetrical conversion mechanisms that occur during the Kirkendall-induced hollowing process. The differences between these two mechanisms have been discussed in detail. In particular, we have discussed how the diffusion rate of vacancies as well as their injection rate can impact the final structure of the hollow nanospheres. Our discussion was further reinforced based on a newly published study reporting on the in situ dynamic TEM imaging of the Kirkendall-induced hollowing process of nanospheres.

For nanotubes, we have summarized the examples demonstrated so far using the Kirkendall effect. We dedicated special attention to oxide nanotubes. Based on the reports published since 2004, we discussed the hollowing mechanisms for one-dimensional materials and pointed out some unusual effects (i.e., formation of segmented and bamboo-like oxide nanotubes) observed in specific cases (i.e., oxidation of nickel nanowires) which, until today, is still not fully understood. The explanation reported so far to explain such unusual effects were discussed. More precisely, the presence of irregularities in nickel oxide nanotubes was related to the diffusion and to the injection rates of vacancies as well as to the confinement in nanowires.

Although huge efforts were dedicated to the comprehension of the fundamental mechanisms involved in the Kirkendall-induced hollowing process of nanomaterials, there are still several studies which must be carried out to expand the comprehension of this phenomenon. Among these, one can mention the study of the oxidation-induced Kirkendall conversion mechanisms of binary and ternary metal alloys. Such a study would be quite interesting since the presence of impurities in metals is expected to impact the diffusion coefficients, which might in turn influence the Kirkendall effect. Until today, only two studies were reported so far on this topic (i.e., oxidation of Ag/Au and Ni/Cr nanospheres) leaving a wide range of possible experiments which deserve to be conducted [73,74]. A very obvious study concerns the oxidation of binary and/or ternary metal alloy nanowires. This must provide additional elements for a better comprehension of the hollowing process since the vacancy confinement in 1D nanostructures differs from the case of nanospheres. Another perspective is the possibility of monitoring the oxidation-induced hollowing process using in situ TEM carried out under conditions similar to those applied ex situ (e.g., oxidation of nanostructures under an oxygen atmosphere at high pressure). Until now the dynamic studies were limited to the oxidation of nanostructures in TEM liquid cells [48]. However, such an experiment requires a very specific temperature-controlled TEM holder, allowing heating of the specimen at high temperature under an oxygen flow. Additionally, as far as we are aware, there are no comparative studies on the Kirkendall effect in monocrystalline and polycrystalline materials.

Another perspective which deserves to be pointed out is the TEM 3D tomography of Kirkendall nanospheres and nanotubes. This would allow a better comprehension of the hollowing mechanisms similar to some other processes such as the galvanic replacement, which has already been monitored using TEM tomography [75].

In terms of fabrication, the Kirkendall effect may be combined with other fabrication processes. An example is to apply electron beam lithography to Kirkendall nanotubes, which allows the design of ordered periodic metal nanoparticles confined inside oxide nanotubes (Figure 14) [64]. Another possibility is the combination of the Kirkendall effect with galvanic replacement, which allows the fabrication of multilevel hollow nanostructures that otherwise cannot be prepared with one of these processes alone [76].

One of the important perspectives of this research topic is the understanding of the Kirkendall-induced hollowing process at the atomic level using computer modeling. It should be noted that a few models were developed so far [58,77,78], but they were limited to the modeling of the basic mechanisms of the hollowing process. Applying these models as well as dynamic simulation would be very helpful to explain the unusual phenomenon observed experimentally, such as the formation of

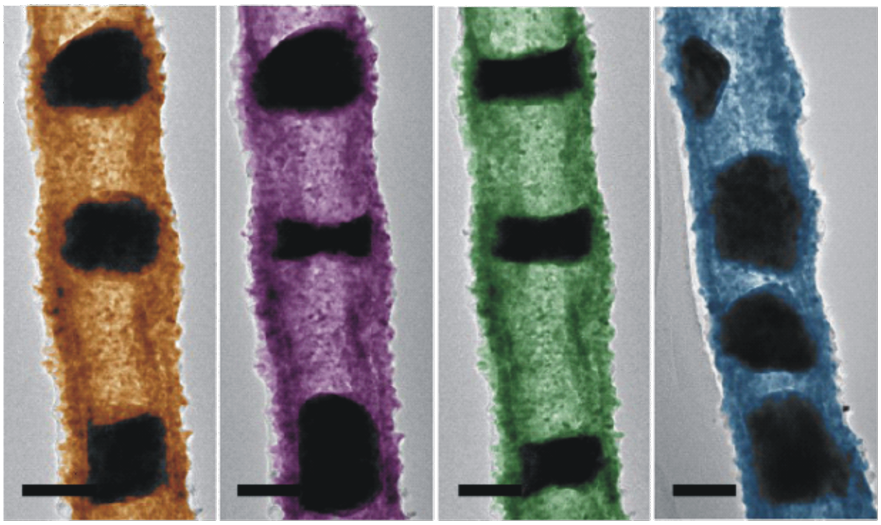

Figure 14: False-color TEM micrographs of some possible periodic Cu nanostructures that can be sculpted using an e-beam inside Kirkendall oxide nanotubes by local heating extracted from the source of a TEM. Scale bar: 100 nm. Figure adapted with permission from [64], copyright 2014 American Chemical Society.

asymmetric hollow nanospheres, segmented and bamboo-like nanotubes.

References

1. Tu, K. N. *Annu. Rev. Mater. Sci.* **1985,** *15,* 147–176. doi:10.1146/annurev.ms.15.080185.001051
2. Roberts-Austen, W. C. *Philos. Trans. R. Soc., A* **1896,** *187,* 383–415. doi:10.1098/rsta.1896.0010
3. Nakajima, H. *JOM* **1997,** *49,* 15–19. doi:10.1007/BF02914706
4. Kirkendall, E. *Trans. AIME* **1942,** *147,* 6.
5. Smigelskas, A. D.; Kirkendall, E. O. *Trans. AIME* **1947,** *171,* 130–142.
6. daSilva, L. C. C.; Mehl, R. F. *Trans. AIME* **1951,** *191,* 155–173.
7. Yin, Y.; Rioux, R. M.; Erdonmez, C. K.; Hughes, S.; Somorjai, G. A.; Alivisatos, A. P. *Science* **2004,** *304,* 711–714. doi:10.1126/science.1096566
8. Gao, J.; Liang, G.; Zhang, B.; Kuang, Y.; Zhang, X.; Xu, B. *J. Am. Chem. Soc.* **2007,** *129,* 1428–1433. doi:10.1021/ja067785e
9. Chen, J. S.; Li, C. M.; Zhou, W. W.; Yan, Q. Y.; Archer, L. A.; Lou, X. W. *Nanoscale* **2009,** *1,* 280–285. doi:10.1039/b9nr00102f
10. Ha, D.-H.; Islam, M. A.; Robinson, R. D. *Nano Lett.* **2012,** *12,* 5122–5130. doi:10.1021/nl3019559
11. Lee, Y.; Jo, M. R.; Song, K.; Nam, K. M.; Park, J. T.; Kang, Y.-M. *ACS Appl. Mater. Interfaces* **2012,** *4,* 3459–3464. doi:10.1021/am3005237
12. Liu, L.; Guo, Y.; Wang, Y.; Yang, X.; Wang, S.; Guo, H. *Electrochim. Acta* **2013,** *114,* 42–47. doi:10.1016/j.electacta.2013.09.152
13. Park, M.-H.; Cho, Y.; Kim, K.; Kim, J.; Liu, M.; Cho, J. *Angew. Chem., Int. Ed.* **2011,** *50,* 9647–9650. doi:10.1002/anie.201103062
14. Xiao, G.; Zeng, Y.; Jiang, Y.; Ning, J.; Zheng, W.; Liu, B.; Chen, X.; Zou, G.; Zou, B. *Small* **2013,** *9,* 793–799. doi:10.1002/smll.201202083
15. Yongfu, Q.; Shihe, Y. *Nanotechnology* **2008,** *19,* 265606. doi:10.1088/0957-4484/19/26/265606
16. Zhang, L.; Wang, H. *ACS Nano* **2011,** *5,* 3257–3267. doi:10.1021/nn200386n
17. Popczun, E. J.; McKone, J. R.; Read, C. G.; Biacchi, A. J.; Wiltrout, A. M.; Lewis, N. S.; Schaak, R. E. *J. Am. Chem. Soc.* **2013,** *135,* 9267–9270. doi:10.1021/ja403440e
18. Liu, S.; Zhang, Z.; Bao, J.; Lan, Y.; Tu, W.; Han, M.; Dai, Z. *J. Phys. Chem. C* **2013,** *117,* 15164–15173. doi:10.1021/jp4044122
19. Hong, J. W.; Kang, S. W.; Choi, B.-S.; Kim, D.; Lee, S. B.; Han, S. W. *ACS Nano* **2012,** *6,* 2410–2419. doi:10.1021/nn2046828
20. Li, Q.; Penner, R. M. *Nano Lett.* **2005,** *5,* 1720–1725. doi:10.1021/nl050994x
21. Scherer, M. R. J.; Steiner, U. *Nano Lett.* **2013,** *13,* 3005–3010. doi:10.1021/nl303833h
22. Du, W.; Liu, R.; Jiang, Y.; Lu, Q.; Fan, Y.; Gao, F. *J. Power Sources* **2013,** *227,* 101–105. doi:10.1016/j.jpowsour.2012.11.009
23. Fan, H. J.; Gösele, U.; Zacharias, M. *Small* **2007,** *3,* 1660–1671. doi:10.1002/smll.200700382
24. Wang, W.; Dahl, M.; Yin, Y. *Chem. Mater.* **2013,** *25,* 1179–1189. doi:10.1021/cm3030928
25. Anderson, B. D.; Tracy, J. B. *Nanoscale* **2014,** *6,* 12195–12216. doi:10.1039/C4NR02025A
26. Yin, Y.; Erdonmez, C. K.; Cabot, A.; Hughes, S.; Alivisatos, A. P. *Adv. Funct. Mater.* **2006,** *16,* 1389–1399. doi:10.1002/adfm.200600256
27. Cabot, A.; Smith, R. K.; Yin, Y.; Zheng, H.; Reinhard, B. M.; Liu, H.; Alivisatos, A. P. *ACS Nano* **2008,** *2,* 1452–1458. doi:10.1021/nn800270m
28. Cabot, A.; Ibáñez, M.; Guardia, P.; Alivisatos, A. P. *J. Am. Chem. Soc.* **2009,** *131,* 11326–11328. doi:10.1021/ja903751p
29. Gusak, A. M.; Tu, K. N. *Acta Mater.* **2009,** *57,* 3367–3373. doi:10.1016/j.actamat.2009.03.043
30. Ibáñez, M.; Fan, J.; Li, W.; Cadavid, D.; Nafria, R.; Carrete, A.; Cabot, A. *Chem. Mater.* **2011,** *23,* 3095–3104. doi:10.1021/cm2006633
31. Nakamura, R.; Lee, J.-G.; Tokozakura, D.; Mori, H.; Nakajima, H. *Mater. Lett.* **2007,** *61,* 1060–1063. doi:10.1016/j.matlet.2006.06.039

32. Nakamura, R.; Lee, J.-G.; Mori, H.; Nakajima, H. *Philos. Mag.* **2008,** *88,* 257–264. doi:10.1080/14786430701819203
33. Nakamura, R.; Matsubayashi, G.; Tsuchiya, H.; Fujimoto, S.; Nakajima, H. *Acta Mater.* **2009,** *57,* 4261–4266. doi:10.1016/j.actamat.2009.05.023
34. Nakamura, R.; Tokozakura, D.; Nakajima, H.; Lee, J.-G.; Mori, H. *J. Appl. Phys.* **2007,** *101,* 074303. doi:10.1063/1.2711383
35. Nakamura, R.; Tokozakura, D.; Lee, J.-G.; Mori, H.; Nakajima, H. *Acta Mater.* **2008,** *56,* 5276–5284. doi:10.1016/j.actamat.2008.07.004
36. Tokozakura, D.; Nakamura, R.; Nakajima, H.; Lee, J.-G.; Mori, H. *J. Mater. Res.* **2007,** *22,* 2930–2935. doi:10.1557/JMR.2007.0362
37. Liang, X.; Wang, X.; Zhuang, Y.; Xu, B.; Kuang, S.; Li, Y. *J. Am. Chem. Soc.* **2008,** *130,* 2736–2737. doi:10.1021/ja7109629
38. Liu, J.; Xue, D. *Adv. Mater.* **2008,** *20,* 2622–2627. doi:10.1002/adma.200800208
39. Shevchenko, E. V.; Bodnarchuk, M. I.; Kovalenko, M. V.; Talapin, D. V.; Smith, R. K.; Aloni, S.; Heiss, W.; Alivisatos, A. P. *Adv. Mater.* **2008,** *20,* 4323–4329. doi:10.1002/adma.200702994
40. Xu, J.; Tang, Y.-B.; Zhang, W.; Lee, C.-S.; Yang, Z.; Lee, S.-T. *Cryst. Growth Des.* **2009,** *9,* 4524–4528. doi:10.1021/cg9005339
41. Zhou, J.; Song, H.; Chen, X.; Zhi, L.; Huo, J.; Cheng, B. *Chem. Mater.* **2009,** *21,* 3730–3737. doi:10.1021/cm901222j
42. Niu, K. Y.; Yang, J.; Kulinich, S. A.; Sun, J.; Du, X. W. *Langmuir* **2010,** *26,* 16652–16657. doi:10.1021/la1033146
43. Railsback, J. G.; Johnston-Peck, A. C.; Wang, J.; Tracy, J. B. *ACS Nano* **2010,** *4,* 1913–1920. doi:10.1021/nn901736y
44. Sutter, E.; Sutter, P. *J. Phys. Chem. C* **2012,** *116,* 20574–20578. doi:10.1021/jp305806v
45. Ha, D.-H.; Moreau, L. M.; Honrao, S.; Hennig, R. G.; Robinson, R. D. *J. Phys. Chem. C* **2013,** *117,* 14303–14312. doi:10.1021/jp402939e
46. Jen-La Plante, I.; Mokari, T. *Small* **2013,** *9,* 56–60. doi:10.1002/smll.201202471
47. Kim, M. J.; Park, J. H.; Lee, K. Y.; Lee, S.; Han, G.-S.; Song, H. J.; Shin, H.; Ahn, T. K.; Jung, H. S. *ACS Appl. Mater. Interfaces* **2014,** *6,* 1145–1151. doi:10.1021/am404809s
48. Niu, K.-Y.; Park, J.; Zheng, H.; Alivisatos, A. P. *Nano Lett.* **2013,** *13,* 5715–5719. doi:10.1021/nl4035362
49. Varón, M.; Ojea-Jimenez, I.; Arbiol, J.; Balcells, L.; Martínez, B.; Puntes, V. F. *Nanoscale* **2013,** *5,* 2429–2436. doi:10.1039/c2nr32657d
50. Yang, Z.; Lisiecki, I.; Walls, M.; Pileni, M.-P. *ACS Nano* **2013,** *7,* 1342–1350. doi:10.1021/nn304922s
51. Yang, Z.; Walls, M.; Lisiecki, I.; Pileni, M.-P. *Chem. Mater.* **2013,** *25,* 2372–2377. doi:10.1021/cm4012266
52. El Mel, A.-A.; Buffière, M.; Ewels, C. P.; Molina-Luna, L.; Faulques, E.; Colomer, J.-F.; Kleebe, H.-J.; Konstantinidis, S.; Snyders, R.; Bittencourt, C. *Carbon* **2014,** *66,* 442–449. doi:10.1016/j.carbon.2013.09.020
53. Zhang, G.; Wang, W.; Yu, Q.; Li, X. *Chem. Mater.* **2009,** *21,* 969–974. doi:10.1021/cm803307f
54. Zhang, F.; Shi, Y.; Sun, X.; Zhao, D.; Stucky, G. D. *Chem. Mater.* **2009,** *21,* 5237–5243. doi:10.1021/cm902231s
55. Muthuswamy, E.; Savithra, G. H. L.; Brock, S. L. *ACS Nano* **2011,** *5,* 2402–2411. doi:10.1021/nn1033357
56. Liu, Y.; Hight Walker, A. R. *ACS Nano* **2011,** *5,* 6843–6854. doi:10.1021/nn200565y
57. Wang, J. X.; Ma, C.; Choi, Y.; Su, D.; Zhu, Y.; Liu, P.; Si, R.; Vukmirovic, M. B.; Zhang, Y.; Adzic, R. R. *J. Am. Chem. Soc.* **2011,** *133,* 13551–13557. doi:10.1021/ja204518x
58. Jana, S.; Chang, J. W.; Rioux, R. M. *Nano Lett.* **2013,** *13,* 3618–3625. doi:10.1021/nl401467r
59. Glodán, G.; Cserháti, C.; Beszeda, I.; Beke, D. L. *Appl. Phys. Lett.* **2010,** *97,* 113109. doi:10.1063/1.3490675
60. Radi, Zs.; Barna, P. B.; Lábár, J. *J. Appl. Phys.* **1996,** *79,* 4096–4100. doi:10.1063/1.361772
61. Fan, H. J.; Knez, M.; Scholz, R.; Hesse, D.; Nielsch, K.; Zacharias, M.; Gösele, U. *Nano Lett.* **2007,** *7,* 993–997. doi:10.1021/nl070026p
62. Jin fan, H.; Knez, M.; Scholz, R.; Nielsch, K.; Pippel, E.; Hesse, D.; Zacharias, M.; Gösele, U. *Nat. Mater.* **2006,** *5,* 627–631. doi:10.1038/nmat1673
63. El Mel, A.-A.; Buffière, M.; Tessier, P.-Y.; Konstantinidis, S.; Xu, W.; Du, K.; Wathuthanthri, I.; Choi, C.-H.; Bittencourt, C.; Snyders, R. *Small* **2013,** *9,* 2838–2843. doi:10.1002/smll.201202824
64. El Mel, A.-A.; Molina-Luna, L.; Buffière, M.; Tessier, P.-Y.; Du, K.; Choi, C.-H.; Kleebe, H.-J.; Konstantinidis, S.; Bittencourt, C.; Snyders, R. *ACS Nano* **2014,** *8,* 1854–1861. doi:10.1021/nn406328f
65. Nakamura, R.; Matsubayashi, G.; Tsuchiya, H.; Fujimoto, S.; Nakajima, H. *Acta Mater.* **2009,** *57,* 5046–5052. doi:10.1016/j.actamat.2009.07.006
66. Ren, Y.; Chim, W. K.; Chiam, S. Y.; Huang, J. Q.; Pi, C.; Pan, J. S. *Adv. Funct. Mater.* **2010,** *20,* 3336–3342. doi:10.1002/adfm.201000498
67. Ren, Y.; Chiam, S. Y.; Chim, W. K. *Nanotechnology* **2011,** *22,* 235606. doi:10.1088/0957-4484/22/23/235606
68. Chun, S. R.; Sasangka, W. A.; Ng, M. Z.; Liu, Q.; Du, A.; Zhu, J.; Ng, C. M.; Liu, Z. Q.; Chiam, S. Y.; Gan, C. L. *Small* **2013,** *9,* 2546–2552. doi:10.1002/smll.201202533
69. Lee, Y.-I.; Myung, N. V.; Choa, Y.-H. *Scr. Mater.* **2013,** *68,* 463–466. doi:10.1016/j.scriptamat.2012.11.020
70. Lu, H. B.; Li, H.; Liao, L.; Tian, Y.; Shuai, M.; Li, J. C.; Hu, M. F.; Fu, Q.; Zhu, B. P. *Nanotechnology* **2008,** *19,* 045605. doi:10.1088/0957-4484/19/04/045605
71. Yang, Y.; Liu, L.; Güder, F.; Berger, A.; Scholz, R.; Albrecht, O.; Zacharias, M. *Angew. Chem.* **2011,** *123,* 11047–11050. doi:10.1002/ange.201102740
72. Güder, F.; Yang, Y.; Goetze, S.; Berger, A.; Ramgir, N.; Hesse, D.; Zacharias, M. *Small* **2010,** *6,* 1603–1607. doi:10.1002/smll.201000561
73. Lewis, E. A.; Slater, T. J. A.; Prestat, E.; Macedo, A.; O'Brien, P.; Camargo, P. H. C.; Haigh, S. J. *Nanoscale* **2014,** *6,* 13598–13605. doi:10.1039/C4NR04837G
74. Wang, C.-M.; Genc, A.; Cheng, H.; Pullan, L.; Baer, D. R.; Bruemmer, S. M. *Sci. Rep.* **2014,** *4,* No. 3683. doi:10.1038/srep03683
75. Goris, B.; Polavarapu, L.; Bals, S.; Van Tendeloo, G.; Liz-Marzán, L. M. *Nano Lett.* **2014,** *14,* 3220–3226. doi:10.1021/nl500593j
76. González, E.; Arbiol, J.; Puntes, V. F. *Science* **2011,** *334,* 1377–1380. doi:10.1126/science.1212822
77. Klinger, L.; Kraft, O.; Rabkin, E. *Acta Mater.* **2015,** *83,* 180. doi:10.1016/j.actamat.2014.09.050
78. Tu, K. N.; Gösele, U. *Appl. Phys. Lett.* **2005,** *86,* 093111. doi:10.1063/1.1873044

License and Terms

This is an Open Access article under the terms of the Creative Commons Attribution License (http://creativecommons.org/licenses/by/2.0), which permits unrestricted use, distribution, and reproduction in any medium, provided the original work is properly cited.

The license is subject to the *Beilstein Journal of Nanotechnology* terms and conditions: (http://www.beilstein-journals.org/bjnano)

The definitive version of this article is the electronic one which can be found at: doi:10.3762/bjnano.6.139

BEILSTEIN JOURNAL OF NANOTECHNOLOGY

Possibilities and limitations of advanced transmission electron microscopy for carbon-based nanomaterials

Xiaoxing Ke*[1,2], Carla Bittencourt[3] and Gustaaf Van Tendeloo[1]

Review

Open Access

Address:
[1]EMAT, University of Antwerp, Groenenborgerlaan 171, 2020 Antwerp, Belgium, [2]Institute of Microstructure and Property of Advanced Materials, Beijing University of Technology, Beijing 100124, China and [3]Chemistry of Interaction Plasma Surface (ChiPS), University of Mons, Place du Parc 20, 7000 Mons, Belgium

Email:
Xiaoxing Ke* - xiaoxing.ke@uantwerpen.be

* Corresponding author

Keywords:
TEM; aberration-corrected; carbon; nanostructures; low-kV imaging

Beilstein J. Nanotechnol. **2015,** *6,* 1541–1557.
doi:10.3762/bjnano.6.158

Received: 16 March 2015
Accepted: 25 June 2015
Published: 16 July 2015

This article is part of the Thematic Series "Atomic scale interface design and characterisation: Theory – Structure and dynamics".

Guest Editor: C. Ewels

© 2015 Ke et al; licensee Beilstein-Institut.
License and terms: see end of document.

Abstract

A major revolution for electron microscopy in the past decade is the introduction of aberration correction, which enables one to increase both the spatial resolution and the energy resolution to the optical limit. Aberration correction has contributed significantly to the imaging at low operating voltages. This is crucial for carbon-based nanomaterials which are sensitive to electron irradiation. The research of carbon nanomaterials and nanohybrids, in particular the fundamental understanding of defects and interfaces, can now be carried out in unprecedented detail by aberration-corrected transmission electron microscopy (AC-TEM). This review discusses new possibilities and limits of AC-TEM at low voltage, including the structural imaging at atomic resolution, in three dimensions and spectroscopic investigation of chemistry and bonding. In situ TEM of carbon-based nanomaterials is discussed and illustrated through recent reports with particular emphasis on the underlying physics of interactions between electrons and carbon atoms.

Review

1 Introduction

For decades the electron microscopy community was strictly divided into biology on the one end and materials science on the other end. Meanwhile, however, the importance of "soft matter", such as zeolites, porous materials, polymers, hybrid materials and carbon-based nanomaterials, is rapidly increasing. Optimal integration of soft matter materials into nanodevices calls for a fundamental interpretation of the structure of the materials, for which classical electron microscopy was actually poorly equipped. Soft matter materials are much more sensitive to electron beam damage compared to traditional metal or inorganic materials, and thus require imaging at low accelerating voltages. Working at lower voltages is not new; actually the first electron microscopes built by Ernst Ruska and Max Knoll were operated at low voltages [1]. However, because the resolu-

tion of an electron microscope scales with the wavelength of the electrons, the spatial resolution at low voltage was not sufficient for high resolution studies. Meanwhile, imaging at low voltage suffers dramatically from aberrations due to the imperfection of the electromagnetic lenses in the electron microscope. Driven by the pursuit of high resolution, manufacturers went on to higher operation voltages in the sixties and seventies of the twentieth century [2-5]. This came at the price of increasing beam damage, and consequently separated the study of hard matter (metal or robust inorganic materials) and soft matter.

Fortunately this has changed over the last decade. The introduction of spherical-aberration-corrected lenses [6] has paved the way out of this dilemma by improving the spatial resolution and increasing the signal to noise ratio at the same time. This has a dramatic impact when imaging at low accelerating voltage of 60–80 kV or even lower. At present the correction of spherical aberration (Cs correction) is a commonly used technique. Meanwhile, the correction of the chromatic aberration (Cc correction) in order to improve the uniformity of emitted electron beams has been demonstrated, but is still in an exploratory phase [7-9]. Particularly for relatively thick samples, the effect of a Cc corrector may be compromised by sample-induced chromatic effects, and the corrector is therefore only really useful to ultra-thin samples. An alternative is to use a monochromator to cut out tails in beam spreading, which reduces the intensity of the beam [10-12]. This again is of benefit for imaging soft matter materials because a lower electron dose means less damage to the material. More importantly, it improves the energy resolution for spectroscopic studies, which is another major step in the increase of performance of electron microscopes. Therefore, the advances of the instruments have led to a dramatic improvement in imaging at low voltage. Atomic resolution has been achieved at low voltages of 60–80 kV or even as low as 20 kV [13], and energy resolution has been increased up to 0.1 eV [12].

These recent progresses in electron microscopy offer an unprecedented opportunity to investigate beam-sensitive soft matter materials, in particular carbon-based nanomaterials, while only doing little damage to the samples. Carbon is one of the most essential elements on earth, named after the Latin word of "carbo" referring to charcoal. The use of charcoal, soot and coal dates back to prehistoric times, when nano-structured carbon materials already existed. Analysis of prehistoric cave paintings in Altamira (Spain) and Lascaux (France) has revealed the presence of carbon nanoparticles [14-16]. Carbon nanoparticles were also essential ingredients in inks and printing pastes used over centuries in various cultures [17]. Another example are carbon nanotubes (CNTs) [18] which found their way into the secret recipe of ultra-sharp Damascus steel, which dates back to seventeenth century, and are believed to be responsible for its extraordinary mechanical properties [19-21]. In the materials mentioned above, nano-structured carbon was used as an essential part to tailor their properties and characteristics. Carbon nanoparticles are mixed with collagen-derived animal glue to achieve a high homogeneity when dispersed into a colloidal solution. CNTs in Damascus steel are found to encapsulate cementite nanowires which might account for its super-plastic behavior. More recently, the report of graphene [22] has triggered extensive studies on its rich physics and has opened up wide applications in photoelectric devices, catalysis supports, battery electrodes, and many more.

The research of carbon nanohybrid materials, including both the fundamental study of carbon nanostructures and the understanding of interface formation between nano-carbon and the host matrix, is essential to the understanding of their unusual electronic, mechanical or thermal behavior, and further assists the optimal design of carbon-based nanodevices in a smart and sustainable manner. Such structural and chemical characterizations become possible at both high spatial resolution and high energy resolution with only limited beam damage thanks to major advances in TEM [23]. In addition to static imaging of the carbon nanostructure, the controlled interaction between electrons and carbon atoms may add a new dimension to the imaging, where electrons probe the carbon lattice during imaging and therefore lead to a dynamic investigation based on the fundamental physics of the materials.

In this review, we start from a brief outline of electron microscopy improved by aberration correction at low voltage, with an emphasis on the interaction between electrons and carbon atoms. The different applications of electron microscopy for carbon-based nanomaterials are then reviewed, including structural imaging at atomic resolution and in three-dimensional (3D) reconstruction, spectroscopy of the chemistry at defects and interfaces, and in situ TEM under external stimuli along with dynamic TEM.

2 Basics of TEM: Lower the voltage

2.1 Aberration correction

Electron beams accelerated at high voltages (tens to hundreds of kilovolts) have wavelengths far below the scale of inter-atomic distances of all materials, so in principle they are able to resolve the structures. As a general rule, the resolving power scales with the wavelength of the accelerated electrons. Using de Broglie equations, the wavelength of a 200 kV electron beam is approximately 0.025 Å, whereas that of 80 kV and 60 kV is about 0.04 Å and 0.05 Å, respectively. It can be seen that even electron beams accelerated by the low voltages of 80 kV and 60 kV are sufficient in resolving the inter-atomic distances at sub-

angstrom level. However in conventional TEM, the resolution at 200 kV is usually approx. 1–2 Å and it is even lower for 120 kV or 80 kV. This raises the question: What limits the resolution of TEM to such a large degree and how to overcome it?

To answer this question we need to consider that the formation of an image relies not only on the illumination source, but is also influenced by a series of electromagnetic lenses before and after electrons interacting with the specimen. Generally speaking, imperfections in the optical system introduce lens aberrations, which are continuously magnified during the propagation of the electron waves. Spherical aberrations and chromatic aberrations are the most well-known aberrations to lower the resolving power of an electron microscope [24]. Spherical aberration induces a blurring of the image in the focal plane, because light rays through the center of the lens and through the edge of the lens deviate when intersecting with the optical axis. Chromatic aberration on the other hand, induces blurring of the image because light rays of different wavelengths (due to the energy spread) fail to intersect with each other on the optical axis. Electron waves of shorter wavelengths and higher energies are refracted stronger. Spherical aberration and chromatic aberration are schematically shown in Figure 1.

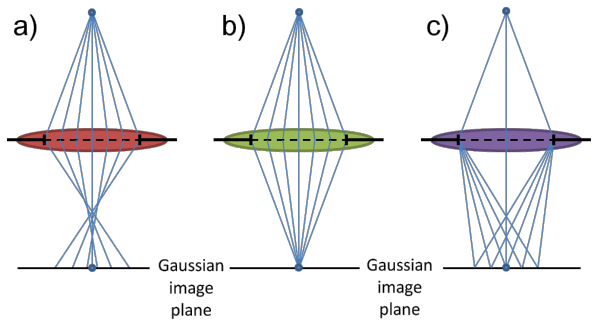

Figure 1: Illustration of (a) spherical aberration (b) ideal lens and (c) chromatic aberration.

It can be seen that lens aberrations limit the resolving power of electron microscopes. For simplicity, the point resolution of a HRTEM is expressed by Equation 1 [25]. A quantitative description of different lens aberrations in electron microscopy has been extensively discussed in the literature [24].

$$\rho_r = 0.66\left(C_3\lambda^3\right)^{\frac{1}{4}}, \quad (1)$$

where λ is the wavelength of the electrons and C_3 is the third-order spherical aberration coefficient of the objective lens. It must be noted that C_3 has a dominant influence on imaging; higher order aberrations are neglected here for simplicity.

The difference in the point resolution is therefore dramatically determined by the value of C_3. A conventional TEM has a C_3 value in the range of millimeters, which results in a reduction of the resolving power. Using a multi-walled carbon nanotube (MWCNT) for demonstration, a high resolution TEM (HRTEM) image acquired at 200 kV using a conventional FEI Tecnai G^2 microscope is shown in Figure 2a, where the spatial resolution is about 1.5 Å. When the accelerating voltage is lowered to 120 kV, not only the resolution is reduced, but there is also a strong contrast delocalization, which relates to spherical aberration [6,26]. A typical example of delocalization is shown in Figure 2b, where a MWCNT is imaged at an operating voltage of 120 kV using the same Tecnai G^2 microscope. A strong delocalization projected in the vacuum in the vicinity of CNT walls is indicated by arrows.

The increased delocalization and limited resolution complicates the interpretation of nanostructures when studied at low voltages. The most straightforward solution, as suggested by Equation 1, is to decrease the value of C_3 by reducing the lens aberration. However, although this suggestion was known for a long time, it was not implemented in the beginning of electron microscopy. The first Cs correctors were developed in the 1990s [6]. State-of-art aberration corrected TEMs (AC-TEM)

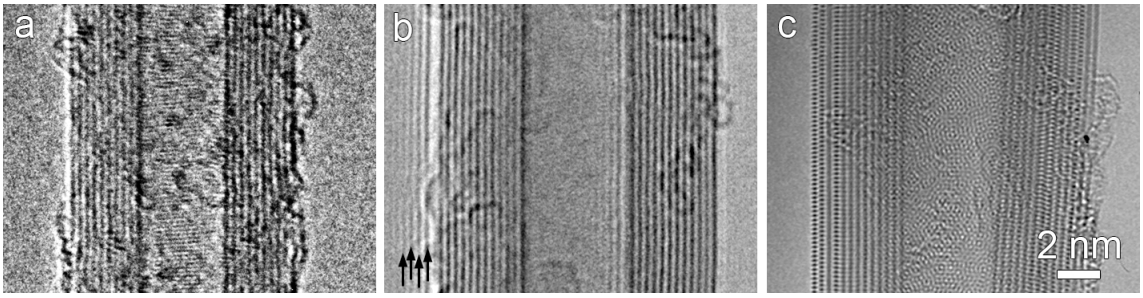

Figure 2: HRTEM images of MWCNTs acquired (a) at 200 kV without Cs correction; (b) at 120 kV without Cs correction, where delocalization is indicated by arrows; and (c) at 80 kV with Cs correction using a monochromated beam.

are now commercially available and the number of worldwide users is increasing exponentially. The development of aberration correctors are not discussed here, but an impressive result using AC-TEM to image MWCNTs at a voltage of 80 kV is demonstrated in Figure 2c to be compared with Figure 2a–b. Neighboring atom columns on the graphitic shell can be unambiguously distinguished. The delocalization is suppressed to a large degree, providing a straightforward interpretation of the surface and interface structure.

After the successful implementation of Cs correctors, there have been strong efforts to also correct chromatic aberration, however these corrections turn out to be more delicate and are still to be improved. Chromatic aberration becomes more important at lower voltages due to a wider relative energy spread compared to high voltage electron waves. An alternative to reduce chromatic aberration is often implemented by cutting electron beam tails using a monochromator, where the energy spread is considerably narrowed. The highly-aligned beam energy minimizes the effect of chromatic aberration, and hence improves the information limit to the sub-angstrom level at low operating voltages [27]. Actually, Figure 2c was obtained using a monochromated electron beam of 80 kV together with Cs correction. It must be noticed that the use of a monochromator will reduce the beam intensity due to a partial removal of the energy spectrum, which effectively minimizes possible damage to the structure, as will be discussed in the next subsection.

The previous discussion of Cs correctors applies to the post-field of the objective lens, which corrects the electron trajectory of the exit electron wave after interaction with the specimen, and provides a more straightforward interpretation of the projected potential of the specimen. When the correction is used in bright-field imaging using a parallel beam the corrector is referred to as “image corrector”. When the Cs corrector is applied to the electron beam before interacting with the specimen, and forms a highly converged electron probe, it is referred to as “probe corrector”. In the latter case we are talking about scanning transmission electron microscope (STEM), where an electron probe scans over a desired area to obtain local structural or spectroscopic information. When working with a highly converged beam at low voltage, a monochromator, reducing the beam energy spread, is desired in combination with a probe corrector.

Introduction of AC-TEM has provided unprecedented spatial resolution at low voltages and has thus largely benefited the studies of carbon-based nanomaterials and nanohybrids. Imaging conditions under 80 kV [28], 60 kV [29], even 30 kV [30] and 20 kV [13] have been demonstrated in studying carbon-based nanostructures.

2.2 Interaction between the electron beam and carbon-based materials

Electron microscopes use electron waves to resolve atomic structures and overcome the diffraction limit of optical microscopes. However, different from optical microscopes, accelerated electrons carry high energy and interact with the material in a highly dynamic manner. Elastically scattered electrons, inelastically scattered electrons (for electron energy loss spectroscopy, i.e., EELS) and X-rays (for energy dispersive X-ray spectroscopy, i.e., EDX), all uniquely characterize the studied materials. Chemical compositions, electron fine structures, even the phonon vibrations [31] produced by electron–matter interactions can be acquired, which is quite exciting for a detailed study. Therefore, electron beams are more than an illumination source, and can be considered as a tool in probing the intrinsic physics and chemistry of the investigated materials.

One should be concerned however, that such probing may modify the structure and introduce artefacts. In this context, low voltage is critical, particularly for beam-sensitive carbon-based nanostructures. The most well-known artefact to be avoided in carbon-based nanomaterials is the so-called “knock-on damage”. When high energy electrons collide with the carbon lattice and the momentum transferred during the collision exceeds the binding energy of the carbon–carbon bonds, carbon atoms can be displaced in competition with a spontaneous recombination, resulting in defects in the lattice, i.e., knock-on damage.

If we consider the collision only, the maximum kinetic energy transferred from the accelerated electrons to the atoms during the collision, which is regarded as a pure elastic head-on one, is expressed as follows [32]:

$$T_{\max} = \frac{2ME\left(E + 2mc^2\right)}{(M+m)^2 c^2 + 2ME}, \qquad (2)$$

where M and m are the masses of the atom and electron respectively, c is the speed of light, and E is the energy of the electron. We have calculated $T_{\max}$ for different accelerating voltages: The results are approx. 25 eV, approx. 20.5 eV, approx. 16 eV and approx. 11.8 eV for incident electrons of 120 kV, 100 kV, 80 kV and 60 kV respectively.

The threshold energy, T_d, needed to displace a carbon atom has been calculated for defect-free graphene as an ideal case. Earlier results have reported a T_d of 15 eV and 22 eV calculated statically and dynamically, as shown in Figure 3a [33]. More recent studies using molecular dynamics simulations based on tight-binding density functional theory [32] and first principle calcu-

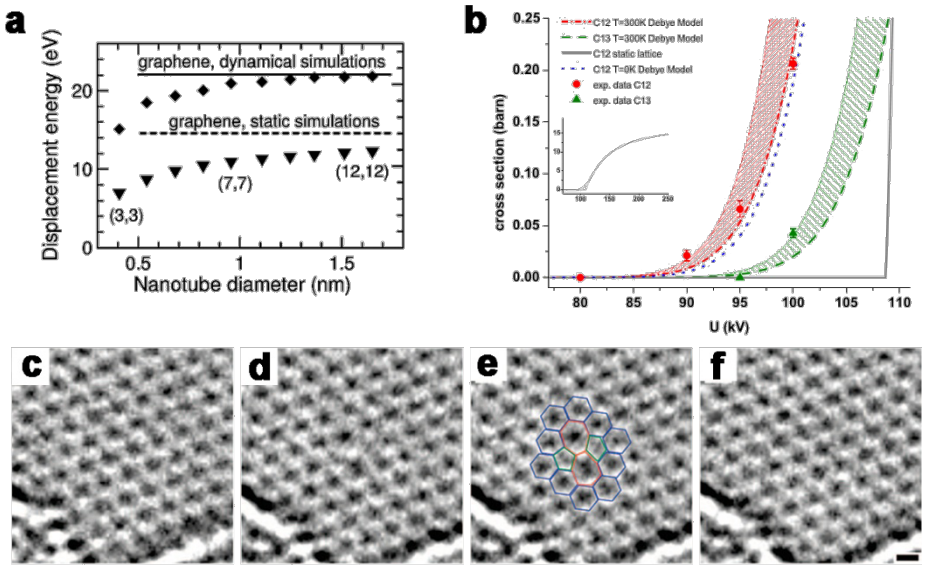

Figure 3: (a) Threshold energy T_d needed to displace carbon atoms from armchair multi-walled carbon nanotubes (SWCNTs) and graphene calculated dynamically (diamonds) and statically (triangles) as a function of tube diameter; the lines are the corresponding results for graphene; reproduced with permission from [33], Copyright (2005) American Physical Society. (b) Measured and calculated knock-on displacement cross sections. The lower boundary of the shaded areas corresponds to the calculated cross section, while the upper boundary is twice the calculated value. The inset shows the calculations for ^{12}C, 300 K and static lattice on a larger energy range; reproduced from [35], Copyright (2012) American Physical Society. (c–f) Metastable Stone–Wales (SW) defects found in HRTEM image sequence: (c) unperturbed lattice before appearance of the defect, (d) SW defect, (e) same image with atomic configuration superimposed, (f) relaxation to unperturbed lattice (after ca. 4s); reproduced with permission from [37], Copyright (2008) American Chemical Society.

lations [34] have agreed on a T_d of 23 eV and 22 eV, respectively, corresponding to an accelerating voltage of about 110 kV using Equation 2. However, HRTEM on defect-free graphene at 100 kV causes damage to the sample, including pentagons, heptagons and octagons [35]. The experimental results clearly show that a T_d of 23 eV and 22 eV (corresponding to an incident beam of approx. 110 kV) is overestimated. Such a difference may indicate that the irradiation of graphene with electrons includes more complicated interactions than only direct knock-on collisions with the carbon nuclei. A better fit is found by taking lattice vibration into account [35], rather than a static lattice approximation used in earlier literature. The damage cross-section rises is nearly zero at 80 keV and increases monotonically afterwards, as shown in Figure 3b. The result is well supported by the experimental results of extensive defect formation at 100 keV [36] (see below in Figure 4c–e) and occasional defects observed at 80 keV as shown in Figure 3c–f [37].

On the other hand, a lower threshold is expected for graphene with defects [38]. A typical example is the edge of a graphene sheet where an electron energy below approx. 50 keV is recommended to minimize the knock-on damage [39], and even this already low value is suggested to be still overestimated. Meyer et al. commented that extended holes (rather than a knock-on vacancy) grow over a wide range from 20 to 100 keV, or even below 20 keV. A mechanism of beam-induced etching with residual water or oxygen in the system is therefore suggested [40]. The strong anisotropic tubular structure of CNTs leads to an anisotropy of the atomic displacement threshold [32,41,42]. The scattering geometry naturally contributes to the variation of the knock-on threshold depending on the nanotube diameter [33]. As shown in Figure 3a, CNTs invariably have a lower knock-on threshold than graphene, whereas the CNTs of smaller diameters are more sensitive to knock-on damage.

The message concluded from the literature study is that the knock-on threshold for defect-free graphene can be regarded to be 80 keV, although the dynamics of the carbon atoms cannot be entirely excluded. A lower voltage of 60 keV is generally safe for analyzing most carbon-based nanostructures. Great care must be taken in investigating extensive defects such as a graphene edge, where a lower voltage may not necessarily mean the better solution, as beam-induced etching will occur [40].

Following the knock-out of carbon atoms, vacancy formation and the subsequent reconstruction of large even-number vacancies takes place, as discussed in detail in [43]. One example is shown in Figure 4a,b. When carbon atoms in CNTs are displaced by electron irradiation, single vacancies (SV), divacancies (DV), and even tetravacancies can be created; a schematic illustration is presented in Figure 4a,b. Displaced carbon atoms may form adatoms (A) on the lattice. Atomistic computer simu-

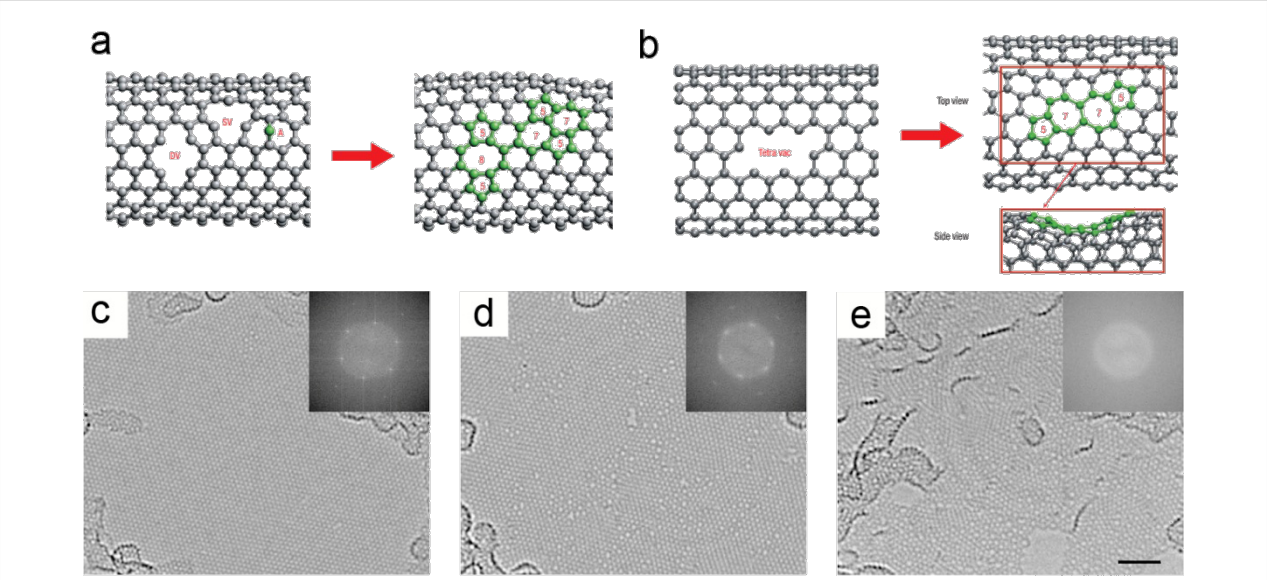

Figure 4: (a–b) Reconstruction of the atomic network of a CNT near vacancies and adatoms is predicted by atomistic computer simulations. SV, DV, tetravacancies and adatoms may transform into a Stone–Wales (5–7–7–5) defect and 5-8-5 defects; reproduced with permission from [43], Copyright (2007) Nature Publishing Group. (c–e) Amorphization of graphene demonstrated by three TEM images and their corresponding Fourier transformations (insets) at (c) a low irradiation dose (1.25 × 10^8 e^-/nm^2), (d) an intermediate dose (2.94 × 10^9 e^-/nm^2) and (e) a high dose (9.36 × 10^9 e^-/nm^2); reproduced with permission from [36], Copyright (2014) Nature Publishing Group.

lations predict that the reconstruction of the atomic network near vacancies and adatoms is very likely to happen, resulting in an agglomeration of 5- to 8-membered rings [44,45]. As shown in Figure 4a, a SV and an adatom may form a metastable Stone–Wales (5–7–7–5) defect or a 5–8–5 defect. A tetravacancy could transform into a Stone–Wales defect, too (Figure 4b). As discussed above, electron beams of voltages exceeding 80 kV have a larger probability in displacing carbon atoms, resulting in structural disorder. Severe continuous illumination may eventually lead to complete amorphization of the lattice at room temperature [36]. As demonstrated in Figure 4c–e, an ordered graphene lattice is transformed into a disordered two-dimensional (2D) carbon glass by continuous irradiation at 100 keV.

It has been suggested to study carbon-based nanostructures at low voltage in order to suppress knock-on damage (elastic collision), allowing for a damage-free study in both TEM and STEM. One may point out that a decrease of the accelerating voltage has the disadvantage of increasing the damage cross section introduced by inelastic scattering [46]. This may lead to effects such as ionization damage and sample heating. These are indeed major concerns in studying polymers and biomaterials [23]. Fortunately, carbon-based nanomaterials, such as CNTs or graphene-based nanohybrids, have excellent electric and thermal conductivity [47,48] and suffer only slightly from damage related to inelastic scattering. Although the previous discussion has pointed out that low operating voltages increase the damage of large holes possibly due to etching, imaging conditions of 60 keV and 80 keV are generally accepted as reasonable. Additionally, the increase of the scattering cross section at low voltage improves the signal to noise ratio for light elements as carbon and results in an enhancement in contrast [38,49].

Following the discussion on lowering the voltage, the dose of incident electrons must be considered as well. Electrons accelerated by voltages close to the knock-on threshold of 80 kV or 60 kV may still displace carbon atoms in a graphene lattice, particularly the ill-bonded atoms at defects, surfaces or interfaces. Lowering the dose can therefore reduce such damage. This can be achieved by, e.g., spreading the electron beam, increasing the spot size, or minimizing the exposure time. In addition, the condenser aperture or spotsize can be tuned to reduce the beam intensity. The sensitivity of the CCD camera then becomes critical in order to maintain an acceptable noise-to-signal ratio. A recent development in an advanced high-resolution fast-detection camera (K2-IS camera from Gatan Inc.) has made a significant improvement in both sensitivity and resolution by the elimination of the traditional scintillation process and the capture of electrons directly on a CMOS (complimentary metal-oxide semiconductor) sensor up to 1600 fps [50]. The high sensitivity and fast acquisition in detecting has made possible the automated and ultra-fast acquisition of a series of under-exposed images from the same region. After drift correction, the images of such a sequence are

stacked and can thus provide a HRTEM image with an acceptable signal to noise ratio with only limited damage to the sample.

The introduction of a high-speed detector may also have an impact on increasing the time resolution. In a molecular dynamics simulations on the reconstruction of vacancies, the time scale is often restricted to picoseconds [45], whereas in TEM the time resolution is at the order of 1 s [51] or 80 ms [52]. Under these conditions, it is more likely that the resulting image shows the time-relaxed state of the sample. A high-speed detector may facilitate the imaging of more intermediate states of the carbon dynamics. To push the time resolution to the limit, a revolutionary change in the electron source technology is required. Progress is being made by groups at Caltech (http://www.ust.caltech.edu/press/uem1.html) and Lawrence Livermore National Laboratory (https://www-pls.llnl.gov/?url=science_and_technology-materials-dtem). They reported TEM results with temporal resolutions of nanoseconds and picoseconds and spatial resolutions of angstroms and nanometers are reported [53-56]. Nevertheless, few results are reported at voltages below 80 kV.

2.3 Imaging conditions and image interpretation

An important question to be answered is: How to determine the ideal imaging conditions? Although AC-TEM, which allows for atomic resolution at low operating voltages, is being promoted to be the standard for research facilities, should we abandon imaging at under more conventional conditions, e.g., 200 kV without Cs correctors? Dating back to the early nineties of last century when CNTs were reported first, much effort was devoted to resolve the structures of CNTs using TEM without aberration correction. Although the exact structure of CNTs could not be directly imaged by HRTEM because of the limited spatial resolution, attention was focused on unfolding the mystery through electron diffraction. Different from the phase contrast projected in the imaging plane, information projected in reciprocal space is much less influenced by lens imperfections. In addition, diffraction patterns reflect the kinetic and dynamic scattering of electrons when interacting with the unique structure of CNTs. Fundamental understanding of the physics during the interaction between the electrons and the carbon lattice is crucial. Together with the real space imaging at higher voltages, the nanostructure and the chirality of CNTs was successfully resolved [57-59].

It is an example to be well remembered. Firstly, the fundamental physics of the lens optics as well as that of the electron–matter interaction must be taken into account when it comes into the interpretation of TEM images. Secondly, a proper understanding of the lens optics in electron microscopes opens up more possibilities in choosing the most appropriate imaging condition for studies of different purposes. Not all carbon-based nanomaterials require imaging using monochromated AC-TEM at 80 kV. When the irradiation damage can be reasonably controlled by limited exposure time, high voltage with a low dose can be considered as an alternative. Thirdly, the development in AC-TEM offers unprecedented spatial resolution to be achieved at low voltage, which (1) provides a relatively straightforward (S)TEM image readily to be interpreted; (2) allows for an extensive timescale for structural investigation before breaking down. Consequently, local structures such as defects or active sites can be investigated in detail. More interestingly, the interaction between electrons and the materials can be imaged in a dynamic manner. Evolution of the structural defects, for instance, is evoked by electrons as a tool and imaged simultaneously. From this point of view, the electron beam is more than an illumination source in producing projections of the investigated materials as in a “shadow play”. It is, to be more accurate, the process or the result of an electron–matter interaction that is projected. This fact is the key to interpreting TEM images or TEM-acquired spectra.

3 Applications to carbon-based nanomaterials

3.1 Structural Imaging: (atomic resolution and 3D)

Earlier studies using TEM to image the structures of carbon-based nanomaterials have limited spatial resolution, as shown above in the example of CNTs. Through the developments in AC-TEM nowadays, not only atomic resolution can be achieved, but also the obtained phase contrast suffers much less from the lens aberration, providing easily interpretable images. Local defects such as vacancies, dislocations, grain boundaries and strain can be revealed in great detail. The fundamental understanding of CNTs, particularly of graphene in the past decade, have largely benefited from the development in electron microscopy.

Taking CNTs again as an example, the direct imaging of a zigzag single-walled CNT (SWCNT) at atomic resolution using AC-TEM operated at 80 kV is able to reveal atomic displacements with picometer precision [60], as demonstrated in Figure 5a–d. The CNT is determined to have a chirality of (28,0) as shown in Figure 5b. By comparing to a simulated CNT with the same chirality (Figure 5a), a displacement map can be obtained (Figure 5c–d) at picometer precision, which further reveals the strain distribution. Strain induced by bending can be mapped in two dimensions, and further proposed to be a dominant non-uniform shear strain. The strain in the nanotube is associated to the modification of its intrinsic physical properties, including bandgap variation and quantum transport disturbance. Therefore, a detailed study of how the atomic

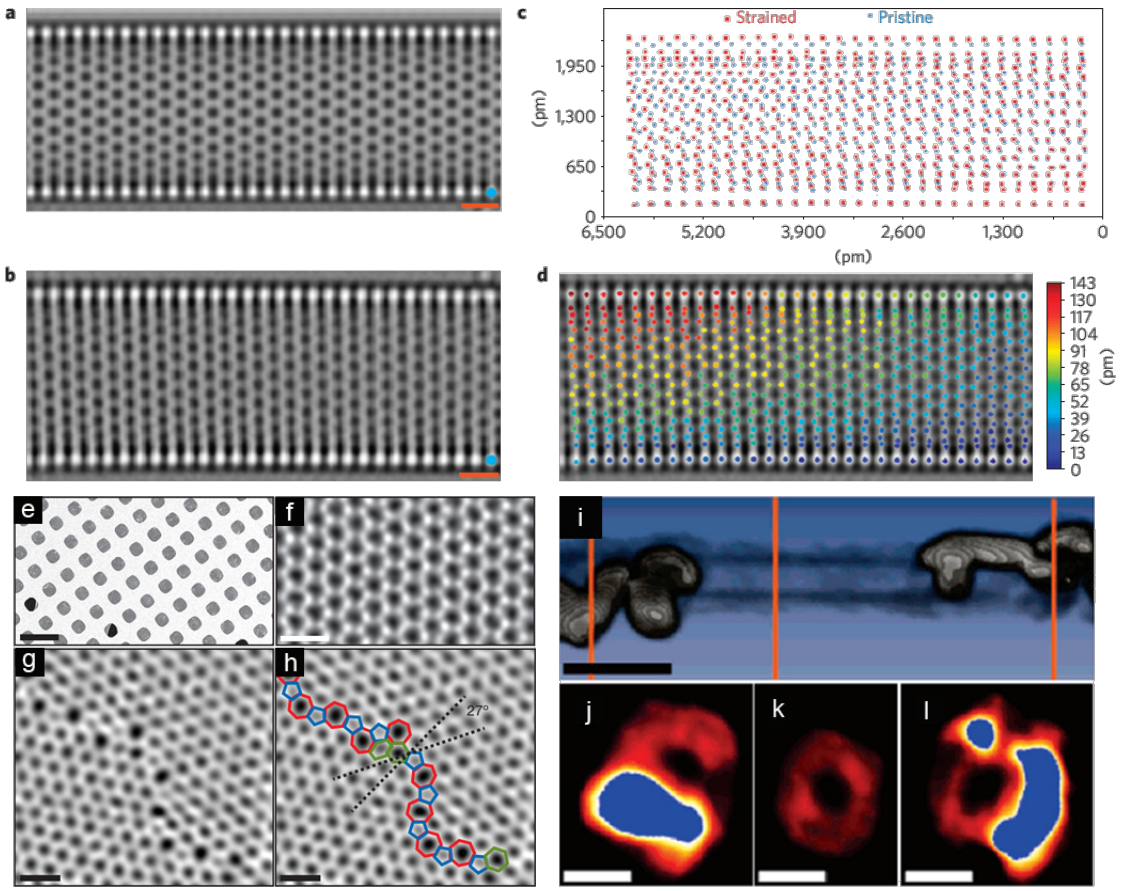

Figure 5: (a–d) Obtaining a 2D displacement map of a (28,0) SWCNT; reproduced with permission from [60], Copyright (2011) Nature Publishing Group. (a) HRTEM image simulation of a (28,0) SWCNT. Scale bar: 500 pm. (b) Experimental AC-TEM image of a (28,0) SWCNT with strain. Scale bar: 500 pm. (c) Overlay of atomic column positions measured from a (28,0) SWCNT in simulated (a) (blue) and experimental (b) (red) HRTEM images. (d) 2D displacement map, overlaid on top of the HRTEM form (b). (e–h) ADF-STEM images of graphene crystals; reproduced from [62], Copyright (2011) Nature Publishing Group. (e) Scanning electron micrograph of graphene transferred onto a TEM grid. (f) ADF-STEM image showing the defect-free hexagonal lattice inside a graphene grain. (g) Two grains intersect with a relative rotation of 27°. An aperiodic line of defects stitches the two grains together. (h) The image from (g) with the pentagons (blue), heptagons (red) and distorted hexagons (green) of the grain boundary outlined. Panels f–h were low-pass-filtered to remove noise; scale bars: 5 Å. (i–l) 3D reconstruction of a CNT in contact with Pd islands; reproduced with permissionfrom [83], Copyright (2007) American Chemical Society. (i) Volume rendering of the geometrically reconstructed CNT (black) with iso-intensity surface of Pd islands (white). Scale bar: 10 nm. (j-l) Cross-section views of the orange slices in (i). Scale bars: 4 nm.

structure responds to strain has contributed to the fundamental understanding of the physics of CNTs and other related nanostructures.

Similarly, AC-TEM has contributed significantly to the fundamental understanding of graphene. Its superior physical properties derived from its unique 2D nanostructure triggered extensive research about how defects in graphene can influence its properties and can further be utilized to tailor its macroscale behavior. By directly imaging a single layer of graphene at atomic resolution, the role of vacancies and ad-atoms can be studied in detail [28]. Non-hexagonal lattices in which C–C bonds are no longer sp^2-hybridized have been identified. These included pentagons, heptagons, and octagons, which are usually paired to form 5–7 pairs or even 5–8 pairs [28,43] as demonstrated in Figure 4a,b. The imaging with AC-TEM confirms the presence of these defects in graphene, and provides evidence for the variations in its electronic properties, mechanical properties and thermal properties [61]. An example is shown in Figure 5e–h, where a grain boundary is imaged on a single graphene layer using annular dark field scanning transmission electron microscopy (ADF-STEM) acquired at 60 kV. An extensive arrangement of the 5–7 pairs together with distorted hexagons is revealed (Figure 5g,h) [62]. It can be deduced that electronic scattering and phonon scattering are very likely to be disturbed at the boundary. The fundamental studies on the atomic structure of graphene have a significant impact on the large-scale applications of graphene. Graphene synthesized through chemical vapor deposition (CVD) often exhibits a polycrystalline morphology with defects such as grain boundaries

[62,63] and therefore suffers from a degradation of its physical properties. Characterization of the intrinsic defects and their further relation to the synthesis conditions, e.g., substrate lattice mismatch and annealing temperature is therefore of great importance.

In addition to the fundamental research on the structures of carbon-based nanomaterials, advanced electron microscopy has provided great opportunities to investigate functionalized carbon-based nanomaterials as well. Carbon nanohybrids found widespread use in nanoscience and nanotechnology: as building blocks for nanoelectronics [64], for drug delivery in biomedicine [65], and as bio-imaging agents when decorated with magnetic nanoparticles [66], just to name a few. The investigation of the interfaces of nanohybrids is often crucial in optimizing their design toward eventual applications. Two important examples are the studies of the interface formation at electrical contacts between CNTs and a metal, which needs to be understood for applications in nanoelectronic devices [67], and nanocatalysts where CNTs are used as conducting bed for efficient charge transfer [68,69]. Systematic studies of different metals on CNTs has been reported, including Au, Pt, Pd, Rh, Cu and Ti [67,70-75]. Early studies using HRTEM have revealed that Au and Pt form mostly well-crystallized nanocrystal islands with limited contact areas with the CNTs walls, whereas Pd and Rh form triangular shaped nanoparticles on CNT walls with an increased area at the contact interface, and Ti forms an amorphous film with continuous coverage around the CNTs. These results are further associated with the wettability of different metals on the CNT surface and explained by electron affinity and binding energy through DFT calculations [67]. Similarly, the electron affinity and binding energy difference can influence the reactions inside the CNTs, although the interior of the CNTs is regarded as inert due to its concave surface [76,77]. Recent studies using AC-TEM at the atomic scale have revealed that transition metals, such as W, Re and Os, encapsulated inside CNTs, can react with inner wall graphitic layers, depending on their affinity and bonding energy with the graphitic layers [78], or even stimulate the formation of nanometer-sized protrusions [77].

Detailed TEM studies on the metal/CNTs interface have also noticed a certain degree of bending in graphitic layers [79]. Conventional 2D imaging is insufficient in this case, as it acquires a projection of a 3D object, resulting in misinterpretation due to the lack of information along the projected direction. A better solution is to use 3D electron tomography to reveal the overall deformation. By acquiring a series of projections over a tilt range, the 3D structure can be reconstructed. As one of the most developed new TEM methods in the past ten years, 3D electron tomography has attracted tremendous attention since the first review paper on 3D electron tomography published by P. Midgley in 2003 [80]. Detailed discussions on data acquisition [80,81] and the reconstruction algorithm [82] can be found elsewhere. The result of the 3D reconstruction of a Pd–CNT interface is in parts presented in Figure 5i–l [83]. It has been reported that the deformation of Au-contacted CNT walls is more prominent compared to Pd-contacted CNT walls (not shwon), which could be associated to higher wettability of Pd over Au nanoparticles on one hand. On the other hand, a deformation mechanism through elastic strain relaxation is also proposed which attributes the deformation to lattice mismatch [79]. Whichever the driving force is, the geometric distortions in the graphitic lattice have been clearly evidenced by 3D TEM, indicating a significant difference in the electronic structure at the metal–CNT contact. The consequent resistance change at the contact is believed to contribute to the already present Schottky barrier in metal–CNT contacts, providing an alternative perspective in studying metal–CNTs contacts.

Undoubtedly, advances in TEM have offered unrivaled opportunities in studying carbon nanostructures in both 2D and 3D in a straightforward manner. Following the large improvement in the spatial resolution of 2D imaging, atomically resolved 3D reconstruction has been achieved and demonstrated on Au nanorods [84]. Encouragingly, only a few projections are required for the reconstruction thanks to an improvement of the reconstruction algorithm [82,84]. For beam-sensitive materials, such as carbon-based nanomaterials, a limited exposure time is preferred. Therefore this novel reconstruction method with a few projections can be extremely useful in obtaining the 3D structure of carbon-based materials at higher spatial resolution and moving it from the nanometer scale [85] toward the atomic scale.

3.2 Advanced spectroscopy of carbon-based materials

In contrast to structural imaging which uses elastically scattered electrons, chemical and electronic structure information can be obtained simultaneously using inelastically scattered electrons or X-rays emitted during electron–matter interaction. By combining analytical techniques including EELS and EDX, modern electron microscopy reaches its ultimate potential in both higher spatial resolution and higher energy resolution.

Compared to EDX which is typically used to detect heavy elements, EELS is more frequently used for light elements and therefore carbon-based nanostructures. Generally speaking, the inelastic scattering of the incident electrons, either with the tightly bound inner shell electrons or with more loosely bound valence electrons, can cause atomic electrons to be excited to unoccupied states, and is reflected as a loss in energy when

recorded using an EELS spectrometer. Not only elements can be identified using EELS, but the fine structure of the spectral profiles also reflects the specific electronic structures and chemical bonds [86,87]. Detailed analysis of the low-loss or valence region of an EELS spectrum (<50 eV) allows one to study the band structure and in particular the dielectric function of a material. In addition to the collective electron excitation modes marked by characteristic plasmon peaks, the joint density of states above the Fermi level is encompassed within the valence-loss region of an EELS spectrum. In combination with theoretical calculations and simulations detailed local information can be obtained. EELS is close to near-edge X-ray absorption fine structure (NEXAFS) analysis used to probe electronic states [88]. One major difference is that the spatial resolution in TEM is much higher than that of in NEXAFS. The bottleneck of EELS was the energy resolution, because in classical filaments or in a "warm emission gun" (Schottky filament) the energy spread of the emitted electron beam is fairly broad and the resolution of the EELS was of the order of 1 eV. The introduction of a chromatic aberration corrector or alternatively a monochromator allows one to overcome this shortage. By reducing the energy spread as discussed in Section 2, the energy resolution can now be down to the 100 meV range and even below. Replacement of the Schottky gun by a cold field emission gun (cold FEG) [89-92] has achieved a remarkable energy resolution of 9 meV as reported recently [31]. From an instrumental point of view, Cc corrector and cold FEG have similar advantages in increasing the beam coherency and provide premium imaging conditions for carbon-based nanomaterials or beam-sensitive materials in general.

Therefore, by combining the high energy resolution of EELS with the high spatial resolution of AC-(S)TEM, chemical information can be probed down to the limit. The remarkable potential of STEM–EELS to investigate carbon nanostructures was reported by Suenaga et al. These authors demonstrated atom-by-atom spectroscopy by probing a graphene edge [29]. Carbon rings were clearly imaged at a low voltage of 60 kV to minimize possible knock-on damage (Figure 6a,b). Fine-structure spectroscopic information of energy-loss near-edge structure (ELNES) spectra was collected simultaneously as probed by a highly converged electron probe. Carbon atoms with single-, double- and triple-coordination were distinguished through the information gathered on the electronic and bonding structures (Figure 6c,d). In comparison, ELNES performed on diamond is also shown here [93] as an example of carbon nanostructure with predominantly sp^3 hybridization (Figure 6e). A unique σ* feature starting at 290 eV is typical for diamond, in contrast to that of graphene, which starts at 292 eV.

One step further, the doping of elements into carbon lattices can be investigated in great details using STEM–EELS, as demonstrated in the work of nitrogen-doped graphene [94] and nitrogen-doped CNT [95]. Substitutional nitrogen defects in graphene are identified by direct imaging using STEM, whereas the EELS spectrum collected at the neighboring carbon columns suggests a C–N bond [94]. Together with the help of first principles calculations, STEM–EELS further reveals the configurations of single N-substitutions in SWCNT as graphitic and pyrrolic [95]. A more striking result is reported in Si-doped graphene [96], in which a sp^3-like trivalent Si substitute and a

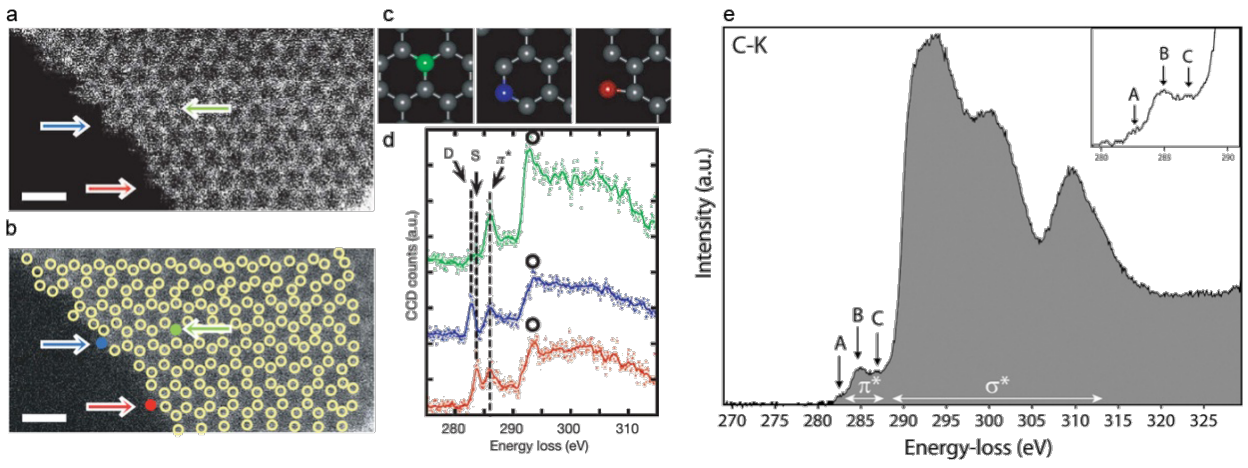

Figure 6: (a–d) Graphene edge spectroscopy; reproduced with permission from [29], Copyright (2010) Nature Publishing Group. (a) ADF-STEM image of a single graphene layer at the edge region. No image-processing has been done. Atomic positions are marked by circles in a smoothed image (b). Scale bars: 0.5 nm. (d) ELNES of carbon K1s spectra taken at the color-coded atoms indicated in (b). Green, blue and red spectra correspond to the normal sp^2 carbon atom, a double-coordinated atom and a single-coordinated atom, respectively. These different states of atomic coordination are marked by colored arrows in (a) and (b) and illustrated in (c). (e) Experimental carbon K-edge ELNES acquired with monochromatic electron illumination. The σ* feature starting at 290 eV is typical for diamond. The π* contribution around 285 eV consists of 3 pre-peaks, at 282.7 eV (A), 285 eV (B), and 286.6 eV (C); reproduced with permission from [93], Copyright (2013) John Wiley and Sons.

more complicated hybridized tetravalent Si impurity are clearly distinguished by atomic-resolved STEM–EELS spectra. It demonstrates the capability of EELS to reveal rich chemical information at an atomic scale. Although the work was performed on graphene/CNTs, chemical information provided by EELS can be used for the study of interfaces in carbon-based nanohybrids. For example, in [97] an attempt is given to resolve the interface of CNT–TiO_2 hybrids. Segregation or mixed metal–carbon phases at the interface of nanohybrids can be evaluated.

Additionally, the introduction of the monochromator and high-resolution electron-loss spectrometers has greatly transformed the field of plasmonics and dielectric property measurements using valence EELS (VEELS). Different from ELNES which deals with the core-loss spectrum, VEELS focuses on the low-loss part of the EELS spectrum in the range of 0–50 eV and therefore is able to probe the optical properties, e.g., to measure the local band gap through a monochromated STEM [98,99]. Before the introduction of a monochromator and/or cold FEG, the energy resolution was limited to approximately 1 eV, which hinders the low-loss part of the EELS spectrum to be interpreted due to a broad tail near zero-loss peak. With the help of a monochromator and/or a cold FEG plasmonic properties can be studied, for instance in graphene. The low-loss EELS spectrum of graphene is dominated by plasmon excitations consisting of two peaks at about 4.5 eV and about 15 eV, referred to as π and π+σ surface plasmons, respectively, as confirmed both theoretically and experimentally in free-standing monolayer graphene [100,101]. Zhou et al. have demonstrated the surface plasmon resonances in monolayer graphene down to the atomic scale [102]. It is further revealed that a single point defect, as imaged by STEM, can act as an atomic antenna in the frequency range of petahertz, and thus enhance the surface plasmon resonance locally. However, more recently, Nelson et al., after extracting the dielectric function from STEM–EELS spectra and comparing it with the calculated results [103], claimed that the commonly referred π and π+σ peaks are not surface plasmons but single-particle interband excitations. Nevertheless, VEELS on graphene has opened up a venue to both the fundamental study and further applications in optoelectronics, plasmonics and transformative optics using carbon-based nanostructures.

Although it has been convincingly shown that STEM–EELS is able to reach the ultimate goal of materials characterization, combining atomic spatial resolution and millielectronvolt resolution on the energy scale, there are still limits that need to be treated with caution. For instance, the delocalization of inelastic scattering is in many cases larger than the probe size, indicating an actual spatial resolution possibly larger than the nominal value [23]. This has to be taken into account when interpreting data. The limit is then set by the physics behind rather than by the instrument. Nevertheless, the delocalization can be used to carry out “remote” spectroscopy by positioning the electron beam outside the sample and virtually “probe” the material, as demonstrated on vibrational spectroscopy acquired from various

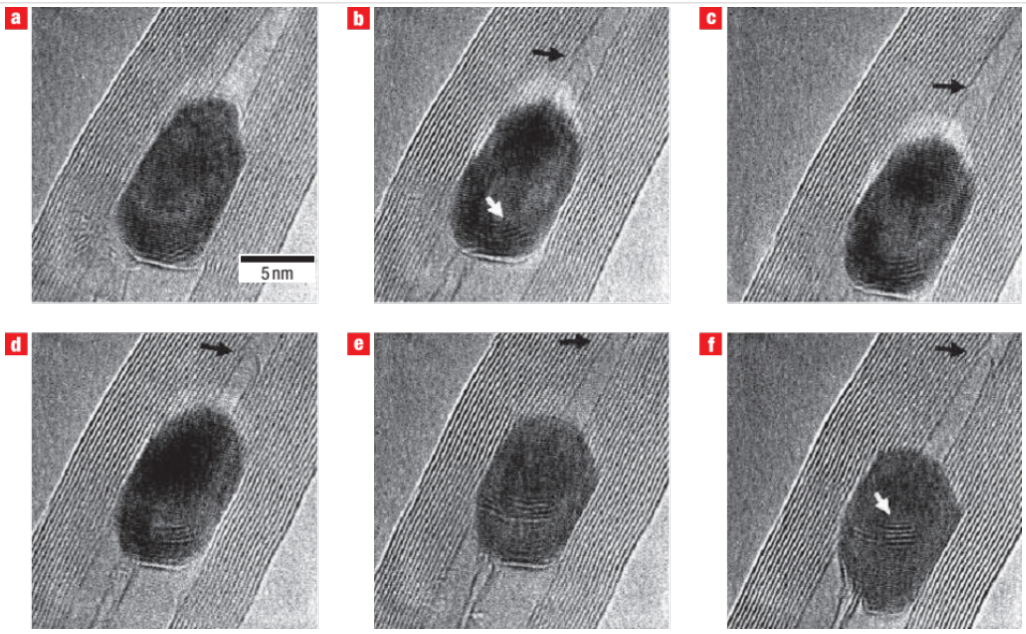

Figure 7: SWCNT growth from Fe with possible occurrence of a carbide phase. The HRTEM images show the growth of a SWCNT inside a MWCNT, which is partly filled with a Fe crystal under electron irradiation (ca. 200 A/cm^2) at a specimen temperature of 600 °C. The tip of the growing SWCNT is indicated by a black arrow. Images taken (a) before the growth, (b) after 5 min, (c) after 6 min, (d) after 7 min, (e) after 13 min, (f) after 15 min of irradiation respectively; reproduced with permission from [105], Copyright (2007) Nature Publishing Group.

materials, both hard and soft [31]. Radiation damage can therefore be avoided in beam-sensitive materials, including carbon-based nanomaterials.

3.3 In situ TEM

In situ studies of "working" processes at the nanometer scale or even the atomic scale are increasingly attracting attention. The dynamics of materials responding to external stimuli adds new perspectives and a new dimension to the study of carbon-based nanomaterials.

One of the most commonly applied stimuli is the temperature. Increasing the temperature has promoted self-healing of the knock-on damage in CNTs and related carbon-based nanohybrids in agreement with the thermodynamics of annealing. In situ heating to 600 °C allows CNTs to be studied at a high voltage of 300 kV while the structure remains defect-free [104]. Furthermore, carbon-based nanohybrids, particularly graphene or CNTs functionalized with metal nanoparticles, can be considered as a unique nanoreactor at elevated temperature. The interaction between energetic electrons and matter plays a unique role in triggering the reaction. Taking CNT growth as an example, the formation mechanism of CNTs was under debate for years until 2007, when Rodriguez-Manzo et al. monitored the nucleation and growth of a SWCNT through an in situ heating experiment using HRTEM [105]. As shown in Figure 7, a MWCNT filled with a Fe nanoparticle was regarded as a nanoreactor, where irradiation by the electron beam upon the MWCNT shells injects carbon atoms into the body of the nanoparticle. Diffusion of carbon atoms at high temperature subsequently leads to the formation of SWCNTs or MWCNTs at the tip of the nanoparticle inside the host nanotube. The experiment was performed in an entirely condensed phase process and revealed the growth mechanism of bulk diffusion of carbon through the body of catalytic particles, including Fe, Co and Ni.

Other external stimuli being introduced into in situ TEM, include mechanical stress [106,107], electrical stimuli [108], and chemical reactions in the gas phase or in liquid cells [50]. Although only a few studies using in situ TEM on carbon-based nanomaterials have been reported, an increase can certainly be expected. For instance, the evolution of defects (such as the shear strain present in CNTs as discussed in Section 3.1) along with the elastic/plastic deformation in CNT-reinforced composites under load can be well studied using similar techniques [109].

In contrast to the external stimuli, which are introduced through dedicated designs of the TEM specimen holder (thermal, mechanical, electrical) or specimen chamber (gas phase, environmental TEM), the contribution of electrons into the dynamic process, which can be regarded as the "internal stimulus", is often overlooked. The interaction between electrons and carbon atoms may alter carbon-based nanostructures during imaging as discussed in Section 2. Unwanted destruction of the nanostructures can be avoided by imaging below the knock-on threshold of 80 kV, whereas active sites such as defects and functional species can still interact with electrons at lower voltages [43,110]. The advantage of this process, however, is the creation of a unique in situ platform in which active nanostructures can be studied at atomic resolution along the process [111]. It has found useful applications in the study of catalysis where functionalized carbon nanostructures are frequently employed as hosts for various catalysts [34].

We can demonstrate this using the example of functionalized graphene anchored by a water-splitting catalyst based on polyoxometalates (POMs). By imaging the nanohybrids at 80 kV, the supporting graphene is protected to a large degree and remains stable, whereas functionalized sites are more active when exposed to the electron beam. Sloan et al. for the first time reported the dynamical movement of discrete C_{2v} $[\gamma\text{-}SiW_{10}O_{36}]^{8-}$ lacunary Keggin ions (a type of POM) at atomic resolution on a monolayer graphene oxide support [111]. A sequence of images recorded during the exposure to electrons demonstrate rotating, flipping and oscillation of the Keggin ions. Ke et al. reported an extensive study from 2D to 3D demonstrating the dynamics of Ru_4POM functionalized on graphene, using the symmetry of Ru_4POM as prior knowledge [112]. Ru_4POM is composed of two rigid Keggion ions ($[\gamma\text{-}SiW_{10}O_{36}]^{8-}$) interconnected by a tetraruthenium core. As shown in Figure 8a, the dynamic movements of an individual Ru_4POM are captured over time. By comparing its projections to its simulated patterns at different tilted positions in 3D space (Figure 8b), the 3D configurations are reconstructed at each time point (highlighted by red squares). The dynamic behavior of each molecule in 3D can therefore be retrieved as a result of its interaction with the electron beam (indicated by arrows in Figure 8b).

The active sites of graphene are less resistant to the exposure of electrons, and therefore provide the anchoring points with a certain degree of flexibility allowing for the movement of the Ru_4POM molecules. Additionally, a continuous deformation of the molecular structure is noticed throughout the imaging. A typical example is demonstrated in Figure 8c–i. The acquired projection of a Ru_4POM (Figure 8d) is more elongated compared to the simulated pattern (Figure 8c). Detailed analysis at the atomic scale indicates that the deformation is mostly focused on the tetraruthenium core, which is the catalytic core as well. As shown in Figure 8f–i, a dilation is applied to the

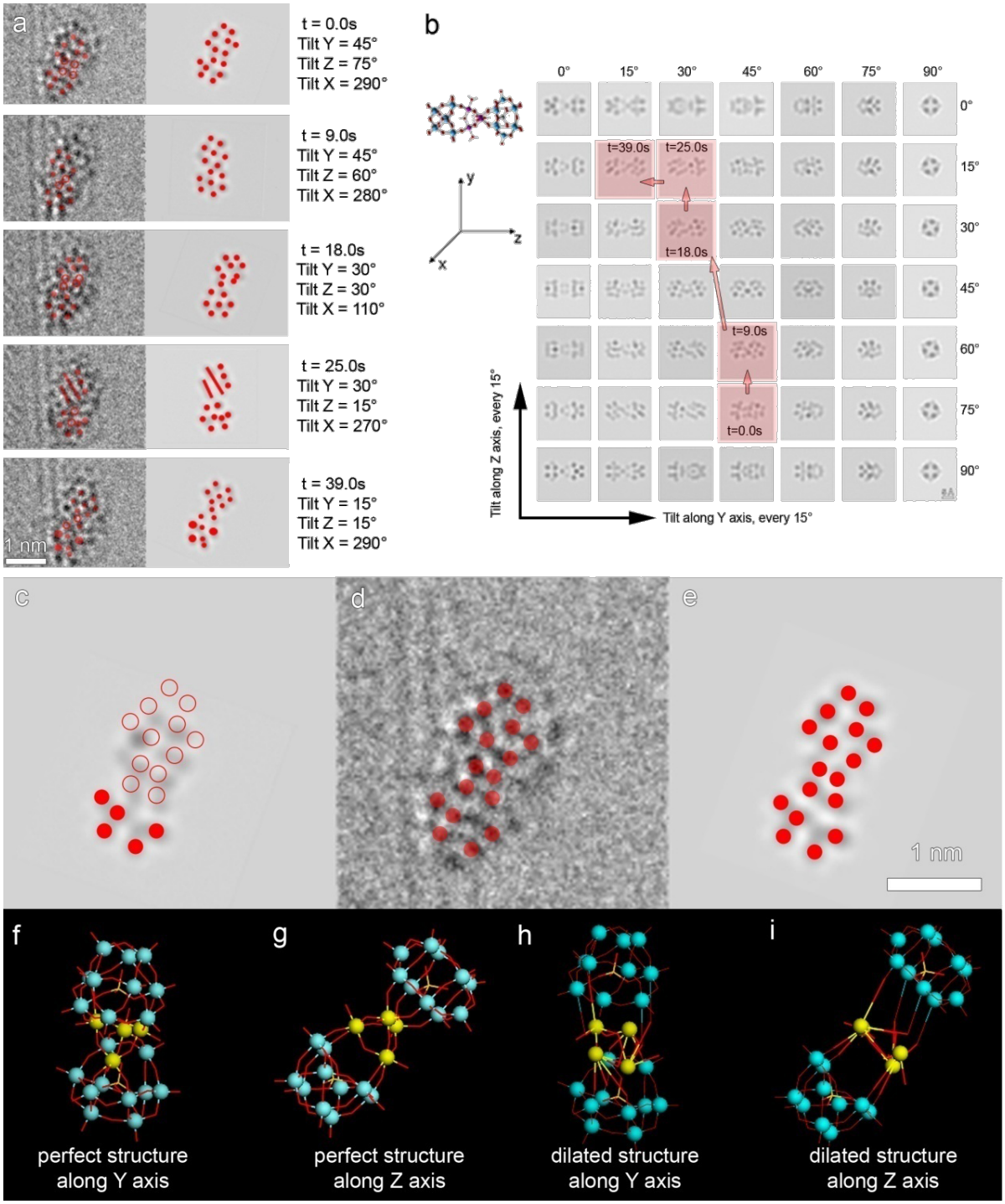

Figure 8: Dynamic study of Ru_4POM functionalized on graphene. (a) Projections from a time sequence of functionalized Ru_4POM together with their corresponding orientations determined from (b). (b) A plot summarizing simulated projections of an ideal Ru_4POM molecule when tilted around the X and Y axes. The orientation changes from (a) are matched to the simulated patterns and highlighted by the red squares. (c) Simulated pattern of a Ru_4POM whose orientation is found to fit into the HRTEM image shown in (a). The solid dot represents the fitted position of W, whereas the circle reveals a mismatch of the simulation and acquired pattern. (d) The acquired HRTEM image of Ru_4POM to be fitted into the simulation shown in (c), where the position of W and Ru scheme proposed in (c) with a distorted Ru_4 core. The fitted dots of Ru and W are indicated by solid red dots. (e) A simulated pattern of the dilated Ru_4POM based on the scheme proposed in (c) with a distorted Ru_4 core. The fitted dots of Ru and W are indicated by solid red dots. (f) The scheme of a perfect Ru_4POM with viewing direction along Y axis and (g) along Z axis. (h) The scheme of the dilated Ru_4POM based on the perfect structure shown in (f) and (g) with a manually distorted Ru_4 core viewed along Y axis (h) and Z axis (i); reproduced with permission from [112], Copyright (2013) John Wiley and Sons.

structure which distorts the Ru_4 core, and provides a simulated pattern (Figure 8e) that fits well to the TEM image as shown in Figure 8d. It is remarkable that the Ru_4POM molecules remain intact after intensive exposure to accelerated electrons, confirming the robustness of this catalyst and hints to the fact that the self-accommodation of the Ru_4 core in its nanostructure may be responsible for the stability.

In situ TEM studies of carbon-based nanostructures have attracted substantial attention since the interaction of electrons and carbon lattices can be monitored at an atomic scale using AC-TEM. Electrons play the roles of probing tool and imaging tool simultaneously, which is unique for carbon-based nanomaterials. The introduction of this internal stimulus together with external stimuli has therefore allowed for the investigation of fundamental physics and chemistry at an atomic scale.

Conclusion

In this review, the possibilities of modern electron microscopy for carbon-based nanomaterials have been discussed. AC-TEM has revolutionized our understanding of the materials by providing unprecedented spatial resolution and energy resolution at lower operating voltages. By minimizing the knock-on damage, extensive studies on the carbon-based nanomaterials at atomic scale are possible both structurally and chemically, from 2D to 3D. Further introduction of external stimuli has added multiple dimensions to the research field, where the dynamics of its response to stimuli can be revealed in detail. The interaction between electrons and carbon is essential when coming into the interpretation of any data, which makes the internal stimulus of electron beams a unique tool in both imaging and probing, allowing a study of fundamental physics and chemistry at atomic scale for carbon-based nanomaterials.

Acknowledgements

X. Ke and C. Bittencourt acknowledge the support of the COST ACTION MP0901. X. Ke and G. Van Tendeloo acknowledge the European Research Council, ERC Advanced Grant No 246791 - COUNTATOMS. C. Bittencourt is a research associate at the National Funds for Scientific Research (FRS-FNRS, Belgium). X. Ke acknowledges the support of National Science Foundation of China (NSFC) (11404016) and Qing-Bai talents project of Beijing University of technology (2015-RD-QB-19).

References

1. Ruska, E. *Biosci. Rep.* **1987,** *7,* 607.
2. Formanek, H.; Müller, M.; Hahn, M. H.; Koller, T. *Naturwissenschaften* **1971,** *58,* 339. doi:10.1007/BF00602786
3. Ottensmeyer, F. P.; Schmidt, E. E.; Jack, T.; Powell, J. *J. Ultrastruct. Res.* **1972,** *40,* 546. doi:10.1016/S0022-5320(72)80042-X
4. Creewe, A. V.; Wall, J.; Langmore, J. *Science* **1970,** *168,* 1338. doi:10.1126/science.168.3937.1338
5. Hashimot, H.; Kumao, A.; Hino, K.; Yotsumot, H.; Ono, A. *Jpn. J. Appl. Phys.* **1971,** *10,* 1115. doi:10.1143/JJAP.10.1115
6. Haider, M.; Uhlemann, S.; Schwan, E.; Rose, H.; Kabius, B.; Urban, K. *Nature* **1998,** *392,* 768–769. doi:10.1038/33823
7. Rose, H.; Wan, W. In *Proceedings of the 2005 Particle Accelerator Conference,* Knoxville, TN, United States of America, May 16–20, 2005; Horak, C., Ed.; IEEE: Piscataway, NJ, United States of America, 2005; pp 44–48.
8. Xin, H. L. L.; Muller, D. A. *Microsc. Microanal.* **2009,** *15* (Suppl. S2), 1474. doi:10.1017/S1431927609095622
9. Takeguchi, M.; Hashimoto, A.; Shimojo, M.; Mitsuishi, K.; Furuya, K. *J. Electron Microsc.* **2008,** *57,* 123. doi:10.1093/jmicro/dfn010
10. Mook, H. W.; Kruit, P. *Ultramicroscopy* **2000,** *81,* 129. doi:10.1016/S0304-3991(99)00193-X
11. Tsuno, K. *Nucl. Instrum. Methods Phys. Res., Sect. A* **2011,** *645,* 12. doi:10.1016/j.nima.2010.12.164
12. Krivanek, O. L.; Ursin, J. P.; Bacon, N. J.; Corbin, G. J.; Dellby, N.; Hrncirik, P.; Murfitt, M. F.; Own, C. S.; Szilagyi, Z. S. *Philos. Trans. R. Soc., A* **2009,** *367,* 3683.
13. Kaiser, U.; Biskupek, J.; Meyer, J. C.; Leschner, J.; Lechner, L.; Rose, H.; Stöger-Pollach, M.; Khlobystov, A. N.; Hartel, P.; Müller, H.; Haider, M.; Eyhusen, S.; Benner, G. *Ultramicroscopy* **2011,** *111,* 1239–1246. doi:10.1016/j.ultramic.2011.03.012
14. Vajtai, R. Science and Engineering of Nanomaterials. In *Springer Handbook of Nanomaterials;* Vajtai, R., Ed.; Springer: Berlin, Germany, 2013; pp 1–36. doi:10.1007/978-3-642-20595-8_1
15. Patel, T. *New Sci.* **1996,** *151,* 32–35.
16. Brady, R. F., Jr. Twenty-first century materials: coatings that interact with their environment. In *Smart Coatings;* Provder, T.; Baghdachi, J., Eds.; ACS Symposium Series, Vol. 957; ACS Publication: Washington, DC, USA, 2007; pp 3–11. doi:10.1021/bk-2007-0957.ch001
17. Swider, J. R.; Hackley, V. A.; Winter, J. *J. Cult. Heritage* **2003,** *4,* 175–186. doi:10.1016/S1296-2074(03)00044-X
18. Iijima, S. *Nature* **1991,** *354,* 56–58. doi:10.1038/354056a0
19. Reibold, M.; Paufler, P.; Levin, A. A.; Kochmann, W.; Pätzke, N.; Meyer, D. C. *Nature* **2006,** *444,* 286. doi:10.1038/444286a
20. Reibold, M.; Pätzke, N.; Levin, A. A.; Kochmann, W.; Shakhverdova, I. P.; Paufler, P.; Meyer, D. C. *Cryst. Res. Technol.* **2009,** *44,* 1139–1146. doi:10.1002/crat.200900445
21. Eletskii, A. V. *Phys.-Usp.* **2007,** *50,* 225–261. doi:10.1070/PU2007v050n03ABEH006188
22. Novoselov, K. S.; Geim, A. K.; Morozov, S. V.; Jiang, D.; Zhang, Y.; Dubonos, S. V.; Grigorieva, I. V.; Firsov, A. A. *Science* **2004,** *306,* 666–669. doi:10.1126/science.1102896
23. Van Tendeloo, G.; Bals, S.; Van Aert, S.; Verbeeck, J.; Van Dyck, D. *Adv. Mater.* **2012,** *24,* 5655–5675. doi:10.1002/adma.201202107
24. Erni, R. *Aberration-corrected imaging in transmission electron microscopy: An introduction;* Imperial College Press: London, United Kingdom. doi:10.1142/p703
25. Williams, D. B.; Carter, C. B. *Transmission Electron Microscopy: A Textbook for Materials Science;* Plenum Press: Berlin, Germany, 1996. doi:10.1007/978-1-4757-2519-3
26. Lentzen, M. *Microsc. Microanal.* **2008,** *14,* 16–26. doi:10.1017/S1431927608080045
27. Tiemeijer, P. C.; Bischoff, M.; Freitag, B.; Kisielowski, C. *Ultramicroscopy* **2012,** *114,* 72–81. doi:10.1016/j.ultramic.2012.01.008

28. Bjorkman, T.; Kurasch, S.; Lehtinen, O.; Kotakoski, J.; Yazyev, O. V.; Srivastava, A.; Skakalova, V.; Smet, J. H.; Kaiser, U.; Krasheninnikov, A. V. *Sci. Rep.* **2013,** *3,* No. 3482. doi:10.1038/srep03482
29. Suenaga, K.; Koshino, M. *Nature* **2010,** *468,* 1088–1090. doi:10.1038/nature09664
30. Konno, M.; Ogashiwa, T.; Sunaoshi, T.; Orai, Y.; Sato, M. *Ultramicroscopy* **2014,** *145,* 28–35. doi:10.1016/j.ultramic.2013.09.001
31. Krivanek, O. L.; Lovejoy, T. C.; Dellby, N.; Aoki, T.; Carpenter, R. W.; Rez, P.; Soignard, E.; Zhu, J.; Batson, P. E.; Lagos, M. J.; Egerton, R. F.; Crozier, P. A. *Nature* **2014,** *514,* 209–212. doi:10.1038/nature13870
32. Zobelli, A.; Gloter, A.; Ewels, C. P.; Seifert, G.; Colliex, C. *Phys. Rev. B* **2007,** *75,* 245402. doi:10.1103/PhysRevB.75.245402
33. Banhart, F.; Li, J. X.; Krasheninnikov, A. V. *Phys. Rev. B* **2005,** *71,* 241408. doi:10.1103/PhysRevB.71.241408
34. Zubeltzu, J.; Chuvilin, A.; Corsetti, F.; Zurutuza, A.; Artacho, E. *Phys. Rev. B* **2013,** *88,* 245407. doi:10.1103/PhysRevB.88.245407
35. Meyer, J. C.; Eder, F.; Kurasch, S.; Skakalova, V.; Kotakoski, J.; Park, H. J.; Roth, S.; Chuvilin, A.; Eyhusen, S.; Benner, G.; Krasheninnikov, A. V.; Kaiser, U. *Phys. Rev. Lett.* **2012,** *108,* 196102. doi:10.1103/PhysRevLett.108.196102
36. Eder, F. R.; Kotakoski, J.; Kaiser, U.; Meyer, J. C. *Sci. Rep.* **2014,** *4,* No. 4060. doi:10.1038/srep04060
37. Meyer, J. C.; Kisielowski, C.; Erni, R.; Rossell, M. D.; Crommie, M. F.; Zettl, A. *Nano Lett.* **2008,** *8,* 3582–3586. doi:10.1021/nl801386m
38. Santana, A.; Zobelli, A.; Kotakoski, J.; Chuvilin, A.; Bichoutskaia, E. *Phys. Rev. B* **2013,** *87,* 094110. doi:10.1103/PhysRevB.87.094110
39. Kotakoski, J.; Santos-Cottin, D.; Krasheninnikov, A. V. *ACS Nano* **2012,** *6,* 671–676. doi:10.1021/nn204148h
40. Molhave, K.; Gudnason, S. B.; Pedersen, A. T.; Clausen, C. H.; Horsewell, A.; Boggild, P. *Ultramicroscopy* **2007,** *108,* 52–57. doi:10.1016/j.ultramic.2007.03.001
41. Crespi, V. H.; Chopra, N. G.; Cohen, M. L.; Zettl, A.; Louie, S. G. *Phys. Rev. B* **1996,** *54,* 5927. doi:10.1103/PhysRevB.54.5927
42. Zobelli, A.; Gloter, A.; Ewels, C. P.; Colliex, C. *Phys. Rev. B* **2008,** *77,* 045410. doi:10.1103/PhysRevB.77.045410
43. Krasheninnikov, A. V.; Banhart, F. *Nat. Mater.* **2007,** *6,* 723–733. doi:10.1038/nmat1996
44. Kotakoski, J.; Krasheninnikov, A. V.; Nordlund, K. *Phys. Rev. B* **2006,** *74,* 245420. doi:10.1103/PhysRevB.74.245420
45. Lee, G.-D.; Wang, C. Z.; Yoon, E.; Hwang, N.-M.; Kim, D.-Y.; Ho, K. M. *Phys. Rev. Lett.* **2005,** *95,* 205501. doi:10.1103/PhysRevLett.95.205501
46. Egerton, R. F.; Li, P.; Malac, M. *Micron* **2004,** *35,* 399–409. doi:10.1016/j.micron.2004.02.003
47. Krasheninnikov, A. V.; Nordlund, K. *Nucl. Instrum. Methods Phys. Res., Sect. B* **2004,** *216,* 355–366. doi:10.1016/j.nimb.2003.11.061
48. Balandin, A. A.; Ghosh, S.; Bao, W.; Calizo, I.; Teweldebrhan, D.; Miao, F.; Lau, C. N. *Nano Lett.* **2008,** *8,* 902. doi:10.1021/nl0731872
49. Jinschek, J. R.; Yucelen, E.; Calderon, H. A.; Freitag, B. *Carbon* **2011,** *49,* 556. doi:10.1016/j.carbon.2010.09.058
50. Liao, H.-G.; Zherebetskyy, D.; Xin, H.; Czarnik, C.; Ercius, P.; Elmlund, H.; Pan, M.; Wang, L.-W.; Zheng, H. *Science* **2014,** *345,* 916–919. doi:10.1126/science.1253149
51. Girit, Ç. Ö.; Meyer, J. C.; Erni, R.; Rossell, M. D.; Kisielowski, C.; Yang, L.; Park, C.-H.; Crommie, M. F.; Cohen, M. L.; Louie, S. G.; Zettl, A. *Science* **2009,** *323,* 1705–1708. doi:10.1126/science.1166999
52. Warner, J. H.; Rümmeli, M. H.; Ge, L.; Gemmling, T.; Montanari, B.; Harrison, N. M.; Büchner, B.; Briggs, G. A. D. *Nat. Nanotechnol.* **2009,** *4,* 500–504. doi:10.1038/nnano.2009.194
53. Armstrong, M. R.; Boyden, K.; Browning, N. D.; Campbell, G. H.; Colvin, J. D.; De Hope, W. J.; Frank, A. M.; Gibson, D. J.; Hartemann, F.; Kim, J. S.; King, W. E.; La Grange, T. B.; Pyke, B. J.; Reed, B. W.; Shuttlesworth, R. M.; Stuart, B. C.; Torralva, B. R. *Ultramicroscopy* **2007,** *107,* 356–367. doi:10.1016/j.ultramic.2006.09.005
54. Baskin, J. S.; Zewail, A. H. *C. R. Phys.* **2014,** *15,* 176–189. doi:10.1016/j.crhy.2013.11.002
55. Browning, N. D.; Bonds, M. A.; Campbell, G. H.; Evans, J. E.; LaGrange, T.; Jungjohann, K. L.; Masiel, D. J.; Mckeown, J.; Mehraeen, S.; Reed, B. W.; Santala, M. *Curr. Opin. Solid State Mater. Sci.* **2012,** *16,* 23–30. doi:10.1016/j.cossms.2011.07.001
56. Campbell, G. H.; McKeown, J. T.; Santala, M. K. *Appl. Phys. Rev.* **2014,** *1,* 041101. doi:10.1063/1.4900509
57. Bernaerts, D.; Amelinckx, S.; Van Tendeloo, G.; Van Landuyt, J. *J. Phys. Chem. Solids* **1997,** *58,* 1807–1813. doi:10.1016/S0022-3697(98)80003-6
58. Bernaerts, D.; Op de Beeck, M.; Amelinckx, S.; Van Landuyt, J.; Van Tendeloo, G. *Philos. Mag. A* **1996,** *74,* 723–740. doi:10.1080/01418619608243538
59. Meyer, R. R.; Friedrichs, S.; Kirkland, A. L.; Sloan, J.; Hutchison, J. L.; Green, M. L. J. *J. Microsc. (Oxford, U. K.)* **2003,** *212 (Pt 2),* 152–157. doi:10.1046/j.1365-2818.2003.01240.x
60. Warner, J. H.; Young, N. P.; Kirkland, A. I.; Briggs, G. A. D. *Nat. Mater.* **2011,** *10,* 958–962. doi:10.1038/nmat3125
61. Fthenakis, Z. G.; Zhu, Z.; Tománek, D. *Phys. Rev. B* **2014,** *89,* 125421. doi:10.1103/PhysRevB.89.125421
62. Huang, P. Y.; Ruiz-Vargas, C. S.; Van der Zande, A. M.; Whitney, W. S.; Levendorf, M. P.; Kevek, J. W.; Garg, S.; Alden, J. S.; Hustedt, C. J.; Zhu, Y.; Park, J.; McEuen, P. L.; Muller, D. A. *Nature* **2011,** *469,* 389–392. doi:10.1038/nature09718
63. Lee, G.-W.; Cooper, R. C.; An, S. J.; Lee, S.; Van der Zande, A.; Petrone, N.; Hammerberg, A. G.; Lee, C.; Crawford, B.; Oliver, W.; Kysar, J. W.; Hone, J. *Science* **2013,** *340,* 1073–1076. doi:10.1126/science.1235126
64. Loh, O. Y.; Espinosa, H. D. *Nat. Nanotechnol.* **2012,** *7,* 283–295. doi:10.1038/nnano.2012.40
65. Bianco, A.; Kostarelos, K.; Prato, M. *Expert Opin. Drug Delivery* **2008,** *5,* 331–342.
66. Wang, J. T.-W.; Cabana, L.; Bourgognon, M.; Kafa, H.; Protti, A.; Venner, K.; Shah, A. M.; Sosabowski, J. K.; Mather, S. J.; Roig, A.; Ke, X.; Van Tendeloo, G.; de Rosales, R. T. M.; Tobias, G.; Al-Jamal, K. T. *Adv. Funct. Mater.* **2014,** *24,* 1880–1894. doi:10.1002/adfm.201302892
67. Felten, A.; Suarez-Martinez, I.; Ke, X.; Van Tendeloo, G.; Ghijsen, J.; Pireaux, J.-J.; Drube, W.; Bittencourt, C.; Ewels, C. P. *ChemPhysChem* **2009,** *10,* 1799–1804. doi:10.1002/cphc.200900193
68. Hao, L.; Jiao, Q.; Hu, Y.; Li, H.; Zhao, Y. *Micro Nano Lett.* **2014,** *9,* 97–99. doi:10.1049/mnl.2013.0624
69. Ma, L.; Zhang, H. M.; Liang, Y. M.; Xu, D. Y.; Ye, W.; Zhang, J. L.; Yi, B. L. *Catal. Commun.* **2007,** *8,* 921–925. doi:10.1016/j.catcom.2006.09.024
70. Suarez-Martinez, I.; Bittencourt, C.; Ke, X.; Felten, A.; Pireaux, J. J.; Ghijsen, J.; Drube, W.; VanTendeloo, G.; Ewels, C. P. *Carbon* **2009,** *47,* 1549–1554. doi:10.1016/j.carbon.2009.02.002

71. Bittencourt, C.; Hecq, M.; Felten, A.; Pireaux, J. J.; Ghijsen, J.; Felicissimo, M. P.; Rudolf, P.; Drube, W.; Ke, X.; Van Tendeloo, G. *Chem. Phys. Lett.* **2008,** *462,* 260–264. doi:10.1016/j.cplett.2008.07.082
72. Quintana, M.; Ke, X.; Van Tendeloo, G.; Meneghetti, M.; Bittencourt, C.; Prato, M. *ACS Nano* **2010,** *4,* 6105–6113. doi:10.1021/nn101183y
73. Suarez-Martinez, I.; Ewels, C. P.; Ke, X.; Van Tendeloo, G.; Thiess, S.; Drube, W.; Felten, A.; Pireaux, J. J.; Ghijsen, J.; Bittencourt, C. *ACS Nano* **2010,** *4,* 1680–1686. doi:10.1021/nn9015955
74. Bittencourt, C.; Ke, X.; Van Tendeloo, G.; Thiess, S.; Drube, W.; Ghijsen, J.; Ewels, C. P. *Chem. Phys. Lett.* **2012,** *535,* 80–83. doi:10.1016/j.cplett.2012.03.045
75. Adjizian, J. J.; De Marco, P.; Suarez-Martinez, I.; El Mel, A. A.; Snyders, R.; Gengler, R. Y. N.; Rudolf, P.; Ke, X.; Van Tendeloo, G.; Bittencourt, C.; Ewels, C. P. *Chem. Phys. Lett.* **2013,** *571,* 44–48. doi:10.1016/j.cplett.2013.03.079
76. Britz, D. A.; Khlobystov, A. N.; Porfyrakis, K.; Ardavan, A.; Briggs, G. A. D. *Chem. Commun.* **2005,** 37–39. doi:10.1039/b414247k
77. Chamberlain, T. W.; Meyer, J. C.; Biskupek, J.; Leschner, J.; Santana, A.; Besley, N. A.; Bichoutskaia, E.; Kaiser, U.; Khlobystov, A. N. *Nat. Chem.* **2011,** *3,* 732–737. doi:10.1038/nchem.1115
78. Zoberbier, T.; Chamberlain, T. W.; Biskupek, J.; Kuganathan, N.; Eyhusen, S.; Bichoutskaia, E.; Kaiser, U.; Khlobystov, A. N. *J. Am. Chem. Soc.* **2012,** *134,* 3073–3079. doi:10.1021/ja208746z
79. Scarselli, M.; Camilli, L.; Persichetti, L.; Castrucci, P.; Lefrant, S.; Gautron, E.; De Crescenzi, M. *Carbon* **2012,** *50,* 3616–3621. doi:10.1016/j.carbon.2012.03.032
80. Midgley, P. A.; Weyland, M. *Ultramicroscopy* **2003,** *96,* 413–431. doi:10.1016/S0304-3991(03)00105-0
81. Ke, X.; Bals, S.; Cott, D.; Hantschel, T.; Bender, H.; Van Tendeloo, G. *Microsc. Microanal.* **2010,** *16,* 210–217. doi:10.1017/S1431927609991371
82. Goris, B.; Roelandts, T.; Batenburg, K. J.; Heidari Mezerji, H.; Bals, S. *Ultramicroscopy* **2013,** *127,* 40–47. doi:10.1016/j.ultramic.2012.07.003
83. Cha, J. J.; Welyand, M.; Briere, J.-F.; Daykov, I. P.; Arias, T. A.; Muller, D. A. *Nano Lett.* **2007,** *7,* 3770–3773. doi:10.1021/nl072251c
84. Goris, B.; Bals, S.; Van den Broek, W.; Carbó-Argibay, E.; Gómez-Graña, S.; Liz-Marzán, L. M.; Van Tendeloo, G. *Nat. Mater.* **2012,** *11,* 930–934. doi:10.1038/nmat3462
85. Ke, X.; Bittencourt, C.; Bals, S.; Van Tendeloo, G. *Beilstein J. Nanotechnol.* **2013,** *4,* 77–86. doi:10.3762/bjnano.4.9
86. Tan, H.; Turner, S.; Yücelen, E.; Verbeeck, J.; Van Tendeloo, G. *Phys. Rev. Lett.* **2011,** *107,* 107602. doi:10.1103/PhysRevLett.107.107602
87. Tian, H.; Verbeeck, J.; Brück, S.; Paul, M.; Kufer, D.; Sing, M.; Claessen, R.; Van Tendeloo, G. *Adv. Mater.* **2014,** *26,* 461–465. doi:10.1002/adma.201303329
88. Guttmann, P.; Bittencourt, C.; Rehbein, S.; Umek, P.; Ke, X.; Van Tendeloo, G.; Ewels, C. P.; Schneider, G. *Nat. Photonics* **2012,** *6,* 25–29. doi:10.1038/nphoton.2011.268
89. Sawada, H.; Tanishiro, Y.; Ohashi, N.; Tomita, T.; Hosokawa, F.; Kaneyama, T.; Kondo, Y.; Takayanagi, K. *J. Electron Microsc.* **2009,** *58,* 357. doi:10.1093/jmicro/dfp030
90. Dellby, N.; Bacon, N. J.; Hrncirik, P.; Murfitt, M. F.; Skone, G. S.; Szilagyi, Z. S.; Krivanek, O. L. *Eur. Phys. J.: Appl. Phys.* **2011,** *54,* 33505. doi:10.1051/epjap/2011100429
91. Houdellier, F.; Masseboeuf, A. I.; Monthioux, M.; Hÿtch, M. J. *Carbon* **2012,** *50,* 2037. doi:10.1016/j.carbon.2012.01.023
92. Piston, D. W.; Kremers, G.-J.; Benninger, R. K. P.; Davidson, M. W. *Microsc. Today* **2009,** *17,* 8. doi:10.1017/S1551929509000194
93. Turner, S.; Shenderova, O.; Da Pieve, F.; Lu, Y.-g.; Yücelen, E.; Verbeeck, J.; Lamoen, D.; Van Tendeloo, G. *Phys. Status Solidi A* **2013,** *210,* 1976–1984. doi:10.1002/pssa.201300315
94. Nicholls, R. J.; Murdock, A. T.; Tsang, J.; Britton, J.; Pennycook, T. J.; Koós, A.; Nellist, P. D.; Grobert, N.; Yates, J. R. *ACS Nano* **2013,** *7,* 7145–7150. doi:10.1021/nn402489v
95. Arenal, R.; March, K.; Ewels, C. P.; Rocquefelte, X.; Kociak, M.; Loiseau, A.; Stéphan, O. *Nano Lett.* **2014,** *14,* 5509–5516. doi:10.1021/nl501645g
96. Ramasse, Q. M.; Seabourne, C. R.; Kepaptsoglou, D.-M.; Zan, R.; Bangert, U.; Scott, A. J. *Nano Lett.* **2013,** *13,* 4989–4995. doi:10.1021/nl304187e
97. Zhang, Y.; Utke, I.; Michler, J.; Ilari, G.; Rossell, M. D.; Erni, R. *Beilstein J. Nanotechnol.* **2014,** *5,* 946–955. doi:10.3762/bjnano.5.108
98. Erni, R.; Browning, N. D. *Ultramicroscopy* **2005,** *10,* 176–192. doi:10.1016/j.ultramic.2005.03.009
99. Keller, D.; Buecheler, S.; Reinhard, P.; Pianezzi, F.; Pohl, D.; Surrey, A.; Rellinghaus, B.; Erni, R.; Tiwari, A. N. *Microsc. Microanal.* **2014,** *20,* 1246–1253. doi:10.1017/S1431927614000543
100. Eberlein, T.; Bangert, U.; Nair, R. R.; Jones, R.; Gass, M.; Bleloch, A. L.; Novoselov, K. S.; Geim, A.; Briddon, P. R. *Phys. Rev. B* **2008,** *77,* 233406. doi:10.1103/PhysRevB.77.233406
101. Gass, M. H.; Bangert, U.; Bleloch, A. L.; Wang, P.; Nair, R. R.; Geim, A. K. *Nat. Nanotechnol.* **2008,** *3,* 676–681. doi:10.1038/nnano.2008.280
102. Zhou, W.; Lee, J.; Nanda, J.; Pantelides, S. T.; Pennycook, S. J.; Idrobo, J.-C. *Nat. Nanotechnol.* **2012,** *7,* 161–165. doi:10.1038/nnano.2011.252
103. Nelson, F. J.; Idrobo, J.-C.; Fite, J. D.; Mišković, Z. L.; Pennycook, S. J.; Pantelides, S. T.; Lee, J. U.; Diebold, A. C. *Nano Lett.* **2014,** *14,* 3827–3831. doi:10.1021/nl500969t
104. Goldberg, D.; Brando, Y. In-Situ TEM of Filled Nanotubes: Heating, Electron Irradiation, Electrical and Mechanical Probing. In *In-situ Electron Microscopy at High Resolution;* Banhart, F., Ed.; World Scientific Publishing Co Pte Ltd: Singapore, 2008. doi:10.1142/9789812797346_0006
105. Rodríguez-Manzo, J. A.; Terrones, M.; Terrones, H.; Kroti, H. W.; Sun, L.; Banhart, F. *Nat. Nanotechnol.* **2007,** *2,* 307–311. doi:10.1038/nnano.2007.107
106. Wang, S. J.; Wang, H.; Du, K.; Zhang, W.; Sui, M. L.; Mao, S. X. *Nat. Commun.* **2014,** *5,* No. 3433. doi:10.1038/ncomms4433
107. Li, B. Q.; Sui, M. L.; Li, B.; Ma, E.; Mao, S. X. *Phys. Rev. Lett.* **2009,** *102,* 205504. doi:10.1103/PhysRevLett.102.205504
108. Shao, R.-w.; Zheng, K.; Wei, B.; Zhang, Y.-f.; Li, Y.-j.; Han, X.-d.; Zhang, Z.; Zou, J. *Nanoscale* **2014,** *6,* 4936–4941. doi:10.1039/c4nr00059e
109. Colla, M.-S.; Amin-Ahmadi, B.; Idrissi, H.; Malet, L.; Godet, S.; Raskin, J.-P.; Schryvers, D.; Pardoen, T. *Nat. Commun.* **2015,** *6,* No. 5922. doi:10.1038/ncomms6922
110. Chuvilin, A.; Kaiser, U.; Bichoutskaia, E.; Besley, N. A.; Khlobystov, A. N. *Nat. Chem.* **2010,** *2,* 450–453. doi:10.1038/nchem.644
111. Sloan, J.; Liu, Z.; Suenaga, K.; Wilson, N. R.; Pandey, P. A.; Perkins, L. M.; Rourke, J. P.; Shannon, I. J. *Nano Lett.* **2010,** *10,* 4600–4606. doi:10.1021/nl1026452

112. Ke, X.; Turner, S.; Quintana, M.; Hadad, C.; Montellano-López, A.; Carraro, M.; Sartorel, A.; Bonchio, M.; Prato, M.; Bittencourt, C.; Van Tendeloo, G. *Small* **2013,** *9,* 3922–3927. doi:10.1002/smll.201300378

License and Terms

This is an Open Access article under the terms of the Creative Commons Attribution License (http://creativecommons.org/licenses/by/2.0), which permits unrestricted use, distribution, and reproduction in any medium, provided the original work is properly cited.

The license is subject to the *Beilstein Journal of Nanotechnology* terms and conditions: (http://www.beilstein-journals.org/bjnano)

The definitive version of this article is the electronic one which can be found at: doi:10.3762/bjnano.6.158